



**The 10th Annual International Conference
of Young Scientists on Energy Issues**

Kaunas, Lithuania, May 29–31, 2013

Organized by

Lithuanian Energy Institute

In cooperation with:

AGA

Lithuanian Nuclear Energetic Association

Reo Investment

European Nuclear Association

Kaunas City Municipality

Chairman of the Conference

prof. Eugenijus Ušpuras

Chairman of the Organizing Committee

dr. Diana Meilutytė-Barauskienė

INTERNATIONAL SCIENTIFIC COMMITTEE

Andres Siirde	Estonia	Mantas Marčiukaitis	Lithuania
Andris Kreslins	Latvia	Namejs Zeltins	Latvia
Alessandro Petruzzi	Italy	Pierre-Etienne Labeau	Belgium
Bernhard Peters	Luxemburg	Panos M. Pardalos	USA
Bjørn C. Hauback	Norway	Ralf Ebinghaus	Germany
Darius Milčius	Lithuania	Sten Bergstrom	Sweden
Enn Mellikov	Estonia	Sigitas Rimkevičius	Lithuania
Eugenijus Ušpuras	Lithuania	Sergej Zhdanok	Belarus
Finn Ravndal	Norway	Victor A. Zhovyansky	Ukraine
Florentin Paladi	Moldova	Vaclovas Miškinis	Lithuania
Luis E. Herranz	Spain	Virginijus Radziukynas	Lithuania
Myriam Lazard	France	Vytautas Martinaitis	Lithuania

The Board of Reviewers was formed from experts in the field of the Conference topics.

Board of Reviewers

Alessandro Petruzzi	Italy	Kristina Brinkienė	Lithuania
Algirdas Gulbinas	Lithuania	Kristina Ukvalbergienė	Lithuania
Algirdas Jasinskas	Lithuania	Liudvikas Pranevičius	Lithuania
Andres Siirde	Estonia	Liutauras Marcinauskas	Lithuania
Andris Kreslins	Latvia	Luis E. Herranz	Spain
Anupras Šlančiauskas	Lithuania	Mantas Marčiukaitis	Lithuania
Artur Rogoža	Lithuania	Marija Eidukevičiūtė	Lithuania
Arturas Klementavičius	Lithuania	Marijus Šeporaitis	Lithuania
Artūras Šmaižys	Lithuania	Martynas Lelis	Lithuania
Arvidas Galdikas	Lithuania	Mindaugas Jakubčionis	Lithuania
Arvydas Adomavičius	Lithuania	Mindaugas Krakauskas	Lithuania
Asta Malakauskaitė	Lithuania	Mindaugas Vaišnoras	Lithuania
Asta Narkūnienė	Lithuania	Mindaugas Valinčius	Lithuania
Audrius Jonaitis	Lithuania	Myriam Lazard	France
Aurimas Lisauskas	Lithuania	Namejs Zeltins	Latvia
Aušra Pažėraitė	Lithuania	Narimantas Listopadskis	Lithuania
Benediktas Čėsna	Lithuania	Nerijus Pedišius	Lithuania
Bernhard Peters	Luxemburg	Nerijus Striūgas	Lithuania
Bjørn C. Hauback	Norway	Panos M. Pardalos	USA
Brigita Abakevičienė	Lithuania	Pierre-Etienne Labeau	Belgium
Dainius Martuzevičius	Lithuania	Raimondas Bliūdžius	Lithuania
Dalia Grigaliūnienė	Lithuania	Raimondas Pabarčius	Lithuania
Dalia Jankūnaitė	Lithuania	Ralf Ebinghaus	Germany
Dalia Štreimikienė	Lithuania	Ramūnas Gatautis	Lithuania
Dalius Tarvydas	Lithuania	Reda Čerapaitė-Trušinskienė	Lithuania
Danas Ridikas	Lithuania	Regina Kalpokaitė-Dičkuvienė	Lithuania
Darius Albrektas	Lithuania	Ričardas Krikštolaitis	Lithuania
Darius Biekša	Lithuania	Rimantas Pranas Deksnyš	Lithuania
Darius Milčius	Lithuania	Rimantas Levinskas	Lithuania
Darius Virbukas	Lithuania	Robertas Alzbutas	Lithuania
Diana Meilutytė-Barauskienė	Lithuania	Robertas Navakas	Lithuania
Diana Adlienė	Lithuania	Robertas Poškas	Lithuania

Diana Šarauškienė	Lithuania	Rolandas Urbonas	Lithuania
Egidijus Norvaiša	Lithuania	Romualdas Kėželis	Lithuania
Egidijus Saulius Juodis	Lithuania	Romualdas Škėma	Lithuania
Egidijus Urbonavičius	Lithuania	Saulė Milčiuvienė	Lithuania
Eglė Biekšienė	Lithuania	Sergej Zhdanok	Belarus
Eglė Jaraminienė	Lithuania	Sigitas Masaitis	Lithuania
Enn Mellikov	Estonia	Sigitas Rimkevičius	Lithuania
Ernestas Narkūnas	Lithuania	Stanislovas Vrubliauskas	Lithuania
Eugenija Farida Dzenajavičienė	Lithuania	Stasys Šinkūnas	Lithuania
Eugenijus Perednis	Lithuania	Sten Bergstrom	Sweden
Eugenijus Ušpuras	Lithuania	Tomas Sabonis	Lithuania
Feliksas Zinevičius	Lithuania	Vaclovas Kveselis	Lithuania
Finn Ravndal	Norway	Vaclovas Miškinis	Lithuania
Florentin Paladi	Moldova	Vaidas Matuzas	Lithuania
Giedrius Laukaitis	Lithuania	Valdas Girdauskas	Lithuania
Giedrius Šiupšinskas	Lithuania	Valdas Ragaišis	Lithuania
Gintautas Miliauskas	Lithuania	Valentinas Klevas	Lithuania
Inga Konstantinavičiūtė	Lithuania	Victor A. Zhovyansky	Ukraine
Inga Radžiūnienė	Lithuania	Vidas Lekavičius	Lithuania
Inga Stasiulaitienė	Lithuania	Viktorija Grigaitienė	Lithuania
Inga Valuntienė	Lithuania	Vilma Čipinytė	Lithuania
Irina Kliopova	Lithuania	Violeta Makarevičienė	Lithuania
Jolanta Dvarionienė	Lithuania	Violeta Vaitkevičienė	Lithuania
Jonas Baltrušaitis	USA	Virginijus Radziukynas	Lithuania
Juozas Gudzinskas	Lithuania	Virginijus Vileiniškis	Lithuania
Jūratė Karbauskaitė	Lithuania	Vitas Valinčius	Lithuania
Jūratė Kriaučiūnienė	Lithuania	Vykintas Šuksteris	Lithuania
Jurij Tonkonogij	Lithuania	Vytautas Martinaitis	Lithuania
Justas Kažys	Lithuania	Vytis Kopustinskas	Lithuania
Karolina Čepurnienė	Lithuania	Vladislovas Algirdas Katinas	Lithuania
Kęstutis Čiuprinskas	Lithuania	Žaneta Stasiškienė	Lithuania
Kęstutis Valančius	Lithuania	Žilvinas Nakutis	Lithuania
Kęstutis Venslauskas	Lithuania	Živilė Rutkūnienė	Lithuania
		Žydrė Kadžiulienė	Lithuania

PREFACE

The International Conference of Young Scientists on Energy Issues 2012 has been organized nine times since 2004. The initiative for such an event came from young, enthusiastic researchers in Lithuanian Energy Institute (LEI). They realised that there are a lot of young, smart and science-oriented young people doing research in the energy area and they do need a place and time to meet each other to share their views, generate ideas, present stories of successful results and failures which definitely occur in the science. The first conference was organized by young researchers with the supervision of experienced scientists from LEI only in 2004.

In 2005 it became a national conference with participants from Kaunas University of Technology, Vilnius Gediminas Technical University, Vilnius University, Vytautas Magnus University – in fact from all science and education institutions of Lithuania involved in energy-related topics. The next year (2006) was devoted to strengthening the status of the conference among young researchers and their experienced supervisors and bringing the message that in a small country we can reach our targets with joint efforts only.

In 2007 the Organising Committee decided to put emphasis on regional and international dimension. The participants from neighbouring countries – Belarus and Poland participated in the conference for the first time. We realised that young researchers facing challenges in energy research need to be brought together as much as possible to create a critical mass, to be competent and competitive for the future research. Thus, the conference is not only intended for the increase of the participants' competence by involvement of best experienced scientists as peer reviewers, involvement of the participants in the review process of their colleagues (educational exercise), but also to expand geographically.

In 2008 we welcomed the participants from Belarus, Estonia, India, Latvia, Lithuania and Russia. In 2009 the outcome of the conference (in terms of scientific papers) was contributed by the young scientists from Belarus, Estonia, Italy, Latvia, Lithuania, Nigeria and Ukraine.

With a growing attention to this annual event the conference proceedings included the papers with scientific results of researchers from various Lithuanian science and research institutions and foreign institutions (Belarus, Estonia, Germany, Italy, Latvia, Nigeria, Norway and Ukraine) in 2010.

In total 69 papers of young scientists' from various Lithuanian science and research institutions and foreign institutions in Belarus, Estonia, Germany, Latvia, Nigeria, Poland, Taiwan and Ukraine were reviewed and accepted for the publication in 2011.

In 2012 even 82 young scientists took part in the conference (CYSENI 2012) and presented the results of their research.

This year (2013), there were 130 abstracts submitted, 100 papers were reviewed and 80 papers were accepted to the conference. The authors are not just from Lithuanian institutions, but also from neighbouring countries: Latvia, Estonia, Poland, Belarus, Ukraine, Moldova, Georgia, Romania, Nigeria, Indonesia and Taiwan.

This event in our institute is usually full of pleasant atmosphere, interesting and valuable discussions, cheerful social program. The greetings and acknowledgments of the participants encourage us to keep these moments in mind and improve the future CYSENI conferences. Regarding the next year we already invite you to the eleventh International Conference of Young Scientists on Energy Issues 2014, which will be held in 29–30 May, 2014 in Kaunas, Lithuania.

CONTENT

I. HYDROGEN AND FUEL CELLS (3)

M. Kodols, S. Didrihsone, J. Grabis

Comparison of nanosized Bi_2WO_6 photocatalysts prepared by different methods I-1

P. Lesnicens, L. Grinberga, J. Kleperis

Explanation the mechanism of hydrogen adsorption in clinoptilolite from thermogravimetric experiments I-10

D. Petrulionis

Comprehensive sintering and conductivity study of 10% SC_2O_3 and 1% CEO_2 co-doped ZRO_2 I-18

II. RENEWABLE ENERGY SOURCES (13)

T.O. Antoshchuk

Investigation of biomass gasifier to produce heat and electricity for industrial applications in Ukraine..... II-26

P. Dumitriu, T. Potlog, V. Mikli, V. Lugh, V. Sergio

CdTe thin film solar cells with nanocrystalline ZnSe buffer layer II-35

R. Džiugaitė-Tumėnienė, V. Jankauskas

Integration and optimization of renewable energy sources in a low energy house II-45

A. Fitriani, A. Purnomo

Utilization of tanjung fruit (*Mimusops elengi*) as renewable energy source for the future II-62

K. Januševičius, E. Biekšienė

Parametric study of the solar assisted heat pump performance..... II-71

A. Putnina, S. Kukle, J. Gravitis

An environmentally friendly method for microfibrillated cellulose extraction from hemp II-81

A. Snegirjovs, P. Shipkovs, M. Vanags, L. Mila, J. Oļeiņiks

Photovoltaic batteries with Modified glazing II-87

R.P. Deksnys, A. Stankevičius

Investigation of solar photovoltaic and wind power generation II-94

K. Vagoliņš, G. Frīdenbergs, P. Šipkovs

The GHG emissions model study for straw fired boilers II-99

T. Vonžodas, M. Valantinavičius

Investigation of performance parameters of low –power water boilers burning biofuel..... II-107

V. Žėkas, V. Martinaitis

Exergy assessment of air flow in the site of the building..... II-116

A.P. Tsitovich, A.A. Khartoni

Experimental investigation of solid sorption cooler with improved low temperature sorber by micro heat pipe effect..... II-127

P. Seniūnas

Review of renewable energy use in Lithuania's energy sector II-136

III. SMART ENERGY NETWORKS (6)

A. Ališauskas, R.P. Deksnys

Investigation of efficiency of power balancing in the power system of the variable speed pumped storage unit III-139

O. Kochukov, A. Mutule

Tasks of transmission planning in competitive energy market III-148

A. Lvovs, A. Obushevs, A. Mutule

Development of the model for small scale asynchronous generator connection impact assessment on distribution network III-156

A. Obushevs, I. Oleinikova

AC and DC optimal power flow models for long-term development planning III-168

<u>N. Radziukynienė</u>	
Multi-criteria effectiveness evaluation methodology for the analysis of switchyard modernization problem	III-177
<u>Yen-Huai Ma, Chen-Hsuan Chang, Chueh-Cheng Wu, Sy-Ruen Huang, Yu-Hua Mo, Chen-Yeon Chu</u>	
Fault identification in micro-hydro power generator based on the short-time fourier transform.....	III-189

IV. ENERGY EFFICIENCY AND SAVINGS (7)

<u>P. Bruzgevičius, V. Stankevičius, A. Burlingis, K. Banionis, D. Pupeikis</u>	
The influence of the fourier number on the calculation accuracy of dynamic thermal transmission in multi-layer enclosures	IV-198
<u>I. Gornevs, J. Blums</u>	
Investigation of electromagnetic harvester with flat structure and low voltage rectifier	IV-206
<u>K. Grinbergs, P. Shipkovs,</u>	
Heat rate optimization opportunities	IV-214
<u>T. Iešmantas, R. Alzbutas</u>	
Methodology for gas transmission network age-dependent reliability assessment considering variation of incident criteria	IV-222
<u>M.A. Klimenko</u>	
Outlook of energy and ecological application of sewage sludge in cement production.....	IV-231
<u>G. Plavenieks, A. Lesinskis</u>	
Analysis of using double by-pass in the air handling unit's with counter flow heat exchangers	IV-237
<u>V. Jurkans, J. Blums</u>	
Improving the efficiency of Peltier cooling with recuperative power Management	IV-243

V. KNOWLEDGES FOR ENERGY POLICY MAKING (10)

<u>K. Biekša</u>	
Sustainable development of regional energy system using process network synthesis method.....	V-253
<u>Z. Gachechiladze</u>	
Electricity competitive market development and regional trading perspective for Georgia	V-264
<u>B. Jokšas, I. Žutautaitė</u>	
Method for criticality assessment of energy infrastructure	V-274
<u>R. Mikučionienė, V. Martinaitis</u>	
Criteria for evaluation of energy efficiency measures in the management of building energetic characteristics.....	V-285
<u>L. Murauskaitė</u>	
The significance of district heating for the promotion of renewable energy sources demand	V-294
<u>S.C. Nwanya, O.V. Ekechukwu</u>	
The energy performance of hospital buildings in Nigeria.....	V-302
<u>L. Rimšaitė</u>	
Third European Union energy package implementation problems: intercourse between full ownership unbundling and foreign investment protection.....	V-310
<u>A.A. Mikhalevich, S.N. Nikitsin, V.A. Tkachou</u>	
Scenarios of development of the Belarusian electricity generation system in context of fuel balance diversification and greenhouse gases emission reduction	V-320
<u>G. Česnakas, A. Čepinskytė</u>	
Global energy security level assessment index: introduction and application	V-330
<u>C.M. Liu, C.Y. Chu, S.Y. Wu, Y.C. Li, Y.P. Chou</u>	
The economic and energy evaluation of bio-hydrogen and bio-methane production processes	V-341

VI. INVESTIGATIONS IN THE FIELDS OF THERMAL PHYSICS, FLUID MECHANICS AND METROLOGY (10)

Y.A. Baranyshyn

Numerical simulations of the non-isothermal growth of carbon nanoparticles from experimental data of soot formation at ethylene pyrolysis in the shock tube..... VI-348

A.A. Brin

Evaporative cooling of water in a natural draft cross-flow cooling tower VI-355

G. Frīdenbergs, A. Lešinskis

Supply water parameters influence on Indirect evaporative air cooling (IEAC) thermal performance VI-361

G. Gubceac, F. Paladi, A. Barsuk

Contributions to the fluid dynamics and phase transitions at low temperatures VI-370

I.M. Kuzmenko, R.M. Prokopets

Gas and fluid film flow simulation in the contact apparatus..... VI-376

J. Ratnieks, A. Jakovičs, S. Gendelis

Stationary heat transfer and airflow simulation for test polygon houses VI-382

O. Simbirskaja, S. Alyokhina

Verification of flow calculation method in the near-disk gaps of high cylinder pressure stage of steam turbine VI-390

A. Tonkonogovas, A. Stankevičius

Dynamic error of the turbine gas meter at complex flow pulsation laws..... VI-397

M. Trepulis

Macro foam convective heat transfer in vertical cylindrical tube VI-404

M.V. Daroshka, P.P. Khramtsov, O.G. Penyazkov

Flow structure visualization behind the shock wave in the shock tube..... VI-413

VII. MATERIALS SCIENCES AND TECHNOLOGY (13)

I.G. Inculet

Window layer thickness influence on then photoelectrical properties of ZnSe-CdTe heterostructures VII-419

P. Bieluszka, G. Zakrzewska-Trznadel

The use of the membrane contactor for extraction OF uranium (VI) from aqueous solutions..... VII-423

S.M. Danilova-Tretiak, L.E. Evseeva, S.A. Tanaeva

Thermal conductivity of conventional Cfrp and CNT-nanocomposites under alternating heat impact..... VII-433

R. Drunka, J. Grabis, A. Patmalnieks

Synthesis and photocatalytic properties of modified TiO₂ nanopores and nanotubes VII-440

E.P. Goncareenco, G.V. Colibaba, E.V. Monaico

Obtaining of the substrates of II-VI compounds and solid solutions for nanoporous structures..... VII-448

A. Graf

Investigation of electrical properties of cadmium sulfide thin films..... VII-457

G. Ovekova, I. Oja Acik, M. Krunks

Optical and structural properties of TiO₂ thin films by chemical spray pyrolysis VII-464

D. Scortescu, A. Mirzac, N. Spalatu and T. Potlog, V. Mikli

Electrophysical properties of the ZnTe/CdTe thin film heterostructures VII-472

T. Unt, M. Kriisa, A. Mere, M. Krunks

Optical properties of sprayed ZNO thin films..... VII-482

S.I. Dmitriev, P.S. Grinchuk, N.V. Pavljukевич

Experimental results and mathematical model for the process of carbon black production in high temperature flow reactor VII-490

P.S. Grinchuk, M.V. Kiyashko

Carbon nanotubes and nanofibers synthesis by chemical vapour deposition in reactor with close gap between catalytic walls VII-499

J. Soon, M. Krunks, V. Mikli

Properties of nio thin films prepared by chemical spray pyrolysis VII-510

S. Lagzdina, A. Sutka, G. Mezinskis

Influence of the precipitation conditions on the morphology, phase purity and physical properties of magnetite nanomaterials VII-519

VIII. INVESTIGATIONS OF COMBUSTION AND PLASMA PROCESSES (8)

V.I. Ignatenko, S.I. Shabunja, V.V. Martynenko

Development of algorithms for simulation of iron rod combustion in oxygen with the detachment of the drop..... VIII-528

V.V. Leschevich, O.G. Penayzkov, S.V. Shushkov

Rapid compression machine study of auto-ignition and combustion of liquid fuels with ultradisperse additives VIII-536

R. Paulauskas, A. Džiugys, N. Striūgas

Numerical models of wood pellet shrinking on pyrolysis..... VIII-543

A. Saliamonas, N. Striūgas, R. Navakas

Optimization of combustion process by characterization of the flame parameters using chemiluminescence phenomenon..... VIII-548

I.N. Shatan

The application of the talbot-images method to the methane-air flame diagnostic..... VIII-559

A. Tamošiūnas, P. Valatkevičius, V. Grigaitienė, V. Valinčius

Electrical and thermal Characteristics of water vapor plasma torch used for thermal plasma reforming VIII-568

U.M. Bahach, S.V. Vasilevich, M.V. Malko

Numerical and experimental studies of biomass pyrolysis VIII-573

K. Zakarauskas, N. Striūgas, G. Stravinskas

Optimization of thermal decomposition process of biomass pyrolysis tars for the production of high calorific gases VIII-583

IX. GLOBAL CHANGE AND ECOSYSTEMS (4)

T. Bauzha, L. Gorbachova

Features of maximum discharges change of mountain rivers in the Carpathian region: a case study of the water courses in the upper part of the rika river basin IX-590

A.V. Epik

Abatement cost analysis for greenhouse gas emission reductions in Ukraine IX-601

A. Jurgelėnaitė

Long-term variations of the heat runoff transferred by the rivers Nemunas and Merkys IX-610

O. Koshkina, L. Gorbachova

Hydro-genetic research methods of the main factors of the spring flood in the Desna river basin..... IX-618

X. FUSION ENERGY (1)

T. Kaliatka

Analysis of thermal hydraulic processes during different operation modes of Wendelstein 7-X experimental fusion reactor..... X-632

XI. NUCLEAR FISSION AND RADIATION PROTECTION (3)

V. Barkauskas, A. Plukis

Preparation of effective cross-section libraries for calculation of spent nuclear fuel inventory of RBMK type reactors..... XI-642

D. Justinavičius

Influence of porous medium permeability on gas migration in the disposal tunnel of conceptual geological repository..... XI-651

A. Šutas

Modelling of heat transfer processes in the dry storage spent nuclear fuel containers using relap5 code XI-659



COMPARISON OF NANOSIZED Bi_2WO_6 PHOTOCATALYSTS PREPARED BY DIFFERENT METHODS

M. Kodols, S. Didrihsone, J. Grabis

*Institute of Inorganic Chemistry, Riga Technical University
Miera str. 34, LV-2169 Salaspils – Latvia*

ABSTRACT

The influence of different preparation methods: combustion synthesis, hydrothermal and microwave assisted synthesis and their conditions on formation and morphology of Bi_2WO_6 nanoparticles has been studied. The pure crystalline Bi_2WO_6 with specific surface area of $26.6 \text{ m}^2/\text{g}$ and platelike and spherical morphology was obtained by using hydrothermal and microwave synthesis. The photocatalytic activity of the prepared Bi_2WO_6 in degradation of methylene blue depended on the specific surface area of samples and particle morphology.

Keywords: bismuth tungstate, photocatalysts, combustion synthesis, hydrothermal synthesis, microwave assisted synthesis, MB degradation

1. INTRODUCTION

Bismuth tungstate Bi_2WO_6 has layered perovskite type structure. Perovskites in general have ABO_3 formula unit, but in bismuth tungstate Bi_2WO_6 this structure forms in $\text{Bi}_{2m}\text{A}_{n-m}\text{B}_n\text{O}_{3(n+m)}$ ($m=1$, $n=1$, $B=W$) which is called Aurivillius structure [1]. Bismuth tungstate have orthorhombic structure which forms from $[\text{Bi}_2\text{O}_2]^{2+}$ layers and WO_6 octaedrons, symmetry group $Pca2_1$, cell parameters $a=5.4373 \text{ \AA}$, $b=16.4302 \text{ \AA}$, $c=5.4584 \text{ \AA}$ [2–5]. Due to the specific crystalline structure, crystallinity and crystallite size Bi_2WO_6 have band gap in range $2.56\text{--}2.70 \text{ eV}$ [6–8].

The last decade Bi_2WO_6 photocatalytic activity has been extensively studied due to the potential application for photo-degradation of organic compounds [5-9], for water splitting under irradiation [11] and for humidity sensors [10]. Shangguan et al. showed that Bi_2WO_6 and Y_2WO_6 solid solution ensured water splitting under visible light [12].

The most popular Bi_2WO_6 preparation methods are sol-gel synthesis, microwave assisted synthesis [14], hydrothermal [8] and solid state synthesis [13]. All methods are useful for different oxide system synthesis and depending on synthesis parameters such as temperature, pH, synthesis time, pressure, and use of surfactants the final product can be obtained with controlled and different particle size distribution, shape morphology, crystallinity, and surface properties. For example: hydrothermally prepared bismuth tungstate morphology changes rapidly at different pH values plate-like structures obtaining at pH 7 but flowerlike structures at acidic environment [5]. The hydrothermally prepared bismuth tungstate nanoparticles has resulted with crystallite size of 17 to 25 nm [16], but microwave synthesis in work [14] provided bismuth tungstate powders with specific surface area $8.1\text{--}10.6 \text{ m}^2/\text{g}$ and crystallite size of 27–30 nm. The studies of bismuth tungstate morphology shows that solid state synthesis results in 3 – 5 μm large particles [17], but sol-gel, hydrothermal method often provides relatively uniform nanosheet particles distributed in the 80 – 100 nm range [16-17].

L. Zhang et al. obtained bismuth tungstate superstructures using hydrothermal method [8, 15] which showed reasonably high photoactivity. The activity of photocatalysts depends strongly on particle size and crystallinity [8] determined by preparation methods. The purpose of the work was to compare the characteristics and photocatalytic activity of Bi_2WO_6 nanoparticles prepared by development of different synthesis methods.

2. EXPERIMENTAL

2.1. Powder preparation

Bi_2WO_6 was prepared by three methods: combustion synthesis, hydrothermal and microwave assisted synthesis. All synthesis were performed in water environment using metal salt solutions at stoichiometric molar ratio Bi: W = 2:1. The differences between techniques – synthesis time and temperature are shown in Fig. 1.

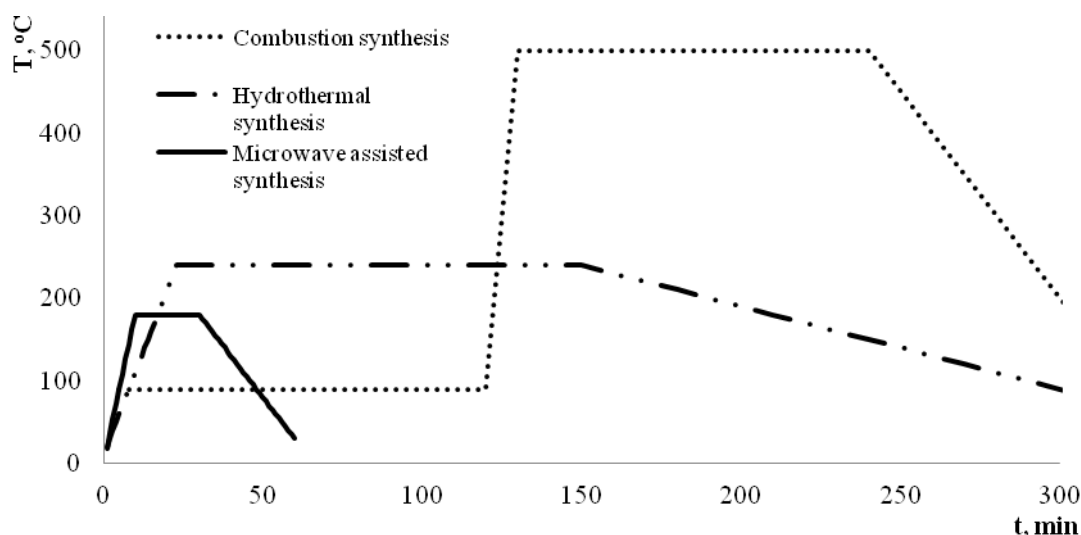


Fig. 1. Temperature and time diagram of the used synthesis methods

Procedure of combustion synthesis. Bismuth nitrate was dissolved in distilled water at 80°C by adding nitric acid which improved solubility of $\text{Bi}(\text{NO}_3)_3$. Tungstic acid was prepared by dissolving tungsten powder in 30 % hydrogen peroxide. Both solutions were mixed together at temperature of 80°C and necessary amount of organic fuel was added. The molar ratio between organic fuel and total nitrate ions was of 0.67. The opaque mixture of reactants was heated at 80–90°C temperature on the hotplate with magnetic stirrer to evaporate water and obtain xerogel. Since the xerogel was formed, the temperature was rose up to 500°C when the spontaneous combustion started and NO_2 was realised. The calcinations process at 500°C continued 2 h till light yellow Bi_2WO_6 powder was obtained and all NO_2 gas was released and carbon residues were burned out.

Procedure of hydrothermal synthesis. The stoichiometric $\text{Bi}(\text{NO}_3)_3 \cdot 5\text{H}_2\text{O}$ and $\text{Na}_2\text{WO}_4 \cdot 2\text{H}_2\text{O}$ salt suspension in water was prepared (Bi:W = 2:1). The pH of the suspension was controlled by adding NH_4OH . The salt suspension was hydrothermally treated in high pressure reactor at 240°C temperature and pressure of 8 bar for 2 h. After synthesis the precipitates were filtered and washed with distilled water, dried in the air.

Procedure of microwave assisted synthesis. Microwave assisted synthesis (MW) was realized in Masterwave Benchtop Reactor (Anton Paar) using above mentioned solutions. The salt suspension was treated in PTFE-TFM reactor at 180°C for 20 minutes with intensive stirring (600 rpm). The reactor pressure was of 13 bar, MW power was of 530 W. After synthesis the precipitates were filtered and washed with distilled water and dried in the air.

2.2. Methods for powder characterization

All powder samples where characterized using X-ray diffractometer Advance D8 (Bruker) with CuK_α irradiation and SolX detector. Data were recorded at scan rate of $0.02^\circ 2\theta$ in the 20–60°

range 2θ . Crystallite size where determined using X-ray diffractometers software EVA12 which algorithm was based on Scherrers equation (1). The SEM images were obtained by using Tescan Mira II microscope with SB/BSE detectors.

$$D = \frac{k\lambda}{B \cos \theta} \quad (1)$$

where D is the crystallite size (nm), k is the Scherrer constant (0.89), λ is the wavelength of the X-Ray radiation (0.15418 nm), B is the width at half maximum intensity in radians, θ – the Bragg angle.

The aqueous solution of MB (0.0225 M) with 0.2 wt% of Bi_2WO_6 nanoparticles was introduced in a quartz reactor. The suspension was treated by ultrasound for 10 min and then it was stirred in dark for 30 min. The MB degradation was studied by irradiation of Hg lamp at distance of 100 mm for 3 h. Samples of the suspension for analysis were taken out each 10 min. Before analysis the Bi_2WO_6 particles were removed from suspension by centrifugation. The degradation of MB was determined by measuring light absorption by solution at wavelength of 662 nm using Jenway-6300 spectrophotometer. The role of UV radiation in degradation of MB was evaluated by illumination of the solution in absence of nanoparticles. The absorption of MB on the surface of Bi_2WO_6 nanoparticles was determined by investigation change of optical density of solution in dark.

3. RESULTS AND DISCUSSION

Different synthesis methods provides to obtain Bi_2WO_6 nanoparticles with specific surface area (SSA) in the range of 17.8–26.6 m^2/g depending on the synthesis method and used fuel. Which is reasonably higher than in previously described microwave assisted synthesis (8.1–10.6 m^2/g) in work [14] but similar to SSA has reported authors [6] obtaining bismuth tungstate through combustion route with SSA of 13.09–25.53 m^2/g . The samples prepared by hydrothermal and MW has highest values of specific surface area (Table 1), because the low temperature of these processes limits particle growth with respect to combustion synthesis.

Table 1. Synthesis parameters for Bi_2WO_6 preparation for as prepared powders

Synthesis type	T, °C	pH	t, min	p, bar	SSA, m^2/g
Combustion (C) using as fuel:	500	~7	120	-	
a) Citric acid (CC)					17.8
b) Ethylene glycol (CE)					25.1
c) Glycine (CGL)					23.6
d) Glycerine (CGC)					23.4
Hydrothermal (HT)	240	9	120	8	26.6
Microwave assisted (MW)	180	7	20	13	26.5

The XRD analysis confirms that pure, crystalline Bi_2WO_6 nanoparticles have been prepared by using hydrothermal and MW as well by combustion synthesis in the presence of glycerine or glycine (Fig. 2). Combustion synthesis of Bi_2WO_6 by using citric acid or ethylene glycol as fuel results in formation extra phases such as $\text{Bi}_{14}\text{W}_2\text{O}_{27}$ and $\text{Bi}_{14}\text{WO}_{24}$ which was reported also previously [5, 18]. The presence of the extra phases can be explained by insufficient reaction temperature for complete formation of bismuth tungstate because additional calcination of the samples prepared by combustion synthesis at 800°C allows obtaining pure Bi_2WO_6 powder (Fig. 3). Authors in work [18] have noted that higher calcinations temperature shows phase change by decreasing the ad-mixture phases and increasing particle growing.

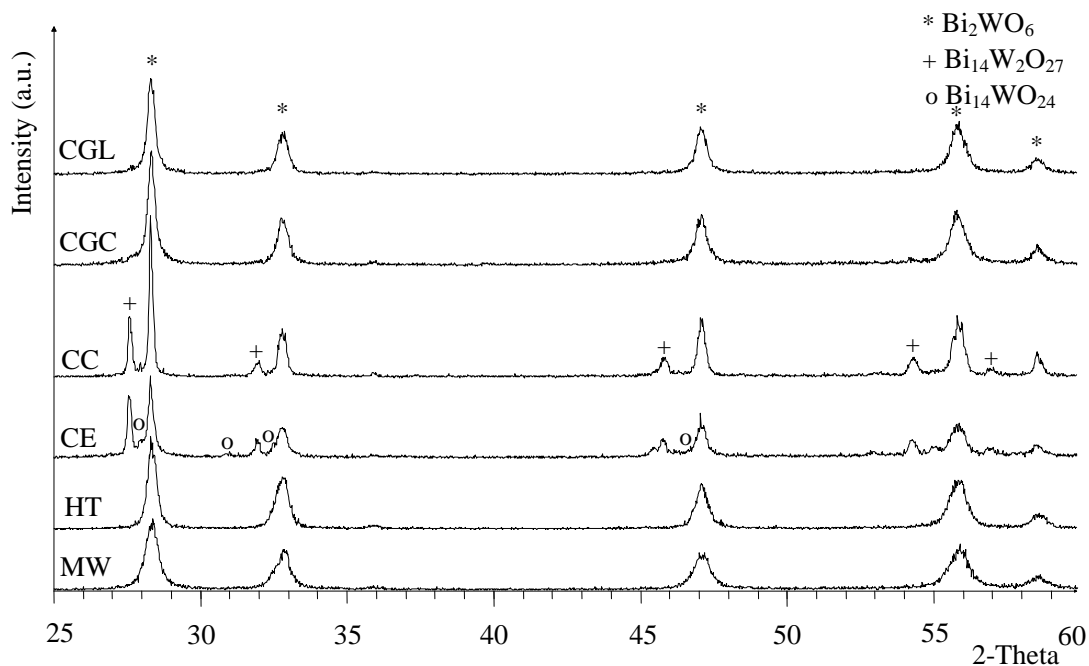


Fig. 2. XRD patterns of Bi_2WO_6 samples prepared by MW, HT or combustion synthesis using ethylene glycol (CE), citric acid (CC), glycerine (CGC) or glycine (CGL)

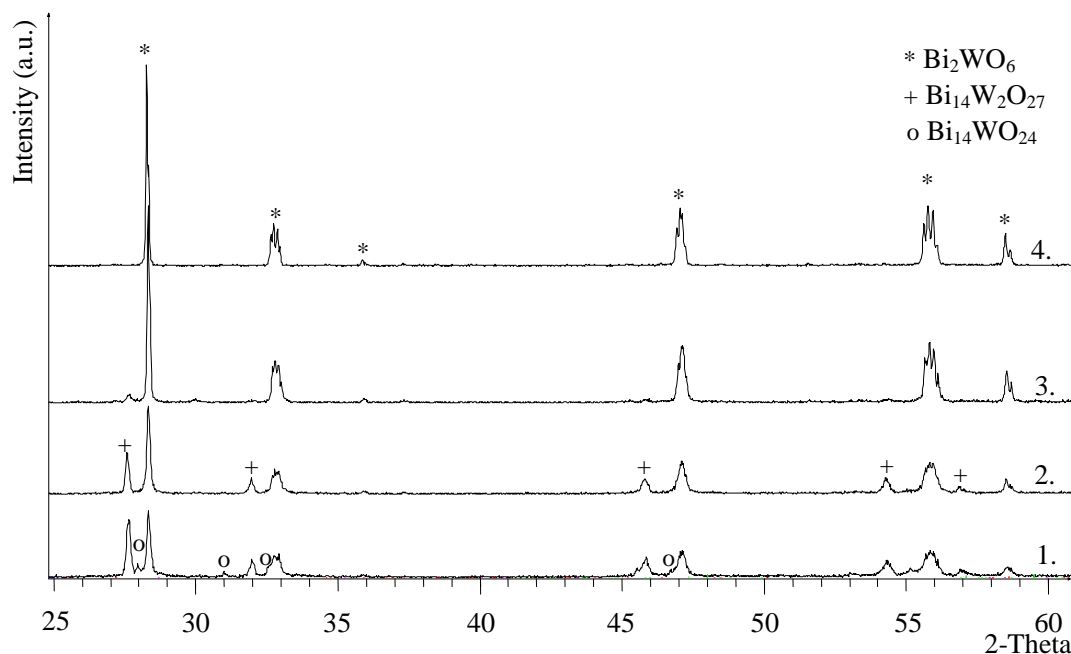


Fig. 3. Dependence of XRD patterns of samples obtained by combustion synthesis in presence of citric acid on calcinations temperature: 1 – 500°C, 2 – 600°C, 3 – 700°C, 4 – 800°C

However additional calcinations promotes particle growth and as result the Bi_2WO_6 crystallite size increase up to 150 nm and specific surface area decreases to 5 m^2/g at 800°C (Fig. 4). Therefore additional calcination can reduce the photocatalytic activity of Bi_2WO_6 .

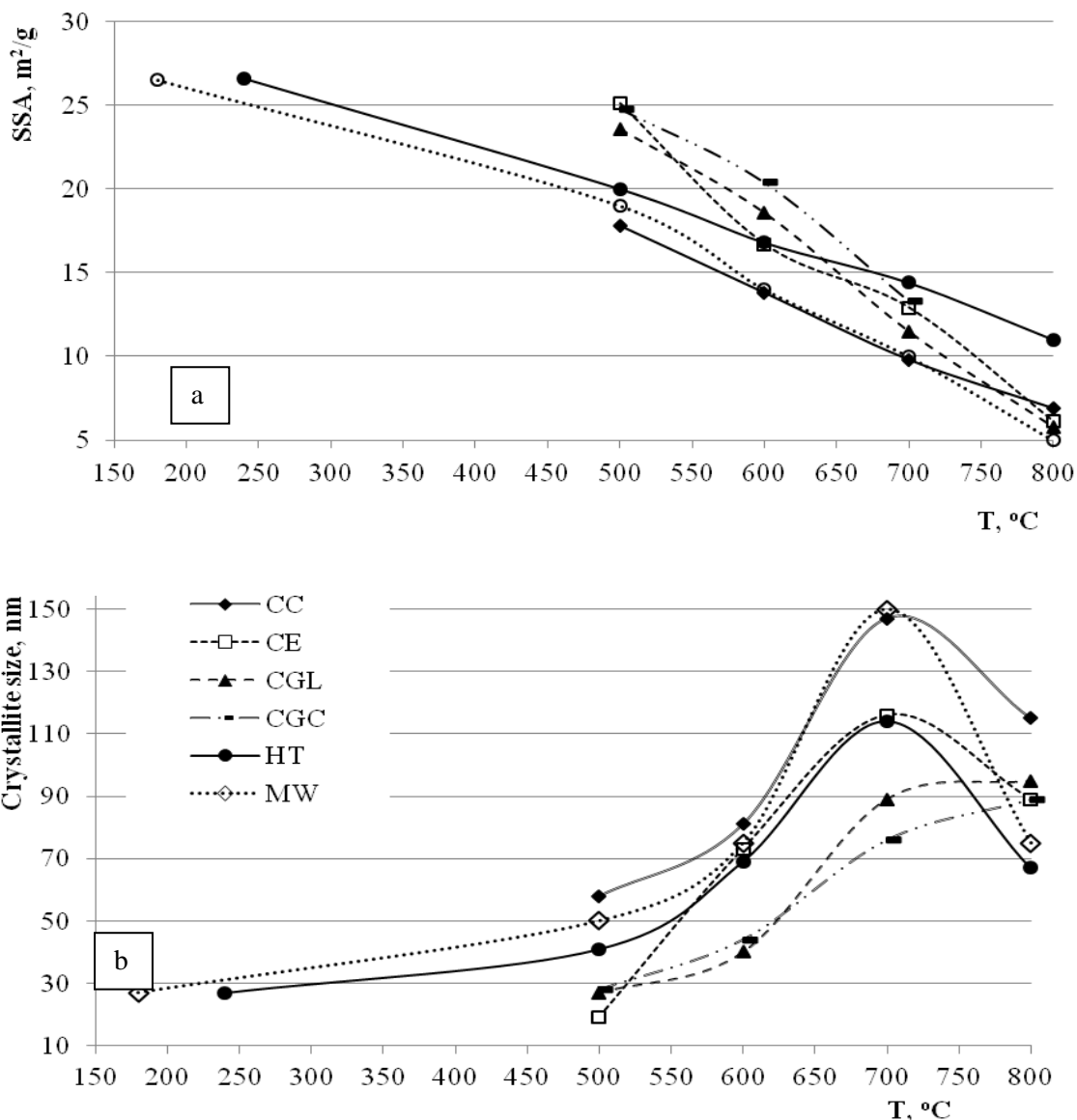


Fig. 4. SSA (a) and crystallite size (b) of the samples depending on calcination temperature

3.1. SEM images

It is clearly seen that preparation method have significant role on different particle morphology formation. Both microwave assisted synthesis and hydrothermally prepared samples have definite close to spherical or plate-like structures respectively (Fig. 5.). The formation of these type structures probably is because of pressure impact during synthesis, lower synthesis temperature and shorter synthesis time (Fig. 1.). Contrary the samples prepared by combustion synthesis have explicitly spongy type agglomerated structure without strictly defined particle boundaries but during calcinations at 800°C particles are growing and crystalline nature of the particle agglomerates is seen clearly.

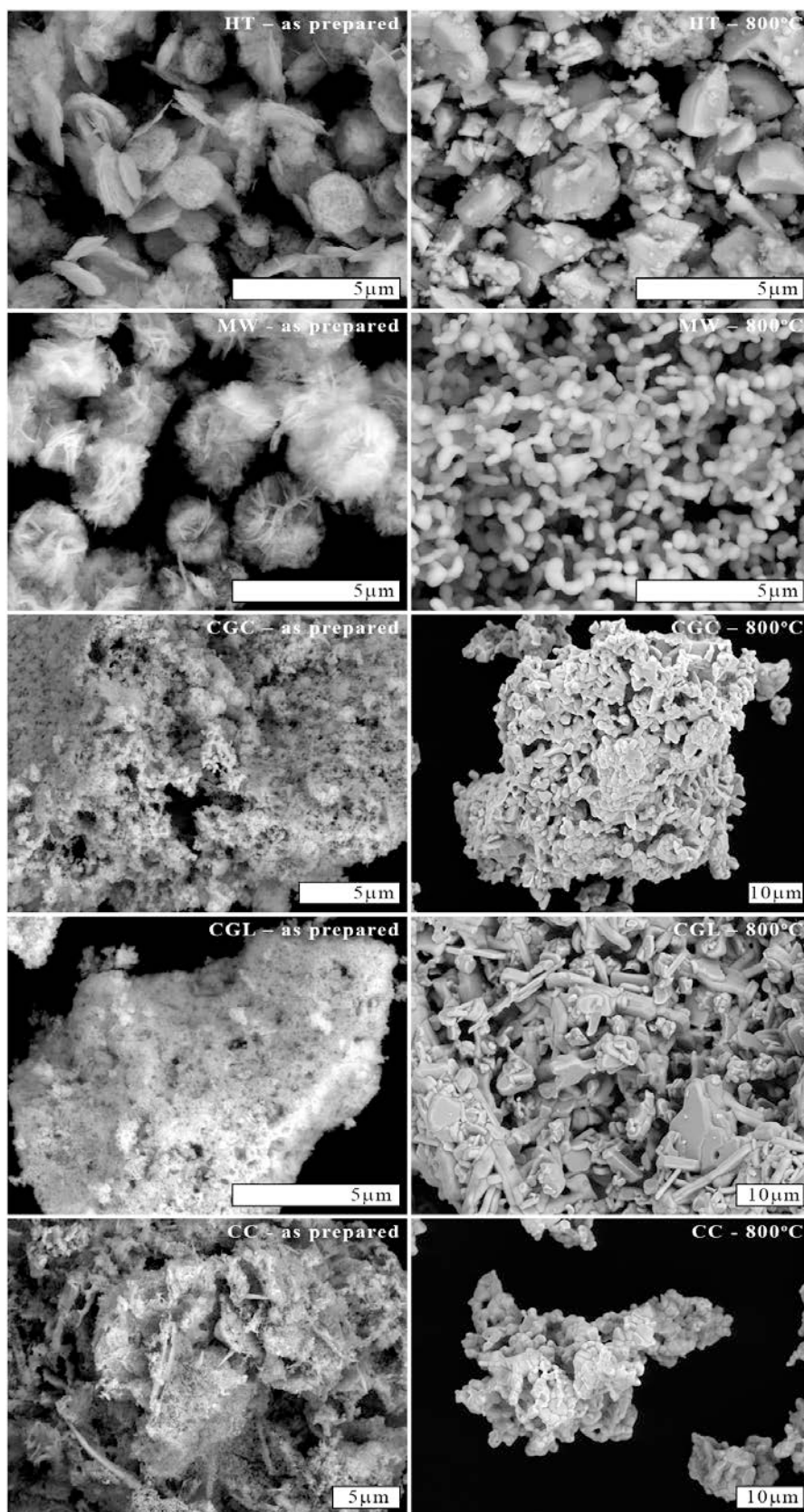


Fig. 5. Bi_2WO_6 particle morphology of the as-prepared and calcinated at 800°C samples obtained HT, MW and combustion synthesis

Notable that used organic fuel does not influence the morphology of the agglomerates of the as-prepared powder – structures are spongy in all cases, but the mode of particle growth changes

during calcinations. Such observations reported also Zhang et. al. in [18] when SEM images showed the aggregation and sintering between the particles at high temperatures. This means that organic fuel influences the particle growth. The particles prepared in the presence of citric acid are more spherical, but in all other cases the particles have needle-plate like shape. One of obstacle which may influence the particle shape formation during additional calcination could be on phase transition count.

3.2. Photodegradation of MB

Studies of degradation of MB solution (Fig.6) by Bi_2WO_6 nanoparticles prepared by HT and CGC synthesis testify similar photocatalytic activity of both samples. Regarding similar specific surface area values of the both samples one can conclude that in this case different morphology of the particles has insignificant influence on the photocatalytic activity.

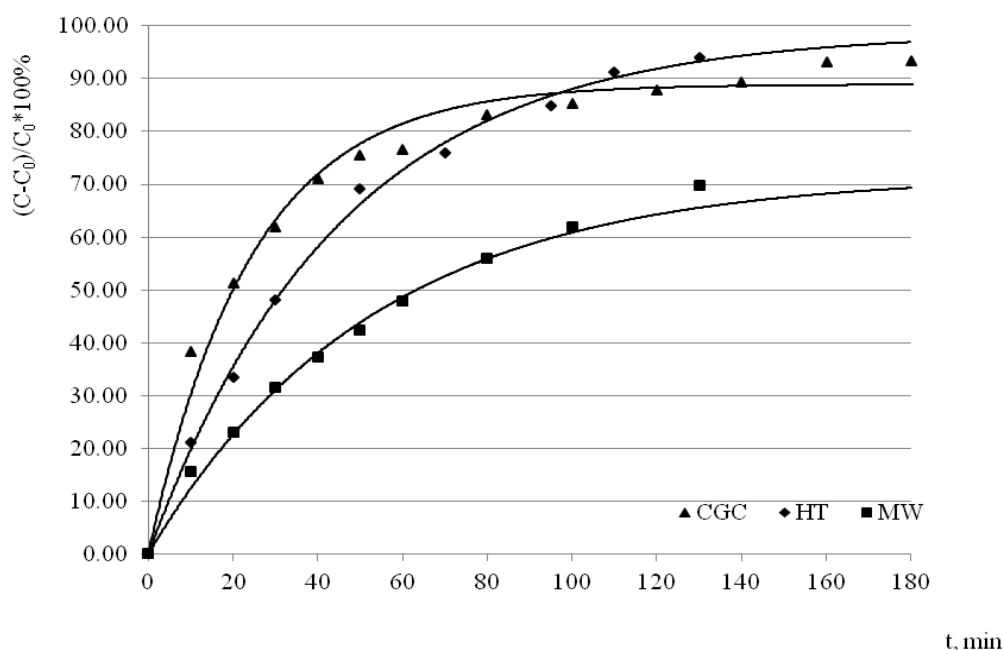


Fig. 6. Degradation of MB by Bi_2WO_6 prepared by HT, MW and combustion synthesis under ultraviolet illumination

Regarding crystallinity it previously known [19] on photodegradation experiments of RhB dye, that high crystallinity have high photocatalytic activity. Reduced photocatalytic activity of the samples prepared by combustion synthesis can be explained by presence of the aggregates because it's specific surface area of $23.6 \text{ m}^2/\text{g}$ is close to that for other samples. The results are contradictious, because previous studies show that crystallinity plays important role on photocatalytic activity but the evidence on morphology effect must be improved. Authors in [20] pointed that uncalcinated flower-like superstructures have weaker photocatalytic activity than calcinated samples.

4. CONCLUSIONS

Hydrothermal and microwave synthesis provide preparation of Bi_2WO_6 nanoparticles with specific surface area of $26.6 \text{ m}^2/\text{g}$ and crystallite size about 28 nm, and with similar photocatalytic activity in MB degradation under UV radiation despite to different particle morphology.

Pure crystalline Bi_2WO_6 with specific surface area of $23.6 \text{ m}^2/\text{g}$ and crystallite size of 27 nm can be prepared by combustion synthesis using as fuel glycerine and glycine.



The lower photocatalytic activity of Bi₂WO₆ nanoparticles prepared by combustion synthesis can be explained by presence of agglomerates.

ACKNOWLEDGMENT

The research was supported by Ministry of Education and Science of Latvia within the state programme in materials science.

REFERENCES

1. KNIGHT K.S., The crystal Structure of russelite; a re-determination using neutron powder diffraction of synthetic Bi₂WO₆, *Mineralogical Magazine*, 1992, Vol. 56, p. 399–409.
2. OSTERLOH F.E., Inorganic Materials as Catalysts for Photochemical Splitting of Water, *Chemistry of Materials*, 2008, Vol. 20, p. 35–54.
3. BEN LIAO Y.H., WANG J.X., LIN J.S., CHUNG W.H., LIN W.Y., Synthesis, photocatalytic activities and degradation mechanism of Bi₂WO₆ toward crystal violet dye, *Catalysis Today*, 2011, Vol. 174, No. 1, p. 148–159.
4. VORONKOVA V.I., KHARITONOVA E.P., RUDNITSKAYA O.G., Refinement of Bi₂WO₆ and Bi₂MoO₆ polymorphism, *Journal of Alloys and Compounds*, 2009, Vol. 487, No. 1–2, p. 274–279.
5. ZHANG L., WANG H., CHEN Z., WONG P. K., LIU J., Bi₂WO₆ micro/nano-structures: Synthesis, modifications and visible-light-driven photocatalyst applications, *Applied Catalysis B, Environmental*, 2011, Vol. 106, No. 1–2, p. 1–13.
6. ZHANG Z., WANG W., SHANG M., YIN W., Low temperature combustion synthesis of Bi₂WO₆ nanoparticles as a visible-light-driven photocatalyst, *Journal of Hazardous Materials*, 2010, Vol. 177, No. 1-3, p. 1013-1018.
7. DUAN F., ZHENG Y., CHENG M.Q., Flowerlike PtCl₄/Bi₂WO₆ composite photocatalyst with enhanced visible-light-induced photocatalytic activity, *Applied Surface Science*, 2011, Vol. 257, No. 6, p. 1972–1978.
8. FU H., ZHANG S., XU T., ZHU Y., CHEN J., Photocatalytic Degradation of RhB by Fluorinated BiWO and Distributions of the Intermediate Products, *Environmental Science and Technology*, 2008, Vol. 42, No. 6, p. 2085–2091.
9. GE L., LIU J., Efficient visible light-induced photocatalytic degradation of methyl orange by QDs sensitized CdS-Bi₂WO₆, *Applied Catalysis B, Environmental*, 2011, Vol. 105, No. 3–4, p. 289–297.
10. ZHENG K., ZHOU Y., GU L., MO X., PATZKE G.R., CHEN G., Humidity sensors based on Aurivillius type Bi₂MO₆ (M=W, Mo) oxide films, *Sensors and Actuators B: Chemical*, 2010, Vol. 148, No. 1, p. 240-246.
11. LAI K., ZHU Y., LU J., DAI Y., HUANG B., N- and Mo-doping Bi₂WO₆ in photocatalytic water splitting, *Computational Materials Science*, 2013, Vol. 67, p. 88–92.
12. LIU H., YUAN J., SHANGGUAN W., TERAOKA Y., Visible-Light-Responding BiYWO₆ Solid Solution for Stoichiometric Photocatalytic Water Splitting, *The Journal of Physical Chemistry C*, 2008, Vol. 112, No. 23, p. 8521–8523.
13. TANG J.W., ZOU Z. G., YE J.H., Photocatalytic decomposition of organic contaminants by Bi₂WO₆ under visible light irradiation. *Catalysis Letters*, 2004, Vol. 92, No. 1–2, p. 53–56.
14. WU L., BI J., LI Z., WANG Y., FU X., Rapid preparation of Bi₂WO₆ photocatalyst with nanosheet morphology via microwave-assisted solvothermal synthesis. *Catalysis Today*, 2008, Vol. 131, No. 1–4, p. 15–20.



15. ZHANG L., WANG W., ZHOU L., XU H., Bi₂WO₆ Nano- and Microstructures: Shape Control and Associated Visible-Light-Driven Photocatalytic Activities, *Small*, 2007, Vol. 3, No. 9, p. 1618–1625.
16. YOUNG D., KIM S., KANG M., Synthesis of Bi₂WO₆ Nanometer Sheet Shaped and Approach to the Photocatalysis, *Bull. Korean Chem. Soc.*, 2009, Vol. 30, No. 3. p. 630–635.
17. ZHANGA G., LU F., LI M., YANGA J., ZHANG X., HUANG B., Synthesis of nanometer Bi₂WO₆ synthesized by sol–gel method and its visible-light photocatalytic activity for degradation of 4BS, *Journal of Physics and Chemistry of Solids*, 2010, Vol. 71, p. 579–582
18. ZHANG S., ZHANG C., MAN Y., ZHU Y., Visible light –driven photocatalyst of Bi₂WO₆ nanoparticles prepared via amorphous complex precursor and photocatalytic properties, *Journal of Solid State Chemistry*, 2006, Vol. 179, p. 62–69.
19. FU H., YANG S., ZHANG S., ZHENG Z., Preparation of Nanosized Bi₂WO₆ using different content of starting materials and their photoactivities, *Journal of Applied Spectroscopy*, 2009, Vol. 76, No. 2, p. 227–233.
20. ZHANG L., WANG W., CHEN Z., ZHOU L., XU H., ZHU W., Fabrication of flower-like Bi₂WO₆ superstructures as high performance visible-light driven photocatalysts, *Journal of Material Chemistry*, 2007, Vol. 17, p. 2526–2532



EXPLANATION THE MECHANISM OF HYDROGEN ADSORPTION IN CLINOPTILOLITE FROM THERMOGRAVIMETRIC EXPERIMENTS

P. Lesnicenoks

*Riga Technical University
Azenes 14/24, LV-1048 Riga – Latvia*

L. Grinberga, J. Kleperis

*University of Latvia
Kengraga 8, LV-1063 Riga – Latvia*

ABSTRACT

Use of thermogravimetric method for hydrogen storage in natural zeolite shows uptake of hydrogen over 6wt%. Some of these are explainable as Langmuir single layer adsorption and filling of the pores. Ion exchange of magnesium and lithium extra framework cations and activation of material with palladium ions is applied to determine possibility to increase effectiveness of zeolites as storage material. Ion exchanged zeolites was checked with EDAX and XRD methods to determine effectiveness of these manipulations. Aim of this paper is to present possibility of hydrogen storage at low pressure and high to standard temperatures. Presented results show significant difference in exchanged ion usefulness for high temperature hydrogen storage as not seen previously. Spillover effect as well as framework strain is considered as benefactors for hydrogen storage in zeolites.

Keywords: zeolite, hydrogen adsorption, clinoptilolite

1. INTRODUCTION

Increasing demand of energy is fueling the research for more efficient and less polluting way to manufacture, store and use energy. Because of that there is increased attention to the alternative and green energy resources, in that count, also hydrogen, as ecologically friendly energy carrier with high energy density. To fully integrate it in energy circulation, it is important to be able to store and to transport it. That is why the hunt for most efficient storage system still continues. So far there are high pressure storage tanks, liquefied hydrogen storage tanks, metal hydrides, some metalorganic frameworks and mesoporous materials that are being investigated [1] [2–4]. In terms of efficiency, European Union demands higher results than those for USA, for example for year 2015 materials have to be able to store 10 wt% in EU and 9wt% in US, to be considered for actual use in stationary or portable hydrogen storage devices.

Mesoporous materials are materials with pore size 2–50 nm, one of these materials is zeolite [5]. Not always natural zeolites can provide best results, so there are some variations of modifications that can apply. Due to its structural variety and almost 3 million theoretical structural possibilities to create zeolite structures [6], it is a promising material for hydrogen storage. Economical convenience is a good reason to seek simple and common materials for storage systems. Natural materials in this case are especially interesting. Investigations about molecular hydrogen storage in zeolites started in 70's and are still continued. Zeolites are crystal aluminosilicates with grid structure which varies depending on chemical structure and proportions of aluminum – silica tetrahedrons [7]. Some of possible structures – RHO, FAU, KFI, LTA and CHA these three capital letters represent IUPAC Commission on Zeolite Materials (Appendix D in the Atlas of zeolite framework types) [8], are shown in Fig. 1. and are considered some of the best in terms with efficiency, showing adsorbance of 2.65-2.86 wt% (weight percent) at -196° C. Zeolite structure strongly depends on silicon – aluminium ratio (Si:Al) [9]. Decreasing this ratio increases surface based ion exchange centers and their coexistent oxygen atom grid, which regulates Lewis basicity. With this manipulation it is possible to increase the amount of adsorbed hydrogen. Proof of this is NaX type zeolite, shown in 2nd Figure, which adsorbs more hydrogen than NaY zeolite even

thou NaX zeolite shows stronger basicity its Si:Al ratio is 1.05, but NaY type zeolite has Si:Al ratio is 2.4 [10].

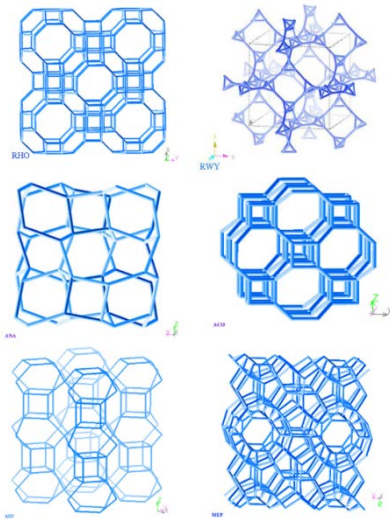


Fig. 1. ACO, MEP, ASV, ANA, RWY and RHO type zeolite frameworks [11]

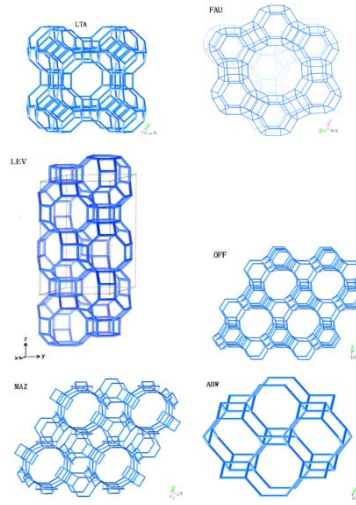


Fig. 2. NaA, NaXm Na-LEV, H-OFF, Na-MAZ and Li-ABW zeolite supercell schematics [12]

In room temperature and normal pressure hydrogen is adsorbed on zeolite surface thanks to weak interactions between gas and surface, cooling this system down to temperature of liquid nitrogen, these forces should increase and condensation of hydrogen on solid surfaces should increase. With Diffuse Reflectance Infrared Fourier transform spectroscopy (DRIFT) it has been confirmed that hydrogen gets adsorbed in reactions with basic anions in zeolites and these reactions increase their power if the amount of grid containing basic oxygen atoms is increased. From these interactions it is expected to achieve hydrogen molecule polarization towards surface, thanks to electrostatic forces. From this it is expected that one of hydrogen gas atoms behaves as acidic environment and interacts with near oxygen on zeolite surface[10].

Adsorption in zeolites can be realized in high, room temperature (RT) or cryogenic temperatures. Each of zeolite structures has different number of adsorption centers which are available to the hydrogen molecules. Also specific surface area is a meaningful criteria in estimation of adsorbed hydrogen amount. At any given temperature hydrogen adsorption must be proportional to surface coverage θ thus it gives information about adsorption constant K . Variations of this constant lead to different values enthalpy and entropy. These values can be combined with bond constant A , temperature T and balance pressure p and called Langmuir type equation (1). If to combine it with Hoff type equation (2) leads to 3rd equation which aloud to calculate enthalpy and entropy values [13, 14]:

$$\theta = \frac{A}{A_M} = \frac{K(T)p}{1+K(T)p} \quad (1)$$

$$K(T) = \exp\left(-\frac{\Delta H^\ddagger}{RT}\right) \exp\left(\frac{\Delta S^\ddagger}{R}\right) \quad (2)$$

$$\ln\left[\frac{A}{(A_M - A)p}\right] = -\frac{\Delta H^\ddagger}{RT} + \frac{\Delta S^\ddagger}{R} \quad (3)$$

Experiments with zeolites, retarding adsorption process and hydrogen storage, usually are not conducted at room temperature, but those few that actually happen at RT temperature show higher

results if they are conducted at higher [9]. RWY zeolite is considered having characteristics closest to ideal – showing highest adsorption results at room temperature and high pressure. Adsorption value will definitely increase increasing the pore diameter of zeolite [11].

As mentioned before, lower temperatures allow increasing amount of adsorbed hydrogen. Measurements that have been done at 77.3 and 90.2 K temperature show two adsorption types. The first one is the fairly strong electrostatic interactions with cation centers, which point to typical Langmuir type adsorption. Second – delocalized adsorption occurs starting with moment when all cation centers are used. It expresses itself as filling of the pores and show lower interaction energy. This adsorption can be investigated using (VTIR) variable temperature infrared spectroscopy. Important is that this process can also be described as Langmuir type adsorption [13].

Aim of this paper is to present possibility of hydrogen storage at low pressure and high to standard temperatures. Presented results show significant difference in exchanged ion usefulness for high temperature hydrogen storage as not seen previously.

2. EXPERIMENTAL

In our work natural zeolite – clinoptilolite from Ukraine is used. Clinoptilolite is a natural zeolite which belongs to heulandite (HEU) class. Its chemical composition has been mentioned in literature [15] as $(K,Na,Ca_{0.5},Sr_{0.5},Ba_{0.5},Mg_{0.5})_6(H_2O)_{20}[Al_6Si_{30}O_{72}]$.

Sample preparation. Samples for investigating the natural zeolites with thermogravimetric method usually were taken from deposit. Also for XRD measurements usually no special sample preparation was needed. For some experiments zeolite samples were prepared with washing in deionized water. Also some of these samples were prepared for ion exchange by washing natural zeolite in deionized water, some samples underwent washing in oxalic acid, as suggested in [15] to purify samples of iron oxides. After that indented cations salt solution was prepared – usually 1 mol/l. Then the washed zeolite samples were introduced to salt solutions such as $MgCl_2$ for 48 hours. After these procedures washed or ion exchange samples are dried at 100° C. For some optical experiments a self supporting zeolite tablets were prepared in press, under 4000 psi high pressure for other experiments finer powder was created by grinding it in mortar for such benefits as lesser adsorption of excited electrons in EDAX.

Sample characterization. Zeolite samples were tested by different methods to find out the properties of the material. For determining the pore size and surface volume of zeolites – the BET method – based on Brunauer-Emmett-Teller theory (Nova 1200 E-Series, Quantachrome Instruments), was used in explaining the physical adsorption of gas molecules on solid surface. For determining species of zeolite sample XRD method was used (X'Pert Pro MPD). The sample composition then was compared to database. Also EDAX - Energy Dispersive Analysis X-Ray was used (EDAX/Ametek - Eagle III microprobe), for determining elemental composition of zeolite samples.

Thermogravimetric hydrogen adsorption method was elaborated in our laboratory [16]. In our experiments thermogravimetric method in differential thermal gravimetry device Shimadzu DTA/TG – 60 have been used for determination of hydrogen sorption in zeolites.

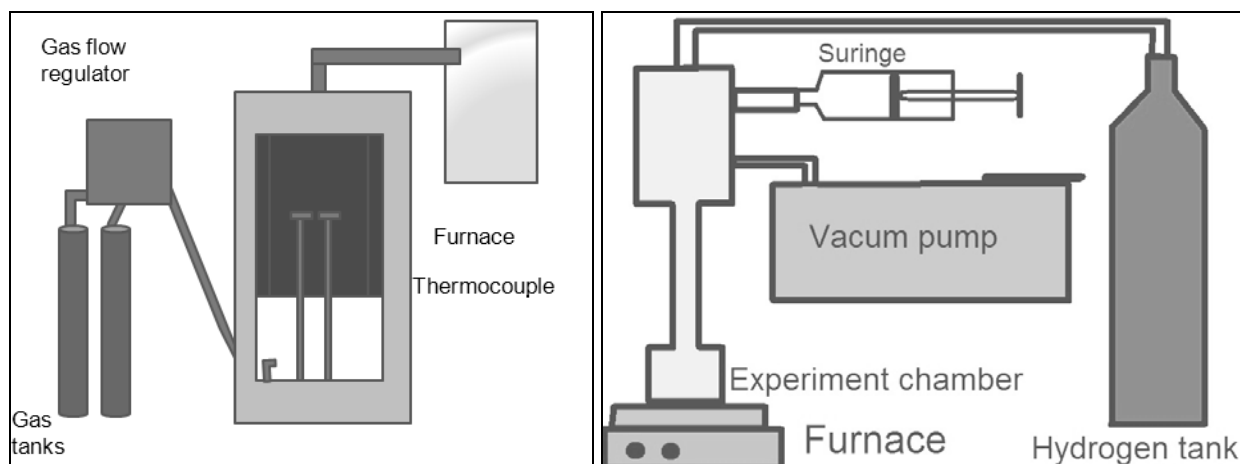


Fig. 3. Schematics of thermogravimeter setup (left) and thermal desorption method (right)

This method was chosen because of its easiness, and high repeatability, but also after it was checked with palladium powder, that indeed, while cooling degassed samples in hydrogen atmosphere, gains weight – by forming PdH_x and heating for second cycle the same amount of weight is lost [16]. So far samples have behaved consistently, adsorbing and desorbing gases at similar rates. Although zeolites do not show the typical hydrating step type weight gain, their exponential graph does match the one of palladium.

To replicate gas and temperature regimes in thermogravimetric experiments, a hermetic steel chamber containing zeolite, was used (Fig. 3, right). This chamber then was heated while vacuum was applied to sample. When the sample reached 300°C , then hydrogen gas (2 bar) was applied on previously vacuumed sample and allowed to cool till room temperature. After this, samples were tested with FTIR spectrometer Advantage 785 (DeltaNu, USA) and mass-spectrometer RGA100 (Setaram, France).

3. RESULTS AND DISCUSSION

Using BET surface analysis method we have determined size of our sample pore surface as $23.03\text{ m}^2/\text{g}$. From that value we can calculate that our zeolite can adsorb on its surface around 1.8 wt% of hydrogen gas, assuming that monolayer of adsorbed molecules is formed:

$$S_{\text{zeolite}} = \frac{23.03}{50} = 0.46\text{ m}^2 \quad (4)$$

$$m_{\text{H}_2 \text{ layer}} = 1.06976 \cdot 10^{20} \cdot 3.34 \cdot 10^{-24} = 3.573 \cdot 10^{-4}\text{ g} \quad (5)$$

$$S_{\text{H}_2} = \frac{\pi d^2}{4} = 0.43 \cdot 10^{-20}\text{ m}^2 \quad (6)$$

$$m_{\text{H}_2} = 3.34 \cdot 10^{-24}\text{ g} \quad (7)$$

$$N = \frac{0.46}{0.43 \cdot 10^{-20}} = 1.06976 \cdot 10^{20} \quad (8)$$

$$\text{wt}\%_{\text{H}_2} = \frac{3.573 \cdot 10^{-4}}{0.02} \cdot 100\% = \sim 1.8\% \quad (9)$$

Both modified and plain zeolites are investigated as possible storage materials. X-ray diffraction spectroscopy (XRD) determined that our natural zeolite samples consist not only of mineral – clinoptilolite ~77%, but also of quartz ~21%, as gathered from mines. EDAX analysis shows Si:Al ratio <4, that is why only clinoptilolite with HEU framework type is considered.

Hydrogen adsorption with volumetric-pressure method usually gets described using isotherms – Fig. 4. High pressure measurements of zeolites are one of the most commonly used in research. Such experiments describe adsorption balance at 50 bar high pressure. Similarly to volumetric method FTIR spectra and masspectrometry wouldn't show increase of hydrogen concentration over significant amounts, but these results most likely point to leaks in delivery of samples, for example in syringe or time from opening sealed chamber and delivering samples to FTIR device.

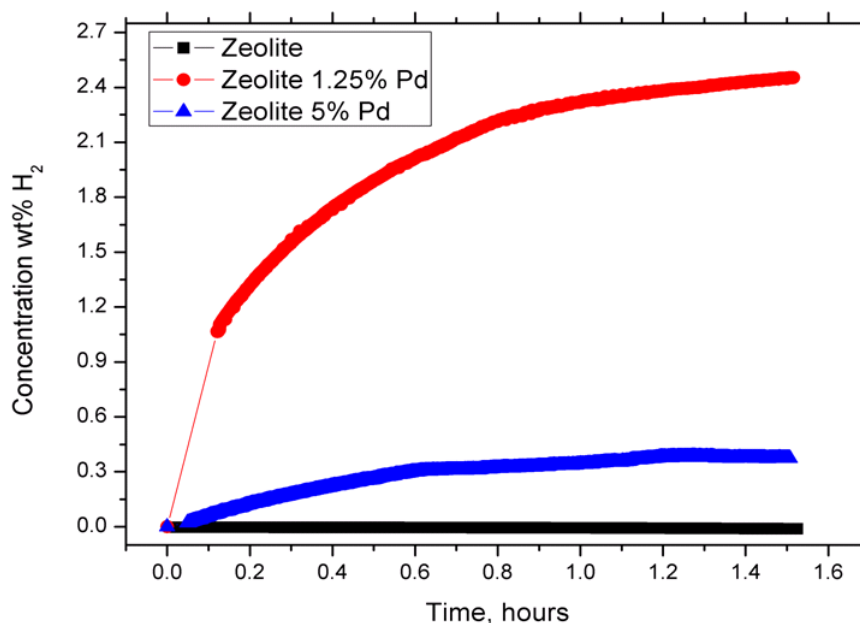


Fig. 4. Zeolite performance within Sievert type device PCT-Pro 200

But there are framework types which can be useful at even higher pressures [3] showing 0.4 wt% high adsorption. Very significant category is materials micro-porosity, and material powder or grain geometry, material compactness and thermodynamic conditions in thermogravimetric and volumetric gas storage devices [17]. To increase Zeolite performance, first the spillover effect was considered, by solution pyrolysis adding palladium to zeolite samples.

Thermogravimetric experiments were performed with ion-exchanged zeolites first. We suspected the ion exchange will have positive effect on hydrogen adsorption capability of zeolites – Fig. 5.

Different metal ions have great importance in promoting hydrogen adsorption in zeolites. That is why, if these metals aren't found enough in a zeolite structure they can be exchanged with ion solutions [13]. Using VTIR spectroscopy faujasite type (Mg,Na)-Y zeolites show the highest standard enthalpy values between other zeolite types and first group metal ion exchanged zeolite sorption results. These results are important for potential usage of zeolites as potential adsorbents for hydrogen storage. These zeolites could in fact store 3–4.5wt% [18].

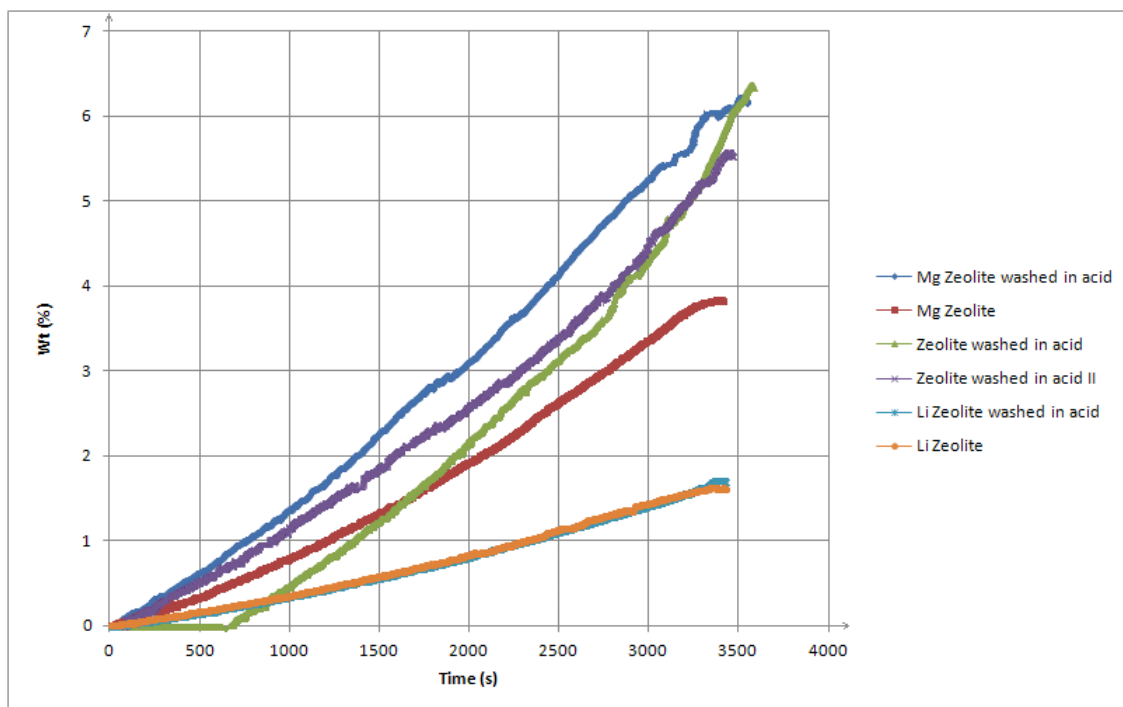


Fig. 5. Results of fine powder zeolite samples. Dark blue being not treated sample, light blue and orange – zeolite treated with CH_3COOLi solution, green and purple – zeolite treated with $\text{C}_2\text{H}_2\text{O}_4$ and blue and red being zeolite treated with MgCl_2

Using thermogravimetry some promising results have been achieved using finer powder samples. Also palladium introduction to zeolite system has proven itself valuable in increased amount of adsorbed hydrogen, as seen on Fig. 6.

To explain results obtained with thermogravimetric method, previously found Hydrogen encapsulation mechanism in zeolite [6, 7] can be discussed. As a possible mechanism for the encapsulation of hydrogen in zeolite may be mentioned that the heat treatment in the presence of inert gas flow at atmosphere pressure leaves the pores in zeolite at slightly stressing state; small hydrogen molecules can easily penetrate in stressed pores while changing gas at high temperature from inert to hydrogen. Also palladium catalyst play a role - hydrogen molecules dissociates on the palladium nano-grains into atoms and due the spillover effect spills from palladium to zeolite were atomic hydrogen fills the pores of zeolite (for spillover effect see [7]). Less-porous fractions of natural clinoptilolite sample (containing quartz) may be involved in spillover process supplying atomic hydrogen to zeolite particles.

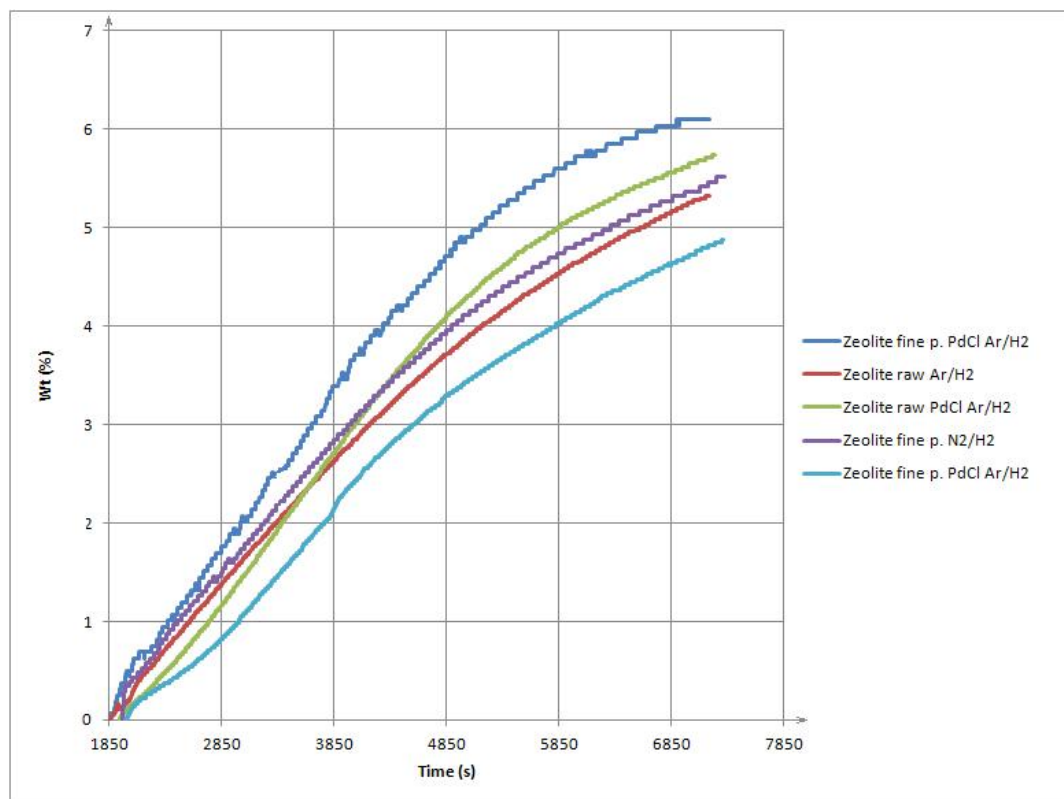


Fig. 6. Zeolite performance in thermogravimeter using different inert gases

4. CONCLUSIONS

Method to measure hydrogen storage capability in solid materials with commercial thermogravimeter instrument is developed. Material firstly is cleaned by desorption at inert gas (argon, nitrogen) flow and then exposed to hydrogen gas flow at higher temperature and cooled down to room temperature at hydrogen atmosphere.

The sample of natural zeolite – clinoptilolite finely grounded showed higher hydrogen adsorption capacity – up to 6 wt%, while slightly lower adsorption capability is observed for Pd-activated coarse ground zeolite, than finely ground zeolite without and with activation, and last - coarse ground zeolite without Pd-activator.

Thermogravimetric results of ion exchanged samples are consistent with [19] where the fact that Mg 2+ -exchanged zeolite Y showed an H₂ adsorption enthalpy of 18 kJ mol⁻¹ suggests that use of cations with no back-donation abilities, but with higher formal charges increases the electrostatic interaction with H₂ and may lead to materials with optimal H₂ binding energies.

Hypothesis that the heating of zeolite in argon (nitrogen) atmosphere activates the pore structure in zeolite material is proposed, where hydrogen encapsulation (trapping) is believed to occur when cooling down to room temperature in hydrogen atmosphere. An effect of catalyst (Pd) on hydrogen sorption capability is explained by spillover phenomena were less-porous fractions of natural clinoptilolite sample (containing quartz) is involved.

Results of ion exchanged samples points to effectiveness of extra framework cation interactions with hydrogen gas as well as deformation of framework leads to increased or decreased amount of adsorbed hydrogen.

Acknowledgement

Authors acknowledge financial support of National Research Program in Material science and IT “IMIS”.



5. REFERENCES

1. AHLUWALIA R.K HUA T.Q., PENG J-K., LASHER S., MCKENNEY K., SINHA J. and GARDINER M. 2010 Technical assessment of cryo-compressed hydrogen storage tank systems for automotive applications *International Journal of Hydrogen Energy* **35**, 4171–84.
2. SAKINTUNA B., LAMARIDARKRIM F. and HIRSCHER M. 2007 Metal hydride materials for solid hydrogen storage: A review *International Journal of Hydrogen Energy* **32**, 1121–40.
3. YU Y., ZHAO N., SHI C., HE C., LIU E. and LI J. 2012 Electrochemical hydrogen storage of expanded graphite decorated with TiO₂ nanoparticles *International Journal of Hydrogen Energy* **37**, 5762–8.
4. ZHENG J., LIU X., XU P., LIU P., ZHAO Y. and YANG J. 2012 Development of high pressure gaseous hydrogen storage technologies *International Journal of Hydrogen Energy* **37**, 1048–57.
5. ANTONELLI D.M. and YING J.Y. 1996 Mesoporous materials *Current Opinion in Colloid & Interface Science* **1**, 523–9.
6. BRUNNER G.O. 1990 Criteria for the evaluation of hypothetical zeolite frameworks *Zeolites* **10** 612–4.
7. WEITKAMP J. 2009 *Encyclopedia of Electrochemical Power Sources: Fuels – hydrogen storage / Zeolites*.
8. MEIER W.M, OLSON D.H. and BAERLOCHER C. 2001 *Atlas of zeolite framework types* (elsevier).
9. CHUNG K.-H. 2010 High-pressure hydrogen storage on microporous zeolites with varying pore properties *Energy* **35**, 2235–41.
10. AZZOZ A. 2012 Achievement in hydrogen storage on adsorbents with high surface-to-bulk ratio – Prospects for Si-containing matrices *International Journal of Hydrogen Energy* **37**, 5032–49.
11. RAHMATI M. and MODARRESS H. 2009 Grand canonical Monte Carlo simulation of isotherm for hydrogen adsorption on nanoporous siliceous zeolites at room temperature *Applied Surface Science* **255**, 4773–8.
12. DONG J., WANG X., XU H., ZHAO Q. and LI J. 2007 Hydrogen storage in several microporous zeolites *International Journal of Hydrogen Energy* **32**, 4998–5004.
13. PALOMINO G.T., BONELLI B., AREÁN C.O., PARRA J.B., CARAYOL M.R.L., ARMANDI M., ANIA C.O. and GARRONE E. 2009. Thermodynamics of hydrogen adsorption on calcium-exchanged faujasite-type zeolites *International Journal of Hydrogen Energy* **34**, 4371–8.
14. GARRONE E., BONELLI B. and OTERO AREÁN C. 2008 Enthalpy–entropy correlation for hydrogen adsorption on zeolites *Chemical Physics Letters* **456**, 68–70.
15. TSCHERNICH R.W. 1992 *Zeolites of the World* (Phoenix: Geoscience Press Inc.)
16. LESNICENOKS P., SIVARS A., GRINBERGA L. and KLEPERIS J. 2012 Hydrogen Adsorption in Zeolite Studied with Sievert and Thermogravimetric Methods *IOP Conference Series: Materials Science and Engineering* **38**, 012060.
17. WEINBERGER B. and LAMARI F.D. 2009 High pressure cryo-storage of hydrogen by adsorption at 77K and up to 50MPa *International Journal of Hydrogen Energy* **34**, 3058–64.
18. OTERO AREÁN C., TURNES PALOMINO G. and LLOP CARAYOL M.R. 2007 Variable temperature FT-IR studies on hydrogen adsorption on the zeolite (Mg,Na)-Y *Applied Surface Science* **253**, 5701–4
19. DINČÁ M. and LONG J.R. 2008 Hydrogen storage in microporous metal-organic frameworks with exposed metal sites. *Angewandte Chemie (International ed. in English)* **47**, 676–679.



COMPREHENSIVE SINTERING AND CONDUCTIVITY STUDY OF 10% Sc_2O_3 AND 1% CeO_2 CO-DOPED ZrO_2

D. Petrulionis

*Faculty of Physics, Vilnius University
Saulėtekio ave. 9/3, LT-10222 Vilnius – Lithuania*

ABSTRACT

Due to their high ionic conductivity compared to conventional yttria stabilized zirconia, solid electrolytes based on scandia doped zirconia are attractive materials for applications in fuel cells operating at intermediate temperatures with relaxed requirements on sealants and structural materials. Sintering properties of the powder are an important consideration determining its viability for commercial applications, while the resultant ceramic's ionic and electronic conductivities determine its performance as an electrolyte. This work is aimed at comprehensive characterization of commercial 10% Sc_2O_3 and 1% CeO_2 co-doped ZrO_2 powder with respect to the above mentioned parameters. The sintering behavior of the powder was determined by non-isothermal dilatometry as well as thermogravimetric analysis. This data was then used to determine appropriate treatment of the powder to obtain dense ceramic pellets. XRD was performed on as-received powder and at appropriate stages of the ceramic preparation process. The microstructure properties of the powder and ceramic pellets were investigated by SEM. Total conductivity of the obtained ceramic was measured in frequencies of 10 Hz to 3 GHz and temperatures between 300 K and 700 K. The electronic contribution to total conductivity of the pellets in reducing and oxidizing atmospheres was determined using a modified Hebb-Wagner technique over an oxygen activity range of 10^{-35} to 10^3 and temperatures between 673 K and 1023 K, which correspond well to the operating temperature and oxygen activity ranges in intermediate temperature fuel cells.

Keywords: Doped Zirconia, Solid Electrolyte, Ionic Conductivity, Electronic Conductivity, Sintering

1. INTRODUCTION

Fuel cells are currently being widely researched as an alternative to batteries and conventional power generation methods at all scales. Current commercial offerings require high operating temperatures to achieve power density and efficiency sufficient for these applications [1]. This limits the choice of materials that can be used for structural components and sealants to an expensive few [2], while introducing problems related to reduced material reliability at high temperatures, unwanted chemical interactions between structural and cell materials as well as bad thermal cycling performance. Therefore, much of the research has been focused on reducing the operating temperature of fuel cells to the intermediate range of 773 K to 1073 K. This is usually achieved by using a more conductive electrolyte [3], which is the focus of this article, or improving reaction kinetics at the electrodes [4].

One of the well-known electrolytes, suitable for operation in the intermediate temperature range is 10 mol. % Sc_2O_3 doped ZrO_2 . [5] Due to the presence of a phase transition in Sc_2O_3 doped ZrO_2 at, depending on dopant amount, 750 K to 900 K from the room temperature stable rhombohedral to the high temperature cubic phase, the cubic phase is usually stabilized with a further addition of small amount of larger ionic radius dopant such as 1 mol. % of CeO_2 . [3] This stabilizes the material's electrochemical and mechanical properties during thermal cycling.

The most important electrochemical properties of a solid electrolyte for its use in fuel cells are its ionic and electronic conductivities, stability with respect to temperature and highly reducing or oxidizing conditions present at the anode or cathode sides of the fuel cell. Good mechanical stability is also important and is usually achieved by limiting the crystallite growth during sintering. This can be achieved by utilizing a lower sintering temperature, which has the added benefits of lower costs associated with materials processing and the possibility of co-sintering with other ceramics.



In this work, sintering as well as comprehensive conductivity studies of commercially produced 10 mol. % Sc_2O_3 and 1 mol. % CeO_2 co-doped ZrO_2 (10Sc1CeSZ) material are presented. Special attention is given to its stability over a wide oxygen activity range, as indicated by its electronic conductivity and low temperature sinterability.

2. EXPERIMENTAL

All of the experiments were carried out on commercial 10Sc1CeSZ powder, manufactured by Fuel Cell Materials. The surface area of the powder was specified to be $11.1 \text{ m}^2/\text{g}$ by the manufacturer.

X-ray diffraction was performed on the as-received material, as well as after heat treatment and sintering. Philips X'Pert PRO diffractometer, equipped with an X'celerator detector, was used. The X-ray gun assembly was operated at 45 kV and 35 mA, producing monochromated $\text{CuK}\alpha$ ($\lambda = 1.541 \text{ \AA}$) radiation. The patterns were recorded in the 2θ range of 12° to 120° and an interpolated step of 0.017 for heat-treated and sintered powders and in the 2θ range of 12° to 73° and an interpolated step of 0.07 for as-received powder.

Non-isothermal sintering curves of a cylindrical 5 mm diameter and 1.41 mm length sample were obtained using a mechanical SETARAM SETSYS Evolution dilatometer. The sample was formed by cold pressing at very low pressure and pressed isostatically at 5000 bar. Measurements were carried out over a temperature range of 293 K to 1773 K and temperature rise speed of 3 K/min. A hemispherical alumina probe with 0.05 N contact force was used. Microstructure was observed using a Hitachi TM3000 SEM. Thermal analysis on the heat treated powder was performed using a NETZSCH TG 209 F1 thermogravimetric analyzer which was coupled to a mass spectrometer. The gravimetric curve was obtained over a temperature range of 293 K to 1473 K, with 10 K/min temperature rise speed.

Total conductivity of the sintered ceramic was characterized by means of two custom impedance spectrometers working in the frequency ranges of 10 Hz to 2 MHz and 300 kHz to 3 GHz, using the two probe method. Measurements in the frequency range of 10 Hz to 2 MHz were carried out using the vector voltmeter–amperemeter method while the system was swept in the frequency domain by means of fixed frequency sine signals. The voltage and current through the system were measured by a two channel TiePie HS3 computer oscilloscope. A custom current to voltage converter, allowing accurate vector current measurement, was used. Two electrode measurements in the frequency range of 300 kHz to 3 GHz were carried out using an Agilent E5062A network analyzer, connected to a heated coaxial line and sample system, with the sample forming a part of the line's inner conductor. The electrical parameters of the sample were calculated from the transmission and reflection coefficients of the system as in [6]. Temperature control loop for both spectrometers was comprised of an Amprobe TMD90 digital thermometer and a Mastech HY 3005 power supply, both of which were connected to a computer.

The electronic conductivity measurements were carried out using a modified Hebb-Wagner method, which is based on the analysis of steady state polarization curves around an ion-blocking microcontact. [7] Due to a slight deviation from stoichiometry present in the oxide, oxygen activity at the blocking electrode can be controlled by applying different DC voltages across the measurement cell. The oxygen activity at the other side of the pellet must be held constant by a reversible electrode, which is conductive to both, oxygen ions and electrons. To ensure fully blocking behaviour of the microelectrode, the measurements were carried out in dry N_2 atmosphere using Platinum as the electrode material. The sample and electrode were fully encapsulated using a glass-based sealant. The electrode to sample contact surface was assumed to be hemispherical, with a measured $100 \mu\text{m}$ diameter. A 1:1 ratio (by charge) mix of CuO and Cu_2O was pressed into pellets and sintered in an inert atmosphere to be used as a reversible electrode and known oxygen activity reference. Voltages between -1 V and +0.4 V were applied across the sample, which

correspond to an oxygen activity range of 10^{-35} to 10^3 . Here the oxygen activity of 1 is defined as the oxygen activity at oxygen partial pressure of $p(\text{O}_2) = 1.013$ bar.

3. RESULTS AND DISCUSSION

3.1. X-ray diffraction

X-ray diffraction measurements of the as-received and heat-treated powder, as well as a ground sintered pellet are shown in Fig. 1. The heat treated and sintered samples were found to have small amounts of the rhombohedral β phase, as indicated in the figure. This is in agreement with a similar study in [8]. No impurities were detected at any stage of the process.

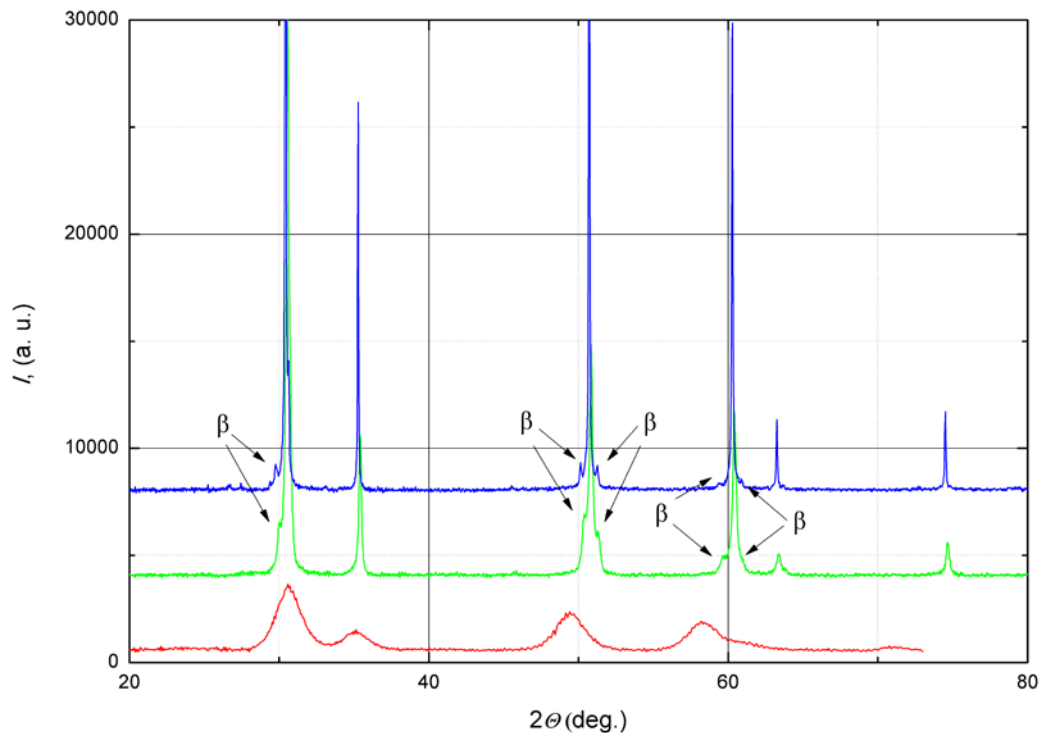


Fig. 1. X-ray diffraction patterns of as-received (bottom), heat treated (middle) and sintered (top) powder. Rhombohedral phase peaks are indicated with β

The low intensity and very wide peaks of as-received powder are indicative of a weakly crystallized material with a small crystallite size. Considerable crystallite growth can be seen to have occurred during the heat treatment of the powder, with further narrowing and higher intensity of the sintered powder peaks corresponding to further growth of crystallites during sintering.

3.2. Sintering

Significant deviations from the expected low temperature behaviour were present in the dilatometric measurements of the as-received powder. Subsequently, FTIR studies were performed, which indicated the presence of adsorbed water, carbonates and other unidentified impurities in the material. The powder was calcined at 873 K for 2 h in order to remove any unwanted compounds, which might otherwise be volatilized when heated and prevent shrinkage of the pellet during the closed pore sintering stage due to gas becoming trapped inside the pores. Subsequent measurement with a thermogravimetric analyzer showed no mass loss up to 1473 K, while a mass-spectrometric analysis of the gas in the working chamber of the analyzer was consistent with no gas being evolved from the heat-treated sample.

Non-isothermal shrinkage curve of the pellet, is shown in Fig. 2. The sintering process starts at 1250 K and is the fastest at 1418 K, with most of the sintering process being finished at 1478 K. This temperature is notably lower than the sintering temperatures previously reported in the literature for conventional sintering of 10Sc1CeSZ [3] and is comparable to the temperatures used in spark-plasma sintering of the compound [9]. This result is also corroborated further by a recent sintering study of the material [8].

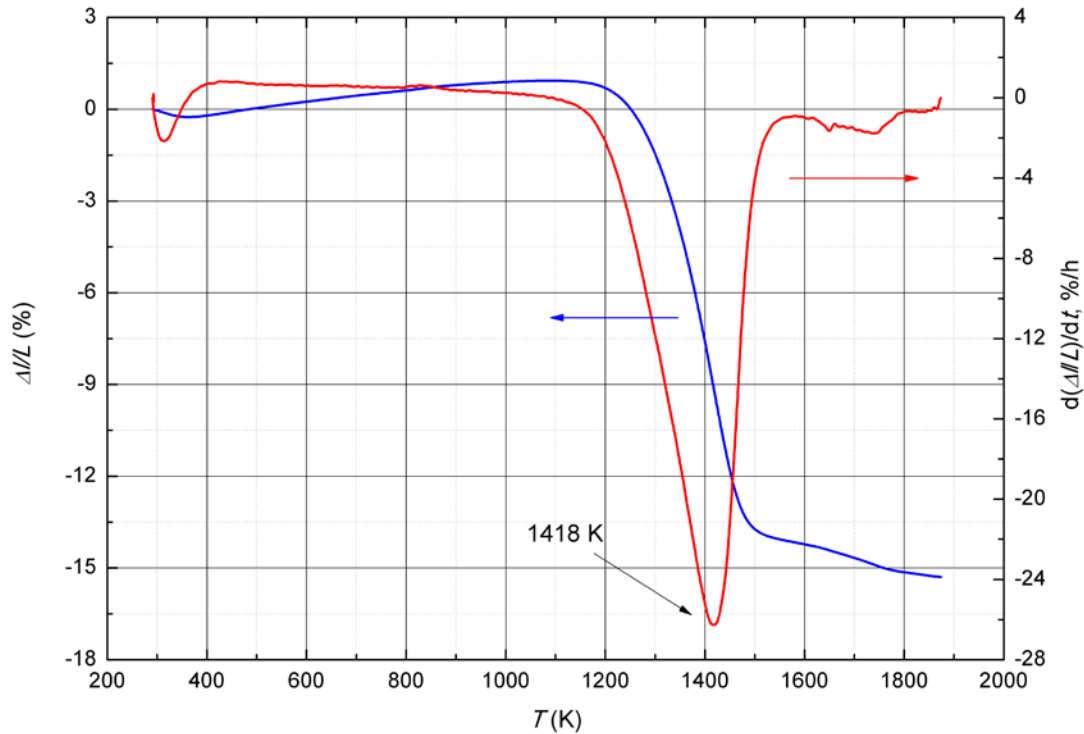


Fig. 2. Linear shrinkage of the pellet (blue) and the linear shrinkage rate (red). Heating rate of 3 K/min.

A conventional sintering profile was used for sintering of the pellets. The sintering temperature of 1423 K was chosen to correspond with the region of fastest shrinkage, as measured by dilatometry. Three pellets were prepared identically to the ones used for dilatometric measurements and sintered for 2 h using the same temperature rise speed of 3 K/min.

All of the pellets were found to be denser than 92 % of the material's theoretical density, as measured by the Archimedes method. It should be noted, that density measurement is complicated by the presence of multiple phases of 10Sc1CeSZ in the samples. The theoretical density of cubic (dominant) structure of the material was chosen as the 100 % density reference. A SEM photograph of the unpolished sintered pellet's surface is shown in Fig. 3.

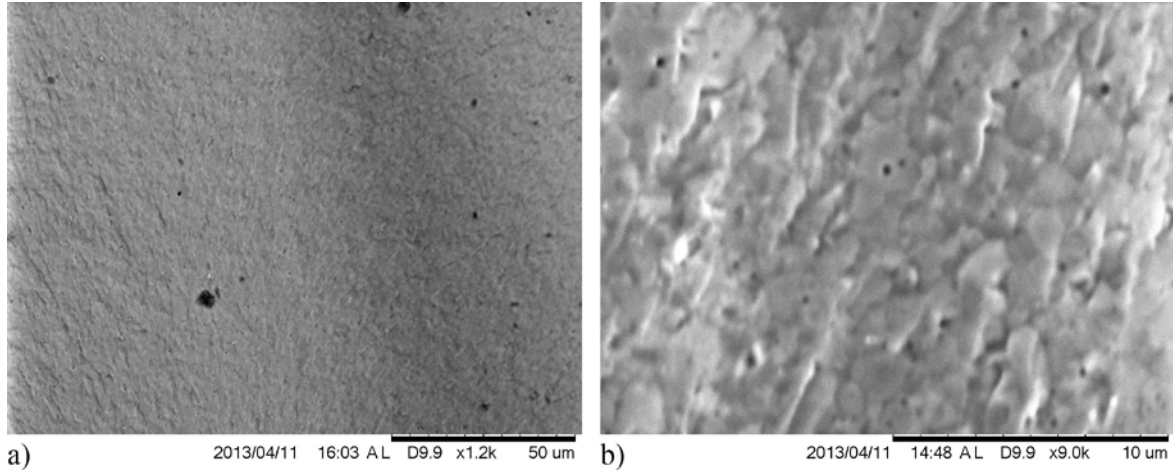


Fig. 3. HF etched fracture surface of the ceramic pellet. The density is 93 % of theoretical, as measured by the Archimedes method

3.3. Ionic conductivity

The frequency dependence of 10Sc1CeSZ total conductivity at various temperatures is shown in Fig. 4a. Two regions of conductivity dispersion are visible at all temperatures, which can be attributed to grain boundary and grain conductivity at medium and high frequencies, as indicated in the Figure. The third dispersion, only present in the low frequency region at high temperatures, is due to the blocking nature of the sample electrodes.

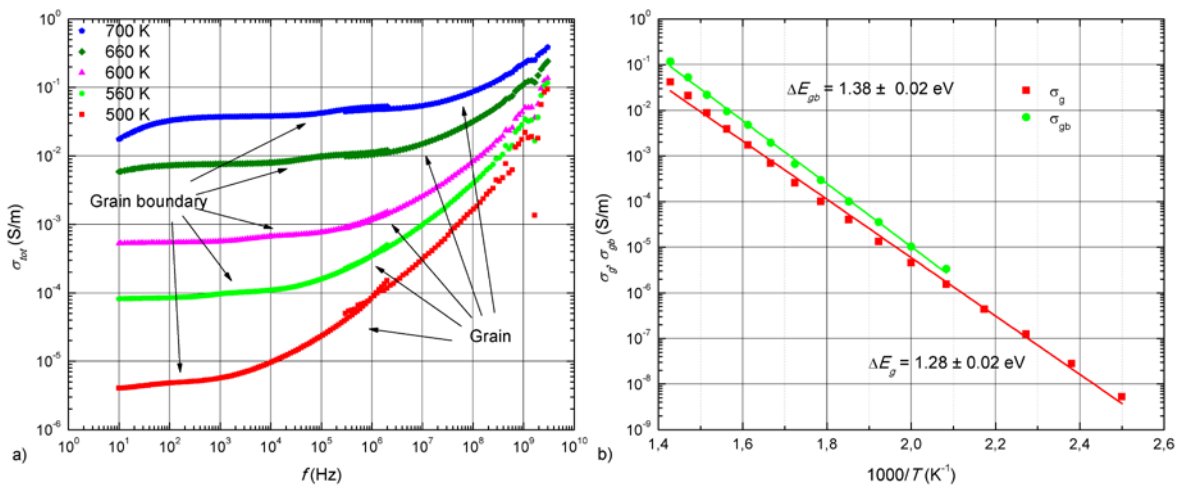


Fig. 4. Total conductivity dependence on frequency for different temperatures (a) and Arrhenius plot of grain boundary and grain ionic conductivities (b)

The temperature dependences of 10Sc1CeSZ grain and grain boundary conductivities are shown in Fig. 4b. The conductivities were calculated by fitting of an equivalent circuit composed of two elements consisting of parallel constant phase element – resistor pairs connected in series, representing the grain and grain boundary conductivity contributions to the total conductivity. The two morphological regions of the ceramic have distinct conductivity activation energies, corresponding to 1.38 ± 0.02 eV for grain boundary and 1.28 ± 0.02 eV for grain conductivity (the accuracy is only indicated for the linear fit of conductivity data).

Complex plane plot of 10Sc1CeSZ resistivity at 600 K is presented in Fig. 5. Two semicircles are visible, with the larger semicircle corresponding to grain and the smaller semicircle corresponding to grain boundary resistivity. Electrode effects also become apparent at very low frequencies.

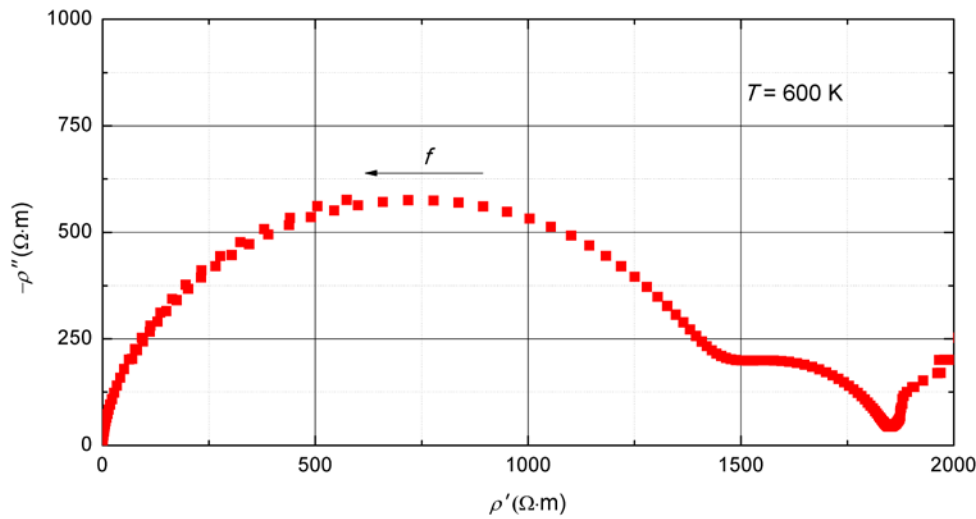


Fig. 5. Complex plane plot of sample resistivity at 600 K. The direction of increasing frequency is indicated with an arrow

These ionic conductivity results are comparable to the ones reported for spark plasma sintered ceramic [9], and are in excellent agreement with a recent study of low temperature sintering of 10Sc1CeSZ [8]. The grain boundary conductivity is not markedly decreased compared to conventionally sintered samples, as reported in the literature. [3].

3.4. Electronic conductivity and stability in reducing and oxidizing atmospheres

The electronic conductivity's dependence on oxygen activity for different temperatures is shown in Fig. 6a. Two regions of electronic conductivity's dependence on oxygen activity can be easily discerned: an oxygen activity dependant region at high oxygen activities, and a region of very weak or absent electronic conductivity's dependence on oxygen activity in the low activity region.

The slope of the electronic conductivity fit at high oxygen activities is in the range of 0.21 to 0.29 at temperatures above 673 K, which corresponds well with the theoretical value of 0.25, predicted by a single process of hole production due to oxygen incorporation into vacancy type defects present in the material as described in [7]. However, at 673 K the slope is 0.10, suggesting more complex processes taking place. Such decrease of the slope can be due to oxidation of Ce^{3+} , present at the microcontact, to Ce^{4+} . This could limit hole conductivity in the high oxygen activity region, similarly to results reported for Fe_2O_3 and Y_2O_3 co-doped ZrO_2 in [10].

At low oxygen activities there is no marked dependence on oxygen conductivity at high temperatures, while the increase in electronic conductivity with decreasing oxygen activity at low temperatures cannot be reliably interpreted due to the high spread of measured data.

The electronic conductivity can be seen to increase with temperature, as depicted in Fig. 6b for two different values of oxygen activity. The conductivity activation energy at high oxygen activity, corresponding to hole conduction due to incorporation of oxygen into the ceramic, is constant at 0.37 ± 0.01 eV, while the activation energy at low oxygen activities is dependent on temperature and is 0.23 ± 0.03 eV below and 0.81 ± 0.04 eV above 873 K. The lowest temperature point of electronic conductivity at high oxygen activity is not fitted due to the presence of different processes in the material at that temperature.

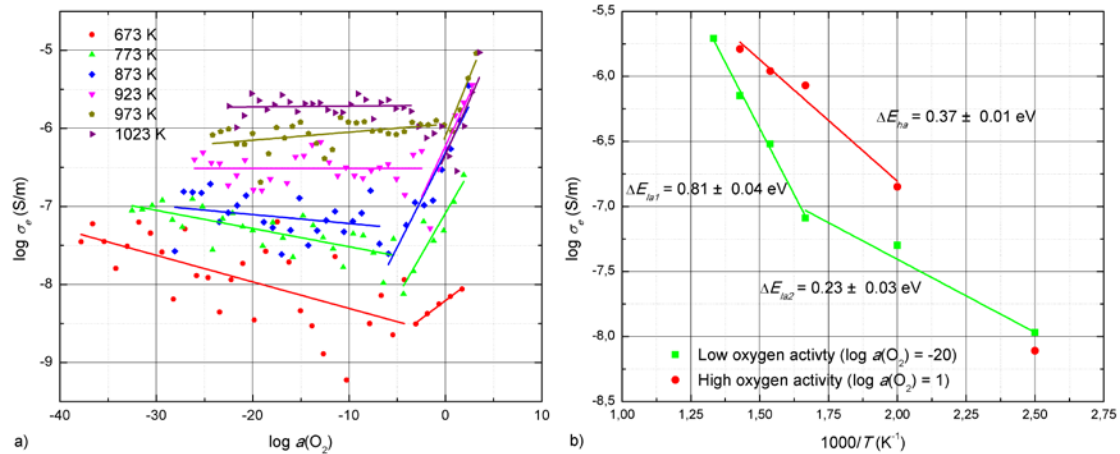


Fig. 6. Electronic conductivity of 10Sc1CeSZ, as it depends on oxygen activity (a) and Arrhenius plots of electronic conductivity at high and low oxygen activities (b)

The ratio of ionic to electronic conductivities of the ceramic can be considered sufficiently high for fuel cell applications at all temperatures.

4. CONCLUSIONS

XRD study of 10 mol. % Sc_2O_3 and 1 mol. % CeO_2 co-doped ZrO_2 showed no crystalline impurities present at any point in the ceramic preparation process. Small amounts of rhombohedral phase of the material were detected, with most of the material having a cubic structure.

Non-isothermal dilatometry of isostatically pressed pellets showed high sintering activity of the powder, heat treated at 873 K for 2h, with the highest densification rate at 1418 K. Subsequently, three ceramic pellets were sintered at 1423 K for electrochemical property investigation. All of the pellets exhibited densities higher than 92 %, with the pellet investigated by impedance spectroscopy reaching 93 % of the material's theoretical density.

Total conductivity investigation of the sintered pellets showed high grain boundary conductivity, comparable to that of spark-plasma sintered ceramic and corroborated by recent studies in the literature, indicating acceptable sintering performance at the reported low sintering temperature.

Measurements of electronic conductivity revealed good stability over a wide range of oxygen activities. The conductivities were in the range of $10^{-8.25}$ S/m to $10^{-5.75}$ S/m at all temperatures.

Together with good ionic conductivity these results indicate acceptable performance of the material for intermediate temperature fuel cells.

REFERENCES

- LIU, B.; ZHANG, Y. Status and prospects of intermediate temperature solid oxide fuel cells, *Journal of University of Science and Technology Beijing*, 2008, Vol. 15, No. 1, p. 84–90.
- WU, J.; LIU, X. Recent Development of SOFC Metallic Interconnect, *Journal of Materials Science & Technology*, 2010, Vol. 26, No. 4, p. 293–305.
- LIU, M.; HE, C.; et. al. Investigation of $(\text{CeO}_2)_x(\text{Sc}_2\text{O}_3)_{(0.11-x)}(\text{ZrO}_2)_{0.89}$ ($x = 0.01-0.10$) electrolyte materials for intermediate-temperature solid oxide fuel cell, *Journal of Alloys and Compounds*, 2010, Vol. 502, No. 2, p. 319–323.
- SETEVICH, C.F.; MOGNI, L.V.; et. al. Optimum cathode configuration for IT-SOFC using $\text{La}_{0.4}\text{Ba}_{0.6}\text{CoO}_{3-\delta}$ and $\text{Ce}_{0.9}\text{Gd}_{0.1}\text{O}_{1.95}$, *International Journal of Hydrogen Energy*, 2012, Vol. 37, No. 19, p. 14895–14901.



5. BADWAI, S.P.S.; CIACCHI, F.T.; MILOSEVIC, D. Scandia–zirconia electrolytes for intermediate temperature solid oxide fuel cell operation, *Solid State Ionics*, 2000, Vol. 136-137, p. 91–99.
6. KEŽIONIS A.; KAZAKEVIČIUS E.; ŠALKUS T.; ORLIUKAS A. Broadband high frequency impedance spectrometer with working temperatures up to 1200 K, *Solid State Ionics*, 2011, Vol. 188, No. 1, p. 110–113.
7. LUBKE, S.; WIEMHOFER, H. D. Electronic conductivity of Gd-doped ceria with additional Pr-doping, *Solid State Ionics*, 1999, Vol. 117, p. 229–243.
8. GROSSO, R. L.; MUCCILO, E. N. S. Sintering, phase composition and ionic conductivity of zirconia–scandia–ceria, *Journal of Power Sources*, 2013, Vol. 233, p. 6–13.
9. GROSSO, R. L.; BERTOLETE, M.; et. al. Ionic conductivity and phase stability of spark plasma sintered scandia and ceria-stabilized zirconia, *Solid State Ionics*, 2013, Vol. 230, p. 48–51.
10. KRAVCHYK, K. V.; BOHNKE, O.; et. al. Ionic and electronic conductivity of 3 mol% Fe₂O₃-substituted cubic Y-stabilized ZrO₂, *Solid State Ionics*, 2012, Vol. 226, p. 53–58.



INVESTIGATION OF BIOMASS GASIFIER TO PRODUCE HEAT AND ELECTRICITY FOR INDUSTRIAL APPLICATIONS IN UKRAINE

T.O. Antoshchuk

*The Gas Institute of National Academy of Sciences of Ukraine
Degtjarivska str. 39, 03113 Kiev – Ukraine*

ABSTRACT

The high cost of natural gas and the deteriorating environmental condition calls for an urgent replacement of alternative fuels in Ukraine. Hydropower, solar, wind, biomass, etc. are the top renewable energy sources in Ukraine. Suffice to say that Ukraine's biomass industry constitutes over two-thirds of the country's potential on the market of renewables. Currently, under 0.5 percent of energy is produced from biomass but the estimated potential is ten times larger. Ukraine is using biomass to generate heat and electricity. From the experience gained, it has been observed that gasification certainly appears to be a better option than combustion in terms of energy efficiency. Produced gas obtained from gasification can be used as gaseous fuel for combustion in boilers and industrial furnaces for heat energy. It can also be used as fuel for diesel piston engines to generate electricity. Gas-generators with designed capacity ranging from 0.5 to 3 MW_{Th}, are currently under investigation at Gas Institute of National Academy of Sciences of Ukraine, together with private companies. So, in consideration of their potential use as an alternative fuel for water heating and industrial applications, biomass conversion technologies under investigation at Gas Institute of National Academy of Sciences, gas cleaning system, use of some software for designing a gasifier along with important results obtained both theoretical and experimental, will be discussed.

Keywords: renewable energy, biomass, gasification, gas-generator (gasifier)

1. INTRODUCTION

According to the Energy Strategy of Ukraine [1], fuels from biomass for various power equipment are very actual for Ukraine at present moment. Due to the different researches, Ukraine that is developing country has considerable consumption of electric and thermal energy. Also Ukraine is one of the biggest exporters of electric energy in Europe, but at the same time the country occupies first places in Europe on purchases of natural gas and oil refining products. Having big metallurgical, chemical and other industrial enterprises Ukraine also is a big consumer of different power fuels, electric and thermal energy. Also the country has developed enough natural resource, agricultural and industrial and woodworking complexes.

Taking into consideration all mentioned above and the fact that Ukraine is the biggest in territory country of the Europe it is possible to make a conclusion, that usage of biomass as alternative, and in some cases, as main fuel presents the paramount problem for the country. Also we should note that country already has program on development of energy saving and energy effectiveness and has series of laws about alternative and green energy [2].

The problem is the next:

- coal is the priority fuel in energy system of Ukraine;
- there is no clear mechanism for transition from coal to biomass as main fuel type;
- the majority of project don't receive enough financing;
- little number of practical implementation of the installations.

Biomass is one of the most popular kind of alternative energy source in Ukraine. Biomass is widely used in direct burning processes in manufacturing equipment of different key industries. Also there is possibility to gasify biomass in special gasifier installations that gives opportunity to receive gaseous combustible fuel, which can be used in different kinds of equipment adjusted for

natural gas as main fuel. But the direct process of burning and gasification both have its advantages and disadvantages (see Table 1) [3].

Table 1. Comparison of direct burning and biomass gasification processes

Direct process of burning	Use after gasification
Advantages	
<ul style="list-style-type: none"> – relative simplicity of fuel feeding equipment; – higher efficiency factor of energy transformation (with use of modern technologies). 	<ul style="list-style-type: none"> – possibility to use raw material of different factions and various mixtures of organic fuels; – less cost of boiler re-equipment, if it worked on a gaseous fuel (only need of burner replacement); – possibility to use raw material with humidity up to 50%; – less environmental influence; – possibility to produce electric energy; – for whole complex: possibility to work on both generator and natural gas or on their mixture.
Disadvantages	
<ul style="list-style-type: none"> – necessity of the previous predrying of fuel; – necessity to install the system of ash removal in boiler; – limitation on size composition of fuel. 	<ul style="list-style-type: none"> – necessity of extra purification of producer gas from tarry substances and cooling before feeding of heat-and-power engineering equipment; – more serious system of automatics that provides simultaneous burning of producer and natural gas; – necessity to place gas-generator outside of boiler room.

Table 2. Comparison of gasification processes characteristics

	Updraft	Downdraft	Combined
Advantages	<ul style="list-style-type: none"> – use of physical heat of gas for heating and subdrying; – low temperature of gas; – possibility of the use of fire-grate. 	<ul style="list-style-type: none"> – stability of process, use of tarry fuels, simplicity of loading, no need in additives. 	<ul style="list-style-type: none"> – stable composition of gas, possibility to use different types of fuel.
Disadvantages	<ul style="list-style-type: none"> – impossible to use tarry fuels, additive of saturated steam; – impossibility of feeding of hopper during work of complex. 	<ul style="list-style-type: none"> – comparatively high temperature of gas; – difficulties at cleaning the grate from ash. 	<ul style="list-style-type: none"> – big height of gasifier; – high temperature of gas; – more complicated service works.

Gasifier is the special installation intended for gasification of different kinds of organic fuel, including biomass. There are different types of gasifiers, each type has its advantages and disadvantages (see Table 2) [4]. Gasifiers vary by the type of fuel burning, the most popular are: updraft and downdraft gasification. Taking into consideration all the above stated advantages and

disadvantages, The team of The Gas Institute together with partners have developed gasifier of combined type, which includes both up-draft and down-draft gasification process. The purpose of this gasifier to receive more clear, high-caloric and universal producer gas.

This work is aiming the following:

- to investigate the working process of combined two-zone gasifier and its functioning on different kinds of solid biofuels;
- to determine the possibilities of power equipment to work on producer gas or on a mixture of producer and natural gas;
- to study operation modes of power equipment working on a mixture of natural and producer gas in combination 70% to 30%;
- to study the functioning of the piston electric engine which used as a fuel producer gas;
- to study the parameters of the power equipment working on generator gas.

2. DESCRIPTION OF GASIFIER

The gasifier complex GTP-3.0 is system designed for production of producer gas by gasification of solid biofuels (biomass)[5]. The wood chips and sunflower husk pellets are used as a fuel in this complex. Aiming the stable operation of the gasifier and sustainable quality of produced gas, the humidity level of raw material should not exceed 15%.

The gasifier has two-zone design, and combines two processes of the gasification – updraft and downdraft, such system allows to neutralize disadvantages of each method of gasification, and allows to receive more qualitative and caloric producer gas.

Also, this gasifier has continuous operation mode and is equipped with appropriate automation, which controls the frequency of gasifier feeding, temperature regime, air and producer gas consumption.

The maximum heat output this gasifier is 1.5 MW.

Producer gas received in this gasifier complex can be used as gaseous fuel for industrial furnaces, power boilers, drying stoves and other industrial equipment that is working on natural gas.

This technology gives possibility to completely substitute natural gas or burn mixture of natural gas and producer gases. For burning of gaseous mixture there is a need to change the burner for special burner device, which is designed to burn both natural gas and producer.

The gasifier complex consists of the next basic aggregates and units (Fig. 1 and Fig. 2):

1. the combined gasifier for solid fuel;
2. hopper of solid fuel;
3. fuel feeding conveyer;
4. sluice for fuel feeder;
5. conveyer of ash removal;
6. sluice feeder of ash removal;
7. ventilator for air input on combustion;
8. ventilator of cooling system of gasifier;
9. cyclone;
10. hopper of ash receiver;
11. power panel;
12. panel of automatic control system;
13. frame.

The prepared fuel is transported with conveyer from the fuel hopper inside the gasifier. The conveyer can be either flat-belt or screw type. The impermeability of gasifier is provided by fuel feeder sluice, where the fuel gets after conveyer.

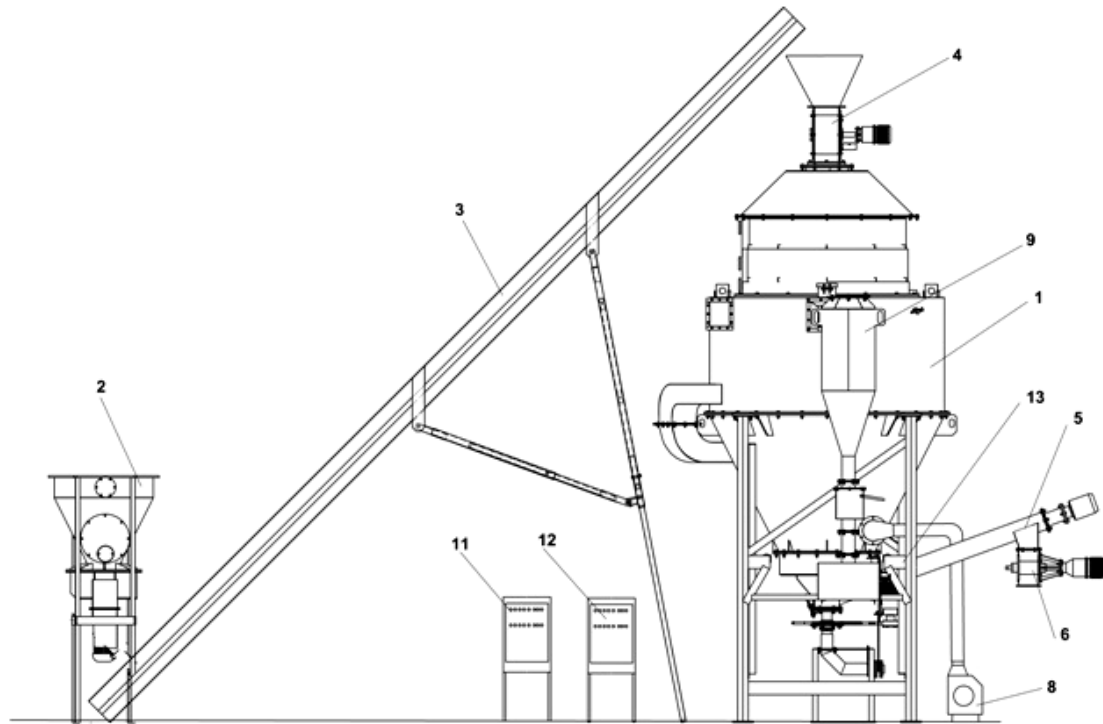


Fig. 1. General view of gasifier complex GTP-3.0

The gasifier is ready for ignition when it is filled with fuel to the appropriate level. The level of fuel is indicated by special level-sensors, which are located in the panel of automatic control system. For ignition in bulk of gasifier should be contain air rarefaction, which is created by means of producer gas-input ventilator. This rarefaction together with the air supplied by air-input ventilator provides quantity of air needed for combustion of solid fuel.

Cooling of gasifier and partial cooling of producer gas is provided by ventilator of cooling system of the gasifier.

Ignition of gasifier is executed through ignition nozzles of upper and down zones, these nozzles are closed after raw material was lit up with flame (300 sec).

Process of ash removal is conducted through the line of removal, which consist of conveyer of ash removal and sluice feeder of ash removal. Regulation of gasifier productivity is made by change of air rarefaction in nozzles of producer gas input.

Creation of producer gas is a result of raw material burning in the reactionary chamber of gasifier in conditions of oxygen deficit. There are next chemical reactions in the zone of burning (zone oxidant input) of zone of downdraft gasification[6]:



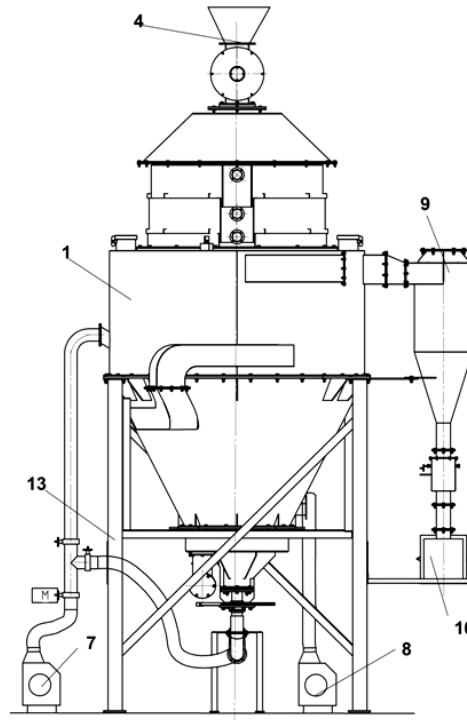


Fig.2. Front view of gasifier complex GTP-3.0

During this process a large amount of heat is produced. Byproducts of oxidation process are tars and other components that later on in low-temperature gasifier parts can condense and turn into pyrolysis tars. At the same time at the bound of combustion zone and renewal of downdraft zone (which is located lower than combustion zone), there goes dominated processes of oxidation of carbon and renewal processes [7]:



That means that CO_2 and water vapor (are products of reaction oxidation and internal moisture of fuel) recover in CO and H_2 , and released oxygen O_2 reacts with carbon of fuel.

Speed of reaction as well as quantity of producer gas is regulated by air supply owing to rarefaction process which is provided by ventilator of producer gas supply.

Functioning of this ventilator provides rarefaction in internal volume of the gasifier, which prevents producer gas to come out. The pressure of producer gas before burner at power rating does not exceed 5 kPa and is provided by ventilator of producer gas input.

Producer gas received in gasifiers is ready to be applied in power equipment. The Gas institute of National academy of science of Ukraine has designed special kind of burner that is working with producer, natural gas and mixture of these gases.

This gasifier complex also has cleaning system of producer gas, this system consists of a cyclone, horizontal and vertical camera of producer gas settling, disintegrator for separation moisture and tar particles, filter for catching small particles of tar and soot.

3. METHODOLOGY OF EXPERIMENT

The methodology of experiment with gasifier complex constricts of bench tests, conducted before final transfer of the complex to the customer. The given gasifier complex was tested on the next types of biofuel: wood chips and pelleted sunflower husks. Complex was working with each type of fuel continuously for 72 hours. The given gasifier complex is of permanent type, which is working continuously with periodic fuel recharge. All tests began with full load of fuel (wood chips or sunflower husks pellets), full load was indicated by sensors.

System has 3 sensors of load: upper level, middle level and lower level.

Solid fuel was transported from hopper via fuel feeder sluice (located on the top of gasifier) with help of fuel feeding conveyer. The sensors of fuel level are connected with panel of automatic control system, and indicate full load of fuel on appropriate level. Also they indicate lack of fuel and on such condition starts automatic mode of fuel reloading. When the fuel was appropriately load, there begging the process of ignition of gasifier. Ignition is made manually through special nozzles.

The upper zone of gasifier should be ignited first, in this zone goes downdraft process of gasification, then the down zone is ignited.

After the ignition was finished the ventilator starts its functioning and gives air into both lower and upper parts of the gasifier.

During the bench tests the main output of producer gas is blocked, and producer gas goes to the candle, where the gas is burnt for the period when the gasifier reaches its power rating (about 20-25 minutes).

The first test sampling of producer gas is made after gas had reached candle (about 5 minutes after the start of work), the next test sampling is made when producer gas is directed on the main power equipment.

In this research as main power equipment there were taken boiler DE-25-14GM [8] and piston electric engine JaMZ-236M2-7 [9].

When gasifier complex has reached its power rating producer gas has to be purified and only then it is directed to main power equipment.

The purification process is the next: received producer gas first was given into the cyclone, then into horizontal and vertical settling cameras, then via canal producer gas went through disintegrator and filter, only after these stages producer gas was ready to reach burner in industrial power boiler or piston electric engine [10].

The capacity of gasifier was regulated with air input, Power inflator regulated by air, the process of gasification. During the process of gasifier functioning the next parameters were under the control:

- temperature in gasifier reactors (with the help of thermocouples)
- pressure of air given into gasifier,
- pressure of gas after output of gasifier;
- pressure of gas before the burner of boiler.
- temperature of producer gas and its consumption before the burner of boiler.

Operation of boiler was started on natural gas, which was given to the special double-fuel burner developed by The Gas Institute of National academy of science of Ukraine, which has industrial power boiler resorted to natural gas that is supplied to the burner gas developed in the Institute of National Academy of Sciences of Ukraine, which has channels for natural gas, producer gas and channel for air.

The operation start of boiler on natural gas was carried in normal mode as prescribed in working instruction.

When the boiler has reached its nominal power there was started supply of producer gas directly to the working boiler, then there were taking test sampling of producer gas obtained from different types of fuel.

On the nominal power of gasifier operation the test sampling were taken every three hour. To simplify the control of the boiler, there was created special software for automatic boiler control, which allows checking of all the parameters of the boiler. Also this software adjusts modes and settings of the boiler for natural gas, producer gas and mixture of these gases.

During the bench tests there have been worked out all the modes of the boiler, according to the old regime card. Basing on test results there has been developed new regime card, in which there is described continuous operation of the boiler on mixture of natural and producer gases generating, in percentage of 70% to 30%.

In the same way there were tests with piston electric engine – producer gas was transferred into the engine. The engine was upgraded with new device of fuel delivery system. Operating on producer gas there was reached power of 45 kW, but the work was unstable. There were defined errors in engine assembling and the reasons of unstable operation. At the moment there are conducting works eliminate errors and upgrade the engine, we plan to make new tests with power engine working on producer gas.

4. RESULTS OF WORK

During these experiments there were obtained the next characteristics of producer gas that are presented in below tables (Table 3, Table 4):

Table 3. Composition of producer gas

No.	Components	Sample Sunflower husk	Sample Wood chips
1	H ₂	9.1	7.74
2	O ₂	0	0
3	N ₂	55.85	51.96
4	CH ₄	2.90	3.07
5	CO	13.0	23.76
6	CO ₂	11.96	9.70
7	C ₂ H ₄	3.83	0.89
8	C ₂ H ₆	0.26	0.21
9	C ₂ H ₂	0.59	0.04
10	C ₃ H ₆	0.30	0.18
11	C ₃ H ₈	0.03	0.06
12	iC ₄ H ₁₀	0.05	0
13	nC ₄ H ₁₀	0.17	0.13
12	H ₂ O	1.96	2.26
	Σ	100	100

Table 4. Power characteristics of producer gas

Parameter	Sample Sunflower husk	Sample Wood chips
Lower heating value, kcal/nm ³	1618	1420
Stoichiometric relationships	1.49	1.29
Theoretic temperature of combustion, K	1979.7	1921.5

The functioning of steam boiler is indicated in regime card of boiler that is set up for two gaseous fuels: natural gas and producer gas (from wood chips). Data of regime card is shown in Table 5

Table 5. Regime card of steam boiler DE-25-14 GM

№	Value	Sym bol	Unit of measure	Load			
				23 %	33 %	39 %	50 %
1	Steam consumption	D_{steam}	ton/hour	5.7	8.3	9.7	12.4
2	Steam pressure	P_{steam}	Bar	12	12	12	12
3	Consumption of natural gas	$B_{\text{n.g.}}$	m ³ /hour	320	510	616	814
4	Consumption of producer gas	$B_{\text{g.g.}}$	m ³ /hour	800	800	800	800
5	Lower heating value of natural gas	$Q_{\text{n.g.}}$	kcal/nm ³	8080	8080	8080	8080
6	Lower heating value of producer gas	$Q_{\text{g.g.}}$	kcal/nm ³	1212	1212	1212	1212
7	Coefficient of excess air	α		1.76	1.61	1.53	1.5
8	Carbon monoxide content	CO	mg/m ³	80	62	56	50
9	Nitric oxide content	NO _x	mg/m ³	120	132	140	148
10	Efficiency of steam boiler	η	%	90.2	91.7	92.3	92.7

5. CONCLUSIONS

There have been run experimental researches of functioning of gasifier of combined type with different kinds of biomass, namely on wood chips from coniferous woods and on sunflower husk.

Both kinds of a biomass were verified to be excellent alternative fuel, with high enough percentage of gasification, as the ash level rests 12% for wood chips and 8% sunflower husk.

The efficiency of gasifier and steam boiler with given biomass fuel made 82% and 92% accordingly, regardless biomass kind.

But taking into consideration that gasifier complex is situated in area where there are many woodworking factories – the decision was made to take wood chips as principal kind of a biomass for this gasifier.

Basic power characteristics of producer gas received from wood chips makes it alternative for natural gas. As it was revealed during the experiment producer gas can substitute up to 50% of natural gas with small loads of steam boiler. Also we have to note that efficiency of boiler working on mixture of producer and natural gas with consequent increase of boiler load does not fall below 90%. Owing to special burner device of double-fuel type. The reconstruction of steam boiler needs only fragmentary works not changing its overall structure and design.

The presented technology of biomass use as kind of alternative fuel has high potential either in Ukraine or in other European countries. This technology does not demand broad capital investments or technical decisions of re-equipment of operating machinery. But the main advantage of the technology is that it is real alternative for traditional kinds of fuel.



REFERENCES

1. *Energy strategy of Ukraine till 2030*. Website of the Ministry of Fuel and Energy of Ukraine. Link to the internet <<http://mpe.kmu.gov.ua/fuel/control/uk/doccatalog/list?currDir=50358>>.
2. V. ZHOVTYANSKY, M. KULIK, B. STOGNIY. *Energy strategy in Ukraine: Analyticity and reference materials in 2 volumes: General provisions of energy-savings* K.: Academperiodika, 2006. ISBN 966-360-047-0.
3. ANTOSHCHUK T.O., PYANYKH K.E. Experience of receiving and use of generating gas in power installations. Proceedings of Conference on Energy efficiency-2010, Kiev, Ukraine, 2010 October 19–21.
4. PYANYKH K.E., ANTOSHCHUK T.O. Production and use of the producer gas for the steam-boiler. Proceedings of Conference on Energy efficiency-2012, St.-Petersburg, Russia, 2012 May 29 – June 1.
5. Patent of Ukraine. Gas-generator of combined type of solid fuel, model №33861. 2008 July 10.
6. Patent of Ukraine. Gas-generator of combined type of solid fuel, model №34149. 2008 July 25.
7. Patent of Ukraine. Gas-generator of combined type of solid fuel, model №34150. 2008 July 25.
8. Product Catalog 2013. OJSC "Biysk Boiler Plant" JSC ("BiKZ"), Link to the internet <www.bikz.ru>
9. Product Catalog 2013. Spetsdizelservis" Ltd., OJSC "Avtodiesel" Yaroslavl Motor Plant, Link to the internet <www.sds.yaroslavl.ru/index.html>
10. *FAO forestry paper 72*. Wood gas as engine fuel. FAO1986 ISBN 92-5-102436-7.



CdTe THIN FILM SOLAR CELLS WITH NANOCRYSTALLINE ZnSe BUFFER LAYER

P. Dumitriu, T. Potlog

Moldova State University

A. Mateevici str. 60, MD 2009 Chisinau – Moldova

V. Mikli

Tallinn University of Technology,

Ehitajate tee 5, 19086 Tallinn – Estonia

V. Lughi, V. Sergio

University of Trieste

via Valerio 6a, 34127 Trieste – Italy

ABSTRACT

Nanocrystalline ZnSe films were prepared by close space sublimation method on SnO₂/ glass substrates to fabricate ZnSe/CdTe heterojunctions. The SnO₂: F film had a thickness of 500 nm, sheet resistance of <10 Ω/□. The SEM and XRD studies of ZnSe thin films on SnO₂/glass substrates show that the structure is cubic zincblende and nanograins sizes depend on the substrate temperature. The lattice parameter showed a dependence on substrate temperature. Because it is difficult the low resistive nanocrystalline ZnSe films to grow the immersion in a solution of ZnCl₂:H₂O were used to dope with chlorine. Effect of annealing and chlorine doping on the composition, structural and optical properties was studied. The EDS spectra of the immersed ZnSe films show the presence of chlorine in the films. Both ZnSe layers treated as well as activated were Zn deficient. The transmission and energy band gap of nanocrystalline ZnSe films decrease after annealing and ZnCl₂:H₂O doping. All ZnSe/CdTe photovoltaic cells were characterized through light and dark current density–voltage (J–V) measurements. The photovoltaic parameters of ZnSe/CdTe thin film solar cells improved after the immersion in a solution of ZnCl₂:H₂O and annealing at 400°C. The cell parameters obtained for the best device are $V_{oc} = 750$ mV, $FF = 43\%$, $J_{sc} = 20.39$ mA/cm², and $\eta = 6.6\%$.

Keywords: ZnSe thin films, ZnCl₂ activation, ZnSe/CdTe thin film solar cells

1. INTRODUCTION

A literature analysis reveals that attempts were made by several workers [1-6] in the past, to obtain reproducible ZnSe films for device applications. More progress has been achieved in fabrication of blue-green light emitting diodes, dielectric mirrors, filters, blue laser diode and other optically sensitive devices [7-12]. There are a number of reports on the different structural, optical and electrical properties of ZnSe polycrystalline thin films prepared by various techniques such as chemical vapour deposition, metal-organic chemical vapor deposition MOCVD, electrodeposition, photochemical deposition, chemical bath deposition (CBD), pulsed laser deposition and thermal evaporation [4–9, 13–15]. Because of its large band gap of 2.67 eV, ZnSe has been used as window layer for the fabrication of photovoltaic solar cells. The use of ZnSe films as a heterojunction partner in II-VI thin-film solar cells has been explored by T. L. Chu et al [16]. The ZnSe/CdTe solar cells grown by close spaced sublimation have yielded fairly good results with an efficiency of 11% [16]. The close spaced sublimation method is considered one of the most promising techniques for A2B6 thin film deposition. Therefore we have prepared the ZnSe thin films of different thickness by close space sublimation method at different substrate temperatures. The different structural parameters of these films were determined and the effect of substrate temperature is studied in this paper. CdTe is recognized as promising absorbers for thin-film photovoltaic devices because of

their near optimum direct band gap of ~ 1.5 eV and their high absorption coefficient. For the fabrication of the CdTe thin films the same method of deposition was used. Also, in this paper we will study ZnSe/CdTe thin film solar cells.

2. EXPERIMENTAL PROCEDURE

ZnSe films were deposited by close space sublimation technique. ZnSe and CdTe of 99.999% purity were used as source materials. The ZnSe thin films were deposited on glass substrate covered with SnO₂ at a system pressure of $\sim 10^{-6}$ Torr. The SnO₂ films were about 500 nm thick with a sheet resistance of 10 Ω/\square . In order to optimize the growth condition, ZnSe films were deposited at different substrate temperatures. The substrate temperature was maintained at 500 K to 650 K. Then the ZnSe films was immersed in ZnCl₂ solution and annealed in the vacuum at 400°C for 40 min. The ZnSe/CdTe thin-film photovoltaic heterojunctions were fabricated on glass substrates with an area of 2×2 cm² covered with a SnO₂ layer with a sheet resistivity of about 10 Ω/\square . We used the optimized component films to fabricate ZnSe/CdTe thin-film solar cells. The ZnSe/CdTe thin-film solar cells were fabricated in a superstrate configuration. The samples with as-grown ZnSe thin films obtained at substrate temperatures 500 K, 550 K, 600 K and 650 K denoted as (M5.1), (M6.1), (M7.1) and (M8.1), respectively. The samples with ZnSe chloride activated films obtained at substrate temperatures 500 K, 550 K, 600 K and 650 K signed as (M5.2), (M6.2), (M7.2) and (M8.2), respectively.

The structure of ZnSe films were examined with a Rigaku X-Ray Diffractometer (XRD) with CuK α_1 /40 kV/40 mA radiation source ($\lambda=1.54056$ Å), Ni filter, in the 2 θ range of 10–90°, scanning speed of 0.5°/min. The XRD analysis was performed using Rigaku software PDXL. The energy dispersive spectroscopy (EDS) analysis of the samples was performed with a JEOL JSM-6390LV scanning electron microscope. The optical transmission spectra were recorded using a JASCO V-670 spectrophotometer. The photovoltaic characteristics of ZnSe/CdTe thin film solar cells were investigated by current-voltage characteristic through the wide band gap components at the room temperature (300 K) and 100 mW/cm² illumination.

3. RESULTS AND DISCUSSIONS

3.1. Structural Analysis of CSS Nanostructured ZnSe thin films

The requirements for window layers in solar cells applications are high conductivity and adequate thickness in order to allow good transmission and uniformity which would avoid the effects of short cutting. Fig. 1 shows the SEM image of as-grown and after ZnCl₂ annealing of ZnSe films on SnO₂/glass substrates. From the SEM image it is clear that the ZnSe films are dense and pinhole free. The grain size is smaller than 1 μm in both cases. Sample M5.2 with ZnSe after ZnCl₂ activation at 400 °C shows a lot of round grains on the surface, and they did not coalesce together. No significant changes in morphology after annealing with the changing of the substrate temperature occurred in samples M6.2 and M7.2.

Fig. 2 shows XRD 2 θ scans, between 20° and 80°, for ZnSe/SnO₂/glass samples before and after ZnCl₂ activation. As seen, the XRD pattern exhibits intensive XRD peaks at 26.52°, 33.79°, 37.85°, 38.84, 42.55, 51.64, 54.51, 61.69, 71.04, 78.44 and 52° which are due to the X-ray diffraction from polycrystalline SnO₂ with tetragonal or orthorhombic structures [17] and four peaks with the smaller intensity for ZnSe phase presented in the Fig. 2. The X-ray diffraction measurements on the as-deposited films and ZnCl₂ treated indicated a cubic ZnSe phase. There is no evidence of formation of a new phase after ZnCl₂ annealing. The crystallite size was calculated using the Scherrer's formula from the full-width at half-maximum (FWHM) [10]:

$$D = \frac{k\lambda}{\beta \cos\theta} \quad (1)$$

where k is a dimensionless shape factor with a value close to unity, λ is the X-ray wavelength, β – the full-width at half-maximum.

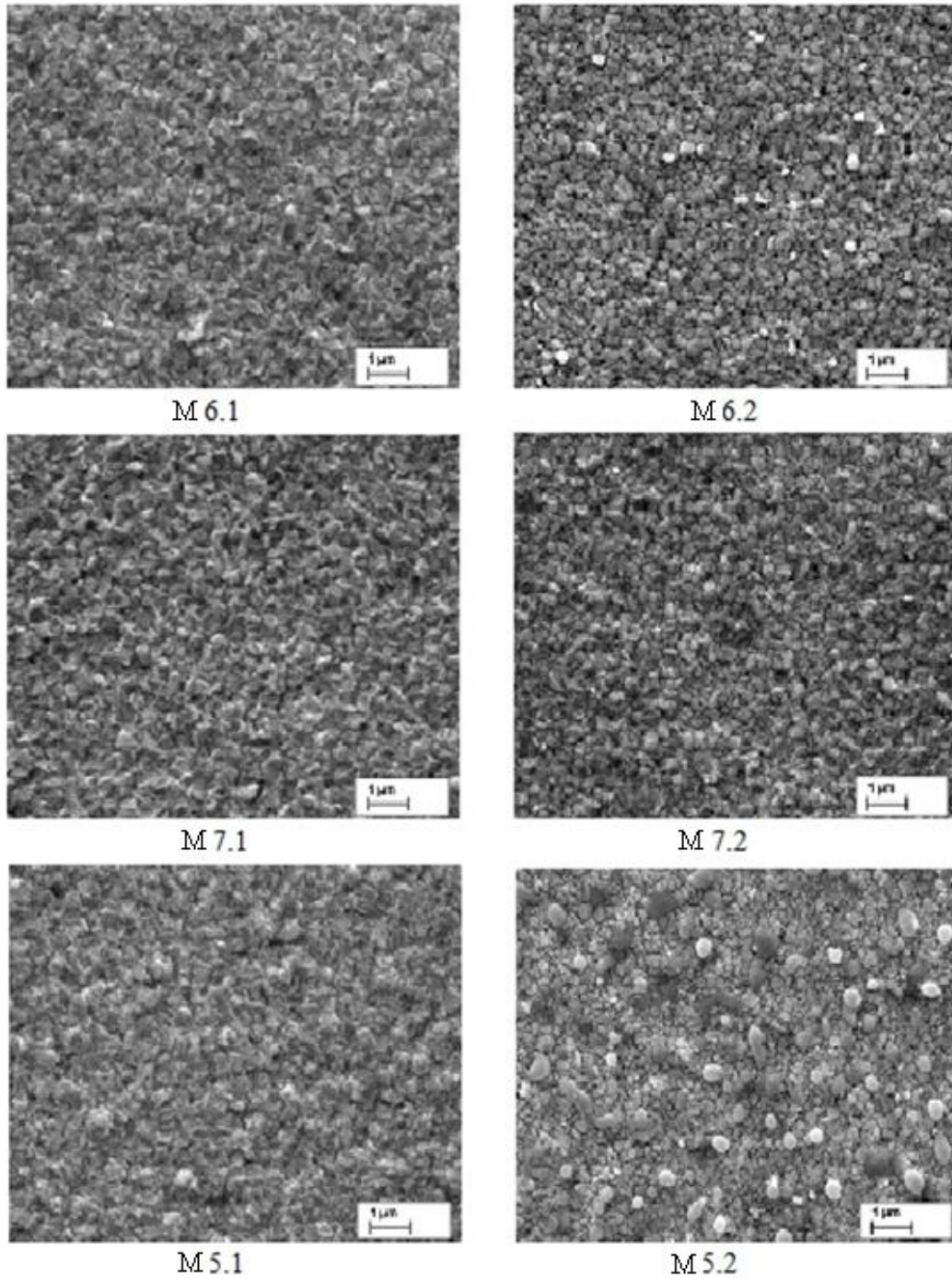


Fig. 1. SEM images of ZnSe films: M5.1, M6.1, M7.1 – as grown; M5.2, M6.2, M7.2 – after ZnCl_2 activation

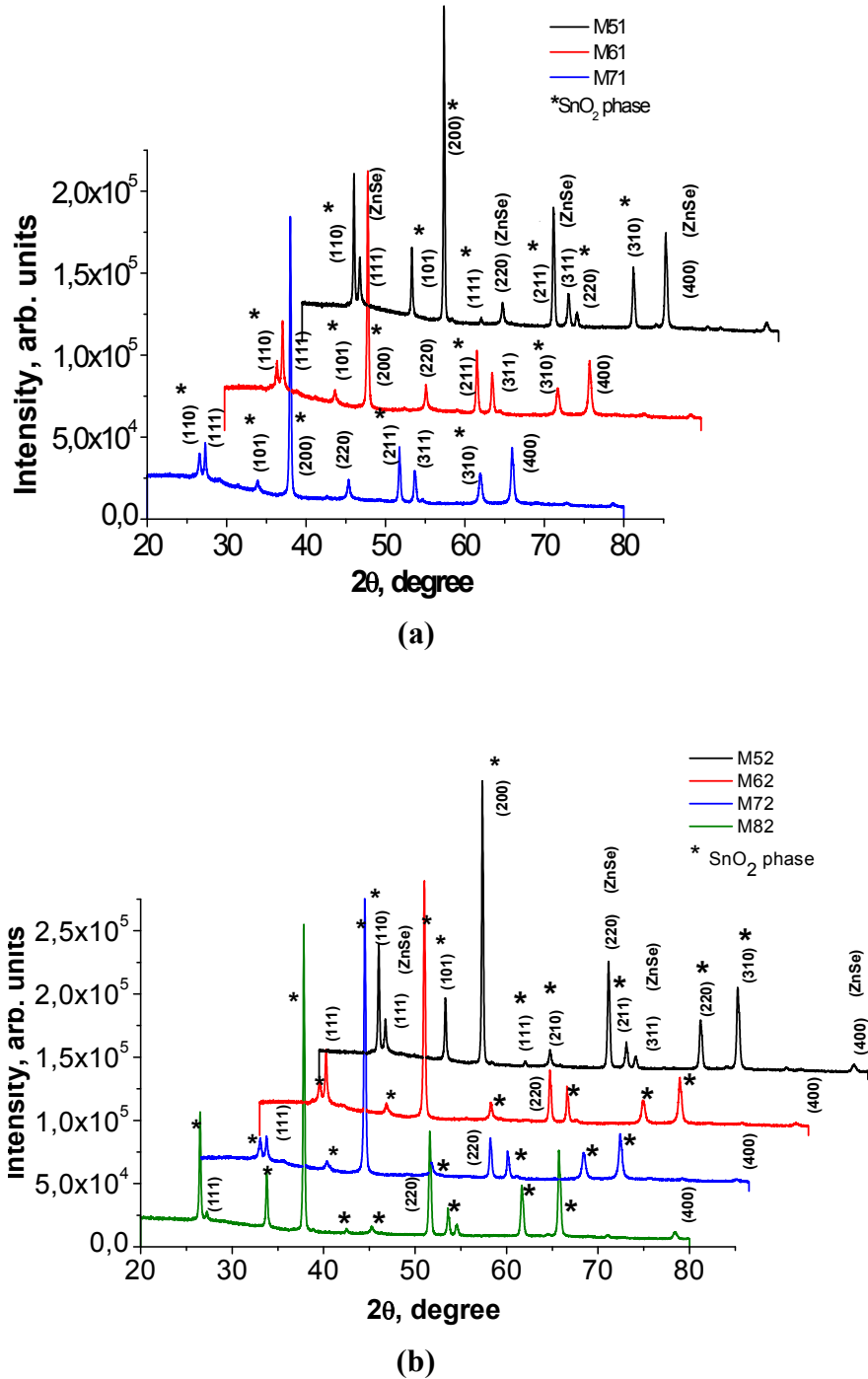


Fig. 2. X-ray diffraction patterns of as-grown (a) and after ZnCl₂ activation (b) ZnSe thin films at different substrate temperatures

The micro strain (ϵ) was calculated from formula [10]:

$$\epsilon = \beta \cos\theta/4 \quad (2)$$

where θ is Bragg angle.

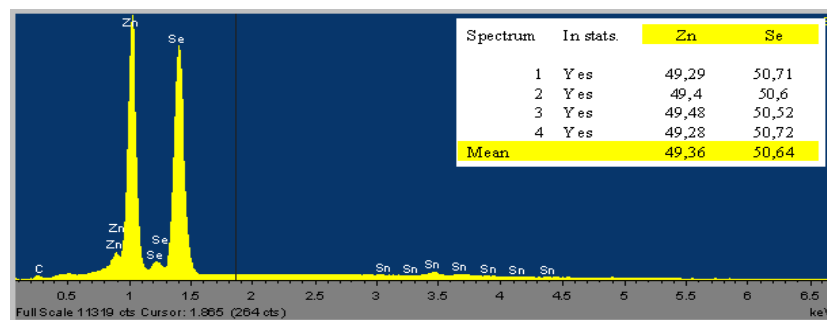
For all the activated samples the ZnSe phase presents a slight lattice-parameter decrease compared to the as-grown ones. The change of lattice constant for the as-deposited with substrate temperatures is not

very prominent and suggests that the film grains are stressed. This can be caused by the lattice mismatch and/or differences in the thermal expansion coefficients between the SnO₂ and the glass substrate.

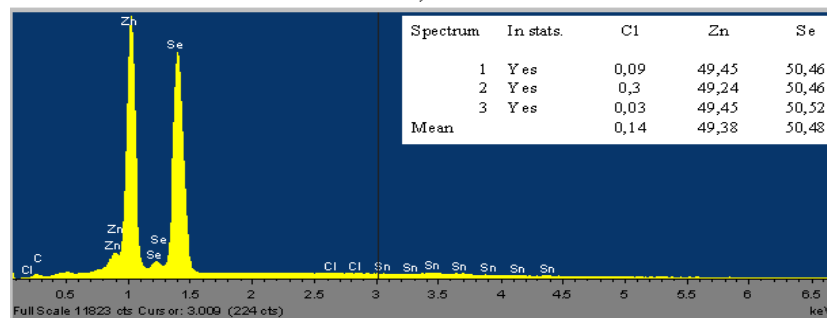
In Fig. 3 is presented energy dispersive X-ray (EDS) analysis of as-deposited and annealed ZnSe thin films obtained at T_s=600 K. The data for the other substrate temperatures are not shown as they all show very similar characteristics. Both the as-deposited and annealed ZnSe films are Zn-deficient as reported by other workers [18]. This is because the vapour pressure of Se is greater than that of Zn and their sticking coefficients are also different. The incorporation of chlorine in the activated ZnSe layers at substrate temperatures is confirmed by the detection of chlorine in a standardless EDS analysis.

Table 1. Structural parameters of as-grown and after ZnCl₂ activation ZnSe/SnO₂ thin films obtained at different substrate temperatures (T_s)

Samples	a(Å)	b(Å)	c(Å)	D, crystallite size (Å)	Strain (%)	Phase name
M51_as grown T _s =500 K	5.6707	5.6707	5.6707	280	0.10	Stilleite, syn
	4.7502	4.7502	3.1932	635	0.15	Cassiterite
M52_ ZnCl ₂ _activated T _s =500 K	4.7517	4.7517	3.1934	644	0.15	tin(IV) oxide
	5.6695	5.6695	5.6695	288	0.000000e+000	Stilleite, syn
M61_as grown T _s =550 K	4.7365	4.7365	3.1881	579	0.20	tin(IV) oxide
	5.6572	5.6572	5.6572	317	0.16	Stilleite, syn
M62_ ZnCl ₂ _activated T _s =550 K	5.6665	5.6665	5.6665	314	0.12	Stilleite, syn
	4.7391	4.7391	3.1905	583	0.20	tin(IV) oxide
M72_as grown T _s =600 K	5.6571	5.6572	5.6571	337	0.23	Stilleite, syn
	4.7392	4.7392	3.1871	647	0.21	tin(IV) oxide
M71_ ZnCl ₂ _activated T _s =600 K	4.738350	4.738350	3.195294	588	0.20	tin(IV) oxide
	5.666307	5.666307	5.666307	287	0.13	Stilleite, syn



a)



b)

Fig. 3. The EDS analyses of as-grown (a) and after ZnCl₂ activation (b) ZnSe thin films

3.2. Optical investigations of CSS Nanostructured ZnSe thin films

The optical transmission spectra of as deposited ZnSe thin films grown at different substrate temperatures were measured in the range of 400–1200 nm at T=300 K and shown in Fig. 4. The transmission slightly changes with the substrate temperature increase. The transmittance of the layers varies between 70%–90%, maximum of 90% being reached for ZnSe layer with a lower thickness – 236.79 Å. For ZnSe chlorine activated films transmittance is smaller. The absorption coefficient, α , was calculated from expression [19]:

$$\alpha = \frac{1}{d} \ln \frac{(1-R)^2}{T} \quad (3)$$

where d is the film thickness, and R and T represent the reflection and transmission coefficient, respectively. The thickness of the ZnSe layers was estimated using the following relation [20]:

$$d = \frac{\lambda_1 \lambda_2}{2(\lambda_1 n_2 - \lambda_2 n_1)} \quad (4)$$

where n_1 , and n_2 are the refractive indexes at two adjacent maxima (or minima) and λ_1 , λ_2 the respective wavelength values. The analysis of the $(\alpha h\nu)^2 = f(h\nu)$ plot of all ZnSe films is linear and it indicates a direct type of transition. The optical band gap values for as-deposited ZnSe films ranged between 2.686 eV (0.633 μm) and 2.690 eV (1.159 μm). The maximum value of E_g is connected with the very small size of crystallites in films. The thick films have a lower absorption value at the forbidden gap region of the ZnSe films. Thinner films have a high absorption value in the band-band absorption region. This effect may be explained by proposing that thicker films have bigger crystallites so they are closer to the crystalline ZnSe, but bigger crystallites sizes give results in larger unfilled inter-granular volumes so the absorption per unit thickness is reduced. One obvious result from the $(\alpha h\nu)^2 = f(h\nu)$ dependence (Fig. 5) for ZnSe films grown at different substrate temperatures and ZnCl₂ activated at 400°C is that the energy gap decreases.

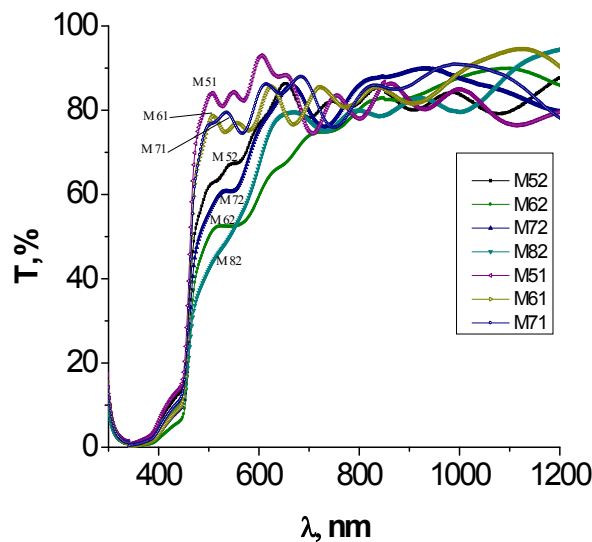


Fig. 4. The transmission spectra of as-grown (M5.1, M6.1, M7.1) and ZnCl₂ activated ZnSe thin films at different substrate temperatures

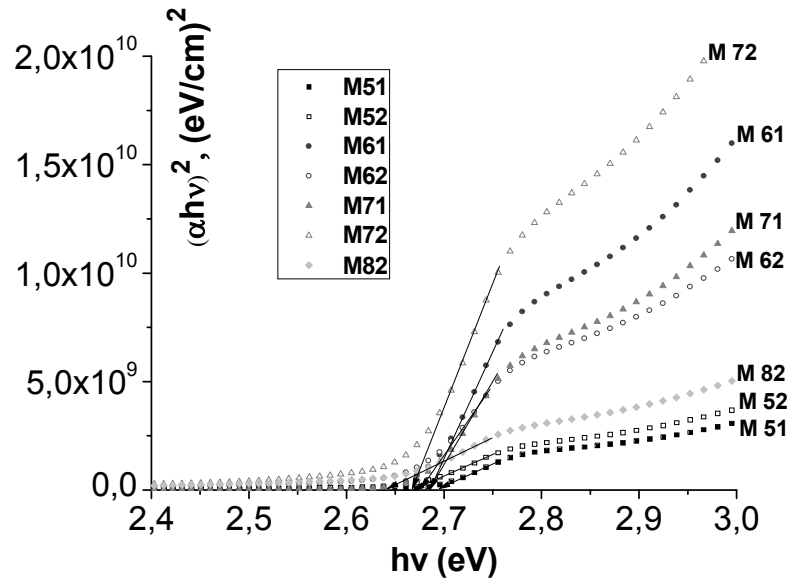


Fig. 5. The $(\alpha hv)^2$ vs photon energy (hv) spectra of as grown (M5.1, M6.1, M7.1) and $ZnCl_2$ activated ZnSe thin films at different substrate temperatures

The size of crystallites increases with the increase of the substrate temperatures and with $ZnCl_2$ activation. This is confirmed by the XRD analysis (Table 1). This is valid for all ZnSe films regardless of the substrate temperature.

Table 2. Optical parameters of as-grown and $ZnCl_2$ activated ZnSe thin films.

Samples	λ_1 , nm	λ_2 , nm	n_1	n_2	d, nm	E_g , eV
M5.1 $T_s = 500$ K as-grown	855	1003	2.511	2.488	1159.10	2.690
M5.2 $T_s = 500$ K annealed	908	1076	2.502	2.481	1167.07	2.667
M6.1 $T_s = 550$ K as-grown	914	1288	2.501	2.466	633.72	2.686
M6.2 $T_s = 550$ K annealed	1091	1422	2.479	2.46	948.98	2.672
M7.1 $T_s = 600$ K as-grown	999	1422	2.489	2.46	678.59	2.683
M7.2 $T_s = 600$ K annealed	937	1408	2.497	2.46	565.07	2.668
M8.2 $T_s = 650$ K annealed	846	1000	2.513	2.489	1098.26	2.640

3.3. Photovoltaic parameters of ZnSe/CdTe thin film solar cells

The photovoltaic characteristics of ZnSe/CdTe thin film solar cells were investigated through the wide band gap components at the room temperature (300 K) and 100 mW/cm^2 illumination. The

current density-voltage (J - V) characteristics of ZnSe/CdTe thin film solar cells with ZnSe activated at different substrate temperatures are illustrated in Fig. 6. The photovoltaic parameters are presented in Table 3. The highest efficiency 6.6 % was achieved for ZnSe/CdTe thin film solar cells with a thicker ZnSe activated buffer layer. As one can see from Table 3 the value of the open circuit voltage (U_{oc}) and the current density (J_{sc}) achieve 0.75 V and 20.39 mA/cm², respectively. The fill factor (FF) is low in general. According to the theory [21] the fill factor is determined by the series resistance, the saturated dark current density (J_o) and the diode quality factor (A).

Table 3. Photovoltaic parameters of ZnSe/CdTe solar cells.

Samples	T_s , K	J_{sc} , mA/cm ²	U_{oc} , V	FF	η , %	R_{sh} , $\Omega \cdot \text{cm}^2$	R_s , $\Omega \cdot \text{cm}^2$
M8.2	650	18.45	0.78	0.37	5.34	168.62	23.66
M7.2	600	10.70	0.74	0.42	3.30	333.33	30.30
M6.2	550	12.13	0.73	0.39	3.46	176.08	34.04
M5.2	500	20.39	0.75	0.43	6.61	380.00	17.02

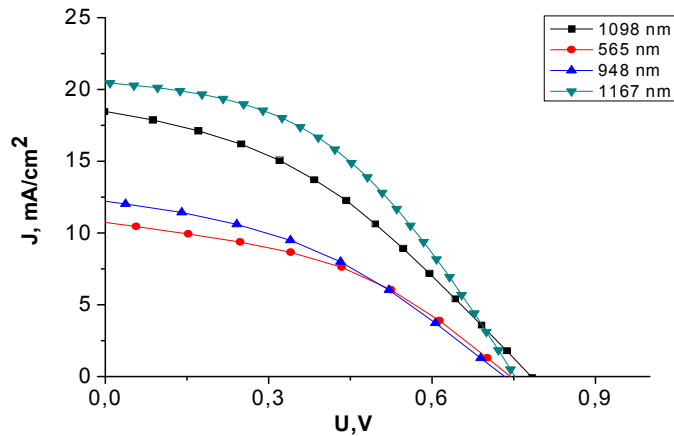


Fig. 6. The current density-voltage (J - V) characteristics of ZnSe/CdTe thin film solar cells with ZnSe activated at substrate temperatures

The dark J_o and A of the ZnSe/CdTe cells are in the range of $10^{-9} - 10^{-7}$ A/cm² and 1.7-3.6, respectively. The low value of FF is mainly determined by the high value of the series resistance which is due to the high resistivity of both ZnSe and CdTe thin films and probably to the fact that the cells wet CdCl₂ treatment may contain oxide on the surface of CdTe.

4. CONCLUSIONS

In situ ZnCl₂ activation promotes the increasing of the crystallites sizes and improvement of the photovoltaic parameters in ZnSe/CdTe thin film solar cells. Also, with the increasing of the substrate temperature the crystallites sizes increases from 280 nm (500 K) to 337 nm (600 K). The analysis of the XRD spectra of the ZnSe films established that activation in ZnCl₂ results in a slight lattice-parameter decrease compared to the as-grown ones. The energy dispersive X-ray (EDS) analysis showed that the as-grown and annealed ZnSe films are Zn-deficient. The transmission and the band gap energy of the ZnCl₂ activated ZnSe thin films decrease. The efficiency of 6.6 % for ZnSe/CdTe thin film solar cells with a ZnSe activated buffer layer was achieved.



ACKNOWLEDGEMENT

This research was supported by the EU 7th Framework Program PEOPLE International Research Staff Exchange Scheme project “Development of Flexible Single and Tandem II-VI Based High Efficiency Thin Film Solar Cells” GA-2008, No. 230861. We also acknowledge PhD student N. Maticiuic from Department of Materials Science, Tallinn University of Technology for X-ray and optical measurements.

REFERENCES

1. VENKATACHALAM, S.; AGILAN, S.; MANGALARAJ, D.; NARAYANDASS, Sa. K. Optoelectronic properties of ZnSe thin films. *Mat. Sci. Semicon. Proc.* Vol. 10, (July 2007), p. 128-132, ISSN 1369-8001.
2. KUMARESAN R., ICHIMURA M. and ARAI E. Photochemical Deposition of ZnSe Polycrystalline Thin Films and Their Characterization, *Thin Solid Films*, 414, 25, 2002.
3. LOKHANDE C.D.; PATIL P.S.; TRIBUTSCH H.; ENNAOUI A. ZnSe thin films by chemical bath deposition method. *Solar Energy Materials and Solar Cells*, V. 55, Nr .4, 1998, p. 379–393.
4. R.B. KALE, C.D. LOKHANDE. Influence of air annealing on the structural, morphological, optical and electrical properties of chemically deposited ZnSe thin films. *Appl. Surface Science*, V. 252, Iss. 4, 2005, p. 929–938.
5. LIANGYAN Chen, DAOLI Zhang, GUANGMEI Zhai, JIANBING Zhang. Comparative study of ZnSe thin films deposited from modified chemical bath solutions with ammonia-containing and ammonia-free precursors. *Materials Chemistry and Physics* V. 120, Iss. 2–3, 15 April 2010, p. 456–460.
6. G. PERNA, M. LASTELLA, M. AMBRICO, V. CAPOZZI. Temperature dependence of the optical properties of ZnSe films deposited on quartz substrate. *Appl. Physics A* , 2006, V. 83, Iss. 1, p. 127–130.
7. M.W. CHO, J.H. CHANG, H. WENISCH. YAO. Blue-Green Light Emitting Diodes with New p-Contact Layers: ZnSe/BeTe. *Phys. Stat. Solidi (a)* V.180, Iss.1, p. 217–223, 2000.
8. M. A. HAASE, J. QIU, J. D. DEP, H. CHENG Blue-Green Laser Diodes. *Applied Physics Letters* 59 (1991) 1272-1274.
9. T. L. CHU, S. S. CHU, Thin Film II-VI Photovoltaics, *Solid State Electronics*. 38 (1995), p. 533–549.
10. A. ENNAOUI, S. SIEBENTRITT, M.Ch. LUX-STEINER, R RIEDL, F. KARG, High Efficiency Cd-Free CIGSS Thin Film Solar Cells with Solution Grown Zinc Compound Buffer Layers, *Solar Energy Materials and Solar Cells* 67, (2001), p. 31–40.
11. SHIMIZU A, CHAISITSAK S, SUGIYAMA T, YAMADA A, and KONGAI M., Zinc-based buffer layer in the Cu(InGa)Se₂ thin film solar cells. *Thin Solid Films*, 361-362: 193–197, (2002).
12. GOKHALE, MILIND R, OMVPE growth and characterization of ZnSe based materials for blue-green laser applications (1995). *Doctoral Dissertations*. Paper AAI9605510. Link to the internet
<<http://digitalcommons.uconn.edu/dissertations/AAI9605510>>
13. J. E. BERNARD, A ZUNGER Electronic Structure of ZnS, ZnSe, ZnTe and their Pseudobinary Alloys, *Physical Review* 36 (1987) 3199-3228.
14. G. GORDILLO, E. ROMERO, C. QUINONES, Study of Structural Properties of Zn(S, Se) Thin Films Deposited by Evaporation, 19th European Photovoltaic Solar Energy Conference, (2004), p. 1780–1783.



15. S. ARMSTRONG, P.K. DATTA, RW. MILES, Properties of Zinc Sulphur Selenide Deposited using a Close-Spaced Sublimation Method, *Thin Solid Films* 403- 404 (2002), p. 126–129.
16. T. L. CHU, SHIRLEY S. CHU, G. CHEN, J. BRITT, C. FERKIDES et al. Zinc selenide films and heterojunctions. *J. Appl. Phys.* 71, 3865 (1992), p.3865–3869.
17. JCPDS X-ray powder files data (Data file 05–0522).
18. G. HODES, in: I. RUBINSTEIN (Ed.), *Physical electrochemistry: Principles, Methods and Applications*, Marcel Dekker Inc., New York, 1995, p. 515–554.
19. ESTRELLA V. NAIR M.T.S. and NAIR P.K., *Semicond. Sci. Technol.* 18, (2003), p. 190.
20. EZEMA F.I., EZUGWU S.C., OSUJI R.U., ASOGWA P.U., EZEKOYE B.A., EKWEALOR A.B.C., and OGBU M.P., *J. Non-Oxide Glasses* 1 (1), (2010), 45.
21. S. M. SZE, *Physics of Semiconductor Devices*, Publ. John Wiley & Sons Inc. (1981).

INTEGRATION AND OPTIMIZATION OF RENEWABLE ENERGY SOURCES IN A LOW ENERGY HOUSE

R. Džiugaitė-Tumėnienė, V. Jankauskas

*Vilnius Gediminas Technical University
Saulėtekio str. 11, LT-10223 Vilnius – Lithuania*

ABSTRACT

This article describes a method for an integration and optimization of renewable energy resources in a low energy house at the conceptual design stage. A multi-energy system, which uses a combination of renewable and non-renewable energy sources to cover the thermal and electric loads of the low energy house, is introduced. The method suggested in the paper is based on the energy hub concept. This approach allows the coupling between the energy demand and the energy supply in the building to be modelled in a synthetic way.

First, the energy demand side parameters are analysed. A model of the low energy house has been created in DesignBuilder and validated using measured data. Using this model, a database of different multi-energy system configurations has been selected and used to train and validate the chosen Building Energy Hub method. This method allows analysing building energy demand and energy supply sequentially, which helps to understand the relationship between the energy inputs and outputs more clearly. Finally, this paper presents a case study on the optimal configuration of multi-energy system that minimises the use of non-renewable sources.

Keywords: low energy house, renewable energy resources, multi-energy system, integration, optimization, building energy hub

1. INTRODUCTION

Over the past decade the European Union is facing unprecedented energy challenges resulting from increased import dependency, concerns over supplies of fossil fuels worldwide and a clearly discernible climate change. In spite of this, Europe continues to waste at least 20% of its energy due to inefficiency. In recent years energy efficiency has improved considerably, however it is still technically and economically feasible to save at least 20% of total primary energy by 2020. Partly because of its large share of total consumption, the largest cost-effective savings potential lies in the residential (households) and commercial buildings sector (tertiary sector), where the full potential is now estimated to be around 27% and 30% of energy use, respectively [1]. Therefore, the increase of energy efficiency and of the energy use from renewable sources is identified as a top priority [2].

The promotion of the use of renewable energy sources in the built environment has led to the spread of multi-energy systems in buildings. However, the design of such systems is a complex task with a large number of design variables and constraints. Therefore, the optimization methods are widely used in order to significantly reduce non-renewable energy consumption, define the optimal configuration of the multi-energy system of the building, and maintain a comfortable indoor environment [3-10].

This paper focus on two main objectives:

- to maximize the use of renewable energy sources in building,
- to reduce the environmental impact of the building.

An object of this study is a multi-energy system of a low energy residential house with integrated renewable energy sources.

2. METHODOLOGY

2.1. The energy hub concept

The energy hub concept was first introduced in 2004 by a research team at the Power System and High Voltage Laboratories of the Zurich ETH led by Goran Andersson and Klaus Fröhlich. This team of researchers developed an integrated modelling framework to simulate and optimize highly interlinked energy systems for a future multi-carrier and multi-product network. The energy hub concept was developed within a European project named “Vision of future energy networks”, concerning the study and the optimization of a series of centralized units that transform, convert, store, and supply various forms of energy linked by a combined electrical, chemical, and thermal energy interconnector [8].

In the energy hub approach, the energy inputs vector, namely the energy supply fluxes, is related to the energy outputs vector that is the energy demands, by a coupling matrix. The coefficients of this matrix are functions of the efficiency of the various energy conversion systems and of the distribution of energy fluxes in the energy generators. As a result, this model provides the best combination of the energy supply fluxes for a fixed, given configuration of the energy system and the optimal configuration of the energy system. The main advantage of the energy hub theory is optimization of any energy system fed by various energy sources under a certain set of assumptions [8]. The use and development of the energy hub concept is growing rapidly. Geidl [11] developed a series of algebraic relations in order to couple system inputs and outputs. Many applications of this concept were focused on the problem of studying and optimizing the electric energy networks. However, Fabrizio [12] extended the applicability of the concept to the building sector. The building energy hub modelling framework has been introduced by Fabrizio et al. [13, 14] in order to size the multi-energy system of the building. Recently, Bayraktar and Fabrizio [8] presented the extended building energy hub concept, which is used for the simultaneous optimization of energy demand and energy supply in buildings. The extended building energy hub extends the set of decision variables of the optimization problem to the relevant aspects of the thermal design in the building.

2.2. Application of the energy hub model to optimize multi-energy system of a case study building

The theoretical background of the applications of the coupling algorithm to model multi-energy systems in buildings is presented by Fabrizio et al. [12]. Therefore, this section introduces the methodology of the optimization of multi-energy system, which is applied to a case study house.

2.2.1. Optimization framework

The optimization framework of this study is summarized in Fig. 1.

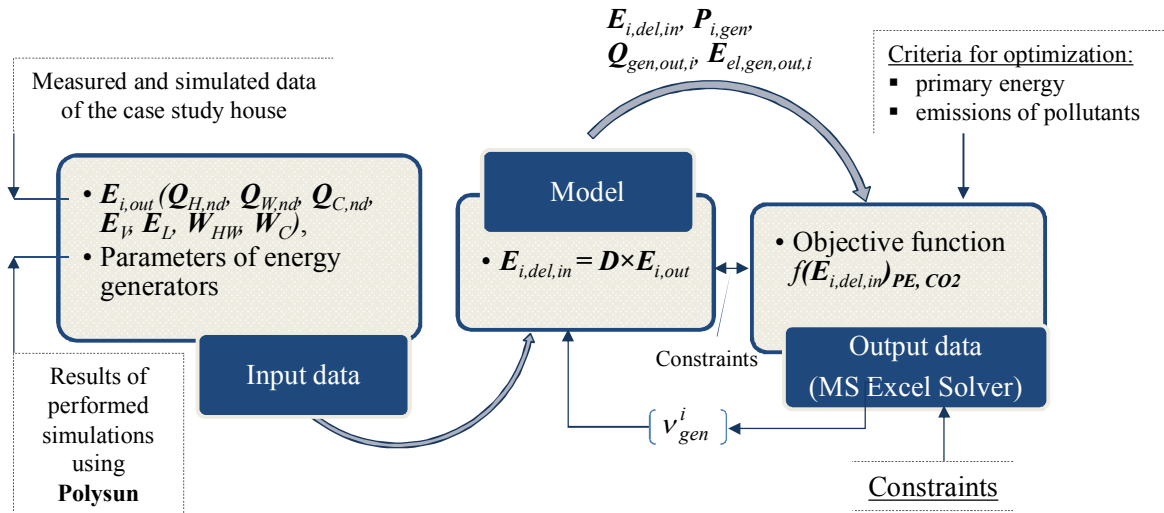


Fig. 1. Optimization framework applied to a case study

The framework consists of three main sequential steps: determination of input data, making the model and obtaining output data. First a model of the case study building has been created in Design Builder and validated using measured data (see section 3). The main parameters related to the energy demand side of the hub have been investigated, i.e. building thermal needs ($Q_{H,nd}$, $Q_{W,nd}$) and electrical energy demand for ventilation (E_V), lighting (E_L) and auxiliary energy for the thermal technical systems (W_{HW}). Then the possible configurations of the multi-energy systems of the house have been identified and simulated using the Swiss simulation program Polysun. The main parameters related to the performance of the selected energy generators have been got, i.e. energy conversion efficiencies of the generators ($\varepsilon_{i,gen}$, $SCOP_{i,gen}$). The formation of the energy hub model is the second step. The physical outputs ($E_{i,out}$) of the hub are one of the inputs of the model together with the parameters (values of efficiencies of energy generators). The model calculates the values of the delivered energy required for energy generators. These values are called energy- wares ($E_{i,del,in}$) at the input port of the hub. These output values of the model (the physical inputs of the hub) are the argument of an objective function to perform the selection. In this study two main objective functions have been defined by means of two selection criteria (maximum use of renewable energy sources, otherwise minimum use of non-renewable energy sources, and minimal emissions of pollutants). The main parameters, which express the selection criterion into a certain objective function, have been defined, i.e. primary energy demand and CO₂ emissions to the environment. Primary energy and CO₂ conversion factors are taken from [15] source. These factors are based on 17 European countries and used in the calculations. MS Excel Solver has been used during optimization process. The solver has iteratively to search for the optimal combination of energy generators that best minimize the objective function.

2.2.2. Mathematical expression of the energy hub model

When the vectors of building energy needs ($E_{i,out}$) and energy-ware ($E_{i,del,in}$) are defined, the coupling between the energy demand and the energy supply of the energy system of the building can be defined as:

$$E_{i,del,in} = D \times E_{i,out}, \quad (1)$$

where D is called a backward coupling matrix that is expressed as a function of the factors v_{gen}^i and energy efficiencies $\varepsilon_{i,gen}$ of energy generators:

$$D = f(v_{gen}^i, \varepsilon_{i,gen}), \quad (2)$$

where v_{gen}^i represents the ratio between the power flow on a line and the total power flow at the output.

In this study the possible combinations of the multi-energy system of the house can be written in a matrix form. The delivered energy to the building energy systems can be expressed as a function of building energy needs and of conversion efficiencies of the energy generators, as it is described by Fabrizio in equation 7.8 [12]. Principal scheme of the possible combinations of the multi-energy system of the house is presented in Fig. 3.

2.3. Design optimization of the multi-energy system of the house

2.3.1. The objective functions

One of the optimization functions of the building energy system is the minimization of a total primary energy consumption, which is expressed by equation:

$$f^{en} = f(E_{i,del,in})_{PE}. \quad (3)$$

Another optimization function of the building energy system is the minimization of emissions of pollutants (namely, carbon dioxide), which is expressed by equation:

$$f^{ev} = f(E_{i,del,in})_{CO_2} \quad (4)$$

2.3.2. Constraints of renewable energy sources

In this study solar energy is the main renewable energy source. In order to assess the solar energy properly and to avoid an overestimation of the energy input, the constraints have to be introduced. For this case, the simulation software Polysun has been used to simulate solar energy to the system of the house.

Polysun simulation software provides dynamic annual simulations of solar thermal systems and helps to optimise them. It operates with dynamic time steps from one second to one hour, thus simulation can be more stable and exact. The program is user friendly and the graphic-user interface permits a comfortable and clear input of all system parameters. All aspects of the simulation are based on physical models that work without empirical correlation terms. In addition the program performs economic viability analysis and ecological balance, which includes emissions from the eight most significant greenhouse gasses, thus the emissions of systems working only with conventional fuel and systems employing solar energy can be compared. Program Polysun was validated by Gantner (2000) and was found to be accurate to within 5-10% [20]. Considering a mean simulation time of 1 minute for a one-year simulation, the software Polysun is chosen to perform the analysis of solar thermal systems.

Sensitivity analysis of solar active parameters has been made (see section 3.3). In this case the period of analysis is one year. The optimal size of solar energy systems has been defined. The total delivered solar energy to the building energy system has been set in the model as the constraint.

2.3.3. Other constraints

Other constraints used in this study are:

- the efficiencies of energy generators are constant,
- the parameters in the objective functions (primary energy factors and emissions factors) are constant.

Mathematically, the problem of the optimization can be described as:

$$\begin{aligned}
 & \text{Minimize} && f(E_{i,del,in})_{PE,CO_2} && (5) \\
 & \text{Subject to constraints} && 0 \leq v_{gen}^i \leq 1, \quad \forall i \in \{\text{thermal, cool, electricity, ...}\}, \quad \forall gen = \{G1, \dots, Gn\}, \\
 & && \sum_{G=G1}^{Gn} v_{gen}^i = 1, \quad \forall i = \{\text{thermal, cool, electricity, ...}\}, \\
 & && E_{i,del,in} \geq 0, \quad \forall i = \{\text{wood, gas, electricity, ...}\}, \\
 & && E_{i,gen} \geq 0, \quad \forall gen = \{G1, \dots, Gn\}, \\
 & && \frac{E_{del,in}^s \cdot v_{SC}^t}{\varepsilon_{SC}} \leq 8605 \text{ kWh/a},
 \end{aligned}$$

where 8605 kWh/a is the maximum value of solar irradiation onto 7.2 m² area of the solar collectors and is defined using simulation software Polysun.

$$\frac{E_{del,in}^s \cdot v_{PV}^e}{\varepsilon_{PV}} \leq 264.6 \text{ kWh/a},$$

where 264.6 kWh/a is the required value of solar irradiation onto 1 m² area of the polycrystalline solar cells, in order to provide 34.4 kWh/a electricity demand. This value is defined using simulation software Polysun.

3. CASE STUDY

3.1. Description of a low energy house

The low energy house in this study is an existing individual family house with five residents. It is built in Vilnius. The main geographical and climatic data, also some relevant house features are shown in Table 1.

Table 1. Main features and climatic data of the house in Vilnius

Geographical and climatic data		House features	
Latitude	N 54° 41'	Total floor area	153.50 m ² (one floor)
Longitude	E 25° 19'		
Degree days	4837 ($\theta_i=23$ °C)	Heated area	153.50 m ²
Average yearly temperature	6.7 °C	Total volume	452.39 m ³
Lowest outdoor air temperature	-23 °C	Orientation of entrance	North-East

The thermal conductivity of the house components are shown in Table 2.

Table 2. The thermal conductivity of house elements

House component	Thermal conductivity (W/m ² K)
External walls	0.120
Roof	0.087
Floor	0.111
Windows	0.802
External door	1.20

Linear thermal conductivity of thermal bridge:	(W/mK)
outside corner	-0.114
roof	-0.095
floor slab	-0.153
window	0.035

As can be seen from Table 2, the super insulation is used to significantly reduce the heat transfer through the walls, roof and floor compared to standard residential houses. The pressurization test for the studied house has been made. The results have shown that the actual measured air-tightness of the house construction is 0.6 h^{-1} at 50 Pa, resulting in approximately 0.05 h^{-1} external air infiltration rate under normal conditions.

3.2. The building energy demand side

Energy need represents energy need in a building for heating, cooling, ventilation, domestic hot water, lighting and appliances. Energy need for heating is caused by heat losses and is reduced by solar and internal heat gains. Net energy need is the energy need minus heat gains, i.e. thermal energy without any system losses needed to maintain indoor climate conditions. The electrical energy for the lighting and appliances is evaluated in this case study.

The actual performance of the house has been monitored from 2nd of October 2010 to 30th of April 2011. The main parameters (outdoor and indoor air temperatures, relative humidity, solar irradiation, indoor air pollution) have been measured. The heat balance of the monitored house for the heating period has been performed using EnergyPlus simulation tool, Passive House Planning Package (PHPP) calculation tool and the actual data of measurements. The methodology and the main results of the evaluation of the house heat and energy balance are described in the article of Dziugaite-Tumeniene et al. [16]. Thus, focusing on the optimization of the energy system of the house, the input data used for the energy demand of the house is shown in Table 3. Normalized data of measurements of the house is used for the building energy demand side in the energy hub.

Table 3. Energy demand of the house

Input data	Symbol, unit	Normalized measured data [16]
Outdoor air temperature	°C	Measured values
Indoor air temperature	°C	23
Transmission heat transfer	kWh/m ² a	51.7
Ventilation heat transfer by mechanical ventilation system	kWh/m ² a	2.95
Internal heat gains from persons	kWh/m ² a	3.10
Solar heat gains	kWh/m ² a	11.30
Recovered ventilation heat losses	kWh/m ² a	37.5
Annual heat demand	kWh/m ² a	40.3
Energy need for space heating	$Q_{H,nd}$, kWh/m ² a	37.4
Energy need for domestic hot water (DHW)	$Q_{W,nd}$, kWh/m ² a	29.1
Energy use for ventilation	E_v , kWh/m ² a	8.4
Energy use for lighting	E_L , kWh/m ² a	7.0
Energy use for appliances	E_A , kWh/m ² a	16.0
Solar irradiation onto 1 m ² collector (or solar cells) area	E_{sol} , kWh/m ²	1195

The monitored non-renewable primary energy demand for space heating, domestic hot water, fans, pumps, lighting (excluding appliances) is $120 \text{ kWh}_{PE}/\text{m}^2$ during heating season [16], which complies with the requirements for the low energy house. However, the energy balance of the

monitored house has shown that the potential energy savings can be achieved by optimizing the energy system of the house.

3.3. The building energy supply side

After the analysis of building energy demand, the optimal configuration of the multi-energy system is investigated. The multi-energy system of the house has to use more renewable energy sources and to cover the thermal and electric loads of the house with the maximum efficiency. Therefore, the various options of energy generators have been selected in order to find the optimal configuration of the multi-energy system. The chosen energy generators exploit solar energy, ground source, biomass and fossil fuels that are still integrated in the system. The overall combination of the multi-energy system and energy flows of the house are shown in Fig. 2.

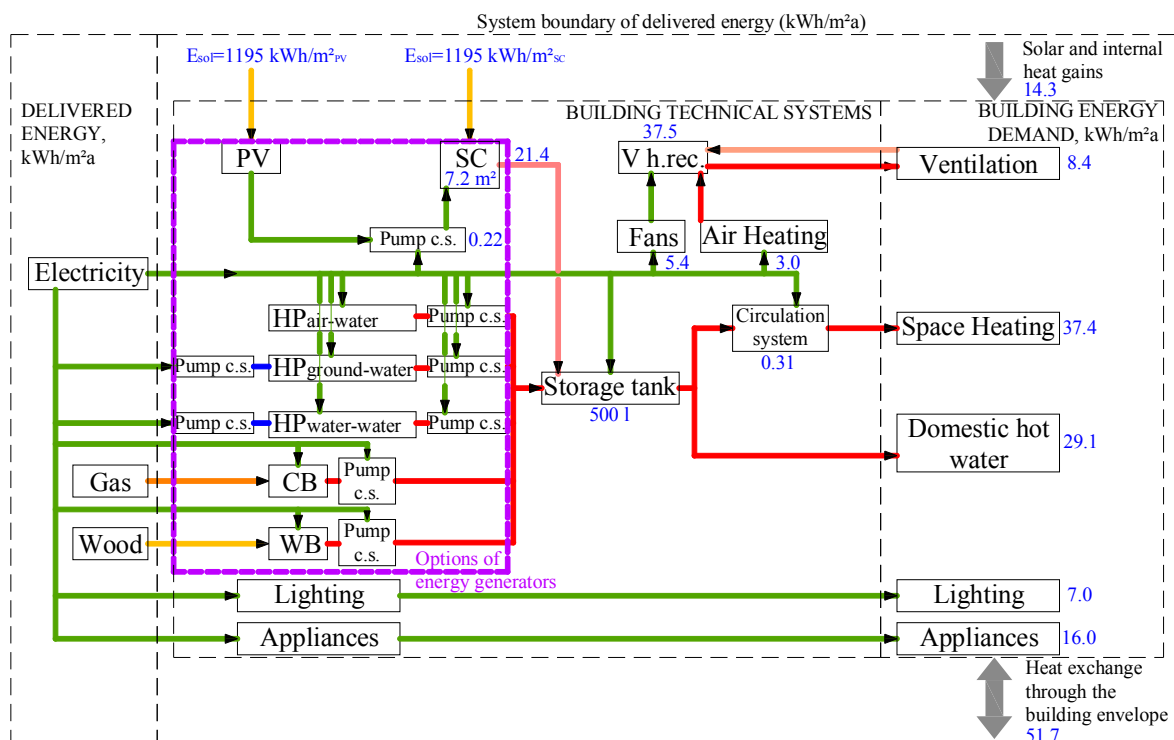


Fig. 2. The overall combination of the multi-energy system of the house

As can be seen from Fig. 2, the building energy supply side consists of selected building technical systems, which supply the amount of net energy needs of heating and electrical energy. In this case the building technical systems are: possible energy generators (different types of heat pumps, condensing boiler, biomass boiler, photovoltaic, solar collectors), storage tank, ventilation unit with heat recovery, and circulation systems. The energy used by the building technical systems is from delivered energy to the building or from on-site renewable energy (without fuels). Therefore, in this case delivered energy to the house is grid electricity, renewable (biomass) and non-renewable (natural gas) fuels. Energy from heat sources of heat pumps (air, ground, water) is also renewable energy, but calculation of delivered energy to heat pumps is based on the data of seasonal coefficient of performance (SCOP) of heat pumps. However, when the share of renewable energy is investigated, then energy taken from heat sources of heat pumps has to be evaluated in the calculations. Photovoltaic and solar collectors are on site renewable energy production systems, which reduce the need for the delivered energy to building. In this case on site renewable energy is not exported to energy networks.

3.3.1. Application of the energy hub to the case study house

The energy hub considered for this case study is presented in Fig. 3.

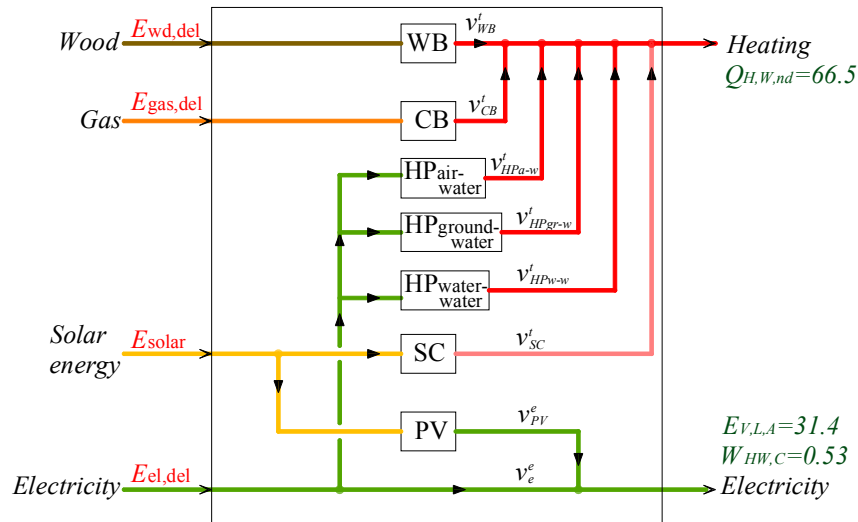


Fig. 3. The energy hub of the case study house

In this case the energy-warens at the input port are: wood, natural gas, solar energy and electricity from the grid. The combination of energy generators provides the possibility to meet the thermal and electrical loads. Thermal load can be met by: wood boiler (WB), condensing boiler (CB), air-to-water heat pump (HP_{a-w}), ground-to-water heat pump (HP_{gr-w}), water-water heat pump (HP_{w-w}), and solar collectors (SC). The electricity can be met by: electricity from the grid (e), photovoltaic system (PV).

The different combinations of multi-energy system have been studied and simulated extensively using the simulation program Polysun. The design efficiencies and mean seasonal efficiencies of the energy generators have been got from the results of the simulations and are presented in the Table 4.

Table 4. The design efficiencies and mean seasonal efficiencies of the energy generators

Energy generator	ε_{gen} , (%)	SCOP
	Simulated values	Simulated values
Wood boiler (WB)	70.9	–
Condensing boiler (CB)	79.7	–
Air-to-water heat pump (HP_{a-w})	–	2.3
Ground-to-water heat pump (HP_{gr-w})	–	3.3
Water-water heat pump (HP_{w-w})	–	3.2
Solar collectors (SC)	37.1	–
Photovoltaic system (PV)	13.0	–

Before the optimization of the multi-energy system of the house, the constraints for solar energy have to be added in the energy hub. Therefore, the sensitivity analysis of solar active parameters is presented in order to select the optimal solar collector and photovoltaic systems for the case study house.

3.3.2. Sensitivity analysis of solar active parameters

The solar collector system of the house has been simulated using Polysun software. The fixed parameters for the simulations are: climate conditions of Vilnius, good quality flat plate collectors, the insulation thickness of the storage tank is 80 mm; the main heating pipes are insulated with the thermal insulation of 40 mm. The main parameters used for sensitivity analysis of the solar collector system are: orientation, tilt angle, absorber area, and storage tank volume.

Solar collector orientation. According to Perednis and Kavaliauskas [17] the optimal orientation of solar collector is south. Deviation of 15° from the south direction to the east or west reduces the solar radiation to the collector surface about 2–4 %. When the deviation is more than 30° , then the solar radiation reduces 15 %. Therefore, the orientation of the solar collectors is not critical parameter. In this case the solar collectors are facing directly towards south.

Tilt angle. The study of Perednis and Kavaliauskas [17] shows that the tilt angle of the collectors to the horizon is $30\text{--}45^\circ$ from January till December, which causes about 15 % more efficient use of solar energy compared with the collectors, installed horizontally. Therefore, the tilt angle of the collectors is not critical factor. In this case the tilt angle of the collectors is 45° in order to increase the solar collector output over the year.

Solar collector area. The solar collector system of the house should obtain 100 % coverage during June to August. The energy demand during the summer only consists of DHW. Therefore, the measured energy demand for DHW, which is 372 kWh/per month (excluding storage tank losses), has been assumed in the selection of the solar collector system. The variation of the auxiliary energy demand for collector areas between 5.4 m^2 and 14.4 m^2 during the warm period is shown in Fig. 4.

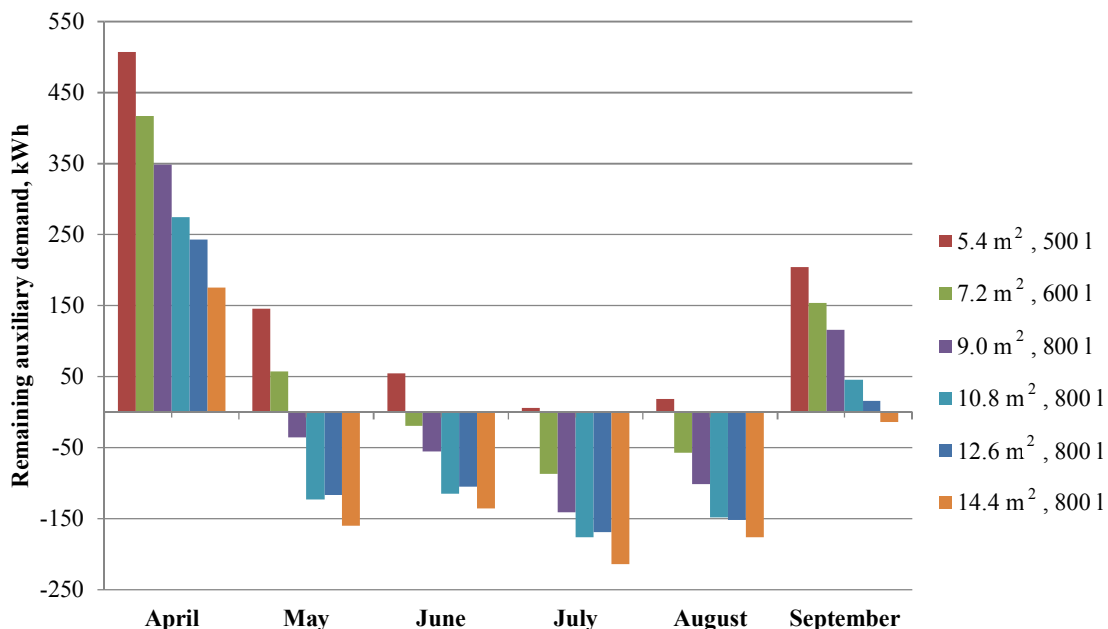


Fig. 4. The dependence of remaining auxiliary energy demand on the collector area during warm period

As can be seen from Fig. 4, the solar collector with 5.4 m^2 area is too small in order to get complete coverage during June to August. It can be seen that if the size of solar collector is increased from 9 m^2 to 14.4 m^2 , the auxiliary energy demand is covered from May to August.

However, the Fig. 4 shows that the solar system with the larger area of collectors will be overheated during the summer. The consequence of the system overheating is that the useful collector output drastically decreases when the area of the collector is increased. Also larger collector will produce non-useful waste heat during the summer, which is harmful for the solar collector. Due to this fact the optimal collector area is about 7.2 m^2 , which covers the energy demand for DHW during the summer months.

Storage tank size. The size of the storage tank is important, when the solar system is optimised. The influence of storage tank sizes on the heat generator energy and solar energy to the system for the 5.4 m^2 and 7.5 m^2 flat plate solar collectors is shown in Table 5.

Table 5. The influence of storage tank sizes on the heat generator energy and solar energy to the system

Solar collector area, m^2	5.4		7.2	
	Heat generator energy to the system (solar thermal energy not included), kWh/m^2	Solar energy to the system, kWh/m^2	Heat generator energy to the system (solar thermal energy not included), kWh/m^2	Solar energy to the system, kWh/m^2
Storage tank volume, m^3				
0.3	53.1	16.1	49.8	19.3
0.4	52.8	16.3	49.1	20.0
0.5	52.5	17.1	47.7	21.4
0.6	51.8	17.3	47.4	21.7
0.7	51.6	17.5	47.2	21.9
1.0	51.1	18.0	46.6	22.5

As can be seen from Table 5, utilization of the solar gains from the solar collector increases, when the bigger storage tank is used. However, this increase is not significant, thus 11 % in case of 5.4 m^2 of solar collector and 14 % in case of 7.2 m^2 of solar collector, when the size of storage tank increases from 0.3 m^3 to 1.0 m^3 . Also it is necessary to pay attention to the heat losses of the storage tank, which become larger when the size of the tank is increased. In this case the optimal size of storage tank for 7.2 m^2 of solar collector can be 0.5 m^3 , because the utilization of the solar gains remains almost constant when the size of storage tank increases from 0.5 m^3 to 1.0 m^3 .

Summary of the results. The overall energy demand for space heating, domestic hot water and energy supplied to the system by solar system and heat generator are shown in Fig. 5.

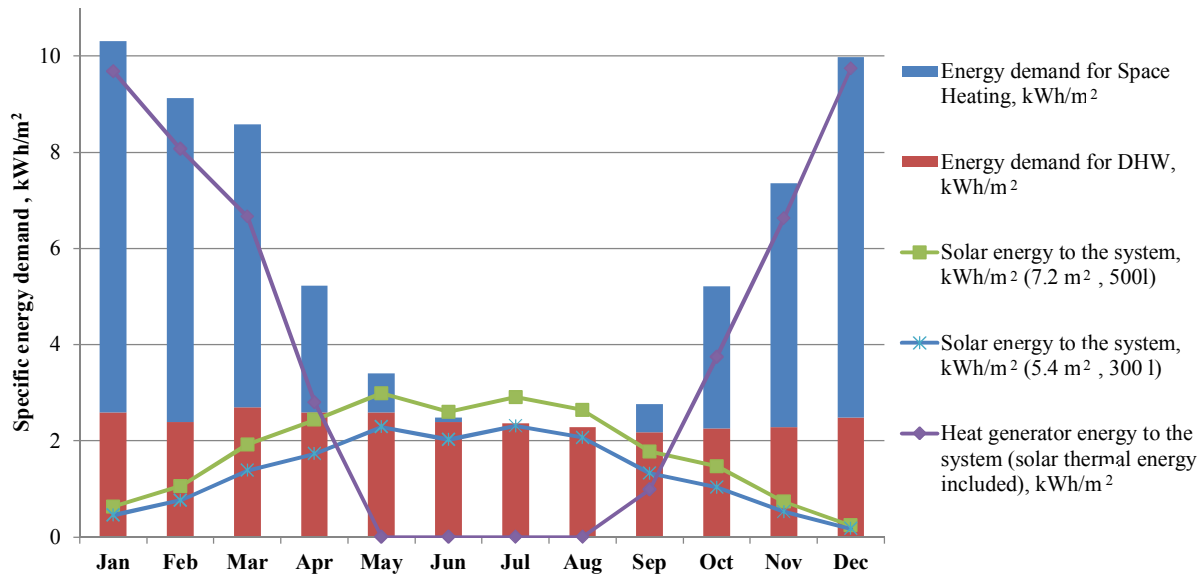


Fig. 5. Specific energy demand of the house

As can be seen from Fig. 5, the remaining auxiliary energy demand, covered by heat generator, is $48.3 \text{ kWh/m}^2\text{a}$, if 7.2 m^2 flat plate solar collectors are selected, which are tilted 45° with the 0.5 m^3 tank. The total annual solar energy to the system is $21.4 \text{ kWh/m}^2\text{a}$ (3281 kWh/a). Therefore, the total annual solar fraction of solar energy to the system is about 31 %. The corresponding annual solar fraction for the DHW coverage is about 68.5 %. In case, when the energy demand for DHW is lower than $372 \text{ kWh/per month}$, then the option of 5.4 m^2 flat plate solar collectors has to be considered.

3.3.3. The selection of photovoltaic system for the case study house

Photovoltaic (PV) energy is also an active use of solar energy, which uses the photovoltaic effect to convert sunlight into electricity. In this case the considered PV system is a stand-alone system, which consists of PV modules, battery charger, accumulator, inverter, inlet panel. Protogeropoulos et al. [18] outlined that when stand-alone renewable power supply system is being considered, an important design factor is its level of autonomy. Here autonomy is defined as the fraction of time, over a year of operation, for which the load can be met. Therefore, in this case the main consumer of electricity produced by PV system is a circulation pump of solar system. According to the uncertainty of solar radiation during the cold period, the water circulation system of solar collectors is the best choice to assure the autonomy for the PV system.

The photovoltaic system of the house has been simulated using Polysun software. The fixed parameters for the simulations are: climate conditions of Vilnius, polycrystalline solar cells, tilt angle is 45° , orientation is to the south.

The monthly solar radiation and the performance of PV system of the house is shown in Fig. 6.

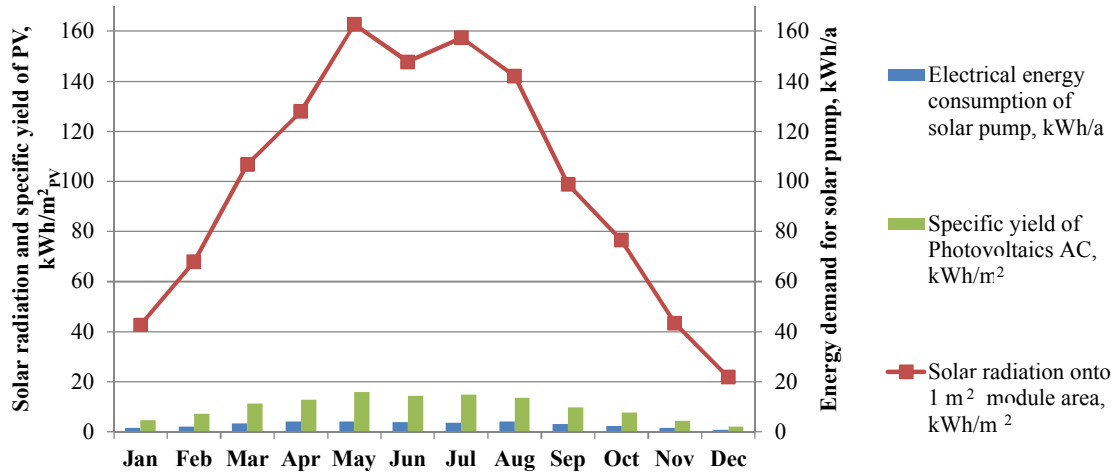


Fig. 6. Monthly solar radiation and performance of photovoltaic system

As can be seen from Fig. 6 that the polycrystalline solar cells of 1 m² with the efficiency of 13 %, covers the annual electricity demand (34.4 kWh/a) for the circulation pump of the solar system.

4. RESULTS

The optimization of the multi-energy system of the house has been performed using reduced gradient optimization algorithm developed by Lasdon et al. [19] and used to optimize nonlinear problems. This optimization method is integrated in a commercially available MS Excel Solver. In this paper the gradient of the reduced objective function of the problem is used to minimize two objectives: primary energy and emissions of pollutants (namely, CO₂).

The energy objective function has been defined by equation (4), where the weighting factors are the non-renewable primary energy factors [15]. The environmental objective function has been defined by equation (5), where the weighting factors are the carbon dioxide emission factors [15].

During the optimization process the constraints for renewable energy sources are foreseen:

- the total annual solar energy to the system is 3281 kWh/a,
- the photovoltaic system will provide electricity demand of 34.4 kWh/a.

The initial decision making matrix has been made and reported in Table 6. The initial guess is a system where all the loads are uniformly distributed over the various energy generators.

Table 6. Initial decision making matrix

Alternatives	Values of factors v	Criteria	
		(E _{i, del, in}) _{PE} , (kWh _{PE} /a)	(E _{i, del, in}) _{CO₂} , (kg _{CO₂} /a)
WB	0.167	336	103
CB	0.167	2433	527
HP _{a-w}	0.167	1738	318
HP _{gr-w}	0.167	1212	222
HP _{w-w}	0.167	1249	229
SC	0.167	0	0
Σ	1	–	–
PV	0.5	7540	2451
Electricity grid	0.5	5759	1054
Σ	1	–	–
Total	–	20268	4903

The optimal configuration of multi-energy system of the house is determined from the minimization of the energy and environmental objective functions or maximizing the share of renewable energy sources. The results of the optimization of the multi-energy system are reported and represented in Table 7.

Table 7. Decision making matrix with minimized values of objective functions

Alternatives	Values of factors v	Criteria	
		$\min f(E_{i, del, in})_{PE}$, (kWh _{PE} /a)	$\min f(E_{i, del, in})_{CO_2}$, (kg _{CO2} /a)
WB	0.69	1386	426
CB	0	0	0
HP _{a-w}	0	0	0
HP _{gr-w}	0	0	0
HP _{w-w}	0	0	0
SC	0.31	0	0
Σ	1	–	–
PV	0.007	106	34
Electricity grid	0.993	11437	2093
Σ	1	–	–
Total (kWh_{PE}/a)	–	12929	2106
Total (kWh_{PE}/m² a)	–	84.2	13.7

As can be seen from the results in Table 7, the optimal configuration of multi-energy system of the house is:

- solar collectors, which will provide 31 % of total annual energy demand for space heating and DHW,
- wood boiler (heating capacity is $P_{WB} = 10$ kW, design efficiency is $\varepsilon_{WB} = 70.9$ %, design temperatures of inlet/ return water are 35/30 °C), which will cover the remaining auxiliary energy demand for space heating and DHW,
- photovoltaic system, which will supply electricity for the circulation pump of solar system.

The final diagram of optimized energy flows is shown in Fig. 7.

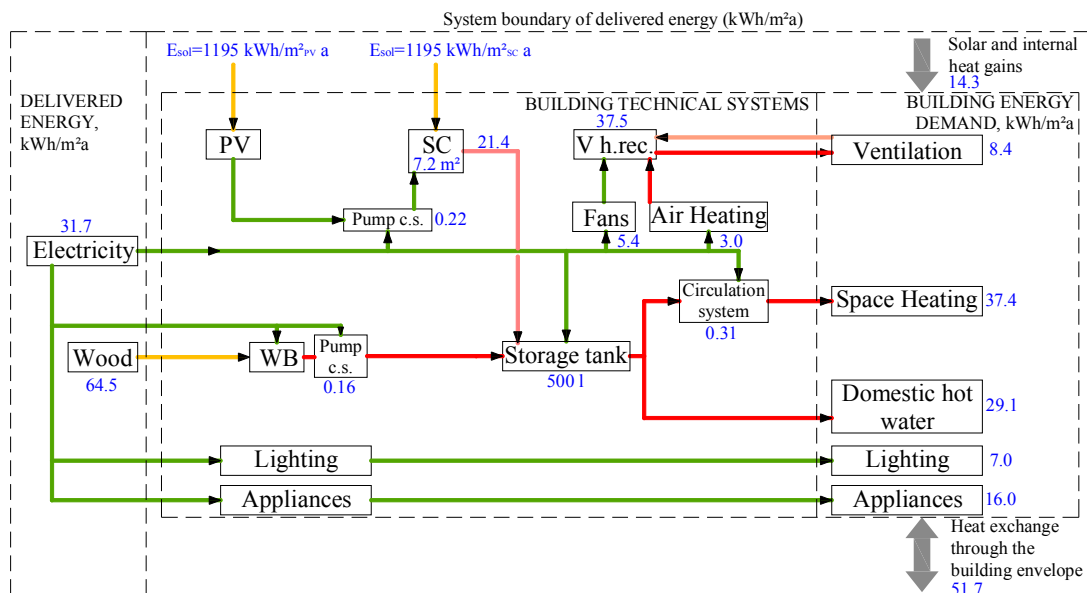


Fig. 7. An optimized multi-energy system of the house

The primary energy required for the case study house is 84.2 kWh/m² a, which is reduced comparing with the reference case (existing installed technical systems of the house) significantly. The consumption of non-renewable energy sources of the house is 27 % of the total consumed primary energy. However, it should be noted that the optimal configuration of multi-energy system could vary according to the defined objective functions and optimization criteria.

In order to get more reliable results of the optimization of the building energy system, the results are compared with the results achieved by Gajbert [21]. Gajbert presents the design solution of a solar combi system with a bio fuel boiler for a high performance residential building. The comparison of results of the case study and other similar survey is presented in Table 8.

Table 8. Comparison of results of the case study and other similar survey

Results	The case study – low energy single family house in Vilnius [16]	High performance apartment building in Stockholm [21]
1. Area of the building, m ²	153.5	1600 (16 apartments of 100 m ²)
2. Design outdoor temperature in winter, °C	-23	-16
3. Heating set point, °C	23	20
4. The thermal conductivity of:		
– External walls	0.120	0.270
– Roof	0.087	0.290
– Floor	0.111	0.300
– Windows	0.802	1.340
5. Air change, h ⁻¹	0.4	0.4
6. External infiltration, h ⁻¹	0.05	0.05
7. Energy efficiency of ventilation system, %	93.3	80
8. The efficiency of biomass boiler, %	70.9	85
9. Net energy demand, kWh/m ² a:	74.9	47.6
– mechanical systems (ventilation, circulating pumps)	8.7	5.0
– space heating	37.4	19
– domestic hot water	29.1	23.6
10. Energy use of technical building systems (system losses are excluded), kWh/m ² a:		
– electricity	8.7	5.0
– solar	21.4	17.3
– biomass	45.1	25.3
11. Delivered energy, kWh/m ² a:		
– electricity	8.7	5.0
– solar	0	0
– biomass	64.5	29.8
12. Non-renewable primary energy, kWh _{PE} /m ² a:	29.5	15.9
13. CO ₂ equivalent emissions, kg _{CO2} /m ² a	6.32	3.3

As can be seen from the Table 8, the main difference between the results is the net energy demand for space heating, which is 49 % higher in the case study. The main reason is that the measured value of energy demand for space heating has been used in the case study. The monitoring of the house of the case study showed that the high indoor air temperature was maintained due to the inefficient control of the heating system and the simulated values of internal heat gains were used in the evaluation of the heat balance of the house. Considering the presented

results, the solar energy system with the biomass boiler is a reasonable design solution in the early design stage of the building.

5. CONCLUSIONS

Recently, there is a great variation in design of multi-energy systems used today and it is difficult to find the best design of the building energy system. The integration of renewable energy sources into the multi-energy system makes this task even more complicated in the early design stage of the building. Therefore, before designing the multi-energy systems with integrated renewable energy sources, the main data has to be known: the building energy demand and its distribution over the year, the best auxiliary energy source for the concrete renewable energy system, or a system design that is suitable for combining renewable energy with the chosen auxiliary energy source, the design of the heating, ventilation, cooling systems, the main parameters of these systems and etc.

Considering these main challenges during the early design of the building energy system, the energy hub model has been applied to optimize multi-energy system of a case study building. After analyzing the results obtained by this method, the following conclusions can be deduced:

- The optimization of the multi-energy system of the house determines that the primary energy consumption of the house has been reduced 52 % comparing with the existing installed energy system of the house.
- The use of renewable energy sources has increased significantly. The main renewable energy sources are wood and solar energy, which cover 73 % of total primary energy used in the house.
- In case of the optimal multi-energy system of the house the environmental impact has been reduced by 46 %.
- The study presents that the energy hub model can be used as an appropriate method for the optimization of multi-energy systems in the early building design stage.

NOMENCLATURE

$E_{i,out}$ – input values of the building energy demand in the model (the physical outputs of the hub), kWh/m²a

$E_{i,del,in}$ – delivered energy, which is expressed per energy carrier i and supplied to the technical building systems through the system boundary (the physical inputs of the hub), kWh/m²a

$E_{el,gen,out,i}$ – electricity production of the generation device i , kWh/m²a

$Q_{H,nd}$ – energy need for space heating, kWh/m²a

$Q_{W,nd}$ – energy need for domestic hot water (DHW), kWh/m²a

$Q_{gen,out,i}$ – thermal output of the generation device i (thermal input required by the distribution systems fed by this generator), kWh/m²a

E_V – energy use for ventilation, kWh/m²a

E_L – energy use for lighting, kWh/m²a

E_A – energy use for appliances, kWh/m²a

W_{HW} – auxiliary energy of the heating and domestic hot water systems without generation, kWh/m²a

D – a backward coupling matrix

$P_{i,gen}$ – design power of energy generator i , kW



v_{gen}^i – the ratio between the power flow of the energy generator i on a line and the total power flow of the energy generator i at the output

$\varepsilon_{i,gen}$ – energy efficiency of energy generator i , %

$SCOP_{i,gen}$ – seasonal coefficient of performance of energy generator i

Subscripts

A – appliances

CO_2 – related to CO_2 emissions

H – heating

L – lighting

PE – primary energy

V – ventilation

W – hot water

del – delivered

el – electricity

gen – generator

i – dummy subscript

in – input

nd – need

out – output

Superscripts

en – related to primary energy use

ev – related to environmental impact

Abbreviations

DHW – domestic hot water

PHPP – Passive House Planning Package

SCOP – seasonal coefficient of performance

REFERENCES

1. Commission of the European Communities 2011. *Communication of commission: Energy Efficiency Plan 2011* [interactive]. COM(2011)109 final [referred on the 3th of March in 2013 y.]. Brussels. 15 p. Link to the internet <<http://eur-lex.europa.eu/LexUriServ/LexUriServ.do?uri=COM:2011:0109:FIN:EN:PDF>>
2. European Parliament and Council 2010. Directive 2010/31/EU of the European Parliament and of the Council of 19 may 2010 due on the energy performance of buildings. *Official Journal of the European Union* L153: 13–35.
3. BAMBROOK, S M., SPROUL, A.B., JACOB, D. Design optimisation for a low energy home in Sydney. *Energy and Buildings*, 2011, Vol. 43, No. 7, p. 1702–1711.
4. IHM, P., KRARTI, M. Design optimization of energy efficient residential buildings in Tunisia. *Building and Environment*, 2012, Vol. 58, p. 81–90.
5. KAYO, G., OOKA, R. Building energy system optimizations with utilization of waste heat from cogenerations by means of genetic algorithm. *Energy and Buildings*, 2010, Vol. 42, No. 7, p. 985–991.
6. LI, H., BURER, M., SONG, Z.-P., FAVRAT, D., MARECHAL, F. Green heating system: characteristics and illustration with multi-criteria optimization of an integrated energy system. *Energy*, 2004, Vol. 29, No. 2, p. 225–244.



7. LUNA-RUBIO, R., TREJO-PEREA, M., VARGAS-VÁZQUEZ, D., RÍOS-MORENO, G.J. Optimal sizing of renewable hybrids energy systems: A review of methodologies. *Solar Energy*, 2012, Vol. 86, No. 4, p. 1077–1088.
8. BAYRAKTAR, M., FABRIZIO, E., PERINO, M. The “extended building energy hub”: A new method for the simultaneous optimization of energy demand and energy supply in buildings. *HVAC&R Research*, 2012, Vol. 18, No. 1-2, p. 67–87.
9. OOKA, R., KOMAMURA, K. Optimal design method for building energy systems using genetic algorithms. *Building and Environment*, 2009, Vol. No. 7, p. 1538–1544.
10. PELET, X., FAVRAT, D., LEYLAND, G. Multiobjective optimisation of integrated energy systems for remote communities considering economics and CO₂ emissions. *International Journal of Thermal Sciences*, 2005, Vol. 44, No. 12, p. 1180–1189.
11. GEIDL, Martin. *Integrated modelling and optimization of multi-carrier energy systems*. Doctoral thesis. ETH (Swiss Federal Institute of Technology) Zurich: 2007. 125 p.
12. FABRIZIO, Enrico. *Modelling of multi-energy systems in buildings*. Doctoral thesis. Politecnico di Torino & Institut National des Sciences Appliquees de Lyons, Torino: 2008. 170 p.
13. FABRIZIO, E., FILIPPI, M., VIRGONE, J. An hourly modelling framework for the assessment of energy sources exploitation and energy converters selection and sizing in buildings. *Energy and Buildings*, 2009, Vol. 41, No. 10, p. 1037–50.
14. FABRIZIO, E., CORRADO, V., FILIPPI, M. A model to design and optimize multi-energy systems in buildings at the design concept stage. *Renewable Energy*, 2010, Vol. 35, No. 3, p. 644–55.
15. HASTINGS, Robert S., WALL, Maria. *Sustainable Solar Housing: Volume 1 - Strategies and Solutions*. London: Sterling, VA, 2007. 315 p. ISBN-13: 978-1-84407-325-2.
16. DZIUGAITE-TUMENIENE, R., JANKAUSKAS, V., MOTUZIENE, V. Energy balance of a low energy house. *Journal of Civil Engineering and Management*, 2012, Vol. 18, p. 369–377.
17. PEREDNIS, E., KAVALIAUSKAS, A. Investigation of solar energy usage for heat production in Lithuania. *Energetika*, 2005, Vol. 4, p. 49–53.
18. PROTOGEROPOULOS, C., BRINKWORTH, B.J., MARSHALL, R.H. Sizing and techno-economical optimization for hybrid solar photovoltaic / wind power systems with battery storage. *International Journal of Energy Research*, 1997, Vol. 21, p. 465–479.
19. LASDON L.S., WARREN A.D., JAIN A., RATNER M. *Design and testing of a generalized reduced gradient code for nonlinear programming*. ACM Transactions on Mathematical Software, 1987. 45 p. ISSN 0098-3500.
20. SORENSEN, Bent, BREEZE, Paul, SUPPES, Galen, J., BASSAM, Nasir El, SILVEIRA, Semida, YANG, Shang-Tian, ROSA, Aldo, V., GUPTA, Harsh, K., ROY, Sukanta, DOBLE, Mukesh, BROUSSELY, Michel, MAEGAARD, Preben, BARBIR, Frano, PISTOIA, Gianfranco, KALOGIROU, Soteris, STORVICK, Truman. *Renewable Energy Focus Handbook, 1st Edition*. Oxford: Elsevier, 2009. 528 p. ISBN 978-0-12-374705-1.
21. GAJBERT, Helena. *Solar thermal energy systems for building integration*. Licentiate thesis. Lund University, Lund: 2008. 308 p. ISBN 978-91-85147-29-8.



UTILIZATION OF TANJUNG FRUIT (*Mimusops elengi*) AS RENEWABLE ENERGY SOURCE FOR THE FUTURE

A. Fitriani, A. Purnomo

Semarang State University

Campus D5 FMIPA UNNES Sekaran Gunungpati Semarang

50229 - Indonesia

ABSTRACT

Mimusops elengi is a medium-sized evergreen tree found in India, Northern Australia, South Asia, Southeast Asia, Europe (Britain, Spain), and Africa. In Indonesia, it is usually planted on edges of roads as shade plants or a green plants and its common name is Tanjung. It produces many fruits which are, during this time, considered as wastes, not consumed by a society because it has no function and no economic value. Seeing that the number of its fruit is abundant, there arose desire to know the content of tanjung's fruits and look for their usefulness.

The result of glucose refractometer test showed that Tanjung's fruits are rich of glucose. The methods of tanjung bioethanol production are as follows: (1) Gelatinase, (2) Inoculation, (3) Fermentation, (4) Stratified distillation, and (5) Alcohol refractometer test. Gelatinase is a process to make Tanjung's fruits become smaller. Then, Tanjung's fruits are inoculated by 1 gram, 3 grams, and 5 grams of *Saccharomyces cerevisiae* during 24 hours, and fermentation process during 2, 4, 6, and 8 days. Ethanol resulted is not pure, so there is stratified distillation to split ethanol and water.

Based on this research findings, 160 grams of Tanjung's fruits can produce 3.5 ml of ethanol 83% with optimum fermentation are 6 days by using 1 gram of *Saccharomyces cerevisiae*. The main advantage of tanjung bioethanol is that tanjung fermentation can reach 13% of ethanol purity levels while molasses fermentation only reach 10% levels. It indicates that tanjung bioethanol have very significant potential to outperform molasses bioethanol which is now become E100 in Brazil. Besides that, tanjung bioethanol is made of fruit wastes which are guaranteed their sustainability of its material and Tanjung's fruits can also be found in many countries accross the world, and be very much deserved to be international renewable energy sources.

Keywords: utilization, tanjung fruits, renewable energy

1. INTRODUCTION

Mimusops elengi is a medium-sized evergreen tree found in tropical forests in South Asia, Southeast Asia (Indonesia, Malaysia, Sri Lanka, Burma, Philippines), India, Spanish, Europe, Africa, and Northern Australia. In English, the common names are Spanish cherry, Medlar, and Bullet wood. In India, the common names are Maulsary and Pogada.^[1] In Indonesia, the common name is Tanjung. In overseas countries, its timber is valuable, the fruit is edible, and it has also traditional medicinal uses^[2]. But in Indonesia, *Mimusops elengi* is just an evergreen tree and its fruit is has no function and it is just a waste.

Indonesia has so many potential natural resources and abundant agriculture products which can be used to innovate and create bioenergy.^[3] In Indonesia there are so many varied agricultural products, unfortunately they are never used maximally and even their function of the product is unknown.^[4] An example of it is Tanjung's fruits. Although the fruits can be found everywhere, not only found in Indonesia, but there is nobody who is interested to utilize the high potential of this fruits. During this time, Tanjung's trees are only used as shade plants or green plants along the highways and their fruits is just treated as wastes.^[5] Based on glucose refractometer test, Tanjung's fruits contain the high glucose so that it's very

much potential to produce ethanols. Ethanols can be used for vehicle engines as a substitute for gasoline or as a mixture with gasoline in a certain percentage. Even, Brazil has been using E100 (100% ethanol).

2. METHODOLOGY

Research objective: The objective of this study is to better identify whether Tanjung's fruit can result in ethanol, to know their process of tanjung bioethanol production, and to determine the yeast concentration for producing the optimum ethanol. There are 3 variables of this experiment. First, manipulated variables are yeast concentrations and fermentation time. Dependent variables are ethanol levels resulted. Control variables are matured Tanjung's fruits, mass of Tanjung's fruits, kind of yeast, the size of fermentation tool, distillator, fermentation room, the time of gelatinase, and the time of steam. There are six steps in this research, so it need so many tools and materials. The table below showed tools and materials which are needed in every steps of research.

Table 1. Tools and materials which are needed in every steps of research

No.	Steps	Tools	Materials
1.	Glucose, protein, and starch test of Tanjung's fruit	Beaker glass, test tube, tripod, refractometer glucose, burner.	Ripe Tanjung's fruit, water, benedict, biuret, lugol reagen.
2.	Gelatinase	Container, scales, pots, napkins, blender, stove, liter measuring cup, stopwatch.	Ripe Tanjung's fruit, water.
3.	Inoculation	Containerr, measuring cup capacity of 1 liter, 50 ml capacity measuring cup, wipes.	Meals of Tanjung's fruit, water, bread yeast (<i>Saccharomyces cereviseae</i>), 70% alcohol.
4.	Fermentation	Container, water hose, napkin, spoon, duct tape, scissors.	Inoculation results, 70% alcohol, water.
5.	Distillation	Distillation flask, water hoses, burners methylated, condenser, thermometer, strainer, scissors, paper towels, napkins, measuring cup capacity of 10 ml, 50 ml and 1 liter.	Ethanol of fermentation process, water, methylated, first distilled ethanol.
6.	Alcohol refraktometer test	Alcohol refractometer.	Ethanol which is resulted from stratified distillation.

The methods of Tanjung bioethanol production are (1) gelatinase, (2) inoculation, (3) fermentation, (4) stratified distillation, and (5) alcohol refractometer test. Gelatinase is a process to make Tanjung become smoother and smaller. Then, Tanjung is inoculated with 1 gram, 3 grams, and 5 grams of *Saccharomyces cereviseae* during 24 hours for yeast reproduction. In the fermentation process, substrate which is resulted from inoculation is mixed with Tanjung's pulp and then it's fermented in anaerob condition during 2, 4, 6, and 8 days to resulting ethanol. That ethanol is not pure, it's still mixed with water, so there is stratified distillation to split ethanol and water so that the ethanol levels increased. The last step which is done on each stage is to test the ethanol level. Ethanol which is produced from Tanjung's fruit fermentation must be tested by using alcohol refractometer. Then ethanol of fermentation is purified by stratified distillation for increase the ethanol level. Elevated of ethanol level is also measured by alcohol refractometer.



Data in this experiment were tested using two-ways analysis of variance (Anova). Analysis of variance is a procedure to test differences in mean or average of populations. The concept of variance analysis is based on the concept of the distribution of F and can be applied for analysis of relationship between more than one variable observed. There were two independent variables in this experiment are the time of fermentation (day) and concentration of yeast (gram), so it must be used two-way Anova technique to determine the relationship between its variables.

3. RESULTS AND DISCUSSIONS

In this experiment, there was no interaction between yeast concentration and fermentation time. There was only 0,1% of difference and it showed that the differences in the levels of ethanol production was not significant. The table below showed interaction of yeast concentration (gram) and fermentation time (day) to the percentage of ethanol level (v/v).

Table 2. Interaction of Yeast Concentration (gram) and Fermentation Time (day) to the Percentage of Ethanol Level (v/v)

Yeast Concentration (gram)	Fermentation Time (day)				Σn	\bar{x}
	2	4	6	8		
1	7	9	13	8	37	9.2
3	7	9.3	13	8	37.3	9.3
5	7	9.3	13	8	37.3	9.3
Σn	21	27	39	24		
\bar{x}	7	9.2	13	8		

The blue colour on the table showed percentage of ethanol levels which are resulted by fermentation process (v/v)

Tanjung's fruits were fermented for 2 days using bread yeast (*Saccharomyces cerevisiae*) as much as 1 gram, 3 grams and 5 grams produces 7% v/v ethanol. It was the lowest ethanol level which was produced. On the fourth day, ethanol level was increased to 9.2% v/v. The highest ethanol level was on the fourth day, ethanol can reach 13% v/v ethanol level. Fermentation on the next day (8 days) showed a decrease in average ethanol production to just 8% v/v ethanol level. But for yeast concentration, 1 gram of yeast on average could produce 9.2% v/v ethanol and 3 grams of yeast along with 5 grams together produced an average yield of 9.3% v/v ethanol. Based on two-way Anova statistical test, the difference of 0,1% showed that the differences in the levels of ethanol production was not significant. It means that there was no interaction between yeast concentration and fermentation time. In other words, the fermentation time and the yeast concentration did not have causal relationship by each other

The table below illustrated the increase of ethanol levels, resulted from fermentation process, and ethanol which had been purified, by using first and second distillation (stratified distillation).

On ethanol fermentation from first distillation, the ethanol levels was increased, approximately 180% v/v until 205% v/v. Then ethanol which was distilled again (second distillation), the ethanol was increased approximately 105% v/v until 140% v/v. The first distillation and second distillation process are called stratified distillation.



Table 3. Increase of ethanol level percentage before and after stratified distillation (v/v)

Fermentation Time (day)	Before Distillation (BD) % (v/v)	After Distillation % (v/v)		Increase of Ethanol Levels % (v/v)	
		Distillation I (DI)	Distillation II (DII)	BD-DI	DI-DII
2	7	28,5	80	205	140
4	9	31,5	81	175	130
6	13	40	83	155	105
8	8	29	80	180	135

Table 4. Interaction of yeast concentration (gram) and fermentation time (day) upon the ethanol volume (ml)

Yeast Concentration (gram)	Fermentation Time (day)				$\sum n$	\bar{x}
	2	4	6	8		
1	250	265	300	260a	1075	268.75
3	250	275	300	250a	1075	268.75
5	250	270	300	270a	1090	272.5
$\sum n$	750	810	900	780		
\bar{x}	250	270	300	260		

Based on the analysis of two-way Anova, Table 4 above showed that the concentration of yeast did not affect the ethanol volume, but the day of fermentation affected the volume ethanol fermentation. On the second days of fermentation, it produced 250 ml of ethanol. Then on the fourth days, ethanol volume was increased up to 270 ml. The optimum ethanol volume was obtained on the sixth days, which was 300 ml. Then ethanol volume was decreased on the eighth day, only 260 ml, but its volume was still more bigger than ethanol volume on the second days.

Table 5. Decrease of percentage ethanol volume before and after stratified distillation (v/v)

Fermentation Time (day)	Before Distillation (BD) (%)	After Distillation (%)		Increase of Ethanol Levels (%)	
		Distillation I (DI)	Distillation II (DII)	BD-DI	DI-DII
2	250	32	2.6	390.6	384.5
4	270	47	3.5	289.7	285.5
6	300	52.5	3.5	285.7	285.5
8	260	34	2.6	382.3	384.5

Table 5 indicated the decrease of ethanol volume before and after stratified distillation process. Before distilling, ethanol levels was decreased by approximately 285.7% until 390.6% after the first distilled. Ethanol of first distillation then is distilled again for purification. The second distillation showed the results of decreased ethanol volume between 285.5% until 384.5%.

The Figure below showed that the ethanol content obtained was successively as follows, the lowest 7%, and 8%, 9%, and 13% on the 2nd days, 8th days, 4th days, and 6th days fermentation time. The highest level of ethanol (13%) was found in 6th day fermentation time on all variations of concentrations of yeast. It showed that yeast concentration did not affect ethanol levels, but the fermentation time was influenced. 1 gram, 3 grams, and 5 grams yeast concentration did not affect the ethanol levels because 1 gram yeast was enough strong to convert all existing glucose of Tanjung's fruits into ethanol. Therefore, 3 grams and 5 grams

yeast concentration did not have significant differences in results when compared with 1 gram yeast concentration.

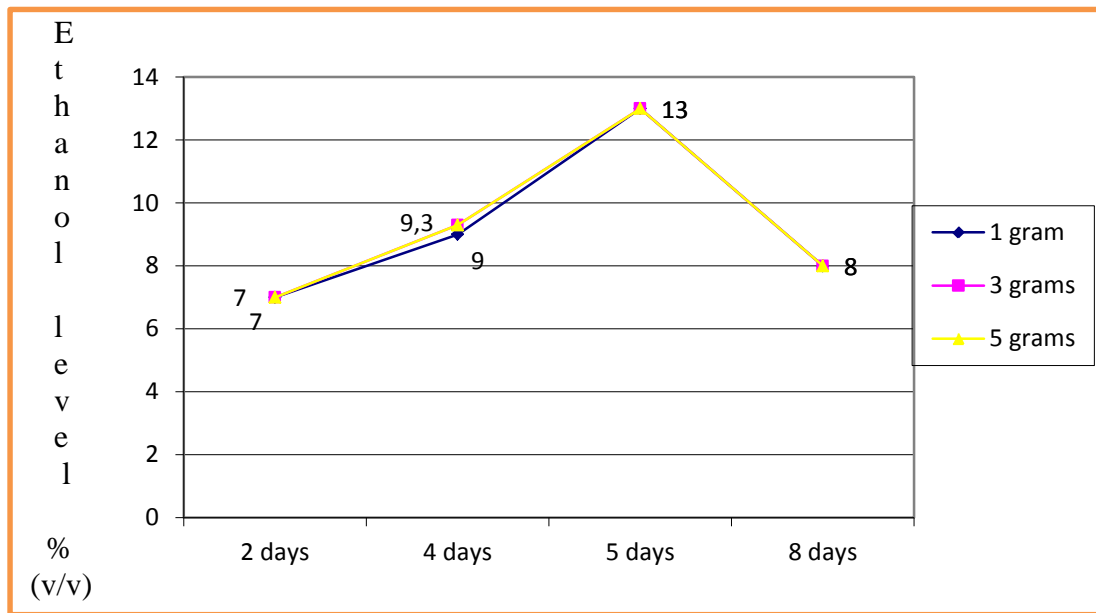


Fig. 1. Interaction of yeast concentration (gram) and fermentation time (day) upon the percentage of ethanol level (v/v)

At second days of fermentation, yeast conditions were in the preparation stage of fermentation, so not all of the existing glucose were converted to become ethanol. Next day, more of glucose were converted into ethanol by fermentation process so that the resulting of ethanol was increased, from 7% v/v in 2 days to 9% v/v in 4 days. The optimum of fermentation was on 6 days, it indicated by the high levels of ethanol production which was 13% v/v. Meanwhile on the 8 days fermentation, the fermentation rate was decreased and produced only 8% v/v ethanol levels. That was because of most of the ethanol converted into other compounds such as acetic acid (CH_3COOH).

The Fig. 2 above illustrated the increase of ethanol levels resulted from fermentation process until ethanol had been purified by using first and second distillation (stratified distillation). Ethanol fermentation when had been done first distillation, the ethanol levels was increased approximately 180% v/v until 205% v/v. Then ethanol which was distilled again (second distillation), the ethanol was increased approximately 105% v/v until 140% v/v.

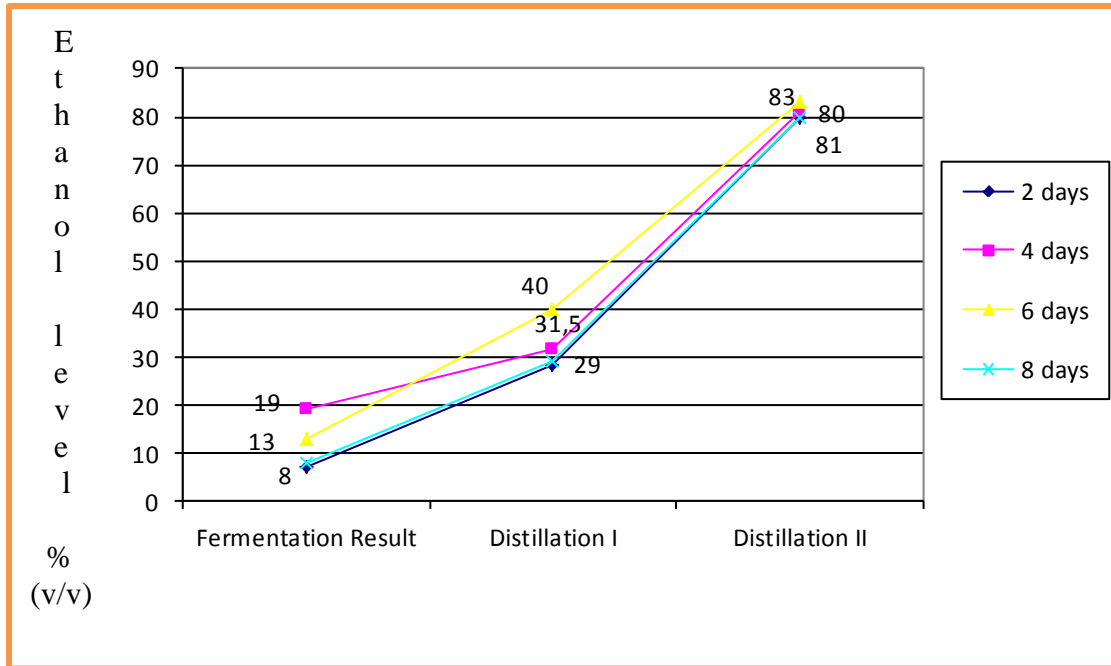


Fig. 2. Increase of ethanol level percentage before and after stratified distillation (v/v)

The Fig. 3 above showed the 2nd days of fermentation produced 250 ml ethanol. On the next day, there was an increase of ethanol volume, from 265 ml become 275 ml for 4th days and exactly 300 ml at 6th days. 6th days fermentation was the optimum point because on the next day (8th days) there was a decrease of ethanol volume become 250 ml until 270 ml.

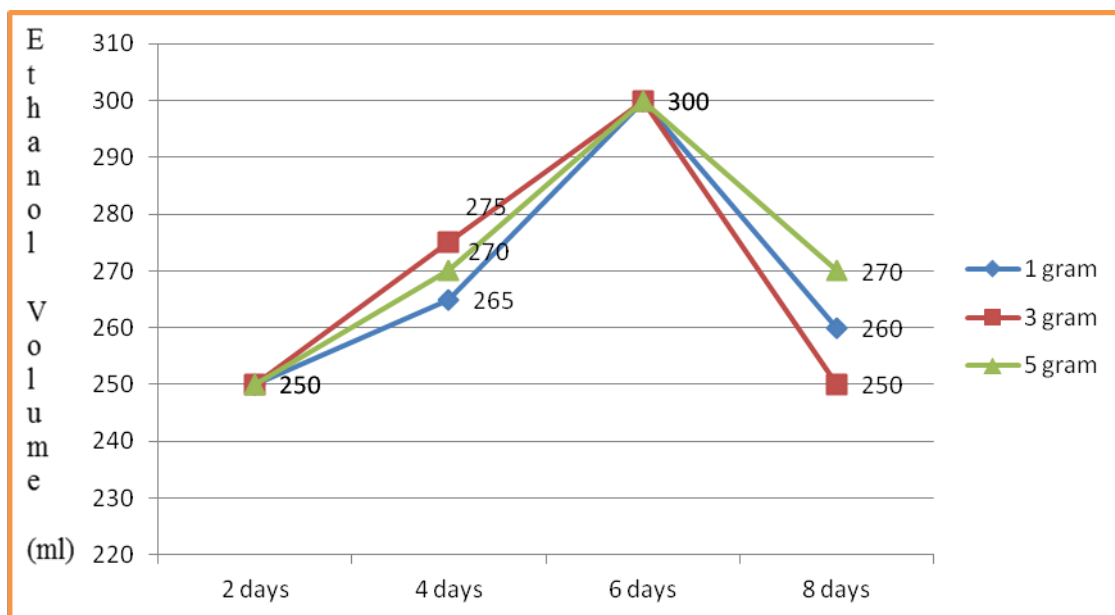


Fig. 3. Interaction of yeast concentration (gram) and fermentation time (day) upon the ethanol volume (ml)

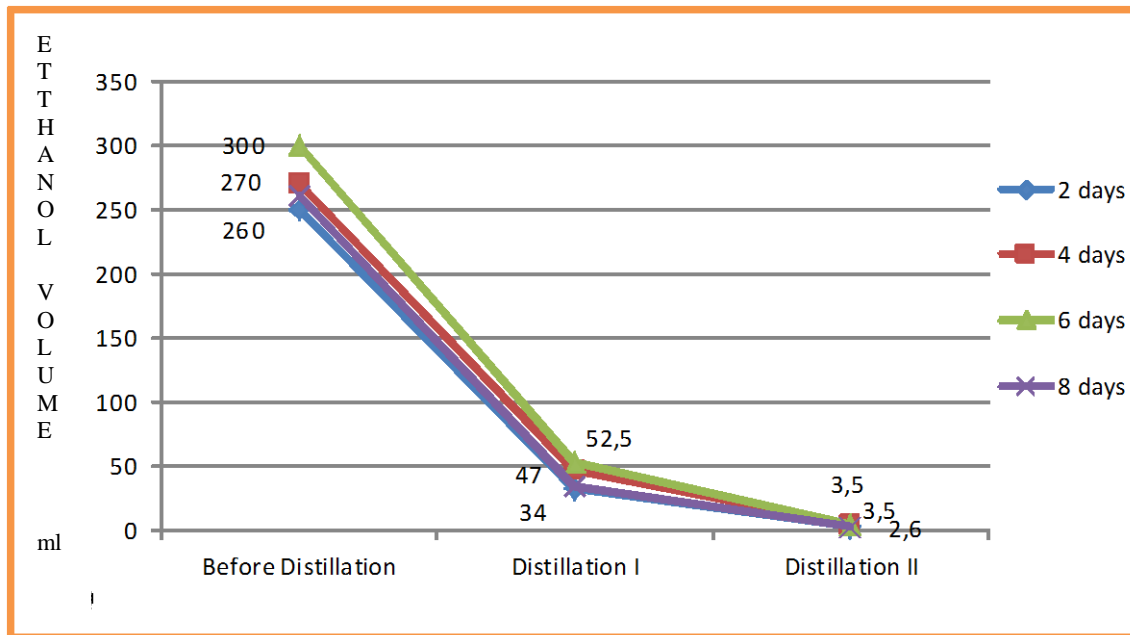


Fig 4. Decrease of ethanol volume before and after stratified distillation (ml)

The Fig. 4 illustrated a decrease of ethanol volume starts on ethanol which was resulted from fermentation process until ethanol which had purified using first and second distillation (stratified distillation). Ethanol fermentation when had done first distillation, the ethanol levels was increased approximately 285.7% v/v until 390.6% v/v. Then ethanol which was distilled again (second distillation), the ethanol was increased approximately 285.5% v/v until 384.5% v/v.

Previous research with 10% (v/v) sugar levels in the beginning could produce ethanol in yield products 23.67%.^[6] The problem which often arose in the fermentation process was inhibition of ethanol product. In addition, ethanol products will affect the growth of yeast, such as ethanol will damage the plasma membrane, protein denaturation, and the changes of growth temperature. Intake of ethanol products must be done in conditions which did not disturb the growth of *Saccharomyces cerevisiae*. One method that can be used is to vacuum fermentation. In these conditions, ethanol and water will evaporate at a temperature suitable to the conditions of living microbes.^[7] Evaporation that occurs continuously caused ethanol levels and fermenters are stable and did not disturb the growth of microbes.

Intake of ethanol products must be done in conditions which did not disturb the growth of *Saccharomyces cerevisiae*. One method that can be used is to vacuum fermentation. In these conditions, ethanol and water will evaporate at a temperature suitable to the conditions of living microbes. Evaporation that occurs continuously caused ethanol levels and fermenters are stable and did not disturb the growth of microbes. The microbial growth need nutrients. Required nutrients are classified into two macro nutrients and micro-nutrients. Macro nutrients such as elements C, N, P, K. Element of C derived from carbohydrate-containing substrate.^[8] Micro elements include vitamins and other minerals also needed, such as Ca, Mg, Na, Cu, Co, Al, Bo, S, Cl, Fe, Mn, Zn, and Mo.

Fermentation processes are usually done by species of the yeast *Saccharomyces cerevisiae*, whereby the sugars in the fruit juice are converted into alcohol and organic acid, that later react to form aldehydes, esters and other chemical components. In the fermentation process, oxygen was still needed even in small amounts. *Saccharomyces cerevisiae* required oxygen to sustain its life.^[9] Besides that, oxygen was needed to maintain the cell

concentration remains high.^[10] Oxygen function was to produce ATP in glycolysis and oxidative phosphorylation. Oxidative phosphorylation process was the most prominent process in the production of ATP. If there was no oxygen (anaerobic), NADH in the mitochondria could not be oxidized back in the citric acid cycle, ATP formation and nutrient solution were interrupted. The efforts to improve production of was with using the *Saccharomyces cerevisiae* starter in the conventional way. Fermentation temperature affected the concentration of alcohol production, fermentation rate, growth rate, lag phase, enzymes and membrane functions.^[11]

In 2010, the potential of biomass is 49.81 Gwe with utilization reached 1.6 GW. Capacity of biofuel production in Indonesia in 2010 is about 272,730 kilo liters for bioethanol but not utilized because lack of ethanol supply for blending^[12]. Ethanol was alternative energy source which had several advantages, such as ethanol were the renewable energy and environmentally friendly due to the less of carbon-dioxide emissions.^[13] Ethanol could be produced by fermentation of raw materials such as monosaccharide and disaccharide (sugar cane, molasses of sugar cane), starchy materials (corn, rice, tubers), and cellulose materials (wood, agricultural waste). With the great potential of Indonesia as an agricultural country, the development of ethanol with fermentation way was very possible.

Results of the research which was conducted by gelatinase, inoculation, fermentation, stratified distillation, and alcohol refractometer test, showed that Tanjung's fruits were rich in glucose, and 160 grams of Tanjung could produced 3.5 ml of ethanol 83% with the optimum fermentation was on 6th days and by using 1 gram of *Saccharomyces cerevisiae*. The advantage of Tanjung's bioethanol was that ethanol of fermentation could reach 13% levels of purity while in molasses fermentation only reached the 10% levels. It indicated that Tanjung's bioethanol had a very big potential to outperform the molasses bioethanol which was now become E100 in Brazil. Tanjung's bioethanol was made of the fruit wastes, and the sustainability of its materials was guaranteed, therefore it deserved to be a national eco-friendly alternative energy resources.

4. CONCLUSIONS

Conclusion: (1) Fermentation of Tanjung's fruit could produce bioethanol which was very potential to become alternative energy; (2) The methods of Tanjung's bioethanol production were gelatinase, inoculation, fermentation and stratified distillation, and alcohol refractometer test; (3) the day of fermentation influenced the ethanol level. In this experiment, the optimal day was 6th days; (4) concentration of yeast (*Saccharomyces cerevisiae*) did not influence the ethanol level production. So, it can be used 1 gram of yeast to make the optimum Tanjung's bioethanol.

Recommendation: In the fermentation process, container as a fermentation tool must be closed and make an isolated condition in 28–30^oC. When ethanol in distillator tool can not flow easy, so it has to make a little hole in the cap container of ethanol. The day of inoculation process is one day (24 hours) with microaeration technique. Although, the purity level of ethanol to become a fuel reach 99.6 to 100% ethanol purity so that it doesn't corrode vehicle engine. Therefore, it is very much necessary to improve the distillation methods and change it into permeability membrane technique to give their result 100% pure ethanol.



REFERENCES

1. KOHLI, R.K., BATISH, D.R., SINGH, H.P. Important Tree Species. India: *Forest and Forest Plants*, 2000, Vol. 2, p. 1–12.
2. GANU., JADHAV., DESHPANDE. Antioxidant And Antihyperglycemic Potential of Methanolic Extract of Bark of *Mimusops Elengi* L In Mice. *Research Journal of Pharmaceutical, Biological and Chemical Sciences (RJPBCS)*, 2010, Vol. 1, No. 3, p. 68.
3. HAMBALI.; ERLIZA.; MUJDALIPAH, SITI. *Teknologi Bioenergi*. Jakarta: Agromedia Pustaka, 2007.
4. PRIHANDANA.; RAMA.; KARTIKA, NOERWIJAYANTI. *Bioetanol Ubi Kayu: Bahan Bakar Masa Depan*. Jakarta: AgroMedia Pustaka, 2007.
5. ENIZA, S., MARZUK, T., PRAYITNO, D. The Effect of Buah Tanjung Meal in Ration upon the Performance of the Japanese Quail (*Coturnix-coturnix japonica*). *Jurnal Ilmiah KULTURA*, 2005, Vol. 40, No. 1, p. 1-5.
6. WIDJAJA, TRI. Produksi Etanol dari Molases Dengan Teknik Immobilized Cell Ca-Alginale dalam Bioreaktor Packed Bed. *Seminar Nasional Fundamental dan Aplikasi Teknik Kimia*, Surabaya: Jurusan Teknik Kimia FTI ITS, 2007.
7. BOHNET, MATTHIAS., ET AL. *Ullmann's Encyclopedia of Industrial Chemistry 6th Completely Revised Edition*, 2003, Vol. 12.
8. HALIMATUDDAHLIANA. *Pembuatan n-Butanol Dari Berbagai Proses*. Medan: USU Digital Library, 2004.
9. TAO, F., MIAO, J.Y., SHI, G.Y., ZHANG, K.C. Ethanol Fermentation by an Acid-tolerant *Zymomonas mobilis* under Non-sterilized Condition. *Process Biochemistry*, 2003, Vol. 40, p. 183–187.
10. HEPWORTH, M. *Technical, Environmental and Economic Aspects of Unit Operation for The production of Bioethanol From Sugar Beet in the United Kingdom*, United Kingdom: Corpus Christi College, 2005.
11. SENER, A.; CAMBAS, A.; ONAL, O. *Effects of Fermentation Temperature of Kinetic Growth *Saccharomyces cerevisiae**. Turkey: University of Cukurova Faculty of Agriculture, 2007.
12. BADAN PENGKAJIAN DAN PENERAPAN TEKNOLOGI. *Outlook Energy Indonesia 2012*. Jakarta: BPPT, 2012.
13. JEON, BO YOUNG., ET AL. Development of a Serial Bioreactor System for Direct Ethanol Production from Starch Using *Aspergillus niger* and *Saccharomyces cerevisiae*. *Biotechnology and Bioprocess Engineering*, 2007, Vol. 12, p. 566–573.



PARAMETRIC STUDY OF THE SOLAR ASSISTED HEAT PUMP PERFORMANCE

K. Januševičius

*Vilnius Gediminas Technical University
Saulėtekio al. 11, LT-10223 Vilnius – Lithuania*

E. Biekšienė

*COWI Lietuva, UAB Energy Division, BU Energy and Environment
Ukmergės str. 369A, LT-06327 Vilnius Lithuania*

ABSTRACT

The rising interest in near zero energy buildings (NZEB) as an energy policy tool to reduce the consumption of primary energy, has increased attention to the renewable energy systems for buildings. Heat pump systems are wide spread solution to reduce energy use. In cold climate due to intense energy use for space heating and domestic hot water (DHW) preparation, it is difficult to reach seasonal performance factor values suggested in the EN 15450 standard. A combination of heat pump and solar thermal collectors helps to meet standard requirements and increases the fraction of the renewable energy use.

In order to improve the performance of the system we need to know parameters that have the greatest impact on it. Thus we create a simulation model of the system in TRNSYS and carry out a parametric study to investigate how different values of the parameters will affect the seasonal performance factor (SPF) of the solar assisted ground source heat pump system. The main parameters considered are borehole size, efficiency of solar collectors and required capacity of circulation pumps. All these parameters can be influenced at the design stage of the system, while the heat demand profile is considered to be predetermined. Different solar assisted heat pump design solutions with serial and parallel solar thermal connections to heat pump loop are modeled. The findings could help directing future research to increase the performance of near zero energy building energy supply for heating systems and avoid decrease of systems efficiency

Keywords: solar assisted heat pump, near zero energy buildings, parametric study, TRNSYS

1. INTRODUCTION

According to the European Union directive 2010/31/ES, from 2020 all buildings will be built as near zero energy buildings [1]. This energy performance criterion was transferred to national construction regulations. These buildings will be labelled as A+ and A++ class, and will have to meet energy efficiency criteria on energy use for space heating, domestic hot water preparation, cooling, ventilation and electricity use. All these energy needs will be assessed by primary energy method [2]. After the first reviews of the new construction regulations highly influenced of the 2010/31/ES directive, it is clearly visible, that heat production systems have a potential to decrease primary energy use. For near zero energy buildings heat pump becomes efficient heat production possibility – feed from renewable energy grid and with high primary energy efficiency, could highly influence fossil fuel use reduction.

At NZEB, which has reduced energy losses and minimized space heating consumption, domestic hot water demand has main influence on SPF value in heat pump systems. Due to higher temperature requirements for DHW preparation, heat pump works on lower coefficient of performance (COP) values. In those circumstances, meeting LST EN 15450:2007 Annex C requirements [3] for target SPF values becomes more complicated than in typical houses.

Meeting requirements of LST EN 15450:2007 minimum or target values at those specific energy needs requires specific solutions. A solar assisted heat pump system may improve overall system performance. While heat pump installations suffers from unfulfilled SPF requirements due

to the design and fitting mistakes, additional complexity of a system may cause more problems for users and installers.

Previous studies [4] have shown the dependence of system performance on solar collector area, borehole length, but does not characterize how strong these relationships are. While there are no design guidelines for solar assisted heat pump systems used at NZEB, the influence of known design parameters to the final system performance should be evaluated.

The trial and error method – widely spread in practice for system design – is not suitable for any new technology. Due to non-performing examples of installations, the system may become unacceptable for near zero energy owners. This paper tries to show possible non-performance causes, which can be easily changed in early design stage.

2. LITERATURE REVIEW

A solar assisted heat pump is not a new concept – the first conceptual systems were discussed in early 70' in Sweden and North America. Later, a solar collector add-on was used to increase seasonal efficiency in the incorrectly sized heat pump systems by regeneration of borehole. Unglazed collectors were mainly used for previous demonstration projects due to high glazed and vacuum tube collector prices. [4]

Long term simulation studies proves, that solar collectors added in heat pump system provides consistent COP for 20 years run time with constant heat demand [5]. According to hydrogeological situation in Lithuania – this solution is only suitable where influence of ground water flow is small. Due to an increase of average yearly source temperature at under-sized borehole heat exchangers, combination with solar collectors can help reduce heat pump energy use [4].

Mainly add-on of solar collectors to heat pump system is suggested as possibility to reduce borehole drilling depth. Reduced drilling cost used for unglazed collectors could reduce installation costs if purpose of solar collectors is ground source regeneration and temperature decrease prevention [6].

The study presented in this paper continues reviewed works by adding more detail to energy demand for space heating and illustrates influence of design parameters at seasonal performance factor. Lack of investigations for solar assisted heat pump use in NZEB at Lithuania, motivated to start this simulation based research.

3. MODELLED BUILDING AND SOLAR ASSISTED HEAT PUMP SYSTEMS

3.1. Modelled building

Systems were sized for a NZEB which is designed to meet Passivhaus [7] standard (15kWh/m^2 heat demand per year for space heating). Floor area of this building is 180m^2 . A heat balance is highly influenced by internal and solar heat gains, due to high thermal constant of the building. A domestic hot water use is set to 30ltr/person daily use, while 4 person family lives in the simulated building. The hot water demand was generated according to the methodology by Jordan U. & Vajen K [8].

Two system layouts where solar thermal collectors are combined in parallel and serial systems are used in this study. These layouts were typically used in previous studies described above. The schemes used can be characterized as solar collector connection to hot side of heat pump (parallel) and cold side (serial). The main difference between these systems comes from the connection of solar thermal collectors – parallel connection allows stand-alone operation of both systems and these systems covers energy supply gaps in the overall season.

3.2. Parallel solar assisted heat pump system

A parallel system (Fig. 1) of solar assisted heat pump is widely used. In this system solar collector and heat pump subsystems operates separately from each other. Solar collectors are connected to the hot side of heat pump. In summer solar thermal collector produces most of the required heat for DHW preparation and heat pump source (ground) has possibility for natural regeneration. Due to the fact that a solar collector system produces heat with the higher efficiency (COP), seasonal performance factor of this system is higher than for the typical heat pump system. Predicted increase of SPF value for this system could vary from 0.5 [9] to 1.2 [6] in near zero energy buildings.

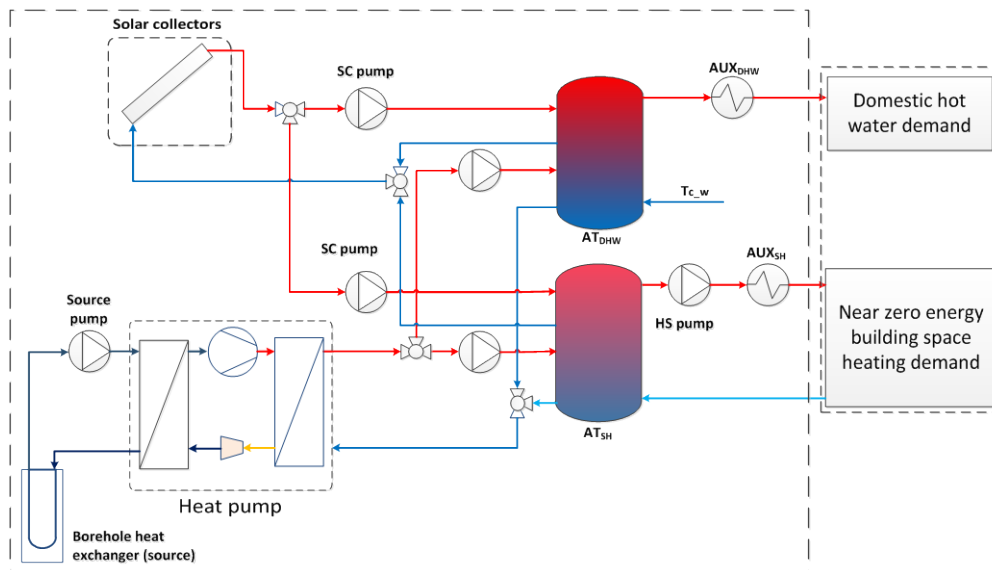


Fig. 1. Parallel solar assisted heat pump system with studied boundaries

3.3. Serial solar assisted heat pump system

In a serial system (Fig. 2) solar collectors are connected at a cold side of a heat pump. The aim of this solution is to increase the incoming source flow temperature to heat pump by adding the solar heat to fluid from a borehole heat exchanger. Contrary than in a parallel system, in the serial system solar and heat pump subsystems closely interacts with each other. The main system operation modes are:

1. The ground source directly feeds heat pump,
2. Heat transferring fluid flows to the borehole and warms up in solar collectors. The heat pump gets increased “source” temperature,
3. Ground regeneration with a solar heat, when heat pump is not operating and solar heat is available.

The previous studies [9] has shown that the serial system has the higher average source temperature, but the seasonal performance factor suffers from the high pump energy use.

Serial system creates conditions to the higher solar thermal collector seasonal efficiency and increase of solar utilization in the comparison with the parallel system, due to low inlet temperatures [9]. For this reason the solar collector operates with the lower losses and higher efficiency.

The potential of a ground source temperature regeneration in this case is assessed without control strategy which takes into account influence of pump energy use and electricity, for SPF value. With this type of control strategy system performance and ground source temperature may be different than presented in this paper.

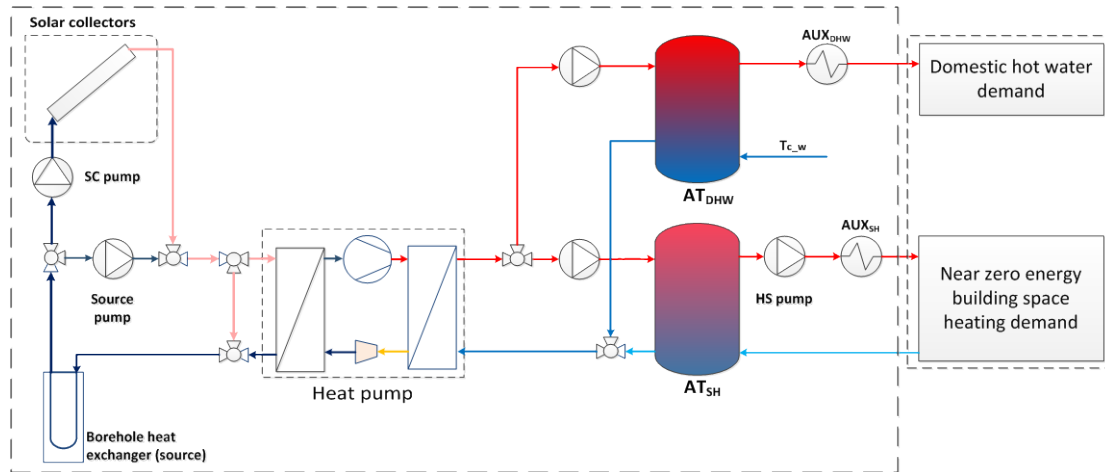


Fig. 2. Serial solar assisted heat pump system

With efficient control strategy, solar heat can be used for heat demand covering or regeneration of ground source if heat production with heat pump is unused. The lack of regeneration strategy can cause high electricity use for pumps. In geological conditions, where ground water flows effects ground temperature, huge amount of solar heat, could be lost. This might happen due to storage losses to surrounding ground without additional long term temperature increase effect. In the serial system the COP values of the heat pump could be from 2 to 6 % higher than in parallel system, depending on solar radiation amounts on the collector's plate.

4. USED METHODS

4.1. Assessed variables

The schemes analyzed in the paper could be characterized by the thermodynamic approach with the main energy flow patterns and influencing parameters that have the impact on the amount of energy supplied to system. The SPF value of the system could be changed by adjusting quality and amount of presented energy flows (Fig. 3).

In the real system the SPF value is affected by heat losses in the piping loop. In this analysis heat losses are not taken into account for the simplification reasons. Accumulation tanks have heat losses as a result of temperature difference between the stored fluid and surroundings. This energy flow was left out of the scope of the study as well as annual heat losses from accumulation tanks depend on many variables. The solutions to reduce these losses are to increase insulation layer on the tank cylinder and right sized dimensions.

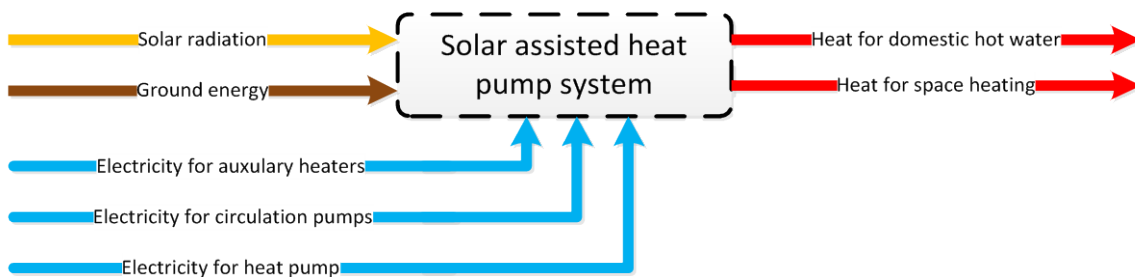


Fig. 3. System energy flows

The energy flows, as shown in the Fig. 3, could be influenced in the design or construction phase. The possible design decision could be caused by the different targets as presented in the Table 1.

Table 1. Causes of the system parameter variation

Parameters	Scenario of parameter change	
	Parameter increase causes	Parameter decrease causes
Solar collector area	Design target to increase solar fraction	Target to reduce system installation costs or limited installation area
Solar collector efficiency	Installation of vacuum tube collectors	Installation of unglazed collectors
Solar collector inclination angle	Design target to increase solar fraction on winter season	Concentration on summer season heat production in solar collectors
Solar collector circulation pump power	Hydraulic scheme complicated and high pressure losses	Simplified – parallel hydraulic scheme
Ground source capacity	Increase of average source outlet temperature	Minimization of borehole length to reduce price or lower resistance
Ground source circulation pump power	Complicated and with high pressure loss	Simplified – parallel hydraulic scheme

According to these parameter values three different scenarios were used in this work (Table 2).

Table 2. Analysed scenarios and values of the parameters

Parameter	Increase scenario	Base scenario	Decrease scenario
Solar collector area	2 X 2,4m ²	3 X 2,4m ²	4 X 2,4m ²
Solar collector efficiency	Vacuum tube collectors 7,1m ² $\eta_0=0,8$ $a_1=1,6$ $a_2=0,0012$	Flat plate collectors 7,2m ² $\eta_0=0,8$ $a_1=4,1$ $a_2=0,0064$	Unglazed collectors 7,2m ² $\eta_0=0,8$ $a_1=29$ $a_2=0$
Solar collector inclination angle	35°	45°	55°
Solar collector circulation pump power	35W	55W	75W
Ground source capacity	2X32m probes V=2770m ³	2X41m probes V=3550m ³	2X65,6m probes V=5680m ³
Ground source circulation pump power	45W	100W	150W

4.2. Seasonal performance factor

The seasonal performance factor (SPF), as calculated according to LST EN 15450:2007 [3], takes into account the power consumption of the heat pump and the source circulation pump; auxiliary energy (E_{aux}) need; the heat output for the space heating (Q_{SH}) and the heat output for the domestic hot water preparation (Q_{DHW}). Usually the SPF is calculated only for the boundary of a heat pump system to express the rate of the total seasonal energy use and production. In this case a SPF_{HP} shows how heat pump system is influenced and SPF_{sys} express overall solar assisted heat pump system performance.

For the performed parametric analysis, yearly SPF values are used to determine sensitivity of system parameter change. For the parallel system heat pump a seasonal performance is calculated for heat pump system by formula (1) which takes into account the electricity use of the heat pump (E_{HP}) and the source pump ($E_{s.p.}$).

$$SPF_{HP} = \frac{Q_{SH} + Q_{DHW}}{E_{HP} + E_{s.p.} + E_{aux}} \quad (1)$$

According to the standard [3] with the chosen boundaries of the system, SPF factor for yearly period is calculated as presented in formula (2). In this case, the energy consumption of the solar collector system circulation pump was added as E_{pumps} :

$$SPF_{sys} = \frac{Q_{SH} + Q_{DHW}}{E_{HP} + E_{s.p.} + E_{pumps} + E_{aux}} \quad (2)$$

For the parallel system both heat pump and overall system SPF value were calculated. Due to solar collector connection to cold side of heat pump in serial system, SPF_{HP} value is equal to SPF_{sys} and annual performance is presented as single performance indicator.

4.3. TRNSYS simulation

The simulation of solar assisted heat pump systems was performed with TRNSYS simulation program [6]. This completely extensible simulation environment is wide spread tool for complex renewable energy system simulation. The models were created with the main system elements as Types:

Type 12C – Energy/Degree-Hours House model with temperature level control is used for weather influenced space heating load generation. The additional heat gains and losses from windows were added with the *Type 35A*. The influence of shading devices was taken in account with the *Type34*.

Type 927 – Water to Water Heat Pump. This Type uses normalized data file interpolation for the performance modelling based on the user-supplied data files containing catalogue data for the normalized capacity and power draw. The content of this file was custom made from the performance data for the heat pump as supplied by the manufacturer *STIEBEL ELTRON*.

Type 557 – Vertical U-Tube ground heat exchanger. This Type provides the possibility to calculate heat rejection and absorption depending on temperatures of heat carrier fluid and the ground. This type uses calculation 3model created by Hellstrom [11].

Type 1 – Solar Collector model which calculates solar collector performance from quadratic efficiency formula with 2nd order incidence angle modifiers taken into account.

The simulation was performed with the integration and convergence toleration of 0.001. The balance between the elements is checked manually in the MS excel environment. The highest errors fit in 2% mismatch value. The flow temperatures fit in the value boundaries of a real system.

Due to the assumptions made during the simulation (neglected piping heat loss, constant power use in pumps and ideal heating system control) the results are not suitable for real system performance prediction, but are appropriate for the comparison. The results clearly show differences and could be used to predict design parameter influence to final SPF value. All cases are simulated in the same conditions and with the same assumptions.

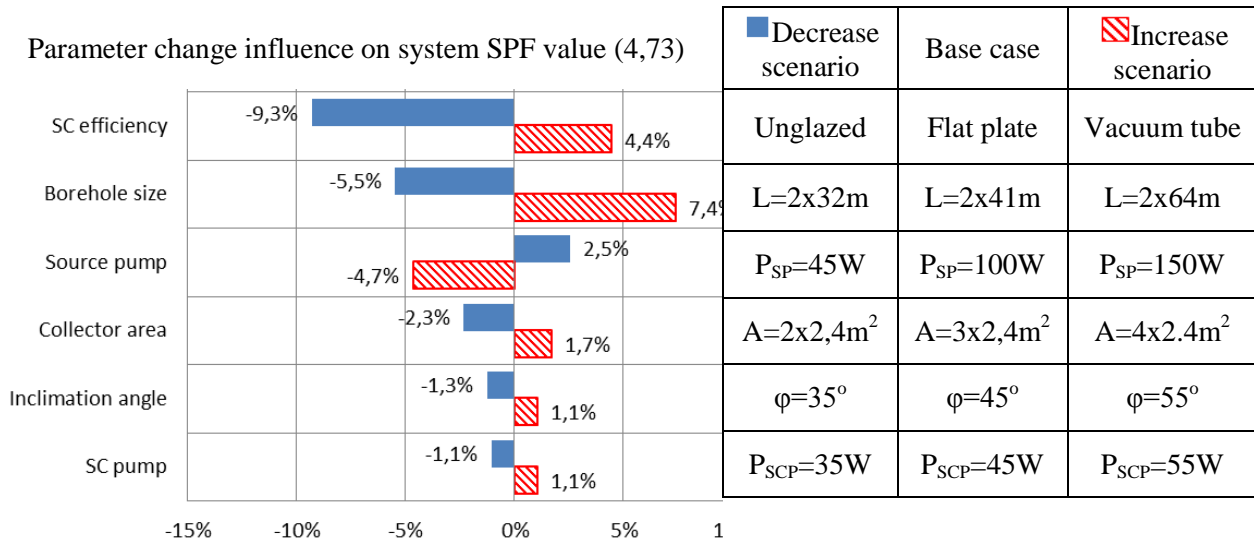
5. RESULTS

The results of the performed simulation are presented as the variation of yearly SPF value. The influence of different parameter change at a fixed range is shown in the tornado chart.

5.1. Parallel system performance

In the base case, the simulated parallel system has reached SPF value of 4,73. This can be explained by the high solar fraction for domestic hot water prepared with the relatively high COP in comparison to the heat produced by the heat pump. Table 3 shows the SPF (non-dimensional) value deviation from the base case scenario due to the changes of the different parameters.

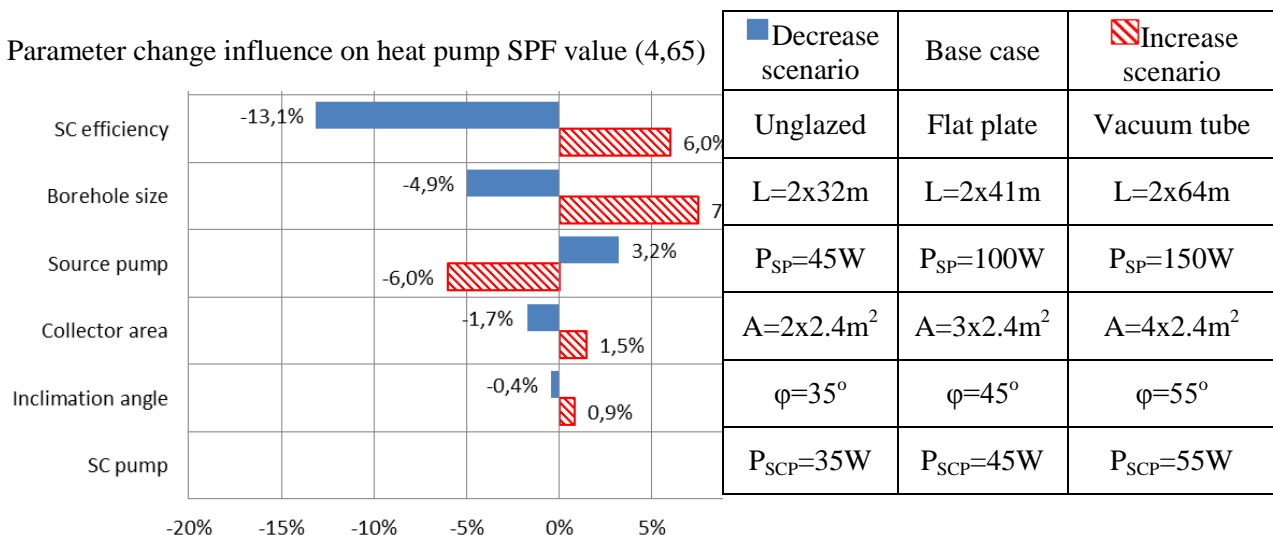
Table 3. Parallel system SPF change



Due to the interaction between the solar collector and heat pump subsystem, separate SPF value for heat pump subsystem was calculated (Table 4.). The trends of parameters influence are the same as at the system level.

For parallel system efficiency of solar collectors makes the high impact to the solar fraction of DHW. In summer the heat pump prepares DHW with the lower COP than solar collectors. As vacuum tube collectors cover the higher fraction of domestic hot water in summer than flat plate collectors, SPF value increases by +6.0% for the heat pump subsystem and by +4.4% at the system level. According to the results, the area and efficiency of the solar collectors should be optimized according to the DHW and space heating demand variation to make the most of energy and economic efficiency, while there is a price difference among unglazed, flat plate and vacuum tube collectors.

Table 4. Parallel system heat pump SPF change



Deeper boreholes have the higher active storage volume. This causes the higher inlet temperature to heat pump and more efficient source regeneration in summer months when solar collectors cover the heat demand. Deeper boreholes increase system performance by +7.4% while undersized ground source decreases SPF value by -5.5%. At a heat pump level influence is from -4.9% to +7.5% of the base case performance.



The solar assisted heat pump is less sensible to the power of the source pump due to reduced heat pump running time when heat demand is covered by solar collectors. The power of the pump power influences SPF value change from -6.0% to $+3.2\%$ in the heat pump subsystem and from -4.7% to $+2.5\%$ at the whole system level.

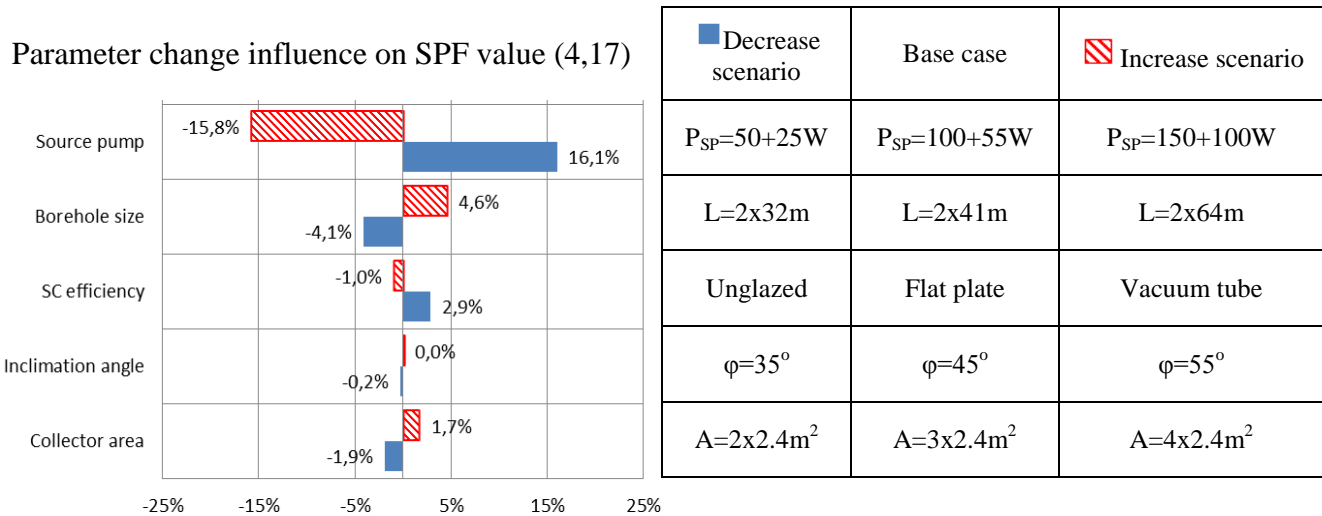
The area of solar collectors directly affects amount of the transformed solar energy. While the larger collector area produces more solar heat, it increases SPF by $+1.7\%$ and $+1.5\%$ at the system and heat pump level. This relates to the decreased heat pump run time and increased heat production with the higher electrical COP on solar collectors. The opposite effect – reduction of area decreases SPF from -2.3% and -1.7% .

The inclination angle of the solar collectors has relatively small influence to the yearly SPF values. Due to this design choice seasonal performance varies from -0.4% to $+0.9\%$ at the heat pump level and from -1.3% to $+1.1\%$ at the whole system level.

5.2. Serial system performance

The serial system in the base case has a SPF value of 4.17. The heat pump in this system works in relatively higher COP values than in the parallel system, due to the higher “source” temperature. The decrease of yearly SPF value is caused by the lack of the direct solar heat use for the DHW preparation with the high COP in summer. Seasonal performance variation is shown in Table 5.

Table 5. Serial system SPF change



Circulation pumps use a high fraction of electricity in the whole system due to the high installed power. In this case, circulation pumps consumption can reach the same electricity amount as in the heat pump due to the high running time on the ground source regeneration. At those circumstances, the power variation of the source pump influences SPF value change from -15.8% to +16.1%.

The size of boreholes impacts the system performance from -4.1% to +4.6%. In the smaller probes, source temperatures fluctuate at the higher ranges than in the deeper ones. This causes more heat pump running periods with the lower COP and less accumulated heat amount. In the system with the larger boreholes, temperature from source has smaller fluctuations due to the stable ground heat extraction.

6. CONCLUSIONS

Some elements of solar assisted heat pumps should be sized more precisely and with more attention to possible heat demand variation than other ones. The elements that need more consideration were detected by the parameter analysis performed in this paper.

1. The borehole size and storage volume have the high influence on the seasonal performance of solar assisted ground source heat pump systems in NZEB. The deeper probes (assuming the same thermal properties of ground layers) have the higher outlet temperatures and recover more easily after the high extraction periods at extreme capacity needs. According to the simulations performed, the smaller borehole size could affect SPF_{sys} value decrease by -5.5% and the higher ground heat storage volume could increase SPF_{sys} value to +7.4% in parallel system in the parallel layout. The performance factor is less sensible to borehole size in the serial system, it could vary from -4.1% to +4.6% due to borehole size change in the same range.

2. The efficiency of solar collectors influences the running time of circulation pumps and outlet temperature of the heat carrier. For the parallel system (solar collectors connected to hot side of heat pump) the increase of efficiency of solar collectors causes higher heat production fraction and decrease of heat pump run time. Due to the higher efficiency of solar collectors SPF_{sys} value increases to +4.4%. The use of unglazed solar collectors with the lower efficiency –decreases the performance factor by -9.3%.

In the case of solar assisted heat pump with the serial layout, () increased solar gains and higher temperatures (due to higher collector efficiency) drive more solar heat to ground source regeneration. This action increases heat pump performance (COP) in cold period, but the rise of the yearly SPF_{sys} value is just +2.9% due to the increased energy consumption in the circulation pump.

Unglazed collectors has small influence (-1.0%) to the seasonal performance in this type of system. Despite the fact that solar heat gains are smaller with this solar collector type, SPF_{sys} value is better due to reduced energy use for ground source regeneration while less unused heat is produced in unglazed collectors.

3. The complexity of systems increases pressure losses and requires higher pump power. The higher power of the circulation source pumps decreases SPF value by -4.7% (for heat pump boundaries -6.0%) in parallel and by -15.8% in serial system case. This problem could be solved by simplifying and optimizing hydraulic loops of heat pump sources and solar collectors. Avoiding the complicated loops and correspondingly high pump power could help increase SPF_{sys} by $+2.5\%$ (for heat pump boundaries -3.2%) and $+16.1\%$ in parallel and serial systems.

4. The changes of the inclination angle and area of the solar collectors at the considered range do not make sensible influence on the yearly SPF value of the system. In shorter (monthly) periods these changes has influence on the running time of the heat pump. According to the simulation results these parameters do not have priority in the design process, but in the complex system could help to increase SPF value.

REFERENCES

1. THE EUROPEAN PARLIAMENT AND THE COUNCIL OF EUROPEAN UNION. Directive 2010/31/EU. On the energy performance of buildings. Brussels. 2010.
2. *Energy performance of buildings. Energy performance certification* (Pastatų energinis naudingumas. Energinio naudingumo sertifikavimas) STR 2.01.09:2012. Vilnius. Environment Ministry of Lithuanian Republic. 2012 (in Lithuanian).
3. *Heating systems in buildings - design of heat pump heating systems*. Lithuanian standard LST EN 15450:2007, Lithuanian department of standardization. 2007.
4. KJELLSON, E., HELLSTROM, G., PERRERS, B. Optimization of systems with the combination of ground-source heat pump and solar collectors in dwellings. *Energy* 2009, Vol. 35, No. 6, p. 2667–2673.
5. XI, C., LIM, L., HONGXING, Y. Long Term of a Solar Assisted Ground Coupled Heat Pump System for Space Heating and Domestic Hot Water. *Energy and Buildings* 2011, Vol. 43, No. 8, p. 1835–1844.
6. BERTRAN, E., PARISCH, P., TEPE, R. Impact of solar heat pump system concepts on seasonal performance - Simulation studies. IEA SHC Task 44 /HPP Annex 38 “Solar and heat pumps system”. 2011 International Energy Agency
7. FEIST, W. *Passipedia* [referred on 25 of February in 2013 y.]
<http://www.passipedia.org/passipedia_en/basics/the_passive_house_definition>
8. JORDAN, U., VAJEN, K. Influence of the DHW Load Profile on the Fractional Energy Savings: a Case Study of a Solar Combi – System with TRNSYS Simulations. *Solar Energy* 2000, Vol. 69, No. 6, p.197–208.
9. JANUŠEVIČIUS, K., JARAMINIENĖ, E. Saulės Kolektorių ir Gruntinio Šilumos Siurblio Sistema Mažaenergiām Pastatui. Pastatų inžinerinės sistemos 2013. (Accepted for publishing in Lithuanian).
10. KLEIN, A., BECKMAN, A., MITCHELL, W., DUFFIE, A., et al. TRNSYS 17 – a transient system simulation program. Madison, Solar Energy Laboratory, University of Wisconsin; USA 2011.
11. HELLSTROM, G. Duct ground storage model, TRNSYS documentation, 1996.



AN ENVIRONMENTALLY FRIENDLY METHOD FOR MICROFIBRILLATED CELLULOSE EXTRACTION FROM HEMP

A. Putnina, S. Kukle

*Riga Technical University
Institute of Textile Technology and Design
Azenes 14/24, LV-1048 – Latvia*

J. Gravitis

*Latvian State Institute of Wood Chemistry
Dzerbenes Str. 27, LV-1006 Riga – Latvia*

ABSTRACT

Microfibrillated cellulose is a new biomaterial having astonishing intrinsic properties. It was first used in nanocomposites due to its environmentally friendly nature and mechanical reinforcement. It has found various other uses and particularly in a high-value applications [1]. That is why significantly has been increasing interest in development of environmentally friendly technologies of microfibrillated cellulose (MFC) extraction from plants.

In this article disintegration of hemp fibres from variety Purini grown in Latvian Agricultural Science Centre of Latgale by steam explosion and ultrasound treatment were investigated with the aim to evaluate steam explosion (SE) pre-treatment influence on hemp fibre microstructure and ultrasound treatment effectiveness investigation on cellulose disintegration processes into microfibrillated cellulose.

The acquired results after steam explosion treatment, water extraction and extraction by 0.4 wt. % NaOH are discussed and interpreted by Fourier transform infrared spectroscopy (FTIR). Scanning electron microscopy (SEM) was used to examine the microstructure of hemp fibres before and after each of the treatment.

Keywords: steam explosion, hemp fibre, cellulose, microfibrillated celluloses

1. INTRODUCTION

Hemp fibres are renewable, cellulose rich material that can be used for production in different areas. However, some of the applications in nanocomposites are limited by such components of the plant cell wall as hemicellulose, pectin/waxes and lignin. Hemp fibers are built from different hierarchical microstructures with microfibrils as basic units.

Different technologies could be used to prepare harvested hemp to further processing. The hemp bast is separated into large fibres bundles during water retting or dew-retting. Additional treatment is required to defibrillation of the fibres bundles into single fibres and small fibres bundles. According to the literature [2] the content of cellulose in hemp fibres increased from 73% to 85–90% by steam explosion in retted hemp fibres, and from 60–64% to 73–75% in raw hemp fibres. It is obvious that retting has to be included before steam explosion.

Enzyme treatment [2, 3, 4], wet oxidation [5, 6], and NaOH treatment [7,8] is used for degradation of pectin and lignin in the middle lamellae between the single fibres. Physical defibrillation includes treatments by steam explosion [9, 10] and ultrasound [11, 12, 13].

During the SE, the biomass is subjected to the treatment with high pressure saturated steam and rapid decompression resulting in substantial breakdown of the lignocellulosic structure, hydrolysis of hemicelluloses, depolymerisation of lignin components and defibrillation [14]. In this research removal of lignin by water and alkali treatment after SE used makes the cellulose accessible for ultrasound treatment and nanotechnological processing.

The high-intensity ultrasonication technique (HIUS) is an environmentally benign and simple method that conducts fiber isolation and chemical modification simultaneously and helps significantly reduce the production cost of cellulose nanofibers and their composites [12].

2. METHODOLOGY

2.1. Materials

Dew-retted hemp fibres of local variety ‘Purini’ grown on the experimental fields of the Latgalian Agriculture Research Center LLZC (Latvia, district Vilani) and NaOH (Commercial grade) are used in this research. The physical properties of hemp fiber are presented in Table 1.

Table 1. The physical properties of hemp (‘Purini’) fiber [15]

Cellulose	64.2 %
Hemicellulose	23.79 %
Lignin	7.96 %
Pectin	1.37 %
Waxes and fats	0.82 %
Moisture content	9.17 %

Hemp fibres were prepared by cutting into uniform size of approximately 2 mm length. This size of fiber allows steam explosion process and ultrasound treatment taking place in the chemical and physical processes to penetrate deeper into the fibers in the inner layers.

2.2. Steam explosion treatment (SE)

Steam explosion treatment conditions are shown in Table 2. After SE treatment follows hydrothermal and alkali treatment (0.4 % wt.NaOH) that allows remove partly constituents from hemp fibers including hemicelluloses, pectins/waxes and oils covering the external surface of the fibers cell wall. Alkali treatment of natural fiber causes swelling of the fiber and subsequent increase of the absorption of moisture. Sodium hydroxide (NaOH) is the most commonly used chemical for bleaching and/or cleaning the surface of plant fibers [18].

After treatment, within a split second, the biomass is decompressed (exploded) to one atmosphere. Empirically, the so-called severity parameter or the reaction ordinate R_0 can be expressed as [16]:

$$R_0 = t * \exp [(T- 100)/ 14.75] \quad (1)$$

The reaction conditions are expressed in terms of a severity factor which combines reaction temperature and retention time as described by Overend and Chornet [16].

Where: duration of the value of treatment time (t, minutes) and temperature (T, °C) express the SEA severity against the base temperature T_{base} or reference = 100 °C. R_0 dimension is minutes but in practice $\log R_0$ is used.

Where: duration of the value of treatment time (t, minutes) and temperature (T, °C) express the SE severity against the base temperature T_{base} or reference = 100 °C [16].

Table 2. Steam explosion treatment parameters

Variants	SE parameters			
	Temperature, °C	Pressure, bar	Time, min	$\log R_0$
Fibres (‘Purini’)	235	32	1	3.97

2.3. High-intensity ultrasonication technique (HIUS)

The fibres were suspended in distilled water and treated with ultrasound (ultrasonic processor UP 200Hp parameters: 200W, frequency 26 kHz, amplitude 90%, sonotrode S26d14, Ø14mm) (HIUS) for 45 min. HIUS produces very strong mechanical oscillating power, so cellulose fibrils can be isolated from cellulose fibers by the action of hydrodynamic forces of ultrasound [13]. In order to control the process temperature, the beaker with the cellulose fibers in water was put in a water bath with thermostat. The fiber suspension was filtered and dried at room temperature to constant mass.

2.4. Fourier Infrared Spectroscopy (FTIR)

Fourier transform infrared (FTIR) spectra of the samples under investigation in KBr pellets by Spectrum One (Perkin Elmer, UK) FTIR spectrometer in the range of 4000-400 cm^{-1} (resolution: 4 cm^{-1}) were recorded. About 2 mg of fiber sample precipitation was milled into powder using ball mill. The fiber particles were then mixed with KBr and pressed into a disc about 1mm thick.

2.5. Scanning Electron Microscopy (SEM)

SEM micrographs of fibres surface were taken using a scanning electron microscope VEGA Tescan 5136M (Czech Republic – UK). Prior to SEM evaluation, the samples were coated with gold by means of a plasma sputtering apparatus.

3. RESULTS AND DISCUSSIONS

It was investigated an disintegration of hemp fibres from dried non-retted or dew-retted stems of hemp plants of Latvian local genotype ‘Purini’ grown at the Agricultural Science Centre of Latgale (Kraslava) of the 2010 vegetation season by steam explosion (235 $^{\circ}\text{C}$, 23 bar) separated (Table 3). Results show that SE treatment at severity of $\log R_0 = 3.97$ followed by treatment in water and NaOH solution allow to remove practically all hemicellulose and non-cellulose compounds from the hemp fibres living dry residue 68,3 %.

Table 3. Modes of hemp fibres samples SE treatment and after-treatment

Sample	Pressure, bar	$\log R_0$	Evaporable fractions, %	Residue, %	Water solub., %	Resid. after wat., %	Alk. solub., %	Precipitation (lignin), %	Resid. after alk. extr., %
Untreated	-	0	0	100	7.3	92.7	4.5	0.2	88.2
SE treated	32	3.97	13.8	86.2	10.8	75.3	7.1	2.3	68.3

From SEM micrographs of ultrasonic treated fibers (Fig.1) can estimate morphological characterization of fibers surface. Individual fibers and their aggregates of cellulose can be easily observed. There can be seen that after HIUS treatment fibers are separate to fibrils. Some surface and structure defects seen on the micrograph could appear during hemp stalk primary processing or combing.

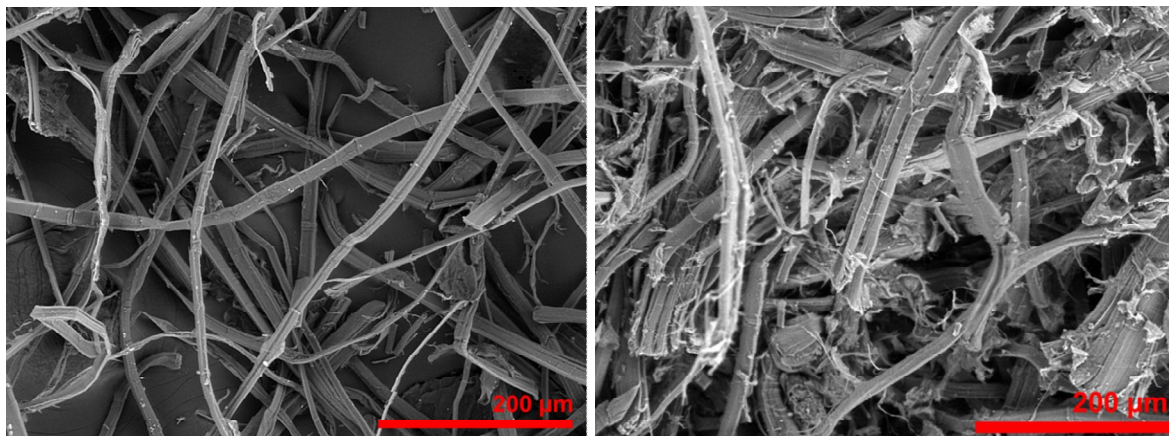


Fig. 1. Steam explosion treated hemp fibres before and after HIUS

Infrared Fourier spectroscopy allows revealing modifications of main cellulose-based structures, non-cellulose compounds through identification of carboxylic acids and esters found in pectin, lignin, and waxes not found in cellulose [17]. The IR bands of hemp lignin are found in the frequency range 1460 cm^{-1} , 1507 cm^{-1} and 1730 cm^{-1} . Intensity of the 990 cm^{-1} band is reduced after treatments decreasing the lignin content ($-\text{HC}=\text{CH}-$ out of plane deformations) (Fig. 2). From FTIR spectra can see that after SE and HIUS treatment decrease peak intensity at the band intensities 1110 cm^{-1} (aromatic C-H in $-\text{plane}$ deformation (typical for S units); plus secondary alcohols plus C=O stretch).

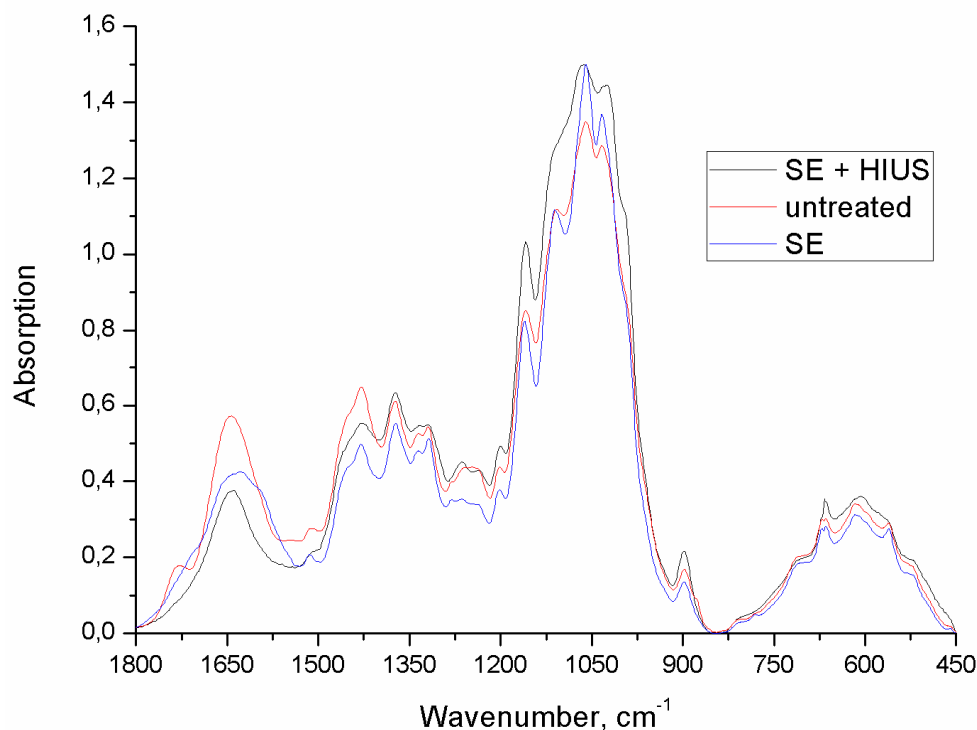


Fig. 2. FTIR spectra of untreated, steam exploded (SE) and after HIUS (SE+HIUS) treated hemp fibres



CONCLUSIONS

Hemp cellulose microfibrils are individualized from bast fibres using steam explosion, hydrothermal, alkali treatment and HIUS. Results of this study have shown that SE treatment combined with following hydrothermal and 0,4 wt. % NaOH treatment allows removing partly constituents from hemp fibers. SEM observations show that the sizes of the different treated fibrils have a diameter range to several micrometers. There can be seen that after HIUS treatment fibres are separate to fibrils, microfibrils and agglomerates of them. FTIR analysis showed differences between the spectra for the untreated, steam explosion treated and ultrasound treated hemp fibres at insets 990 cm^{-1} and 1110 cm^{-1} .

ACKNOWLEDGEMENTS

This work has been supported by the European Social Fund within the project «Support for the implementation of doctoral studies at Riga Technical University».



INVESTING IN YOUR FUTURE



REFERENCES

1. LAVOINE, N., DESLOGES, I., DUFRESNE A., BRAS, J. Microfibrillated cellulose – Its barrier properties and applications in cellulosic materials: A review. *Carbohydrate Polymers*, 2012, Vol. 90, p. 735–764.
2. THYGESEN A. Properties of hemp fibre polymer composites -An optimisation of fibre properties using novel defibration methods and fibres characterisation, PhD thesis, The Royal Agricultural and Veterinary University of Denmark, ISBN 87-550-3440-3.
3. MADSEN, F.T., BURGERT, I., JUNGNIKL, K., FELBY, C., THOMSEN A.B. Effect of enzyme treatment and steam explosion on tensile properties of single hemp fiber. 12th International Symposium on Wood and Pulping Chemistry (ISWPC), 2003, Madison, P80.
4. BRÜHLMANN F., LEUPIN M., ERISMANN K.H., FIECHTER A. Enzymatic degumming of ramie bast fibers. *Journal of Biotechnology*, 2000, 76, 43–50.
5. THOMSEN, A. B., RASMUSSEN, S., BOHN, V., NIELSEN, K.V., THYGESEN, A., Hemp raw materials: The effect of cultivar, growth conditions and pretreatment on the chemical composition of the fibres. R-1507, Risø National Laboratory, Denmark, 2005.
6. MWAIKAMBO LY, ANSELL MP. The effect of chemical treatment on the properties of hemp, sisal, jute and kapok for composite reinforcement. *Die Angewandte Makromolekulare Chemie*, 1999, 272, 108–116.
7. WANG H.M., POSTLE R., KESSLER R.W., KESSLER W. Removing pectin and lignin during chemical processing of hemp for textile applications. *Textile Research Journal*, 2003, 73, 664–669.
8. GARCIA-JALDON, C., D. DUPEYERE, M. R. VIGNON. Fibres from semi-retted hemp bundles by steam explosion treatment. *Biomass and Bioenergy* Vol. 14, No. 3, 251-260, 1998.
9. VIGNON M.R., GARCIA-JALDON C., DUPEYRE D. Steam explosion of the woody hemp chénevote. *International Journal of Biological Macromolecules*, 1995, 17, 395–404.



10. ZIMMER H., KLOSS D. Ultraschallaufschluss von Hanf. Ziele-Technologie-Anwendungs-Resultate-Qualitätsmanagement. Nova-Institut, Proceedings of the Bioresource Hemp '95 Symposium, 3–5 March 1995, Frankfurt, Germany.
11. KLINKE H.B., AHRING B.K., SCHMIDT A.S., THOMSEN A.B. Characterization of degradation products from alkaline wet oxidation of wheat straw. *Bioresour Technol*, 2002, 82. 15–26.
12. CHENG Q, WANG S, HAN Q. A novel process to isolate fibrils from cellulose fibers by high-intensity ultrasonication. Part II: Fibril characterization. *J Appl Polym Sci*, 2009, Vol. 113, p. 1270–1275.
13. CHENG, QINGZHENG, Fabrication and Analysis of Polymeric Nanocomposites from Cellulose Fibrils." PhD diss., University of Tennessee, 2007.
http://trace.tennessee.edu/utk_graddiss/137,
14. KUKLE S., GRAVITIS J., PUTNINA A. Processing Parameters Influence on Disintegration Intensity of Technical Hemp Fibres. *Journal of Biobased Materials and Bioenergy*, 2012, Vol.6, No.4, p. 440-448.
15. KUKLE S., STRAMKALE V., KALNIŅA D., SOLIŽENKO R. Comparison of HEMP Fibre Properties. 6th International Textile, Clothing & Design Conference "Magic World of Textile": Book of Proceedings, Horvātija, Dubrovņiki, 7.-10. Oct., 2012. – p. 76–80.
16. M. HEITZ, E. CAPEK-MONARD, P.G. KOEBERLE, J. GAGNO, E. CHORNET, R.P. OVEREND, J. D. TAYLOR, E. YU. Fractionation of *Populus tremuloides* at the Pilot Plant Scale: Optimization of Steam Pretreatment Conditions using the STAKE II Technology. *Bioresource Technology* 35 (1991) 23-32
17. WANG Q, FAN XR, GAO WD, CHEN J. Characterization of bioscoured cotton fabrics using FT-IR ATR spectroscopy and microscopy techniques. *Carbohydrate Research* 2006; 341, 2170–2175
18. OUAJAI, S.; SHANKS, R.A., Composition, structure and thermal degradation of hemp cellulose after chemical treatments. *Polymer Degradation and Stability*, 2005. 89(2): p. 327–335.



PHOTOVOLTAIC BATTERIES WITH MODIFIED GLAZING

A. Snegirjovs, P. Shipkovs, M. Vanags, L. Mila

*Institute of Physical Energetics
Aizkraukles 21, LV-1006 Riga – Latvia*

A. Snegirjovs, P. Shipkovs

*Riga Technical University
Azenes 16/20, LV-1048 Riga – Latvia*

J. Oļeiņiks

*GroGlass LTD
Katlakalna 4b, LV-1073, Riga – Latvia*

ABSTRACT

Photovoltaic (PV) battery's efficiency increasing is one of the central purposes of PV industry. It is possible to increase solar panel's production of electricity by improving characteristics of solar panel glazing.

Crystal anti-reflective thin film coating on glass was designed specifically for monocrystalline and multicrystalline silicon wafer modules. Developed glazing takes into consideration: silicon crystalline cell light wavelength sensitivity; temperature conditions and need to reject heat in the spectrum that cells do not use for energy production (near infrared radiation); the Sun's position over solar panel during the day and the year (angle of light beam incidence).

Efficiency of regular and modified glazing of PV batteries was investigated in real weather conditions in solar energy testing polygon. It was determined that PV batteries glazing types have different impact on PV batteries production in similar environment conditions. Efficiency increasing was in high solar radiation intensity conditions for modified glazing of PV batteries, because this glazing reduced PV batteries warming from infrared radiation. But difference of energy production was lower in cloudy days, especially when PV module's temperature was low. Annual energy production of modified glazed PV batteries in comparison with regular glazed PV batteries is about 2% higher.

Keywords: photovoltaic batteries, glazing, renewable energy

1. INTRODUCTION

Replacing fossil fuels energy with renewable energy is one of the topical issues currently in the world. Special emphasis is placed on solar energy use. Solar energy is fully renewable energy and its amount is practically unlimited. The most important limitation of photovoltaic (PV) technology use is efficiency of PV Cells, what is relatively low now. Therefore economically benefit is PV batteries using in high solar intensity regions (like California, USA, and Spain) [1].

Photovoltaic battery's efficiency increasing is one of the central purposes of PV industry. A lot of efficiency improvements are investigated and insert in PV batteries materials and production methods.

Electricity generations of PV cells are defined by the silicon materials properties. Therefore it is possible to increase solar panel's production of electricity by improving characteristics of solar panel glazing [2].

PV cell efficiency defines external quantum efficiency (EQE) of equipment. EQE is function of photon flow that comes in PV environ, and it does not depend on PV cells number of transitional. This means that it is important to achieve as much as possible to get photons in PV environ and these not reflected in air from PV panel protective glass.

Refractive index of air is about 1, while refractive index of glass is about 1.5, what shows that from 25 to 40% of solar radiation may be reflected from glass surface. Antireflection layer application reduces solar radiation reflection up to 1%. The main function of this layer has gradual increasing of refractive index with thin layers between air and glass. Also antireflective layer can be achieved by thin layer of destructive interference. The main principle is that glass has been covered by thin layer what thickness corresponds to quarters of fixed wavelength. Reflective rays from layer and glass surface interfered. Taking into account that thickness of layer is quarters of wavelength, this interference is destructive. This means that both rays quench each other, theoretical result of reflecting rays is zero [3-6].

Efficiency of regular and modified glazing of PV batteries was investigated in real weather conditions in solar energy testing polygon [7]. One of PV batteries set's glasses are covered by metal oxide layer, what is selective antireflective. The regular glazing is used for second set.

2. METHODS

Two similar PV batteries sets were used in experiment. Characteristics of PV batteries are: $P_{MPP} = 232.45$ W, $V_{MPP} = 29.2$ V, $I_{MPP} = 7.96$ A, $V_{OC} = 37.2$ V, $I_{SC} = 8.3$ A. Each PV batteries set includes kit of 4 batteries. One of PV batteries set has regular glazing, and second has glazing with antireflective covering. The covering consists of six metal oxide thin layers. The total thickness of covering is 300 nm.

The comparing of spectral transmittance for extra clear glass, unilateral and bilateral coated glazing is displayed in Fig. 1. It is shown that one side and double side covered glazing have maximal radiation transmittance in Si PV cells in EQE region. Radiation transmittance of covered glazing is higher by comparing with extra clear glass radiation transmittance in Si PV cell EQE region. Glass covering has low radiation transmittance in short wavelength, what makes degradation of PV cells. Also glass covering reduces solar radiation transmittance in infrared wavelength what decreases efficiency of PV batteries because it is related to warming of PV cells. This indicates that the coating should be auspicious.

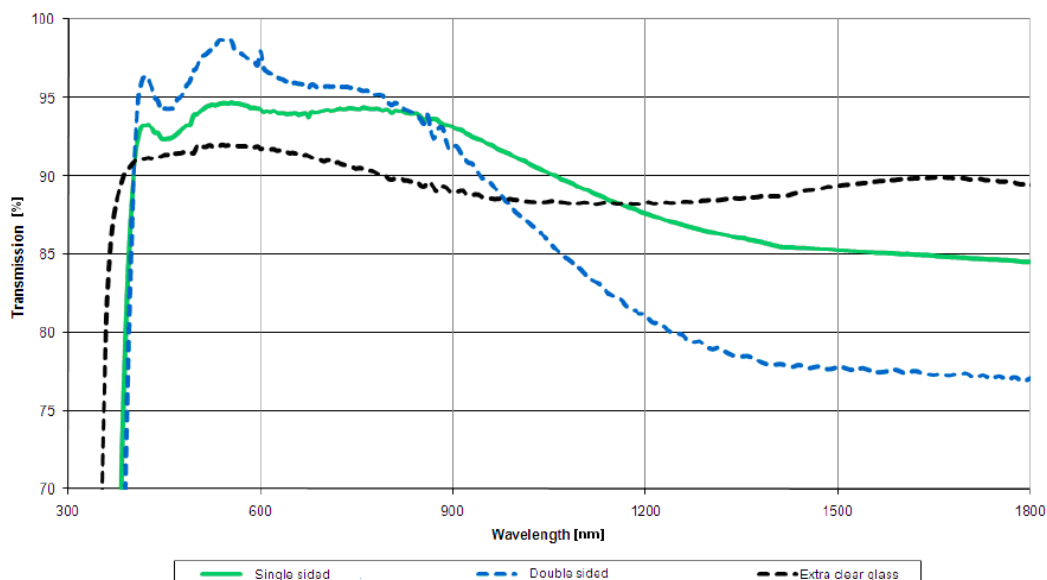


Fig. 1. The spectral transmittance of clear glass, single and double sided coated glazing

Both sets are separately connected to its own grid inverter with following parameters: $P_{DCmax} = 1320$ W, $V_{DCmax} = 400$ V, $V_{PV} = 100...320$ V, $V_{DCnom} = 120$ V, $I_{PVmax} = 12.6$ A, $P_{ACnom} = 1200$ W,

$V_{ACnom} = 220...240$ V, $I_{ACnom} = 5.2$ A. Each solar set is connected in series. Kit of 4 PV batteries gives 120V in inverter DC input. AC sides of invertors are connected to central electricity network. Grid connection for each inverter goes through a separate fuse. Bluetooth communication card has been built-in each grid inverter, by what the inverter intercommunicates with the computer. The most important parameters are saved with special program every 5 min, such as: PV voltage, PV current, AC voltage, AC current, AC frequency. Inverter work hours, total energy production, daily energy production, operating status, etc. Also save information about outdoor air temperature, PV batteries surface temperature and solar radiation intensity. The testing period is 49 days.

3. RESULTS AND DISCUSSION

Fig. 2 shows variations of power values from two sets for 49 days. In 32 days momental power of both sets exceeded 700 W, in 8 days the limit of 500W has not reached but in 1 day the limit of 100 W has not reached.

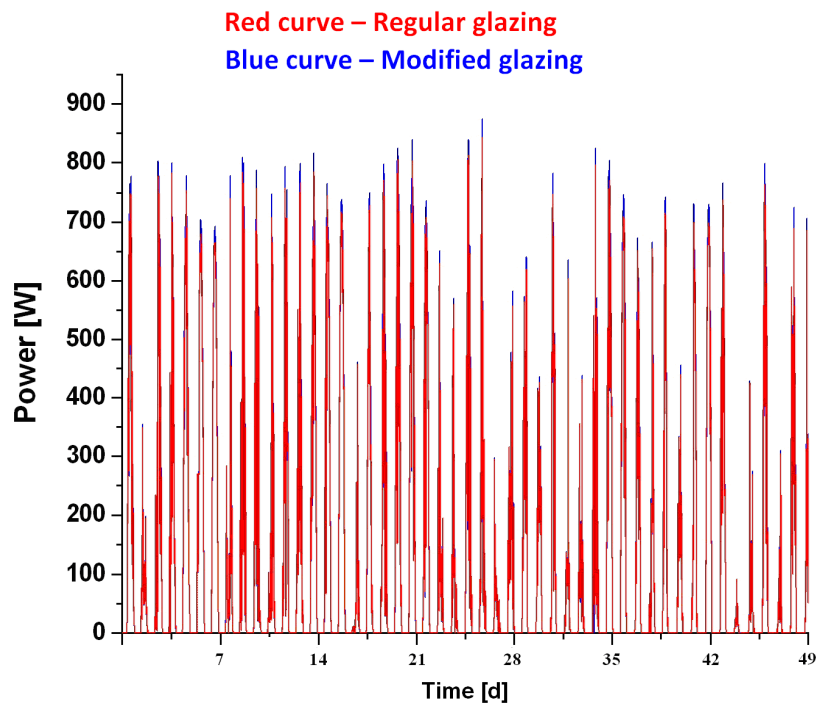


Fig. 2. Power values of both sets for 49 days

The increase in the difference of output energy of regular and modified glazing PV batteries in time is shown in Figure 3. The curve can be divided into several distinct regions. Gain of difference is surging to 22nd test day then spread curve get lower a slope of rise up to 35th day of testing. The differential slope of curve rises again till the end of testing time. At the end of test modified glazing set has been supplied 2.98 kWh more energy as set with usual glazing.

The produced energy difference of both sets depended on outdoor air temperature (Fig. 3). The average temperature during the testing period was 15 °C. Whereas testing period was from August till October, the daily temperature gets lower.

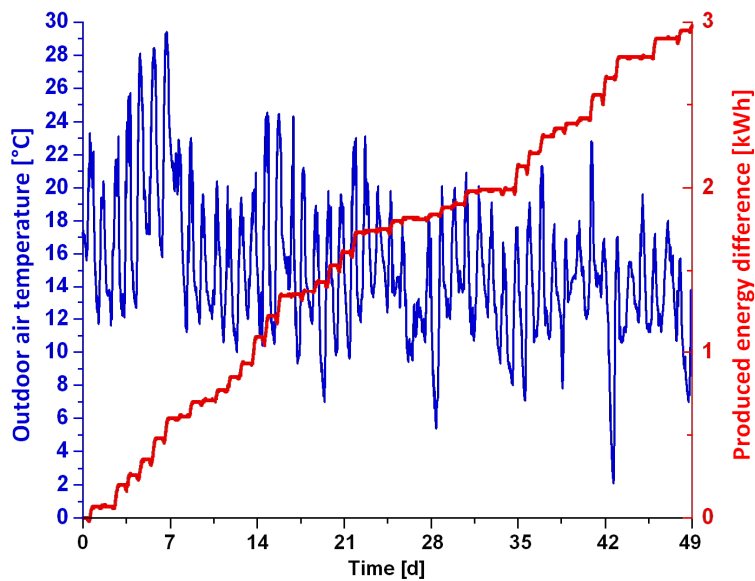


Fig. 3. An outdoor temperature and produced energy difference between both types of glazing in 49 days testing period

In the time when the outdoor temperature was lower, the decrease of slope of curves was observed. But in the hottest days in the end of August the difference is growing more rapidly than in the middle of testing period when temperature was lower. In the days when the temperature's variations are not as pronounced the difference growing less.

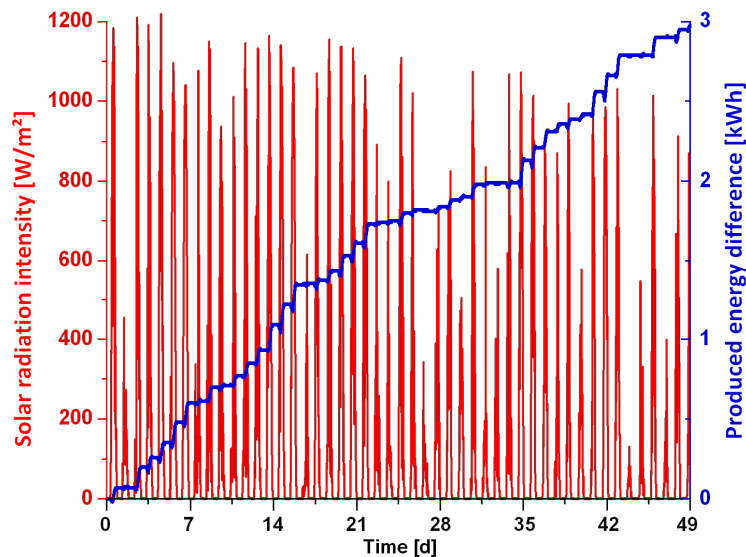


Fig. 4. Solar radiation intensity and produced energy difference between both types of glazing in 49 days testing period

Fig. 4 shows the dynamic of difference between produced energy of regular and with modified glazing PV batteries plus the solar radiation density. When solar radiation density is lower or the sky is not clear, the slope of curve gain is less, but when peak of the sun's radiation density is high, the difference gain is greater.

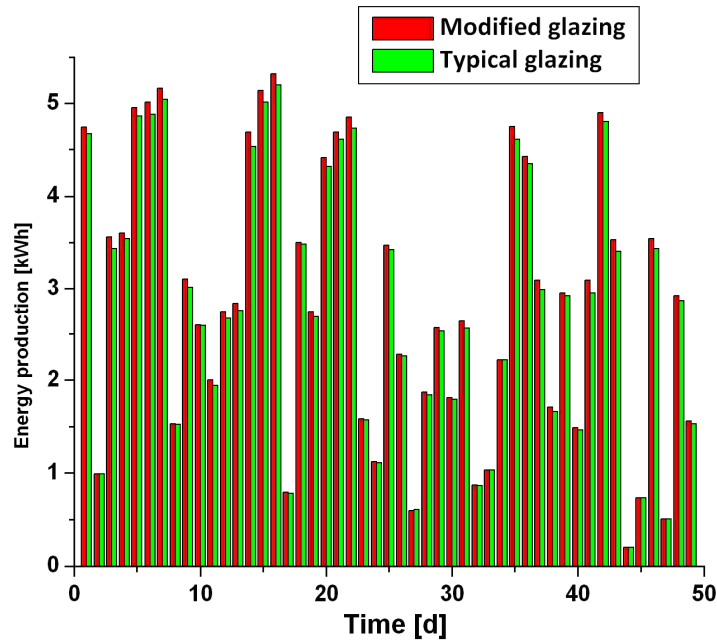


Fig. 5. Daily production of both sets

The dynamic of daily produced energy of two sets in the testing period is shown in Fig. 5. The top of the produced energy is in the 16th day of the period, while the below – 44th day of the testing period. Average daily production of modified glazing set is 2.866 kWh but a typical glazing set produced 2.805 kWh, which is by 2.13% less than modified glazing set.

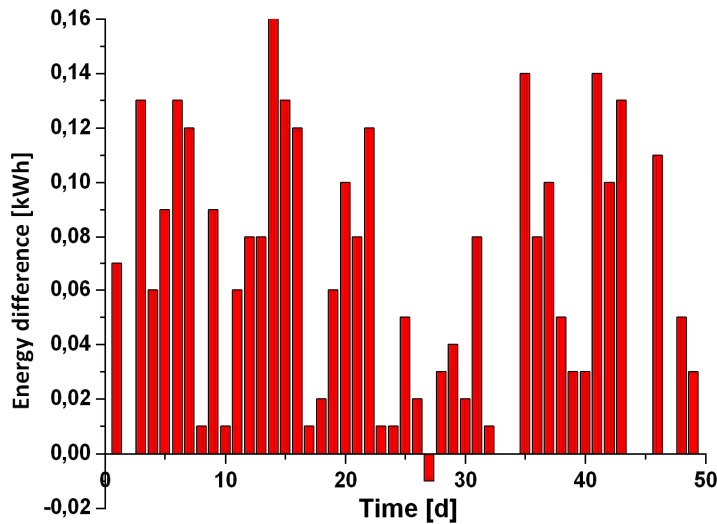


Fig. 6. Difference between daily energy production of both sets

Fig. 6 shows daily energy production output gap in the testing period. By the 42 days the modified glazing set produced more energy than set with a typical glazing. Both sets produced equal in 6 days, but only in 1 day set with typical glazing produced more than modified glazing set.

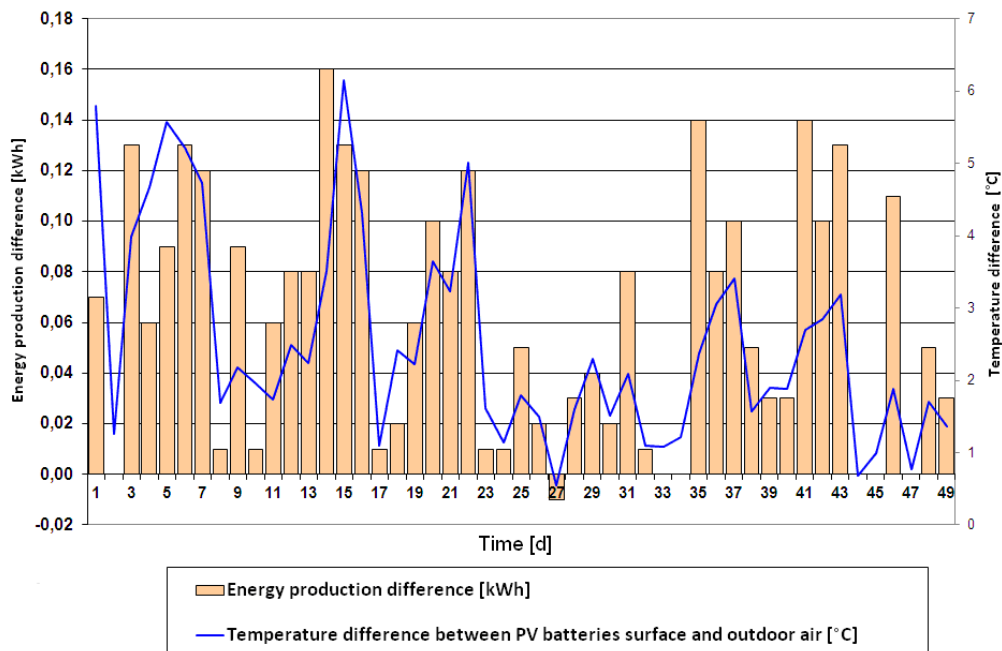


Fig. 7. Daily energy production difference and temperature difference

Fig. 7 depicts a graph where on the one–ordinates has been postponed temperature difference between temperature in PV modules and outdoor temperature but on the second–ordinates shown produced energy difference. This figure shows that the dynamic of “y” values are matched. On the merits difference of temperatures shows heating up of solar PV cell. The more the sun heats up the battery, the greater growths difference between output energy of the both sets, or modified glazing solar set dominated in conditions when the solar radiation density is high, because are additional panel heating and indecreades efficiency of PV cell.

4. CONCLUSIONS

Analysis shows that PV batteries set with modified glazing generated 140 kWh in the electricity network in 49 days time period from August 21 till October 8. While regular glazing PV batteries set generated 137 kWh. Therefore, set with modefing glazing generated 2.98 kWh, or up to 2.16% more electricity.

The difference of energy production from PV sets depends on environmental conditions (ambient temperature, solar radiation intensity).

Experiment show that the difference of energy production is reduced close to zero at low ambient temperatures, and even reaches negative value. The difference rice up when ambient temperature is increasing.

Efficiency of PV batteries with modified glazing increasing in high solar radiation intensity conditions, because this glazing reduced PV batteries warming up from infrared radiation.

ACKNOWLEDGMENT

This work has been supported by State Research Program “LATENERGY”.



REFERENCES

1. KING C., Site data analysis of CPV plants, Conference Record of the IEEE Photovoltaic Specialists Conference, p. 3043–3047.
2. PIETRUSZKO S.M., BLAZEJEWSKA K., MALINOVSKA, Development of photovoltaics in the Central and Eastern European States, Conference Record of the IEEE Photovoltaic Specialists Conference, p. 219–222.
3. ROGER J., COLARDELLE P., Antireflecting silicon solar cells with titanium dioxide, Proceedings of the Eighth IEEE Photovoltaic Specialists Conference, Seattle, USA, 1970, p. 84–87.
4. STELLA P.M., SOMBERG H., Integrally covered silicon solar cells, Proceedings of the Ninth IEEE Photovoltaic Specialists Conference, Silver Springs, USA, 1972, p. 179–184.
5. LUFT W., Status of TiOx antireflective coating in the US, in: Proceedings of the 10th IEEE Photovoltaic Specialists Conference, Alaska, USA, 1973, p. 174–179.
6. BRANDHORST H.W. Jr., Current status of silicon solar cell technology, in: Technical Digest of the IEEE International Electron Devices Meeting, Washington, USA, 1975, p. 331–334.
7. SHIPKOV S., KASHKAROVA G., LEBEDEVA K., Solar energy use for sustainable development, 29th ISES Biennial Solar World Congress 2009, ISES 2009 2 , p. 1881–1887.



INVESTIGATION OF SOLAR PHOTOVOLTAIC AND WIND POWER GENERATION

R.P. Deksnys, A. Stankevičius
Kaunas University of Technology
Studentų g. 48, LT-51367 Kaunas – Lithuania

ABSTRACT

Integration of the solar photovoltaic and wind power stations that use renewable energy keeps progressing in Lithuanian power system. Assessment of the influence of intermittent power stations with variable power output is highly significant for the operating regimes and frequency management in the energy system.

In this paper, energyPRO program consists of solar photovoltaic and wind power parks in the model. Based on the data of Lithuanian Hydrometeorological Service, power generation by the power plants in farms under consideration has been estimated, and distributions of variance in power generation and their parameters as well as dependencies of correlation coefficients of power generation variation have been calculated. The inter correlation between power generations in solar photovoltaic and wind farms, and that between power generation and the load have been determined.

Keywords: correlation, energyPRO, power generation

1. INTRODUCTION

Rapidly increasing numbers of wind and solar power plants generating renewable energy as well as variable and only partly predictable power generation and electricity production by these plants raises problems to energy systems and electrical power market because makes it difficult to continuously ensure a balance between electrical power generation and consumption, the exchange of power generation and trade in electric power with neighbouring countries [1-2]. For this reason it is necessary to have some extra operating power reserves in any energy system in order to ensure its reliable operation. Amount of required additional power reserves depends on the size and load of the power system, as well as on the throughput of electric power systems and their links with neighbouring power systems, thus it is limited.

Successful integration of wind and solar power plants into energy systems requires not only for increased power transfer throughput of power systems but also for improved technologies and ability to duly control and adjust variable power generation by wind power plants. In order to ensure reliable and safe operation of energy system and to possibly use renewable wind and solar power more efficiently, it is absolutely necessary to have reliable indicators of power generation plants operation and characteristics that enable maximum integration of these power plants into the energy system and prevent from potential problems and restrictions of operating regimes control within energy system.

2. CHARACTERIZATION OF THE OBJECT UNDER RESEARCH

The model under investigation was comprised of solar power generation farms PVP1 and PVP2 located at the distance of 186 km from each other, wind power farms WPP1 and WPP2 located at the distance of 80 km from each other, and load power of the electrical power system in the region under research. For the purpose of calculations of power generation farms the installed capacity of 30 MW was selected. Simulation used measurement data of wind speed and solar radiation for one hour time-steps recorded by the Lithuanian Hydrometeorological Service (LHMT) in the one year period of 01/07/2010 to 30/06/2011 at Kaunas (PVP1), Šilutė (PVP2, WPP2), and

Šventoji (WPP1) power plants. Measurements of wind speed were taken at Šilutė and Šventoji hydrometeorological stations at the height of 10 m above ground surface. Requirement for power generation in the region under research amounts for 169.1 GWh.

Power generation by wind and solar power plants were calculated based on data supplied by LHMT, using software “energyPRO”, whereas parameters of power generation variation, correlation coefficients between fluctuations in power generation were obtained using SPSS software package.

3. METHODS FOR CALCULATION OF POWER GENERATION BY SOLAR AND WIND POWER PLANTS

Power generation by solar and wind power plants can be calculated using the following methods:

Method of solar calculation (Photovoltaic);

The electricity production from a Photovoltaic module, P_{pv} , can be expressed as follows:

$$P_{pv} = P_{max} \cdot \frac{I_s}{I_{STC}} \cdot [1 - \gamma_s \cdot (T_{cell} - T_{STC})] \quad (1)$$

where P_{max} is the installed capacity, I_s is the solar radiation, I_{STC} is the radiation under standard conditions, γ_s is the temperature coefficient for module efficiency, T_{cell} is the operation cell temperature, T_{STC} is the cell temperature at standard conditions.

The operation cell temperature is calculated by the following formula [3]:

$$T_{cell} = T_{at} + I_s \cdot \left(\frac{NOCT - 20^\circ C}{800W / m^2} \right), \quad (2)$$

where T_{at} is the ambient temperature, $NOCT$ is the Nominal Operating Cell Temperature.

Hereto come losses from the pv-module to the grid, λ_{misc} , such as miscellaneous PV array losses and other power conditioning losses.

The power production at grid becomes:

$$P_{elec} = P_{pv} \cdot (1 - \lambda_{misc}) \quad (3)$$

where P_{elec} is the electricity production to the grid from the photovoltaic plant.

Method of wind warm calculation;

Calculated wind speed at hub height:

$$WS_c(t) = WS_m(t) \cdot \left(\frac{H_h}{H_m} \right)^\alpha \quad (4)$$

where $WS_c(t)$ is the wind speed calculated at time t , $WS_m(t)$ is the wind speed measured at time t , H_m is the Height of measurements, H_h is the Hub Height, α is the Hellmann coefficient.

Calculation of production at time t :

$$P(t) = PC(WS_c(t)) \cdot P_{Max} / P_{MaxPC} \quad (5)$$

where $PC(WS_c(t))$ return then power from the power curve based on the calculated wind speed at hub height and linear interpolation on power curve, P_{Max} is the Max Power stated, P_{MaxPC} is the Max power value found in power curve. $P(t)$ is the production at time t .

Based on the data of LHMT, and using above mentioned methods, it was estimated that operating (Fig. 1) under its average capacity of 7.79 MW with the duration of operation at its installed capacity being 2274 h, WPP1 (Šventoji hydrometeorological station) is supposed to generate 68.22 GWh of electrical power per year, resulting in its installed capacity efficiency of

25.96 %. In the same period of time, WPP2 (Šilutė hydrometeorological station) is supposed to generate 59.67 GWh of electrical power. The average annual capacity of this power farm amounts for 6.81 MW, the duration of operation at its installed capacity – 1989 h, and its installed capacity efficiency 22,71 %. The regional solar power farm PVP1 (Kaunas hydrometeorological station), operating under its average capacity of 3.85 MW with the duration of operation at its installed capacity of 1125 h, is expected to generate 33,76 GWh of electrical power per year, resulting in its installed capacity efficiency of 12.85 %, whereas PVP2 (Šilutė hydrometeorological station) is expected to generate 33.82 GWh of electrical power per year, resulting in its installed capacity efficiency of 12.87 % when operating under its average capacity of 3,86 MW with the duration of operation at its installed capacity being 1127 h.

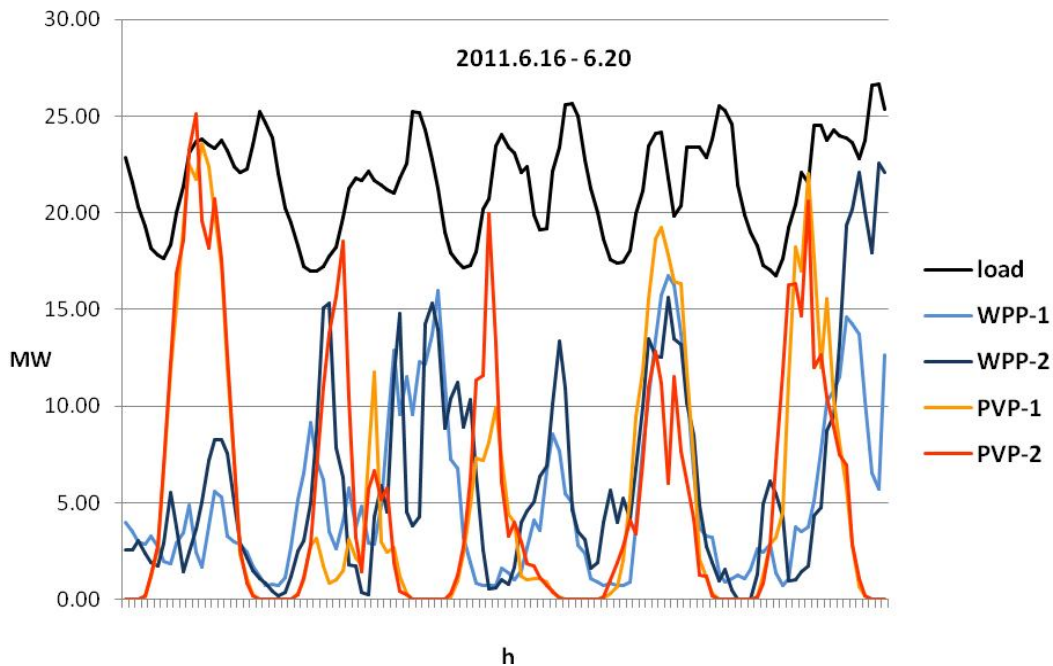


Fig. 1. Fluctuations in power generation of solar and wind power plants

4. INVESTIGATION OF THE VARIATION OF POWER GENERATION BY POWER PLANTS

For the purpose of the assessment of variation in power generation by solar and wind power plants, the study of correlation and standard deviations was carried out based on the data representing the entire period covered by the research.

Variation in power generation might be determined as follows:

$$\Delta P_i = P_{i+1} - P_i, \quad (6)$$

where P_i and P_{i+1} – average power generation over consecutive selected time steps.

The following formula is used to determine correlation coefficient between power generation of two WPPs [4]:

$$r_{12} = \frac{\sum_{i=1}^n (\Delta P_{1,i}) (\Delta P_{2,i})}{\sqrt{\sum_{i=1}^n (\Delta P_{1,i})^2} \sqrt{\sum_{i=1}^n (\Delta P_{2,i})^2}}, \quad (7)$$

where ΔP_{1i} and ΔP_{2i} – the i^{th} variation in power generation of the first and second farms, respectively.

The following formula is used to determine standard deviations of variation in power generation:

$$\sigma = \sqrt{\sum_{i=1}^n \frac{1}{n-1} (\Delta P_i - \overline{\Delta P})^2}, \quad (8)$$

where n – number of measurements made under research, $\overline{\Delta P}$ – average value of variation of power generation, that in this particular case is equal to zero.

Analysis of results obtained shows that correlation coefficients of variation in power generation (Fig. 2) between two investigated WPP are weakly positive and below 0.15, whereas those between WPP and loads – negative but low and amounting for -0.02 – -0.05 . The calculated standard deviations (Table 1) amount for 2.06 MW for WPP1, and 2.17 MW for WPP2, whereas their standard deviations calculated including the load are increased and equal to 2.62 MW and 2.56 MW, respectively. Such a variation in deviations will increase operating power reserves necessary for an energy system.

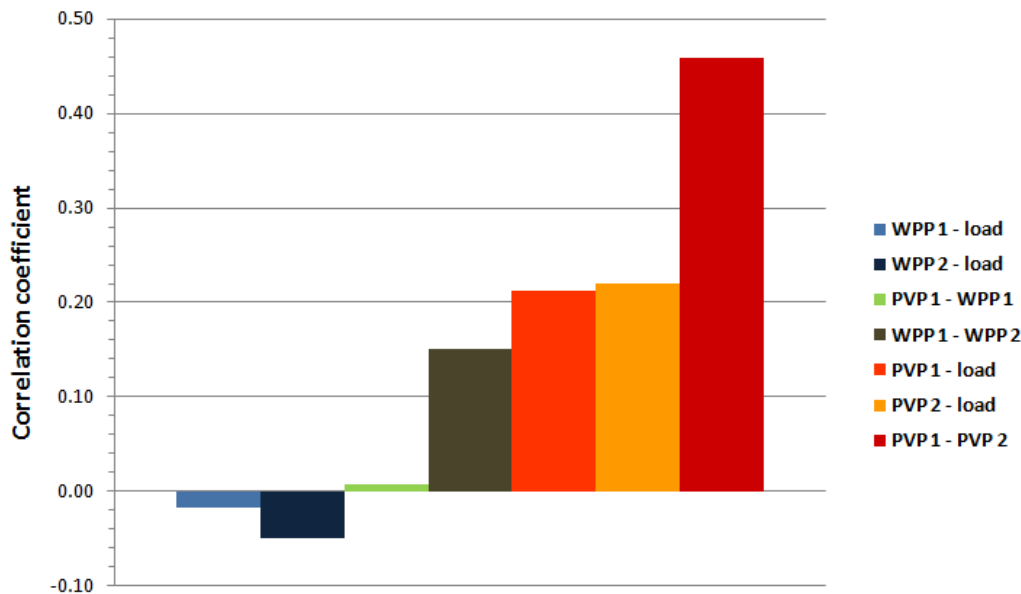


Fig. 2. Correlation of power variation between power parks and between power parks and the system load

The correlation coefficients of the variation in power generation by two solar power plants (PVP) under investigation were found to be positive and below 0.46, whereas those between PVP and loads – also positive, however lower and equal to values 0.21 – 0.22. The calculated standard deviations for solar power plants amount for 2.47 MW for PVP1, and 2.59 MW for PVP2, whereas their standard deviations calculated including the load were found not to increase due to the positive correlation of variation in power generation and remain in range of 2.46 MW and 2.60 MW, respectively. Such a variation in deviations is not expected to significantly increase operating power reserves.

Table 1. Parameters of variations of WPP and PVP power generation

Object	Parameters	Object				
		load	WPP1	WPP2	PVP1	PVP2
load	r_{12}	-----	-0.02	-0.05	0.21	0.22
	σ , MW	1.24	2.42	2.56	2.52	2.61
WPP1	r_{12}	-0.02	-----	0.15	0.01	-0.01
	σ , MW	2.42	2.06	3.21	3.23	3.30
WPP2	r_{12}	-0.05	0.15	-----	-0.04	-0.05
	σ , MW	2.56	3.21	2.17	3.23	3.30
PVP1	r_{12}	0.21	0.01	-0.04	-----	0.46
	σ , MW	2.46	3.23	3.23	2.47	4.32
PVP2	r_{12}	0.22	-0.01	-0.05	0.46	-----
	σ , MW	2.60	3.30	3.30	4.32	2.59

The maximum correlation coefficient of variation in power generation of 0.46, and standard deviation of 4.32 MW obtained between the solar power plants shows that development of solar power plants must be well-balanced to the local demand for load.

Findings obtained through this research show that it's worth developing solar and wind power plants generating renewable energy in as large territories as possible while ensuring more even loading on power transfer network and fuller use of throughput of electric power systems.

CONCLUSIONS

The correlation of variation in power generation between wind power farms was found to be positive, whereas that between power farms and load – weakly negative, consequently penetration of wind power plants into the electrical power systems is expected to increase operating power reserves.

The variation in power generation by solar and wind power farms were found not to correlate, and their joint standard deviations were found to increase, consequently solar power plants are not expected to serve for stabilization of variation in power generation by wind power plants.

The correlation of variation in power generation between the solar power plants and load was found to be positive, their joint standard deviations were found not to increase, consequently penetration of solar power plants into the electrical power systems is not expected to require for significant operating power reserves.

REFERENCES

1. DEKSNYS R.P., STANIULIS R., ŠULGA D. *Posibilities of wind power plants penetration into electric power system*. Electrical and Control Technologies ECT – 2008: 3rd International conference. Kaunas: Technologija, 2008. ISBN 978-9955-25-484-3. p. 27–31.
2. AŽUBALIS M., AŽUBALIS V., SLUŠNYS. D. *Estimation of the Feasible Wind Power in a Small Power System*. Electronics and Electrical Engineering. Kaunas: Technologija, ISSN 1392 – 1215. 2011. No. 1(107). p. 79–82.
3. LUQUE A., HEGEDUS S. *Handbook of Photovoltaic Science and Engineering. Books:* Wiley, 2003, ISSN 0471491969, p. 1168.
4. ERNST B. *Short – Term Power Fluctuations of Wind Turbines from the Ancillary Services Viewpoint*. Institut für Solare Energieversorgungstechnik Königstor 59 D-34119 Kassel Germany, <http://www.iset.uni-kassel.de>



THE GHG EMISSIONS MODEL STUDY FOR STRAW FIRED BOILERS

K. Vagoliņš, G. Frīdenbergs, P. Šipkovs
Riga Technical University
Azenes street -16/2nd floor, LV-1010 – Latvia

ABSTRACT

Latvia (EU) is obligated to report anthropogenic greenhouse gas emissions annually to the UNFCCC. Inventories of greenhouse gas emissions and methodologies used have to be well based and documented. The aim of this report is to give input to Latvia greenhouse gas inventory of straw fired boiler sector. The emission factors for the industrial processes used in the inventory are based both on plant-specific factors and the IPCC default values. Modelled emission factors for the non-CO₂ greenhouse gases from combustion are mainly based on studies in plant design and maintenance, operating conditions and composition of fuels. In addition, knowledge of emission generating processes has increased world-wide.

In this study, the non-CO₂ emission factors (mainly CH₄ and N₂O, and at a lesser extent, CO and NMVOC) for straw fired boiler used in the Latvian greenhouse gas inventory are evaluated based on domestic and international literature, available measurement data and calculated data.

Results of this study revealed many potential areas for improvements in the inventory. The time dependency and uncertainties of the emission factors are also considered. In addition, effect of load and straw mixes on emissions is examined. Areas for further research are also indicated.

Keywords:

1. INTRODUCTION

The publication provides a research methodology and the presentation of the Latvian model-research available biomass for energy in order to assess the GHG emissions from the agricultural biomass life cycle. Cycle of biomass production, harvesting, processing and use, as well as prepared forest products for energy production.

Division of simple benchmarks for available biomass resources in Latvia ranking of GHG emission reductions in their production process and the use of the output of useful energy unit, taking into account the effectiveness of technologies available on the market.

2 RESEARCH METHODOLOGY

Taking into account the results of calculations simple benchmarks for biomass resources ranking the GHG emission reductions in their production process and the use of the output of useful energy unit is designed, taking into account the effectiveness of technologies available on the market. Ranking is the basis of the analysis and recommendations on the use of biomass for efficiency opportunities in Latvia:

1. Specific estimates of emissions due allowance for the use of biomass energy (fuel, electricity) consumption throughout the life cycle of biomass such as crops is evaluated by energy consumption in tillage, fertilization, crop care, harvesting, primary transportation, recycling, energy use and the use of by-the return of nutrients life cycle or deposit.

2. Set of operations consumed emissions are calculated as energy resource (fuel or electricity) emissions using the specific research.
3. Emissions from mobile vehicles specific operations such as emissions EMT mass transport is given by:

$$E_{mt} = D_p \times E_i \quad (1)$$

where D_p – the total fuel consumption in the operation, l; E_i - specific emission $\text{gCO}_2\text{eq} / \text{l}$ for each fuel, usually used transport in such operation.

4. Emissions of biomass processing or reprocessing operations that use electricity, such as the E_s emissions pumping motors are calculated as follows:

$$E_s = E_{el} \times P_{el} \quad (2)$$

where E_{el} – emissions from the production of 1 kWh of electricity on Latvia's average, using Latvia Ministry of the Environment (2007) the accepted value of $E_{el} = 363 \text{ gCO}_2/\text{kWh}$; P_{el} – power consumption of the particular operation occurs, kWh.

5. The recommended emission calculation procedure is as follows: first, calculate consumed operations required to carry out energy (fuel or electricity) use. Below the calculated value is used to calculate the energy used to carry out the operation of production, harvested from 1 ha or for 1 day output, as well as the calculated value is used to convert the resource consumption of energy per unit of production or the production of 1 MJ net energy (net energy – energy from biomass to replace fossil energy resources, such as energy furnace heat output) by the following formulas:

$$E_{MJ} = E_{op} \div P_{sar} \quad (3)$$

where E_{OP} – day operations emissions gCO_2eq ; P_{sar} - daily production of useful energy, MJ.

$$E_{MJ} = E_{ha} \div P_{ha} \quad (4)$$

where E_{ha} – 1 ha management issue, $\text{gCO}_2\text{eq}/\text{ha}$, P_{ha} - from 1 ha of useful energy output, MJ.

3. GHG EMISSIONS MODEL-RESEARCH FOREST PRODUCTS AND STRAW FOR USE IN THERMAL POWER GENERATION

Forest products and straw belonging to the solid biomass with a high cellulose and lignin content, yet difficult to use them to others, such as anaerobic digestion for biogas production methods, methods other than incineration. Forest biomass and straw is used for heat energy production by incineration, but the combustion efficiency is different for different application techniques. The task of this research are:

- Take model-research forest products (wood) biomass, and straw, getting GHG emission values of forest wood and straw biomass for use in thermal energy,
- Develop a simple benchmarks available Latvian forest products and agricultural producers straw biomass thermal energy ranking of GHG emission reductions;
- Recommendations for the choice of technology or efficiency required for GHG emissions from forest and agricultural biomass reduction over time.

Forest products (wood) and straw materials production, transportation, processing and use and GHG emissions ($\text{gCO}_2 \text{ eq}$) is attributed to biomass combustion process to obtain useful energy unit (1 MJ), or applied to agricultural land (straw) 1 ha to 1 t dry matter (forest biomass). How common criteria of various biomass production and use technology is used to

compare process GHG emissions (gCO₂ eq) attributed to biomass combustion is obtained 1 MJ of useful energy (gCO₂ eq / MJ), and are accounted for in the calculation of the specific combustion efficiency. This means that the resulting net energy increases increasing the use efficiency of the plant. The study uses data on Latvian access to the equipment, the combustion efficiency (efficiency ratio) is chosen slightly larger than the average in the country (currently the average of wood combustion efficiency of furnaces in the country is around 70%, the Latvian-made AK series boiler (AS “Comfort”, Miami, FL) energy efficiency reaches 88% bio fuel with moisture content up to 50% and 92% pellets with humidity up to 12% [2]. Model-research has been selected water boiler with solid biofuels (wood chips) combustion efficiency of 82% (manufacturing, Ltd., “Two”, Riga) and water to the boiler and straw (straw batches) the combustion efficiency of 87% (AGB STRAW), which satisfies the calculations use the best technology available, and thus count the average furnace parameters gradual improvement in the coming years.

Cereal and canola straw obtained from the harvest in the conventional agricultural processor. Provided for straw fuel is transported and stored until a certain time of processing. Straw is the relative humidity (14–20%), low density, because of the variety of Stacking technology, for example, uses Stacking small, round, medium-sized and large (Heston) bales. Small rectangular bale size is 0.36 x 0.5 x 0.8 m and a weight of about 14 – 18 kg. Medium-size rectangular bales are 0.8 x 0.8 x 1.7 m, and a mass of about 150 kg. Round bale length is 1.2 m, diameter 1.5 m and weight varies from 200-300 kg. Large square or rectangular Heston dimensions of 1.2 x 1.3 x 2.4 m and a mass of about 450 kg. The most centralized power in large bales. Use of straw as a fuel for heat production in Latvia dates back to 1999th The Danish support, equipping Saulaine Technical College furnace boiler house with a big Heston bale combustion.

Common crop straw resources available for energy production in Latvia can be calculated using the following formula:

$$S_e = S_r - S_z - S_p - S_b - S_t \quad (5)$$

$S_e = 1255 - 12.5 - 584 - 125 - 10 = 522$ [thousand. t].

Where S_e – maximum amount of straw available for energy production, thousand tons; S_r – grown straw yield, thousand. t. (2007 straw yield of 1255 thousand. tons., calculations); S_z – grown crop losses straw harvesting, transport and storage, process losses taken 1% of the total production of straw, thousand tons.; S_p – straw, leaving the calculation of the minimum needs of litter [1] for livestock thousand. t.; S_b – straw, fodder, feed the required amount (based on the use of oat straw) within 10% of the total harvested crop straw, thousand. t.; S_t – straw for technical uses (paper pulp, building products manufacturing, etc.), adopted S_t – 10 thousand tons.

Technically, the available surplus straw in Latvia makes one third of the volume (174 thousand. tons) of the theoretical (522 thousand. tons) of surplus straw for intensive farming conditions, to ensure stable soil organic matter preservation. Assuming that the average calorific value of straw is 4.0 MWh / t, it can be assumed that the Latvian 2007th The energy use of technically had access to 14% of the total straw yield of 2.5 PJ of energy. In practice, this means that two years of surplus straw into the soil, but in the third year they are harvested and used for energy.

The total emissions straw for heat energy production can be calculated as:

$$E_{kop} = E_{izv} + E_g + E_{AP} + E_{tt} + E_{izm} - E_{ua} - E_{as} - E_{koġ} + E_{BP} \quad (6)$$

where, E_{kop} – total emissions gCO₂eq/MJ, E_{izv} – raw materials (straw) production emissions gCO₂eq/MJ, E_g – emissions associated with land use change, gCO₂eq/MJ, E_{ap} – harvest

processing such as straw pellets production emissions gCO₂eq/MJ; E_{tt} – crop or product loading, packing, transporting, unloading emissions from crop to crop conversion business use (for example in combustion furnace), assuming a distance gCO₂eq/MJ; E_{izm} – crop production or processing of energy (such as combustion and combustion process) using emissions gCO₂eq/MJ; E_{ua} – C capture and sequestration, emissions, adopt E_{ua} = 0; E_{as} – C replacement emissions, gCO₂eq/MJ taken E_{as} = 0; E_{koġ} – Emissions savings of cogeneration be adopted E_{koġ} = 0; E_{BP} – by-products (straw ash transport and incorporation into the field) for the emissions gCO₂eq/MJ.

Emissions from the production of raw materials:

$$E_{izv} = K_s (E_{aa} + E_m + E_p + E_{rn}) + E_{ss} + E_t, \quad (7)$$

where K_s – coefficient, which is evaluated by the energy potential of straw (combustion energy) with respect to all the harvest (grain and straw), potential energy (combustion energy) E_{aa} – tillage (plowing, cultivating, sowing) emissions gCO₂eq/MJ:

$$E_{aa} = E_a + E_k + I \quad (8)$$

where E_a – plowing emissions gCO₂eq/MJ; E_k – cultivation emissions gCO₂eq/MJ; I – field emission, gCO₂eq/MJ; E_m – fertilizer emissions (assuming that the fertilizer is mixed with 3 times) gCO₂eq/MJ; E_p – Integration of pesticide emissions (assuming treatment of crops with pesticides and conditioning agents out 3 times), gCO₂eq/MJ; E_m – harvest emissions gCO₂eq/MJ; E_{ss} – stacking straw emissions gCO₂eq/MJ; E_t – straw bale transport from the field to the storage unit shall issue (adopted transport distance 10 km), gCO₂eq/MJ;

Straw production required for tillage, fertilization, plant protection and harvesting applies to straw, as well as on the grain, so the straw feedstock cultivation and harvesting emissions to be reduced by a factor K_s:

$$K_s = \frac{M_s Q_s}{M_s Q_s + M_g Q_g} \quad (9)$$

where M_s, M_g – the straw and grain yield from 1 ha, t; Q_s, Q_g – from 1 ha of harvested grain and straw combustion energy, GJ.

Using the calculation of the average grain Zemgale 4.65 t/ha and wheat straw 2.94 t/ha yield 2007th year [source: CSB] to the combustion energy of wheat 15.8 MJ/kg and straw 15.0 MJ / kg obtain the coefficient K_s value of 0.459.

Straw bale fuel production and use of emissions compiled Table 3.1.

Table 3.1. Straw bale fuel production and use of emissions

Emissions	Fuel	kWh	Job people.-h/ha	K _s	Emissions kgCO ₂ eq/ha	Emissions gCO ₂ eq/MJ
E _a	18		1.36	0.459	53.6	1.4
E _k	15		0.33	0.459	44.6	1.2
E _s	7		0.33	0.459	20.8	0.6
E _m	6		0.64	0.459	17.9	0.5
E _p	6		0.2	0.459	17.9	0.5
E _{rn}	18		2	0.459	53.6	1.4
Total (straw growing with grain):						5.6

E_{ss}	12		1.67	1	77.8	2.1
E_{tt}	4		1	1	25.9	0.7
E_{dm}		12	6	1	4.4	0.1
E_d			6	1	83.5	2.3
E_{pt}	0.3	0.1	0.2	1	1.9	0.1
Total (only the collection and use of straw):						5.3
Total:	86.3	12.1	19.7		401.9	10.9

Recently rapid start of establishment in the biomass, including straw pelleting technology that enables high-quality fuel burn, as well as to carry it long distances. The treatment may also include emissions from straw handling, grinding, drying, to ensure a moisture content of 14 to 18% range, if necessary. Manufacturing is a small emission from the burning of whole straw bales without further drying.

The prospect of a fuel pellet production from energy plants (wood, straw, canary, etc.) biomass pellet furnaces because they can burn a higher quality, have low moisture content (7–9%) with the increase of combustion energy (Fig. cf. 1.). Described below straw pelletizing plants with the capacity of 0.6 t/h (made in Lithuania, installed capital) mill are placed straw bales with moisture 14–16%, with the crushing, grinding, pressing and ventilation processes material moisture is reduced to 8%. Straw treatment – pellet production process emissions EAP (pellet production process emissions) are summarized Table 3.2.

Table 3.2. Straw treatment - pellet production process emissions

Operations	Installed capacity kW	Load factor	Energy, kWh/ha	Emissions kgCO ₂ eq/ha	Emissions gCO ₂ eq/MJ
Transportation	5	0.3	6.3	2.3	0.1
Crushing	15	0.7	44.1	16.0	0.4
Milling	55	0.8	184.7	67.0	1.8
Moisturing (with steam)	15	1	63.0	22.9	0.6
Pellet pressing	75	1	314.8	114.3	3.1
Ventilation, separation	30	1	125.9	45.7	1.2
Tot E_{ap}	190		732.4	265.8	7.2

Cumulative emissions of pellets for energy production is obtained by summing the use of straw bale total emissions 10.9 gCO₂eq/MJ (see Table 1.) The emissions from the pellet production process gCO₂eq/MJ 7.2 (see Table 2.), which shows the total straw pellets in emissions of 18.1 gCO₂eq/MJ heat energy.

4. STRAW FUEL EMISSIONS RANKING

Straw fuel production and use of emissions compared to fossil fuel emissions per 1 MJ of energy shown in Fig 1.

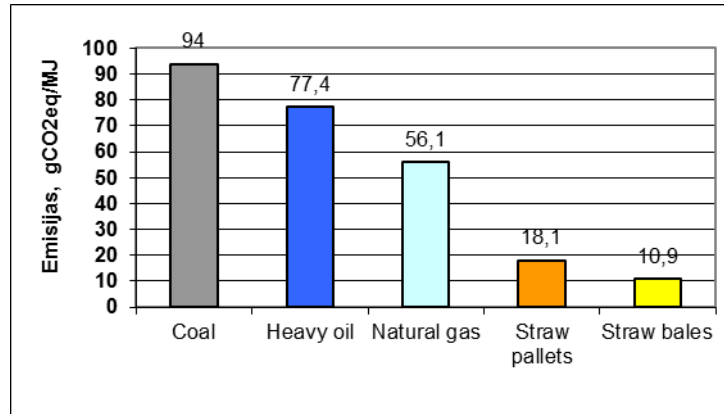


Fig 1. Straw bale, straw pellets and fossil fuel emissions of heat energy

Emission savings from replacing the thermal energy of fossil fuels with straw or straw pellets is shown in Fig 2.

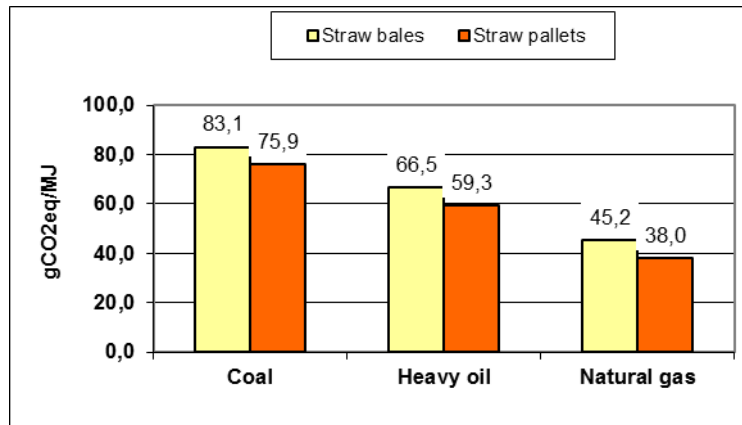


Fig. 2. Straw bale and straw pellets in thermal power generation emissions savings relative to fossil fuels

Straw bale and straw pellets in thermal power generation emissions savings relative to the percentage of fossil fuels shown in Fig. 3.

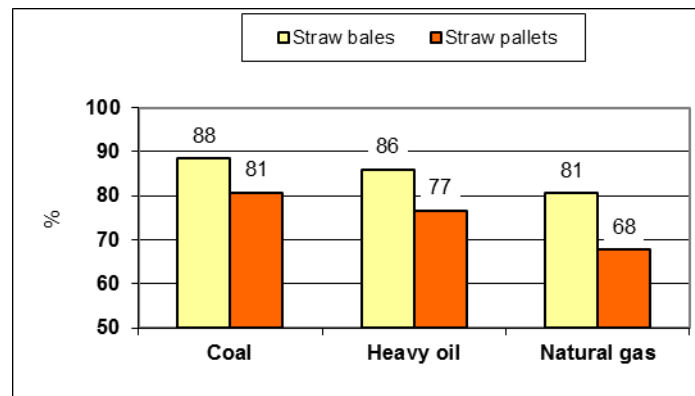


Fig. 3. Straw bale and straw pellets in thermal power generation emissions savings relative to the percentage of fossil fuels

Table 3. Ranking coefficient K_{50} and K_{35} values straw bale and straw pellet application of heat energy emissions from fossil energy resources

Ranking coefficients, %	Against coal		Against heavy oil		Against natural gas	
	Straw bales	Straw pallets	Straw bales	Straw pallets	Straw bales	Straw pallets
K_{50}	38	31	36	27	31	18
K_{35}	53	46	51	42	46	33

5. ANALYSIS AND RECOMMENDATIONS FOR THE USE OF STRAW THERMAL POWER

Ranking coefficient values are positive, confirming that the straw and straw pellets can be used for biofuels criteria of 35% and 50% reduction in emissions.

The main factors that can affect the ranking coefficient value is incinerated straw moisture and combustion efficiency.

In practice, the straw is usually harvested and collected in good weather, but the main effect of the fuel energy value of straw is damp, the energy used straw to protect it from rain, straw bales or rolls stored in barns, covered with a roof, or at least a cover with a damp soundproof cover. Straw for heating water supplied must be 14 – 22% range. To prepare the pellets without additional drying straw should be air-dried condition, ie humidity should be no more than 14–15%.

Ledmane water boiler efficiency combustion of straw bale is 0.87. Straw pellets are suitable for combustion in furnaces manufactured in Latvia (AS “Comfort”, LLC “Two”, furnaces) to pellet combustion efficiency to 0.92.

Although the chip manufacturing emissions reaches 88% of the straw mining emissions, the main advantage is the straw pellet better quality straw combustion of material within the temperature range (650–750 °C), which is higher than the dioxin formation temperatures, but at the same time less than the temperature at which the begins to form NO_x compounds. In addition, the granules are economically transported over long distances, ensuring that the use of the energy production point of view of strategic importance for energy companies, such as increased habitat cogeneration or pellets can be exported. Perhaps the straw-phase with the grain will not count emissions from straw and residues for energy production estimates, the proposal will be accepted by the 16th Paragraph (European Parliament and Council directive on renewable energy promotion), which provides: "(..) It is assumed that the human food or animal feed unusable waste, crop residues (including straw, bagasse, husks, corn cob and walnut shell) and residues from processing (other than biofuel processing residues) of the life cycle greenhouse gas emissions up to the collection is zero ... ". In this case, the above estimated energy use emissions straw straw-subtracted along with grains emissions – 5.6 $\text{gCO}_2\text{eq/MJ}$, resulting in total emissions from the use of straw bale will reduce to 5.1 $\text{gCO}_2\text{eq/MJ}$ and pellets to 12.3 $\text{gCO}_2\text{eq / MJ}$.

The calculation takes into account only the direct straw-tech GHG emission sources, but not included several key emission sources, such as fertilizer production, pesticide production, agricultural machinery and other production equipment manufacturing indirect emissions, which does not include the proposals emerging EU directive. Such calculations would require straw-depth analysis of the life cycle.



REFERENCES

1. NIKOLAISEN, L. *Straw for Energy production*. Copenhagen: 1998, 53p.
2. *Ecoenergy, Wood fuelled boiler biomass energy services district heating*. Ecoenergy Limited: British Gas – 2009, 4 p.
3. BŪVNICĪBAS, ENERĢĒTIKAS UN MĀJOKĻU VALSTS AĢENTŪRA. *Atjaunojamo energoresursu potenciāls Latvijā*. Rīga, SIA ‘‘Gandrs’’: 2010, 60 p.
4. ADAMOVIČS, A; DUBROVSKIS, V; PLŪME, I; JANSONS, Ā; LAZDIŅA, D; LAZDIŅŠ, A. *Biomassas izmantošanas ilgtspējības kritēriju pielietošana un pasākumu izstrāde*. Rīga: 2011, 146 p.



INVESTIGATION OF PERFORMANCE PARAMETERS OF LOW – POWER WATER BOILERS BURNING BIOFUEL

T. Vonžodas, M. Valantinavičius

Lithuanian Energy Institute

Breslaujos str. 3, LT-44403 Kaunas – Lithuania

ABSTRACT

In Lithuania, as in other European countries, the increasing availability of residential heating with biofuels, using a variety of heating equipment: water boilers, ovens, open and closed fireplaces and air heaters. However, most of the devices are technically obsolete, but not being used for biofuels or just not properly equipped, so the heating system with the following devices do not perform and significantly increase environmental pollution.

These problems can be solved only by the gradual replacement of obsolete equipment with new ones, which meet modern efficiency and emissions requirements. Perform Lithuania manufactured boilers operating on different principles of performance testing, improving boiler combustion chamber design shows that at the very least with a newly manufactured boilers are improving and have a positive impact in order to address two main objectives – to achieve the highest and economically viable biofuel combustion plants, the efficiency and reduce the volatile and particulate matter emissions to the environment.

Keywords: Biomass, wood fuel, water boilers, efficiency, emissions

1. INTRODUCTION

Most of renewable energy resources are solid biofuels: various types of wood fuels, straws and other plant biomass for energy production. Wood fuel is one of the major and the most widely used fuel in household sector and power plants because its resources are the largest ones, it is the most easily available and, if paying no attention to its use efficiency and pollution caused, it does not require a sophisticated equipment and preparation. In Lithuania the potential of this fuel is not adequately evaluated and can reach 1000–1050 ktOE or 4.85–5.93 million m³ of wood. Now 910 ktOE of it is already being in use [1]. In recent 20 years wood fuel use were constantly on the increase with growing demand in the household sector for home heating and cooking and more of it used in central heating plants. According to 2011 years data [1] it was used about 61.3 %, 19.5 % and 6 % of total wood fuel amount in household sector, central / district heating plants and cogeneration power plants, respectively. Left amount of this fuel was used for heating and technological processes in the industry, service- and agriculture sectors. Biofuel use is fast growing not even in the freshly installed heating systems, but, too, in less effective old heating systems which parameters of efficiency and pollution are much worse. In Lithuania about 90 % of household sector has technically dated heating systems which need to be renovated. These heating systems, comparing with the new ones, discharge more pollutants such as carbon monoxide (CO), volatile organic compounds (VOC), particulate matter (PM) and polycyclic aromatic hydrocarbons (PAH) to the environment.

All these pollutants enhance (especially during heating season) the background contamination of residential areas/districts heated with biofuel, and the contamination with solid particles SD10 (solid particles < 10 µm in diameter) often exceed permissible concentrations.

It is obviously essential to install new modern and less polluting heating systems using biofuel as well as to change the old ones while biofuel use is continuously increasing in household sector. Only in this way it is possible to avoid increasing environment pollution.

These problems solving should be based on experience of such countries as Austria, Germany, Sweden, Finland and Denmark. In these countries for a few decades lots of attention has been paid to the technology progress of biomass thermal decomposition systems and important results have been reached, especially in pollutant decreasing field. In these countries the major goal of scientific research is to create/design low polluting (so called „zero pollution“) biomass thermal decomposition heating systems applying various technological solutions [2]. For developing these technologies the major attention is paid to:

- Research and application of new biofuel types and mixtures;
- Research of biomass combustion technology in small-, medium- or high power plants [3];
- Design and improvement of new innovative combined-cycle systems;
- Design and improvement of tools for combustion products cleaning [4];
- Research of technologies of biomass gasification and pyrolysis;
- Improvement and installation of automatic control systems of thermal decomposition processes and devices.

It must be emphasized that though the new technologies of biomass use for energy production are being developed rapidly, the direct biofuel burning will still remain the major way for heat and even electricity energy generation in small- and medium-power systems. In the European countries scientific and applied works and tools of legal basis are being developed for promotion of biofuel use, preparation and installation prove the long-term importance of the problem and it can be a proper/good mark/guide for solving problems of heat energy provision in Lithuania.

Further on this paper we will analyze performance parameters, like efficiency and emissions of most widely used low – power water boilers. For future investigations different types of biofuels and their influence to combustion process for different types of boilers will be analyzed.

2. REQUIREMENTS FOR BIOFUELS COMBUSTION INSTALLATIONS

Lithuania by far the main focus was on medium and high-power boilers fired with biofuels, installation and development to replace fossil fuels for local fuel and as quickly as possible to reduce dependence on fossil fuel imports. Since 1993., when biofuels started to use in district heating boilers installed in boilers total installed capacity increased to 650 MW. However, solid biofuel for energy production has grown rapidly not only in district heating, but also for households in rural and urban areas in private homes. Statistical data confirms that biofuel are still largely consumed in households.

We have to admit that in Lithuania, produced by small and medium-power boilers technological progress was on little attention. Only a few major manufacturers focused on the research and testing of small scale heating boilers, in order to maintain the competitiveness of their products in other EU markets. It was not given to legal measures to encourage producers to achieve the highest energy targets and to be certified. Technical Regulations [5, 6] Lithuania implementing European Parliament and Council Directives 92/42/EEC and 2002/91/EC, did not provide water heating boilers for heating buildings and fired with biofuels, and energy efficiency requirements for the periodic inspection.

In recent years, this situation is changing as boilers manufactured in Lithuania because of introduction of mandatory conformity assessment standard BS EN 303-5:2012 [7]. The

truth of this procedure do not include all requirements of the standard, but still pushing manufacturers to develop boilers for better efficiency and pollution parameters.

In view of this, there is an urgent need to continue the development of the legal framework in order to:

1. To establish uniform requirements for the classification of biofuels as well as quality indicators;
2. To establish uniform requirements for boilers efficiency and their testing;
3. The application of the mandatory and incentives for manufacturers, producing higher efficiency boilers.

In order to solve first task, developed and validated standards already been prepared, that standardize the classification of solid biofuels [8], and forms the basis for convergence requirements of its quality indicators to evaluate and conditions of the fuel market.

The second problem is dealt with in accordance with BS EN 303-5:2012 standard [7], which provides solid fuel fired boilers with the requirements specified in Table 1.

Table 1. Efficiency requirements in accordance with BS EN 303-5 2012

Boiler class	Applied standard	The boiler output in kW	Efficiency	Efficiency formula
			%	
5	LST EN 303-5 2012	10	88	$\eta = 87 + \log Q_n$
		300	89	
4	LST EN 303-5 2012	10	82	$\eta = 80 + 2 \log Q_n$
		300	84	
3	LST EN 303-5 2012	10	73	$\eta = 67 + 6 \log Q_n$
		300	82	
2	LST EN 303-5 2000	10	63	$\eta = 57 + 6 \log Q_n$
		300	72	
1	LST EN 303-5 2000	10	53	$\eta = 47 + 6 \log Q_n$
		300	62	

Note. Q_n – Boiler nominal power in kW.

The third problem is solved by the requirements governed by the general provisions for boiler efficiency and emissions of pollutants into the environment mitigation, as well as national measures, such as: Denmark incentives for home residents acquiring not less than Class 3 boilers.

Some countries have already reached high performance indicators. (Austria (Fig. 1). Data suggest that solid-fuel-fired boiler efficiency average reached 90% and significantly reduced its distribution, representing a significant growth of fossil fuel use efficiency.

However, a review of the overall situation, it can be said that the efficiency improvement and emission reduction is directly related to fossil fuel combustion in small devices features:

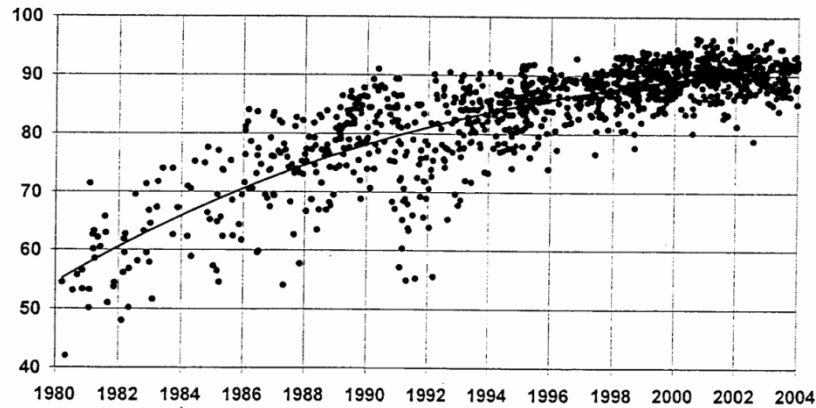


Fig. 1. Solid fuel boilers use in Austria [9], performance of efficiency variation statistics

- The complex regulation of combustion process because of its inertness and the proper combustion air supply;
- Water temperature control and periodic load, if any are made, causes combustion instabilities that occur in emission elevations compared to the routine process;
- Wood fuel (biofuel) (firewood, pellets, briquettes, mixtures ...) and a variety of their properties;
- Variety of types of boilers.

Very significantly the combustion process and improve the regulation of pre-solid preparation, for example: pellets or briquettes. This allows automate the prepared fuel supply into the combustion chamber and bring it to the burning of gaseous or liquid fuel combustion process.

It should be pointed out one major character that gets fired boilers with solid fuel: this is a very uneven emission into the environment of constantly changing the intensity of the combustion process, particularly in periodically charging the boiler fuel. Since it cannot be avoided, it is necessary to establish procedures for measuring emissions from the boilers operation of such controls.

3. EXPERIMENTAL EQUIPMENT AND METHODS

Solid biofuel combustion own specific requirements of research and requires sophisticated equipment and apparatus. This enables to carry out the main operating parameters and the CO , and C_xH_y emissions continuous measurement, recording and calculation. The study results of these measurements are to be recorded relatively high frequency (recommended every 20 seconds) throughout the study. The average results are performed at the end of the study.

The investigations were performed with four same capacity (~25 kW) heating boilers working in different principles. That gas generative, grate boiler with natural draught, grate boiler with forced draught and pellet boiler. They were burned with pellet and logs at nominal heating output.

The test device consists of a boiler being investigated, mounted on a precise balance, by means of which fuel consumption is observed. The boiler is connected to the cooling and the measurement system of the thermal parameters. The combustion products are being analysed by the continuous measurement system. The concentrations of the particulates are being measured by the gravimetric method.

This equipment is suitable for all complexes of parameters to measure and fully meets the EN 303-5:2012 standard requirements. Although they are applied to Lithuania just now, applied these requirements have already been used by the other European countries.

Frequently on evaluating the combustion quality is used the measurement of CO_2 in exhaust gas instead of the exceed air ratio or O_2 concentration. According to this parameter one can judge by the proper regulation and function of the device.

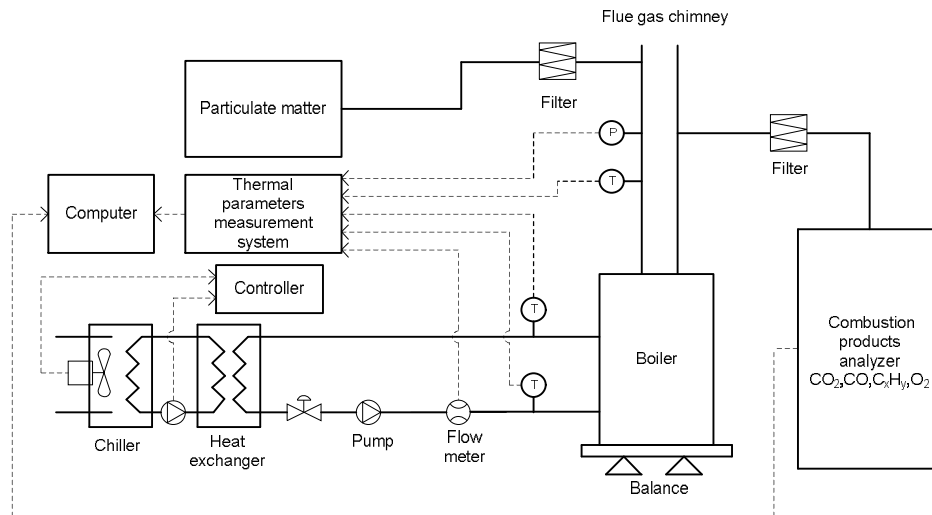


Fig. 2. Water boilers research unit general scheme

4. RESULTS

The investigations were performed with four same capacity (~ 25 kW) heating boilers working in different principles. They were burned with pellet and logs at nominal heating output. In pictures 3–5 the changes of CO_2 , CO , C_xH_y concentrations of all the boilers are shown at nominal heating output during the two combustion periods.

As it can be seen from this figure, the control of the pellet boiler is constant. In this case the exhaustion of carbon dioxide varies in narrow limits during the entire test. The combustion is not constant in other types of boilers. Therefore the concentration of carbon dioxide varies in wide limits during all the combustion time. However, the average concentrations of carbon dioxide differ not in big limits ($\sim 1.5\%$) in all types of boilers.

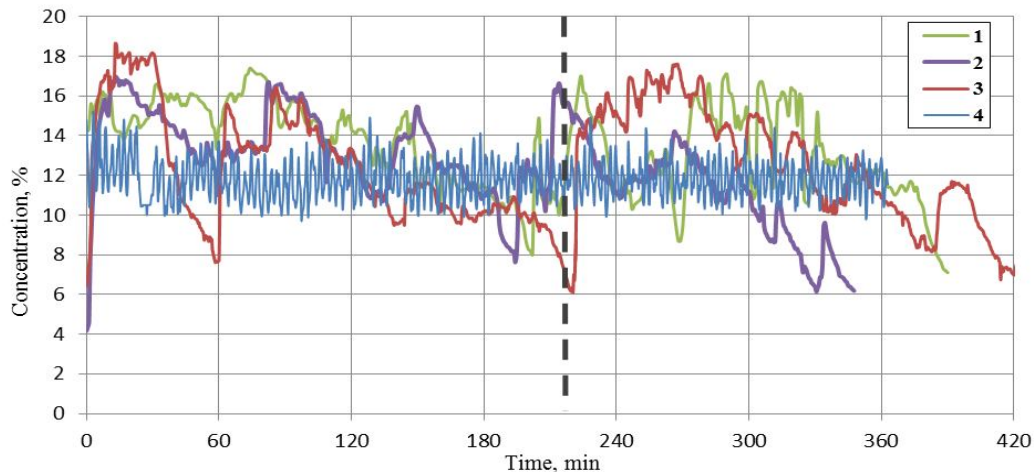


Fig. 3. The comparison of carbon dioxide concentration in exhaust gas of different types of boilers, 1 – gas generative, 2 – grate boiler with natural draught, 3 – grate boiler with forced draught, 4 – pellet boiler

The different view can be seen in Figure 4 that shows the change of the concentrations of carbon monoxide. The concentrations of carbon monoxide differ in all types of boilers. Gas generative boiler has the highest rate of carbon monoxide exhaustion. Carbon monoxide can appear in the smoke for a few reasons:

- badly organized, incomplete combustion;
- inconstant combustion;
- the oxygen is badly mixed with the fuel;
- the deficit of the air or the abundance of it;
- low temperature in a furnace;
- etc. [6].

According to this year enacted LST 303-5:2012 standard, this boiler not meet the minimum requirements for pollution.

The exhaustion of carbon monoxide (CO) in grate – boiler fire with forced draught highly depends on the chamber's temperature. Therefore, it can be seen a huge jump of carbon monoxide (CO) concentration at the beginning of the test. The feeding of the primary and the secondary air makes great influence to the combustion of this boiler. The blast makes the combustion better by regulating the feeding of primary and secondary air according to the oxygen level in a chimney. Therefore the concentration of carbon monoxide (CO) diminishes when the boiler reaches the working temperature. The further jumps of carbon monoxide concentration depend on the fuel being on the grate. The fallen fuel without the gaps of air combusts with the deficit of air. Therefore, the concentration of carbon monoxide (CO) becomes higher.

The pellet boiler reaches the best results because it has constant and good combustion, qualitative fuel and good control. The pulsation (the jumps) can be seen in the diagram of carbon monoxide (CO) concentration of the pellet boiler. These jumps appear because of the feeding of the fuel into the combustion chamber. The fuel is fed by the specified doses. When the new dose of the fuel is fed, the concentration of the carbon monoxide jumps up. It returns when the combustion becomes constant.

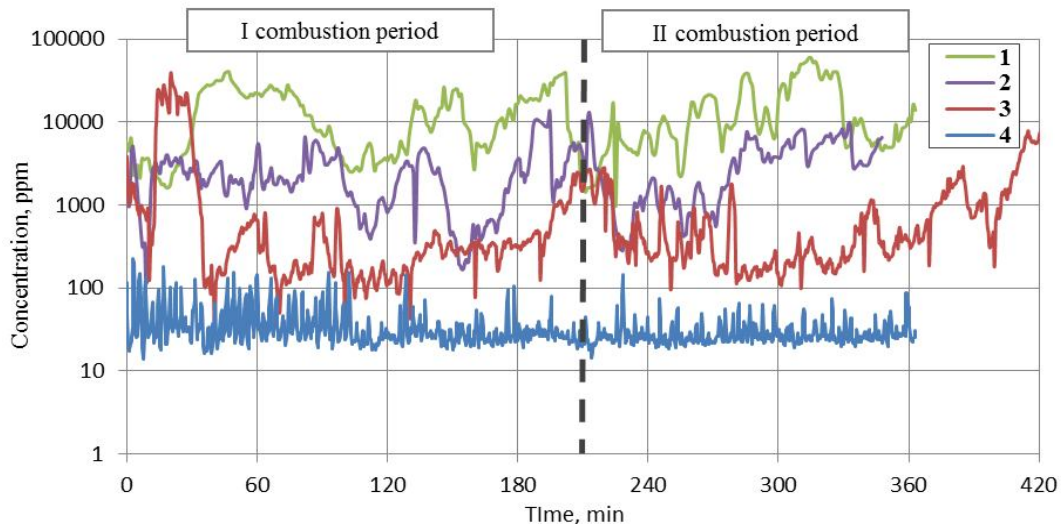


Fig. 4. The comparison of carbon monoxide concentration in exhaust gas of different types of boilers, 1 – gas generative, 2 – grate boiler with natural draught, 3 – grate boiler with forced draught, 4 – pellet boiler

The concentration of hydrocarbons (C_xH_y) can be seen in the diagram below (Fig. 5). As it can be seen the same tendency remains for the hydrocarbons (C_xH_y) as for the carbon monoxide (CO). The difference of the concentrations is for the same reasons as it has been mentioned before. The gas generative boiler extremely distinguishes from the others. The exhaustion of the hydrocarbon in the pellet boiler are constant during all the test.

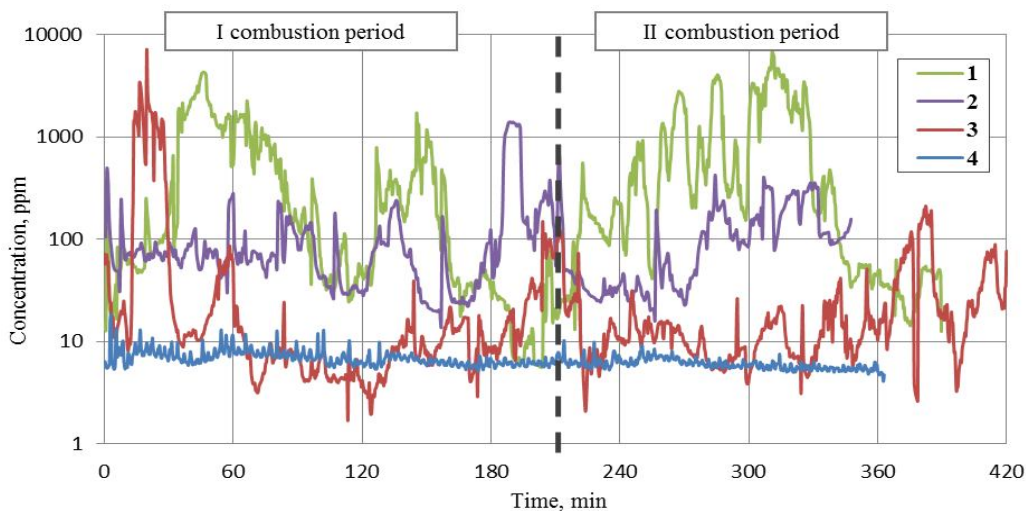


Fig. 5. The comparison of concentration of hydrocarbons in exhaust gas of different types of boilers, 1 – gas generative, 2 – grate boiler with natural draught, 3 – grate boiler with forced draught, 4 – pellet boiler

Research summary of the results presented in Table 3, shows that boiler, fired by wood pellets, particulate matter (PM) emissions are by almost 4 times less than the lower combustion boiler, operating on a natural draft. This difference arises not only because of specially prepared wood pellet fuel has better properties, but also the fact that the fuel of such a type is efficiently burn in the boiler. The gas generating boiler for two-stage combustion exhausts less particulate in comparison to the Grate boilers.

Table 2. The average values of the emissions and efficiency of different types of boiler.

Boilers type	CO ₂ , %	CO, ppm	C _x H _y , ppm	PM at 10% O ₂ , mg/m ³	Efficiency coefficient, %
Pellet boiler	11.81	36	6.6	21.5	89.8
Grate boiler with forced draught	12.39	1508	77	75.4	84.8
Grate boiler with natural draught	12.41	2887	125.7	82.8	82.1
Gas generative	13.41	14463	635	68.4	83.0

All discussed results are shown in the (Table. 2.). It can be seen that the pellet boiler has the greatest coefficient of efficiency as compared with the other boilers. This coefficient can be greater than 90%. This is because the pellet boiler has the better fuel quality and this fuel can be combusted more effectively. The gas generative boiler is in the worst first class and it lags from the grate boiler. But it can be considered that the gas generative boiler could compete with the grate boiler after improving the construction of the gas generative boiler.

5. CONCLUSIONS

1. CO emissions from the pellet boiler are 400 times smaller than the gas generating boiler and emissions of C_xH_y 100 times smaller. PM emissions from pellet boiler are almost 4 times smaller than the other boilers. Also the efficiency of the pellet boiler is almost 7 percent higher.
2. The growth rate of the consumption of wood fuels in the production of energy needs will slow down as the most accessible fuel reserves for the most part have already been used to a great extent. The collection of logging residues, storage and transportation infrastructure growing of short rotation plants of purpose production in the future would allow increasing the use of wood fuel and could partially compensate for the growing need of wood fuel.
3. More and more attention needs to be paid to wood fired boilers to increase efficiency and reduce pollution. For example, using pressed wood fuels (pellets, briquettes) one can mechanize and automate the combustion process and to manage it more effectively.
4. It could be said that the manufacturers in Lithuania should guarantee that their products fulfil the requirements of the fourth or fifth class of boilers by the standard LST EN 303-5:2012 in order to keep competitive in the market of boilers.

REFERENCES

1. Lithuanian statistical department – *Fuel and Energy Balance 2011*, ISSN 2029-5944. Vilnius, 2011.
2. OBERNBERGER I. *The present state and future development of industrial biomass combustion for heat and power generation* // ASME-ATI-UIT 2010 Conference on Thermal and Environmental Issues in Energy Systems. Sorrento, Italy, 16–19 May 2010.



3. OBERNBERGER I., THEK G. *Combustion and Gasification of solid biomass for heat and power production in Europe – State-of-the-Art and relevant future developments.*// Proc. of the 8 th European Conference on the Industrial Furnaces and Boilers. Vilamoura, Portugal, April 2008.
4. OBERNBERGER I., CHRISTOPH M. *Survey on the present state of particle precipitation devices for residential biomass combustion with a nominal boiler capacity up to 50 kW* // IEA Bioenergy project Task 32 report. Graz, Austria, December 2011.
5. *New hot water boilers fired with liquid or gaseous, technical procedures*, approved by the Minister of Economy of the Republic of Lithuania in 2002. February 11. Order No. 45 (Žin., 2002, Nr. 115–5164).
6. *Boilers installed in buildings using renewable solid or liquid fuels with a rated output of no less than 20 kW and heating systems with older than 15 years and not less than 20 kW rated output power boilers which use renewable solid or liquid fuel efficiency checking technical regulation adopted by the Lithuanian Minister of Economy on February 28, 2006.* Order No. 4–73 (Official Gazette, 2006, no. 27-902).LST EN 303-5:2012.
7. *Heating boilers. Part 5. Manually and automatically loaded solid fuel heating boilers with heat output up to 500 kW.* Terminology requirements, testing and marking. LST EN 15359:2012.
8. *Solid recovered fuel. Technical requirements and class.* LST EN 15357:2011
9. *European Wood-Heating Technology Survey: An overview of combustion principles and the energy and emissions performance characteristics of commercially available systems in Austria, Germany, Denmark, Norway, and Sweden.* Energy Research and Development Authority, Final report 10-01 April 2010.
10. TISSARI, J., LYYRAANEN, J., HYTOONEN, K. *Fine particle and gaseous emissions from normal and smouldering wood combustion in a conventional masonry heater.* Atmospheric Environment, Vol. 42, Issue 34, November 2008, p. 7862–7873



EXERGY ASSESSMENT OF AIR FLOW IN THE SITE OF THE BUILDING

V. Žėkas, V. Martinaitis

*Vilnius Gediminas Technical University
Saulėtekio str. 11, LT-10223 Vilnius – Lithuania*

ABSTRACT

The strategic aim to increase the amount of RE integration into the site of the building creates the new engineering challenges. One of the main challenges is locally disposable RE flows optimal usage and selection of RE transformers' combination corresponding to the adjacent exact situation. The air flow reaching the site of the building, in the form of RE, usually is treated only as a medium of heat products transfer on the site. Air heat pumps of broad application, along with their required air flow, as energy supply option, is not attributed to the typical form of the RE. In order to get the comprehensive understanding of renewing energy disposable on site, the air flow in this study, is treated as RE flow. The principle of exergy analysis is applied in this study. It provides the interpretation regarding the selection of possible reference parameters of exergy analysis. The study covers the time period of one year. The obtained data of exergy analysis allows to know the quality of disposable air flow energy as well as to perform the more objective selection of RE transformers combination.

Keywords: air flow, exergy analysis, disposable renewable energy

1. INTRODUCTION

One of the key objectives of European Union energy policy [1] and thus the guidelines of renewable energy (RE) [2] is 20% RE share in final energy consumption in 2020. EU-27 energy statistics [3] show that there is 10 % of RE share in 2010. Compared to 5 % share of 1995, the progress is visible, but still not enough to achieve the key objectives. On the global level [4] the integration of RE is up to 14 % (according to 2000 statistics). Achieving the key objectives, the different and more complex integrated RE use solutions must be continued to explore through G.O.L.D (Global Optimized Local Designed) and IWBDP (Integrated Whole Building Design Process) concepts. The goal of this study is the integrated approach to the RE potential, available on the site and disposable by the local energy user. The user – nearly zero energy building planned to erect on site. The study aims to analyze the physical origin of RE potential. This includes solar, wind and ground RE sources. Also, according to unconventional interpretation, the air flow heat potential is evaluated as well. Exergy analysis is applied to estimate the potential.

2. RENEWABLE ENERGY ASSESSMENT

Although the origin of any RE is the same – the sun (a phenomenon sometimes seen through the energy), the usual RE sources are - wind energy (mainland and offshore), solar (thermal diffused and concentrated photovoltaic), water (flow and flood – tidal) geothermal and biomass energy (including the biofuels). Various computer simulation tools and methods [5, 6] are applied for RE potential evaluation and energy use planning. The basic principle of different kind potential evaluation is three levels assessment: theoretical, technical and economical. Theoretical energy amount is determined using physical formulas; technical – potential energy amount influenced by human activity, performance, availability and other factors; economical – the amount of energy that is cost-effective to be absorbed at the given

economic conditions. From the point of view of building economic activity demand for light, heat and cooling, the typical division of RE energy flows shall be supplemented with one more form of RE – thermal energy flow of air.

Any specific form of energy has totally different transforming technology. The sun is unique because of radiation energy; wind, hydro energy, wave, flood and tidal energy – because of kinetic flow energy; geothermal and air - because of the temperature potential; biomass – because of chemical potential. Hybrid RE systems [7, 8] are being developed and analyzed. Usually they are associated with electricity generation. Considering hybrid RE transforming direction on the basis of heat pump technology, the use of air as thermal energy flow becomes more popular [9-11]. Following the same logic, that wind turbines are for wind energy harnessing, solar panels – for solar energy, ground source heat pump – for geothermal energy, then the air heat pumps – for air thermal energy. Therefore, the air, in this study, is considered as one more RE source. Widely known [12, 13] free cooling or passive cooling system highlights the sense of the air flow as an energy source – cool. Though, in the passive use of solar energy [14] the air flow becomes the localized fluid that transfers the heat in the thermodynamic system and hardly can be called the energy source.

3. AIR FLOW IN THE SITE OF THE BUILDING

In this study, the *air flow* is the flow of moving air mass (Fig. 1) that reaches the area of selected site. *Site* – area meeting the needs of single family house. Actually, there are no restrictions for another site selection. *Site control volume* – area limited by imaginary boundaries, above and below the ground (Fig. 2).

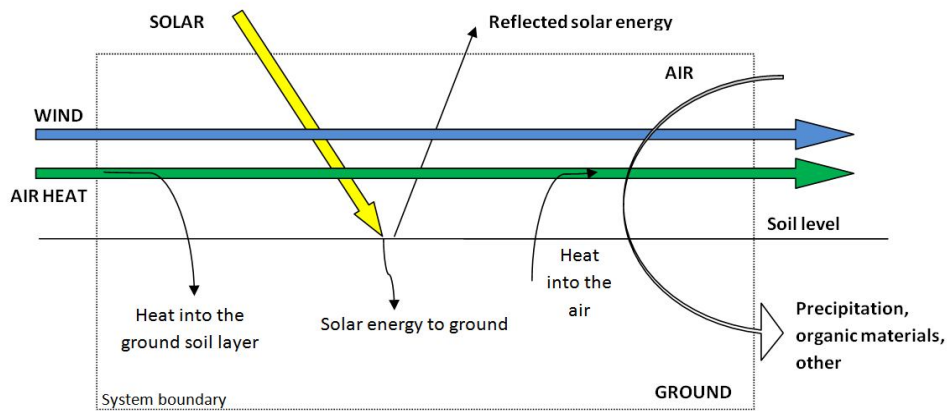


Fig. 1. RE flows reaching the site



Fig. 2. Site control volume

In this study, the air flow reaches the site control volume with some speed that over kinetic air mass flow energy is characterized by the wind. It is also assumed, that air mass crosses the control volume in a plane perpendicular to a site plane. Air flow analysis determines the theoretical potential of the air heat flow. Progressing to the technological level of potential use, the possible plane or technological holes and air flow rate have to be evaluated and the active or passive user's systems could use the reaching air flow (Fig. 3).

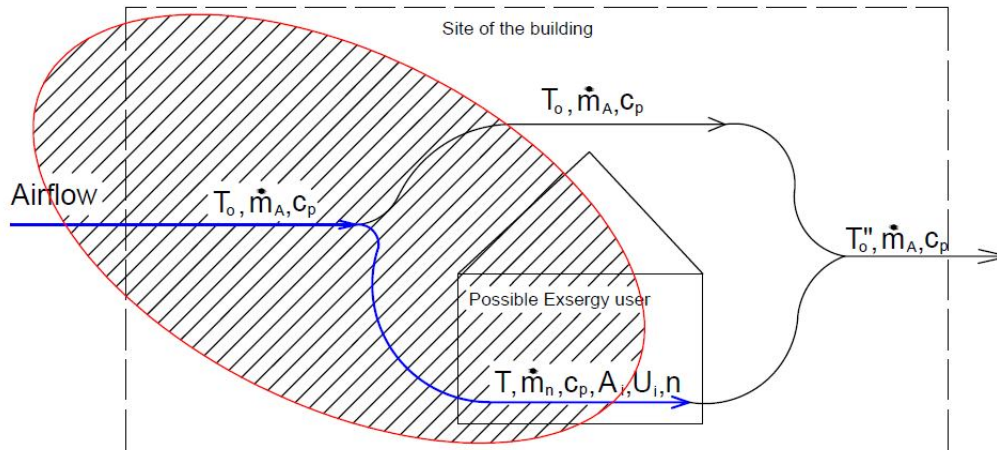


Fig. 3. Exergy analysis boundaries: T – temperature, $^{\circ}\text{C}$; m – air flow rate, kg/s ; c – specific heat of air, J/kg K ; A – area of external envelope, m^2 ; U – heat transfer coefficient $\text{W/m}^2\text{K}$; n – number of residents

Fig. 3 shows the boundaries of the analyzed possible user and the incoming air flow system. The study analyses the exergy flow needed for users parameters support in the system.

4. EXERGY ASSESSMENT OF THE AIR FLOW

Dincer [15, 17] emphasizes the advantages of exergy use. He considers the exergy analysis as a tool that best indicates the environmental impact of the energy source; it is an efficient method of engineering systems development and analysis, based on mass and energy conservation principles and the second law of thermodynamics; it is a method to select the best option of energy source use, evaluating the generated waste or losses; it is objective evaluation method of sustainable development process. Exergy characterizes the maximum possible work of the system. Potential work is the driving force that occurs because of the difference between the system parameters and reference environment parameters. The main shortcoming of RE sources exergy analysis is that originally it is applied for technological equipment analysis and evaluation [16-18]. Exergy analysis is also applied for building engineering systems and building sustainability analysis and evaluation [19-23]. Exergy is also found in RE sources evaluation [24-28]. RE flows are analyzed on a global scale. Space radiation (including the Sun) is also treated as RE causing wind, ocean surface fluctuations, rainfall, biomass, ocean thermal gradient, floods and tides and geothermal energy. The numerical values of global energy flows are developed. Different nature of RE flows, namely thermal variation, motion energy, potential energy or particles concentration compared with reference environment, determines the forms of exergy. Physical nature exergy describes the potential work influenced by temperature, pressure, speed and position change. Chemical and nuclear exergy describes the potential influenced by substances concentration or chemical composition difference and possible transformation. This exergy list can be supplemented by

ongoing process-oriented forms of exergy, that is, mechanical, thermal and radiation exergy. The study object is one of the component of complex RE flow reaching the site – air heat flow exergy evaluation. The air flow transmitted heat flow thermal exergy amount is determined.

5. IDENTIFICATION OF REFERENCE ENVIRONMENT PARAMETERS

Reference environment must be larger than the analyzed system and its parameters are relatively steady. Analyzing the natural sources, the environment parameters can be sea, earth crust or atmosphere. Usually, the starting point of energy systems analysis is natural environmental conditions, for example 1 atm and 25 °C. Various studies [29–30] analyze the influence of reference environmental parameters on the systems exergy analysis results. The conclusions state that if the analyzed system operating parameters are more similar to reference environment parameters then their selection influence is greater. Analysis of energy systems, similar to reference environment parameters, emphasizes the importance of not only the objective selection of steady reference environment parameters but also of dynamic reference environment principles. Authors analyze this issue in various studies [22, 31, 32] and conclude that the dynamic reference point makes the significant influence to building energy supply problems solving by applying the principles of exergy analysis. Reference environment parameters selection is the essential stage of exergy analysis.

Analyzing the air reaching the site and the possible user, building energy and exergy flows, the characteristics of the process must be taken into account. Exergy reference parameter T_0 is always dynamic, while the system state key parameter T is steady with the slight variations depending on the season.

Relation of reference environment with possible building on site is presented in Fig. 4.

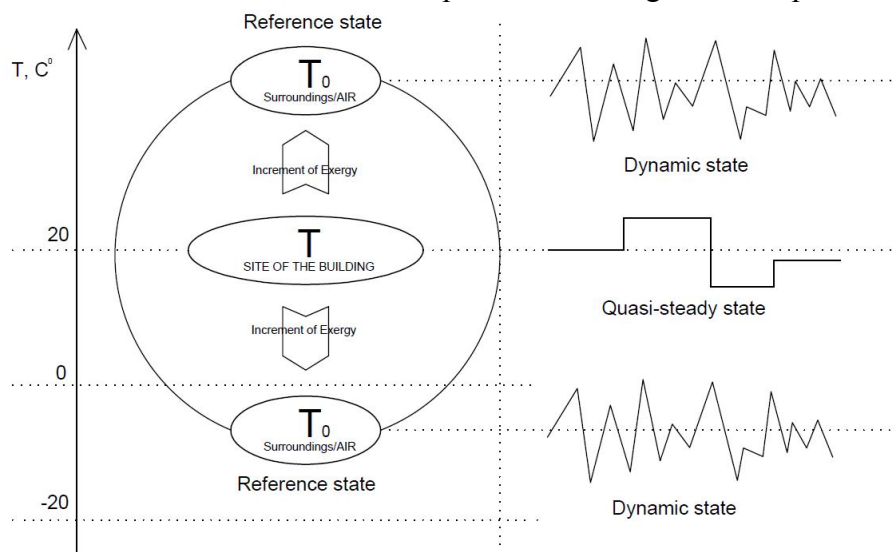


Fig. 4. Reference environment and system relation

This study determines the case, when the building is not erected, but the simulation is that the possible user air volume on site is with the characteristic parameter T . Potential user (building) exergy flow is determined on the basis of system and environment temperature differences. Exergy – operation potential of different environment and indoor temperatures, that can be used to cover building energy needs directly or through technological solutions. Building site energy and exergy flow temperature T – quasi-steady state is 19 °C during the cold period, 20 °C – transition period, 25 °C – the warmest period.

Minimum exergy flow needed for building heating, cooling and ventilation is determined by:

$$\dot{E}x_{Building} = \left(\sum U_i \cdot A_i + n \cdot \dot{m}_n \cdot c_p (T - T_0) \right) \left(1 - \frac{T_0}{T} \right) \quad (1)$$

Where $\dot{E}x_{Building}$ – exergy flow for building, W, \dot{m}_n – fresh air flow for residents, kg/s, c_p – specific heat of air, J/kg K, T_0, T – reference environment and system temperature, °C, n – number of residents; A – area of external envelope, m²; U – heat transfer coefficient W/m²K.

Air flow transferred heat exergy:

$$\dot{E}x_{air} = \dot{m}_A c_{p,avg} \left(1 - \frac{T_0}{T} \right) \quad (2)$$

Where $\dot{E}x_{air}$ – air heat flow exergy reaching the site, W, \dot{m}_A – air flow rate, kg/s, $c_{p,avg}$ – specific heat of air, J/kg K.

Exergy flows comparison can provide significant information for energy/exergy supply planning from locally available energy sources and selecting the optimal hybrid RE transformer or applying the passive RE use measures.

6. CASE STUDY RESULTS

6.1. Object of the case study

The study contains the analysis of air flow thermal exergy reaching the building site (Table 1, Fig. 5).

Table 1. Technical details of freely chosen site

Site area:	100×100 m
Site buildings:	Undeveloped territory
Buildings near the site:	Non
Vegetation in the site:	Grass/field
Vegetation near the site:	Grass/field
Terrain:	1 percent over all slope to the NE side
Site coordinates:	54.792863, 25.279806 (WGS)
Site control volume geometrical dimensions (100×100×52 m) are selected according to air space demand for wind turbine installation; the central site area is provided for residential building construction, not creating shadows for neighbouring objects and installation depth of heat pump horizontal collector.	

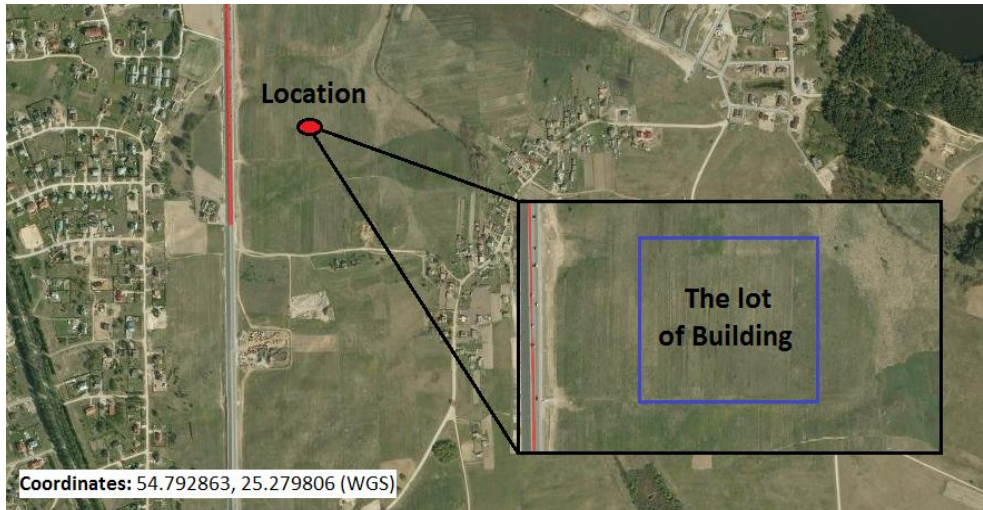


Fig. 5. Analyzed site location

6.1. Exergy flow

Dynamics of air flow thermal exergy amount reaching the site within the year period is presented in Fig. 6.

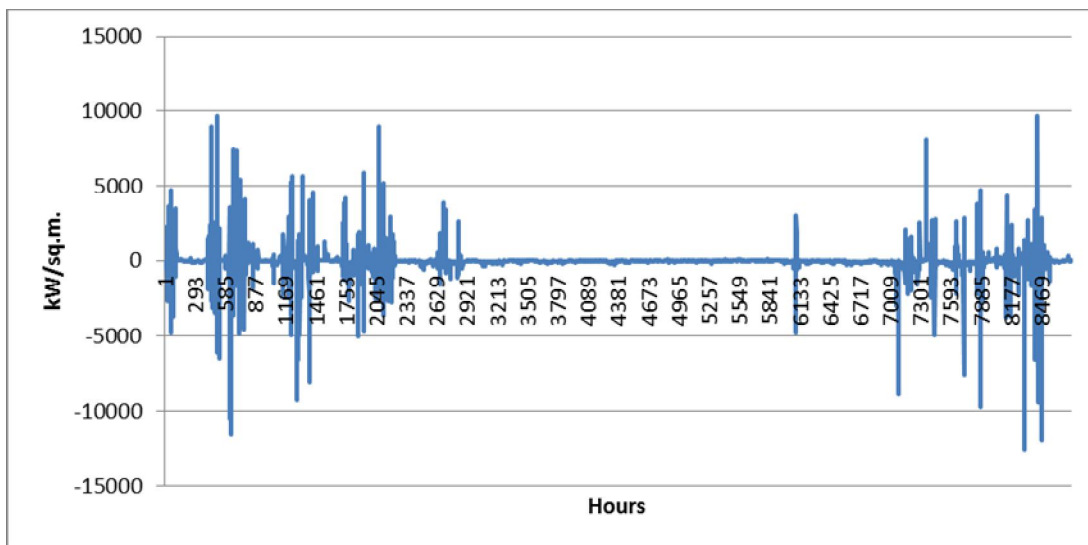


Fig. 6. Exergy flow to the building site

Two key periods of the year: cold (1–3000 and 7000–8760 year hours) and warm (3000–7000 year hours) can be distinguished in exergy amount dynamics analysis. Exergy extremes are very clear in the cold period of the case study, while the exergy amount to the building site is quite stable during the warm period. Exergy amount dynamics in July is presented in Fig. 7.

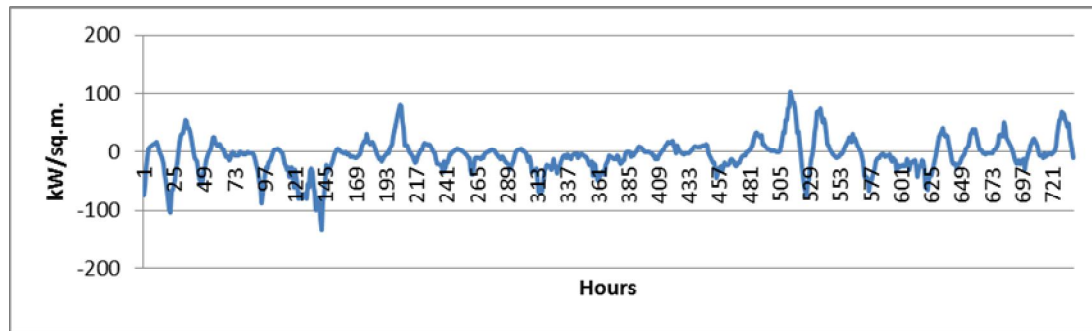


Fig. 7. Exergy amount dynamics in July

The results are that in summer disposed exergy amount fall into ± 100 kW/sq.m limits. The heat flow interpretation shows that the part-time air flow reaching the building site can transmit the heat, the other part-time – to remove the heat, otherwise, to cool. On the technological level, the totally different solutions have to be made in cold and warm periods. Only in such case, the larger exergy amount reaching the building site can be used. On the other hand, the obtained 100 kW/sq.m. exergy flow is quite difficult to compare with exergy flow required for building cooling needs [20] of 20–40 mW/sq.m. In low energy building rather small but steady exergy amount is needed for heating, cooling and ventilation needs. Air flow exergy analysis, in case of significantly larger exergy potential, must focus on technological air flow use options only. Since the individual technology or solution cannot be determined for each exergy amount or mark (plus or minus) case, the part of exergy flow will remain unused. Also, if the need and exergy amount will pass each other in time, the accumulation option must be evaluated. Such or similar issues become the second step of complex RE flow analysis.

6.2. Statistical assessment of results

Statistical analysis tools are applied for more detailed identification of prevailing exergy flow values. STATISTICA program data evaluation results are presented in Fig. 8 and Table 2. The time interval between the estimates is one day.

Values frequency histogram (Fig.8) is developed by setting air exergy amount values in one variation line.

Histogram results show that 81% of all exergy flow values fall into ± 200 kW/sq.m. values limit. All the other exergy amount values are discrete and distorting the weighted center of flow values. More consistent air flow supply exergy analysis shall include the evaluation of exergy amount weighted centre within the set limits. Statistical indicators are presented in Table 2.

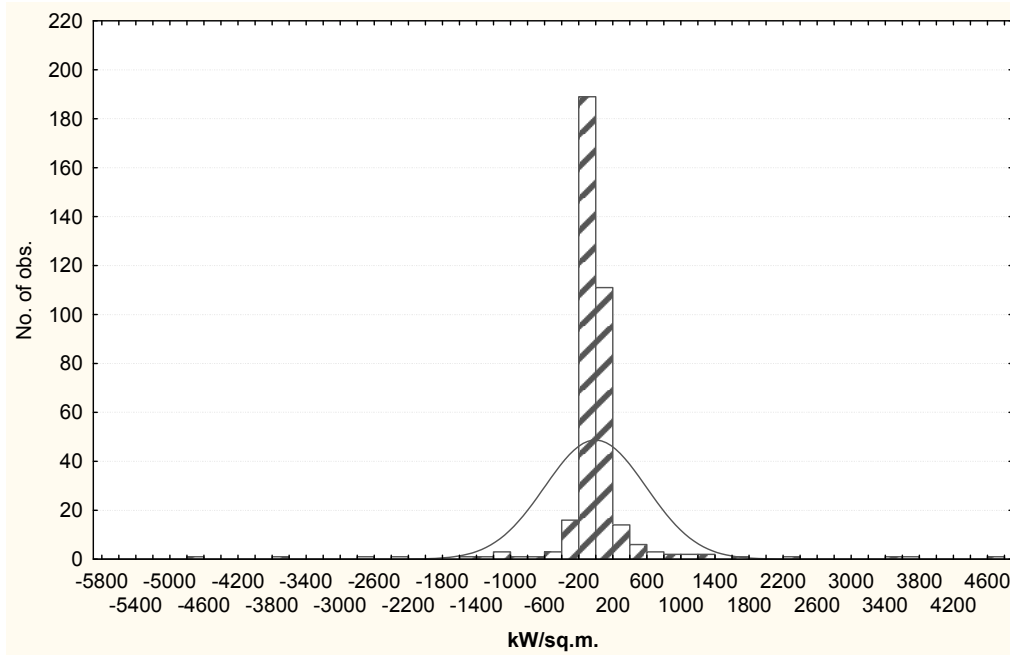


Fig. 8. Values frequency histogram

Table 2. Exergy flow statistical indicators

No.	Characteristic	Value
1.	Valid No.	364
2.	Mean	-4.07
3.	Median	-24.22
4.	Minimum	-4746.35
5.	Maximum	4765.81
6.	Lower Quartile	-74.73
7.	Upper Quartile	33.87
8.	Range	9512.16
9.	Quartile Range	108.59

Result of exergy values mathematical average determination is -4.07 kW/sq.m. flow value, while the average result of extreme values impact eliminating the median is -24.22 kW/sq.m. According to the fact that 81 % values are within ± 200 kW/sq.m and during the warm period ± 100 kW/sq.m. values limit, the extreme values impact is more important for summer technological solutions. In both cases, the negative exergy value shows that the temperature of energy flow supplied to the building site is lower than the system temperature. Taking the phenomenon as heating or cooling, the constant exergy lack is prevailing within the year period and must be compensated by additional exergy amount. This can be compensated by electricity, biomass or other energy forms use.

According to quartile values, the prevailing exergy flow in positive exergy (heat supply) values is 33.87 kW/sq.m. and in negative exergy (heat extract) values -74.73 kW/sq.m. Active and passive heating and cooling technological solutions should help to determine the equipment capacities based on these values. It should be noted, that the determined air flow thermal exergy amount reaching the building site is a theoretical one. Technological exergy amount evaluation shall be resulted by maximum potential exergy amount technological solutions.

7. CONCLUSIONS

In this study, the complex analysis of RE flow reaching the building site is one of the main measure to evaluate a sustainable RE integration. The study includes the concept approach to the air heat flow as another RE source. The air in RE integration analysis is usually problematic and is not evaluated as one more RE source. The air is interpreted as a medium for other processes only.

To evaluate exergy amount of air flow, the reference parameters are set as dynamic, while the system parameters are quasi-steady state. Such interpretation of reference environment is rather unconventional, but accepted as the only appropriate in the analysis of air as energy/exergy flow.

The presented case study demonstrates that the detail analysis of RE sources develops a data base for theoretical and optimal technologies combination selection. The evaluation shows that exergy amount changes and different dynamics of values are quite significant within the various periods of the year:

- ± 200 kW/sq.m. air thermal exergy potential and dynamic exergy flow are disposed in cold period;
- ± 100 kW/sq.m. rather steady exergy flow is disposed in warm period.

It is noted, that significantly higher exergy amount than the one needed for the building is available on site. The main task is the technological evaluation of exergy potential. The need and supplied exergy flow pass with each other and related accumulation phenomena must be identified as well as the coincidence of the need and exergy marks.

In general, it is concluded, that the exergy analysis of air flow must be developed and applied in complex RE potential determination as well as potential quality characterization in the user perspective.

REFERENCES

1. *Communication from the Commission to the European Council and the European Parliament – an energy policy for Europe* {SEC(2007) 12} Brussels, 10.1.2007, [referred on the 1th of January in 2013 y.]. Link to the internet < <http://eur-lex.europa.eu/LexUriServ/LexUriServ.do?uri=CELEX:52007DC0001:EN:NOT> >
2. *Communication from the Commission to the Council and the European Parliament - Renewable energy road map - Renewable energies in the 21st century: building a more sustainable future* COM(2006) 848 final, Brussels, 10.1.2007, [referred on the 1th of January in 2013 y.]. Link to the internet < <http://eur-lex.europa.eu/LexUriServ/LexUriServ.do?uri=CELEX:52006DC0848:EN:NOT> >
3. EU energy in figures. *Statistical pocketbook 2012*. European Commission. ISSN 1977-4559.
4. UNDP. *World energy assessment 2000 – energy and the challenge of sustainability*. New York: UNDP; 2000 (ISBN 9211261260).
5. ANGELIS, Dimakis A., and other. Methods and tools to evaluate the availability of renewable energy sources. *Renewable and Sustainable Energy Reviews*, 2011, Vol. 15, p. 1182–1200.
6. BORGES, Carmen, L.T. An overview of reliability models and methods for distribution systems with renewable energy distributed generation. *Renewable and Sustainable Energy Reviews*, 2012, Vol. 16, p. 4008– 4015.



7. BAJPAI, P., DASH, V. Hybrid renewable energy systems for power generation in stand-alone applications: A review. *Renewable and Sustainable Energy Reviews*, 2012, Vol. 16, p. 2926–2939.
8. LUNA-RUBIO, R., TREJO-PEREA, M., VARGAS-VAZQUEZ, D., RIOS-MORENO, G. J. Optimal sizing of renewable hybrids energy systems: A review of methodologies. *Solar Energy*, 2012, Vol. 86, p. 1077–1088.
9. PARDO, N., MONTERO I., MARTOS J., URCHUEGUĞA J.F. Optimization of hybrid – ground coupled and air source – heat pump systems in combination with thermal storage. *Applied Thermal Engineering*, 2010, Vol. 30, p. 1073–1077.
10. NAMA, Y., OOKA, R., SHIBA, Y. Development of dual-source hybrid heat pump system using groundwater and air. *Energy and Buildings*, 2010, Vol. 42, p. 909–916.
11. KARAGIORGAS, M., GALATIS, K., TSAGOURI, M., TSOUTSOS, T., BOTZIOS-VALASKAKIS, A. Solar assisted heat pump on air collectors: A simulation tool. *Solar Energy*, 2010, Vol. 84, p. 66–78;
12. ARTMANN, A., MANZ, H., HEISELBERG, P. Climatic potential for passive cooling of buildings by night-time ventilation in Europe. *Applied Energy*, 2007, Vol. 84, No. 2, p. 187–201.
13. KHALED, A., AL-SALLAL, Laila Al-Rais. Outdoor airflow analysis and potential for passive cooling in the modern urban context of Dubai. *Renewable Energy*, 2012, Vol. 38, No. 1, p. 40–49.
14. CHAN, H.Y., SAFFA, B. RIFFAT, J.Z. Review of passive solar heating and cooling technologies. *Renewable and Sustainable Energy Reviews*, 2010, Vol. 14, p. 781–789.
15. DINCER, I. The role of exergy in energy policy making”. *Energy Policy*, 2002, Vol. 30, p. 137–49.
16. KORONEOS, C., Spachos T., Moussiopoulos N. Exergy analysis of renewable energy sources. *Renewable Energy*, 2003, Vol. 28, p. 295–310;
17. DINCER, I., ROSEN, M.A. *Exergy. Energy, Environment and Sustainable Development. First edition*, 2007. ISBN:978-0-08-044529-8.
18. HEPBASLI, A. A key review on exergetic analysis and assessment of renewable energy resources for a sustainable future. *Renewable and Sustainable Energy Reviews*, 2008, Vol. 12, p. 593–661.
19. BIEKŠA, D. *Pastato inžinerinių sistemų procesų integravimo vertinimas taikant eksergijos kriterijų*. Daktaro disertacija. ISBN: 978-9955-28-223-5.
20. SHUKUYA, M. Exergy concept and its application to the built environment. *Building and Environment*, 2009, Vol. 44, p. 1545–1550.
21. YUCER, C.T., HEPBASLI, A. Thermodynamic analysis of a building using exergy analysis method. *Energy and Buildings*, 2011, Vol. 43, p. 536–542.
22. TORIO, H., ANGELOTTI, A., SCHMIDT, D. Exergy analysis of renewable energy-based climatisation systems for buildings: A critical view. *Energy and Buildings*, 2009, Vol. 41, p. 248–271;
23. El SHENAWY, A., ZMEUREANU, R. Exergy-based index for assessing the building sustainability. *Building and Environment*, 2013, Vol. 60, p. 202–210.



24. WALL, G., GONG, G. On exergy and sustainable development—Part 1 Conditions and concepts. *Exergy an International Journal*, 2001, Vol. 1, No. 3, p. 128–145.
25. HERMANN Weston A. Quantifying global exergy resources. *Energy*, 2006, Vol. 31, No. 12, p. 1685–1702.
26. VALERO, A., VALERO, A., MARTINEZ, A. Inventory of exergy resources on earth including its mineral capital. *Energy*, 2010, Vol. 35, p. 989–995.
27. BEYENE, A., MACPHEE, D., ZEVENHOVEN, R. *Anthropogenic Heat and Exergy Balance of the Atmosphere*, Perugia, Italy; Proceedings of ECOS 2012 – The 25th international conference;
28. SHUKUYA, M., KOMURO, D. Exergy-Entropy process of passive solar heating and global environmental systems, *Solar Energy*, 1996, Vol. 58, p. 25–32.
29. ROSEN, Marc A., DINCER, I. Effect of varying dead-state properties on energy and exergy analyses of thermal systems. *International Journal of Thermal Sciences*, 2004, Vol. 43, p. 121–133.
30. UTLU, Z., HEPBASLI, A. Parametrical investigation of the effect of dead (reference) state on energy and exergy utilization efficiencies of residential–commercial sectors: A review and an application. *Renewable and Sustainable Energy Reviews*, 2007, Vol. 11, p. 603–634.
31. YALCIN, A. GOGUS, Camdalı U., MEHMET, Kavsaoglu S. Exergy balance of a general system with variation of environmental conditions and some applications. *Energy*, 2002, Vol. 27, p. 625–646.
32. ZHOU, Y., GONG, G. Exergy analysis of the building heating and cooling system from the power plant to the building envelop with hourly variable reference state. *Energy and Buildings*, 2013, Vol. 56, p. 94–99.



EXPERIMENTAL INVESTIGATION OF SOLID SORPTION COOLER WITH IMPROVED LOW TEMPERATURE SORBER BY MICRO HEAT PIPE EFFECT

A.P. Tsitovich, A.A. Khartonik
Luikov Heat & Mass Transfer Institute
P. Brovka, 15, 220072 Minsk – Belarus

ABSTRACT

Sorption cooler using renewable power sources (solar energy) was created and experimentally investigated. Sorption cooler consists of two high temperature adsorbers with complex sorbent (activated carbon fiber with microcrystals of $MnCl_2$) and heat pipe thermal control and the third low temperature sorber (activated carbon fiber with $BaCl_2$). Ammonia was chosen as a working fluid. The cooler thermal management is based on heat pipes. The sink of the cold is the air flow. The system can work as a resorption cooler without any liquid in a cycle or can have both sorption and condensation in low temperature sorber. Presence of liquid in porous structure causes the effect of micro heat pipes during the process of evaporation increasing effective thermal conductivity in the sorbent bed of the system. Also combination of adsorption/condensation and evaporation/desorption increases the amount of heat and cold generation in adsorber in the same or reduced time.

Keywords: solid sorption, heat pipe thermal management, complex sorbent, renewable power sources, micro heat pipe effect

1. INTRODUCTION

Growing demands of human civilization cause more usage of refrigerators. People need to chill agricultural products, fish and other food. But different ecology acts of law prevent using of conventional refrigerators. Reduction in use of synthetic refrigerants and production of CO_2 provides a new opportunity for sorption systems using environment friendly coolants and renewable power sources like solar energy [1–2].

Physical adsorbents like zeolite, silica gel, activated carbon and alumina oxide have highly porous structures and can selectively catch and hold refrigerants [3]. After they get saturated, they can be regenerated simply by being heated. If an adsorbent and a refrigerant are placed in the same vessel, the adsorbent would maintain the pressure by adsorbing the evaporating refrigerant. The process is intermittent because the adsorbent must be regenerated when it is saturated. For this reason, multiple adsorbent beds are required for continuous operation. Conventional working pairs are activated carbon and methanol, or ammonia, and silica gel and water. Current solar adsorption technology can provide a daily ice production of 4–7 kg per unit square meters of solar collector with a solar-to-cooling COP (coefficient of performance) between 0.1 and 0.15 [4]. Thermal management helps solid sorption systems to work effectively [5].

Although mechanical compression chillers often have higher COP than chemical pumps, conventional refrigerators can lose in overall effectiveness because of additional transforming of heat energy to electricity to drive an electric pump. Sorption systems can use heat energy directly from heat power sources [6].

The main idea of this research is to build and investigate a small portable chip chiller using renewable power source as a main power supply and gas flamer as secondary back-up power supply.

2. THE STRUCTURE AND WORK BASICS OF THE COOLER

A small portable chip cooler using renewable power source can be built if we take a solar concentrator as a primary power source and a set of sorbent beds which are heating and cooling alternatively [7]. We can use also a gas flamer as a secondary back-up system to power the cooler during nights or to apply additional energy to the system. Activated carbon fibre (ACF) “Busofit” is used for ammonia adsorption/desorption. The micro/nano crystals of MnCl_2 and BaCl_2 are used as the chemical sorption material to increase the sorption capacity of the sorbent bed. The original heat pipes (thermosyphon) are used as heat exchangers for external heat recovery and adsorbers thermal control [8].

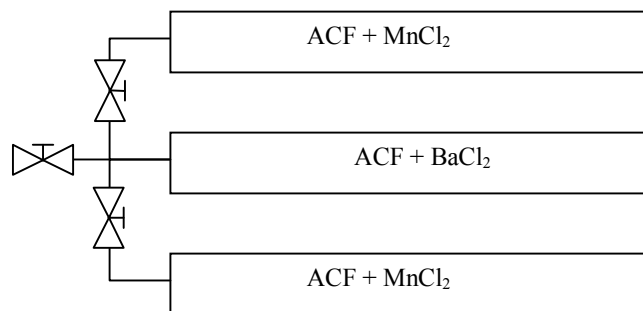


Fig. 1. The schematic of the three adsorbers cooler

The schematic of the three adsorbers cooler is shown on Fig. 1 – Fig. 2. The experimental set-up includes two adsorbers ($\text{ACF} + \text{MnCl}_2$) with relatively high temperature and one relatively low temperature adsorber ($\text{ACF} + \text{BaCl}_2$). Original heat pipes (thermosyphons) are proposed as thermal management system.

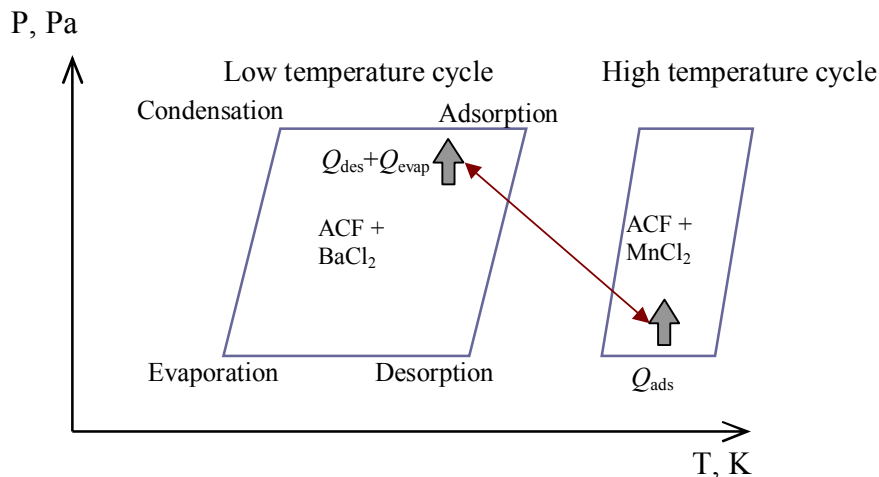


Fig. 2. Thermodynamic scheme of the three adsorbers cycle with complex utilization of energy of low temperature adsorber

Clapeyron diagram shows the main processes in the system, Fig. 2. The low temperature cycle can be expanded with the help of processes of condensation and evaporation. In this case additional evaporation heat Q_{evap} is added to heat of desorption Q_{des} in low temperature sorber. It increases the total amount of adsorbate available and results in increasing of heat of adsorption Q_{ads} in high temperature sorber.

The system management consists only in opening and closing valves to change the direction of the fluid inside the heat exchangers.

The main characteristic of the cooler efficiency is the COP for cooling:

$$COP_C = \frac{Q_{des} + Q_{evap}}{Q_{ads}} \quad (1)$$

Dynamics of the cooling cycle is defined by the Specific Cooling Power (SCP):

$$SCP = \frac{Q_{des} + Q_{evap}}{\Delta w \tau}, \quad (2)$$

where Δw is the adsorbate uptake exchanged during the cycle; τ is the time of the cycle.

The quality of sorbent material affects both the COP and SCP, and its proper choice is of prime importance. The choice of sorbent material should be based on comprehensive analysis that takes into consideration both thermodynamic and dynamic aspects. Kinetic properties of the sorbent material have the strong influence on the dynamic behaviour heat and mass transfer inside the sorbent bed and contribute to the specific power of the cooler.

The mass of each adsorber is equal to the sum of masses of the adsorbent, metal of adsorber and heat pipe heat transfer system. The mass of the low temperature sorber includes the mass of $BaCl_2$ (270 g), the mass of the ACF “Busofit” (340 g) and the mass of steel case (1220 g). The mass of the high temperature adsorber includes the mass of $MnCl_2$ (230 g), ACF “Busofit” (250 g), steel case (1220 g) and thermosyphon (900 g).

3. THE THERMAL MANAGEMENT SYSTEM

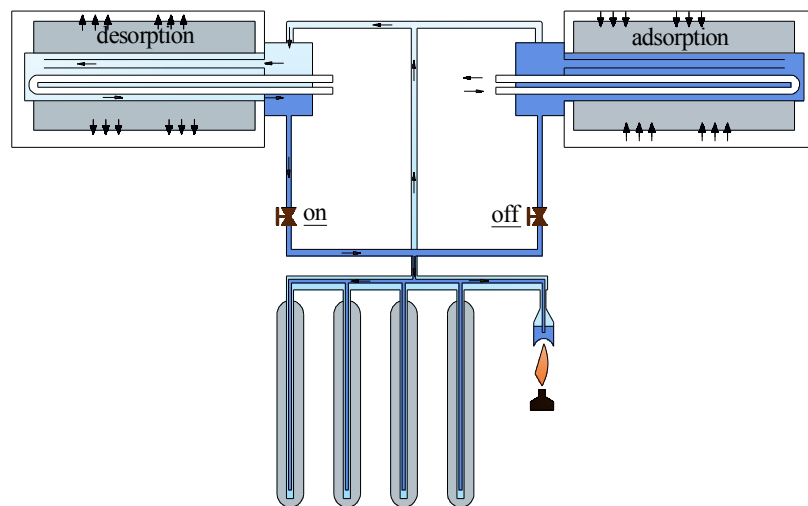


Fig. 3. Solar heater with two adsorbers, solar collectors (with flame as the back-up), vapour-dynamic thermosyphon, two loop thermosyphons and two valves

The scheme of the thermal management system is shown on Fig. 3–4. Vapor-dynamic thermosyphon can have several evaporators to obtain the heat from renewable power sources (sunlight) and a gas flamer for back-up or an additional power source. It is made from stainless steel. The working fluid is water. The evaporators of the vapour-dynamic thermosyphon are disposed inside the vacuum glass solar collectors. The thermosyphon condensers are placed inside two high temperature adsorbers. Such vapour-dynamic thermosyphon has low thermal resistance ($R = 0.01 - 0.05 \text{ K/W}$), its length is one meter. The vapour and liquid minichannels and two-condensers are switched on and off, alternatively, Fig. 4. To heat adsorbers the constant heat flow from the thermosyphon evaporator (solar energy) was transformed into intermittent heat flow

generating in condensers by alternative closing/opening valves, Fig. 4, disposed on liquid pipes of the vapour-dynamic thermosyphon.

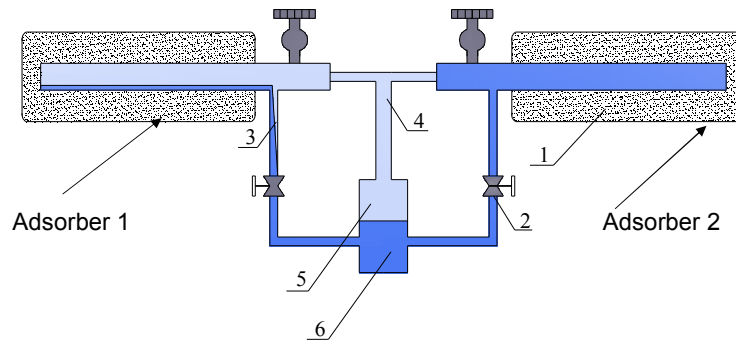


Fig.4. Schematic diagram of the vapour-dynamic thermosyphon: 1 – condensers, 2 – valves, 3 – liquid line, 4 – vapour line, 5 – evaporator, 6 – liquid pool of the evaporator

The advantages of this vapour-dynamic thermosyphon are: 1) low thermal resistance; 2) ability to transport the heat flow over a long distance in the horizontal position, which is difficult to achieve, using conventional thermosyphons; 3) possibility to transform the constant heat load in the evaporator to intermittent heat load in condensers (Fig. 5).

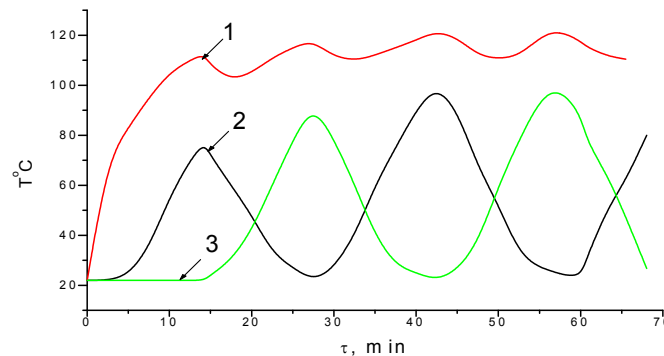


Fig. 5. Transformation of constant heat load to intermittent one: 1 – the evaporator of the thermosyphon, 2 – condenser I, 3 – condenser II

The cooling of the sorbent bed inside the high temperature adsorbers was performed by stainless steel loop heat exchangers. The loop heat exchanger was made as a 2 mm tube placed inside the annular gap of the vapour-dynamic thermosyphon condenser. The working fluid is water. When the vapour-dynamic thermosyphon is closed (valve closed) the loop thermosyphon cools the sorbent bed, realizing two-phase heat transfer inside the annular gap. The low temperature adsorber (ACF + BaCl₂) has the liquid loop system of thermal control (heat exchanger to transfer the cold from the adsorber to the air). Thus the process of the heating/cooling of the sorbent bed in adsorbers is performed.

4. THE SORPTION SYSTEM

The sorption system consists of the low temperature adsorber (ACF + BaCl₂ microcrystals) and two high temperature adsorbers (ACF + MnCl₂ microcrystals) connecting by valves.

The mass of ammonia inside two high temperature adsorbers is higher than the mass of the adsorbed ammonia in third low temperature adsorber. Thus there is a possibility to store ammonia in the low temperature adsorber in two qualities (adsorbed gas inside the sorbent material only and both adsorbed gas in micro pores and the liquid in its macro pores).

Such three adsorbers cooler has some advantages:

1. The liquid is disposed inside the capillary porous media and uniformly distributed along its volume (non sensitive to gravity due to the capillary forces action).
2. During the time of cold generation, the intensive two-phase heat transfer occurs inside the porous media. The effective thermal conductivity of the sorbent bed is at least ten times more (micro-heat pipe effect [9]) to compare with the resorption cooler.
3. Two-phase micro-jets of ammonia during the evaporation inside the porous media impact the loop heat exchanger and the adsorber envelope ensuring the uniform cooling.

The cooler is working as follows:

1. Initially three adsorbers have the same temperature. The valves are opened
2. At the time τ_1 the high temperature adsorbers start to be heated by sun, the pressure in the adsorbers is increasing, heat and mass transfer between high and low temperature adsorbers is initiated.
3. The heat absorbed by the high temperature adsorbers from the source of energy (solar collectors, gas flame) due to the pressure drop is transferred to the low temperature adsorber by the ammonia flow. The low temperature adsorber during the time of ammonia adsorption dissipates this energy to the surrounding through the loop heat exchanger.
4. At the time τ_2 one of high temperature adsorbers starts to cool down to the ambient temperature (by loop heat exchanger) and begin to suck the ammonia from the low temperature adsorber. The cold generation inside the low temperature adsorber is divided to two stages. Initially there is a volumetric evaporation of the liquid ammonia inside the porous media of the sorbent bed following the intense two-phase heat transfer. The second stage is based on desorption/regeneration of ammonia vapour in the sorbent bed. The cold from the low temperature adsorber is dissipated to the ambient with the help of the heat exchanger. The total time of cooling is equal to the time of the liquid evaporation and the time of the ammonia vapour adsorption/decomposition:
5. At the time τ_3 the cold generation is finished. The ammonia is accumulated in the medium temperature adsorbers, the valves are switched off. The cooler is ready for the next cycle operation.

If we have two adsorbers filled with different sorbent beds, the cycle is separated in two main phases corresponding to two pressure levels. Due to the effect of adsorption/desorption of the ACF this pressure difference is dynamically changing during the cycle (completely different comparing with chemical reactors). The carbon fibre as a fast sorbent material starts to react with ammonia in the early stage of heating/cooling time (up to 5 min) and accomplish its reaction after the chemical reaction of the salt is finished. The dynamic of the pressure change in the reactor is also fast and starts before the salts are beginning to react. During the regeneration stage carbon fibre as a host material helps to distribute microcrystals through the whole volume of a sorbent bed (ammonia capillary condensation, salts dissolution in the liquid ammonia, salt rich liquid ammonia penetration into the sorbent material due to capillary forces).

The micro/nano crystals deposit on the filament surface increase the sorption capacity of the sorbent compound “Busofit+ BaCl₂” 2–3 times. The activated carbon filaments and micro/nano crystals enhanced the COP of the system to compare with conventional chemical heat pumps.

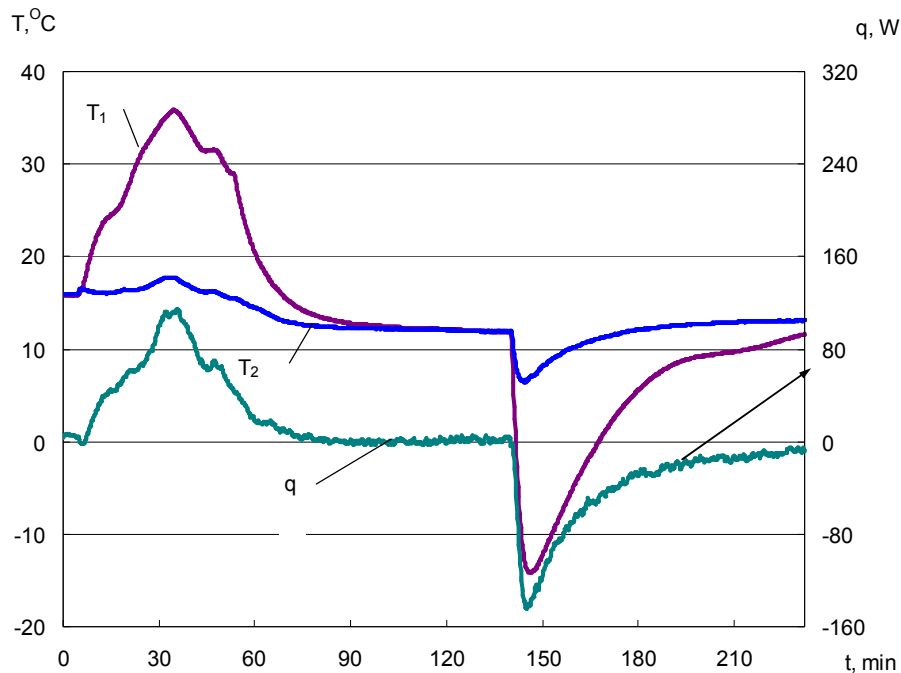


Fig. 8. Temperature changing with time in: T_1 – the low temperature adsorber (ACF +BaCl₂), T_2 – mean temperature of liquid inside the loop heat exchanger, q – heat flow to/from the liquid heat exchanger to the sorbent bed inside the low temperature adsorber

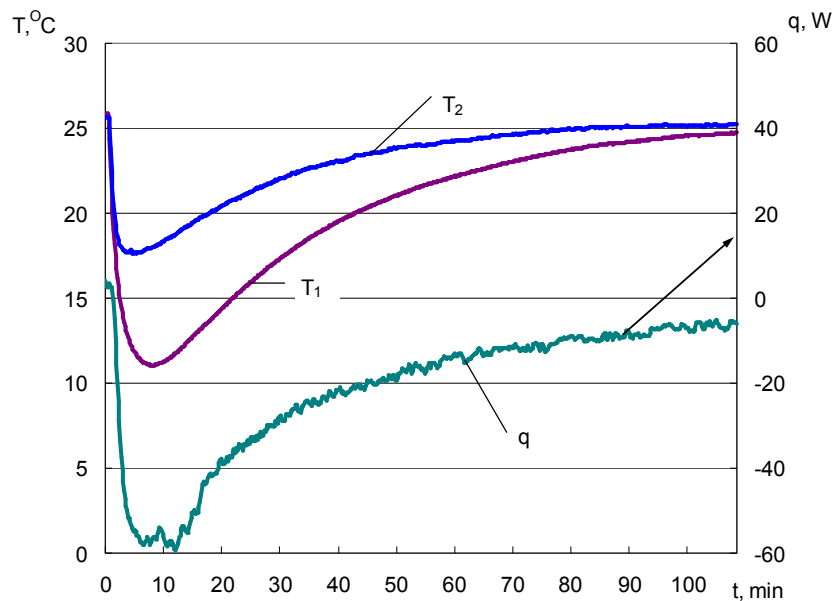


Fig. 9. Temperature changing with time during resorption process in: T_1 – the low temperature adsorber (ACF +BaCl₂), T_2 – mean temperature of liquid inside the loop heat exchanger, q – heat flow to/from the liquid heat exchanger to the sorbent bed inside the low temperature adsorber

The second case is adsorption coolers with new effects due to the evaporation of ammonia inside the porous bed, Fig. 10. The amount of ammonia driven to the low temperature sorber is much higher and liquid ammonia is condensated and accumulated in the pores of the sorbent bed. The temperature evolution in two adsorbers during the cycle of heating/cooling shows the temperature decrease in the low temperature adsorber at least 12 °C–15 °C to compare with the resorption cooler.

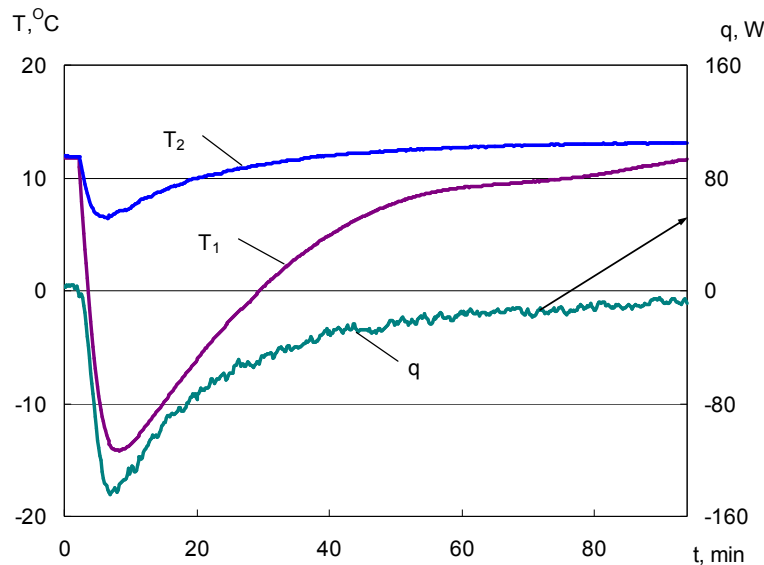


Fig. 10. Temperature changing with time when using the effect of micro heat pipes in: T_1 – the low temperature adsorber (ACF + BaCl₂), T_2 – mean temperature of liquid inside the loop heat exchanger, q – heat flow to/from the liquid heat exchanger to the sorbent bed inside the low temperature adsorber

For such a cycle we have the cold generation at least of two times more. The mass flow meters were used for the calculation of the degree of advance of chemical reactions and physical adsorption. Instantaneous cooling and heating rate was also recorded. The cooling capacity obtained is equal 250–300 KJ.

The process of evaporating of ammonia inside macro pores and condensation in them too causes increasing in the effective conductivity of sorbent bed (micro heat pipe effect). Much higher amount of heat transferred through the sorbent in less time. The specific cooling power of low temperature adsorber is up to 107 W/kg (for the sorbent bed). The time of the cooling cycle is near 35 min. to compare with one hour for the conventional resorption cycle.

6. CONCLUSIONS

A three bed cooler with two high temperature sorbent (ACF + MnCl₂) bed and a low temperature bed (ACF + BaCl₂) was created and experimentally investigated. Complex compounds sorbent materials such as active carbon fibre and microcrystals of the salts on its surface allow to obtain larger amount of heat (cold) than usual simple sorbent. Heat pipe thermal management of adsorbers gives an easy opportunity to successfully use renewable power sources. Using of micro heat pipe effect allows obtaining much higher power output from sorption devices. The cooling capacity obtained in experiments is up to 250–300 KJ. . The specific cooling power of low temperature adsorber is up to 107 W/kg (for the sorbent bed). The time of the cooling cycle is reduced twice in compare with the conventional resorption cycle. It shows that energy from renewable power sources (solar power) can be used effectively. The investigated cooler can be used as a part of the systems for maintain humidity and temperature in museums and other closed spaces [10].

REFERENCES

1. ZIEGLER, F. Sorption heat pumping technologies: Comparisons and challenges, *International Journal of Refrigeration*, 2009, Vol. 32, p. 566–576.



2. VASILIEV, L.L., KANONCHIK, L.E., BABENKO, V.A. Thermal management of the adsorption-based vessel for hydrogenous gas storage, *Journal of Engineering Physics and thermophysics*, 2012, Vol. 85, № 5, p. 909–918.
3. WANG, L.W., WANG, R.Z., OLIVEIRA, R.G. A review on adsorption working pairs for refrigeration, *Renewable and Sustainable Energy Reviews*. 2009. Vol. 13 (3), p. 518–534.
4. JAKOB, U., KOHLENBACH, P. Recent Developments of Sorption Chillers in Europe, *IIR Bulletin*, 2010, p. 34–40.
5. CRITOPH, R.E. The use of thermosyphon heat pipes to improve the performance of a carbon-ammonia adsorption refrigerator. Proceedings of the IV Minsk International Seminar “Heat Pipes, Heat Pumps, Refrigerators”, Minsk, Belarus, September 4–7, 2000, p. 35–41.
6. AKISAWA, A., MIYZAKI, T. Multi-bed adsorption heat pump cycles and their optimal operation, *Advances in Adsorption Technology*, Edited by B.B. Saha and K.C. NG, p. 241–279, 2010 Nova Science Publishers, Inc. ISBN-10: 1608768333.
7. ALYOUSEF, Y., ANTUKH, A.A., TSITOVICH, A.P., VASILIEV, L.L. Three adsorbers solar cooler with composite sorbent bed and heat pipe thermal control, *Applied Thermal Engineering*, 2012, Vol. 38, p. 124–130.
8. VASILIEV, L.L. Heat pipes to increase the adsorption technology efficiency, *Advances in Adsorption Technology*, 2010, Nova Science Publishers, Inc., Edited by B.B. Saha and K.C. NG, p.505-538. ISBN-10: 1608768333.
9. BABENKO, V.A., KANONCHIK, L.E., VASILIEV, L. Jr. Heat and Mass Transfer Intensification in Solid Sorption System, *Journal of Enhanced Heat Transfer*, 1998, Vol. 5, № 2, p. 111–125.
10. ARISTOV, YU.I., VASILIEV, L.L., GLAZNEV, I.S., GORDEEVA, L.G., ZHURAVLEV, A.S., KOVALEVA, M.N. Physicochemical bases of autonomous maintenance of humidity and temperature in closed spaces, *Journal of Engineering Physics and Thermophysics*, Vol. 85, № 5, p. 977–986.



REVIEW OF RENEWABLE ENERGY USE IN LITHUANIA'S ENERGY SECTOR

P. Seniūnas

*Lithuanian Energy Institute
Breslaujos g. 3, LT-44403 Kaunas – Lithuania*

ABSTRACT

Nowadays the demands electricity power of the world including Lithuania are increasing. It is also now widely recognized that the fossil fuels (coal, petroleum and natural gas) and other conventional resources, presently being used for generation of electrical energy, may not be either sufficient or suitable to keep pace with increasing demand of the electrical energy of the Lithuania. So generation of electrical power by most of fossil fuels causes pollution, which is likely to be more acute in future.

Lithuania has a good potential in biomass, hydro and wind power. Also now becoming more and more popular solar, biofuel, hydro power, which produce electrical power and keep pace of increasing energy demand. These renewable energy sources are Lithuania's main goal to replace some fossil fuels (coal, petroleum and natural gas) in future and to increase the share of renewable energy in energy mix to 23% by 2020. Aim of this article is to present a review of the renewable energy situation and assessed potential of renewable's in Lithuania. Also this article presents balances and renewable share of all fuel types to the energy sectors. Also the problems related to the use of renewable energy sources in Lithuania.

Keywords: Renewable energy sources, hydro, wind, solar power, fossil fuel

1. INTRODUCTION

This paper gives a short overview of energy the conditions in the energy sector of Lithuania, analyses the current situation and provides overview of the latest developments in the Lithuanian energy sector. Currently renewable energy sources becoming more and more developed (requirements of electricity demands in Lithuania are increasing) in Lithuania, renewable energy sources (including biomass, solar, wind, geothermal and hydropower) that use indigenous resources have the potential to provide energy services with zero or almost zero emissions of both air pollutants and greenhouse gases [1].

The development of renewable energy sources will ensure an attractive alternative to traditional energy because the combustion of fossil energy sources substantially increases environmental pollution and accelerates climate warming, which causes natural disasters more and more frequently. The use of renewable energy sources not only helps to resolve problems of climate changes, but also creates conditions to combat poverty and problems of energy and economic exclusion. [2] So it is extremely important to use renewable energy sources as widely as possible. Each year the total energy share from renewables in Lithuania are growing continuously, because possibilities of wider use of local fossil resources (oil, peat) are limited both in Lithuania and other Baltic countries. The Lithuania's target is to increase the share of renewable energy sources to at least 23% of the country's final gross energy consumption by 2020. It is most important to create favourable conditions for the development of renewable energy sources in the country. The following development directions of renewable energy sources have been established for all three sectors (electricity, heating and transport) [2].

The current situation of RES (renewable energy sources) in Lithuania is very promising. Conditions for the development of energy share from renewables, because the country has a great potential in biomass, wind and hydropower energy. These are the main renewable sources (biomass, wind and hydropower energy), but also there are some other sources such as solar, geothermal

energy that are becoming more popular [3-4]. So all these RES can be developed and help Lithuania to reach its goals by 2020.

2. METHODOLOGY

The analysis is based on the application of methodology of Lithuania's energy statistics data (which was collected and calculated) comparative analysis and detailed analysis of changes in tendencies of economic development and structure of the country's energy balances. Developing and increasing total share of renewable energy sources final gross energy consumption every year.

3. RESULTS

The research on the current situation in the energy sector in Lithuania has shown that the main tasks, challenges of the development of renewable energy sources in the energy sector concerning the priorities of EU strategies are:

- To coordinate actions of market participants in separate sectors and to involve municipalities in the promotion of the use of RES.
- To improve and implement support schemes which would create favourable conditions for the use of RES.
- To ensure that all administrative procedures intended for projects for RES would be proportionate, simple and transparent.
- By effectively developing electricity, thermal energy and gas infrastructure, to create favourable conditions for the implementation of projects for RES and to coordinate the development of RES with the principle of distributed generation.
- To increase use of all types biomass for thermal energy and electricity production.
- To increase the use of RES and electricity in the transport sector.

Main challenges of the Lithuania's energy sector and the development of renewable energy sources is to ensure that the share of RES in the country's total final consumption of energy, which amounted to 15.3% in 2008, would reach at least 23% in 2020, to seek the following procedures [2]:

- To increase the share of RES consumed in all kinds of transport from 4.3% of the final consumption of energy in the transport sector in 2008 to 10% in 2020;
- To increase the share of electricity produced from RES from 4.9% in the country's total consumption in 2008 to 21% in 2020;
- To increase the share of RES in heating and cooling from 28% in the gross final consumption of this sector in 2008 to 36% in 2020, and increase the share of district heating produced from RES from 14.9% in 2008 to 50% in 2020.

During the last couple of years Lithuania has developed the use of RES. Also it has begun active work to develop RES in all energy sectors in order to achieve ambitious target, to increase the share of energy from renewable sources in gross final consumption of energy in 2020 – 23%. Heating and electricity sectors are very important, because there are very complicated to implement RES and use them properly in all municipalities and cities of Lithuania. Results show how much Lithuania implemented RES into energy sectors, what the future expectations are.

4. CONCLUSION

In conclusion energy sufficiency and properly use of RES in the country is an issue of economic development, quality of life and state security. The main goal of the energy sector in Lithuania is to ensure balanced, secure and sustainable supply of all kind of energy for national economy and for better, cheaper energy.



Lithuania has good conditions for the development of renewable energy sources, because the country has a great potential in biomass, wind and hydropower energy. These RES that was mentioned before have the biggest total share from renewables to all energy sectors. Every year RES usage is becoming higher and higher. So Lithuania can reach its ambitious target, which are that the total share of energy from renewables (in gross final consumption of energy) there will be 23% in 2020.

REFERENCES

1. STREIMIKIENE, D.; BURNEIKIS, J.; PUNYS, P. *Review of renewable energy use in Lithuania. Renewable and Sustainable Energy Reviews*. 2005, 9, p. 29–49.
2. European Commission. *National Renewable Energy Action Plan*. 2010.
3. Republic of Lithuania. *National renewable energy action plan of Lithuania*. 2010.
4. VACLOVAS, M.; KONSTANTINAVIČIŪTE, I.; TARVYDAS, D.; *Major changes in the Lithuanian energy sector during two decades. Energy economy, policies and supply security: surviving the global economy crisis*. 2010, p. 207–209.



INVESTIGATION OF EFFICIENCY OF POWER BALANCING IN THE POWER SYSTEM OF THE VARIABLE SPEED PUMPED STORAGE UNIT

D. Ališauskas, R. P. Deksnys

Kaunas University of Technology

K. Donelaičio str. 73, LT-44029 Kaunas – Lithuania

ABSTRACT

This article analyzes possibilities of effective usage of variable pumped storage unit in power system. The main function of variable pumped storage unit is power compensation while ensuring power reliability and quality of voltage and frequency parameters. In this investigation exciter and control system of pumped storage unit is evaluated as well as structure and functional peculiarities in generator and pump regimes. Probability of oscillations in power system is being modelled with integrated wind plant parks and reaction of variable pumped storage unit to entailed power variation. Iterations, statistical and numerical integration methods were applied for establishing parameters and characteristic. The criteria of effective reliability, voltage and frequency parameters and security indexes are determined.

Keywords: variable pumped storage unit, exciter and control system, generator regime, pump regime, quality of voltage, quality of frequency

1. INTRODUCTION

The modern technologies are perfecting existent power plants and building new plants. New variable speed generators are being installed in the pumped storage plants of Europe. The variable speed generators can work as the motor. These units are recommended as having high reaction in powers variation of the power system. It ensures stability of the power system. Also efficiency raises comparing with the synchronous generators.

Nowadays the renewable energy is being installed in the power systems broadly. These are sun, wind, biomass plants. The Sun and wind plant parks are generating the variable active power which depends on conditions of the nature. This event is originating the balancing problem of the power system [1].

The fundamental principles of the asynchronous machines are applied for the variable speed generators. These principles are perfecting the excite control system of the variable speed generators and searching for new ideas. One of ideas ensures the quality of the voltage and frequency. It is determined by balance of active and reactive powers in the power system. Important aspect in balancing powers is power system reliability.

For analysis the structure and principle circuits and mathematical models of the wind plant parks, the power systems and the variable speed pumped storage units are created. The fundamental theory of the automation control, which is certificate IEEE, is applied for structure of the excite control system [3, 4].

The systems of the algebraic and differential equations are describing models. The methods of numerical integration and iteration are applied for system analysis.

2. MATHEMATICAL MODELS OF THE VARIABLE SPEED PUMPED STORAGE UNIT AND CONTROL EXCITER SYSTEM

2.1. Mathematical model of the variable speed pumped storage unit

Electrical part of the variable speed pumped storage unit is analyzed according to evidences of the classical electrotechnical theory. Large power pumped storage unit is selected for analyzing. The inside stator and rotor winding structure of electrical part of the pumped storage unit is identical to structure of the asynchronous motor with double feed rotor [4].

Dynamic mathematical model of the variable speed pumped storage unit is described the system of differential equations of d q coordinate system Fig. 1:

$$\left\{ \begin{array}{l} \underline{e}_{ds} = \underline{i}_{ds} r_s + \frac{d\underline{\psi}_{ds}}{dt} + j\omega_s \underline{\psi}_{qs} \\ \underline{e}_{qs} = \underline{i}_{qs} r_s + \frac{d\underline{\psi}_{qs}}{dt} + j\omega_s \underline{\psi}_{ds} \\ 0 = \underline{i}_{qs0} r_s + \frac{d\underline{\psi}_{qs0}}{dt} \\ \underline{e}_{dr} = \underline{i}_{dr} r_r + \frac{d\underline{\psi}_{dr}}{dt} - j(\omega_s - \omega_r) \underline{\psi}_{qr} \\ \underline{e}_{qr} = \underline{i}_{qr} r_r + \frac{d\underline{\psi}_{qr}}{dt} - j(\omega_s - \omega_r) \underline{\psi}_{dr} \\ 0 = \underline{i}_{qr0} r_r + \frac{d\underline{\psi}_{qr0}}{dt} \end{array} \right. , \quad (1)$$

where $\underline{i}_s, \underline{i}_r$ are currents' vectors of stator and rotor; $\underline{e}_s, \underline{e}_r$ are electromotive vectors of stator and rotor; $\underline{\psi}_s, \underline{\psi}_r$ electromagnetic flux vectors of stator and rotor; r_s, r_r active resistance of stator and rotor; ω_s, ω_r angle frequency of stator and rotor.

For determining mechanic angle we express movement equation of rotor:

$$\frac{d\theta_r}{dt} = \frac{T_e \pm T_m + D\theta_r}{J}, \quad (2)$$

where T_e, T_m are electromagnetic and mechanical driving torques moment; D is damping factor, J is mechanic moment of inertia.

Then differential equation (1) we transform from polar coordinates to space Park's coordinates' system in matrix form:

$$\begin{bmatrix} i_{ds} \\ i_{qs} \\ i_{dr} \\ i_{qr} \end{bmatrix} = \begin{bmatrix} \left(r_s + \frac{d}{dt} L_s \right) & \theta_s L_{ss} & \frac{d}{dt} L_{sm} & \theta_s L_{sr} \\ -\theta_s L_{ss} & \left(r_s + \frac{d}{dt} L_s \right) & -\theta_s L_{sm} & \frac{d}{dt} L_{sr} \\ \frac{d}{dt} L_{sm} & \theta_m L_{ms} & \left(r_r + \frac{d}{dt} L_r \right) & \theta_m L_{mr} \\ -\theta_m L_{ms} & \frac{d}{dt} L_{sm} & -\theta_m L_{mr} & \left(r_r + \frac{d}{dt} L_r \right) \end{bmatrix}^{-1} \begin{bmatrix} e_{ds} \\ e_{qs} \\ e_{dr} \\ e_{qr} \end{bmatrix}, \quad (3)$$

where L_s , L_r are leakage inductance of stator and rotor; L_m is magnetizing inductance.

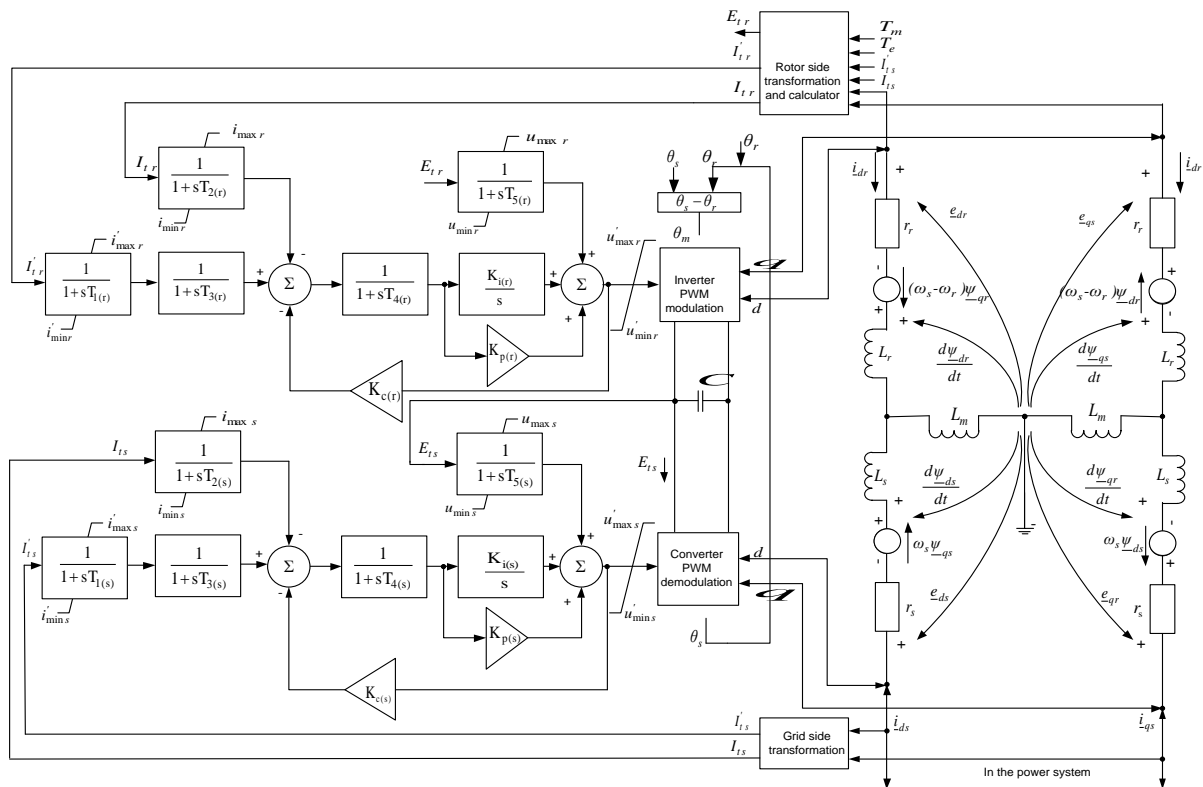


Fig. 1. Structural scheme of variable speed pumped storage unit and its excitation

Given matrix (3) and movement equation (2) we rearrange into state space equations. Having applied Cauchy's state space equation we express variable solutions of rotor angular position and current of stator and rotor:

$$\begin{cases} \underline{i}(t) = e^{\mathbf{A}(t)} \underline{i}(t) + \int_0^t \left(e^{\mathbf{A}(t-\tau)} \mathbf{B} \underline{e}(\tau) \right) d\tau \\ \theta_r(t) = e^{\mathbf{A}(t)} \theta_r(t) + \int_0^t \left(e^{\mathbf{A}(t-\tau)} \right) d\tau \end{cases}, \quad (4)$$

where \mathbf{A} , \mathbf{B} are state equation matrixes; τ is time change.

Angle velocity ω_s , ω_r is integrated for determining angle relations of variable speed pumped storage unit between mutual conditions of stator and rotor:

$$\begin{cases} \theta_s = \int \omega_s dt \\ \theta_r = \int \omega_r dt \\ \theta_m = \theta_s - \theta_r \end{cases}, \quad (5)$$

where θ_s , θ_r or θ_m are angular position of stator, rotor and mechanical.

From the first differential equation we express induction and angle frequency of inside rotor and stator is substituted by electrical and mechanical angles (3).

From this solution (4) we express electro motion vectors:

$$\begin{bmatrix} e_{ds} \\ e_{qs} \\ e_{dr} \\ e_{qr} \end{bmatrix} = \begin{bmatrix} \left(r_s + \frac{d}{dt}L_s\right) & \theta_s L_s & \frac{d}{dt}L_m & \theta_s L_s \\ -\theta_s L_s & \left(r_s + \frac{d}{dt}L_s\right) & -\theta_s L_s & \frac{d}{dt}L_m \\ \frac{d}{dt}L_s & \theta_m L_m & \left(r_r + \frac{d}{dt}L_r\right) & \theta_m L_r \\ -\theta_m L_m & \frac{d}{dt}L_s & -\theta_m L_r & \left(r_r + \frac{d}{dt}L_r\right) \end{bmatrix} \begin{bmatrix} i_{ds} \\ i_{qs} \\ i_{dr} \\ i_{qr} \end{bmatrix}, \quad (6)$$

Summary active power P_e and reactive power Q_e may be computed by use of proposed mathematical model of variable speed pumped storage unit power circuits and method of solution:

$$\begin{cases} P_e = 3(e_{ds}i_{ds} + e_{qs}i_{qs} + e_{dr}i_{dr} + e_{qr}i_{qr}) \\ Q_e = 3(e_{qs}i_{ds} - e_{ds}i_{qs} + e_{qr}i_{dr} - e_{dr}i_{qr}) \end{cases}. \quad (7)$$

Gross output or consumed power of the variable speed pumped storage unit depends on water potential power. We are expressing moments of driving of electromagnetic and mechanic:

$$\begin{cases} T_e = \frac{P_{\max}}{\omega_s} \\ T_m = \frac{kG\sqrt{H^3}}{\omega_m} \end{cases}, \quad (8)$$

where k is the proportionality factor, H is the pressure height and G is a position of deflection wheel.

According to this described mathematic model when the meanings of electro motion, current vectors and condition angle meanings are known we establish active as well as reactive power in variable speed pumped storage unit in pump and generator work regimes.

2.2. Excitation control block structure

Variable speed pumped storage unit structure of excitation control system has analogical mathematically described control elements as well as control system of wind power station [4, 5]. Excitation control system structure is modified assuming pumped storage unit's working regimes in proportional integral PI elements and negative feedback. Dynamic mathematic model excitation control stabilization structures made of grid side and rotor side control blocks. Grid side control block is integrated into converter demodulator and rotor side

control block is inverter modulator. Modulator and demodulator are controlled by impulse width modulation. Excitation control structure has to ensure stable functioning of pumped storage unit [6, 7].

Stator's and rotor's control currents $i_{(dq)s} \rightarrow I_{ts}$, $i_{(dq)r} \rightarrow I_{tr}$ as well as rotor's voltage $e_{(dq)r} \rightarrow E_{tr}$ are transformed. Control system grid's and rotor's sides elements' basic constant parameters are time constants $T_{x(s,r)}$, integration factors $K_{i(s,r)}$, proportion factors $K_{p(s,r)}$ and negative feedback compensation factors $K_{c(s,r)}$. Calculation rotor side parameters are reconciled with mechanic parameters of pumped storage unit and electromagnetic and mechanic driving torques [8].

The control exciter system structures of synchronous blocs are created from mathematical equation to describe function blocs. These function blocs are widely investigated. Calculation of parameters is executed by standard fundamental theoretical electronical methods.

Variable speed pumped storage unit with excitation control system are integrated into power system equivalent circuit bus 4 Fig. 2.

3. MODEL OF THE POWER SYSTEM

For power system power flow distribution analysis transmission grid equivalent circuit with loads (RL1-RL15), generators (G5-G8), variable speed pumped storage units (VSPSU1, VSPSU 2) and synchronous pumped storage units (G1-G4) presented in Fig. 2. The synchronous and variable speed hydro units are connected parallelly in one bus.

For power system wind power park, which is integrated into the 9th bus we describe only generated power Fig. 2. Wind power park's on dominant wind speed which depends on the season. A 24 hours load graphic and generated power by other generators are also evaluated. According to meteorological prognosis paying attention to seasons wind power generated power is described using probability Weibull's distribution:

$$\left. \begin{aligned}
 H_{VP} &= \left(\left(\frac{k}{\frac{v_{vid}}{\Gamma\left(\frac{2}{k}\right)}} \right) \left(\frac{v}{\frac{v_{vid}}{\Gamma\left(\frac{2}{k}\right)}} \right)^{k-1} \cdot e^{-\left(\frac{v}{\frac{v_{vid}}{\Gamma\left(\frac{2}{k}\right)}} \right)^k} \right) \\
 P_{VPP} &= P_{VP(nom)} n H_{VP}
 \end{aligned} \right\} \quad (9)$$

where H_{VP} is Weinbull's parameter for wind power station, $P_{PV(nom)}$ nominal power of wind power station, P_{PVV} generate active power of wind power stations, Γ is gamma function, k is form factor, v is v_{vid} wind and medium wind speed, n number of wind power stations.

330 kV and 110 kV is made up, transmission grid lines are changed into equivalent reactance's (R1-R26). Power system is integrated into IPS/UPS system by connections (IC1, IC5). In the equivalent system connections (IC6, IC7) are foreseen with neighbouring

European power systems.

In the equivalent circuit power flow analysis is oriented to the 4th bus in which variable speed pumped storage unit is integrated and the 9th bus which is wind power park.

We use Newton-Raphson's method for analyzing and determining power system active and reactive power flows. This method is described in scientific literature [9].

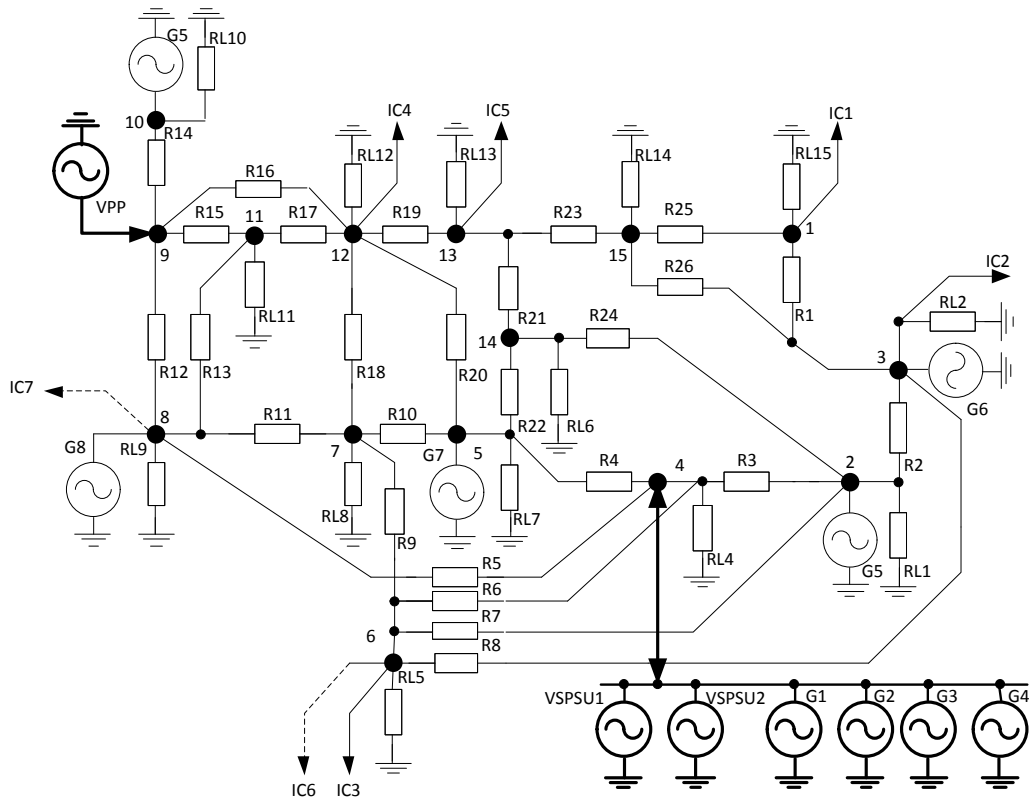


Fig. 2. Equivalent simplified circuit of power system transmission grid

Fulfilling analyzing of reliability active and reactive powers of the synchronous and the variable speed hydrounits are used power laws of reserve [9, 10]:

$$P(T) = \frac{\lambda}{\lambda + \mu} \left(1 - e^{-(\lambda + \mu)T} \right), \quad (10)$$

where T is timescale, μ is recovery state, λ is failure state.

We are accepting as generate and load powers in hydrounits $t=0$ moment of time. Then their failure is $t=T$ moment of time. From here we are doing assumption that operation of hydrounits to generating and loading active and reactive powers. We know that active power fulfils control of frequency of power system, while reactive power fulfils control of voltage [11].

Power system equivalent circuit is formed from power flow analysis and wind power park generated power (9) mathematical models which allow to fulfil thorough power flow distribution analysis between the 9th and the 4th buses.

4. DYNAMICS MODELLING OF THE VARIABLE SPEED PUMPED STORAGE UNIT IN THE POWER SYSTEM

Variable speed pumped storage unit and its mathematical model excitation control system according to technical characteristics and some specifications correspond to 2x250 MW active power real pumped storage unit. Active power of the synchronous pumped storage units is 4x225 MW. Synchronous and variable speed pumped storage units are modeled at the moment of start in regime of generator and pump.

We are accepting that active and mechanic powers are approximately equal:

$$P_e \approx P_m . \quad (11)$$

Wind power park's installed power bearing in mind expansion tendencies is 500 MW. Autumn season's wind power stations' generated power is being modelled.

Lithuania's PS 330 kV and 110 kV transmission grid simplified equivalent circuit model is formed. The 9th bus is the model in Palanga district and the 4th bus is Kruonis PSPP. We are modelling 1900 MW of active power in the power system.

5. RESULTS OF ANALYSIS

For selected the synchronous and the variable speed pumped storage units and their systems' excitation control and power energetics work regimes are established limits of mathematic models algebraic and solutions of differential equations convergence. Elementary power system and synchronous and variable speed pumped storage units parameters are substituted by per units' system.

Applying Newton Raphson's method power flow distribution, variations and influence to power system grid are selected and the variable speed pumped storage units power circuits are evaluated. Numerical integration method is applied for establishing and the variable speed pumped storage units systems of excitation control operation characteristics of dynamic processes and reliability. In 60 seconds interval medium wind power generated power and power system loads are mathematically simulation in different scenarios (S1-S5) Fig. 3.

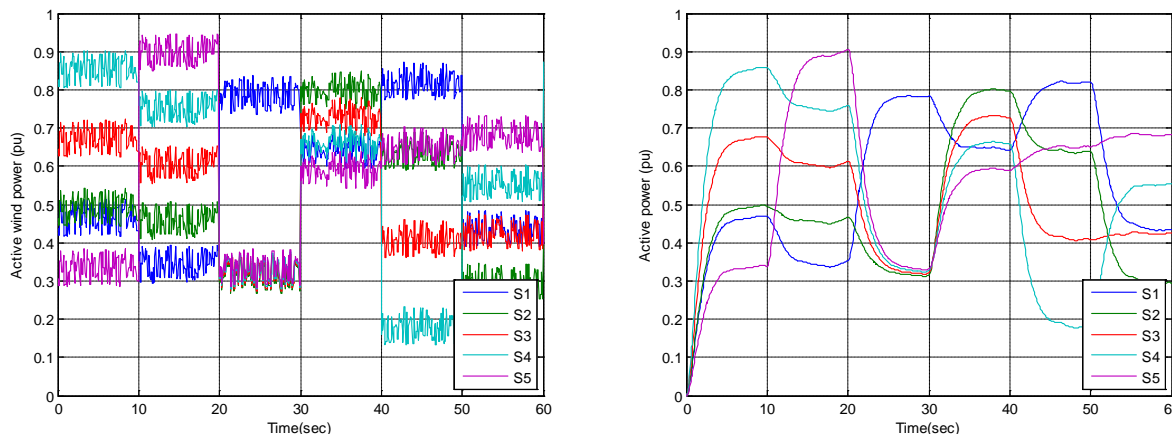


Fig. 3. Active power of wind power stations and power system

Having identified power system power balance with generators and loads power distribution in the system is imitated mathematically. Since investigation is related to power system and its excitation control system we determine active and reactive power changes in bus 4 Fig. 4, 5.

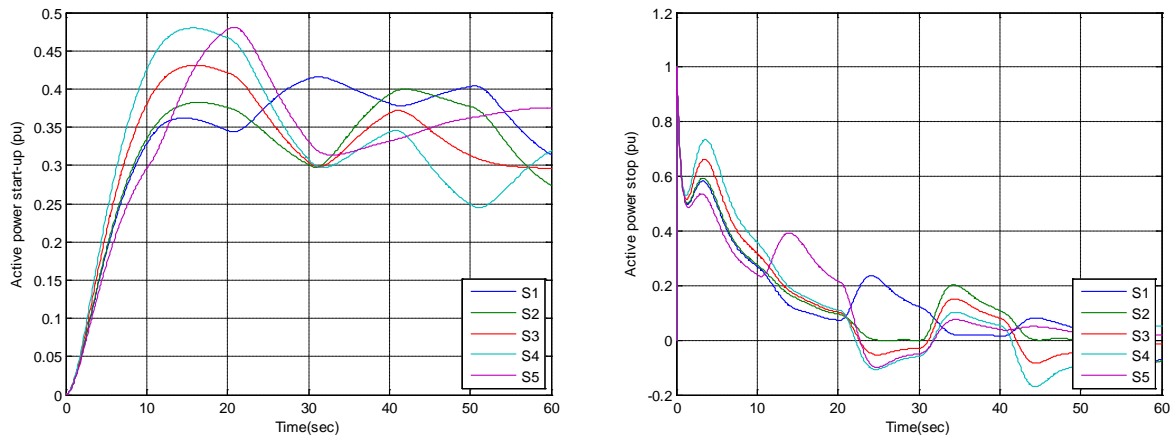


Fig. 4. Active power start-up and stop

Moment of rotor inertia and its control system compensate and stabilize power fluctuations. Adequately they react to power fluctuations. If disconnect first hydro unit, automatically connected second hydro unit in the power system Fig. 4, 5.

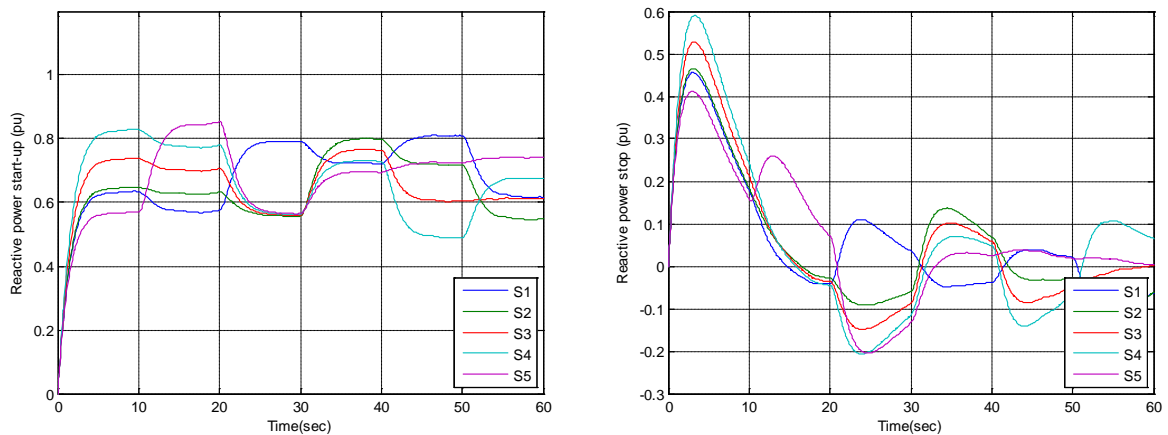


Fig. 5. Reactive power start-up and stop

Sensitivity correction allows reconciling excitation control so that in variable speed pumped storage units turbines would not intervene water hammer. Variable speed pumped storage units ensure dynamic processes of power system reliability. This ensures active and reactive power balance in the power system as well as frequency and voltage reliability.

This is a theoretical and practical model was applied. The main focus of attention is designed for variable speed pumped storage unit system analysis. Analysis was used to ETAP 11 and MATLAB software packages.

6. CONCLUSIONS

1. Mathematical model of the variable speed pumped storage units allow analyzing static and dynamic processes in system.
2. Variable speed pumped storage unit maximum possible active power change of 140 MW in generator operation conditions and corresponding change of 90 MW when the unit operates as a pump.
3. The variable speed pumped storage units over synchronous pumped storage units are advantaged, because starting and stopping time about 15 seconds.



4. Variable speed pumped storage units ensure effective powers balance and high reliability in different scenarios.

REFERENCES

1. *The Strategy approved by Resolution No XI-2133 of the Seimas of the Republic of Lithuania of 26 June 2012*. Link to the internet: <http://www.lrv.lt/EP/strategija-EN.pdf>
2. RODRIGUEZ, J. BERNET, S. BIN, W. PONTT, J. KOURO, O. S. Multilevel Voltage-Source-Converter Topologies for Industrial Medium-Voltage Drives. *IEEE Trans*, 2007, Vol. 54, No. 6, p. 2930–2945.
3. IEEE Recommended Practice for Excitation System Models for Power System Stability Studies, *IEEE Standard 421.5-1992*.
4. SUUL, J. A. UHLEN, K. UNDELAND, T. Variable speed pumped storage hydropower for integration of wind energy in isolated grids – case description and control strategies. *NORPIE*, 2008, p. 8.
5. LUNG, J. K. HUNG, W. L. KAO, W. S. Modeling and dynamic simulations of doubly fed adjustable-speed pumped storage units. *IEEE T. Energy Conver*, 2007, Vol. 22(2), p. 250–258.
6. MUNTEANU, I. BRATCU, I. U. CUTULULIS, N. A. CEANGA, E. Optimal Control of Wind energy Systems. *Springer*, 2008.
7. NAGURA, O. HIGUCHI, M. TANI, K. OYAKE, T. Hitachi's adjustable-speed pumped-storage system contributing to prevention of global warming. *Hitachi Review*, 2010, Vol. 59(3), p. 99–105.
8. TAKAHASHI, R. TAMURA, J. TADA, Y. KURITA, A. Model derivation of an adjustable speed generator and its excitation control system. *14th Power Systems Computation Conference*, 2002, p. 200–205.
9. STOTT, B. ALSAC, O. Fast Decoupled Load Flow. *IEEE Transactions on Power Apparatus & Systems*, Vol. 93, p. 859–869.
10. TERRENCE, L. Probability and Probabilistic Reasoning for Electrical Engineering, *Prentice Hall*, 2006.
11. MODARRES, M. KAMINSKY, M. KRIVTSOV, V. “Reliability Engineering and Risk Analysis: A Practical Guide, Second Edition”, *Marcel Dekker*, 1999.



TASKS OF TRANSMISSION PLANNING IN COMPETITIVE ENERGY MARKET

O. Kochukov, A. Mutule
Institute of Physical Energetics
Aizkraukles 21, LV-1006 - Latvia

ABSTRACT

The main objective of this paper is to show the ways of improving electricity generation and transmission long-term planning methods. Paper reveals differences in approach to long-term planning in different market organization models, showing similarities and differences in tasks and procedures. Performing of some procedures is a complicated task, which requires creation of special computer models of interconnected systems. There is given a small test case, providing model for justification of building real interstate link – “LitPol”. Since the calculations are simplified and the results might be inaccurate, there are given only a review of the method. The model is developed using newest development of Laboratory of Power System Mathematical Modelling - PSPlanner software that also is going to be briefly presented.

Keywords: future electric power systems, transmission planning, cost-benefit analysis component, LitPol Link

1. INTRODUCTION

Electricity supply has special characteristics which make the service unique as compared to other types of industry. The end product has to be delivered instantaneously and automatically upon the consumer's demand, therefore power system configuration have to be very precise and accurate. Since there are plenty of changing parameters in a power system, such as loads, its future development is essential. Power system planning objective is to determine a minimum cost strategy for long-range expansion of the generation and transmission systems adequate to supply the load forecast within a set of technical, economic and political constraints [1]. Moreover, careful planning of the electric sector is of great importance since the decisions to be taken involve the commitment of large resources, with potentially serious economic risks for the electrical utility and the economy as a whole. Together with development of electricity market all over the world, planning procedure became even more complicated, as small modification of a project terms could lead to significant re-distribution of costs and profit between market players.

2. ECONOMIC EFFICIENCY OF INTERSTATE ELECTRIC TIES (IET)

From the one hand, there are a lot of problems related to dividing costs and sharing benefits, especially in competitive market condition. From the other hand, IET could give huge advantages for partner systems, they are [2]:

- Possibility to use larger and more economical power plants
- Reduction of the necessary reserve capacity in the system
- Utilization of most favourable energy resources
- Possibility of building new power plants at favourable locations
- Increase of reliability in the systems etc.
- Development of energy market

2.1. Procedure of IET evaluation in monopole market conditions

The first and most complicated task is to perform general evaluation of IET economic efficiency. It is realized by comparing several development scenarios – new tie construction options

with isolated operation scenarios, which could include local generation development or other options. Economic efficiency is the base of justification of a project. In this step all above mentioned effects should be taken into account and calculated for particular power systems. It is always preferable to have single-criteria calculation, when all effects are adjusted to single unit of measurement, so that in target function they could be summarized as follows [5]:

$$NPV = \sum_{t=1}^T \frac{-K_t - C_t + I_t}{(1+d)^t}, \quad (1)$$

where NPV – net present value, K_t – capital investments in year t , C_t – other costs in year t , I_t – income (benefit) in year t , d – coefficient of discounting, T – object lifetime

NPV is calculated for each development plan separately. The plan with highest NPV is the most cost-efficient.

K_t in one case could mean investments in IET and as alternative – investment in new local generation units in other case.

C_t could include annual costs for maintenance of IET, power plant or other equipment, costs for energy import or production, energy losses costs, adjusted costs for non-delivered energy, CO₂ emission costs etc. C_t is separate summand just for convenience.

I_t summarize all benefits from construction of a new tie or new power plant (might be also another tie or even plan with no development actions). It could include direct incomes, like income for generated and sold energy in local market, income for energy export, income from energy transit etc. Benefits could be also indirect, like possibility of building new power plants at favourable locations, utilization of most favourable energy resources, reduction of the necessary reserve capacity in the system etc., but for technical reasons it is more convenient to calculate the costs of opposite effects in another development scenario.

For example, we know that most likely construction of IET between System-1 and System-2 will reduce necessary reserve capacity in both systems. The scenario of isolated system will include normal reserve capacities and the scenario with IET will include reduced values, what gives certain benefit to systems. The amount of reduction depends on load curves of systems, where general idea is to cover one system load minimums with another system load's maximums. The higher is this effect, the more benefit systems can get. Fig. 1 displays an example, how effective such overlay can be.

In this example one system has load maximum value of 40 MW in winter and another system has load maximum of 140 MW in summer (green circles highlight maximums). In this case summary load maximum for both systems is:

$$P_{SUMMARY} = P_{MAX}^1 + P_{MAX}^2 = 140 + 40 = 180GW \quad (2)$$

But as we can see, the maximum of united system's curve is only 166 GW. If necessary reserve capacity is 10% from maximal load, totally it will be 18 GW in case of isolated operation and 16.6 GW in case of united operation (1.4 GW difference). Now the monetary effect can be calculated – it depends on costs for construction of additional capacities (it can vary from 500–3000 EUR / kW).

Of course such a huge effect could be achieved only interconnecting systems with different seasons of load maximum. In smaller systems located on similar latitude this effect would not be so significant.

The market structure in monopole conditions is relatively simple – one company is responsible for power generation, transmission, distribution and sales. In this case all costs of IET project have to be covered by this company and respectively only this company (sometimes also consumers) will benefit from IET.

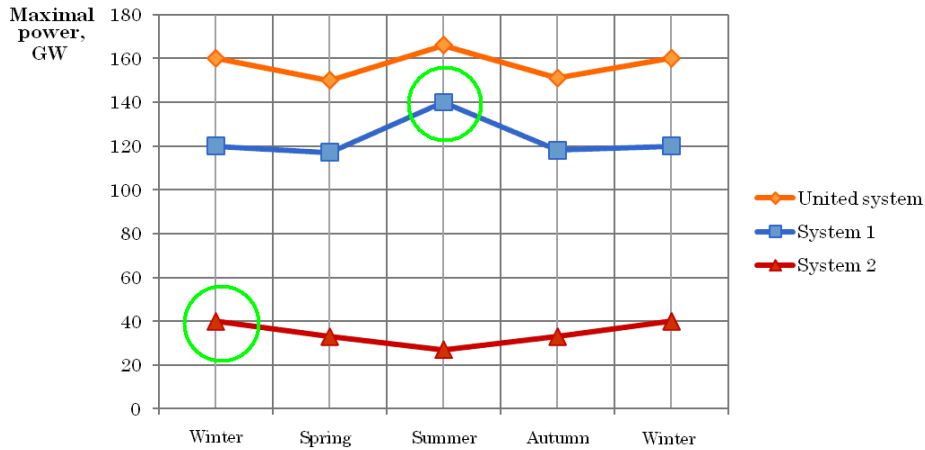


Fig. 1. Load curve overlay of two systems

2.2. Procedure of IET evaluation in competitive market conditions

Generally, in competitive market conditions there is forbidden to merge generation, transmission and energy sale functions in frame of one company. In this situation choosing of IET financing sources is not anymore obvious.

Multiple companies involved in local markets might benefit from construction of a new tie. Fig. 2 shows IET connecting two systems with wholesale energy markets and gives an idea of potential participants of IET project.

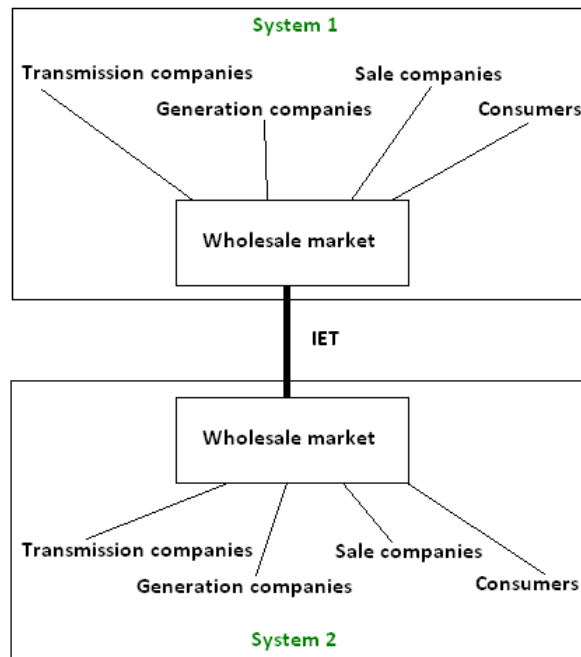


Fig. 2. IET in competitive market conditions

Transmission companies might receive additional transit profit, generation companies will have alternative for development of local capacities, sale companies will be able to buy energy for lower price and sell it for higher prices.

Justification of IET project becomes an iterative task and NPV is calculated for each project participant separately. IET is justified if the terms of a project satisfy all the participants. If this condition is not fulfilled at least for one participant, the terms are adjusted and process is restarted. Fig. 3 shows general algorithm of IET project justification in competitive market conditions [2].

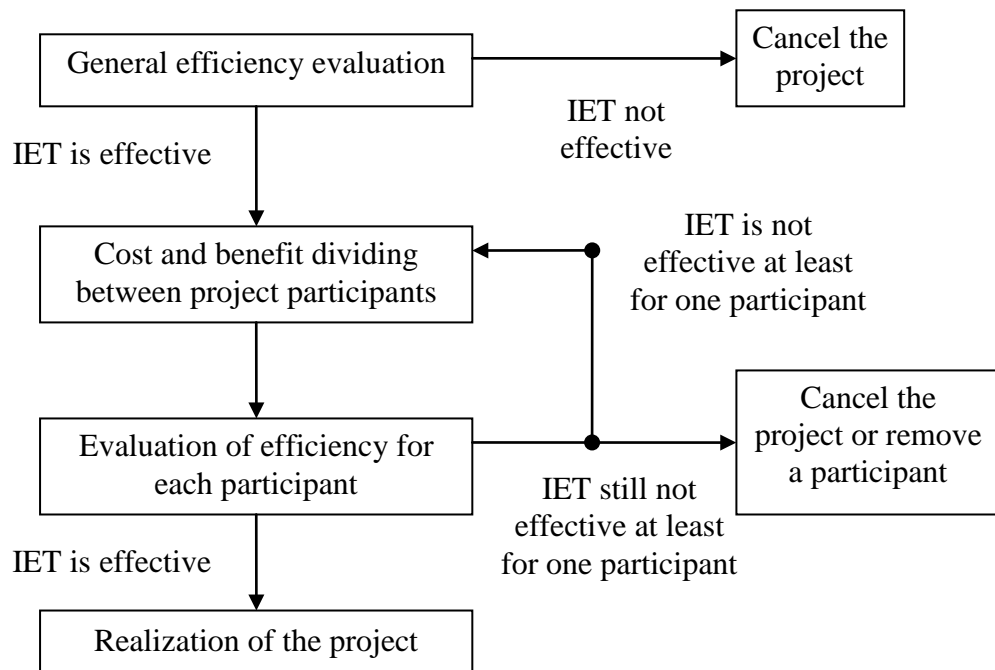


Fig. 3. Algorithm of IET project justification in competitive market conditions

General efficiency evaluation in this case will be similar as it was described in Chapter 2.1, when IET construction scenario was compared with isolated operation scenario, taking into consideration all above mentioned criteria. On this stage volumes of future energy trade should be defined by calculating power flows through IET in different operational states. Power flows respectively will depend on generation curves, load curves and market prices on both sides. Though the task is similar to the general justification task in monopole market conditions, calculations would give different results due to different power flow distribution principles.

Cost and benefit dividing between project participants is urgent task that directly influence NPV of each participant. Variable values in this case are: transit price (\$/MWh), energy import and export prices for each partner etc.

Though algorithm is allowing infinite participants, the simplest case is having two participants – one from each side. Most likely it would be transmission companies, which would own IET and benefit from payments for transit later on. The main criteria for IET justification in this case would be:

- Price difference in systems;
- Power flow through IET (it have to be big enough to cover investments and annual costs);
- Transit price (it influences import/export volumes and profit of transmission companies).

If energy prices are possible to forecast and a normal profit of sale companies is known, it is easy to calculate power flows through tie at different transit prices, as they will also influence price difference. The task of transmission company is to define an optimal transit price, that will give maximal profit and cover investment amortization and annual costs for IET. Such approach could lead to removal of one or several participants or users.

3. COMPUTER MODEL FOR IET EVALUATION

The method described above is hardly realized without using special computer models due to large number of variables, like: scenarios, development steps, operation states, prices etc. For these purposes it is offered to use *PSPlanner* (Power System Planner) software, which is newest development of Laboratory of Power System Mathematical Modelling, Latvian Institute of Physical

Energetics. The software is able to make full economic justification of generation and transmission projects.

3.1. Object description

LitPol Link was chosen as an object for showing the process of modelling for transmission justification purposes.

The LitPol Link project include interconnection between Poland and Lithuania consisting of 400kV overhead double-circuit transmission line Alytus-Elk (48+105 km), the modern substation in Alytus, including back-to-back AC-DC 2x500 MW converter and upgrade of the existing network infrastructure on both sides (see Figure 4). The total budget of the project is about 1.15 B€ The new tie is planned to be open in 2015 (500 MW) and 2020 (1000 MW total) [3].

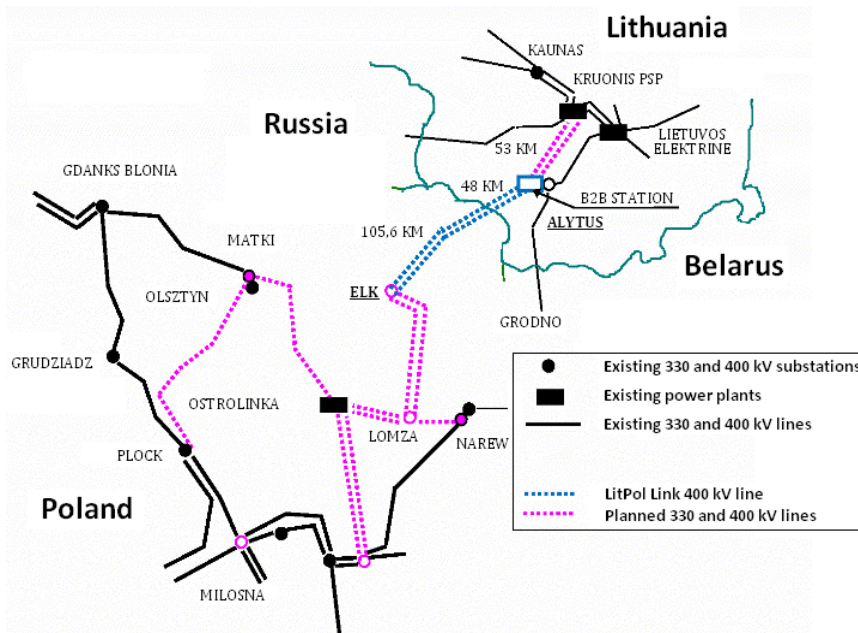


Fig. 4. LitPol Link and upgraded infrastructure of Poland and Lithuania [4]

The new power interconnection will allow Lithuania and other Baltic States to join the Western European Electricity System, to have diversity of suppliers, higher reliability of power supply and to remove dependency from primary energy sources hold by eastern neighbours [3].

3.2. The model

Fig. 5 shows model for LitPol Link justification in PSPlanner software. The model consists of nodes – substations with defined load (white circles) belonging either to Lithuania or Poland, power plants (circles with „G“ inside) and transmission lines. There are existing substations with real names and several imaginary (equivalent) substation with „Eq.X“ name, which model a part of the network that is not directly included to this scheme due to huge volume. Equivalent nodes have both equivalent generation and load.

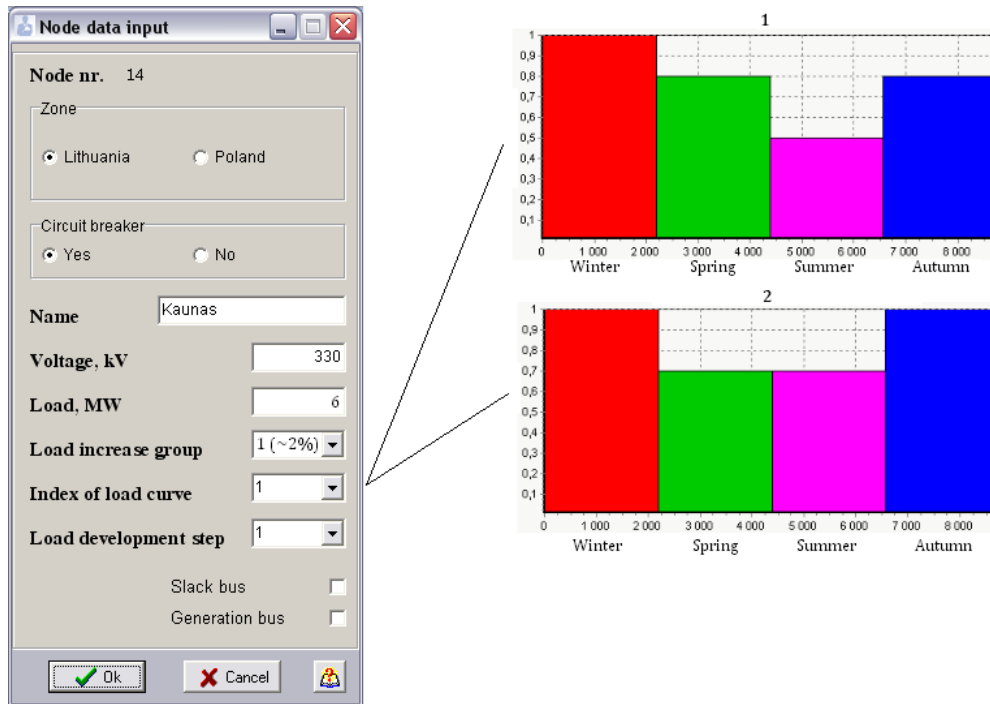


Fig. 6. Example of load curve selection for node „Kaunas“

The programme is able to calculate market-based power flows for particular operational state (for example Spring, 2016) or for whole user-defined period together with other technical-economic parameters, like NPV, giving a comparison of formed scenarios, so that user could make a correct justified power system development decision.

4. CONCLUSIONS

There are several significant differences in transmission planning in different market conditions. Even a small change in project terms could lead to re-distribution of costs and benefits between project participants. A project is beneficial if it is beneficial to all participants. One of the ways of setting costs and benefits for participants is circular redistribution, as it is shown on Fig. 3.

In order to make justification of a development project it is necessary to use computer models, allowing to consider variable power system parameters and market structure of participants, observing consequences in long perspective. Particularly, the model should include possibility to make market-based power flow calculation, precise economic evaluation and flexible input parameter data base, e.g. load curve. Several nodes of a model may be equivalent, covering a part of a network or including lower voltage network.

The presented model after detalisation will be capable to deal with LitPol Link justification with certain approximation, though this topic is not included in this work.



REFERENCES

1. KRISHANS, Z.; MUTULE, A.; MERKURIEV, Y.; OLENIKOVA, I. *Dynamic Management of Sustainable Development: Methods for Large Technical Systems*. London: Springer, 2011. 5–6, p. 52–60.
2. Л. С. БЕЛЯЕВ, С. В. ПОДКОВАЛЬНИКОВ, В. А. САВЕЛЬЕВ, Л. Ю. ЧУДИНОВА. Эффективность межгосударственных электрических связей. – Novosibirsk: “Наука”. – 2008. – 237 p.
3. LitPol Link homepage <http://www.litpol-link.com/en/news/litgrid-and-abb-signed-an-agreement-for-design-and-construction-of-litpol-link-hvdc-converter-station.html>
4. LitGrid homepage <http://www.litgrid.eu/index.php?1937543676>
5. Z. KRISHANS, A. MUTULE, Y. MERKURIEV, I. OLENIKOVA. *Dynamic Management of Sustainable Development: Methods for Large Technical Systems*. London: Springer, 2011. p. 5–6, p. 52–60.
6. Euroelectric. *Statistics and prospects for the European electricity sector*, 37th edition.
7. International Energy Agency. *Projected costs of generating electricity*. 2010. 200 p.



DEVELOPMENT OF THE MODEL FOR SMALL SCALE ASYNCHRONOUS GENERATOR CONNECTION IMPACT ASSESSMENT ON DISTRIBUTION NETWORK

A. Lvoys, A. Obushevs, A. Mutule
Institute of Physical Energetic
Aizkraukles str. 21, LV-1006 Riga – Latvia

ABSTRACT

It is expected that the production of electrical energy from renewable energy sources and liberalized market further development can cause changes in the distribution network operating modes, as with time more small scale power plants will operate in liberalized market rather than ones with subsidies. Such situation can cause more frequent starts and stops of power plants comparing to current situation. To assess the impact of asynchronous generator connection to the existing network, taking into account technical limitations, there was created small scale HPP electric model, which simulates asynchronous machine transient processes.

Mathematical model of small scale HPP was developed for simulation of HPP electricity production. The developed model consists of generator and network parts and is capable of modelling various generation and load interaction scenarios. Different generation and load scenarios have been modelled to evaluate generator connection impact on the existing network, taking into account technical constraints.

Load – generating interaction scenarios modelling were implemented in Matlab environment. Power flow model was tested in Power World environment in order to verify the accuracy of its operation. Network and HPP simulations were carried out using the widely accepted IEEE 37 node test feeder [1].

Paper focuses on description of model and electrical machine and results of case study performed to test proposed mathematical model. The elaborated model can be used for representing wide range of HPPs in assessment analysis of distribution network, as well as adapted for modelling of other types of power plants that use asynchronous generators.

Keywords: Hydroelectric power generation, mathematical model, power distribution, transient process

1. INTRODUCTION

The paper presents the achievements of Institute of Physical Energetics (IPE) in SmartGrids ERA-NET Project named “Efficient identification of opportunities for Distributed Generation based on Smart Grid Technology (SmartGen)” (Project) during the second stage of Project realization. The Project involves partners from four European countries – Balslev (Denmark), Bacher Energie (Switzerland), Sweco (Norway) and IPE (Latvia).

During the first year of Project IPE have developed approach for small scale hydro power plant (HPP) generation optimization under market (uncertainty) conditions. The approach was based on calculations of stable operation modes of HPP and the main goal of the approach was to find optimal operation schedule of HPP that would ensure maximal economical profit of HPP owner. Results of the first stage of Project realization have been presented at various international conferences, as well as included in their proceedings [2–4].

The second stage of Project implementation in Latvia continued with research in the field of HPP operation, but with bigger focus on technical side – study of transient processes (changes of currents and voltages) of asynchronous machine (generator) and their impact on the distribution network. Latvian biggest distribution system operators JSC “Sadales tīkls” had major interest to the results of the study, as there are more than 140 small scale HPPs in operation in Latvia and before

the study Latvian DSO was not able to make full scale analysis of transient processes appearing, when starting of generation at small scale HPPs.

The paper presents developed model for assessment of transient processes, describes electrical machine used, as well as presents results of the model testing.

2. MATHEMATICAL MODEL OF ASYNCHRONOUS GENERATOR INDUCED TRANSIENT PROCESS IN A DISTRIBUTION GRID

It is expected, that the production of electrical energy from renewables and liberalization of energy market for small scale HPPs in Latvia can cause changes in the distribution network operation modes. Changes in Latvian distribution network in future could be related with the fact that till the moment there have been given a lot of permissions for small scale HPPs and also with the fact that in future small scale energy sources operate in liberalized market that will result in more frequent starts and stops of generators that will try to operate in hours with maximal electricity price. Up to now it is not known how will bigger amount of small scale HPP and their starts and stops will affect distribution network. The model developed and presented in this paper, as well as in previous papers [2-4] is tended to help DSOs in evaluation of the HPPs affect.

This section gives theoretical description for a small HPP impact assessment for load – generator interaction scenario, which will then be used in the model tests on the basis of real example. To assess the impact of a new generator connection to existing network, taking into account technical limitations as thermal limitations (according to maximal allowed current) of power lines and values of voltages in nodes of network, electric model of small scale HPP was created (see flow chart at Fig. 1), which simulates transient process of asynchronous machine.

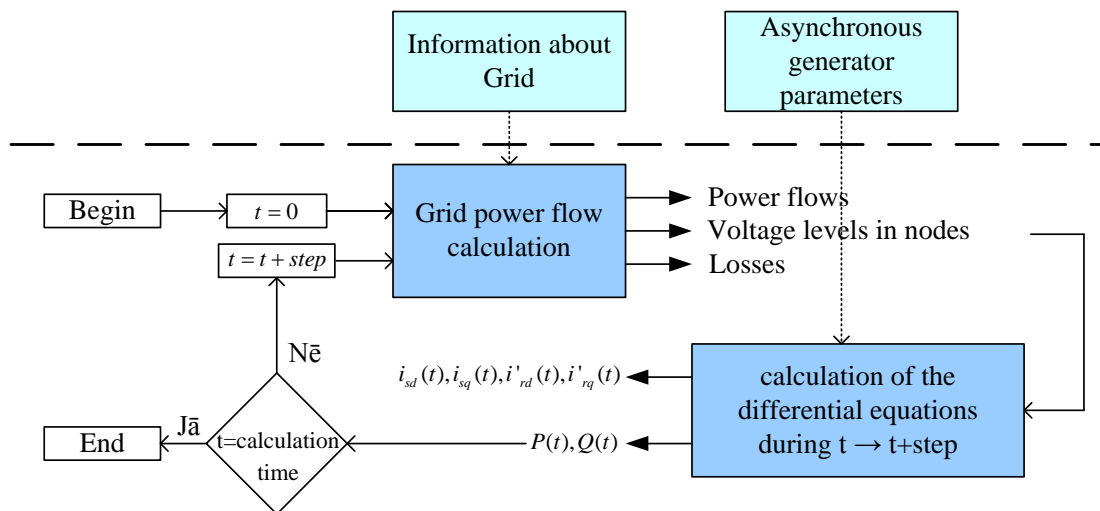


Fig. 1. Block diagram of the developed model

Flow chart consists of two parts – information input part (above dashed line) and calculation part (below dashed line), that represents developed model. The latter is based on two mathematical submodels – power flow model and asynchronous generation model.

Information input part

In this part, information about grid and HPP is inputted in the model.

Information about grid consist of following data:

- Power line and transformer impedances;
- Types of loads (load curves) and load values at load points of grid;
- Information about grid voltage and voltage regulation possibilities;
- Base (slack) node;

- Allowable voltage unbalance (for network simulations).

Information about HPP asynchronous machine comprises the following data:

- The maximum installed capacity of generator;
- Nominal voltage level;
- Rated frequency;
- Stator resistance and leakage inductance;
- Rotor resistance and leakage inductance;
- Magnetizing inductance;
- Combined rotor and load inertia constant;
- Number of pole pairs;
- Shaft mechanical torque;
- Initial value of slip.

After information on the grid and generator is entered, calculation can be performed. Calculation part of the model begins with step “zero” – when HPP is not connected to the grid. When the calculations for step “zero” have been performed, we received initial state of the grid with known values of power flows, voltage levels in nodes, as well as losses in power lines.

At the next time step “ $t=t+\text{step}$ ”, generator is connected to the network. Using data of the grid from initial state ($t=0$), differential equations, that describe electrical machine, should be solved. As the result we receive active and reactive power that is produced and consumed by generator, as well as currents of generator. These results then are put in grid power flow calculations and calculation process is repeated. Calculation interval “step” is chosen small enough to see dynamics of transient processes.

Calculations have been performed for such time period that is big enough for transient process.

3. MATHEMATICAL SUBMODEL OF ASYNCHRONOUS GENERATOR

Electrical machine used in the transient process model (see section 2) has been assumed as idealized electrical machine and calculations are made using per unit system in dq coordinate system. Used idealized machine, usage of per unit system, as well as equations that have been created and used for evaluation of transient processes are being described further.

3.1. Idealized electrical machine

Identification all mathematical relationships is practically impossible, so the solution is in approximation of the number of factors. It means that we set aside the so-called second level factors, whose impact on the transient process is not important.

The differences between idealized and real machine [5–8]:

- The magnetic circuit is not saturated;
- Hysteresis phenomena and losses of the steel are not taken into account;
- Distribution of magnetization forces is assumed to be sinusoidal, higher harmonics are not taken into account;
- Leakage inductive impedance is assumed to be independent from rotor position.

3.2. Asynchronous machine equations in relative values

In case of usage per unit system (p.u.), all values are expressed as part of the base rate. The base values are different for different machines. When studying transient process of electrical machine, machine nominal values are being used as base values. 3-phase winding is placed in both

stator and rotor. Rotor winding parameters are being reduced to the stator side. Stator and rotor windings are connected in star connection.

Advantages:

- Electrical machines equations in p.u. usually are in simplest form;
- The calculations are made with numbers that are close to "1" or some certain value;
- Control of calculations becomes simpler, as deviation of values of parameters due to mistakes can be easily noticed;
- Comparison of different types of machines and machines with different power becomes more simple, enabling the establishment of common criteria;
- In many cases, eliminates the need to recalculate values with one units to values with another units;
- Maximum and effective values expressed with the same number.

Disadvantages:

- Equations in p.u. are often simpler, but it is more difficult to understand the physical side;
- Depending on choice of one or another p.u. system, the relationship between parameters of machine is changing. It should be taken into account in equation-creating and equation-solving process;
- Currently there is no one universally recognized p.u. system. This makes it difficult to compare results of research performed by different authors;
- Confusion of relative value and physical units is possible.

Following base units are used in calculations in relative values:

$$f_b = f_n \quad - \quad \text{base frequency [Hz];}$$

$$U_b = \sqrt{2} \cdot U_{fn} \quad - \quad \text{nominal stator voltage amplitude, phase voltage value [V];}$$

$$I_b = \sqrt{2} \cdot I_{fn} \quad - \quad \text{nominal current amplitude [A];}$$

$$Z_b = \frac{U_b}{I_b} \quad - \quad \text{base resistance } [\Omega];$$

$$P_b = \frac{3}{2} \cdot U_b \cdot I_b \quad - \quad \text{base power [W];}$$

$$\omega_b = \omega_{\text{sinhr.}} \quad - \quad \text{angular base frequency [rad/s];}$$

$$L_b = \frac{Z_b}{\omega_b} \quad - \quad \text{base value of inductance [H];}$$

$$M_b = \frac{P_b \cdot p}{\omega_b} \quad - \quad \text{base value of torque [Nm];}$$

$$T_j = \frac{J \cdot \omega_b^3}{P_b \cdot p} \quad - \quad \text{Inertia constant of machine [p.u.]}$$

3.3. Asynchronous machine equations in dq coordinate system in relative values

Induction motor unit can be operated in generator or motor mode. Operation mode is determined by the mechanical shaft torque:

If M_{sl} has positive value, then machine works in motor mode;

If M_{sl} has negative value, then machine works in generator mode.

Electrical part of machine is described by a fourth-order differential equation, but mechanical part by second order differential equations. All electrical parameters reduced to the stator side.

Stator and rotor values are presented as two-axis system – d q coordinate system (see Fig. 2.). Following subindexes are used in Fig. 2 [8]:

- d – d-axis value;
- q – q-axis value;
- r – value related to rotor;
- s – value related to stator;
- l – leakage inductance;
- m – magnetizing inductance.

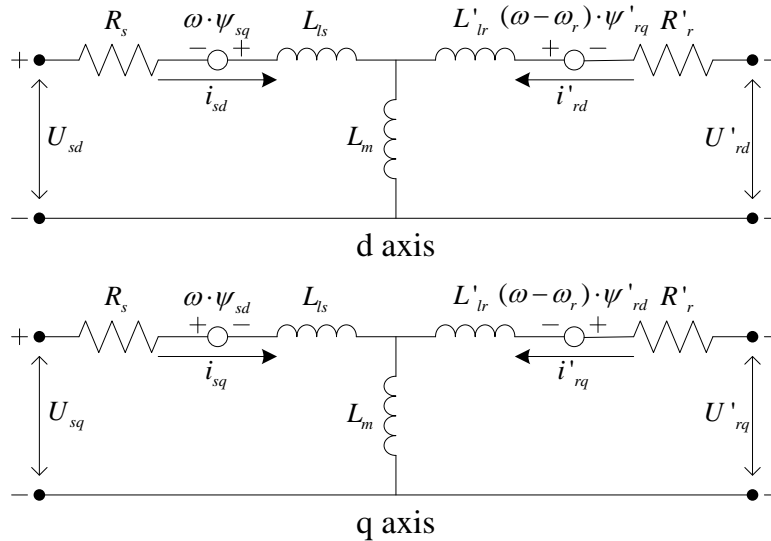


Fig. 2. Induction machine circuit schemes in d q coordinates

For description of asynchronous machine, the system of following differential equations has been used:

$$\left\{ \begin{array}{l} U_{sd} = R_s \cdot i_{sd} - \omega \cdot \psi_{sq} + \frac{d\psi_{sd}}{d\tau} \\ U_{sq} = R_s \cdot i_{sq} + \omega \cdot \psi_{sd} + \frac{d\psi_{sq}}{d\tau} \\ U'_{rd} = R'_r \cdot i'_{rd} - (\omega - \omega_r) \cdot \psi'_{rq} + \frac{d\psi'_{rd}}{d\tau} \\ U'_{rq} = R'_r \cdot i'_{rq} + (\omega - \omega_r) \cdot \psi'_{rd} + \frac{d\psi'_{rq}}{d\tau} \\ T_j \cdot \frac{d\omega_m}{d\tau} = M_{em} - M_{sl} \\ \frac{d\Theta_m}{d\tau} = \omega_m \end{array} \right. \quad (1) \quad \text{where:} \quad \left\{ \begin{array}{l} \psi_{sd} = L_s \cdot i_{sd} + L_m \cdot i'_{rd} \\ \psi_{sq} = L_s \cdot i_{sq} + L_m \cdot i'_{rq} \\ \psi_{rd} = L'_r \cdot i'_{rd} + L_m \cdot i_{sd} \\ \psi_{rq} = L'_r \cdot i'_{rq} + L_m \cdot i_{sq} \\ L_s = L_{ls} + L_m \\ L'_r = L'_{lr} + L_m \\ M_{em} = \psi_{sd} \cdot i_{sq} - \psi_{sq} \cdot i_{sd} \end{array} \right.$$

Where asynchronous machine parameters are defined as follows (all quantities are referred to the stator):

- R_s, L_{ls} – stator resistance and leakage inductance;
- R'_r, L'_{lr} – rotor resistance and leakage inductance;
- L_m – magnetizing inductance;



- L_s, L_r – total stator and rotor inductances;
- U_{sd}, i_{sd} – d axis stator voltage and current;
- U'_{rd}, i'_{rd} – d axis rotor voltage and current;
- U_{sq}, i_{sq} – q axis stator voltage and current;
- U'_{rq}, i'_{rq} – q axis rotor voltage and current;
- Ψ_{sd}, Ψ_{sq} – stator d and q axis fluxes;
- Ψ'_{rd}, Ψ'_{rq} – rotor d and q axis fluxes;
- ω_m – angular velocity of the rotor;
- Θ_m – rotor angular position;
- p – number of pole pairs;
- ω_r – electrical angular velocity ($\omega_r = \omega_m \cdot p$);
- Θ_r – electrical rotor angular position ($\Theta_r = \Theta_m \cdot p$);
- M_{em} – electromagnetic torque;
- M_{sl} – shaft mechanical torque;
- T_j – combined rotor and load inertia constant;
- J – combined rotor and load inertia coefficient.

The active and reactive power changes during the transient process determined according to the following expressions:

$$\left\{ \begin{array}{l} P(t) = U_{sd} \cdot i_{sd} + U_{sq} \cdot i_{sq} \\ Q(t) = U_{sq} \cdot i_{sd} - U_{sd} \cdot i_{sq} \\ S(t) = P(t) + jQ(t) \end{array} \right\}. \quad (2)$$

If a squirrel-cage rotor is used ($U'_{rd} = 0, U'_{rq} = 0$) and $\omega = \omega_{\text{sinhr.}} = 1$ ($U_{sd} = U_{\text{GRID}}, U_{sq} = 0$), machine's differential equations look as shown in (3) [9].

$$\left\{ \begin{array}{l} \frac{d\Psi_{sd}}{d\tau} = U_{sd} - R_s \cdot i_{sd} + \omega \cdot \Psi_{sq} \\ \frac{d\Psi_{sq}}{d\tau} = U_{sq} - R_s \cdot i_{sq} - \omega \cdot \Psi_{sd} \\ \frac{d\Psi'_{rd}}{d\tau} = -R'_r \cdot i'_{rd} + (\omega - \omega_r) \cdot \Psi'_{rq} \\ \frac{d\Psi'_{rq}}{d\tau} = -R'_r \cdot i'_{rq} - (\omega - \omega_r) \cdot \Psi'_{rd} \\ T_j \cdot \frac{d\omega_m}{d\tau} = M_{em} - M_{sl} \\ \frac{d\Theta_m}{d\tau} = \omega_m \end{array} \right\} \quad (3)$$

To solve Eq. (3), the fourth-order Runge–Kutta method was used.

4. TESTING OF TRANSIENT PROCESS MODEL

For model testing purposes, an asynchronous motor/generator with squirrel-caged rotor has been chosen, with the parameters as follows:

$P_n = 160000 \text{ VA}$	$R'_s = 0.007728 \Omega$
$U_n(V_l) = 400 \text{ V}$	$L'_{lr} = 0.000152 \Omega$
$F_n = 50 \text{ Hz}$	$L_m = 0.00769 \Omega$
$R_s = 0.01379 \Omega$	$J = 2.9 \text{ kg}\cdot\text{m}^2$
$L_{ls} = 0.000152 \Omega$	$p = 2$

Modelling of load-generation interaction has been done in Matlab environment. Power flow model have been additionally tested in PowerWold environment to prove it's precision. Simulation of grid and HPP operation has been performed using widely known IEEE 37 node test feeder scheme. Each load point in the test feeder represents some type of load with its own load diagram.

Calculations have been performed for 2 HPP connection cases – without and with synchronization. In addition to these calculations, the model has been tested using not only IEEE 37 node test feeder, but also scheme that represents grid with unlimited power source. Taking into account constraints of paper volume, results of model tests with grid with unlimited power source are not included in the paper.

Figs. 3, 4 and 5 show results of calculations as active and reactive power flows, currents and nodal voltages, respectively, in case of connection *without synchronization* ($M_{sl} < 0$ – generator mode ($M_{sl} = -950 \text{ N}\cdot\text{m}$), slip=1).

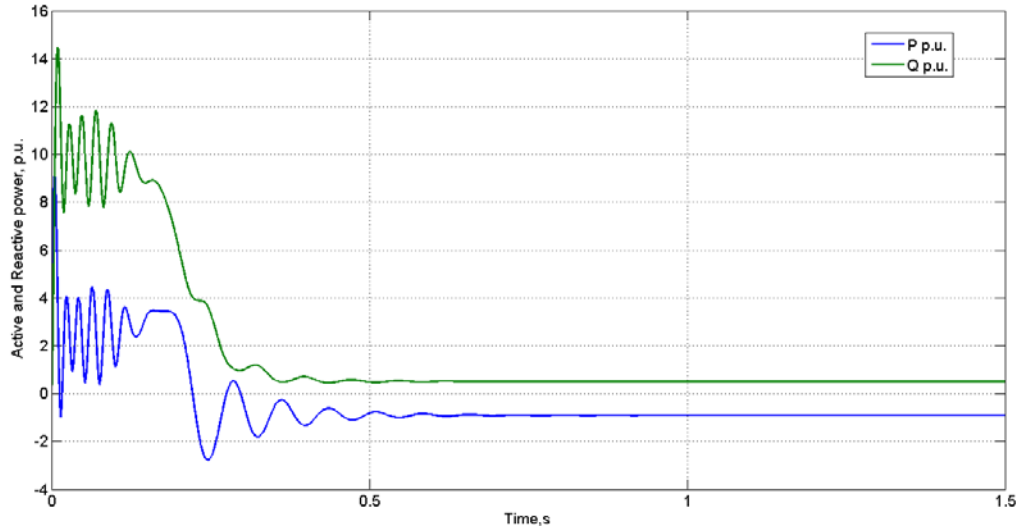


Fig. 3. Changes of active and reactive power of asynchronous generator in case of connection without synchronization (slip=1)

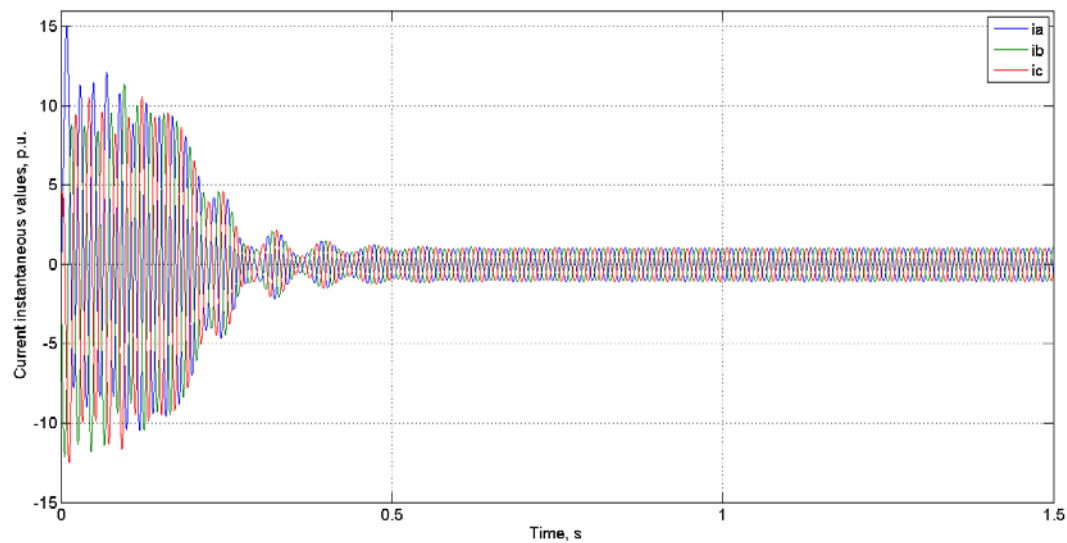


Fig. 4. Changes of momentary values of currents of asynchronous generator in case of connection without synchronization (slip=1)

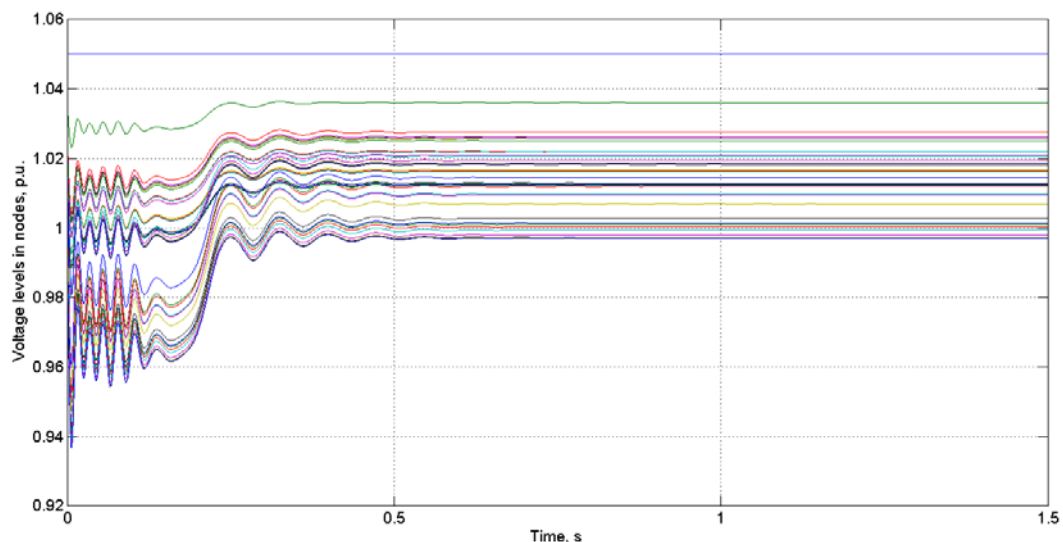


Fig. 5. Changes of voltage in network nodes in case of connection without synchronization (slip=1)

Results of calculations show that connection of generation to the grid without synchronization results in appearing of oscillations of electrical parameters in the grid for time period of 0.3 seconds. These oscillations can result in disturbances of protection operation as well as of sensible electronics, e.g. computers.

Figs. 6, 7 and 8 show results of calculations in case of connection *with synchronization* ($M_{sl} < 0$ - generator mode ($M_{sl} = -950 N \cdot m$), $slip = -0.025$). This connection technique is usually used in real life, especially for generators with big power. Before connection to grid, water gate doors of HPP are opened and water pushes blades that in their turn makes rotor to rotate. At the moment when rotation of asynchronous machine exceeds network's frequency value by 2.5–5%, synchronization of machine begins and it is connected to grid.

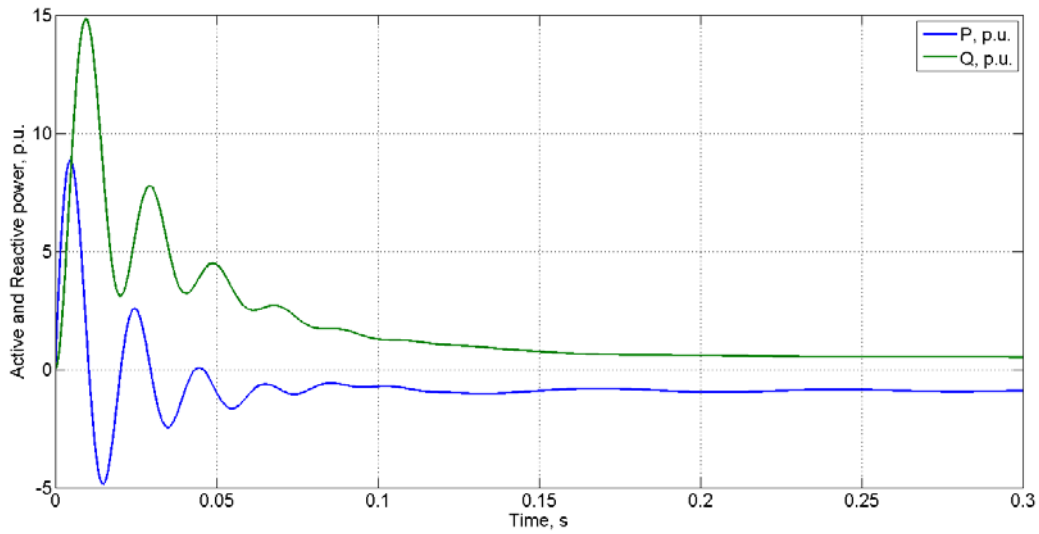


Fig. 6. Changes of active and reactive power of asynchronous generator in case of connection with synchronization ($slip = -0.025$)

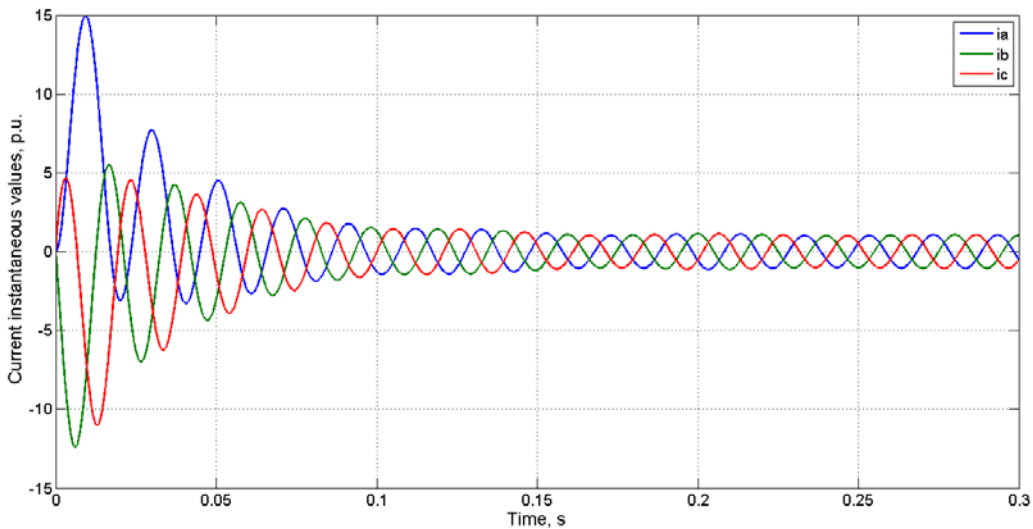


Fig. 7. Changes of momentary values of currents of asynchronous generator in case of connection with synchronization ($s = -0.025$)

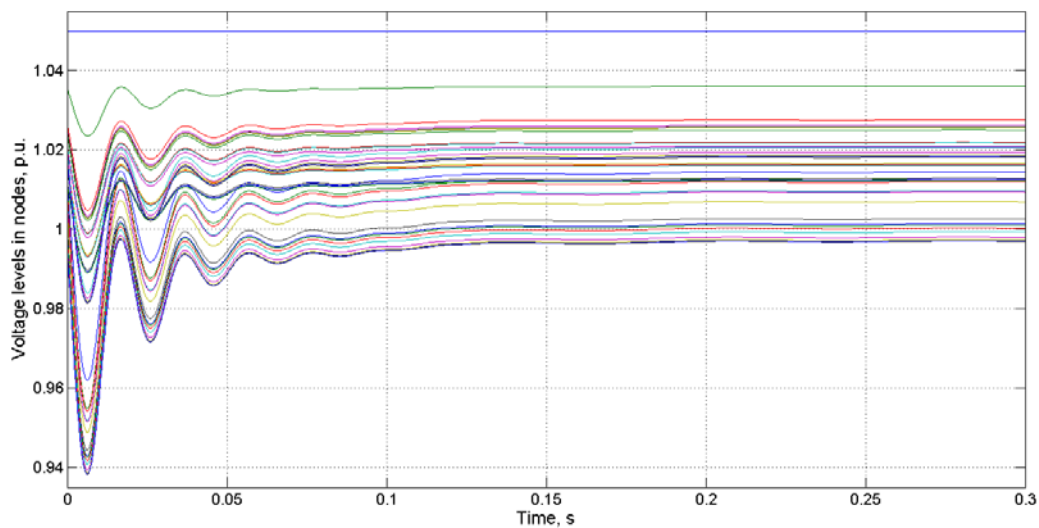


Fig. 8. Changes of voltage in network nodes in case of connection with synchronization ($slip = -0.025$)

In case of connection with synchronization (slip value “-0.025”), oscillations of electrical parameters in the grid appear for time period 0.1 second. Comparing results of two simulations, it can be seen that synchronization of generator helps reduce time of oscillations, but not their amplitude.

Results obtained from the calculations are similar to the results obtained through measurements in real grid by personnel of Latvian DSO – JSC „Sadales tīkls”. The fact confirms that developed model works well.

To make these calculations in PowerWorld, active and reactive power consumption/production of the HPP’s generator have been put into PowerWorld after they have been obtained from the model (1)-(3). Figs. 9, 10 and 11 have been plotted in PowerWorld and show changes of currents, voltages as well as losses in the grid in three states: 1) before the generator is connected to the grid ($t = 0$ seconds); 2) the worst moment of the generator connection to the grid ($t = 0.0064$ seconds); 3) state of the grid after generator synchronization. It should be underlined that all the parameters showed in Fig. 9, 10 and 11 can be obtained also by using the developed model, but PowerWorld gives better visualisation possibilities.

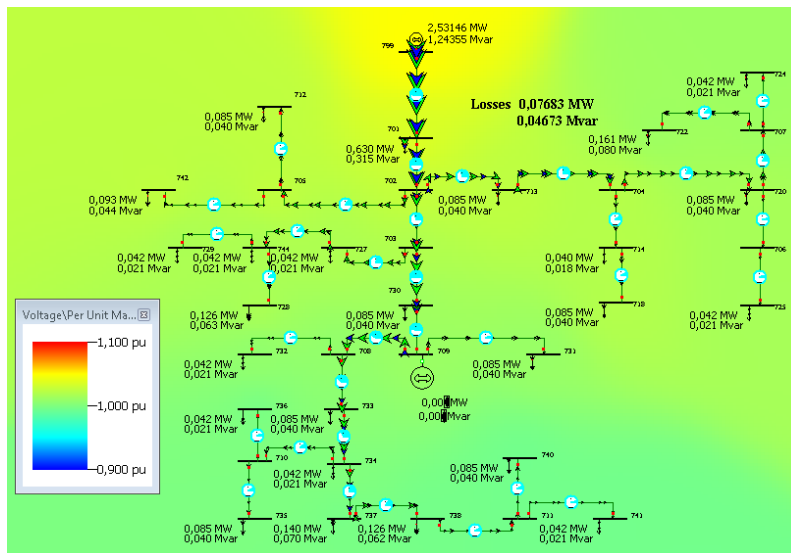


Fig. 9. The studied grid before generator starts

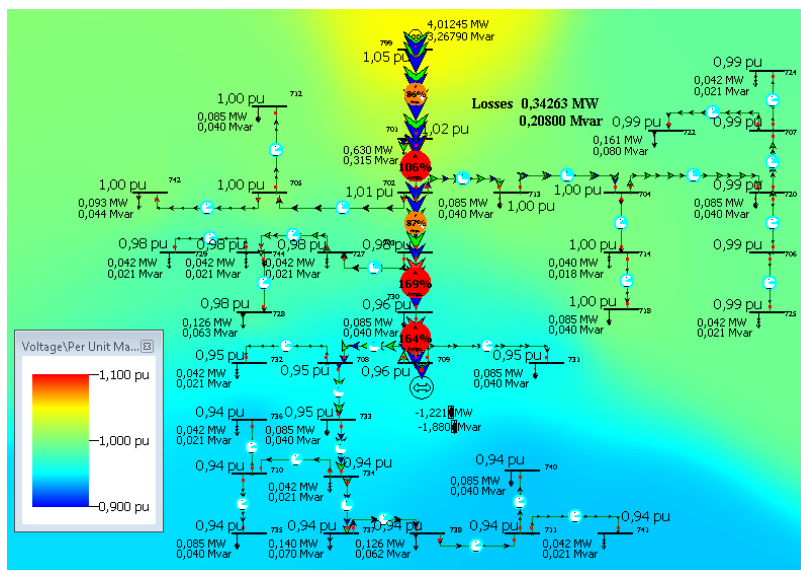


Fig. 10. The studied grid at generator start moment (0.0064s)

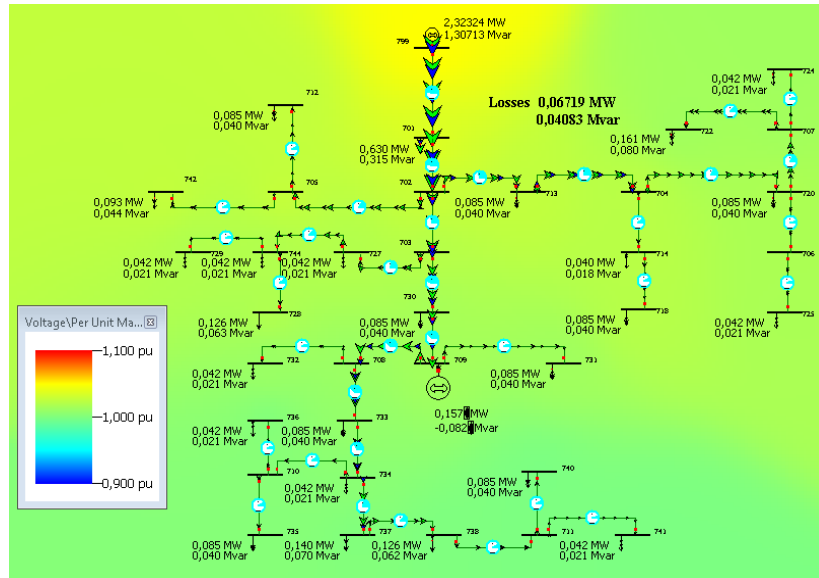


Fig. 11. The studied grid after generator is fully synchronised

Results given at this section represent the worst operation mode – the combination of load in the network and generation at which current and voltage values are the worst. The results are only theoretical, as there have been used theoretical IEEE 37-node test feeder scheme. In case if aforementioned results would be obtained for real distribution network and generator, the conclusions would be that the network can normally operate with tested HPP generator if it is synchronized with the network before connection. In case if generator is connected to the network without synchronization, there could be some problems due to tripping of relay protection if there would be used relatively small time of tripping. Calculations for real network haven't been performed because of confidentiality of real network data.

Calculations with the test feeder gives idea of possible model usage in real life. For example there could be real network and there could be several places for generator connection. Using the model there could be performed calculations and obtained results on values of voltage drops and currents, as well as duration of transient process for all the possible HPP connection points. Modelling can also take into account changing network loads – calculations can be performed for low, middle and high load periods. This, in its turn, will allow personal of DSO to make decision on possibility of generator connection to some node in the network, as well as decide on maximal allowed power of generator.

5. CONCLUSIONS

Model in Matlab environment has been developed for full scale calculations of transient processes. The model allows one to see values of currents and voltages occurring during transient processes at very short time frame after generator start – 0-0.3 seconds.

The model presented at the paper has significant value for distribution system operators, as it can be used for coordination of HPP development and relay protection devices installed in the grid. The significance of the model for DSOs is also described by the possibility to use results of the model for evaluation of HPP effect on power quality parameters in the grid, as DSO is responsible for major power quality parameters. The model is important for developers of projects of small scale HPPs as well, as it allows evaluating effect of HPP connection on the grid before making investments in HPP construction. In case of construction of new HPP and having different connection options, the developed model allows to choose the best location for construction of power plant, as it can help to choose such place in the grid that needs no or needs less investments



to grid in comparison to other possible locations. In case of reconstruction of existing power plant (by improvement of generation capacities) or having plans to operate in power market, the developed model makes it possible to evaluate further impact of HPP to the grid and identify the need for network improvement. So, it allows both DSO and HPP owner to evaluate possibilities for improvement and plan their investments.

The model, developed by the authors of the paper, accomplish previously created model for optimization of HPP's generation schedule. Both developed models together offer a tool for extensive evaluation and planning of HPP projects from technical and economical side.

Taking into account that the developed models have been created in Matlab environment, they can be used by wide number of professionals and the models have almost unlimited opportunities for improvement and development of functionality. For example, the models can be accomplished with separate module for evaluation of HPP operation on relay protection of grid.

REFERENCES

1. IEEE PES Distribution System Analysis Subcommittee's Distribution Test Feeder Working Group. <http://ewh.ieee.org/soc/pes/dsacom/testfeeders/>
2. MUTULE, A., OBUSEV, A., LVOV, A. The Approach for HPP Generation Optimization under Liberalized Electricity Market. IEEE ICSET 2012. Proceedings of the 3rd IEEE International Conference on Sustainable Energy Technologies. [USB]. Kathmandu, Nepal: IA/PELS Joint Chapter, IEEE Singapore Section. 2012, September 24–27.
3. MUTULE, A., LVOV, A., OBUSEV, A., SEGERBERG, H., BACHER, R. SmartGen model solutions for Distributed Generation and Load Management. LMPS 2012. Proceedings of the 5TH International conference on LIBERALIZATION AND MODERNIZATION OF POWER SYSTEMS: SMART TECHNOLOGIES FOR JOINT OPERATION OF POWER GRID. [CD]. Irkutsk, Russia: Energy Systems Institute, Russia; Technical University of Dortmund, Germany; Otto von Guericke University of Magdeburg, Germany; IEEE PES Russian (Siberia) Chapter; IEEE PES German Chapter. 2012 August 6–10.
4. OBUSEV, A., LVOV A., MUTULE, A. Estimation of Small Scale HPP Affect on Distribution Network Reliability under Market Conditions. PQ2012. Conference Proceedings of "The 8th International Conference "2012 Electric Power Quality and Supply Reliability. PQ2012". [USB]. Tartu, Estonia: Tallinn University of Technology. 2012 June 11–13.
5. ВОЛЬДЕК, А.И. *Электрические машины*. Л.: Энергия, 1974. 840 с.
6. КОПЫЛОВ, И.П. *Электрические машины*. М.: Энергоатомиздат, 1986. 360 с.
7. КОПЫЛОВ, И.П. Математическое моделирование электрических машин. М.: Высшая школа, 2001. 327 с.
8. БУРБЕЛЮ, М.Й. Динамічна компенсація реактивної потужності в пускових режимах електроприводів. Монографія. Вінниця: УНІВЕРСУМ-Вінниця, 2010. 104 с.
9. МЕРКУРЬЕВ, Г.В.; ШАРГИН Ю.М. *Устойчивость энергосистем. Расчеты: Монография*. СПб.: НОУ "Центр подготовки кадров энергетики", 2006. 300 с.



AC AND DC OPTIMAL POWER FLOW MODELS FOR LONG-TERM DEVELOPMENT PLANNING

A. Obushevs, I. Oleinikova

Institute of Physical Energetics

Laboratory of Power System Mathematical Modelling

Aizkraukles 21, LV-1006 Riga – Latvia

ABSTRACT

Increasing integration in the Baltic electricity market and Europe-wide interconnection establishment makes it necessary to consider markets principals for power system development planning. The Optimal Power Flow (OPF) is one of the fundamental problems in power system analyses. Long-term development planning typically requires a large number of repetitive OPF solutions. In this comparison, the calculation speed of the OPF solutions beside their accuracy is observed. The full alternating current OPF is accurate, but takes long solution time. The direct current OPF is a simple approximation of OPF that is very fast but is not so accurate.

The paper first provides a general explanation of proposed method of zonal prices determination, which is based on Interior Point Method (IPM) for finding maxima of Social Welfare or minimization costs of production subject to power system constraints. Comparison of ACOPF and DCOPF models was implemented in Matlab environment.

The papers second part provides case studies using both a small 4 node system and a somewhat larger 98 node model of the BRELL Ring (electricity ring of Belarus, Russia, Estonia, Latvia and Lithuania) transmission grid. Results are provided comparing both the accuracy (generation levels, line flows, and voltage angles) and the computational requirements of the two models.

Keywords: electricity market, optimal power flow, power system, power system development

1. INTRODUCTION

Liberalised electricity market effects the power system development. It is determined by the condition that electricity generators are independent from transmission and distribution operators and their interests differ. This fact creates higher uncertainty conditions for the perspective forecasts than before and power system development planning and optimisation is hampered. In this connection in development tasks it is necessary to consider price formation mechanisms, for a more detailed definition of benefits and costs with the introduction of new or liquidation of old power system elements.

Pricing mechanisms for competitive electricity markets determine either a uniform price (UP), a set of nodal or locational marginal prices (LMP), or only a few zonal marginal prices (ZMP). Each of above mentioned mechanisms is characterized by level of complexity, ability for appropriate allocation of investments as well as rightfully allocates costs for final consumers. According to aforementioned methods of price determination, the optimal prices in a transmission network are the nodal prices resulting from an OPF performed by a centralized dispatcher. Also due to that reasons the evolution of market structures worldwide introduces a nodal pricing principle as the proclaimed benchmark of congestion management, effectiveness and conformity with economic theory and physical laws.

In this paper summarized long-term planning methodology is described, that takes into account liberalised electricity market. To compare AC and DC models annual calculations for two experimental networks have been produced.

2. LONG-TERM DEVELOPMENT PLANNING

A mathematical model of power system is the system, which makes it possible to calculate and assess criteria of the analysed system with a view to make justified decisions on system sustainable development. The development optimization is hampered by the fact that is pursued in conditions with information uncertainty. The information uncertainty should be taken into consideration in the process of decision-making, and appropriate methods have to be applied. In the process of system sustainable development management the following uncertainty groups shall be taken into consideration: physical uncertainties, financial uncertainties and regulators uncertainties. For sustainable development of large technical systems development process may be described with the following basic definition characteristics:

Development actions reflect activity – new system object construction, as well as existing objects extension, reconstruction and modernization. The actions are assigned by user according to the specific task, experience.

Development state – technical system development state in optimization task is specified by system graph, its elements parameters and other technical, economical, ecological etc. parameters. Development state is marked with $e(t)$, where t – sign or sign group which determines development state reciprocal dissimilarities. Development states forming scheme is presented in Fig. 1.



Fig. 1. Development states forming scheme

Development step – large technical system development step is time period when no any development action is realized - system graph and its parameters are not changed. In development step period it is assumed that annual consumption of the first year of development step, twenty four hours, seasonal and monthly consumption is preserved for the period of all further years. In such a way calculation real continued process is modelled by discrete development process. In the initial phase of estimation period development steps are shorter, the next development steps length is longer but the last development steps are the longest.

Development process – in estimation period which is divided into T steps, may be various development states $e(t)$. Sequence of states $e(t)$, if $t = 1, 2, \dots, t, \dots, T$, be named as large technical system development process or development plan, which will be marked with $g(k)$ and described as sequence of states $g(k) = e(0), e(1), e(2), \dots, e(t), \dots, e(T)$.

Objective function for power system development plan displays and integrates technical, economic, power supply reliability, ecological etc. parameters depending on specific technical system. Objective function is an system development plan g quality criterion, denoted as $F(T, g)$. Further on, the objective function will be calculated by a formula:

$$\max F(T, g) = \max_{g \in \{G\}} \sum_{t=1}^T F(t, e(t)) \quad (1)$$

where: t – development step serial number; T – number of development steps in estimation period; $F(t, e(t))$ – system quality criterion in development step t and development state $e(t)$; g – development process; $\{G\}$ – set of all possible development plans.

Each development process is characterized by number of realized development actions and its realization moment, as well as by each development action realization type. Fig. 2. represents small

example with 2 development actions, development step 1 year and 16 development states. The total number of development plans in this example will be 16.

In real tasks the number of comparable development plans attains astronomic quantity, therefore it is required to apply specialized dynamic optimization methods in power system sustainable development management process [1].

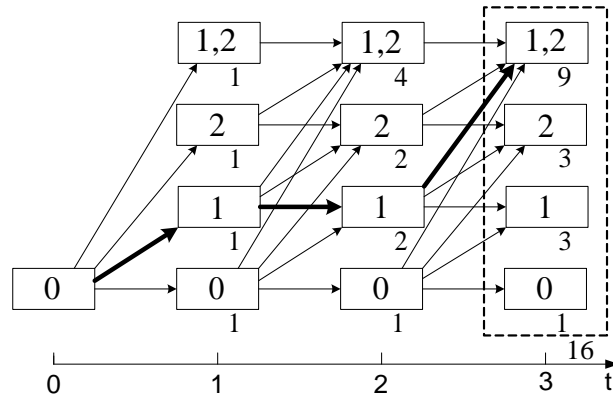


Fig. 2. Development states forming scheme example

To consider the impact of liberalized electricity market to technical and economic criteria each development state should be observed at hourly base. Application of hourly calculation based on OPF allows taking into account the major trends of production and consumption during the day, taking into account consumption time shifting when considering multiple time zones, demand response, distributed generation, etc.

3. OPF IMPLEMENTATION IN DEVELOPMENT TASKS

The objective function of an OPF problem may take many different forms according to the different applications. The general objective in OPF is to maximize social welfare which comprises producers' and consumers' surpluses or minimize costs of production. The costs and benefits may be defined as polynomials or as piecewise-linear functions [2–3]. The problem can be formulated schematically as:

$$\max_{x,s,d} B(d) - C(s) \quad (2)$$

subject to

$$h(x, s, d) = 0 \quad (3)$$

$$g(x, s, d) \leq 0. \quad (4)$$

Where $C(s)$ supplier function; $B(d)$ consumer function; $h(x, s, d)$ equality constraints of active and reactive power balance; $g(x, s, d)$ inequality constraints of power flow limit of line, bus voltage limits;

The constraints of OPF include: active and reactive balance equations; upper and lower bounds on the generator active power outputs; upper and lower bounds on the generator reactive power outputs; branch transfer capacity limits; node voltage limits.

When using DC network modelling assumptions, the standard OPF problem as presented above can be simplified to a quadratic program with linear constraints and a quadratic cost function. The DC power flow greatly simplifies the power flow by making a number of approximations such as:

1. Ignoring the reactive power balance equations;
2. Assuming all voltage magnitudes are identically one per unit;

3. Ignoring line losses;
4. Ignoring tap dependence in the transformer reactance.

OPF development has been closely following the progress in numerical optimization techniques and computer technology. Many different approaches have been proposed to solve the OPF problem. These techniques include nonlinear programming, quadratic programming, linear programming, mixed programming, as well as interior point and artificial intelligence algorithms [4].

The most successful IPMs are based on using a primal–dual formulation and applying Newton’s method to the system of equations arising from the barrier method. This method has been widely used in power system optimization problems because of its favourable convergence, robustness, and insensitivity to infeasible starting points. The primal-dual interior point method (PDIPM) has become the algorithms of choice for solving OPF for long-term development planning strategies [4–10].

4. DESCRIPTION OF CALCULATION APPROACHES

To compare different methods are applied two approaches: the hourly calculation (considered the whole year as a whole), and using the typical schedules for consumption and production by month (monthly characterize trends for 24 hours). Therefore, to determine the criteria for a one development state is necessary produce 8760 calculations using first approach and 288 calculations with second approach.

5. CASE STUDIES AND CALCULATION RESULTS

Configuration of 4 node system contains: four nodes, four generators with quadratic or piecewise cost functions, 5 branches with maximal permissible power and annual loads. Configuration and parameters of the considered system is presented in Fig. 3. Calculations were made in the MATLAB software using 1.90 GHz AMD Turion 64 x2 PC with 4096 MB of RAM.

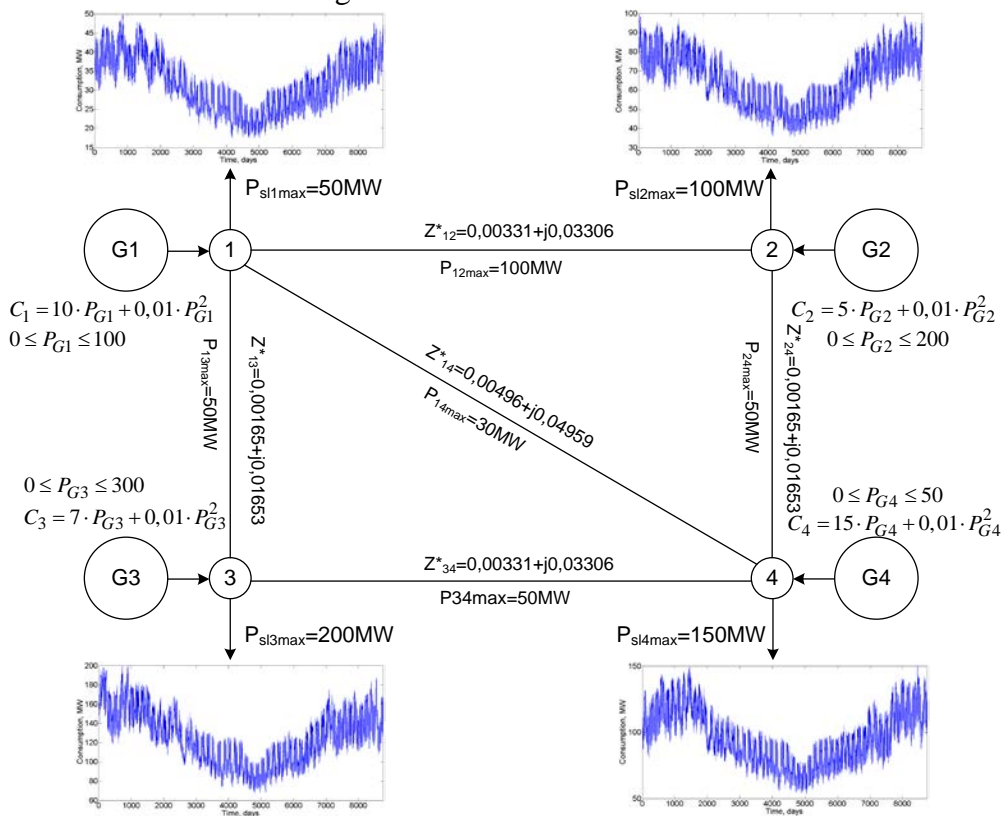


Fig. 3. 4 node system with grid parameters

Figs 4 and 5 show the results of calculations using the above described approaches for AC model taking into account power system constraints. Application of the approach with typical schedules speeds up calculation process and preserves the main trends of the system, but smoothing of the consumption and production peaks does not give a full technical evaluation of development state.

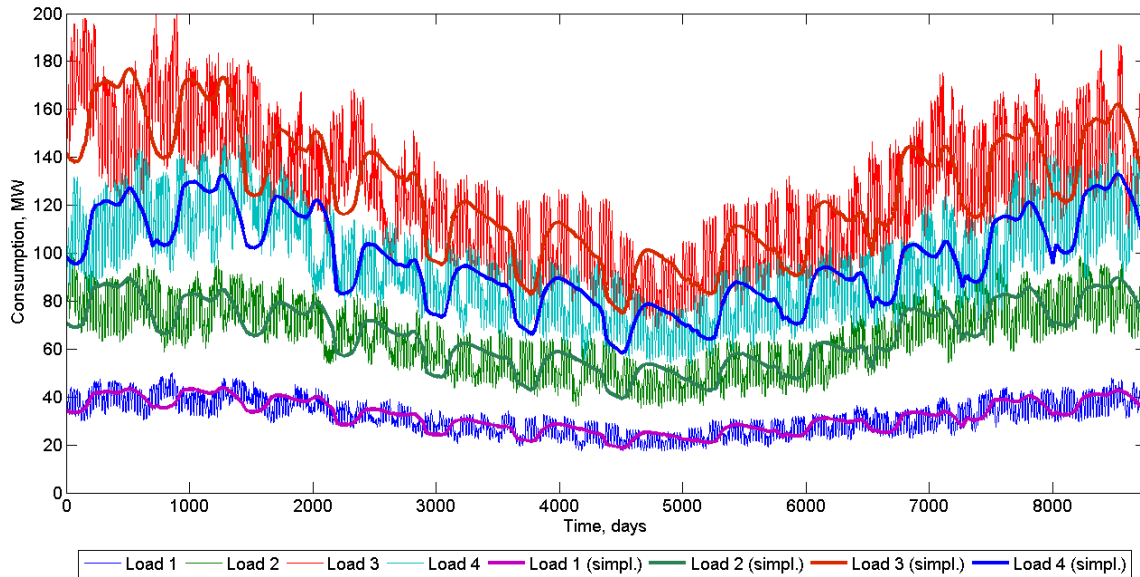


Fig. 4. 4 node system consumption profiles at full and simplified calculations

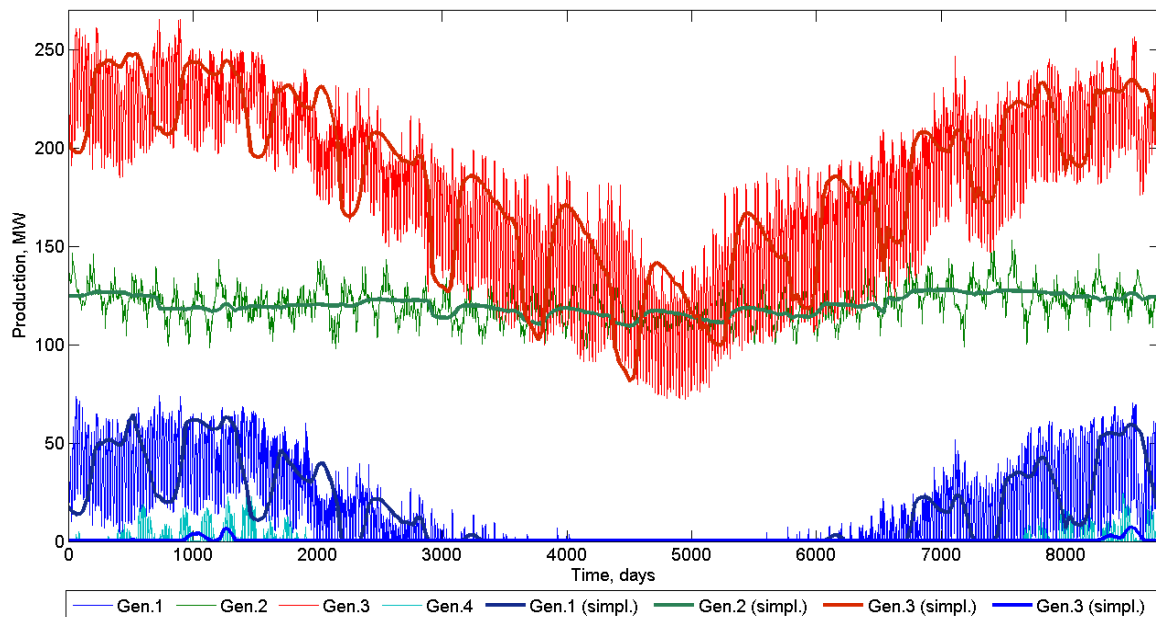


Fig. 5. 4 node system generation profiles at full and simplified calculations

Configuration of the Baltic scheme contains: 98 nodes, 15 generators (Estonian, Latvian and Lithuanian biggest generations), 143 branches (mainly 330 and 750 kV lines) and 35 loads (Baltic States). The rest part scheme does not include in calculations Russian and Belarus generating and consuming units due to insufficient information. Consideration of such scheme would be more interesting, due to the fact that large generating capacity from Russia and Belarus create in the Baltic networks power flows that will affect price formation and market performance in general. This calculation is planned to make in the future. Configuration of the considered system is presented in Fig. 6.

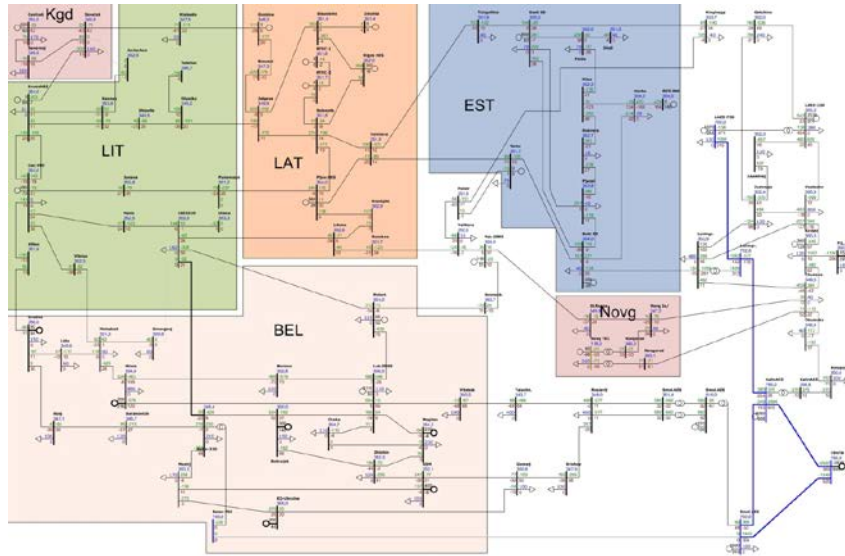


Fig. 6. Baltic scheme

Tables 1 and 2 shows calculation results for four nodes system for comparison ACOPF and DCOPF models with different approaches. Taking into account constraints of paper volume, only part of results are presented. Calculations were made for different conditions of the system (with congestions and without them) and using polynomials or piecewise costs functions. Traditionally, when optimizing the operation of a regulated power system, the objective function in (2) takes a simple smooth quadratic form. The electricity market, however, does not use quadratic cost because it does not cognitively match how market participants want to trade in the real world [6].

Table 1. 4 node system case without simplification

Name	Costs of production, €	Total production per year, MWh/year	Total consumption per year, MWh/year	Calculation time, seconds
Without Congestions				
DC without limits (polynomials)	21250166	2805405	2805405	338.06
DC without limits (Piecewise)	21265159	2805405		381.84
AC without limits (polynomials)	21262709	2806701		1066.65
AC without limits (Piecewise)	21277741	2806706		1204.02
With Congestions				
DC with limits (polynomials)	22437402	2805405	2805405	338.61
DC with limits (Piecewise)	22455709	2805405		385.10
AC with limits (polynomials)	22447357	2806305		1103.53
AC with limits (Piecewise)	22464853	2806371		1000.14

Table 2. 4 node system case with simplification

Name	Costs of production, €	Total production per year, MWh/year	Total consumption per year, MWh/year	Calculation time, seconds
Without Congestions				
DC without limits (polynomials)	21234295	2805424	2805424	11.61
DC without limits (Piecewise)	21249341	2805424		13.01
AC without limits (polynomials)	21246743	2806709		27.66
AC without limits (Piecewise)	21261863	2806716		32.81
With Congestions				
DC with limits (polynomials)	22406685	2805424	2805424	11.70
DC with limits (Piecewise)	22424455	2805424		13.22
AC with limits (polynomials)	22415876	2806395		29.62
AC with limits (Piecewise)	22433627	2806397		33.36

Tables 3 and 4 show similar calculations results for Baltic scheme. The results are annual values of total consumption and generation, costs of production, as well as the time taken for the calculation. In DC models difference between production and consumption of electric power equal zero, because losses of networks not taking into account.

Table 3. Baltic scheme without simplification

Name	Costs of production, €	Total production per year, MWh/year	Total consumption per year, MWh/year	Calculation time, seconds
Without Congestions				
DC without limits (polynomials)	205861256	26174077	26174077	584.69
DC without limits (Piecewise)	208096998	26174077		1054.69
AC without limits (polynomials)	209802978	26381625		2497.18
AC without limits (Piecewise)	212096986	26382080		3631.15
With Congestions				
DC with limits (polynomials)	213140547	26174077	26174077	618.85
DC with limits (Piecewise)	215763098	26174077		1056.45
AC with limits (polynomials)	215817709	26394673		2479.49
AC with limits (Piecewise)	218429201	26395308		3539.94

Table 4. Baltic scheme with simplification

Name	Costs of production, €	Total production per year, MWh/year	Total consumption per year, MWh/year	Calculation time, seconds
Without Congestions				
DC without limits (polynomials)	205975660	26210556	26210556	17.34
DC without limits (Piecewise)	208188513	26210556		32.76
AC without limits (polynomials)	209908095	26418094		79.62
AC without limits (Piecewise)	212166352	26418641		116.68
With Congestions				
DC with limits (polynomials)	213136192	26210556	26210556	17.98
DC with limits (Piecewise)	215859391	26210556		33.08
AC with limits (polynomials)	215804646	26431930		76.14
AC with limits (Piecewise)	218500249	26433685		114.98

From the results of calculation can be seen a significant acceleration of the process of calculating for one development stage using approach with the typical schedule. From Tables 1 and 2 DC model calculation without simplification takes 338 s (5.63 min), in turn with simplifications 11.70 s (0,19 min), or in 29 times faster than usual. From Tables 3 and 4 AC calculation without simplifications takes 3631.15 s (60.52 min), in turn with simplifications 116.68 s (1.95 min.), or in 31 times faster than usual. Annual values of these calculations do not differ among themselves significantly.

6. CONCLUSIONS

The paper describes the course of the research from description of the problem, possible solutions and value calculation. This research reflects one of the many problems, which need to be solved in imminent future and then utilized for power transmission network modeling and development tasks.

The paper first provides a general explanation of large technical system development process description and proposed method of prices determination, which is based on Interior Point Method for finding maxima of Social Welfare or minimization costs of production subject to power system constraints. Application of hourly calculation based on OPF allows taking into account the major trends of production and consumption during the day, taking into account consumption time shifting when considering multiple time zones, demand response, distributed generation, etc. Proposed approach with typical schedules speeds up calculation process 30 times and preserves the main trends of the system, but smoothing of the consumption and production peaks does not give a full technical evaluation of development state. Annual values of these calculations do not differ significantly between themselves.

Considering the complexity and dimension of development tasks, as well as information uncertainty conditions, appropriate method for the steepest calculating of OPF to define criteria is simplified DC method (typical schedules) with polynomials or piecewise costs functions. For short-term analysis of several years, and subject to initial information availability can be used the full AC model.



ACKNOWLEDGMENT

This work has been supported by the European Social Fund within the project «Support for the implementation of doctoral studies at Riga Technical University», Nr. 2009/0144/1DP/1.1.2.1.2/09/IPIA/VIAA/005.

REFERENCES

1. KRISHANS Z., MUTULE A., MERKURYEV Y., OLENIKOVA I., “Dynamic management of Sustainable Development: Methods for Large Technical Systems”, in Hardcover, 1st ed., Springer, 2010.
2. WEBER J.D. “Individual Welfare Maximization in Electricity Markets Including Consumer and Full Transmission System Modeling”. Link to the internet: <<http://powerworld.slappylab.com/DocumentLibrary/WelfareMaximization.pdf>>.
3. KAUSTUV. “IPSOL: An interior point solver for nonconvex optimization problems”. Link to the internet < <http://www.stanford.edu/group/SOL/dissertations/kaustuv-thesis.pdf>>.
4. Xi-Fan Wang, Yonghua Song, Malcolm Irving. “Modern Power Systems Analysis”. Springer, 2008, 559 p. ISBN 978-0-387-72852-0.
5. OBUSEVS, A., OLENIKOVA, I. “Modeling of Zonal Prices with Application in Long-Term Development Planning Strategies” Conference of Young Scientists on Energy Issues “CYSENI 2012”, Kaunas, Lithuania, May 24–25, 2012.
6. H. WANG, C. E. MURILLO-S´ANCHEZ, R. D. ZIMMERMAN, AND R. J. THOMAS, “On computational issues of market-based optimal power flow” Power Systems, IEEE Transactions on, Vol. 22, No. 3, p. 1185–1193, August 2007.
7. RAY D. ZIMMERMAN, CARLOS E. MURILLO-S´ANCHEZ, MATPOWER – A MATLAB Power System Simulation Package, User’s Manual, School of Electrical Engineering, Cornell University, 2011. Link to the internet: <<http://www.pserc.cornell.edu/matpower/manual.pdf>>.
8. RAY D. ZIMMERMAN, CARLOS E. MURILLO-S´ANCHEZ & DEQIANG (DAVID) GAN, MATPOWER v 4.1 (MATLAB Power System Simulation Package). Link to the internet: <<http://www.pserc.cornell.edu/matpower/>>.
9. RAY D. ZIMMERMAN, CARLOS E. MURILLO-S´ANCHEZ, ROBERT J. THOMAS, “MATPOWER’s Extensible Optimal Power Flow Architecture”. Link to the internet: <<http://www.pserc.cornell.edu/matpower/MATPOWER-OPF.pdf>>.
10. TARJEI K. “Utilizing Matpower in optimal power flow”. Link to the internet: <http://www.elkraft.ntnu.no/~tarjei/matpower_opf.pdf>.



MULTI-CRITERIA EFFECTIVENESS EVALUATION METHODOLOGY FOR THE ANALYSIS OF SWITCHYARD MODERNIZATION PROBLEM

N. Radziukynienė

*Lithuanian Energy Institute
Breslaujos str.3, LT-44403 Kaunas – Lithuania*

ABSTRACT

The paper presents a methodology for evaluation of competing scenarios in terms of multi-criteria effectiveness in various real life problems. It is based on ideas of Multi-criteria decision making model known as weighted sum model. It suggests 2 parallel evaluations using different benchmark scenarios as *user expectation* scenario and “*best-projected value*” scenario. The methodology is validated on the numerical set-up related to power substation modernization by 4 competing scenarios.

Keywords: multi-criteria effectiveness, competing scenario, benchmark scenario, switchyard, user expectation, best projected values

1. INTRODUCTION

In the last several decades, many real-life problems are increasingly addressed using multi-criteria approach. It is an instrument to measure the effectiveness (utility) of problem solution alternatives through evaluation of several selected attributes (mostly called criteria) of the solution. Since the best problem solution is on target, the decision on such a solution should rest upon an analytical procedure. Such a procedure is complicated in its essence, and one of the major reasons is criteria conflicts. Here often two approaches for dealing with conflicting criteria are addressed: the benefit to cost ratio approach and the benefit minus cost approach [1].

This instrument is mostly named multi-criteria decision-making (MCDM) and sometimes multi-criteria decision analysis (MCDA) and it yields the ranking of a finite set of alternatives in terms of a finite number of decision criteria.

MCDM is found as very suitable to energy sector as there are many energy infrastructures which are unique, extended, expensive, and with huge social and environmental impacts. Despite of such a high suitability, the authors in [2] state that this instrument has not received adequate attention in sustainable energy problems.

According to many authors, MCDM is divided into Multi-Objective Decision Making (or MODM) and Multi-Attribute Decision Making (or MADM) [3].

MODM studies decision problems in which the decision space is continuous. A typical example is mathematical programming problems with multiple objective functions. First reference to this problem, also known as the “*vector-maximum*” problem, is attributed to [4].

MADM concentrates on problems with discrete decision spaces. In these problems the set of decision alternatives has been predetermined.

There are a number of MCDM methods, and they are classified to following major groups:

- 1) Additive methods (the criterion effectivenesses are summed up), e.g. weighted sum model (WSM), analytic hierarchy process (AHP);
- 2) Multiplicative methods, e.g. weighted product model (WPM), multiplicative AHP;
- 3) Other methods, e.g.
 - ELECTRE (*Elimination and Choice Translating Reality*) method,
 - TOPSIS (*Technique for Order Preference by Similarity to Ideal Solution*) method [5].

There is a great number of methodologies realizing the MCDM methods and approaches. For instance, the paper [6] presents multi-criteria methodology to support the selection of repair contracts in a context where information is imprecise, when decision makers are not able to assign

precise values to importance parameters of the criteria used for contract selection. Utility functions are integrated with the variable interdependent parameters method to evaluate alternatives through an additive value function regarding mean time to repair, contract cost, the geographical spread of the candidate's (bidder's) service network, the candidate's reputation and the compatibility of company cultures.

Nevertheless, despite of the multi-year experience in their development and application, some authors argue that there is no way to know which the "right" ranking of alternatives is and which is not [1].

Specifically, the validity of the benchmark alternative (reference point) is one of the most puzzling. Notably it refers to the fairness of one particular alternative appointed to be as a yardstick (benchmark alternative) for competing alternatives. In general, insufficient reasoning of benchmark alternative ("why its criteria values are taken as reference values against other alternatives") is a weakness of multi-criterion approach. Often the authors attempt to do without the benchmark alternative by developing realistic alternatives and considering the optimal alternative as the best from them. For instance, the pair comparison approach was used for competing scenarios of wind power information system [7]. It has not defined the reference point at all.

The so-called ratio system is one of the traditional reference point approach. The study [8] employs this approach to evaluate 6 climate change mitigation policies for Lithuania. The policies are compared against Maximal Objective Reference Point (vector). This Point is found according to ratios of the type $x^*_{ij} = w_j x^*_{ij} / \sqrt{(x^2_{1j} + x^2_{2j} + \dots + x^2_{mj})}$, where x_{ij} denotes i^{th} alternative of j^{th} objective (i.e. criterion) and w_j is weight of the j^{th} objective. Each coordinate j^{th} of Maximal Objective Reference Point can be described as $r_j = \max x^*_{ij}$ (in case of maximization). This Point was used as a yardstick: the Tchebycheff distances of each alternative from this Point were calculated. In result, policies were ranked in consistent order but the same procedure of calculation seems not to be straightforward from a user viewpoint.

Regarding to deficiencies of traditional techniques dealing with reference points, the theoretical study [9] suggests multiple reference points instead. Multiple reference points are deemed easily to be implemented in a parallel algorithmic framework. The reference points can be uniformly distributed within a region that covers the Pareto Frontier. The authors realized an evolutionary algorithm based on an the scalarizing function that does not impose any restrictions with respect to the location of the reference points in the objective space.

When summarizing this review, we argue that existing approaches are either problematical (fairness of reference points) or sophisticated (not straightforward). Consequently, the objective of the paper is to develop a straightforward MCDM methodology with reasoned choice of benchmark scenario (reference points). The suggested methodology uses in parallel two simple multi-criteria effectiveness evaluation methods. The methodology was validated on numerical case of electrical network modernization problem.

2. NOVEL MULTI-CRITERIA METHODOLOGY

The scope of methodology is evaluation of effectiveness of competing scenarios (plans, strategies, projects) with the view to distinguish the best (i.e. most effective) one.

The theoretical approach to evaluation features the following characteristics:

- it is balanced approach: 2 evaluation methods with different rationales are combined to a consistent viewpoint in order to increase confidence of evaluation;
- it is multi-criteria approach: single criteria are normalized to effectiveness scale and aggregated to one scenario performance index;
- it is quantitative approach: both single-criterion and multi-criteria effectivenesses (performance indices) are measurable; they are computed according to formalized rules;
- it is attributable to weighted sum model category;

- it is benchmarking-specific: as being competing, scenarios are comparable in terms of effectiveness to reference point (benchmark scenario) and can be aligned to priority ranks by their effectiveness.

The methodology is a composite procedure. 5 steps can be distinguished:

1. choice of performance criteria and establishment of criteria weighing order;
2. development of competing scenarios;
3. multi-criteria evaluation according to user expectations (method A);
4. multi-criteria evaluation according to “best-projected values” (method B);
5. sensitivity analysis of the developed scenarios to the variation of user expectations and criteria weighing orders.

Effectiveness is considered as total usefulness (value) of the developed scenario.

At 1st step, the system (organization, structure) experiencing a problem is identified and this problem which can be solved in several alternative ways is formulated. These ways can be viewed as scenarios competing for the best effectiveness. A user is a person (inter alia legal body) who will use the results of scenario development to make a respective decision. A user is assumed to:

- formulate the problem’s scope and define the criteria as indicators to measure performance of the system under consideration, e.g. $R1$ (investment), $R2$ (environmental impact), $R3$ (electricity exports), $R4$ (sustainability index);
- set the criterion reference values as its expectation levels, i.e. numerical values which, if achieved by any scenario, would completely satisfy the user, e.g. $R1(A) = \$4.5$ million, $R2(A) = 60$ thous. tons of solid particles, etc.
- weigh the significance of criteria for the performance of considered system, e.g. $w1$ (for criterion $R1$) is 0.28, $w2=0.14$, etc., subjected to the condition

$$\sum_{i=1}^N w_i = 1 \quad , \quad (1)$$

where N – number of performance criteria.

At 2nd step, the project developer(s) analyzes the problem and works out several future scenarios for the user’s system (i.e. considered system), say, $S1, S2, \dots, S_M$, where M – number of competing scenarios. In result, the scenario criterion values can be tabulated in arrays as follows:

$$\begin{aligned} &R1(S1), R2(S1), \dots, R_N(S1) \\ &R1(S2), R2(S2), \dots, R_N(S2) \\ &R1(S_M), R2(S_M), \dots, R_N(S_M), \end{aligned}$$

where, for instance, $R_N(S1)$ is a value of (N -th) criterion in scenario $S1$.

At 3rd step, the user (or developer) addresses the user expectation method (hereinafter also method A) to aggregate the obtained criterion values to scenario multi-criteria effectivenesses. Firstly, the criterion values are normalized with respect to the expectations $R1(A), R2(A), \dots, R_N(A)$ according to the rules (2a), (2b), i.e. single-criterion effectivenesses are derived, e.g:

$$C1(S1, A) = 1 - \frac{R1(S1) - R1(A)}{R1_{\max} - R1_{\min}} \quad , \quad \text{when } R1_{\min} \text{ is better than } R1_{\max} \quad , \quad (2a)$$

$$C1(S1, A) = 1 + \frac{R1(S1) - R1(A)}{R1_{\max} - R1_{\min}} \quad , \quad \text{when } R1_{\max} \text{ is better than } R1_{\min} \quad , \quad (2b)$$

$$R1_{\min} = \min \{R1(S1), R1(S2), \dots, R1(S_M)\}, \quad (3a)$$

$$R1_{\max} = \max \{R1(S1), R1(S2), \dots, R1(S_M)\}, \quad (3b)$$



The effectiveness of a scenario is expressed on the instance of SI as follows:

$$PI(SI,A) = w_1 C1(SI,A) + w_2 C2(SI,A) + \dots + w_N C_N(SI,A) \quad (4)$$

where $PI(SI,A)$ is a performance index (multi-criteria effectiveness) of scenario SI pursuant to expectations-based evaluation (method A). The weighed single-criterion effectivenesses, e.g. $w_1 C1(SI,A)$, show a real contribution of a criterion to multi-criteria effectiveness. In result, the scenarios are aligned to priority rank A by the PI magnitude and the first one (with the biggest PI value) should be regarded as a winner.

At 4th step, a role of criterion reference values is designated to the “best-projected values” across the all scenarios (method B). Such a value is either R_{min} or R_{max} (see expressions 2a, 2b). The benchmark scenario consists of “best-projected values” $R1(B), R2(B), \dots, R_N(B)$ and their effectivenesses $C1(B)=C2(B)=\dots=C_N(B)=1$. Similarly to 3rd step, the same criteria values $R1(SI), R2(SI), \dots, R_N(SI)$ are normalized with respect to the “best-projected values”, e. g.

$$C1(SI,B) = 1 - \frac{R1(SI) - R1(B)}{R1_{max} - R1_{min}}, \text{ when } R1_{min} \text{ is better than } R1_{max}. \quad (5a)$$

$$C1(SI,B) = 1 + \frac{R1(SI) - R1(B)}{R1_{max} - R1_{min}}, \text{ when } R1_{max} \text{ is better than } R1_{min}. \quad (5b)$$

where $C1(SI,B)$ – single-criterion effectiveness of value $R1(SI)$ pursuant to method B . This normalization results in the similar array:

$$\begin{array}{c} C1(SI,B), C2(SI,B), \dots, C_N(SI,B) \\ C1(S2,B), C2(S2,B), \dots, C_N(S2,B) \\ \dots\dots\dots \\ C1(S_M,B), C2(S_M,B), \dots, C_N(S_M,B). \end{array}$$

It should be noted that this array has a number of null-value and unit-value elements determined by criterion values R_{min} and R_{max} , respectively. Also, the “criterion rose” can be constructed like that in Fig.1 where the “best-projected” scenario plays a central role and its loop embraces the loops of developed scenarios. Here the scenarios loops cannot overrun the central loop at any point $C1(B)=C2(B)=\dots=C_N(B) = 1$.

Finally, the usefulness of each scenario is found as expressed for SI :

$$PI(SI,B) = w_1 C1(SI,B) + w_2 C2(SI,B) + \dots + w_N C_N(SI,B), \quad (6)$$

where $PI(SI,B)$ is a performance index (multi-criteria effectiveness) of scenario SI pursuant to “best-projected” evaluation approach (method B). As seen, the indices under this approach never exceed the unit value ($PI \leq 1.0$), and this is contrary to the eventual overruns ($PI > 1.0$) under the first approach. Then a new priority rank of scenarios (rank B) is obtained and should be compared with the rank A .

At the 5th step, the sensitivity of both ranks shall be examined to the variation of weighing orders W and, additionally, to user expectations level L (for the rank A only).

3. ELECTRICAL SWITCHYARD MODERNIZATION PROBLEM (NUMERICAL SET – UP)

A big industrial company with its own power plant was chosen as a numerical set-up to validate the methodology. The considered system is company’s own 110/6 kV switchyard. The

problem is as how to modernize it in most rational way. Company’s administration played a role of a user and Lithuanian Energy Institute – that of scenario developer. The user presented the list of criteria and 3 levels of their expectation values (Table 1). Ambitious level *L2* reflects optimistic prospects and suggests higher expectations than basic level *L1*. Conversely, mean level *L3* refers to pessimistic prospects and suggests rather poor expectations.

Table 1. User-defined expectation values of criteria (applicable to method *A* only)

expectation level <i>L</i>	R1(A)	R2(A)	R3(A)	R4(A)
	short-circuit level, kA	annual probability of switchyard outage	damage and O&M cost reduction index, points	modernization cost, million LT
<i>L1</i> (basic)	20	0.015	40	14.50
<i>L2</i> (ambitious)	14	0.0001	20000	12.00
<i>L3</i> (pessimistic)	50	0.45	15	20

Also the user presented the criteria weighing orders (Table 2). Order *W2* expresses preferences to technical effectiveness against cost-effectiveness while *W3* represents opposite view. Order *W4* assumes non-differentiated weights.

Table 2. User-defined criteria weights

weighing order <i>W</i>	w_1	w_2	w_3	w_4
<i>W1</i> (basic)	0.15	0.3	0.2	0.35
<i>W2</i> (tech-preferred)	0.2	0.45	0.25	0.1
<i>W3</i> (cost-preferred)	0.1	0.25	0.2	0.45
<i>W4</i> (non-differentiated)	0.25	0.25	0.25	0.25

In response to such a problem formulation, 4 modernization scenarios have been developed: *S1* – part-renovation; *S2* – full-renovation; *S3* – new construction with 2 6-kV busbars; *S4* – new construction with multiple 6-kV busbars. The sketch of *S3* is presented in Fig. 2.

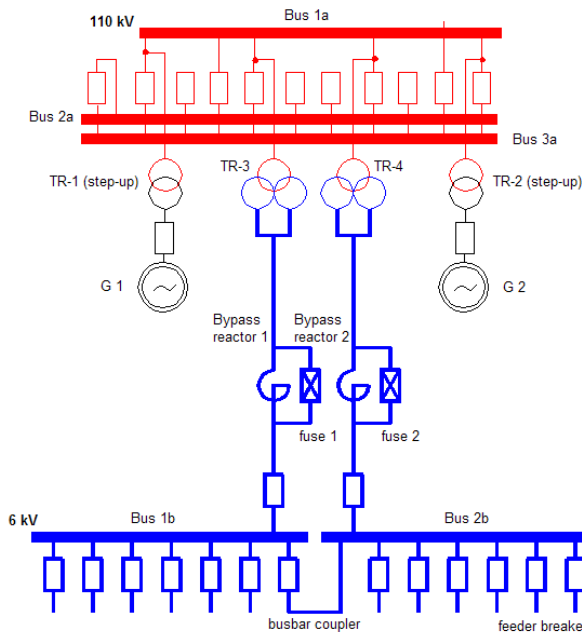


Fig. 2. Sketch of the switchyard of industrial company, modernization scenario *S3*

The scenarios' results in terms of criteria values are presented in Table 3 and their distribution ranges – in Table 4.

Table 3. Criterion values $R1(S1)$, $R2(S1)$, ..., $R4(S4)$ of the developed scenarios

Scenario	$R1$, kA	$R2$, annual probability	$R3$, points	$R4$, million LT
$S1$	65.11	0.9963	1	10.5
$S2$	65.11	0.0718	14	20.9
$S3$	14.09	0.0249	40	23.7
$S4$	13.3	0.00003611	27690	20.05

Table 4. Distribution ranges of criteria $R1$, $R2$, $R3$ and $R4$ across the developed scenarios

	$R1$, kA	$R2$, annual probability	$R3$, points	$R4$, million LT
R_{min}	13.3	0.00003611	1	10.5
R_{max}	65.11	0.9963	27690	23.7
$R_{max} - R_{min}$	51.81	0.99626389	27689	13.2

4. RESULTS AND THEIR DISCUSSION

This section presents the realization of the steps 3–5 of the methodology for the considered numerical set-up. Firstly, we address the method A and proceed with the normalization of criterion values according to (2a), (2b). Fig. 3 presents the normalization results under basic expectation level while Fig. 4 and 5 – under ambitious and mean expectations, respectively.

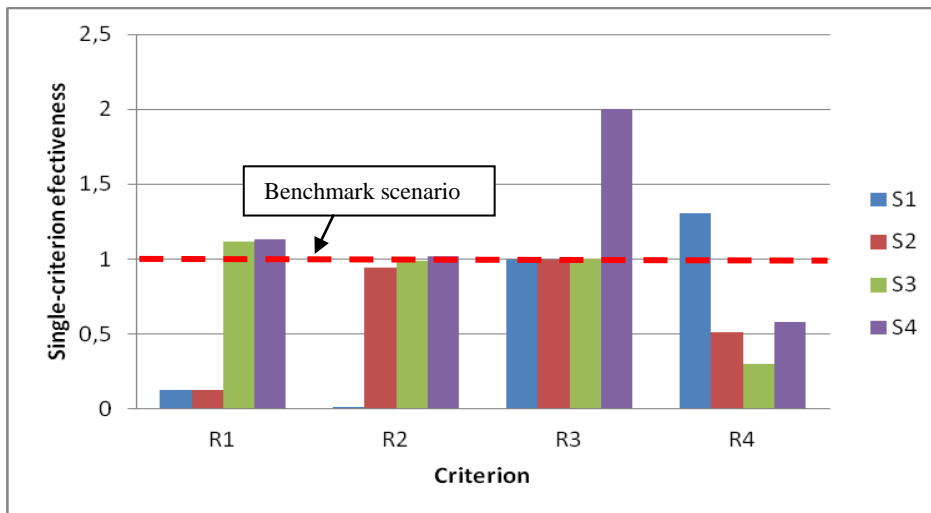


Fig. 3. Single-criterion effectivenesses $CI(S1,A)$, $CI(S2,A)$, ..., $CI(S4,A)$ of the developed scenarios under the basic expectation level $L1$ and basic weighing order $W1$

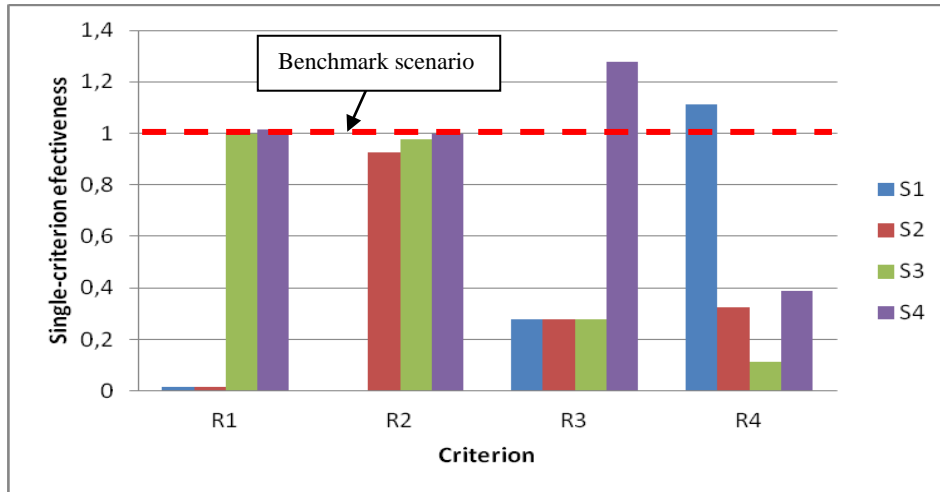


Fig. 4. Single-criterion effectivenesses $C1(S1,A)$, $C1(S2,A)$, ..., $C4(S4,A)$ of the developed scenarios under the ambitious expectation level $L2$ and basic weighing order $W1$

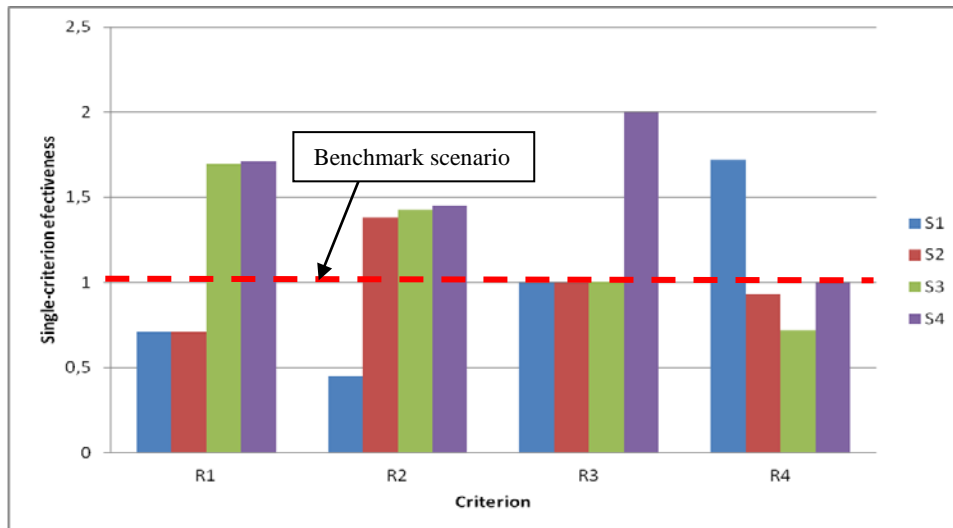


Fig. 5. Single-criterion effectivenesses $C1(S1,A)$, $C1(S2,A)$, ..., $C4(S4,A)$ of the developed scenarios under the mean expectation level $L2$ and basic weighing order $W1$

Upon having calculated the single-criterion effectivenesses, we compute the multi-criteria effectivenesses (performance indices) of scenarios by means of expression (4). The scenarios ranks are presented in Fig. 6 for different expectation levels and in Fig. 7 – for different weighing orders.

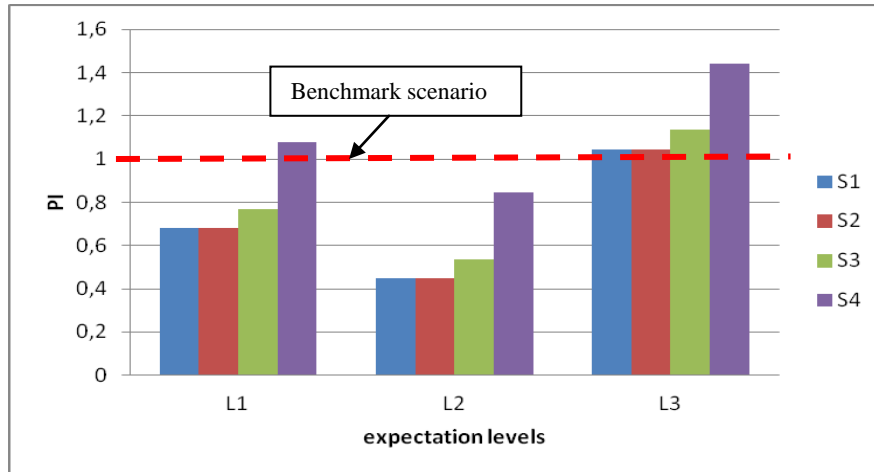


Fig. 6. Sensitivity of performance indices $PI(S1,A)$, $PI(S2,A)$, $PI(S3,A)$ and $PI(S4,A)$ to the variation of expectation levels under the basic weighing order $W1$

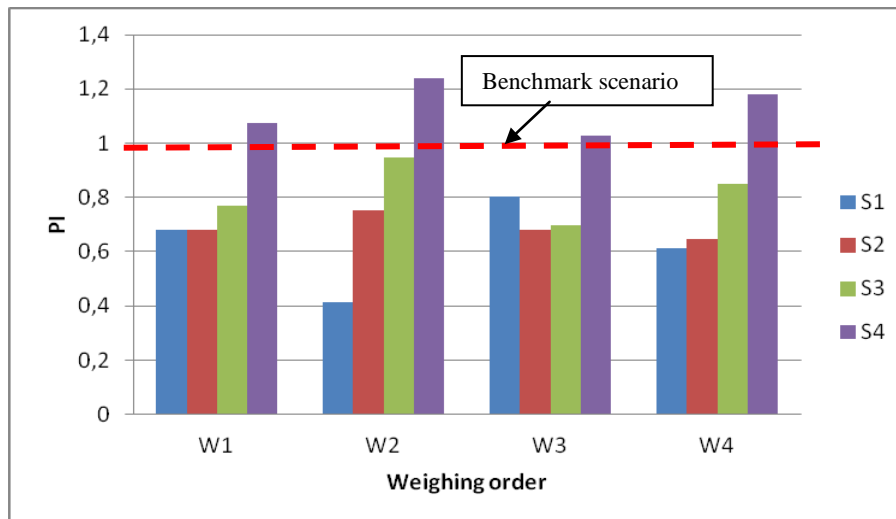


Fig. 7. Sensitivity of performance indices $PI(S1,A)$, $PI(S2,A)$, $PI(S3,A)$ and $PI(S4,A)$ scenarios to the variation of weighing order under the basic expectation level $L1$

As seen from Fig. 6 and Fig. 7, the scenario priority rank A is 1) $S4$; 2) $S3$; 3-4) $S2$, $S1$ and it can be regarded as dominating. It could be deduced that robustness of this rank against variation of expectation level L is very high – it is insensitive to switching to other level (Fig. 6). Nevertheless, the multi-criteria effectiveness PI is very sensitive to the expectation level: the higher the level, the poorer the effectiveness. The robustness against variation of weighing order W is rather high – i.e. the rank's sensitivity is rather weak (Fig. 7). Namely, $S4$ is on the top of the rank for any W , and the second place is taken by $S3$ for 3 weighing orders.

As for tech-preferred and cost-preferred weighing orders $W2$ and $W3$, both induce different scenario priority ranks, but with the same top scenario $S4$ (Fig.7). Also the difference in the magnitude of effectiveness is evident: if technical performances $W2$ are preferred against cost-effectiveness $W3$, $S4$ performs better ($PI=1.24$) than in vice-versa case ($PI=1.02$)

Further we examined the obtained scenario ranks by the second method. We constructed a new benchmark scenario based on “best projected values” taken from the Table 4. These values are taken as reference values (Table 5).

Table 5. Reference criteria values (“best-projected values”) of the benchmark scenario according to method *B*

	Value	Scenario yielding the value
$R1(B)$, kA	13.3	S4
$R2(B)$, annual probability	0.00003611	S4
$R3(B)$, points	27690	S4
$R4(B)$, million LT	10.5	S1

The normalization of criterion values was done using (5a) and (5b) and the results are plotted in Fig. 8. It indicates the specificity of normalization to produce a number of extreme values (zeros or units) of single-criteria effectivenesses, e.g. $R3$ -effectivenesses are 0 in $S1$, $S2$ and $S3$ and 1 for $S4$.

The performance indices were calculated using (6) and are presented, with sensitivity analysis viewpoint, in Fig. 9.

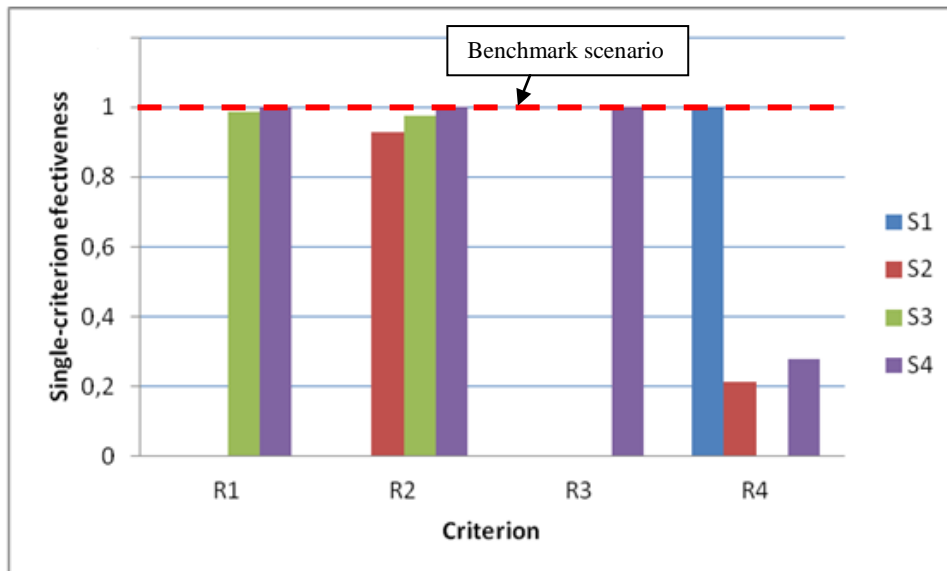


Fig. 8. Single-criterion effectivenesses $C1(S1,B)$, $C1(S2,B)$,..., $C4(S4,B)$ of the developed scenarios under the basic weighing order $W1$

Contrary to clearly dominating scenario priority rank *A*, the respective rank *B* as 1) $S2$; 2) $S4$; 3) $S1$; 4) $S3$ is less dominant – it is obtained for two weighing orders ($W3$ and $W4$). Specifically, its top priority is different – $S2$ (instead of $S4$ in rank *A*).

It could be regarded that robustness of the rank *B* against variation of expectation levels is fair, i.e. it is rather sensitive to variation of weighing order.

In conclusion, the winning switchyard modernization scenario according to user expectations (method *A*) is $S4$ – new construction with multiple 6-kV busbars. It is PI in tech-preferred weighing order $W2$ reaches the highest value. On the other hand, according to “best-projected values” (method *B*), $S2$ (full-renovation) appears as winning scenario, with considerably better PI in cost-preferred weighing order $W3$ against tech-preferred order $W2$.

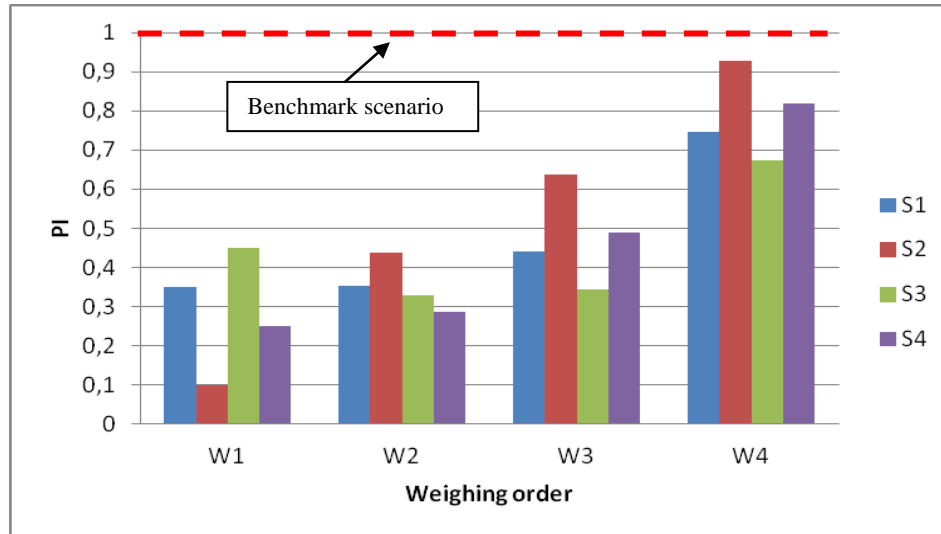


Fig. 9. Sensitivity of performance indices $PI(S1,B)$, $PI(S2,B)$, $PI(S3,B)$ and $PI(S4,B)$ to the variation of weighing order

And final remark: method B is applicable to competing scenarios only (specifically, at least 2 scenarios) as it needs “best-projected values” from either one. Conversely, method A suits to the “no-competition” case when only one scenario is developed (method enables quantification of such single scenario).

4. CONCLUSIONS

1. The suggested multi-criteria effectiveness evaluation methodology has simple rationale and transparent procedure of application. Both single-criterion and multi-criteria effectivenesses seem to be not far abstracted from physical meaning.
2. The methodology suggests scenario ranking according to 2 methods which allow measure the scenario “distances” from user expectation and from “best-available” (best-projected) criteria values. In case of several scenarios with similar effectiveness according to method A , method B could be additionally used to identify the best scenario. Nevertheless, it cannot be excluded that certain situations may occur when methods result in different choice of the best scenario.
3. It is easy in application. It suggests to use a “criteria rose” chart to get general impression on effectivenesses of single criteria
4. It is user-friendly and convenient for the practitioners.
5. It seems to be transferable from energy thematic area to many other thematic areas when competing scenarios should be screened for their effectiveness.

REFERENCES

1. TRIANTAPHYLLOU E., BAIG K., *The Impact of Aggregating Benefit and Cost Criteria in Four MCDA Methods*. IEEE Transactions on Engineering Management, May 2005, Vol. 52, No. 2, p. 213–226.
2. WANG J.J., JING Y.Y., ZHANG C.F., ZHAO J.H., *Review on multi-criteria decision analysis aid in sustainable energy decision-making*. Renewable and Sustainable Energy Reviews 13 (2009) p. 2263–2278.
3. ZIMMERMANN, H.J., *Fuzzy Set Theory and Its Applications*. Kluwer Academic Publishers, Second Edition, Boston, MA, 1991.



4. KUHN, H.W. AND A.W. TUCKER., *Nonlinear Programming*. Proc. 2nd Berkeley Symp. Math. Stat. Prob., 1951, p. 481–492.
5. TRIANTAPHYLLOU E., SHU B., NIETO SANCHEZ S., RAY T., *Multi-Criteria Decision Making: An Operations Research Approach*. Encyclopedia of Electrical and Electronics Engineering, (J.G. Webster, Ed.), John Wiley & Sons, New York, NY, 1998, Vol. 15, p. 175–186.
6. JORGE DE MELO BRITO A., TEIXEIRA DE ALMEIDA FILHO A., TEIXEIRA DE ALMEIDA A. *Multi-criteria decision model for selecting repair contracts by applying utility theory and variable interdependent parameters*. IMA Journal of Management Mathematics (2010) 21, p. 349–361.
7. NEMURA A., KLEMENTAVIČIUS A. *Multi-criterion assessment of preferences for communications alternatives of wind power park information system*. Informatica. ISSN 0868-4952. 2008. Vol. 19, No. 1, p. 63–80.
8. STREIMIKIENE D., BALEZENTIS T. *Multi-objective ranking of climate change mitigation policies and measures in Lithuania*. Renewable and Sustainable Energy Reviews 18, February 2013, p. 144–153.
9. FIGUEIRA J. R., LIEFOOGHE A., TALBI E.-G. and WIERZBICKI A. P. *A parallel multiple reference point approach for multi-objective optimization* European Journal of Operational Research, Volume 205, Issue 2, 1 September 2010, p. 390–400.



FAULT IDENTIFICATION IN MICRO-HYDRO POWER GENERATOR BASED ON THE SHORT-TIME FOURIER TRANSFORM

Yen-Huai Ma, Chen-Hsuan Chang, Chueh-Cheng Wu, Sy-Ruen Huang,
Yu-Hua Mo, Chen-Yeon Chu
Feng Chia University
Wenhwa Rd. 100, 407 Taichung – Taiwan

ABSTRACT

A condition monitoring system of vertical axis turbine micro-hydro power generation system is proposed in this study and the short-time Fourier transform is applied in identifying the fault. There are many low-head (small drop) waterway, usually only used for irrigation or transportation but not power generation in the world. This study intends to use a vertical turbine generator in the existing canal or irrigation channels to research micro-hydroelectric power including system design, generating power estimation, lightweight blade design, turbine efficiency assessment, and condition monitoring system. The high flux permanent magnet synchronous generator inside the unit is gearless drive system has benefits of small size, light weight and flexible structure design. There are many mechanic components in micro-hydro turbine generator. Not only the fault caused by electric, the damage of mechanical but also affects the generated electrical power, therefore, the condition monitoring system of vertical axis micro-hydro turbine system necessary. The study uses the short-time Fourier transform method to identify the fault of micro-hydro generator. The method reduces the cost and has abilities of detecting electric and mechanic faults.

Keywords: Vertical Axis Turbine Micro-hydro Generator, Condition Monitoring System (CMS), Short-Time Fourier Transform (STFT)

1. INTRODUCTION

Hydroelectric power has been developed and widely used in the world. This power generation method can be large-scale power plant and also is a clean, renewable energy. In addition, hydroelectric power generation costs per kWh is clearly lower than other currently widely used energy such as thermal power, nuclear power, solar power, wind power, etc. [1], therefore, almost all the developed countries in the face of the threat of excessive greenhouse gas emissions take hydropower as priority development. One of the best regulatory power in the electric power grid is hydropower which can immediately start up power generation usually plays an important role in the power grid, to assume the important function of emergency reserve. Ordinary coal-fired thermal power must allow sufficient burning of coal to generate enough steam to start power generation. Regulation performance, with hydropower comparable only oil and natural gas to generate electricity.

This study proposes a vertical turbine structure as shown in Fig. 1, to explore the feasibility of micro-hydropower in the existing canal or irrigation channels and design it easy to remove from water if necessary such as flood or maintenance.

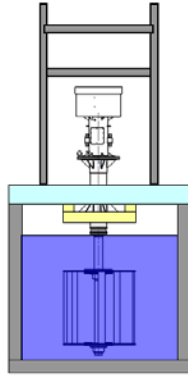


Fig. 1. Micro-hydro power generator

Water energy conversion and the conversion of wind energy is similar to the process of converting energy includes two procedures: the first program absorb kinetic energy is converted to mechanical energy in the rotor axis from the hydro. The second procedure: the first program mechanical energy is converted into useful electric energy, shown in Fig. 2. Water energy and wind energy are very similar, so the wind in the literature, we can see that the horizontal-axis wind turbines used to power for fluid mechanics simplified analysis, research and development related to hydrodynamic performance prediction for rotor theory of modern wind power and hydroelectric power is available. However, in the analysis presented in the minority after appropriate fully tested, by direct comparison with actual measurements on the wide range of configurations and conditions.

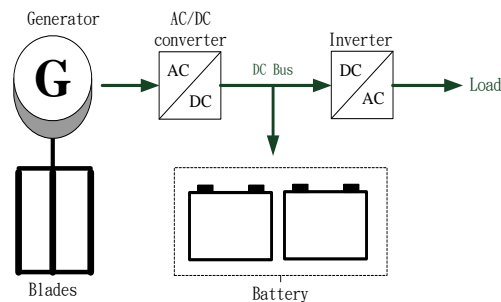


Fig. 2. Block diagram of the energy converter

Micro hydro turbine generator as the independence of the voltage source supply unit, its internal high magnetic flux density permanent magnet synchronous generator is popularity for industry applications, especially gearless drive system advantages, such as small size, light weight and flexible The design of the structure. The recent trends to make weigh the benefits exceed the cost of the power generation system, the development of the power generation system capacity range of up to several hundred kilowatts [2]. Given these trends, one of the best micro-hydro turbine conversion system topology, the power output of the synchronous generator, the convergence of a simple three-phase rectifier diodes and DC-DC power tracking circuit is more than three-phase IGBT PWM converter AC-DC converter, a solution that is more cost-effective [3–6].

DC-DC buck – boost converter feedback as the maximum power point tracking circuit output current of the wind turbine [7]. Power switch voltage stress is greater than the boost converter. The leakage inductance of the generator and the cable cannot be used as a considerable DC inductor. Control scheme is based on an independent wind power generation

system, which requires the parameters in the DC end into a large-capacity battery as a balance between the two media. [5]

Condition monitoring technology has been in power production, aerospace, marine propulsion, and fluid industry used in wind turbines. In this thesis, the application of condition monitoring technology and micro-hydro machine. Example of a condition monitoring technology application monitoring control and data acquisition system (SCADA). Although there are many SCADA systems and has not been included in any condition monitoring and wind turbine condition monitoring, but it does have the potential for future development. For the further development of the specific fault monitoring technologies to researchers and engineers to develop and judgment turbines, such as literature [9] [12]. Improved signal processing technology can improve the condition monitoring technology potential, because of its convenience and low cost per unit. So far, condition monitoring technology and more use of the Fourier transform (FT), the literature also use other condition monitoring techniques, using FFT processing non-stationary signals. [13] The micro hydro drive variable as follows: water flow rate, of non-stationary time and frequency domain electrical and mechanical signals, at the same time should be used more advanced signal numerical analysis method to do state diagnosis.

The micro-hydro power generator is consisted of many mechanical components. In addition to electrical failure, damage to the mechanical components, will also affect the amount of micro-hydro. The damage caused by the electrical element on the output power will have a drastic change, for example, stopped by the system due to the damage of the important components of the output power or system microchip can also cause damage to the serious power distortion. Mechanical failure on the electrical characteristics of the changes are not obvious, such as blade breakage, split or rotating blades of a foreign body embedded when the turbine is still powerful hydraulic continue to rotate. No valid judgment mechanism detects downtime to repair, make micro-turbine to continue to lead to more serious damage generated compromised. Depend on the reliability of these mechanical power generation equipment, which contributed to the turbine condition monitoring and fault diagnosis. [9-12] Improved turbine condition monitoring and fault diagnosis can also help to improve these mechanical reliability. In particular, micro-hydro turbine is susceptible to load fluctuations as well as the turbine itself subjected to extreme environmental conditions malfunction. In this research paper, the application of short-time Fourier transform (STFT) is applied condition monitoring and fault diagnosis, which the electrical signal from the a micro-hydro power generator with condition monitoring system, analysis of machine failure in micro-water theory.

2. THE VERTICAL MICRO-HYDROELECTRIC TEST PLATFORM AND OPERATING STUTS MONITORING SYSTEM

Water energy and wind energy is very similar to the natural water from high and low drop. The formation of the kinetic energy of the drop of water under the effect of gravity, at the high water from a river or reservoir to a low at the diversion and use of water pressure or flow rate shocks turbine to rotate, so water energy into mechanical energy, and then driven by the turbine generator rotating AC cutting the magnetic field lines. Water quality, and its density is much larger than the wind, and when this mass has a speed that will produce the kinetic energy of the water, that is, with $1/2 [\text{mass} \times (\text{speed})^2]$ proportional. Through the mass of water in unit time with the available power (in water) within a unit time, through the kinetic energy of the area is:

$$P_w = \frac{1}{2} \rho A V \cdot V^2 = \frac{1}{2} \rho A V^3 \quad (1)$$

ρ = The density of water the (approximate 1.225 kg/m³) at sea level. V = the velocity of water (m/s). A = water through the area of the blade, that is, the water normally after (m²). Clearly force can be obtained in the sum of the (approximate) of the available power, the power of only can actually draw a portion. Drawn by a hydraulic turbine power, as follows:

$$P = K \frac{1}{2} \rho A V^3 \quad (2)$$

$$k = C_p N_g N_b \quad (3)$$

Where C_p = coefficient of performance or power coefficient (approximate 0.593). N_g = generator efficiency. N_b = gearbox / bearings efficiency. The torque generated by the hydro-turbine is as follows:

$$T_s = \frac{P}{\omega_r} \quad (4)$$

T_s = Hydro turbine side of the mechanical torque. P = the hydro turbine side of the power output. ω_s = hydro turbine side of the rotor speed.

Micro-hydro system monitoring interface planning and design: micro-hydroelectric system monitoring interface contains of four parts: hydraulic characteristics of the micro water generators characteristics measurement, Canal or irrigation channels of measurement, data collection and monitoring. The four parts of the system, network transmission interface. Understand their mutual conversion efficiency by the establishment of the mechanism of measurement of its primary purpose for the establishment of the water flow, water flow rate, turbine, converters, etc., application charts with data processing, etc., showing the various results of the analysis. Figure 3 presents monitoring system design of the micro-hydro power generator.

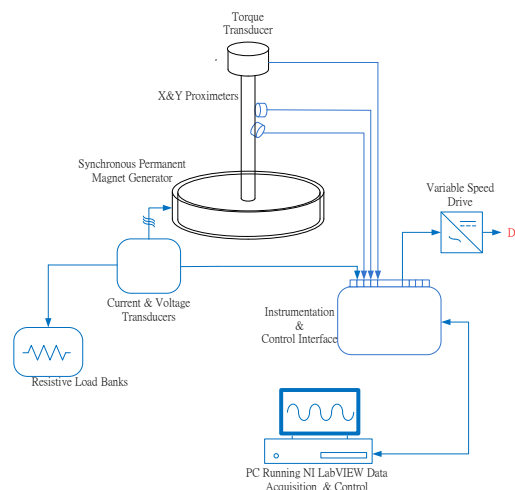


Fig. 3. Monitoring interface system design of the micro-hydro power generator

Independent generator set, limited to maintain safety and the quality of the electricity supply in the regulations required. The main switching element includes a main circuit breaker, which is used to connect or disconnect the generator from the grid connection. Measuring transformers, power transformers and current sensors for measurement purposes is

easier to manage and measure the high voltage and current conversion. Grounding is implemented according to the requirements specified by the grid operator.

Micro hydro because of mechanical failure caused by the unbalanced state of the rotor are the following: (1) foreign body embedded micro-hydro turbine blades in the water; (2) micro hydro turbine blade attacks by foreign matter or form due to the high intensity of the hydraulic blade broken; (3) lengthy operation or affect the blade fatigue damage. The above listed micro hydro failure will have a certain impact on the output power of the micro-hydro system, but its impact slowly, i.e. these factors affect the micro-hydro not a direct result of micro-hydro motor stop. Therefore, the short time generating output cannot be fault diagnosis. The generator output power for a period of time only can be used for failure analysis to determine mechanical failure.

3. FAULT DIAGNOSIS AND ANALYSIS OF MICRO-HYDROELECTRIC USING SHORT-TIME FOURIER TRANSFORM (STFT)

Hydroelectric torque sensor is very accurate but expensive, therefore, there are some low cost detecting sensors such as terminal electrical signal which can capture the current and voltage source signal to analysis. Years continuous condition monitoring system will increase the burden of the system memory using a high sampling frequency, transient detection and high sampling frequency instrument will improve the instrument cost, does not apply to long-term monitoring. General for a long time condition monitoring system to measure terminal voltage or the effective value measurement target project. Low sampling frequency can reduce equipment costs, but also greatly reduces memory use, condition monitoring system can run much longer period of time, without memory overflow situations. High sampling frequency will be making detection of the fault operation requires very fast processing speed. For some complex calculation algorithm of the fault system in the design of high sampling frequency mechanism cannot use. However, low sampling point is often lost a lot of instant or transient phenomena, such as surges, phase shift and frequency drift. The detection system is a low sampling frequency of the measurement system. The system records every two seconds, the voltage and current RMS value cannot be used for fault detection method, the transient measurement method proposed in the previous literature. This paper presents the electrical output of the micro-hydro machine fault diagnosis to short-time Fourier.

The short-time Fourier transform (STFT) is a commonly used mathematical analysis methods for the analysis of non-stationary signals. A one-dimensional function, a window function, the function of sliding along the timeline and select the function to do the short-time Fourier transform, the signal after the conversion to a two-dimensional function solution can be obtained. Mathematically, this can be written:

$$\text{SFST}\{x(t)\}(\tau, \omega) \equiv X(\tau, \omega) = \int_{-\infty}^{\infty} x(t) \omega(t - \tau) e^{-j\omega t} dt \quad (5)$$

In the formula (5), $\omega(t)$ is a window function, (τ, ω) is a two-dimensional function, which is $x(t) \omega(tT)$ after the Fourier transform of a complex function of the resultant, and this two-dimensional function represents the phase and amplitude of the signal in time and frequency. Usually function solutions are two vectors Timeline τ and the frequency axis ω resolution, STFT can suppress any jump discontinuous phase. Usually window function is selected in the range is set to be long and the time t is not usually transient or high-resolution as selected.

In the non-continuity of the values in the case of discrete time or signal, the converted data can be broken up into blocks (usually overlap with each other, to reduce boundary calculation error). The blocks of each part is decomposed after the Fourier transform, you will

get a complex matrix, which records the amplitude and phase of each point in the function of time and frequency function. This can be expressed as:

$$\text{STFT}\{x[n]\}(m, \omega) \equiv x(m, \omega) = \sum_{n=-\infty}^{\infty} x[n] \omega[n - m] e^{-j\omega t}. \quad (6)$$

4. RESULTS

The system in the monitoring of electrical characteristics of the output waveform of the state under the normal state shown in Fig. 5.

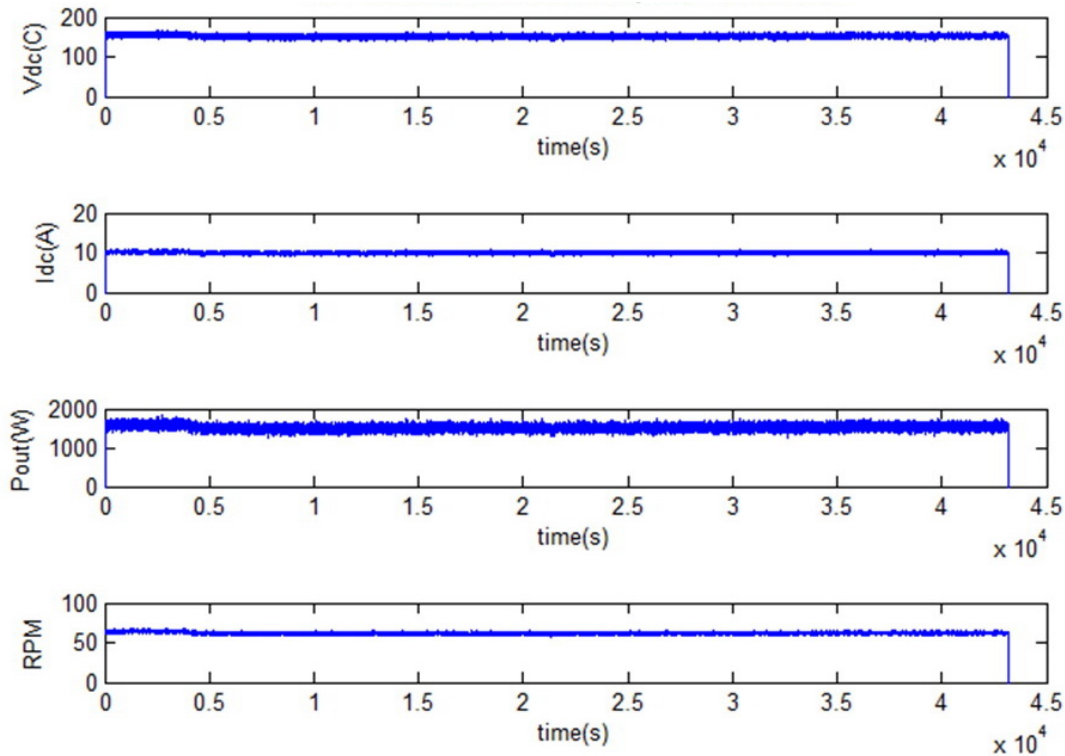


Fig. 4. Micro-hydro power generator output data

This study selected micro-hydro failure which for some values of the short-time Fourier transform analysis to verify the method proposed in this paper. Micro-hydroelectric generators in one day due to the falling water of the branches embedded in the leaves, making the turbine rotational imbalance. Fig. 5 shows the electrical signal: (a) before fault, (b) in fault happening and (c) after fault happening. Three sets of waveform to general output waveform to do the fault detection is difficult. Fault waveform of Fig. 6 (b) has an undulating, but may be due to the amount of water to enhance speed becomes high in the voltage is increased, will cause a misjudgement of the situation. The diagram (c) of the voltage variation is larger, but the manner of the system monitoring electricity is fragmented manner, shown in Fig. (c) is the waveform shown, but also cannot be determined in this fragment that. Fig. 6 is one day data of DC voltage output waveform. Indeed it can be seen from the waveform singular point of the system voltage and the voltage change waveform of a day, but the description need to use a day data for analysis, the detection performance is low.

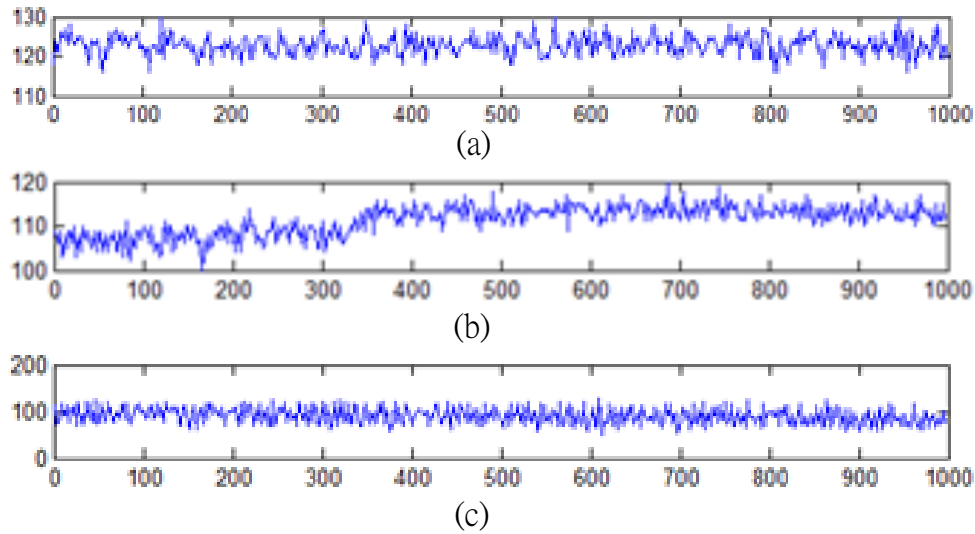


Fig. 5. Wave forms of monitoring system of micro-hydro power generator: before fault (a), in fault happening (b), and after fault happening (c)

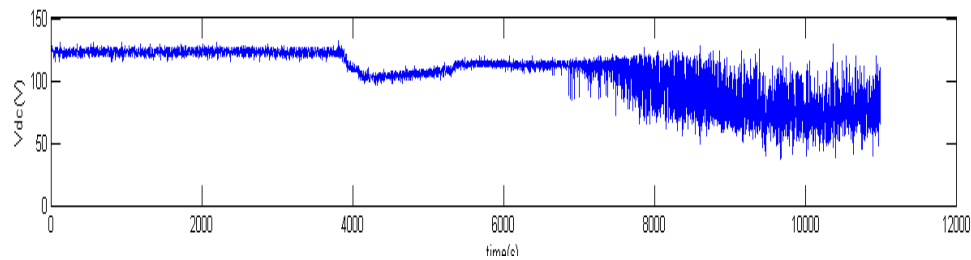


Fig. 6. Electrical signals of micro-hydro power generator (one day)

The proposed application of the short-time Fourier window function is defined as fragments of the signal in the micro-hydro system status monitoring signal window function. The system reads DC voltage value after a period of time, and then to do a short-time Fourier analysis, resulting in the value of the one time domain and frequency domain vector. By the time of diagnosis, the time domain and frequency domain draw a three-dimensional pattern to show distortion of the time domain and frequency domain in the period of before fault, fault happening and after fault happening. This method can effectively do micro-hydro machine fault diagnosis. Fig. 7 shows a part of the output waveform is detected through the frequency three-dimensional map in the window function using short-time Fourier transform analysis. It shows that data before the fault is very smooth. When the fault occurred, the time domain and frequency domain is less stable. After the fault, the frequency domain in the low-frequency and high-frequency part is also unstable.

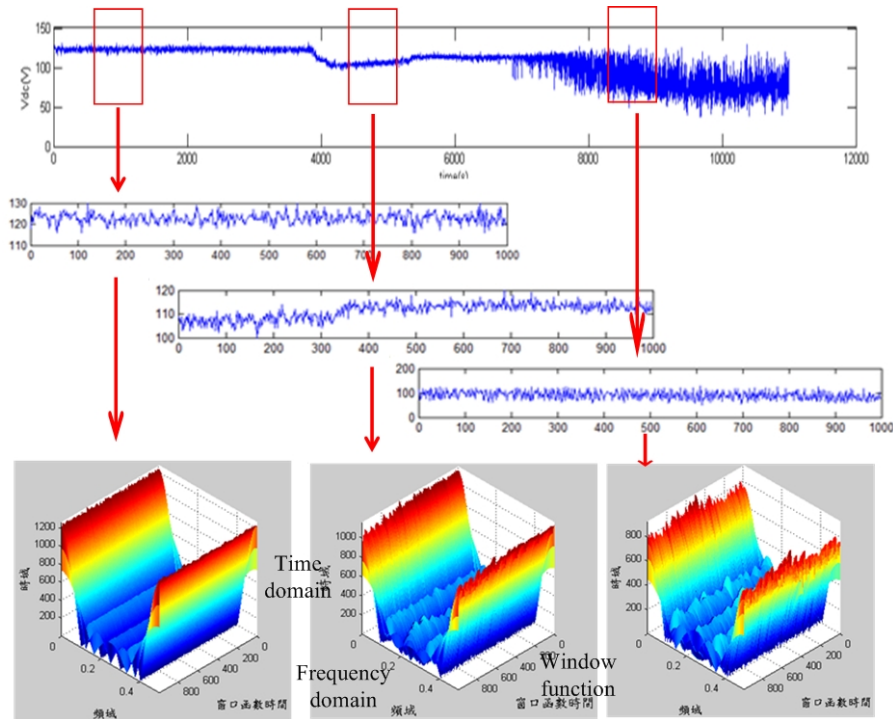


Fig. 7. Original signals transformed to easy detection wave form by short-time Fourier transform

5. CONCLUSION

This study presents a vertical axis turbine micro-hydro power generator with condition monitoring system and application of the short-time Fourier fault diagnosis using the low cost detection system which is different from wind turbine sensor elements. Condition monitoring system using the electrical characteristics of the micro-hydroelectric output signal, to improve the availability of micro-hydroelectric and reduce the cost of maintenance operation. This study proposes a new micro-hydroelectric power monitoring technology to a new system architecture. From this study can be achieved to reduce the cost of investment, both of electrical and mechanical fault detection ability. Proposed micro hydro machine failure detection method of the study, using the short-term Fourier transform to the voltage waveform.

Distortion waveform through the high and low frequency bands can determine the state of micro-hydraulic motor blades embedded by tree branches and other foreign matter. Compared to the traditional wind turbines detecting technology, the new micro-hydroelectric power status detection is simple, and cheap. There are many kinds of faults impacting micro-hydro generators, however, this study just only discusses the branches embedded. Future researches can apply this proposed method to verify other micro-hydroelectric faults.

ACKNOWLEDGEMENTS

The authors thank the National Science Council of Taiwan for supporting the research under the grants of NSC 101-2632-E-035-001-MY3.



REFERENCES

1. California Levelized Energy Costs for Different Generation Technologies in US Dollars Per Megawatt Hour (2007).
2. YUTIAN SUN, QINGFEI GAO, “The Design and Operation of 700mw Class Totally Air-Cooled Hydroelectric Generators,” *Rocon 2009, Eurocon '09. IEEE*, p. 501–508, 2009.
3. SEUNG-HO SONG, SHIN-IL KANG, NYEON-KUN HAHM, “Implementation and Control of Grid Connected AC-DC-AC Power Converter for Variable Speed Wind Energy Conversion System,” *Applied Power Electronics Conference and Exposition, APEC '03, Eighteenth Annual IEEE*, Vol. 1, p. 154–158, 2003.
4. LEE D.C., LEE G.M., LEE K.D., “DC-Bus Voltage Control of Three-Phase AC/DC PWM Converters Using Feedback Linearization,” *IEEE Transactions on Industry Applications*, Vol. 36, No. 3, p. 826–833, 2000.
5. SINGH B.N., CHANDRA A., AL-HADDAD K., PANDEY A., KOTHARI D.P. “A Review of Three-Phase Improved Power Quality AC-DC Converters,” *IEEE Transactions on Industrial Electronics*, Vol. 51, No. 3, p. 641–660, 2004.
6. THIYAGARAJAH K., RANGANATHAN V.T., IYENGAR B.S.R., “A High Switching Frequency IGBT PWM Rectifier/Inverter System for AC Motor Drives Operating From Single Phase Supply,” *IEEE Transactions on Power Electronics*, Vol. 6, No. 4, p. 576–584, 1990.
7. TAFTICHT T., AGBOSSOU K., CHERITLA. “DC Bus Control of Variable Speed Wind Turbine Using a Buck-Boost Converter,” *IEEE Power Engineering Society General Meeting*, 2006.
8. TEODORESCU R., BLAABJERG F. “Flexible Control of Small Wind Turbines With Grid Failure Detection Operating in Stand-Alone and Grid-Connected Mode,” *IEEE Transactions on Power Electronics*, Vol. 19, No. 5, p. 1323–1332, 2004.
9. YANG, W., TAVNER, P.J., WILKINSON, M.R., “Condition Monitoring and Fault Diagnosis of a Wind Turbine Synchronous Generator Drive Train” *Renewable Power Generation, IET*, Vol. 3, No. 3, p. 1–11, 2009.
10. BIN LU., YAOYU LI, XIN WU., “A Review of Recent Advances in Wind Turbine Condition Monitoring and Fault Diagnosis” *Power Electronics and Machines in Wind Applications, 2009. PEMWA 2009. IEEE.*, p. 1–7, 2009.
11. AMIRAT, Y., BENBOUZID, M.E.H., BENSACKER, B., WAMKEUE, R., “Condition Monitoring and Fault Diagnosis in Wind Energy Conversion Systems: A Review” *Electric Machines & Drives Conference, 2007. IEMDC '07. IEEE International*, Vol. 2, p. 1434–1439, 2007.
12. WENXIAN YANG., TAVNER, P.J., WILKINSON, M., “Wind Turbine Condition Monitoring and Fault Diagnosis Using Both Mechanical and Electrical Signatures” 2008. *AIM 2008. IEEE/ASME International Conference on Advanced Intelligent Mechatronics*, p. 1296–1301, 2008.
13. Z.K. PENG., F.L. CHU. ”Application of the Wavelet Transform in Machine Condition Monitoring and Fault Diagnostics: a Review with Bibliography” *Mechanical Systems and Signal Processing*, Vol. 18, No. 2, p. 199–211, 2004.
14. V.K. RAI., A.R. MOHANTY., ”Bearing fault diagnosis using FFT of Intrinsic Mode Functions in Hilbert–Huang Transform” *Mechanical Systems and Signal Processing*, Vol. 21, No. 6, p. 2607–2615, 2007.



THE INFLUENCE OF THE FOURIER NUMBER ON THE CALCULATION ACCURACY OF DYNAMIC THERMAL TRANSMISSION IN MULTI-LAYER ENCLOSURES

P. Bruzgevičius, V. Stankevičius, A. Burlingis, K. Banionis

*Kaunas University of Technology
Institute of Architecture and Construction
Tunelio str. 60, LT-44405 Kaunas – Lithuania*

D. Pupeikis

*Kaunas University of Technology
Studentu str. 48, LT-51367 Kaunas – Lithuania*

ABSTRACT

The research is done by analyzing the different cases of dynamic thermal transmission. The dynamic thermal transmission simulation is based on finite-difference calculation method. The great impact on the accuracy of calculation has a criteria of similarity, which is also known as Fourier number. This number shows the similarity of thermal variation in conditional layers of enclosures. Most scientists recommend to use 0.5 value of Fourier number and perform calculating of a transient heat transfer in all cases. The value of Fourier number is determined in order to acquire the reliable calculation results with optimal accuracy. The research analyses the two cases of wall construction. In both cases the thickness and thermal transmittance of wall is the same, the difference is only in location of insulation layer. This layer is placed in first case – on interior of wall, in second case – on the exterior of wall construction. To compare the results of simulation with experimental research, transient heat transfer calculation spreadsheet was created. Our research has shown that value of Fourier number equal to 0.5 is not sufficient for calculations of transient heat transfer in multilayer wall.

Keywords: building envelope, transient heat transfer, Fourier number, multilayer enclosure

1. INTRODUCTION

Unsteady heat transfer can be characterized by the concept of heat transfer when heated (frozen) material's temperature varies continuously in time. In examining a simple case where the heat flow moves in one direction only, the differential heat conduction equation is expressed applying the finite difference method [1-3]:

$$\frac{\Delta\theta}{\Delta t} = a \frac{\Delta^2\theta}{\Delta x^2}, \quad (1)$$

where: $\Delta\theta$ – changes of temperature over a time step, (°C); Δt – time step, (s); Δx – layer's thickness, (m).

Calculation accuracy of unsteady heat transfer using the finite elements method depends on the selected values of Fourier and Biot numbers.

The Fourier number is designated by the symbol F_o and the equation for every layer of this number is [1, 4, 5]:

$$F_o = \frac{a \cdot \Delta z}{d^2} \quad (2)$$

where: a – the thermal diffusivity, (m²/s); Δz – the time step, (s); d – thickness of conditional layer, (m).

The thermal diffusivity of the material:

$$a = \frac{\lambda}{\rho \cdot c_p}, (m^2 / s) \quad (3)$$

where: λ – thermal conductivity, (W/(m·K)); ρ – material density, (kg/m³); c – specific thermal capacity, (J/(kg·K)).

The dependence of conditional layer thickness on the Fourier number and time step:

$$d = \sqrt{\frac{a \cdot \Delta z}{F_o}}, (m) \quad (4)$$

where: a – thermal diffusivity of material, (m²/s); d – thickness of conditional layer, (m); Δz - the time step, (s).

Fourier number F_o – shows the thickness (depth) of “equalization” in the layer during the selected time step Δz , i.e., the part of layer thickness Y for the temperature to equalize in the homogeneous layer from the initial moment during the time period Δz , when the temperature drop on both sides of the layer, whose thickness is Y , is 1K.

Suppose, there is an expanded polystyrene (EPS) layer with the following characteristics: $\lambda=0.07$ W/(m·K); $\rho=25$ kg/m³; $c_p=1340$ J/(kg·K), $d= 50$ mm, $\Delta z=0.1$ h, then, the calculations are performed according to [4]: $F_o \approx 0,301$ and $1/F_o \approx 3.322$.

Thus, if $\Delta z=0.1 \cdot 3.322 \approx 0.3322$ h, then $F_o \approx 0.9999$ and $1/F_o \approx 1.000$; in other words, during this time period, the temperature equalizes in all the thickness of the layer.

$$F_o = A \cdot \Delta z = \frac{\lambda \cdot \Delta z}{\rho \cdot c_p \cdot d^2} \quad (5)$$

where: A – thermal diffusion of layer, (1/s).

The Biot number is usually expressed as:

$$Bi = \frac{h \cdot d}{\lambda} \quad (6)$$

where: h – surface heat transfer coefficient, d – thickness of the surface layer of the enclosure, λ – thermal conductivity coefficient of the surface layer of the material.

The Biot number can also be expressed in the following way:

$$Bi = h_s \cdot \Delta R_{S.L.} = \frac{h_s}{\Lambda_{S.L.}} = \frac{\Delta R_{S.L.}}{1/h_s} \quad (7)$$

where: h_s – surface heat transfer coefficient; $\Delta R_{S.L.}$ – thermal resistance of the first surface layer; $\Lambda_{S.L.}$ – thermal conductance of the first surface layer (the inverse proportion of thermal resistance).

According to [6, 7], the limit value of the Fourier number is equal to 0.5. The values of this number higher than 0.5 causes significant errors in temperature calculations. In some cases, the temperature calculation average error increases significantly when the value of the Fourier number reaches 0.47 [8].

In case of transient heat transfer, the temperature in plane surrounding by different materials of enclosure is determined by the following equation (8):

$$\Theta'_n = \Theta_n + \left(\frac{\Theta_{n-1} - \Theta_n}{\Delta R_{n-1}} - \frac{\Theta_n - \Theta_{n+1}}{\Delta R_n} \right) \cdot \frac{2 \cdot \Delta z}{d_{n-1} \cdot c_{n-1} \cdot \rho_{n-1} + d_n \cdot c_n \cdot \rho_n} \quad (8)$$

where: Θ'_n – temperature of plane n at the present time moment; Δz – time period (calculation time step), (s); d_n – thickness of layer between “ n “ and “ $n+1$ “ planes, (m); c_n – specific thermal capacity

of layer between “ n ” and “ $n+1$ ” planes, $(J/(kg \cdot K))$; ρ_n – the material of layer between “ n ” and “ $n+1$ ” planes density, kg/m^3 ; $q'_{n/(n-1)}$ – the potential of heat flow density between “ n ” and “ $n-1$ ” planes at the time moment after time period Δz , (W/m^2) ; $q'_{(n+1)/n}$ – heat flow density between “ n ” and “ $n+1$ ” planes at the initial time moment z , i.e. the heat flow rate due to temperature difference $(\Theta_n - \Theta_{n+1})$, W/m^2 ; χ_{n-1} or χ_n – coefficient of area thermal capacitance of the layer “ $n-1$ ” and “ n ”, $(J/(m^2 \cdot K))$; $S_{(n+1)/(n-1)}$ – the average thermal receptivity of the material of both layers “ $(n-1)$ ” and “ n ”, $(W/(m^2 \cdot K))$; $\Delta t_{n/n}$ – temperature change in the plane “ n ” after the time period Δz passed from the initial time moment.

According to [4], it is recommended that the first surface layer thickness amounted to $1/2$ (or less) of the thickness of other layers, since it is important for obtaining the required Biot number. For the calculation of a unidimensional temperature field, when F_o is inside the enclosure, the stability criteria is the following: $(1-2 \cdot F_o) \geq 0$, from here $F_o \leq 0.5$;

When Bi is displayed on the surface of the wall, the stability criteria is the following: $(1-2 \cdot F_o - 2 \cdot Bi \cdot F_o) \geq 0$, from here $F_o \cdot (1+Bi) \leq 0.5$.

The second criterion with Bi is more sensitive than the first one; therefore, it has to be used for determining the critical (the largest allowed) calculation time step Δz :

The positive $Bi \leq 0.1$ is preferred.

The maximum allowed F_o is determined applying:

$$F_o \leq \frac{0,5}{1 + Bi} \quad (9)$$

Using the maximum allowed F_o , the maximum allowed time step is calculated:

$$\Delta z \leq \frac{F_o \cdot d^2}{a} \quad (10)$$

The finite elements difference explicit method is used for calculating new values using the already know ones.

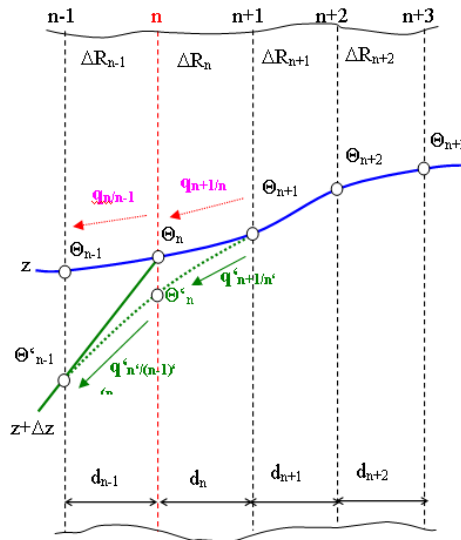


Fig. 1. Principle scheme for calculating the interlayer temperature of the enclosure

It is unclear whether the same rules affect multilayer enclosure. So in this research analyses two cases of wall construction. In both the cases the thickness and thermal transmittance of wall is the same, the difference is only in location of insulation layer. This layer is placed in first case – on interior of wall, in second case – on the exterior of wall construction. What are the optimal values of Fourier number of multilayer enclosure?

2. MATERIALS AND EQUIPMENT

Two building (wall) models were made for the experiments. Heat transfer coefficient of the internal surface of the enclosures of models WM-I and WM-II, which describes the surface heat transfer coefficient of the enclosure with the environment, is the following:

$$h_s = Nu \cdot \left(\frac{\lambda}{s} \right) + \frac{4 \cdot \sigma \cdot \left(\frac{T_s + T_{air}}{2} \right)^3}{\frac{1}{\varepsilon_1} + \frac{1}{\varepsilon_2} - 1}, (W/m^2 K) \quad (11)$$

where: $\sigma = 5.6704 \cdot 10^{-8}$ Stefan–Boltzmann constant, ($W \cdot m^{-2} \cdot K^{-4}$); s – thickness of air boundary layer, (m); Nu – Nusselt number calculated according to [9]; λ – thermal conductivity of still air, ($W/(m \cdot K)$); T_s – temperature of the surface, ($^{\circ}C$); T_{air} – surround air temperature, ($^{\circ}C$); ε_1 – emissivity of surface; ε_2 – emissivity of surrounding.

The measured thermal properties of materials used in wall models WM-I and WM-II are presented in Table 1. The thermal conductivity values of the materials were measured according to [10, 11] in lambda apparatus which meets the requirements of [12, 13]. The density of materials was determined in accordance with [14, 15].

The thermal capacitance values of common construction materials used in the experiment were selected from literature sources in accordance to the type and density of the materials. Models WM-I and WM-II were made of materials commonly used in practice Fig. 2. Five walls of the model 600x600x600 mm (length x width x height) were made of polystyrene boards $d_1=50+50$ mm. Heterogeneous enclosure of the models consists of two medium density wood fibre boards (MDF), with the thickness of $d_2=18+18$ mm, and one expanded polystyrene (EPS) board, $d_1=50$ mm.

Internal and external volumes of the models are identical, but the position of MDF massive layer in heterogeneous enclosures is different: in WM-I, it is oriented to the interior, and in WM-II, it is oriented to the exterior.

The thermal properties of the wall construction materials were measured and the results are presented in Table 1.

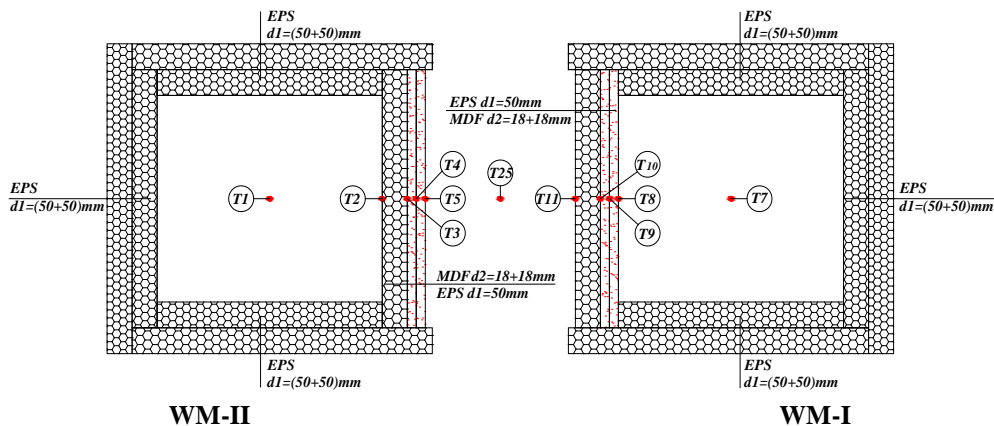
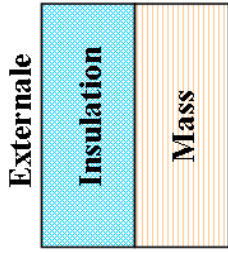


Fig. 2. Structural scheme of thermocouple arrangement in models. T– thermocouples

Table 1. The walls studied: WM-I and WM-II with the same values of thermal transmittance U , but with different values of internal areal thermal capacity

Wall models		
	WM-I	WM-II
Insulation (EPS - expanded polystyrene)		
Conductivity λ , (W/m·K)	0.039	0.039
Density ρ , (kg/m ³)	15.807	15.807
Thermal capacity c , (J/kg·K)	1450	1450
Mass (MDF - medium density wood fibreboard)		
Conductivity λ , (W/m·K)	0.12	0,12
Density ρ , (kg/m ³)	787.22	787.22
Thermal capacity c , (J/kg·K)	1430	1430
Thermal transmittance U_{wall} , (W/(m ² ·K))	0.57	0.57

3. EXPERIMENTAL AND RESULTS

In order to determine the accuracy of the calculation method, the experiment was carried out. On the basis of the experiment, the calculation program was created for the evaluation of unsteady heat exchange in multi-layered enclosures (using MS Excel). In conditional layers of the enclosure, temperature fluctuations are calculated using finite elements method, and the values of internal enclosure layers are estimated according to the equations given in Chapter 1.

The experiment was carried out by imitating climatic conditions in the climatic test chamber, in the Laboratory of Building Thermal Physics at Institute of Architecture and Construction of Kaunas University of Technology, (KTU ASI). Two spatial models, differing in the position of their high thermal resistance layer, i.e. inside and outside of the model, were constructed in the chamber. The aim of the experiment was to change the temperature of the surroundings by cooling and heating it and observe temperature changes in the walls and the interior of the models. In order to ensure the accuracy of the experiment, the values of thermal parameters of the materials were determined and the thermocouples measuring the temperature were calibrated.

During the experiment, the temperature was measured every one second and the average of one minute was recorded (one minute time step is also acceptable in calculations). Data accumulator DL-3 scanned the values of automatically measured temperatures, recorded them and presented in MS Excel format.

During the experiment, the dynamic temperature oscillation consisting of seven cooling and heating cycles was created in the climatic chamber using cooling and heating devices (Fig. 3). Before the experiment, steady temperature of $\Theta_i = +18.56$ °C was settled in the climatic chamber and inside the models WM-I and WM-II. Dispersion limits of the thermocouples (under steady state conditions) (T1...T25) were the following: $A_e = \pm 0.25$ °C Fig. 4.

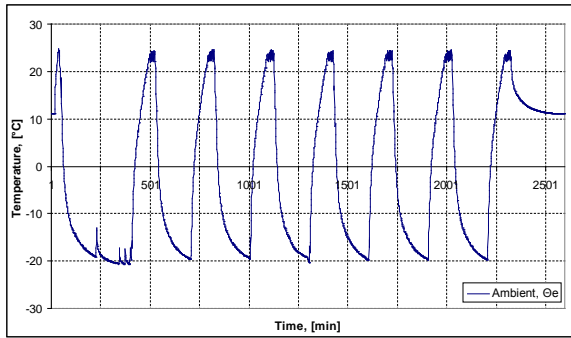


Fig. 3. The measured temperature of ambience during experiment

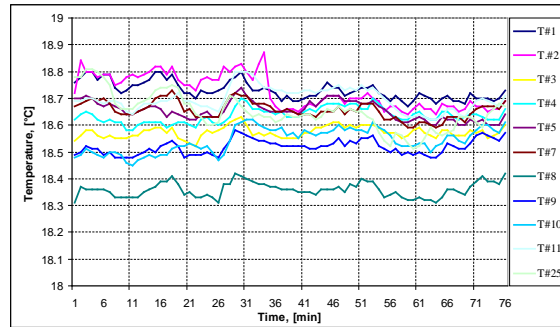


Fig. 4. Scattering of measured temperatures

The experiment begins with the cooling cycle, which lasts for three hours. The temperature in the climatic chamber is lowered to $\Theta_e = -20\text{ °C}$. When this cycle is over, a two-hour heating cycle begins, when the temperature is raised up to $\Theta_e = +25\text{ °C}$. The temperature oscillation amplitude is equal to $A_e = (+25\text{ °C}) - (-20\text{ °C})$.

Using the outdoor air temperature oscillation data obtained during the experiment, calculations were performed in order to determine the temperature of the indoor air and wall interlayers. The temperatures were compared with the values measured during the experiment. The accuracy of the calculations in the non-homogeneous (multi-layered) enclosure depends on the Fourier number, which defines the conditions of gradual change and the selection of the rational number of conditional layers. When there is a significant difference among the Fourier number values of different layers in multi-layered enclosure $F_{oMDF} = 0.3553$ and $F_{oEPS} = 0.3266$, the temperature distribution (blue curve) obtained using the calculation program correlate with the experimental data (red curve) Fig. 5, but does not match within a desirable accuracy.

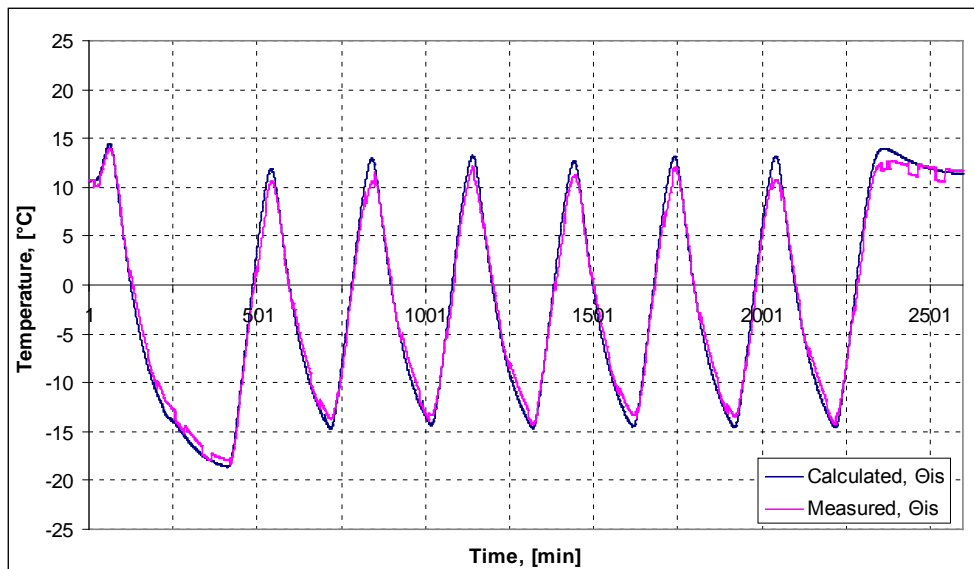


Fig. 5. Correlation of experimental temperature value of the internal surface of multi-layered enclosures of WM-I model with temperature values obtained using the calculation program, when $F_{oMDF} = 0.3553$; $F_{oEPS} = 0.3266$

Thus, the experiment clearly shows that the least distorted calculation results were obtained when the layers of multi-layered enclosure made of different materials were divided into rational layers so the values of the Fourier number for both layers were closely equal. In case of the experimental calculation, the values were $F_{oMDF} = 0.177$ and $F_{oEPS} = 0.1633$. The blue curve,

representing the distribution of the temperature calculated using the calculation program, completely correlates with the red curve representing the experimental data in Fig. 6.

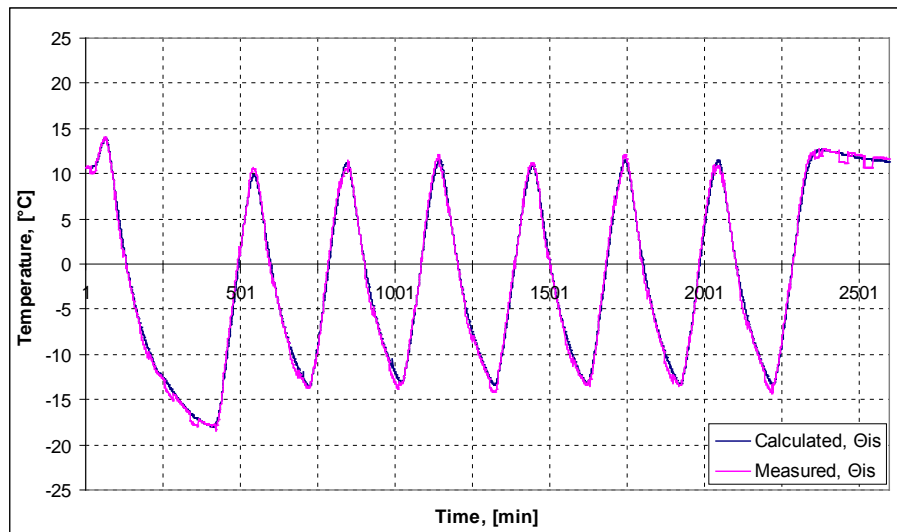


Fig. 6. Correlation of experimental temperature value of the internal surface of multi-layered enclosures of WM-I model with temperature values obtained using the calculation program, when $F_{oMDF}=0.177$; $F_{oEPS}=0.1633$

The optimal accuracy can be obtained as Fourier number is around $Fo=1/6=0.1666$ [1]; but one has to remember that the lower Fo value also means a bigger amount of calculation. The calculation analysis has shown that the least disagreement between calculated and experimental-measured values for model with massive layer inside the model was acquired with $Fo\approx 0.17$ (absolute error in temperature amplitude was -0.4%). Calculation results with $Fo\approx 0.085$ gave $+3.90\%$, and with $Fo\approx 0.23$ gave $+3.3\%$ absolute error in temperature amplitude values.

The calculation method is sufficiently accurate for carrying out further research.

4. CONCLUSIONS

Our research has shown that 0.5 value of Fourier number to calculate a transient heat transfer in multilayer walls is insufficient. The least distorted calculation results were obtained when the multi-layered enclosure was divided into conditional layers so that their values of the Fourier number were almost uniform and the value of Fourier number was around to $1/6$, i.e. around 0.17.

REFERENCE

1. STANKEVIČIUS, V.; BARKAUSKAS, V. Building physics. Kaunas. Technologija, 2000. 281 p. ISBN 9986-13-740-3.
2. PHOKIN, K. PH. Physics of building's envelope. 5th Edition. Moscow. ABOK-PRESS, 2006. 256 p. ISBN 5-98267-023-5.
3. BOGOSLOVSKIJ, V. N. Building physics. Moscow. 1982. 331 p.
4. INCROPERA, Frank, P.; DEWITT, David, P.; BERGMAN, Theodore, L.; LAVIN, Adriene, S. Fundamentals of Heat and Mass Transfer. 6th Edition. New York. John Wiley&Sons, 2007. 1024 p. ISBN 978-0-471-45728-2.
5. HAGENTOFT, C. E. Introduction to Building Physics. Lund, 2001, p. 125–135.
6. KARBAUSKAITĖ, J., STANKEVIČIUS, V., BURLINGIS, A., MORKVĖNAS, R. The Assessment of Freezing Risk in Apartment Buildings after the Supply Break Proceedings of the



- 8th Symposium on Building Physics in the Nordic Countries Copenhagen, Denmark, 2008 June 16–18, p. 1341–1347.
7. HENSEN, L. M., NAKHI, E. A. Fourier and Biot Numbers and the Accuracy of Conduction Modelling. Proceedings of the Conference on Building Environmental Performance: Facing the Future, University of York, 1994, p. 247–256.
 8. PUPEIKIS, D., BURLINGIS, A., STANKEVIČIUS, V. The Effect of the Fourier Number on Calculation of an Unsteady Heat Transfer of Building Walls. *Journal of Civil Engineering and Management*, 2010 Vol. 16, No. 2, p. 298–305.
 9. LST EN 673:2011 Glass in building – Determination of thermal transmittance (U value) – Calculation method. Brussels, 2011. 18p.
 10. LST EN 12667:2002. Thermal performance of building materials and products. Determination of thermal resistance by means of guarded hot plate and heat flow meter methods. Products of high and medium thermal resistance. Brussels, 2002. 53p.
 11. STANKEVIČIUS V., KAIRYS L. The effect of stochastically dependent physical parameters on the material's thermal receptivity coefficient. *Materials Science*. 2005, Vol. 11, No. 2, p. 188–192.
 12. ISO 8301:1991. Thermal insulation. Determination of steady-state thermal resistance and related properties. Heat flow meter apparatus. 1991. 40 p.
 13. ŠADAUSKIENĖ J., BLIŪDŽIUS R., RAMANAUSKAS J., GRICIUTĖ G. Analysis of distribution of properties of expanded polystyrene in production and their changes in exploitation conditions. *Materials Science*, 2009 Vol. 12, No. 4, p. 372–376.
 14. LST EN 1602:1998 Thermal insulating products for building applications – Determination of the apparent density. Brussels, 1998. 5 p.
 15. LST EN 1602:1998/AC:2003 Thermal insulating products for building applications – Determination of the apparent density. Brussels, 2003. 2 p.



INVESTIGATION OF ELECTROMAGNETIC HARVESTER WITH FLAT STRUCTURE AND LOW VOLTAGE RECTIFIER

I. Gornevs

*Institute of Radio Electronics
Riga Technical University
Azenes 12, Riga, LV-1048 – Latvia*

J. Blums

*Institute of Technical Physics,
Riga Technical University
Azenes 14, Riga, LV-1048 – Latvia*

ABSTRACT

As electronics decrease in size, power consumption moves toward the level of energy found in environmental vibration sources, making energy harvesters more promising as renewable energy sources. Wearable and portable electronics are considerable as main field for such research, because of requiring compact energy sources which can be exploited effectively. Depending on available volume and frequency range, different physical principles are used to convert mechanical energy into electrical. Harvesters using electromagnetic inductance produce higher power in low frequencies, therefore they were chosen for current research. It is shown that flat construction inductors have low occupied volume and it is possible to estimate shape of generated voltage pulses as well as produced power, considering inductor shape, conductor and relation between size of magnet and inductor. Accordingly it is possible to find best fitting parameters of harvester for needed results in specific situation. Generated voltage level of harvesters in many occasions is low and fully dependent on effective transformation. To increase effectiveness, low voltage rectification system is under investigation. It utilizes field effect transistors, creating equivalent of the diode with threshold voltage level under 100 mV.

Keywords: energy harvesters, electromagnetic harvester, low voltage rectification, efficiency, power management

1. INTRODUCTION

There has been a growing interest in devices suitable for generation of power from human motion over the last few years [1]. The interest in this kind of energy sources is associated also with apparel integrated devices, imparting new functions (health monitoring, communication, positioning, entertainment, etc.). Nowadays such devices are powered by batteries or rechargeable accumulators. Considering the fact that batteries have to be replaced and accumulators to be recharged, it is not suitable way. Mobile power sources are necessary for successful operation of such devices.

Integrated electronic devices should be utilized easily, should not essentially change size and weight of the clothing and should not lose operation after laundry care process. Many proposed electromagnetic harvesters, which convert mechanical energy of human motion into electrical energy, are created as three-dimensional devices with conventional cylindrical coil and a magnet moving inside it [2, 3]. This construction is not suitable for integration into clothing as each item of the apparel consists of two-dimensional parts. So flat structure for electromagnetic harvester is one of the ways to deal with the problem.

In the efforts of making perfect combination of low power consumer and generator, specific problems were observed, one of them is low generated voltage level. For now most effective way to

correct that is usage of switching power supplies, but they require direct current at input. Ordinary method of rectification will not help because of high threshold level (consequently – high efficiency losses). Here come their equivalents with lowest threshold – active rectification systems in various kinds of implementation like [4-6], however they require continuous control during the operation. The best passive variant in this perspective is backward diode [7], sadly it has downside when higher voltages (approximately 0.6V and up) could also be present – it starts conducting in both directions.

Consequently, overcoming this obstacle could greatly help using low power generators expediently and developing self-powered systems. So another approach for low voltage rectification is presented in this paper. Its threshold voltage is close to the one of a backward diode (below 100 mV) and is controllable. It is also capable to withstand higher reversed voltages like ordinary diodes and necessity for control can be temporary. Proposed solution can be used with low voltage levels where common rectifiers are not satisfactory or active rectification is not implementable or preferable.

2. ELECTROMAGNETIC HARVESTER WITH FLAT STRUCTURE

2.1. Experimental model

Electromagnetic harvester works according to mechanism of electromagnetic induction. Conductor placed in altering magnetic flux creates potential difference across it, so when a permanent magnet is moved along a conductor, or vice versa, an electromotive force is created. If the wire is connected to an electrical load, current will flow, consequently converting the mechanical energy of motion into electrical energy.

In the study conductor was formed as spiral shaped wire on a flat plane. Windings were isolated and placed as close as possible, to reduce total area and make it more suitable for integration into clothing. Diameter of coil was 25 mm, it had 50 windings of copper wire with diameter 0.22mm. Magnet was chosen with a flat structure that can produce strongest magnetic field – neodymium (Nd₂Fe₁₄B) magnet [8]. Measured magnetic inductance near its surface was 0.2 T, size was 18x18x2 mm.

To test the generator in controlled conditions, automated manipulator was created. It can move magnet along the coil in controllable speed and distance from it.

2.2. Mathematical model

To characterize coils as electric generators, principal mathematical model for specific shape and parameters can be created. To simplify calculations we assume spiral shaped coil as one round winding of conductor, which is crossed by perpendicular magnetic flux produced by rectangular magnet which size is a lot bigger than diameter of a coil. According to Faraday's law (1):

$$\varepsilon = B \frac{dS}{dt} \quad (1)$$

ε – electromotive force [V], B – magnetic induction [T], S – area of a loop of the conductor crossed by magnetic field [m²], t – time [s].

To calculate electromotive force, crossed area of circle at specific moment of time must be known. It can be estimated as area of segment ACB (fig.1):

$$S_{segment} = S_{sector} - S_{triangle} = \alpha r^2 - (r-h)\sqrt{r^2 - (r-h)^2} \quad (2)$$

α – half of sector AOBC angle, r – radius [m], h – height of segment [m].

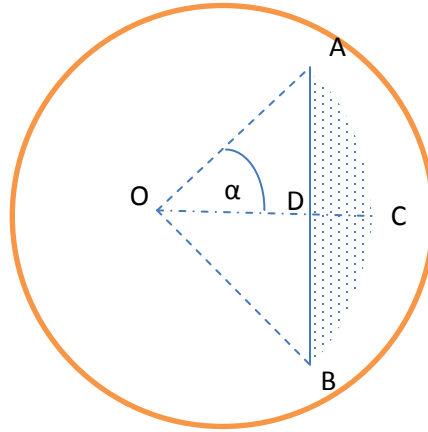


Fig.1. Calculations of circle crossed area as segment ACB

Trajectory of magnet motion is along the diagonal, so momentary path is equal to segment height DC (3). Accordingly, angle α will follow equation (4).

$$h = vt \quad (3)$$

t – time of movement [s], v – speed of a magnet (magnetic field) [m/s].

$$\alpha = \arccos\left(\frac{r-h}{r}\right) \quad (4)$$

Putting (3) and (4) into equation (2), then into (1), after derivation we get equation that describes generated electromotive force for one round winding:

$$\varepsilon = 2rvB\sqrt{1-\left(1-\frac{vt}{r}\right)^2} \quad (5)$$

After getting evaluation of electromotive force for coil with one winding, according to Joule-Lenz law (6) it is possible to calculate produced energy (7). It is assumed that generated voltage V is equal to electromotive force ε .

$$E = \int P dt = \int \frac{V^2}{R} dt = \int \frac{\varepsilon^2}{R} dt \quad (6)$$

$$E = 5.33 \frac{B^2 r^3 v}{R} \quad (7)$$

E – energy [J], V – voltage [V], R – resistance of winding [Ω].

Equation (7) gives maximal possible generated energy of specific coil by the complete coverage of the winding by magnetic field (meaning $t=2r/v$).

3. LOW VOLTAGE RECTIFIER

3.1. Basic principle

Basic principle of formation of a channel of N-type enhancement mode metal oxide-semiconductor field-effect transistor (MOSFET) is shown in Fig. 2. While applied voltage to the gate (V_{GS}) is zero, there is no path for current to go from drain to source or vice versa (not taking

parasitic body diode into concern) (Fig. 2. a), but specific gate voltage (threshold voltage V_{th}) will attract free electrons and repel holes, thus forming channel underneath the gate (Fig. 2. b).

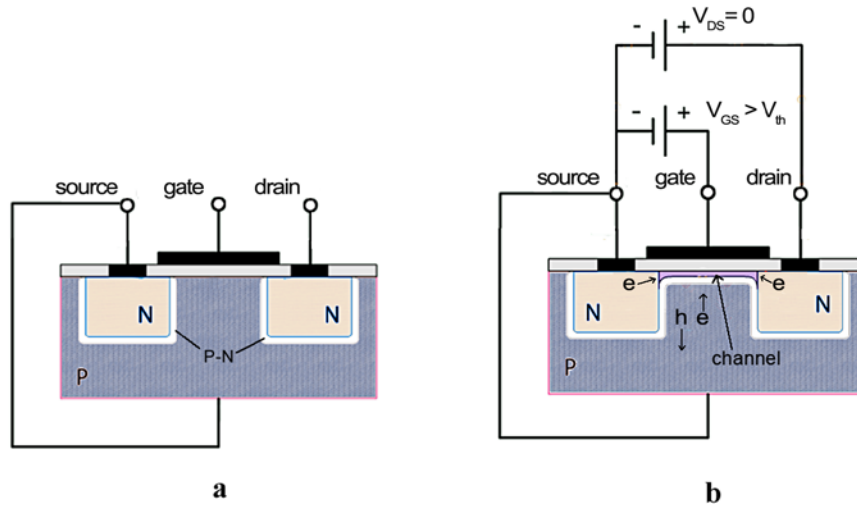


Fig. 2. Basic structure of N-type enhancement mode MOSFET (a) and formation of the channel (b). Movement of electrons and holes is shown with arrows (e and h)

Voltage applied to the drain-source region will pinch the channel (Fig. 3a), because it is lowering drain voltage relatively to the gate and the channel, while source-gate voltage stays fixed. If drain-source voltage is raised more, pinch region will move away from drain even more, hence blocking current flow. In normal operation narrowing of the channel is called saturation of transistor, it occurs when $V_{DS} > (V_{GS} - V_{th})$. To overcome that, gate-source voltage must be raised.

The idea is to use gate-source voltage identical to the threshold voltage to form a small channel, which will pinch and block any current flow with any drain-source voltage applied. But in the opposite direction (when source-drain voltage is applied) current will flow, because gate-drain voltage will be raised, opening the channel near the drain (Fig. 3b).

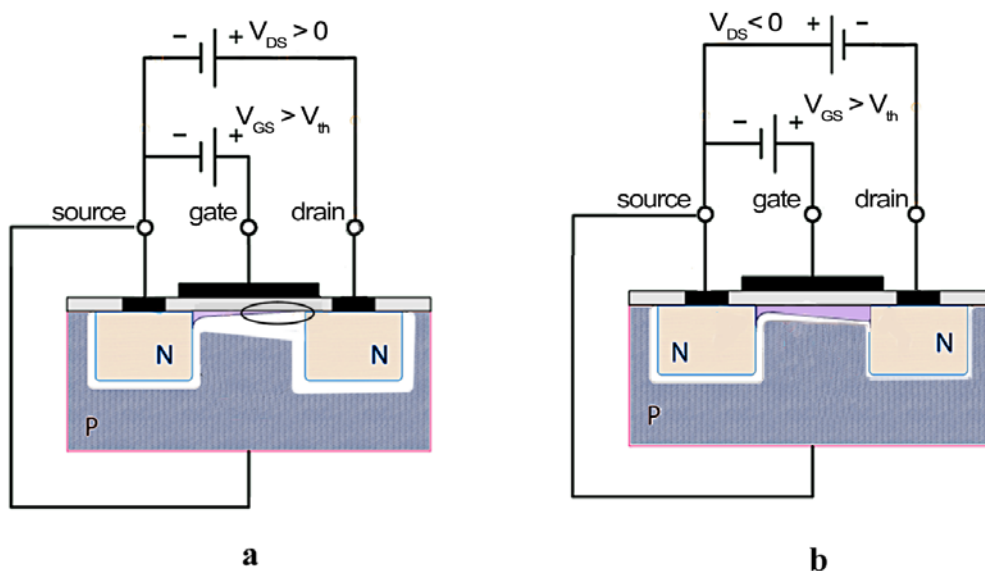


Fig. 3. Pinching of the channel (encircled) when drain-source voltage is applied (a) and its opening when source-drain voltage is applied (b)

Theoretically, forming a small channel with applied $V_{GS} = V_{th}$ will create rectifier between source and drain regions with zero opening voltage.

3.2. Experimental Current-Voltage characteristics

Tests were made for various MOSFETs. The aim of this research is not a comparison of different models or manufacturers but a demonstration of the effect, so it is shown on a one of *IRF* series power MOSFET *IRF7832*. Practical measurement shows that previously described principle is present and has some limitations. Gate-source voltage changes threshold voltage of the rectifier (Fig. 4a) and also raises reverse current (Fig. 4b).

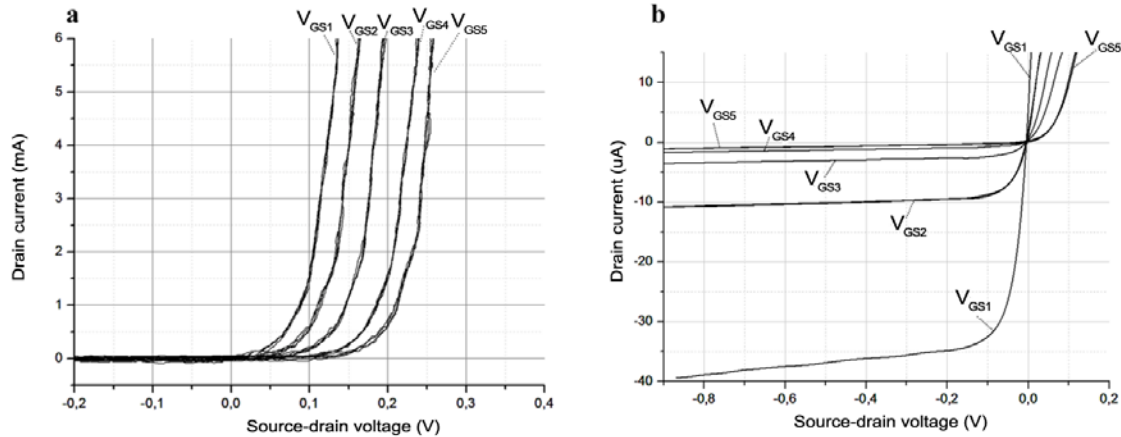


Fig. 4. Current-voltage (IV) curves of proposed rectifier forward current (a) and reverse current (b) with different gate-source voltage applied ($V_{GS1}=1.6V$, $V_{GS2}=1.5V$, $V_{GS3}=1.4V$, $V_{GS4}=1.3V$, $V_{GS5}=1.2V$)

As it is seen in Fig. 4a and b, changing gate-source voltage alters rectification “mode”. Acquired IV curves can be used to calculate resistance of specific rectifier as function of current.

4. RESULTS AND DISCUSSION

Electromagnetic harvester modelled with mathematical equation (5) for qualitative evaluation of produced signal shape comparing with experiments is shown in Fig. 5a, b.

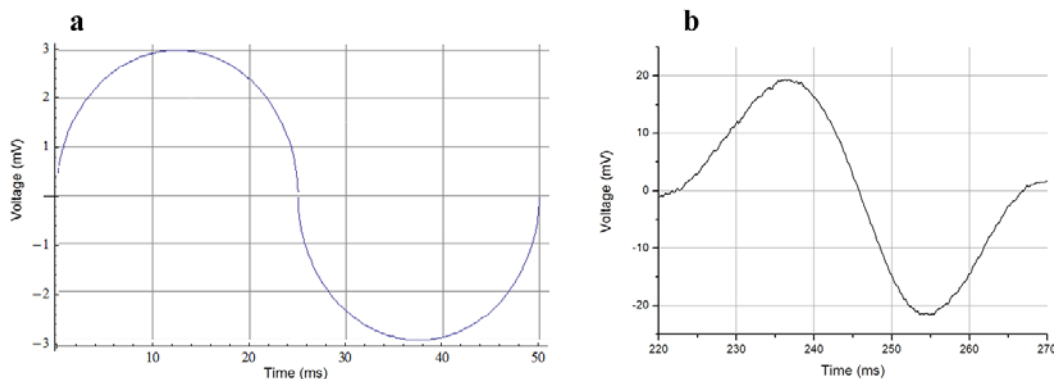


Fig. 5. Mathematical (a) and experimental model (b) for qualitative comparison

Dissimilarities in shape were created by non-ideal shape of the magnetic field. We still need to take into account that equation was made for one round winding, but spiral shaped coil consists of 25 windings, that increases generated voltage level accordingly. Also self-inductance was not included in calculations. Furthermore, with equation (7) it can be noted that generated energy is in

direct relation to the speed of the magnet, it is proven experimentally (Fig. 6). Produced energy was measured on a load resistance that is equal to the resistance of the coil.

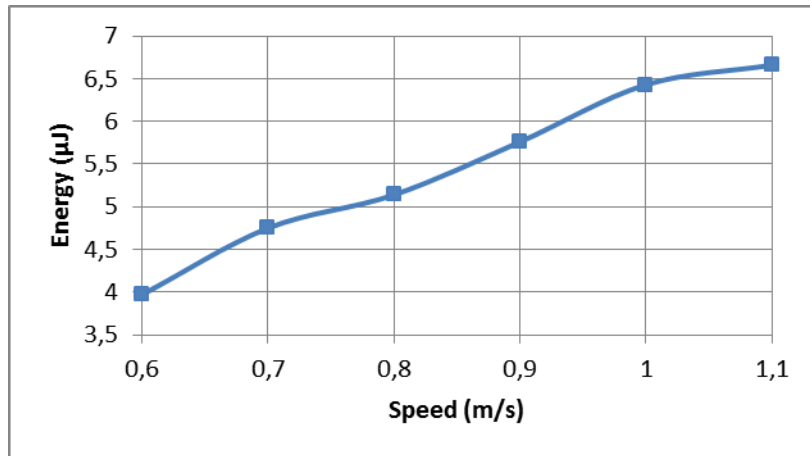


Fig. 6. Generated energy of one impulse related to magnet speed

If the energy generated at speed of 1.1 m/s, which is approximate speed of hand movement during walking speed of 6 km/h [9], is related to total volume of the generator (including magnet), energy and power densities can be obtained. Power density of $176 \mu\text{W}/\text{cm}^3$ for only one coil makes the proposed generator superior to the majority of low frequency electromagnetic motion harvesters listed in [1].

Having the mathematical model gives an opportunity to predict generated signal and adjust it to what is needed by changing properties of a coil and/or a magnet. It is also possible to make equations for different shapes of a coil, to exploit flat structured electromagnetic generator even further.

Practical implementation of such generator was also tested in [9]. Three coils were connected in series and placed one on another, three such structures then were connected in series and placed beside each other at specific distance. Generator was integrated into one side of a jacket, while flat neodymium magnet was placed into sleeve (Fig. 7.). Generated voltage was measured with PicoScope®2205 oscilloscope on a load resistance, which was equal to coils resistance.

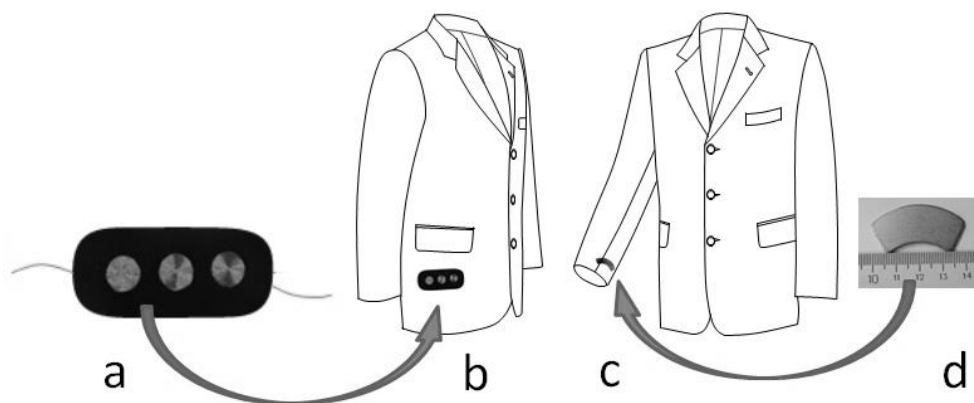


Fig. 7. Jacket with the electrical generator, a – set of flat spiral shaped coils, b – location of the inductive elements, c – location of the magnet, d – neodymium magnet [9]

While person wearing the jacket moves hands along body (walking etc.), altering magnetic flux produces electrical energy in the coils. Peak power generated while walking at 6 km/h for such device is 14 mW, but mean power up to 0.21 mW, which was defined as net generated energy on the load resistance divided by the time of the movement. These parameters fully depend on wearer's individual type of movements, that is why harvester must be optimized for it [9].

With one 3-layer coil it is possible to show improvements over existing rectifier elements, in this case, Schottky diode, as it has low threshold voltage. The same transistor as the one for IV curves measurement was used, applied gate-source voltage was 1.5 V (Fig. 4, V_{GS2}). Schottky diode was 1N5822. In a half-wave rectifier circuit drain and source were connected as cathode and anode of a diode. Magnet was moved along the coil with automatic manipulator at constant speed and distance. Produced pulses had amplitude of 220 mV, load resistance was equal to resistance of the coil – 3.7 Ω . Measurements were made with PicoScope®2205 oscilloscope. Rectified half period for Schottky (Fig.8. a) and MOSFET (Fig.8. b) is further used to calculate effectiveness.

From Fig .4. a and b rectifier resistance is calculated as a function of forward current and reverse voltage for selected operation mode (gate-source voltage). It is done using curve fitting algorithms to get formula for instantaneous resistance calculations from measured voltage and current. As only half-period rectifier was used, reverse leakage current was taken as energy losses due rectification, so in this case actual efficiency of proposed solution can be evaluated as:

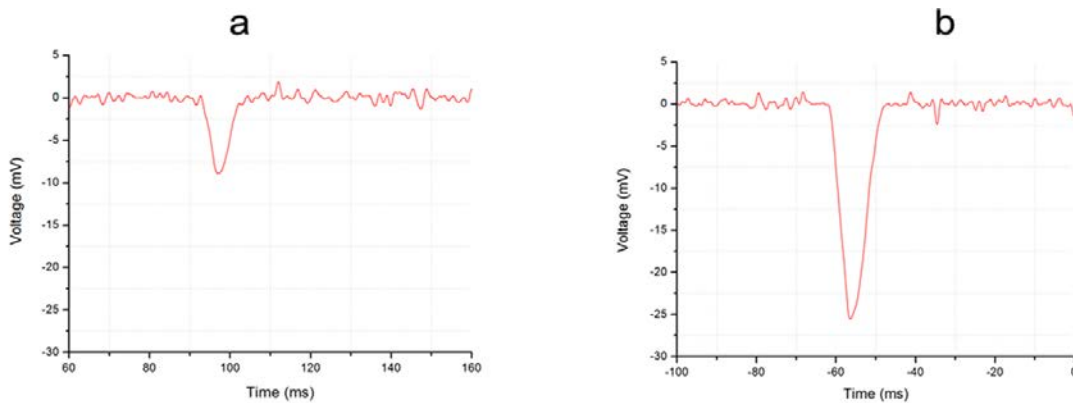


Fig. 8. Rectified half period of the signal with amplitude 220 mV from electromagnetic generator on a load resistor, a – using Schottky diode, b – using proposed rectifier

$$\eta = \frac{E_{load}}{E_{load} + E_{rect} + E_{leak}} \cdot 100\% \quad (8)$$

η – efficiency coefficient of specific rectifier, E_{load} – energy on a load after rectifying [J], E_{rect} – energy dissipated on a rectifier due rectification [J], E_{leak} – energy dissipated on a rectifier and a load during reversed voltage [J].

As load resistance is very low, both rectifiers resistances give relevant losses. Calculated efficiency for Schottky diode is $\eta_{Schottky} = 3.04\%$, while $\eta_{proposed_rectifier} = 11.14\%$. Even though leakage current of Schottky diode for 0.2 V of reverse voltage is only 0.9 μ A, comparing to 9.4 μ A of the proposed rectifier at same voltage level (Fig.4. b), acquired energy on a load compensates it.

While proposed rectifier reverse resistance is much lower than the one of Schottky diode, it is linear as function of reverse voltage, meaning that after some point leakage current will not rise as steeply as for Schottky. So for specific reverse voltage region proposed rectifier can be assumed as fixed current source. But if generated current is low, lower leakage current is preferable.

As proposed rectifier has controlled threshold level, it makes it more easy to use in different schematics. It is possible to find more suitable rectifier mode for specific situation, regarding what

is more relevant – small threshold or small leakages, or some combination of them. Since different models of transistors have different parameters, they can also be adjusted in different range, giving more possibilities for altering the rectifier.

5. CONCLUSION

Electromagnetic harvester with a flat structure was presented. It is possible to make low occupied volume motion energy harvester that can be also suitable for integration into apparel. Because of flat profile, overall power density is higher than for many of previously stated harvesters. With mathematical model it is possible to predict shape of generated pulses and maximal possible energy. Since generated voltage level is low, appropriate way to rectify it is being researched.

Low voltage rectifier with controllable threshold voltage and leakage current was described. It is possible to set and alter these parameters within some range with constant voltage. Unlike for active rectifiers, there is no need for constant monitoring of incoming signal polarity. Its usage for rectifying voltage amplitude of 220 mV increases effectiveness from 3% to 11%, when compared to Schottky diode.

REFERENCES

1. MITCHESON P. D., E. YEATMAN M., RAO KONDALA G., HOLMES A.S., T. C., Green Energy Harvesting From Human and Machine Motion for Wireless Electronic Devices, *Proceedings of the IEEE*, 2008, Vol. 96, No. 9.
2. SAHA C.R., O'DONNELL T., WANG N., MCCLOSKEY P., Electromagnetic generator for harvesting energy from human motion, *Sensors and Actuators A*, 2008, Vol. 147, p. 248–253.
3. TROESTER G., T. VON BUEREN, Design and optimization of a linear vibration-driven electromagnetic micro-power generator, *Sensors and Actuators A*, 2007, Vol. 135, p. 765–775.
4. SEEMAN M. D., SANDERS S. R., RABAEY J. M., An Ultra-Low-Power Management IC for energy-Scavenged Wireless Sensor Nodes, in *Proc. IEEE PESC Conf.*, 2008, p. 925–931.
5. DAYAL R., Design and Implementation of a Direct AC–DC Boost Converter for Low-Voltage Energy Harvesting, *IEEE Trans. Industrial Electronics*, June, 2011, p. 2387–2396.
6. TOMASZ M., Use a self-powered op amp to create a low-leakage rectifier, *EDN*, October, 2011, p. 61–62.
7. IGUMNOV D., KOSTYNINA G., *Basics of semiconductor Electronics*. Telekom. 2011. 394 p. (in Russian).
8. FRADEN J. *Handbook of Modern Sensors: Physics, Designs, and Applications*, 4th Ed. USA: Springer. p. 73, ISBN 1441964657.
9. TARLECKA G., BLUMS J., VILUMSONE A., GORNEVS I., The structure of the electromechanical converter and it's integration in apparel. *Scientific Journal of Riga Technical University. Material Science. Textile and Clothing Technology*. 2011, Vol. 6, p. 123–129.



HEAT RATE OPTIMIZATION OPPORTUNITIES

K. Grinbergs, P. Shipkovs
Riga Technical University
Azenes 16/20, LV-1048 Riga – Latvia

P. Shipkovs
Institute of Physical Energetics
Aizkraukles 21, LV-1006 Riga – Latvia

ABSTRACT

Heat generation at industrial boiler houses is extremely unstable. This is due to external air temperature, which require a large capacity reserve. Evaluating of deviation in boiler house heat loads from average heat consumption throughout the year, one must conclude that generated heat either considerably exceeds or falls short of average consumption. These deviations from the average are a normal reaction to fluctuations in external air temperature. A boiler house should be designed considering the peak load reserve, although this reserve is often so high that capacity would be sufficient for heating considerably larger areas. Having analyzed this, the question arises about what impact the selection of boiler house capacity and the amount of sold thermal energy has on heat tariffs. In our research will analyze the situation with a certain operating natural gas boiler house, evaluating expenses related to creating and operating this boiler house. However, in the future it is necessary to diversify thermal energy use it would allow to balance heat consumption between calendar months. Therefore in second part of our research we will analyze the impact of thermal energy consumption on heating prices.

Keywords: heat rate, thermal energy costs, cost optimization

1. INTRODUCTION

Decreased heat consumption in summer period considerably reduce heat-producing equipment efficiency, since the amount of sold heat shrinking much more than the heat energy losses in the supply network. Heat losses invested in isolated water pipes are calculated by the following formula [1, 4]:

$$N_{loss} = \frac{K(t_1 + t_2 - 2t_{gr}) \cdot L}{1000}, (kW) \quad (1)$$

where: K – specific heat loss coefficient [W/m⁰K], t₁ – incoming coolant (water) temperature [°C], t₂ – outgoing heating medium temperature [°C], t_{gr} – soil temperature [°C], L – longitude of constant diameter heating pipe [m].

These calculations are created to determine the heat losses during its transportation to a certain distance, but in reality coolant continuously circulates in the heating network, so the actual heat losses are considerably higher. Heating network efficiency in annual terms is given by following formula [1]:

$$n = \frac{Q_{sold}}{Q_{released}} \cdot 100, \quad (2)$$

where: Q_{sold} – amount of heat energy sold, MWh/ per year, Q_{released} - release heat energy amount, MWh/ per year.

The above-mentioned formula refers the actual boiler house efficiency per year and shows real heat loss impact. Fig. 1 shows existing regional boiler houses heat energy sold analysis and deviation from the average heat sold indicators per year. Fig. 2 shows that the increase in outdoor air temperature considerably decreases the heating facilities efficiency. If in February on 7 MWh

sold 1 MWh is consumed in heat energy loss, then for example in July on 1.5 MWh sold 1 MWh is consumed in heat energy losses. Occurs significant drop in boiler house efficiency, which affects cost of thermal energy to the consumer.

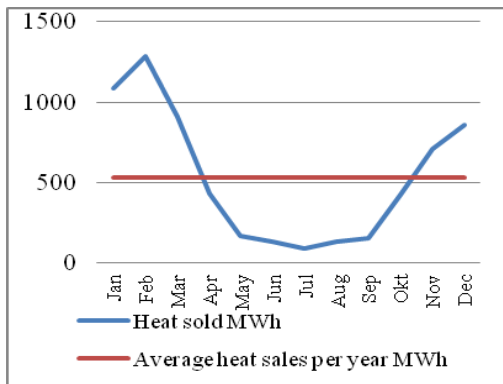


Fig. 1. sold heat changes in annual terms

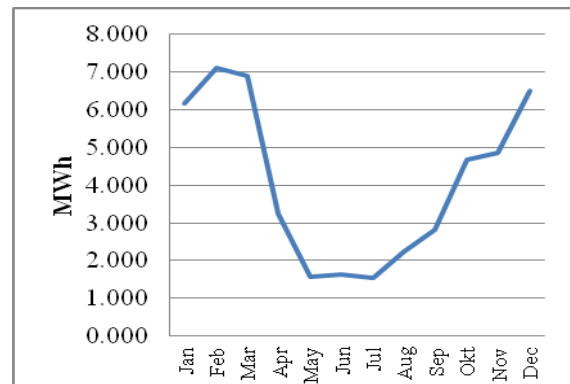


Fig. 2. Sold heat amount on heat loss

Considering the aforementioned circumstances, a simulation has been created in order to evaluate expenses that are related to creation and operation of an existing boiler house, and considers two other variants. In one case, the capacity of the boiler house is reduced to the requirement for a given year (calculated actual heat load for the year). In the other, the capacity is selected without considering peak loads observed during the year. The purpose is to evaluate installation and operation expenses for three distinct boiler house capacities and calculate the amount of heat overspent by the average heat consumer on “excess” load in centralised heating networks, considering the expense items composing the heating tariff. As well as the boiler house capacity the heat energy consumption on customer side has affect on heat tariffs. So another simulation has been created in order to evaluate the heat energy consumption impact on reducing heat tariff.

2. HEATING TARIFF EXPENSE ITEMS INTENSITY ON HEAT ENERGY PRICE

Table 1 (data has been adopted from approved heat energy rate of existing regional boiler houses [2]) provides three examples of heat tariff calculation. Each of the table columns shows various boiler house capacities with the relevant installation and maintenance expenses. The first column specifies the current boiler house capacity, the second indicates the actual required capacity for a given year, and the final column specifies the capacity without accounting for peak loads. Each of the columns details the expenses as part of the heat tariff, allowing to determine the price per MWh by dividing the total expenses by the amount of heat that would be sold. In order to allow an assessment of the impact of each expense item, it is assumed that the amount of heat generated and delivered to consumers will remain unchanged.

Table 1. Expense items constituting the heat tariff

Expense item	4.2 MW	3.12 MW	1.6 MW
Installed boiler capacity, MW	4.2	3.12	1.6
Heat delivered to consumers, MWh	6233	6233	6233
Heat supply network losses, MWh	1030	1030	1030
Heat output, MWh	7263	7263	7263
Heat supply and distribution losses, %	14	14	14
Duration of facility operation, h	1729.3	2327.9	4539.4
Fixed costs, EUR	62777	59139	54476



Labour costs EUR year	49610	49610	49610
Fixed asset depreciation EUR year	10133.59	8524.57	4584.81
Equipment maintenance and repair expenses EUR year	3033	1004.51	281.27
<i>Variable costs, EUR</i>	361750.2	358358.9	353817.5
Fuel expenses (assuming natural gas prices of 418.12 EUR/1000 m ³)	346264.1	346264.1	346264.1
Electricity costs EUR year	14744.89	11353.57	6812.13
Natural resource tax, EUR year	741.2	741.2	741.2
<i>Total expenses, EUR year</i>	424527	417498	408294
Heat tariff with different heat sale volumes, EUR	68.1	67.0	65.5

An analysis of the data in the table brings about the conclusion that, the higher the capacity of the boiler house, the more expensive its operation. Fixed expenses do not change or change only slightly, depending on the capacity of the boiler house and amount of heat generated (labour costs, fixed asset depreciation). However, variable expenses change in direct proportion to the amount of heat generated: consumption of fuel, electricity (the lower-capacity equipment would also consume less power) [2]. The expense items specified in Table No. 1 show that differences in expenses for different boiler house capacities are considerable, although their impact on the heat tariff is low. The heat tariff is primarily affected by the fixed assets used to generate the heat because, even though the purchase is an immediate expense, accounting of these expenses is gradual, as the expenses are written off with gradual depreciation of a fixed assessment. Table 2 shows the fixed assets for each boiler house capacity and the calculated depreciation value is reflected in Table 1. The fixed asset depreciation period is specified subjectively by a specialist (usually the economist or accountant), because it must account for the fact that the impact of a fixed asset on the heat tariff can be altered by changing the depreciation period. Therefore, it is often much more profitable to choose more expensive equipment with a longer service life than to use equipment without a known service life.

Table 2. Calculation of fixed asset depreciation

N. in a row	Depreciation, years	Value (EUR) of fixed assets at the b/h capacity 4.2	Depreciation value (EUR) of the current year, the power 4.2MW	Value (EUR) of fixed assets at the b/h capacity 3.12	Depreciation value (EUR) of the current year, the power 3.12MW	Value (EUR) of fixed assets at the b/h capacity 1.6	Depreciation value (EUR) of the current year, the power 1.6MW
1	12	15308.29	1275.69	13040.40	1086.70	9213.32	767.78
2	12	15308.29	1275.69	13040.40	1086.70	9213.32	767.78
3	8	10347.27	1293.41	9284.20	1160.52	3685.33	460.67
4	8	10347.27	1293.41	9284.20	1160.52	3685.33	460.67
5	5	963.86	192.77	765.41	153.08	368.53	73.71
6	5	963.86	192.77	765.41	153.08	368.53	73.71
7	5	5315.38	1063.08	4394.05	878.81	2267.90	453.58
8	20	36853.30	1842.66	30474.84	1523.74	15946.14	797.31
9	8	3756.20	469.53	2905.74	363.22	1630.05	203.76
10	5	2055.28	411.06	1559.18	311.84	892.98	178.60
11	5	1063.08	212.62	921.33	184.27	524.45	104.89
12	10	4039.69	403.97	3118.36	311.84	1488.31	148.83
13	5	1034.73	206.95	751.24	150.25	467.75	93.55
		<i>107356.48</i>	<i>10133.59</i>	<i>90304.75</i>	<i>8524.57</i>	<i>49751.95</i>	<i>4584.81</i>

Table 2 indicates that, although the initial value of equipment at purchase was different in terms of expenses, their impact on the heat tariff is reduced considerably with depreciation, representing 2.4%, 2.2% and 1.1% respectively (as seen in Table 2). This leads to the conclusion that the choice of boiler house loads does not significantly restrict initial expenses and the initial value of a fixed asset does not play a major role. Thus, a higher capacity reserve cannot considerably increase the price of heat for consumers, provided that the number of units is selected accordingly.

3. IMPACT OF CHANGES IN HEAT SALES ON THE HEAT TARIFF

On the basis of the aforementioned, long-term solutions must provide a way to balance heat consumption throughout the year, i.e. increase heat sales during the summer period. Heat consumption may vary widely, and it is in the interest of the producer and particularly the user to sell as much heat as possible, which would eventually result in a lower tariff. To analyse the potential gains from increasing, an assumption will be made and the heat producer's potential gain will be studied [2, 3]. Table No. 3 specifies different EUR/MWh tariffs across a wide amplitude of heat sales. Each column summarises the expenses that compose a specific heat tariff depending on the input parameters. The table includes several subjective items which might not apply in certain conditions. For instance, the specified capacity of heat generation equipment would not be necessary at lower heat output. Projected heat losses in the networks are unchanged because the length and configuration of heating networks are assumed to be constant. Fixed expenses do not change because this is a study of heat tariffs at constant heat generation equipment capacity. Thus, the heat tariff changes solely due to variable expenses. The number of these subjective assumptions undoubtedly affects the precision of calculations, but the trend can be analysed. The purpose is to study how much the heat tariff changes if heat sales increase. The tariff is calculated based on the currently applicable methodology. Fig. 3 (data taken from the Table 3) reflects heat tariffs given different amounts of heat actually sold. Considering that fixed expenses remain unchanged, the tariff reduction is achieved thanks to increased turnover, since the increase in heat sales affects the impact of fixed costs on the tariff. The purpose of any heat tariff calculation is to reduce the impact of fixed costs because, depending on the type of fuel, variable costs (mostly expenses on fuel) have very low impact (unless one considers the choice of fuel itself).

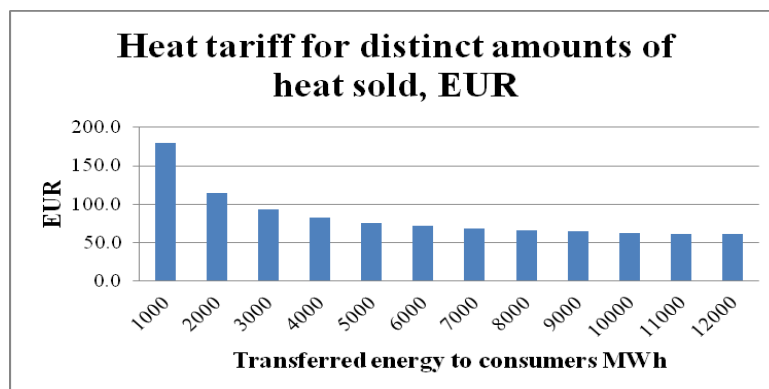


Fig. 3. Heat tariff changes

As the cost per MWh is reduced, the share of profit shrinks as well, but the most important matter is the change in profit as the amount of heat sold increases.



Table 3. Heat tariff changes with variable sales

Installed boiler capacity, MW	4.2	4.2	4.2	4.2	4.2	4.2	4.2	4.2	4.2	4.2	4.2	4.2
Heat delivered to consumers, MWh	1000	2000	3000	4000	5000	6000	7000	8000	9000	10000	11000	12000
Heat supply network losses, MWh	1200	1200	1200	1200	1200	1200	1200	1200	1200	1200	1200	1200
Heat output, MWh	2200	3200	4200	5200	6200	7200	8200	9200	10200	11200	12200	13200
Heat supply and distribution losses, %	55	38	29	23	19	17	15	13	12	11	10	9
Duration of facility operation, h	523.8	761.9	1000.0	1238.1	1476.2	1714.3	1952.4	2190.5	2428.6	2666.7	2904.8	3142.9
<i>Fixed costs, EUR</i>	70870	70870	70870	70870	70870	70870	70870	70870	70870	70870	70870	70870
Labour costs	49609	49609	49609	49609	49609	49609	49609	49609	49609	49609	49609	49609
Fixed asset depreciation	15591	15591	15591	15591	15591	15591	15591	15591	15591	15591	15591	15591
Equipment maintenance and repair expenses	5670	5670	5670	5670	5670	5670	5670	5670	5670	5670	5670	5670
<i>Variable costs, EUR</i>	109132.3	158737.9	208343.4	257949.0	307554.6	357160.2	406765.8	456371.3	505976.9	555582.5	605188.1	654793.7
Fuel costs (assuming a natural gas price of 418.12 EUR/1000 m ³)	104885.2	152560.3	200235.3	247910.4	295585.5	343260.6	390935.7	438610.8	486285.8	533960.9	581636.0	629311.1
Electricity costs	4022.6	5851.0	7679.5	9507.9	11336.4	13164.8	14993.3	16821.7	18650.1	20478.6	22307.0	24135.5
Natural resource tax, EUR	224.5	326.6	428.6	530.7	632.7	734.8	836.8	938.9	1040.9	1143.0	1245.0	1347.1
<i>Total expenses, EUR</i>	180002	229608	279213	328819	378425	428030	477636	527241	576847	626452	676058	725664
Heat tariff for distinct amounts of heat sold, EUR	180.0	114.8	93.1	82.2	75.7	71.3	68.2	65.9	64.1	62.6	61.5	60.5
Profit, 5% of tariff	9.00	5.74	4.65	4.11	3.78	3.57	3.41	3.30	3.20	3.13	3.07	3.02
Heat tariff with profit, EUR	189.00	120.54	97.72	86.31	79.47	74.91	71.65	69.20	67.30	65.78	64.53	63.50
Profit increase thanks to increased turnover, EUR	9000.11	11480.39	13960.67	16440.95	18921.23	21401.51	23881.79	26362.07	28842.35	31322.62	33802.90	36283.18

3.1. Changes in profit

Profit is assumed to constitute 5% of the eventual price per MWh sold. Fig. 4 (data taken from the table 3) shows that the price of heat falls with increasing turnover, although profits increase thanks to higher sales. It is essential to aim at achieving just such a situation.

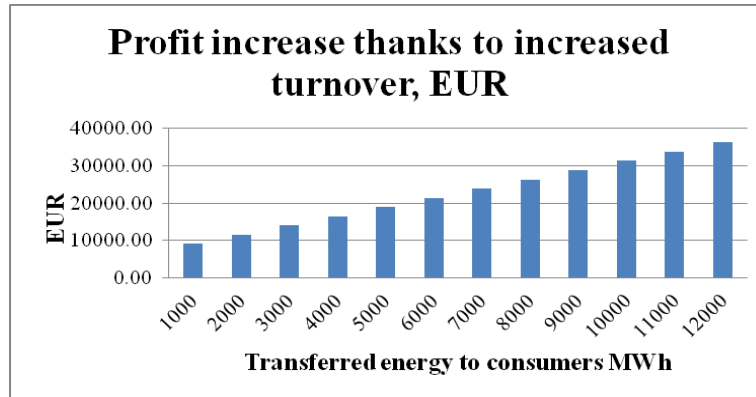


Fig. 4. Changes in profit

3.2. Impact of increased fuel consumption

Increased demand leads to reductions in other tariff cost positions, i.e. fuel costs. Differentiated natural gas tariffs are composed based on the amount of natural gas consumed by the consumer, i.e. a larger consumer receives better prices for their natural gas. Consumers are arranged in tiers: the higher the tier, the lower the delivery price. If the heat producer's consumption increases, their natural gas consumer tier may change, reducing the delivery price. Natural gas is one of the most expensive fuel types. The influence of natural gas costs on the heat tariff may approach 80%. Fig. 5, (data taken from the table 3) shows the reduction in heat tariffs that might be achieved by a change of delivery tiers and reduction in delivery pricing. However, a delivery tier change is possible only at a certain consumption level; in this case, the threshold would be 1000000nm³. Fig. 3, shows how this amount is achieved only in column 9. As heat sales increase to reach a higher natural gas delivery price tier, the heat tariff may be reduced by up to 4%.

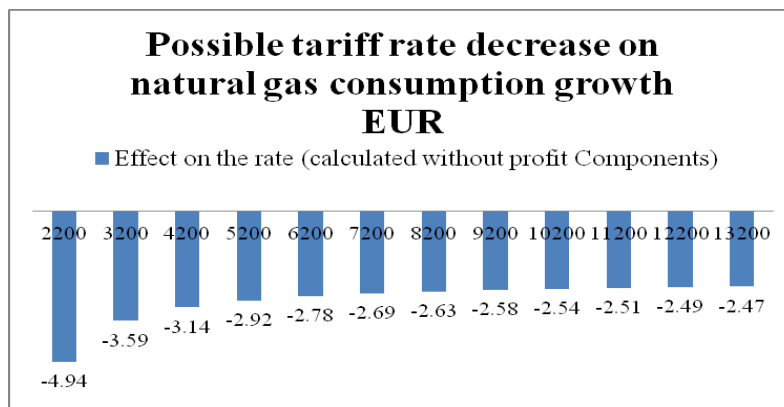


Fig. 5. Impact of fuel costs

Table 3 reflects data with increasing heat generation rather than heat sales; it is assumed that the amount of heat sales would increase accordingly – otherwise, the resulting tariff would not become lower.

3.3. Heat applications

What are the ways to increase heat sales? Obviously, heat is necessary during the heating period, to maintain comfortable indoor temperatures when the outside air temperature drops. During the summer period, heat sales shrink considerably; fixed costs remain constant, heat is still lost within the networks, and the energy efficiency of boiler houses is reduced. Although the heat tariff calculation includes this consideration, and the consumers accept it, there are ways to change the situation. Heat can also be used for the reverse purpose during the summer period – namely, for indoor cooling. Currently, indoor spaces are cooled using electric equipment. However, current technology allows the use of equipment that will provide cooling with the application of thermal energy [3]. Given a certain level of consumption, such a solution could be a long-term interest both for the heat producer and for the user. Fig. 6, (data taken from the table 3) includes a green line representing the fixed price of electricity and a purple line plotting the price of heat. In a certain situation, using thermal energy instead of electricity to cool indoor spaces would be 2.4 times cheaper if heat prices are reduced with increasing consumption.

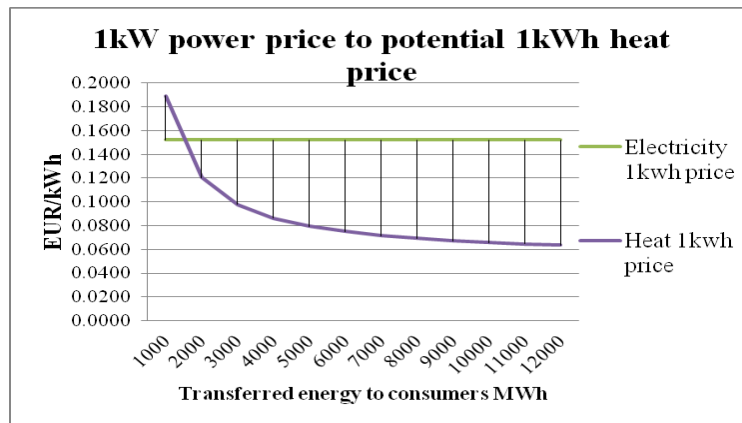


Fig. 6. Change in heat prices compared to electricity

4. CONCLUSIONS

The heat producer would not considerably increase heat tariffs for consumers by opting for higher-capacity facilities, given long-term operation and fixed cost depreciation.

With increased heat sales and lower natural gas delivery price, the heat tariff may be reduced.

If heat sales are increased, the tariff may be reduced owing to increased turnover. Future activities should focus on implementing projects that allow maximum use of heat within the centralised network, and sales do not solely on indoor heating.

Municipal governments with a small territory and concentrated infrastructure should design detailed plan ensuring infrastructure access to the industrial zones. Only maximum centralisation of heating networks will be able to achieve higher energy efficiency.

Increased heat sales are binding on both the producer and the consumer in the long term. The deciding factor is which side would take initiative, namely, whether the heat producer would provide the service in a centralised fashion or the consumer would install the appropriate equipment.

The above mentioned activity complex would lead to a thermal energy cost reduction for the consumer, in order to achieve this state is to overcome prejudice, associated with the use of heat meaning.



REFERENCES

1. RUBĪNA M., Siltumapgāde, Problēmas un risinājumi pašvaldību administratīvajās teritorijās, LZA Latvijas Fizikālās Enerģētikas institūts (FEI), Rīga, 2002.
2. Heat supply tariff calculation methodology, Riga, 2010 April 14.
3. RUBĪNA M, ŽĪGURS Ā, CRARS A., Advantages of district cooling in modern urban environment, RTU, Rīga, 2008,
4. ŽĪGURS A., TURLAJS D., KRĒSLIŅŠ A., CERS A., SOROČINS A., Improvement of Efficiency of District Heating Systems in Latvia, RTU, Rīga, 2010.



METHODOLOGY FOR GAS TRANSMISSION NETWORK AGE-DEPENDENT RELIABILITY ASSESSMENT CONSIDERING VARIATION OF INCIDENT CRITERIA

T. Iešmantas, R. Alzbutas

Lithuanian Energy Institute

Breslaujos str. 3, LT-44403 Kaunas – Lithuania

ABSTRACT

In order to quantify the risks posed by gas transmission networks, several international pipeline incident databases have been established. However, incidents reporting criteria differ and even changes of those criteria occur over time as a result of modifications in regulatory documents. This makes issues for practitioners seeking to decrease the uncertainty and apply as much data as possible. Due to this, practitioners avoid joint usage of those databases or even someone has to discard from analysis a quite relevant part of a sample contained on one database. Such issues may highly affect reliability and safety assessment results. In order to resolve these issues a new methodology will be presented.

Through the Bayesian framework the theoretical model will be applied to real gas transmission pipeline network incidents sample, which itself is non-homogeneous because it is affected by various criteria at different times. Finally, the new method effectiveness and its possible extensions will be demonstrated and discussed.

Keywords: Reliability, pipelines, networks, gas, Bayesian framework

1. INTRODUCTION

Gas transmission pipeline network is of great importance to any country using natural gases in its various technological processes. However, the usefulness cannot overshadow the threat posed to people and property by gas leakage or other incidents in the system. The importance of recognizing such events has been already expressed in EU Council Directive 96/82/EC (for this see [4, 5]). Upon the gas leakage event if ignited jet fire, flash fire or explosion could be a risky outcome [1]. In addition to this kind of risk, leakage of significant volume could lead to cascading events [2], i.e. loss of pressure and decrease of flow rate at the failed node or whole pipeline will lead even to degraded characteristics in other parts of the network, hence failing to achieve required or acceptable performance measures.

In order to quantify these risks, several widely recognized pipeline incident databases have been established. Organizations that initiated these databases are: US Department of Transportation Pipeline and Hazardous Materials Safety Administration Office of Pipeline Safety (further OPS), European Gas pipeline Incident data Group (EGIG), United Kingdom Onshore Pipeline Operators' Association (UKOPA), Canadian National Energy Board (NEB). Even though these databases are quite extensive (some more than others), their accident data seems to be never used together, i.e. statistical information carried by one database was not used to support information contained in another. Qualitative comparisons like Papadakis' [3] do not fill the gap as well. This is understandable since each database contains data about pipelines operated in remote geographical regions with varying soil types, under different incident data collection criteria. For longer time period even in single database there is variation of these criteria. Hence, direct integration of data into one analysis and sample raises suspicions about the validity of resulting inferences.

The purpose of this paper is to move beyond the qualitative pipeline accident database comparison and by providing a methodology to draw guidelines for quantitative integration of all available statistical information to improve reliability evaluation. In Section 2, we will review four

natural gas transmission pipeline network accidents databases; section 3 is devoted for development of a new methodology, which takes into consideration various incident data collection criteria; in section 4 we will apply our methodology to OPS database and demonstrate its effectiveness.

2. A BRIEF REVIEW OF PIPELINE ACCIDENT DATABASES

Mostly used and cited international pipeline incidents databases are as follows:

1. OPS (data from 1970 to 1990 in [7] , from 1991 to 2011 in [6]);
2. EGIG [8];
3. UKOPA [9];
4. NEB [10].

However, these databases are not identical and differ in covered time periods, incident criteria, geographical location of pipeline networks, etc. Main differences and similarities are summarized in the following table.

Table 1. International pipeline databases: similarities and differences

Name (Location)	Incident criteria	Database record types
OPS PHMSA (USA)	1970–1983: damage higher than 5000 \$; 1984–2002: damage higher than 50000 \$; 2003–2012: damage higher than 50000 \$; leaks above 84000 m ³ .	Incident frequencies and causes; detailed information for each incident as independent study; In all periods fatalities and injuries were recorded, explosions and fires as well.
EGIG (Europe)	All detectable unintentional gas releases.	Number of incidents, causes, distribution by detection methods, pipeline diameter, diameter, wall thickness, age, cover type; ignition frequency grouped by hole size and pipe diameter; injuries.
UKOPA (Great Britain)	All detectable unintentional gas releases.	Incidents frequency and causes; leakage volume distribution grouped by detection methods, pipeline diameter, wall thickness, soil type, age, type of cover.
NEB (Canada)	All detectable unintentional gas releases; the death of or serious injury to a person;	Incident frequencies.

As we can see, the data collection criteria highly differ for OPS database – whole time series is divided into three regions (Fig. 1), which cannot be analyzed as a one sample without appropriate model. Incident criteria can be thought as the basis for screening out insignificant events or applying censoring procedure.

It is important to realize, that the data represented by these databases do not cover every country and the usage of it to analyze samples from other, not covered by database, gas transmission networks might be questionable. On the other hand, samples from small countries like the one from Lithuanian gas pipeline network are not representative enough and then there is no other choice but to use the international experience.

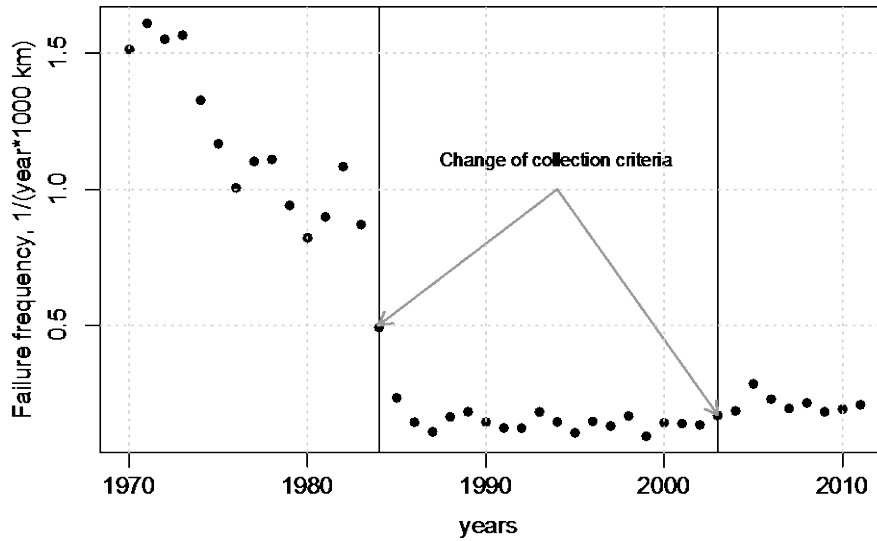


Fig. 1. Influence of collection criteria to incidents frequency (OPS database)

Regarding Lithuanian gas transmission pipeline network, data are quite scattered due to relatively short length of the pipelines and due to information collection of just accidents that resulted to gas explosions or fires. The criterion was changed in 2004 and since then all incidents resulting to gas leakage are recorded. To obtain more clear demonstration and to avoid the profusion of zero frequencies we pooled incidents data as well as pipeline lengths into 5-years bins (Fig. 2).

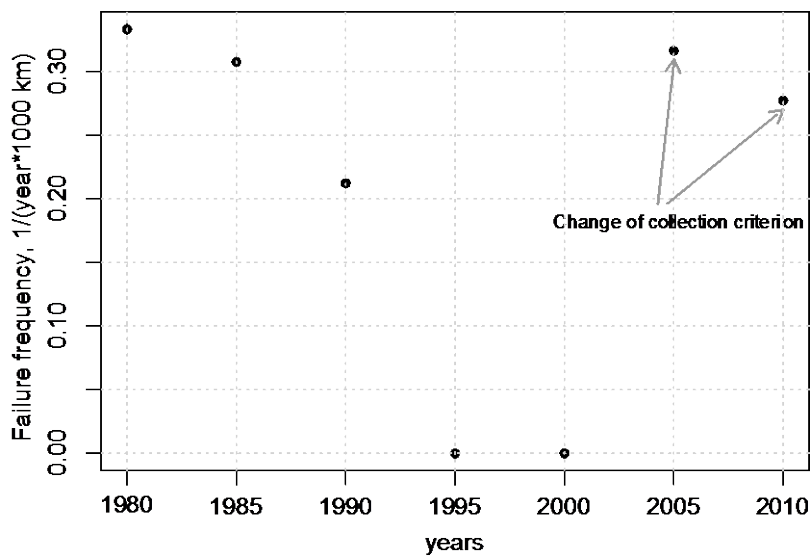


Fig. 2. Incidents frequency change over time for Lithuanian natural gas transmission network

Current state-of-art situation of pipeline reliability analysis involves physical (cracking, degradation, etc.) analysis (stochastic/deterministic) or statistical incidents investigation. In the following sections we confine ourselves to the second option due to several reasons – scientific literature covering physical analysis issues is quite well developed and the statistical incidents data aspects are left somewhat underrepresented. The usual approach is to concentrate on several (but possibly falsely thought) main characteristics like mean and variance and to conclude from these measures the overall state of pipeline system reliability.

3. NETWORK RELIABILITY ASSESSMENT CONSIDERING VARIATION OF INCIDENT CRITERIA

We present here the methodology of modelling incidents count data, when the incident definition changes over time. Although we will consider poissonian data, the methodology can be extended to other distributions. Suppose we have a number of incidents X over some time period Δ when the length of pipeline system is L and the exposure is $E = \Delta L$. However, to make things more clear we assume that $\Delta = I$ time units and drop this variable from our further notation. We assume that the incidents rate at the age t is the function of age and incident criteria at that time C_t , i.e.

$$\lambda = \lambda(t; C_t), \quad (1)$$

where C_t might be a set of different criteria, which we will assume to be mutually independent of each other and the occurrence of incidents can fall just in one of the categories defined by the set. In addition, let C denote the set of all criteria used, so that $C_t \subseteq C, \forall t$. However, this is not entirely correct, because in reality an incident could satisfy more than one criteria and model is an approximation of the phenomena. Further we will demonstrate how to construct sets of criteria in a way, to satisfy assumptions as close as possible.

One of the reasons why we would like to incorporate data under different collection criteria is to infer the current state or to predict reliability of network with highest certainty level possible. Hence, this requires incorporation of all available information into analysis. However, when we analyze data from databases we cannot observe how many incidents were collected under one or another criteria – just pooled sample is available to us. For example consider OPS database: in 1984 one of the criteria were tighten from 5000 \$ to 50000\$, but until this change, accidents with damage over 50000\$ were still observed. However, it is not possible to deduce how many accidents fell in this category and how many under the category with damage less that 50000\$ and more than 5000\$. The same is for the shift of criteria in 2003. Without knowing how many accidents fell under each category, how can we estimate overall state of network reliability? Or even more, how can we predict future incidents?

To answer that, we assume that each data point X_t is a sum of multinomial random variables – the number of incidents under each criteria out of overall number of accidents follows multinomial distribution with parameters p and X_t , where $p = (p_1, \dots, p_K)$ and K is the cardinality of C . More formally, if X_t^1, \dots, X_t^K are number of incidents under each criteria, then the distribution of vector of incidents (X_t^1, \dots, X_t^K) conditional on $\sum_{c_i} X_t^j$ is as follows:

$$(X_t^1, \dots, X_t^K) | \sum_{c_i} X_t^j = X_t \sim \text{Multinomial}(p, X_t), \quad (2)$$

where p is the probability vector of incidents. The unconditional distribution for each vector component is then:

$$X_t^j | p_j, \lambda(t) \sim \text{Poisson}(p_j E_t \lambda(t)); \quad (3)$$

p_j is the probability of incidents under j^{th} criterion.

Since the information of how many accidents X_t^j have occurred under each criterion is not available to us, all that could be done is to model the pooled sum $\sum_{c_i} X_t^j = X_t$ together with probability vector p . From the properties of Poisson distribution we easily conclude with a Criterion-Dependent-Poisson (CDP) model

$$X_t \sim \text{Poisson}(E_t \Lambda(t)), \quad (4)$$

where $\Lambda(t) = \lambda(t) \sum_{C_i} p_i$ and the summation is over those probabilities that correspond to the collection of criteria C_i . Hence, when we observe accidents satisfying all our criteria, we have that the sets C_i and C coincide, from what follows that $\Lambda(t) = \lambda(t) \sum_{C_i} p_i = \lambda(t)$, while in the case when we observe just accidents under subset of C , the incident rate will be always smaller than $\lambda(t)$, as expected.

Further we will illustrate the model with two accident criteria. Suppose we have an incident count time series $X = (X_1, \dots, X_T)$ and two criteria, i.e. $C = \{C^1, C^2\}$. For the half of the observation time, the data were collected according to criterion C^1 , while at the age $T/2 + 1$ the threshold was lifted to criterion C^2 . In reality it would be rarely the case that these two criteria are mutually independent. Sometimes might happen that accidents satisfying C^1 meets C^2 as well, e.g. C^1 is the damage of size 1000 \$, while C^2 is for 1000 \$ damage and greater than 10,000 m³ leakage. However, we can instead introduce another criterion $C'' = C^1 \setminus C^2$, which accounts for accidents under C^1 but not C^2 . This transformation gives us a set of mutually independent accidents $C' = \{C'', C^2\}$ for which we can assign probabilities $p = (p_1, p_2)$.

The probability of data to be in category $C^1 = C'' \cup C^2$ is then $p_1 + p_2 = 1$, while to be in category C^2 is p_2 . Hence, we have a following CBP model:

$$X_t \sim \begin{cases} \text{Poisson}(E_t \lambda(t)), & t = 1, T/2 \\ \text{Poisson}(E_t \lambda(t) p_2), & t = (T/2 + 1), T \end{cases}. \quad (5)$$

This model enables analyst to use all available data in order to evaluate and predict pipeline system reliability. Such possibility leads to more accurate inferences, since there is no need to discard part of statistical information. The general framework does not differ much from simple case presented above, and schematically can be represented as in flow-chart Fig. 3.

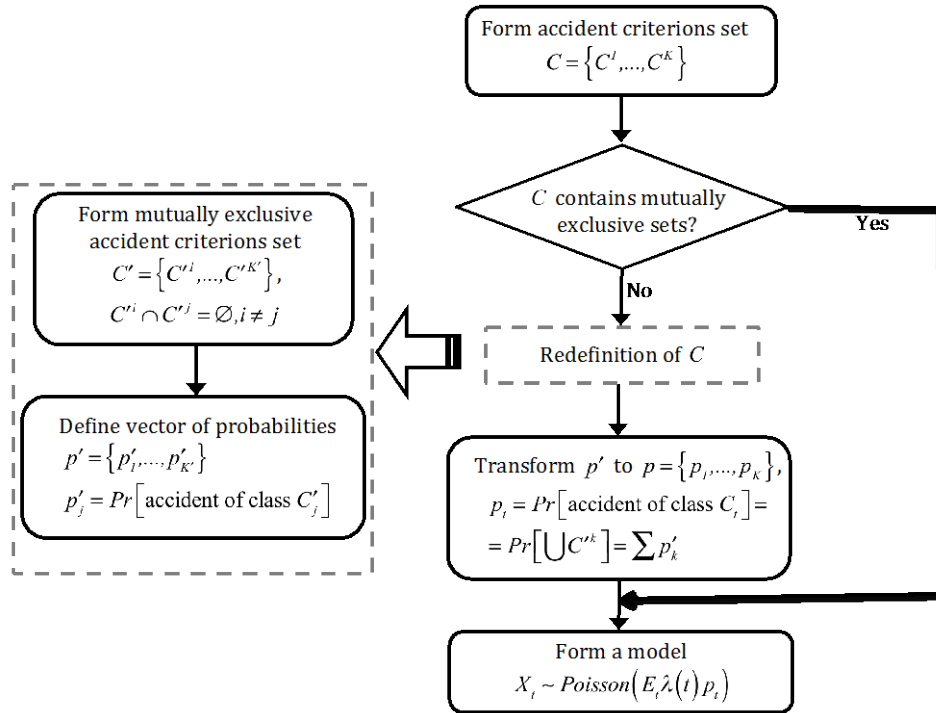


Fig. 3. Methodology of pipeline network reliability model construction under different accident criteria

4. CRITERION-BASED-POISSON MODEL FOR OPS PIPELINE GRID DATA

In this section we will demonstrate the application of CDP model for OPS gas transmission accident database sample. Until 1983 accidents were recorded to OPS if the damage were above 5000 \$, or there were events with injuries or deaths. Then the criterion were increased to 50000 \$ in 1984 and finally additional criterion were introduced in 2002 – leakage above 84000 m³. Accidents with deaths and injuries were always recorded, so that we can discard it from our set of criteria, so that we are left with 3 not mutually exclusive criteria. Hence, we form the set

$$C = \{C^1 (> 5000\$), C^2 (> 50000\$), C^3 (> 50000\$ \text{ or } 43000 \text{ m}^3)\}.$$

None of the criteria are mutually exclusive and following relations hold:

$$C^2 \subset C^1, C^3 \subset C^1, C^2 \subset C^3;$$

hence we have that redefinition of C is needed. However, it is not so trivial with C^3 , since accident in this group might be of damage greater than 50000 \$ but with leakage less than 43000 m³ or vice versa. It may also happen that an accident falls in both categories. This leads to following redefinition of the set of accident criteria:

$$C' = \left\{ \begin{aligned} &C^{1'} (> 5000\$, < 50000\$, < 43000 \text{ m}^3), \\ &C^{2'} (> 5000\$, < 50000\$, > 43000 \text{ m}^3), \\ &C^{3'} (> 50000\$, < 43000 \text{ m}^3), \\ &C^{4'} (> 50000\$, > 43000 \text{ m}^3) \end{aligned} \right\}$$

where all criteria are mutually exclusive and the following expressions holds:

$$\begin{aligned} C^1 &= C^{1'} \cup C^{2'} \cup C^{3'} \cup C^{4'} \\ C^2 &= C^{3'} \cup C^{4'} \\ C^{\infty} &= C^{2'} \cup C^{3'} \cup C^{4'} \end{aligned}$$

If we denote $p' = (p^{1'}, p^{2'}, p^{3'}, p^{4'})$ a probability vector for C' , then it is obvious, that probability vector for C will be $p = (1, p^{3'} + p^{4'}, p^{2'} + p^{3'} + p^{4'})$ or (since $\sum p^{k'} = 1$) $p = (1, 1 - p^{1'} - p^{2'}, 1 - p^{1'})$. It should be mentioned, that the last expression of probability vector should be used to avoid identifiability problems. Having this, the final expression of the model is as follows:

$$X_t \sim \begin{cases} \text{Poisson}(E_t \lambda(t)), t = \overline{1, 14} \\ \text{Poisson}(E_t \lambda(t)(1 - p^{1'} - p^{2'})), t = \overline{15, 33} \\ \text{Poisson}(E_t \lambda(t)(1 - p^{1'})), t = \overline{34, 42} \end{cases}$$

To enable Bayesian analysis we have used uniform distributions for probabilities as an expression of prior beliefs about the proportion of data in each category. Such prior can be interpreted as a non-informative since no value is given a priority, but under small data samples uniform prior distribution might result to too broad confidence limits. By performing goodness-of-fit checking procedures the power law trend $\lambda(t) = \theta t^{\theta_2}$ has been validated as having the best fit.

We compared replicated values from our model and from a simple model that accounts just accidents occurred after the last change of criterion in regulatory documents, i.e. since years 2003. Surprisingly, 95 % credibility intervals in the inference region of Fig. 4 are almost identical for both cases contrary to the expected wider intervals for partial sample. Hence, this leads to the conclusion that in this particular OPS case it does not matter whether all available data is used or just a part of the sample. The differences should become more obvious in case of even smaller data samples. However, when we look at the prediction region, superiority of using all available data becomes clear – smaller sample leads to rapidly increasing credibility bounds, while CDP model under full data sample provides much more certain values – a very natural result, since with more data we are more certain about inferences we make. This is especially important in long-term reliability.

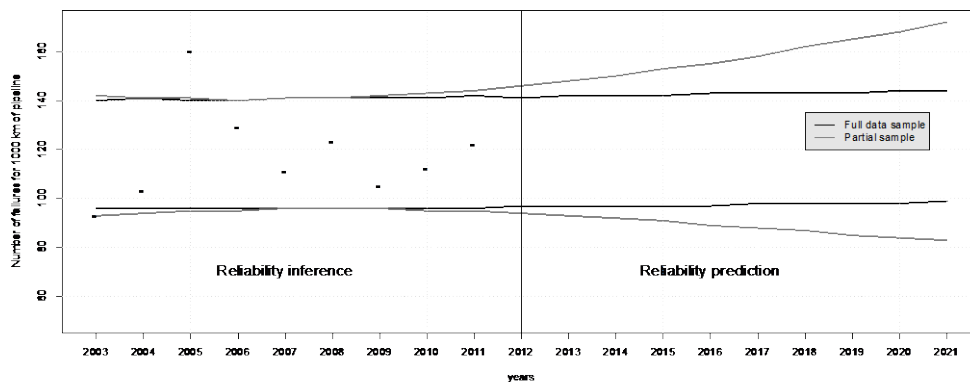


Fig. 4. 95 % credibility intervals for replicated and predicted data; points represents statistical data

The probabilities of incidents falling in one or another category (see Fig. 5) are somewhat a redundant result – although it allows efficient inclusion of all available pipeline reliability data, it could be left without any further consideration if the modification of accident criterion is not planned. However, it might be used to analyze how the change of criteria would influence reliability predictions and how it would affect general risk level (for example, under stricter criterion small leaks might not be recorded leading to unaccounted risk). It might turn out to be beneficial to go back to some of previous criterion.

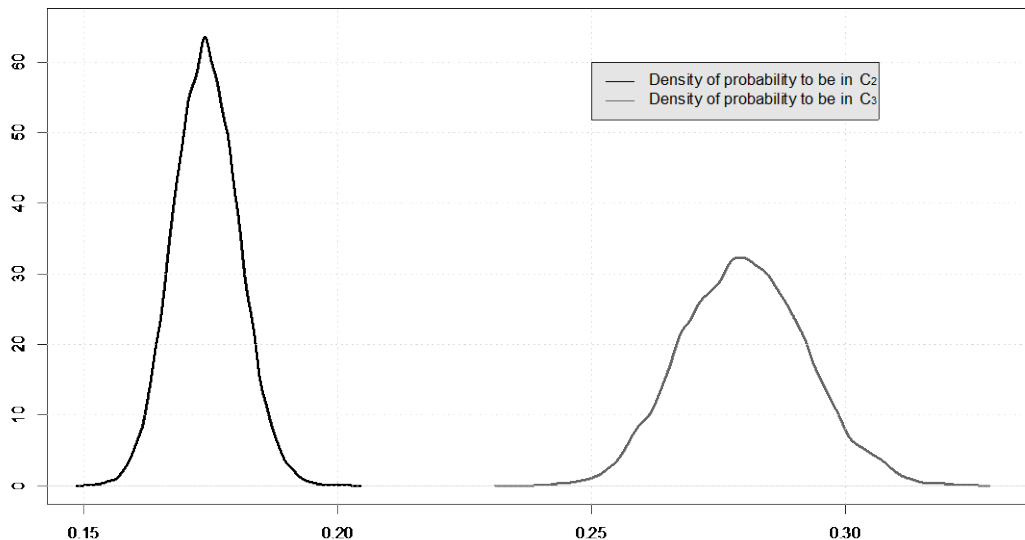


Fig. 5. Densities of probabilities of incidents in pipeline network to fall in categories C_2 and C_3 ; x axis represents probability

We conclude this section by stressing the validity of proposed model and its usefulness due to ability to account for data collected under varying incidence criteria.

5. CONCLUSIONS AND COMMENTS

In this paper we have provided a short review of international natural gas pipeline network incidents databases, their differences and difficulties arising in inferences about data contained there.

Most important result of this paper is a new model, which we called Criterion-Dependent-Poisson model for the purpose to properly incorporate whole available data no matter what was the criterion of incident registration. We have demonstrated that it provides a coherent way to handle changes of data collection criterion and to use all statistical information instead of part of it, hence resulting to more valid inferences as well as predictions.

At first sight our model might seem to be of limited use when number of different criteria is high compared to the size of data sample that they represent. However Bayesian analysis as a contrast to the frequentist framework is able to handle such issues and still provide reasonable conclusions. But situations of high number of criteria is not expected in any database, whether it is international or some local (e.g. representing one country) since the change of criteria is change in legislation which, as international experience shows, does not occur very often.

In our model development we said nothing about the dynamics of probability vectors. We treated it as a being a time-independent. Theoretically, there is no difficulty to impose so functional form on it with dependence on time covariate. However, it is not clear what forms might be



assumed and whether it is needed at all. Hence, further testing and probably some theoretical in-depth analysis would be needed to answer this.

At the beginning we briefly touched issues with Lithuanian incident sample: small, scattered, several different incidence criteria – even the usage of CDP model is questionable due to high number of resulting parameters (compared to size of the sample). But we leave it as an open question – it will be covered in our further research where extension of CDP to hierarchically structured model will be stated.

6. REFERENCES

1. JO, Y.-D.; AHN, B. J. Analysis of hazard areas associated with high-pressure natural-gas pipelines. *Journal of Loss Prevention in the Process Industries* 2002, No. 15, p. 179–188.
2. HAN, Z.Y.; WENG, W.G. An integrated quantitative risk analysis method for natural gas pipeline network. *Journal of Loss Prevention in the Process Industries* 2010, No. 23, p. 428–436.
3. PAPADAKIS, G. Major hazard pipelines: a comparative study of onshore transmission accidents. *Journal of Loss Prevention in the Process Industries*, 1999, No. 12, p. 91–107.
4. PAPADAKIS, G.; PORTER, S.; WETTIG, J. EU initiative on the control of major accident hazards arising from pipelines. *Journal of Loss Prevention in the Process Industries*, 1999, No 12, p. 85–90.
5. PAPADAKIS, G. Assessment of requirements on safety management systems in EU regulations for the control of major hazard pipelines. *Journal of hazardous materials*, 2000, No. 78, p. 63–89.
6. PHMSA pipeline incidents database: <<http://primis.phmsa.dot.gov/comm/reports/safety/>> (viewed at 2013-02-25);
7. GOLUB, E.; GREENFELD, J.; DRESNACK, R.; GRIFFIS, F.H.; PIGNATARO, L.J. Pipeline accident effects for natural gas transmission pipelines. Final report. New Jersey Institute of Technology (August, 1996).
8. EGIG *Gas Pipeline Incidents*, European Gas Pipeline Incident Group. (Secr. Gasunie N., 2008).
9. McCONNELL, R.; HASWELL, D.J.V. *UKOPA Pipeline Product Loss Incidents (1962–2010)*. (Ambergate, 2011).
10. MICHAEL BAKER JR. (Inc.), *Comparison of US and Canadian Transmission Pipeline Consensus Standards*. 1–11 (2008).



OUTLOOK OF ENERGY AND ECOLOGICAL APPLICATION OF SEWAGE SLUDGE IN CEMENT PRODUCTION

M.A. Klimenko

*A.M. Pidhorny Institute of Mechanical Engineering Problems
Pozharsky str. 2/10, 61046 Kharkiv – Ukraine*

ABSTRACT

Accumulation of a great amount of sewage sludge complicates work of treatment facilities. Unlike other waste amount of sewage sludge cannot be reduced due to change of economical and social policy in the society.

Existent methods for sewage sludge processing are reduced to sewage of sludge volume and change of their structure for the subsequent application. Due to a great amount of heavy metals, probable helminthes infection, sewage sludge requires an additional processing, which is not always technologically possible or economically sound.

Technology developed makes it possible to utilize sewage sludge as mineral addition in cement production, practically, without after-treatment.

Most economically sound method for sewage sludge treatment it is proposed to apply natural freezing that makes it possible to reduce the initial specific resistance of sludge and to improve its dehydrating ability, that, in its turn, will reduce energy costs for drying sludge.

Introduction of technology makes it possible to reduce a risk of further contamination of soil, ground water and underground waters and to improve the ecological situation and social-hygienic conditions of population residence near treatment facilities and sewage sludge sites.

In addition, the utilization technology makes it possible to lower cement cost due to saving of energy and material resources and to reduce expenditures on sewage sludge storage.

Keywords: sewage sludge, inert additive, cement production, natural freezing, utilization, energy saving

1. INTRODUCTION

During the next decades, considerable increase of energy consumption will be expected due to economic development and population growth. This will result in the intensified load on the power supply system and will require increased attention to energy use efficiency. One of possible solutions to avoid growing power consumption is to save natural resources, to search for alternative resources, to recycle raw materials and to use waste. Along with ferrous and nonferrous metallurgy, fuel processing and chemical industries, production of building materials, including cement, is one of main components of energy balance of the industry.

Cement production requires the significant amount of energy and costs for energy carriers are about 35–40% of the cost of the final product, the portion of the fuel exceeds a half of a value.

With the expansion of cement production up to 80–90 million tons per year in the years to come, gas demand will be increased by 9–11 billion m³ per year, and a problem reduction of fuel consumption reduction will be more acute [1].

Nowadays, energy-saving technologies in EU countries hold a huge niche in the sphere of waste utilization and generate heat and electricity using waste of 4th and 5th risk classes. They have been used in municipal services and private households, and the industry [2].

The equipment of cement enterprises, in which technological processes are at temperatures up to 1700 °C, minimizes the content of hazardous substances in exhaust gases, and makes chemical bonding in clinker minerals of toxic materials released from the waste during the processing due to higher temperatures. It is on the the adventures of the treatment technology in contrast to waste



treatment plants or other industrial productions. In addition, the combustion of fuel-containing waste in cement kilns makes it possible to reduce the consumption of expensive fuel (gas, oil, coal) significantly and to lower costs of the cement production.

The technology for utilization of sewage sludge developed will reduce the power consumption during the cement production due to the use of the organic part of the sludge as an additional energy-carrier and recycle the sewage sludge that will improve the environmental situation and socio-sanitary conditions of the population residence in the vicinity of water treatment plants and sludge beds [3÷6].

2. RESEARCH AIM

The aim of the study is to develop a technology for sewage sludge utilization by using it as a mineral and organic additive in cement clinker production that will make it possible to lower environmental risks during the sludge storage on sludge beds and to reduce resource intensity and power intensity of cement production.

3. PRACTICE REALISATION

Existent methods for sewage sludge treatment reduce sludge volume and change a structure for the further use. Up till now the universal technologies providing economically sound and ecologically clean and complete utilization of sewage sludge have not been developed yet. The reason is inconstancy of sewage sludge composition, which depends on specificity of wasting sewage of productions, and peculiarities of its treatment.

The analysis of the flowchart and material balance of the cement production shows that the sludge treatment according to the technical requirements for the cement clinker does not require the additional specialized equipment, does not result in increase of power intensity of the production and does not change the technological cycle of the clinker production. The sludge as a mineral additive enters the clinker at the grinding stage. To use the sludge as an additive, its moisture must not exceed 15% according to State Standard B V.2.7 – 112:2002 [7].

The initial moisture of the sludge on sludge beds is 70–95%. To improve the process of dehydration and to lower costs, the natural freezing of sludge at sludge beds is proposed to reduce the initial specific resistance of sludge significantly and to improve its dehydrating ability. The improvement of sludge dehydration on sludge beds after its spring thawing is explained by change of its initial physical and chemical structure of the sludge, due to which different forms of moisture bond in the sludge are redistributed and the amount of free moisture is increased and promotes its removal through the filter base of beds, and favours the rate of the evaporation [8].

The sludge after freezing and thawing is dehydrated mechanically, without additional reagents and conserves the structure closer to the environment and the composition. The further dewatering on filling filters and band press filters is the most efficient. The long term storage of sludge after thawing results in deterioration of its water loss ability.

Up till now the advantages gained due to freezing and thawing of the sludge have not been applied to the utmost because the complete freezing of the whole layer of the sludge does not occur. Under sludge freezing on sludge beds the solid phase is concentrated at their base and the depth of the layer of the coated sludge is 1.0–1.4 m, while the depth of soil freezing in the zone of the temperate continental climate is from 0.08 to 0.64 m and depends on the height of the snow cover and, as a result, the significant part of the sludge is not frozen, i.e., the physical and chemical structure remains unbroken.

The intensification of sludge freezing can be achieved by the periodic removal of the upper layer of the frozen sludge from the surface of beds that improves the heat exchange between the sludge and the environment.

The design-theoretical study of the heat conductivity in a layer of the sewage sludge is conducted [9].

Fig. 1 shows the temperature change in a half-meter layer of sludge at a time.

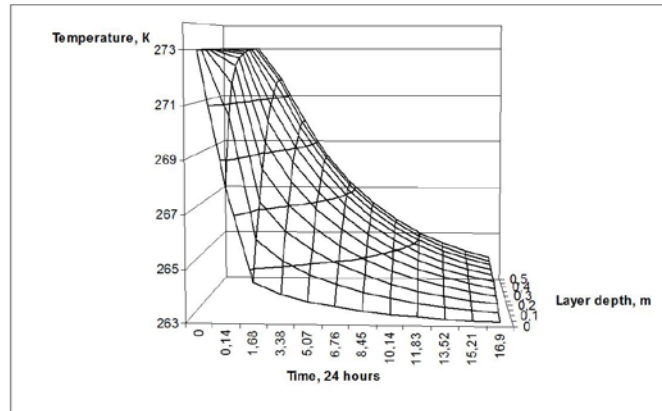


Fig. 1. Dynamics of temperature change in the sludge layer at the average outdoor temperature $-10\text{ }^{\circ}\text{C}$

The design-theoretical investigation of heat and mass transfer in the sludge layer shows that the sludge layer will be completely frozen to the depth of 0.5 meter at the average temperature of $-10\text{ }^{\circ}\text{C}$ in 17 days. That makes it possible to apply the natural freezing to improve the sewage sludge drying in the climatic conditions of Ukraine.

To determine the potential of multiple application of the sludge, physical and chemical properties and a composition of sewage sludge of the major industrial centers have been investigated. The analysis of a sludge composition shows that its mineralogical composition corresponds to the content of cement clinker components. The sewage sludge can be added up to 10% in volume as an inert additive according to State Standard B V.2.7 – 112:2002. The sewage sludge as a raw material cannot be used in the cement production because its composition does not correspond to the ratio of components of the raw mixture of the cement clinker.

To calculate the natural gas saving, the rotary kiln of production rate 75 t/h and with overall dimensions 5x185 m used in the cement production by the wet mode is selected.

Table 1. Basic performances of the rotary kiln with the wet mode of cement clinker production

Index	Standard size, m 5x185
Production rate, G_k , t/h	75
Slime moisture, w_{slime} , %	36
Temperature of exhaust gases, $T_{\text{e.g.}}$, $^{\circ}\text{C}$	250
Equivalent fuel consumption for clinker kilning, B_k , kg/t	211
Heat consumption for clinker kilning, kJ/kg	6100
Moisture of additive, w_{sludge} , %	15

Taking into account that the sewage sludge has a different composition in various cities the data of industrial metropolises given in [10] have been used for calculation. Table 2 represents data on the sludge combustion heat at the initial moisture w_{in} and at the required moisture $w_{\text{sludge}} = 15\%$.

Table 2. Combustion heat of sewage sludge having different composition

Sewage sludge of industrial metropolises	Combustible mass, %	Q_L^D , MJ/kg	Q_L^O , MJ/kg	w_{in} , %	Q_L^W at w_{in} , MJ/kg	Q_L^W at $w_{sludge} = 15\%$, MJ/kg
1	23.6	19.7	24.8	70.3	5.86	16.74
2	26.4	20.3	24.9	67.63	6.57	17.25
3	27.6	17.6	22.9	64.09	6.32	14.96
4	29.5	19.6	23.3	64.93	6.87	16.66
5	24	19.3	25.2	68.65	6.05	16.4
6	25.9	16.5	24	62.31	6.22	14.03

The computational analysis shows that the combustion heat changes insignificantly for the sludge of different composition. The conclusion can be drawn that it is possible to use the sewage sludge of any industrial metropolises to reduce the natural gas consumption in the cement production. But the main criterion that shows the possibility of the sewage sludge utilization is its mineral and organic composition that affects the quantity of the additive and the quality of the final product.

Consider the calculation of fuel saving by adding 3, 5, 7 and 9% of the sewage sludge [12]. The sludge consumption in the clinker is,

$$G_0 = G_k \cdot \delta_{sludge}, \quad (1)$$

where δ_{sludge} is a portion of sludge entered the kiln.

The necessary amount of the sewage sludge is,

$$G'_{sludge} = G_{sludge} / \delta_{org}, \quad (2)$$

where δ_{org} is a portion of the combustible part.

The sewage sludge combustion heat at the given slime moisture $w_{slime} = 36\%$ and sludge $w_{sludge} = 15\%$ is,

$$Q_L^{W'} = Q_L^W \cdot \frac{100 - w_{slime}}{100 - w_{sludge}} \quad (3)$$

where Q_H^P is the sewage sludge combustion heat, kJ/m^3 .

Then, the amount of heat released at the sludge combustion per hour is,

$$Q_{sludge} = Q_L^{W'} \cdot G'_{sludge} \quad (4)$$

The amount of heat available in the kiln is,

$$Q_k^{av} = Q_k \cdot B_k \quad (5)$$

Then, the fuel saving due to the use of the organic part of the sludge is

$$E = Q_{sludge} / Q_k^{av} \quad (6)$$

and the natural gas saving is,

$$E_{n.g.} = \frac{q_{cl} \cdot G_k}{Q_L^D} \cdot E, \quad (7)$$

where q_{cl} is the heat consumption for clinker kilning, kJ/kg, Q_L^D is the natural gas consumption heat, kJ/m³.

The annual saving of the natural gas in the kiln is

$$E_{year} = E_{n.g.} \cdot T, \quad (8)$$

where T is the number of hours of kiln operation per year (7920 hours were taken for calculation).

The equivalent fuel saving in tons of equivalent fuel per year is

$$E_{eq} = E_{year} \cdot \frac{Q_{eq,t}}{Q_L^D \cdot 1000}, \quad (9)$$

where $Q_{eq,t}$ is equivalent fuel combustion heat, kJ/m³.

The data on natural gas saving in the kiln are represented in Fig. 2.

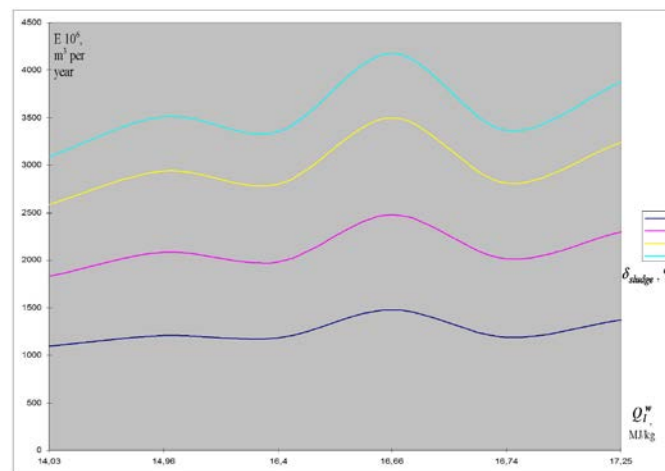


Fig. 2. Natural gas saving due to sewage sludge as an additive

As follows from Fig. 2, the natural gas saving with the practically identical sewage sludge combustion heat will grow with the increase of the portion of organic substances. For the kiln studied, the natural gas saving is from 1.4 to 5.2 %, that confirms the economic expediency of its utilization.

4. CONCLUSIONS

The technology for the utilization of the sewage sludge in industrial metropolises has been offered. The analysis of the technology shows the possibility of the sludge use as the mineral and organic additive in the cement clinker production.

The introduction of the technology will reduce a risk of the further contamination of soil, ground waters and underground waters and better the ecological situation and social-sanitary conditions of the population residence near treatment plants and sewage sludge beds.

For the most economically and energy efficient method for the sewage sludge treatment the natural freezing is proposed that makes it possible to reduce the initial specific resistance of the sludge and to improve its dehydrating ability, that, in its turn, will lower energy costs for sludge dewatering.

The advantage of technology for utilization given in comparison with the existent ones is its cheapness and simplicity of its implementation due to absence of additional energy expenditures and the need of the additional technological equipment.



The technology for utilization developed will lower costs of cement due to saving of energy and material resources. Natural gas savings for the cement kiln studied due to the organic part of sewage sludge as an additional energy carrier will be 1.4–5.2%.

REFERENCES

1. БУТТ Ю.М., ТИМАШЕВ В.В. *Портландцемент*. – М.: Стройиздат, 1974. – 328 с.
2. ДРОЗД Г.Я. *Технико-экологические записки по проблеме утилизации осадков городских и промышленных сточных вод*. – Донецк: ИЭП НАН Украины, 2001. – 340 с.
3. ЯКОВЛЕВ С.В., ВОРОНОВ Ю.В. *Водоотведение и очистка сточных вод*. – Москва: Изд-во Ассоциации строительных вузов, 2004. – 704 с.
4. ДИКАРЕВСКИЙ В.С. *Обработка осадков сточных вод*: Уч. пособие “Водоснабж. и водоотвед.” СПб. ПГУПС-ЛИИ НТ. —, 2001. — 35 с.
5. ХАКИМОВ Ф.И., КЕРЖЕНЦЕВ А.С., СЕВАСТЬЯНОВ С.М. *Рекомендации по утилизации илов городских очистных сооружений*. – М.: Госкомэкологии России, 1999. – 54 с.
6. БАТЛУК В.А. *Основы экологии и охрана окружающей среды. Учебное пособие*. – Львов: Афиша, 2001. – 336 с.
7. ДСТУ Б В.2.7-112-2002, Цементы. Общие технические условия, – Киев: Госкомградостроительства Украины, 2002. – 18 с.
8. СТЕПАНЕНКО Н.И., РЯХОВСКАЯ А.И., РОМАНЕНКО О.А. *Химия и технология воды*. – 1985. № 2. – С. 79 – 80.
9. КЛИМЕНКО М.А. Перспективы обработки осадка сточных вод естественным холодом для утилизации в цементном производстве. Сучасні проблеми машинобудування. Тези доповідей конференції молодих вчених та спеціалістів. Харків, 2012 р. – с. 69.
10. ЯКОВЛЕВ С.В., ВОРОНОВ Ю.В. *Водоотведение и очистка сточных вод*. – М.: Изд-во Ассоциации строительных вузов, 2004. – 704 с.
11. АЛЕКСЕЕВ Б.В., БАРБАШЕВ Г.К. *Производство цемента: Учебник для сред. ПТУ*. – М.: Высшая школа, 1985 – 264 с.
12. ПЬЯЧЕВ В.А., КАПУСТИН Ф.Л. *Тепловые и технологические расчеты вращающихся печей для обжига цементного клинкера*. – Екатеринбург: УПИ, 1992. – 34 с.



ANALYSIS OF USING DOUBLE BY-PASS IN THE AIR HANDLING UNIT'S WITH COUNTER FLOW HEAT EXCHANGERS

G. Plavenieks, A. Lesinskis

Riga Technical University

Institute of Heat, Gas and Water technology

Azenes str. 16-20, LV 1010 Riga – Latvia

ABSTRACT

The European Union (EU) energy consumption is growing each year, and along with their dependencies on external oil and gas suppliers. EU buildings consume 40% of the total energy consumption in Europe. Predicts that by the year 2020, two times increase in energy consumption of air handling systems, and it should be limited to the higher standards for air handling units. Using counter flow heat exchanger in the ventilation system, it will reduce considerably heat energy consumption of ventilation, but the same time create pressure loses. The paper presents analysis of using double by-pass in the air handling units. In the article will be represented possible air flows and pressure reduction models of air handling units with double by-pass of counter flow heat exchangers. Objective of my work is to improve ventilation systems performances in terms of sustainability, indoor comfort and economics. Reduction of energy consumption, improvement of energy efficiency and optimization of air handling units is important to address the improvement of indoor air quality.

Keywords: counter flow heat exchanger, air handling units.

1. INTRODUCTION

The Europe Union's (EU) as well Latvian energy consumption is growing each year, and along with their dependencies on external oil and gas suppliers. EU buildings consume 40% of the total energy consumption. Predicts that by the year 2020, two times increase in energy consumption of air-handling systems, and it should be limited to the higher standard for air handling units. EU member states intend to reduce the total energy consumption in buildings by making the buildings well-insulated and tighter [1].

In private houses mechanical ventilation with heat recovery has become as in common use. Natural ventilation is not suitable for use in cold climate due to cold supply air create drafts and heat loses of ventilation. According to researchers in the Scandinavian countries, mechanical ventilation with heat recovery is compared to natural ventilation and extracts fans, and is found to be most effective system for maintaining a low humidity level. But biggest challenge to find solutions to avoiding ice formatting in the heat exchanger, reduced electricity consumption for the fans and pressure drop reduction [2].

This paper presents analyses of air-to-air heat recovery in air handling units. In the article will be represented possible using configurations of air handling with cross flow heat exchanger. Reduction of energy consumption, improvement of energy efficiency and optimization of air handling units is important to address the improvement of indoor air quality as well.

2. METHODOLOGY

Analyzing the sources of literature with practical measurements and tests of the counter flow heat exchangers, it can be concluded that effective from the point of view of heat recovery will be the rotating regenerators and cross flow heat exchangers. In this study I had made research of the use of the cross flow heat exchangers due high efficiency heat recovery. The increasing prices of heat and cold resources as well as prices of electricity, this may be an important factor to ensure energy efficiency. However, the using of cross flow heat exchangers is limited and as the main deficiencies- the geometric size and high pressure losses compared to other heat exchangers.

By this time one of the most common ways to prevent freezing in the heat exchangers is by totally by-passing the cold supply air when it is below a certain temperature (for example -5°C). Another way is to by-pass only part of the cold air stream, just enough so that freezing does not start. By mechanically blocking part of the heat exchanger the flow in the cold corner can be reduced and thus prevent freezing [3, 4, 5, 6, 7, 8, 9, 10, 11, 12, 13, 14, 15].

My main objective of the study is to develop a ventilation system solution with low pressure losses. Now counter flow heat exchangers pressure loss would probably be reduced by supplementing the scheme of air handling unit. The basic idea behind the new configuration would be to use heat recovery on demand. As the basic configuration of the air handling unit took part in the supply of filter and fan and exhaust side by analogy – just the fan and filter and counter flow heat exchanger.

Two bypass dampers will be used in my research, first will be placed on the supply side, but the second on the exhaust side of air handling unit. Outdoor air will flow into the supply side of air handling unit, flowing through a filter and into the heat exchanger. Part of the exhaust side of air handling unit- air flows through part of the exhaust filter and the heat exchanger. Using this principle of air handling unit scheme, you can specify several energy-efficient operating modes using two bypass dampers of the counter flow heat exchanger. In this case, the pressure loss is studied only an optimization feature and is not a condition of the supply air as it enters the room.

$T_{\text{outside}} < T_{\text{supply set point}}$ first (winter) mode occurs when the outdoor air temperature is below the set supply air temperature. On the supply part of air handling unit bypass dampers will be 100% closed, part of the exhaust bypass damper also will be 100% closed and counter flow heat exchanger works for 100%. Consequently, air handling unit working in maximum mode, using 100% heat recovery cross exchanger.

Both bypass dampers are 100% closed and cross flow heat exchanger works for 100%.

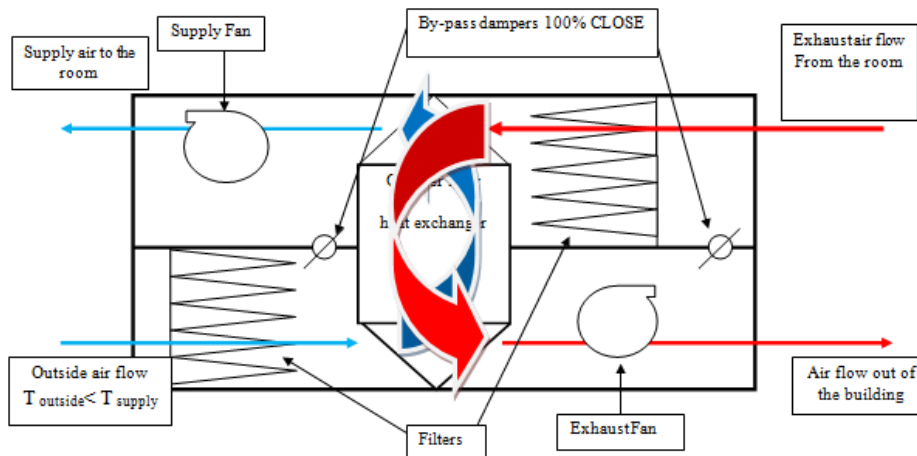


Fig. 1. Scheme of air handling unit with counter flow heat exchanger by using double by-pass dampers-both bypass dampers are 100% closed and cross flow heat exchanger works for 100%

$10^{\circ}\text{C} < T_{\text{outside}} < T_{\text{supply set point}}$ second mode occurs when the outdoor air temperature is 10°C , but not more as $T_{\text{supply set point}}$. On the supply part of air handling unit bypass dampers will be 100% closed, part of the exhaust bypass damper also will be 50% open and counter flow heat exchanger works for 50%. Consequently, we obtain a reduction of pressure loss of 50% of the exhaust side filter and just 50% of the exhaust air passes through the cross flow heat exchanger.

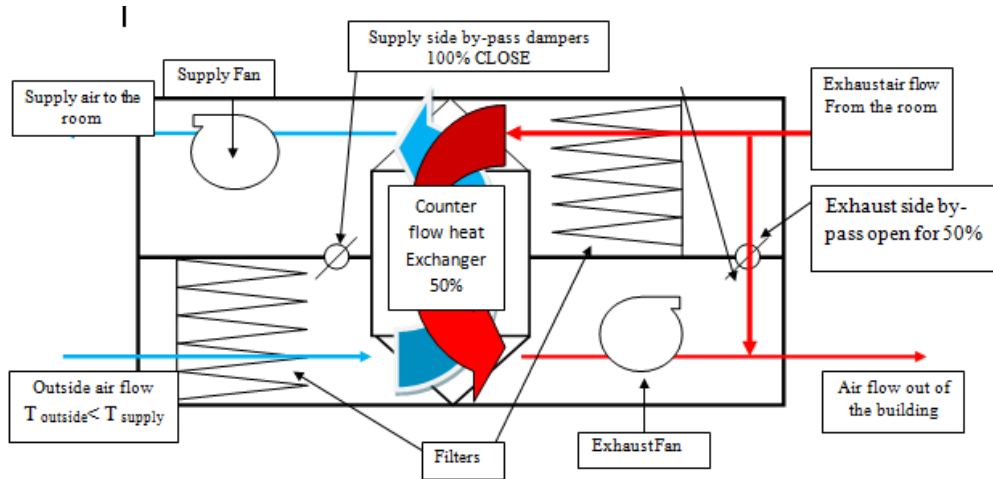


Fig. 2. Scheme of air handling unit with counter flow heat exchanger by using double by-pass dampers, supply side bypass dampers are 100% closed, but exhaust side bypass dampers are 50% open and cross flow heat exchanger works for 50%

$T_{\text{outside}}=18^{\circ}\text{C} \leq T_{\text{supply set point}}$ When the outdoor air temperature reaches 18°C , but not more than $T_{\text{supply set point}}$, then start the next mode-supply part bypass dampers open 100% and on the exhaust air side bypass damper 100% open and counter flow heat exchanger working for 0%. Consequently, we obtain a reduction of pressure loss of 100% of the exhaust side filter and the exhaust air does not flow through the counter flow heat exchanger. Both bypass dampers 100% open and counter flow heat exchanger is bypassed.

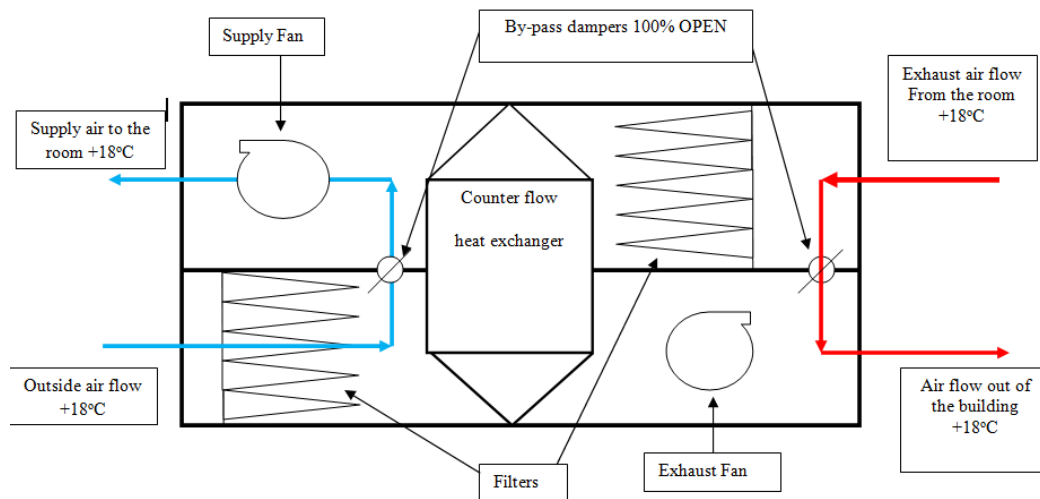


Fig. 3. Scheme of air handling unit with counter flow heat exchanger by using double by-pass dampers, both bypass dampers 100% open and counter flow heat exchanger is bypassed

$T_{\text{outside}} \geq T_{\text{supply set point}}$, when outside air temperature is more than $T_{\text{supply set point}}$, than next modes will start – supply part by-pass for 100% open, exhaust part bypass for 100% open and heat exchanger is bypassed for 100%. Consequently, we obtain a reduction of pressure loss of 100% of the exhaust side filter and the exhaust air does not flow through the counter flow heat exchanger. Both bypass dampers 100% open and counter flow heat exchanger is bypassed.

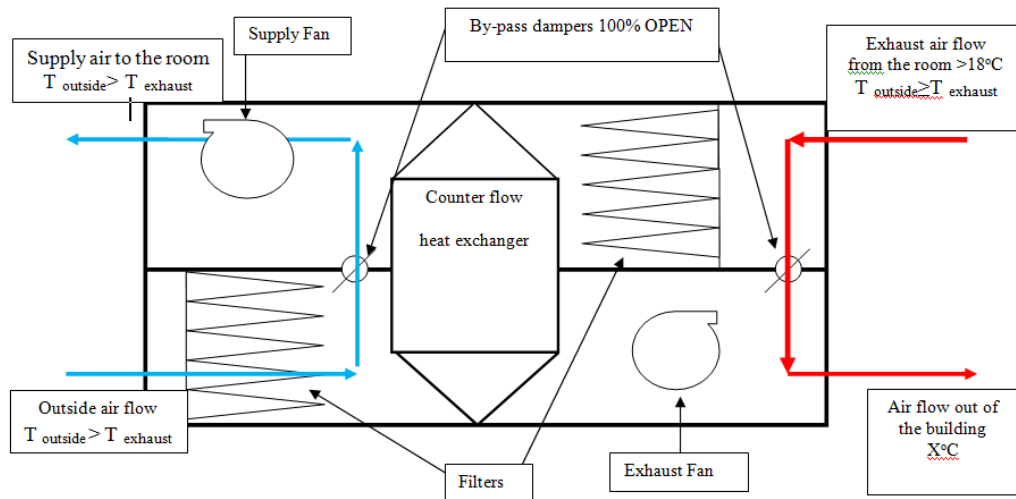


Fig. 4. Scheme of air handling unit with counter flow heat exchanger by using double by-pass dampers

$T_{\text{outside}} \leq T_{\text{exhaust}}$ When during summer outside air temperature is less than T_{exhaust} , then next mode will start – supply part by-pass for 100% open, exhaust part by-pass for 100% open and heat exchanger is bypassed for 100%. Consequently, we obtain a reduction of pressure loss of 100% of the exhaust side filter and the exhaust air does not flow through the counter flow heat exchanger. Both bypass dampers 100% open and counter flow heat exchanger is bypassed. This mode can call free cooling without using exchanger.

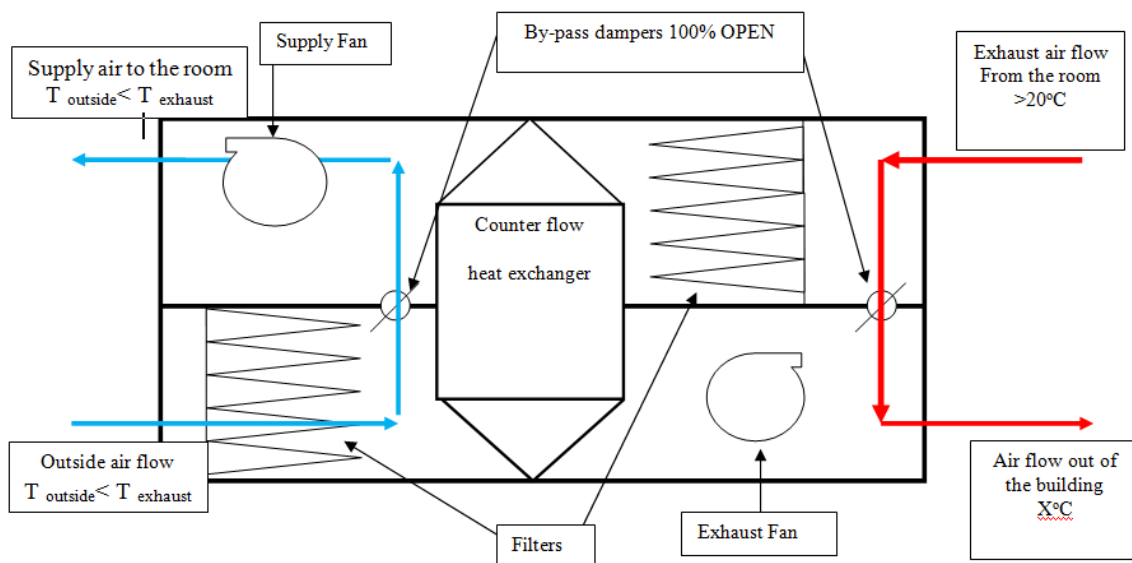


Fig. 5. Scheme of air handling unit with counter flow heat exchanger by using double by-pass dampers- mode of free cooling

In all modes, when both bypass dampers 100% open and counter flow heat exchanger is not used, air does not flow through the exhaust filter. This mode reduces the pressure losses in air handling unit elements – heat exchanger and exhaust filter. Significant energy savings compared to traditional mode will be provided, in this case we have possibility to avoid pressure drops of heat exchanger and exhaust filter.

3. RESULTS AND DISCUSSIONS

This scheme of air handling unit with two bypass dampers can reduce the pressure losses and provides significant energy savings compared to traditional mode. Traditional mode air passes through all components of air handling units, but using double bypassing air goes through only part of air handling components reducing internal pressure drops in air handling unit. To search for more economical solutions, should investigate the counter flow heat exchangers geometric size optimization capabilities, as well as reduce the weight that should be done when you change heat exchanger plates from traditional materials to for example polymer or nano materials that can provide not only mass heat transfer, but also moisture transfer [16]. Constant or variable supply and exhaust air quantity can provide fans with electronically communicated (EC) motors or permanent magnet motors. Using of air handling units with double bypass of heat can perform defrosts function with the exhaust air, but it requires a more in-depth analysis. Economic effects, we can calculate by hours, how long at the specific mode of air handling unit running. Similar solution of bypass scheme can also be used for air handling units with rotating regenerator, but this still needs to be looking for solutions.

4. CONCLUSIONS

Based on the analysis one of the most effective combination for air handling unit with heat recovery is counter flow heat exchanger combination with double bypass dampers. Using the following double bypass dampers system in the air handling unit, there will be always possible to provide fresh supply air. There is great potential of energy savings using double by-pass dampers for counter flow heat exchangers, but it depends of climate conditions in each case. It is possible reduce pressure drops inside air handling unit by bypassing of counter flow heat exchanger and filter of extract part of air handling unit in some modes air ventilation and air conditioning of building.

ACKNOWLEDGEMENT

I thank Research and development centre of Systemair AB (Sweden) for co-operation and supporting the work.

REFERENCES

1. EIROPAS PARLAMENTA UN PADOMES DIREKTĪVA 2012/27/ES.
2. Mechanical ventilation with heat recovery in cold climates [referred on the 2th of January in 2013 y.] Link to the internet <http://web.byv.kth.se/bphys/reykjavik/pdf/art_157.pdf >
3. КРЕСЛИНЬ А.Я. Автоматическое регулирование систем кондиционирования воздуха. Москва: Стройиздат, 1972. 96 с.
4. КРЕСЛИНЬ А.Я. Оптимизация энергопотребления системами кондиционирования воздуха. Рига: РПИ, 1982. 154 с.
5. КРЕСЛИНЬ А.Я. Оптимальные алгоритмы функционирования систем Вентиляция и кондиционирование воздуха промышленных и сельскохозяйственных зданий: межвуз. сб. науч. тр. – Рига: Риж. политехн. ин-т, 1981. – [Вып.13], с. 22–43.
6. КРЕСЛИНЬ А.Я. Основные понятия и принципы оптимизации и идеализации систем кондиционирования микроклимата Вентиляция и кондиционирование воздуха : межвуз. науч.-техн. сб. – Рига : Риж. политехн. ин-т, 1979. – [Вып.11], с. 3–13.
7. БОГОСЛОВСКИЙ В.Н., Поз И.Я. Теплофизика аппаратов утилизации тепла систем отопления, вентиляции и кондиционирования воздуха. М.: Стройиздат 1983. 319 с.
8. БАРКАЛОВ Б.В., КАРПИС Е.Е. Кондиционирование воздуха в промышленных, общественных и жилых зданиях. Москва: Стройиздат, 1982. 312 с.



9. ХАУЗЕН Х. Теплопередача при противотоке, прямотоке и перекрестном токе: Пер. с нем. – М.: Энергоиздат, 1981. 384 с.
10. MATHISEN K., SKOGESTAD S., WOLFF E. Bypass selection for control of heat exchanger networks, *Computers & Chemical Engineering*, Vol. 16, Supplement 1, May 1992, p. S263–S272, ISSN 0098-1354, 10.1016/S0098-1354(09)80031-8.
11. MARDIANA- IDAYU A., RIFFAT S.B. Review on heat recovery technologies for building applications, *Renewable and Sustainable Energy Reviews*, Vol. 16, Iss. 2, February 2012, p. 1241–1255, ISSN 1364-0321, 10.1016/j.rser.2011.09.026.
12. LAVERGE J., JANSSENS A., Heat recovery ventilation operation traded off against natural and simple exhaust ventilation in Europe by primary energy factor, carbon dioxide emission, household consumer price and exergy, *Energy and Buildings*, Volume 50, July 2012, p. 315–323, ISSN 0378-7788, 10.1016/j.enbuild.2012.04.005.
13. NYMAN M., SIMONSON C. J. Life cycle assessment of residential ventilation units in a cold climate, *Building and Environment*, Vol. 40, Iss. 1, January 2005, p. 15–27, ISSN 0360-1323, 10.1016/j.buildenv.2004.04.011.
14. ВИШНЕВСКИЙ Е.П. Особенности обеспечения эффективной работы пластинчатых теплообменников рекуперативного типа в суровых климатических условиях // С.О.К. – 2005. – № 1.
15. <http://www.heatex.com/Documents%20and%20Tools/~media/Files/TechnicalDocumentati on/Heatex_TechInfo_110120.ashx> [referred on the 2th of January 2013].
16. T'JOEN C., PARK Y., WANG Q., SOMMERS A., HAN X., JACOBI A., A review on polymer heat exchangers for HVAC; R applications, *International Journal of Refrigeration*, Vol. 32, Iss. 5, August 2009, p. 763–779, ISSN 0140-7007, 10.1016/j.ijrefrig.2008.11.008.



IMPROVING THE EFFICIENCY OF PELTIER COOLING WITH RECUPERATIVE POWER MANAGEMENT

V. Jurkans

*Institute of Radio Electronics
Riga Technical University
Azenes 12, LV-1048 Riga – Latvia*

J. Blums

*Institute of Technical Physics,
Riga Technical University
Azenes 14, LV-1048 Riga – Latvia*

ABSTRACT

Peltier elements offers new qualities in various cooling applications, but do not compare well with traditional cooling systems due to a low efficiency. This paper claims an approach to increase Peltier element based cooling system efficiency using advanced power management system. It is realized by using Peltier element as Thermo Electro Generator periodically turning excess heat to electricity. This method is effective in several specific applications that suffer from weak heat dissipatoin. Such system was created to expose potential gain for human body microclimate controlling system. Experiments revealed that it is possible to recuperate up to 3% of supplied energy at 3 to 5 °C temperature difference between hot and cold side of Peltier element. Main advantages and drawbacks are presented, including further study opportunities. Research opens new direction for improving cooling ability of Peltier elements, thus bringing it one step closer to efficiency of gas compression based cooling systems.

Keywords: Peltier, recuperation, efficiency, excess heat, power management

1. INTRODUCTION

Thermoelectric systems have been gaining interest lately because of necessity for cooling devices in various applications that is increasing constantly. Starting with household applications such as food refrigeration and air conditioning, and moving towards to measuring equipment and high speed computers. Requirements for comfort and quality are increasing as much as need for higher sensitivity in various measurements and lower temperatures for high density microcircuits or overclocked computers. Since cooling systems based on Peltier effect have no moving parts and don't use any liquids and gases, they ensure quiet, reliable, environment friendly and easily controlled operation, having many advantages over mostly used gas-compression systems. In spite of that, Peltier effect based cooling systems are less efficient than gas compression systems, causing hard work all over the world to make this kind of systems truly superior.

Some studies show that it is possible to get higher cooling performance using microstructures with different arrangement of elements in thermoelectric coolers [1]. As Pradeep Bansal mentions in his review [2], some studies report better results using nano crystalline powders of p-type BiSbTe [3] and significant advancements are taking place in the development of thermoelectric nano composites, to provide higher performance [4].

Table 1 shows comparison of various refrigeration types. It is clear why there is so much challenge to raise efficiency of Peltier cooling.

Table 1. Comparison between different types of refrigeration

Type	COP ¹	Advantages	Disadvantages
Acoustic refrigeration [5]	~0.8 [6]	Low cost and high reliability [7]	Low power density [8], low cooling capacities, large physical size, heat conduction between the heat exchangers and hence poor performance of the heat exchangers [9]
Thermoelectric refrigeration [10]	~0.4–0.5	Has no moving parts environment friendly, high reliability, low weight, and flexible operation [11]	Low efficiency
Magnetic refrigeration [12]	~4–10	Environment friendly, high efficiency	High cost of materials and magnets, limitations of physical properties of materials, and time delay required to reach the required temperature lift [13]
Stirling cycle refrigeration [14]	~0.8	Environment friendly, perspective in energy saving	Low efficiency.
Gas compression refrigeration [15]	~4.5–5	Cheap, efficient, very popular	Large physical size, uses hazardous fluids, non-flexible operation
Adsorption refrigeration [16]	0.39 [17]	Large scale refrigeration	Low efficiency
Compressor-driven metal hydride heat pump [18]	1.8–2.5	Environment friendly, can compete with vapor compression technology.	High cost of metal hydrides, non-availability of suitable materials with fast reaction kinetics, and the need for improved hydrogen compressor technology [19]

From a somewhat different perspective, the present work investigates a way to increase overall efficiency of Peltier element based cooling system by manipulation of different operation modes of thermoelectric elements. Such an approach considers possibility to recuperate the part of energy that is used to achieve temperature difference between cold and hot side of Peltier element, thus returning excess energy. Using thermoelectric cooler as generator could be an opportunity for applications where an overheating of cooling system is possible or in situations when cooling is necessary only occasionally. For example, these conditions can be found in specific calculation or measurement systems, or wearable cooling systems. The aim of this paper is to show that the recuperation is possible and reveal possible benefits for this method. Impact of recuperation has not been reported in other studies of Peltier based cooling systems.

2. PRINCIPLES OF OPERATION

The main idea of researched approach is to use Peltier element (PE) as thermoelectric generator after the temperature difference is made between hot and cold side of cooling element. This approach is visualized in Fig.1. When cooling is needed, Peltier element is commutated with power supply (Fig.1, a) to transport the heat. If cooling isn't needed or it can't be done due some reasons, system uses Peltier element as power generator that is commutated to some load or energy harvester (Fig.1, b).

¹ Coefficient of performance – ratio of the heating or cooling provided over the electrical energy consumed. COP = Q/W.

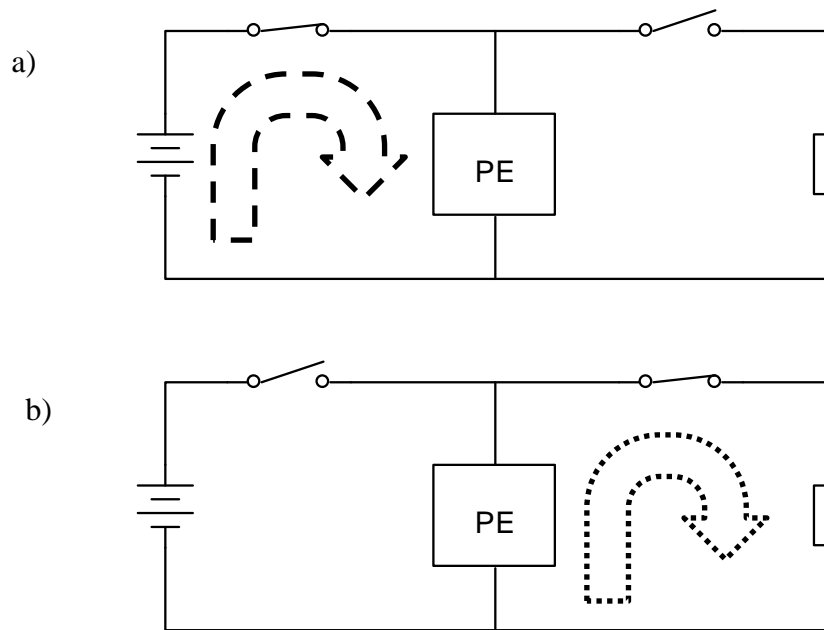


Fig. 1. Energy flow in cooling system with energy recuperation. a) energy is used for cooling purposes. Electrical energy is supplied to Peltier element and it is working as a heat pump b) Peltier element is disconnected from power supply and commutated as source of electrical energy. As Peltier element generates voltage from temperature difference, recuperated energy can be used for other needs or accumulated

Problem that has to be considered is the fact that there is heat backflow during the recuperation mode because Peltier element doesn't transport the heat but acts as a thermal conductor. This consideration narrows applications this approach could be used in. Possible gain could be achieved in systems that don't need constant cooling or have elements that reduce heat backflow, for example heat pipes (heat-transfer devices that combines the principles of both thermal conductivity and phase transition).

Measurements of possibilities to improve thermoelectric cooler efficiency were made with several systems that potentially could use this kind of manipulation.

3. FIRST EXPERIMENT: COOLING SYSTEM WITH HIGH HEAT FLOW

3.1. Methods

For these experiments Peltier based cooler model, that is able to imitate various situations and applications, was made. Resistive heat source, Peltier element and heat dissipator, that uses air convection, were integrated into one system, which is controlled by custom programmable controller, to try to find the possibilities of this recuperational approach – transforming heat generated at cooling process to electricity.

System is capable of delivering 40 W of heat load for Peltier element, which can receive about 60 W of electric power for transporting heat from this load to heat dissipator, that has an ability to transport more than 100 W of heat load by having 0.2 °C/W thermal resistance. Recuperated energy is received using electronic configuration shown in Fig. 2.

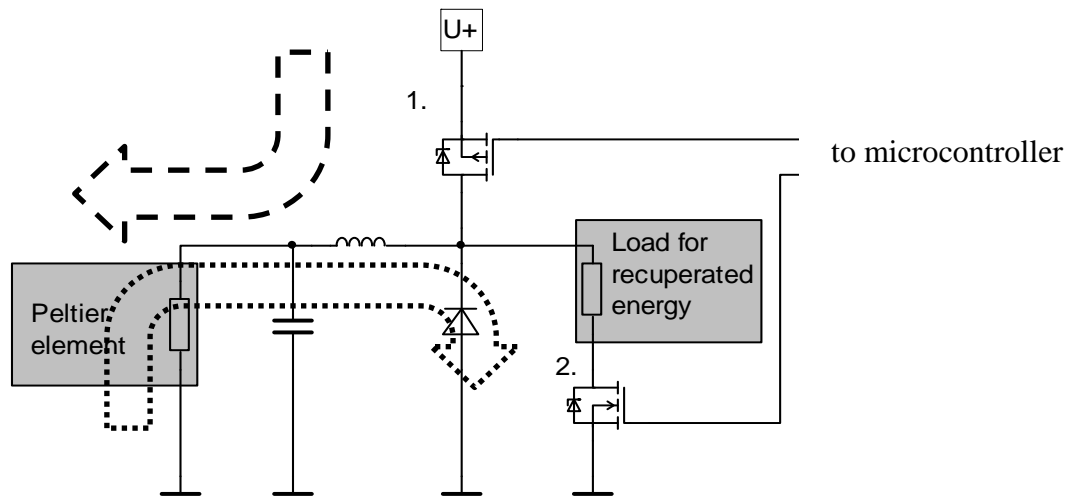


Fig. 2. Electronic schematic of output stage for Peltier element supplemented with recuperation. It consists of power supply ($U+$), two MOSFET switches, electronic filter, Peltier element and resistive electrical load. Arrows show flow of energy : dashed line – supplied energy, dotted line – recuperated energy

Fig. 2 shows output stage that has a possibility to commutate Peltier element as electro generator. Output consists of step-down dc/dc converter realized with MOSFET Nr.1. that produces power flow to Peltier element, this process is represented with dashed arrow. An additional MOSFET No. 2 can provide thermoelectric generation mode by allowing the current flow from Peltier element to the load through it. It is represented with dotted arrow. Output stage is controlled with AVR® microcontroller.

System measures temperatures at different points of construction using digital thermal sensors DS18B20 (manufactured by Texas Instruments). Temperatures are logged for further analysis of experiments using different cooling algorithms. System also measures current flowing through and voltage applied to Peltier element. Bipolar current and voltage measurements are possible to gather information not only for measuring supplied power but also monitor power that is being recuperated. System is able to communicate with computer to log all measured values.

First aim of study is to find out if recuperation occurs not only in theory. In search of possible applications of recuperation, system varied power of heat load for Peltier cooler to imitate application where there is need to change amount of cooling rapidly. System was programmed to keep resistive heat load temperature constant at one level that is lower than room temperature. With such quite various heat load it is very likely to see recuperation and find out what are the conditions for better results.

3.2. Results and discussion

System was programmed and tuned to keep heat source at $2\text{ }^{\circ}\text{C}$ lower than ambient temperature, using PID controller² algorithm. As ambient room temperature was $20\text{ }^{\circ}\text{C}$, Peltier element had to keep heat source at constant $18\text{ }^{\circ}\text{C}$ regardless of supplied heat power. In spite of large thermal inertia it was possible to keep heat source at $18\text{ }^{\circ}\text{C}$ even if it was driven with 25 W of power. As it often happens, because of thermal inertia, system has a little overshoot, thus cooling

² Proportional-Integral-Derivative controller [20]

the heat source a little below 18 °C. From perspective of recuperation it is right moment to generate electricity.

Temperatures of Peltier element and heater can be seen in Fig. 3.

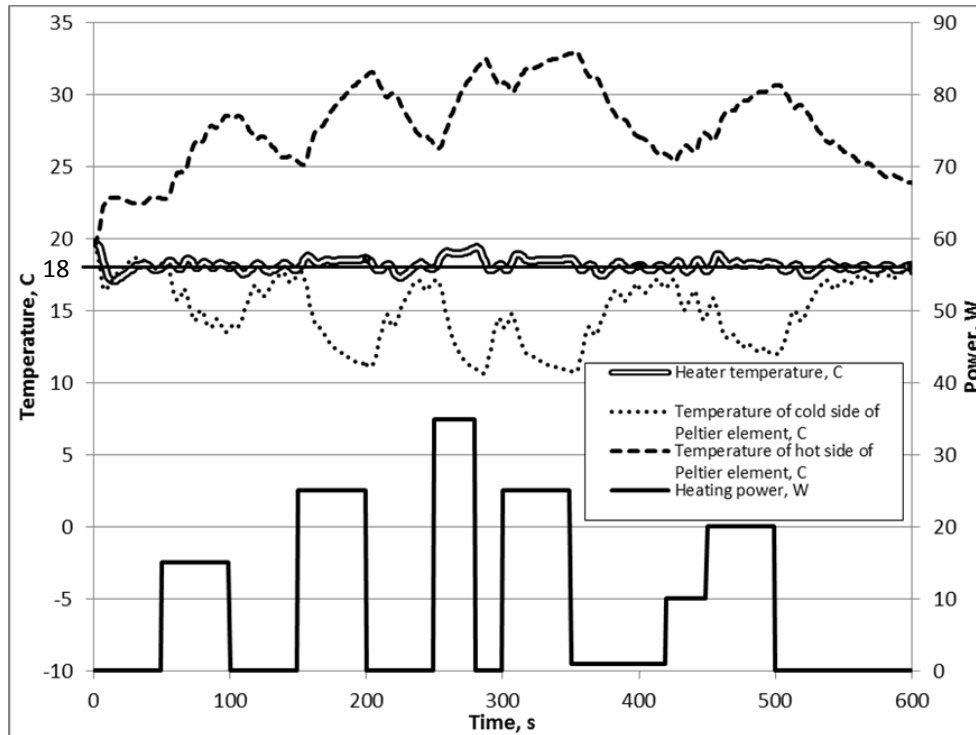


Fig. 3. Thermal data and heat load of first experiment

As we can see, temperature of heat load fluctuates around 18 °C. At the moments when recuperation is possible, temperature difference between cold and hot side of Peltier element often has reached 15 °C. In Fig. 4 we can see power that is supplied to and recuperated from Peltier element.

Energy recuperated from Peltier element is well below 1% compared to supplied electrical energy, although we can clearly see, that electric power can be generated and understand how to get better results. Recuperated power could be so small because of large heat power applied to system. Because of large heat quantities need to be transported, we need Peltier element to work at high power. Thus very high power is supplied to reach necessary temperature differences, which, in turn, can be used for recuperation. Because of large thermal inertia, it takes much longer to generate temperature difference between Peltier element sides.

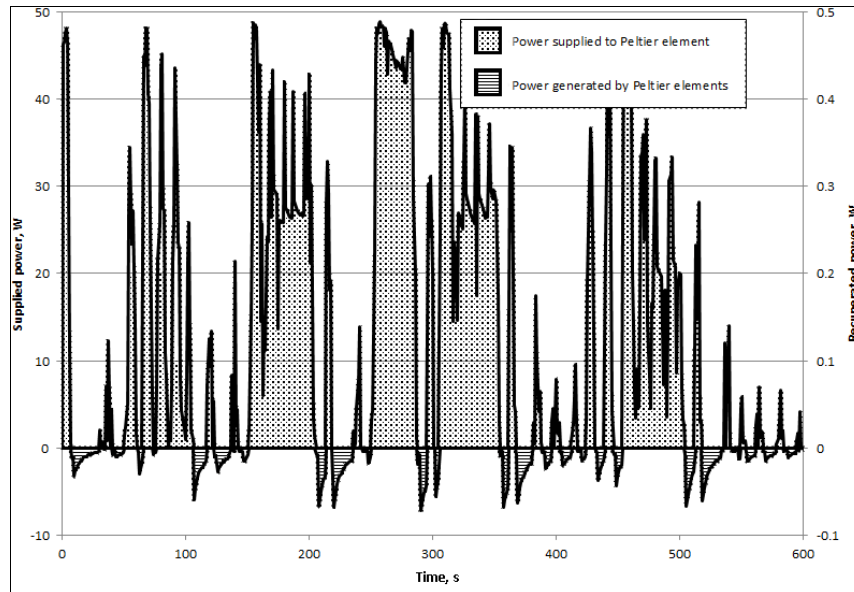


Fig. 4. Supplied and recuperated power in first experiment

4. SECOND EXPERIMENT: COOLING WITH INSUFFICIENT HEAT DISSIPATION

4.1. Methods

Considering previous results, it was decided to try to implement an approach of recuperation in system that operates with smaller powers and has smaller thermal inertia.

Such approach could be used in human body microclimate controlling system that uses Peltier elements. Such system has been made, analyzed and described in several researches in Riga Technical University [21]. Because of small thermal inertia, PID controller of the system works more stable than the one used in previously described experiment and doesn't cool cold side lower than needed so recuperation could not be activated during normal cooling period.

Because of limitations in mass and space in wearable electronics, system has difficulties dealing with excess heat in hot side radiators. When hot radiator reaches critical point heat starts to flow back. This moment could be used for recuperation during partial thermal shutdown, otherwise cooling system warms the body.

Experiments with human body microclimate controlling system have shown, that system becomes ineffective because of generated heat if it doesn't has ability to dissipate heat fast enough. Heat starts to diffund to cold side of Peltier element, thus causing decrease of efficiency and stop of cooling process [21].

To realize recuperation in this system, additional elements were implemented the same way it was shown in Fig. 2.

For the analysis of microclimate control system it was used with a person who was doing physical activities (running) to produce heat and activate system. As soon as system suffers excess heat on Peltier elements, recuperation mode was switched on. For electrical measurements PicoScope®2205 PC oscilloscope was used. Thermal data was gathered by Agilent® 34972A data logger.

4.2. Results and discussion

Two experiments were made using the microclimate system with and without recuperation of energy. Data of full experiment is shown in Fig. 5 and Fig. 6 to illustrate the context of experiment,

understand better the usage and estimate the impact of suggested method. In both experiments identical actions of subject and timing were repeated. Microclimate control system has to keep bodies temperature under 29 °C, preventing the overheating of human during physical activities.

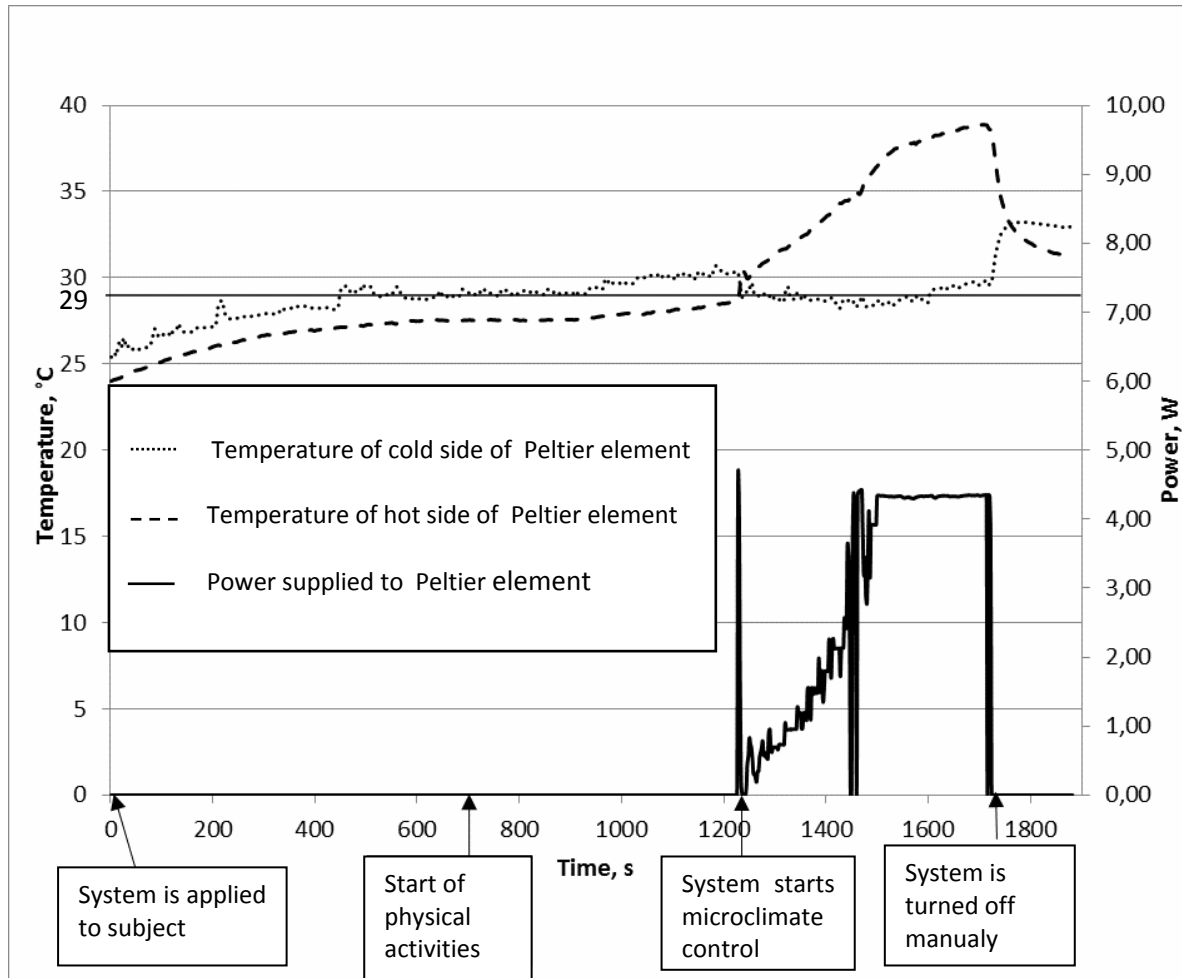


Fig. 5. Data and explanations of experiment without recuperation

The system is applied to person – the subject of our experiment. Once temperatures are stabilized, subject starts physical activities to create excess heat. At 29 °C system starts temperature control, thus transporting away waste heat of human body. Heat is transported to copper plate (50×50×3 mm) which is then connected with thin copper foil to increase heat dissipation keeping flexibility of clothing. Temperature of this heat dissipator is increasing as heat is being transported. After a while system reaches its maximum power. As we can see system loses its ability to work as cooler once hot radiator reaches certain temperature because of fact that it can not deal with the excess heat.

In experiment with recuperation, system is programmed to limit heat dissipators temperature. System is allowed to work only 10 seconds if it is working at maximum power. From this perspective temperature of cold side isn't as low as it would be without this partial thermal shutdown, but on the other hand, cooling can be prolonged.

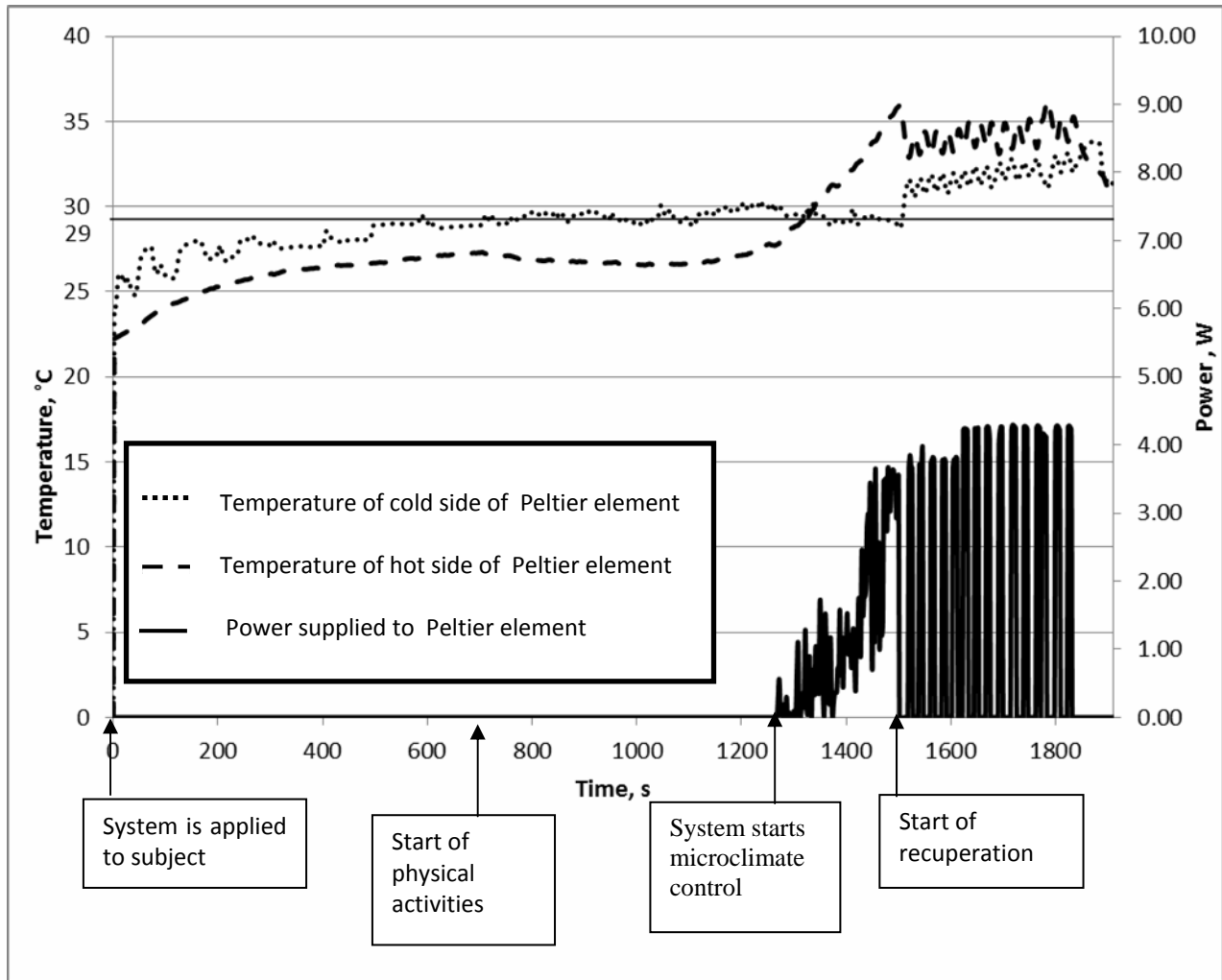


Fig. 6. Data and explanations of experiment with recuperation

As we can see (Fig. 6), system starts to switch between the cooling and generator modes once it reaches maximum power level. As the result, hot side temperature isn't as high as without recuperation. Although the cold side temperature is higher it doesn't affect the subject because main excess heat of persons body already has been drained away, therefore helping to deal with the main peak of it.

Fig. 7 represents the power supplied and generated in experiment with recuperation. We can see that each time system commutates Peltier element as thermoelectric generator, small amount of electrical energy can be recovered. System supplies 90 to 100 Joules of energy to Peltier during one pulse. Recuperated amount reaches 3 Joules thus delivering up to 3% of supplied energy.

According to the law of conservation of energy, these 3% are not only gathered as electric energy, but also transported away from cooling system as heat, hence lowering the heat load for the heat dissipator.

It is possible to increase total recuperated energy in this experiment if we use temperature difference that occurs because of heat flow to the Peltier element before it starts to cool down the cold side. From 0 to 1250 second of experiment this heat flow generates about 2 to 3 °C temperature difference which can be used for recuperation as well.

To increase recuperated energy further, it is necessary to reduce losses in cables and other nodes. According to this problem, Peltier elements should be connected in series and voltages should be raised, thus lowering the currents necessary for same power.

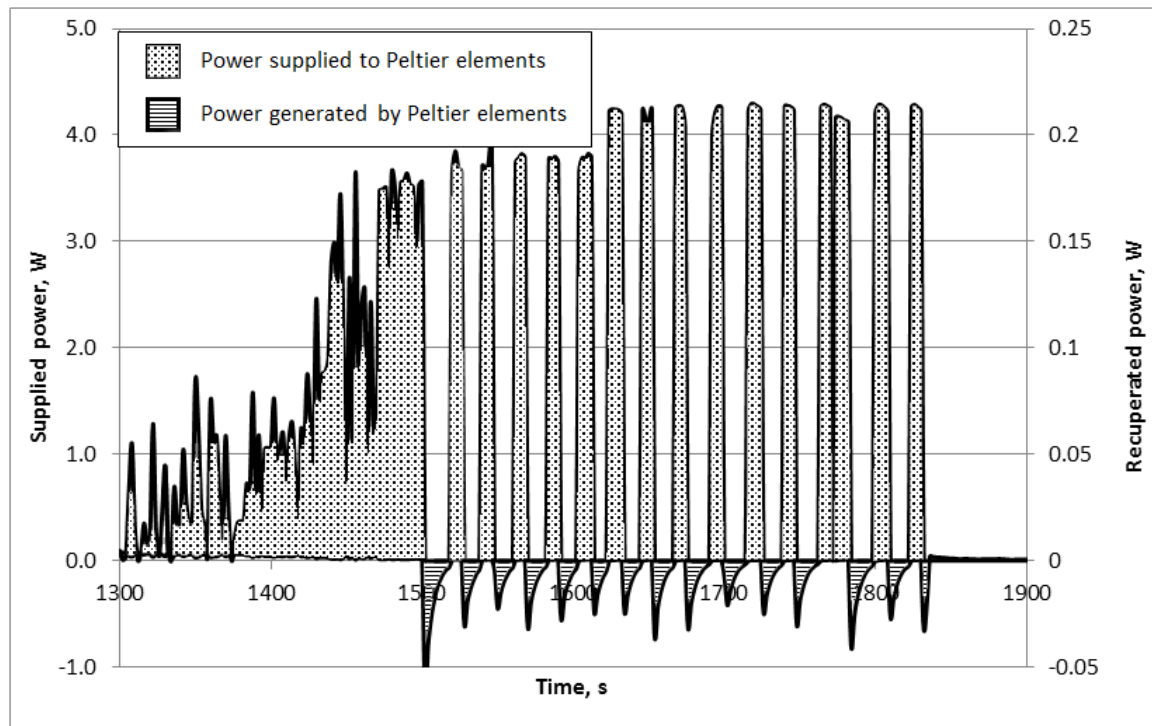


Fig. 7. Supplied and recuperated power in second experiment.

Due to the loss of cooling intensity it is recommended to use this approach in systems that suffer from excess heat in hot side radiator, hence causing the heat backflow, for example human body microclimate controlling system. Instead of turning off the system or generating more excess heat, it would be preferable to use recuperation. This study investigates recuperated electrical energy that could be dissipated on simple resistive electrical load. Further studies should be made to find most optimal ways to harvest this energy, store it in accumulators or supercapacitors and use it effectively.

5. CONCLUSION

An approach to increase efficiency of Peltier element based cooling systems has been presented in this paper. This approach offers to use Peltier device periodically changing working mode from cooling to thermoelectric generator. It has been experimentally proved that it is possible to recuperate electrical energy supplied to Peltier element during cooling process, thus perspective decreasing overall energy consumption. Paper shows the possibility to use this advanced control method either for large or small power systems. Experimental data shows that it is possible to return up to 3% of electrical energy supplied to Peltier element based cooling system.

6. REFERENCES

1. I-YU HUANG, JR-CHING LIN, KUN-DIAN SHEA, MING-CHAN LI, JIANN-HENG CHEN, JIN-SHUN Kuo. 2008. *Sensors and Actuators A* 148, p. 176–185.
2. BANSAL, P., VINEYARD, E., ABDELAZIZ, O. 2012. Status of not-in-kind refrigeration technologies for household space conditioning, water heating and food refrigeration. *International Journal of Sustainable Built Environment* 1, p. 85–101.
3. YANG, B., AHUJA, H., TRAN, T.N., 2008. Thermoelectric technology assessment: Application to air-conditioning and refrigeration. *HVAC&R Res.* 14, p. 635–653.



4. LAN, Y., MINNICH, A.J., CHEN, G., REN, Z., 2010. Enhancement of thermoelectric figure-of-merit by a bulk nanostructure approach. *Adv. Funct. Mater.* 20, p. 357–376.
5. SWIFT, G.W., 1988. Thermoacoustic engines. *J. Acoust. Soc. Am.* 84: p. 1145–1180.
6. POESE, M.E., SMITH, R.W., GARRETT, S.L., VAN GERWEN, R., GOSSELIN, P., 2004. Thermoacoustic refrigeration for ice cream sales. In: *Proc. 6th IIR Gustav Lorentzen Conf.*
7. ZINK, F., VIPPERMAN, J.S., SCHAEFER, L.A., 2010. Environmental motivation to switch to thermoacoustic refrigeration. *Appl. Therm. Eng.* 30, p. 119–126.
8. BROWN, D.R., FERNANDEZ, N., DIRKS, J.A., STOUT, T.B., 2010. The prospects of alternatives to vapour compression technology for space cooling and food refrigeration applications. A Rep. by PNNL-19259 for US Dept. of Energy.
9. WETZEL, M., HERMAN, C., 1997. Design optimization of thermoacoustic refrigerators. *Int. J. Refrig.* 20, p. 3–21.
10. NOLAS, G.S., SHARP, J., GOLDSMID J., 2001. *Thermoelectrics: Basic Principles and New Materials Developments.*
11. RIFFAT, S.B., MA, X., 2003. Thermoelectrics: A review of present and potential applications. *Appl. Therm. Eng.* 23, p. 913–935.
12. GIAUQUE, W. F.; MACDOUGALL, D. P., 1933. Attainment of Temperatures Below 1° Absolute by Demagnetization of Gd₂(SO₄)₃·8H₂O. *Phys. Rev.* 43 (9). 768 p.
13. KITANOVSKI, A., EGOLF, P.W., 2010. Innovative ideas for future research on magnetocaloric technologies. *Int. J. Refrig.* 33, p. 449–464.
14. SIER R., 1999. *Hot air caloric and stirling engines. Vol.1, A history*
15. WHITMAN, W. C., JOHNSON, W. M., TOMCZYK, J. 2005. *Refrigeration & Air Conditioning Technology (5th ed.)*.
16. SAPALI, S. N., 2009. *Lithium Bromide Absorption Refrigeration System. Textbook Of Refrigeration And Air-Conditioning.* 258 p.
17. LU, Z.S., WANG, R.Z., WANG, L.W., CHEN, C.J., 2006. Performance analysis of an adsorption refrigerator using activated carbon in a compound adsorbent. *Carbon* 44, 747–752.
18. MAZUMDAR, S., GOPAL, M. R., BHATTACHARYYA, S., 2004. Performance of Compressor Driven Metal Hydride Cooling Systems Under Different Operating Conditions. *International Refrigeration and Air Conditioning Conference.* 9.
19. MUTHUKUMAR, P., GROLL, M., 2010. Metal hydride based heating and cooling systems: A review. *Int. J. Hydrogen Energy*, p. 3817–3831.
20. SAHTA I., BLUMS U., BALTINA I., JURKANS V., 2011. Thermoregulatory system's integrated in the clothes effect on the human microclimate. *150 Years of Research and Innovation in Textile Science: Book of Proceedings*, p. 856–860.
21. BENNETT S., 1993. *A history of control engineering, 1930–1955.* 48 p.



SUSTAINABLE DEVELOPMENT OF REGIONAL ENERGY SYSTEM USING PROCESS NETWORK SYNTHESIS METHOD

K. Biekša

Lithuanian Energy Institute

Laboratory of Regional Energy Development

Breslaujos str. 3, LT-44403 Kaunas – Lithuania

Phone: +370 680 16985

Email: biekša@mail.lei.lt

ABSTRACT

The scarcity or abundance of local energy resources depends on regional geographic conditions, geological structure of land, soil structure, water, forests and other natural resources. The supply of renewable energy resources (RES) and development of RES technologies also depends from economic, social and environment aspects for energy resources extraction and energy production. Usually economic instruments such as criteria of efficient use of investment and operational capital are used for evaluation of energy production technologies in the region. Therefore environmental and social impacts of energy production technologies are considered as negligible factors for influencing the final energy prices. Process synthesis analysis (PNS) method helps to assess the use of energy production technologies through evaluating energy flow in the region from the use of RES, other local energy resources and fossil burning fuel technologies. PNS method is evaluates the economic influence in the region according technological and economic factors of energy production. The method optimizes the delivery and distribution network of energy resources and the final energy according availability, supply and demand of the energy resources and the final energy. In the article energy economic sectors are analyzed in two regions of Lithuania. Energy economy development models in investigated regions are created base on PNS method and the use of RES. Evaluation of regional energy economy systems and the comparative analysis of energy economic models are carried out in investigated regions.

Keywords: renewable energy resources, energy process network synthesis analysis, regional energy economy

1. INTRODUCTION

Regional energy economy development is a complex system and it depends on three factors of sustainability: economy, environment and social life. Every aspect is crucial for the future development of the region because every municipality needs to balance their local economy for the best living standards for local inhabitants. Our generation has a challenge to cope with the energy problems. They need wisdom to use fossil resources for energy production useful and efficiently. At the same time they need to increase the use of alternative energy technologies without influencing much the environment, economy and social sectors. The way to achieve an optimal performance of the regional energy economy is not a simple solution however the best option is to start the developing process from the own yard. Municipalities or local communities are the right target regions which can initiate the bottom up development process however supervision from above is also needed. This article investigates possibilities of the smallest regional unit – community – to achieve sustainable energy economy development scenario. The community – the smallest administrative unit of Lithuania – was chosen as a target region. Follow the comparable projects (by the plot of the territory and population) done in other countries (Austria) community or elderate was considered as the best area for investigation. Good practice experience gained from regional development projects in other countries were treated as positive examples for local regional development projects in Lithuania. Community was chosen because the “bottom-up” approach has a potential for sustainable development in the region. Regional development is currently has less

serious political trouble and level of changes within region is less complex. Regional developing projects need a broad approach but less central governing, more local initiatives and less big money or top-down project development. Consequently the statements of sustainable development – “think globally act locally” is the right proverb for regional economy development.

The objective of this article is to evaluate local energy potential in the community and to investigate energy economy development options. Target group – two small communities in Vilnius region municipality – Riese and Avizieniai elderate (community). The task is to determine the best energy production technology and to describe the best available technologies for production of energy to cover energy needs in the regions

2. PROCESS NETWORK SYNTHESIS ANALYSIS METHOD

The objective of process network synthesis (PNS) program is to identify the most favorable, optimum process network [2]. Program has been developed for the P-Graph (process graphs) based methodology to provide PNS model can be used for analysis of the local regional energy economy and evaluation of energy economy development trends in the region. Process synthesis is expected to solve problems of creating an optimal, integrated and cost efficient structure to convert raw materials to products, more or less ignoring the world outside the factory gate [5]. The more information about energy demand in the region we know the more detail and accurate scenario we can get. Process Network Synthesis is a method to optimize material and energy flow within a region. The main aim is to find a network consisting of operations of processes technologies to transform raw materials into products (including energy). This method requires the optimization of process structures as well as the optimization of continuous flows such as material flows in a processing unit [3]. A combination of methods will definitely lead to an optimum. Process synthesis approaches have already been employed to generate complex process structures in industries, based on input-output relations for process steps and the properties of material and energy flows. These methods can be applied to regional material flow networks as well as to optimizing renewable resource utilization pathways.

Using the following information presented below it is possible to generate an optimal technology network for a hybrid energy solution [3]:

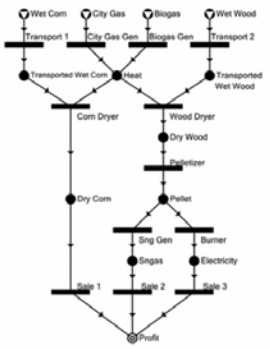
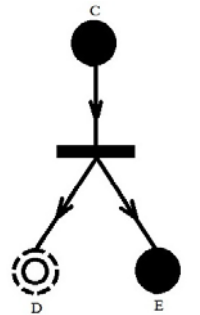
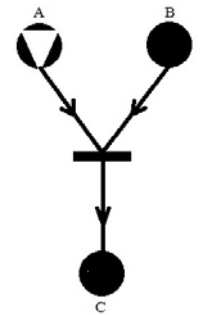
- Regional resources (land components with the according basic conditions or numbers of available resources per year)
- Existing infrastructure (district heating station, biogas plant, heating network, etc.)
- Existing or ongoing projects (expansion of heating networks, further customers, possible markets for agricultural products and refining products, etc.)
- Material and energy flows of technologies for disposition of incoming agricultural products or rather waste and by-products of the technologies and farming.
- Investment and operating costs of the technologies available.

PNS method requires optimization of energy production process structures as well as the optimization of continuous flows of energy material flows in processing (energy production) unit [1]. The following information such as regional resources, existing infrastructure, existing or ongoing projects, material or energy flows of technologies from agricultural, farming or other activities, investment and operating costs of technologies, prices and costs for resources, products and services provided by network it is possible to generate an optimal technology network for energy solution.

PNS method is based on P-graph structure as unique bipartite graph representing the structure of a process system. In P-graph the operating units are denoted by horizontal bars and their input and output materials by solid circles [3]. A P-graph is a directed graph; the direction of the arcs is the direction of the material flows in the network; it is directed to an operating unit from its input materials and from an operating unit to its output materials. P-graph is a bipartite graph. One set of

nodes (horizontal bars) represents the operating units and the other (solid circles) the material streams. Relations of the operating units are realized through material streams. In P-graph representation there are arcs from each input material (stream) to the operating unit consuming it and from each operating unit to its output materials (streams). In a table below in column (a) is shown an example where in one operating unit two separate materials are produced (a main product D and by-product E). In column (b) is shown as a single operating unit receiving material (raw resources) A and by-products from other processes B as its inputs, produces a material which is subsequently fed to another operating unit where material C (by-product) is generated.

Table 1. Principle of PNS structure using P-graph method

 <p>P-graph representation of the process structure</p>	 <p>(b) Materials C, D, and E, and operating unit ({C}, {D, E})</p>	 <p>(a) Materials A, B, and C, and operating unit ({A, B}, {C})</p>	<table border="1"> <tr> <td></td> <td>Operating unit</td> </tr> <tr> <td></td> <td>Raw material</td> </tr> <tr> <td></td> <td>Product</td> </tr> <tr> <td></td> <td>Intermediate material</td> </tr> <tr> <td></td> <td>Byproduct</td> </tr> </table> <p>A Legend of symbols</p>		Operating unit		Raw material		Product		Intermediate material		Byproduct
	Operating unit												
	Raw material												
	Product												
	Intermediate material												
	Byproduct												

3. INVESTIGATION OF TARGET REGIONS

A set of available energy infrastructure were investigated before applying PNS model. Investigated regions were chosen according similar case studies done in Austria. Community as target region was chosen because its size of the territory and population are similar. Possibility to use renewable energy technologies were emphasized with major application of solar and biomass technologies. Nowadays the target region is more energy consumer neither energy producer therefore the application of energy production technologies was recommended in order to use local available energy resources. Consequently the possibilities of decentral and central energy production technologies units were proposed. PNS program investigates energy flow within the target region and gives results of the optimum energy distribution network.

3.1. Geographical and land characteristics

Investigated communities are situated in the outskirts of Vilnius city close to each other. These are neighboring communities of Vilnius city. The biggest village called Riese is situated in Avizieniai community and Didzioji Riese is situated in Riese community. However both these villages nowadays constitute one residential dwelling district nevertheless they belong to the different communities. That is why these both communities were taken for investigation. Due to expansion of Vilnius development housing projects these communities are suffering from unexpected expansion of real estate projects and uncontrolled decentralize planning of housing projects. Communities are lacking of infrastructure in the outskirts.

Riese community is situated in the central part of Vilnius region municipality. It accounts around 4'216 inhabitants (5.09% from the overall population in the region). **Avizieniai** community is situated in the central part of Vilnius region municipality as well but to the west south from Riese community. It accounted 4276 inhabitants (Lithuanian Statistics, 2003) however due to expansion

of housing development projects the population has increased by 60% and now lives 6845 inhabitants (7.6 % from the overall population in Vilnius region).

Table 2. Geographical-physical characteristics of investigated regions

Community	Population	Area, ha	Forests, ha	Agricultural land, ha	Built-up territories, ha	Water and other land, ha
Riese	4216	10220	1840	5398	1226	1756
Avizienu	6845	4500	1305	2295	675	225

The major part of territory is allocated for agricultural purposes (respectively in Riese 59% and in Avizieniai 51%) and this is slightly higher than the average 46% in Vilnius region and near the average rate (53.8%) in Lithuania. Most of agricultural land is not used directly because the prices of land have increased very much in the recent years due to development of real estate projects. Land owners usually waiting for the best time to sell the land and don't use it for agricultural purposes. Unused agricultural land plot accounts about 62% from all available agricultural land plot.

Forests occupy respectively around 19% of the territory in Riese community and 29% in Avizieniai community. Other land (water bodies, roads, built-up territory) occupy respectively 24% of the territory in Riese community and 24% in Avizieniai community.

Therefore in municipality of Vilnius region the rate of using agricultural land could be much higher because the potential is the same as in the rest part of Lithuania. Consequently the potential of land use for energy production is also high. However due to expansion of new real estate development projects approximately 40% of agricultural land and 5% of forest land is going to be built up [6]. The land productivity rate in investigated communities is 36.6 (average in Lithuania is 42.3) [7]. The average farm size in suburban communities was 4 ha (countries' average – 10.4 ha). Distribution of agricultural land in suburban communities was as follow: grain 24 % (countries' average – 34.9%); potatoes and industrial plants – 10.9 % (7.6%); root plants and vegetables – 3.6 % (1.8%); grassland and other crops – 51.5 % (47.8%); fallows and unused land – 10% (7.9%). The distribution of land allocated for cattle: number of cattle per 100 ha of land territory – 33.8% (35.3%); number of pigs per 100 ha of land territory – 28.7% (42.9%) [6].

3.2. Development problems

The neighborhood of Vilnius city is causing the problems for unsustainable and rapid development of suburban territories. Agricultural land and forests are allocated for real estate development projects without detail planning procedures usually leaving aside social, economic and even landscape and architectural aspects. The driving force for real estate development project is the rising prices of land plots. Following the concept of general plan development of Vilnius region the average rate of agricultural land use is only 40%. However this index has advantage to a positive approach of sustainable development principles of modeling sustainable region scenario using renewable energy resources. Planners say that there are two main trends for development of these regions from the viewpoint of land use and planning. First is a compact city model, other – is geographical decentralization of the city with a conceptual idea of small satellites of green villages [6]. The aspiration of sustainable regional energy economy development is a safe, environment friendly, modern and smart region model. However before modeling the regional energy economy we need to identify the energy consumption capacities, patterns and trends. Therefore the next chapter analyzes the energy consumption data in the region.

3.3. Energy consumption

3.3.1 Collection of information

Energy in the region usually is needed for heating and electricity in general. Energy for heating of buildings is divided according the use of buildings: residential and other buildings (public, administrative, commercial), according the number of floors and the year of construction. Data of heated plot of buildings were taken from Lithuanian statistics [7], National land service [8] and from Lithuanian energy ministry report of energy distribution within municipalities [4]. As well there were carried out the sociological investigation in the target communities in the period from August 2012 to February 2013 where interviewed about 120 respondents. Data about buildings which is heated using central heat network were taken from local company JSC “Nemencines komunalininkas” which operates and supervise local district network in Riese and Avizieniai communities. One of the main problems is to find appropriate data in community level because all mentioned data bases in the references [4,7,8] are available for municipality level only.

3.3.2 Information about buildings

Consequently the data about buildings area and energy consumption in it were recalculated according the share of inhabitants and households in investigated communities. The plot of buildings is presented in a table below. The largest group of building is individual dwellings houses. The total plot of individual dwellings is five times larger than multistory houses plot. Buildings area and its plot are presented in a table below

Tabel 3. Distribution of building plot in investigated communities

Community	Individual houses 1-2 floors, m ²	Multistoried houses, 3 and more floors, m ²	Other buildings, m ²	Total are of buildings, m²
Rieses	105'911	27'102	15'492	148'504
Avizieniu	171'954	44'002	25'152	241'108

(Source: National land service, 2011)

One household consist of 2.5 inhabitants [8]. The number of household in Riese community is 1686 (4.37% from the total number of households in Vilnius region) and in Avizieniai community – 2738 (7.09%). The total heated area in buildings account 148 thous.m² in Riese community and 241 thous.m² in Avizieniai community. According installed heat system the total heated are in Riese community is 62 thous.m² and 146 thous.m² in Avizieniai community. Energy user groups were investigated according the heating system installed in houses as well using report [4] and the date are presented in table 4.

Table 4. Distribution of buildings according installed heat system

Community	Natural gas, m ²	Electric boilers, m ²	Biomass boilers, m ²	Liquid fuel boilers, m ²	Central heat network users, m ²	Total plot, m²
Rieses	3'891	1'652	16'834	34'881	5'662	62'920
Avizieniu	6'317	2'682	27'332	56'518	53'764	146'613

(Source: Ministry of Energy, Report, 2011)

3.3.3 Energy consumption in buildings

Primary energy needs for heating, preparation of hot water, electricity for living dwellings, public houses and other premises were calculated according legislative norms for energy demands and consumption of buildings and according resolution for energy use in buildings of National control commission for prices and energy regulation. It was presumed that old buildings (built before 1990 year) consume 225 kWh per 1m², buildings built after 1992year have value 145 kWh

per 1m^2 and new houses - $120\text{ kWh per }1\text{m}^2$. Energy needs for buildings are presented in a Table 5 below.

Table. 5. Energy demand for dwelling house in communities

Region	Population		Number of household	Annual total heat demand (norm value 225 kWh/m^2)			Annual total heat demand (norm value 145 kWh/m^2)			Annual total heat demand (norm value 120 kWh/m^2)		
				Living dwellings	Other	Total	Living dwellings	Other	Total	Living dwellings	Other	Total
				MWh	MWh	MWh	MWh	MWh	MWh	MWh	MWh	MWh
	vnt.	%										
Vilniaus r.	96.484	100%	38.594	295.046	165.983	461.028	190.141	44.013	234.154	157.358	36.425	193.783
Riešė	4.216	4,37%	1.686	12.892	7.253	20.145	8.308	1.923	10.232	6.876	1.592	8.468
Avižieniai	6.845	7,09%	2.738	20.932	11.776	32.707	13.489	3.123	16.612	11.164	2.584	13.748

The total energy needs for heating of buildings account about $19'435\text{ kWh}$ in Riese community and $31'555\text{ kWh}$ in Avizieniai community. Electricity consumption in the region is calculated according average energy use norm (data are gathered from sociological pool). One household consume around 4800 kWh per year (400 kWh per month). Therefore the total electricity demand is around 8093 MWh in Riese community and 13142 MWh in Avizieniai community. Total electricity demand is 21235 MWh .

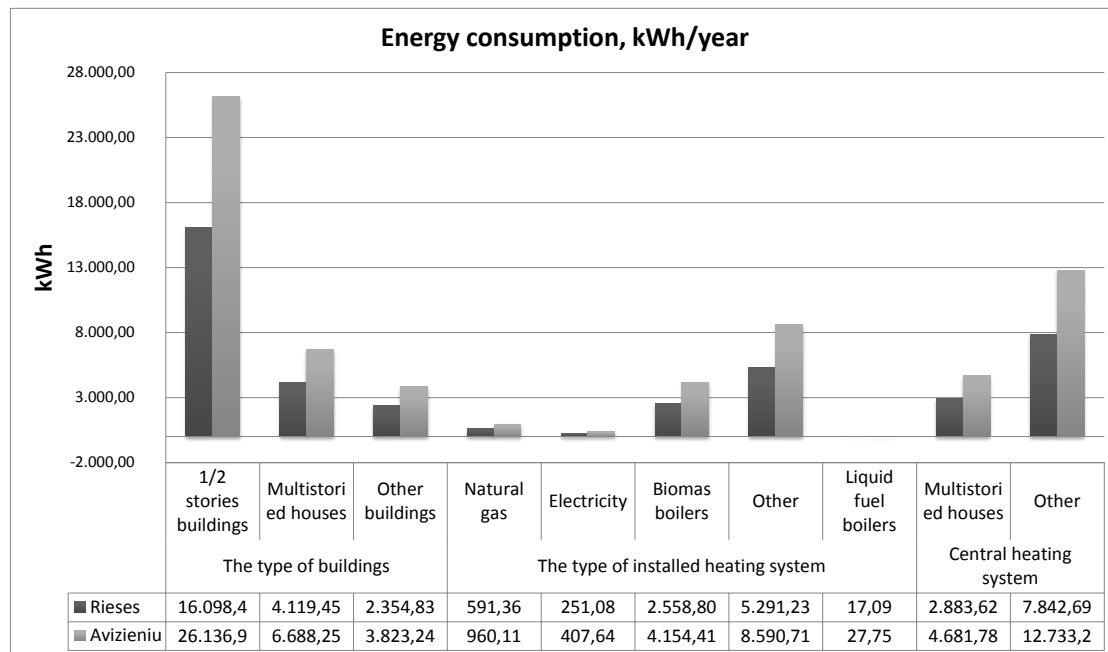


Fig. 1. Energy consumption in buildings [7, 8]

3.3.4 Energy consumption in the central heating network

Local operator of district heating network JSC “Nemenčines komunalinikas” has provided information about distribution and supply of central heat energy for investigated communities. Using 2 decentral natural gas boilers in Riese community there were supplied 768 MWh of heat energy. Using 5 decentral gas boilers there were supplied $6'783\text{ MWh}$ of heat energy to Avizieniai community. Totally there were supplied $7'551\text{ MWh}$ of heat energy and were used $1'315\text{ thous.nm}^3$ of natural gas. Total heated plot of buildings is $49'677\text{ m}^2$. Average energy consumption rate is 152 kWh/m^2 .



4. MODELLING THE REGIONAL ENERGY SCENARIO

4.1. The status quo model

Existing regional energy infrastructure consists of the following components: electricity network, natural gas network, local (individual) biomass and electric heat boilers for heating buildings and preparation of hot water, central heating system. Electricity to users is supplied through electricity network by the company “Litgird” which gets electricity from various producers (half of electricity is imported). There are no local electricity production facilities in the region so far, however the boom of solar PV installations can change the situation after 1st of March, 2013. There are two natural gas fired boiler plants in Riese community and five natural gas fired plants in Avizieniai community which are producing heat for local living and other buildings. The rest 80% of buildings are heated up using individual heat boilers. Approximately 50–80% of it is using natural gas boilers and about 30% is using biomass burning boilers. 70% of households are preparing hot water using electric boilers and around 30% are using natural gas boilers. Transport system is based on a mixture of public and private vehicles. There is a municipality bus system which operates in the region. However cars and buses infrastructure is based on using fossil fuel (diesel, gasoline, and liquid natural gas). There is no train or tram infrastructure in the region.

The energy infrastructure is based mostly on fossil fuel use. However about 30% of energy is produced using renewable energy sources – biomass, which is imported from other regions. There is no data available about quantities of locally produced biomass fuel (firewood), but considering the similar structure of private forests distribution there is probability that forest owners use their own forest as energy resources for heating purposes. Municipal building sector and multistory house sector get heat from a central heating plant or using decentral individual heat boilers. Local central heat boilers operated by local heat distribution company use only natural gas for central heat production. Industrial sector is mostly equipped with natural gas or biomass heat boilers however there is lack of information about energy use in industry or business sector. The main focus of PNS analysis is to develop regional energy economy infrastructure which can support energy needs using renewable energy resources, can generate additional energy amount and will increase the regional added net value.

4.2. Modeling energy scenario using PNS program

PNS programs have investigated 65 materials and sub-products and 44 energy production technologies (operating units). Maximal structure of PNS model consists of 23 available energy production technologies which use 39 primary and secondary materials. PNS algorithm has excluded 25 energy production technologies and 28 primary materials and sub-products. The main criteria of modeling energy economy scenarios are the balance of energy flow, the payout period and energy prices. It is important to choose the adequate capacity of production, to evaluate investment and operating costs. However the use of renewable raw materials based on biomass is under consideration in this article. The idea was taken from Austrian case studies with application of green biorefinery technologies where grass as raw material is used. The second approach is that biomass (land, forests) creates a boundary of regions [5]. The third aspect is that the situation in bio-resources (grass land, arable land, forests) in Austria and other EU countries have similar problems as in Lithuania as well. The problem is that grassland becomes a serious surplus problem for agriculture [5]. The percentage of utilized grassland in investigated communities reaches only 40%. The grassland will decrease considerably over the next decade will influence farm income as well as landscape [5]. So we are not alone in battle field of finding the solution for regional energy development using biomass resources.

The green biorefinery could be the solution for applied high tech technologies in the region, because green biomass (grass silage) can generate bulk chemical (lactic acids and amino acids), fine

chemical, fibers and fiber products and energy from biogas generations [5]. The other idea is to create sustainable regional energy economy minimizing transportation costs which are still based fossil fuel. Removing water content from biomass, compacting biomass (granulating, palletizing, chopping) can considerably save transport costs. Transport may play a significant role in setting up the whole production chain [5]. A number of energy productions steps (pressing, chopping, palletizing, biogas generation) can be done locally or centrally and the right mixture of local and central production can significantly influence local energy economy [5]. Choosing the right structure is one of the main driving forces in the final energy price of energy production technologies.

The creation of PNS model was based on following materials: (1) agricultural fields and its sub-product which can be grown (several sorts of grass (miscanthus, sudangras), short rotation plants (lot. *Salix viminalis*), rape, maize and other sort of crops); (2) forests land (input material are wood log, woodchips, wood residues); (3) agricultural meadow (input material – grass silage); (4) livestock input (input material – mainly house manure); (5) solar thermal collector and solar PV modules installed on roofs of buildings; (6) wind energy application in small (up to 2 kW) and industrial cases (from 150 kW).

The following operating units as energy production technologies were investigated:

1. Drying, pressing and storing of biomass (straw, crops, grass; output – biomass fuel);
2. Drying and pressing of plant seeds (output material – plant oil, press cake);
3. Drying and chopper of wood products (input product – wood products, wood residues, scrap wood; output products – woodchips);
4. Briquettes making technology (output products – wood briquettes);
5. Wood palletizing technology (output products – wood pallets);
6. Grass silage technology (output product – pressed grass, milk and amino acids, fertilizers);
7. Different types of combined heat production technologies (use of natural gas boilers, introduction of CHP plant using biomass; output product – heat and electricity):
 - a. Direct burning technologies (output – heat and/or electricity);
 - b. Organic Ranken Cycle (ORC; output – electricity and/or heat);
 - c. Gasification process (output – heat, biogas);
 - d. Pyrolysis process (output – charcoal, pyrolysis oil, excess of heat).
8. Biogas plant (input – residues from livestock (horse farms), grass silage, mixture of different biomass; output – bio gas supplied to existing natural gas network or used locally in electric generation).

During modeling of optimal energy network structure the priority was given to reconstruction of natural gas network, expansion of district heat network and use of RES technologies. The substitution of natural gas is to use cleaned biogas produces at fermenter using biomass is quite promising because of investment costs of cleaning biogas is 375 thous. Eur and operation costs 109 thous. Eur per year. To clean 1m³ of gas costs around 1.9 Eur. Delivery of biogas to gas network theoretically is possible and the price is around 10 Eur per 100 m³ of delivered biogas to gas station. Biogas to natural gas network can also be supplied using wood or straw gasification technology where synthetic gas is produced from using wood and biomass drying technological units. The costs of gasification unit is 1,68 mln. Eur, the price of produced 1MWh of synthetic gas is around 165 Eur, but it is increasing if the capacity of synthetic gas production is lower. The size factor is thing of matter. Production of biogas at fermenter is various from 1.4 to 0.7 Eur per 1m³ of biogas. The major aspects for developing of regional energy systems is the use of biomass for heat production and production of biomass fuel (wood pellets). The drying of wood biomass costs around 4 Eur/t and draying of straw is around 8 Eur/t. Chopping of dried biomass cost around 0.4 Eur/t. Then biomass chops goes to pelletizing or biomass fired boilers or CHP plants.

The second choice were driven more by environment issues. Consider the expansion of houses area and increase of density of built-up areas the quality of air is important. Therefore from

the ecological viewpoint it is worth to upgrade existing central heat boilers houses from natural gas burning to biomass burning technologies. This technological application is showing remarkable decrease in final energy price. The best and cheap way is to install or upgrade existing furnace boiler houses because investigation show that the energy price for heat energy is only 0.03 Eur/kWh (30 Eur/MWh). Using ORC (organic ranken cycle) technology shows that the heat energy price is slightly higher is around 0.07 Eur/kWh. However using ORC technology we can getting electricity, where the cost of electricity production is around 0.15 Eur/kWh. ORC technology due to the large investments (about 2.76 mln. Eur with a capacity of 1200 kW) was rejected by PNS program. The same situation is with micro gas turbines (MGT) where the price for electricity production is 0.24 Eur/kWh. At the same time the energy production price at solar PV models is around 2.5 Eur/kWh however due high feed-in tariffs (0,41 Eur/kWh) solar PV models were included in PNS model and its is still economically valuable according PNS if the feed-in tariffs is above 0.25 Eur/kWh.

Economic indicators are the main driving factors for the energy economy modeling. PNS model has provided information about energy prices. The heat energy prices are lowest where biomass resources are used (wood residues, wood logs, wood pallets, and wood briquettes). The price per 1kWh of energy is around 0.05 Eur (0.17 Litass/kWh). Heat energy price is higher if the resource is natural gas. Energy price is around 0.11 Eur/kWh. Compare energy price of central heating system it is slightly less and is around 0.08 Eur/kWh. However this is not a final price because about 30% of energy price is compensated by municipality of Vilnius district. Electricity produced using RES is sold through applied feed in tariffs which is compensated via public service obligation financing mechanism. However it is interesting to notice that electricity produced using wind power generators is the cheapest (0,10 Eur/kWh) among investigated technologies. Average electricity price for consumers in Lithuania is costa about 0.13 Eur/kWh, while energy imported from Latvia or Belarus cost only 0.05 Eur/kWh. The most expensive way of producing electricity is to use Solar PV modules, the price than is around 0.38 Eur/kWh. However solar PV models technologies is developing very fast and consequently the investment cost is reducing as well.

Scrap wood and woodchips is used in pyrolysis technology for making pyrolysis oil as a substitute of oil products and for making a charcoal. Calculating production capacity of charcoal and pyrolysis oil the price for scrap wood should be less than 125 Eur/t. However if the price is higher PNS is excluding pyrolysis option from energy structure. Wood logs, wood residues, damaged wood, short rotation biomass are used in PNS process for heat production at central heat boiler house and in individual houses as well. However PNS has excluded wood for pelletizing technologies and chopping of wood because the quantity of available damaged wood is not available in the investigated region. Chopping, pelletizing or pyrolysis technologies only are valuable if all wood resources in Vilnius region municipality are considered.

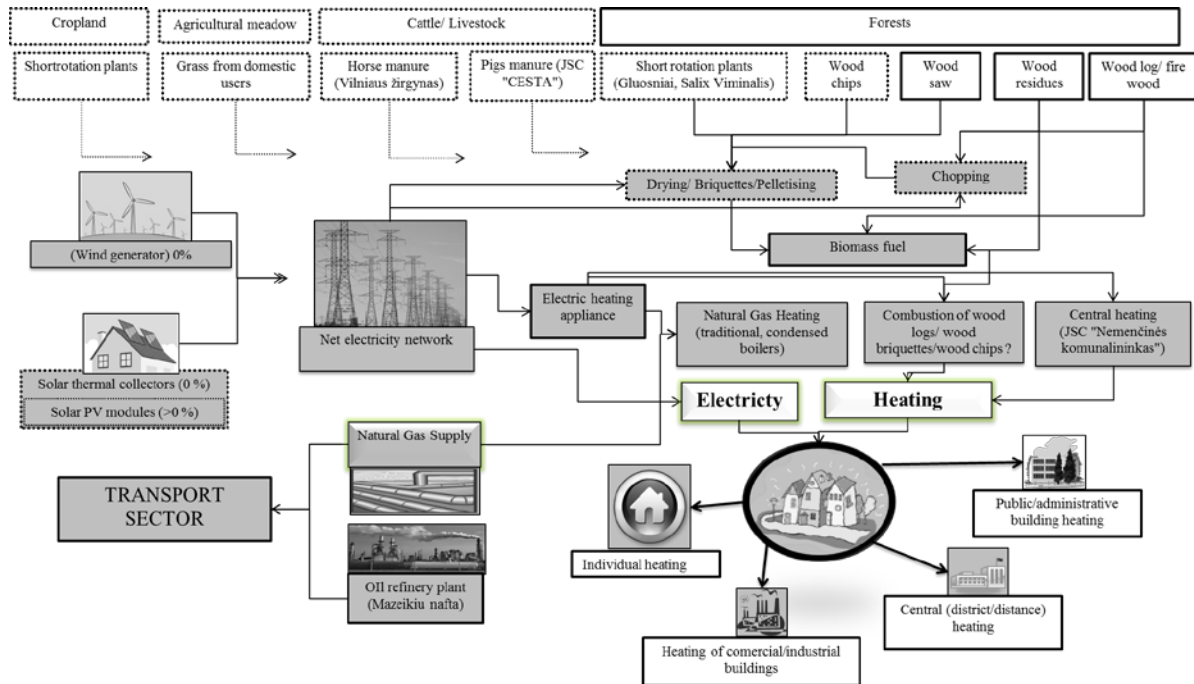


Fig.2. Optimal energy structure by PNS analysis

5. CONCLUSIONS

It is a crucial for PNS algorithm to assess available energy sources (input materials) and energy production technologies with all energy flows. To achieve sustainability of energy use within the region the balance of energy flows should be achieved. A surplus of energy is having an advantage because energy as fuel can be exported outside the region and can generate a net added value. If energy consumption rate is less than energy production capacity this means that regions are not sustainable from energy use viewpoint. Excess of energy (energy products) should be imported outside the regions. If there is no infrastructure to do this (in case of heat excess delivery) there will be a problem of overinvesting and getting increased energy prices. So there is always a problem to find equilibrium between consumption and production. It is good of course to have an excess of energy which can be exported but if the energy prices or price of energy products is too high compare to other regions that will cause the loss of investments and will influence the region economy as well.

It's important to notice that not only economic and ecological factors are important to implement innovative structures. Often we forget about the social component and the culture aspect of regional development. A bottom up approach is necessary because the best solutions or ideas are usually coming from local communities. However regulations mechanisms and promotion tools for innovation and investments are necessary as a top down tool to establish the best regional energy economy scenario. Higher feed-in tariffs for RES technologies gives a chance to foster a faster development of new energy production technologies which open gates to decentralize energy economy model in regions. The advantages of PNS methods are that local energy resources are selected with the maximum efficient rate of it use and that technologies are evaluated according energy production flow.



6. REFERENCES

1. NARODOSLAWSKY, M. Ecological impact of renewable resource based energy technologies. International conference on process integration, modeling and optimization for energy saving and pollution reduction. Rome, Italy. 2009 10–13 May.
2. VARGA, V., HECLK, I., FRIEDLER, F. PNS Solutions: a P-Graph based programming framework for process network synthesis. Chemical engineering transactions. 2010. Vol. 21. p. 1387–1392.
3. NARODOSLAWSKY, M., KETTL, K.-H., NIEMETZ, N., SANDOR, N., EDER, M., Ecological evaluation of biogas feedstock from intercrops. TUG, Graz. 2011, p. 4.
4. LR ENERGETIKOS MINISTERIJA. (2009). Šalies savivaldybėse esamų atsinaujinančių energijos išteklių (biokuro, hidroenergijos, saulės energijos, geoterminės energijos) ir komunalinių atliekų panaudojimas energijai gaminti. LEI, galutinė ataskaita.
5. HALSZ, L., POVODEN, M., NARODOSLAWSKY, M. Sustainable processes synthesis for renewable resources. 2005. Resources, Conservation and Recycling 44. P. 293–307.
6. ALEKNAVIČIUS, P., VALČIUKIENĖ. J. Kaimiškojo kraštovaizdžio raidos ypatumai Vilniaus miesto įtakos zonoje. Vandens ūkio inžinerija, 2011, 38 (58), p. 32–41.
7. Lithuania Statistic. www.stat.gov.lt. Access to Internet on 2012.12.09.
8. National land service www.nzt.lt. Access to Internet on 2012.12.09.



ELECTRICITY COMPETITIVE MARKET DEVELOPMENT AND REGIONAL TRADING PERSPECTIVE FOR GEORGIA

Z. Gachechiladze

*Technical University of Georgia
Kostava str. 77, 0175 Tbilisi - Georgia*

ABSTRACT

Liberalization processes in Georgian power sector have been gaining more actuality over recent years. Reform has already produced impressive results. End user tariffs have risen and companies along the industry value chain have been privatized and are profitable. Power energy sector development policy is to continue to commercialize the sector. Against this backdrop of reform, increased private ownership of hydropower generation is a logical next step forward.

Regional economies and energy markets are also expanding fast. Demand for power in neighbouring Turkey, could double till 2020. An increasing and irreversible international appetite for electricity generated from renewable sources, and the highly productive nature of its rivers position Georgia to become a significant provider of export power in the midterm. The addition of a new, soon to be completed HVDC transmission line between Georgia and Turkey is a significant step towards realization of the country's export potential. When other new transmission lines become operational, total capacity between Georgia and Turkey will reach about 1.400 MW, ten times more than currently available.

Multiple changes have already been made to stimulate increased commercial activity in the industry. Barriers to market entry have been removed and there is wholesale competition in power generation. Tariffs and tariff policies intended to secure the sector's economic sustainability and enable service providers to achieve cost recovery have been adopted. The use of direct contracts between power generators and wholesale purchasers has been expanded. Transmission and distribution networks are managed on an open access basis. Energy sector reforming still proceeds and target remains full market opening, including retail competition. It is already proven that Georgian experience of very fast recovery, reaching electricity independency and success in development of power sector over last few years remains an interesting sphere of investigation for regional and post Soviet Union countries.

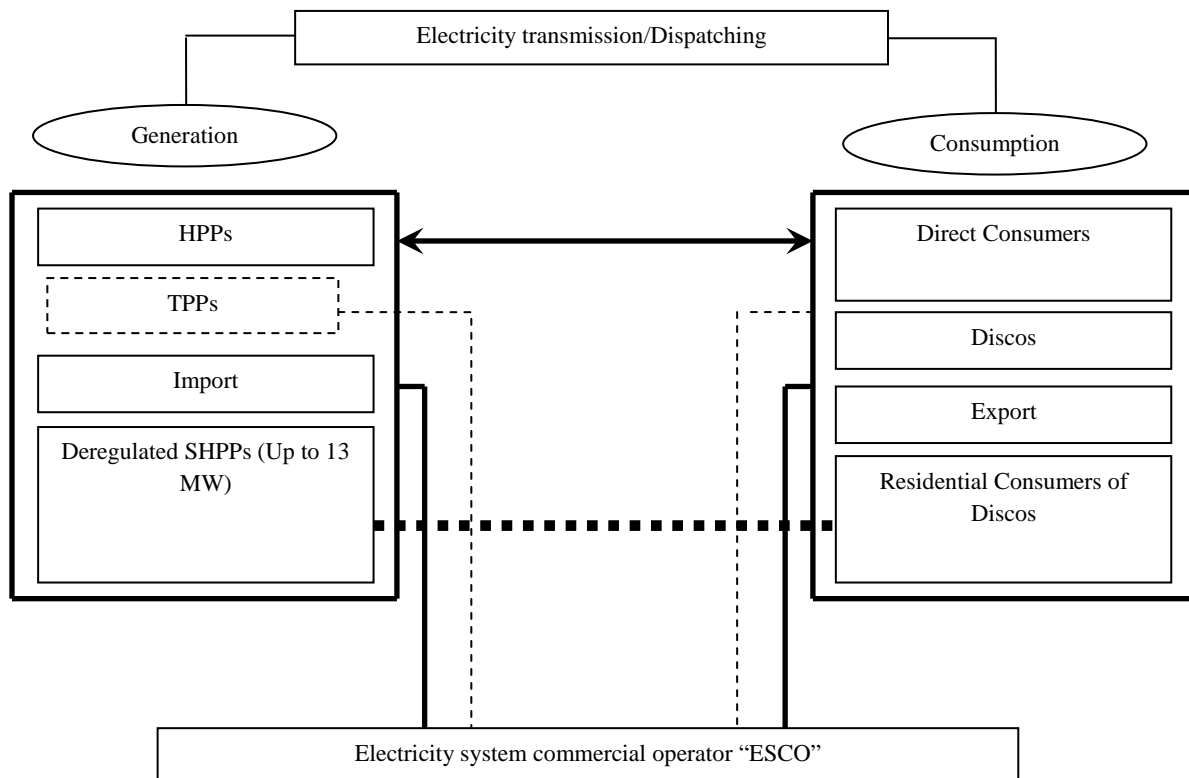
Keywords: Liberalization, electricity trading, Hydro-power generation, wholesale competition

1. INTRODUCTION

During the 1990s, many developed and developing countries began to restructure their electric power sectors to improve their performance. The restructuring programs have included privatization of state-owned enterprises, the separation of potentially competitive segments (generation and retail supply) from natural monopoly segments (distribution and transmission), the creation of competitive wholesale and retail markets. While these restructuring initiatives are ongoing, there is much to learn from both the successes and problems associated with the experience to date. This paper provides a brief review of the reforms in Georgia in this regard, current electricity market performance assessment and the implications for future reforms.

The first stage of reforms carried out in the power sector of Georgia is associated with the establishment of Electricity system commercial operator of (ESCO) and Georgian power market has transferred to the system of bilateral contracts. ESCO keeps records of the trade processes of wholesale power market and promotes the transparency of functioning of power sector.

Current model of electricity trade in Georgia is shown in the following drawing.



- ↔ Direct contracts
- Balancing electricity
- - - Reserve capacity
- ■ ■ ■ Standard contracts about selling/purchasing electricity
- Direct contracts about Transmission/Dispatching service

In order to provide the balance, ESCO purchases and sells balancing electric energy and reserve capacities. According to the new market rules, the holders of a licensee in power sector, qualified producers (consumers, which annual consumption attains 3.000.000 kWt.hr) concluded a short-term (1 month) or long-term direct contracts on the purchase and sale of electric energy. Contracts are concluded between power consumers and power producers, while agreements on the purchase of balance capacities are executed with commercial operators.

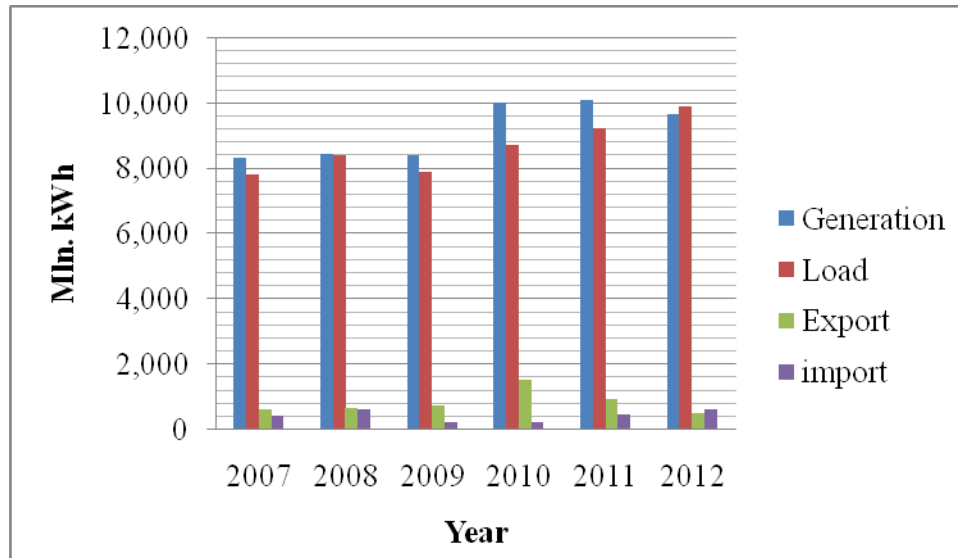


Fig. 2. Electricity balance of Georgia in between 2007–2012 years

Today the Georgian power market is in stable condition. 2007–2012 power balance gives a clear idea of improvement of system operation, where is clearly seen the increase in volume of power generation and its export during these years, at the same time the transmission losses for 2010 were equal only to 1,74%. Establishment of contractual relationships provides the 100% index of payments. Improved operation of power market has significant effect on the current processes of system updating, the processes of construction of new transmission lines and power plants that to a great extent improves the quality of energy independence of Georgia.

The analysis of current situation in Georgian electric power industry shows that the current model, in which electricity trade is based on mainly bilateral contracts, can be considered only as transitional model in order to introduce competition and timely and without painful consequences harmonize with the EU directives and principles. Under the terms of decrees of the Ministry of Energy and Natural resources of Georgia concerning the main directions of national policy in this regard, the process of power market opening is mapped out up to 2017 and is accepted that all consumers should have free choice by this period.

With the purpose of implementation of competitive market model in electric power industry is necessary the study of conjuncture features of competition in this field and assessment of readiness for market opening for competition by well-known criteria. This paper presents analyses of readiness of Georgian power market to comply with the EU principles of electricity market organization and functioning.

2. METHODOLOGY

Analyzing the sources of literature about electricity market performance [1, 2, 3, 5, 6, 7, 8], it can be concluded that an ideal indicators of market performance assessment is one that provides in a simple number a measure of the ability to exercise market power. Some of the earliest work in electricity markets was based on analyzing market share and the Herfindahl-Hirschmann Index [1, 2, 8]. Criticisms of these measures, in particularly the appropriateness of these static measures in a dynamic market such as electricity, has led to the development of other indices which take into account demand conditions and not just the supply side (for instance RSI, PSI) [4, 5, 7]. The aim of this section is to briefly review the features and applications of these indices to assess the real situation.

Hence, main objective of the study is to assess of the readiness for change-over to competitive model of management in electric power industry via the following major criteria: market opening, market share, Herfindahl-Hirschman index, residual supply index and regulating force [1, 2, 4, 5, 6].

Opening of power market is determined by ratio of total index of sale of electricity generated by generation facilities to direct consumer (P_{Lm}) to the total consumption of system (P_C).

$$MO = \frac{\sum P_{Lm}}{\sum P_c} (\%) \quad (1)$$

Georgian power market opening index data are shown in the following graph (see Fig. 3).

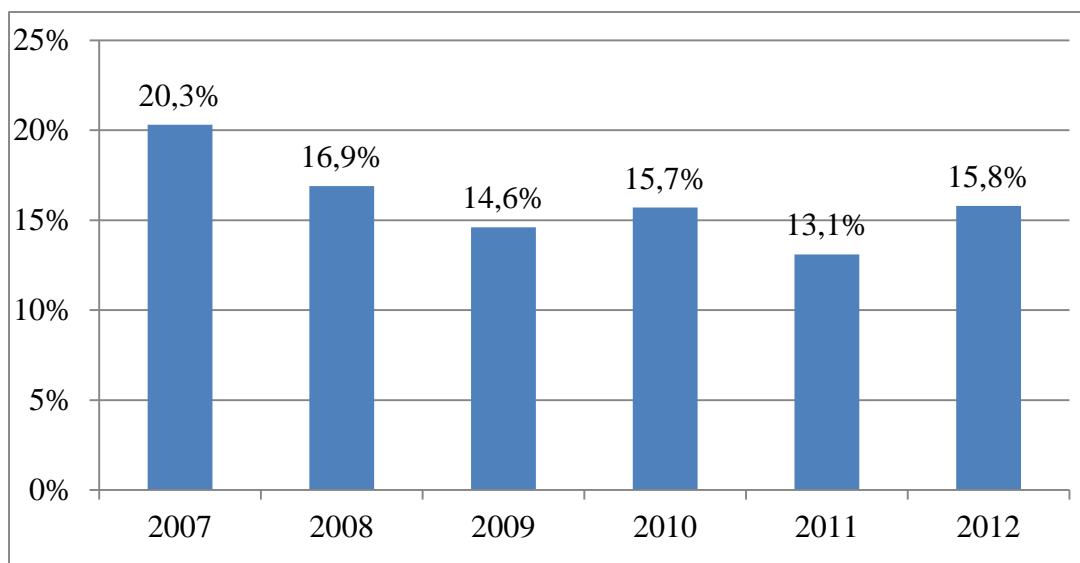


Fig. 3. Georgian power market opening characteristic 2007-2012 years

As is seen from Fig. 3, this index significantly falls behind the indices of EU member states, where it is almost equal to 100%. According to some economists' opinion [2] optimum level of market openness is 60–70% and the mentioned index depends on the consumption level in the country and on the consumer's structure.

Herfindahl-Hirschman index (HHI). By means of Herfindahl-Hirschman index (HHI) is implemented the measurement of concentration of total power market. The motivation behind these indices is that the more concentrated a market, the more likely is the ability of its participants to exercise market power. The concentration of total power market is determined by the following formula:

$$HHI = \sum_{i=1}^n s_i^2, \quad (2)$$

where s_i is the market share of market entities.

Power market estimation carries out via three indicators:
when $HHI < 1000$, the market is not concentrated;
when $1001 < HHI < 1800$, the market is moderately concentrated, and
when $HHI > 1801$, highly concentrated.

Herfindahl-Hirschman index virtually represents the impartial quantitative measure of competitiveness. When calculating this index, is necessary to determine the market shares of the companies at the market.

Georgian power market passed from moderately concentrated (in 2008) to highly concentrated (in 2010). This fact is explained by substantial increase in power generation by the largest power producer Enguri Hydroelectric Power Plant due to high water flow in this year. In 2010, the share of electric energy generated by Enguri HPP became equal to 41.8% compared to total generation.

According to the memorandum of understandings, regarding construction of new HHPs, concluded with the Ministry of Energy of Georgia in 2017 the power market will become non-concentrated taking into account the terms of putting all planned new power plants in operation.

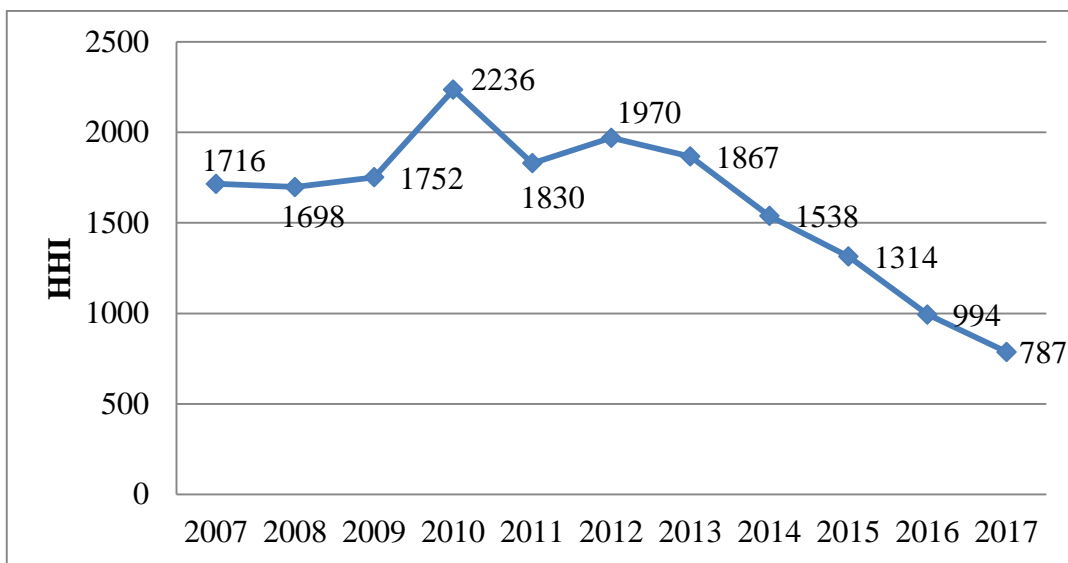


Fig. 4. HHI index dynamics 2007–2017 years

The HHI values for electricity supply sectors in EU Member states ranged in September 2006 from 1209 in UK (England and Wales) to 9800 in Greece . The HHI for the Nordic electricity markets are low, ranging from 836 in Finland to 1745 in Sweden, still reaching 3123 in East Denmark [4].

It is noteworthy that for a variety of EU member state according to 2007 data, among 25 member states only 8 had moderately concentrated power market, 12 of them had highly concentrated market and 5 of them were distinguished by extremely high concentration. As to Georgia, at present the most of power generation and all distribution facilities are privatized and represent the private ownership.

Residual supply index estimates the satisfaction degree of the consumer’s requirements and measures for company the capacity of residual delivery at the market (in percents), after capacities offered by that company at the market are depleted.

$$RSI = \frac{\text{system's gross generation} - \text{company's generation}}{\text{total demand}} \% \quad (3)$$

where, total generation is determined as full supply of power system minus reserve capacities and including import.

If RSI for specific company is more than 100%, other suppliers have the opportunity of market dominance and mentioned company has only low impact on the market price. On the other

hand, if index value is less than 100% for the company it means that the mentioned company is the dominant (principal) supplier at the market and theoretically is capable to have the massive impact on the formation of electricity price. In table 8 are given the results of calculation of RSI indices for major large power producers of Georgia, whereof is seen that Enguri Hydroelectric Power Plant represents the major producer of electricity in order to satisfy consumers' requirements and at the same time the volume of balancing electric energy sold by the Enguri HPP will be important in the process of balancing electricity price formation.

Table 1. RSI index calculation for three largest producers according to Georgian energy balance forecast

Producer		2010	2011	2012	2013	2014	2015	2016	2017
1	Enguri HPP	68%	59%	57%	58%	66%	73%	89%	108%
2	Energo-pro	98%	79%	76%	77%	85%	91%	106%	125%
3	Inter Rao-Ues	111%	88%	85%	85%	93%	99%	114%	132%

The level of development of regulator in Georgia can be considered via regulating strength criterion [7]. According to the EU directive 2009/72/EC, each member state is obliged to have independent regulating agency or body in order to provide non-discriminatory relation, competition and effective market performance. Under Strength of Regulator each country is scored on whether they have ex ante regulation or (=1, ex post=0), ministerial involvement (no=1, some=0.5, yes=0), network access conditions set by the regulator (yes=1, no=0), dispute settlement (yes=1, no=0) and strong information acquisition powers (yes=1, no=0). According to this index Georgia is at the high level and is distinguished by the almost maximum value – 4 of evaluative characteristics for abovementioned regulating force. Only network access conditions are set by the TSO. It can be said that this fact is another step forward for improvement of the liberalization processes.

3. DISCUSSION

Possibility of Georgia's integration with EU energy system was reflected in the document of the Parliament of Georgia: "Basic directions of the state policy in energy sector of Georgia". According to these directions, for the year of 2017 each consumer will be able to choose supplier which could be any generator. This means that Georgia should transform its existing market structure towards competitive retail sale market, which requires carrying out certain necessary activities and steps. In order to further develop the current market structure, certain steps must be taken towards that direction. In order to develop competition in electricity market, the following development and capacity building is supposed to be done by this time, including developing market service provider entities:

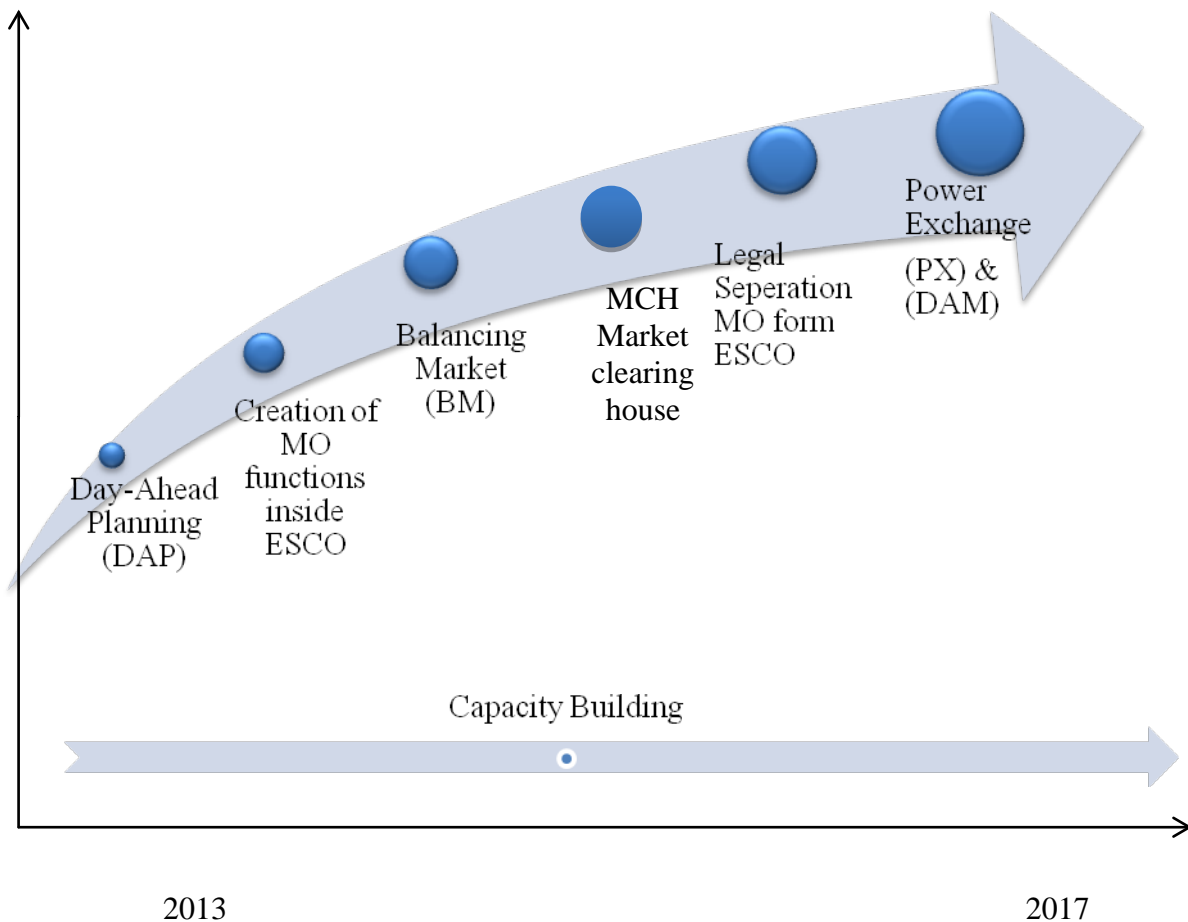


Fig. 5. Evolution path of the market design structure

Competitive electricity trading in Georgia is mostly limited to bilateral sales to end-consumers and export sales utilizing island mode. Bilateral electrical energy sales are dependent on finding large energy end-consumers. Therefore further growth of bilateral consumers is quite limited. Island mode sales to Turkey will cease when Turkey joins the ENTSO-E. New Georgian HPPs need a new mechanism that allows for open access on the Georgian electrical transmission networks and an opportunity for competitive trading in regional power markets.

However, to enter the competitive power markets of Turkey and/or Southeast Europe, Georgian HPPs will need transmission paths, trading tools, and risk mitigation options so that they can compete effectively with other power traders in those markets. The realization of the road map described in figure 5 is essential for constructing and planned HPPs in Georgia because they need market mechanism to sell generated electricity at acceptable price to cover long-run costs. Georgian power sector middle-term export potential is assessed in the Fig. 6 that is based on all the memorandum of understanding contracted between Ministry of Energy and Natural Resources of Georgia and private investors aiming to invest in Georgian hydro power.

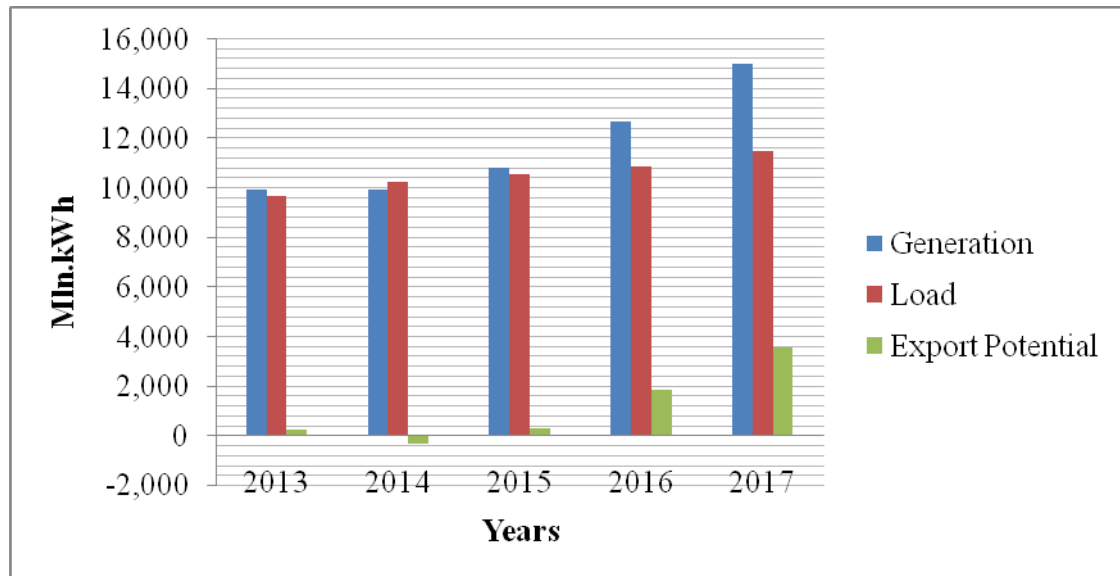


Fig. 6. Electricity export potential of Georgian power sector

It is necessary that the new electricity market model be developed in accordance with the principles of EU legislation on competitive electricity markets and movement toward the convergence of regional energy markets. Such convergence is a principal requirement of the Eastern Partnership, the forum for the EU's discussion of strategic partnership agreements with Belarus, Armenia, Azerbaijan, Georgia, Moldova and Ukraine.

During the Georgia-Turkey negotiations it became clear that there is a need to add new features to Georgia's present electricity sector in order to harmonize the electricity trading mechanism with regional markets, in particular, those of Turkey and Southeast Europe, which in turn are harmonized with EU Directives. Harmonization does not require strict compliance with such Directives. It does, however, require that the laws and regulations applicable in Georgia enable reciprocal electricity trading across borders. As other regional markets continue to develop and refine their operations, Georgia will also need to change the structure and rules governing the electricity market. Harmonization, therefore, will be a continuous process. The new electricity market model should provide a framework for the development of an electricity trading mechanism that is expected to be a more enduring structure than the existing model.

As a result of the research, presumable Georgian competitive electricity market functional model was created (see drawing 7).

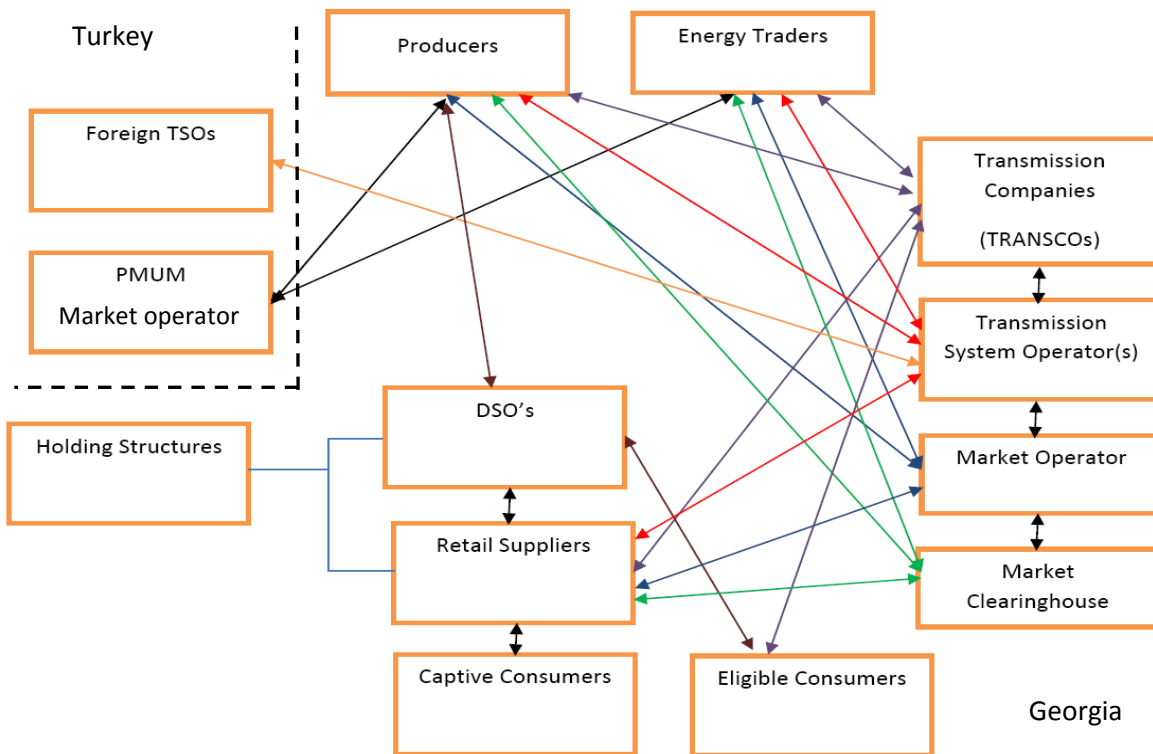


Fig. 7. Georgian electricity market model for 2017 year

4. CONCLUSIONS

On the basis of analysis fulfilled above, it is possible to conclude that despite fast renewal of Georgian power system, there still exist many problems that are incompatible to competition and electricity market operation concept. For the full liberalization of Georgian power market and creation market based mechanisms, it will be needed to increase demand elasticity, as well as to increase number of market participants on the generation side, to avoid dominance of one or several power generating company.

The main need of transition of Georgian power system to competitive electricity market model is to ensure that the potential benefits resulting from Georgia's geographic location and natural resources run directly to electricity consumers and electricity sector investors. Such fundamental changes in the industry management model shall result in the following benefits:

- In the long-term, Georgian domestic consumers will benefit from a secure supply of electrical energy, from quality services at reasonable and ultimately cost-reflective prices and from reduced reliance on imports of expensive and foreign-controlled energy sources;
- Decreasing the energy import dependency, including gas import dependence;
- Economic benefits for Georgia which derive from maximizing the price of electricity sales to Turkey and the EU;
- Improved transparency and reliability of sales by Georgian HPPs through the implementation of a bilateral contracts and balancing market (which properly assigns the risk (costs) of non-delivery) for energy transactions;



REFERENCES

1. MURRAY, Barry. *Power markets and Economics: Energy costs, Trading, Emissions*. John Wiley & Sons, 2009, 279 p. ISBN 0-471-98507-4.
2. JOSKOW, P. Electricity sector restructuring and competition: Lessons learned. *Cuaderonos de Economia*, 2003, № 121, p. 548–558.
3. JAMASB T.; POLLIT, M.; NEWBERY, D. Electricity sector reform in developing countries: a survey of empirical evidence on determinants and performance. *World bank policy research working paper* 2005, p. 35–49.
4. RANGEL, L. Competition Policy and Regulation in Hydro-Dominated Electricity Markets. *University of Auckland Energy Centre*. 2007, Vol. 3, №15, p. 67–98.
5. VENTSOA M., BAILLO A. Electricity Market Modeling Trends. *Energy Policy*, 2005 № 33, p. 123–145.
6. BELYAEV Lev. *Electricity market reforms*. New York: Springer, 2006, 270 p. ISBN 978-1-4419-5611-8.
7. FRANCOIS, Leveque. *Electricity Reform in Europe, Towards a Single Energy Market*. Northampton: Edward Elgar, Cheltenham, 2009, 314 P.
8. САЈЛИИ, Хант. *Конкуренция и выбор в энергетике*. London: n/e/r/a, 2000, 260 p.

METHOD FOR CRITICALITY ASSESSMENT OF ENERGY INFRASTRUCTURE

B. Jokšas

*Lithuanian Energy Institute
Breslaujos str. 3, LT-44403 Kaunas – Lithuania*

I. Žutautaitė

*Vytautas Magnus University
Vileikos str. 8, LT-44404 Kaunas – Lithuania*

ABSTRACT

The protection of critical infrastructure has become the topical subject of the economy and national security in all countries. Critical infrastructure is defined by an asset, system, part thereof or technical networks. All sectors' activities are included in this network, such as energy supply, transport services, water supply, gas and oil supply, information and communication technology systems. That is considered important for maintenance of physical integrity, energy security and economic welfare. It is not possible to attain the acceptability level of political, energy sustainability or economic development if infrastructure networks of the country are at risk or vulnerable. Although, one of the main issue of critical infrastructure assessment is there is no single measure unit that can accurately reflect “interdependency” among critical infrastructure sectors.

The criticality of infrastructure element is described by others system elements functionality reduction when considered element is out of order.

Assessment of system ability to perform its functions is allowed by created model, when system element is out of order or energy supply is interrupted. This model is designed using Matlab platform. The pilot numerical experiment was performed to demonstrate the implementation of the application of developed methodology for the assessment of infrastructure functionality and criticality.

Keywords: Critical infrastructure, energy sector, network system, criticality, functionality

1. INTRODUCTION

Nowadays, one of the main issues is how to ensure national and energy security of the state. The secure operation of the state infrastructure could ensure the essential functions of society. All infrastructure sectors' activities such as energy supply, transport services, water supply, gas and oil supply, information and communication technology systems are elements of one network system.

Critical infrastructure elements defined as system elements whose services are so vital that their incapacity or destruction would have a debilitating impact on the deface or economic security of any state: electric power, gas and oil production and distribution, and etc. Critical infrastructure is described like complex network system, where sector's elements are connected in one level.

In our work the definition of critical infrastructure is used as same as in EU directive 2008/114/EC [1] defined as asset, system or part thereof located in (Member) States which is essential for the maintenance of vital societal functions, health, safety, security, economic or social well-being of people, and the disruption or destruction of which would have a significant impact in a (Member) State as a result of the failure to maintain those functions.

The energy infrastructure will be analyzed in this work only.

Disturbances in one infrastructure sector often spread to other dependent infrastructures. So disturbances could spread within system and to make negative impact for others elements. This

property is called *interdependence* [2]. There are defined several types of interdependencies: physical, cyber, logical, geographic.

Once the infrastructure systems are disturbed by external or internal disturbances, the failures can spread to other interdependencies infrastructure systems. Sometimes failure can even return to the originated infrastructures which may cause the whole systems to lose their function and collapse. For example of infrastructure system disruptions could be major power blackout in Europe on November 4, 2006. Another external disruption example is Russia Ukraine gas supply disruption on January 2009, when gas supply was disturbed for other 18 European countries.

It is becoming increasingly important to take these interdependencies into account when assessing the vulnerability of technical infrastructures.

An “energy system” is defined as a set of tightly coupled domains that collaborate together in order to provide a service. So system and its elements could function properly, if all system elements could provide service for each other (included resources) (for example: gas pipelines, gas compressor station, CHP, power plant and etc.). Therefore interdependencies analyses of infrastructure elements are one of the main issues.

The work of systems could be analyzed by two complementary options:

1. The structural approach could tell “what is the system made of?”
2. The functional approach could tell: “how is it working?”

The structural analysis let to identify the boundary between the system and its environment. In structural analysis, energy system could be compounded of the transmission lines that connect the nodes (storages, pipelines, power plants and etc.) and it represent the links of the network and it are a schematic representation of dependencies and interdependencies

The functional analysis is focused on the analysis of the function, but not on the list of components. Most of functional analysis methods are called input-output approaches (efficiency analysis methods), and the main issue of this analysis is to identify the trouble spots and especially the places where there is waste and then proceed to remove the inefficiency.

There are several papers that analyzed interdependencies of partial infrastructure system [1–4]. In these papers authors analyzed systems of interdependencies between electricity substation, water treatment plant and water supply for consumers. The others authors analyzed oil and gas industries or railway infrastructure. Authors presented a network model designed for interdependencies between infrastructure systems at different scales. The system of Infrastructure is considered as a network. Authors suggested that optimal performance of the network under normal and extreme conditions may be found by minimizing the cost of commodity flow. Authors used Monte Carlo method for the realization of simulation in this work.

Another issue is a vulnerability analysis of infrastructure. Approaches for modelling interdependent technical infrastructures are proposed by authors in the papers [4–10]. Authors used graph theory for modelling approach for fictional electrified railway network or power transmission grids. These approaches are consisted of several systems and interdependencies between the systems. They presented how the model can be employed in a vulnerability analysis.

Critical components identification and edge attack strategies analysis are the other issues which are investigated by authors in paper [6, 7, 10–12]. Some authors used power and gas pipeline systems as example and they analyzed critical components in these systems. The other authors analyzed how to identify the most critical elements of electrical transmission system. Graph theory for topological analysis of system is used as main tool for modelling infrastructure system and analyzing interdependent infrastructure systems vulnerability. Authors introduced how to estimate network’s dynamic functionality and proposed an alternative to the electrical reliability degree, the expected electrical distance could be used to evaluate the importance of different network components.

Some papers proposed methodology for assessing the holistic criticality [13–16]. The authors introduced the formal definition of interdependencies between different infrastructures and their respective sectors. Authors are used risk analysis method for criticality assessment of infrastructure

system. Separation layers of interdependencies are proposed in these papers as well. Some of the authors used multi-objective optimization and principal component analysis.

The criticality analysis of infrastructure elements will be helpful to design or improve the infrastructures in the long run or short term. The criticality assessment of infrastructure taking into consideration of elements functionality is essential. The cascading failures in some infrastructure sectors are important for criticality analysis as well.

A general energy infrastructure model, descriptions of elements concept (generation technologies, supply technologies and etc.) are presented in this paper. The authors propose the developed a methodology for the assessment of infrastructure functionality and criticality. As example of energy infrastructure, the heat generation and gas pipeline systems were analyzed in more details with regard to interdependency between separate elements of infrastructure systems. The criticality indicators estimates of considering part of energy infrastructure were obtained by applying developed methodology for the assessment of infrastructure criticality.

2. DESCRIPTION OF CRITICAL INFRASTRUCTURE

2.1 Schematic representation of critical infrastructure

The infrastructure that represents the energy sector was analyzed in this paper. The energy infrastructure could be comprises of consumers, generation technologies, fuel supply technologies, energy supply technologies and etc. The simplified scheme of the energy infrastructure is presented in Fig. 1.

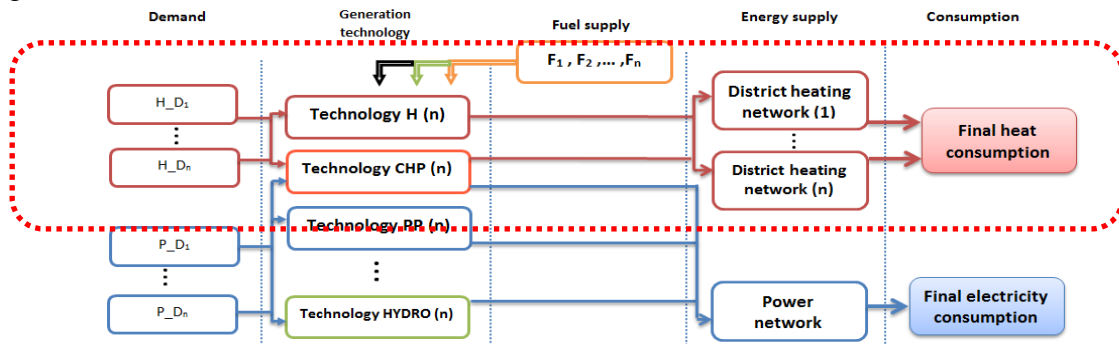


Fig. 1. The scheme of energy infrastructure

In this work, the red-dotted line part of energy infrastructure was analyzed in more details.

2.2 Description of energy generation technology

The energy generation technologies used in energy infrastructure are presented in this subchapter. In our work we use the concept of input-output method. So it allows us to compare the operation of simulation system and real system.

The technology that is used to generate electricity and heat could be described by the following expression:

$$Tch_i = \{P_i; Q_i; \eta_{el}; \eta_h\}, \quad (1)$$

where P_i – the installed electric capacity in to i^{th} technology (MW); Q_i – the installed thermal capacity in to i^{th} technology; η_{el} – the efficiency of primary energy conversion for electricity using main fuel; η_h – the efficiency of primary energy conversion for heat using main fuel.

The main parameters characterizing the energy-generating technologies are:

- thermal capacity of plant Q_i (MW);
- electrical capacity of plant P_i (MW);

- efficiencies, which convert the primary energy source of heat energy and electrical energy $0 < \eta_{el} < 1$ and $0 < \eta_h < 1$;
- coefficient indicating power / heat production ratio $0 < \sigma_i < 1$;
- generation technology uses fuel Fu_i (tone of oil equivalent, toe);
- the reliability indicator r_i .

Gas pipeline supply technology and generation technologies (Combined Heat and Power (CHP), Power plant, Hydro power plant) are described in more details.

Gas pipeline supply technology. In this work we assumed that gas supply network is grouped by segments. The segment of pipe line is denoted parts of pipeline from boundary of the State to the generation technologies that used gas. Some segments of pipeline are composed of same parts of pipeline. This method has been simplified to facilitate the calculation of the assessment. The quantity of natural gas which is provided to the generation technology could be estimated by following equation [17]

$$Q_i = 2.489 \cdot 10^{-9} \cdot E \cdot SG^{-0.425} \cdot D^{2.725} \cdot \left(\frac{P_{in}^2 - P_{out}^2}{L} \right)^{0.575}, \quad (2)$$

where Q_i – flow rate of i-th pipeline (millions of m³/hr - mm³/hr); SG – specific gravity of the gas; E – efficiency; D – internal pipeline diameter (mm); L – pipeline length (km); P_{in} – inlet pressure (Bar); P_{out} – outlet pressure (Bar).

Generation technology (Combined Heat and Power (CHP)). The combined heat and power plants generally are built near the cities. So this heat and power generation plants are oriented in local customers demand. As well as these plants have much higher efficiency of utilization of primary energy-fuel, they replace condensing power plant and boiler-house that correspondingly serve for electricity and heat production. Therefore, these CHP generation technologies are assumed to simplify in our model.

We made assumptions that heat is the main products produced by technology. The electricity power in this case is generated as a by-product. The other assumptions made in CHP generation approach are that: this technology uses one main fuel for the generation process (for example, natural gas, biomass, etc.) and the alternative fuel is used in the case when supply of main fuel is limited or not supplied. The CHP generation technology approach is shown in Fig. 2.

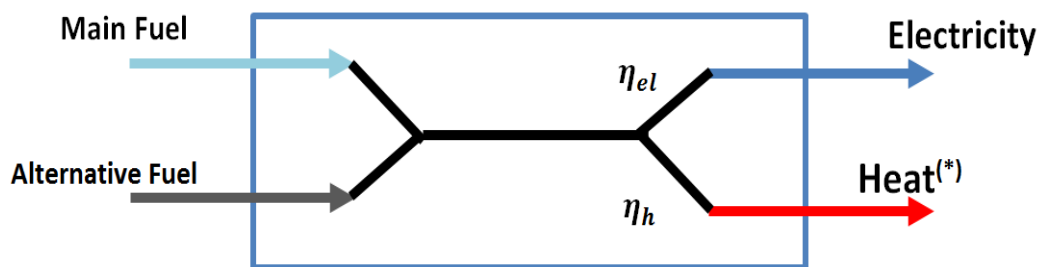


Fig. 2. The scheme of CHP generation technology approach * – main products; η_{el} – the efficiency of primary energy conversion for electricity using fuel; η_h – the efficiency of primary energy conversion for heat using fuel

The total CHP efficiency is [18],

$$\eta_{CHP} = \frac{P_i + \frac{Q_i}{2}}{F}, \quad (3)$$

the efficiency of the main (electricity) output,

$$\eta_{el} = \frac{P_i}{\frac{P_i + Q_i}{\eta_{CHP}}}, \quad (4)$$

and the efficiency of related (heat) output

$$\eta_h = \frac{Q_i}{\frac{P_i + Q_i}{\eta_{CHP}}}. \quad (5)$$

Where: F – used fuel for generation (t.o.e.); Q_i – the amount of generated heat (MWh); P_i – the amount of generated electricity.

Generation technology (Power plant). This type of generation technology is only used for power generation. The by-product is not used for central heating system. The heat which have been generated are supplying to cooling towers. The power plant generation technology approach is shown in Fig. 3.

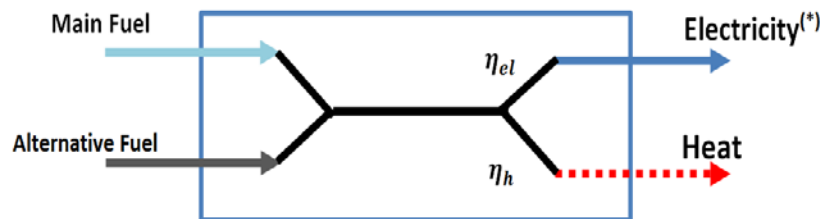


Fig. 3. The scheme of Power plant generation technology approach
* – main products ; η_{el} – the efficiency of primary energy conversion for electricity using fuel; η_h – the efficiency of primary energy conversion for heat using fuel

Generation technology (Hydro power plant). Hydroelectric power generation technology could be described as follows

$$p_i = F(Q_w; H_h; \eta), \quad (6)$$

where p_i – the generated output power (MW); Q_w – water flow in cubic meters per seconds; H_h – hydraulic head height in meter; η – the efficiency.

3. ASSESSMENT OF FUNCTIONALITY AND CRITICALITY

The functionality and criticality of infrastructure are assessed using functional analysis approach. The functionality of elements could be defined for two issues:

- The functionality of elements could be described, how much quantitatively i^{th} element could satisfy demands of other system elements. This type of element functionality allows us to say how much i^{th} element satisfies demands together with related could provide elements.
- The technical functionality of elements could be described as ability of the i^{th} element to satisfy the actual demand; this ability is expressed as a percentage. This type of element functionality, could tell what is the technically ability of the i^{th} element to satisfy demands.

The reduction of the functionality of one element could lead the operation of others elements. Thus this behavior must be taken into account performing the assessment of functionality of all system or others separate elements. Functionality f and technical functionality fT of the i^{th} element

depending on the other elements demand could be estimated by following equation (when the k^{th} element was assumed to be out of order)

$$f_i^{(k)}(t) = 1 - \frac{\sum_{j=1, j \neq i, k}^N D_{ji}(t) - \sum_{j=1, j \neq i, k}^N S_{ij}(t)}{\sum_{j=1, j \neq i, k}^N D_{ji}(t)}, \quad i = 1, 2, \dots, N, \quad (7)$$

and

$$fT_i^{(k)}(t) = \begin{cases} 1, & D_{ji}(t) \leq TechA_{ij}(t) \\ 1 - \frac{\sum_{j=1, j \neq i, k}^N D_{ji}(t) - \sum_{j=1, j \neq i, k}^N TechA_{ij}(t)}{\sum_{j=1, j \neq i, k}^N D_{ji}(t)}, & D_{ji}(t) > TechA_{ij}(t) \end{cases} \quad (8)$$

$$i = 1, 2, \dots, N,$$

where $(k) - k^{\text{th}}$ index means, that k^{th} element is out of order; $D_{ji}(t)$ – the quantity of demand of resource from i^{th} element to j^{th} element at time moment t ; $S_{ij}(t)$ – the quantity of recourse which i^{th} elements could supply to j^{th} element at time moment t ; $TechA_{ij}(t)$ – i^{th} element ability to satisfy demand of j^{th} element at time moment t .

The elements within infrastructure may be not equivalent. They can be ranked according to the number of served consumers.

The supplier, which has the greatest number of consumers, gets the highest weighted coefficient. The weighted coefficient is defined by α_i that satisfies equality

$$\sum_{i=1}^N \alpha_i = 1. \quad (9)$$

In the case of equivalent elements, the weighted coefficients are $\alpha_i = 1 / N$, N – number of suppliers.

Then functionality indicator of infrastructure system could be estimated using following equation 10.

$$Sf^{(k)}(t) = \sum_{i=1}^N f_i^{(k)}(t) \cdot \alpha_i, \quad i = 1, 2, \dots, N, \quad (10)$$

where $(k) - k^{\text{th}}$ index means, that k^{th} element is out of order; $f_i(t)$ – the estimate of the i^{th} element functionality; α_i – the weighted coefficient of i^{th} element.

The reliability indicator for final consumer, cf shows how much the demand of energy is satisfied ($0 \leq cf \leq 1$).

$$cf_i^{(k)}(t) = 1 - \frac{\sum_{j=1, j \neq k}^N NSE_{ji}(t)}{\sum_{j=1, j \neq k}^N D_{ij}(t)}, \quad i = 1, 2, \dots, M, \quad (11)$$

where M – number of the final consumers in the energy system; $NSE_{ji}(t)$ – not supplied energy from j^{th} element for demands of i^{th} consumer at time moment t ; $D_{ij}(t)$ – the quantity of demand of resource from i^{th} element to j^{th} element at time moment t .

As the review of the literature shows there is no general understanding of what criticality of infrastructure is. This issue faces main challenges:

- the subjective standpoint on criticality leading to the identification of different types of criticality (for instance, performing structural analysis, the criticality is defined using the number of connections of element);
- the evolution of a critical situation (evaluation of the cascade effect of disturbance);
- the necessity to indicate the part of infrastructure for the assessment its criticality.

The criticality of the k^{th} element could be assessed with regard to the functionality of the all system $Sf^{(k)}(t)$ that is obtained when the k^{th} element was assumed to be out of order. Performing the selection which one has most impact to the functionality of the system. Or the other way, the criticality of the k^{th} element may be estimated using the reliability indicators of final consumers obtained in case when k^{th} element is out of order

$$C^{(k)}(t) = 1 - \sum_{i=1}^M cf_i^{(k)}(t) \cdot \beta_i, \quad k = 1, 2, \dots, N, \quad (12)$$

where N – number of the elements in the energy system; $cf_i^{(k)}(t)$ – the reliability indicator that shows how much the energy demand is satisfied for the i^{th} element; β_i – the weighted coefficient of the i^{th} final consumer within system (for instance, weighted coefficients are estimated with regards to the energy demand of consumer, and they satisfy equality $\sum_{i=1} \beta_i = 1$).

For instance, $C^{(k)}(t) = 1$ means that disruption of i^{th} element work stops operation of all the energy infrastructure at time t .

4. LITHUANIAN ENERGY CRITICAL INFRASTRUCTURE MODELLING

The methodology for the assessment of infrastructure functionality and criticality (presented in the section 3) was applied for the Lithuania energy infrastructure. The pilot numerical calculations was performed for the part of Lithuania energy infrastructure (presented in the subchapter 2.1, see Fig. 1, part marked red-dotted line). The simplified scheme of the Lithuania gas supply and heat generation model is shown in the Fig. 4.

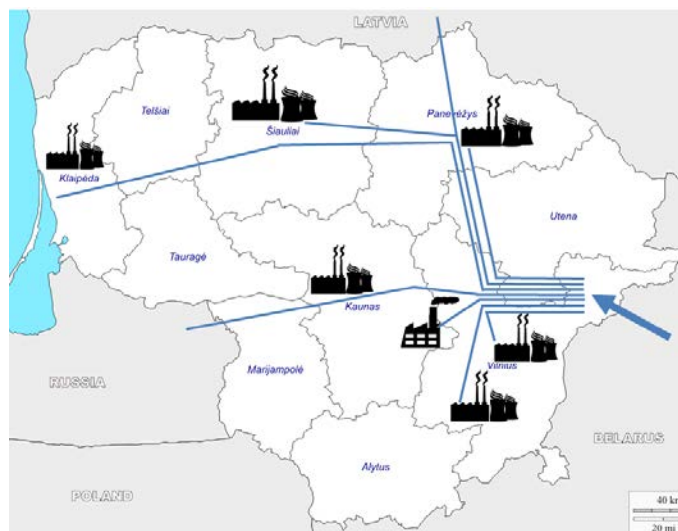


Fig. 4. The scheme of Lithuania gas supply and heat generation infrastructure

Several assumptions for the considering energy infrastructure were made:

1. Lithuanian heat generation system is composed of seven combined heat and power plants. They are located in bigger Lithuania cities.

2. The heat generation technologies are as described in the subchapter 0.
3. The main fuel is gas, the alternative fuel is oil. The reserve fuel is included in all CHP. The list of CHP is showed in the Table 1.

Table 1. The list of heat generation technology of model

Combined heat and power plants	Installed electric capacity MW	Installed thermal capacity MW
Kaunas CHP	170	389
Vilnius CHP 2	24	928
Vilnius CHP3	360	604
Klaipėda CHP	10.8	43.8
Mažeikiai CHP	160	558
Šiauliai CHP	3	44
Panevėžys CHP	35	33

Note, plants heat generation technology of public heat was not included in this modelling. It will be included in the futures works and it lets to simulate and assess the energy infrastructure system closer to real one.

Some system modelling assumptions:

- Lithuania gas network was divided in to the pipeline segments.
- the each segment of gas network is connected to separate heat generation technology;
- heat demand of final consumer is satisfied by one generation technology.

Thus, seven segments of gas network with different lengths and diameters are analyzed in numerical example. As shown in Fig. 4 all segments of gas network have common part of pipeline, let say symbol SG represents this part. The capacities of pipeline segments transmission are showed in the Table 2.

Table 2. The list of the capacities of pipeline segments transmission

	The capacity Mm ³ /quarterly period
SG1:form SG to Kaunas	372.3
SG2:form SG to Vilnius2	394.2
SG3:form SG to Vilnius3	20.98
SG4:form SG to Klaipėda	150.56
SG5:form SG to Mažeikiai	32.85
SG6:form SG to Šiauliai	100.37
SG7:form SG to Panevėžys	250.93

SG represents common part of gas pipeline (as shown in Fig. 4).

Heat demands used in the model are showed in the Table 3.

Table 3. Heat demands of Lithuania model

	Vilnius TWh	Kaunas TWh	Klaipėda TWh	Mažeikiai TWh	Šiauliai TWh	Panevėžys TWh
1 year	2.9366	1.5787	0.9925	0.1639	0.5168	0.131
2 year	3.0633	1.6967	1.0868	0.180	0.5563	0.8502
3 year	2.7509	1.5197	0.9588	0.161	0.4892	0.7679

The calculations are intended for the determination of impact to the Lithuanian heat supply infrastructure system, when the activity of considering system is influenced by the disturbance(s).

The disturbances in the infrastructure might occur due to:

- the disruption of gas supply networks elements work;
- the disruption of CHP work;
- the disruption of fuel reserve work.

For the pilot calculations eleven scenarios of disturbance in power system were selected (see Table 4) to assess its effect to system performance.

The work of energy infrastructure was modelled in different disturbance scenarios described in the Table 4. The simulation was performed using program code written in Matlab software platform. The influence of disturbances to the energy infrastructure functionality was assessed by calculation of system functionality indicators (equation 10) and reliability indicators for final consumers (equation 11). The obtained indicators were used to assess the criticality (equation 12) of the infrastructure elements. Numerical values of the criticality of elements in considering scenarios are presented in Fig. 5.

Table 4. The list of disturbance scenarios

The number of scenario	The description of scenario
SC1	Kaunas CHP (389 MW) is out of order.
SC2	Vilnius CHP 2 (928 MW) is out of order.
SC3	Vilnius CHP3 (604 MW) is out of order.
SC4	Klaipėda CHP (43,8 MW) is out of order.
SC5	Mažeikiai CHP (558 MW) is out of order.
SC6	Šiauliai CHP (44 MW) is out of order.
SC7	Panevėžys CHP (33 MW) is out of order.
SC8	The common part 1 is out of order. It disconnected gas network segments SG6 to Šiauliai and SG5 to Mažeikiai.
SC9	The common part 2 is out of order. It disconnected gas network segments SG4 to Klaipėda, SG6 to Šiauliai, SG5 to Mažeikiai and SG7 to Panevėžys.
SC10	The common part 3 is out of order. It disconnected gas network segment SG1 to Kaunas.
SC11	The common part 4 is out of order. It disconnected all gas network segments.

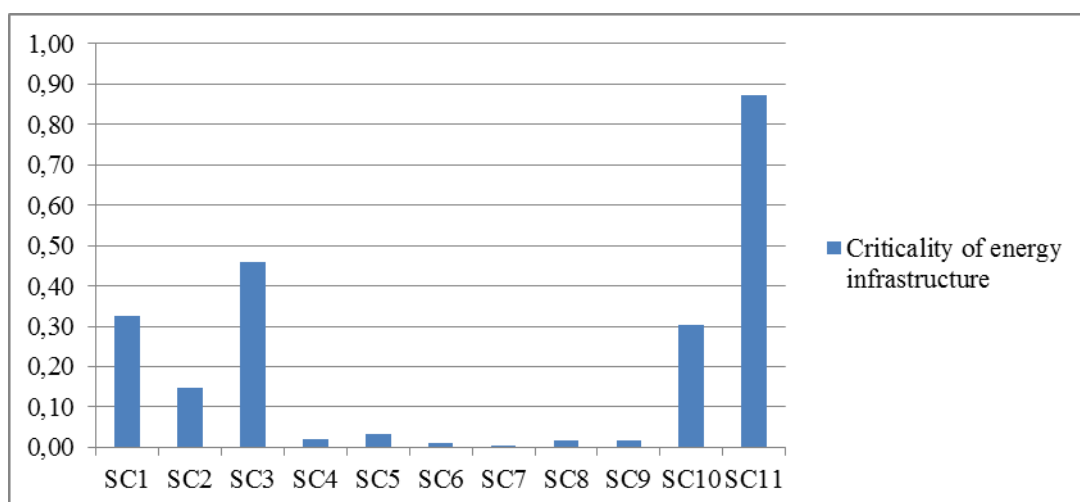


Fig. 5. The criticality of elements in considering scenarios

Obtained results may be used to identify more critical scenario (or element of infrastructure).

5. RESULTS AND CONCLUSIONS

The way of understanding the term “criticality assessment” of infrastructure taking into account infrastructure ability to operate was proposed.

The developed methodology for the assessment of infrastructure functionality and criticality is proposed in the research work.

The pilot numerical experiment was performed to demonstrate the implementation of the application of developed methodology for the assessment of infrastructure functionality and criticality. The criticality level of system is the higher when, the more important element is removed from the system or this element is related with other elements, it could be seen from the results presented in Fig. 5. The estimated criticality indicators may be used to identify critical element(s) in infrastructure.

REFERENCES

1. HOLDEN, R., et al., A network flow model for interdependent infrastructures at the local scale. *Safety Science*, 2013, Vol. 53, p. 51–60.
2. CHAI, C.L., et al., Application of social network theory to prioritizing Oil & Gas industries protection in a networked critical infrastructure system. *Journal of Loss Prevention in the Process Industries*, 2011, Vol. 24, p. 688–694.
3. SKEA, J., M. CHAUDRY, and X. WANG, The role of gas infrastructure in promoting UK energy security. *Energy Policy*, 2012, Vol. 43, p. 202–213.
4. XIA, Y., et al., Railway infrastructure disturbances and train operator performance: The role of weather. *Transportation Research Part D: Transport and Environment*, 2013, Vol. 18 p. 97–102.
5. VAN DER VLEUTEN, E. and V. LAGENDIJK, Interpreting transnational infrastructure vulnerability: European blackout and the historical dynamics of transnational electricity governance. *Energy Policy*, 2010, Vol. 38, p. 2053–2062.
6. EUSGELD, I., et al., The role of network theory and object-oriented modeling within a framework for the vulnerability analysis of critical infrastructures. *Reliability Engineering & System Safety*, 2009, Vol. 94, p. 954–963.
7. MURRAY, A.T. and T.H. GRUBESIC, Critical infrastructure protection: The vulnerability conundrum. *Telematics and Informatics*, 2012, Vol. 29, p. 56–65.
8. RYU, D.H., H. KIM, and K. UM, Reducing security vulnerabilities for critical infrastructure. *Journal of Loss Prevention in the Process Industries*, 2009, Vol. 22, p. 1020–1024.
9. NAN, C., I. EUSGELD, and W. KRÖGER, Analyzing vulnerabilities between SCADA system and SUC due to interdependencies. *Reliability Engineering & System Safety*, 2013, Vol. 113, p. 76–93.
10. BOMPARD, E., R. NAPOLI, and F. XUE, Analysis of structural vulnerabilities in power transmission grids. *International Journal of Critical Infrastructure Protection*, 2009, Vol. 2, p. 5–12.
11. WANG, S., et al., Vulnerability analysis of interdependent infrastructure systems under edge attack strategies. *Safety Science*, 2013, Vol. 51, p. 328–337.
12. ZIO, E. and L.R. GOLEA, Analyzing the topological, electrical and reliability characteristics of a power transmission system for identifying its critical elements. *Reliability Engineering & System Safety*, 2012, Vol. 101, p. 67–74.
13. THEOHARIDOU, M., P. KOTZANIKOLAOU, and D. Gritzalis, A multi-layer Criticality Assessment methodology based on interdependencies. *Computers & Security*, 2010, Vol. 29, p. 643–658.



14. SABIO, N., et al., Holistic minimization of the life cycle environmental impact of hydrogen infrastructures using multi-objective optimization and principal component analysis. *International Journal of Hydrogen Energy*, 2012, Vol. 37, p. 5385–5405.
15. HASSAN, M.N., Y.E. HAWAS, and M.A. MARAQA, A holistic approach for assessing traffic safety in the United Arab Emirates. *Accid Anal Prev*, 2012, Vol. 45, p. 554–64.
16. AMOUZANDEH, A., et al., Holistic Analysis of Underground Infrastructure Subjected to Fire. *Procedia Engineering*, 2011, Vol. 14, p. 41–51.
17. LYONS, W.C., *Standard handbook of petroleum and natural gas engineering*. Texas: Gulf Professional Publishing. 1996. Volume 1. 484p. ISBN 0-88415-642-7.
18. *Catalog of CHP Technologies*. Combined Heat and Power Partnership. 2008. [referred on the 3th of april in 2013 y.] < http://www.epa.gov/chp/documents/catalog_chptech_full.pdf>



CRITERIA FOR EVALUATION OF ENERGY EFFICIENCY MEASURES IN THE MANAGEMENT OF BUILDING ENERGETIC CHARACTERISTICS

R. Mikučionienė, V. Martinaitis

*Vilnius Gediminas Technical University
Saulėtekio Av. 11, LT-10223 Vilnius – Lithuania*

ABSTRACT

Renovation of the existing buildings is one of the aims of the society, actually reflected in the Energy efficiency Directive. Qualitative renovation begins by choosing energy efficiency measures (EEM). Criteria should be defined for all kinds of decision making methods. In order to increase sustainability of the renovation five main criteria (primary energy savings, environmental impact, economical rationality, comfort and Life cycle analysis criteria) are defined and analysed. The attributes representing each criterion are defined. The defined criteria are commonly used separately or in groups, e.g. 2E or 3E evaluation. The model for integration of criteria from different fields of science (energy, environment, economy, health and building construction) is presented. The sensitivity analysis for estimation of weight for each criterion is presented and the impact of each criterion for decision making is described.

Keywords: Building renovation, Energy efficiency measures, Sustainability, Criteria

1. INTRODUCTION

The one of major energy consumers in the world is buildings sector [1]. The requirements for new buildings are tightening all the time. But rate of new buildings construction in Europe is about 1% and rate of renovation for existing buildings is only about 1-2% per year according different sources [2]. The newest Energy Efficiency Directive [3] is reflected to the fact that global energy savings will be achieved when majority of the buildings will be energy efficient. Renovation of the existing buildings is straight way to this aim. When decision to renovate building is made, the qualitative renovation begins by choosing energy efficiency measures (EEM). But to choose EEM – to make decision which alternative is the best – the criteria should be defined first. Criteria should be defined for all kinds of decision making methods.

The evaluation and prioritization of EEM depends on the chosen criteria. The most commonly used criterion is economical evaluation, because „money or cost“ is understandable and clear to evaluate. Payback is easily motivating and is popular advisor for decision making. A lot of studies for evaluation of EEM are done with only one economic criterion. Another reason of popularity of this criterion is that often loans are needful to implement EEM. For investors only EEM with financial benefit are appropriate [4]. So the economic criterion is often used among scientists to evaluate EEM. The Greek scientists [5] in intelligent decision support model for assessing energy saving measures use only economic criteria and define it by three attributes: payback period, net present value (NPV) and internal rate of return (IRR). These attributes of economic criteria are most popular [6]. The economical evaluation of EEM done in another study [7] is evaluated by four attributes: NPV, IRR, payback period evaluating depreciation of the building and ratio of savings and investment. Method for optimization of the building in design stage [8] is based on economic criteria, which is evaluated by energy savings in terms of money.

Another popular criteria for evaluation of EEM is energy efficiency or energy saving. It is related with economic criteria, because without saving will be no financial benefit of implementation of EEM. So the measure which is economically feasible has energy savings as well. As described in [8] the measures are evaluated by energy savings. The energy efficiency criteria often is used together with criteria of environmental impact and in literature is presented as 2E criteria [9] and with economic criteria 3E evaluation [10]. Environmental and energy efficiency

criteria usually are met Life cycle analysis (LCA) [11], [12]. But LCA usually is performed for separate building elements, or not for impact of whole building [13]. The LCA evaluation together with energy efficiency lets to analyze the EEM in two-fold benefit, related to energy savings and improvement of buildings element conditions [6].

The state-of-the-art and sustainable evaluation of EEM usually is performed using not only one criterion, but composing several ones. The selection of criteria depends on the aim of analysis.

Model for selection of renovation actions [14] evaluate EEM by two criteria: environmental impact and functionality. The environmental impact is expressed by the potential of reduction of CO₂ emissions. The functionality criteria is expressed in by 10 aspects, which evaluate how easily the retrofit action can be carried out, does it require new methods for implementation of EEM, which do not exist, evaluate effect of comfortability and reliability, space requirements, impact on physical characteristics of building, usability and serviceability. This model focuses on the complexity of the renovation process and effect for inhabitants.

The another example of criteria selection for specific purpose is study for EEM evaluation in political aspects [15]. This study is performed by Multi Criteria Decision Making (MCDM) analysis for promotion of retrofit actions. The analysis is performed by 10 ungrouped criteria: energy savings, demand savings, total implementation cost, welfare, employment – economy benefits, benefits in other resources, budget share, evaluation capability, market transformation, compatibility with strategic objectives. The aim of this MCDM analysis is to find optimal EEM in governmental point of view. Such criteria as employment, market transformation and compatibility with strategic objectives evaluate the specific (political in this case) benefit. The sustainable renovation of hotel buildings for Energy Performance Contracting Project [16] has quality, energy system management, project cost benefit, energy consumption and resources saving, health and safety, stakeholders satisfaction criteria. The stakeholder's satisfaction criterion is also the specific one, which is profitable only for stakeholders. The special criteria are useful for specific cases, but focusing for sustainable and comprehensive evaluation should have comprehensive and universal indicators.

The multi criteria evaluation of sustainable EEM performed by [17] use four criteria: use of energy, thermal comfort, cost and environmental impact. This combination of criteria comparing with others is sustainable, but is focused more on usage of the building, and not in life cycle aspects. Sustainable office building renovation presented by [18] has five criteria: sustainable site – evaluating current situation of building, energy efficiency, water efficiency, material and resources – evaluation renewability and waste management and indoor environment quality.

All described criteria can be divided into quantitative and qualitative criteria. The quantitative criteria (investment cost, energy savings and etc) are indicators which can be calculated and evaluated objectively. The qualitative (aesthetics, comfort and etc) are subjective and evaluation of them depend on decision maker. But sustainable evaluation of renovation should be evaluated according both quantitative and qualitative factors [19].

Summarizing the described studies with different purposes of EEM evaluation and different criteria, the conclusion is that to evaluate EEM is sustainable and universal aspect should be used the complex of criteria, which involve energy efficiency, environmental impact, economical rationality, comfort and life cycle duration.

2. SUSTAINABLE EVALUATION OF ENERGY EFFICIENCY MEASURES

In order to increase sustainability of the renovation the criteria for EEM evaluation reflecting sustainable attitude should be chosen. In this section of the paper the five main criteria (energy efficiency (EE), environmental impact (EI), economical rationality (ER), comfort (C) and Life cycle duration (LCD)) are defined and analysed. Defined attributes characterizing each criterion are described.

2.1. Energy efficiency

The sustainability firstly meets EE requirements [9], [16], [17], [19]. The expression of EE usually is described as saved energy. Saved energy is calculated as difference of annual energy consumption (recalculated to normal year) before and after renovation. The saved energy can be in different form (electricity or heat), so to evaluate it universally recalculation to the primary energy should be done. The primary energy saving is more comprehensive attribute of EE criteria, because it reflects the usage of renewable energy.

Another attribute characterizing EE is change of heat load. This attribute prioritize the complex renovation and selection of several EEM at the same time. For example the retrofit of building envelope will not make changes in the load of heat substation if the renovation of heat substation is not performed.

Two attributes of EE for sustainable EEM evaluation are defined, to characterize the saved primary energy and to prioritize the complexity in renovation process.

2.2. Environmental impact

EI is also popular in sustainable evaluation [9], [17], [19]. EI can be expressed as climate change (in units kg of CO₂ eqv.), depletion of ozone layer, acidification and other pollutant extracted to the air [11]. The most popular is evaluation of impact to climate change, which is presented by calculation of the emitted amount of pollutant to the CO₂ gases equivalent. But the renovation process impacts environment in two lines. One line is reduction of pollution by reduction of energy use. Another line is emitted pollutants during the renovation process and manufacturing and transporting the materials for renovation. The EI criteria can be evaluated by two attributes (saved pollution and emitted pollution by renovation process), or can be expressed by the ratio of these indicators. The usage of the described ratio as only one attribute of EI criteria simplify the calculation process for decision making and is more appropriate to use.

2.3. Economical rationality

Economical rationality criterion also has to be assed in sustainable development. Direct attributes of economic criterion as payback period, NPV and IRR present financial benefit of renovation. As it is described in the 1st part, these attributes are most popular [6]. The clearest one is payback period. The payback period can be the simple one and the real one. The real payback period reflects depreciation of money in time, so it is more accurate when payback period is longer than one year. For planning renovation important is initial investment. This attribute lets to sort EEM measures to groups of small and big investment needful EEM.

The renovation profit and economical rationality of it can be expressed by cost of conserved energy (CCE) [6]. The attribute lets to compare the implementation of EEM with doing nothing. The present situation is evaluated as the building condition and energy consumption is at present time. If CCE of EEM is bigger than price of energy it shows, that is not rational to implement EEM, it is cheaper to consume energy. CCE is calculated as ratio of investment and savings for lifetime of measure considering the discount rate for that period. The savings in long period are evaluated with discount rate, to evaluate the value of saved money in long period at the present time. The risk of change in energy prices is not evaluated, because is not possible to create one undoubted scenario for long period. The Analysts usually create few opposite (optimistic and pessimistic) scenarios of change in oil or natural gas prices [20]. The model for evaluation of EEM is created referring present situation and evaluating the clear and undoubted change.

Implementation of EEM, especially renovation of building envelope, increases the value of building as well. The rehabilitation of building element can be evaluated by coefficient of buildings element rehabilitation. This coefficient depends on life time of building element and the actual age of building element. [6] Multiplying the coefficient of buildings element rehabilitation by

investment cost the increase of building element value is presented. This attribute lets to prioritize the EEM with big investment cost, but which are obligatory for rehabilitation building element [9].

So concluding the review of economical rationality attributes to evaluate thorough view of economical benefit not only the real payback period, NPV, IRR and initial investment has to be evaluates but CCE and increase in the value of building has to be defined as well.

2.4. Comfort

Complex and sustainable evaluation of EEM usually requires meeting comfort conditions. But term comfort is used and expressed not uniformly in scientific society. The most popular criteria are thermal comfort [17] or indoor environmental quality (IEQ) [18] [21], [22]. Thermal comfort evaluates the only thermal characteristics of indoor environment, but it is not enough to satisfy human comfort. The overall comfort is formed from physical and personal comfort. The physical comfort depends on thermal comfort, air quality, acoustic comfort and luminosity [23]. The personal comfort depends on persons physiological and psychological features. The limits of requirements for physical comfort usually are described in standards. Evaluating the impact of EEM it can be defined in binary question for decision maker: meet requirement (evaluation - 1) do not meet requirements (evaluation - 0). The personal part of comfort can be evaluated only by survey with inhabitants. It is known that impossible to satisfy comfort needs to 100 % of inhabitants because of people personal features. Usually scientists focus on 90 % of inhabitants. So another attribute of comfort evaluation inhabitants opinion about comfort expressed by the number of hour per day when 90% of inhabitants where satisfied by comfort.

2.5. Life cycle duration

Life cycle duration of building indirectly is evaluated in EI and ER criteria evaluating by ratio of saved pollution and emitted pollution by renovation process and evaluating coefficient of building rehabilitation and increase of building value. But sustainable supervision of the buildings is actual question of today [9]. So the recommended periodicity of renovation by [9] is taken into account. The reference point is 20 years period of complex renovation periodicity. The extension of the building is evaluated by the impact of EEM implementation for whole building and its life cycle duration.

2.6. Evaluation of criteria

The selection of criteria and assessment of their attributes is incomplete information for decision maker. Each attribute of the criteria has different units, different optimization functions. The structure for evaluation of attribute values and criteria should be created. Usually the normalization method is used to unify the values [24]. The normalization process is based by comparing attribute values of analysed alternatives with the best result, and evaluation the difference from the best value. Another question for decision maker is weight of each criterion. The weight can be defined proportionally (equal for each criteria) or different weights can be provided for criteria. Weighting of criteria depends on the expected result by decision maker [14] and is useful for prioritizezation of special criteria.

In Fig. 1 the procedure of EEM evaluation is presented in the sequence of operations. All operations are obligatory when analysis is multi criteria.

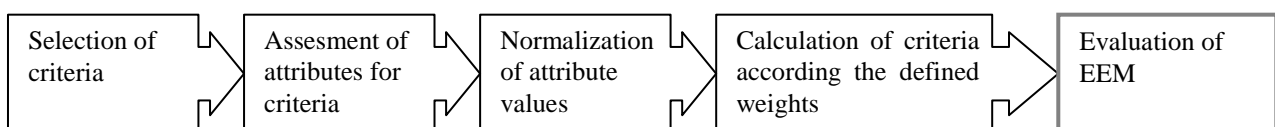


Fig. 1. Sequence of operations for EEM evaluation

Sustainable evaluation of EEM can be performed only estimating multicriteria. And multicriteria should cover and be integrated from different fields of science: energy, environment, economy, comfort and construction.

3. EVALUATION OF CRITERIA SENSITIVITY ANALYSIS OF DEFINED CRITERIA WEIGHTS

The evaluation of criteria is presented by analysing three different EEM for public building in Lithuania, city of Birštonas, built 30 years before, without complex renovation, only windows are changed and without mechanical ventilation. Chosen EEM are: insulation of external walls (V1), change of heat substation equipment with modern automation (V2) and implementation of ventilation system with recuperation (V3). Recuperation in ventilation system is heat recovery from extracted air to supplied air by heat recovery unit or heat exchanger. The evaluation of separate EEM was chosen for sensitivity analysis, because separate EEM have wider range of criteria values, when combination of EEM. In the Table 1 these three described variants are evaluated by each attribute in criteria tree. Each attribute is described by measurement units and function of optimization. Values of attributes for each variant are calculated and the best result for each attribute is presented in Table 1.

Table 1. Criteria for EEM with attributes which are presented by function of optimization and the values of three variants

Criteria	Attribute	Units of attribute	Function of optimization	V1	V2	V3	The best result of attribute
EE	Savings of primary energy	MWh	max	89.31	34.35	-28.19	89.31
	Reduction of heat load	kW	max	0	13.9	-14.9	13.95
EI	Ratio of CO ₂ savings and emitted CO ₂ by implementing EEM	-	max	15.75	2.87	-	15.75
ER	Investment	Lt	min	234195,00	20000,00	355779,00	20000,00
	Real payback period	year	min	17.2	2.8	-	2.8
	Cost of conserved energy	Lt/MWh	max	14.86	18.20	-	18.20
	Net present value	Lt	max	135293.30	48144.08	-	135293.30
	Internal rate of return	%	max	8.7%	8.6%	-	8.7%
	Increase of building value	Lt	max	140517.00	-	-	140517.00
C	Duration when 90% of habitants are satisfied	h	max	4	4	4	4.00
	Keeping of standard indoor climate parameters	0/1	0	1	1	1	1.00
LCD	Extension of buildings lifecycle	m	max	13.7	1.5	3.0	13.74

In Table 2 normalized values of attributes for each variant are presented. The normalization of attributes is done by SAW (Simple additive weighting) method, when value of attribute is divided by the best value of the attributes. These values can be added together to evaluate the point of each criteria. The Fig. 1 presents the values of criteria of three analysed variants, when weights of criteria are proportionally segmented.

Table 2. Criteria for EEM with normalized attribute values

Criteria	Attribute	Function of optimization	V1	V2	V3
EE	Savings of primary energy	max	0.5	0.19	-0.158
	Reduction of heat load	max	0	0.5	0
EI	Ratio of CO ₂ savings and emitted CO ₂ by implementing EEM	max	1	0.18	-
ER	Investment	min	0.0142	0.17	-
	Real payback period	min	0.0268	0.17	-
	Cost of saved energy	max	0.1361	0.17	-
	Net present value	max	0.1667	0.06	-
	Internal rate of return	max	0.1667	0.17	-
	Increase of building value	max	0.1667	0	-
PC	Duration when 90% of habitants are satisfied	max	0.5	0.5	0.5
	Keeping of standard indoor climate parameters	0/1	0.5	0.5	0.5
LCD	Extension of buildings lifecycle	max	0.5	0.11	0.2183

The Figs. 2–3 are constructed in the way that the variant which delineate bigger area has bigger point of criteria evaluation: base case and free scenarios are presented.

Case (a) in Fig. 2 shows the evaluation when weighting factors are equal (Base case). This case show, that the best variant is V1 – insulation of external walls and the worse one is V3-implementation of mechanical ventilation. Installation of mechanical ventilation in the building, which had only natural ventilation is not energy saving, so there is no impact to environment, and not paying back measure, so only to criteria are evaluated. But it is obvious to implement it for comfort conditions, especially when windows are changed. So if evaluation is only 3E, this variant will not get any points at all. The case study shows how important to have criteria covering all fields for sustainable evaluation.

The sensitivity analysis of criteria weights is performed by changing factors and analysing the change of results. Free scenarios with different weighting factors are presented: green, rational and comfort. Green scenario prioritises environmental impact (weighting factors (WF) – 0,3) criteria, and second priority is energy savings and life cycle duration. The rate of EEM in this scenario remains the same, as in base case, but V1 has better point in green scenario comparing with base case.

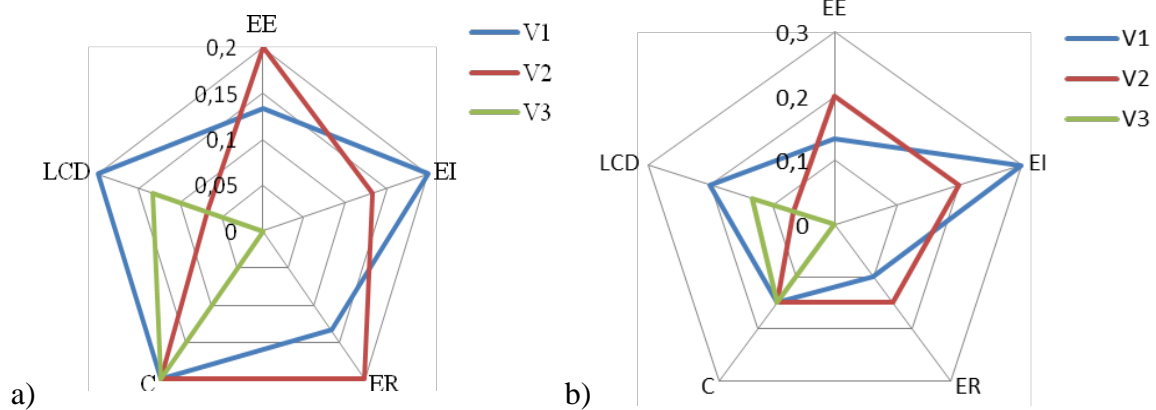


Fig. 2. The distribution of criterion values with different variation of criteria weight. a) Base case (all WF are equal $1/5=0.2$). b) Green scenario (EE=0.2; EI=0.3; ER=0.15; C=0.15; LCD=0.2)

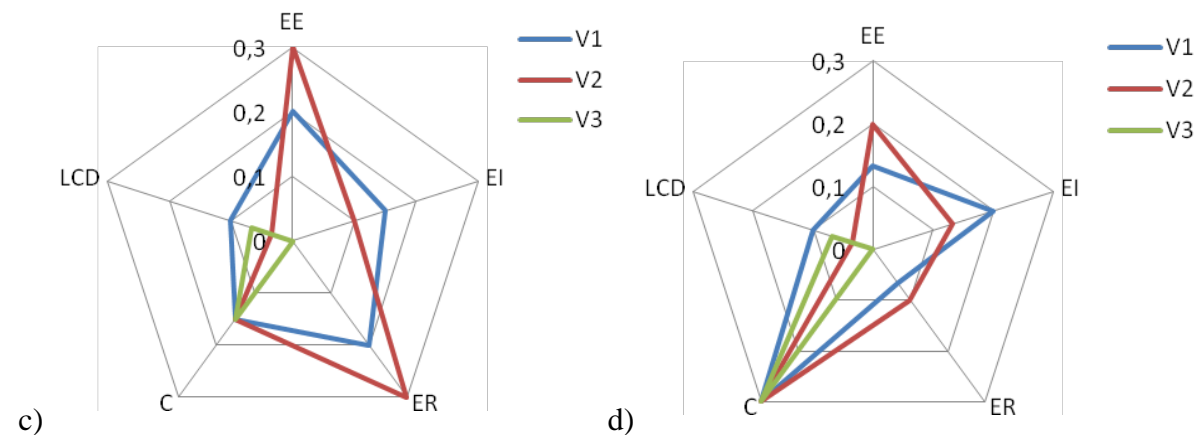


Fig. 3. The distribution of criterion values with different variation of criteria weight. c) Rational scenario (EE – 0.3; EI – 0.15; ER – 0.3; C – 0.15; LCD – 0.1). d) Comfort scenario (EE – 0.2; EI – 0.2; ER – 0.1; C – 0.3; LCD – 0.1)

Rational scenario is constructed in the way, that most important criteria is EE and ER (WF – 0.3), and second priority is C (WF – 0.25). Such distribution of criteria weights lets to prioritize V2 – renovation of heat subsystem. This EEM is feasible in aspect of ER and lets to reduce not only energy consumption, but heat load as well.

In comfort scenario the comfort criterion is prioritised, but the rate of variants does not change comparing with initial case, when all factors have the same weights, because all variant has the same maximal value of comfort criteria.

The conclusion of sensitivity analysis is that distribution of WF depends on the priority of decision maker and of the aim for evaluation. For sustainable evaluation of EEM when all dive criteria are equally important the base case suits best. WF can change the results, as in rational scenario, but cannot change it significantly. If EEM is not feasible in majority of criteria, as V3 variant is, will not be the best variant nevertheless.

The rating of WF and estimation of most important criteria depends on political social psychological factors influencing the decision maker. There is no answer which way is the best, it can change according to situation.

4. CONCLUSIONS

EEM evaluation in sustainable and universal point of view should be performed with complex of criteria, which involve energy efficiency, environmental impact, economical rationality, comfort and life cycle duration.

Complex or multicriteria analysis of EEM needs clear structure and sequence, to define the values criteria according the calculations of defined attributes.

The sensitivity analysis of criteria WF showed that different weights can change the result, when criteria factors are close each other cannot change the result significantly.

The rating of WF and estimation of most important criteria depends on political social psychological factors influencing the decision maker. There is no answer which way is the best, it can change according to situation.

REFERENCES

1. EUROPEAN COMMISSION, Energy efficient buildings PPP Road map and longer term strategy. Luxemburg: Publications Office of the European Union, 2010, 52 p.
2. THE BUILDINGS PERFORMANCE INSTITUTE EUROPE, Europe's buildings under the microscope. Brussels: Buildings Performance Institute Europe, 2011, 132 p.
3. THE EUROPEAN PARLIAMENT AND THE COUNCIL, Energy efficiency Directive 2012/27/EU Brussels, 2012, 56 p.
4. VERBRUGGEN, A., MARCHOHI, M.A., JANSSENS, B., The anatomy of investing in energy efficient buildings, *Energy and Buildings*, 2011, Vol. 43, No. 4, p. 905–914.
5. DOUKAS, H., NYCHTIS C., PSARRAS, J., Assessing energy-saving measures in buildings through an intelligent decision support model, *Building and Environment*, 2009, Vol. 44, No. 2, p. 290–298.
6. MARTINAITIS, V., ROGOŽA, A., BIKMANIENĖ, I., Criterion to evaluate the 'twofold benefit' of the renovation of buildings and their elements, *Energy and Buildings*, 2004, Vol. 36, No. 1, p. 3–8.
7. NIKOLAIDIS, Y., PILAVACHI, P. A., CHLETISIS, A., Economic evaluation of energy saving measures in a common type of Greek building, *Applied Energy*, 2009, Vol. 86, No. 12, p. 2550–2559.
8. PETERSEN, S., SVENDSEN, S., Method for component-based economical optimisation for use in design of new low-energy buildings, *Renewable Energy*, 20012, Vol. 38, No. 1, p. 173–180.
9. UŽŠILAITYTĖ, L., Pastato renovacijos periodiškumo įtaka jo gyvavimo ciklo energijos sąnaudoms, *Energetika*, 2010, No. 2, p. 146–153.
10. OLIVEIRA, C., ANTUNES, C. H., A multiple objective model to deal with economy–energy–environment interactions, *European Journal of Operational Research*, 2004, Vol. 153, No. 2, p. 370–385.
11. BLOM, I., ITARD, L., MEIJER, A., LCA-based environmental assessment of the use and maintenance of heating and ventilation systems in Dutch dwellings, *Building and Environment*, 2010, Vol. 45, No. 11, p. 2362–2372.
12. DYLEWSKI, R., ADAMCZYK, J., Economic and environmental benefits of thermal insulation of building external walls, *Building and Environment*, 2011, Vol. 46, No. 12, p. 2615–2623.
13. VERBEECK, G., HENS, H., Life cycle inventory of buildings: A calculation method, *Building and Environment*, 2010, Vol. 45, No. 4, p. 1037–1041.
14. ALANNE, K., Selection of renovation actions using multi-criteria 'knapsack' model, *Automation in Construction*, 2004, Vol. 13, No. 3, p. 377–391.



15. NEVES, L. P., MARTINS, A. G., ANTUNES, C. H., DIAS, L. C., A multi-criteria decision approach to sorting actions for promoting energy efficiency, *Energy Policy*, 2008, Vol. 36, No. 7, p. 2351–2363.
16. XU, P., CHAN, E. H. W., ANP model for sustainable Building Energy Efficiency Retrofit (BEER) using Energy Performance Contracting (EPC) for hotel buildings in China, *Habitat International*, 2013, Vol. 37, p. 104–112.
17. CHANTRELLE, F. P., LAHMIDI, H., KEILHOLZ, W., MANKIBI, M. E., MICHEL, P., Development of a multicriteria tool for optimizing the renovation of buildings, *Applied Energy*, 2011, Vol. 88, No. 4, p. 1386–1394.
18. JUAN, Y.-K., GAO, P., WANG, J., A hybrid decision support system for sustainable office building renovation and energy performance improvement, *Energy and Buildings*, 2010, Vol. 42, No. 3, p. 290–297.
19. RISHOLT, C. B., TIME, B., HESTNES, A. G., Sustainability assessment of nearly zero energy renovation of dwellings -based on energy, economy and home quality indicators, *Energy and Buildings*, 2013, Vol. 60, No. 5, p. 217-224. .
20. RUIJVEN, B. van, and VUUREN, D. P. van, Oil and natural gas prices and greenhouse gas emission mitigation, *Energy Policy*, Vol. 37, No. 11, p. 4797–4808.
21. BROWN, N. W. O., MALMQVIST, T., BAI, W., MOLINARI, M., Sustainability Assessment of Renovation Packages for Increased Energy Efficiency for Multi-family Buildings in Sweden, *Building and Environment*, 2013, Vol. 61, No. 3, p. 140-148.
22. FRONTCZAK, M., ANDERSEN, R. V., WARGOCKI, P., Questionnaire survey on factors influencing comfort with indoor environmental quality in Danish housing, *Building and Environment*, 2012, Vol. 50, p. 56–64.
23. FRONTCZAK, M., WARGOCKI, P., Literature survey on how different factors influence human comfort in indoor environments, *Building and Environment*, 2011, Vol. 46, No. 4, p. 922–937.
24. KAKLAUSKAS, A., ZAVADSKAS, E. K., RASLANAS, S., Multivariant design and multiple criteria analysis of building refurbishments, *Energy and Buildings*, 2005, Vol. 37, No. 4, p. 361–372.



THE SIGNIFICANCE OF DISTRICT HEATING FOR THE PROMOTION OF RENEWABLE ENERGY SOURCES DEMAND

L. Murauskaitė

Lithuanian Energy Institute

Breslaujos str. 3, LT-44403 Kaunas – Lithuania

ABSTRACT

The stimulation of energy producers and consumers for the use of renewable energy sources (RES) is one of the major goals of energy policy in Lithuania. Among other priorities of the development of energy from renewable sources, envisages utilisation of the existing region infrastructure and further development of necessary infrastructure while creating conditions for the development of RES. District heating infrastructure is suitable for implementing RES technologies on the demand side and consequently achieving energy and environmental policy goals. The paper presents justification of RES demand support measures on the example of solar thermal and geothermal energy. In this paper scenario of the use of solar thermal energy for the preparation of hot water is analysed, also scenario of the use of geothermal energy for the space heating purposes. Moreover, all analysed scenarios are in apartment buildings that are still connected to district heating system. Simulation of techno-economic analysis was done using EnergyPro modelling software package. Economic evaluation of the use of RES was done by the levelised cost of energy method.

Keywords: district heating, RES demand, solar thermal energy, geothermal energy

1. INTRODUCTION

Many countries around the world for various reasons, such as energy security and climate change, pursue an energy policy focusing on energy efficiency and an increase in the share of renewable energy sources (RES) [1-2]. Lithuania also promotes RES both in electricity and district heating sectors [3-4].

District heating network gain in importance, as it facilitates large scale renewable energy integration and a more even matching between supply and demand [5]. District heating is expected to remain competitive in high heat density city districts and large city areas, even at ambitious heat reduction targets due to energy efficiency measures [6-7]. The building sector uses on average 40% of total energy consumption in the EU countries [8]. Papers mainly deal with future buildings [9-10], but usually do not include existing buildings, which are expected to remain for many decades to come due to the long lifetime of buildings [11]. Some papers have addressed important issues of how to reduce the heat demand in existing buildings, and have come to the conclusion that reduction of the demand involves a significant investment cost, but results in operational savings [12-13]. However, the share of buildings that already exist today is expected to remain high for many years. Therefore, the possibility to integrate RES on the demand side of district heating in the apartment building was chosen for analysis. Main sources for investment in the apartment building in Lithuania are:

- the Programme for the renovation/upgrading of multi-apartment buildings (15 percent of investments);
- Climate Change Programme funding (15 percent of investments);
- soft loans from Jessica fund. The possibility of 20 year period of the loan with a fixed annual interest rate of percent.

This paper analyses several combinations of flat plate and vacuum solar collectors with accumulation tank systems of various sizes in apartment building. Heat from the district heating system is used as an additional heat source for the preparation of domestic hot water. Moreover,

geothermal heating by using ground source heat pump is analysed. The influence of variations in the main indicators on the final economic results has also been evaluated.

2. METHODOLOGY

EnergyPRO by EMD [14] modelling software package 4.1 has been used. EnergyPRO is typically used for techno-economic analysis of different energy projects such as district heating cogeneration plants. The model is specifically suited for simulating cogeneration plants and district heating systems with multiple energy producers. Other types of projects, e.g. geothermal, solar collectors, etc. can also be analysed and detailed within the software. EnergyPRO provides the user with a detailed financial plan in a standard format. This includes presentation of the operating results for the project, monthly cash flows and key investment figures such as Net Present Value (NPV), Internal Rate of Return (IRR) and Payback Time. The reason for choosing energyPRO is its ability to model storages and solar thermal production, and geothermal production, as well as to connect district heating.

EnergyPRO evaluates characteristics of solar collector and its inclination and orientation to the sun, accurately models hourly amount of produced heat. Savings are evaluated as produced heat price meets an average Lithuania's city district heating price (259.9 Lt/MWh).

The formula for a solar collector is as follow:

$$Y = A \cdot \left((I_{beam} \cdot K_{\theta} + (I_{diffuse}) \cdot K_{60^{\circ}}) \cdot \eta_0 - a_1 \cdot (T_m - T_a) - a_2 \cdot (T_m - T_a)^2 \right) \quad (1)$$

where: Y – heat production, [W]; A – solar collector area [m^2]; I_{beam} – beam radiation on a horizontal plane, [W/m^2]; K_{θ} - incidence angle modifier; $I_{diffuse}$ – diffuse radiation on an inclined plane, [W/m^2]; T_m – solar collectors average temperature, [$^{\circ}C$], that is an average between the temperature of the cold water entering the collector and the hot water leaving the collector; T_a – ambient temperature, [$^{\circ}C$].

The efficiency of the solar collector is defined by three parameters: η_0 – intercept (maximum) of the collector efficiency, [-]; a_1 – the first-order coefficient in collector efficiency equation, [$W/(m^2 \ ^{\circ}C)$]; a_2 – the second-order coefficient coefficient in collector efficiency equation, [$W/(m^2 \ ^{\circ}C^2)$].

The radiation is split into beam radiation and diffuse radiation. Since the diffuse radiation per definition has no incidence angel is used the incidence angle modifier or K_{θ} at 60° .

Economy in energyPRO basically is monthly based. Net present value (NPV) calculation every monthly payment are brought back to Present (start of the Planning period) on a monthly basis.

The Internal Rate of Return (IRR) is the discount rate that makes the net present value of all cash flows from a particular project equal to zero. The higher a project's internal rate of return, the more desirable it is to undertake the project. The IRR is found by iterations using Newton's method. EnergyPRO calculates the Nominal IRR. The difference between the Nominal and the Real IRR is in practice equal to the average inflation in the planning period.

Pay Back Time is defined as the month, in which you are able to pay back your loans (the month in which the money in the cash account equals remaining debts in the loans).

The use of geothermal energy in energyPRO is modelled as an electrical heat pump. There must be defined electricity consumption and heat production when calculations are specified. Electricity consuming heat pumps increases the complexity of energy system calculations.

Levelised cost of energy (LCoE) is the price of energy which has to be set that at the chosen (stated) discount rate, which is equal to capital price, all discounted expenditures are equal to income; and the net present value (NPV) equals 0.

This method is very convenient, because all main criteria can be concentrated in it – net present value (equal to 0), internal return rate (as we determine it). The main advantage is that this

indicator can be compared to the competitive price of energy in the market. In other words, the levelised cost of energy shows that the project will have, for example, 10 % IRR (that is determined), if the price of district heating (or any other producer/supplier) would not be lower than the price that is calculated by the formula:

$$LCOE_s = \frac{\sum_{i=1}^{i=n} \frac{(I_i + e_i - Z_i)}{(1+r_n)^i}}{\sum_{i=1}^{i=n} \frac{G_i}{(1+r_n)^i}} \quad (2)$$

where: LCOEs – simple levelised cost of energy; I_i – capital investments; e_i – annual operational and maintenance costs; Z_i – external benefit of renewable energy (could be negative); r – stated periodic discount rate; n – years of lifetime; i – serial number of the year; G_i – yearly amount of produced and consumed energy; r_n – stated discount rate (discount rate for RES can be lower than for fossil fuel).

This method is suitable for the evaluation of a wide spectrum of different options. The result obtained, for example, 1 kWh levelised cost of heat can be compared to officially confirmed district heating price, and the feasibility of a project can be decided. The LCoE can be calculated by any of energy development scenarios of the analysed object (apartment, house, city, district, etc.).

It must be noticed that the main criterion is not the price of solar collector's and its installing, but also the price of a heat unit that is produced by solar collector and effectively consumed. It is possible and even necessary to calculate how much the produced heat for apartment buildings will cost with chosen type of solar collector. The application of this method allows estimation of all technical aspects of economical projections to the levelised cost of the heat unit. Initial calculations show that the increasing heat prices make the use of solar collectors for domestic hot water preparation competitive in some cities.

Moreover, if ecological, economic and social benefit would be comprehensive evaluated in a long term period and on that basis would be given support for users who produce energy using solar energy, the demand for advanced solar technologies would increase noticeably.

3. RESULTS AND DISCUSSION

Modelling is being done by evaluating the demand of hot water, working period of flat and vacuum solar collectors in a year, their efficiency. Depending on the type of the collector, its area, heat loss parameters the program calculated the price of hot water made by collector, the payback period of the system, etc. Moreover, modelling of geothermal heating is being done with existing electricity price.

Apartment building that is typical in Lithuania was chosen for analysis. It has five floors and three stairways, the number of flats is 45, area of the house is 2950 m². The annual demand of space heating is about 350 MWh, the annual demand of hot water heating is about 170 MWh with total 520 MWh heating demand. This data is an average of 20 typical for Lithuania non-renovated apartment buildings [15].

Modelling assumptions are made using various sources, available statistical data, studies, reports, papers, websites [15–17]. The paper deals with the possibility to install on the roof of the apartment building the solar collectors system. Solar collectors are selected taking into account the intensity of solar radiation and fluctuation of hot water system needs in apartment building. Fig. 1 shows annually aggregated solar radiation in Lithuania. Solar radiation data is an average of 1990–2005 for Kaunas city (the biggest city approximately in the middle of Lithuania). First year of investment (2013) is shown in a graph. As could be seen, the biggest potential of the effectively use of solar collector in Lithuania is in the summer time, approximately from the beginning of April to the end of September.

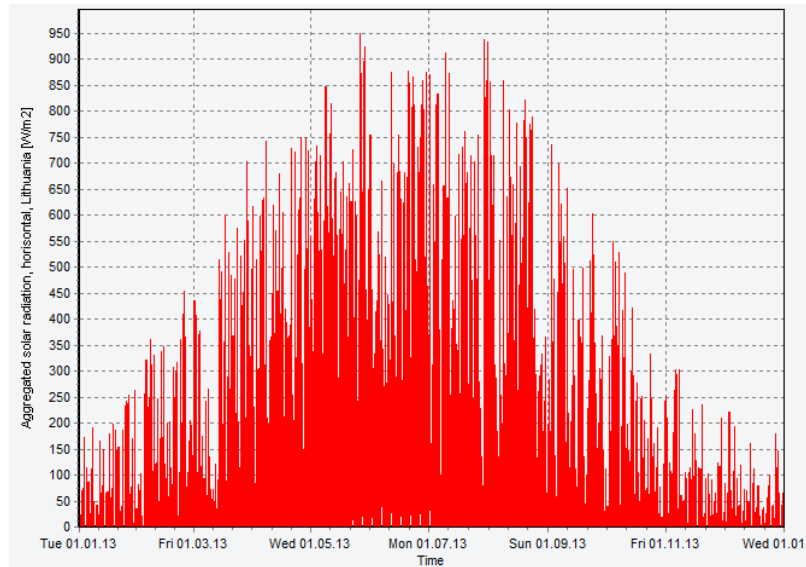
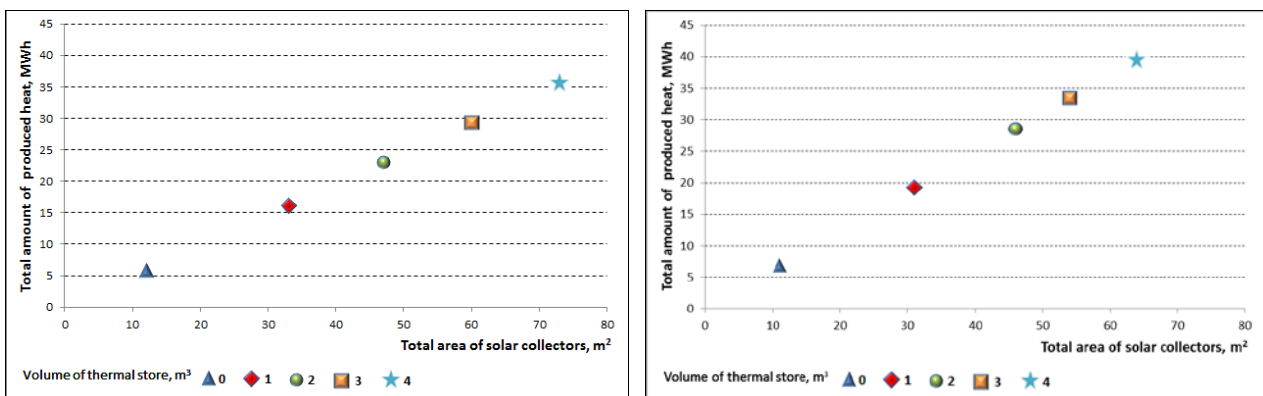


Fig. 1. Aggregated solar radiation, horizontal in Lithuania (annually, EnergyPRO)

A solar hot water system typically includes solar collectors mounted on the roof and a separate thermal storage tank beside the conventional water heater (district heating) [18]. The produced hot water from the solar collector is supplied to the hot water system or accumulated in thermal store. In case when solar collector produced heat or accumulated heat are not enough to ensure the need for hot water system, missing part is supplied from district heating network.

The main difference is a type of solar collector. Flat-plate collectors are cheaper and less efficient than vacuum-tube collectors. EnergyPRO enables to determine the maximum technical potential of solar collector area. Analysis has taken into account various volumes of thermal store, from no thermal store at all to 4 m³. Fig. 2 presents modelling results.



a) Flat-plate solar collectors

b) Vacuum-tube solar collectors

Fig. 2. Modelling results of total amount of annually produced heat (MWh), total area of solar collectors (m²) and volume of thermal store (m³)

The assumed area of solar collectors can provide only part of the hot water demand. The larger volume of thermal store, the larger may be solar collector area and more hot water produced. The maximum modelled flat-plate solar collector area of 73 m² with 4 m³ thermal store can produce only 36 MWh heat annually, vacuum-tube solar collector area of 64 m² and the same thermal store only about 40 MWh. Smaller area of vacuum-tube solar collector could produce larger amount of

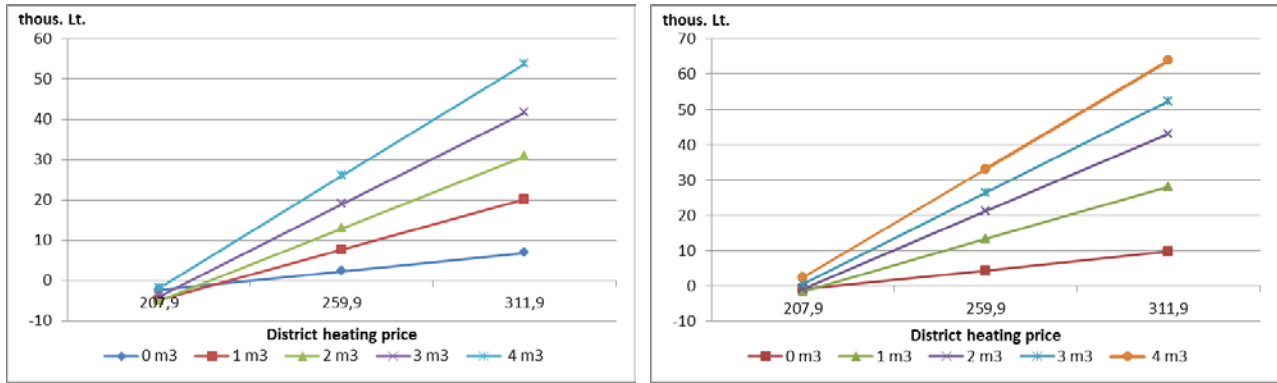
hot water than flat-plate solar collector. Theoretically it is possible to increase the area of solar collectors and volume of thermal store, but there is a problem with space for thermal storage tanks. Heat pump was chosen 60 W capacity, with possibility to cover about 210 MWh heating demand. The rest of the heating demand is supplied by district heating network.

Therefore, it is essential to stay connected to an additional heat source – district heating – for the rest of the hot water demand. The main issue is that only consumers can expect benefit for the use of solar collector. District heating company losses part of income because of lower hot water demand. Moreover, loss in district heating network remains the same. Therefore, other users of district heating pay more for grid losses.

Calculations of the use of solar collectors showed that *payback time* is approximately 12–14 year. Flat-plate solar collectors payback time varies between 13–14 year, vacuum-tube solar collectors payback time varies between 12–13. The assumption of stable district heating price was taken into account. Savings are calculated as heat amount from solar collectors multiplying by district heating price of 259.9 LTL/MWh (1 EUR = 3.4528 LTL). More economically attractive solar collector's systems according this indicator is smaller size with lower payback time. Payback time for heat pump is only about 8 year.

Investments for solar collectors are done assuming of 20 years lifespan, when it is used soft loan with 3 percent annual interest. The assumption of no exploitation expenses is taken into account. The same assumptions are made for heat pump. The main reason for the same conditions of calculation is a possibility to compare two most popular renewable energy alternatives for district heating. After market survey of the price of solar collectors, thermal store and installation expenses, the largest system 73 m² of flat-plate solar collectors system cost about 110–120 thousand litas, 64 m² vacuum-tube solar collectors system cost about 120-130 thousand litas and more (it depends on the quality of selected type of solar collectors). Heat pump price with full installation is about two times higher, approximately 200-230 thousand litas.

Economic calculations of *Net Present Value* indicator showed that the most attractive NPV is for the biggest solar collector's systems. The main reason for such result is high district heating price. Therefore, there is essential to make sensitivity analysis calculations. Fig. 3 shows sensitivity analysis of NPV results. An average district heating price in Lithuania is selected as a basis (259.9 Lt/MWh), and 20 percent increases and decreases of the district heating price was calculated. The results have showed that 20 percent decrease gives negative NPV values for flat-plate solar collectors, but larger scale vacuum-tube solar collectors system has positive values. Summing up the results, 20 percent decrease of the average district heating price is economically unacceptable investment for flat-plate solar collectors and very risky for vacuum-tube solar collectors. The current situation in Lithuania shows that small cities (such as Moletai, Ignalina, Sirvintos) already have lower price for district heating, and investment in solar collectors is unnecessary and generates financially loss. On the other hand, for more than 10 cities that uses natural gas as a fuel for district heating, investments in solar collectors are very attractive. The main risk is future plans of district heating companies to change natural gas fuel into biomass and significantly reduce price. NPV calculations for heat pump showed that NPV remains very economically attractive even with 20 percent lower district heating price (NPV=64 thous.Lt). Therefore, investment in heat pump is more economically acceptable than in solar collectors.



a) Flat-plate solar collectors

b) Vacuum-tube solar collectors

Fig. 3. Sensitivity analysis of NPV with different district heating price and different area of solar collectors/thermal store combinations

IRR calculations result with the average Lithuanian district heating price (259.9 LTL/MWh) showed that investment in solar collectors are very risky, because IRR varies about 4–5 percent. The main conclusion is that without government support (for soft loan with 3 percent interest rate) investments in solar collectors are financially unacceptable. Economically attractive investments with 6–7 percent IRR for flat-plate solar collector or 7–8 IRR for vacuum-tube solar collectors could be just for cities with district heating price over 310 LTL/MWh. IRR calculations for heat pump showed that even without government support investment remains economically acceptable with the average Lithuanian district heating price (IRR=12 percent). Calculations with high district heating price (311,9 LTL/MWh) showed that IRR is over 17 percent. On the other hand, with low price for district heating (207,9 Lt/MWh) heat pump becomes very risky investment, because IRR is only over 5 percent.

Levelised cost of energy calculations can be compared to the competitive price of energy in the market. Solar collectors levelised cost of energy indicator varies 219–233 Lt/MWh with 3 percent discount rate. Heat pump levelised cost of energy indicator is 307 Lt/MWh with 3 percent discount rate, because external benefit is lower for the heat pump. The main reason is that heat pump consumes electricity to produce heat, and Lithuania produces electricity mainly from natural gas.

Without taking into account external benefit, heat pump has better financial indicators and is more attractive investment. On the other hand, it requires more than two times higher investments cost and consumes electricity. The risk of changes in district heating and electricity prices, and lower demand of heating after renovation of apartment buildings should be taken into account in further researches.

4. CONCLUSIONS

Analysis of the results showed that vacuum-tube solar collectors are more effective than flat-plate solar collectors, but requires higher investments. On the other hand, they are more attractive because of shorter payback time, higher NPV values and higher IRR values. Sensitivity analysis showed that vacuum-tube solar collectors are more economically acceptable, when district heating price varies of 20 percent. The main conclusion from the sensitivity analysis could be done that for cities in Lithuania, who uses biomass as a fuel and have the lowest district heating price, investment in solar collectors for apartment buildings generate financial loss and is unacceptable. On the other hand, such investment is attractive for cities with the highest district heating price in Lithuania.

Investment in heat pump has better financial indicators than solar collectors with lower payback time, higher IRR and high NPV values even when district heating price varies 20 percent. On the other hand, it requires more than two times higher investments cost and consumes

electricity. If external benefit is taken into account, heat pump levelised cost of energy becomes higher than solar collectors.

The main risk is future plans of district heating companies to change natural gas fuel into biomass and significantly reduce price. Moreover, investment in renewable energy on the demand side is beneficial only for apartment building residents. From the macroeconomic point of view, it is socially unjust, because loss of district heating network should be paid by the rest of consumers. If the installation of solar collectors and heat pumps in apartment buildings increase in larger scale, it should be changes in district heating prices as well.

ACKNOWLEDGEMENTS

This research was supported by the Research Council of Lithuania (IEP-01/2012).

REFERENCES

1. Directive 2009/28/EC of the European Parliament and of the Council on the promotion of the use of energy from renewable sources and amending and subsequently repealing Directives 2001/77/EC and 2003/30/EC. Official Journal of the European Communities, 5.6.2009, L 140/16.
2. International Energy Agency. Global renewable energy. IEA/IRENA joint policies and measures database [referred on the 2nd of March in 2012]. Link to the internet <<http://www.iea.org/policiesandmeasures/renewableenergy/>>
3. The National Strategy for the Development of Renewable Energy Sources. Official Gazette, 2010, No. 73-3725.
4. Law on Renewable Energy of the Republic of Lithuania. Official Gazette, 2011, No. 62-2936.
5. BEN HASSINE, I., EICKER, U. Impact of load structure variation and solar thermal energy integration on an existing district heating network. *Applied Thermal Engineering*, 2013, Vol. 50, No. 2, p. 1437–1446.
6. PERSSON, U., WERNER, S. Heat distribution and the future competitiveness of district heating. *Applied Energy*, 2011, Vol. 88, No. 3, p. 568–576.
7. ABERG, M., HENNING, D. Optimisation of a Swedish district heating system with reduced heat demand due to energy efficiency measures in residential buildings. *Energy Policy*, 2011, Vol. 39, No. 12, p. 7839–7852.
8. KORONEOS, C., TSAROUHIS, M. Exergy analysis and life cycle assessment of solar heating and cooling systems in the building environment. *Journal of Cleaner Production*, 2012, Vol. 32, p. 52–60.
9. NIELSEN, S., MÖLLER, B. Excess heat production of future net zero energy buildings within district heating areas in Denmark. *Energy*, 2012, Vol. 48, No. 1, p. 23–31.
10. DALLA ROSA, A., CHRISTENSEN, J.E. Low-energy district heating in energy-efficient building areas. *Energy*, 2011, Vol. 36, No. 12, p. 6890–6899.
11. LUND, H., MÖLLER, B., MATHIESEN, B.V., DYRELUND, A. The role of district heating in future renewable energy systems. *Energy*, 2010, Vol. 35, No. 3, p. 1381–1390.
12. ATKINSON, J.G.B., JACKSON, T., MULLINGS-SMITH, E. Market influence on the low carbon energy refurbishment of existing multi-residential buildings. *Energy Policy*, 2009, Vol. 37, No. 7, p. 2582–2593.
13. HEISELBERG, P. ET AL. Application of sensitivity analysis in design of sustainable buildings. *Renewable Energy*, 2009, Vol. 34, No. 9, p. 2030–2036.
14. EMD International. EnergyPRO user's guide. Aalborg. 2011.
15. LDHA: Lithuanian District Heating Association, 2012 – [referred on the 2nd of March in 2013]. Link to the internet <<http://www.lsta.lt/>>.



16. National Control Commission for Prices and Energy, 2012- [referred on the 2nd of March in 2013]. Link to the internet <<http://www.regula.lt/en/>>. Link to the internet <<http://www.regula.lt/en/>>
17. Statistics Lithuania, 2012 – [referred on the 2nd of March in 2013]. Link to the internet <<http://www.stat.gov.lt/en/>>.
18. HANG, Y., QU, M., ZHAO, F. Economic and environmental life cycle analysis of solar hot water systems in the United States. *Energy and Buildings*, 2012, Vol. 45, p. 181–188.



THE ENERGY PERFORMANCE OF HOSPITAL BUILDINGS IN NIGERIA

S.C. Nwanya

*Department of Mechanical Engineering
University of Nigeria
410001 Nsukka – Nigeria*

O.V. Ekechukwu

*National Universities Commission
Abuja, Nigeria*

ABSTRACT

The negative effects of deteriorated indoor environments have been recognised in Nigerian hospitals. This paper presents a summary of how Nigerian hospitals prioritize their energy supply under alternative sources of power. It also, identified lighting function as possible area for energy optimization in Nigerian hospitals. The specific objectives of the study include estimating how much of the total energy requirements are used in patient rooms, calculating metrics for assessing energy performance and estimating emission reductions achieved through renewable energy systems in hospitals. The research used a systematic field survey followed by in-depth statistical analysis. The field survey investigated four categories of hospitals, namely rural, urban, specialist and teaching hospitals; focusing on medical equipment and ventilation facilities in addition to patient population, lighting points, and manpower requirements. Then, questionnaires were administered randomly among 70 hospitals in Nigeria. Results of the analysis show that stand-alone auto-generation is predominantly used in all the hospitals, when grid utility supply is unavailable or unreliable. Although, auto-generation presents attractive solutions, it is restrictive to emergency usage. Emergency usage is insensitive to microclimatic changes at the detriment of in-patients. For more efficient lighting, the 57.73 % utilization of tungsten bulbs in patient rooms is reduced through application of photovoltaic (PV) system. Based on analysis, it is shown that photovoltaic system has potential economic viability comparable to conventional sources. The paper concludes that cost-effective energy supply will add to the value of hospital service delivery in Nigeria, where expenditure on healthcare is less than 5 % of the Gross Domestic Product (GDP).

Keywords: energy performance, building energy index, lighting energy indicator, hospital building, Nigeria.

1. INTRODUCTION

Unreliable power supply in hospitals is a daunting challenge that affects cost-effective service delivery in Nigeria. Recent health cases have demonstrated that reliable power supply to hospital building is a precondition to success in service delivery. Power disruptions result in a disruption of treatment programme or the inability to reliably use electrical appliances such as laboratory equipment [1]. It is important to note that health service as a national priority cannot be actualized without efficient and reliable energy supply. Energy provides the motive force that powers hospital machinery. In monetary terms, the cost of this input factor has been on the increase in Nigeria because of unreliable power supply and self-generation. The world health organization (WHO) states that health and energy are inter-dependent factors which largely determine the progress of rural development [2]. According to studies by Al-karaghoul and Kazmerski [3] and Jimenez and Olson [4] the relationship between health and energy is compelling. However, this is an indirect relationship and it is tied to the use of appliances or functions operated on energy. In Nigeria, the compelling need for adequate energy supply to hospitals as in other economic sectors has been observed. But, the willingness to devise appropriate remedial strategies for improving energy performance in ill-fated hospital buildings is lacking.

The issue of energy performance of buildings is of great concern because it translates to cost [5]. An energy strategy for hospitals, therefore will be critical in achieving lasting health improvements [2]. Nigeria is located between latitude 4°N and 14°N in the equatorial and tropical region of Africa and this underscores the importance of energy input factor for improving comfort for patients. Indoor comfort has a strong influence on recovery rate of in-patients and its cost implications are factored in hospital bills. With rising energy prices, taking control of energy usage will enable a hospital achieve savings and generate positive corporate image towards host community. Also, Pinzone et al, [6] and Stankovic et al. [7], opine that availability of energy influences the mood of patients and beneficially effects the welfare and productivity of staff. This preceding fact explains in part why the rising energy cost component of hospital bill is believed to be responsible for high level apathy to accessing modern health care services in Nigeria.

Several authors have reported the rising energy consumption pattern of hospital buildings. For example, [1] and [8] observed the importance of electricity as an increasingly essential commodity in remote healthcare facilities. Hospital buildings are usually complex facilities that operate continuously for 24 hours a day; seven days a week; and consume energy on a large scale in different ways [9, 10]. The various ways energy is consumed include lighting, heating, ventilation, cooling, communication and operating of equipment. The factors that influence hospital energy use intensity such as facility size, climate, weather, operating schedule and the suite of activities have been discussed[11]. At the same level of energy consumption, indoor air quality is improved [12]. Since the variability in energy use is almost a certainty due to these factors, there is need to use energy metrics to measure specific performance targets at the level of hospital facility. Methodology for the calculation of the energy performance of buildings is well documented[13]. Chen [14] reviewed the tools for predicting performance in hospital buildings. According to [15] one of the main buildings with a great potential to apply measures of energy saving is the hospitals. By increasing energy efficiency, hospitals can improve the bottom line and free up funds to invest in new technologies and improve patient care [16, 17].

In Nigeria, literature on energy utilization in hospital buildings is scanty, thus highlighting a number of shortages that remain to be addressed. Among the issues to be addressed is lack of metrics for appraising the energy usage or how energy requirements are prioritized in hospital facilities. Underlying the foregoing argument is the justification for this study, since country specific information is essential for comparative analysis.

The hospital sector is of interest because it consists of consumers with similar equipment and can therefore be considered to be fairly homogenous. Nigeria is endowed with a variety of energy sources such as coal, crude oil and natural gas, that can provide reliable generation options, yet sick-building syndrome symptoms, illumination and thermal lapses have been observed in hospital buildings as evidence of energy deprivation related issues. The syndrome exists when a deteriorated part of the building is neglected and it constitutes nuisance to the environment.

The overall purpose of this study is the determination of some of the energy performance framework for evaluating hospital energy utilization in particular. To achieve this identified target, the specific objectives of the study are as follows: to estimate some of the energy performance indices in hospital buildings; to determine the quantities of energy usage and their consumption pattern within the hospital location; and to compare the usage of lighting facilities in hospital buildings with a view to planning for energy efficient measures.

1.1 Significance of study

It is therefore pertinent to study the energy consumption profile of hospital building as this will aid good policy formation in both health and energy sector of the economy.

2. METHODOLOGY

The study sets to achieve its goals using a systematic field survey followed by in-depth statistical analysis methodology. In carrying out the field survey, the hospitals are stratified into four categories rural, urban, specialist and teaching. A concise function and ownership descriptions of these categories are as follows: rural hospital – mostly private owned, patient catchment within host community and involved mainly in primary care and ambulatory services; urban hospital - act as a comprehensive health system, missionary / local government ownership and offers secondary and primary care services; specialist hospitals – act as hub of an integrated health system for a State government; and teaching hospitals – are attached to universities, involve in teaching, research and acute care services.

As a part of the survey, an energy audit is required to establish a reference base of energy use that will be analysed for performance. A walk-through audit approach was used to obtain historical energy consumption from four representative hospitals, using data from utility bills, plant/equipment records and patient turnover. The energy performance assessment embraced all services of the hospital including lighting, ventilation and, cooling. The needs assessment will include an inventory of the types of equipment used and power required to operate each device.

The instrument for primary data collection is a well structured, pretested questionnaires. The survey questionnaire was framed to emphasize on operating characteristics of hospital buildings such as gross internal floor area(m²), on-time (hours), bed space, thermal characteristics of medical equipment(name plate power rating), ventilation facilities in addition to patient census and energy consumption values for the buildings. Then, the questionnaires were administered randomly among 70 hospitals in Nigeria.

In order to calculate energy performance metrics, the collected data are collated according to category of hospital by type of service. The significance of this approach is that the amount of power used to operate the equipment daily will influence the choice of energy supply source to hospital. According to [11], the starting point for the calculation is energy use information from utility and fuel bills. These records are stratified into costs and amount of each type of energy used on daily basis. The former is summed into monthly values. Then, the energy consumptions, regardless of source, are expressed in kWh. Finally, full analysis of consumption for each fuel and utility type with costs and operating conditions is carried out based on total energy requirements. In order to relate results of this study to existing benchmarks, some energy metrics were calculated.

The total energy demand/consumption, X is a summation of all energy consumed for lighting, water pumping, equipment/ appliance operation, ventilation/cooling, and refrigeration/ sterilization. The general expression for X is as follows:

$$X = \sum_{i=1}^n (X_{grid} + X_{gen} + X_{ren})_i \quad (1)$$

Where i= individual hospital energy demand, grid = grid electricity, gen = self generated electricity from generator, ren =self generated from renewable /solar.

It is also possible to disaggregate bulk demand into components such as lighting. An estimate of the lighting energy for illumination is calculated as follows:

$$L_{l,t} = \sum \{(P_n \times F_c) \times [(t_D \times F_o \times F_D) + (t_N \times F_o)]\} / (1000) \text{ [kWh]} \quad [13] \quad (2)$$

Where $L_{l,t}$ = total energy for illumination function per hospital (including incandescent and compact/fluorescent), P_n = total installed lighting power in W, F_c = illuminance factor, t_D = daylight time usage, F_o = occupancy factor, F_D = daylight dependency factor, t_N = non-daylight usage and t = time period in hours.

3. RESULTS AND DISCUSSIONS

In this study, an audit of energy consumption was carried out for Nigerian hospitals in order to determine how they prioritize their energy supply from different sources. Major energy services such as lighting, ventilation, communication, water pumping and operation of medical equipment were given priority attention in line with the hospital categories. In addition, the patient population, manpower requirements and building parameters were among the responses obtained from the 70 hospitals randomly sampled. Two key performance indicators are considered in this study: building energy index and energy use performance factor (efficacy,). The extent of service we can derive from a given amount of every supply to a hospital building determines the performance level.

Based on the field data, a cross-sectional analysis was carried out the responses. All the urban, specialist and teaching hospitals rely on the national grid and fossil fuels (generators) for electricity. Sometimes, fuelwood and kerosene are used as alternative to national grid in rural hospitals for heating and sterilization needs. The photovoltaic energy is sparingly used for lighting and storage. Table 1 shows estimated consumption of a typical rural hospital.

Table 1. Estimation of daily energy consumption per equipment for a typical rural hospital

Equipment function	Qty of Equipment (a)	Power Rating, watt (b)	Total watts (c)	On-time (hours/day) (d)	Watt-hour (e)	kWh $f = \left(\frac{e}{1000}\right)$
Vaccine refrigerator	2	60	120	6	720	0.72
Centrifuge	2	575	1150	6	6900	6.9
Microscope	2	15	30	6	180	0.18
Autoclave	1	1,564	1,564	6	9384	9.384
Oxygen concentrator	1	300	300	6	1800	1.8
Computer desktop	1	150	150	10	1500	1.5
Printer	1	65	65	10	650	0.65
Monitor	1	65	65	10	650	0.65
TV (colour)	1	60	60	10	600	0.6
Ceiling fan	13	40	520	6	5200	5.2
kerosene stove	2	9500	19000	1	19000	19.0
Standing fan	3	40	120	6	720	0.72
Compact lamp	25	15	375	8	3000	3.0
Incandescent	16	60	960	8	7680	7.68
Borehole-sumo pump	1	2 horsepower	1492	6	8952	8.952
Gross Total of energy used	-					66.936

The facts used to reach a decision on the energy performance of hospital buildings are based on energy consumption by end use in Nigeria. Results analysis for the representative rural, urban, specialist and teaching hospitals showed a significant pattern of energy end-uses. For example, an average hospital in Nigeria depending on its status uses energy as follows: rural – 66.936kWh/day, urban – 343. 23 kWh/day, specialist – 454.872 kWh/day and teaching – 1944.394 kWh/day. A descriptive interpretation for the total energy requirements, is that 2.4 %, 12.2 %, 16.2 % and 69.2 % are consumed daily by rural, urban, specialist and teaching hospitals, respectively. Also, Fig. 1 shows the energy performance according to functions by type of hospital. As shown in Fig. 1, lighting function has the highest energy usage, seconded by equipment operations in all the hospital categories. However, this may not represent the order of significance in hospital functions. The

observed trend rather identified area for energy optimization in the hospital, though outside the scope of this study.

Energy demand per hospital bed space can be calculated using equation 3.

$$M = \frac{\sum FX}{\sum F} \quad [\text{kWh}] \quad (3)$$

Where M = mean energy demand per bed space, X = energy demand, F = number of bed spaces.

Based on survey data and results analysis regardless of energy source, a statistic value of 3.346 kWh/ bed space/ day; 2.367 kWh/ bed space/day, 4.548 kWh/bed space/day and 19.443 kWh/bed space are consumed, respectively by a typical rural, urban, specialist and teaching hospitals. Using Power Holding Company of Nigeria, PHCN tariff rate of ₦12.89 (\$ 0.083) per 1 kWh, the average cost of energy per bed space in the representatives hospitals are ₦ 43.12, ₦ 30.51, ₦ 58.62 and ₦ 250.62, respectively. Their corresponding building energy index (BEI) is calculated as the quotient of gross energy consumed over the built-up area. The respective BEI values for the hospitals are as follow: rural- is 0.13 kWh/m², urban - 0.077 kWh/m², specialist – 0.088 kWh/m² and teaching – 0.277 kWh/m². The low BEI implies that building has lower rates of sick building syndrome symptoms.

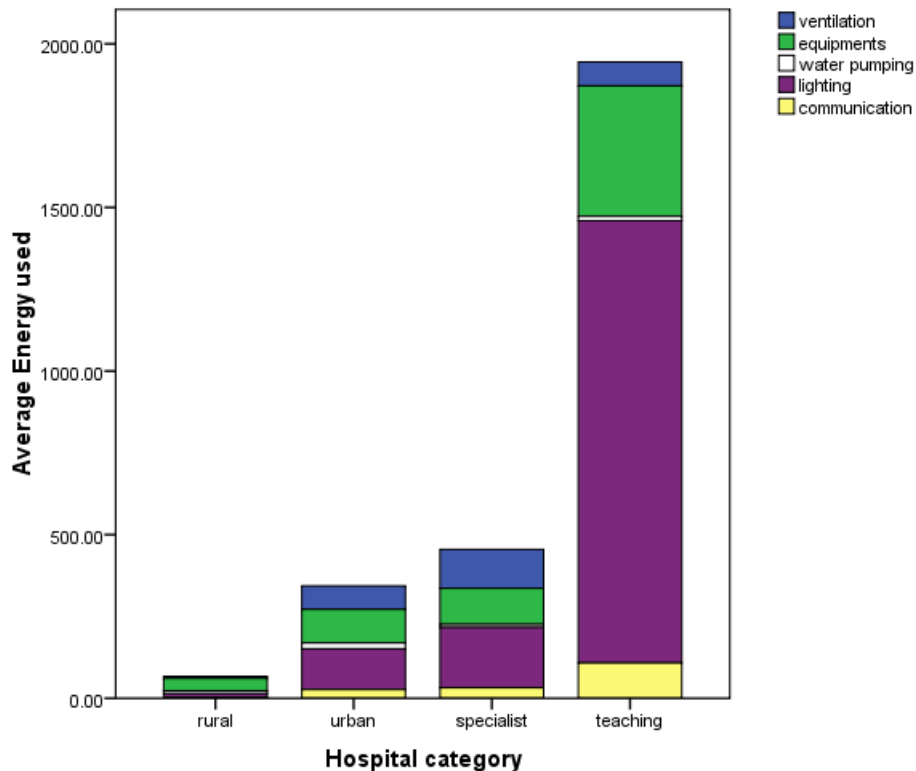


Fig. 1. Component bar chart of energy usage in hospital according to function and type of hospital

3.1 Self generation of electricity by generator

In this survey, all the hospitals were observed to have installed stand-by generators. An average hospital according to the status considered in this study consumes 11 litres, 20 litres, and 40 litres of gasoline per day for rural, urban and specialist hospitals, respectively. The teaching hospital uses 100 litres of diesel per day. Using average commercial gasoline price of ₦ 100 per litre and ₦ 120 per litre for diesel, these hospitals spend ₦ 1100, ₦ 2000 and ₦ 4000 for gasoline and ₦ 12,000 for diesel per day. This cost of electricity by a generator is expensive compared to grid electricity that is between ₦ 40001 – ₦ 8000, ₦ 8001 – ₦ 12000, ₦ 12001 – ₦ 30000 and ₦

50000 per month for rural, urban, specialist and teaching hospitals, respectively. This cost of energy services is shifted to patients and it has rebound effect of limiting the ability to access healthcare, particularly in rural areas. The use of generators for running hospital services represents a potential deprivation and it is a proxy indicator of energy poverty in Nigeria.

As observed in this study, the crucial services of lighting and mechanical power for running equipment depend on liquid petroleum products. Although, auto-generation presents a second best attractive solution, it is restrictive to emergency usage. Emergency usage is insensitive to microclimatic changes at the detriment of in-patients.

3.2 Lighting System In Nigerian Hospitals

Lighting function is a key component in hospitals for night and theater activities. the calculation of lighting energy numeric indicator, LENI follows equation 4.

$$LENI = \frac{L_{L,t}}{A} \quad (4)$$

Where $L_{L,t}$ = total energy for illumination function per hospital, A = area of hospital occupied patients.

The lighting energy numeric indicators for the categories of hospital under study are as follows: 0.02 kWh/m², 0.03 kWh/m², 0.04 kWh/m² and 0.19 kWh/m² for rural, urban, specialist and teaching hospitals. It was observed from the survey that a large part of the lighting energy expenditure by hospitals is due to mismatch between the adoption of eco-friendly technologies and the persistent use of conventional electrical accessories. A case on hand is the compact fluorescent and incandescent lamps. The hospitals consume much more energy for the same duration of time in running incandescent lamps compared to compact fluorescent. For more efficient lighting, the overall 57.73 % utilization of tungsten bulbs in patient rooms can be reduced through application of photovoltaic (PV) system. Therefore, PV presents great opportunity for energy savings in hospitals.

The basic step in employing PV system for energy savings is to get its sizing right. Photovoltaic power system sizing- To properly size a photovoltaic system the following is required.

- Accurate data on the solar radiation of the concerned area
- The peak load of the system to be powered together with variation of this demand on daily/seasonal bases.
- Accurate data on the characteristics of the solar cells employed in the design of the plant.

The above data are then used to calculate the following:

No of PV modules (for stand-alone systems)

$$P_{pv} = \frac{E_l + \left(\frac{E_l D * B_E}{C_R} \right) * 100}{K} \quad (5)$$

Where P_{pv} is the photovoltaic module array size in peak watt, E_L is the daily energy requirement (kWh/day), D is the number of storage days, C_R is the charge recovery of the battery efficiency (days), B_E is watt-hour efficiency of the battery, K is the annual average equivalent peak hour per day (sunshine period).

4. CONCLUSION

This paper presents a summary of how Nigerian hospitals prioritize their energy supply under alternative sources of power. It estimated the total energy requirements used in patient rooms and calculated metric for assessing energy performance in rural hospital buildings. The research used a

systematic field survey followed by in-depth statistical analysis. The field survey investigated four categories of hospitals, namely rural, urban, specialist and teaching hospitals; medical equipment; ventilation facilities in addition to patient population, lighting points, and manpower requirements. Then, questionnaires were administered randomly among 70 hospitals in Nigeria.

Results of the analysis show that an average hospital in Nigeria, depending on its status, uses energy as follows: rural – 66.936kWh/day; urban – 343.23 kWh/day; specialist - 454.872 kWh/day and teaching – 1944.394 kWh/day. A statistic energy value of 3.346 kWh/ bed space/ day; 2.367 kWh/ bed space/day, 4.548 kWh/bed space/day and 19.443 kWh/bed space are consumed, respectively by a typical rural, urban, specialist and teaching hospitals. The respective BEI values for the hospitals are as follow: rural – is 0.13 kWh/m²; urban -0.077 kWh/m²; specialist – 0.088 kWh/m² and teaching – 0.277 kWh/m². The low BEI implies that building has lower rates of sick building syndrome symptoms. Also, stand-alone auto-generation is predominantly used in all the hospitals, when grid utility supply is unavailable or unreliable. Although, auto-generation presents attractive solutions, it is restrictive to emergency usage.

Emergency usage is insensitive to microclimatic changes at the detriment of in-patients. For more efficient lighting, the 57.73 % utilization of tungsten bulbs in patient rooms is reduced through application of photovoltaic (PV) system. Much of the hospital energy consumptions can be reduced by a significant amount with cost-efficient measures such as PV system. Further study on cost allocation system for energy supply to hospital is being recommended.

REFERENCES

1. BOSCH, J.P., GLASER, E. Powering Health: Electrification Options For Rural Health Centers. United States Agency For International Development, USAID, 2012- [referred on the 2nd of March in 2013 y.]. Link to the internet <pdf.usaid.gov/pdf_docs/PNADJ557.pdf>.
2. World Health Organization, WHO. Solar Energy and Rural Health Care. WHO fact sheet N132, Geneva, Switzerland, 1996-[referred on 28th of February in 2013 y.]. Link to the internet <who.int/inf-fs/fact132.html>.
3. AL-KARAGHOULI, A., KAZMERSKI, L.L. Optimization and life-cycle cost of health clinic PV system for a rural area in Southern Iraq using HOMER software. Solar energy, 2010, Vol. 84, p. 710–714.
4. JIMENEZ, A.C., K. OLSON. Renewable energy for rural health clinics. National renewable energy laboratory, NREL Colorado, USA, 1998- [referred on 20th of February in 2013 y.]. Link to the internet <nrel.gov/docs/legosti/fy98/25233.pdf>
5. DEGELMAN, L. O., V. I. SOEBARTO. VITAL SIGNS: whole building energy performance-simulation. [referred on the 8th of April in 2013 y.] Link to the internet <<http://arch.ced.berkeley.edu/vitalsigns/res/downloads>>
6. PINZONE, M., E. LETTIERI, C. MASELLA. Sustainability in healthcare : Combining organizational and architectural lvers. International J. Engineering Business Management 2012, Vol. 4, No. 38, 1–9.
7. STANKOVIC, S., N. CAMPBELL, O. MAKIMOVIC, T. CVJETKOVIC. Evaluation of energy efficiency measures applied in public buildings (Schools and Hospitals) in Serbia. Spatium Inter. Review, 2009, No. 20, 1–8.
8. Hospitals Sector Overview, CTV024. Carbon Trust: making business sense of climate change. [referred on the 20th of February in 2013 y.]. Link to the internet <carbontrust.com/media/39216/ctv024_hospitals.pdf>.
9. GORDO, E. Energy efficiency in a hospital building case study: Hospitnis da Universidade de Coimbra, Portugal. Energetics IYCE 2011. Proceedings of the 2011 3rd international youth



- conference on energetics [referred on 21st of February in 2013 y.]. Link to the internet <ieeexplore.ieee.org>.
10. HU, S.C., CHEN, J.D., CHUAH, Y.K. Energy cost and consumption in a large Acute hospital. *International Journal on Architectural Science*, 2004, Vol. 5. No. 1, p. 11–19.
 11. SINGER, B.C., P. MATHEW, S. GREENBERG, W. TSCHUDI, SARTOR, D. Hospital energy benchmarking guidance- version 1.0. Ernest Orlando Lawrence Berkeley National Laboratory, California, 2009, p. 1–52.
 12. SEPPANEN, O. Scientific basis for design of ventilation for health, productivity and good energy efficiency. Presented in the Indoor air congress 2008, Copenhagen.
 13. CEN/TC 169 N 0618. PrEN 15193: Energy Performance of Buildings – Energy Requirements for Lighting. [referred on the 8th of April in 2013 y.]. Link to the internet <www.iar.unicamp.br/./en_15193-1_energy_requirements>
 14. CHEN, QINGYAN. Ventilation performance prediction for buildings: a method overview and recent application. *Building and Environment*, 2009, Vol. 44, No. 4, p. 848 – 859.
 15. Life04 EMV. Guideline for energy efficiency measures in hospitals. Life-Environment EMAS and Information Technology in Hospitals, Life04 EMV/GR/000114. [referred on the 27th of February in 2013 y.]. Link to the internet <ec.europa.eu/environment/life/project>
 16. YILDIZ, J. Identification of the building parameters that influence heating and cooling energy loads for apartment buildings in hot-humid climates. *Energy*, 2011, Vol. 36, p. 4287–4296.
 17. E-Source Customer Direct. Managing Energy Costs in Hospitals. US Energy Information Administration, 2010, 1–4. Link to the internet:



THIRD EUROPEAN UNION ENERGY PACKAGE IMPLEMENTATION PROBLEMS: INTERCOURSE BETWEEN FULL OWNERSHIP UNBUNDLING AND FOREIGN INVESTMENT PROTECTION

L. Rimšaitė

*Mykolas Romeris University
Ateities str. 20, LT-08303 Vilnius - Lithuania*

ABSTRACT

This topic was chosen considering third European Union energy package and Lithuania's decision to implement the strictest model of energy market liberalisation. The creation of internal energy market remains a priority goal defined in the European Union legislation. European Council emphasised the importance to exclude the existing obstacles in order to create internal energy market by 2014. The main idea of creating European Union internal energy market is to ensure competition, affordable energy supply for households and businesses also to provide possibility for consumers to choose energy supplier and to pay a competitive price for energy sources. Third European Union energy package provides three options for the creation of competitive internal energy market. According to European Commission full ownership unbundling is the most effective way to create energy market however it is the most controversial model. The weaker forms of market liberalisation such as independent transmission operator and independent system operator limit the ability to abuse the dominant position in market although leaves space for certain discriminatory behaviour. It is important to analyse the difference between privately owned companies with foreign investors and publicly owned corporations when Member State decides to implement full ownership unbundling model. Although third energy package had to be implemented by March 2011, not all member states fulfilled such obligation. This work gives an overview of third energy package implementation in Member States. Moreover, this article provides a deeper analysis of market liberalisation models with a relation to arbitral tribunal practice on indirect expropriation of foreign investment in energy field and identifies the intercourse between full ownership unbundling and foreign investment protection under bilateral investment treaties and Energy Charter Treaty in energy market.

Keywords: Third energy package, full ownership unbundling, independent system operator, transmission system operator, foreign investment protection, indirect expropriation

1. INTRODUCTION TO THE EUROPEAN UNION ENERGY LAW

The problem of the research. The paper focuses on the implementation problem of the Third energy directive package (hereinafter - TEP) in European energy market. Author considers that there are certain restrictions to choose liberalisation model mainly the international commitments in bilateral investment treaties (hereinafter – BIT) and the Energy Charter Treaty (hereinafter – ECT) which implies higher protection level to foreign investment. A major complication is at the outset, the energy markets are almost completely controlled by vertically integrated utilities in Europe. Third energy directive package allows Member States to choose out of three liberalisation models: independent system operator (hereinafter – ISO), independent transmission operator (hereinafter – ITO), full ownership unbundling. Arguably the major obstacle in the creation of internal energy market and allowing more competition in market are vertically integrated utilities. European Union's core goal is to prevent vertically integrated utilities from using control over their networks to reduce competition, oblige Member States to choose market liberalisation model. Prior to liberalisation the vertical character of firms in a natural monopoly position was seen as a major advantage for cost of service changes however integrated companies that have obligations to shareholders and compel a resistance to liberalisation.

The object of research. Third energy package relation with foreign investment protection standards.

The aim of research. To provide analysis of Third energy package implementation models and their relation to foreign investment protection standards.

Relevance of the research topic. This research analyzes main aspects of energy market liberalisation models of third energy package in natural gas and electricity sector also Member States practice on implementation of liberalization models and full ownership unbundling model intercourse with foreign investment protection.

Methodology of research.

1. *Systemic analysis method* was applied to analyse legal regulation of natural gas and electricity market, Third energy package and evaluate its main provisions on legal regulation.

2. *Document analysis method* was applied to obtain information from legal acts and compare the results by indentifying main implementation problems.

The process of creating EU internal energy market began slowly but in recent years has accelerated. In 1996 first electricity directive 96/92/EC [1] was adopted, main goal was to create instruments for electricity sector liberalisation and to eliminate state monopolies in electricity field. A bit later directive 98/30/EC concerning common rules for the internal market of natural gas (First Gas directive) was adopted [2]. First energy directive package provided partial market liberalisation. As this regulation was not sufficient to create market liberalisation the second regulatory package was adopted in 2003. The second energy package contains directive 2003/54/EC concerning common rules for the internal market in electricity and directive 2003/53/EC concerning common rules for the internal market in gas and related regulations. The Second energy directive package included unbundling whereas energy transmission networks has to be run independently from supply and generation. According to directives market for non – households are to be liberalised until 2004. For private households deadline is July 2007. After these deadlines consumers would be able to choose energy supplier freely in competitive market. However market concentration is still very high and market monopolies abandon such customer rights.

The Second energy package provided further liberalisation forms: accounting unbundling, management unbundling, legal unbundling, ownership unbundling. One of the European Commission benchmarking reports conclusion showed significant distortion between different member states, lack of binding rules concerning cross border trade issues [3]. In July 2009 European Parliament and Council adopted new Electricity directive 2009/72/EC and Gas directive 2009/73/EC which aims at introducing common rules for distribution transmission generation and supply of both electricity and gas sectors. According to Gas directive consumers will have more information about gas suppliers. Electricity directive provided right for consumers to buy electricity from different market suppliers via existing networks as well as the direct lines.

The aim to create single European energy market has to be based on market liberalisation criteria implemented in single member states. The rise of competitiveness might cause some market problems mainly price indexation, consumer opposition which may cause bigger government regulation and opposite reaction to investors.

2. REGULATORY CHANGES IN ENERGY MARKET LIBERALISATION

Third energy package provides certain criteria for unbundling of vertically integrated utilities. According to Directive 2009/73/EC vertically integrated utility is natural gas company or company group when the same person is directly or indirectly entitled to exercise control over and where the undertaking performs at least one of functions of transmission, distribution, LNG, or storage and at least one of functions of production or supply of natural gas.[4] An alternative for full ownership unbundling (OU) Commission contained independent system operator (ISO) model, independent transmission operator (ITO) model. ISO model has it's implementation difficulties. First of all there might be a conflict between the network undertaking and ISO concerning competence. Problem arises when investment decisions are under ISO control and all the financial assets stays at network undertaking [5] Another problem is network expansion when there is indistinctness who controls these functions and who covers investment expenses also profit sharing problems may arise. There is also a liability problem when the investments are detrimental.

There are two ISO models: Deep ISO and Shallow ISO. When talking about Deep ISO model we could analyse *de facto* expropriation, when the network owner loses the investment control and the responsibility for the third party access to storage facilities. There is also possible situation when ISO makes investment plan, but network owner disagrees with it. Despite the network owner will investment plan is being implemented, because this function belongs to ISO and network owner only accomplishes plan [5]. Deep ISO is used in USA; in Europe we can find the similar model in England. We can give an example Scotland situation in electricity field, there England and Wales's network operator "National Grid" participates in market as ISO for Scotland transmission networks. These networks belong to Scotland vertically integrated utility.

Gas and Electricity Directives also provide third model for the creation of EU internal energy market, ITO. When this model is implemented transmission system operator remains part of vertically integrated utility [5]. However there are certain unbundling rules. This model is the most liberal for the creation of internal energy market because vertically integrated utility remains network owner, but there is a certain obligation to ensure protection for independent decision making in the separate fields.

Electricity and Gas Directives provide third party access to storage facilities. The aim of such option is to create internal energy market also to ensure competition in energy field. Third party access ensures consumers to choose supplier. Third party access is one of the core instruments to create single competitive energy market. It is responsibility of the Member State in which the production is located to ensure the use of storage facilities is not abused by producers though the creation of priority access to storage facilities [6]. Directive stress that Member States may choose one of procedures. According to Gas Directive they have possibility to implement regulated third party access or negotiated third party access. Access has to be granted without discriminatory obligations, it has to be transparent, objective. However there might be a problem because network undertakings are monopolistic and often use seek ways to avoid access granted to third parties [38]. Their often arguments are insufficient capacities. Allocation of storage capacity shall be made transparent by detailed publication of timing, organisation and aggregated results of applied allocation mechanisms on the internet in local language as well as in English [7]. Some authors notice that third party access to storage facilities may be granted using competition laws [3]. Any unjustified refusal to grant access to storage facilities is a violation of EU competition rules. In *Marathon* case, the Netherlands undertaking Gasunie refused to grant access to storage facilities to Norwegian subsidiary of US oil and gas producer Marathon. Such undertakings actions were considered as breach of competition laws, because third party access to storage facilities is one of instruments for market liberalisation. After deliberations with Commission Gasunie undertaking has increased transparency as regards access to networks. Gasunie will introduce balancing system to avoid situations where suppliers are charged high prices for the gas supplied by Gasunie to unexpected increase in consumption by their customers.

TEP determines main elements of competition in electricity and gas markets and the legal tasks of member states and undertaking. Free competition in these sectors cannot be managed by reason of high priority of service. Competition in energy market is still restricted but in common legal frame. Some undertakings still have exclusive special rights and compensations but these measures are necessary to ensure safety and competition to the market.

3. THE OVERVIEW OF EUROPEAN ENERGY MARKET LIBERALISATION ACCORDING TO THE THIRD ENERGY DIRECTIVE PACKAGE

The third energy directive package implies several options of the creation of internal energy market in Europe: full ownership unbundling, (hereinafter - OU), independent transmission operator (hereinafter - ITO) independent system operator (hereinafter - ISO).

In Lithuania electricity market the OU model was implemented by the 1 October 2012. Within the framework of third energy package shares of the vertically integrated company group

UAB “Visagino Atominė Elektrinė” have been transferred to be held in trust by the Ministry of Economics. Shares of the electricity transmission system operator AB “Litgrid”, which were controlled by UAB „Visagino Atominė Elektrinė”, have been transferred by reimbursement to the newly established AB “Litgrid” subsidiary company *EPSO-G*, and is acting under the responsibility of the Ministry of Energy. To improve better management of energy group companies on 13 February 2013 Government adopted a resolution which implemented a transposition of UAB “Visagino Atominė Elektrinė” shares from ministry of Economics to ministry of Finance [8]. In gas market Lithuania has also chosen OU model and vertically integrated utility AB „Lietuvos dujos“ submitted the terms and conditions for ownership unbundling to the National Control Commission for Prices and Energy [9].

Czech Republic has chosen the strictest model according to the third energy directive package, OU in electricity market and ITO model in gas market[10]. According to the third energy directive package member states are allowed not to implement OU if on 3 September 2009 transmission system is owned by vertically integrated utility. When the undertaking is not a part of vertically integrated transmission system only OU model can be implemented in such cases. In electricity market the electricity transmission operator ČEPS, a. s. could not be regarded as a part of vertically integrated utilities it was not feasible to apply Article 9 (8) Directive 2009/72/EC and the only possible model to choose was OU. In gas market it is possible to implement ITO or ISO models as the RWE Transgas, s. r. o. (today NET4GAS, s. r. o.) was owned by a vertically integrated undertaking, a part of which was also RWE Transgas, a. s. as a gas importer and supplier [10].

Finland is integral part of Nordic electricity market. It has formed an integrated wholesale market with Denmark, Norway, Sweden *The Nord Pool Spot* exchange. According to the third energy directive package company Fingrid which owns main Finnish grid and significant cross-border connections was unbundled from electricity production and supply activities. Fingrid was transformed to transmission network company factually unbundled from electricity production [11]. According to the directive 2009/72/EC Fingrid transmission network company has been factually unbundled from electricity production. The gas market is vertically integrated where supplier Gasum Oy is sole importer and operator of transmission network [11]. On the Finnish natural gas market only users with consumption of more than 5 million cubic meters and with remote metering can trade in the secondary market with the gas that they have acquired for their own use. The Russian natural gas exporter Gazprom and Gasum Oy has entered into an agreement for Russian natural gas exports to Finland until the 31st of December 2026 [12]. The importer and wholesaler of natural gas is Gasum Oy. The shareholders of Gasum Oy are Fortum Plc, the Russian natural gas company Gazprom, the State of Finland, Ruhrgas and three Finnish forest industry companies. According to Natural Gas Act the local distribution of natural gas must be unbundled into distribution and sales. In the corresponding manner, the transmission and wholesale of natural gas must be unbundled by Gasum Oy. Moreover, the businesses not belonging to the natural gas branch must be unbundled into separate businesses [12]. Due to the lack of competition in gas market Finland has certain exemption from EU energy law regime.

Greece regulatory framework regarding the Electricity market has been established by Law 2773/1999, which was lastly modified by law 3426/2005 with the view to transpose the provisions of the Directive 2003/54/EC, to boost the liberalization process, and to enhance security of supply. The electricity market model consists of two separate markets, a wholesale electricity market, and a capacity assurance market. The market is open to generators registered with the generation unit register and holding a supply license; to suppliers holding a supply license; and to self-supplying customer. Greece was among eight member states that pushed towards third option ITO model. According to the law 3428/2005 liberalisation of natural gas market article 32 accounts unbundling model is implemented in compliance with second energy directive package[13]. When implementing such model national regulatory authority RAE will be under close monitoring of

transparency in vertically integrated utilities. If market transparency is not achieved vertically integrated companies will be obliged to switch to OU model later on.

Ireland implemented ITO model for gas and electricity markets. There is one TSO EirGrid and one DSO, ESB Networks which is the owner of transmission and distribution networks. Full market opening took place in advance of the adoption of Third energy package in 1 July 2007 [14]. The Single Electricity Market is wholesale market for electricity market for the island of Ireland, regulated jointly by the Commission for energy regulators and its counterpart in Belfast, the Northern Ireland Authority for Utility Regulation, and together referred to as the Regulatory Authorities[14].

In Romania implementation of 2009/73/EC Directive requirement opt for one of the three unbundling models for transmission system meetings were held with TSO and it's owner MECMA to identify the applicable model to SNTGN Transgaz SA. The option for independent system operator is concessionaire of the network and not its holder. The same situation is in the electricity model where the option for independent system operator as TSO is the concessionaire of the electricity grid and not its holder. The legal unbundling of the electricity generation, supply, transmission was made according to GD no.627/2000. The result was establishment of CN Transelectrica SA- Romania's sole TSO, and SC Electrica SA as DSO.

Denmark has chosen to implement full ownership unbundling in Danish Natural Gas supply Act. According to the situation in gas market the only option was to implement full ownership unbundling. In electricity market there are few options, because TSO can be unbundled in several ways. There is a possibility to implement full ownership unbundling model, ISO model, to implement the art. 9 of 9 paragraph[15]. None of TSO's can choose to set up an ISO model. In Danish energy market there is one TSO for gas and 11 TSO's for electricity market.

France has chosen the most liberal model the ITO model for electricity and gas markets. As regards supply activities in gas, CRE has approved in its deliberation of February 11th, 2010, the principles for account unbundling applied by GDF SUEZ for its supply activity to eligible and ineligible customers but some adjustments are still necessary [16].

Hungary in electricity market has implemented ISO model according to the second energy directive [17]. Later it has chosen the ITO model in electricity market which is operated as a single subsidiary within vertically integrated utility. In gas market the vertically integrated utilities were physically separated from other business activities [17]. The vertically integrated company of the E.ON Ruhrgas International GmbH subsidiary registered in Hungary (E.ON Hungária Zrt.) is the former public utility wholesale trader E.ON Földgáz Trade Zrt., which is legally completely unbundled from the gas storage licensee E.ON Földgáz Storage Zrt [17].

Italy electricity market has to be fully unbundled according to directive. Transmission System Operator may not, either directly or indirectly, engage in the generation or supply of electricity, or operate – even on a temporary basis – generation infrastructure or plants [18]. The same ownership unbundling rules apply to gas market [18].

Luxemburg has not implemented third energy directive package. So far according to the second directive the country has chosen to implement legal and accounts separation for vertically integrated utilities [19].

Poland has chosen legal and organisational unbundling in gas market to TSO according to second directive. The process to full unbundling is rather slow as the operators often remain within vertically integrated utilities and well-developed group structures [20]. In Poland majority of distribution system operators work with corporate groups which are part of vertically integrated utilities.

Slovakia has not chosen the gas market TSO unbundling model according to the 3rd Directive package [21]. Country has decided to implement ownership unbundling to electricity market in 2001 [21]. Legal unbundling for distribution system operator was introduced in 2007.

Spain has opted for ownership unbundling model in energy markets[22]. Spanish Act 17/2007 brings Red Electrica de Espana as sole TSO for electricity market. Act 5471997 also brings new

market participants the traders [22]. Their role is to acquire energy from producers to sell it to the market. The unbundling regime has led Spain energy market to the competitive energy market for gas and electricity with choice for consumers to choose energy supplier.

Cyprus has an isolated and small energy market that makes difficult to create internal energy market. The country has secured a possibility to derogate from article 9 on unbundling from transmission systems and transmission system operator [23].

Estonia has chosen to unbundle electricity market TSO according to 3rd Directive package. In April 2010 Nord Pool Spot extended to Estonia through creation of Estlink price area with the day ahead trading power exchange. In Estonia the TSO (Elering AS) is separated by ownership from all other electricity production and sale undertakings from 27 January 2010. 100% of its shares belong to the Estonian state[24]. As the Estonian natural gas market is a small one and similarly to Finland, Latvia and Lithuania pipeline interconnections with the central Europe do not exist, the Directive 2009/73/EC, that treats of common rules for the internal market, sets forth an exemption for Estonia in Article 49, which do not apply to Estonia the ownership unbundling obligation of the transmission system from the producer and/or seller until any of the Baltic countries and Finland is directly connected to the interconnected system of any Member State other than Estonia, Latvia, Lithuania and Finland [24].

In Germany the major energy companies E.ON, (electricity and gas) Vattenfall, (electricity) RWE (gas), EnBW were opposing TEP unbundling requirements. However later on E.ON has agreed to sell its assets to independent TSO. Soon afterwards Vattenfall decided to sell its transmission grid. However RWE and EnBW have decided not to sell their transmission grid.

Netherlands in electricity market has adopted unbundling act which makes obligation for vertically integrated companies to unbundle their activities. At the end of 2010, all (but two) DSOs were separated (fully ownership unbundled) from the integrated company. Due to a court decision part of the law on unbundling lost force. As a result, the two integrated companies that are not yet unbundled announced to postpone their activities regarding unbundling. The Ministry of Economic Affairs, Agriculture and Innovation lodged an appeal in cassation by the Supreme Court of the Netherlands, the decision is scheduled in October 2011 [25].

Sweden has failed to fulfil obligations under first and second directives. In 2008 Commission brought action against it[26]. After this case Sweden decided to adopt the bill implementing the obligations of Second electricity directive. Also several amendments were proposed under which vertically integrated utility operating in electricity market must be separated from undertakings responsible for operation and generation or supply of electricity market. According to the second gas directive Sweden has chosen to implement the exemption rule which allows to vertically integrated utilities serving less than 100 000 customers to remain integrated. For Sweden the Commission is most likely to be in favour of OU model because ISO model is not effective to this country.

Belgium electricity market prescribes legal unbundling for TSO. The OU model can be implemented when certain conditions regarding the shareholder structure of TSO are adapted in the Electricity Act [27]. Gas Act implements to partially transpose Second gas directive. The proposal aimed at OU and shareholding unbundling that prohibited market shareholders to have transmission assets.

Latvia has chosen OU model in gas market as it is monopolistic utility AS Latvijas Gaze which E.ON owns 47.23% assets, AAS Gazprom owns 34%, SIA Itera-Latvija 16% and several others own 2.76%. On December 2009 Latvian parliament postponed the implementation of third package in gas market until 4 April 2014. The decision was motivated because of only one external supplier AAS Gazprom. Such derogation is possible under article 49 Directive 2009/7/EC. In electricity market country has chosen ISO model.

In Portugal electricity and gas market many 3rd Directive measures are transposed to national law. Country has chosen to unbundle electricity and gas markets TSO's. The operators of the RNTGN, the LNG terminal and the underground natural gas storage infrastructure that are part of

the REN group, have been independent from market agents in operational, legal and ownership terms since 2006 [28].

Slovenia has unbundled electricity sector in early 1990's transfer, production and distribution were separated. Also Slovenia has decided to take similar measures to electricity DSO. Republic of Slovenia is holding 100% stake in ELES d.o.o. (TSO for electricity) and 100% shares of HSE d.o.o. (operator of a number of power plants in Slovenia). According to TEP members of supervisory body have to represent different ministries within the Slovenian government. In gas market Slovenia is highly dependent on external gas importer Gazprom and the dominance of vertically integrated state owned company. Slovensky Plynarensky Priemysel (SPP) is currently responsible for the supply of all gas in Slovakia, which in turn imports all its gas on the basis of contracts with Russia's Gazprom. SPP is also the owner of the transmission and distribution networks. Following the legal unbundling of the networks, access is available to other potential suppliers but as yet there has been no penetration by other new entrants and therefore no customer switching. Approximately two-thirds of the gas consumed in Slovakia is by large industrial users and it is expected that this market will develop rapidly in the future [29]. One TSO is legally unbundled from its parent company Geoplin d.o.o. In DSO gas market all the participants provide service to less than 100 000 customers only accounts unbundling is implemented [29].

Bulgaria adopted ITO model in energy market. Main activities in generation, supply and transmission are controlled by Bulgarian Energy Holding [30]. The state owns 100% shares of his holding. Bulgaria has one of the largest energy companies in the region the national champion. Bulgarian Energy Holding will be reorganized according to ITO model. Legal and organisational unbundling will be implemented to Bulgartransgas to separate transmission from gas storage system.

United Kingdom electricity and gas markets were fully liberalised in 1990's when customers had an opportunity to choose their energy supplier. First and Second Gas and Electricity directives are considered as fully implemented. Public electricity supply companies National Grid and the Scottish retained vertically integrated generation, transmission, distribution, supply utilities. Although ownership remains with vertically integrated utility the operations are managed by ISO National Grid [31]. The Utilities Act required legal separation of supply and distribution functions in electricity market. Requirements to separate licences put in place all common mechanisms to enable third party access to storage facilities on published tariffs.

Austria legislation provides legal unbundling electricity and gas market TSO unbundling. OU has not been introduced to this energy market. Austria is one of the eight members that opted for third way (ITO) model. In Austria some TSO can be identified as ISO although they do not own transmission networks they work through operations of management agreements. Even implementation of ISO model require further changes in Austria legislation.

Malta has not yet published its timetable for transposition of TEP to national legislation. However it is expected that Government will transpose TEP by 2013. Malta has applied for derogation from Chapter IV and Articles 20(1) and 21(1) of Directive 2003/54/EC. Due to the small size of the market and the lack of any interconnection with other countries, there is currently no competition in the Maltese electricity market. Malta is not supplied with natural gas and no internal gas market exists. The possibility of undersea electrical and gas interconnections with Sicily is being investigated, but no action is planned for the time-being.

After short overview of TEP implementation in Member States we can conclude that States choose various liberalisation models. There is no unanimous opinion whether OU model is the best to create single market. It depends on each state situation in energy market and the market players, whether it is vertically integrated utility or TSO performs independently and depends on functions that are generated by such undertaking.

4. FULL OWNERSHIP UNBUNDLING AND FOREIGN INVESTMENT PROTECTION

When implementing the third energy package requirements the States obligation under bilateral investment treaties (hereinafter – BIT) must be taken into consideration also its obligations under Energy Charter Treaty (hereinafter – ECT). The main purpose of such treaties is protection of foreign investment. Bilateral investment treaties are concluded between developed and developing countries where main principles of foreign investment are discussed. These treaties implement *ex post* foreign investment protection standards. Expropriation is not illegal *per se* under international law. Legal expropriation of foreign property must be under such conditions: referred to public interest, absence of discrimination, due process of law, compensation that is promptly adequate and effective [32]. Nowadays direct expropriation and nationalization of foreign property became rare. The most difficult questions for a tribunal are to certify whether the expropriation was in the first place. Under international law not all state measures interfering with property are expropriation. State measures, *prima facie* a lawful exercise of powers of governments, may affect foreign interests considerably without amounting to expropriation [33]. Thus, foreign assets and their use may be subjected to taxation, trade restrictions involving licenses and quotas, or measures of devaluation. While special facts may alter cases, in principle such measures are not unlawful and do not constitute expropriation [33].

Analysing the concept of indirect expropriation we can state that formally the status of investor usually remains however he loses the right to control its property. *Tippets* case illustrates this situation when the Iranian government managers were appointed to private owned company [34]. The degree of interference by the manager with the owner's property rights constituted a taking of property. The tribunal stressed that government interest to expropriate investment is less important than the action itself [34]. Similar conclusion was reached in *Tecmed* case where tribunal found that intention of the state is less important than its action against aliens [35]. For instance the certain measures of state destroy foreign investor's commercial value.

In *Revere Copper* case the claimant through its subsidiary entered into agreement with the Government of Jamaica containing the stabilisation clause with respect to taxes and financial burdens [36]. The Government in violation of such agreement drastically increased the taxes and royalties. In this situation an increase of taxes to a certain extent when an investment becomes economically unsustainable constitutes expropriation.

Under most BIT provisions including ECT the existence of public purpose is the requirement for the legality of an expropriation. There are two criteria to identify the regulatory expropriation and a simple regulation: motive or purpose orientated test which helps to identify the existence of an intention to expropriate other is quantitative test that takes closer look to a severity of the measure's effect on investor's property. *Metalclad v. Mexico* case is worth mentioning as the tribunal found indirect expropriation when the refusal of a construction permit by the municipality had destroyed the investor's ability to pursue previously approved project [37].

After the deeper analysis of the arbitral tribunal practice of indirect expropriation we can conclude that not every legitimate public purpose underlying a regulatory measure exclude the existence of an expropriation. To identify the expropriation tribunal has to found the State's intent to act in commercial role as a party to the contract or in its sovereign capacity because not every breach of contract by a State that results in economic loss to investor is identified as expropriation. After a closer investigation of arbitral tribunal practice there is a reasonable doubt whether countries are absolutely free to choose the third energy directive package liberalisation model. According to the BIT and ECT there is an obligation not to expropriate foreign investor's property. When a country has chosen to fully unbundle vertically integrated utility there is a doubt whether such model is sufficient for the creation of internal energy market. Despite the fact that full ownership unbundling is the best model to create internal competitive energy market and European Commission is in favour of such model States are not absolutely free to choose such strict model

because of their international obligations under BIT. We have to agree with such position because the states which have chosen more liberal implementation model did not reach these goals.

CONCLUSIONS

1. The intent to create internal energy market was obvious as the three energy directive packages were adopted. However none of them provided clear directions for creation of single competitive energy market.
2. Third energy directive package provides three market liberalisation models: the full ownership unbundling, independent system operator, independent transmission operator. After the deeper analysis of European countries decision to implement one of these models we can conclude that there is no unanimous choice and still the countries make their decision depending on political economical matters.
3. Lithuania has chosen the full ownership unbundling model in electricity and gas market. There are no legal obstacles to unbundle electricity market because it is state owned company the only question is who will control transmission networks and who will be responsible for generation and supply activities. The bigger challenge was the implementation of ownership unbundling model in gas market, however the vertically integrated utility AB „Lietuvos dujos“ prepared the unbundling plan to be implemented until 2014 which was approved by the National Control Commission of Prices and Energy.
4. The deeper analysis of arbitral tribunal practice shows that indirect expropriation might be ascertained even if a Member State underlies a regulatory measure under legitimate public purpose. There is still a reasonable doubt whether full ownership unbundling is appropriate and sufficient liberalisation model and *ultima ratio* measure for Member States to create the internal competitive energy market in the European Union

REFERENCES

1. Directive 96/92/EC concerning common rules for internal market in electricity. [1996] OJ.L 027/24.
2. Directive 98/30/EC concerning common rules for the internal market of natural gas. [1998] OJ L. JONES, CHRISTOFER. W. *EU Energy Law. Vol. I. The internal Energy market*. Leuven: Claeys & Casteels, 2006.
3. Directive 2009/73/EC concerning common rules for the internal market in natural gas and repealing Directive 2003/55/EC [2009] OJ L 211/94.
4. GRIFFIN, M.J.; PULLER, L.S. *Electricity Deregulation Choices and Challenges*. Chicago: The University of Chicago Press, 2005.
5. KOTLOVSKI, A. Third-party Access Rights in the Energy Sector: A Competition Law perspective. *Utilities Law Review*. 2007, 16(3), p. 101–113.
6. Amendment of the guidelines of good practice for third party access (TPA) for storage system operators (SSO). 2011. Ref: C11-GST-15-03.
7. Resolution No. 141 of the Government of the Republic of Lithuania of 13 of February 2013. (State Gazette 2013, Nr. 18-898).
8. The National Control Commission for Prices and Energy 2012.06.15 Decision No. O3-145.
9. The Czech Republic's National Report on the Electricity and Gas Industries for 2010. <http://www.energy-regulators.eu/portal/page/portal/EER_HOME/EER_PUBLICATIONS/NATIONAL_REPORT_S/National%20Reporting%202010/NR_En/E10_NR_CzechRep-EN.pdf> [referred on 25 of May 2012]
10. The Annual Report 2011 – Energy Market Authority, Finland.
11. Natural gas market act (508/2000). Finland.



12. Greece Law No. 3428 Liberalization of Natural Gas Market art. 32.
13. Commission for energy regulation (CER) – Ireland’s national report 2011 to the European Commission.
14. Denmark national report 2011. Danish national regulatory authority.
15. CRE national report to DG ENER.
16. Hungarian Energy Office Annual report to the European Commission 2011.
17. The Italian Regulatory Authority for Electricity and Gas (AEEG) 201.
18. Institut Luxembourgeois de Régulation. 2011.
19. National Report to the Commission the president of the energy regulatory Office in Poland. 2011.
20. Regulatory Office for Network Industries. National Report 2011.
21. Spanish energy regulator’s annual report to the European Commission. 2011.
22. Cyprus National report to the European Commission. 2010.
23. Estonia national report to the European Commission. 2010.
24. National reports Energiekamer. 2010 Netherlands.
25. European Union Court of Justice Case C-274/08.
26. Belgium Annual report 2011 to the European Commission synopsis.
27. Portugal Annual report to the European Commission. 2011.
28. Slovenia internal market factsheet.
<<http://www.ebrd.com/downloads/legal/irc/countries/slovenia.pdf>> [referred on 16 th of May 2012].
29. State Energy and Water Regulatory Commission (SEWRC) Bulgaria. The annual report to the European Commission. 2011.
30. Great Britain and Northern Ireland national reports to the European Commission. 2011.
31. DOLZER, R. Indirect Expropriations: New Developments? *Environmental Law Journal*. 2002, 11, p. 64–91
32. BROWNLIE, I. *Public International Law*. Oxford University Press, 6th Edition, 2003.
33. *Tippets, Abbett, McCarthy, Stratton v. TAMS-AFFA Consulting Engineers of Iran*, Iran-US Claims Tribunal, 22 June 1984, 6 Iran-US CTR 219.
34. *Technicas Medioambientales Tecmed S.A. v The United Mexican States*, Award, 29 May 2003, 43 ILM 133 (2004).
35. *Matter of Revere Copper and Brass Inc. v. Overseas Private Investment Corporation*, Award, 24 August 1978, 56 ILR 268.
36. *Metalclad Corp. V. United Mexican States*, Award, 30 August 2000, 5 ICSID Reports 226.
37. MOEN, K.B. Gas Directive and Third Party Transport Rights – What Pipeline Volumes are Available. *Energy & Natural Resources Law Journal*. 2003, 13: 25–36 .



SCENARIOS OF DEVELOPMENT OF THE BELARUSIAN ELECTRICITY GENERATION SYSTEM IN CONTEXT OF FUEL BALANCE DIVERSIFICATION AND GREENHOUSE GASES EMISSION REDUCTION

A.A. Mikhalevich, S.N. Nikitsin, V.A. Tkachou

*Institute of Power Engineering of National Academy of Sciences of Belarus
Akademicheskaya str. 15/2, 220072 – Belarus*

ABSTRACT

Heat and electricity production is based substantially on consumption of fossil fuels. However, its combustion leads to significant GHG emissions. At present, the international community is concerned about the problem of reducing GHG emissions. Power generation industry, as one of the major GHG emitters, could make a significant contribution to solving the problem. Therefore, it is necessary to take into account measures for GHG emission reduction in case of modelling of the power generation system' expansion.

For Belarus, which is largely dependent on one fuel imported from one country, an important issue is also the diversification of energy resources and their suppliers. For example, in the structure of fuel consumption for electricity and heat generation the share of natural gas exceeds 90%, and all of it is imported from Russia.

This paper considers different long-term scenarios of the Belarusian power generation sector development in a context of the fuel mix diversification for electricity and heat generation, and minimizing GHG emissions. MESSAGE modelling tool was used for scenarios simulation.

The following scenarios were considered for taking into account the diversification of fuel mix: 1) decreasing the share of natural gas for heat and electricity generation to 50% by 2025; 2) reducing the share of one energy supplier to 50% by 2035, and 3) combination of the foregoing limitations. These scenarios have been modelled with implementation of a carbon tax on greenhouse gas emissions.

Keywords: energy security, carbon tax, scenario modelling, power system, greenhouse gases

1. INTRODUCTION

Solving of energy security problems represents currently one of the main goals in the sustainable development strategy of the different states. This applies largely to countries that do not have enough domestic energy resources, and the Republic of Belarus is one of such countries. In the energy balance of the Republic of Belarus predominates one type of fuel (natural gas) and one energy supplier (Russia). For example, the share of natural gas for heat and electricity generation exceeds 90%. Therefore, the problem of energy balance diversification is particularly important if the main goal of the long-term energy planning is improving of the energy security.

In addition, the long-term energy planning should take into account environmental factors. The main greenhouse gas in the Republic of Belarus is the carbon dioxide (CO₂). Share of CO₂ in 2009 amounted to 64.7% of the total GHG emissions. Moreover, a significant contribution to GHG emissions in Belarus (34.6%, or 30.3 million tonnes of CO₂) makes electricity and heat generation [1].

Different scenarios of development of the Belarusian power generation system up to 2050 depending on the diversification by energy resources was considered in the paper. Emission factors per unit of heat and electricity production for all scenarios were calculated. These emission factors were considered by authors as environmental indicators. Diversification of energy resources for heat and electricity generation by type, as well as by energy suppliers was selected as indicators of energy resources diversification. The "carbon tax" or a tax on the burning of carbon-containing fuels, which reflects the increase in the cost of fossil fuels, was used to account for the influence of

environmental factors. For the biomass such tax was not applied because of the concept of "zero balance" for the biomass burning.

2. METHODOLOGY

For the calculation was used MESSAGE model (Model for Energy Supply Strategy Alternatives and their General Environmental Impacts) [2], developed by the International Institute for Applied Systems Analysis (IIASA) for the energy systems optimization. Basic principle of the MESSAGE model is to optimize the objective function with the given constraints that define the area containing all possible solutions. The objective function helps to choose the best solution according to the criteria specified.

General form of the objective function can be expressed in form of equation:

$$B_j = \sum_{t=1}^T [\bar{I}_{j,t} - \bar{S}_{j,t} + \bar{F}_{j,t} + \bar{L}_{j,t} + \bar{M}_{j,t} + \bar{CT}_{j,t}] \quad (1)$$

where B_j – is the objective function corresponding to the plan of energy system development, t – time in years (1, 2, ..., T), T – the duration of the study period (total number of years).

The bar over the symbol means the discounted value with the discount rate i .

Usually, the objective function consists of the capital (or investment) cost (I), the salvage value (or depreciated cost at the end of the simulation period) (S), the fuel cost (F), the cost of fuel stocks (L), operating and maintenance costs (M), and may include also the "carbon" tax (CT). The optimal plan is defined as a minimum of B_j for all j .

The energy resources price forecast as well as the heat and electricity demand forecast have to be included as input data of calculations.

Energy resources prices forecast used in this study was based on analysis of the forecasts made by International Energy Agency [3], British Petroleum [4], World Bank [5] and the international agreements signed by the Republic of Belarus (in particular those relating to the Eurasian Economic Area and Customs Union), as well as author's expert assumptions. This forecast is shown in Fig. 1.

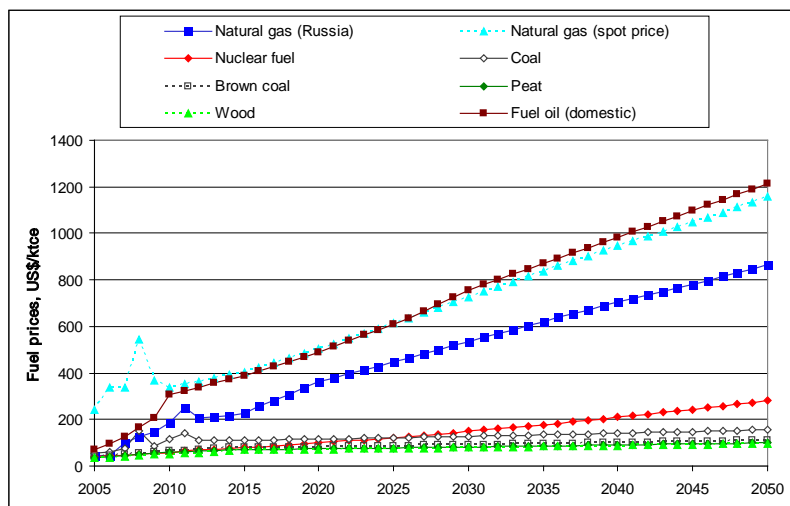


Fig. 1. Energy resources price forecast

As was mentioned above, Belarus is country with poor energy resources. Belarus has small oil reserves with annual production app. 1.6–1.7 million tones and a lot of peat. Peat reserves in Belarus are more than 200 million tce but peat production in Belarus is limited for environmental reasons with maximum potential of 3 million tce. It should be noted that commercial reserves of

brown coal in Belarus are 86 million tons with potential annual production up to 2 million tones. In this study it was supposed that the price for domestic brown coal will be twice lower than for imported coal. Possibility of hydro power plants construction is limited to 250 MW. At sites suitable for the construction of wind turbines, can be build up to 20000 MW.

The only natural gas supplier to Belarus is Russia. Belarus consumes app. 21–22 billion cubic meters of natural gas annually and app. 17–18 billion is consumed for electricity and heat generation. LNG can be considered as an alternative to natural gas supply from Russia. However, particularly after the sale of the gas-main pipelines to Gazprom, projects for construction and/or sharing of LNG terminals with neighboring countries look dubious, since it is unlikely that Gazprom will agree to use its gas networks by other suppliers to deliver the natural gas to Belarus.

Poland and Russia were considered as potential coal suppliers for Belarus in this study. The undertaken analysis demonstrated that price of Russian coal could be a little lower than Polish one. The total annual consumption of imported coal was limited to 10 million tons because of limitations of the capacity of the Belarusian railway.

As possible options for the development of nuclear energy in Belarus three possible technologies were considered: Russian AES-2006 project with capacity 1170 MW, the French reactor (EPR) with capacity of 1600 MW and Korean reactor (OPR-1000) with capacity of 950 MW. The first two types of reactors are new developments with a lifetime of 60 years, have increased levels of protection, however higher capital and operating costs. The Korean reactor belongs to the older generation with a lifetime of 40 years, has lower capital and operating costs. In the present study it was assumed that the reactor supplier will also supply the fuel for it. Despite the prevailing point of view that it is possible to provide fuel for nuclear reactors by different suppliers, the unfortunate experience of supply of nuclear fuel by Westinghouse Company for Ukrainian nuclear power shows otherwise.

It has been assumed by forecasting of the electricity and heat demands that measures of increasing energy efficiency, such as the ban on incandescent light bulbs, increasing energy efficiency in the construction sector etc would be implemented. These assumptions allows to estimate the electricity consumption in 2020 equal 39 billion kWh. According to these data the growth rate in electricity consumption in 2010–2020 will be in average of 1.5% per year. At the period 2021–2030 electricity consumption growth rate will slightly increase and absolute electricity consumption exceed 47.6 billion kWh. At the period 2031–2040 absolute value of the electricity consumption will reach 55.7 billion kWh. In the future the growth rate in electricity consumption will be reduced to an average of 1.3% per year, and electricity consumption in 2050 will amount to 64.2 billion kWh.

Heat consumption forecast for 2020 gives a value of 77.7 million Gcal, that is slightly below the forecast, given in the concept of energy security of Belarus [5] (81.3 million Gcal low scenario). In the future, as the share of energy efficient apartment building (with a specific heat consumption up to 60 kWh/m²) will increase, total heat demand will slow down, reaching in 2030 79.7 million Gcal, by 2040 – 80.9 million Gcal, and in 2050 – 81.4 million Gcal.

Table 1 shows the parameters of the generating capacities for electricity and heat generation that are considered in this study as possible candidates for replacement of retired capacities and for new construction in Belarus. Technical and economic parameters for coal power plant, coal CHP, NPP have been taken from [6]. Data for other generation units are based on analysis of the existing experience of their implementation in Belarus.

Table 1. Technical parameters of power installations for heat and electricity generation

Technology	Capacity, MW	Investment costs, US \$/kW	Electrical efficiency	Heat efficiency	Life time, years
NPP (Russia)	1170	3500	0.34	-	60
NPP (South Korea)	954	2500	0.30	-	40
NPP (France)	1630	4000	0.34	-	60
Combined cycle GT	400	1000	0.55	-	30
Coal PP	460	2500	0.42	-	30
Gas turbine	110	750	0.35	-	25
CHP reconstruction	80	750	0.27	0.58	30
Combined cycle CHP	65	1500	0.45	0.4	25
Wood and peat CHP	2	3500	0.2	0.5	25
Industrial CHP	10	1200	0.4	0.5	20
Coal CHP	100	3000	0.24	0.42	30
Brown coal CHP	100	3000	0.23	0.41	30
Utility boilers	400	125	-	0.91	40
Industrial boilers	1000	125	-	0.90	40
Small boilers	300	155	-	0.87	35
Wood and peat boilers	600	100	-	0.6	35
Hydro*	5	3700	0.4	-	50
Wind*	5	1800	0.27	-	20

* Capacity factor is shown in case of hydro and wind units but not efficiency

3. RESULTS

3.1. Scenarios with constraints on diversification of energy resources

The natural gas is used predominantly in Belarus for generation of heat and electricity. For example, electricity generation by burning of natural gas increased from 74% to 92% in 10 last years. This is one of the factors endangering the energy security of the country, especially in light of the fact that Belarus has no own natural gas reserves. In order to analyze the influence of diversification by fuel type on the structure of generating capacity, a scenario "constraint by fuel type" has been studied. This scenario imposed limitation on use of natural gas for the electricity and heat generation. It was assumed that in 2020 the share of natural gas used for the electricity and heat generation will not exceed 70% and in 2030 – 50%.

More than 80% of energy resources used in Belarus are imported from Russia. This fact also poses a threat to energy security. To see the influence on the energy system structure of possible limitations on the fuel import from a single supplier (in this case – from a single country) scenario with the following restrictions on the import of energy resources was simulated: by 2020 the share of imported Russian energy resources should not exceed 70% and by 2035 – 50%. The alternative ways for imported energy resources also considered (LNG, coal from Poland).

Due to limited size of article further attention will be focused on analysis of the fuel mix for electricity and heat production.

Results of calculations of energy resources consumption for selected scenarios are shown in Fig. 2. The share of natural gas for the heat and electricity generation in the baseline scenario (Fig. 2a) is reduced from over 80% to 35% by the end of the forecasting period.

The share of coal in total energy resources consumption increased up to 40% in 2032 and then slightly reduced to the end of the period (up to ~35%) because the coal price growth rate is lower than for natural gas. Total installed capacity of coal-fired condensing power plants in this case reaches 3.200 MW, which is about 30% of the total installed capacity in 2050. By 2025 the total

installed capacity of coal-fired CHP will reach 1,000 MW and 300 MW brown coal-fired CHP will be put in operation. These generation units will partially substitute the CHP on natural gas. Since 2016 an intensive wind turbine construction begins and by 2035 will reach their maximum potential installed capacity of 2.000 MW.

In accordance with performed study the optimal using of nuclear power in the generation mix based on using of two units of Russian AES-2006 technology with capacity of 1.170 MW each will realize only if the first unit begins its operation in 2037 and the second one – in 2044.

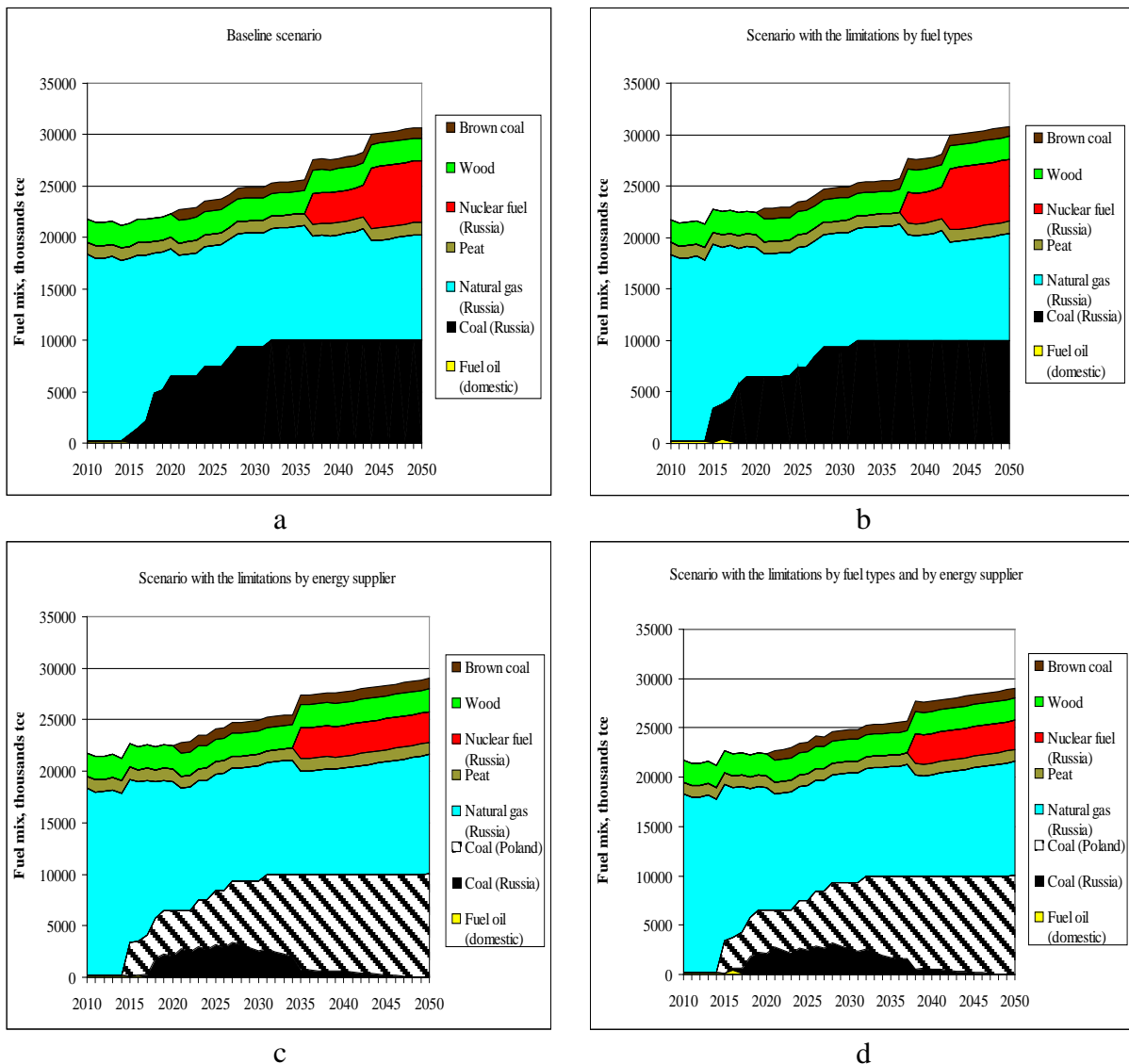


Fig. 2. Fuel mix for electricity and heat generation: a – baseline scenario; b – scenario with the limitations by energy resources types; c – scenario with the limitations by energy suppliers; d – scenario with limitations by fuel types and energy suppliers

In addition up to 1.300 MW of the industrial CHP and 800 MW of the CHP on domestic fuels (peat, biomass) will be constructed. The optimal solution also suggests construction up to 455 MW of CCGT on CHP and up to 290 MW of hydro. By the end of the considered period total installed capacity of the electricity generation system will increase up to 11.5 GW.

As shown on the Fig. 2b the fuel mix for electricity and heat generation is almost identical to the structure in the baseline scenario. The only difference is more intensive coal consumption in the first years after applying of the limitations by fuel and operating of the coal power plants begins

three years earlier – in 2015. In this case diversification by energy resources in long-term planning of the Belarusian energy system will be natural (the optimal) process without applying any additional limitations.

In case of limitations on fuel import from a single supplier there will be some changes in the structure of energy consumption (Fig. 2c). Firstly, the Russian coal is used only up to 2035 with a maximum consumption of 2.5 million tons of coal equivalent per year, and by the end of the considered period it completely displaced by Polish coal. Thus, the share of Polish coal in total energy consumption increases to the end of considered period up to 35%. Secondly, in this case the optimal solution is construction only one nuclear power unit of the Russian type AES-2006. This will influence the fuel mix for electricity and heat generation.

As it was mentioned above, the implementation of limitations on one fuel type consumption (natural gas) hardly makes a difference comparing to the baseline scenario. Therefore, the scenario "with limitations by fuel types and energy supplier" (Fig. 2d) is virtually identical to the scenario "with limitations by the supplier" (Fig. 2c). Thus, to show the influence of the limitations by the fuel type and energy suppliers on the structure of fuel consumption, only baseline scenario and scenario with two limitations will be considered further.

3.2. Scenarios with a carbon tax

Implementation from 2016 "carbon tax" results in changes in the optimal structure of the generating capacity. The diversification of the fuel mix for the electricity and heat production results in significant increase of the coal share in fuel balance and accordingly to the growth of greenhouse gas emissions in the energy sector. It was tasked to analyse how to reduce GHG emission or at least not increase. In order to analyse what would happened with increase of fossil fuels cost due to carbon tax scenarios with a carbon tax of 25, 50 and 75 dollars per ton of CO₂-equivalent were modelled. The structure of fuel mix for these scenarios is shown in Fig. 3.

With the "carbon tax" of \$25 per tonne of CO₂-equivalent (Fig. 3b) coal technologies already are not competitive. Coal power plants in this case have to be put in operation later (since 2027). The share of coal consumption in 2028 will be then less than 20%. From this time, the coal consumption will increase, as in the baseline scenario. It should be noted here that the first nuclear unit (Russia) according to this scenario will be put in operation earlier – in 2018, and the second one – in 2041.

Increase the value of "carbon tax" to \$50 per tonne of CO₂-equivalent leads to greater replacement of the coal power plants by nuclear units. In the scenario "with tax 50" (Fig. 3c) coal power plants are competitive only since 2036, and to the end of the considered period the share of coal consumption is less than 30%. However, in this scenario the Russian nuclear technology will be presented by three units. They have to be putted in operation in 2018, 2027 and 2033, respectively.

With "carbon tax" of \$75 per tonne of CO₂-equivalent coal power plants have to be replaced fully by nuclear power plants (Fig. 3d). The share of coal consumption in this case is around 10%, and this coal consumed only by the coal CHP. Nuclear power plants have to be constructed in this case more intense, and by 2050 the total nuclear power plants installed capacity reaches 5.850 MW.

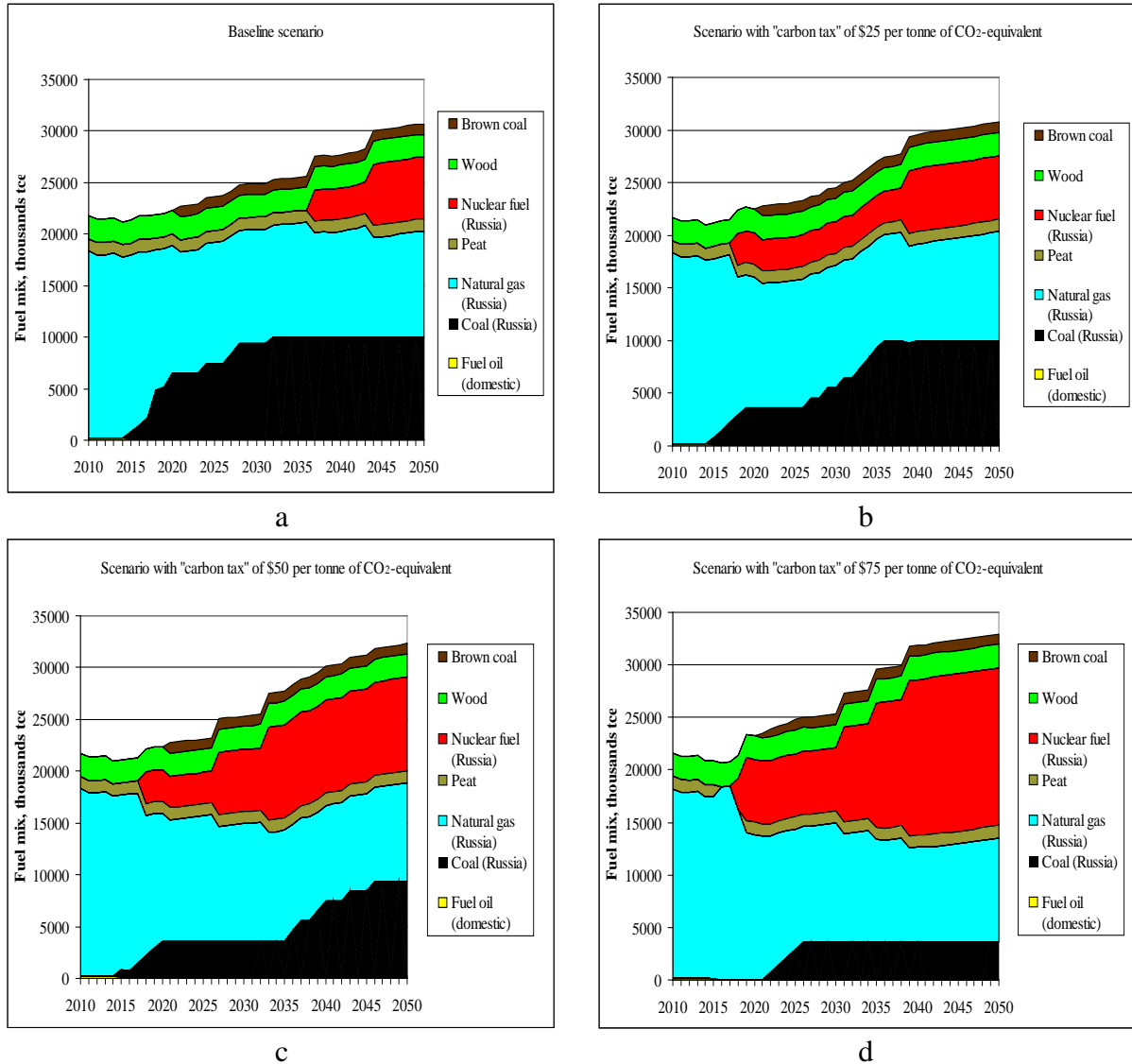


Fig. 3. Fuel mix for electricity and heat generation: a – baseline scenario without "carbon tax"; b – baseline scenario with "carbon tax" of \$25 per tonne of CO₂-equivalent; c – baseline scenario with "carbon tax" of \$50 per tonne of CO₂-equivalent; d – baseline scenario "carbon tax" of \$75 per tonne of CO₂-equivalent

With constrains by fuel types and by energy supplier it is evident the necessity of replacement of coal power plants by nuclear plants. In scenario with "carbon tax" of \$75 per tonne of CO₂-equivalent the share of coal in the fuel mix for electricity and heat generation does not exceed 15%. It should be noted that with requirements for diversification by suppliers the Russian nuclear power units will be replaced partially by Korean ones.

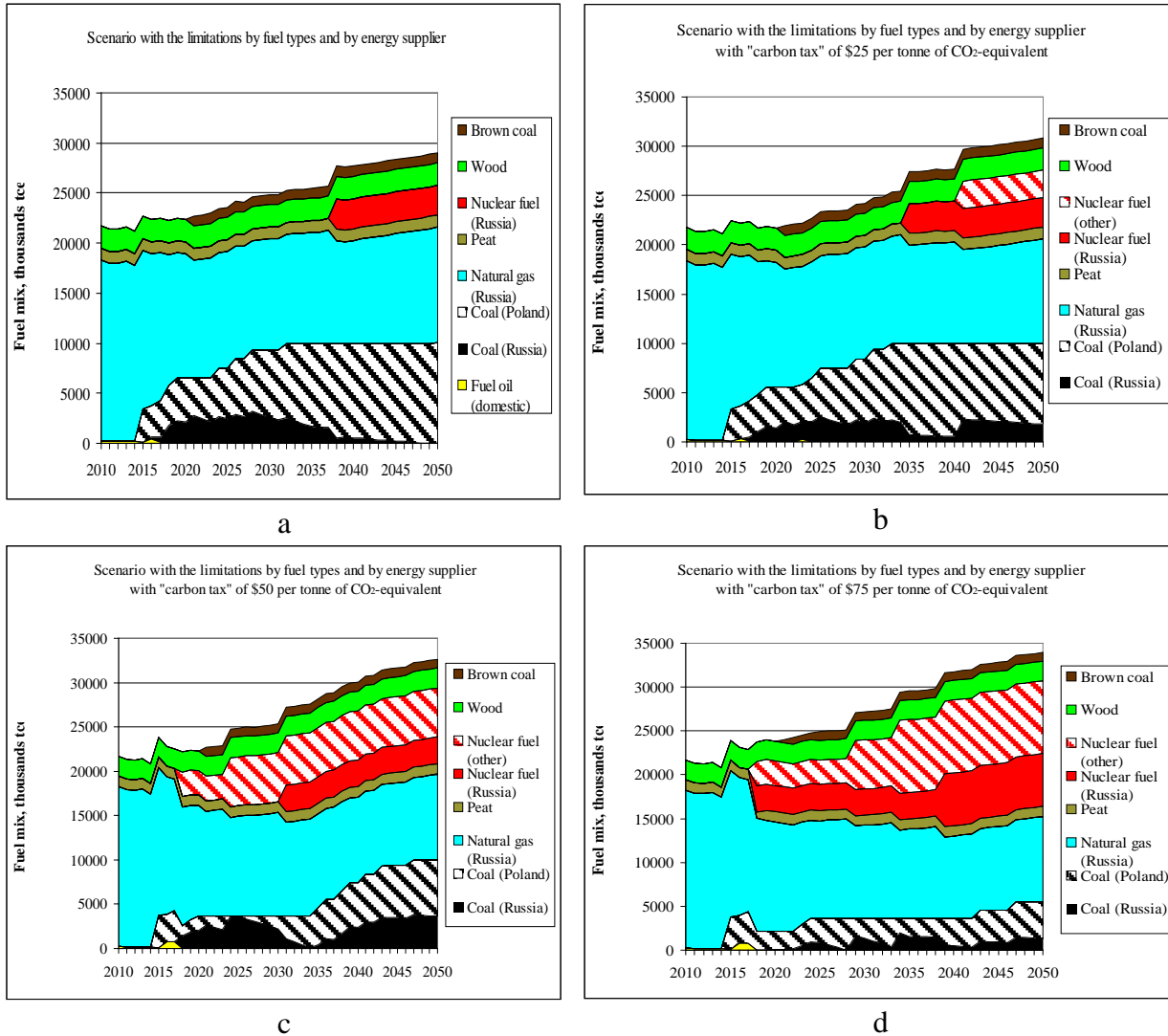


Fig. 4. Fuel mix for electricity and heat generation in the scenarios with the limitations by fuel types and by energy supplier: a – without "carbon tax»; b – with "carbon tax" of \$25 per tonne of CO₂-equivalent; c – with "carbon tax" of \$50 per tonne of CO₂-equivalent; d – with "carbon tax" \$75 per tonne of CO₂-equivalent

3.3. The emission factors

The ratio of GHG emissions per unit of heat and electricity produced was chosen as an environmental factor for the scenarios modelled. Considering the values of this factor for different countries [7, 8], it could be seen that the CO₂ emission factor takes into account the following:

- structure of fuel balance for heat and electricity generation,
- share of electricity and heat produced using renewable energy sources (RES),
- share of electricity and heat produced by CHP plants,
- fuel utilization rate for heat and electricity production.

As could be seen for countries that use for the electricity and heat generation more fuel with high carbon content the specific CO₂ emissions factor is higher. For example, in fuel balance for electricity and heat generation in Poland, coal share exceeds 90%, and the CO₂ emission factor is one of the highest in the world (1.087 tones of CO₂/MWh in 2008). From the other side, France has one of the lowest emission factors (0.078 tones of CO₂/MWh) due to the prevailing share of nuclear energy in the structure of generation capacities. Iceland, Norway and Sweden have large

share of renewable sources in power generation systems, thus the emission factors for these countries are also low (0.001, 0.006 and 0.041 tones of CO₂/MWh, respectively).

At present, the value of this factor in the Republic of Belarus is about 0.27 tones of CO₂/MWh. It is quite low because of using of natural gas for electricity and heat generation. The emission factor for natural gas is by 1.7 and 1.4 times lower then emission factor for coal and fuel oil respectively. In addition, because of the high share of combined heat and electricity generation with CHP the efficiency of fossil fuel use (the ratio of electricity and heat generated from fossil fuels to the fossil fuels consumed for this reason) in Belarus is quite high. However, in the case of ensuring the diversification by fuel types for electricity and heat generation the emissions factor can considerably varies, depending on the way of diversification. The results of emission factors calculations for the considered scenarios are shown in Fig. 5.

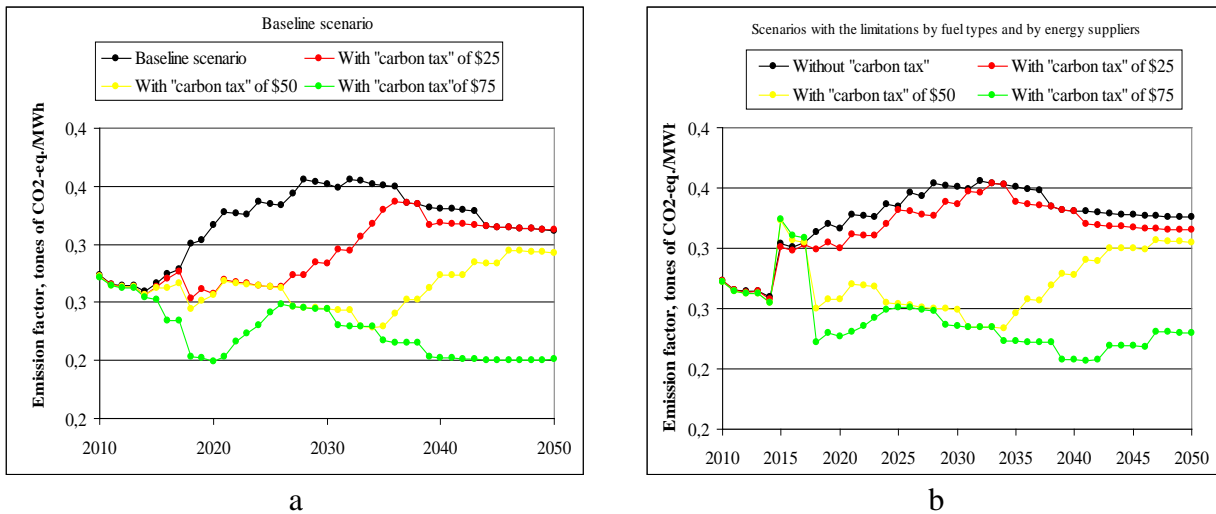


Fig. 5. Dynamics of changes of the CO₂ emission factor for the electricity and heat generation:
 a – baseline scenario; b – scenario with the limitations by fuel types and by energy suppliers

Minimums of the emission factor shown in the left and right panels of Fig. 5 coincide with periods of increasing role of renewable and nuclear capacities.

In the baseline scenario (Fig. 5a), the emission factor increases to a maximum of 0.36 tones of CO₂/MWh (in 2032), and then reduced to 0.31 tones of CO₂/MWh by the end of the period. With the "carbon tax" \$25 per tones of CO₂-eq. total GHG emissions associated with electricity and heat generation for the entire period will be reduced by about 9% compared to the baseline scenario. It is necessary to note that the emission factor in this scenario will decrease to 0.31 tones of CO₂/MWh by 2050. In scenario with "carbon tax" of \$50 per tones of CO₂-eq. it possible to achieve reduction of total CO₂ emissions by 18% and the emissions factor values to 2050 will be equal 0.29 tones of CO₂/MWh. The greatest GHG emission reduction can be expected for the scenario with the "carbon tax" of 75\$ per tones of CO₂-eq. In this case, the total amount of GHG emissions over the whole period will be more than 30% lower than in the scenario without "carbon tax". Moreover, despite the increasing in the electricity and heat generation in this scenario, the emission factor by 2050 is reduced to 0.20 tones of CO₂/MWh. Similar changes for the emission factor are observed in scenarios with limitations by fuel types and by energy suppliers (Fig. 5b). Since the implementation of limitations by fuel types and by suppliers of energy resources in these scenarios, there is a sharp increasing of emissions, but further the dynamics of the emission factor is similar to the baseline scenario. In this scenario "carbon tax" allows to achieve GHG emissions reduction by more than 25%.

4. SUMMARY

The study showed the importance of considering different scenarios of the energy system development in the long-term period to define conceptual ways with regard to the factors of energy and environmental security. Analysis of the results leads to following conclusions for the Belarusian energy system:

- diversification by energy suppliers influences more significantly on fuel mix for electricity and heat generation than energy resources diversification,
- the base scenario of energy sector development results in diversification of fuel mix without any additional limitations,
- diversification by energy suppliers results in replacement of the Russian nuclear and coal power plants by power plants based on using of Polish coal,
- limitations on the import of fuel from single supplier results in replacement of coal power plants by nuclear power plants,
- "carbon tax" promotes the replacement of coal power plants by nuclear power plants,
- implementation of "carbon tax" of \$75 per tones of CO₂-eq. could lead to reduction of GHG emissions in the electricity and heat generation system by 30%.

REFERENCES

1. National inventory report of the anthropogenic emissions by sources and removals by sinks of greenhouse gases not controlled by the Montreal Protocol for 1990–2009 // United Nation Framework Convention on Climate Change [Electronic resource] / Mode of access: http://unfccc.int/national_reports/annex_i_ghg_inventories/national_inventories_submissions/items/5270.php. – Date of access: 04.02.2013.
2. MESSAGE: Model for Energy Supply Strategy Alternatives and Their General Environmental Impacts / User Manual. – Vienna, 2004. – 244 p.
3. International Energy Agency (2011). “World Energy Outlook 2011”. IEA. – Paris – 2011. – 696 p.
4. BP (2012a) Energy Outlook 2030, London: BP plc. [Electronic re-source] / Mode of access: <http://www.bp.com>. Date of access: 20.01.2013.
5. World Bank, Development Prospects Group. Commodity Price Forecast Update. [Electronic re-source] / Mode of access: <http://www.worldbank.org/prospects/commodities>. Date of access: 20.01.2013.
6. Projected Costs of Generating Electricity / International Energy Agency, Nuclear Energy Agency, Organisation for Economic Co-operation and Development. Paris. – 2010. – 216 p.
7. Statistics & Balances // International Energy Agency. [Electronic resource] / Mode of access: <http://www.iea.org/stats/index.asp>. – Date of access: 09.02.2013.
8. CO₂ emission from fuel combustion / OECD/IEA. – 2011. – 130 p. International Energy Agency. [Electronic resource] / Mode of access: http://www.iea.org/publications/free_new_Desc.asp?PUBS_ID=2143. – Date of access: 09.01.2013.



GLOBAL ENERGY SECURITY LEVEL ASSESSMENT INDEX: INTRODUCTION AND APPLICATION

G. Česnakas, A. Čepinskytė

Vytautas Magnus University

K. Donelaičio g. 52 – 114, 44244 Kaunas – Lithuania

ABSTRACT

This paper introduces a global energy security level assessment index methodology, focusing on its elements, as well as the application of the suggested index in the assessment of national energy security level. The paper presents criticism of already existing global energy security level assessment methodologies and suggests an improved approach.

The newly suggested global energy security index combines energy data and political factors data. Eight indicators are introduced. Each indicator is composed of two variables. The first variable is a share of each country's production or reserves of a specific resource (coal, oil, natural gas, uranium) in the global production or reserves. The second one is the level of political stability of each country that has reserves of the respective resources or produces them. The data of the variables are normalised and the values of the variables are calculated by weighting them. This leads to a single number denoting global energy security level that can be compared on the annual basis.

The proposed energy security index takes into account all the states that have reserves and produce resources. Furthermore, it accentuates that the changes in political stability of the countries with the greatest reserves or the biggest production capacities are more important than such changes in the countries less significant in terms of resources. The analysed indexes omit the nuclear fuel element and use the data where small changes have great impact on the final index result. The proposed approach allows measuring global energy security more accurately and independently from the results previous years. Finally, this study suggests that in the assessment of energy security of a particular state the value of the global energy security index should depend on the energy intensity in that state.

Keywords: oil, natural gas, coal, uranium, energy security, index

1. INTRODUCTION

In recent years, development of the concept of energy security has acquired great intensity. Until 1973, energy security was perceived by consumer states essentially as the variety of supplies and sorts of conventional energy resources (oil, natural gas, etc). By contrast, today there are more than 45 definitions of energy security. They include economic, ecologic, political, social, even cultural and informational factors. Professor David Victor (Stanford University) asserts, “Energy security is like a Rorschach inkblot test – you can see whatever you want to see in it” [1]. Energy security is understood as the opportunity to ensure adequate and reliable supplies of energy resources and that energy is affordably priced and supplied by means that do not threaten national values and aims [2]. Thus the main subject of energy security is the state. Because of that, energy security becomes inevitably connected to political and geopolitical aspects.

Furthermore, it is important to underline that recently there have been increasing attempts to quantitatively measure national, regional and global energy security. There is a growing variety of indexes, as well as variables used to calculate them [3]. There are arguments suggesting that purely quantitative approach gives the ‘illusion of objectivity to weighting choices that are by their nature quite subjective’ [4]. Nevertheless, there are no better tools to measure energy security across a broad number of cases avoiding traditional descriptive approach.

The aim of this article is twofold. First, it is to assess some of the methods, which measure global energy security level. Second, it is to suggest a new method, while discussing its potential

inclusion into national energy security level assessment indexes of various energy consuming states and taking into account peculiarities of each states.

2. THE KEY ELEMENTS OF ENERGY SECURITY LEVEL ASSESSMENT INDEXES AND THE ROLE OF GLOBAL ENERGY SECURITY FACTOR

Energy security level indexes are constructions that consist of a few or more smaller thematic blocs (sub-indexes). The most common thematic blocs are the following: technical, political, economic and environmental (there are attempts to introduce a social block). These blocks are further divided based on the fuel types. In most cases three main types of fuel are distinguished: oil, natural gas and coal. Nuclear fuel is usually not included into the assessment of energy security level and neither are renewable resources (due to their special characteristics). Each block is assigned an individual value.

Essentially all definitions and energy security assessment indexes rely on four areas that are called the four A's: availability (geological), accessibility (geopolitical), affordability (economic) and acceptability (environmental and social) [5]. For the most part availability and accessibility determine affordability and acceptability.

Availability and accessibility are tightly intertwined with one another. Geological factors are inseparable from territoriality of a state. Due to this interaction between availability and accessibility it is essential to combine two types of variables in order to create indicators necessary to measure global energy security level. Variables that belong to the first type are related to geographic distribution of reserves and production. Variables of the second type cover external and domestic political factors of the states this way affecting security of reserves and supply of resources as well as their prices.

In order to measure global energy security level it is crucial to relate the data of reserves and production capacities on the one hand and political variables on the other. Before this is done, it is necessary to normalise these factors, so they can be compared. The correlation between them will allow calculating global energy security level that reflects security of global energy resources reserves and their production.

3. ANALYSIS OF EXISTING INDEXES

Arguably the most widely known methodology to measure global energy security was developed by the U.S. Chamber of Commerce Institute for 21st Century Energy in the 'Index of U.S. Energy Security Risk' (introduced in 2010) and 'International Energy Security Risk Index' (introduced in 2012). These indexes focus on four energy security sectors – geopolitical, economic, reliability and environmental. They consist of 37 indicators - metrics. In this article only six indicators are analysed as they are used to measure global energy security level focusing on the political aspects of the states. The following 'Global Fuel Metrics' are:

1. Security of World Oil Reserves;
2. Security of World Oil Production;
3. Security of World Natural Gas Reserves;
4. Security of World Natural Gas Production;
5. Security of World Coal Reserves;
6. Security of World Coal Production.

The methodology to calculate all of them is identical. Global reserves or production of a particular resource is weighted by each country's Freedom House freedom ranking and application of diversity (Herfindahl-Hirschman) index. The year 1980 is chosen as the basic year which is then set at 100 as a starting point to which metrics of all other years are compared [6]. The year 1980 is the point of comparison based on the argument that this year was the worst year for the U.S. energy security situation since the 1970s. However, this does not mean that this was the worst year for all

indicators. The aforementioned six indicators are differently weighted in the index. All of them combined have 10.95 per cent impact on the final index result.

The six suggested metrics have certain shortcomings. The number of metric compared to the types of energy resources is not sufficient. The index does not include nuclear fuel, which made up 5.7 per cent of world primary energy supply in 2010 [7]. Nuclear fuel is produced and enriched in highly secured mines and laboratories. The supply disruption is highly unlikely to happen, but it remains the element of energy security and its supply is dependent on political aspects of supplying countries.

In the ideal case, if there were statistics of global biofuel and biomass production and its trade, there would also be possibilities to create such metrics in the index. Nevertheless, this kind of fuel remains not of strategic importance. Production and trade of biofuel is dominated by private sector. These types of fuel could be included in environmental but not in geopolitical sub-index.

The most significant limitations of the metric of the index are related to political variables. Objective statistical data on reserves and production of energy resources is weighted together with the Freedom in the World Index (FWI) index provided by the Freedom House¹. It measures freedom according to two very broad categories: political rights and civil liberties. The average of the political rights and civil liberties ratings determines the overall status of country: free (1.0 to 2.5), partly free (3.0 to 5.0), or not free (5.5 to 7.0) [8].

The main issues are related to the FWI itself. Freedom of the country is not necessarily connected to the security of reserves and supply². The stability of energy resources suppliers is much more important to energy security than democracy or freedom. Countries with deep social, religious or ethnical divisions and tensions are less reliable suppliers. The index has to take into account a broader scope of issues and variables due to the complexity of political aspect.

FWI ranges from 1 to 7 and the smallest possible change is 0.5 point. This means that the minimal change in the spectre of 100 % is basically equal to 7.143 %, i.e. a very significant change. This way energy security index becomes highly impacted by small changes in the FWI. This part of the index faces amplification of small differences between paths/scenarios. FWI leaves out economic, social and military factors that are crucial for the security of reserves and supply.

Furthermore, both 'Index of U.S. Energy Security Risk' and 'International Energy Security Risk Index' lack indications as to when global energy security level enters critical, pre-critical and secure conditions. Critical condition means that security level is unacceptable and actions must be taken to eliminate the causes of such condition. Pre-critical condition is when security level is tolerable, however, it is likely that threats to security might emerge. Secure conditions mean that security level is acceptable, security is ensured [9]. The levels of each condition are decided pursuant to technical specifications or assessments of experts. The 'Index of U.S. Energy Security Risk' does not allow determining whether a negative change of 20 points from 100 points is a big change or a small one, whether the situation in 1980 was critical or safe and if it was critical, whether it has advanced to a safe one or has just become safer than before, yet still critical?

4. METHODOLOGICAL DESCRIPTION

Shortcomings of the indexes discussed above can be reduced by combining their strongest methodological elements and complementing them with new ones. Considering accessibility of the data and aiming to measure global energy security that integrates accessibility and affordability, we use the metrics that cover four types of fuel: oil, natural gas, coal and nuclear fuel. The data about reserves and production of these resources (and in the case of nuclear fuel – mining and enrichment of uranium) are publicly accessible. In this study we shall rely on the data provided by the U.S.

¹ FWI provides an annual evaluation of the progress and decline of freedom in 195 countries and 14 related and disputed territories.

² The United Arab Emirates for the last 20 years the has been a reliable supplier, even though the country remains not free.

Energy Information Administration (EIA) and World Nuclear Association (WNA). To measure political stability of the states Failed State Index (FSI) shall be used. FSI was introduced in 2005 by the U.S. think-tank “Fund for Peace” and the “Foreign Policy Journal” and has been published annually ever since.

Eight indicators are used in calculating the index of global energy security level:

- Security of global oil reserve.
- Security of global gas reserve.
- Security of global coal reserve.
- Security of global uranium production³ [10].
- Security of global oil supply.
- Security of global gas supply.
- Security of global coal supply.
- Security of global uranium enrichment.

Each indicator consists of two variables. The first variable is a share of each state’s specific type of fuel reserves and production (enrichment) in the global reserves and production (enrichment) of that type of fuel. This share is normalised and is given an expression in per cents. The second variable is each state’s stability index. Again, it is normalised and expressed in per cents where 100 per cent marks the maximal stability of a state and 0 per cent – the minimal stability of a state. Each state’s share in global reserves of each type of fuel is multiplied by the second variable – state’s political stability. The results are then added up and eight independent indicators are created.

Example: Calculating the indicator (1):

$$SGOR = \sum \frac{or_x}{wor} \times \left(1 - \frac{fsi_x}{120}\right) \quad (1)$$

SGOR – Security of Global Oil Reserve, or_x – oil reserve of country x, wor – world oil reserve, fsi_x – stability of state x.

The advantage of this method is that while calculating the value of each indicator, a due regard is paid to the correlation between state’s reserves, production (enrichment) capabilities on the one hand and that state’s political stability on the other.

States having greater reserve or greater production capacities (or have higher enrichment capabilities) have more impact on the value of the indicator than the states with lesser resources or production capabilities. Therefore, small changes in political stability of the first type of states have a more significant impact on the value of the indicator than big changes in the second type of states. This way global energy security level is measured more objectively. The higher value of the indicator means the higher level of energy security. Accordingly, the lower value of the indicator shows the lower level of security.

Another advantage of the method is that each indicator can be used both separately (in calculating national energy security level and taking into account the specifics of consumers in individual states) and combined together (in calculating global energy security level).

In assessing global energy security level it is important to take into consideration the value of each fuel type, i.e. the share in the global primary energy consumption, proportionately calculating the impact of each fuel type to the final global energy security level. According to International

³ In the case of nuclear fuel, it is mining and enrichment of uranium that are measured rather than reserves and production capabilities. This is because uranium can be used for the purposes of electricity production as well as in military industry. Therefore, in measuring global energy security it is not the uranium resources that matter, but uranium mining and enrichment capabilities that are used in energy industry. In energy industry reserves and production are less important than enrichment capabilities, because without enrichment nuclear fuel could not be used for energy generation.

Energy Agency (IEA) ‘Key World Energy Statistics 2012’, the share of different resources in the World primary energy supply in 2010 was as follows:

- Oil – 32.4 %;
- Coal/peat – 27.3 %;
- Natural gas – 21.4 %;
- Biofuels and waste – 10 %;
- Nuclear – 5.7%;
- Hydro – 2.3%;
- Other – 0.9%.

In calculating global energy security level using the proposed methodology, biofuels and waste, hydro and other types of primary energy supply resources were eliminated and the 100 per cent of share was proportionally divided among the four types of fuel that were included into the index. Based on the assumption that production (enrichment) is more important to global energy security than reserves and uranium mining, the weights were assigned as follows: 2/3 of the weight was given to production and enrichment and the remaining 1/3 of the weight - to reserves and uranium mining proportionally. Indicators, variables and weight coefficients are provided in Table 1.

Table 1. Indicators of global energy security index

Indicator	Acronym of indicator	Variables	Weight
Security of global oil reserve	SGOR	Crude oil proved reserves of each state × failed state level of each state	0.12
Security of global gas reserve	SGGR	Proved reserves of natural gas reserves of each state × failed state level of each state	0.083
Security of global coal reserve	SGCR	Total recoverable coal of each state × failed state level of each state	0.1
Security of global uranium production	SGUP	Uranium production from mines of each state × failed state level of each state	0.023
Security of global oil supply	SGOS	Annual oil supply of each state × failed state level of each state	0.25
Security of global gas supply	SGGS	Gross natural gas production of each state × failed state level of each state	0.167
Security of global coal supply	SGCS	Total primary coal production of each state × failed state level of each state	0.21
Security of global uranium enrichment	SGUE	Primary conversion capacity of each state × failed state level of each state	0.047

Example: calculating the global energy security level (2):

$$\begin{aligned}
 GES = & SGOR \times 0.12 + SGGR \times 0.0834 + SGCR \times 0.023 + SGUP \times 0.023 \\
 & + SGOS \times 0.25 + SGGS \times 0.167 + SGCS \times 0.21 + SGUE \times 0.047
 \end{aligned}
 \tag{2}$$

The value of the Global energy security (GES) index varies between 100 per cent (maximal security) and 0 per cent (minimal security). Both 100 per cent and 0 per cent values are only theoretically possible. Vytautas Magnus University Energy Research Centre suggests introducing security level conditions. The levels of the conditions were determined based on the suggestions of FSI methodology developers. According to them, states having stability of 0–25 per cent are in the ‘alert’ zone, states with stability between 25.1 – 50 per cent are in the ‘warning’ zone and states having stability higher than 50.1 per cent are in the ‘monitoring’ or moderate zone. Accordingly, following the consultations with experts, the similar security level conditions of the proposed index are introduced. The security level lower than 25 per cent marks critical condition; the security level

that is between 25.1 and 50 per cent indicates pre-critical condition; finally, the security level above 50 per cent means that security level is normal.

5. THE NATURE OF VARIABLES

Applying the methodology in practice it is important to mention a few specific factors related to variable data. Annual data on oil, natural gas and coal reserves and production is obtained from the EIA. The EIA also provides data on the territorial subjects that are not recognised as sovereign states by the United Nations (UN). For the purposes of this study the data of such territories were added to the data of the respective states recognised by the UN.

The EIA does not always present the data from all countries. When the data of a certain country is missing, it is assumed that the data remains unchanged from the last published data. The EIA periodically reviews and adds the data and thus accordingly, the data is periodically reviewed and renewed in the methodology.

The annual data on uranium production and the primary conversion capacity is obtained from the World Nuclear Association. It is noteworthy that not all of the data by the World Nuclear Association is renewed periodically. This is due to insignificant changes. Because of this reason, the present study relies on the same annual data until they are renewed.

In order to determine political stability of the countries, the present study uses FSI that is published annually by the U.S. think-tank the Fund for Peace and the Foreign Policy Journal [11]. FSI always reflects the results of the year before. The index consists of 12 indicators that are further divided into 100 sub-indicators. The index is calculated for 178 states. First, the data is collected from news articles, essays, magazine pieces, speeches, and government and non-government reports. They are then exposed to content analysis software that scans the documents using Boolean phrases on indicators within the Fund for Peace CAST framework. Second, quantitative data from reputable institutions, such as the UNHCR, WHO, UNDP, Transparency International, World Factbook, Freedom House, World Bank, and other reliable sources are incorporated. Finally, the results are compared with insights from a separate qualitative review of each indicator for each country [12]. Aggregated data are normalised and scaled from 0 to 10, where 0 is the absolute stability and 10 is the absolute instability. Therefore, the total result of the index varies between 0 and 120. FSI focuses on a spectrum of risk factors that affects the security of supply of energy resources. It also gives an overall idea of the stability of each state.

6. RESULTS OF THE RESEARCH

This section provides a global energy security assessment that is based on the proposed methodology. The study has shown that the global energy security level changes are rather insignificant (Fig. 1). In the analysed period year 2006–2011, pursuant to the suggested index methodology the highest level of global energy security was reached in 2007 (46.76 %). The biggest change during the study period was during 2007–2008, when security level dropped by 1.72 %. The main reason for this change was the global economic crisis, which also caused the decline of political stability in many countries. However, since 2008 the situation has been improving. Such trends are influenced by increasing stability of the states and growing production in the states that are characterised by a greater political stability. In the analysed period the global energy security level remained in the pre-critical level. It nearly reached secure level in 2007 and missed it only by 3.24 %.

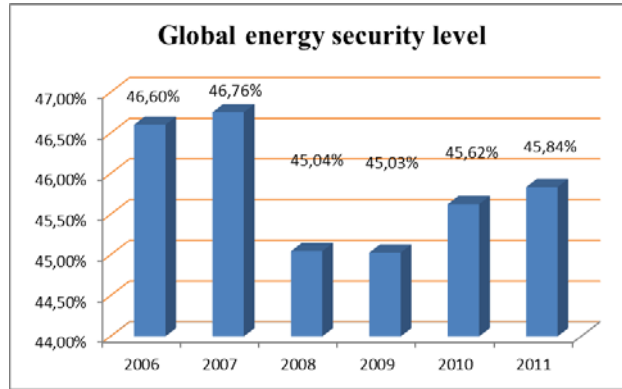


Fig. 1. Global energy security level

The pattern shows that global energy security level changes very slowly and this is related to the slowly changing geo-energetic positions of the states. The expansion of production of certain fuel in a particular state takes a lot of time until it becomes significant on the global scale. The changes are also related to continuing explorations of the reserves and changing technologies allowing the increase in extraction of resources in the regions where previously extraction was unavailable and unaffordable. The aspect of political stability is usually also slowly changing. It usually takes more than a decade to increase stability of the state if the circumstances are favourable. Due to political elements global energy security can decrease very rapidly. For example, if a global crisis emerges as a result of economic failures or large-scale wars. The methodology has shown that energy security decreases more rapidly than it increases.

Global energy security level index allows calculating energy security annually and independently from previously presented data (unlike the Index of U.S. Energy Security Risk' and 'International Energy Security Risk Index'). The annual results of the suggested index could be compared independently, and the index is more precise.

Since global energy security index consists of eight separate indicators and their values are summed up only in the final stage, it is easy to measure global security level of reserve and production of each resource applying the same formula (1). The presented Fig. 2 and Fig. 3 show the dynamics of the changes of each indicator of global security level index.

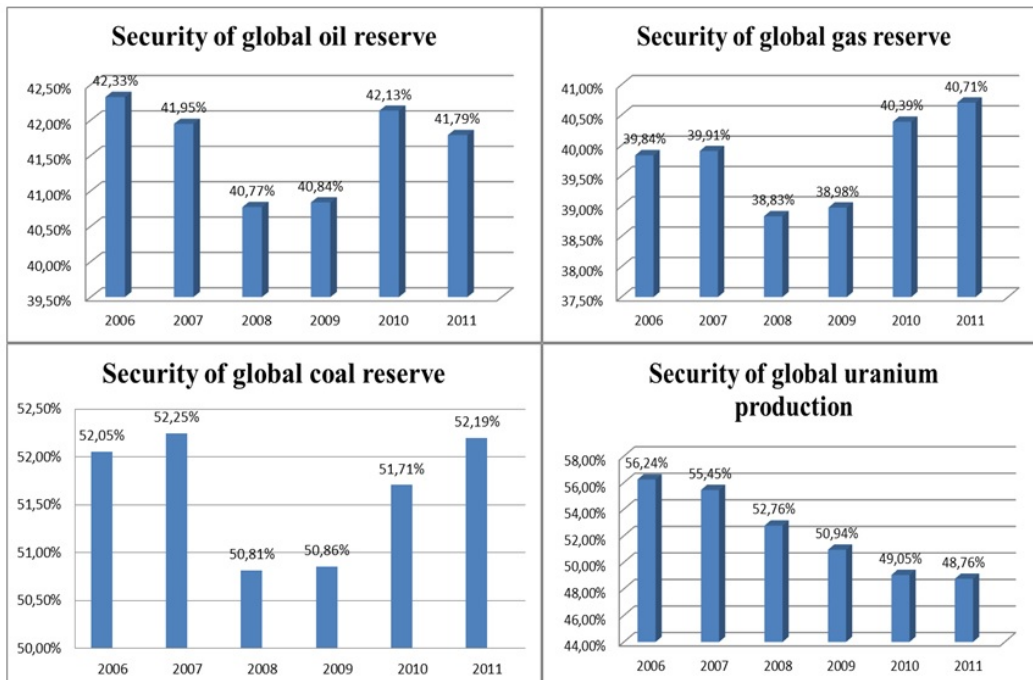


Fig. 2. Security of global oil, gas, coal reserves and global uranium production

Fig. 2 shows that the lowest security was in the gas reserve sector, while the highest - in the coal reserve sector. The security of global uranium production was constantly decreasing due to the expansion of mining in less stable countries. The security of global coal reserve in the researched period remained above 50%, i.e. in the secure zone.

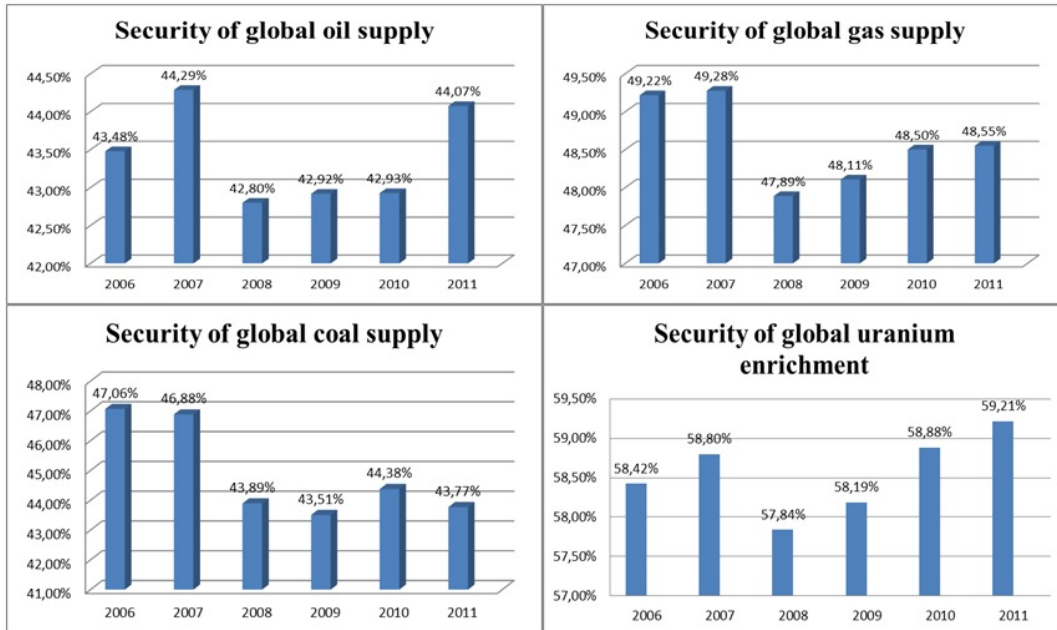


Fig. 3. Security of global oil, gas, coal production and global uranium enrichment

Fig. 3 shows that the global oil supply was the least secure, while the global gas supply in 2007 nearly entered secure zone. The global uranium enrichment security level remained in the secure level, well above 50%. It must be underlined that Fig. 2 and Fig. 3 show global patterns, and do not reflect energy security of the individual state or region. For example, these figures do not reflect Russian – Ukrainian energy crisis in 2006 and 2009 as they do not measure security of export and transit.

The index suggests that there are two ways to increase global energy security. First, it is necessary to expand the production of energy resources in more stable countries. Second, more efforts should be made to stabilize the countries having largest reserves and production capabilities.

7. APPLICATION OF THE INDEX

The index can be used either as a separate research model or incorporated into broader energy security level research models/indexes. When applied individually, the index allows exploring long-term global energy security changes in a long-term perspective (10 and more years). If incorporated into a broader national energy security research model, the index becomes a constituent part of the energy security related to political field Fig. 4. Political sector is commonly divided into the fields of domestic and global politics.

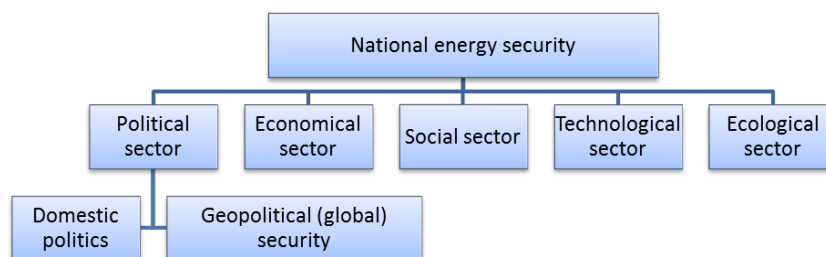


Fig. 4. Elements of national energy security index

Global energy security level assessment index covers four most important types of fuel. Not all of them are necessarily consumed in a specific state. For instance, Lithuania currently does not use coal or uranium to produce energy. However, these types of fuel are still not disregarded while assessing Lithuanian national energy security level and incorporating global energy security level index. Each type of fuel and energy is important in global energy security level assessment and it is essential to incorporate it into each state's national energy security level assessment. This is because energy systems of each and every state essentially make up one uniform energy complex where different types of fuel are interacting.

For example, comparing the total primary energy structure in 1973 and 2010, a share of oil dropped from 46.1 per cent to 32.4 per cent [13]. This had an impact on the sectors of natural gas, coal and nuclear energy and thus the effect was felt in energy security systems of various states in the world. In the absence of natural gas or nuclear energy development in the total primary energy structure, competition between states for oil and coal would become more intense. Accordingly, the prices would grow more dramatically. Similarly, currently increasing or decreasing demand for coal affects global energy structure and global energy security level.

Nevertheless, it is debatable as to what share in the national energy security index should be given to the global energy security level. It is important to stress that global energy security index is incorporated into the national energy security level indexes of consumer states while its incorporation into energy security level indexes of exporter states should be improved.

Assuming that all five sectors in the national energy security level index are to have the same share, i.e. 20 per cent, it is suggested to divide the global energy security level index as shown in Table 2.

Table 2. Share of global energy security level index in national energy security level index

Share in index	Energy use (kg of oil equivalent per capita)
1%	$x < 500$
2%	$500 < x < 1000$
3%	$1000 < x < 1500$
4%	$1500 < x < 2000$
5%	$2000 < x < 2500$
6%	$2500 < x < 3000$
7%	$3000 < x < 3500$
8%	$3500 < x < 4000$
9%	$4000 < x < 4500$
10%	$4500 < x$

The share of the global energy security level in the energy security index of a consumer state should be related to energy intensity. That is, the more energy is consumed by that state (per capita or GDP), the more this state is dependent on the changes of the global energy security level. Accordingly, the bigger share of the index should be given to the global energy security level. By contrast, developing states that do not consume much energy (per GDP unit or per capita) are not actively engaged in the global energy system. Therefore, the share of global energy security level in their national energy security level index should be smaller.

The global energy security level index affects national energy security level index only insignificantly and further discussions on the impact of global energy security level on national energy security are essential.

CONCLUSIONS

The suggested methodology reflects the logic of the global energy system: the changes of political stability in the states producing large amount of resources are much more important to the

global energy security than changes of political stability in minor producers. The value of the index changes for two reasons. The first reason is geographic redistribution of energy resources reserves and production (most often) or enrichment. This is a slow process that depends on technological progress and long-term substantial investments. The second reason is changes in political stability. The changes of political stability emerge in shorter term as compared to redistribution of production.

The suggested methodology is designed to measure global energy security in the long time period. This corresponds to the structures of global energy and international systems, as drastic changes in the systems are rare. The application of the methodology has to extend in time.

When included into national energy security index, the introduced index plays only a minor role. Global energy security changes are quite insignificant when calculating national energy security level. Further debates on the inclusion of the global energy security level into national energy security level index are needed.

The introduced index could be extended to other fields, such as export of energy resources. Global security of energy export could be determined by enhancing the role of exporting countries in the index results.

The limitations of this methodology are related to the data of the indicators. This applies especially to FSI, as there are no possibilities to measure global energy security level beyond 2004. Also, there will always remain questions how reliable is the data of FSI. Another limitation is that the application of this methodology does not allow predicting the global energy security level developments in the future, i.e. the index is retrospective. The index allows only vague interpretations of the future global energy security level while evaluating experience of the past.

ACKNOWLEDGEMENT

This research was funded by a grant (No. ATE-06/2012) from the Research Council of Lithuania.

REFERENCES

1. SOVACOL K. B. Introduction: Defining, measuring, and exploring energy security. Sovacol K. B. (ed.), *The Routledge Handbook of Energy Security*. New York, NY: Routledge, 2011, p. 3.
2. YERGIN D., Energy security in the 1990s'. *Foreign Affairs*, 67 (1), 1988, p. 110–132.
3. APERC. *A quest for energy security in the 21st century: Resources and constraints*. Asia Pacific Research Centre: Tokyo, 2007; STIRLING, A. Diversity and ignorance in electricity supply investment: Addressing the solution rather than the problem. *Energy Policy*, 22(3), 1994, p. 195–216; KENDELL, J.M. *Measures of oil import dependence*. U.S. Energy Information Agency: Washington, DC, 1998; JANSEN, J. C., van ARKEL, W.G., BOOTS, M.G. *Designing indicators of long-term energy supply security*. Energy Research Centre of the Netherlands: Petten, Netherlands, 2004; SCHEEPERS, M., SEEBREGTS, A., de JONG, J., MATERS, H. *EU standards for energy security of supply*. ECN/Clingendael International Energy Programme: Petten & the Hague, 2007; GUPTA, E. Oil vulnerability index of oil importing countries. *Energy Policy*, 36(3), 2008, p. 1195–1211.
4. von HIPPEL, D. F., SUZUKI, T., WILLIAMS, J. H., SAVAGE, T., HAYES, P. Evaluating the energy security impacts of energy policies. Sovacol K. B. (ed.). *The Routledge Handbook of Energy Security*. New York, NY: Routledge, 2011, p. 85
5. APERC. *A quest for energy security in the 21st century: Resources and constraints*. Asia Pacific Research Centre: Tokyo, 2007.; KRUYT, B., van VUUREN, D. P., de VRIES, H.J.M., GROENENBERG, H. Indicators for energy security. *Energy Policy*, 37(6) (2009), p. 2166–81.
6. U.S. CHAMBER OF COMMERCE INSTITUTE FOR 21ST CENTURY ENERGY. *Index of U.S. Energy Security Risk: Assessing America's Vulnerabilities in a Global Energy Market*,



- edition 2012*, p. 24; 29–34, 2012 – [referred on the 28th of February in 2013 y.]. Link to the internet <http://www.energyxxi.org/sites/default/files/pdf/us_energy_risk_index_2012.pdf>.
7. The International Energy Agency. *Key World Energy Statistics, edition 2012*. 2012 – [referred on the 28th of February in 2013 y.]. Link to the internet <<http://www.iea.org/publications/freepublications/publication/kwes.pdf>>.
 8. The Freedom House. *Freedom in the World 2012: Arab Uprisings and their Global Repercussions*. 2012 – [referred on the 28th of February in 2013 y.]. Link to the internet <http://www.freedomhouse.org/sites/default/files/FIW%202012%20Booklet_0.pdf>.
 9. Vytautas Magnus University and Lithuanian Energy Institute. *Lithuanian Energy Security: Annual Review 2011–2012*. Kaunas: VDU leidykla, 2013, p. 11.
 10. World Nuclear Association. *World Uranium Mining*. [referred on the 28th of February in 2013 y.]. Link to the internet <<http://www.world-nuclear.org/info/inf23.html>>; World Nuclear Association. *Uranium Enrichment*. [referred on the 28th of February in 2013 y.]. Link to the internet <<http://world-nuclear.org/info/inf28.html>>
 11. Official website of the Fund for Peace. [referred on the 28th of February in 2013 y.]. Link to the internet <<http://www.fundforpeace.org/global/?q=fsi>>
 12. Governance Assessment Portal. *Failed States Index*. 2012 – [referred on the 28th of February in 2013 y.]. Link to the internet <<http://www.gaportal.org/global-indicators/failed-states-index>>.
 13. International Energy Agency. *Key World Energy Statistics (2012)*. p. 6.



THE ECONOMIC AND ENERGY EVALUATION OF BIO-HYDROGEN AND BIO-METHANE PRODUCTION PROCESSES

C.M. Liu, C.Y. Chu, S.Y. Wu, Y.C. Li, Y.P. Chou

*Feng Chia University
Taichung 40724 – Taiwan*

ABSTRACT

Earth is facing energy crisis, but the past energy crisis, this will be long-term and sustained crisis. The main reasons, the first is the rapid increase of the population, human needs expansion, as well as the pollution caused by the "city" and "industrial" development. With the continuous development of human economic activities, human life has become more convenient and more progress. In progress at the same time, energy is drastically reduced harm to the environment in which we live. Therefore, the development of alternative renewable energy and reduce greenhouse gas emissions has become an important issue.

This study was aimed at economic and energy evaluation of bio-hydrogen and bio-methane production by Aspen Plus software. Assess the cost only for the process of bio-hydrogen and bio-methane production, not consider separation bio-hydrogen, storage, transportation, energy conversion and application. Waste molasses was the feeding substrate which was from amino acids producing process and can be ignored the cost of feedstock. It was found that the total capital cost for bio-hydrogen and bio-methane facilities is 3.3 million USD which based on Annual Percentage Rate of 1.37%. The annual payback cost is 0.33 million USD per year by dividing to 10 years. The return on investment (ROI) is 3.1 years by using waste molasses to sale bio-hydrogen/bio-methane/CO₂, that was predicted by Aspen Plus Software based on mass and energy balance simulation.

Finally, the total energy output was 3.5 times high than the energy input the system which assumed the efficiency for heating converter is 15%. However, the total energy output was 11.8 times high than the energy input the system which assumed the efficiency for electricity converter (Fuel Cell) is 50%. Therefore, this system is very impressive for heating and energy recovery from the factory with high organic wastewater by renewable energy of bio-hydrogen and bio-methane.

Keywords: Energy Crisis, Bio-hydrogen, Bio-methane, Waste Molasses, Fuel Cell

1. INTRODUCTION

Earth is facing energy crisis, but the past energy crisis, this will be long-term and sustained crisis. The main reasons, the first is the rapid increase of the population, human needs expansion, as well as the pollution caused by the "city" and "industrial" development. With the continuous development of human economic activities, human life has become more convenient and more progress. In progress at the same time, energy is drastically reduced harm to the environment in which we live. In recent years, due to the rise of some emerging economies, fossil fuel consumption improved dramatically, including in international oil prices from 43.06 U.S. dollars / barrel in 2009 rocketed to 111.94 \$ / barrel [1]. In addition, the heavy use of fossil fuels not only accelerate the depletion of energy and greenhouse gas emissions are the main cause of global climate anomalies. Therefore, the development of alternative renewable energy and reduce greenhouse gas emissions has become an important issue.

Renewable energy sources such as wind, water, solar, ocean energy, and biomass energy. Biomass refers to the use of biomass converted into electricity with thermal energy, biomass refers to biological organic matter, such as agricultural waste such as rice straw, bagasse, etc.; forestry waste, such as tree branches, wood chips; well as their daily lives use of waste paper, etc. Biomass

energy development since the technology has become more skilful, and stromal derived waste, can reach the waste recycling and energy production, for the attention of the global environment and energy, biomass energy has attracted increasing attention [2].

In recent years, the biomass rapid development of major bio-diesel, bio-hydrogen production. Due to the combustion of hydrogen only produces water vapour and hydrogen from water, inexhaustible, inexhaustible, and can be recycled by nature, is an endless supply of energy carriers, absolutely in line with today's environmental awareness [3]. Bio-hydrogen production is a new kind of green energy, can not only solve the current oil shortage crisis, may also slow down the car exhaust emissions, improving the global warming issues. In addition, hydrogen has a high energy, the heat generated per unit weight value of 34,300 kcal / kg, about 2.5 times the methane, petrol three times [4-6]. Hydrogen is regarded as one of the most important energy source in the future.

Biohydrogen production has some benefits such as 1. reduction in waste management costs, 2. increased income from agricultural food production via its waste conversion to energy, 3. reduction of carbon dioxide emissions owing to the utilization of sustainable biomass, and 4. replacement of fossil fuel by biofuels [7]. The processing of waste presents a financial burden on the state; using waste as feedstock for hydrogen production may alleviate this burden while adding value as a byproduct [8] and [9]. This study uses the wastewater as the basis to do the economic evaluation.

This study uses the wastewater as the basis to do the economic evaluation. The amounts of waste were illustrated that the source were stable in Taiwan and easy to get, one plant of beverage wastewater at least 3000 m³/day. The materials were determined that the potential of waste materials produced hydrogen in the practical applications; the database were obtained from Aspen Plus simulation and the real data in lab. Two different databases were compared with each other to reveal the potential of hydrogen production for the practical applications. From the results, a reference commercial model value was obtained.

2. MATERIALS AND METHODS

2.1. Raw material

The feeding substrate of Condensed Molasses Solubles (CMS) (Vedan Enterprise Corporation, Taiwan) were varied from 90 to 110 total sugar/L. It was diluted by tap water at the substrate concentration of 60 g COD/L. This feeding substrate of CMS contained various nutrients and other fermentation products such as microbial protein, amino acids, organic acids, vitamins, and coenzymes [10]. The suspended sludge system was started up at HRT 8 h with a substrate concentration of CMS 60 g COD/L after thermal pre-treatment.

2.2. Process description

An overview process is shown in Fig. 1 which included three parts such as feedstock, biohydrogen production by dark fermentation and application. The evaluation data of hydrogen and carbon dioxide production rates with CMS was from our previous study, which was obtained in a continuously stirred anaerobic pilot plant with a working volume of 380 L (biohydrogen production fermentor) and 2,400 L (biomethane production fermentor).

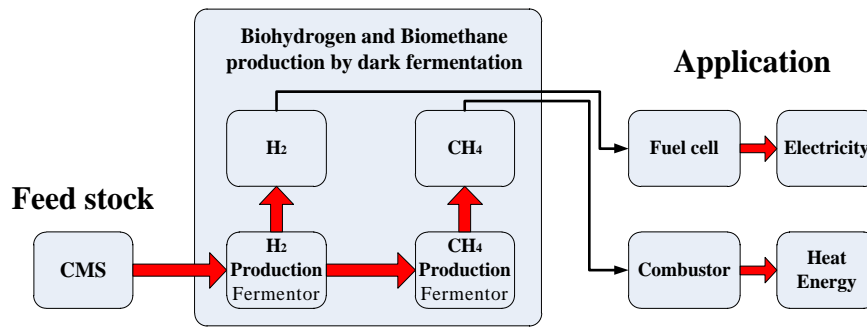


Fig. 1. The flowsheet of a biohydrogen and biomethane production process

2.3. Evaluation condition and processes

The optimal conditions of biohydrogen production were obtained with a substrate concentration of 20 g total sugar/L, pH 5.75, temperature of 37 °C and hydraulic retention time (HRT) of 4 h. As per the results, the hydrogen production rate was 17.8 m³/m³/d, the CO₂ rate was 26.7 m³/m³/d. The optimal conditions of biomethane production were obtained with a substrate concentration of 45.0 g SCOD/L, pH 7.2, temperature of 37 °C and hydraulic retention time (HRT) of 24 h. As per the results, the methane production rate was 4.14 m³/m³/d, the CO₂ rate was 1.15 m³/m³/d [11].

Aspen Plus software was used for process design and economic evaluation of this study which was similar to that reported by the Biological Hydrogen Production (BHP) process [12] and Renewable Energy Laboratory (NREL) [13] etc. The evaluation parameters and biogas production performance from pilot plant is show in Table 1.

Table. 1. Biogas production performance from pilot plant

Evaluation parameters	Biohydrogen production	Biomethane production
The working volume of the fermentor	0.38 m ³	2.4 m ³
^a The working volume of the fermentor for commercial scale	22.8 m ³	675 m ³
Hydraulic retention time, HRT	4 h	24 h
Substrate concentration (g/L)	20.0	45.0 g SCOD/L
^b Production rate (m ³ / m ³ /d)	17.8	4.14
^b CO ₂ production rate (m ³ / m ³ /d)	26.7	1.15

^a Simulated by Aspen Plus software.

^b Adopted from our previous study [10].

3. RESULTS AND DISCUSSIONS

3.1 Mass and energy balance from biohydrogen and biomethane production process

The biohydrogen and biomethane production pilot system was consisted of six functional units (Fig. 2): (a) feedstock tank; (b) feedstock pretreatment heater; (c) pump for feedstock; (d) fermentor for biohydrogen; (e) fermentor for biomethane; (f) absorber for algae. Operating parameters was fixed at the optimal conditions by our previous study [11]. The flowchart of continuous two-stage fermentative process is shown in Fig. 2.

The materials and energy flows by simulation result is show in Fig.3 and Table 3. The main metabolites are assumed as acetic acid and butyric acid for simplifying the simulation procedure. The simulation data of the mass and energy balance between the input and output can be defined as a reasonable results.

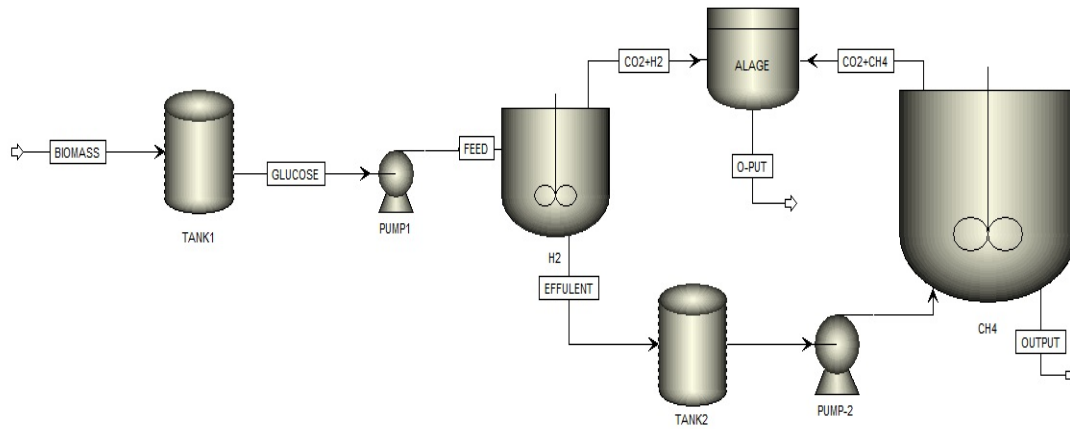


Fig. 2. Flowchart of continuous two-stage fermentative process

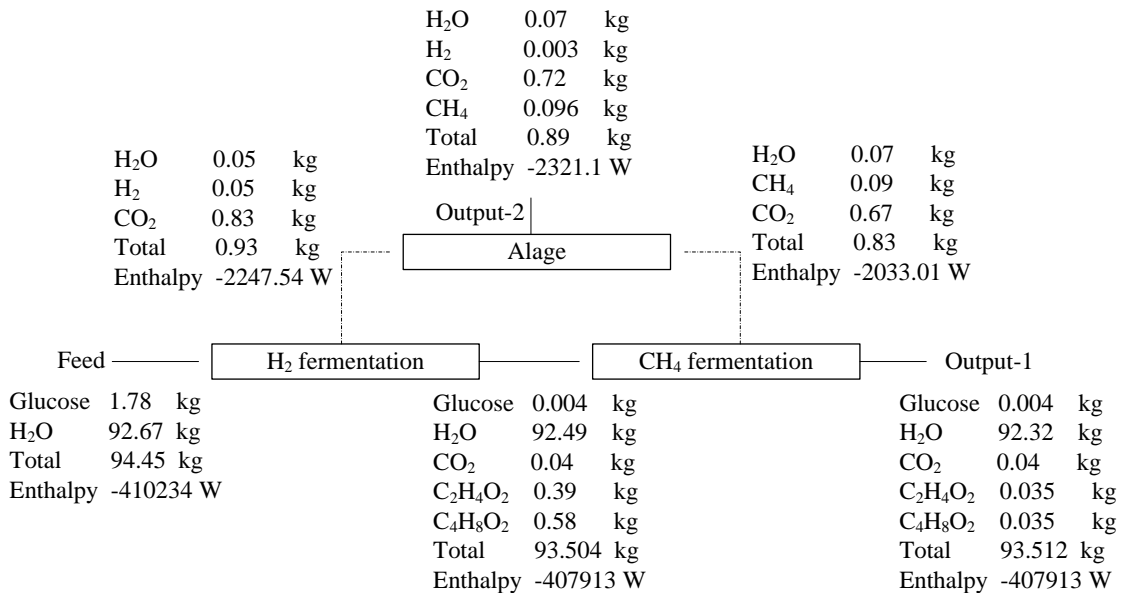


Fig. 3. The materials and energy balance from simulation result

Table. 2. Mass and energy balance

Input			Output			
Feed			Output-1		Output-2	
Item	kg	kW	kg	kW	kg	kW
Glucose	1.78	-410	0.004	-408	-	-2
H ₂ O	92.67		92.32			
C ₂ H ₄ O ₂	-		0.035			
C ₄ H ₈ O ₂	-		0.035			
H ₂	-		-			
CO ₂	-		0.04			
CH ₄	-		-			
Total	94.4		93.5			



3.2. Analysis of Economic Benefits

Table 3 is shown the equipment costs of biohydrogen and biomethane production stages which were obtained from the domestic vendors in Taiwan. The fixed cost was equipment amortization without land cost. The variable costs were operation and maintenance (including salary and equipment supplies). The fixed and variable cost estimates of biohydrogen and biomethane production processes are shown in Table 4. The reduction in carbon dioxide emissions can be calculated by the terms of the suppression amount equivalent to 2.508 tons of carbon dioxide each kiloliter of oil fuel. (Assuming that at normal temperature and pressure, the gas volume was 24.5 L for 1 mole, according to the normal temperature was 25C in Taiwan) The energy gain from biohydrogen production: $133.927 \text{ m}^3 \text{ H}_2/\text{y} = 10.933 \text{ kg H}_2/\text{yr} \times 34.000/9,200$ (Calorific value of hydrogen 34,000 kcal/kg; Calorific value of fuel oil 9.200 kcal/L) = 40.404 L fuel oil/y = 40.4 KL fuel oil/y which was derived that the reduction of carbon dioxide emissions from biohydrogen is 101.32 tons per year in this study. Moreover, the reduction of carbon dioxide emissions from biomethane production is 2110 tons per year in this study. (Calorific value of methane 12.855 kcal/kg; Calorific value of fuel oil 9.200 kcal/L)

Table. 3. The equipment costs of biohydrogen and biomethane production stages

Item	Price (NTD)
Stage I: Equipment of biohydrogen production: mixed tank, biohydrogen fermentor and other accessories (Influent Pump, pH tank, stirrer, pH transmitter, pressure transmitter, piping & valve, electrical system, control panel, walk way)	20.000,000
Stage II: Biomethane fermentor system and MBR.	29.800,000
Total (1 USD= 30 NTD)	49.800,000

Table. 4. The fixed and variable costs of biohydrogen and biomethane production

The costs	Price (NTD)
Fixed cost: Equipment amortization (APR 1.37%)	5.710,000
Variable cost: Operation and maintenance costs (including salary and equipment supplies)	3.870,000
Total (1 USD= 30 NTD)	9.580,000

Assuming the industry factory operates 330 days a year. The products of biohydrogen, biomethane and bio-CO₂ were purified to 99.9%. The prices of hydrogen, methane and CO₂ were referring Gas Company in Taiwan.

The biohydrogen production rate was calculated by the Table 1 as eqs. (1) and (2) where the working volume of the fermentor was use the commercial scale. Therefore, the biohydrogen profit was calculated by eq. (3). The biomethane production can be calculated by Table 1 as eqs. (4) and (5). Therefore, the biomethane profit was calculated by eq. (6). Furthermore, the bio-CO₂ production can be calculated by Table 1 as eqs. (7) and (8). Therefore, the bio-CO₂ profit was calculated by eq. (9). Based on the above three points, the economic profit of the two-stage fermentation by waste molasses was 3.076 million NTD/year.

$$(17.8 \text{ m}^3/\text{m}^3/\text{d})(22.8\text{m}^3) = 405.84 \text{ m}^3 \text{ H}_2/\text{d} \quad (1)$$

$$405.84 \text{ m}^3 \text{ H}_2/\text{d} \times 330 \text{ d}/\text{y} \approx 133.927 \text{ m}^3 \text{ H}_2/\text{y} \quad (2)$$

$$133.927 \text{ m}^3 \text{ H}_2/\text{y} \times 80 \text{ NT}\$/\text{m}^3 \approx 10.710,000 \text{ NT}\$/\text{y} \quad (3)$$

$$(4.14 \text{ m}^3/\text{m}^3/\text{d})(675\text{m}^3) = 2794.5 \text{ m}^3 \text{ CH}_4/\text{d} \quad (4)$$



$$2587.5 \text{ m}^3 \text{ CH}_4/\text{d} \times 330 \text{ d/y} \approx 922.185 \text{ m}^3 \text{ CH}_4/\text{y} \quad (5)$$

$$922.185 \text{ m}^3 \text{ CH}_4/\text{y} \times 17 \text{ NT\$/m}^3 \approx 15.670,000 \text{ NT\$/y} \quad (6)$$

$$\frac{(26.7 \text{ m}^3/\text{m}^3/\text{d})(2.28 \times 10^4 \text{ L}) + (1.15 \text{ m}^3/\text{m}^3/\text{d})(6.75 \times 10^5 \text{ L})}{1,000 \text{ L/m}^3} \approx 1385 \text{ m}^3 \text{ CO}_2/\text{d} \quad (7)$$

$$\text{CO}_2/\text{y rate} = 1385 \text{ m}^3 \text{ CO}_2/\text{d} \times 330 \text{ d/y} \approx 457.050 \text{ m}^3 \text{ CO}_2/\text{y} \quad (8)$$

$$457.050 \text{ m}^3 \text{ CO}_2/\text{y} \times 9.6 \text{ NT\$/m}^3 \approx 4.380,000 \text{ NT\$/y} \quad (9)$$

Assess the cost only for the process of bio-hydrogen and bio-methane production, not consider separation bio-hydrogen, storage, transportation, energy conversion and application. Waste molasses was the feeding substrate which was from amino acids producing process and can be ignored the cost of feedstock. It was found that the total capital cost for bio-hydrogen and bio-methane facilities is 3.3 million USD which based on Annual Percentage Rate of 1.37%. The annual payback cost is 0.33 million USD per year by dividing to 10 years. The return on investment (ROI) is 3.1 years by using waste molasses to sale bio-hydrogen/bio-methane/CO₂, that was predicted by Aspen Plus Software based on mass and energy balance simulation.

3.2 Assessment of energy performance

The energy consumption for each unit of fermentation process by Aspen Plus is shown in Table 5. The energy Input, A is 51.5 kW × 3.600 (kJ/h)/kW = 185.400 kJ/h. The heating values of hydrogen and methane are 285.8 and 889.5 kJ/mol, respectively at temperature of 20C and 1 atm. Therefore, the Energy Output, B can be calculated by eq. (10) which was take into account the biohydrogen and biomethane production rates in this study. Hence, the energy performance can be calculated by energy output divided by energy input that resulted in 4.366,998 (kJ/h) / 185.400 (kJ/h) = 23.5. Finally, the total energy output was 3.5 times high than the energy input the system which assumed the efficiency for heating converter is 15%. However, the total energy output was 11.8 times high than the energy input the system which assumed the efficiency for electricity converter (Fuel Cell) is 50%. Therefore, this system is very impressive for heating and energy recovery from the factory with high organic wastewater by renewable energy of bio-hydrogen and bio-methane.

$$\begin{aligned} B \text{ (kJ/h)} &= 0.74 \text{ (L/h/L)} \times 22.800 \text{ (L)/24.5 (L/mol)} \times 285.8 \text{ (kJ/mol)} + \\ &0.17 \text{ (L/h/L)} \times 675.000 \text{ (L)/24.5 (L/mol)} \times 889.5 \text{ (kJ/mol)} = \\ &= 4.366,998 \text{ kJ/h.} \end{aligned} \quad (10)$$

Table. 5. Energy consumption for each unit of fermentation process by Aspen Plus

Operating unit	Energy consumption (kW)
Biohydrogen Fermentor	8.7
Biomethane Fermentor	2.8
Pump	40
Total (kW)	51.5



4. CONCLUSIONS

This study was aimed at economic and energy evaluation of bio-hydrogen and bio-methane production by Aspen Plus software. It was found that the total capital cost for bio-hydrogen and bio-methane facilities is 3.3 million USD which based on Annual Percentage Rate of 1.37%. The return on investment (ROI) is 3.1 years by using waste molasses to sale bio-hydrogen/bio-methane/CO₂, that was predicted by Aspen Plus Software based on mass and energy balance simulation. Finally, the total energy output was 3.5 times high than the energy input the system. However, the total energy output was 11.8 times high than the energy input the system. Therefore, this system is very impressive for heating and energy recovery from the factory with high organic wastewater by renewable energy of bio-hydrogen and bio-methane.

5. ACKNOWLEDGMENT

The authors gratefully acknowledge the financial support of the National Science Council of Taiwan (NSC 101-2218-E-035-002-MY2); Taiwan's Bureau of Energy (grant no. 101-D0204-3); Feng Chia University (FCU-10G27101).

REFERENCE

1. 經濟部能源局，油價資訊管理與分析系統，<http://210.69.152.10/oil102/>, 2012.
2. 吳耿東、李宏台，生質能源—化腐朽為能源，科學發展，第 383 期，第 20–27 頁，(2004).
3. 柯賢文，未來的氫能經濟，科學發展，第 399 期，第 68-75 頁，(2006).
4. 張嘉修、李國興、林屏杰、吳石乙、林秋裕，以環境生物技術生產清潔能源—氫氣，化工，第 49 卷，第 6 期，第 85–104 頁，(2002).
5. 吳石乙、林祺能、張建勝、陳人豪、邱茗煥、張嘉修，流化床中乙烯醋酸乙醯酯固定化產氫菌之醱酵產氫研究，第 28 屆廢水處理技術研討會論文集，(2003).
6. 蔡俊宇，利用棉花纖維素酸化降解糖為基質進行稱物產氫. 逢甲大學化學工程學系碩士班論文,(2009).
7. BALAT M., BALAT M., Political. Economic and environmental impacts of biomass-based hydrogen, Int J Hydrogen Energy, 34 (2009), p. 3589–3603
8. DAS D., KHANNA N., VEZIRO_GLU T.N., Recent developments in biological hydrogen production processes, Chem Ind Chem Eng Q, 14 (2008), p. 57–67
9. KOTAY S.M., DAS D., Biohydrogen as a renewable energy source prospects and potentials, Int J Hydrogen Energ, 33 (2008), p. 258–263
10. LAY C.H., WU J.H., HSIAO C.L., CHANG J.J., CHEN C.C., LIN C.Y., Biohydrogen production from soluble condensed molasses fermentation using anaerobic fermentation. Int J Hydrogen Energy, 35 (2010), p. 13445–13451
11. LIN C.Y. ET AL., Bioenergy technology research center. Taiwan's Bureau of Energy project final report (grant no. 101-D0204-3) 2012.
12. ADEN, A., RUTH, M., IBSEN, K., JECHURA, J., NEEVES, K., SHEEHAN, J., WALLACE, B., MONTAGUE, L., SLAYTON, A., LUKAS, J. (2002) Lignocellulosic biomass to ethanol process design and economics utilizing co-current dilute acid prehydrolysis and enzymatic hydrolysis for corn stover. NREL/TP-510~32438.
13. CLAASSEN, P.A.M., VAN GROENESTIJN, J.W., JANSSEN, A.J.H., VAN NIEL, E.W.J., WIJFFELS, R.H. (2000) Feasibility of biological hydrogen production from biomass for utilization in fuel cells. *Proceedings of the First World Conference on Biomass for Energy and Industry*, II, Seville, Spain, p. 1665–1667.



NUMERICAL SIMULATIONS OF THE NON-ISOTHERMAL GROWTH OF CARBON NANOPARTICLES FROM EXPERIMENTAL DATA OF SOOT FORMATION AT ETHYLENE PYROLYSIS IN THE SHOCK TUBE

Y.A. Baranyshyn

A.V. Luikov Heat and Mass Transfer Institute

15, P. Brovka str., 220072 – Belarus

Phone: 375 17 284 15 20

Email: Baranishin-83@mail.ru

ABSTRACT

Today there are a lot of experimental data on the soot formation, and works in this area are in progress. Different theoretical models to describe the growth of carbon particles are proposed. Note, however that a full quantitative and qualitative understanding of this process is still lacking. In this paper, we propose a simple model for the non-isothermal growth of carbon nanoparticles in the gas phase due to condensation of carbon atoms into primary carbon particles. Numerical simulation of heat transfer of carbon particles is carried out. Our experimental data on the process of soot formation at pyrolysis of an ethylene and argon mixture in a shock tube over the temperature range from 2000 to 3500 K are used as the initial conditions for our calculations. A comparison of the experimental and theoretical results is presented. The results have shown that the proposed simple model of growth and heat transfer of carbon nanoparticles can be used to determine the basic parameters of soot particles.

Keywords: numerical simulation, carbon nanoparticles, soot, shock tube

1. INTRODUCTION

Study of the formation of carbon particles (soot) has attracted the attention of scientists for many years and nowadays this problem is still actual. Soot is formed at various conversions of hydrocarbon fuel, and it is important to know the optimal regimes of its production. This is because, on the one hand, soot is one of the main pollutants that influence the operation of engines and industrial power installations, climate changes and the mankind's health. On the other hand, black carbon is a widespread industrial product. Moreover, with the discovery of new forms of carbon (fullerenes, nanotubes, graphene) the formation processes of condensed carbon particles are the focus of attention in a wide range of research.

Of late, a huge amount of experimental and theoretical data on the soot formation in flames (diffusion and pre-mixed), reactors, engines, and shock tubes [1–5] is accumulated. In addition to the traditional methods based on combustion and pyrolysis of hydrocarbons, various carbon nanoparticles are now synthesized by other methods, such as chemical vapour deposition (CVD), electric arc plasma reactors, microwave radiation, electron beams, and laser ablation.

However up to now, no self-consistent theoretical description of all stages of the soot formation process is available. The kinetics of carbon particles and their subsequent growth are a complicated scientific challenge. This is mainly due to the complexity of research object. The basic problem for experimental studies is that primary carbon particles are actually nanoparticles. Additionally, a short growth time of primary carbon nanoparticles is a serious obstacle for experimental detection of parameters of heat and mass processes during the particle growth. The modern level of measurement technique does not meet all the requirements of such studies and cannot directly support theoretical research.

This work presents the calculation results of the basic parameters of a cloud of soot nanoparticles using our experimental data on ethylene pyrolysis in the shock tube [6] at high temperatures (2000–3500 K) and pressures (7.0–11.5 atm) and our proposed physical-mathematical



model for the non-isothermal growth of carbon nanoparticles in the gas phase. At present, it is impossible to record the initial stage of development of carbon nanoparticle cloud parameters experimentally.

2. SIMULATION OF THE GROWTH AND HEAT AND MASS TRANSFER OF CARBON NANOPARTICLES

2.1. Experimental data of the soot formation at ethylene pyrolysis in the shock tube

Work [6] presents the results of our experimental studies of the soot particle formation and growth. It was carried out in the stainless steel shock tube 7.1 m in length and 50 mm in diameter. The ethylene – argon mixture (5% C₂H₄ – 95% Ar) was used as a working gas. In our study, the pyrolysis temperature was 2000 – 3500 K. The pressure of the gas behind the reflected shock wave was 7.0–11.5 atm and the density of the gas mixture was 1.61–1.63 kg/m³. In all our experiments, pyrolysis took place behind the reflected shock wave.

In this work, one of the greatest interest is the behaviour of the temperature of soot carbon particles. It was measured using a pulse photoemission pyrometer with a time resolution of 10⁻⁶ s via the quartz rod mounted in the wall side of the shock tube. It was found that in the growth of soot particles, their temperature much exceeded the initial temperature of the gas phase (temperature difference was up to 900 K) at the initial stage of registration, but it then decreased with a rate of ~ 10⁶ K/s up to the quasi-stationary value that was below the initial temperature of the gas (up to 550 K). Such soot particles temperature behaviour agrees with the predictions and experimental results of some authors [7, 8].

Moreover, the soot produced at pyrolysis was analysed under a bitmapped electron microscope Carl Zeiss Supra 55. It was found that the average soot particle radius decreased from 25 to 15 nm with the growth of the pyrolysis temperature from 2100 to 2800 K.

2.2. Simple physical-mathematical model for the non-isothermal growth of carbon nanoparticles in the gas phase

To explain the behaviour of the temperature of soot carbon particles during their formation and growth [6] we proposed the simple physical-mathematical model for the non-isothermal growth of carbon particles to the free-molecular approximation. It was assumed that the particles were growing due to the condensation of carbon atoms from a mixture of supersaturated carbon vapour and carrier gas (argon) that is formed as a result of shock wave heating of a base mixture (ethylene – argon).

There is a relationship between a particle radius R and a number of carbon atoms g in it:

$$R(g, \varepsilon) = (3gv_a / 4\pi\varepsilon)^{1/3}, \quad (1)$$

where ε is the particle-to-circumscribed sphere volume ratio, v_a is the volume per carbon atom in the condensed phase.

Growing carbon nanoparticles may have different geometrical shapes slightly different from the sphere, and also have some pores. They can be formed during condensation of carbon atoms at the particle surface. Thus, the use of the particle-to-circumscribed sphere volume ratio in our equations owes us to take into account partially the real particle geometry. We restrict our consideration here only to the typical case $\varepsilon = 0.9$.

To describe the non-isothermal growth of the nanoparticle we use the idea of the thermal motion of preserved carbon atoms in the nanoparticle as the motion in the potential hole. The depth of this potential hole is equal to the sublimation energy per carbon atom. This value is well known from scientific literature.

Supersaturation, S , of the carbon vapour is determined as:

$$S = n/n_s(T), \quad (2)$$

where n and $n_s(T)$ are the number density of the carbon vapour and the saturated vapour at the temperature T , respectively.

The average free path of carbon atoms is much larger than the diameter of soot, therefore, we use the free-molecular approximation of transfer processes in the gas phase. It should also be noted that for relatively high supersaturation of the carbon vapour, the critical radius of a carbon particle is smaller than the size of a single atom. Actually, any ternary collisions lead to the formation of stable carbon clusters. Below we analyze only the growth of nanoparticles with an initial radius equal to one nanometer and with a temperature equal to that of the gas mixture of the supersaturated carbon vapour consisting only of carbon atoms and carrier gas. The non-isothermal growth of the particle and its temperature change are described by the following system of the ordinary differential equations:

$$\frac{dR}{dt} = \frac{m}{\rho_c \varepsilon \sqrt{2\pi m k}} \left[\frac{nkT}{\sqrt{T}} - \frac{p_s(T_c)}{\sqrt{T_c}} \right], \quad (3)$$

$$\frac{dT_c}{dt} = \frac{3}{Rc} \left[-(cT_c - U) \frac{dR}{dt} + \frac{3\Pi v_a}{\varepsilon} - \frac{\sigma_{SB}^* (T_c^4 - 300^4) v_a}{\varepsilon} \right], \quad (4)$$

where c is the heat capacity per carbon atom in the condensed phase; k the Boltzmann coefficient; m the mass of the carbon atom; $p_s(T_c)$ the equilibrium pressure of the saturated carbon vapour at the temperature T_c ; T_c the carbon particle temperature; ρ_c the mass density of the carbon particle ($\sim 2000 \text{ kg/m}^3$); and σ_{SB}^* is the effective Stefan–Boltzmann coefficient. An expression for energy fluxes in the gas phase to the particle can be written as follows:

$$\Pi = \frac{1}{\sqrt{2\pi m k}} \left[\frac{nkT(cT + U + 0.5kT)}{\sqrt{T}} - \frac{p_s(T_c)(cT_c + U + 0.5kT_c)}{\sqrt{T_c}} + \frac{kn_{car}}{\sqrt{2\pi m_{car} k}} \left[\frac{2kT^2}{\sqrt{T}} - \frac{2kT_c^2}{\sqrt{T_c}} \right] \right], \quad (5)$$

where the subscript *car* stands for the carrier gas (argon).

According to this model, the temperature of particles changed due to latent heat release and absorption at condensation of carbon atoms into carbon particles and at evaporation from them, due to the interaction of collisions with the carrier gas and radiation heat exchange with the chamber walls (300 K).

It is worthy to emphasize that the optical properties and especially radiative emissivity of carbon nanoparticles drastically differ from thermal radiative emissivity of a macroscopic black body [9]. That is why we have used the calculated effective Stefan–Boltzmann coefficient σ_{SB}^* [9].

We have also taken into account a feedback between the growth of particles and the carbon vapour state. The first additional equation is for the change in the carbon vapour number density $n(t)$ due to condensation:

$$\frac{dn}{dt} = -4\pi R^2 \frac{N_c}{\sqrt{2\pi m k}} \left[\frac{nkT}{\sqrt{T}} - \frac{p_s(T_c)}{\sqrt{T_c}} \right], \quad (6)$$

where N_c – the number density of primary carbon nanoparticles.

We can thus describe the carbon vapour depletion during the growth of black carbon nanoparticles.

The change in the gas mixture temperature due to energy exchange with nanoparticles is governed by the following equation:

$$\frac{dT}{dt} = -4\pi R^2 \frac{N_c \Pi}{nc + nc_{car}} \quad (7)$$

The system of ordinary differential equations (3, 4, 6, 7) has been solved by means of the software Mathcad 14. We have used the fourth-order Runge – Kutta method.

2.3. Results of numerical simulation of the carbon nanoparticle growth

We used the above-presented physical-mathematical model and experimental results to simulate the behaviour of the main carbon particle parameters (temperature and size) and to determine the parameters of a cloud of primary soot nanoparticles.

The method for determination of parameters of carbon nanoparticles is as follows. The given system of ordinary differential equations (3, 4, 6, 7) includes two variable parameters. One of them is the number density, n , of carbon atoms responsible for the carbon vapour supersaturation degree S at a given temperature. The second parameter is the number density, N_c , of primary carbon nanoparticles (condensation centers of carbon atoms from the gas phase). These parameters have been chosen so as to satisfy the available experimental data [6]. First, the number density of carbon atoms in the mixture, which is not measured at present, has been chosen so that the maximum calculated temperature of nanoparticles would be equal to the experimentally recorded temperature (Fig. 1a). In our calculations, through subsequent variations of another unmeasured parameter – initial number density of primary carbon particles, which is a constant parameter in our model, we obtained close calculated and experimental finite size values of nanoparticles (Fig. 2b). In our calculations, experimental values of the gas mixture temperature and the pressure behind the reflected shock wave were used as initial gas phase parameters. The initial radius of a carbon particle was taken as equal to 1 nm, its initial temperature – as equal to the initial gas temperature. Modelling was performed for the 1 ms interval, since it is the characteristic time of experiments in our shock tube.

Fig. 1a and 1b illustrate the temperature and the radius of a nanoparticle calculated at different values of the parameter N_c during the process of its growth. It is seen that starting with the moment of growing a particle its temperature increases rapidly to a maximum value that exceeds the initial gas temperature. For a time period of the order of 10^{-4} s it then decreases and reaches a stationary value.

As seen from the data in Fig. 1b, during the first several tens of microseconds the radius of particles increases almost linearly, and then, as the supersaturation degree of the carbon vapour decreases, the rate of its growth decreases and by the time of $\sim 10^{-4}$ s it reaches the stationary value.

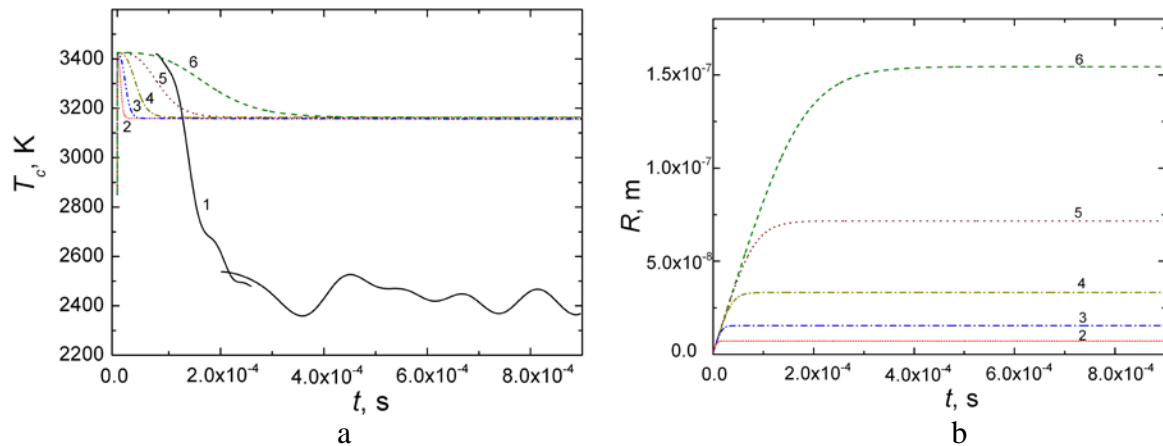


Fig. 1. Carbon nanoparticle temperature (a) and radius (b): 1 – experimental data at $T_i = 2850 - 2880$ K; calculation at N_c : 2 – 10^{18} m^{-3} , 3 – 10^{17} , 4 – 10^{16} , 5 – 10^{15} , 6 – 10^{14}

In the course of the calculations made, we managed to establish that in all experiments, the initial number density of primary carbon nanoparticles was near 10^{17} m^{-3} . Such a value of the parameter N_c allowed us to obtain in calculations the time history of the temperature of soot nanoparticles at the initial stage of its recording which is similar to the one in the experiment (Fig. 2a, but it should be noted that the cooling-down of particles began earlier than in the experiment). Moreover, at such values of the parameter N_c the calculated finite radius of carbon nanoparticles (Fig. 2b) well correlated with the carbon soot analysis data obtained using the electron microscope [6] where the average radius of nanoparticles in different experiments was $\sim 15\text{--}25 \text{ nm}$. Calculation results for the finite radius of particles and the time, t , of their growth at different initial conditions are presented in Table 1 (subscript 1). It is seen that the sizes of the particles coincide with the experimentally recorded ones, whereas the growth time, which does not exceed $30 \mu\text{s}$, is well consistent with the process time.

During the mathematical simulation we managed to reproduce the dynamics of heating of particles and their cooling. However the experimental quasi-stationary temperature of carbon particles is by several hundreds of degrees lower. As mentioned above, in calculations the cooling of particles has begun earlier. To our mind, this is due to the fact that we do not take into consideration physical-chemical changes occurring in the mixture and the important process of coagulation of nanoparticles during their growth.

It is interesting to note that our values of the carbon vapour supersaturation S are close (of one order) to its estimated maximum value, assuming that at the first stage, an ethylene molecule decays into a stable methane molecule and a carbon atom by the formula (Table 1):

$$S_{\max} = 0.5 p_{C_2H_4} / p_s(T_i), \quad (8)$$

where T_i is the initial gas temperature.

Further, we therefore performed the remodelling of the process of growth of carbon particles for the initial number density of primary carbon nanoparticles $N_c = 10^{17} \text{ m}^{-3}$ and for the supersaturation degree of carbon vapour that was maximum possible in these experimental conditions. Calculation results are demonstrated in Fig. 2. It is seen that in this case, at the initial stage of growth of carbon nanoparticles their temperature becomes still larger than the initial temperature of the gas mixture, whereas the dynamics of fall in temperature is retained, but the stationary value increases as well. In what follows, the rate of growth of particles increases slightly, which results both in increasing their finite radius by $1\text{--}6 \text{ nm}$ and in decreasing the growth time by $\sim 5 \mu\text{s}$ (Table 1, subscript 2). Now, if in one's mind, the curve for the experimentally recorded particle temperature is projected (Fig. 2), then it is well consistent with the curve for the temperature calculated at the maximum supersaturation degree of the carbon vapour before it reaches a stationary value. So our simplified model of the carbon particle growth can be useful for estimation of the parameters of the cloud of primary carbon particles.

Table 1. Calculation results of carbon particle and carbon vapour parameters at different conditions.

T_i, K	S_1	$S_{2\max}$	$n_{c1} \cdot 10^{-23}, \text{m}^{-3}$	$n_{c2} \cdot 10^{-23}, \text{m}^{-3}$	R_1, nm	R_2, nm	$t_1, \mu\text{s}$	$t_2, \mu\text{s}$
2410	$1.158 \cdot 10^6$	$4.226 \cdot 10^6$	1.6	5.8	25	24	15	15
2620	$1.038 \cdot 10^5$	$2.775 \cdot 10^5$	2.3	6.2	18	24	25	16
2850	$5.075 \cdot 10^3$	$2.221 \cdot 10^4$	1.4	5.9	15	23	30	18
3100	$1.204 \cdot 10^3$	$2.072 \cdot 10^3$	3.6	6.2	20	22	21	17
3190	$3.61 \cdot 10^2$	$9.87 \cdot 10^2$	2.3	6.2	17	23	30	25
3200	$2.42 \cdot 10^2$	$8.78 \cdot 10^2$	1.7	6.0	16	22	28	20
3270	$1.64 \cdot 10^2$	$5.34 \cdot 10^2$	1.9	6.1	16	22	29	23
3330	$1.16 \cdot 10^2$	$3.45 \cdot 10^2$	2.1	6.3	16	21	27	23
3460	67	$1.35 \cdot 10^2$	3.1	6.4	18	21	32	22

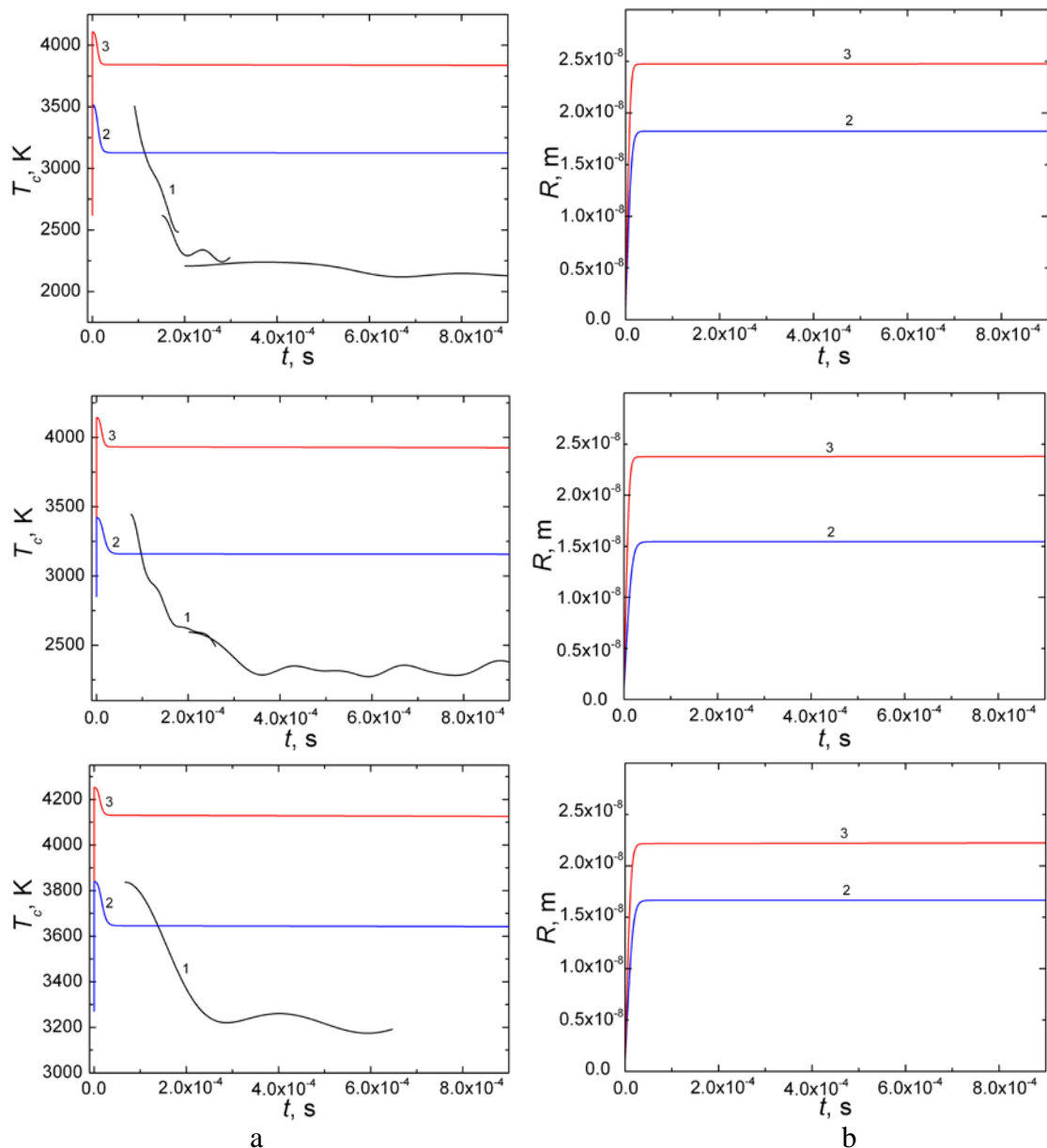


Fig. 2. Carbon nanoparticle temperature (a) and radius (b): 1 – experimental data at T_i : 2580 – 2640 K, 2850 – 2880, 3270 respectively; 2 – calculation at $N_c = 10^{17} \text{ m}^{-3}$; 3 – calculated at $N_c = 10^{17} \text{ m}^{-3}$ and maximum S

3. CONCLUSIONS

The paper presents the simple physical-mathematical model for the non-isothermal growth of carbon nanoparticles in the gas phase. It is shown that the set of experimental data for the pyrolysis of the ethylene – argon mixture in the shock tube at temperatures 2000–3500 K and pressures 7.0–11.5 atm and the mathematical model for the non-isothermal growth of a cloud of carbon nanoparticles in the gas phase allow one to estimate the number density of carbon atoms and carbon nanoparticles and to model the behaviour of the size and temperature of soot particles. These parameters at the initial pyrolysis stage are not defined.

It is of interest and significance to extend the set forth approach to the analysis of the initial formation stage of carbon nanoparticles at pyrolysis of other hydrocarbon fuels.



ACKNOWLEDGEMENT

The author thanks Penyazkov O., Fisenko S. and Kasparov K. for their help in carrying out the work.

REFERENCES

1. HAYNES, B., WAGNER, H. Soot formation. *Progress in energy and combustion science*, 1981, Vol. 7, No. 4, p. 229–273.
2. KERN, R., XIE, K. Shock tube studies of gas phase reactions preceding the soot formation process. *Progress in energy and combustion science*, 1991, Vol. 17, No. 3, p. 191-210.
3. KENNEDY, I. Models of soot formation and oxidation. *Progress in energy and combustion science*, 1997, Vol. 23, No. 2, p. 95–132.
4. BHASKARAN, K., ROTH, P. The shock tube as wave reactor for kinetic studies and material synthesis. *Progress in energy and combustion science*, 2002, Vol. 28, No. 2, p. 151–192.
5. EREMIN, A. Formation of carbon nanoparticles from the gas phase in shock wave pyrolysis processes. *Progress in energy and combustion science*, 2012, Vol. 38, No. 1, p. 1–40.
6. BARANYSHYN, Y., PENYAZKOV, O., KASPAROV, K., BELAZIORAVA, L. Soot particles characterizations at pyrolysis of ethylene in shock tube. CYSENI 2010. Proceedings of annual conference of young scientists on energy issues. [CD]. Kaunas: Lithuanian Energy Institute. 2010 May 27–28.
7. ZHIL'TSOVA, I., ZASLONKO, I., KARASEVICH, Yu., WAGNER H. Nonisothermal effects in the process of soot formation in ethylene pyrolysis behind shock waves. *Kinetics and catalysis*, 2000, Vol. 41, No. 1, p. 87–101.
8. ISHII, K., OHASHI, N., TERAJI, A., KUBO, M. Soot formation in hydrocarbon pyrolysis behind reflected shock waves. 22nd international colloquium on the dynamics of explosions and reactive systems. [CD]. Minsk. 2009 July 27–31.
9. MARTYNENKO, Y., OGNEV, L. Thermal radiation from nanoparticles. *Technical physics. The Russian journal of applied physics*, 2005, Vol. 75, No. 11, p.1522–1524.



EVAPORATIVE COOLING OF WATER IN A NATURAL DRAFT CROSS-FLOW COOLING TOWER

A. A. Brin

*A.V. Luikov Heat and Mass Transfer Institute
National Academy of Sciences of Belarus
P. Brovki str. 15, 220072 Minsk – Belarus*

ABSTRACT

The new two-dimensional mathematical model of the performance of a natural draft cross-flow cooling tower is presented. It is worth to mention that the simulation of a cross-flow cooling tower is most difficult task in compare with natural draft cooling tower because we have to combine two-dimensional description of heat and mass transfer in air flow with falling water droplets. Our model includes a positive feedback between aerodynamics of cooling tower and a rate of evaporative cooling. It takes into account the values of heat and mass transfer coefficients, temperatures, flow rate and pressure of water and meteorological conditions. The self-consistent iterative algorithm of its solution is proposed and discussed. The simulation results, which included profiles of air temperature at the rain zone, are displayed. It is shown that the main parameter, affecting on the thermal efficiency of a natural draft cross-flow cooling tower, is the average droplet radius. Also, the thermal efficiency depends on water temperature difference between inlet and outlet of cooling tower, which by-term depends on several parameters, such as flow rate through the cooling tower, air temperature, relative humidity of air, inlet water temperature. The range of change of final droplet temperatures is calculated.

Keywords: cooling tower, evaporative cooling, natural draft, simulation

1. INTRODUCTION

Cooling towers are huge and important parts of modern power plants with water flow rates 30 000 tons per hour and more. Therefore better understanding of their performance is the goal of many engineers and researchers at the field of heat and mass transfer. Evaporative cooling of water in the cooling tower depends on atmospheric conditions (temperature, humidity and wind conditions), design and geometric parameters of the tower, and total mass flow rate of water. High accuracy simulation of cooling tower performance can help correctly to choose many parameters of cooling tower. Additionally, the simulation of cooling tower performance helps significantly reduce its long and expensive testing at variable atmospheric conditions.

New approach to simulation performance of several types of cooling towers was developed in our works. In particular, this approach is applied to a natural draft cooling tower with the pack, to the simulation of performance of mechanical draft cooling towers [1, 2]. We give here the expansion of our approach to simulation of the performance of natural draft cross-flow cooling towers. We discuss the new advanced mathematical model of natural draft cross-flow cooling tower performance, the iterative algorithm of its solution and the results of its numerical simulation. It is worth mentioning that the simulation of cross-flow cooling towers is the most difficult task compared to previous performed because we have to combine two-dimensional description of heat and mass transfer in air flow with falling water droplets. The sketch of the natural draft cross-flow cooling tower is shown in Fig. 1.

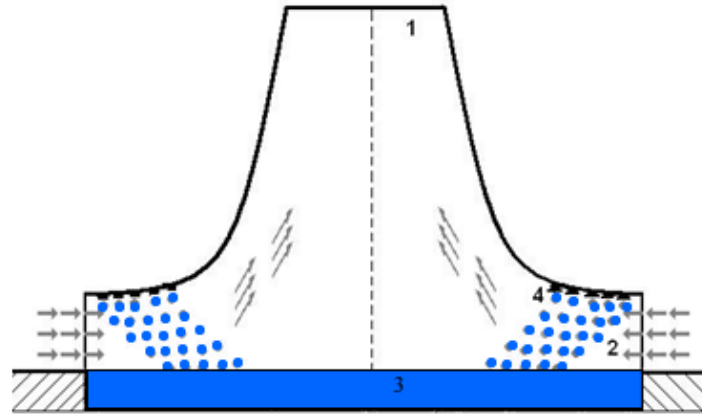


Fig. 1. The sketch of the cross-flow cooling tower: 1 – cooling tower orifice, 2 – cooling tower window, 3 – water collecting pond, 4 – spray system; area with blue droplets is so called rain zone

We assume that a wind velocity is smaller than the inlet velocity of air, so we can use the cylindrical symmetry for the description of the air flow. Our mathematical model solves the boundary value problem for two partial differential equations (PDE) and the coupled system of ordinary differential equations (ODE). The system of PDE describes large-scale turbulent heat transfer and water vapour transfer of diffusion type at vertical direction in the rain zone of the cooling tower. The system of ODE describes the process of evaporative cooling of the monodisperse ensemble of water droplets, which falling in cross-flow of air. Use limits of monodisperse approximation for description of an ensemble of droplets were investigated in [1].

We substantially use our earlier results [1, 2], verified with experimental ones [3]. Following our general approach we describe the aerodynamics of a cooling tower at the integral approximation. Air flow is turbulent therefore we use the effective values for the diffusion coefficient of water vapour in air and for the heat conductivity coefficient of moist air, which are based on experimental results [4]. To obtain the solution of our non-linear mathematical model we use the iterative procedure. Usually it takes only three iterations for the convergence of the heat and aerodynamic parts of the solutions.

For description of cooling tower performance we use effective dimensionless parameter, so called the thermal efficiency of cooling tower η :

$$\eta = \frac{T_{w0} - T_{pool}}{T_{w0} - T_{lim}}, \quad (1)$$

where T_{w0} – inlet water temperature, T_{pool} – average temperature of water in the cooling tower pool, T_{lim} is the limiting temperature of evaporative cooling, which is determined from the equation $\rho_s(T_a) \cdot \psi = \rho_s(T_{lim})$, ψ – humidity of air. It is worth to note that the limiting temperature of evaporative cooling T_{lim} is equal to the temperature of the wet-bulb thermometer, and it is important that the thermal efficiency of cooling tower η practically does not depend on the humidity surrounding cooling tower air.

2. MATHEMATICAL MODEL

The system of PDE describing heat and mass transfer in the rain zone of the cross-flow cooling tower includes the equations for the temperature field of gaseous mixture and for the field of the number density of water vapour. The equation for the temperature field $T_a(r, z)$ of the moist air is:

$$u_a \frac{\partial T_a}{\partial r} = \frac{\lambda_a}{\rho_a c_a} \frac{\partial^2 T_a}{\partial z^2} + I_t, \quad (2)$$

where u_a – average velocity of air flow, T_a – temperature of the vapour-air mixture, λ_a , ρ_a , and c_a – coefficients of air heat conductivity, density of the vapour-air mixture and specific thermal capacity of air, respectively, r – radial coordinate, z – vertical coordinate, $I_t = 4\pi R_d^2 N_d \alpha(\text{Re})(T_w - T_a)$ – heat source. For moist air the efficient (turbulent) heat conductivity λ_a , based on experimental data, is expressed as $\lambda_a = 0.04\lambda_{\text{am}} \text{Re}_h^{0.8}$, where λ_{am} – molecular heat conductivity coefficient of the moist air, the (turbulent) Reynolds number for air flow is defined as $\text{Re}_h = \rho_a h u_a / \mu_a$, where h – height of inlet window of the cooling tower, N_d – number of droplets per unit of volume, depending on droplet velocities and their initial density.

The equation for the number density of water vapour $n(r, z)$ in the rain zone is:

$$u_a \frac{\partial n}{\partial r} = D \frac{\partial^2 n}{\partial z^2} + I_n, \quad (3)$$

where D – effective (turbulent) coefficient of diffusion, $I_n = 4\pi R_d^2 N_d \gamma(\text{Re})(n - n_s)$ – diffusion source. For moist air the Lewis number Le has the constant value about one for all the Reynolds numbers, where $\text{Le} = \lambda / \rho c D$. Therefore for self-consistency we accept that the effective diffusion coefficient D is determined by the following expression, which has the same structure as the expression for the turbulent heat conductivity, $D = 0.04 D_m \text{Re}_h^{0.8}$, where D_m is the molecular diffusion coefficient of water vapour in air.

For droplets the Reynolds number Re is defined as following: $\text{Re} = 2\rho_a R_d v_1 / \mu_a$, where ρ_a – density of air, R_d – droplet radius, μ_a – air viscosity, v_1 – absolute velocity of falling droplets which is defined by the expression $v_1 = \left((v_r - u_a)^2 + v_z^2 \right)^{0.5}$, where v_r and v_z are radial and vertical components of the droplet velocity.

The equation for the droplet growth, based on mass conservation law for droplet is:

$$\frac{dR_d}{dl} = - \frac{\gamma(\text{Re})(\rho_s - \rho)}{\rho_w v_1}, \quad (4)$$

where dl – element of a droplet trajectory, ρ and ρ_s are mass densities of the vapour and saturated vapour at given temperature, ρ_w – mass density of water, $\gamma(\text{Re})$ – mass transfer coefficient, depending on the Reynolds's number: $\gamma(\text{Re}) = D_m (2 + 0.5 \text{Re}^{0.5}) / 2R_d$.

The equation for the changing of falling droplets temperature along their trajectory is:

$$\frac{\partial T_w}{\partial l} = \frac{3 \left[\alpha(\text{Re})(T_a - T_w) + \gamma(\text{Re})(U - c_w T_w)(\rho_s - \rho) \right]}{c_w \rho_w R_d v_1}, \quad (5)$$

where T_w – temperature of the water droplets, U – specific latent heat of the evaporation of water, c_w – specific heat capacity of water, $\alpha(\text{Re})$ – heat transfer coefficient, depending on the Reynolds number $\alpha(\text{Re}) = \lambda_{\text{am}} (2 + 0.5 \text{Re}^{0.5}) / 2R_d$.

The equation for change of droplet velocity along the trajectory is:

$$\frac{dv_1}{dl} = \frac{g}{v_1} - C(\text{Re}) \frac{\rho_a \left(v_z^2 + (v_r - u_a)^2 \right)^{0.5}}{2v_1} \frac{\pi R_d^2}{m}, \quad (6)$$

where m – mass of the droplet, $C(\text{Re})$ – drag coefficient [1]. In the cylindrical systems of coordinates, related with the symmetry axes of the cooling tower, the equation for change of droplet velocity along radial direction r is:

$$\frac{dv_1}{dr} = -C(\text{Re}) \frac{\rho_a (v_r - u_a)}{2} \frac{\pi R_d^2}{m}. \quad (6')$$

The equation for change of droplet velocity along vertical coordinate z is:

$$\frac{dv_1}{dz} = \frac{g}{v_z} - C(\text{Re}) \frac{\rho_a v_z}{2} \frac{\pi R_d^2}{m}. \quad (6'')$$

The boundary conditions for the system of the differential equations (2)–(6) (for the droplets at $z = h$) have the following values: inlet radiuses $R_d|_{z=h} = R_{d0}$, inlet water temperature $T_w|_{z=h} = T_{w0}$, inlet velocity of droplets $v|_{z=h} = v_0$. For gaseous mixture (for $z = h$) we have the condition that air temperature is equal to inlet water temperature $T_a|_{z=h} = T_{w0}$, the condition that the density of water vapour is equal to the density of saturated vapour at the inlet water temperature $\rho|_{z=h} = \rho_s(T_{w0})$. For $z = 0$ we have $T_a|_{z=0} = T_{wp}$, where T_{wp} – surface temperature of water in the pool, $\rho|_{z=0} = \rho_s(T_{wp})$. Inlet air is characterized by the temperature T_{a0} and by the relative humidity ψ_0 . For simulation we convert relative humidity to the corresponding number density of water vapour. We neglect the processes of breaking and coagulation of droplets, therefore there is the law for the conservation of the number of droplets along the trajectory:

$$N_0 v_0 = N_d v_d, \quad (7)$$

where N_0 and v_0 are, correspondingly, initial number of droplets per unit of volume and droplet velocity. Following the expression (7) we can assume that increasing droplet velocity leads to decreasing the number density of droplets. Immediately we have important conclusion that at lower part of the rain zone air flow should be less heated and less moistened.

3. RESULTS

We present numerical results for the cross-flow cooling tower with following parameters: height $H = 80$ m, inlet radius $R_{in} = 40$ m, outlet radius $R_{out} = 20$ m, height $h = 10$ m and length $l = 10$ m of the cooling tower window. For these parameters our mathematical model gives that the inlet velocity of air is about 2.6 m/s, so we assume the velocity of a ground wind is smaller than this value. For all results below we assume that the initial air temperature is 25 °C, and relative humidity is equal to 60 %. The influence of atmospheric condition was investigated carefully at our previous publications [1–3], therefore below we conduct simulation for the same atmospheric conditions. It is worth to note that for one millimetre size droplets and parameters of the cooling tower described above, the contributions of turbulent heat and mass transfer are weak compared to direct impact of evaporative cooling of droplets.

The change of droplets radius is presented in Fig. 2. Curves 1 and 2 show dependence of the droplet evaporation droplet on its vertical position at the inlet of rain zone. The initial droplet radius was used as the scale at the transition to dimensionless values.

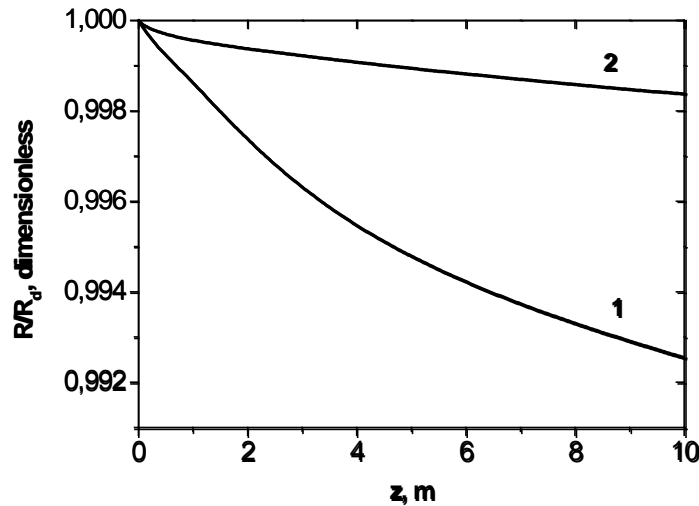


Fig. 2. Change of dimensionless droplets radius along vertical position:
 1 – $R_d = 1$ mm, 2 – $R_d = 1.5$ mm

The change of temperature of falling droplet is presented in Fig. 3.

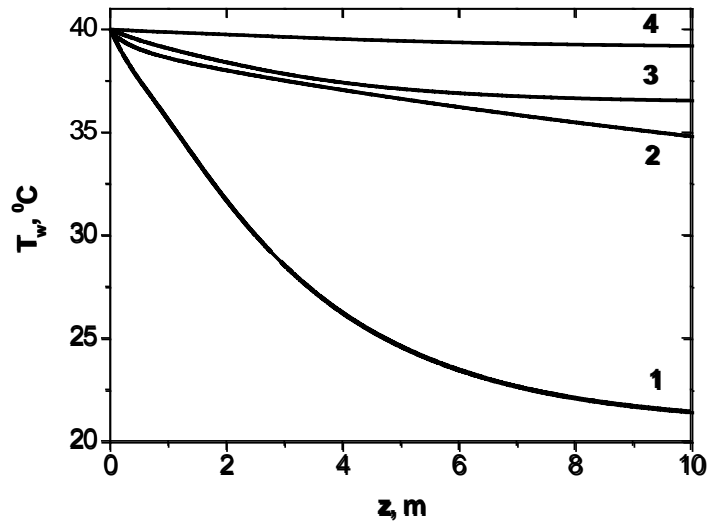


Fig. 3. Change of droplets temperature T_w along vertical position:
 1 and 3 – $R_d = 1$ mm, 2 and 4 – $R_d = 1.5$ mm

Curves one and two describe droplets at the inlet of the rain zone, curves three and four describe droplets at the outlet of the rain zone. There are two important effects: effect of droplet size and effect of position of evaporative cooling at the rain zone. The minimal droplets radius is limited by the spray design, water pressure at supplying system and conditions that all droplets will fall to collecting pond of cooling tower. Conditions for evaporative cooling of droplets differ significantly in the rain zone of cross-flow cooling tower. The main reason is the heated air at the top part of the rain zone and its increasing humidity.

The temperatures of moist air for three different heights h in the rain zone of cooling tower for droplets with initial radius 1 mm are presented in Fig. 4. The fast heating of upper part of air flow, where the temperature and residence time of droplets are much larger than at the bottom, is obvious.

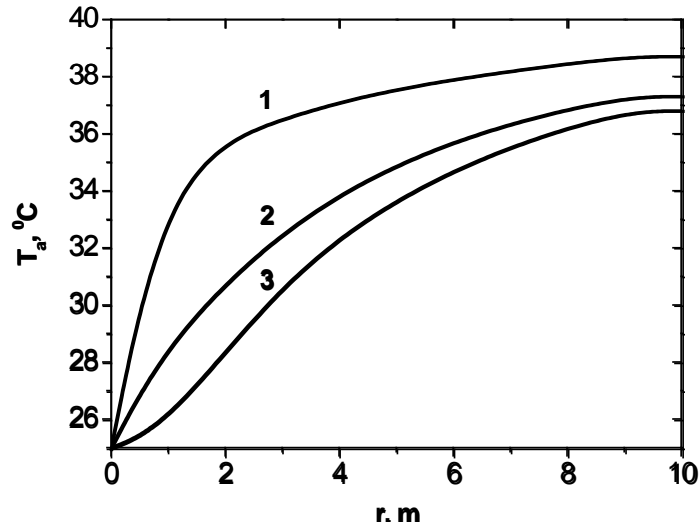


Fig. 4. Vapour-air mixture temperature T_a along the rain zone:
1 – $h = 1$ m, 2 – $h = 4$ m; 3 – $h = 7$ m

Behaviour of air temperature at the lower part of the rain zone is the manifestation of decreasing of contribution from falling droplets. The main physical reason is that the increasing of droplet velocity leads to decreasing of the number density of droplets, according to the continuity equation. The second factor is decreasing of residence time. Increasing of transfer coefficients does not compensate these factors.

4. CONCLUSIONS

The new advanced mathematical model of natural draft cross-flow cooling tower which includes partial and ordinary differential equations is presented. The specific of cooling towers of such type is two-dimensional character of heat and mass transfer processes in the rain zone. The characteristic spatial scale of the evaporative cooling defines by the droplet radius R_d , the characteristic spatial scale of the aerodynamic process is about the height of inlet window H . Typical estimation of the ratio H/R_d is about 10^4 , therefore we use detailed description of evaporative cooling of falling droplets and only integral description of convective flow of moist air in the cooling tower.

5. REFERENCES

1. FISENKO, S.P., BRIN, A.A., PETRUCHIK, A.I. Evaporative cooling of water in a mechanical draft cooling tower. *International Journal of Heat and Mass Transfer*, 2004, Vol. 47, p. 167–177.
2. FISENKO, S.P., PETRUCHIK, A.I. Towards to the control system of mechanical draft cooling tower of film type. *International Journal of Heat and Mass Transfer*, 2005, Vol. 48, p. 31–35.
3. PETRUCHIK, A.I., SOLODUKHIN, A.D., STOLOVICH, N.N., FISENKO, S.P. Toward the analysis of experimental data on thermal efficiency of evaporative cooling tower. *Applied Energy: Russian Journal of Fuel, Power and Heat Systems*, 2000, Vol. 37, № 6, p. 142–149.
4. ZHUKAUSKAS, Algirdas A. *High-Performance Single-Phase Heat Exchangers*. Hemisphere Publishing Corporation, 1989. 515 p.

SUPPLY WATER PARAMETERS INFLUENCE ON INDIRECT EVAPORATIVE AIR COOLING (IEAC) THERMAL PERFORMANCE

G. Frīdenbergs, A. Lešinskis

*Riga Technical University
Azenes street -16/2nd floor, LV-1010 – Latvia*

ABSTRACT

This paper reported a review, calculations and measurements based on study of working water flow parameters influence on the Indirect Evaporative Air Cooling (IEAC) thermal performance. It was considered from a multiple aspects of previous researches of concept, system configuration, operational mode and industrialization, as well as the future focuses and commercialization. Calculation model has been obtained from the governing equations of heat and mass transfer in primary and secondary air and water flows. Parameters of water affecting on evaporative cooling performance such as mass flow rates and flow configuration have been obtained. Model was validated against theoretical data from the literature and good agreement between the prediction and measurement was achieved. The calculated results show that closed cycle working water flow characteristics affect supplied air parameters less than 4 %. It affects cooling efficiency, which mostly depends on mass flow rates ratios of primary and secondary air flows and spacing between plates of wet and dry passages.

Keywords: IEAC, air cooling, working water flow influence, thermal performance, heat and mass transfer

1. INTRODUCTION

To determine the parameters experimental stand device was studied (Fig. 1). The two main discovered parameters influencing on cooling performance are water consumption and water exchange cycle [1].

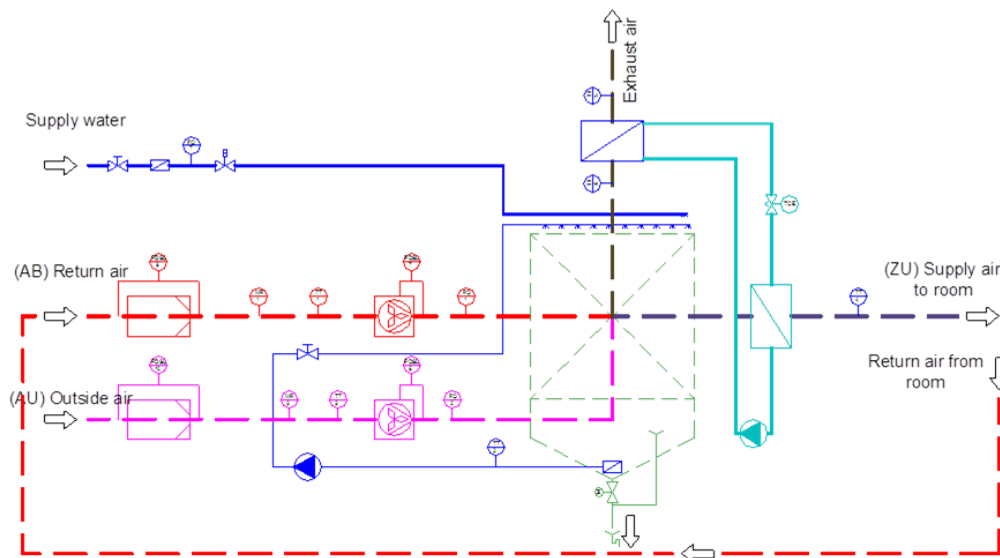


Fig.1. Practical model of studied device [2]

1. The water consumption of evaporative air conditioners includes the water evaporated to provide the cooling effect.
2. Water exchange cycle – is water dumped off with predicted period of time for the purpose of cleaning and avoiding high salt concentration.

2. WATER EVAPORATION

The psychrometric chart in Fig. 2 illustrates the evaporation process (blue line) when air passes through the wet side of indirect evaporative air conditioner. At given entry air conditions (t_1, t'_1) and evaporation effectiveness (ε_e), the dry-bulb temperature of the leaving air (t_2) can be calculated according the Eq. 1. In ideal conditions the wet-bulb temperature of the leaving air is the same as the wet-bulb temperature of the entering air. Then the humidity ratios of both entering and leaving air can be determined from the psychrometric chart (Fig. 1). The water consumption rate for cooling purpose can be estimated using Eq. 2 [3, 4, 5].

$$t_2 = t_1 - \frac{\varepsilon_e}{100} \times (t_1 - t'_1) \quad (1)$$

$$\dot{m}_e = \rho \dot{V} (w_2 - w_1) / 1000. \quad (2)$$

Where \dot{m}_e – water consumption rate, kg/h; \dot{V} – air volumetric flow rate, m³/h; ρ – air density, 1.2041 kg/m³; w_1, w_2 – humidity ratios of entering and leaving air, g moisture/kg dry air.

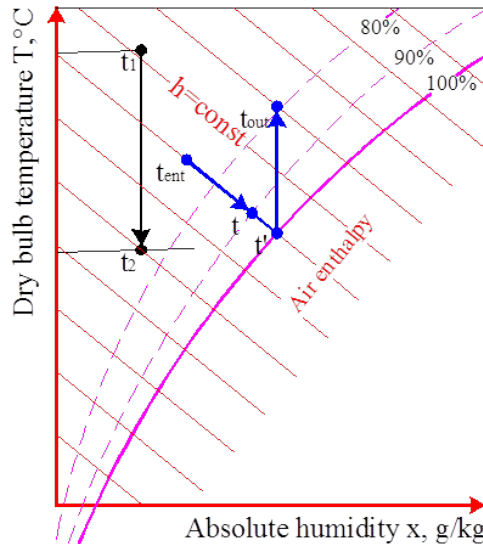


Fig. 2. Psychrometrics of two-stage evaporative cooler [2]

The water consumption rate due to evaporation varies depending on the air flow rate, the temperature and humidity of the outside air and the pad characteristics. Some manufacturers quote indicative figures for water consumption but these can only be used as approximate values. In an effort to provide independent values of the water required for evaporation, the water consumption rates for cooling purposes can be calculated in different locations. The design temperature and humidity can be based on typical historical data and be used to represent the maximum cooling conditions [6].

Furthermore, the amount of water consumption for cooling purpose has been calculated based on hourly weather conditions in a typical hot day and a typical summer day from one available climate data source in Riga, Latvia: (Table 1) data supplied by METEO [6]. It is assumed that cooling to be switched on at full speed during hours when the outside temperature exceeds 27 °C and represents the maximum water consumption on those days in the calculation. The total water consumption and the average consumption rate of the typical summer day are shown in Table 1.

Table 1. Evaporated water consumption in typical days in Riga

Location	Period requires cooling	Total daily water consumption (L/day) for random various air flow rates		Average hourly water consumption rate (L/hr) for random various air flow rates	
		9360(m ³ /h)	16200(m ³ /h)	9360(m ³ /h)	16200(m ³ /h)
Riga typical summer day	10:00am~19:00pm	481.5	833.3	48.1	83.3
	11:00am~20:00pm	538.8	932.5	53.9	93.3

The water consumption rate for cooling purposes is dependent on the humidity ratio difference of the entering and leaving air and the air flow rate. The sizes selected in Table 1 are based on maximum cooling requirements on the hottest part of the day. Typically, the fan utilised in residential evaporative air conditioners has a variable speed and runs on low speeds for the majority of operating time. The evaporated water consumption in Table 1 was calculated based on the maximum fan speed, thus it should be considered as overestimates.

3. WATER EXCHANGE CYCLE

3.1. Modelled device

The cell element selected for numerical analyses (Fig.3.) is shown in Fig. 4. The element consists of half the height of the dry channel, the plate wall and half the height of the wet channel. Energy balance equations were applied to each single element, with consideration of a pre-set boundary condition. This allowed the temperature and humidity distribution across the dry and wet channel sections to be established.

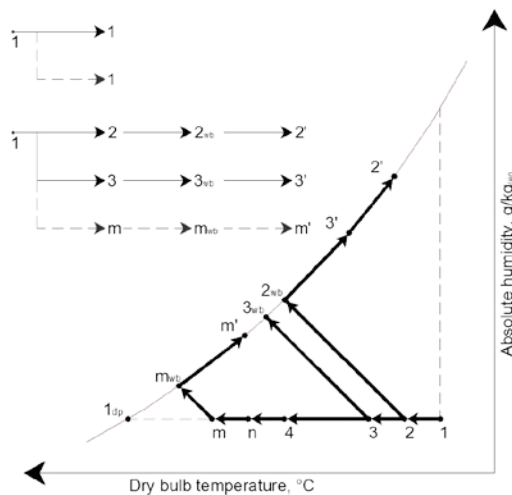


Fig. 3. Selected IEAC cooler operation cycle in H-x diagram [2]

To simplify the modelling process and mathematical analysis, the following assumptions were made:

1. The heat and mass transfer is in steady state. The IEAC enclosure is considered as the system boundary [7].
2. The wet surface of the fibre-sheet is completely saturated. The water vapour is distributed uniformly within the wet channel.

3. A temperature gradient for the channel cross-section was set to zero. Heat transfer in the separating plate is considered in the vertical direction only. Within the working fluid, the cross-stream convective heat transfer is considered as the dominant mechanism of heat transfer.

4. Each element has a uniform wall surface temperature. An analysis carried out by Zhao et al. [7] showed that the thermal conductivity of the plate wall has a little impact on the magnitude of the heat and mass transfer rates, due to its small thickness (0.24 mm). The temperature difference between dry and wet sides of the wall can be ignored.

5. Air is treated as an incompressible gas.

The mass balance in the wet channel can be expressed by Eq. 3 [7]:

$$\left(\frac{\dot{m}_{a,f2}}{2}\right) dw_{a,f2} = h_m(\rho_{w,a2} + \rho_{a,f2}) \quad (3)$$

Where $\dot{m}_{a,f2}$ – air mass flow rate, kg/s

$w_{a,f2}$ – humidity ratio of moist air, kg/kg dry air

h_m – mass transfer coefficient, m/s

ρ – density, kg/m³

The general energy balance within the element in Fig. 4 can be expressed as Eq. 4 [2,7]:

$$dQ_1 = dQ_1 + dQ_2 \quad (4)$$

Where Q – heat flux, W/m²

The energy balance in dry passages – dry passage air involves the forced convective heat transfer, leading to change of the enthalpy of the air. Energy balance in a dry passage could be written as Eq. 5:

$$dQ_1 = h_1(t_{a,f1} + t_w)dA = \left(\frac{\dot{m}_{a,f1}}{2}\right) di_{a,f1} \quad (5)$$

Where A – heat transfer area, m²

i – specific enthalpy of air, J/kg

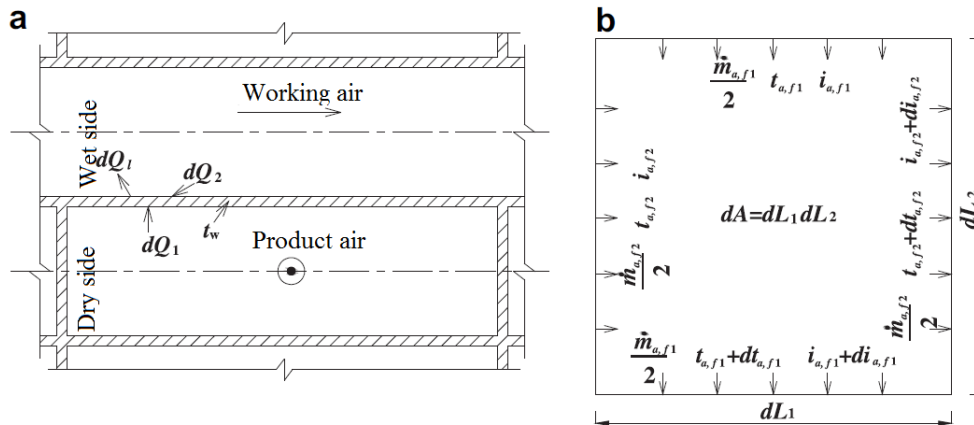


Fig. 4. Cell element (a) applied for numerical simulation, differential illustration (b)

The energy balance in wet passages – wet passage air involves the forced heat and mass exchange, which leads to a change of enthalpy of the air within the passages. The energy balance within the passages can be written as Eq. 6:

$$dQ_1 - dQ_2 = \left(\frac{\dot{m}_{a,f2}}{2}\right) dw_{a,f2} \quad (6)$$

where, for the forced convective heat and mass transfer occurring in the wet passages respective Eq. 7 and Eq. 8 can be written [8]

$$dQ_2 = h_2(t_{a,f2} + t_w)dA \quad (7)$$

$$dQ_1 = (\rho_{w,a2} + \rho_{a,f2})\gamma dA \quad (8)$$

The air flow within the pipes remains in a laminar flow state when $Re_D < 2300$ and becomes turbulent flow when $Re_D > 4000$. Due to the passage size and air velocity, the air flow within the passage is considered to be laminar. In this case, the thermal entry length for laminar flow can be calculated as follows (Eq. 9) [5, 9, 10]:

$$\frac{L}{d} = 0.05Re \cdot Pr \quad (9)$$

For both entry region and fully developed flow conditions, the Nusselt number can be calculated using the following equation 10 [11]:

$$Nu = 1.86 \left(\frac{Re \times Pr}{\frac{L}{d}} \right)^{1/3} \left(\frac{\eta_{a,f}}{\eta_{w,a}} \right)^{0.14} \quad (10)$$

The thermal entrance Nusselt numbers are higher than those for the fully developed case. For the developing flow conditions in the entry region, the Nusselt number can be calculated as presented below by Eq. 11 [7, 11]:

$$Nu = 3.66 + \frac{0.0688 - Re - Pr \left(\frac{d}{L} \right)}{1 + 0.04 \left[Re - Pr \left(\frac{d}{L} \right) \right]^{2/3}} \quad (11)$$

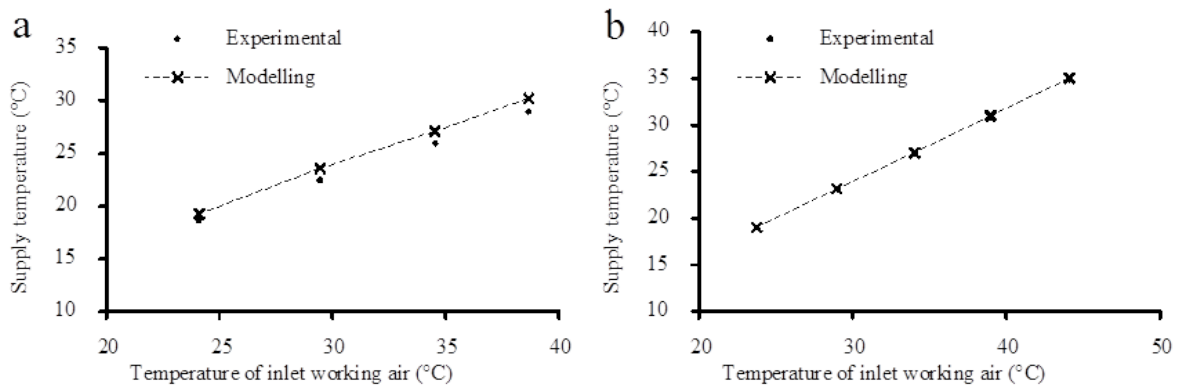


Fig. 5. Experimental validation of supply air temperature. (a) Case 1. (b) Case 2

Case 1 and Case 2 was modelled at constant air flow rate $150 \text{ m}^3/\text{h}$ (to compare with C. Zhan past calculations [5]) and dry bulb 25 till $40 \text{ }^\circ\text{C}$. In Case 1 $RH=35\%$, in Case $RH=50\%$, that is main difference.

The mass transfer coefficient between wet passage air flow and the wet surface of the wall may be calculated using the following 12 equation [12]:

$$\frac{h}{h_m} = \rho c_p Le^{2/3} \quad (12)$$

The mathematical expression for wet-bulb effectiveness ε_{wb} can be written as follows (Eq. 13) [18]:

$$\varepsilon_{wb} = \frac{t_{db,wk,in} - t_{db,su}}{t_{db,wk,in} - t_{wb,wk,in}} \quad (13)$$

The theoretical energy efficiency coefficient of performance (**COP**) of the system can be defined as the ratio of cooling capacity and fan power consumption [7, 12, 13]:

$$COP = \frac{\Phi_0}{P} \quad (14)$$

Cooling capacity (Φ_0) can be expressed as Eq. 15 [14, 15]:

$$\Phi_0 = m_{pt}(i_{wk,in} - i_{wkpt,in}) \quad (15)$$

Where m_{pt} – product air mass flow rate, kg/s
 $i_{wk,in}$ – specific enthalpy of inlet working air, J/kg
 i_{pt} – product air enthalpy, J/kg

The theoretical fan power (P), can be written as Eq. 16 [5]:

$$P = \Delta p_{wk} V_{wk} + \Delta p_{pt} V_{pt} \quad (16)$$

Where Δp_{wk} – working air pressure loss, Pa
 V_{wk} – working air flow rate, m³/s
 Δp_{pt} – product air pressure loss, Pa
 V_{pt} – product air flow rate, m³/s

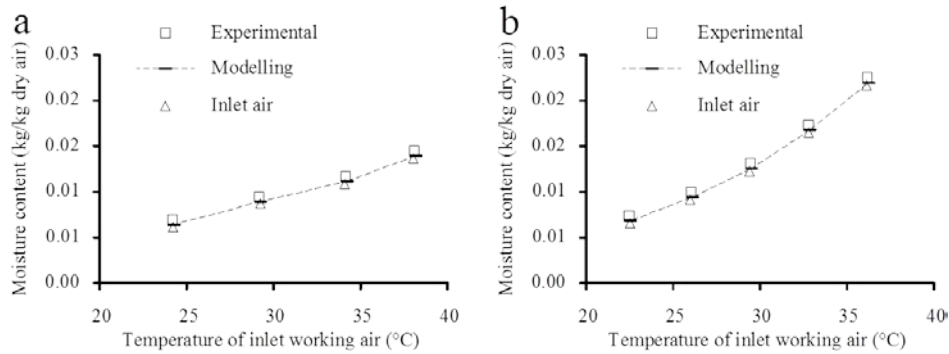


Fig. 6. Experimental validation of supply air moisture content in case 1 (a) and case 2 (b)

It should be emphasized that the energy efficiency obtained from the simulation is an ideal value, which involves use of the theoretical fan power. Actual fan power will be 120–170 % of the ideal value, leading to a drop in the calculated efficiency by 60–80 % [15]. It should be noted that in this paper all the subsequent figures related to COP are ‘ideal’ rather than ‘practical’ values [16].

3.2. Results

The result of the calculation is determined the temperature distribution of the heat exchanger plates, which then will explore the heat transfer across the heat exchanger volume, as well as allow for the calculation of geometrical effects on the final parameters. Below (Fig. 7) are presented three parameters calculation visualization graphs. The more accurate the data needed for further research.

For this operating condition, the temperature profiles of dry, wet air and the exchanging wall are presented in Fig. 7 a, b, c, the heat flux in Fig. 7 a, b, c, it can be seen that the temperature of supply air in dry channels decreases along its direction of flow, and the temperature of working air in the dry channels.

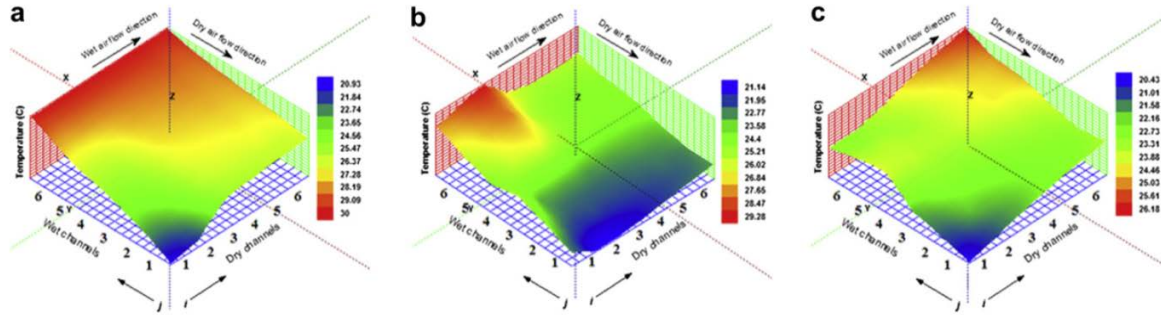


Fig. 7. Temperature distribution across the heat exchanger plate dry side (dry passages) (a), wet side (wet passages) (b) and wall (c)

As shown in Fig. 8 a, the convective heat transfer decreases along the flow path of dry air as a result of the observed (see Fig. 9 a and c) decrease in the temperature difference between the dry channel air and the wall. The heat transfer rate in dry channels is higher if they have bigger air mass flow rates [16-21]. Referring to Fig. 8 b, the wet air is not initially saturated and has a higher temperature than the wet wall close to the entrance of the wet channels (comparison of Fig. 7 b and c). These results in heat being transferred to the water reserved on the wet side of the wall leading to the evaporation of the water. After travelling to a critical point, the temperature of wet air is lower than that of the wet wall, so the convective heat flux has become negative (as shown in Fig. 8 b), this means that the wet air picks up both sensible and latent heat from the wall.

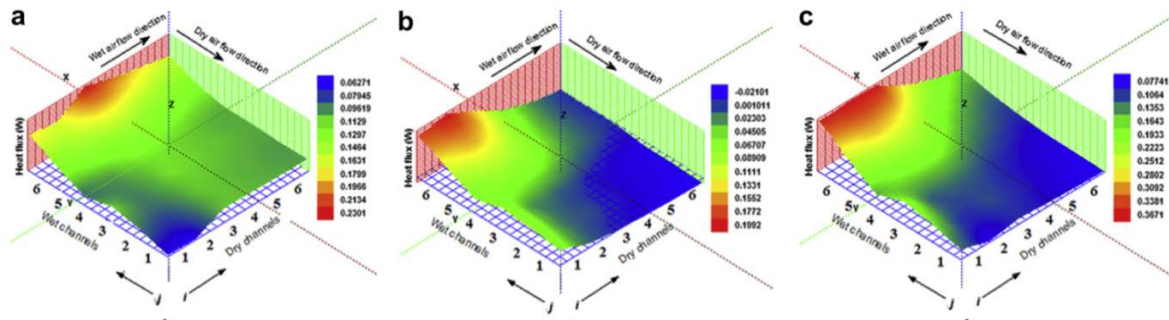


Fig. 8. Heat transfer rate across the heat exchanging plate dry (a), wet (b) side and on the wall (c)

The supply air temperature and the return air temperature just behind the first part of the heat exchanger were in good agreement with the measured data. The model underestimated the temperature of the exhaust air because it does not take into account the fact that the return air is heated by the recirculated water in the second part of the heat exchanger (Fig. 9).

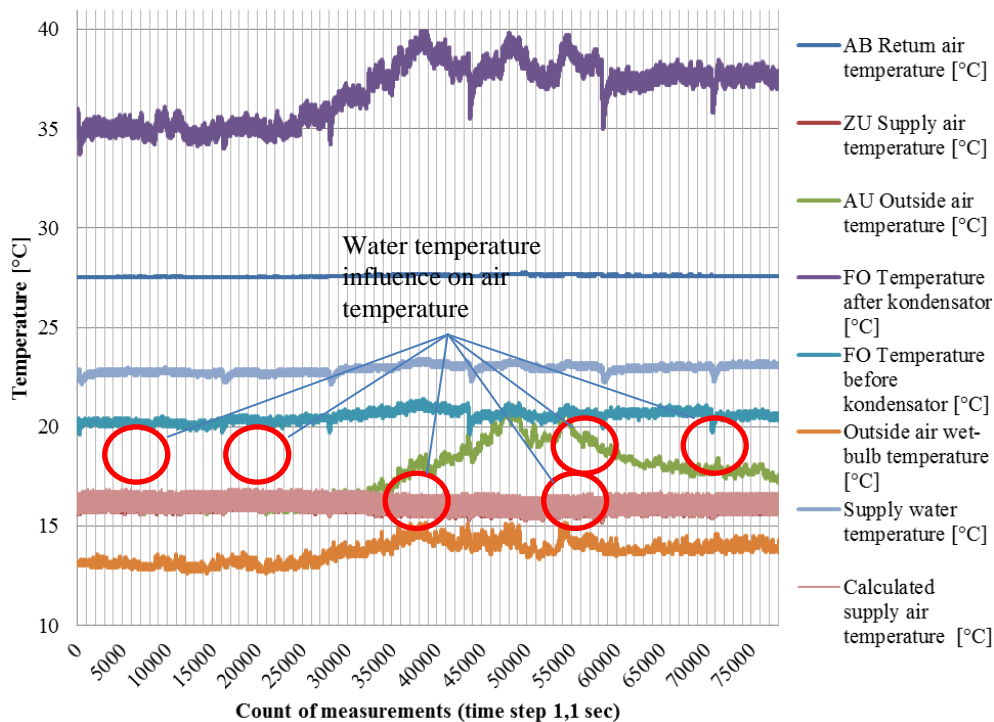


Fig. 9. The observed and calculated water temperature fluctuations on IEAC heat exchanger

CONCLUSIONS

Comparing the two major components of water usage in evaporative air conditioners (water used for the cooling effect and water dumped/bled off), it may be concluded that if the water bleeding/dumping system is well designed, set and maintained, the total water consumption will be largely dominated by the moisture evaporation which is essential in operating the evaporative cooler. However, if not properly adjusted, the water bleeding/dumping rate is of the same order of magnitude as the evaporation rate and can lead to considerable wastage of valuable water.

In this context, it is important to compare the water consumption of evaporative air conditioners with total domestic water consumption. Latvian households consumed on average 48 m³ of water per inhabitant in 2008, 46 m³ in 2009, 47 m³ in 2010 but for example in 1990 it was about 85 m³ of water per inhabitant [22]. The recent water saving efforts have reduced these values. Latvia has one of largest water resources per capita in Europe. That is reason why water consumption have not restrictions for IEAC installing in Latvia region.

REFERENCES

1. SUPPLE, R.G., BROUGHTON, D.R., "Indirect evaporative cooling – Mechanical cooling design", ASHRAE Transactions, Vol. 91, Part 1B – 1985. – p. 319–328.
2. FRĪDENBERGS, G., LEŠINSKIS, A., *Evaluation of indirect evaporative cooler in public buildings*, RTU, 2012 – p. 6–48.
3. HASAN A, SIREN K. *Theoretical and computational analysis of closed wet cooling-towers and its applications in cooling of buildings. Energy and Buildings* – 2002 – p. 34.
4. KALS WA. *Wet-surfaces air coolers*, Chemical Engineering – 1971. – p. 68.
5. Zhiyin D, CHANGHONG Z, ZHAN C, RIFFAT SB. *Indirect evaporative cooling: Past, present and future potentials*, Renewable and sustainable energy reviews – 2012. – p. 1–28.



6. Latvijas Metroloģijas centra data base [referred on the 3th of January in 2012 y.]. <www.meteo.lv/pdf_base/meteor_2009.html>
7. ZHAO X, DUAN Z, ZHAN C, RIFFAT SB. *Dynamic performance of a novel dew point air conditioning system for the UK climate*. International Journal of Low Carbon Technology 2009.
8. HALASZ, B., *A general mathematical model of evaporative cooling devices*, Rev. Gén. Therm., FR, Vol. 37 – 1998. – p. 245–255.
9. COSTELLOE B, FINN D. *Indirect evaporative cooling potential in air e water systems in temperate climates*. Energy and Buildings, 2003.
10. SETHI VP, SHARMA SK. *Survey of cooling technologies for worldwide agricultural greenhouse applications*. Solar Energy, 2007.
11. CERCI Y. *A new ideal evaporative freezing cycle*. International Journal of Heat and Mass Transfer 2003 – p. 1–11.
12. PARKER RO, TREYBAL RE. *The heat-and-mass transfer characteristics of evaporative coolers*, Chemical Engineering Progress Symposium Series – 1961 – p. 57.
13. PETERSON JL. *An effectiveness model for indirect evaporative coolers*, ASHRAE Transactions – 1993. – p. 99.
14. CIBSE KNOWLEDGE SERIES: *sustainable low energy cooling: an overview*. Plymouth PL6 7PY, UK: Latimer Trend & Co. Ltd, 2005.
15. STABAAT, P., MARCHIO, D, *Simplified model for indirect-contact evaporative cooling-tower behaviour*, Applied Energy 78 (2004), - 2003 – p. 433–451.
16. MACLAINE-CROSS, I. L., BANKS, P. J., *A general theory of wet surface heat exchangers and its application to regenerative evaporative cooling*, Journal of Heat Transfer, Vol. 103, No. 3, – 1981. – p. 579–585.
17. MCCLELLAN, C. H., *Estimated temperature performance for evaporative cooling systems in five locations in the United States*, ASHRAE Transactions, 94 (2), – 1988. – p. 1015–1090.
18. MIZUSHINA RIT, MIYASHITA H. *Characteristics and methods of thermal design of evaporative coolers*, International Chemical Engineering – 1968 – p. 3–8.
19. MIZUSHINA RIT, MIYASHITA H. *Experimental study of an evaporative cooler*, International Chemical Engineering 1967. – p. 4–7.
20. NIITSU Y, NAITO K, ANZAI T. *Studies on characteristics and design procedure of evaporative coolers*, Journal of SHASE, Japan – 1969. – No.7 – p. 12–23.
21. SCHIBUOLA, L., *High-efficiency recovery for air-conditioning applications in a mild climate: a case study*, Applied Thermal Engineering, Vol. 17, No. 5 – 1997. – p. 447–454.
22. Rīga's municipal government's corporation "Rīgas Ūdens" data base [referred on the 4th of April in 2013 y.]. <<https://www.rigasudens.lv/par-uznemumu/vesture/>>



CONTRIBUTIONS TO THE FLUID DYNAMICS AND PHASE TRANSITIONS AT LOW TEMPERATURES

G. Gubceac, F. Paladi, A. Barsuk

State University of Moldova

A. Mateevici str. 60, Chisinau MD-2009 – Moldova

ABSTRACT

The parametric modelling of phase transitions and analysis of the role of an intermediate liquid state in irreversible relaxation processes at low temperatures were performed. As an example, one can consider the systems with two stable states ($L1$ and C that means liquid and crystalline, respectively, and the third one – intermediate fluid state, namely $L2$). Such $L2$ state has been experimentally discovered in supercooled liquids. The models include one order parameter and three control parameters in the Landau-type kinetic general potential of 6th degree, and have been developed to study the impact of both asymmetry (heterogeneity) and external field on phase transitions in the presence of an intermediate fluid state. First of all, the intrinsic dynamics are studied, and the mean transition time is calculated. We noticed that the presence of the intermediate liquid state may indeed enhance the nucleation rate, and, furthermore, an increase in the heterogeneity of system accelerates the transition dynamics, while the presence of an external field would increase the mean transition time. In the previous work, analytical solutions were also obtained according to the Descartes-Euler method for solving polynomial equations. Depending on the values of its control parameters, the potential has one, two or three possible minima, and the problem dealt with the construction of the equilibrium phase diagrams. It is also worth mentioning that the presently obtained results are general and suggest a complete set of different transition scenarios in the entire parameter plane.

Keywords: fluid dynamics, phase transitions, relaxation time

1. INTRODUCTION

The theory of phase transitions in supercooled liquids and glasses based on the cluster concept, and taken into account the recent discovery of the generation and extinction of crystal nuclei in supercooled liquids at very low temperatures, has been developed. In particular, the generation and extinction of crystal nuclei was found at low temperatures in supercooled liquids of *o*-benzylphenol, salol and 2,2'-dihydroxybenzophenone, and this brought up a new concept of irreversible structural relaxation in supercooled liquids and glasses [1–3]. The practical value of this research is determined by the importance of understanding the connection between physical properties, microscopic structure of the substance and macroscopic conditions of materials processing, which is vital to produce new materials with advanced technological properties.

Prof. M.Oguni from Tokyo Institute of Technology discussed for the first time the importance of α and β relaxation processes in supercooled liquids which are characterized in terms related to the structural regions of the liquid [4, 5]. Thus, relaxation α was defined as the molecular rearrangement within the cluster, and the corresponding β type – rearrangement of particles in the gap between clusters. So when supercooled liquid is heated to the transition temperature region, first a metastable crystalline state is formed, and, at the next step, a stable structure with an ordered arrangement of molecules grows in clusters at higher temperatures due to the α relaxation process. The model is based on experimental data for organic molecular compounds, but this mechanism could be applied to any supercooled liquid and inorganic polymers, when the size of structural units involved in the rearrangement correlated motion is small compared with the size of cluster.

In the previous work [6], the generic kinetic model involving one order parameter was developed to study the impact of both asymmetry and external field on phase transitions in the presence of intermediate metastable state. Analytical solutions were obtained according to the Descartes-Euler method for solving polynomial equations. Depending on the values of its control

parameters, the potential has one, two or three possible minima, and the problem dealt with the construction of the equilibrium phase diagrams. In general, the universal features of transition scenario can be described by a six-degree potential with four control parameters which are associated with coupling the system to an external field, diffusion, asymmetry and viscosity. So they are related to parts of the effective potential describing intrinsic transition dynamics based just on diffusion and viscosity coefficients, as well as linear and cubic terms in order parameter associated to the coupling of material to an external field and the asymmetry of the system, respectively. When a Landau-type potential possessing a single order parameter associated to the fluid phase and a particular set of three control parameters have been considered, one could assess the effects of asymmetry and coupling of system to an external field in the presence of an intermediate state, but not to study the bifurcation process quantitatively in the entire parameter plane.

2. THEORETICAL FRAMEWORK OF THE MODEL

Kinetic potential $U(x; \lambda, \mu, \xi)$ involving a single order parameter x and the coefficient of asymmetry ξ has the form

$$U(x; \lambda, \mu, \xi) = -\lambda \frac{x^2}{2} + \xi \frac{x^3}{3} + \mu \frac{x^4}{4} + \frac{x^6}{6}, \quad (1)$$

where λ and μ are control parameters related to the intrinsic transition dynamics. The kinetic potential $U(x; \lambda, \mu, \eta)$ involving a single order parameter x and the coupling coefficient with an external field η has the form

$$U(x; \lambda, \mu, \eta) = \eta x - \lambda \frac{x^2}{2} + \mu \frac{x^4}{4} + \frac{x^6}{6} \quad (2)$$

We consider the model for diffusion in a double-well potential, where the probability density $p(x, t)$ of a particle obeys the Fokker-Planck equation, FPE:

$$\partial_t p(x, t) = \partial_x [U'(x)p(x, t)] + D \partial_x^2 p(x, t).$$

The stationary distribution is

$$p_s(x) = N \cdot \exp[-U(x)/D]. \quad (3)$$

The shape of $U(x)$ is shown in Fig. 1, corresponding to **a**, **c** and **b** which are two minima, and a central maximum. The system is thus most likely to be found at **a** or **c**.

In 1940 Kramers introduced what is called the Kramers equation in which he considered

motion under the influence of a potential $V(x)$ which was double well [7]. In the case of large damping, the corresponding Smoluchowski equation could be used, and the escape problem is reduced to the one presently under consideration:

$$\frac{\partial \hat{p}}{\partial t} = \beta^{-1} \left\{ V'(x) \hat{p} + kT \frac{\partial \hat{p}}{\partial x} \right\}. \quad (4)$$

We take the motion of a particle in a fluctuating environment. The motion is in one dimension and the state of the particle is described by its position x and velocity v . This gives the differential equations

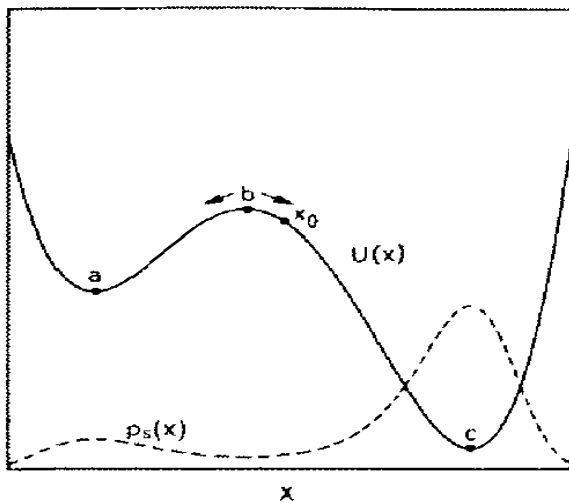


Fig. 1. Plot of $p_s(x)$ and $U(x)$ for a double well potential

$$\hat{Z}_t = \sum_k B_{ik}^{-1}(x) \left[2D_k(x) - \frac{\sum_j \partial}{\partial x_j} B_{kj}(x) \right], \quad (5)$$

and we have $\frac{dx}{dt} = v$ and $m \frac{dv}{dt} = -V'(x) - \beta v + \sqrt{2\beta kT} \xi(t)$ which are essentially Langevin's equations in which, for simplicity, we write $6\pi\eta a = \beta$ and $V(x)$ is a potential whose gradient $V'(x)$ gives rise to a force on the particle. By making the assumption that the physical fluctuating force $\xi(t)$ is to be interpreted as $\xi(t)dt = dW(t)$, we obtain:

$$mdv = -[V'(x) + \beta v]dt + \sqrt{2\beta kT} dW(t), \quad (6)$$

for which the corresponding FPE is

$$\frac{\partial p}{\partial t} = \frac{\partial}{\partial x}(vp) + \frac{1}{m} \frac{\partial}{\partial v} \{ [V'(x) + \beta v] p \} + \frac{\beta kT}{m^2} \frac{\partial^2 p}{\partial v^2}. \quad (7)$$

The equation can be slightly simplified by introducing new scaled variables

$$y = x\sqrt{m/kT}, \quad u = v\sqrt{m/kT}, \quad U(y) = V(x)/kT, \quad \gamma\beta/m,$$

so that the FPE takes the form

$$\frac{\partial p}{\partial t} = \frac{\partial}{\partial y}(up) + \frac{\partial}{\partial u} [U'(y)p] + y \frac{\partial}{\partial u} \left(up + \frac{\partial p}{\partial u} \right), \quad (8)$$

which is called the *Kramers' equation*. Using the notations for the two minima, and a central maximum in Fig.1, i.e. **a**, **c** and **b**, respectively, let's define

$$M(x, t) = \int_{-\infty}^x dx' p(x', t), \quad (9)$$

$$N_a(t) = 1 - N_c(t) = M(b, t), \quad (10)$$

and

$$N_0(t) = (c - a)p(x_0, t). \quad (11)$$

Further, let's define the corresponding stationary quantities by

$$n_a = 1 - n_c = \int_{-\infty}^c p_s(x') dx', \quad n_0 = (c - a)p_s(x_0). \quad (12)$$

From the FPE

$$\partial_t p(x, t) = \partial_x [U'(x)p(x, t)] + D \partial_x^2 p(x, t) \quad (13)$$

and the form of $p_s(x)$

$$p_s(x) = N \cdot \exp[-U(x)/D] \quad (14)$$

we can write

$$dM(x, t) = D \cdot p_s(x) \partial_x [p(x, t) / p_s(x)] \quad (15)$$

which can be integrated to give

$$d_t \int_a^{x_0} dx M(x, t) / p_s(x) = D [p(x_0, t) / p_s(x_0) - p(a, t) / p_s(a)]. \quad (16)$$

This Equation contains no approximations. We are forced to introduce a less rigorous argument than is desirable in order to present the essence of the method. Since we believe the relaxation within each well is rather rapid, we would expect the distribution in each well to approach the same shape as the stationary distribution, but the relative weights of the two peaks to be different. This can be formalized by writing



$$p(x,t) = \begin{cases} p_s(x)N_a(t)/n_a, & x < b \\ p_s(x)N_c(t)/n_c, & x > b. \end{cases} \quad (17)$$

This would be accurate to lowest order in D except in a region of magnitude \sqrt{D} around \mathbf{b} . If we substitute these into Eq. (16), we obtain

$$k(x_0)\dot{N}_a(t) = D[N_0(t)/n_0 - N_a(t)/n_a] \quad (18.1)$$

$$\mu(x_0)\dot{N}_c(t) = D[N_0(t)/n_0 - N_c(t)/n_c] \quad (18.2)$$

with

$$k(x_0) = \int_a^{x_0} p_s(x)^{-1} [1 - \psi(x)] dx \quad (19.1)$$

$$\mu(x_0) = \int_{x_0}^c p_s(x)^{-1} [1 - \psi(x)] dx \quad (19.2)$$

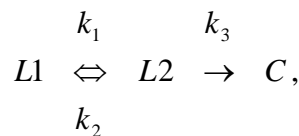
and

$$\psi(x) = \begin{cases} n_a^{-1} \int_x^b p_s(Z) dz, & x < b \\ n_c^{-1} \int_x^b p_s(Z) dz, & x > b. \end{cases} \quad (20)$$

Note that if x is finitely different from \mathbf{a} or \mathbf{c} , then $\psi(x)$ vanishes exponentially as $D \rightarrow 0$, as follows directly from the explicit form of $p_s(x)$.

3. NUMERICAL RESULTS AND DISCUSSION

The notations C , $L1$, and $L2$ represent accordingly crystalline and two liquid phases. Since passage from state $L1$ to state C occurs through an intermediate state $L2$, the overall rate process can be represented schematically as



where the state C is treated as an absorbing barrier and $k_i, i = \overline{1,3}$ are given by the general equation for transition rate [7]:

$$k_i = \frac{1}{2\pi} (-U''(x_{\min}) U''(x_{\max}))^{1/2} \exp\left[\frac{-\Delta U_i}{(q^2/2)}\right]. \quad (21)$$

Here U'' is the second derivative of $U(x)$ for the given Eqs. (1) and (2), and the potential barriers $\Delta U_i = U(x_{\max}) - U(x_{\min})$, where x_{\min} is the value of x associated to a minimum of $U(x)$, x_{\max} corresponds to the maximum of $U(x)$ separating this “reference” minimum from an adjacent second minimum x'_{\min} . Note that the validity of Eq. (21) implies that ΔU_i must be much larger than $q^2/2$, which is the variance of the white noise process $F(t)$ accounting for the thermodynamic fluctuations [8], and the transition rate is given from x_{\min} to x'_{\min} .

Figs. 2 and 3 represents the common logarithm of mean transition time τ between liquid $L1$ and crystalline C phases versus λ in the region of coexistence of states $L1$ and $L2$ for parameter values $\mu = -2$ and $q^2 = 0.1$.

The dynamics involves three transitions, i.e. $L1 \rightarrow L2$, $L2 \rightarrow L1$, and $L2 \rightarrow C$, so the probabilities p_{L1} and p_{L2} to find the system in states $L1$ and $L2$ (with $p_C = 1 - p_{L1} - p_{L2}$) satisfy the rate equations

$$\begin{aligned} \frac{dp_{L1}}{dt} &= -k_1 p_{L1} + k_2 p_{L2}, \\ \frac{dp_{L2}}{dt} &= k_1 p_{L1} - (k_2 + k_3) p_{L2}. \end{aligned} \quad (22)$$

The overall transition rate from $L1$ to C is given by the lowest in absolute value eigenvalue κ of the matrix of transition probabilities included in Eq. (22) per unit time, so the corresponding mean transition time is $\tau_{L1 \rightarrow C} = |\kappa|^{-1}$. See also [8] for $k_2 = k_3$.

$$\kappa = \frac{1}{2} \left[-(k_1 + k_2 + k_3) + \sqrt{-4k_1 k_3 + (k_1 + k_2 + k_3)^2} \right],$$

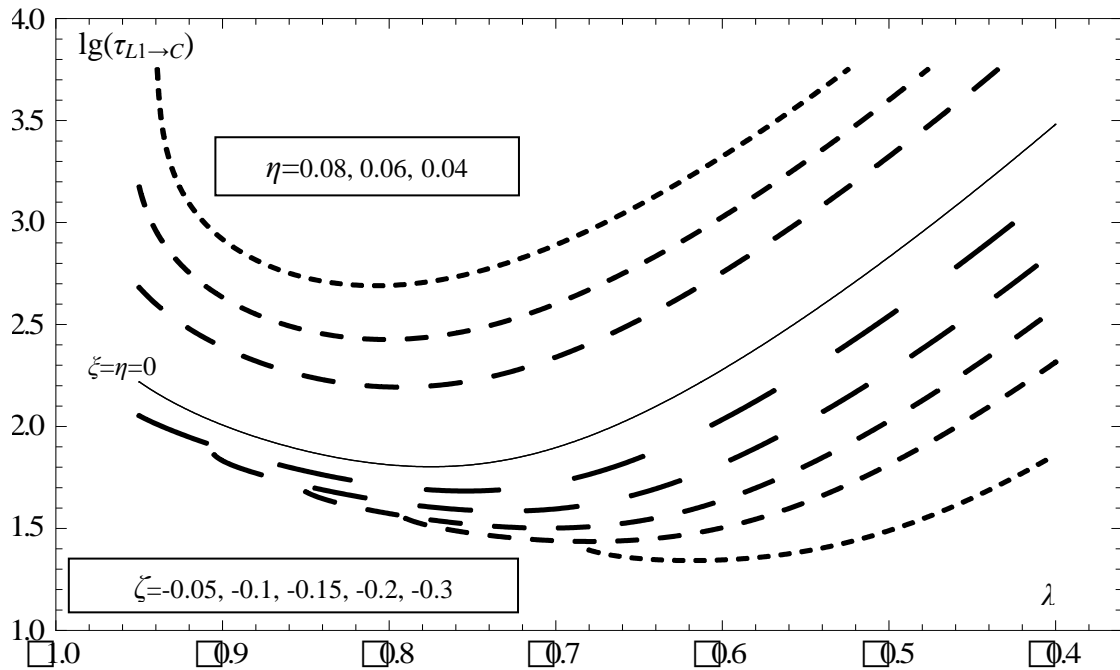


Fig. 3. Common logarithm of the mean transition time τ between liquid $L1$ and crystalline C phases versus λ in the region of coexistence of states $L1$ and $L2$, where the system goes through minima. Solid curve stands for $\eta=0$ and $\xi=0$, and dashed lines correspond to the above-shown values of η and ξ coefficients, from top to bottom respectively. Parameter values $\mu=-2$ and $q^2=0.1$.

In Fig. 3 solid curve stands for $\eta=0$ and $\xi=0$ (the intrinsic transition dynamics), and dashed lines correspond to the $\eta=0.08, 0.06, 0.04$, and $\xi=-0.05, -0.1, -0.15, -0.2, -0.3$, from top to bottom respectively. One can conclude that the mean transition time decreases as the system enters in the region of existence of the intermediate state $L2$, where it goes through minima at negative values of λ corresponding to the coexistence regions of states $L1$ and $L2$, i.e. $U(L1)=U(L2)$ for different values of ξ and η , when the barriers ΔU_i for the transitions $L1 \rightarrow L2$ and $L2 \rightarrow L1$ become the same. Due to smallness of potential barriers in comparison to q^2 , the validity of Eq. (21) is not met in the region close to $\lambda=0$. We notice that the presence of the intermediate state may indeed enhance the



nucleation rate, and, furthermore, an increase in the heterogeneity of system accelerates the transition dynamics, while the presence of an external field would increase the mean transition time.

4. CONCLUSIONS

As shown by the mean transition time in both cases, while the asymmetry of system increases, there is an increase in the stability of either liquid or crystalline phases depending on the sign of parameter ξ . However, the impact of an external field on the system in the presence of an intermediate state would reduce the stability of system. It is also worth mentioning that the obtained results are general and suggest a complete set of different transition scenarios in the entire parameter plane.

The phenomenon of relaxation of metastable states in solid \leftrightarrow liquid transitions is studied more superficial than gas \leftrightarrow liquid phase transitions. In general, the largest and smallest values of order parameter correspond to minima of free energy functional F , while the intermediate value corresponds to an unstable state (F has a local maximum or saddle point), and these three extrema are identified with the crystalline and two liquid phases [9]. In case of a single-component glass which can be characterized in terms of the pressure P and volume V , the relation between P and V could be obtained using the equation $P(V, T, x) = -(\partial F / \partial V)_{T, x}$. Note that $P(V, T, x)$ can be derived from experimental data and this equation may be further used to determine the V -dependence of $F(V, T, x)$. Then F can be applied to get the entropy $S = -(\partial F / \partial T)_{V, x}$, and in this way specific heats and other thermodynamic quantities for the system may be defined [10].

REFERENCES

1. PALADI, F.; OGUNI, M. Anomalous generation and extinction of crystal nuclei in nonequilibrium supercooled liquid o-benzylphenol. *Physical Review B*, 2002, Vol. 65, No. 14, 144202 (6 pages), doi:10.1103/PhysRevB.65.144202.
2. PALADI, F.; OGUNI, M. Generation and extinction of crystal nuclei in an extremely nonequilibrium glassy state of salol. *Journal of Physics: Condensed Matter*, 2003, Vol.15, No. 23, p. 3909–3917, doi:10.1088/0953-8984/15/23/306.
3. TOMITAKA, S. et al. Thermal and dielectric studies of 2,2'-dihydroxybenzophenone: progress of crystal nucleation and growth below the glass transition temperature. *Journal of Thermal Analysis and Calorimetry*, 2005, Vol. 81, No. 3, p. 637–643.
4. HIKIMA, T. et al. Determination of potentially homogeneous-nucleation-based crystallization in o-terphenyl and an interpretation of the nucleation-enhancement mechanism. *Physical Review B*, 1995, Vol. 52, No. 6, p. 3900–3908.
5. HIKIMA, T.; HANAYA, M.; OGUNI, M. Discovery of a potentially homogeneous-nucleation-based crystallization around the glass transition temperature in salol. *Solid State Communications*, 1995, Vol. 93, No. 8, p. 713–717.
6. PALADI, F. Effects of asymmetry and external field on phase transitions in the presence of an intermediate metastable state. *Physica A: Statistical Mechanics and its Applications*, 2010, Vol. 389, No. 10, p.1986-1992, doi:10.1016/j.physa.2010.01.015.
7. GARDINER, C.W. *Handbook of Stochastic Methods: for Physics, Chemistry and the Natural Sciences* 3rd ed. Berlin: Springer, 2004, 415 p. ISBN 9783540208822.
8. NICOLIS, G.; NICOLIS, C. Kinetics of phase transitions in the presence of an intermediate metastable state: a generic model. *Physica A*, 2005, Vol. 351, p. 22–39, doi:10.1016/j.physa.2004.12.006.
9. ORTOLEVA, P.J. Glass transitions: A chemical kinetic/Landau theory. *J. Phys. Chem. B*, 1997, Vol. 101, No. 41, p. 8324–8330.
10. LANDAU, L.D.; LIFSHITZ, E.M. *Statistical Physics (Course of Theoretical Physics, 3rd edition)*, Part 1, Vol. 5, Moskow: Butterworth-Heinemann, 1980, ISBN 978-0-7506-3372-7.



GAS AND FLUID FILM FLOW SIMULATION IN THE CONTACT APPARATUS

I.M. Kuzmenko, R.M. Prokopets
*NTUU Kyiv polytechnical institute
Peremogy str. 37, 03056 – Ukraine*

ABSTRACT

The purpose of the paper is to describe the mathematical models and obtain calculation results of the velocity field when gas flow and fluid film are in motion in the channel of the regular packing of the contact apparatus.

The problem is examined in a vertical cylindrical channel. The fluid film flows down under the gravity force along the internal wall. In the center of the channel there is a forced gas flow. The film thickness is by a factor lower than the channel diameter.

The mathematical model is described by an equation of the fluid motion under the gravity force, an equation of the gas flow motion affected by differential pressure and an equation of continuity in the gas flow. The last equation makes it possible to determine the flow velocity projections upon the cylinder axis and its radius.

The system of these equations of the mathematical model does not have any analytical solution and has been solved numerically

The solution of the system of equations has been obtained with the help of MATLAB. The field of velocities in the gas flow and fluid film has been determined in relation to the differential pressure and the inlet velocity of air on the assumption of their cocurrent flow motion.

Keywords: mathematical model, contact apparatus, gas flow, velocity, channel

1. INTRODUCTION

Gas flow in systems with heat and mass exchange occurs in a number of industry processes [1-5]. For example, in the contact apparatus. However, description of these processes involves simultaneous consideration of changes in temperature, gas humidity and conditioned by velocity filed in apparatus.

The numerical studies of heat and mass exchange by direct contact between phases for the case of inclined surfaces are described in [1, 2] as well as turbulent [3, 4] and laminar [5] air movement in the channel. All works are based on calculation of velocity field in the channel with cocurrent movement of phases. However, none of the works shall describe the velocity field.

Therefore, using the formulation of problem in work [5], we will calculate the velocity field in the packing channel of contact apparatus, such as a cooling tower, with cocurrent movement of phases.

We shall additionally consider that walls of packing are made of porous material, such as mesh, with cell size up to 1 mm and therefore, the film of water that moves through the mesh shall not stop near the wall.

That is to say, the purpose of this study is a numerical simulation of phase velocity field in the contact apparatus channel system with a mesh packing.

The relevance of this study is demonstrated by an increased number of publications. Results of numerical simulation will be used for calculation of heat and mass exchange in the contact apparatus.

2. STATEMENT OF THE PROBLEM

The problem is considered in a vertical axisymmetrical channel with cocurrent air flows (in the center of channel) and water film (on the wall of channel). Movement of air flow is forced due to the pressure gradient $\Delta p / \Delta x$. In our case, the channel length exceeds its diameter $x > 2R$, thus, the pressure gradient $\Delta p / \Delta r$ shall be neglected. The water film movement is gravitational – under action of gravity. Geometry of considered problem shall be a vertical tube with stream flowing down as a stream of gas and liquid shown in Fig. 1.

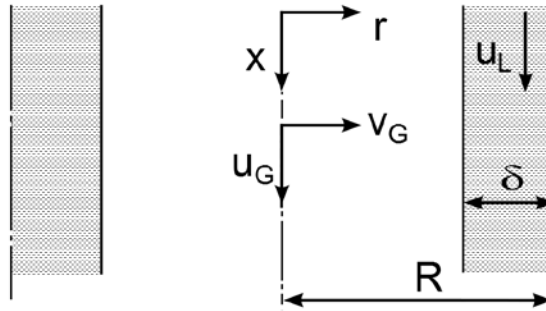


Fig. 1. Geometry of the problem

Boundary conditions shall be set to the upper channel boundary, radius R with a water film of thickness δ . The conditions include: value of absent air velocity radial component $v_G = 0$; air velocity axial velocity component u_G ; velocity of gravitationally flowing down water film u_L . The pressure gradient in the channel $\Delta p / \Delta x$ shall be constant and preset [6].

We assumed that air and film movement is laminar and their thermophysical properties are constant at a temperature 10°C in the channel.

2.1. Mathematical model

Considering the above assumptions, the equation of water film motion (Momentum) in cylindrical coordinates shall be as follows:

$$\frac{1}{r} \frac{\partial}{\partial r} \left[r \mu_L \frac{\partial u_L}{\partial r} \right] + \rho_L g = 0, \quad (1)$$

where μ_L , ρ_L – are viscosity and density of water.

For the air flow, the continuity and motion equation shall be as follows. Continuity

$$\frac{\partial u_G}{\partial x} + \frac{\partial v_G}{\partial r} = 0, \quad (2)$$

considering that thermophysical properties is constant. Momentum

$$\rho_G \left(u_G \frac{\partial u_G}{\partial x} + v_G \frac{\partial u_G}{\partial r} \right) = - \frac{dp}{dx} + \frac{1}{r} \frac{\partial}{\partial r} \left[r \mu_G \frac{\partial u_G}{\partial r} \right] - (\rho_0 - \rho_G) g, \quad (3)$$

where μ_G , ρ_G – are viscosity and density of air. Index „0” relates to input data. Equation (3) shall be simplified as the last sum is equal to zero.

The boundary conditions at the channel input shall be as follows:

$$x = 0: u_G = u_{G0}, v_G = 0, u_L = u_{L0}. \quad (5)$$

The symmetry condition in the center of film profile moved along the mesh packing $r = R$:

$$\frac{du_L}{dr} = 0. \quad (6)$$

The symmetry of air velocity profile concerning the axis x $r = 0$:

$$\frac{\partial u_G}{\partial r} = 0. \quad (7)$$

Continuities of velocity and temperature shall be ensured at phase-to-phase boundary $r = R - \delta$:

$$u_G|_{R-\delta} = u_L|_{R-\delta}. \quad (8)$$

2.2. Model verification

Due to inability to obtain an analytical solution of the system (1–3) with boundary conditions (4-8), equations shall be solved numerically. Therefore, differential equations shall be reduced to linear algebraic equations by applying the mesh scheme. Further, the system of linear algebraic equations was sequentially solved at each step in MatLab package in cycles on x and r using the built-in problem solver.

The calculation shall be performed as follows. Since the air and film movement is directed downward, begin to calculate from the upper tube outlets, for which we know the boundary conditions (5). The calculation involves two cycles: cycle of the velocity field calculation along the x axis includes a cycle of consistent calculations of air and water velocity in the r axis. In the r cycle, movement shall be from the center using the boundary conditions (7) to interphase boundary where the boundary conditions are implemented (8) and then using equation (1) for calculation of water film velocity up to value $r = R$. For the latter, the boundary conditions (6) shall be used.

If the value is calculated at all points, the results shall be presented in the form of matrix for axial velocity u_G , u_L and radial velocity air component v_G .

The model verification was performed on the basis of evaluated local axial velocity provided $\Delta p/\Delta x = 0.01$ Pa, $u_{G0} = 1$ m/s, $u_{L0} = 0.25$ m/s; $v_{G0} = 0$ m/s at 11x11 grid. The results are presented in Figure 2. The calculations are used for channel of 0.02 m length and 0.01 m radius.

For the model verification the comparison was executed with the calculations [2] conducted under the evaporation from the film, running off the angled surface in laminar flow of moist air.

The results known, provided in the Fig. 2 represented by the line, were obtained with the air initial velocity of 1 m/s at 0.02 distance from the overall length of the channel on condition that the film thickness was 0.1 of the channel radius. The results were provided in the Fig. 2 in the dimensionless form.

Besides the Fig. contains modelling results represented by the points. The results were received with the initial velocity of 1 m/s at the distance 0.02 cm, the film thickness is 0.3 of the channel radius.

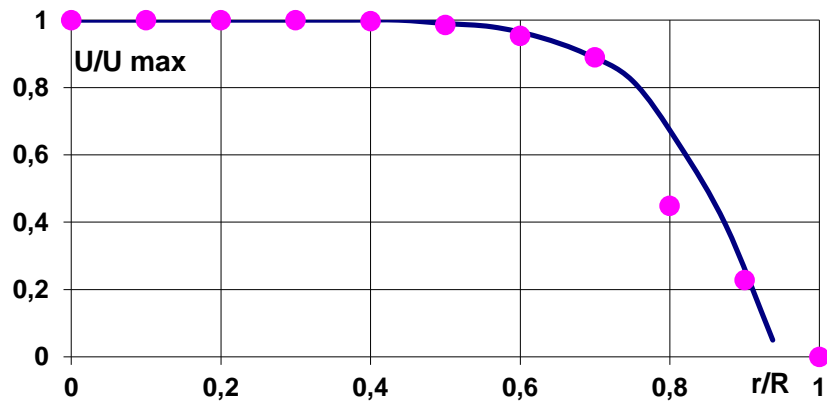


Fig. 2. Model verification (line – results [2], points – given model)

Judging by the Fig. 2, velocity varies from the maximum in the flow centre to zero near the wall.

Besides, maximum deviation between the received and already known results is in the point $r/R = 0.8$, combining the movement of film, water and air. In all other instances the model fully complies with the known result.

3. SIMULATION RESULTS

The simulation was performed for the channel with the following geometry: length $x = 0.02$ m and radius $R = 0.01$ m. Results are presented in Figures 3–5, which show the axial air velocity field u_G and water film u_L (at the left) and radial air velocity v_L (at the right) in the channel. The $x-r$ axes shall have applied points of 11x11 grid for the air velocity field u_G and water film field u_L and 11x8 grid for radial air velocity v_L . The grids may differ as water film radial velocities shall not be considered.

Figs. 3–5 show influence of starting air flow velocity u_{G0} and pressure drop $\Delta p/\Delta x$ for velocity field change. There are shown velocities (at the left u and at the right v) of air and water on Figures 3–5 in axes $x-r$. Figures show change in air velocity due to maximum center velocity for film surface velocity. That is, the boundary layer is formed. The thickness of this layer increases starting from the top of the channel and determines the heat and mass exchange in the channel. But boundary layers were not specified in the water film; it is explained by its not significant thickness and velocity.

Figs. 3–4 show that the boundary level at starting air flow velocity $u_{G0} = 1$ m/s, is independent from pressure drop $\Delta p/\Delta x$. Therefore, the visually determined boundary layer thickness complies with $r_8 - r_4 = 0.007 - 0.003 = 0.004$ m for values of Fig. 3.

Fig. 5 shows field of axial air velocity u_G and water film velocity u_L in the channel and radial v_L air velocity. The calculation was performed under condition $\Delta p/\Delta x = 0.02$ Pa, $u_{G0} = 1$ m/s, $u_{L0} = 0.25$ m/s, $v_{G0} = 0$ m/s.

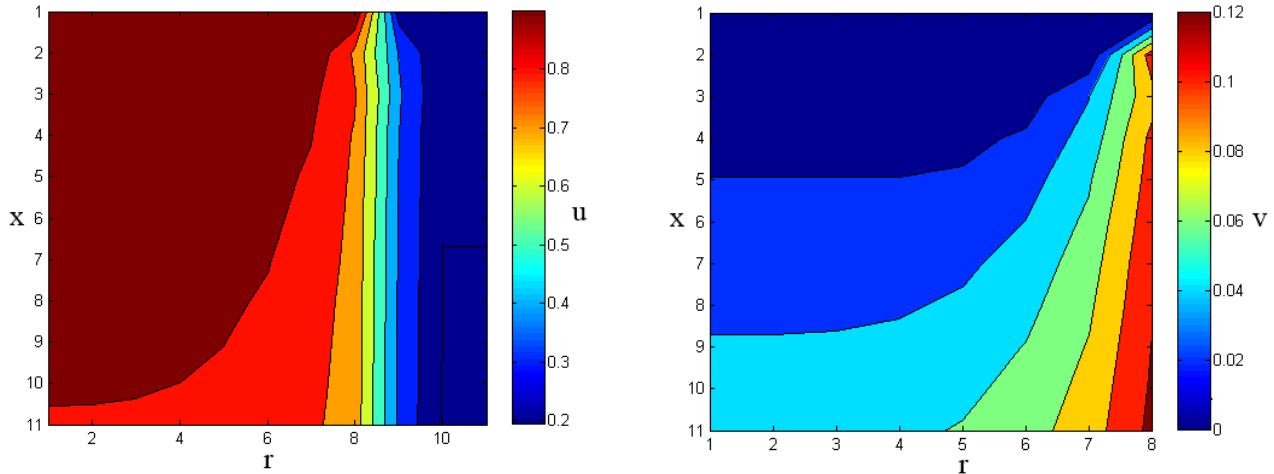


Fig. 3. Field of axial air velocity u_G and water film velocity u_L in (at the left) and radial v_L air velocity (at the right). The calculation was performed under condition $\Delta p/\Delta x = 0.01$

$$\text{Pa}, u_{G0} = 1 \text{ m/s}, u_{L0} = 0.25 \text{ m/s}, v_{G0} = 0 \text{ m/s}$$

As we see in Fig. 5, with an increase of u_{G0} to 1.5 m/s the visually determined boundary layer has a thickness $r_8 - r_5 = 0.007 - 0.004 = 0.003$ m, i. e. the velocity increase causes the boundary layer thickness reduction.

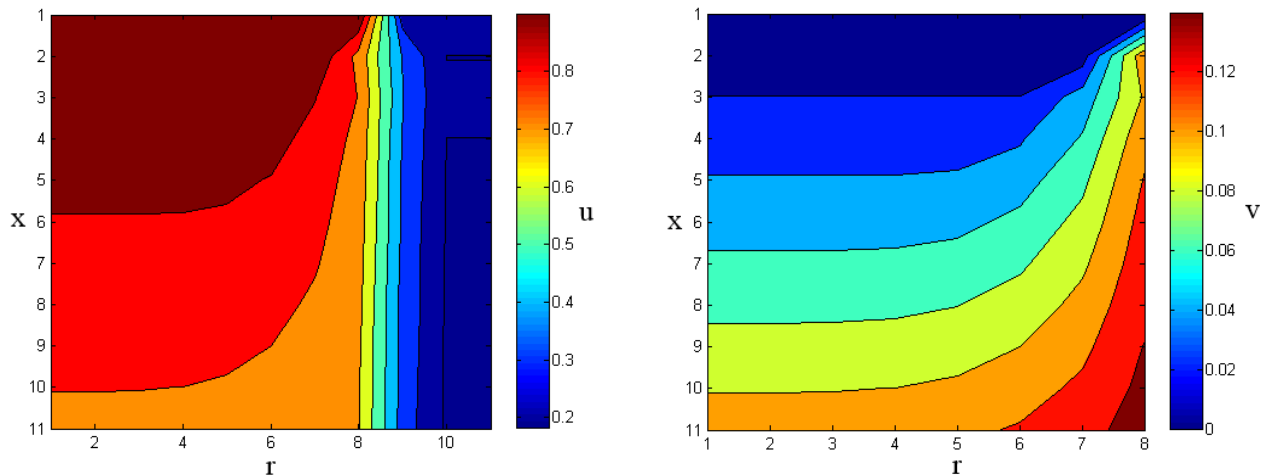


Fig. 4. Field of axial air velocity u_G and water film velocity u_L in the channel (at the left) and radial v_L air velocity (at the right). The calculation was performed under condition

$$\Delta p/\Delta x = 0.02 \text{ Pa}, u_{G0} = 1 \text{ m/s}, u_{L0} = 0.25 \text{ m/s}, v_{G0} = 0 \text{ m/s}$$

Besides, comparison of Figs. 3 and 4 shows that pressure drop increase $\Delta p/\Delta x$ decreases local axial flow velocity u_G . However, the local radial velocity v_L increases causing the growth of convective mass and heat transfer in the channel. Since the pressure drop is practically caused by flow friction, the channel with rough walls will have an increased pressure drop and heat-mass exchange.

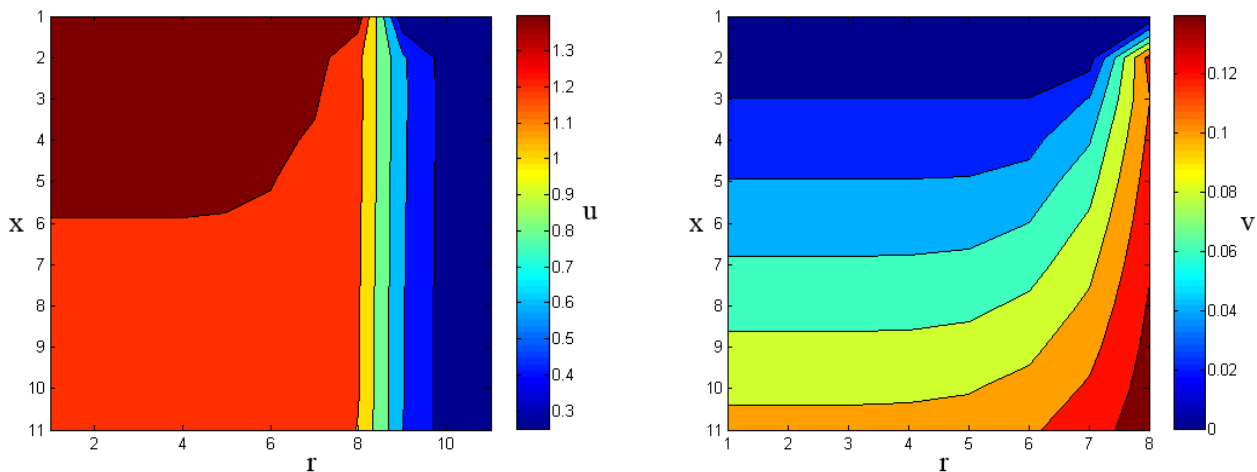


Fig. 5. Field of axial air velocity u_G and water film velocity in the channel (at the left) and radial v_L air velocity (at the right). The calculation was performed under condition $\Delta p/\Delta x = 0.02$ Pa, $u_{G0} = 1.5$ m/s, $u_{L0} = 0.25$ m/s, $v_{G0} = 0$ m/s

CONCLUSIONS

Thus, this mathematical model describes the laminar velocity field in the channel of mesh packing. The model verification showed that the relative deviation of local velocity for different grids shall not exceed 10%.

The thickness of boundary layer in the air is up to 0.004 m and depends on the distance from the top edge of the channel and the initial velocity.

Pressure drop $\Delta p/\Delta x$ that depend on the channel surface roughness has no influence on the boundary layer thickness. However, $\Delta p/\Delta x$ increase causes the decrease in axial air flow velocity and increase in transverse ones. The latter causes an increase in heat and mass transfer.

Ends of boundary layers were not specified in the water film; it is explained by its not significant thickness and velocity.

REFERENCES

1. CHOU, Y., RUEY-JEN, Y. The evaporation of a saturated porous layer inside an inclined airflow channel. *International Journal of Heat and Fluid Flow*, 2007, No. 28, p. 407–417.
2. SAOULI, S., BOUMAZA, M., SETTOU, N., AIBOUD-SAOILI, S., DAGUENET, M. Numerical study of the evaporation of a falling Ostwaldian film along an inclined flat plate into a laminar stream of humid air. HEFAT 2005. 4th International Conference on heat Transfer, Fluid Mechanics and Thermodynamics. Cairo, Egypt. 2005 September 19–22.
3. FEDDAOUI, M., MEFTAH., H., MIR, A. The numerical computation of the evaporative cooling of falling water film in turbulent mixed convection inside a vertical tube. *International Communications in Heat and Mass Transfer*, 2006, No. 33, p. 917–927.
4. ZHANG, H., TAO, W., HE, Y., ZHANG, W. Numerical study of liquid film cooling in a rocket combustion chamber. *International Journal of Heat and Mass Transfer*, 2006, No. 49, p. 349–358.
5. M'BAREK, F., BELAHMIDI, M., MIR, A., BENDOU, A. Numerical study of the evaporative cooling of liquid film in laminar mixed convection tube flows. *Int. J. Therm. Sci*, 2001, No. 40, p. 1011–1020.
6. ROUCH, P. *Computation fluid dynamics*. Moscow: Mir, 1980. 618 p. ISBN 10(13): Rouch.



STATIONARY HEAT TRANSFER AND AIRFLOW SIMULATION FOR TEST POLYGON HOUSES

J. Ratnieks, A. Jakovičs, S. Gendelis

*University of Latvia
Zellu street 8, LV-1002 – Latvia*

ABSTRACT

Energy efficiency of houses is highly topical problem nowadays, low energy consumption buildings are being built around the world, however, the thermal comfort is an issue that must be dealt with. For this purpose the test polygon of five houses with various construction solutions are being built in Riga, Latvia for which the aim is to acquire the best energy efficiency together with thermal comfort.

This work deals with stationary heat transfer and airflow simulations in test houses, the ANSYS/CFX software is used for the study. The modelling approach includes two model types. The first type is a 3D air region with heat transfer coefficient (third type) boundary conditions on outer surfaces to account for structures heat insulation. The second model type is a full 3D model including walls for lightweight plywood and rock wool construction. The heating is done with air to air heat pump and the room is being ventilated with an opening near the ceiling. The analyses are made for different velocities. The methodology for airflow and heat transfer simulations is developed and results are discussed.

Keywords: fluid dynamics, thermal comfort, energy efficiency

1. INTRODUCTION

The aim of this work is to develop a methodology to compute airflow and thermal behaviour of different building structures, taking into account humidity, rain and thermal radiation. The equations governing airflow are nonlinear and difficult to solve and usually numerically unstable, therefore the thermal radiation and humidity is left for further studies and heat exchange due to transmission and convection are studied. The second section deals with the experimental test polygon built in Riga with description of constructions used and methodology described. Two different modelling strategies are being studied the first being only the fluid domain with solid domain replaced with boundary conditions and the second include also the real thickness and material properties of the solid domains. The modelling approach, assumptions used and implementation in ANSYS/CFX as well as governing equations and meshing are described in section three: “mathematical model”. Sections four and five are results and discussion respectively.

2. EXPERIMENTAL SETUP

The project within which this particular research is done deals with both – energy efficiency of different building constructions made in Latvia, suitable for local climate conditions [1], and ensuring A class thermal comfort criteria defined by [2]. To achieve the aim all the available construction solutions were identified and five building structures that appeared to be sustainable were set up in Riga (Fig.1). These constructions include lightweight constructions with small thermal inertia and massive constructions with high thermal inertia. Also the life cycled for each construction type differs. the wooden log and rock wool construction (LOG); plywood, rock wool and fibrolite construction (PLY); clay brick wall with rock wool insulation layer (CER); lightweight aerated concrete with rock wool insulation layer (AER) and innovative clay brick construction where macroscopic holes are filled with insulating material to avoid convection in them (EXP) (Fig. 2). The thermal transmittance for all cases for walls are $U=0.16 \text{ W/m}^2\text{K}$. For doors and windows thermal transmittance is $U=1 \text{ W/m}^2\text{K}$, so the heat losses through them will be higher. For

every structure there are air – air heat pump installed and total energy consumption is measured throughout the year including both heating and cooling. For periods of time when the construction is not available to keep the thermal comfort conditions there is a penalty function introduced.

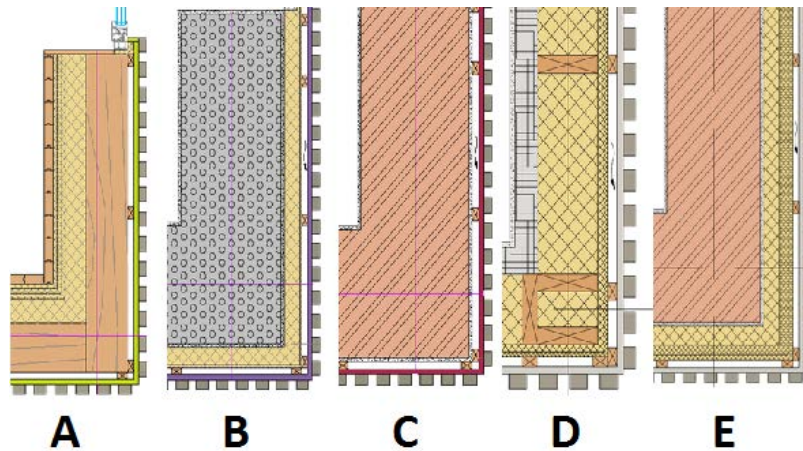


Fig. 1. Different construction types used in the project: a) LOG, b) AER, c) EXP, d) PLY, e) CER



Fig. 2. Test polygon at building stage on the left and finished stage on the right

3. MATHEMATICAL MODEL

3.1. Modelling approach

Two different cases are being considered in this work. As the roof is not being heated, it is removed from the mathematical model and heat losses through ceiling are computed as there was no roof construction present. As the thermal transmittivity is equal for all cases a good approximation would be to exclude the walls from the model and replace them with boundary conditions (Fig. 3a). Third type boundary conditions are suitable for modelling as the outside temperature can be adjusted and thermal transmittivity can be modelled by setting the correct heat transfer coefficient value. The downside of this method is that thermal capacity is not taken into account that is important for time dependent simulations as the outside weather conditions change rapidly, however it gives a good limit of what happens when there is no thermal inertia in the construction.

The second approach is to use a model with walls included (Fig. 3b) and material properties defined properly. This kind of approach is needed to correctly predict thermal behaviour of construction during daily cycles and reaction to sudden outside conditions. For this particular case the plywood is removed to avoid thin regions, but its influence is taken into account by changing material properties for rock wool and fibrolite, the thermal conductivity is higher for the latter. The rock wool is on the outside (cold side) and fibrolite on inside (Fig. 1d).

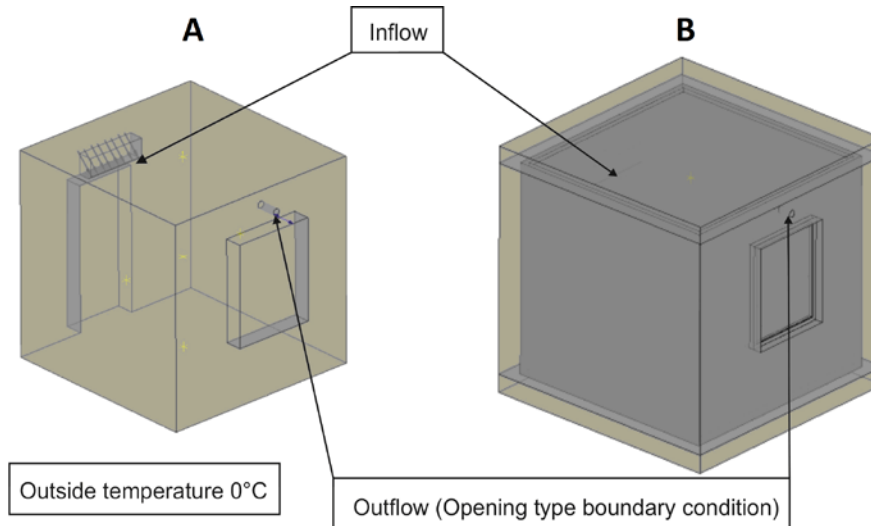


Fig. 3. Mathematical models: a) concentrated thermal resistance model b) full walls model

An issue for computational fluid dynamics (CFD) has always been validity of results. For many other physics equations there are analytic solutions that help to determine the correctness of numerical solutions. In CFD the only analytic solution is a Poiseuille flow in an infinite tube that is not valid in this study, so the only verification is by experiment. As the experimental results are not available yet the validation will be made by calculation of thermal balance and evaluating symmetry of the problem. There are also five monitor points in the model to see the development of temperature and velocity fields. They are marked with yellow labels (Fig. 3) two are equidistant from symmetry plane.

3.2. Governing equations and implementation in ANSYS/CFX

The Reynolds averaged Navier Stokes (RANS) equations are used for conservation of momentum along with energy conservation equation and continuity equation [3, 4, 5]. To model the buoyancy the Boussinesq approximation [3, 4] is used in which the density is assumed constant and the body force is temperature dependent. The temperature is taken from heat transfer equation.

Typically the airflow in a room is turbulent and it can easily be shown (Eq. 1) by Reynolds number that characterize the flow. As the characteristic length can be chosen 1.5 m, density is 1.225 kg/m^3 and dynamic viscosity $1.983 \cdot 10^{-5} \text{ kg/s}\cdot\text{m}$ the velocity, at which Reynolds number exceed 2000 that is typical value when flow become turbulent, is 1.1 cm/s

$$\text{Re} = \frac{\rho \cdot L \cdot v}{\mu} \quad (1)$$

where ρ – density, L – characteristic length, v – velocity and μ – dynamic viscosity.

The k - ω shear stress transport (SST) turbulence model is used that is built-in ANSYS/CFX software [3, 4]. This turbulence model was chosen because it is two parameter model that has the best performing parts of k - ω and k - ϵ turbulence models [4].

3.3. Boundary conditions

To model the source an inlet boundary condition was used for which the inflow air velocity and direction need to be provided in this case the velocities are 0.1 m/s, 0.2 m/s and 0.3 m/s and at all cases the inflow temperature is constant $T=25^\circ\text{C}$. The other options involved the mass flow and pressure difference, but as the Boussinesq approximation keep the density constant over the domain the post-processing is easier with the velocity approach. For mass sink there was an opening type

boundary condition to perfectly balance the mass inside domain as it was the only mass sink available in the model.

For the concentrated thermal resistance case the third type boundary conditions were used to model the thermal resistance of the wall and natural convection. The outside temperature were set to 0°C and the heat transfer coefficient was calculated (eq. 2) taking into account convection and thermal resistance of the wall [5].

$$U = \frac{1}{R_{wall} + R_{convOut}} \quad (2)$$

Where U – heat transfer coefficient [$W/(m^2K)$], R_{wall} – thermal resistance of the wall, $R_{convOut}$ – thermal resistance due to convection on the outside boundary. As example, the thermal resistance of wall is $R_{wall}=1/U=6.25$ [m^2K/W] and $R_{convOut}=0.04$ [m^2K/W].

For the full wall model the outer wall boundary condition is first term on the right side disappear and the heat transfer coefficient accounts only for natural convection.

The fluid solid boundaries for fluid flow are modelled as no slip walls.

3.4. Meshing

For both cases maximum mesh size for fluid domains were 4 cm and for the full wall model the maximum mesh size was 5 cm for solid domains. For mass source and sink regions the mesh was made smaller by using sphere of influence at the sink and at the source to get the mesh resolution below 1 cm. The inflation was used on the walls with 5 boundary layers all over the domain except for source and sink boundaries.

4. RESULTS

4.1. Concentrated thermal resistance model

First calculations were made with the concentrated thermal resistivity model, the convergence criteria were set to 10^{-4} that it never reached, but after 3000 iterations the solution started to oscillate around certain value. The thermal balance acquired was below 0.4% off that is good for CFD simulations. However the model had noticeable asymmetry (Fig. 4). Further study was to make time-dependent calculations after the asymmetric result was achieved. This approach gave more symmetrical results, but for larger time steps the thermal balance diverged and more heat was leaving the system then was pumped in.

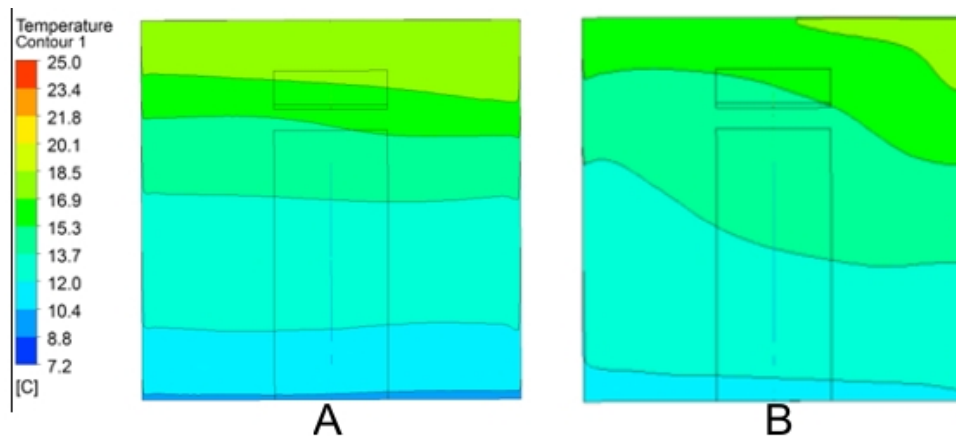


Fig. 4. Concentrated thermal resistance model a) Time-dependent solution after 120 seconds with time step 0.1 s b) stationary solution

As this model had limitations on further studies because of thermal inertia and the full model showed more numerical stability the former was discarded and only the latter was studied.

4.2. Full wall model

Studies with full wall model had previous asymmetry for large number of stationary iterations and time-dependent analysis took considerable computational time to achieve symmetrical velocities and temperature profiles. The studies showed that by choosing good initial temperature guess after 100 iterations (Fig. 5a) the thermal balance was fine, as showed later. For time dependent simulation (Fig. 5b) seemingly stationary solution was acquired after 4 minutes of simulation time (Fig. 6) with time steps being 0.1 s.

The calculations were made for three different cases with velocities being 0.1 m/s, 0.2 m/s and 0.3 m/s. The former is a boundary case with air exchange of 0.6 h⁻¹ as planned for experiment. This shows that feedback to air pump is necessary to keep the inside temperature habitable. The velocity profile for 0.3 m/s simulation is shown in Fig. 5.

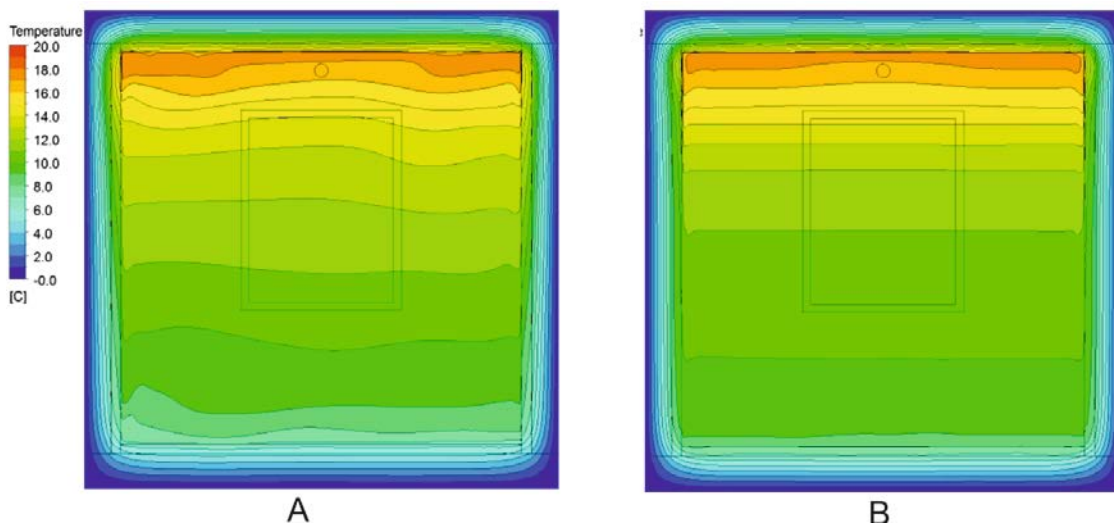


Fig. 5. Temperature fields for inflow velocity 0.3 m/s for a) stationary solution
b) time-dependent solution

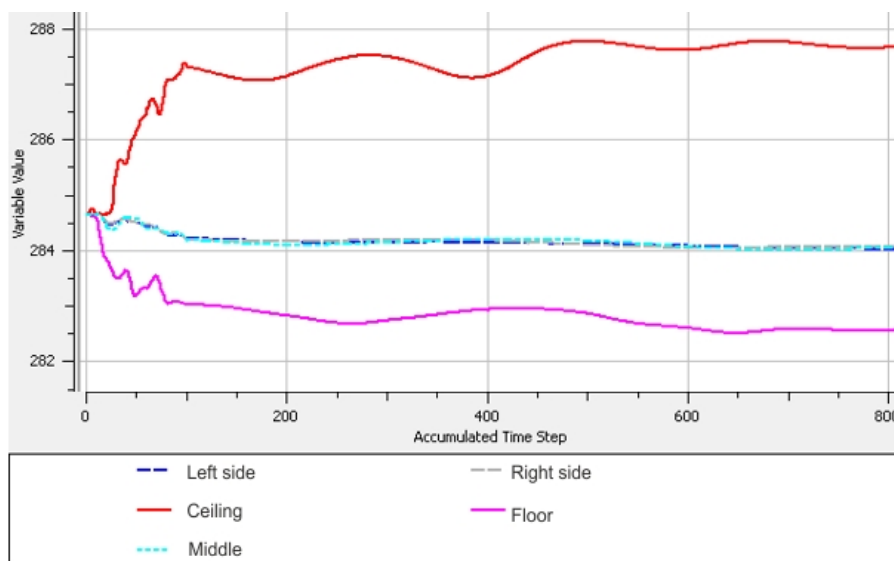


Fig. 6. Monitor point temperature values for each stationary iteration for stationary run and timestep for transient run (inflow velocity 0.2 m/s)

Heat balance calculations were carried out after 100 iterations of stationary solver and initial temperature adjusted to reduce heat balance error. When satisfactory result was obtained, time-dependent solver was run and thermal balance calculated once more (Table 1).

For walls, ceiling, floor, window and doors the heat losses were computed as area integral of heat flux (Eq. 3). At the mass sources and sinks (ventilation and heat pump (table 1)) velocity and temperature were integrated over the surface (eq.4)

$$P_{\phi} = \int_s \vec{\Phi} d\vec{S} \quad (3)$$

$$P_j = C_p \rho \int_s T \vec{v} d\vec{S} \quad (4)$$

Where P_{ϕ} – heat losses through solids [W], Φ – heat flux [W/m^2], C_p – specific heat at constant pressure [$\text{J}/(\text{kgK})$]; ρ – density [kg/m^3], T – temperature [K], v – velocity [m/s].

Table 1. Heat balance for various inflow velocities for the full wall model for time-dependent solver run with stationary solution initial values

Inlet velocity, m/s	0.1	0.2	0.3
heat losses, W			
walls	-40.89744	-54.2686	-60.0715
door	-9.34263	-12.9553	-14.005
window	-9.08604	-11.8835	-13.6166
ceiling	-19.11222	-24.4689	-27.6394
floor	-9.60057	-11.8228	-16.255
ventilation	-61.55	-141.18	-253.78
total	-149.5889	-256.5791	-385.3675
heat gain, W			
heat pump	132.19	262.29	390.91
difference, W	-17.3989	5.7109	5.5425
error, %	13.2	2.2	1.4

The heat losses through construction elements are higher with high inflow velocities. This is reasonable because the overall temperature in the model is higher and therefore temperature difference between inside and outside. Heat loss through ceiling is higher than loss through floor for the temperature differences. The heat gain is proportional the inflow speed as it should be but the ventilation losses differ because the outlet temperature can vary as it does.

5. DISCUSSION

Although the experimental verification is not yet unavailable this would not help to verify model yet because the solar influence and humidity is not taken into account. At this point it is possible only to make some qualitative remarks on the solution. First of all the authors would like to point out that velocity vectors near the doors and window are directed toward the floor that is physically expected as the temperature near these regions is low (Fig. 7), also the hot air near the inflow is rising that gives that proves that the buoyancy is working correctly (Fig. 8).

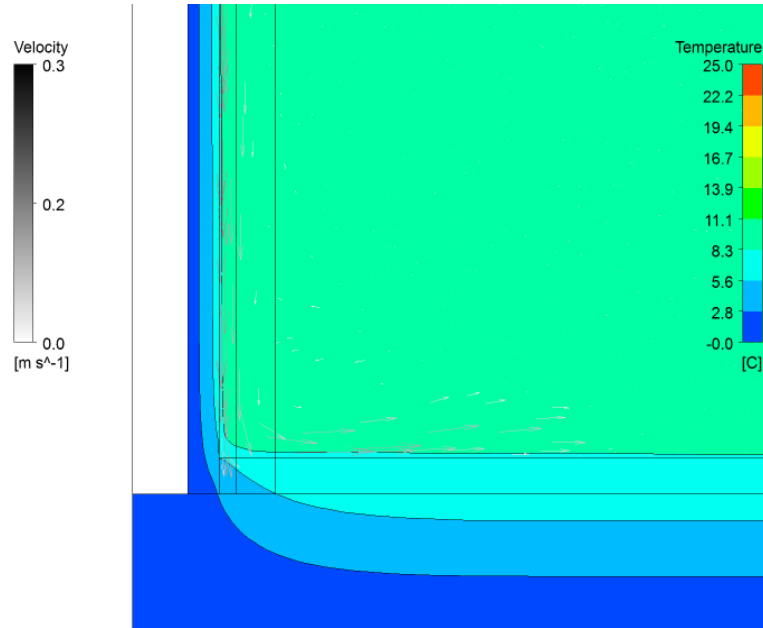


Fig. 7. Temperature field and velocity vectors near the doors region

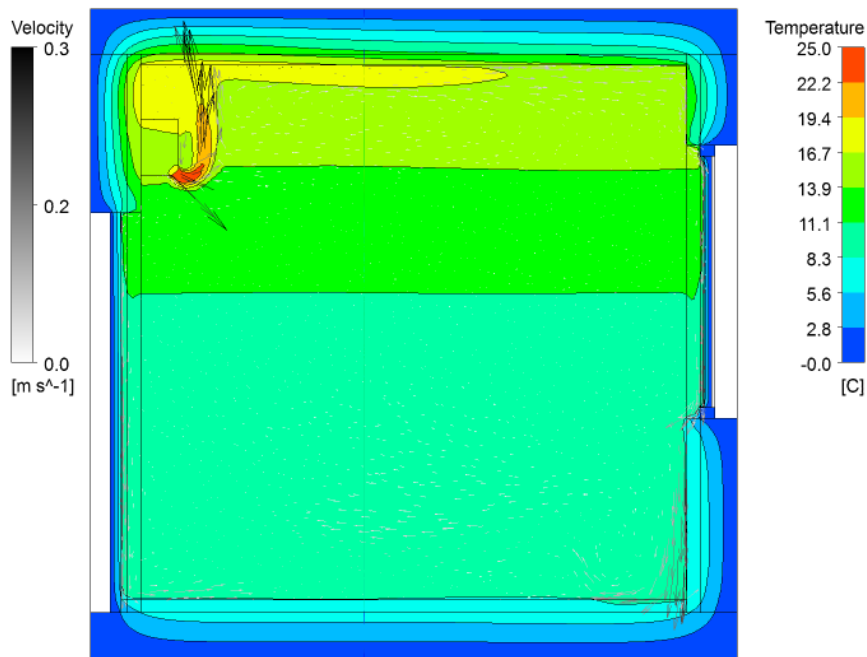


Fig. 8. Temperature field and velocity vectors on plane near the symmetry plane

As previously mentioned the thermal conductivity coefficient for rock wool is smaller than for fibrolite. The isotherms on the rock wool layer are closer to each other that mean the temperature gradient there is higher (Fig. 9).

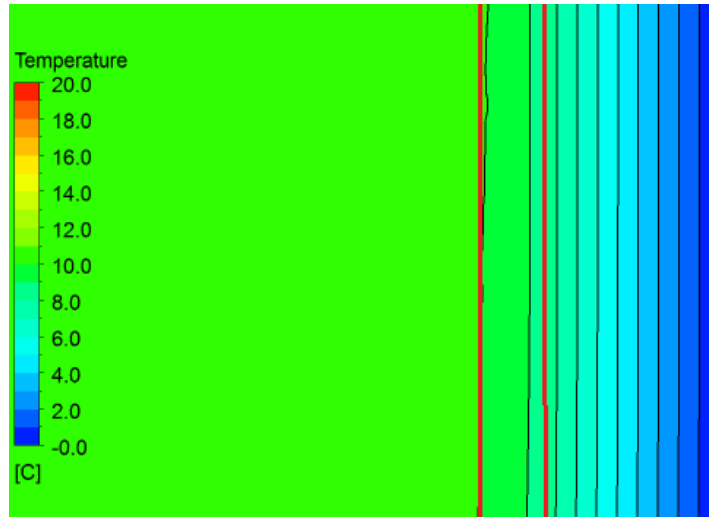


Fig. 9. Isotherms on the solid cross section (domain boundaries are marked with red)

6. CONCLUSION AND FURTHER STUDIES

Stationary solution for both problems gives unphysical results for given mesh and therefore a methodology that involve time-dependent calculations have been developed. The results have been qualitatively analyzed using symmetry and thermal balance and no physical inconsistency have been found that proves the methodology developed is useful for this kind of simulations.

Further work will concentrate on the thermal radiation implementation in the model and humidity impact on results will be considered. The feedback to heat pump will be included in the model to increase the inlet velocity to get inhabitable temperature distribution in room. Empirical observations have indicated that 0.6 m/s is enough.

7. ACKNOWLEDGEMENT

This work has been supported by the European Regional Development Fund in Latvia, project Nr. 2011/0003/2DP/2.1.1.1.0/10/APIA/VIAA/041.

8. REFERENCES

1. OZOLINS Ansis, JAKOVICS Andris, Heat and moisture transport in multi layer walls interaction and heat loss at varying outdoor temperatures, 2012, Latvian Journal of Physics and Technical Sciences, N6(I), p. 32–43
2. LVS EN ISO 7730, Ergonomics of the thermal environment – Analytical determination and interperatation of thermal comfort using calculation of the PMV and PPD indices and local thermal comfort criteria, 2006, third ed.
3. ANSYS Inc., Ansys CFX solver theory guide, 2011.
4. MENTER, FLORIAN R., Two-equation eddy-viscosity turbulence models for engineering applications, *AIAA-Journal*, 1994, Vol. 32(8), p. 1598 – 1605.
5. GENDELIS, STANĪSLAVS, Complex analysis of thermophysical processes in buildings, 2012, University of Latvia, PhD Theses.



VERIFICATION OF FLOW CALCULATION METHOD IN THE NEAR-DISK GAPS OF HIGH CYLINDER PRESSURE STAGE OF STEAM TURBINE

O. Simbirska, S. Alyokhina

*A. N. Podgorny Institute for Mechanical Engineering Problems of the
National Academy of Sciences of Ukraine
Dm. Pozharsky 2/10, UA-61046 Kharkiv – Ukraine*

ABSTRACT

In the multi-stage steam turbines in addition to the torque on the rotor each stage produces an axial force, which tends to move the rotor in the direction of the steam flow. For preventing shifting of the rotor is necessary to balance or significantly decrease the acting forces in the axial direction. Therefore it is necessary to conduct research of gas-dynamic processes and determine of the steam flow influence to the lateral surface of a rotor discs and stator diaphragms.

The main research problem is the occurrence of separation phenomena in certain areas of the gap. The additional complexities are in the modelling of flow in gap with consideration of the rotor rotation and the vapour flow through the discharge orifice.

The calculation was made using modern program packages. Based on a comparison of experimental and numerical results “SST” $k-\omega$ turbulence model was chosen. The width of axial gaps correspond to the true values of the turbine stages. As a result the velocity field and the pressure distribution on the gap's walls were obtained.

Keywords: steam turbine, near-disk gap, pressure distribution.

1. INTRODUCTION

In the multi-stage steam turbines steam moving in near-disk gap creates pressure on the rotor discs. Produced force tend to shift the rotor in the direction of the steam flow along the axis of rotation. For preventing shifting of the rotor is necessary to balance or significantly decrease the acting forces in the axial direction. In this case the different direction of flow in low, medium and high pressure cylinder (LPC, MPC and HPC) or double flow cylinder and the discharge orifice in the disks are used.

The steam flow in the gap between the lateral surface of the rotor disks and stator diaphragms it is actually a steam flow within radial-annular diffuser. Despite the great number of published research and experimental data, the effective method does not yet exist for calculating the characteristics of such flows, particularly in diffuser with rotating wall. The main problem is the occurrence of separation phenomena in certain areas of the gap.

The additional complexities are in the modelling of flow in gap with consideration of the rotor rotation and the vapour flow through the discharge orifice. The rotation of the rotor causes the "pumping effect" when the fluid are in the rotational motion and centrifugal force pushes it from the rotation axis to the periphery. In such a way because of the rotation of the disk in the limited space circular motion occurs when there is no flow rate through the gap, or the complex structure of moving from the center to the periphery of the flow, which is significantly influenced by the flow rate [1].

Practically all of investigations of flows in this area are experimental, conducted on simplified models and are not fully reflecting the real geometry of the object [2, 5].

At present, modern numerical methods and software packages based on those methods allow to simulate three-dimensional viscous turbulent flows, including such phenomena as the separated flows, vortex zones and other unsteady effects. However, the most important question is the choice of adequate turbulence model and the correct formulation of the boundary conditions.

2. PROBLEM DEFINITION

For the verification of the numerical method for calculation of the flow in the gap between the rotor disc and stator used the results of experimental investigation [2, 3] on the installation, which represents a disk of constant thickness, rotating in the casing (Fig. 1). The model is a flat radial diffuser with ratio $R_0/r_{in} = 3.89$. External disk radius $R_0 = 200$ mm, axial gap S varied from 1.8 to 7.8 mm.

In the experiment, the pressure measurements on interior face were conducted at a fixed and a rotating disk.

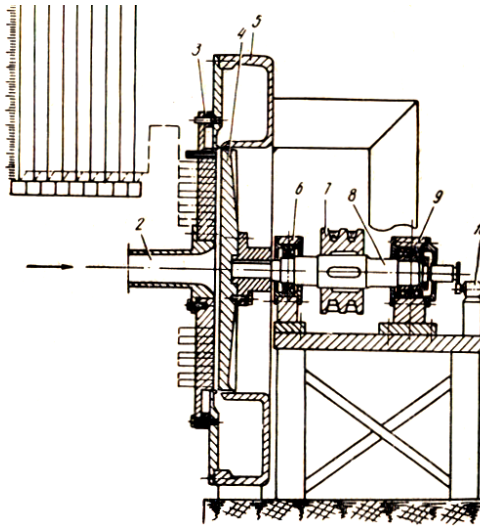


Fig. 1. Experimental installation for the investigation of flow in the near-disk space:
1 – cistern-type manometer battery, 2 – air supply pipe, 3 – cover, 4 – rotating disk,
5 – casing, 6 – front support, 7 – drive pulley, 8 – shaft, 9 – rear support, 10 – tachogenerator

For numerical research was built finite element model (Fig. 2). In the first stage the numerical experiment was conducted without rotation.

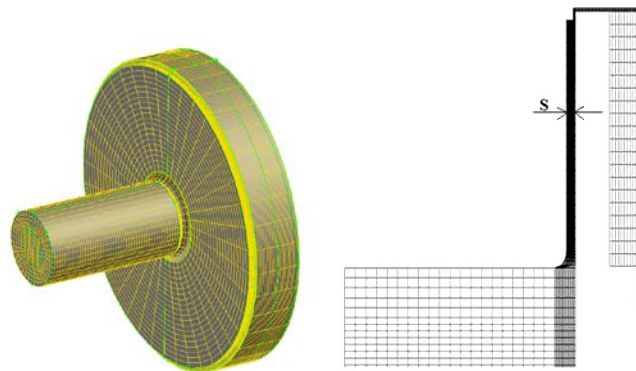


Fig. 2. The computational model of near-disk axial gap

A mathematical model of the process included the following equation:

- Continuity (sources and sinks of mass absent);
- The quantity of motion of a viscous fluid Navier-Stokes equations;
- Energy (for air).

In order to close system of differential equations was supplemented by the equation of state of ideal gas.

Solution of the differential equations of the mathematical model it is advisable to conduct with modern computer software packages help (Fluent, CFX, STAR-CD, etc.), using the finite volume method [6].

3. RESULTS OF CALCULATION

Comparison of theoretical and experimental characteristics of the flow in the gap space was based on the static pressure distribution on the inner face of the cover. Investigations were performed for four values of the relative gap $S/R_0 = 0,009; 0,019; 0,029; 0,039$, which correspond to the turbine stages gaps in the HPC and MPC.

Choice of turbulence model was carried out for all values of the gap. The change of static pressure along the radius was reviewed for most commonly used turbulence models: "Standard" k-e model [7], "RNG" k-e [8], "Realizable" k-e [9], "Standard" k- ω [10], "SST" k- ω [11] (Fig. 3).

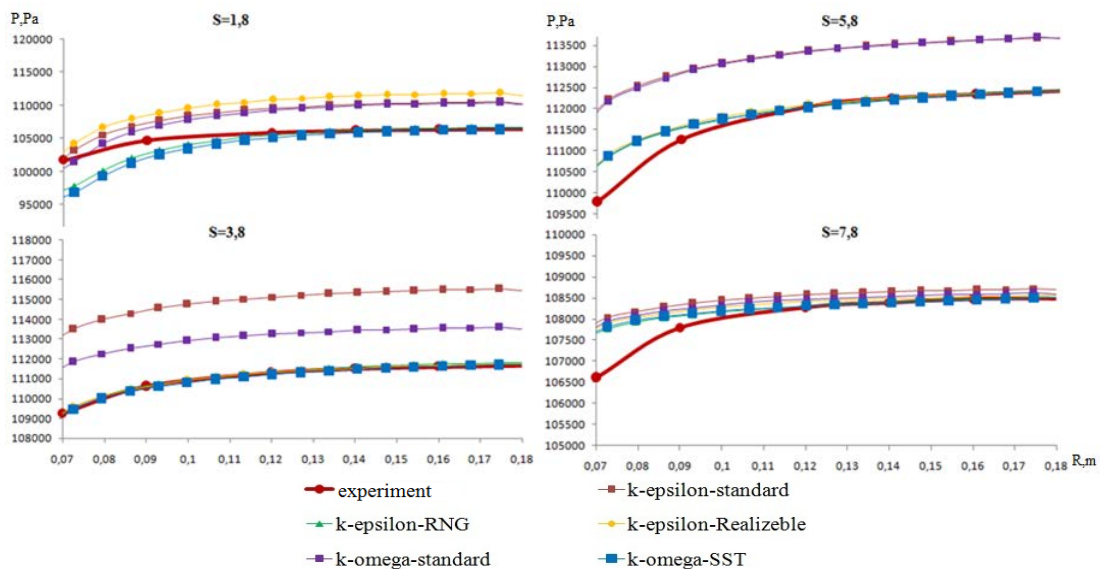


Fig. 3. Static pressure distribution along the radius of the diffuser wall with different models of turbulence

For gap $S = 3.8$ mm is observed better agreement between the calculated and experimental data. In this case, a good agreement shown such turbulence model as "RNG" k-e, "Realizable" k-e, "SST" k- ω . For the other gaps good agreement at the radius $R = 0.12-0.18$ m show "RNG" k-e and "SST" k- ω turbulence model. At radius $R = 0.07-0.12$ m for gap $S = 1.8$ mm, the experimentally obtained pressures are higher than calculation, and for gaps $S = 5.8$ mm and $S = 7.8$ mm the calculation pressures are higher than the experimental.

For gaps $S = 1.8$ mm and $S = 3.8$ mm the pressure remains constant in gap width (Fig. 4), this is evidence that the structure formed by closed boundary layers. For a gap 5.8 mm and 7.8 mm at

the radius $R = 0.18$ m a slight decrease in pressure observe near the disc ($D_p = 15$ Pa) (Fig. 5). At a radius 0.07 m there is a evident pressure increase near the disc ($D_p = 54$ Pa). This may be caused by the influence of the entrance flow form in the annular gap.

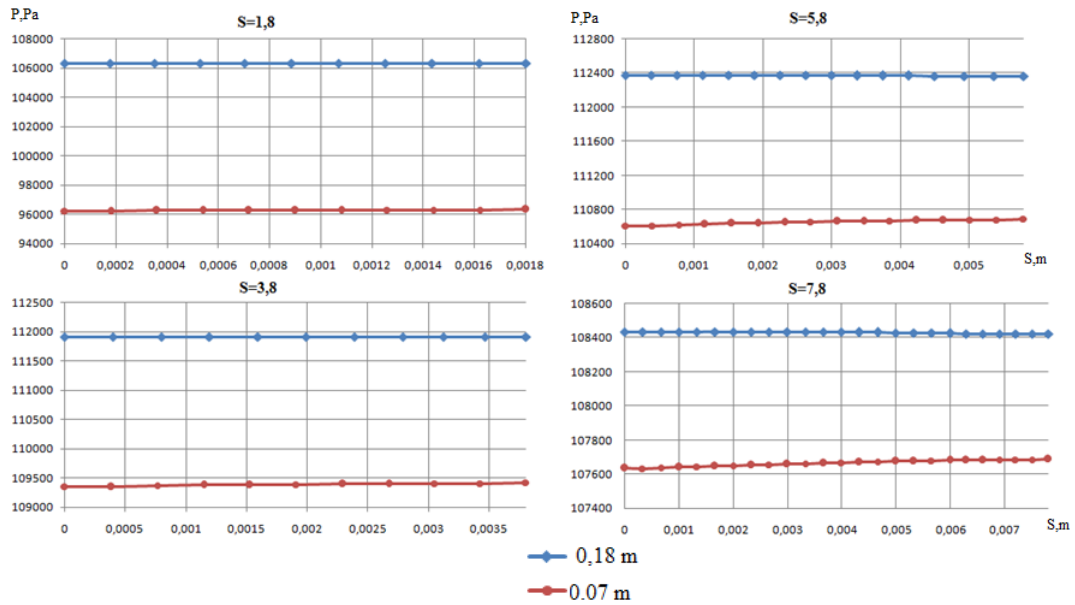


Fig. 4. Calculated static pressure distribution across the gap width in the cross section at a radius of 0.18 m and 0.07 m

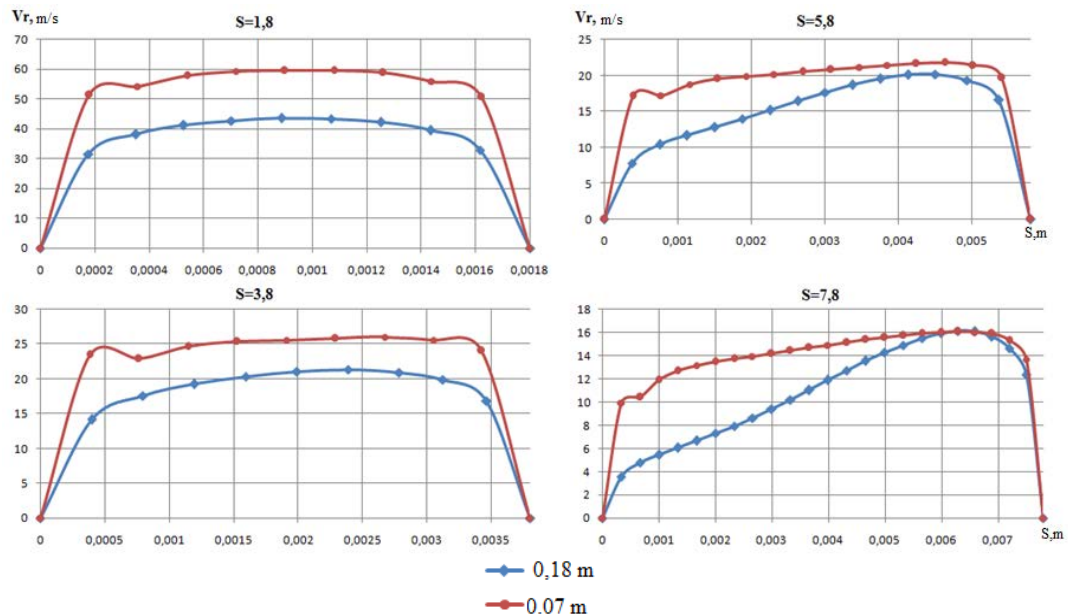


Fig. 5. Calculated radial distribution of velocity across the gap width at a radius of 0.18 m and 0.07 m

For small gaps flow has a form of closed boundary layers with a power law velocity distribution. By increasing the gap the core is formed in the center of the flow, the boundary layer increases near the cover and decreases near the disk. The flow is pressed against the disk surface, because of a protrusion on the edges cover surface at the outlet of gap.

Comparison of the calculated and experimental results shows the feasibility of using the "SST" $k-\omega$ model of turbulence for further annular diffuser calculations. When $S = 3.8$ mm pressure values are the same in the whole radius range, when $S = 1.8$ mm calculated values are lower, and when $S = 5.8; 7.8$ m higher than experimental.

A similar approach was used for the flow calculation in the near-disk axial gap of the typical design turbines, with a capacity of 300-350 MW. Computational model includes the pressure breakdown labyrinth, axis radial annular diffuser and camera on the exit. The ratio $r/R = 0.84$ (External radius $R = 0.8528$ m internal radius $r = 0.7158$ m).

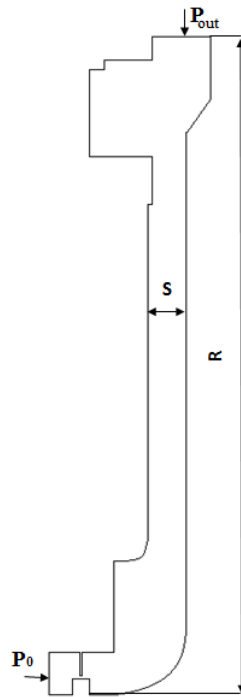


Fig. 6. Computational model of near-disk axial gap in typical HPC stage

Flow considered without rotation, pressure is 80000 Pa at the inlet, and atmospheric at the exit, medium temperature 100° C.

In contrast to the classical scheme in real construction the steam flow is jetting out from the gap between the last tooth seal. In the gap the jet is speeding and is leaking upon the concave surface of the disk and this place, in practice, often have cracks. Then the steam is moving to the surface of the disk and the reverse current arises near the stator with generation of circular motion in the camera.

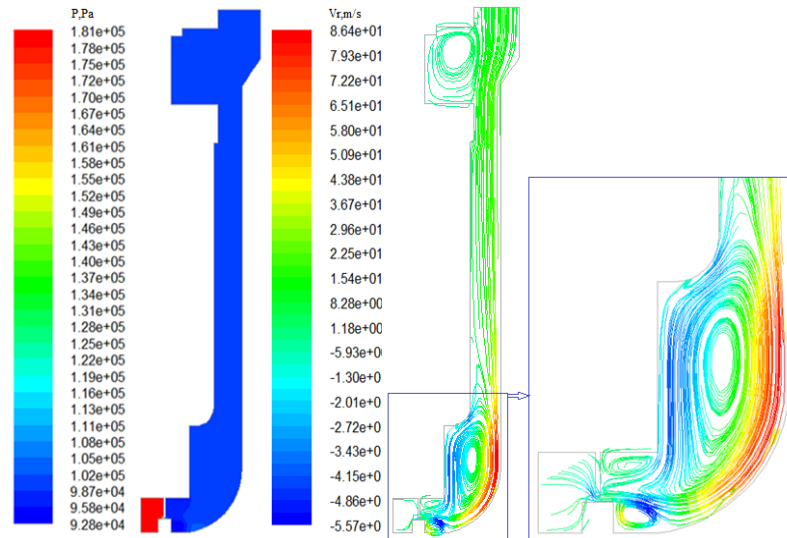


Fig. 7. The distribution of the static pressure and flow lines in the cross section of the near-disk gap

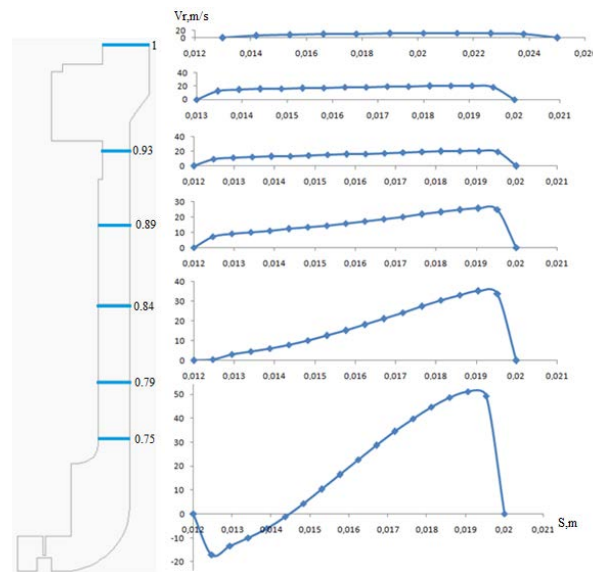


Fig. 8. The distribution of radial velocity across the width of the gap

The near-disk gap with stationary disk and jet flow at the entrance does not work as axis radial diffuser practically. The pressure increase is observed only at the entrance of gap, and at large radiuses the static pressure in the gap remains almost constant, the change does not exceed 100 Pa.

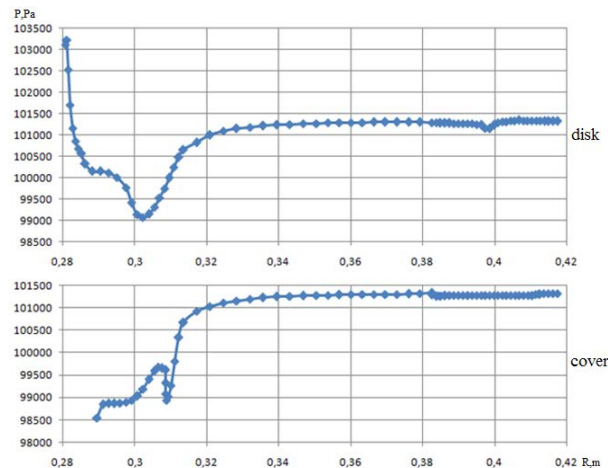


Fig. 9. The distribution of static pressure along the radius on the gap walls

4. CONCLUSIONS

Investigating the flow in the near-disk gap the "SST" $k-\omega$ turbulence model was chosen based on comparison of experimental and numerical results.

The flow structure in the near-disk gap for turbine of standard construction (300- 350 MW) was obtained.

Investigation of flow in the near-disk gap of real turbines (with allowed disc rotation and flow through the discharge orifice) are planned in the future.

REFERENCES

1. ШВЕЦ И. Т., ДЫБАН Е.П. *Воздушное охлаждение деталей газовых турбин*. Киев: Наукова думка, 1974, 487 с.
2. СЕДАЧ В. С. Коэффициенты расхода при течении через разгрузочные отверстия в дисках паровых турбин. *Паровые и газовые турбины*, 1960, № 2, с. 117–131.
3. СЕДАЧ В.Н., ГОЛОЩАПОВ В.Н. Влияние рас хода через полость между вращающимся диском и стен кой на распределение давления по радиусу. *Энергетическое машиностроение*, 1967, № 4, с. 51–58
4. МОРОЗОВ Б.И. Экспериментальное исследование протечек в ступенях турбины. *Труды МЭИ*, 1957, Вып. 28, с. 27–35.
5. БОНДАРЕНКО Г.А. Исследование гидродинамики потока между корпусом и дисками рабочих колес турбомашин. *Компрессорное и энергетическое машиностроение*, 2009, № 4 (18), с. 37–40.
6. ФЛЕТЧЕР К. *Вычислительные методы в динамике жидкостей*. М.: Мир, 1991, 552 с.
7. LAUNDER B. E., SPALDING D. B. *Lectures in Mathematical Models of Turbulence*. London: Academic Press, 1972, 124 p.
8. CHOUDHURY D. *Introduction to the Renormalization Group Method and Turbulence Modeling*. Fluent Inc. Techn. Memorandum, 1993, 107 p.
9. SHIH T.H., LIOU W.W., SHABBAR A., YANG Z., ZHU J.A. New $k-\epsilon$ Eddy-Viscosity Model for High Reynolds Number Turbulent Flows – Model Development and Validation. *Computers Fluids*, 1995, Vol. 24 (3), p. 227–238.
10. WILCOX D.C. Reassessment of the scale-determining equation for advanced turbulence models. *AIAA J*, 1988, No. 11 (26), p. 1299 – 1310.
11. MENTER F. R. Two-equation eddy viscosity turbulence models for engineering applications. *AIAA J*, 1994, No 11 (32), p. 1299 – 1310.



DYNAMIC ERROR OF THE TURBINE GAS METER AT COMPLEX FLOW PULSATION LAWS

A. Tonkonogovas, A. Stankevičius

Lithuanian Energy Institute

Breslaujos str. 3, LT-44403 Kaunas – Lithuania

ABSTRACT

Turbine gas meters (TGM) are widely used for the accounting of natural gas, and also as standards in the facilities for restoring of gas flow volume unit. Their metrological parameters straight influence efficiency of energy use. For TGM appearance of the so-called dynamic error δ because of TGM rotor inertia is characteristic. This error is well investigated for the elementary flow pulsation laws. However, in practice TGM usually work under conditions of complex pulsation laws, sometime at sign-altering pulsations when flow direction periodically varies.

Response and dynamic error of turbine gas meter at different law of pulsations and at different conditions of pulsation has been studied. Earlier developed semi-experimental method has been used for numerical simulation, according to which the equation of TGM response on sharp flow change is being applied for calculations on each step of time t . The experimentally defined time constant of inertia T is being used as key parameter of process. The big advantage of the method is its suitability for any law of flow pulsation.

Keywords: turbine gas meter, response, dynamic error

1. INTRODUCTION

Turbine gas meters (further TGM) are widely used for the accounting of natural gas, and also as standards in the facilities for restoring of gas flow volume unit. Their metrological parameters straight influence efficiency of energy use. For TGM appearance of the so-called dynamic error δ because of TGM rotor inertia is characteristic. This error is well investigated for the elementary flow pulsation laws. However, in practice TGM usually work under conditions of complex pulsation laws [1].

Because of different reasons in gas flow always there are pulsations. As a result of the turbine meters rotor inertia its rotation frequency and correspondingly meter reading always lag from the true momentary flow rate value. In the phase of flow rate decreasing the lag always bigger than in the phase of increasing, so the average reading of the meter is always bigger than the average value of the flow rate. This is the reason of appearing the typical for turbine meters dynamic error which is always positive.

The problem of the turbine meters dynamic errors is known for tens of years. One of the first to evaluate and predicate the dynamic error was W.F.Z. Lee [2]. Unfortunately according to [2] at low values of the response parameter the dynamic error becomes negative, what is impossible by nature of this error.

N. Lehmann [3] got analytical solution for transient processes in the turbine gas meters and presented dynamic error calculation results for gas flow pulsations of rectangular form, which are not occur in practice. Between of influenced parameters the parameter that defines the turbine meter rotation inertia is absent. The N. Lehmann results are involved in the PTB (Germany) normative document G13 [4].

The most known are the results of the K. N. Atkinson [5]. They are obtained for sine flow rate pulsations. K.N. Atkinson results are included into ISO document [6]. Analogical results were presented by R.J. McKee [7].

All known results are obtained for rectangular or sine flow pulsations while according to investigations, for example, B. Lee et al. [8] in real conditions the flow pulsation occurs by complex law.

All obtained results are based on solution of differential equation of turbine meter rotation in the transitional flow, which contains a certain number of hard-to-evaluate parameters. This is the main reason that different investigators results are fragmentary and often disagreed.

Although the problem, which occurs in practice [9], has been known for a long time there is no exhaustive knowledge on transient processes in turbine meters simulation and meters response and dynamic errors evaluation.

Our method [10], which previously has been developed and applied for numerical simulation of the TGM response and dynamic error at the simple flow pulsation laws [9], this time has been used for calculations with pulsations at different complex laws.

2. METHODOLOGY

Any arbitrarily defined curve of flow rate change over time is replaced by the stepped line around a given curve, as shown in Fig. 1. At each step of time Δt_i to calculation of the meter's readings the equation of its response to a rectangular (stepped) change in flow is used. Experiments show that this response to TGM occurs exponentially [10].

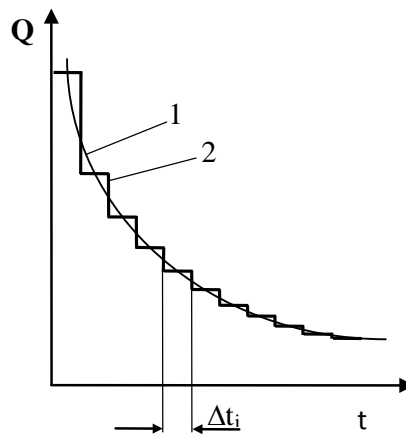


Fig. 1. Replacement of an arbitrarily given flow change curve (1) by stepped line (2) with a length of the step Δt_i

The main and only determining the process parameter is the index of inertia of the TGM T , sometimes called the time constant of inertia and relatively easy may be determined experimentally [11].

The method allows eliminating presently used traditional differential equation for the TGM rotor rotation, which incorporates a number of difficult – defined parameters. The combination of these parameters is replaced by a single parameter T . The method is universal, it may be applied not only to the turbine gas meters, but also to the flow rate meters and the meters of various liquids, not only with rotating sensors but also with moving sensors of other type. It is also basically applied to the some meters of other parameters such as temperature, pressure and flow velocity. The only limitation of the method is the requirement that the meter's response law should be unchangeable during all process of change of metered parameter.

2.1. Mathematical model

For calculations it can be used either the method of finite differences, or method solution of differential equation of the process [8]. We have used the first method which has some advantages in the processing, generalizing and graphical representation of the calculations results.

Distribution of the TGM rotor's rotation frequency ω on the space of time equal to the period of flow pulsation $\Delta t_0 = 1/f$ has been sought. This period has been broken down to sufficiently large number n of time intervals Δt_i :

$$\Delta t_i = \Delta t_0 / n. \quad (1)$$

On each such i^{th} interval (i^{th} step in time) final rotation frequency ω_{fin_i} has been determined by the known from calculation on the previous $(i-1)^{\text{th}}$ step final frequency $\omega_{fin_{i-1}}$, which is equal to initial frequency ω_{fin_i} for the given i^{th} step, by the equation:

$$\omega_{f_i} = \omega_Q + (\omega_i - \omega_Q) \frac{t}{T}. \quad (2)$$

Here ω_Q – rotation frequency, corresponding to the current flow rate Q , which is determined taking into account the revolution coefficient k_{rev} by the equation

$$\omega_Q = Q / k_{rev}. \quad (3)$$

The index of TGM inertia T has been calculated at each step depending on the current flow by the equation presented in [9].

$$T = \frac{C_T}{Q_i^m}. \quad (4)$$

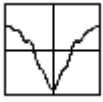
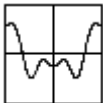
Parameters C_T and m in equation (4) have been determined for the given TGM experimentally [9]. As the boundary condition equality of rotation frequency on the ends of the segment Δt_0 has been used:

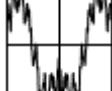
$$\omega_{fin_1} = \omega_{fin_n}. \quad (5)$$

2.2. Flow rate pulsing laws used for calculation

Calculations have been carried out for several complex pulsation laws which have been close to the met in practice [8].

Table 1. Studied laws of pulsations

Law number	Pulsation law equation	Waveform	Coefficient C_a in equation (6)
1	$\bar{Q} = 1 + \Delta \bar{Q}_{nom} \cdot \cos(2\pi t f) - 0,25 \Delta \bar{Q}_{nom} \cdot \cos(4\pi t f) + 0,09 \Delta \bar{Q}_{nom} \cdot \cos(6\pi t f) - 0,05 \Delta \bar{Q}_{nom} \cdot \cos(12\pi t f) + 0,07 \Delta \bar{Q}_{nom} \cdot \cos(14\pi t f) - 0,04 \Delta \bar{Q}_{nom} \cdot \cos(18\pi t f)$		42.71
2	$\bar{Q} = 1 + 2/3 \Delta \bar{Q}_{nom} \cdot \cos(2\pi t f) + 1/2 \Delta \bar{Q}_{nom} \cdot \cos(4\pi t f) - 1/4 \Delta \bar{Q}_{nom} \cdot \cos(8\pi t f)$		48.93

3	$\bar{Q} = 1 + 4/5 \Delta \bar{Q}_{nom} \cdot \cos(2\pi f t) - 1/4 \Delta \bar{Q}_{nom} \cos(8\pi f t) +$ $1/7 \Delta \bar{Q}_{nom} \cdot \cos(16\pi f t) - 1/12 \Delta \bar{Q}_{nom} \cos(20 \cdot \pi f t)$		38.26
4	$\bar{Q} = 1 + \Delta \bar{Q}_{nom} \cdot \cos(2\pi f t) - 0,35 \Delta \bar{Q}_{nom} \cdot \cos(6\pi f t) + 0,25 \Delta \bar{Q}_{nom} \cdot$ $\cos(28\pi f t) - 0,09 \Delta \bar{Q}_{nom} \cos(46\pi f t) - 0,05 \Delta \bar{Q}_{nom} \cdot \cos(96\pi f t) +$ $0,07 \Delta \bar{Q}_{nom} \cdot \cos(120\pi f t) - 0,04 \Delta \bar{Q}_{nom} \cdot \cos(150\pi f t)$		35.60

Each law has been obtained according to the principle of Fourier by summing of the elementary cosine laws with different amplitudes and frequencies. Table 1 shows the pulsation law equation and waveform for all studied laws. In table also are presented values of coefficient C_a , which in equation (6) characterizes the limit value of the dynamic error.

The calculation of the response to the flow pulsation, i.e. a change in the time meter's readings; dynamic error and amplitude of the readings pulsation have been carried out in the wide ranges of frequency f and amplitude of flow rate pulsation.

3. RESULTS

3.1. Turbine gas meter response

The results of TGM response calculation are shown in Fig. 2.

At sufficiently low pulsation frequencies ($f < 0.01$ Hz), meter's inertia practically does not manifest itself, and the TGM readings coincide very closely with the curve of flow rate pulsation. With increasing frequency, meter readings are increasingly lagged behind the actual flow rate. At all flow pulsation laws TGM with increasing frequency first stops to respond to constituents with small amplitude, then on the components with increasing amplitude.

With increasing frequency, amplitude of readings pulsation TGM decreases, a shift of the pulsation phase appears, and pulsation law increasingly approaches to the cosine. At sufficiently high frequencies ($f > 1$ Hz) due to inertia TGM stops to respond to flow rate pulsation, and its rotation frequency remains constant. However exceeding the frequency which corresponds to average flow rate value. This exceeding determines the dynamic error of TGM.

At sufficiently low pulsation frequencies ($f < 0.01$ Hz), meter's inertia practically does not manifest itself, and the TGM readings coincide very closely with the curve of flow rate pulsation. With increasing frequency, meter readings are increasingly lagged behind the actual flow rate. At all flow pulsation laws TGM with increasing frequency first stops to respond to constituents with small amplitude, then on the components with increasing amplitude.

With increasing frequency, amplitude of readings pulsation TGM decreases, a shift of the pulsation phase appears, and pulsation law increasingly approaches to the cosine. At sufficiently high frequencies ($f > 1$ Hz) due to inertia TGM stops to respond to flow rate pulsation, and its rotation frequency remains constant. However exceeding the frequency which corresponds to average flow rate value. This exceeding determines the dynamic error of TGM.

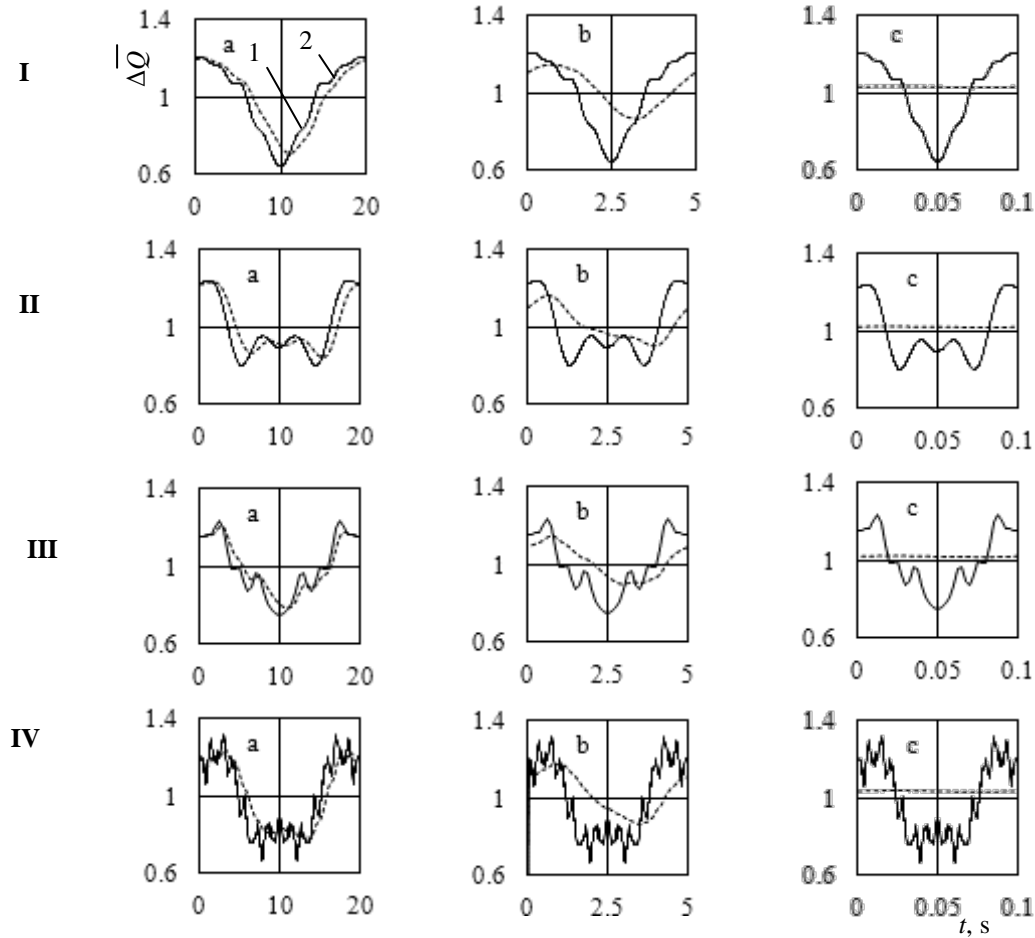


Fig. 2. Response of turbine gas meter to flow pulsations. I - IV – pulsation in accordance with Table 1 $\Delta\bar{Q} = 0.25$; a, b, c - $f = 0.05; 0.2; 10$ Hz respectively. 1 – real flow rate; 2 – TGM response

3.2. Dynamic error and amplitude of the turbine gas meter readings

Dependence of the TGM dynamic error and readings pulsation amplitude on the flow rate frequency at various amplitudes of flow rate pulsation is presented on Fig. 3 and 4 for four flow rate pulsations laws presented in Table 1.

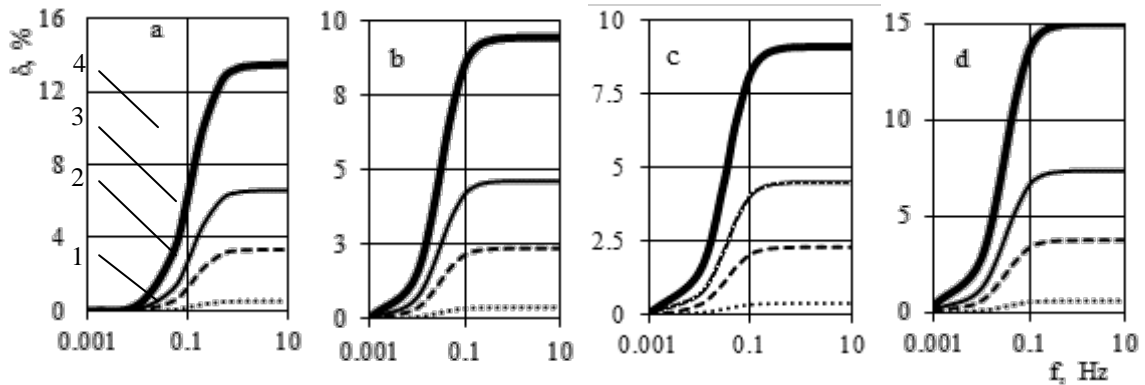


Fig. 3. Dependence of TGM dynamic error on flow rate pulsation frequency; a, b, c, d – the pulsation laws 1 – 4 according to Table 1; 1–4 – $\Delta Q = 0.1; 0.25; 0.35; 0.5$ respectively

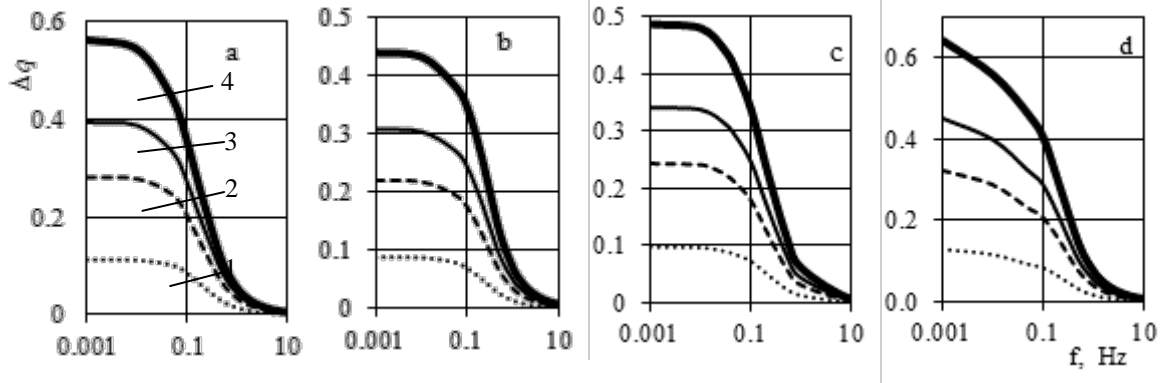


Fig. 4. The amplitude of the TGM readings pulsations on the pulsation frequency; designations are the same as in Fig. 3

The character of the changing of dynamic error is qualitatively the same as in the case of simple pulsation laws. At sufficiently low frequencies, when the meter's inertia does not manifest itself, the dynamic error is close to zero. With increasing of pulsation frequency dynamic error begins to increase. With reaching a certain value of frequency rate of the error growth reaches its maximum value, and with further increasing in the frequency begins to decrease. Dynamic error in this case continues to grow until at a frequency about 1 Hz reaches its maximum limit value δ_{lim} , and after that with further growth of frequency remains unchanged. This occurs at the same time, when the TGM rotor rotation frequency stops pulsing and depend on the frequency of pulsations.

Thus, the dependences of the TGM dynamic error and response on the pulsation frequency correspond to one another. The character of these relationships is exactly the same as for the simple laws of pulsation.

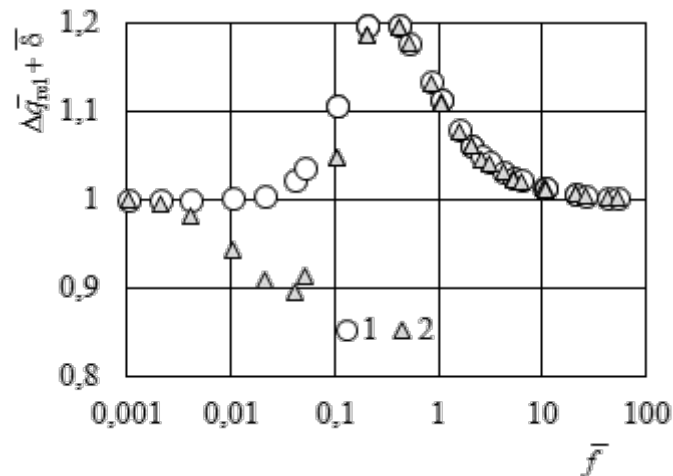


Fig. 5. Dependence of the sum of dynamic error and the amplitude of oscillation frequency readings to pulsation frequency. 1 and 2 – the pulsations number 1 and 4, respectively

Also dependences of flow rate pulsation frequencies for the dynamic error and the pulsation amplitude complies with each other, as it follows from the joint consideration of Fig. 3 and 4. Dependence of the sum of two parameters $(\Delta\bar{q} / \Delta\bar{Q} + \delta / \delta_{lim})$ in the dimensionless form of the frequency is presented in Fig. 5 for the two complex laws. For sufficiently small and sufficiently large values of frequency sum is equal to one, at intermediate values deflects up to 20% in one or another direction, depending on the pulsation law.

3.3. Limit value of dynamic error

Limit value of dynamic error δ_{lim} depends only on the amplitude of flow rate pulsation $\Delta\bar{Q}$.

$$\delta_{lim} = C_a \Delta\bar{Q}^2. \quad (6)$$

Constant C_a in this equation depends only on the law of pulsation. For the simple laws of pulsation – rectangular, triangular and cosine laws $C_a = 100, 50$ and 33.5 respectively. Values of C_a for the studied complex pulsation laws are presented in Table. 1. They are close to the values of C_a for cosine and triangle laws.

CONCLUSIONS

Previously by ourselves developed method of numerical simulation of turbine gas meter behaviour in pulsing flows has been applied for close to the practice complex pulsation laws. The method is universal and it may be applied not only to the turbine gas meters, but also to the flow rate meters and the meters of various liquids, not only with rotating sensors but also with moving sensors of other type. Method allows simulating response and dynamic error of turbine gas meter for any pulsations under various laws, including the field conditions.

It is determined, that dynamic error of turbine gas meter, depending on the law of flow pulsation, can reach up to 15 %. Limit value of dynamic error δ_{lim} depends only on the amplitude of flow rate pulsation $\Delta\bar{Q}$ by square law. Dependence of TGM dynamic error and response on the pulsation frequency corresponds to each other.

REFERENCES

1. CHEESEWRIGHT R., ATKINSON K.N., CLARK C., HORST G.J.P., MOTORAM R.C., VILJEER J., Field tests of correction procedures for turbine flow meters in pulsate flows, *Flow measurement and instrumentation*. 1996, Vol. 7 No. 1, p. 7–17.
2. LEE W.F.Z., KIRIK M.J., MILLINGTON B. Gas turbine flow meter measurement in pulsating flow. *Journal of engineering for gas turbines and power*. 1975, Vol. 97, p. 531–539.
3. LEHMANN N. Dynamisches Verhalten von Turbinenradgaszahlern. *Das gas und wasserfach – GWF-131*. 1990, Nr. 4, Gas Erdgas, p. 160–167.
4. Technische Richtlinien Messgeräte für Gas (PTB) G13, 1994-12.
5. ATKINSON K.N. A software tool to calculate the overregistration error of a turbine meter in pulsating flow, *Flow measurement and instrumentation*. 1992, 3 No. 3, p. 167–172.
6. ISO/TR 3313:1998(E) Measurement of fluid flow in closed conduits – Guidelines on the effects of flow pulsations on flow-measurement instruments.
7. MCKEE R.J. Pulsation effects on single- and two rotor turbine meters, *Flow measurement and instrumentation*. 1992, 3 No. 3, p. 151–166.
8. LEE B., CHEESEWRIGHT R., CLARK C. The dynamic response of small turbine flow meters in liquid flows, *Flow measurement and instrumentation*. 2004, 15 No. 5–6, p. 239–248.
9. TONKONOGOVAS A., STANKEVIČIUS A. The influence of gas flow pulsing on performance of thermal power plant // 8th international conference of young scientists on energy issues CYSENI 2011, Kaunas, Lithuania, May 26–27, 2011. Kaunas: LEI, 2011. ISSN 1822-7554, p. 310–317.
10. TONKONOGIJ J. “The new equation of rotation of the turbine gas meter in unsteady flows”, *Energetika*, ISSN 0235-7208, 2009, Vol. 55, Iss. 3, p. 172–177.
11. TONKONOGIJ J., PEDIŠIUS A. “Numerical simulation of the turbine gas meters behavior in the pulsing flow” *Journal of heat transfer research*, ISSN 1064-2285, 2008, Vol. 39, Iss. 7, p. 559–570.



MACRO FOAM CONVECTIVE HEAT TRANSFER IN VERTICAL CYLINDRICAL TUBE

M. Trepulis

*Kaunas University of Technology
Institute of Energy Technology
K. Donelaičio str. 20, LT-44239 Kaunas – Lithuania*

ABSTRACT

At Kaunas University of Technology various heat transfer studies with macro foam are carried out since 1998. Stable macro foam is produced by blowing air through the perforated plate and pouring water with detergent on it at the same time.

This paper reports experimental data for adiabatic flow and laminar convective heat transfer of macro foam in vertical cylindrical 80 cm x 0.15 cm diameter tube. Validation was carried out in order to find the experimental equipment heat loss. Experimental unit was first tested with the air because of its physical properties are known. Then the experiment was carried out with different foam porosity and flow rates. The results were compared with that of the heat transfer in vertical upward and downward statically stable foam flow and flat-surface cooling of two-phase flow of foam and afterwards compared with the heat transfer of colloidal gas aphrons (CGA) in horizontal mini-channels. The results show that macro foam heat transfer coefficient falls between air and water.

Keywords: macro foam, heat transfer coefficient, vertical tube, flat surface cooling

1 INTRODUCTION

1.1 Motivations

Stable macro foam is produced by blowing air through the perforated plate and pouring water with detergent on it at the same time. For water and detergent supply in foam generation pure gravity flow system is used. Water and detergent (0.5% concentration) tank stands upper than foam entrance level in the experimental tube. Firstly liquid solution is supplied from the main tank to a smaller one to ensure the constant liquid pressure. Flow rate is adjusted by valve (see Fig. 1). When liquid reach the perforated plate from top the air is blowing from underneath at the same time and foam is generating.

It has been reported that aqueous foam made of water and surfactant solutions (macro foam as well as micro foam) have stable bubbles with a reproducible size distribution (see Fig. 2), demonstrate high stability, and can be easily pumped through tubes still keeping their structure (Sebba, 1987, [1]). Macro foam and Colloidal gas aphrons (micro foam) are subject to the same physical phenomena as those taking place in foams including (i) liquid drainage, (ii) interbubble gas diffusion, and (iii) Gibbs–Marangoni effects (Bhakta and Ruckenstein, 1997 [2]).

Heat transfer process is interesting field in two-phase aqueous foam flow, as it can be applied for developing energy-efficient heat exchangers. Low primary energy resources consumption can be achieved with such foam heat exchangers by enhancing the heat transfer rates. To improve heat exchangers, two main strategies have been applied in the past: complex channel geometry of heat exchangers has been introduced; and application of advanced heat transfer fluid as working medium in heat exchangers.

Previous studies of aqueous foam flow were focused on investigation in foam generation and deterioration problems (Herzhaft, B., 2005, [3]). Physical properties of foam flow have been examined by (Feitosa, K., 2008, [4]). Complex rheological behaviour of foam has been studied by (Ireland P.M. 2009, [5]). Foam dynamic behaviour in viscous flows and foam-drop formation were studied by (Bazhlekov, I., 2001, [6]). Different applications of aqueous foam flow have been

considered in the past. It includes fire fighting and food applications, oil recovery, textile and cosmetics (Feitosa, K., 2008, [4]). The Heat Transfer Mechanism in Aqueous Foam Flow in a Channel (I. Gabrielaitienė, J. Gylys, R. Jonynas, T. Ždankus, 2011 [7])

However, even though the flow properties of macro foam and CGA (Colloidal gas aphrons) have been discussed qualitatively in the literature, to the best of my knowledge, no quantitative data on the macro foam heat transfer coefficient calculation using axial location method in heated tube has been reported. In this paper the same calculation methodology [11] is used as it was with micro foam and the results are compared between. The results are also compared with earlier experiments with macro foam [7] when metal plate was used instead of tube.

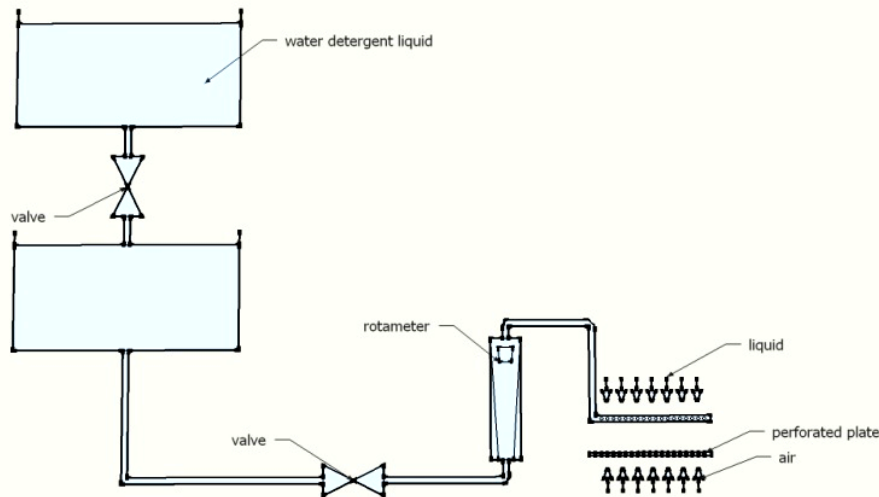


Fig. 1. Schematic of foam generation process

1.2 Macro foam structure

The influence of volumetric void fraction on foam structure is shown on Fig. 2. Foam pictures were obtained by camera, as the transparent plastic was inserted in the experimental channel entrance plastic tube. Aqueous foam structure consists of bubbles with liquid between them and forms a channel network, i.e., Plateau borders. Such highly structured geometry of liquid foam (liquid films bounded by Plateau borders and junctions) and mechanics at the film level influence the heat transfer rates. In Fig. 2 it is seen that a Plateau borders are more apparent, rather than the liquid films, which forms the bubbles walls as they are very thin. For the wettest foam porosity ($\beta=0.996$) on the experiment, an average bubble diameter was relatively small and range from 3 mm to 7 mm (see Fig. 2 (a)). Such wet foam provides better heat transfer condition, than dry foam ($\beta = 0.998$), where larger bubbles appears in the main stream and some small bubbles closer to walls. The bubble shapes are more polyhedral in the channel centre, where foam is dry, and more spherical close to the channel walls, where the foam is wetter. Similarly, the bubbles are more polyhedral for relatively dry foam (see Fig. 2 (c)) and more spherical for relatively wet foam (see Fig. 2 (a)). The average diameter range for the dry foam was from 13 mm to 17 mm (see Fig. 2 (c)), while the average diameter range for $\beta=0.997$ was between 8 mm and 12 mm (see Fig. 2 (b)). Similar results were obtained by previous experiments (Gabrielaitiene, J. Gylys, 2011, [7]).

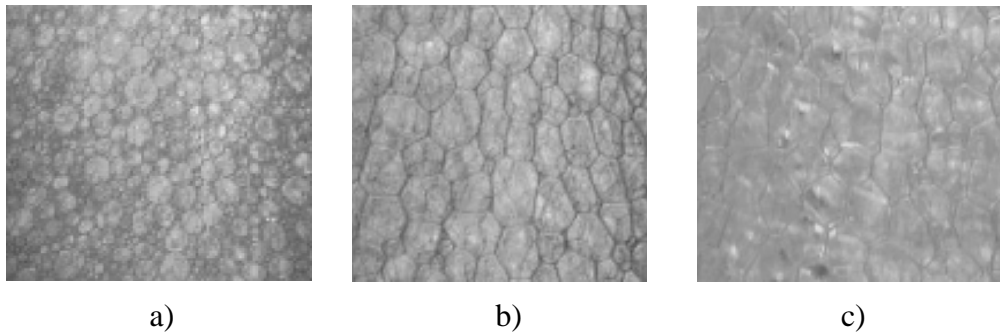


Fig. 2. Foam porosity during experiment a) $\beta=0.996$, b) $\beta=0.997$, c) $\beta=0.998$

2 EXPERIMENTAL SETUP

Fig. 3 shows a schematic of the cross-section of the test section. The calculation design is similar to that used by Warriar et al. 2002, [8] to study boiling heat transfer in mini-channels except that there is only one channel and it is heated straight with electrical current. Cylindrical tube stays in vertical position and is heating with transformer. Power supply is made from two transformers, where the first one 9 A autotransformer is necessary to adjust current and voltage and the second one is shell type single phase simple transformer. Only the second winding in the second transformer have been changed with 95 mm^2 copper wire in case to achieve high current for extended time. This self made power supply unit has voltage ranging from 0 to 1.5 V and current ranging from 0 to 1650 A. Only 95 mm^2 wire doesn't fit for over 300 A for extended time because it's getting hot. The wire is fitted to the tube by copper bended bus. The buses are soldered to the tube for better tube - bus contact. Cylindrical tube is made from stainless steel 0.5 mm thick with active heating height of 0.8 m. All outer side of the tube was covered with insulation. The flow channel has a hydraulic diameter D_h of 0.15 m defined based on the wetted perimeter.

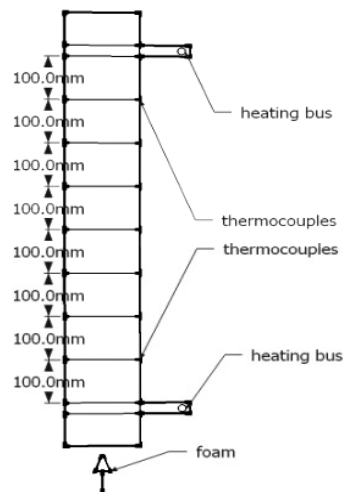


Fig. 3. Schematic cross-section of the test section

The inlet and outlet temperatures are measured by type-E thermocouples. Moreover, to measure the surface temperature along the stainless steel tube, twenty eight type E thermocouples were soldered to the surface. There are four thermocouples per axial location and the temperature readings at each axial location did not differ by more than ± 0.2 ($^{\circ}\text{C}$) for all heat transfer experiments. The seven axial location measured from the entrance are 0.1 m, 0.2 m, 0.3 m, 0.4 m, 0.5 m, 0.6 m and 0.7 m. The average of four temperatures is taken as the temperature of the heated surface at that axial location.

As mentioned by Warriar et al. (2002) [8], it was not possible to measure the fluid flow temperature inside the channels because the thermocouples were in contact with the channel walls leading to a higher temperature reading. Instead, the local fluid temperature is computed using the local energy balance equation. All the thermocouples readings are recorded every second by an Picotech TC 08 data acquisition system connected to a computer.

2.1 Experimental procedure

The experimental setup, which consist of water and detergent supply tank, volumetric pump, frequency converter for adjusting air flow rate, single flow flowmeter (rotameter type) for liquid and gas separate and heating transformer. At first, water tank is topped up with water mixed with detergent (phosphoric compound and stabilizers) of 0.5% concentration. Then it is pumped by gravity throw flowmeter to test section there the air comes from volumetric pump. The foam generation section consisted of a perforated metal plate with holes of diameter 1 mm staggered at 5 mm distance. The liquid solution was supplied from smaller tank to ensure equal distribution of the liquid. Air level is adjusting with frequency converter and, before reaching test section, cross flow meter. A heat flux may be applied by imposing a current across the heated tube. Each experiment is allowed to run for at least 10 minutes in case to reach steady state condition. Then the data acquisition unit is turned on to record temperatures. Current and voltage are measured with current clamp. The typical experiment duration to each test takes around 20 minutes. The process is repeated for different flow rates.

Experimental work was performed by changing the values of volumetric void fraction and foam velocity. The heat transfer process efficiency was evaluated by calculating the heat transfer coefficient for each foam porosity and speed. The current and voltage were recorded at the beginning of a run and were monitored during the course of the run. The current and voltage were used to determine the power density applied to the tube.

Table 1 Uncertainty associated to each experimental measurement

Measured quantity	Measured uncertainty
Volume, V	±5 mL
Mass, M	±1.0 g
Volumetric flow rate, Q_f	±5.0 %
Temperature, T	±0.2 °C
Voltage, U	±1.0 %
Current, I	±3.0 %

The volumetric flow rate of single phase water is measured directly with the flowmeter. The flowmeter is first calibrated by pumping single phase water into a graduated cylinder. A stop watch is used to measure the time it takes to fill a certain volume. The error in the flowmeter reading is estimated to be ±5% at 25 °C. The mass flow rates for the water experiments are calculated by multiplying the density of water at the inlet temperature (Munson et al., 1994, [9]) by the volumetric flow rate. The error associated with the water mass flow rates is the same as the error of the graduated cylinder used for the calibration of the flowmeter.

The experiments were repeated for different values of volumetric void fraction. Volumetric void fraction was defined by the following equation:

$$\beta = \frac{G_g}{G_l + G_g} \quad (1)$$

The G_g and G_l are the volume flow rate [m^3/s] of gas and liquid flow before entering a foam generation section.

The thermocouples have been calibrated by flowing air through the test section under adiabatic conditions at temperature ranging from 20 to 25 °C. The mean difference between all the

thermocouples and the air temperature (measured at the inlet and outlet of the test section) was ± 0.2 °C.

Table 1 shows the list of experimentally measured variables and the associated experimental uncertainty.

3 CONVECTIVE HEAT TRANSFER

Single and two-phase (liquid/gas) convective heat transfer in channels have been the subject of intense studies (Morini, 2004, [10], H. Tseng, 2005, [11] J. Gylys, 2008, [12]). It is beyond the scope of this work to make a thorough review of the topic. Instead, at first the validation of experimental apparatus and test procedure is carried out with single-phase air, because it is not suitable for water validation. Then it is reported experimental data for the local temperatures and local heat transfer coefficients for convective heat transfer to macro foam under imposed heat flux.

3.1 Heat loss

To determine the heat loss of the power supply to the surrounding environment, an energy balance is performed on the heated air. The total power input is expressed by Joule's law

$$q_{total} = UI \quad (2)$$

where U is the voltage measured in volts and I is the current measured in ampere. The actual heat input into the test section $q_{channels}$ must account for the heat loss to the surrounding and is given by

$$q_{channels} = q_{total} - q_{loss} \quad (3)$$

It can also be calculated from the energy balance on the single phase air:

$$q_{channels} = m_{air} \times c_{p,air} (T_{air,out} - T_{air,in}). \quad (4)$$

Where m_{air} is the mass flow rate and $c_{p,air}$ is the specific heat of air at the average temperature in the tube. It was found that the heat loss to the environment q_{loss} varies linearly with the total power input q_{total} and represents at around 23% of the total heat input over the range from 150 to 200 W. In other words, at least 77% of the total power consumed is supplied to the test section.

3.2 Local temperature profile

As previously mentioned, the local fluid temperature along the channels is not measured. Instead, it is estimated using the energy balance equation,

$$T_f(x) = T_{f,in} + \frac{q_{channel}}{m_f c_{p,f}} x = T_{f,in} + \left(\frac{T_{f,out} - T_{f,in}}{L} \right) x, \quad (5)$$

where $T_{f,in}$ and $T_{f,out}$ are the measured fluid inlet and outlet temperatures, m_f is the total mass flow rate of the working fluid, and x is the axial location of the thermocouples along the tube surface measured from the channel entrance ($x = 0$). The uncertainty in the calculated fluid temperatures is estimated to be 10%. Fig. 4 a and b show the typical wall and fluid temperature profiles along the channel for air and foam, respectively.

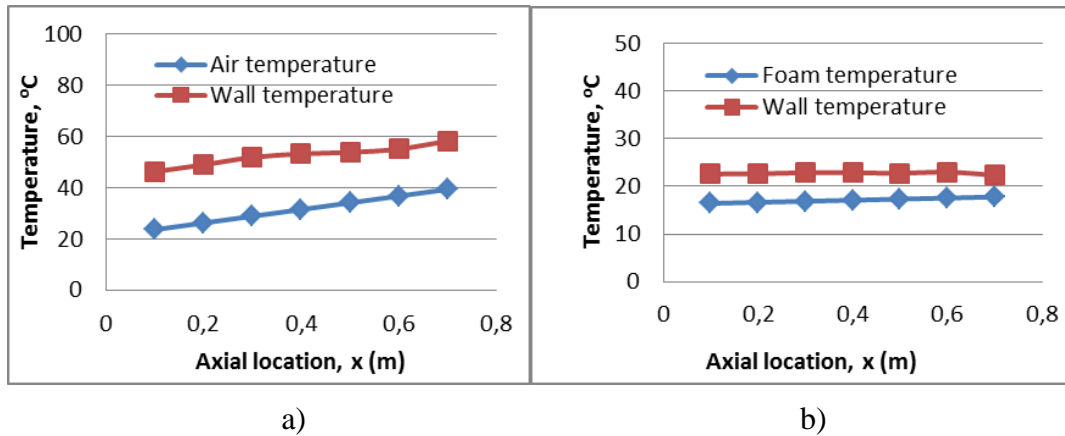


Fig. 4. (a) Fluid and wall temperatures for single phase air at total volumetric flow rate of $2.93 \times 10^{-3} \text{ m}^3/\text{s}$ (0.15 m/s) and power input of 85 W. (b) Fluid and wall temperatures for foam at total volumetric flow rate of $2.94 \times 10^{-3} \text{ m}^3/\text{s}$ (0.15 m/s) and power input of 170 W

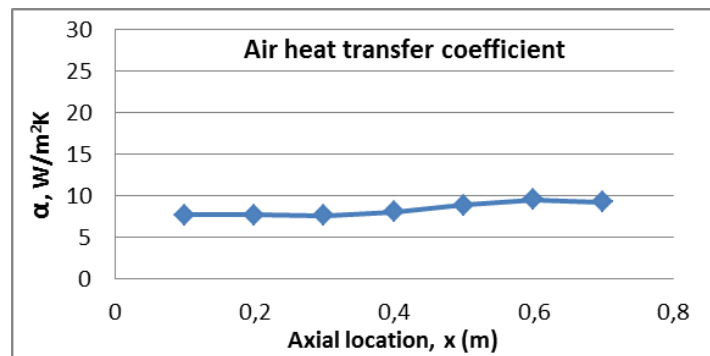


Fig. 5. Air heat transfer coefficient during experimental setup validation

In both cases, the volumetric flow rate is $2.93 \times 10^{-3} \text{ m}^3/\text{s}$ (0.15 m/s) for air and $2.94 \times 10^{-3} \text{ m}^3/\text{s}$ for foam, the total heat input in the channels is 85 W for air flow for validation purpose and 170 W for foam flow. The difference between the fluid and the wall surface temperature stays similar for both air and foam. However, the temperature difference is much larger for air due to smaller specific heat and heat transfer coefficient.

3.3 Heat transfer coefficient

The wall heat flux q''_w is calculated from the overall heat input q_{channel} for experimental channel and is given by,

$$q''_w = \frac{q_{\text{channel}}}{A_t}, \quad (6)$$

where A_t is the total heated surface area of the channel. Then, the local heat transfer coefficient can be calculated according to

$$h(x) = \frac{q''_w}{T_w(x) - T_f(x)}, \quad (7)$$

where $T_w(x)$ is the measured wall temperature at the location of the thermocouple and $T_f(x)$ is the local fluid temperature calculated using Eq. (5).

4 RESULTS AND DISCUSSION

Fig. 6 shows the plot of the heat transfer coefficient versus the volumetric flow rate in the thermally fully developed region of micro foam (porosity around 0.70) done by Howard Tseng [11] with micro channel and for macro foam (porosity 0.996) from current experiment.

It indicates that, the heat transfer coefficient for both cases is independent of mass flux. However, macro foam heat transfer coefficient is lower by almost 8 times compared to that obtained Colloidal gas apherons and equal to around $200 \text{ W/m}^2 \text{ K}$. This can be attributed to the larger porosity of macro foam resulting in significant reduction in the effective thermal conductivity and specific heat. Micro foam contains around 30% of water and macro foam only 0.4%. From results it can be seen, that more aqueous foam, the more effective thermal conductivity as increased amount of water, increase heat transfer coefficient value.

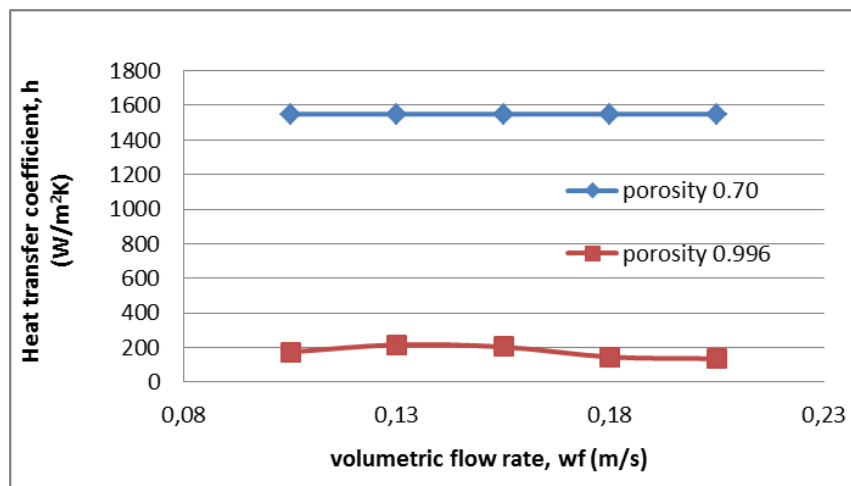


Fig. 6. An average heat transfer coefficient versus the volumetric flow rate in a channel for different foam porosity under uniform heat flux in micro foam [10] and macro foam

In Fig. 7 heat transfer rates are plotted for the different values of volumetric void fraction, (β) and are compared between previous experiments of I. Gabrielaitiene, J. Gylys [7] and present work. The experimental results show that the average heat transfer coefficient is highest $175 \text{ W/m}^2 \text{ K}$ for ($\beta = 0.996$) foam, and decrease as porosity increase ($120 \text{ W/m}^2 \text{ K}$ for ($\beta = 0.997$)). In previous experiments [7], the average heat transfer coefficient of a wettest foam ($\beta = 0.996$) is higher than heat transfer coefficient of a drier foam ($\beta = 0.997$) by about 20%. Average heat transfer coefficients are $172.9 \text{ W/m}^2 \text{ K}$ and $144.8 \text{ W/m}^2 \text{ K}$ for foam $\beta = 0.996$ and foam $\beta = 0.997$, respectively for experiments with plate (I. Gabrielaitiene, J. Gylys, [7]). In wetter foam, the amount of liquid in Plateau borders and junctions has increased. The gravity and capillary forces facilitate the liquid drainage from the foam and increase the thickness of liquid film, composing on the heated surface and channel walls. Present work with cylindrical tube has similar results, except that the curves aren't so straight. It can be explained, that foam drainage and uneven foam porosity over the channel, has grater influence for tube than for plate cooling. Cooling plate takes only small part of the whole channel area so there is not all uneven porosity and drainage influence seen in the results. That makes slight different in tube and plate cooling extreme values.

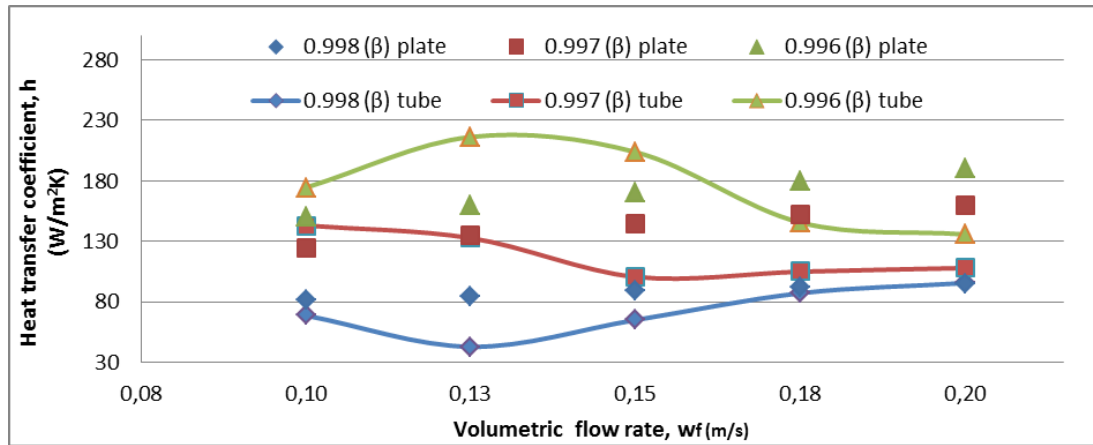


Fig. 7. Comparison of heat transfer coefficient for the different values of volumetric void fraction between plate experiment and cylindrical tube experiment, (h (W/m²K) dependence on flow rate (m/s))

In Fig. 8, there is plotted the heat transfer rate dependence on different porosity and compared between previous plate experiment with current work. There are seen slightly different heat transfer values over the foam velocity in Gabrielaitiene, J. Gyllys [7] experiment with plate: from 0.10 to 0.25 m/s. Foam velocity was modified by changing the flow rate of the gas. For example, for foam ($\beta = 0.998$), heat transfer rates have increased from 83.9 W/m²K to 110 W/m²K (30% increase). For foam ($\beta = 0.997$), heat transfer rates have increased from 135 W/m²K to 165 W/m²K; while for foam ($\beta = 0.996$), heat transfer rates have increased from 150 W/m²K to 192 W/m²K. This contains 22% and 29% increase for the foam ($\beta = 0.997$) and foam ($\beta = 0.996$), respectively. In present work there is not seen exact mass flow rate and heat transfer rate correlation. It was not seen in micro foam experiments (Howard Tseng, [11]) either. Current curve deviation might arrive from not constant drainage in different mass flows and uneven foam porosity over the channel.

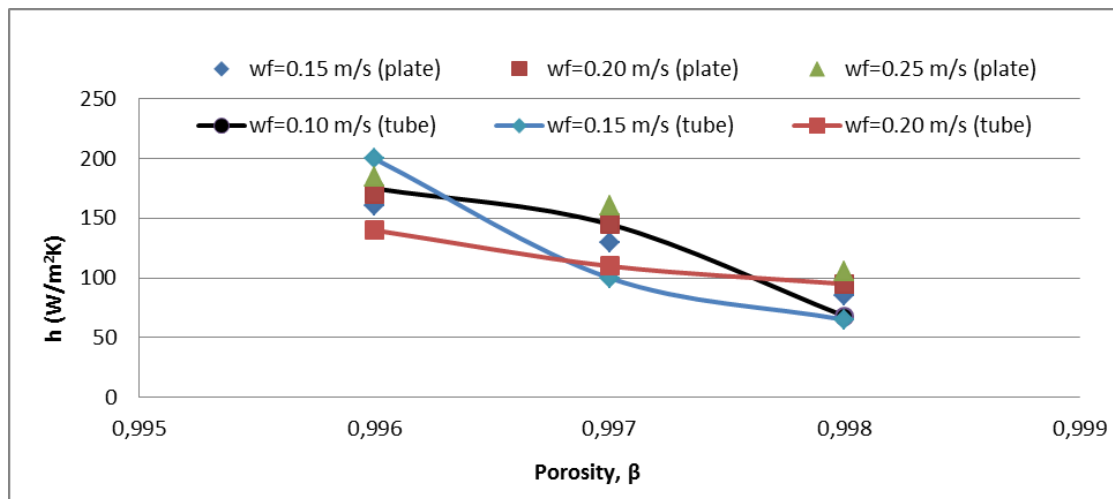


Fig. 8. Comparison of heat transfer coefficient for the different values of volumetric void fraction between plate experiment and cylindrical tube experiment, (h (W/m²K) dependence on porosity (β))

5 CONCLUSIONS

The present study was concerned with heat transfer properties of macro foam flowing in single cylindrical tube channel with hydraulic diameter of 0.15 m. First, well-known properties and correlations for single phase air were used to validate the experimental apparatus and data analysis. Experimental studies were performed for macro foam and the following conclusions can be drawn:

1. The average heat transfer coefficients for CGA under imposed heat flux are independent of the mass flow rate.
2. The heat transfer coefficient for aqueous foam made of water and surfactants is higher than for single phase air due to added liquid resulting in raised specific heat and thermal conductivity.
3. By foam porosity decreasing, the heat transfer coefficient raises, as more water are added and specific heat rises.
4. Even small amount of added water to make foam, rise heat transfer coefficient by few times. For example, 0.998 porosity (0.2% water) foam has around 8 times greater heat transfer coefficient than air.

Future works should include liquid drainage from the foam and emphasise different porosity over the channel axial locations in order to assess their interaction with the heated walls and influence for heat transfer coefficient.

REFERENCES

1. SEBBA, F. *Foams and Biliquid Foams-Aphrons*. New York: John Willey & Sons, 1987. 236 p. ISBN 0471916854.
2. BHAKTA, A., RUCKENSTEIN, E. Decay of standing foams: Drainage, coalescence and collapse. *Advances in Colloid and Interface Science*, 1997, Vol. 70, p. 1–124.
3. HERZHAFT, B., KAKADJIAN, S., MOAN, M. Measurement and modeling of the flow behavior of aqueous foams using a recirculating pipe rheometer. *Colloids and Surfaces A: Physicochemical and Engineering Aspects*, 2005, Vol. 263, No. 1–3, p. 153–164.
4. FEITOSA, K., DURIAN, D.J. Gas and liquid transport in steady-state aqueous foam. *European Physical Journal*, 2008, Vol. 26, No. 3, p. 309–316.
5. IRELAND, P.M. Coalescence in a steady-state rising foam. *Chemical Engineering Science*, 2009, Vol. 64, No. 23, p. 4866–4874.
6. BAZHLEKOV, I., VAN DE VOSSE, F.N., MEIJER, H.E.H. Boundary Integral Method for 3D Simulation of Foam Dynamics. *Computer Science*, 2001, Vol. 2179, No. 1, p. 401–408.
7. I. GABRIELAITIENĖ, J. GYLYS, R. JONYNAS, T. ŽDANKUS, The Heat Transfer Mechanism in Aqueous Foam Flow in a Channel, *Recent Researches in Engineering and Automatic Control conference in Tenerife*, 2011.
8. WARRIER, G.R., DHIR, V.K., MOMDA, L.A. Heat transfer and pressure drop in narrow rectangular channels. *Experimental Thermal and Fluid Sciences*, 2002, Vol. 26, p. 53–64.
9. MUNSON, B.R.; YOUNG, D.F.; OKIISHI, T.H. *Fundamental of Fluid Mechanics*. New York: John Wiley & Sons, 1994.
10. MORINI, G.L. Single-phase convective heat transfer in microchannels: a review of experimental results. *International Journal of Thermal Sciences*, 2004, Vol. 43, p. 631–651.
11. HOWARD TSENG, LAURENT PILON, GOPINATH R. WARRIER, Rheology and convective heat transfer of colloidal gas aphrons in horizontal mini-channels. *International Journal of Heat and Fluid flow*, 2006, Vol. 27, p. 298–310.
12. GYLYS, J.; GABRIELAITIENE, I.; ZDANKUS, T., S. SINKUNAS; Experimental research of heat transfer from an in-line tube bundle to a vertical foam flow. *Heat Transfer Research*, 2009, Vol. 40, No. 5, p. 455–472



FLOW STRUCTURE VISUALIZATION BEHIND THE SHOCK WAVE IN THE SHOCK TUBE

M.V. Daroshka, P.P. Khramtsov, O.G. Penyazkov

A.V. Luikov Heat and Mass Transfer Institute of NAS of Belarus

P. Brovki str. 15, Minsk 220072 – Belarus

ABSTRACT

The averaged Talbot-interferometer method was used to visualize the structure of the flow behind the incident and reflected shock fronts in the shock tube. Distributions of time-averaged density and temperature of the air throughout the whole flow field were measured for shocks with $M=1.3-1.6$. It is found that the thickness of the boundary layer in the observation area is about 7–9 mm, and the density in the boundary layer behind the shock front raises sharply. This leads to an increase of 6–7 % of the average density of the flow at about 3 mm from the shock tube wall. The area occupied by the boundary layer reaches half the cross sectional area of the shock tube. Thus shown that the flow behind the shock wave can not be considered uniform and undisturbed due to the influence of the boundary layer.

Keywords: shock tube, visualization, Talbot-interferometer

1. INTRODUCTION

Currently the shock tube is used more and more frequently in the study of the kinetics of chemical reactions in the gas phase and in the heterogeneous transformation of matter. An important advantage of the shock tube is the simplicity of obtaining the required thermodynamic conditions behind the incident and reflected shock waves. In the experiments, it is assumed that the flow behind the shock wave is uniform and undisturbed, or at least, is that the effect of the perturbation caused by the boundary layer is small. To study this phenomenon visualization of the flow structure behind the incident shock wave was made by the averaged Talbot-interferometry method.

In the work [1] the visualization of the flow with variable density is carried out using conventional optical techniques such as shadow photograph and schlieren-method. It should be noted that these methods require sophisticated optical equipment. Speckle photography technique [2] provides quantitative information about the deflection angles of the whole investigated flow field. Based on the results of measuring deflection angles by the speckle photography method, the authors of the works [3, 4] showed how to change the visible structures of a turbulent flow after the passage of an incident shock wave.

Speckle photography is very simple method to implementation and not require complicated optical scheme but there are difficulties that arise during the processing of speckle images due to the effects of random interference and lack of sensitivity range of this method.

The technique of optical diagnostics of turbulent flows based on the Talbot effect [5] is completely free of the mentioned shortcomings. At the same time the deflection angles can be defined at any point of the phase object with high spatial density, which is determined by the period of a Talbot grating. Registration of ordered interference picture in the plane of self-reproduction provides one to automate processing of Talbot image using computers and improve the measurement accuracy. In the works [6, 7] the Talbot effect was used to determine the distribution of helium average concentrations in the case of axisymmetric and two-dimensional jets outflows freely into the ambient air.

2. METHODOLOGY

2.1 Experimental setup

In Fig. 1. the developed for this research experimental setup scheme is shown. The shock tube with square cross-section 50×50 mm is used to generate shock waves of varying intensity. Interaction of the incident shock wave with the turbulizing grid creates velocity and density pulsations after the shock wave passage. Flow pulsations cause fluctuations of the local refraction index, which can be measured by Talbot – interferometer.

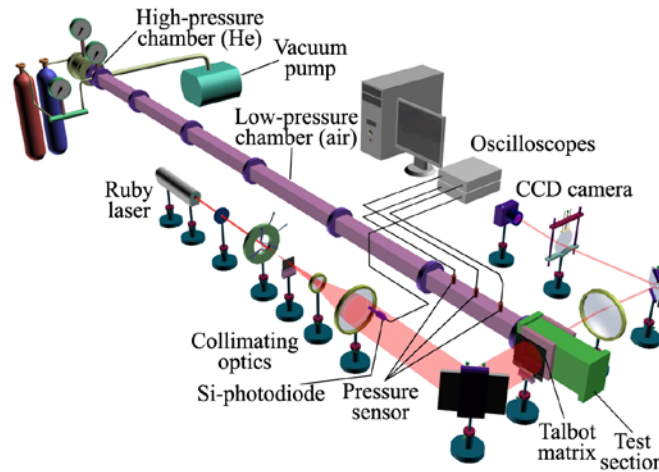


Fig. 1. Experimental setup and optical scheme for structure visualization

Talbot image formation happens by the following principle. A pulse of light from a ruby laser passes through the aperture diaphragm and the neutral filter and then is converted by a collimator into the wide-aperture light beam with an approximately plane wave front. Talbot-grating is tightly clamped between a pair of plane-parallel plates of high optical quality and placed on the way of the laser beam just behind the collimator.

The test section is placed at some distance from the Talbot-grating (no more than z_1). The screen is located at a distance z_N , depending on the required sensitivity of the method. Length z_N provided by

$$z_N = 2p^2 N / \lambda, \quad (1)$$

where N is an integer, determines the position of the planes of self-reproduction, where field distribution duplicates the distribution on the grid [5], p is the Talbot-grating period, λ is the wavelength. The image on the screen is recorded with the required spatial and temporal resolution with the help of a digital camera.

2.1 Calculations

Turbulizing grids cause fluctuations of density and velocity following the incident shock wave in the test section of the shock tube. To initiate the turbulence in the flow behind the shock front the grids with 12×12 and 3.5×3.5 mm square cells were used. To avoid the influence of chemical reactions on turbulence characteristics, the experiments were carried out in the air. Mach number of the incident shock waves varied in the range $M = 1.3$ – 1.6 . Measurement of the laser pulse duration was carried out with a silicon photodiode. As can be seen from a typical oscillogram (Fig. 2) laser illumination time is equal 400 microseconds. Visualization of the flow structure was carried out behind the incident and reflected shock fronts.

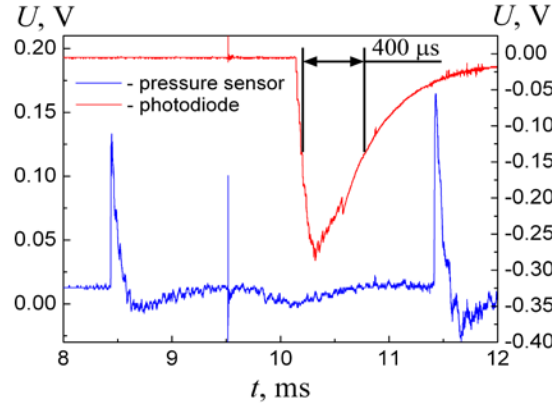


Fig. 2. Typical signals from pressure sensor and photodiode

From the images of time-averaged Talbograms the local deflection angles of light beams $\langle \varepsilon_x \rangle$ over the entire flow field were measured. Assuming that the refractive index varies perpendicular to the flow, we obtain the following formula for the calculation of its gradient dn/dx [8]:

$$\frac{dn}{dx} = \frac{n_0 \langle \varepsilon_x \rangle}{L}. \quad (2)$$

Here n_0 is the initial value of the refractive index, L is path length in the optical inhomogeneity. After integrating the previous expression along the X-axis, we obtain [8]

$$n(x) = n(x_0) + \int \frac{dn}{dx} dx. \quad (3)$$

Taking into account that we are dealing with the experimentally measured discrete values, we get:

$$n(x_i) \approx n_0 + \sum_i \frac{n_0 \langle \varepsilon_x \rangle}{L} \Delta x_i. \quad (4)$$

Here Δx_i is the distance between the i and $i+1$ maximum along the X-axis.

The data for the deflection angles can be numerically integrated, if the value of the refractive index of undisturbed medium n_0 is known. Integration was carried out from the center towards the edges of the flow.

Taking into account the fact that the mean density behind the shock wave can be calculated from initial conditions and the shock wave Mach number, the absolute values of refraction indices and density of turbulent flow behind the shock wave can be found from the geometrical optics relations. The relationship between the refractive index and flow density is carried by the equation

$$n - 1 = K \rho. \quad (5)$$

Here ρ is density, $K = 0.00022635 \text{ m}^3/\text{kg}$ is Gladstone-Dale constant [9]. Thus the density profile $\rho(x)$ across the flow was obtained by

$$\rho(x_i) \approx \rho_0 + \frac{n_0}{KL} \sum_i \langle \varepsilon_x \rangle \Delta x_i. \quad (6)$$

If the pressure and composition of the gas is constant across the boundary layer, then using the equation of state we can obtain the temperature profile $T(x)$ [9]:

$$\frac{T}{T_0} = \frac{\rho_0}{\rho} = \frac{n_0 - 1}{n - 1}. \quad (7)$$

In this equation n_0 , ρ_0 , T_0 are the refractive index, density and temperature in the undisturbed flow outside the boundary layer, respectively.

3. RESULTS AND DISCUSSION

3.1 Flow structure visualization behind the incident shock wave

Fig. 3 and Fig. 4 illustrates the measured distribution of local deflection angles, calculated air density and temperature profiles for grids with 12×12 and 3.5×3.5 mm cells respectively behind the incident shock wave. Results were shown at three different positions along the window. As can be seen from these figures, the greatest deflection angles and, consequently the highest density gradients in the flow are observed near the walls of the shock tube in the boundary layer. Thus, the greatest change in the density and deflection angles occurs across the flow. The mean calculated velocity of the flow behind the shock wave in these experiments was 160.5 and 134 m/s.

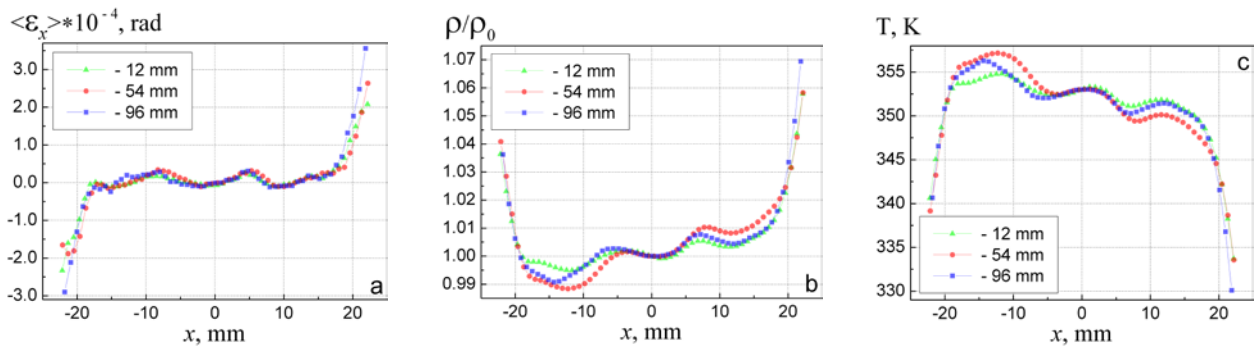


Fig. 3. Parameters in the flow behind the incident shock wave with 12×12 mm grid: a – deflection angles, b – air density ($\rho_0 = 1.029 \text{ kg/m}^3$), c – air temperature ($T_0 = 353 \text{ K}$)

The dependence of deflection angles for the 12×12 mm grid in the middle has oscillations with a period $\approx 12\text{--}14$ mm, and for the 3.5×3.5 mm grid is almost flat.

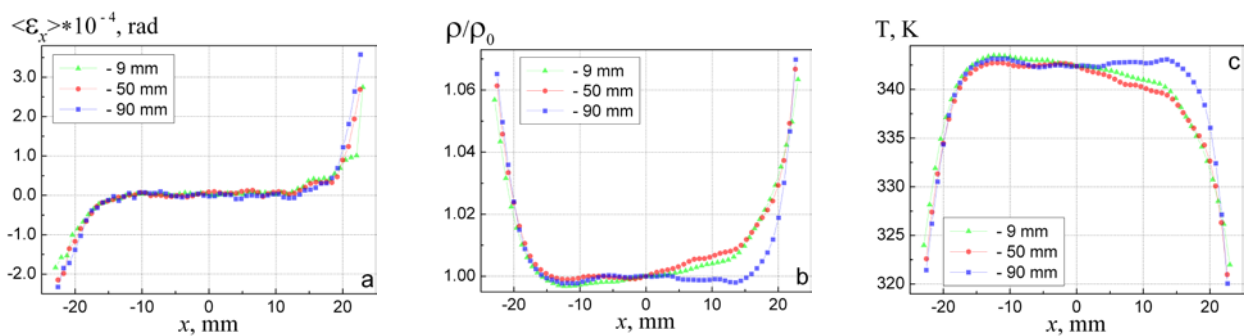


Fig. 4. Parameters in the flow behind the incident shock wave with 3.5×3.5 mm grid: a – deflection angles, b – air density ($\rho_0 = 0.963 \text{ kg/m}^3$), c – air temperature ($T_0 = 342 \text{ K}$)

The boundary layer thickness in the observation area is about 7–9 mm, and the density of the air in the boundary layer behind the shock front begins to increase sharply. This leads to the increase of 6–7% of the average flow density at the distance of ≈ 3 mm from the shock wall. Measurements show that for the case of the turbulizing grid with a 12×12 mm cells, oscillation of the average flow density across tube have the scale $\approx 11\text{--}13$ mm, which is comparable to the size of the cell. For the grid with a 3.5×3.5 mm cells the dependence of the average angles of deflection

across the tube is smoother. The absence of significant fluctuations of density in the flow behind the shock wave is noted (Fig. 4).

It is seen from Fig. 3c, 4c that in the boundary layer the flow temperature decreases towards the shock tube walls. This is because the temperature of the walls is approximately 293 K, which is less than the temperature of the hot flow.

3.2 Flow structure visualization behind the reflected shock wave

The results of investigation of the flow structure behind the reflected shock wave are shown in Fig. 5, 6.

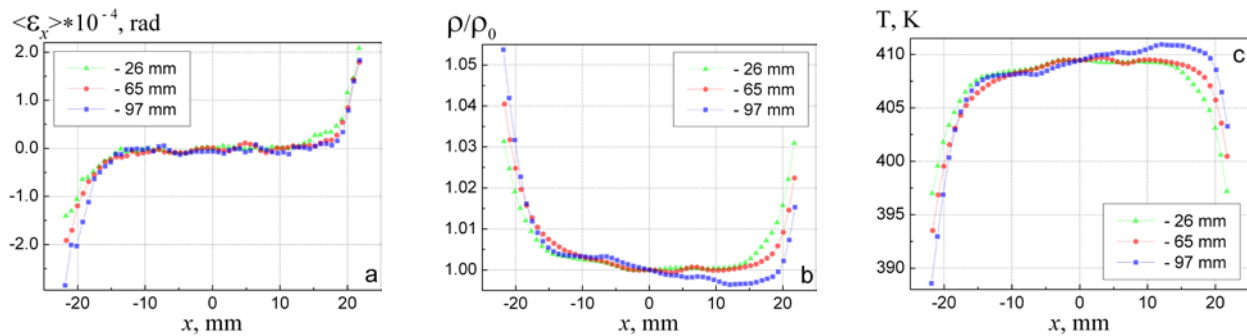


Fig. 5. Parameters in the flow behind the reflected shock wave with 12×12 mm grid: a – deflection angles, b – air density ($\rho_0 = 1.48 \text{ kg/m}^3$), c – air temperature ($T_0 = 409 \text{ K}$)

As well as in the case of the incident shock was observed the presence of a refractive index gradient in the flow behind the reflected shock. After integration we obtain the density distribution such as in the boundary layer. The influence of turbulizing grids on the flow structure for this case was not detected.

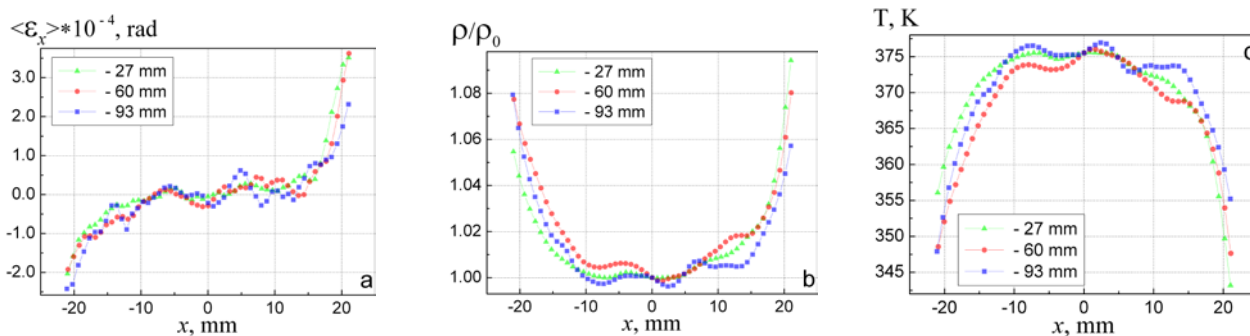


Fig. 6. Parameters in the flow behind the reflected shock wave with 3.5×3.5 mm grid: a – deflection angles, b – air density ($\rho_0 = 1.216 \text{ kg/m}^3$), c – air temperature ($T_0 = 376 \text{ K}$)

4. CONCLUSIONS

Application of the Talbot-interferometry method are showed by its usage for visualization and study the flow structure behind the incident and reflected shock waves in the shock tube.

In the experiments were measured the refractive index gradients over the entire flow and then were reconstructed refractive indices. Distributions of time-averaged density of the air throughout the whole flow field behind the incident and reflected shocks were calculated for 12×12 and 3.5×3.5 mm grids. Temperature profiles across the flow were found.



It is found that the thickness of the boundary layer in the observation area is about 7–9 mm. This leads to an increase of 6–7% of the average density of the flow at ≈ 3 mm from the shock tube wall. The area occupied by the boundary layer reaches half the cross sectional area of the shock tube. Therefore, the existence of the boundary layer has a significant effect on the uniformity of the flow behind the shock wave.

REFERENCES

1. MERZKIRCH, W. *Flow Visualization*: second edition. Academic Press, Orlando. 1987.
2. MERZKIRCH, W. *Experimental Thermal and Fluid Science*, 1995, Vol. 10, p. 435–443.
3. VITKIN, D., MERZKIRCH, W., FOMIN, N. *Journal of Visualization*, 1998, Vol.1, No. 1, p. 29–35.
4. FOMIN, N., LAVINSKAYA, E., MERZKIRCH, W., VITKIN, D. *Shock Waves*, 2000, Vol. 10, p. 345–349.
5. TALBOT, F. Facts relating to optical science. IV. *Philos. Mag.*, 1836, Vol. 9, p. 401–407.
6. DOROSHKO, M.V., PENYAZKOV, O.G., RANKIN, G., SEVRUK, K. L., KHRAMTSOV, P.P., SHIKH, I.A. *J. Eng. Phys. Thermophys.*, 2006, Vol. 79, p. 937–942.
7. DOROSHKO, M.V., KHRAMTSOV, P.P., PENYAZKOV, O.G., SHIKH, I.A. *J. Eng. Phys. Thermophys.*, 2008, Vol. 81, p. 48–54.
8. VASIL'EV, L.A. *Tenevye metody*. Moscow: Nauka, 1968. 400 p [in Russian].
9. SKOTNIKOV, M.M. *Tenevye kolichestvennyye metody v gazovoy dinamike*. Moscow: Nauka, 1976. 160 p. [in Russian].



WINDOW LAYER THICKNESS INFLUENCE ON THE PHOTOELECTRICAL PROPERTIES OF ZnSe-CdTe HETEROSTRUCTURES

I.G. Inculet

Moldova State University

Mateevici str. 60 A, MD-2009 Chisinau – Moldova

ABSTRACT

Zinc selenide is one of the most promising binary compounds with the band gap of about 2.7 eV at room temperature, is transparent for wavelengths higher than 460 nm. The growth of ZnSe films by Close-Space-Sublimation (CSS) method is examined. It is shown that films deposited on glass substrates are polycrystalline with wurtzite-zinc-blende polytypism. The spectral dependencies ZnSe thin film on glass substrates were studied in the wavelength region of 350 nm – 1000 nm at room temperature. The heterostructures were obtained by successive deposition of ZnSe (at and CdTe thin film by CSS method on glass substrates coated with SnO₂ layer. The electrical and photovoltaic parameters of ZnSe-CdTe solar cells depend on the ZnSe film thickness. Optimal technological conditions of ZnSe and CdTe layers deposition were determined.

Keywords: CdTe solar cell, ZnSe window

1. INTRODUCTION

Thin film devices can be made from many semiconductor materials, but in practice, only a few materials are stable enough to be of interest for making commercial devices and modules [1]. The most investigated materials are amorphous silicon, copper indium diselenide and cadmium telluride. Significant increase in solar cell efficiency can be achieved by optimizing the physical and technological parameters of the heterostructure and good matching with solar spectrum. This can be achieved by using a system of nondestructive testing of solar cell parameters at all stages of it obtaining. ZnSe-CdTe heterojunction is of a perspective one for using in solar energy conversion due to the ZnSe optical parameters. Researchers [2] calculated the lattice mismatch using the electron affinity of the semiconductors and found 12.5%. Zinc selenide is one of the most promising binary compounds with the band gap of about 2.7 eV at room temperature, it is transparent for wavelengths higher than 460 nm. In ZnSe-CdTe heterostructure, ZnSe was used as an optical window. CdTe thin film, with $E_g=1,45\text{eV}$, was used as an active absorber. The given paper is to elucidate the effect of window layer thickness on the solar cell parameters calculated from current-voltage dependencies at different temperatures and illumination.

2. METHODOLOGY

The typical structure of a ZnSe-CdTe solar cell consists of 4 layers deposited on a glass substrate: first layer is transparent conducting oxide (TCO) which acts as a front contact, second layer – ZnSe thin film which is called window layer, a CdTe film which is the absorber layer made on top of ZnSe and the last – back contact on top of the CdTe layer.

ZnSe-CdTe heterostructures were obtained by successive deposition of ZnSe and CdTe thin films by Close-Space-Sublimation (CSS) method on glass substrates coated with SnO₂ layer with a conductivity of $10^5 \Omega^{-1}\cdot\text{m}^{-1}$. SnO₂ layer was used as a contact for ZnSe and Ni for CdTe layer.

The CSS has been used extensively for the deposition of CdTe and ZnSe thin films. This technique is based on the reversible dissociation of compounds at high temperature, for example:



This process involves heating the source compound to a higher temperature than the substrate. The influence of growth conditions on electro-physical properties of layers were analysed. It was established that when ZnSe thin films are grown, the substrate temperature influence on the crystalline structure of the layers is not so strong as it is in case of CdTe layers. Optimal technological conditions of ZnSe layer deposition were determined: substrate temperature $T_s=445^\circ\text{C}$ and $T_{ev}=880^\circ\text{C}$ for evaporator. The ZnSe layer thickness was modified by varying the time of growth. Then CdTe layer was deposited, at optimum conditions $T_s=345^\circ\text{C}$ for substrate and $T_{ev}=630^\circ\text{C}$ for evaporator. The thickness of absorbing material deposited by this method is about $4\ \mu\text{m}$. For to increase the heterostructures photosensitivity they were introduced into CdCl_2 solution [3], and annealed at temperature of 400°C at atmospheric pressure.

3. RESULTS AND DISCUSSIONS

The requirements for window layers in photovoltaic devices applications are high conductivity and adequate thickness in order to allow good transmission and uniformity which would avoid the effects of short cutting. We did not find any major influence of the substrate temperature on the morphology and structural properties of the ZnSe layers with a thickness less than $0.5\ \mu\text{m}$. The SEM images of ZnSe CSS films deposited at different substrate temperatures are illustrated (in Fig. 1). The SEM micrograph shows the device quality nature of the surface without any pinholes. No significant changes in morphology occurred.

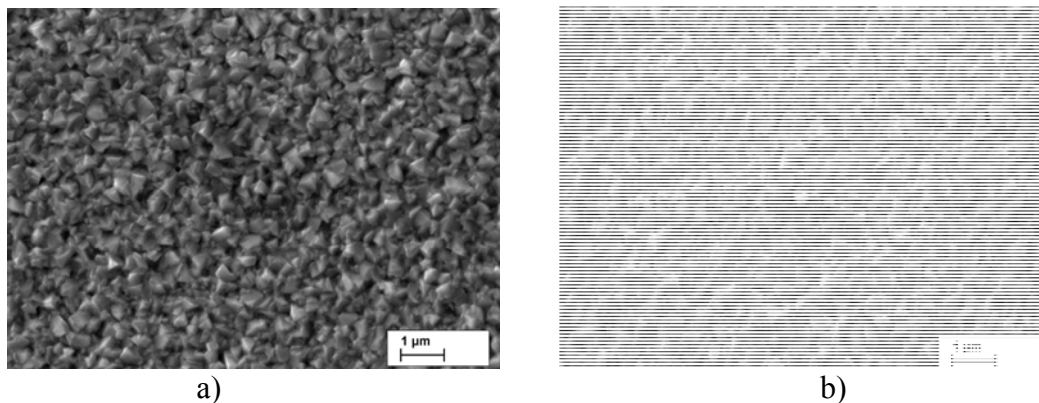


Fig. 1. SEM image of ZnSe thin films deposited on glass substrate at different substrate temperature: a) – 250°C , b) – 345°C

It is well known that the most important feature of thin layers used as optical window is their optical transmission. That is why the spectral dependencies CSS deposited ZnSe thin films on glass substrates were studied in the wavelength region of $350\ \text{nm} - 1000\ \text{nm}$ at room temperature. The energetic resolution of the measurements does not exceed $2\ \text{meV}$. The optical transmission is high in the visible and infrared region and its maximum is up to 85% at the wavelength of $600\ \text{nm}$ and minimum at $350\ \text{nm}$ wavelength.

The optical absorption spectra of ZnSe films deposited onto a glass substrate were studied at room temperature in the wavelength range of $350-1000\ \text{nm}$. The variation of optical absorption with wavelength (in Fig. 2) reveals a very low absorption of energy in VIS-IR regions. This makes ZnSe a good window layer for solar cell application.

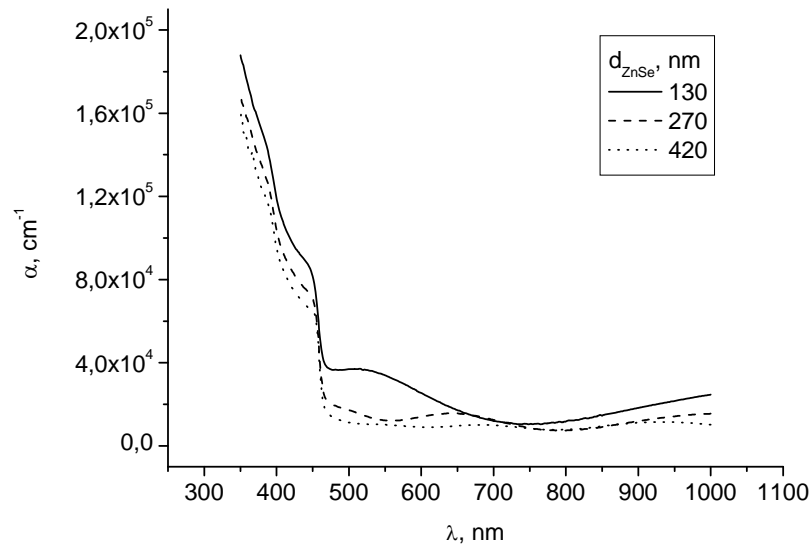


Fig. 2. Dependence of absorption coefficient for ZnSe layer deposited by CSS

To find whether the band gap is direct or indirect, the absorption coefficient α dependence on the photons energy $h\nu$ was compared with the equation related to direct band gap optical transition [3]:

$$\alpha(h\nu) = A \cdot (h\nu - E_g)^{1/2}, \quad (2)$$

where E_g is the band gap of the ZnSe films, α is the absorption coefficient, A is the constant and $h\nu$ is the photon energy. The $\alpha^2(h\nu)$ versus $h\nu$ plots gave us a band gap of 2.68 eV, which is close to ZnSe gap value of 2,7 eV. Hence, straight line segments in short wavelength region confirms the direct band gap nature of ZnSe films [6].

The influence of series and parallel resistances on current flow mechanism through the HJ can be described by the relation [3]:

$$I_{dir} = I_0 \left(e^{\frac{qU - IR_S}{nkT}} - 1 \right) + \frac{U - IR_S}{r_{SH}} - I_L. \quad (3)$$

Series resistance R_S , shunt-resistance r_{sh} , and diode quality factor n describe the nonidealities. The photovoltaic parameters determined from J-V dependencies as dark and illumination are given in Table 1.

Table 1. Photovoltaic parameters of the ZnSe-CdTe solar cell

$d_{ZnSe},$ nm	$R_S,$ $\Omega \cdot 10^{-4} \cdot m^2$	$r_{sh},$ $\Omega \cdot 10^{-4} \cdot m^2$	$U_{OC},$ V	$J_{SC},$ A/m ²	$U_{max},$ V	$J_{max},$ A/m ²	FF	$\eta,$ %
130	20.6	132.2	0.635	140.8	0.394	97.1	0.43	3.83
270	65.1	210.5	0.620	177.5	0.354	126	0.41	4.5
420	87.2	190.7	0.590	163.0	0.327	112	0.38	3.66

The measurement of external quantum efficiency gives an indication about cell sensitivity to light at different photon energies. At long wavelengths, absorption threshold shift indicates that the CdTe layer bandgap value has decreased. Interdiffusion of an element or elements into the CdTe could reduce the bandgap, and therefore, the shift in the spectral response long wavelength region



occurs. However, the incorporation of zinc would increase the band gap of CdTe, where selenium is a more likely candidate, as this can, depending on the mole fraction, lower the CdTe bandgap. It was established that a buried junction will produce a larger spectral response for short wavelengths.

4. CONCLUSION

CdTe based solar cells fabricated with a conventional structure which includes SnO₂/glass as support and ZnSe as a window layer was investigated. The structures were obtained by successive growth of ZnSe, CdTe thin films by close space sublimation with T_s=445°C and T_{ev}=880°C for window layer, T_s=345°C and T_{ev}=630°C for active layer. It was shown that the optical transmission for the ZnSe is high in the visible and infrared region. The $\alpha^2(h\nu)$ plots gave a band gap of 2.67–2.68 eV. The treatment conditions in CdCl₂ enhances electrical and photovoltaic parameters of ZnSe-CdTe solar cells, annealed at temperature 400°C at atmospheric pressure. The best solar cell efficiency obtained from calculation based on current-voltage characteristics at illumination was for heterostructure with 270 nm window layer thickness.

REFERENCES

1. BERGER, L. *Semiconductor Materials*, Boca Raton, CRC Press, 1997, p. 15–30.
2. BUBE, R.; BUCH, F.; FAHRENBRUCH, Y; MITCHELL, K. *IEEE Transaction on Electron Device*, Vol. 24, 1977, p. 487–492.
3. VALDNA, V.; BUSCHMANN, F.; MALLIKOV, E., *J. of Cryst. Growth*, 1996, p. 164–167.
4. MADELUNG, O. *Semiconductors: Data Handbook* Springer, New York 2004.
5. ENNAOUI, M. *Condensed Matter*, Vol. 3, No 1, 2000, p. 8–15.
6. SADAQ, A.; *Properties of Group-IV, III–V and II–VI Semiconductors*, John Wiley&Sons, Ltd, 2005, p.103–143.



THE USE OF THE MEMBRANE CONTACTOR FOR EXTRACTION OF URANIUM (VI) FROM AQUEOUS SOLUTIONS

P. Bieluszka, G. Zakrzewska-Trznadel

Institute of Nuclear Chemistry and Technology

Dorodna 16, 03-195 Warsaw – Poland

Phone: (+4822)5041316

Email: p.bieluszka@ichtj.waw.pl, g.zakrzewska@ichtj.waw.pl

ABSTRACT

Raising role of the nuclear power industry, including governmental plans for the construction of the first Nuclear Power Programme in Poland, creates increasing demand for the uranium-based nuclear fuels. Very important element of this Programme will be the search for economic and efficient technologies of production of uranium from Polish deposits. The project implemented by Institute of Nuclear Chemistry and Technology concerns the development of effective methods for uranium extraction from low-grade ores and phosphorites for production of pure yellow cake – U_3O_8 . The new approach for the liquid-liquid extraction by the membrane method was proposed in the work.

In the present experiments the Liqui-Cel[®] Extra-Flow 2.5×8 Membrane Contactor produced by CELGARD LLC (Charlotte, NC) company was applied. The membrane contactor is the main component of the installation for liquid-liquid extraction. In the process of membrane extraction the uranyl ions from aqueous phase are transported through the membrane into organic phase. The flow of two phases in the system was arranged in cocurrent mode. The very important element of the work was a selection of extracting agents appropriate for the membrane process. After preliminary experiments comprising tests of membrane resistivity and determination of extraction efficiency, di(2-ethylhexyl)phosphoric acid was found to be most favorable. Another important aspect of the work was the adjustment of hydrodynamic conditions in the capillary module. To avoid the membrane wettability by organic solvent and mixing two phases equal pressure drops along the membrane module to minimize the transmembrane pressure, were assumed. Determination of pressure drop along the module was conducted using Bernoulli equation. The integrated process of extraction/re-extraction conducted in continuous mode with application of two contactors was designed. The membrane extraction can be considered as a one of the alternative processes for purification and concentration of uranium solutions after leaching uranium ores and phosphorites.

Keywords: uranium; membrane contactor; extraction

1. INTRODUCTION

The most important minerals of uranium are: uraninite UO_2+UO_3 , carnotite $K_2(UO_2)_2(VO_4)_2 \cdot 2H_2O$, brannerite (UTi_2O_6) , coffinite $(USiO_4 \cdot nH_2O)$, and uranophane $(H_3O)Ca[UO_2][SiO_4]_2$ [1, 2]. Uranium is also found in phosphate rock, lignite, monazite sands and can be recovered commercially from these sources [1]. An important step for obtaining uranium oxide from ores is the purification of uranium after leaching and concentration with use of known physical and chemical methods. Treatment involves removal of associated metals, such as molybdenum, vanadium, iron, arsenic, zinc, copper, nickel and rare earth elements. At the same time leads to concentration of the solution, from which the next step is precipitation of the end-product: diuranian or oxide, depending on the used reagents. The leaching of the ore is usually carried out either by sulphuric acid or sodium carbonate [1, 3]. For purification and concentration of the solution is generally used: liquid extractions, ion exchange, integrated processes, such as ion exchange / liquid-liquid extraction. The new approach for the liquid-liquid extraction of uranium will involve the membrane enclosed in a small volume of the device – the membrane module. The term “membrane contactor” is used to identify membrane systems that are employed to “keep in contact” two phases. On the contrary of the more “traditional” idea of membranes as media for

performing separations thanks to their selectivity, membrane contactors do not offer any selectivity for a particular species with respect to another, but simply act as a barrier between the phases involved, by allowing their contact in correspondence of well defined interfacial area. The two phases are separated by the membrane and species are transferred from one phase to the other by only diffusion. Extraction with the use of membrane contactors has many advantages above conventional methods of the extraction of uranium, like no fluid/fluid dispersion, no emulsion formation, no flooding at high flow rates, low solvent holdup, known and constant interfacial area, etc. One of the biggest drawbacks of membrane extraction may be the formation of concentration polarization and fouling [4]. There is also the risk of wetting the membranes during long-term operation of the module. For proper operation of membrane contactors it is important to maintain appropriate conditions for the hydrodynamic flow of solutions over the membrane surface in order to eliminate such a danger [5, 6].

The most wide application of membrane contactors is processes with the use of supported liquid membranes. The transport of species in a supported liquid membrane can occur by simple permeation through the liquid immobilized into the micropores or by facilitated transport. In the former case the species is transferred by a solution-diffusion mechanism and the affinity between the liquid phase and the species determines the selectivity of the process. The facilitated transport occurs when the species that diffuses through the liquid is subjected to a reversible chemical reaction (the so-called complexation). The permeation of the complex takes place in parallel with the solution-diffusion of the species into the liquid phase and is usually higher than the simple permeation (see Fig. 1) [4, 7, 8]. In order to compare the transport of free species with that of the complex, a facilitation factor (F) is often used, which is defined as the ratio of the flux achievable in presence of carrier to the flux obtained in a carrier-free membrane [4, 9].

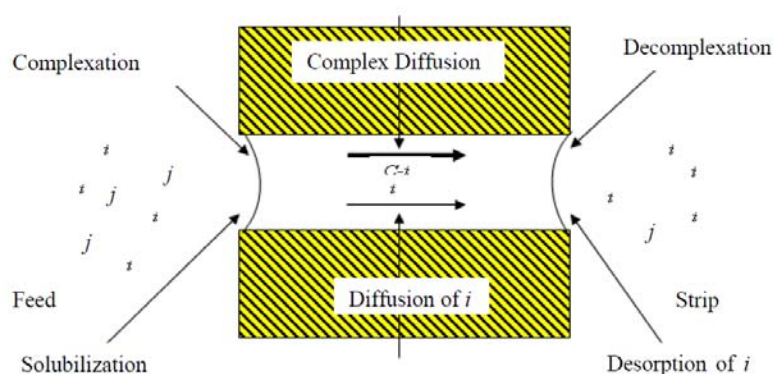


Fig. 1. Transport of i through the immobilized liquid as a complex and as a free species
 $F = \text{Flux in presence of carrier} / \text{Flux without carrier}$

A generic form of the reversible chemical reaction between a species i and a carrier C is:



Depending on the specific application, the transport of the complex can be controlled by acting on different parameters, such as temperature and pH of the feed and streams [4, 10, 11]. In a hollow fiber membrane contactor, the organic phase is immobilized in a porous polymeric support, like a polypropylene hollow fiber, preventing emulsification of the organic phase in the feed solution. This is shown in Fig. 2.

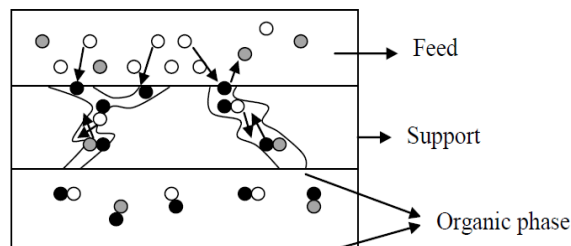


Fig. 2. The extraction process using porous hollow fibers to separate the aqueous feed solution physically from the organic solution (white, gray, and black dots represent the impurity ion, the counter ion, and the carrier, respectively)

During the extraction in the membrane contactor, ions are taken up by the organic phase from the feed phase until thermodynamic equilibrium is reached. At equilibrium, the distribution coefficient, D is calculated by:

$$D = \frac{C_o}{C_w}, \quad (2)$$

where C_o is concentration of the component in organic phase, C_w is concentration of the component in water phase. For a batch process, the flux of the component J [$\text{mol}\cdot\text{m}^{-2}\cdot\text{s}^{-1}$] is equal:

$$J = -\frac{dC_w}{dt} \frac{V}{A}, \quad (3)$$

with V the volume of the solvent [m^3], A the contact area [m^2], and t the time [sec]. The flux can be corrected for the feed concentration, resulting in the permeability, P [m/sec], defined as:

$$P = -\frac{1}{C_w} \frac{dC_w}{dt} \frac{V}{A} = -\ln \frac{C_{w,t=2}}{C_{w,t=1}} \frac{1}{A t_2 - t_1}. \quad (4)$$

The membranes for membrane contactors are usually microporous and symmetric, and can be both hydrophobic and hydrophilic[12].

2. EXPERIMENTAL

2.1. Description of measuring apparatus

2.1.1. Extraction experiments

In the present experiments the small, laboratory installation for extraction of uranium equipped with the membrane contactor Liqui-Cel® Extra-Flow 2.5×8 produced by CELGARD was used. The membrane contactor was connected to two circuits: the aqueous and organic phases and the system of measuring devices, which control the parameters of the process (see Fig. 3).

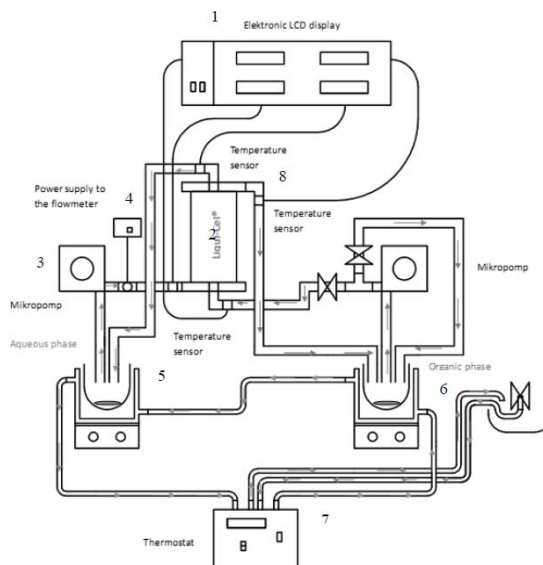


Fig. 3. The scheme of the installation for extraction of uranium (1) Electronic LED display; (2) Hollow fiber contactor; (3) Micropump; (4) Power supply to the flow meter; (5) Aqueous feed phase; (6) Organic phase; (7) Thermostat (8) Temperature sensor

The very important element of the work was a selection of extracting agents appropriate for the membrane process. In the laboratory experiments the partition coefficients for uranium extraction by different extractants, like e.g.: tributylphosphate (TBP), triethylamine (TEA), di(2-ethylhexyl)phosphoric acid (D2EHPA), tri-*n*-octylamine (TnOA) and trioctylphosphine oxide (TOPO) were determined. TnOA and D2EHPA were found to be most favourable extractants for uranium in this experiment; TBP and TEA in the environment of 5% H₂SO₄ were found the weakest extracting agents tested. The classification of the extractants was showed below (see Fig. 4).

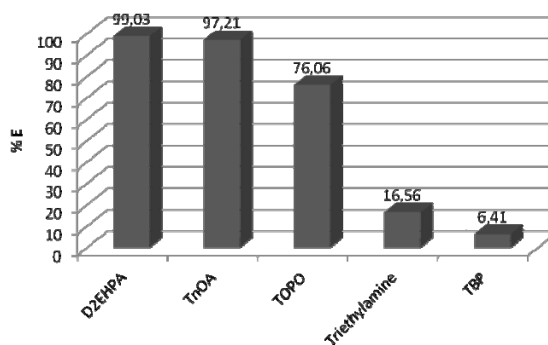


Fig. 4. Extraction efficiency of uranium from model solutions of uranyl nitrate (UO₂(NO₃)₂·6H₂O) in 5% H₂SO₄

After preliminary experiments comprising test of membrane resistivity and determination of extraction efficiency, D2EHPA was found to be most favourable for the membrane extraction process. Membrane extraction was carried out with the model solutions of uranyl nitrate in 5% H₂SO₄ using 0.2 M D2EHPA, which was dissolved in kerosene or toluene. During the membrane extraction the uranyl ions from aqueous phase are transported through the membrane into organic phase. The flow of two phases was arranged in cocurrent mode. The organic phase flowed inside a thin capillary tubes made of polypropylene and the aqueous phase was washed the capillaries. The flow of aqueous (feed phase) and organic phase was generated by two micropumps of small yield below 200 L/h. The volume of two phases circulating in the system was 400 mL. The temperature

of aqueous and organic phases was controlled by a thermostat. The extraction was carried out at 25 °C. Electronic LCD display coupled with PT-100 temperature sensors showed temperature at the inlet and at the outlet of the membrane module. The characteristics of the membrane are shown in Table 1.

Table 1. Characteristics of Celgard X50-215 Microporous Hollow Fiber Membrane

Material	Polypropylene X-50
Membrane Geometry	Capillary
Wall Thickness (nominal)	40 μm
Internal Diameter (nominal)	220 μm
Outer Diameter (nominal)	300 μm
Effective Pore Size	0.04 μm
Porosity	40%
Burst Strength	400 PSI (15.5 kg/cm ²)
Total Membrane Surface Area (Internal)	1.9 m ²
Total Membrane Surface Area (Outer)	2.6 m ²
Number of Capillaries	11 000

2.1.2. Selection of process conditions

The very important element of the work was the choice of hydrodynamic conditions in the membrane contactor. This procedure was designed to avoid the membrane wettability by organic solvent and mixing two phases. For this reason equal pressure drops along the membrane module to minimize the transmembrane pressure, were assumed. If the pressure difference between the shell and inner side of the fiber wall (transmembrane pressure) exceeds the critical pressure, the organic phase will be pushed out of the most susceptible pores of the support. The system will be unstable and the aqueous feed solution will get contaminated with the organic phase[12]. Determination of pressure drop along the module was done using Bernoulli equation:

$$\frac{p_1}{\gamma} + z_1 + \frac{u_1^2}{2g\alpha_1} = \frac{p_2}{\gamma} + z_2 + \frac{u_2^2}{2g\alpha_2} + Z_{1,2}, \quad (5)$$

where p_1 is pressure at the inlet p_2 and the outlet of the module [Bar], α_1 and α_2 are Coriolis coefficients (for laminar flow are equal 0.5 and turbulent flow are equal 1), γ is specific weight of the liquid, [kg/m²·s²]. $Z_{1,2}$ is resistance to fluid flow along the module:

$$Z_{1,2} = \lambda \frac{Lu^2}{D2g}, \quad (6)$$

where z_1 is level of the inlet z_2 and of the outlet [m], g is gravitational acceleration [m/s²], λ is dimensionless drag coefficient, which is a function of Reynolds number and roughness of the pipe:

$$\lambda = \frac{64}{\text{Re}}, \quad (7)$$

$$\text{Re} = \frac{uD}{\nu}, \quad (8)$$

where ν – kinematic viscosity [m²/s] is equal:

$$\nu = \frac{\mu}{\rho}, \quad (9)$$

The equations describing pressure drop:

$$\Delta p_1 = \frac{L(\rho_1 g d_{h1}^2 + 32\mu_1 u_1)}{d_{h1}^2}, \quad (10)$$

$$\Delta p_2 = \frac{L(\rho_2 g d_{h2}^2 + 32\mu_2 u_2)}{d_{h2}^2}. \quad (11)$$

Assuming equality of pressure drops along the membrane in organic and water phases:

$$\Delta p_1 = \Delta p_2. \quad (12)$$

After transformation:

$$u_2 = \frac{d_{h2}^2 \mu_1}{d_{h1}^2 \mu_2} u_1 + \frac{(\rho_1 - \rho_2) g d_{h2}^2}{32\mu_2}, \quad (13)$$

where μ_1 is dynamic viscosity (physical) of the aqueous phase μ_2 and organic phase at temperature 20 °C [kg/m·s], ρ_1 is density of the aqueous phase ρ_2 and organic phase at 20 °C [kg/m³], u_1 is linear flow rate at the inlet u_2 and at the outlet of the fluid [m/s], L is the length of the pipe [m], d_{h1} is the hydraulic diameter of the part of the module outside of the capillaries [m] and it is equal:

$$d_{h1} = \frac{D^2 - d - n d_o^2}{D + n d_o + d}, \quad (14)$$

where D is the diameter of the membrane module [m], d_o is the outer diameter of the capillary [m], d is the outer diameter of the empty space in the module [m], n is number of capillaries d_{h2} is the hydraulic diameter of the part of the module inside the capillaries:

$$d_{h2} = d_i, \quad (15)$$

where d_i the inner diameter of the capillary [m]. After numerous transformations a linear relationship was obtained (see equation 13):

$$u_2 = A u_1 + B, \quad (16)$$

where A and B are the coefficients of the equation. On the basis of the above relationship the conclusion was formulated that velocity of aqueous and organic phases should remain in close relationships expressed by linear function. The values of the average volumetric flow rates were set with use of the above relationship. For the aqueous phase (feed) the flow rate was equal 98.11 L/h, for organic phase was equal 5.95 L/h.

3. RESULT AND DISCUSSION

3.1. Experiments with model solutions

3.1.1. Extraction

The model solutions of uranyl nitrate $\text{UO}_2(\text{NO}_3)_2 \cdot \text{H}_2\text{O}$ were applied in the membrane extraction experiments. Chemical analysis was performed using the method of ICP-MS (Inductively Coupled Plasma Mass Spectrometry). The experimental results were summarized in the kinetic graphs of the extraction efficiency, expressed as a percentage of uranium extracted in time of experiment – %E=f(t). Graphs were approximated according to least squares method:

$$\sum_{i=1}^N (f(x) - y_i)^2, \quad (17)$$

where:

$$f(x) = K(1 - \exp(-t_i / T)), \quad (18)$$

where K and T are approximation coefficients.

The degree of the extraction was calculated by the formula:

$$\%E = \frac{100D}{D + \frac{V_w}{V_o}}, \quad (19)$$

where D is a partition coefficient (see equation 2), V_w and V_o are the volumes of the aqueous phase and organic phase. The membrane extraction process dependence on time and concentration of uranium (U) are shown in Fig. 5.

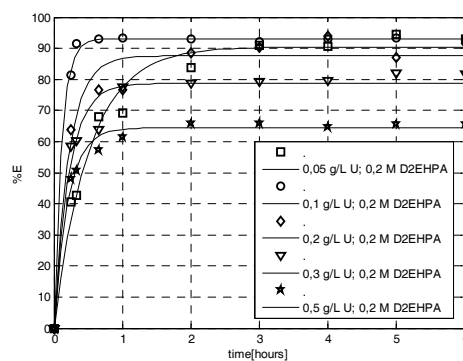


Fig. 5. Membrane extraction using D2EHPA as extractant in toluene, aqueous phase flows inside the capillaries of the membrane contactor

After analyzing the results, it is evident that the kinetics of membrane extraction process using D2EHPA in toluene at different concentrations of uranium is similar. The fastest extraction was with solutions containing low concentrations of uranium for example 0.1 g/L. For this concentration extraction efficiency reaches a constant value after less than one hour. Kinetics of uranium extraction for concentration of 0.05 g/L was different from the other (Fig. 5), however after two hours for all initial concentrations of uranium the equilibrium was established.

3.1.2. Extraction/re-extraction

Experiments of membrane re-extraction process were conducted with the same installation (see Fig. 3). In order to carry out the re-extraction experiment, the aqueous phase (feed phase) after membrane extraction was removed from the apparatus. In place of the removed feed phase the solution of 1 M Na_2CO_3 or $(\text{NH}_4)_2\text{CO}_3$ was introduced (stripping phase). The volume of stripping phase was the same like feed phase and organic phase (see description of measuring apparatus and extraction experiments). The results of the experiments are shown in the Table 2 below.

Table 2. The results of the experiments for extraction/re-extraction process

Stripping phase – $(\text{NH}_4)_2\text{CO}_3$						
C_a [g/L]	C_b [g/L]	D	%E	C_c [g/L]	%re-E	% R
0.169	0.154	10.51	91.12	0.132	85.71	78.11
0.253	0.236	13.81	93.28	0.198	83.90	78.26
0.485	0.450	12.87	92.78	0.450	100.0	92.78
Stripping phase – Na_2CO_3						
0.191	0.177	12.72	92.70	0.145	81.92	75.92
0.263	0.250	19.33	95.06	0.171	68.40	65.02
0.452	0.427	17.15	93.43	0.427	100.0	94.50

Where C_a – concentration of uranium in feed phase after dilution in the installation, C_b concentration of uranium in the organic phase after extraction experiment, C_c concentration of uranium in the stripping phase after re-extraction experiment, %reE percent of uranium re-extraction, was calculated by:

$$\%reE = C_c / C_b \cdot 100\% \quad (20)$$

%R percent recovery of uranium was calculated by:

$$\%R = C_c / C_a \cdot 100\% . \quad (21)$$

A comparison of extraction/re-extraction experiments was summarized in the above tables, where initial feed concentration – C_a had a similar values in re-extraction with $(NH_4)_2CO_3$ and Na_2CO_3 experiments. Higher values of %reE and %R were noticed for the re-extraction with $(NH_4)_2CO_3$ (see Table 2). The highest values of %reE and %R were observed for the higher uranium concentration in the feed solutions – C_a and in this case %R had higher value for the re-extraction with Na_2CO_3 than for $(NH_4)_2CO_3$.

The integrated process of extraction and re-extraction conducted in continuous mode is now under investigation. This process includes two membrane modules, one for extraction and the other for back extraction (stripping). In such a system there is no saturation of the metal-extractant, because the reagent is continuously regenerated in the module for the re-extraction. The advantage of the integrated membrane process over one-stage installation with one single membrane module may also rely on the fact that the overall mass transfer coefficient resulting from the integrated process is greater than the coefficient of mass transfer obtained in a single membrane module [13].

3.2. Experiments with real post-leaching solutions

The extraction with real solutions were conducted using the results of the experiments for model solutions. The real solutions were obtained after leaching of uranium ores (1) sandstones of the Lower and Middle Triassic from Berybaltic Syncline and 2) brown shale from Podlasie Depression) with solutions of sulfuric acid and alkaline solutions of $NaOH/Na_2CO_3$. The process of acid leaching was conducted by using $KMnO_4$ as an oxidant at temperature of 60 °C in 1 hour. For the alkaline leaching H_2O_2 as an oxidant at temperature of 60 °C was applied and time of leaching was 0.5, 1 and 2 hours. In both cases, granulation of ore samples was less than 0.2 mm.

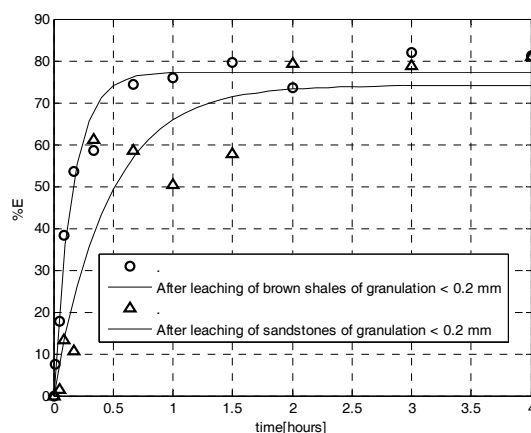


Fig. 6. Comparison of membrane extraction performed on real solutions after acid leaching of brown shales and sandstones

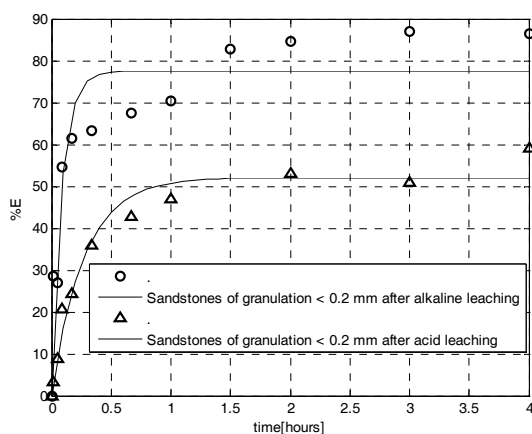


Fig. 7. Comparison of membrane extraction performed on real solutions after acid and alkaline leaching of sandstones

After analysing the results of the experiments one can see that the extraction efficiency of uranium was slightly higher for the samples obtained after leaching of brown shales (see Fig. 6). For this case $\%E = 79.39$ and $D = 3.85$. For the real solutions obtained after leaching of sandstones $\%E = 74.22$ and $D = 2.88$. For slightly higher percentage of extraction of uranium may have impact higher initial concentrations of uranium in real solutions after leaching of sandstones. In this case initial concentration of uranium was $8.09 \cdot 10^{-3}$ [$\mu\text{g}/\text{mL}$]. For real solution after leaching of brown shales the initial concentration of uranium was equal $6.23 \cdot 10^{-3}$ [$\mu\text{g}/\text{mL}$]. In case of experiments shown in Fig. 7 one can see that the higher extraction efficiency of uranium was for real solution after alkaline leaching.

4. CONCLUSIONS

Membrane Contactors such as Celgard X50-215 Microporous Hollow Fiber Membrane enable a variety of applications for recovery and / or removal of heavy metals from different process streams. They can be used for removal or recovery of metals from wastewater from industry and the separation of metallic contaminants from wastewater. In the present project membrane contactors have been used to obtain uranium from aqueous solutions at different steps of processing of uranium ores and secondary raw materials. The resulting high levels of extraction using D2EHPA and various advantages of the membrane extraction enable it to consider, as an alternative method for the extraction carried out in the mixer-settler arrangement. Most of the published studies on the metals extraction using membrane contactors were carried out with use of the modules Liqui-Cel® Extra-Flow produced by CELGARD company. These modules contain microporous hollow fibers made of a polypropylene (PP). The polymers exhibit a very stable thermal properties and are resistant to a wide range of organic compounds. Modules Liqui-Cel® Extra-Flow have a central shield in the shape of baffle, which on one hand increases the efficiency of the process, but on the other hand is a velocity component in the perpendicular direction to the membrane surface [14]. After preliminary re-extraction experiments, which have been carried out with the model solutions, high percentage of re-extraction and recovery of uranium were obtained. Experiments carried out with the real solutions obtained after leaching of uranium ores confirmed the results of preliminary experiments. Appropriate selection of hydrodynamic conditions in the membrane contactor eliminated the possibility of wetting the membrane and allowed stable working conditions of the apparatus. Experiments showed that alkaline leaching is more selective for uranium in presence of other metals but concentration of uranium is less compared to concentration of uranium after acid leaching, which is more effective.



ACKNOWLEDGEMENT

The studies were supported by the POIG project, No 01.01.02-14-094-09-00 “Analysis of the possibility of uranium supply from domestic resources”.

REFERENCES

1. EDWARDS, C.R., OLIVER, A.J. Uranium processing: A review of current methods and technology. *JOM*, 2000, Vol. 52, No. 9, p. 12–20.
2. FRONDEL, J.W., FLEISCHER, M. Glossary of Uranium and Thorium-Bearing Minerals. Bulletin 1250, 4th edition (Reston, VA: U.S. Geological Survey (1967)).
3. SINGH, S., CHAKRAVORTTY, V., DASH, K.C., Solvent Extraction of Uranium(VI) by LIX-54 and its Mixtures. *Journal of Radioanalytical Nuclear Chemistry. Articles*, 1988, Vol. 122, No. 1, p. 137–142.
4. DRIOLI, E., CRISCUOLI, A., CURCIO, E., Membrane contactors: fundamentals, applications and potentialities. Membrane Science and Technology Series 11, Elsevier B.V., Amsterdam 2006.
5. BODZEK, M., KONIECZNY, K., Wykorzystanie procesów membranowych w uzdatnianiu wody (The use of membrane processes for water treatment), Oficyna Wydawnicza Projprzem-EKO, Bydgoszcz 2005, in Polish.
6. BODZEK, M., BOHDZIEWICZ, J., KONIECZNY, K., Techniki membranowe w ochronie środowiska (Membrane methods for environmental protection), Wydawnictwo Politechniki Śląskiej, Gliwice 1997, in Polish.
7. MULDER, M.H.V., Basic principles of membrane technology, second edition, Kluwert Academic Publishers, The Netherlands 1996.
8. BAKER, R.W., Membrane Technology and Applications, McGraw-Hill, New York (2000).
9. WAY, J.D., NOBLE, R.D., Facilitated transport, in: W.S.W. Ho and K.K. Sirkar (Eds.), Membrane Handbook, Champan and Hall, New York (1992).
10. ARGURIO, P., Membrane processes coupled with metal binding reactions in water treatment. PhD thesis (2002). ISBN 88-8276-164-9. Department of Chemical and Materials Engineering. University of Calabria, Rende (CS) Italy.
11. NEPLENBROEK, T., Stability of supported liquid membranes. PhD Thesis (1989). ISBN 90-90031 32-4. University of Twente, Enschede, The Netherlands.
12. KOOPMAN, C., WITKAMP, G.J., Extraction of heavy metals from industrial phosphoric acid in a transverse flow hollow fiber membrane contactor. *Separation Science and Technology*, 37(6), 2002, p. 1273–1290.
13. KUMAR, A., HADDED, R., ALGUACIL, F.J., SASTRE A.M., Comparative performance of non-dispersive solvent extraction using a single module and the integrated membrane process with two hollow fiber contactors. *Journal of Membrane Science*, 2005, 248, p. 1–14.
14. GEBELMAN, A., HWANG, S.T., Hollow fiber membrane contactors. *Journal of Membrane Science*, 159 (1999), p. 61–106.



THERMAL CONDUCTIVITY OF CONVENTIONAL CFRP AND CNT-NANOCOMPOSITES UNDER ALTERNATING HEAT IMPACT

S.M. Danilova-Tretiak, L.E. Evseeva, S.A. Tanaeva

*A. V. Luikov Heat&Mass Transfer Institute of NAS of Belarus
Brovki str. 15, Minsk 220072 – Belarus*

ABSTRACT

The aim of this paper is to investigate the influence of low temperatures and thermal cyclic loading on thermal conductivity of epoxy/carbon nanotube nanocomposites and carbon fiber reinforced plastics. Some tests on thermal cyclic loading in a range of 77.3 K – 403 K were performed. The sample was placed into liquid nitrogen and then replaced to air-oven. Amount of thermal cycles was variable. Measurements were carried out in monotonous regime at temperature range from 123 K to 398 K. It was shown that multiple thermal cycling results in significant decrease of thermal conductivity of unidirectional CFRP. CNT-loading greatly increases both thermal conductivity of epoxy composite and its cryogenic stability.

Keywords: thermal conductivity, nanocomposite, carbon nanotube, thermal loading

1. INTRODUCTION

Carbon fiber reinforced plastics (CFRP) are widely used in civilian and military aircraft and space structures. These materials work at low temperatures and they are undergone periodical heating and cooling. They must withstand a deep cooling and repeated thermal cyclic loading without essential change of their properties.

Thermal cycling leads to essential, sometimes anomalous, changing of thermal properties due to destruction of the material under investigation. Powder and particle fillers improve the resistance of polymer composites to thermal cyclic loading. Nano-fillers improve mechanical and thermal properties at much lower concentration of filler. Using of carbon nanotubes (CNT) for reinforcement of polymer matrix nanocomposites allows to overcome such disadvantage of polymeric materials as its destruction under alternating heat impact.

Polymer composite materials can undergo thermal fatigue and cycling thermal loads at low temperatures for example in cryogenic or space and military technique. As a result high thermal stress arises in materials due to difference between thermal expansion coefficients of binder and filler. During exploitation of these composite materials in condition of high temperature differences the defects (such as breaks and micro-cracks) occur that leads to pores appearance and thermal properties changes.

To provide reliable work of equipment made of composites at low temperature it is necessary to have materials characterized with high cryogenic stability that is they must withstand both deep cooling and multiple cycling thermal loads without essential change of their properties. Artificial thermal cycling allows to predict material state in different temperature conditions. Tension at thermal loading is similar to tension at mechanical one. So many investigators have studied destruction of materials at multiple mechanical loads. But thermal cycling is more aggressive and the material has to have highest strength and cryogenic stability to accept the same amount of thermal cycles as during mechanical loading and mostly save its properties. Some authors investigated synergetic influence of thermal and mechanical cycling on polymer composites destruction [1–3]. Influence of cycling on mechanical properties of composites has been studied [4–7] whereas their thermal properties in conditions of cycling are almost unknown. But it should be noted that breaks and cracks in composites serve like “bridges” for heat transfer and it influences on composites` thermal properties such as thermal conductivity and thermal diffusivity. Micropores

and interphase surface destructions that appear at initial stages of thermal cycling already lead to changes of composite properties [8].

It is important to understand the mechanisms and consequence of destructive action of low temperatures on polymer composites properties for making appropriate new age constructive materials with nanofillers using. The most interesting in this sense are carbon nanotubes due to their outstanding mechanical, electric and thermal properties. Carbon nanotubes exhibit extremely high thermal conductivity due to carbon atoms assembled in a graphitic structure. Theoretical value of thermal conductivity $\lambda \sim 6600$ W/(m·K) for single-wall CNT at room temperatures have been predicted [9]. Measurement of multi-wall CNT gave values of thermal conductivity $\lambda \sim 200\text{--}3000$ W/(m·K) at room temperatures [10, 11]. It was shown that including carbon nanopowders into epoxy resin enhance both thermal conductivity of nanocomposite and its cryogenic cycling stability [12].

The aim of this paper is to investigate the influence of low temperatures and alternating heat impact on thermal conductivity of epoxy/carbon nanotube nanocomposites and carbon fiber reinforced plastics in temperature range of 77.3 K – 403 K.

2. METHODOLOGY

2.1. Materials

Polymer composites on the basis of epoxy with different nanofillers were investigated.

Polyacrylonitrile fibers were used as filler for unidirectional CFRP producing. These fibers contain a chain of carbon connected to one another. Concentration was 70 vol. %, orientation of fibers was unidirectional. The samples were prepared in two manners to provide heat flux along and across fibers.

Nanopowders containing carbon nanotubes (single-wall and multi-wall) were used as fillers for epoxy nanocomposites. All carbon nanopowders were produced by high-voltage atmospheric pressure discharge [13] at Heat&Mass Transfer Institute (Minsk, Belarus). As-prepared carbon nanomaterials were treated with nitric acid and toluene to get purified CNT and then heated at high temperatures. The degree of grafitization was determined by Raman spectroscopy. Degrees of grafitization for nanofillers with multi-wall carbon nanotubes and single-wall carbon nanotubes were 47 and 61.5% respectively.

The samples were produced by mechanical and ultrasound mixing. Polyethylenepolyamin was used as a hardener. The best result was observed at the next processing scheme: 16 hours at room temperature, 3 hours at 333 K, 3 hours at 403 K. Density of all nanocomposites under investigation was approximately the same ($1110 \text{ kg/m}^3 \pm 1\%$). According to previous studies [12] two concentrations of nanopowder were chosen – 0.1 and 1.0 mas.%.

2.2. Thermal cycling

Two types of cryogenic thermal cycling were used. First the sample was cooled to a liquid nitrogen temperature during approximately 20 minutes and then heated under adiabatic conditions at a rate of 6 K/min up to upper limit temperature (type I). During cycling type II the sample undergoes cooling-heating as “heat impact”. In this case the sample was cooled from high temperature to nitrogen boiling temperature during 10 min and after that it was heated to 403 K in drying box.

The samples were cooled and heated according type I before and after certain amount of thermal cycles type II.

2.3. Thermal properties measurements

Thermal conductivity measurements were carried out using a monotonous regime method [14], in the temperature range from 123 to 423 K. This method implies such heating-cooling regime where low temperature gradients and almost uniform temperature rate field are saved simultaneously inside the sample. The sample is placed into adiabatic tank, it is heated by special heating element, heat flow is measured by heat flow meter and it is converted to thermal conductivity on the basis of Fourier's law. The method is realized in the IT- λ -400 and IT-C-400 installations [14]. The relative error was about 5%. The samples for thermal conductivity measurements were disks with 15 mm diameter and 1.4 mm thickness. Thermal conductivity was measured both during thermal cycling of type I and after each series (5, 10, 15, 25) of thermal cycles type II.

Influence of thermal cycling on thermal properties was investigated for nanocomposites with 0.1 mas.% and 1.0 mas.% single- and multi-wall carbon nanotubes. At first thermal conductivity was measured for all samples in temperature range 123–398 K. Then thermal cycling was carried out with amplitude 77.3–403 K. Samples filled with single-wall CNT undergone 5, 10, 15, 25 thermal cycles whereas samples with multi-wall CNT were exposed to cycling 5, 10 and 15 times.

3. RESULTS AND DISCUSSIONS

Dependence of thermal conductivity λ on temperature for unidirectional CFRP is presented in Fig. 1.

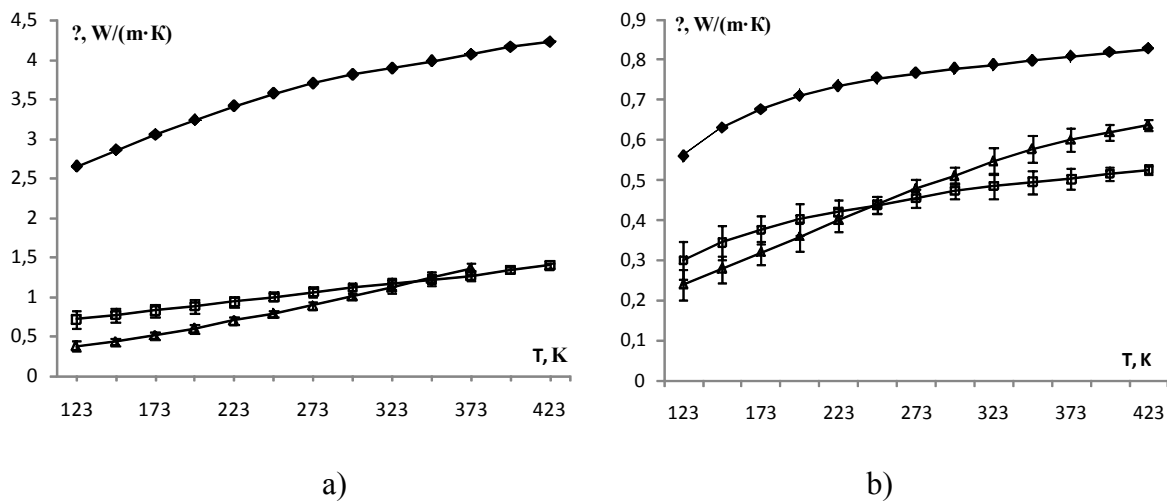


Fig. 1. Thermal conductivity of CFRP at heat flux direction along (a) and across (b) fiber under thermal cycling: \blacklozenge – initial thermal cycle, \square – 5 heat impacts, \triangle – 10 heat impacts

The main feature of CFRP is distinct anisotropy of their properties including thermophysical ones. Anisotropy is defined by fibers orientation in matrix in one or different directions. Anisotropy ratio for CFRP under investigation is 5. Adhesive interaction of matrix and surface of reinforcing fibers is important in these materials. It is seen that thermal cycling leads to sharp reducing of thermal conductivity even at low number of heat impacts. Additional thermal cycling leads to further changing of material structure and curves character alters also. The most significant reducing is observed in direction parallel to fibers (up to 70% while reducing in direction perpendicular to fibers is 45% in average). It can be expected that cracks appearance occurs mainly perpendicularly to fibers. It is proved by SEM-images (Fig. 2).

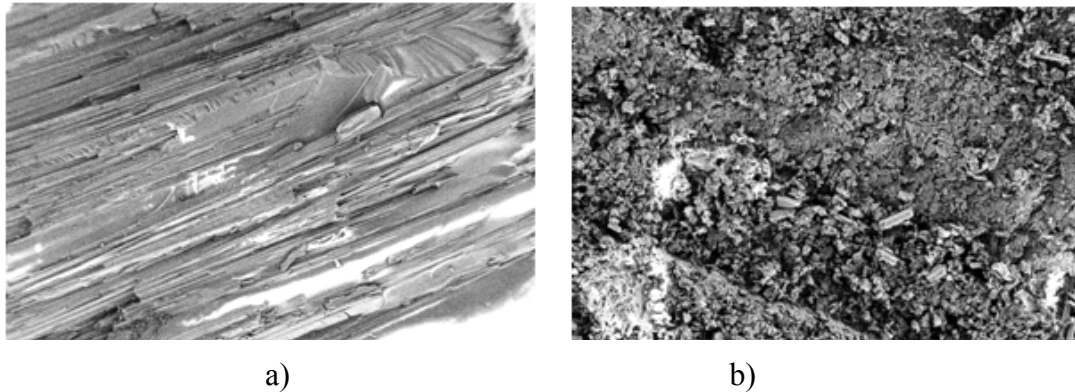


Fig. 2. Scanning electronic microscope (SEM) images of CFRP surface along (a, magnification is 137 \times) and across (b, magnification is 1 kX) fibers after thermal cycling

Dependence of thermal conductivity on temperature for polymers filled with CNT is presented in Fig. 3, 4. It is shown that thermal cycling like “heat impact” leads to reducing of thermal conductivity generally. CNT concentration influences on the process of temperature reduction.

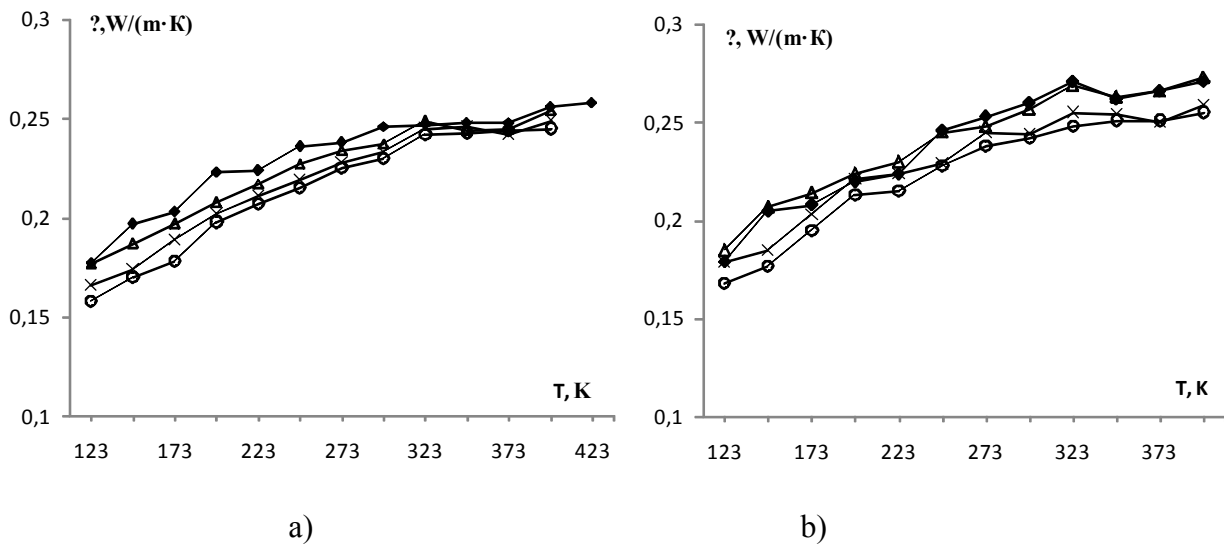


Fig. 3. Thermal conductivity of CNT-nanocomposites filled with single-wall CNT under thermal cycling: a) – 0.1 mas.%; b) – 1.0 mas.%; \blacklozenge – initial thermal cycle, \blacktriangle – 10 heat impacts, \times – 15 heat impacts, \circ – 25 heat impacts

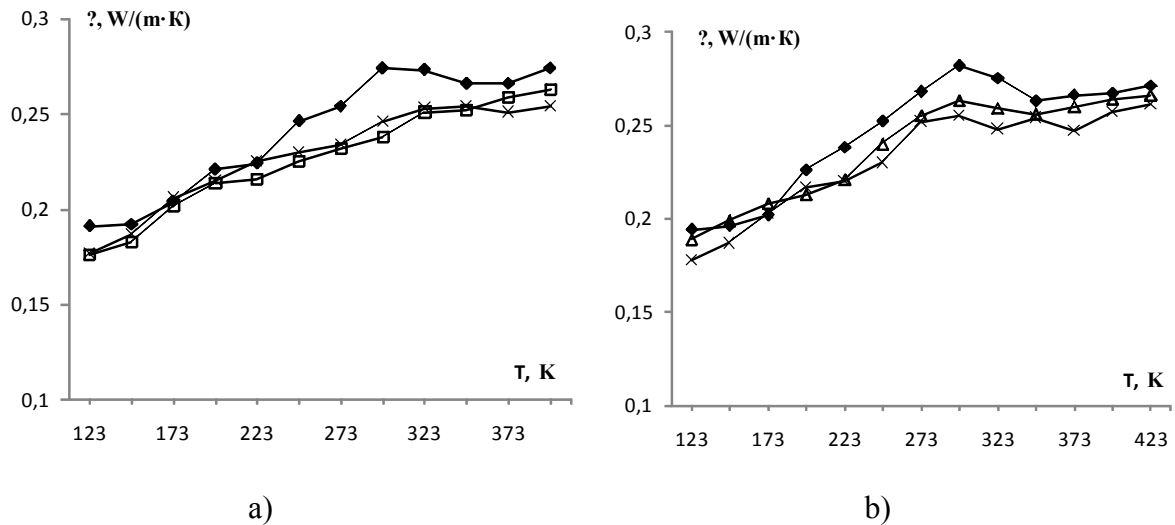


Fig. 4. Thermal conductivity of CNT-nanocomposites filled with multi-wall CNT under thermal cycling: a) – 0.1 mas.%; b) – 1.0 mas.%;

◆ – initial thermal cycle, □ – 5 heat impacts, Δ – 10 heat impacts, × – 15 heat impacts

So, after 5 thermal cycles thermal conductivity of composite with 0.1 mas.% single-wall CNT increased slightly in all temperature range. Similar behaviour was observed while investigation of thermal cycling influence on mechanical properties of composites [15]. Strength and rigidity rise was detected at initial period of cycling that authors explained as final curing of binding component. After 10, 15 and 25 cycles thermal conductivity of the material decreased. Comparison of thermal and mechanical properties of composites is quite in order because these properties are interrelated as it has been proved by different authors [16–18 et al].

Increase of CNT concentration up to 1.0 mas.% leads to rise of cryogenic stability of the composite. As a result thermal conductivity remained the same after 10 heat impacts. But after 15 and 25 impacts thermal conductivity decreased not more than 10% in all temperature range. This result marks both composites with single-wall and multi-wall CNT. For composite filled with multi-wall CNT decreasing of thermal conductivity was observed at temperatures higher than 223 K. It is more evident at low CNT concentration.

But generally, nanocomposites under investigation are more stable to heat impacts in comparison with composites filled with CFRP. Even 25 thermal cycles on CNT-nanocomposites lead to thermal conductivity decrease not more than 10% whereas 10 thermal cycles reduce thermal conductivity of CFRP up to 70%. It is seen in Figs. 1, 3, 4. Thermal stability of CNT-nanocomposites is also higher than of CFRP especially if we regard thermal conductivity of last sample along fibers. In investigated temperature range thermal conductivity of composites rises in average. But variation of this parameter for CNT-nanocomposites is about 40–50% while for CFRP it is 60%.

The results of structure investigation of nanocomposites before and after thermal cycling are shown in Fig. 5. Nanofiller agglomerates can be seen before thermal action. After thermal treatment surface became smoother and material looks like homogeneous. Such self-healing of the composite occurs through high adhesion of CNT to epoxy that prevents cracking of the polymer and vitrification because during thermal cycling the composite is heated beyond glass-transition temperature.

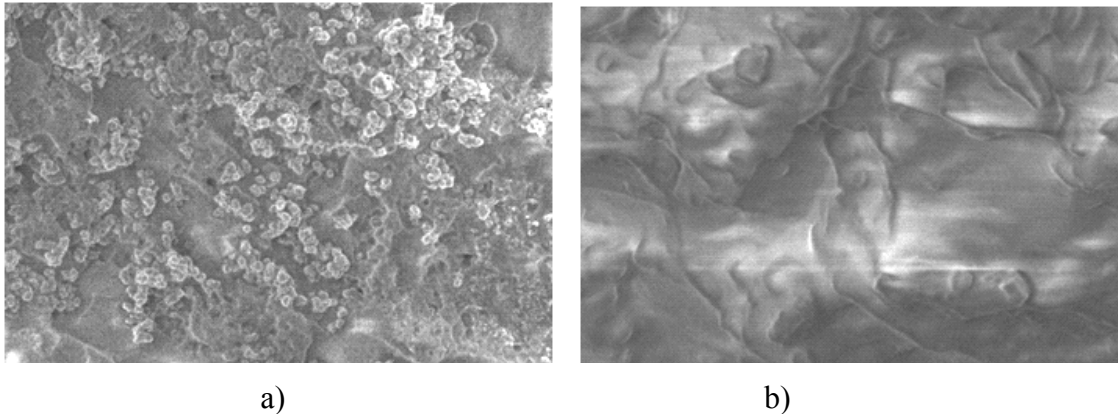


Fig. 5. SEM-images of epoxy nanocomposite filled with 1.0 mas.% of multi-wall CNT before thermal cycling (a, magnification is 19 kX) and after 10 thermal cycles (b, magnification is 28 kX)

4. CONCLUSIONS

It was shown that multiple thermal cycling leads to significant decrease of thermal conductivity of carbon fiber reinforced plastics even at low number of heat impacts. That indicates appearance of micro-cracks in the material.

Using carbon nanotubes as a filler of polymer composite (even at low concentration 0.1 mas.%) leads to significant increase of its cryogenic stability. Thermal conductivity remains almost the same even at 25 heat impacts. That indicates high adhesive ability of polymer to nanotubes.

So, to create more cryogenic stable material it is advisable to use CNT as a filler of polymer composite.

ACKNOWLEDGMENT

The authors of this paper acknowledge Dr. Filatov S. and members of Lab. of Synthesis and Analysis of micro- and nanoscaled systems (Heat&Mass Transfer Institute) for structure investigation of nanocomposites carried out on scanning electron microscope Carl Zeiss Supra™ 55.

REFERENCES

1. AHLBORN, K. Durability of carbon fiber reinforced plastics with thermoplastic matrices under cyclic mechanical and cyclic thermal loads at cryogenic temperatures. *Cryogenics*, 1991, Vol. 31, p. 257–260.
2. EGGERS, H., HARTUNG, W., KNAACK, S. Damage in carbon fibre reinforced epoxy after thermal cycling and T-fatigue loading. *Cryogenics*, 1991, Vol. 31, p. 265–268.
3. JU, J., MORGAN, R.J. Characterization of microcrack development in BMI-carbon fiber composite under stress and thermal cycling. *J. Comp. Mat.*, 2004, Vol. 38, No. 22, p. 2007–2024.
4. HARTWIG, G., HUBNER, R. Thermal and fatigue cycling of fiber composites. *Cryogenics*, 1995, Vol. 35, p. 727–730.
5. TOMPKINS, S.S., WILLIAMS, S.L. Effects of thermal cycling on residual mechanical properties of C6000/PMR-15 graphite polyimide. AIAA/ASME/ASCE/AHS 23rd Structure, Structural Dynamics and Materials Conf., New Orleans, May 10–12, 1982, Vol. 1, p. 239–246.
6. HENAFF-GARDIN, C., DESMEUZES, J.L., GALLIOT, D. in “*Fatigue under Thermal and Mechanical loading*”, ed. B.Seysener, Kluwer Acad. Publisher, Netherlands, 1996, p. 285–295.



7. LUHYNA, N., INAM, F. Carbon nanotubes for epoxy nanocomposites: a review on recent developments. Proc. of 2nd Int. Conf. on Advanced Composite Materials and Technologies for Aerospace Applications, Wrexham, UK, 2012, p. 80–86.
8. PARK, S.Y., CHOI, H.S., CHOI, W.J., KWON, H. Effect of vacuum thermal cyclic exposures on unidirectional carbon fiber/epoxy composites for low earth orbit space applications. *Composites: Part B*, 2012, Vol. 43, p. 726–738.
9. BERBER, S., KWON, Y.K., TOMANEK, D. Unusually high thermal conductivity of carbon nanotubes. *Phys.Rev. Lett.*, 2000, Vol. 84, p. 4613–4616.
10. YANG, D.J., WANG, S.G., ZHANG, Q., SELLIN, P.J., CHEN G. Thermal and electrical transport in multi-wall carbon nanotubes. *Phys. Lett.A*, 2004, No. 329, p. 207–213.
11. CAHILL, D.G., GOODSON, K., MAJUMDAR, A. Thermometry and thermal transport in micro/nanoscaled solid-state devices and structures. *J. Heat Transfer*, 2002, No. 124, p. 223–241.
12. EVSEEVA, L., TANAEVA, S. Influence of carbon nanotubes concentration on thermophysical properties of epoxy nanocomposites at low temperatures. *Mechanics of Composite Materials*, 2008, No. 5, p. 697–708 (available in Russian).
13. ZHDANOK, S.A., BUYAKOV, I.F., CHERNUKHO, A.P., KRAUKLIS, A.V., SOLNTSEV, A.P., SHASHKOV, A.E. Carbon nanotubes syntesis under nonequilibrium conditions in *Nanotechnology in Physics, Chemistry and Biotechnology*, St-Petersburg, Russia, 2002.
14. PLATUNOV, E.S., BARANOV I.V., BURAVOY S.E., KUREPIN V.V. *Thermophysical measurements*. St.-Peterburg, 2010 (available in Russian).
15. KORZH, D.D., LAPOTKIN, V.A. Investigation of carbon plastics under alternative cyclic heat impact. *Mechanics of Composite Materials*, 1991, No. 6, p. 1108–1112 (available in Russian).
16. ZINCHENKO V.F., LATISHENKO V.A. Correlation between modulus of interlayers shear and thermal conductivity of directed fiberglass. *Polymer mechanics*, 1970, No. 6, p. 985–989 (available in Russian).
17. BODRYAKOV V.Yu., PETRUSHKIN V.V., Povzner A.A. Correlation between elastic and thermophysical properties of Scandium. *Physics of metals and metal science*, 2000, Vol. 89, No. 4, p. 5–9 (available in Russian).
18. BUKH A. Correlation between Young`s modulus and some other mechanical and physical properties of pure metals in dependence if their location in Mendeleev table. *Physics of metals and metal science*, 2005, Vol. 99, No. 1, p. 25–30 (available in Russian).



SYNTHESIS AND PHOTOCATALYTIC PROPERTIES OF MODIFIED TiO₂ NANOPORES AND NANOTUBES

R. Drunka, J. Grabis

*Riga Technical University
Institute of Inorganic Chemistry
Miera street 34, Salaspils, LV-2169 Latvia*

A. Patmalnieks

*University of Latvia
Institute of Microbiology and Biotechnology
Kronvalda bulv. 4, Riga, LV-1586, Latvia*

ABSTRACT

Synthesis and modification of TiO₂ nanotubes and nanopores with dopants were investigated to optimize nanostructural TiO₂ catalysts photocatalytic properties. Self-organized TiO₂ nanotube-layers were formed by electrochemical anodization of titania foil in a (NH₄)₂SO₄/HF electrolyte. Doped with sulfur nanotubes and nanopores were prepared by their treatment in H₂S flow or by using method of micro arc oxidation in sulphur containing electrolyte. Doped with nitrogen nanotubes were obtained by their treatment N₂ flow. Doped with tungsten oxide nanotubes were prepared by anodization of TiO₂ foil mechanically rubbed with tungsten particles or by additional anodization of the as-prepared TiO₂ nanotubes in peroxitungstic acid sol and ethanol-water electrolyte.

The catalytic activity was determined by degradation of methylene blue (MB) solution under UV and visible light illumination. The photocatalytic activity of the prepared TiO₂ nanotubes depends on the preparation conditions, the presence of WO₃, S and N increases their activity. During illumination the degradation of MB reaches 85–90% depending on applied dopants. Sulfur doped nanotubes have higher activity with respect to nitrogen and WO₃ doped nanotubes.

Keywords: titania nanotubes, nanopores, sulfur, nitrogen, tungsten oxide dopants, methylene blue decomposition

1. INTRODUCTION

Titania nanotubes due to large specific surface area and relatively simple and cost-effective preparation methods are a promising material for photocatalytic decomposition of organic compounds, splitting water and for dye-sensitized solar cells [1, 2]. The titania nanotubes have been prepared by hydrothermal alkaline treatment of TiO₂ nanoparticles [3], by using tetraisopropyl orthotitanate modified with acetylacetone and lauryamine [2] or by well-known electrochemical anodization of Ti foil in HF-containing electrolytes [4, 5, 6]. However due to wide band-gap (3.2 eV) titania exhibits high photocatalytic activity under ultraviolet (UV) illumination. Only 5% from sunlight is UV radiation but about 45% is visible light. A large number of investigations aimed at increase TiO₂ photocatalytic activity under visible light have been carried out over the last years. It is established that photocatalytic activity of TiO₂ nanoparticles and nanotubes can be increased by doping with nitrogen, carbon and sulphur [7, 8]. The improved photocatalytic activity of TiO₂ nanoparticles and mesoporous films has been achieved by doping with such metal oxide as WO₃ [9].

Micro arc oxidation is a new electrochemical oxidation method, which has been developed in recent years. The mechanism of micro arc oxidation is mainly based on dielectric breakdown and spark discharge [10]. Although, it is difficult to compare modified TiO₂ nanotubes and nanopores effectivity for photo catalysis, because conditions of preparation methods differ.

The aim of the present work is to determine characteristics of TiO_2 nanotubes and nanopores doped with WO_3 , sulfur and nitrogen in dependence on doping mode and to compare their photocatalytic activity.

2. EXPERIMENTAL

2.1. Catalyst preparation

The flow chart (Fig. 1) illustrates the formation process of nanotubes and nanopores and their doping with nitrogen, sulphur and tungsten oxide. All used chemicals were analytical grade. The anodization parameters were chosen on the basis of literature data and preliminary studies [11].

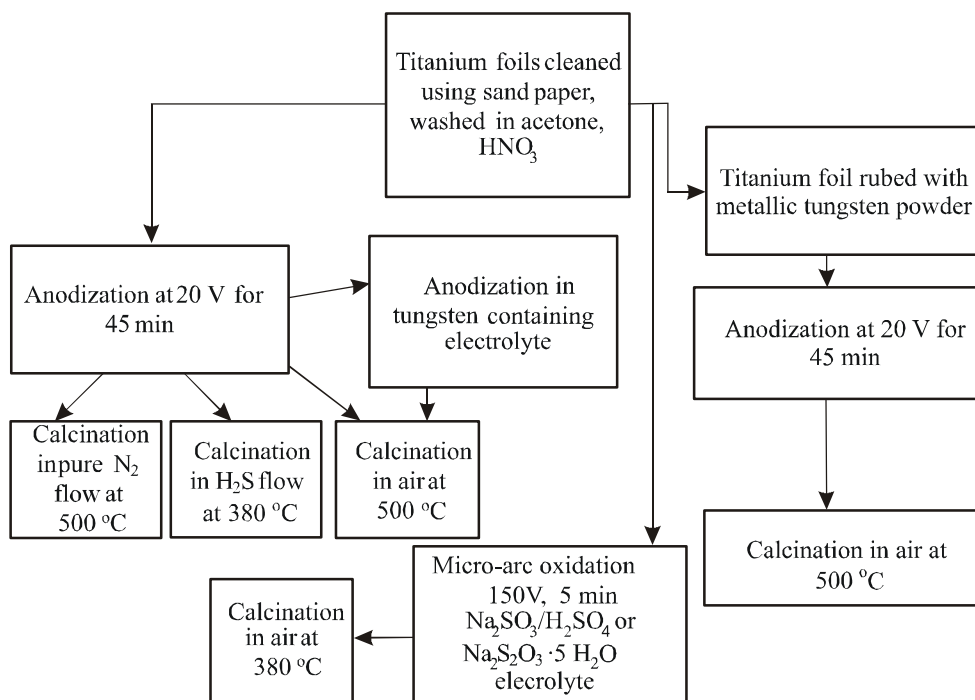


Fig. 1. The flow chart of the preparation of TiO_2 nanotubes and nanopores doped with nitrogen, sulfur or tungsten oxide

2.1.1. TiO_2 nanotubes preparation

Self-organised TiO_2 nanotubes were prepared by electrochemical anodization of titania foil (99.7%, Sigma Aldrich) in $(\text{NH}_4)_2\text{SO}_4/\text{HF}$ electrolyte, using Pt foil as counter electrode (Fig. 1). Ti foil was cleaned with sandpaper to remove TiO_2 layer from the surface, boiled in 6 M HNO_3 solution at 80 °C for 30 min and washed with deionised water and acetone. Anodization was performed at a constant potential of 20 V DC power supply for 45 min, with Ti foil as the anode and a platinum foil as the cathode. The as-anodized Ti foils were washed with distilled water and then dried in air.

2.1.2. Preparation of doped TiO_2 nanotubes and nanopores

Nanotubes and nanopores doped with sulfur were prepared by their treatment at 380 °C in H_2S flow for 2 h. For H_2S gas synthesis reaction between FeS and HCl in Kipp's apparatus was used.

Beside this the sulphur doped TiO₂ nanopores were prepared by Ti foil treatment using micro arc oxidation in sulphur containing electrolyte made by dissolving 10.0 g Na₂S₂O₃·5H₂O in deionised water at constant DC potential of 150 V during 5 min. During anodization process on the surface of Ti foil small sparks were visible. After anodization electrolyte solution changes its colour from colourless to yellow.

Doped with tungsten oxide nanotubes were prepared by anodization of Ti foil mechanically rubbed with tungsten particles for 5 min and then anodized for 45 min. Conditions of Ti foil preparation and anodization were the same as in pure TiO₂ nanotube preparation.

Another method to modify TiO₂ nanotubes with WO₃ was by using additional anodization of the as-prepared TiO₂ nanotubes in peroxitungstic acid sol and ethanol-water electrolyte for 45 min.

After the anodization prepared samples were calcinated in air for 2 h at 500 °C to get crystal anatase.

Doped with nitrogen nanotubes were obtained by their treatment at 500 °C for 2 h in N₂ 99.99% flow. Before starting heating process the system was purified by nitrogen flow for 30 min. The flow rate was 10 ml per minute.

The phase composition was determined by using X-ray diffraction analysis (D8 Advance, Bruker AXS). The microstructure of the obtained samples was investigated by using SEM (Jeol JSM - 6490).

2.2. Photocatalytic measurements

Photocatalytic activity of the prepared samples was evaluated by decomposition of MB water solution under UV radiation (high pressure Hg lamp, 120 W) and under visible light (Philips CFL GENIE fluorescent lamp 40 W). The MB solution (100 ml, 7.6·10⁻³ g/l) was introduced in a quartz reactor equipped with TiO₂ nanotube/Ti and electrode. The sources of light were at distance of 110 mm from the quartz reactor. During the experiments every 15 min suspension samples (2 ml) were taken out. The degradation of MB under illumination in presence and absence of the electrodes was determined by measuring light absorption by solution at light wave length of 662 nm using JENWAY-6300 spectrophotometer. As reference with 100% transmission was used deionized water.

3. RESULTS AND DISCUSSION

XRD patterns of the as-anodized foils show only substrate Ti maxima indicating that TiO₂ nanotubes are X-ray amorphous. Calcination of the as-anodized TiO₂ foils, including doped samples at 500 °C (sulfur doped at 380 °C) for 2 h leads to crystallization of TiO₂. All XRD patterns of the calcinated samples are similar and beside intensive Ti maxima exhibit also weak maxima of anatase phase (Fig. 2). Influence of dopants on phase composition or on shift of the diffraction maxima are not observed.

The very similar SEM images of calcinated pure TiO₂ and doped nanotubes indicate that influence of the dopants and their introduction mode on formation of the titania nanotubes is negligible (Fig. 4). Prepared TiO₂ nanotubes diameter is 40–150 nm and length 7–9 μm (Fig. 3). Sulfur doped TiO₂ nanopores prepared using micro arc oxidation method are with diameter 50–350 nm. Depth of TiO₂ nanopores is much smaller than length of TiO₂ nanotubes and reaches only 0.2–1 μm.

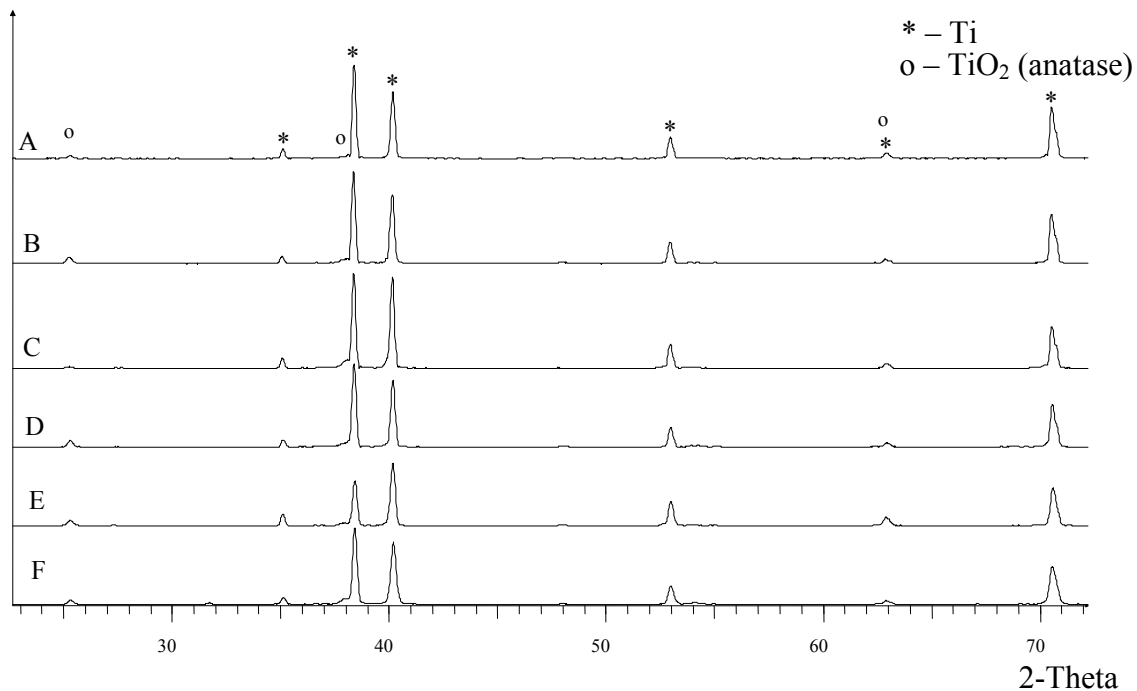


Fig. 2. XRD patterns of TiO₂ samples: pure TiO₂ nanotubes (A); TiO₂ nanotubes doped with WO₃ (rubbed with W) (B), TiO₂ nanotubes doped with WO₃ (additional anodization) (C), TiO₂ nanotubes doped with nitrogen (D), TiO₂ nanopores doped with sulphur (micro arc oxidation) (E) and TiO₂ nanotubes doped with sulphur (treatment in H₂S) (F)

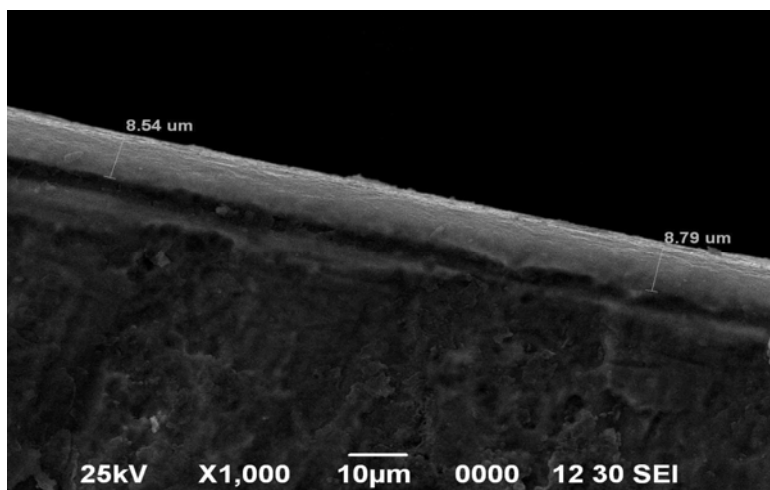
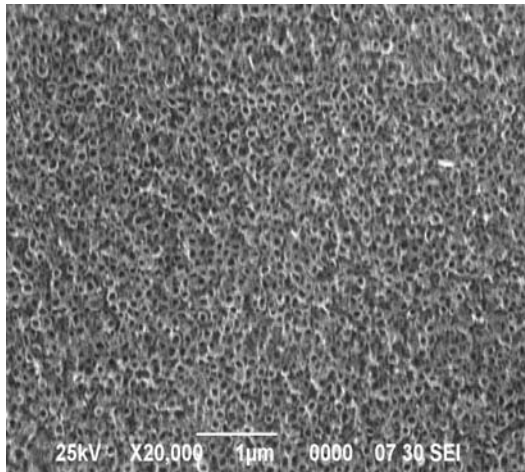
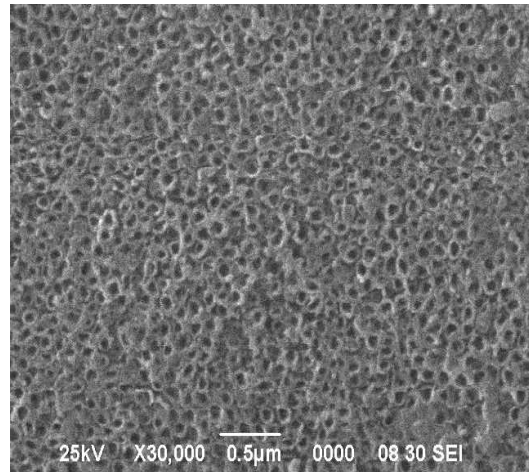


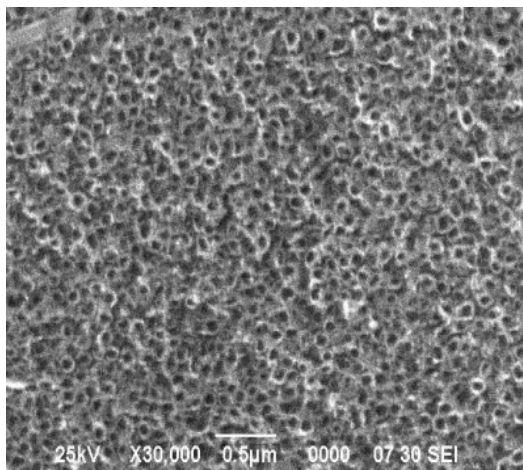
Fig. 3. SEM cross view image of pure TiO₂ nanotubes sample



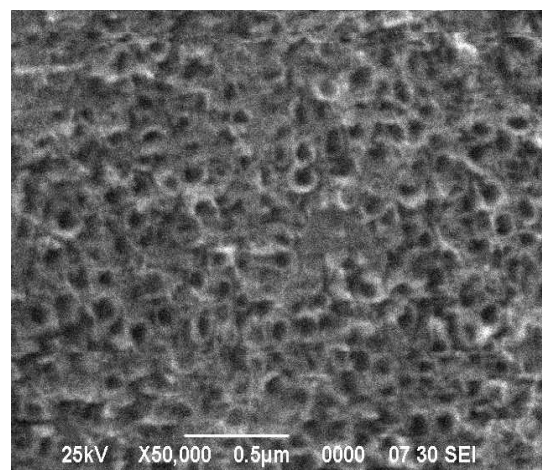
a)



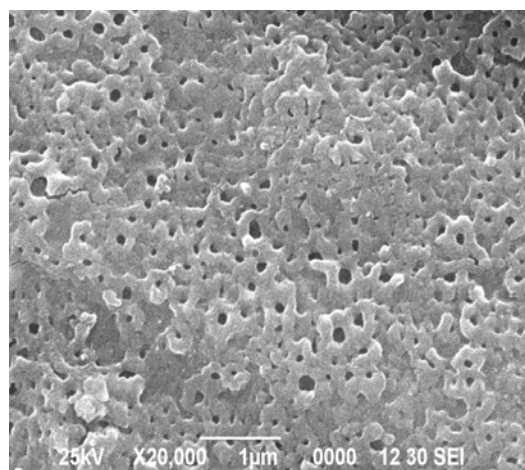
b)



c)



d)



e)

Fig. 4. SEM images of pure TiO_2 nanotubes (a), nanotubes doped with nitrogen (b), nanotubes doped with WO_3 (c), nanotubes doped with sulphur (d), and nanopores doped with sulphur (e)

Despite to the similar morphology of prepared nanotubes the photocatalytic activity of all doped samples is higher with respect to pure TiO_2 nanotubes (Fig. 5). The highest photocatalytic activity for degradation of MB under UV radiation is estimated for TiO_2 nanotubes doped with sulphur in H_2S flow at 380°C and in N_2 flow. The degradation of MB reaches 93% during 250 min. Nanotubes doped with WO_3 using various methods indicate lower photocatalytic activity especially at the first 200 min. of degradation process. Different photocatalytic activity of the doped TiO_2 nanotubes can be explained by better incorporation of nitrogen and sulfur into titania lattice promoted by gas phase process. The estimated decrease of the photocatalytic activity of TiO_2 nanotubes or nanopores doped with sulphur using micro arc oxidation with respect to doped samples in H_2S flow confirms this conclusion. Obviously micro arc oxidation promotes formation of sulphur on the surface of TiO_2 .

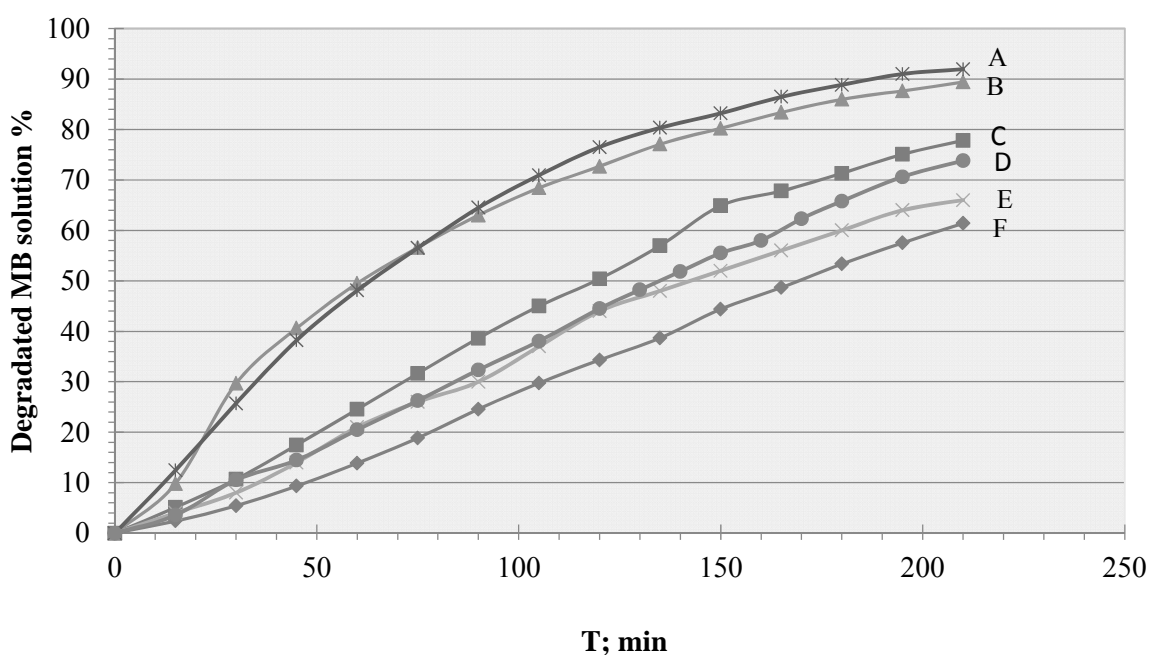


Fig. 5. Degradation of methylene blue solution under UV radiation: TiO_2 nanotubes doped with sulphur (treatment in H_2S) (A), TiO_2 nanotubes doped with nitrogen (B), TiO_2 nanotubes doped with WO_3 (additional anodization) (C), TiO_2 nanotubes doped WO_3 (rubbed with W) (D), TiO_2 nanopores doped with sulphur (micro arc oxidation) (E) and pure TiO_2 nanotubes (F)

The doped TiO_2 nanotubes show some photocatalytic activity under illumination of visible light (Fig. 5). The higher photocatalytic activity under visible light illumination is estimated for TiO_2 nanotubes doped with sulphur in H_2S flow at 380°C . The photocatalytic activity of TiO_2 doped with nitrogen in nitrogen flow is very high at starting period, but then decreases. During illumination of 250 min the degradation of MB reaches 4–11% depending on applied dopants in visible irradiation. Nanotubes doped with WO_3 shows much lower activity with respect to nitrogen and sulphur doped nanotubes. Photocatalytic activity of sulfur doped TiO_2 nanopores under visible light can reach 7%. Pure TiO_2 nanotubes photocatalyst do not show any activity under visible light illumination.

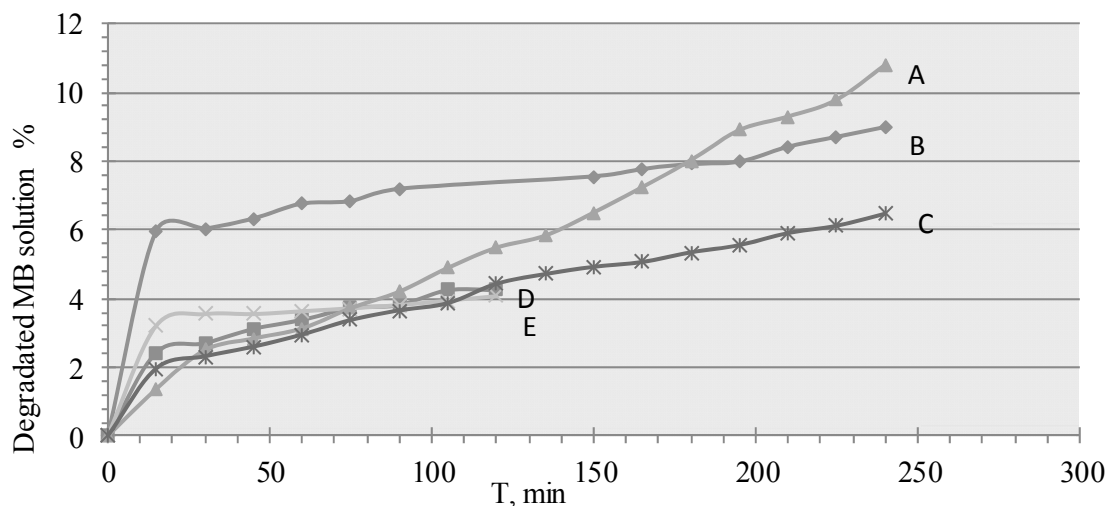


Fig. 6. Degradation of MB solution under visible light illumination: TiO₂ nanotubes doped with sulphur (treatment in H₂S) (A), TiO₂ nanotubes doped with nitrogen (B), TiO₂ nanopores doped with sulfur (micro arc oxidation) (C), TiO₂ nanotubes doped with WO₃ (rubbed with W) (D), TiO₂ nanotubes doped with WO₃ (additional anodization) (E)

Dopants increase photocatalytic activity with respect to pure TiO₂ nanotubes under visible light illumination, but the activity is not as high as it is under UV irradiation.

Generally all of the prepared TiO₂ nanostructure specimens have shown photocatalytic properties, but there is a difference in their activity. As is shown in Fig. 2, none of the prepared samples have shown any dopant containing phase in the XRD patterns, but all of the modified TiO₂ nanostructures have higher photocatalytic activity than pure TiO₂ nanotubes under UV irradiation and under visible light illumination. Sulfur and nitrogen doped TiO₂ nanotube samples have with higher photocatalytic activity under UV and visible light illumination with respect to WO₃ doped nanotubes and sulphur doped TiO₂ nanopores photocatalysts. The sulfur doped TiO₂ nanopores are with higher activity in visible light illumination than WO₃ doped TiO₂ nanotubes.

CONCLUSIONS

Anodization and micro arc oxidation are eligible methods for preparation TiO₂ photocatalysts.

Modification with sulfur, nitrogen and WO₃ allows to improve photocatalytic activity of TiO₂ nanotubes by 33% under UV illumination and up to 11% under visible light illumination.

One of the best method to improve photocatalyst activity is its treatment in dopant containing gas atmosphere.

Micro arc oxidation method allows to prepare sulfur doped TiO₂ nanopore photocatalyst in one step anodization process.

ACKNOWLEDGMENTS

This work has been supported by State Research Program LATENERGI.

REFERENCES

- HASHIMOTO, K., IRIE, H., FUJISHIMA, A. TiO₂ Photocatalysis: A Historical Overview and Future Prospects. *Jpn. J. Appl. Phys.*, 2005. Vol. 44, No. 12, p. 8269–8285.
- ADACHI, M., MURATA, Y., OKADA, I., YOSHIKAWA, S. Formation of titania nanotubes with high photo-catalytic activity. *Chem. Lett.*, 2000. Vol. 29, No. 8, p. 942–943.



3. JITPUTTI, J., PAVASUPREE, S., SUZUKI, Y., YOSHIKAWA, S. Synthesis of TiO₂ nanotubes and its photocatalytic activity for H₂ evolution. *Jpn. J. Appl. Phys.*, 2008. Vol. 47, No. 1, p. 751–754.
4. LEI, L., SU, Y., ZHOU, M., ZHANG X., AND CHEN. X., Fabrication of multi-non-metal-doped TiO₂ nanotubes by anodization in mixed acid electrolyte. *Materials Research Bulletin*, 2007. Vol. 42, No. 12, p. 2230–2236.
5. KANECO, S., CHEN, Y., WESTERHOFF P., CRITTENDEN, J. C. Fabrication of uniform size titanium oxide nanotubes: Impact of current density and solution conditions. *Scripta Materialia*, 2007. Vol. 56, p. 373–376.
6. MACAK, J. M., SHMUKI, P. Self-organized porous titanium oxide prepared in Na₂SO₄/NaF electrolytes. *Electrochimica Acta*, 2005. Vol. 50, p. 3679–3684.
7. ASAHII, R., MORIKAWA, T., OHWAKI, T., AOKI, K. TAGA, Y. Visible-light photocatalysis in nitrogen-doped titanium oxides. *Science*, 2001. Vol. 293, p. 269–71.
8. VITIELLO, R.P., MACAK, J.M., GHICOV, A., TSUCHIYA, H., DICK, L.F.P., SCHMUKI, P. N-Doping of anodic TiO₂ nanotubes using heat treatment in ammonia. *Electrochemistry Communications*, 2008. Vol. 8, p. 544–548.
9. YANG, L., XIAO, Y., LIU, S., LI, Y., CAI, Q., LUO, S., ZENG, G. Photocatalytic reduction of Cr (VI) on WO₃ doped long TiO₂ nanotube arrays in the presence of citric acid. *Applied Catalysis B: Environmental*, 2010. Vol. 94, p. 142–149.
10. JIANFENG, LI, W., JIAYOU, F.,L. Micro arc oxidation of s-containing TiO₂ films by sulfur bearing electrolytes. *J. of Mat. Proc. Techn.* 2009, Vol. 209, p. 762–766.
11. DRUNKA, R., GRABIS, J., JANKOVIČA, DZ., PATMALNIEKS, A. Preparation and photocatalytic activity of doped TiO₂ nanotubes. *Latvian J.Chem.* 2011. No. 3/4, p. 250–255.



OBTAINING OF THE SUBSTRATES OF II-VI COMPOUNDS AND SOLID SOLUTIONS FOR NANOPOROUS STRUCTURES

E.P. Goncareenco, G.V. Colibaba

*Moldova State University
A. Mateevici 60a, MD-2009 –Moldova*

E.V. Monaico

*Technical University of Moldova
Stefan cel Mare 168, MD-2004 –Moldova*

ABSTRACT

The wide band-gap II-VI semiconductors and solid solutions on their basis have large perspectives to be used in optoelectronics, solar energy and spintronics. Substrates of these materials could be widely utilized for fabrication of nanoporous matrices (templates) used for obtaining nanowires and nanotubes with various diameters and lengths. These nanostructures can be used as elements of LEDs, plate lenses, components of integrated optical circuits etc. One of the most interesting applications is solar energy converters with improved performance and cost effectiveness due to increased optical absorption in the region of nanostructured p-n junction and smaller necessary thickness of corresponding layers. The easiest and cost-effective method to obtain nanoporous structures is anodic etching. However, the technology development for II-VI compounds is still on the beginning stage.

This paper deals with the problems of growing homogeneous substrates of the widest band gap II-VI semiconductors (ZnSe, ZnS, ZnO) and solid solutions on their basis (ZnCdS, ZnSSe) with controlled electrical parameters. Prospects of these materials utilization for preparing nanoporous matrices by means of electrochemical etching are also estimated. Various methods of growth and doping of II-VI compounds are analyzed by examination of their morphology, electrical, luminescence and optical properties. The results of nanostructuring using various electrolytes are shown. The prospects of ZnSe and ZnCdS utilization for obtaining nanoporous arrays with porous diameters up to 30 nm are demonstrated. Also, the complexity of obtaining the nanoporous matrices on ZnS, ZnSSe and ZnO substrates is analyzed.

Keywords: zinc oxide (ZnO), zinc selenide (ZnSe), solid solution, anodic etching, nanoporous structure

1. INTRODUCTION

Wide band-gap II-VI semiconductors, such as ZnSe, ZnS and ZnO, have wide perspectives for application in photonics, optoelectronics and spintronics, for example, as solar energy converters, light emitting devices, substrates for nanoporous matrices. They have wide potential to produce the sets of nanowires and nanotubes of various materials with defined values of diameter and length [1–3]. These nanostructures are interesting for investigation of contact phenomena between nanotube materials grown in the nanoporous semiconductor matrix. They may be used as flat lenses, elements of complex integrated circuits, high-efficient solar energy cells etc. [4, 5].

The easiest and cost-effective method of obtaining nanoporous matrices is electrochemical etching. The important technological task is the development of fabrication technology for nanotemplates based on wide band gap II-VI semiconductors (ZnSe, ZnS, ZnO), as the properties of these nanostructures can be easily controlled by external irradiation, applied electric field etc. However, to use electrochemical etching technology, it is necessary to manipulate with electrical parameters of initial material (substrates), which allows controlling the pore diameter. For example, the first test nanoporous structures with minimal diameter of the pore of 400 nm were obtained using commercially available ZnSe substrates with electrical conductivity of $10^{-1} (\Omega \cdot \text{cm})^{-1}$. In addition, porous layers were non-uniform because of non-homogeneous substrates.

The present paper deals with ZnSe, ZnS, ZnO compounds and solid solutions on their basis, such as ZnSSe and ZnCdS. Growth technology of uniformly doped materials with controlled electrical parameters, electrical and luminescent properties of these materials, as well as estimation of their prospects for obtaining nanoporous structures by electrochemical etching are discussed.

2. EXPERIMENTAL TECHNIQUE

The growth of the II-VI semiconductors and solid solutions on their basis was carried out in sealed evacuated quartz ampoules using physical or chemical vapor transport method (PVT or CVT respectively). The influence of the growth temperature (from 975 to 1080 °C), post-growth cooling (from 0.5 to 10 °C), design and temperature profile of the growth chamber, as well as growth rate (from 0.5 to 10 mm/day) on the structural perfection of the samples was analyzed. The ZnSe and ZnS samples were obtained by PVT method; ZnO – by CVT method using HCl, H₂ and CO as vapor transport agents, and ZnCdS, ZnSSe solid solutions using HCl vapors.

The samples of II-VI compounds and solid solutions were cut on plain substrates with ~1 mm thickness for thermal treatment. Finally, the samples were exposed to mechanical and chemical polishing using Br-CH₃ solution and boiling water solution of NaOH.

Photoluminescence (PL) was excited by a nitrogen laser ($E_{\text{exc}} \approx 3.68$ eV, $I_{\text{exc}} \sim 10$ mW/mm²) and registered in the 350 to 800 nm range using a monochromator with reciprocal dispersion of 1.4 nm/mm. Electrical parameters were calculated from the Hall effect measurements using a six-probe method.

Electrochemical etching was carried out in various electrolytes in the dark at room temperature. Anodization was performed in potentiostatic regime [6]. Applied voltage to Pt electrodes was varied from +5 to +30 V depending on the substrate conductivity. The light-induced etching treatment of ZnO crystals was carried out using ultraviolet (UV) mercury lamp with 350 W power. A TESCAN Scanning Electron Microscope (SEM) was used to study morphology of the samples.

3. RESULTS AND DISCUSSION

3.1. ZnSe single crystals

The best results were achieved for the ZnSe crystals grown by the PVT method with the subsequent thermal annealing in Zn+Al melt. Doping conditions (900 °C, 100 hours, 1 at.% Al) allowed obtaining of homogeneous ZnSe substrates with large area and conductivity of 20 (Ω·cm)⁻¹ (Fig. 1(a)) [7]. Homogeneous nanoporous structures were fabricated on their basis with the diameters up to 40 nm using K₂Cr₂O₇:H₂SO₄:H₂O electrolyte (Fig. 1(b)) [8]. However, technology for other II-VI semiconductors and solid solutions on their basis, which have wider band gap, as well as their prospects as nanoporous matrices, are of great interest.

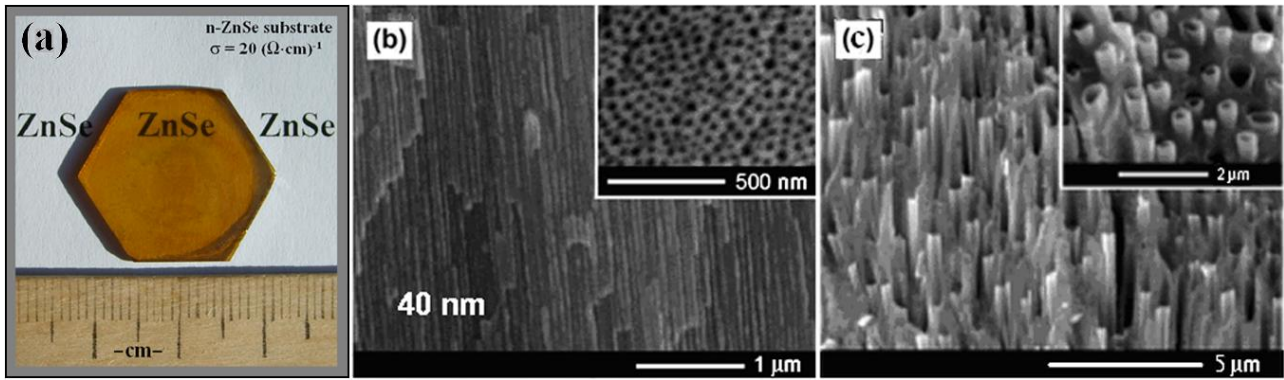


Fig. 1. Exterior view of the high-conductive ZnSe substrate (a), SEM images of nanopores fabricated on the ZnSe substrates with electron concentration of $2 \cdot 10^{18} \text{ cm}^{-3}$ (b), and Pt nanotubes grown in these pores (c). The insets illustrate a top view

3.2. ZnS single crystals

The ZnS samples grown by PVT method with growth temperature and rate of $1050 \text{ }^\circ\text{C}$ and $1\text{--}1.5 \text{ mm/day}$ respectively, have a high density of subgrain boundaries. This is attributed to lower pressure of the ZnS vapours (approximately 0.3 mmHg at $1050 \text{ }^\circ\text{C}$) and liability to polytypism [9]. The most optimal parameter of the growth rate is 0.5 mm/day at $1050 \text{ }^\circ\text{C}$ providing lower density of structural defects.

To increase the electrical conductivity of the ZnS samples, the doping from Zn+Al melt was carried out at various temperatures (from 900 to $1040 \text{ }^\circ\text{C}$) and Al concentrations ($0\text{--}2 \text{ at.}\%$). From the dependence of the resistivity on Al concentration and doping temperature (Fig. 2(a)), the optimal conditions of annealing are determined to be $900 \text{ }^\circ\text{C}$ during 100 hours and $0.5 \text{ at.}\%$ Al. In this case, the charge carrier concentration is $\sim 2 \cdot 10^{16} \text{ cm}^{-3}$ and resistivity is $0.3 \text{ } \Omega \cdot \text{cm}$. However, the investigated material has extreme surface resistance ($\sim \text{M}\Omega/\text{mm}^2$) due to the surface levels which influence the electrical properties of the material because of the raised conduction band bottom (Fig. 2(b)).

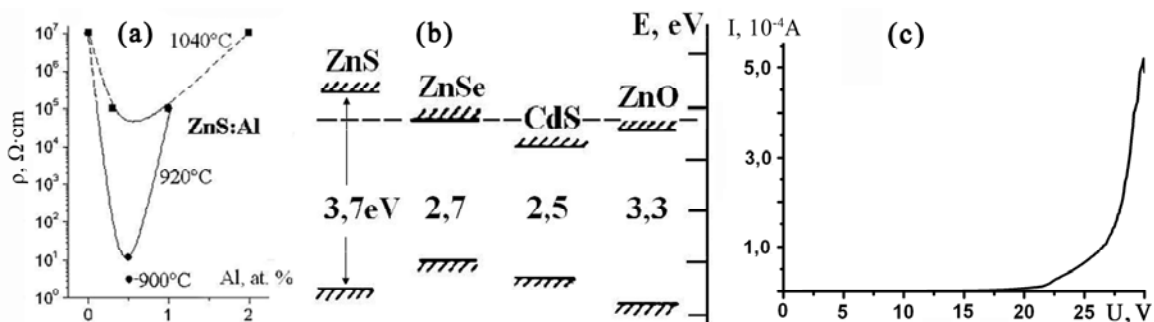


Fig. 2. (a) Resistivity of the crystals ($T = 300 \text{ K}$) after annealing during 100 hours at various temperatures and Al concentrations in Zn+Al melt. (b) Energy diagram of II-VI compounds. (c) Volt-ampere characteristic of the ZnS single crystal during electrochemical etching

The attempts to realize electrochemical etching using various electrolytes (HCl , $\text{HCl:H}_2\text{SO}_4$, $\text{HCl:H}_3\text{PO}_4$) were unsuccessful. The sample surface has been intact after 20 minutes etching at the voltages up to 30 V , as a result of extremely low values of current due to high surface resistance (Fig. 2(c)).

In this regard, we propose to use the solid solutions on the ZnS and ZnSe basis, which have lower surface resistance and wider band gap comparing to ZnS and ZnSe respectively.

3.3. ZnSSe single crystals

It is advisable that the final material corresponds to the composition of the initial material of growth for solid solution. This is very difficult to achieve using PVT method, because of the different pressures of the saturated vapours (for ZnS and ZnSe, these values differ for 3 times [9]). Thus, it is better to use CVT method and HCl vapors as transport agent due to effective interaction with both sulphides and selenides. The results of the thermodynamic calculation for chemical vapour transfer for ZnS, ZnSe and CdS compounds are presented in Fig. 3(a).

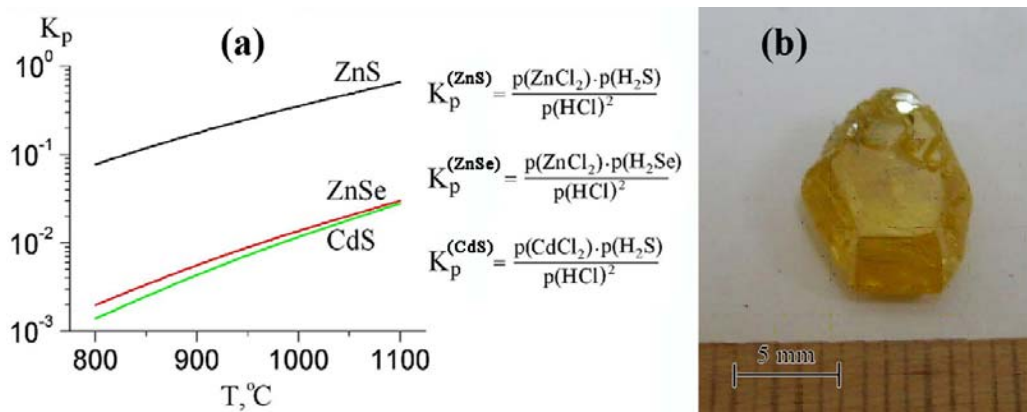


Fig. 3. (a) Temperature dependence of reaction constants corresponding to the CVT process, (b) view of obtained $ZnS_{0.5}Se_{0.5}$ single crystal

Another difficulty in obtaining of ZnSSe solid solutions is the absence of commercially available substrates of these compounds with various compositions and controlled parameters. Thus, it was necessary to synthesize the seed which was extended to the size of 1 cm^3 . Homogeneous crystals with ZnSe:ZnS proportion of 2:1, as well as 1:1 (Fig. 3(b)), were grown using HCl as a transport agent.

The values of the band gap of ZnSSe solid solution were estimated from investigations of exciton PL band. PL spectra are presented in figure 4 for $ZnS_{0.5}Se_{0.5}$ and $ZnS_{0.33}Se_{0.67}$ solid solutions, as well as ZnSe sample doped with Cl impurity for comparative analysis. The value of band gap energy increases depending on the ZnS concentration in the solid solution (Fig. 4, inset). The presence of Cl impurity in the samples is indicated by self-activated long-wave PL band.

Similar to ZnS, the resistivity of grown ZnSSe samples is high ($10^8 \Omega \cdot \text{cm}$). The decrease of the resistivity can be achieved by thermal annealing in Zn vapours at the following conditions: temperature – 900 °C, duration – 30 hours, Zn vapour pressure – 1 atm. However, even in this case, the surface resistance of the sample cannot be dropped to the level of $1 \text{ K}\Omega/\text{mm}^2$, and it increases with increasing Zn concentration in the samples. At the same time, electrical conductivity of the crystals is approximately equal to $0.3 (\Omega \cdot \text{cm})^{-1}$.

As in the case of ZnS samples, current intensity at electrochemical etching is very low for obtaining some results with the use of HCl, HCl:H₂SO₄, HCl:H₃PO₄ electrolytes. Voltage of 30 V and duration of 20 minutes were useless for obtaining of ZnSSe-based nanotemplates.

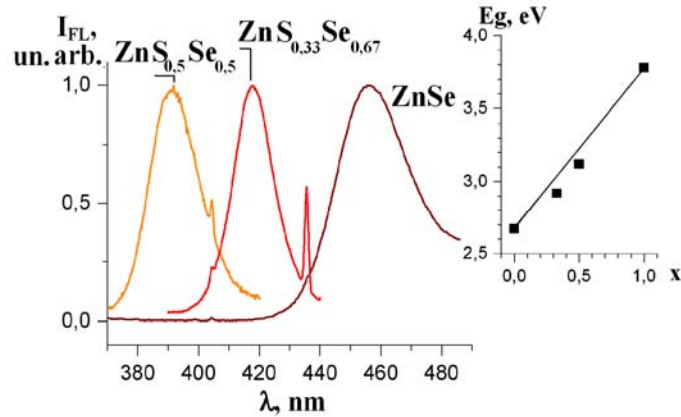


Fig. 4. Edge PL spectra for $\text{ZnS}_{0.5}\text{Se}_{0.5}$, $\text{ZnS}_{0.33}\text{Se}_{0.67}$ and ZnSe samples. Inset: the band gap energy calculated from the edge PL band shift

3.4. ZnO single crystals

The growth of ZnO single crystals by PVT method needs considerable values of saturated vapours pressure of initial material, which, unfortunately, could not be reached even at the temperature of quartz softening. Therefore, the CVT method was used with H_2 , HCl and CO transport agents [10]. Thermodynamical calculation of corresponding reactions is shown in Fig. 5.

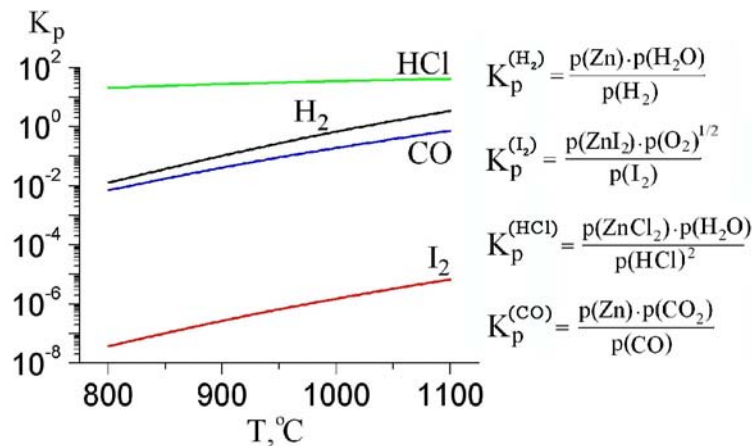


Fig. 5. Temperature dependence of reaction constants corresponding to the CVT method for ZnO

The use of H_2 as a transport agent provides high growth rate of the crystals, however, the strong mechanical contact between the sample and the quartz walls of growth chamber leads to the destruction of both growth chamber and grown crystals during a post-growth cooling (Fig. 6(a)). HCl transport agent is more favourable for the growth of ZnO single crystals due to insignificant mechanical contacts between the crystal and the walls of growth chamber that reduces structural defects generated during a post-growth cooling. At the same time, $\text{ZnO}:\text{HCl}$ single crystals have a large ratio between the crystal length and diameter that is a disadvantage, in our view (Fig. 6(b)). Thus, in order to combine the advantages of the both growth technologies, a mixed H_2+HCl transport agent was proposed. The high growth rate of the single crystals (1 mm/day) and moderate mechanical contact between the crystals and ampoules were obtained experimentally. Thus, the crystals with controlled values of the electric conductivity of $0.5\text{--}9 (\Omega \cdot \text{cm})^{-1}$ and charge carrier concentration of $(2\text{--}6) \cdot 10^{17} \text{ cm}^{-3}$ were obtained [7, 10].

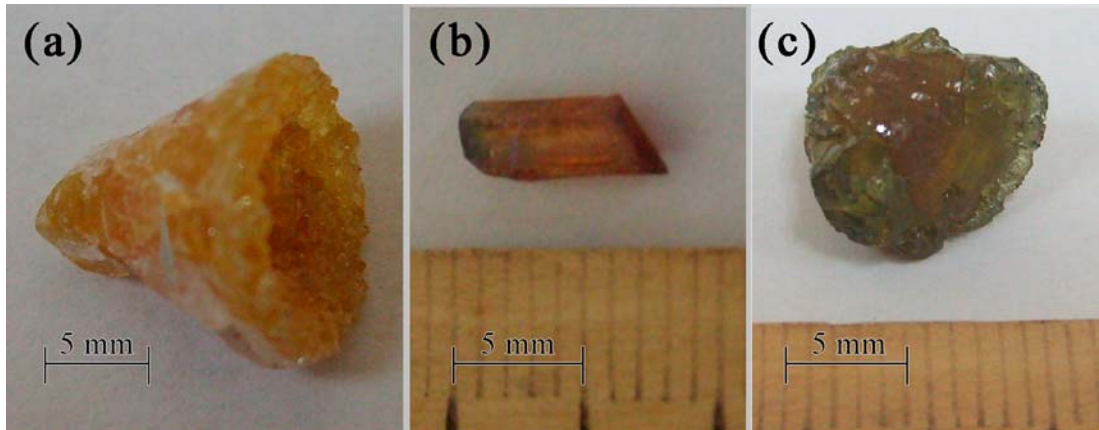


Fig. 6. View of the ZnO single crystal obtained by CVT method using transport agent: (a) H₂, (b) HCl, (c) H₂+HCl

The CO transport agent allows growing the most qualitative ZnO single crystals (Fig. 7(a)). The crystals have no volume structural defects, are optically transparent in the visible spectral range after annealing in vacuum (in comparison with ZnO:H and ZnO:HCl) and are characterized by intense edge luminescence (Fig. 7). Deviation from the ZnO:CO crystal stoichiometry allows both varying the electrical parameters for one order of magnitude (Fig. 7(b)) and essential modification of PL and optical properties of the crystals (Fig. 7(c, d)) [10].

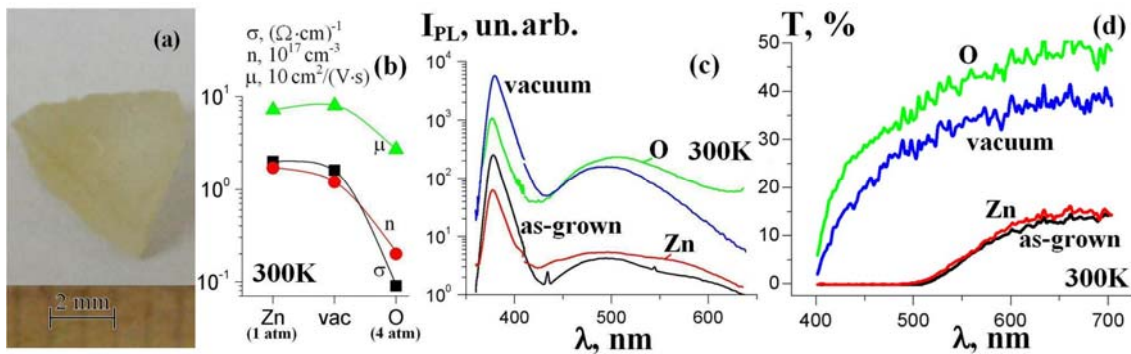


Fig. 7. (a) ZnO single crystal grown with the use of CO transport agent, (b) electrical, (c) PL and (d) transmission properties of ZnO:CO before and after annealing in various media

The NaCl (0.1 M) and KOH (0.1 M) electrolytes have no substantial influence on the surface states of the ZnO samples (Fig. 8(a)) after light-induced electrochemical etching during 15 minutes. Light-induced etching treatment with oxalic acid (0.3 M) allows realization of nanostructuring on the zinc oxide surface. However, the obtained nanostructures do not represent arranged pores as in the case of ZnSe samples (Fig. 1, 8(b)).

The results of nanostructuring performed during 10 minutes in the dark, at 20 V, in 3% water solution of HCl at room temperature are shown in Fig. 8(c). It is clearly seen that the obtained pores have specific geometry that is caused by gradual dissolution of the pore walls during electrochemical etching due to instability of zinc oxide relative to acid solution.

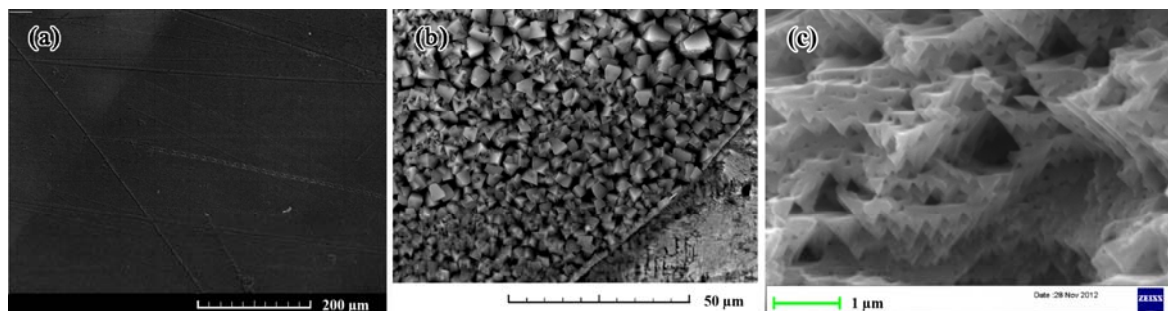


Fig. 8. Surface SEM view of the ZnO single crystals after electrochemical etching under UV irradiation using: (a) KOH electrolytes, (b) oxalic acid electrolyte (right bottom angle is the border of light-induced etching), (c) SEM view of the ZnO porous surface layer (HCl electrolyte)

3.5. ZnCdS single crystals

Taking into account big difference in saturated vapor pressures of initial components, PVT method is difficult to apply for growing ZnCdS crystals. Therefore, CVT method with HCl transport agent was used. The samples with maximum length of 1 cm and diameter of 8 mm and various ratios of the initial components (ZnS:CdS – 2:3, 1:1, 2:1) were obtained. Also, CdS and ZnS crystals doped with Cl impurity were grown for comparative analysis.

Band gap of the ZnCdS found from PL investigations at room temperature is varied from 2.5 to 3.5 eV depending on the initial material ratio (Fig. 9, inset). Thermal annealing of the ZnCdS:Cl solid solution in Zn+Cd vapors was carried out for reducing resistivity. The following results were obtained for the $Zn_{0.4}Cd_{0.6}S:Cl$ sample with 2.85 eV band gap, which is larger than that of ZnSe: charge carrier concentration – $2 \cdot 10^{18} \text{ cm}^{-3}$, electrical conductivity – $20 (\Omega \cdot \text{cm})^{-1}$, and mobility – $70 \text{ cm}^2/(\text{V} \cdot \text{s})$. These materials have no surface resistance.

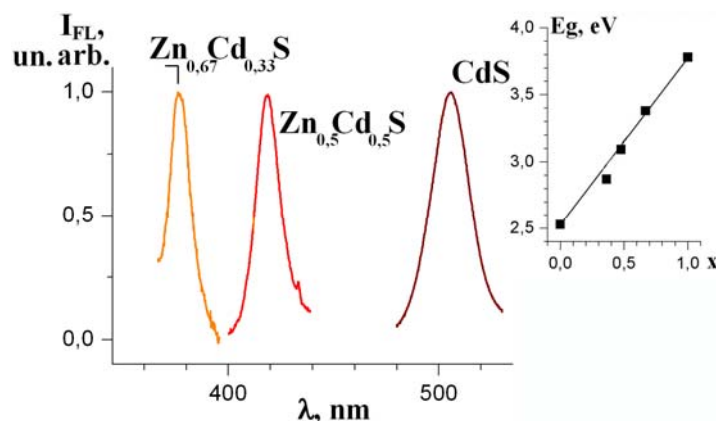


Fig. 9. Edge PL spectra of the $Zn_{0.67}Cd_{0.33}S$, $Zn_{0.5}Cd_{0.5}S$ and CdS. Inset: the band gap energy calculated from the edge PL band shift. T = 300 K

Electrochemical etching was carried out in static conditions at 18 V, in 5% HCl electrolyte, at room temperature during 20 minutes. The obtained nanoporous structure of the $Zn_{0.4}Cd_{0.6}S:Cl$ solid solution (Fig. 10) is characterized by the following parameters: thickness of the pore walls – 20 nm, diameter of the pores – 30 nm, and depth – 20 μm.

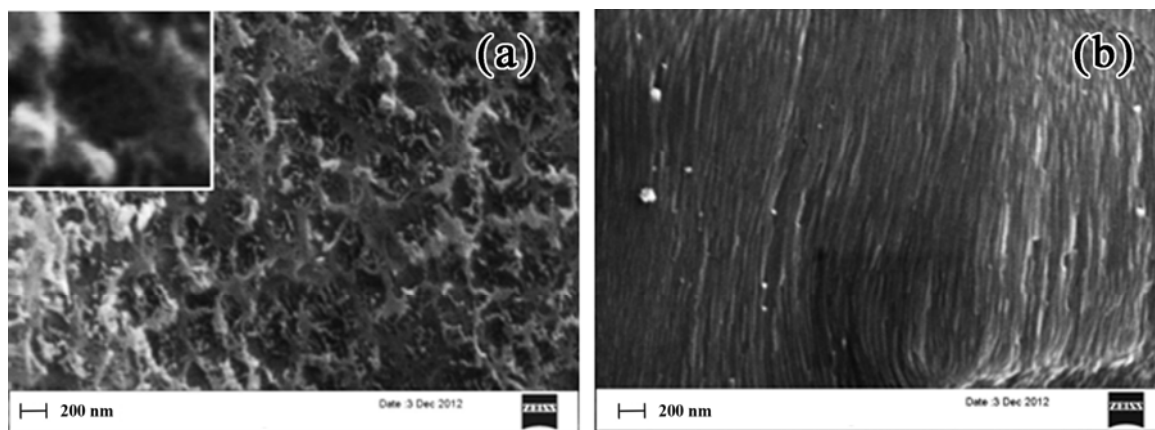


Fig. 10. Surface view of the ZnCdS after electrochemical etching: (a) top, (b) side

4. CONCLUSIONS

The obtaining of nanotemplates could not always be successfully carried out by electrochemical etching for II-VI semiconductor compounds and solid solutions on their basis. For example, despite the fact that ZnS single crystals have the maximal band gap energy among these compounds and moderate resistivity (after annealing – $0.3 \Omega \cdot \text{cm}$), unfortunately, they have enormous surface resistance ($> \text{M}\Omega/\text{mm}^2$). The ZnSSe samples are also characterized by high surface resistance. We suppose this is caused by the surface levels due to the raised conduction band bottom, which influences on the electrical properties of the materials. For ZnO and $\text{Zn}_x\text{Cd}_{1-x}\text{S}$ (with composition x less than 0.5), conduction band is placed lower than the conventional level corresponding to the position of the ZnSe conduction band bottom (that is not characterized by significant surface resistance). This fact is favourable for low surface resistance and opens new prospects for using these materials. Analysis of nanoporous structure obtained on the ZnSe and ZnCdS reveals vast utilizing potential for these materials due to successful obtaining of the pores with diameters down to 30 nm.

Wide band gap ZnO material is widely investigated in the nanoworld. However, this material is not so good for obtaining nanoporous structures by electrochemical etching because of its poor chemical resistance.

Summarizing, the most promising materials from the wide band gap II-VI compounds and solid solutions on their basis for nanostructuring by electrochemical etching are ZnSe and ZnCdS. If some binary II-VI compound does not suit for obtaining nanoporous structures by the discussed method, the solid solution on its basis may be used for this purpose.

ACKNOWLEDGEMENTS

We acknowledge Dr. V. Popa for help in light-induced electrochemical etching of ZnO. The research was supported by the Supreme Council for Science and Technological Development of the Academy of Sciences of Moldova under Projects 11.836.05.07A and 11.817.05.11F.

REFERENCES

1. ШАЛИМОВА, К.В. *Физика полупроводников*. Москва: Энергоатомиздат, 1985. 392 p.
2. MONAICO, E., TIGHINEANU, P., LANGA, S., HARTNAGEL, Hans L., TIGINYANU, I. ZnSe-based conductive nanotemplates for nanofabrication. *Phys. Stat. Sol. (RRL)*, 2009, Vol. 3, p. 97–99.



3. TIGINYANU, I., MONAICO, E., MONAICO, E. Ordered arrays of metal nanotubes in semiconductor envelope. *Electrochemistry Communications*. 2008, Vol. 10, Issue 5, p. 731–734.
4. JIE, J.S., ZHANG, W.J., BELLO, I., LEE, C.S., LEE, S.T. One-dimensional II–VI nanostructures: Synthesis, properties and optoelectronic applications. *Nanotoday* 2010, Vol. 5, Issue 4, p. 313–336.
5. SERGENTU, V.V., URSAKI, V.V., TIGINYANU, I.M., FOCA, E., FÖLL, H., BOYD, Robert W. Design of negative-refractive-index materials of the basis of rods with a gradient of the dielectric constant. *Applied Physics Letters*. 2007, Vol. 91, 081103.
6. LANGA, S., CARSTENSEN, J., CHRISTOPHERSEN, M., FÖLL, H., TIGINYANU, I.M. *J. Appl. Phys. Lett.* 2001, Vol. 78, p. 1074–1076.
7. COLIBABA, G.V., GONCEARENCO, E.P., NEDEOGLO, D.D., NEDEOGLO, N.D. Growth of wide band-gap II–VI compound substrates with controlled electric parameters. *Moldavian Journal of the Physical Sciences*, 2012, Vol. 11, N 4, p. 361–365.
8. TIGINYANU, I.M., URSAKI, V.V., MONAICO, E., ENACHI, M., SERGENTU, V.V., COLIBABA, G., NEDEOGLO, D.D., COJOCARU, A., FÖLL, H. Quasi-Ordered Networks of Metal Nanotubes embedded in Semiconductor Matrices for Photonic Applications. *Journal of Nanoelectronics and Optoelectronics*, 2011, Vol. 6, p. 1–10.
9. AVEN M., PRENER J.S. *Physics and Chemistry of II–VI Compounds*. North-Holland, Amsterdam, 1967, 844 p.
10. COLIBABA, G.V., GONCEARENCO, E.P., NEDEOGLO, D.D., NEDEOGLO, N.D. Growth of ZnO crystals by CVT methods. *Moldavian Journal of the Physical Sciences*, 2012, Vol. 11, N 4, p. 366–370.



INVESTIGATION OF ELECTRICAL PROPERTIES OF CADMIUM SULFIDE THIN FILMS

A. Graf

*Tallinn University of Technology, Department of Physics
Ehitajate tee 5, 19086 Tallinn – Estonia*

ABSTRACT

The investigation of the electrical properties of chemical bath deposited (CBD) cadmium sulfide (CdS) films was the main objective of this work. Namely, sheet resistance, carrier concentration and mobility as a function of temperature and a role of chlorine doping were studied with the aim of understanding how annealing conditions influence on the electrical properties of CdS films. All CdS films were deposited on glass substrates by chemical bath deposition technique in a standard bath (i.e. at certain concentration of the components, same pH and temperature of the bath for all our films). After deposition, films were annealed in hydrogen atmosphere at different temperatures between 200 and 400 °C. Duration of annealing (5–120 min) was taking into account as well.

The electrical properties of the annealed CdS films were characterized using a four probes van der Pauw Hall effect measurement method. It was shown that electrical properties of CdS films can be easily controlled by annealing in hydrogen atmosphere and chlorine doping to achieve appropriate electrical properties for using them in thin film solar cells. Furthermore, it was the first systematic study of the dynamics of changes in the electrical properties as a function of temperature for our CBD CdS films.

The study results and possible mechanisms of changing in the electrical properties under different preparing conditions are discussed below.

Keywords: Cadmium Sulfide, Solar Cells, Chemical Bath Deposition, Thin Films, Hall Measurement

1. INTRODUCTION

As cadmium sulfide has wide band gap (2.4 eV), it is used as a buffer and n-type window layer in cadmium telluride and copper indium gallium selenide (CIGS) based solar cells. Nevertheless, the complete devices and individual layers of devices are the subjects of processing/performance studies, which are sometimes empirical in order to establish the means by which they are effective. The CBD method appears to be a relatively simple, in expansion method to prepare homogenous films with controlled composition. In particular CBD is widely used for achieving good-quality CdS thin films. The CBD method gives poor crystalline quality of CdS layers in comparison with other deposition techniques but films which deposited by this method gives best photoconductivity and morphological properties such as roughness and pinhole density as compared with films processed by other techniques [1]. It has been identified as one of the techniques for growing polycrystalline and epitaxial CdS films at low cost [2].

Regardless of the deposition technique, the characterization of the post-deposited films and optimization of the deposition processes are still open subjects for research. A large number of studies have been carried out to achieve this goal in order to produce CdS thin films with good optoelectronic properties suitable for photovoltaic applications. For this purpose, the CdS thin films should have several properties: (i) relatively high transparency and not too thick to avoid absorption in the buffer layer and favour the absorption in the CIS layer, (ii) not too thin to avoid short circuiting, (iii) relatively low resistivity so as not to alter the fill factor of the solar cell and higher photoconductivity so as not to alter the solar cell spectral response [3].

A good window layer must fulfil several characteristics: low carrier recombination, low sheet resistance, and being a good match to CdTe. It is the purpose of this work to study how annealing conditions influence on the electrical properties of CBD CdS films. Here, we report our systematic study of the dynamics of the changes in the electrical properties of CBD CdS films in annealing process in H_2 at normal (atmospheric) pressure.

2. PREPARATION

CdS thin films have been prepared on glass substrates using CBD technique under different preparation conditions. All CdS thin films were deposited on $2.5 \times 2.5 \text{ cm}^2$ substrates from a bath containing cadmium salt (CdSO_4) as a source of cadmium, thiourea as a source of sulfide, ammonium sulphate ($(\text{NH}_4)_2\text{SO}_4$) and ammonia (NH_3) in an aqueous solution. For some samples the NH_4Cl dopant was added in the deposition bath at concentration $X = 1\%$, where X is the chlorine concentration $[\text{Cl}]$ relative to the cadmium salt concentration $[\text{Cd}]$ in the deposition solution ($[\text{Cl}]/[\text{Cd}]$). The bath temperature ($85 \text{ }^\circ\text{C}$) and pH (~ 9.5) were constant. After deposition CdS layers were thermally pretreated in vacuum for removing of residual water at $200 \text{ }^\circ\text{C}$ for 1 h. The concentrations of the components, temperature and pH of the solution bath for CdS, can be varied over a working range and each group use its own specific recipe [4]. Annealing in H_2 at normal pressure from 5 to 120 min was provided at temperatures from 200 to $400 \text{ }^\circ\text{C}$. Deposited films were yellow in colour and their thickness was measured using scanning electron microscopy (SEM), and it was estimated to be $325 \pm 30 \text{ nm}$. All films have mixture of hexagonal and cubic structure. Similar observations of the structure of CBD CdS films have been reported by other authors [5].

3. EXPERIMENTAL DETAILS

3.1. Sheet resistance measurement

To measure the electrical properties of all annealed CdS films on glass four dots of liquid In – Ga eutectic mixture were painted onto the corners of films. The ohmic behaviour of contacts was followed by the shape of $I - V$ curves, which is necessary condition for using van der Pauw technique.

Our measurement system includes four point probes, temperature detector, heating element, which allowed us to change temperature of a sample in the 300–400 K range, and sample stage for square samples with an area up to 1 cm^2 . Temperatures were measured using a chromel-alumel thermocouple junction attached to the surface of the sample (Fig. 1).

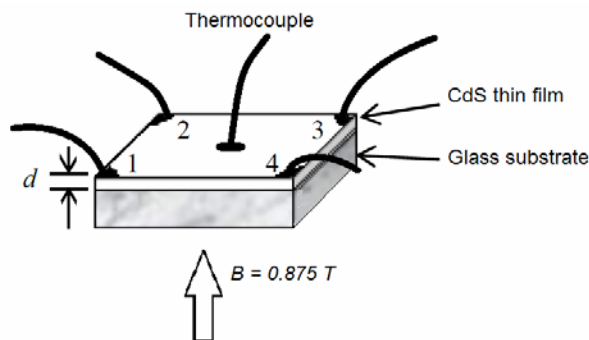


Fig. 1. Schematic configuration of DC Hall effect measurement for a square shaped CdS film using van der Pauw method

By passing a 0.50 mA direct current (DC) I through two contacts on the sample, the voltage V_1 was measured at two other contacts with an APPA 109N multimeter. The same procedure is followed for the second configuration of connections to measure V_2 . Smoothly increasing the temperature (1 – 2 K/min) for avoiding temperature gradients, that may cause noisy and erratic instrument readings, and measuring voltages in accordance with the van der Pauw technique [6], the sheet resistance ρ_s of a film as a function of temperature was determined from an equation (1)

$$\rho_s = \frac{\pi}{\ln 2} \cdot \frac{V_1 + V_2}{2I} \cdot f, \quad (1)$$

where f is correction function [7]. To obtain a more precise measurement of ρ_s several reciprocal measurements were taken and averaged. The sheet resistance was measured in the dark.

3.2. Hall effect measurement

With the constant magnetic field $B = 0.875 T$, that is perpendicular to the plane of the sample (Fig. 1), switched on, the current I is applied along one diagonal of the sample, while the Hall voltage V_H is measured along the other diagonal. Then, the magnetic field's polarity is inverted, and a second measurement is made. The same procedure is also followed for the second configuration of connections. After results were averaged. By measuring the Hall voltage, we can calculate carrier concentration

$$n = \frac{IB}{eV_H d} \quad (2)$$

and mobility μ

$$\mu = \frac{1}{en\rho_s d}, \quad (3)$$

where e is electron charge and d is sample thickness.

We emphasize that interpretation of the Hall effect in polycrystalline semiconductors is not simple, especially when the contribution of the boundaries is appreciable [8]. Therefore we are not so interested in absolute values of the electrical parameters, but in dynamics of changes of these parameters.

4. RESULTS AND DISCUSSION

4.1. Influence of annealing time on sheet resistance

The observation for the effect of annealing on the sheet resistance was done with respect to annealing time, at a certain annealing temperature. We prepared five CdS films using CBD method. All samples were annealed at the same temperature – 400 °C in H_2 atmosphere. 400 °C is the optimal annealing temperature for the production of dense and textured polycrystalline thin films, i.e. increase in annealing temperature accelerates sintering of as deposited polycrystalline CdS. Duration of annealing varied from 5 to 120 min for

different samples. On the other hand, at such annealing temperature higher sheet resistance is observed. Moreover, with prolonged annealing CdS films acquire porous structure.

Results are presented in Fig. 2. Rapid increase of sheet resistance with increasing of duration of annealing is observed.

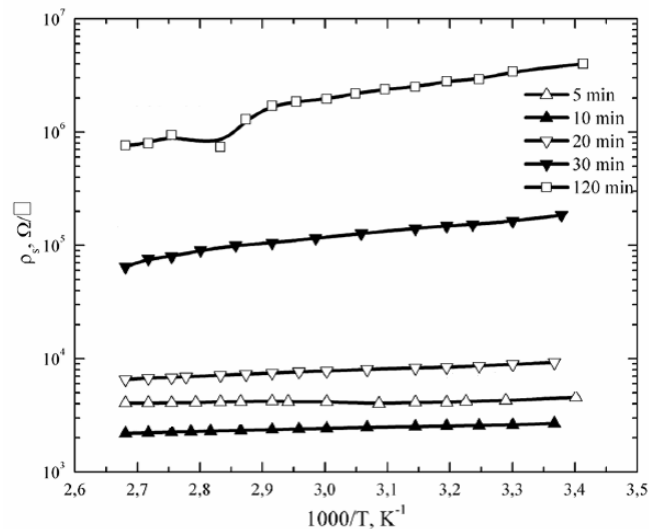


Fig. 2. The dependences of the sheet resistance versus the inverse measurement temperature for the CdS films annealed at 400 °C for individual periods of time listed in the figure

The sheet resistance decreases as the measurement temperature is increased, this agrees with semiconductor behaviour. At high temperature of annealing the concentrations of electrons presumably decreases and consequently resistivity increases.

4.2. Influence of annealing temperature on sheet resistance

To study, how annealing temperature affects sheet resistance, we prepared five samples annealed in H₂ atmosphere for 60 min at different temperatures. This duration of annealing in H₂ is average time of stabilization for annealing temperatures in the 200–400 °C range, when the resistivity of CdS films achieves minimum value [9]. Results are presented in Fig. 3.

Increase in annealing temperature accelerates the fall of sheet resistance as it shown in Fig. 3. Furthermore, the sheet resistance starts to grow significantly in films that are annealed at temperatures above 300 °C.

Lower sheet resistance annealed at temperatures below 300 °C for 60 min can be explained considering that annealing at such temperatures in H₂ atmosphere promotes improvement of the electrical contacts within via grain coalescence, removal of oxide barriers between grains and precipitates [10]. At high temperature of annealing, as it was mentioned before, the concentrations of electrons decreases, causing the resistivity to increase.

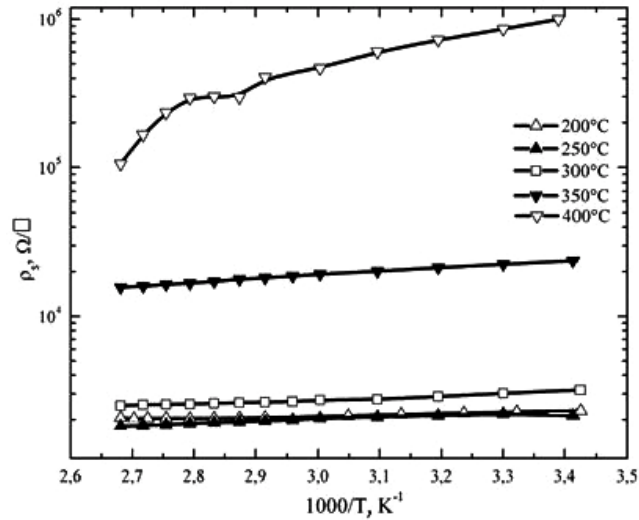


Fig. 3. The dependences of the sheet resistance versus the inverse measurement temperature for the CdS films annealed for 60 min for individual annealing temperatures listed in the figure

4.3. Influence of chlorine doping on sheet resistance

To show a role of chlorine dopant on electrical properties of CdS films we added ammonium chloride salt. Duration of annealing in H₂ was 60 min. In Fig. 4 we compared sheet resistances of CdS films with chlorine dopant (“with Cl”) and without chlorine dopant in deposition bath (“without Cl”).

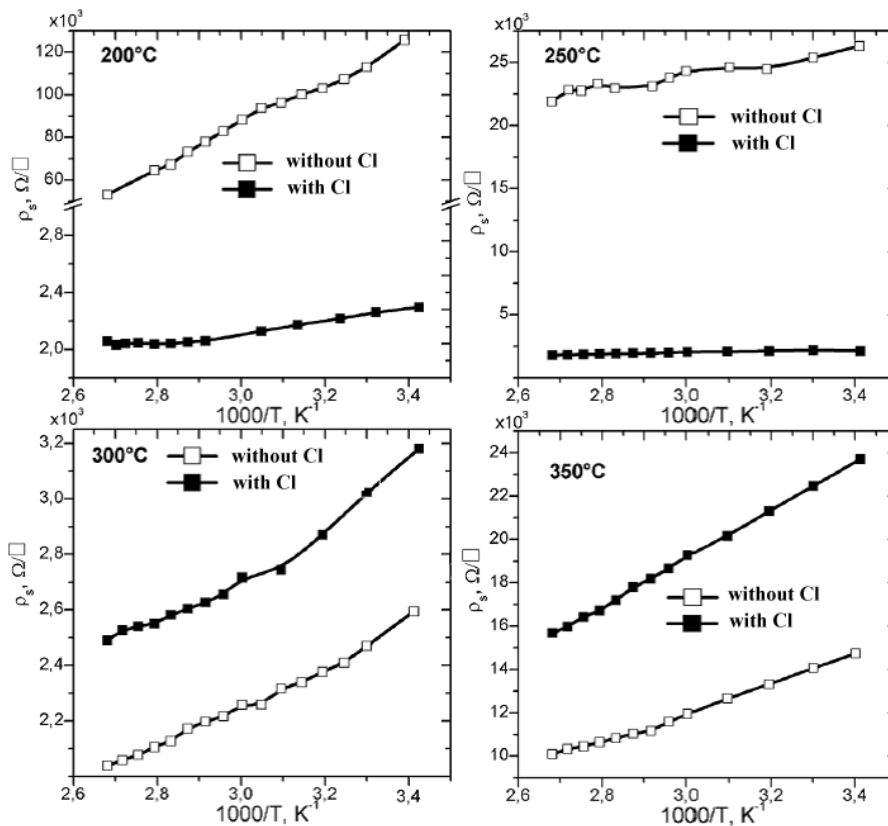


Fig. 4. Comparing of sheet resistances of CdS films as a function of the inverse of the temperature annealed in H₂ at different temperatures from 200 to 350 °C

Results of electrical measurements of CdS thin films with different [Cl]/[Cd] concentrations (Fig. 4) show that the doping of CdS affects remarkably the properties of our samples at annealing temperatures below 300 °C. At higher annealing temperatures sheet resistances vary much less for samples with and without chlorine dopant due to removal of chlorine by vaporization (detailed description in Ref. [11]).

4.4. Hall effect measurement

Hall effect measurements were impracticable for most samples, since Hall voltage V_H was unstable: voltage reading varied more than Hall voltage itself. Samples, where it was able to measure Hall voltage and thus calculate carrier concentration and mobility are presented in Table 1.

Table 1. Electrical properties of annealed CdS films

Duration of annealing, min	Temperature of annealing, °C	[Cl]/[Cd], %	Electron concentration ($\times 10^{19}$, cm^{-3})	Electron mobility ($\text{cm}^2/\text{V}\cdot\text{s}$)
60	200	1	1.50 ± 0.10	5.91 ± 0.34
60	300	1	0.68 ± 0.27	7.1 ± 2.2
60	250	1	1.22 ± 0.32	5.0 ± 1.7
60	250	0	0.98 ± 0.24	6.4 ± 1.2

Unstable Hall voltage is observed at annealing temperatures above 300 °C, which is probably connected with structural changes in CdS films like effect of grain boundaries on electron scattering. However, it is noteworthy that the absolute mobility values are in the order of $10^{-1} \text{ cm}^2/\text{V}\cdot\text{s}$ when compared to $350 \text{ cm}^2/\text{V}\cdot\text{s}$ electron mobility for single crystal CdS [12]. This three orders of magnitude reduction in electron mobility is the consequence of the nature of polycrystalline thin films. Any improvements in this parameter will contribute to increasing the electrical conductivity of CdS layers and therefore it enhances the performance of solar cells made, incorporating these CdS layers.

5. CONCLUSION

This work demonstrates some information on the dynamics of the change in the electrical properties of CdS films according to their preparation. Annealing results of CBD CdS films show that electrical properties of CdS can be controlled by annealing temperature and time in H_2 atmosphere, and by chlorine doping. The investigated thin films were found to behave as semiconductors.

From the obtained results, we can conclude that optimum annealing condition in hydrogen atmosphere is in the 200–300 °C range. These annealing temperatures give lower resistance. Chlorine doping helps also to achieve lower resistance. In the high temperature region rapid growth of resistance is observed. On the other hand, production of dense and textured polycrystalline thin films is needed.

Further work is required to perform an optimization of the post-deposition parameters in order to get the CdS film with the best properties for producing better CdS films necessary for thin film solar cell development.



6. ACKNOWLEDGEMENTS

The author would like to thank N. Maticiuc for the preparation of samples, A. Gavrilov and J. Hiie for much helpful comments and fruitful discussion of the issues this paper takes up, and V. Mikli for SEM measurements.

REFERENCES

1. MAHDI, M.A., et al. Structural and optical properties of chemical deposition CdS thin films. *Int. J. Nanoelectronics and Materials.*, 2009, Vol. 2, p. 163–172.
2. OLADEJI, I.O., et al. Comparative study of CdS thin films deposited by single, continuous, and multiple dip chemical processes. *Thin Solid Films*, 2000, Vol. 359, p. 154–159.
3. MOUALKIA, H., et al. Growth and physical properties of CdS thin films prepared by chemical bath deposition. *J. Phys. D: Appl. Phys.*, 2009, Vol. 42.
4. MATICIUC, N., HIIE, J., POTLOG, T. Influence of technological conditions on the properties of CBD CdS layers. *Proceeding of International Semiconductor Conference, CAS 1*, 2012, Sinaia (Romania), p. 187–190.
5. HAIDER, A. J. Annealing Effect on Structural, Electrical and Optical Properties of CdS Films Prepared by CBD Method. *J. of Semiconductor Technology and Science*, 2008, Vol. 8, p. 326–332.
6. L. J. VAN DER PAUW. A method of measuring the sheet resistance and Hall coefficient on Lamellae of arbitrary shape. *Philips Tech. Rev.*, 1958, Vol. 20, No. 8, p. 220–224.
7. ПАВЛОВ, Л. *Методы измерения параметров полупроводниковых материалов*. Москва: Высшая школа, 1987, 239 с. (PAVLOV, L. *Methods for Measuring Parameters of Semiconducting Materials* [in Russian]).
8. GARCIA-CUENCA, M. V. On the Hall effect in polycrystalline semiconductors, *J. Appl. Phys.*, 1985, Vol. 58 (2), p. 1080–1082.
9. MATICIUC, N., HIIE, J., POTLOG, T., VALDNA, V., GAVRILOV, A. Influence of annealing in H₂ atmosphere on the electrical properties of thin film CdS. *Mater. Res. Soc. Symp. Proc.*, 2011, Vol. 1324.
10. HIIE, J., QUINCI, F., LUGHI, V., SERGO, V., VALDNA, V., MIKLI, V., KÄRBER, E., RAADIK, E. Chlorine doping of cadmium sulfide on the example of CBD CdS. *Mater. Res. Soc. Symp. Proc.*, 2009, Vol. 1165.
11. MATICIUC, N., HIIE, J., RAADIK, T., GRAF, A., GAVRILOV, A. The role of Cl in the chemical bath on the properties of CdS thin films. *Thin Solid Films*, 2012, In Press.
12. CHAURE, N. B., et al. Investigation of electronic quality of chemical bath deposited cadmium sulphide layers used in thin film photovoltaic solar cells. *Thin Solid Films*, 2003, Vol. 437, p. 10–18.



OPTICAL AND STRUCTURAL PROPERTIES OF TiO₂ THIN FILMS BY CHEMICAL SPRAY PYROLYSIS

G. Oyekoya, I. Oja Acik, M. Krunks
Tallinn University of Technology
Ehitajate tee 5, 19086 Tallinn – Estonia

ABSTRACT

TiO₂ thin films prepared by spray pyrolysis have attracted so many interests due to its versatility and cost effectiveness. TiO₂ films have different applications such as electrodes in solar cells, photocatalyst and gas sensor devices. The aim of this study was to determine the structural and optical properties of the sprayed TiO₂ thin films as the function of the substrate and annealing temperature. In the present work TiO₂ thin films were deposited onto cleaned glass and silicon(100) substrates using chemical spray pyrolysis technique. The spray solution containing titanium (IV) isopropoxide, acetylacetone and ethanol were sprayed at substrates temperature between 260 °C to 500 °C. The thin films were deposited at a spray rate of 3 ml/minutes by employing 2 spray pulses (60 seconds spray and 60 seconds pause). The resulting TiO₂ films were later annealed at 400 °C. The TiO₂ films were characterized by FTIR, XRD and UV-VIS measurements. According to XRD and FTIR analysis, as-deposited TiO₂ films grown below 500 °C are amorphous and consist organic residues. Crystalline TiO₂ films with anatase structure could be obtained by deposition at 500 °C or by post-deposition annealing at 400 °C and above. The E_g values in the range of 3.1–3.2 eV for as deposited and 3.2–3.4 eV for annealed TiO₂ films are obtained.

Keywords: TiO₂, chemical spray pyrolysis, structural properties, optical properties, annealing

1. INTRODUCTION

Titanium is the ninth most common element in the earth's crust and it is typically thought of as being chemically inert [1]. Titanium dioxide (TiO₂) is a white solid inorganic substance that is thermally stable, non-flammable, poorly soluble, and not classified as hazardous.

TiO₂ exists naturally as minerals: anatase, rutile or brookite. The rutile and anatase forms have been intensively studied and have significant technological usefulness, owing, in large measure, to their optical properties: both are transparent in the visible and absorb in the near ultraviolet [2]. The physical properties of TiO₂ make it suitable for thin film applications, because of their good transmittance in the visible region, high refractive index and chemical stability. In fact, over 96% of the worldwide use of titanium is in the oxide form, TiO₂ (titanium dioxide), thus creating a high demand. They are used very often as single -layer or multi layer optical coatings [3]. The high dielectric constant ϵ of TiO₂ (the largest ϵ among simple metal oxides) opens prospects for the use of TiO₂ thin films in microelectronic devices [5, 6], e.g in capacitors or as a gate dielectric in metal-dielectric-semiconductor devices. TiO₂ films have also been suggested as photoanodes in the process of photo-electrolysis of water (in solar energy conversion systems) [7], photocatalysis [8] and as a window layer in photovoltaic solar cells; e.g. so called Grätzel cell [9] and eta-solar cell [10]. TiO₂ is used also as a gas sensor [11], geo-material [12] and promoter in catalytic reactions [13].

However, the characteristics of TiO₂ films are strongly dependent on the preparation methods and the deposition parameters. TiO₂ films have been prepared by many technologies, including chemical bath deposition (CBD) [14, 15], electron-beam evaporation [16], reactive electron beam evaporation [17], magnetron sputtering [18, 19], sol-gel [20, 21–25] and thermal oxidation [26, 27].

The sol-gel technique has emerged as one of the most promising techniques. This method produces samples with good homogeneity and simplicity at low cost [28]. The term sol-gel refers to a process in which solid nanoparticles dispersed in a liquid (a sol) agglomerate together to form a continuous three-dimensional network extending throughout the liquid (a gel) [29]. The sol-gel

processing are particularly efficient in producing thin, transparent, multi-component oxide layers of many compositions on various substrates, including glass [30].

However, one of the deposition techniques of TiO₂ thin films is Chemical Spray Pyrolysis which involves a simple technology in which an ionic solution (containing the constituent elements of a compound in the form of soluble salts) is sprayed over preheated substrates with the help of carrier gas. In all spray processes, the significant variables are: ambient atmosphere, solution flow rate, nozzle-to-substrate distance, droplet size, solution concentration and quantity, carrier gas and its flow rate, substrate temperature, substrate motion, etc. [31–33].

In the present study, the spray pyrolysis technique was used to prepare thin films of TiO₂ because the technique is simple and involves low-cost equipments and raw materials.

Moreover, the deposition rate and the thickness of the films can be easily controlled over a wide range by changing the spray parameter [34]. According to literature, TiO₂ films have been deposited by spray pyrolysis usually from alcohol based precursor solution (Ethanol, methanol, 2-propanol, 2-butanol) [35, 36–44] although occasionally aqueous hydrogen peroxide solutions have been employed as well [45–47]. Commonly used Ti-sources for TiO₂ film preparation by spray pyrolysis are Tiacac [35, 36, 39, 41] as well as TiCl₃ [42], TiCl₄ [43], Titanium (IV) isopropoxide (TTIP) [37, 40, 44, 45] and Ti metal powder [47, 48].

Spray pyrolysis deposition have been performed at substrate temperatures between 200 °C and 500 °C followed by annealing at higher temperatures (600 up to 950 °C) to promote the formation of desired crystalline phase. Crystalline TiO₂-anatase films have been obtained in the substrate temperature range of 300–500 °C [35, 36–40, 43–47], where as the formation of crystalline TiO₂-rutile phase takes place after further annealing around 800 °C [36, 37, 45].

The aim of the study is to investigate and present the original results on the optical properties of sprayed TiO₂ films using UV-Visible Spectrophotometer. These results are complemented with the review of the structural and morphological study of sprayed TiO₂ films.

2. EXPERIMENTAL

The precursor solution contains titanium (IV) isopropoxide (TTIP) as a titanium source, acetylacetone (AcAc) as a stabilizer and ethanol as a solvent was prepared using AR grade materials from Fluka. TTIP concentration of 6 vol.% and TTIP: AcAc molar ratio of 1:2 was used as starting solutions. The solution was atomized by a pneumatic spray system using compressed air as the carrier gas, the flow rates used were 3 ml/min. Cleaned glass and silicon (100) were used as substrates and the films were deposited using a pulsed solution feed at substrate temperatures (T_s) in the range 260 to 500 °C. The pulse used for deposition consisted of 1 min spray time and 1 min pause with the number of spray pulses ranges from 2 to 3. After the deposition, all the thin films were annealed at 400 °C for 1h or at 500 °C for 30 min.

XRD patterns were recorded by a Bruker AXS D5005 diffractometer. FTIR transmittance spectra of the films on Si(100) wafers in the spectra region of 4000–400 cm⁻¹ on a Perkin Elmer GX-1 spectrometer.

The optical transmission spectra of the films were measured in the wavelength range of 200–2500 nm on a JASCO UV-Visible Spectrophotometer and optical band gaps were calculated. The surface morphology of the films was characterised by AFM, carried out on an NT-MDT Solver 47 Pro system in the non-contact tapping mode with a resolution in the range of 3 nm. The sample was studied in 2 μm × 2 μm area scans. The surface morphology of the sample was analysed through 2D and 3D AFM scans and roughness analysis. The surface roughness analysis was performed according to the ISO 4287/1 standard. The root mean square (RMS) roughness was calculated over the scanned surface area (2 μm × 2 μm) with an accuracy of ±0.1 nm [48].

3. RESULTS AND DISCUSSION

3.1. UV-VIS Studies

The total transmittance spectra of the as-deposited TiO₂ films grown at temperatures of 260, 300, 400 and 500 °C and of these films after annealing at 400 °C for 1 hour are shown in Figures 1 and 2, respectively.

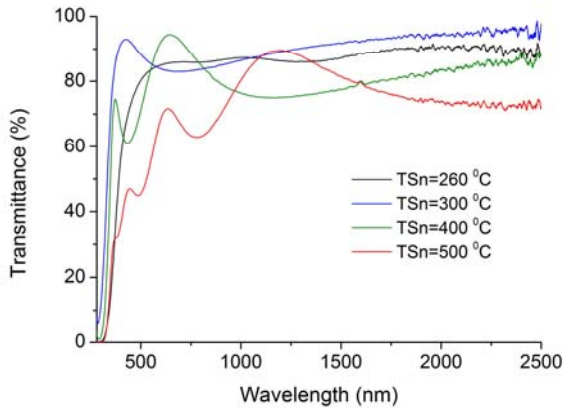


Fig. 1. Total transmittance spectra of the as-deposited TiO₂ films on glass substrate deposited at 260, 300, 400 and 500 °C

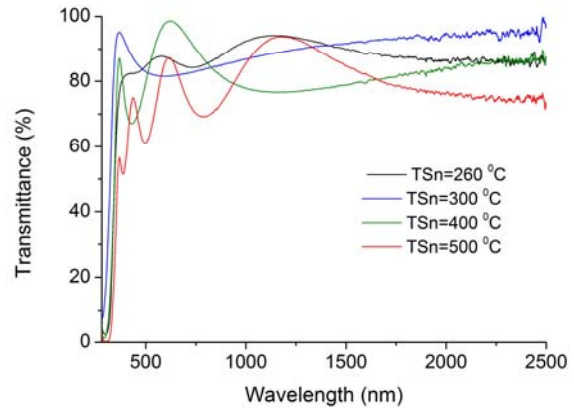


Fig. 2. Total transmittance spectra of the TiO₂ films on glass substrate deposited at 260, 300, 400 and 500 °C and annealed at 400 °C

The TiO₂ films grown at 260 °C, 300 °C and 400 °C exhibit total transmittance above 80% in visible and near-infrared spectral region (Fig. 1 and 2). The film grown at 500 °C has lower total transmittance in this spectral region. The annealing at 400 °C has no big effect on the total transmittance spectra of TiO₂ films. According to the optical transmittance spectra (Fig. 1 and 2), the number of interference fringes is lower for the films deposited at temperatures below 400 °C than for the film deposited at 500 °C. This indicates that the films deposited below 400 °C are thinner compared to the film deposited at 500 °C.

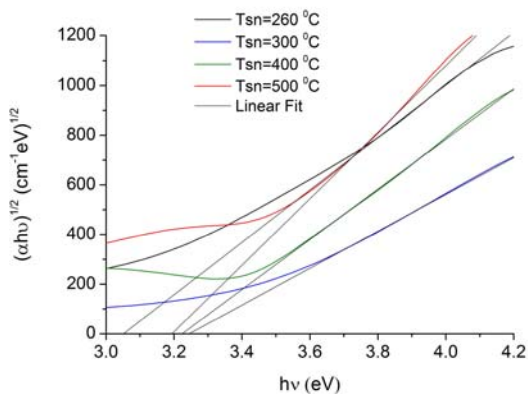


Fig. 3. Plot of $(\alpha h\nu)^{1/2}$ against $h\nu$, of the as-deposited TiO₂ thin films deposited at 260, 300, 400 and 500 °C for indirect band gap evaluation

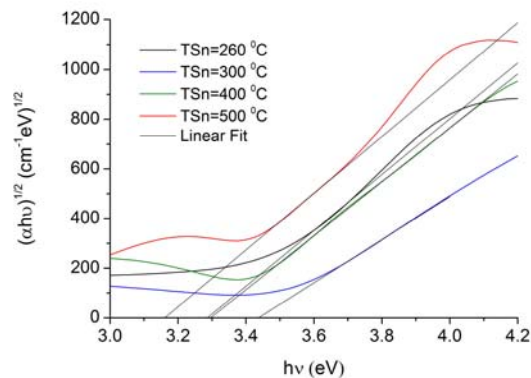


Fig. 4. Plot of $(\alpha h\nu)^{1/2}$ against $h\nu$, TiO₂ thin films deposited at 260, 300, 400 and 500 °C and annealed at 400 °C for indirect band gap evaluation

The absorption coefficient and the optical band gap (E_g) values were determined from the total transmittance data. The theory of inter band optical absorption shows that the absorption edge, the optical absorption coefficient (α) varies with the photon energy ($h\nu$) according to the equation 1,

$$(\alpha h\nu)^n = A (h\nu - E_g), \quad (1)$$

where A and E_g are constant and the band gap energy, respectively and n is a number which characterizes the transition process. The term takes the value 2 for a directly allowed transition and $\frac{1}{2}$ for an indirectly allowed transition. A method for determining E_g involves plotting $(\alpha h\nu)^n$ against photon energy $h\nu$. The E_g values for indirect transition were obtained by the extrapolation of the plot of $(\alpha h\nu)^{1/2}$ against $h\nu$ from the spectral data. According to the literature, TiO_2 has indirect band gap [52]. Thus, the plot of $(\alpha h\nu)^{1/2}$ versus $h\nu$ is created as shown in Fig. 3 and 4. The indirect band gap values of as-deposited TiO_2 films are in the range of 3.2–3.2 eV. E_g values of TiO_2 films deposited at 260–400 °C and annealed at 400 °C are in the range of 3.3–3.4 eV. However, the TiO_2 film deposited at 500 °C and annealed at 400 °C exhibit E_g value of 3.2 eV. The results coincide with the results published in literature, where E_g values of 3.3 and 3.4 eV have been reported for sprayed TiO_2 films deposited in the temperature range of 350–500 °C [52].

3.2. FTIR Spectroscopy study

IR-spectra of the as-deposited TiO_2 films prepared at different substrate temperatures and the film annealed at 500 °C are given in Fig. 5. Strong absorption in the frequency region of 400–1000 cm^{-1} corresponds to Ti-O-Ti bonding and indicates the formation of a titanium oxide network [49]. As the deposition temperature is increased the absorption band with the maximum close to 440 cm^{-1} , characteristic for TiO_2 anatase state also increases. The absorption at 1545, 1452 and 1415 cm^{-1} , recorded for the films prepared at temperatures of 300–435 °C, could belong to asymmetrical and symmetrical vibration of M-O-C groups [49, 50] and CH_2 or CH_3 groups, respectively [51]. The absence of above-mentioned absorptions at substrate temperature of 500 °C indicates that relatively pure films could be already exist at this temperature (Fig. 5). Annealing at 500 °C leads to significant sharpening of absorption bands in the region of 600–400 cm^{-1} and clearly indicates the formation of anatase phase, independent of substrate temperature.

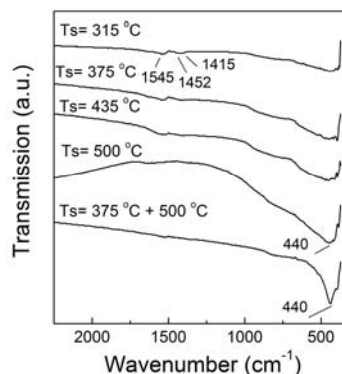


Fig. 5. FTIR spectra of as-deposited TiO_2 films and annealed TiO_2 film at 500°C. The TiO_2 films were deposited on Si- substrate [53]

3.3. X-Ray Diffraction study

XRD showed the as-deposited films prepared at substrate temperatures below 500 °C are amorphous. The (101) peak of anatase (PDF 21-1272) becomes apparent for the films deposited at 500 °C (Fig. 6). Annealing at 500 °C results in anatase phase regardless of the deposition temperature as the clearly detected (101) and (200) peaks of anatase in XRD patterns confirm.

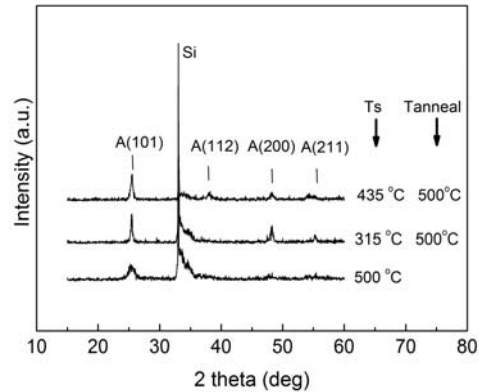


Fig. 6. XRD patterns of as-deposited and annealed TiO₂ films. The TiO₂ films were deposited on Si- substrate [53]

3.4. AFM study

The surface morphology of the TiO₂ films was characterised by AFM 3D images acquired over a 2 μm × 2 μm area (Fig. 7). The TiO₂ film shows agglomerated grains with diameters of ca. 30–200 nm. The calculated root-mean-square roughness of the TiO₂ film deposited at 450 °C and annealed at 500 °C is 1.65 nm [48]. TiO₂ films grown at higher temperatures exhibit a higher rms roughness values. For example, rms roughness of 2.6 nm have been reported for TiO₂ film deposited at 375 °C and annealed at 700 °C [53].

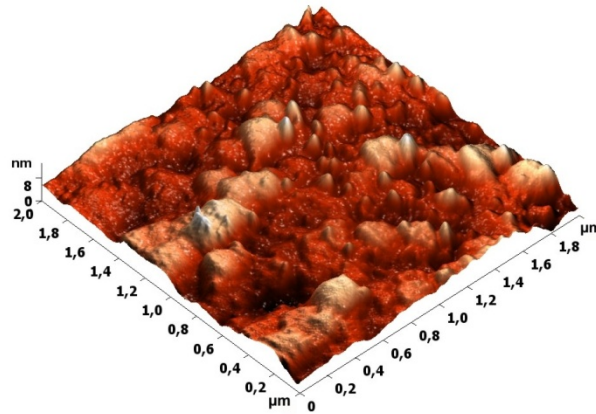


Fig. 7. AFM micrograph of the TiO₂ film on glass substrate deposited at 450 °C and annealed at 500 °C [48]

CONCLUSIONS

In this study, TiO₂ were prepared by chemical spray pyrolysis technique. The E_g values in the range of 3.1–3.2 eV for as-deposited and 3.2–3.4 eV for annealed TiO₂ films are obtained. According to FTIR study, TiO₂ films deposited up to 435 °C contain organic residues. The films deposited or annealed at 500 °C are free from contaminants. As deposited TiO₂ films grown at temperatures below 500 °C are amorphous according to XRD. The deposition or annealing at 500 °C results in crystalline TiO₂ films with anatase structure. TiO₂ film deposited at 450 °C and annealed at 500 °C is relatively smooth, exhibiting a rms roughness of 1.65 nm. In conclusion, as it can be seen from optical results that there are more fringes(interferences) when the samples were annealed. Meanwhile fringes sometimes may be due to the presence of undesired surfaces with



undesired structures [54]. However, it is discovered that, annealed TiO₂ films has higher transmittances but with no big difference than as-deposited TiO₂ films.

ACKNOWLEDGEMENTS

This study was financially supported by the Estonian Ministry of Education and Research under target financing project SF0140092s08, the Estonian Science Foundation under grants ETF7788, ETF9081, ETF8509, TUT base financing project B24 and by the European Union through the European Regional Development Fund (Projects: 3.2.0101.11-0029 and 3.2.1101.12-0023). The authors thank Dr. Valdek Mikli for AFM measurements and analysis.

REFERENCES

1. Titanium Dioxide Stewardship Council, About Titanium dioxide, March 2012. <www.photocatalysis-federation.eu.>
2. ZALLEM R.; MORET M.P.; Solid State Communications 137, 154 (2006).
3. <<http://cleanair.bz/otheruses.html>.> Date viewed 25/02/2013.
4. MACLOED H.A. Thin-Film Optical Filters, 2nd ed., Adam Hilger Ltd., Bristol, 1986, p.71.
5. WALLACE, R. M. Appl. Surf. Sci. 231–232 (2004), p. 543–551.
6. CAMPBELL, S.A., KIM, H.S., GILMER, D.C., B. HE, B., MA, T. Res. Develop. 1999, Vol. 43, p. 383–392.
7. MOR, G. K.; VARGHESE, O. K.; PAULOSE, M.; SHAKAR, K.; GRIMES, C. A. Sol. Energ. Mater. Sol. Cell. 2006, Vol. 90, p. 2011–2075.
8. CARP, O., HUISMAN, C.L., RELLER, A. Progr. Solid State Chem. 2004, Vol. 32, p. 33–177.
9. O'REGAN, B. GRATZEL, M.; Nature 353, (1991), p. 737–740.
10. KAISIER, I.; ERNST, K.; FISCHER, Ch.-H.; KONENKAMP, R.; ROST, C.; SIEBER, I.; LUX-STEINER, M.Ch.; Sol. Energy Mater. Sol. Cell.2001, Vol. 67, p. 89–96.
11. MOSELEY, P.T.; Meas. Sci. Technol. 1997, No. 8, p. 223–237.
12. JONES, F.H. Surf. Sci. Rep. 2001, Vol. 42, p. 75–205.
13. HADJIIVANOV, K.J.; KISSURSKI, D.G.; Chem. Soc. Rev, 1996, Vol. 25, p. 61–69.
14. MORE, A.M.; GUJAR, T.P.; GUNJAKAR, J. L.; LOKHANDE, C. D.; JOO, O. S. Growth of TiO₂ nanorods by chemical bath deposition method: Applied Surface Science. 2008, Vol. 255, No. 5, p. 2682–2687.
15. ZHU, H.; YANG, J.; FENG, S.; LIU, M.; ZHANG, J.; and LI, G. Growth of TiO₂ nanosheet-array thin films by quick chemical bath deposition for dye-sensitized solar cells, Applied Physics A, 2011, Vol. 105, p. 769–774.
16. YAO, J.K.H.Y. Li, Z.X. Fan et al. Comparison of TiO₂ and ZrO₂ films deposited by electron-beam evaporation and by sol-gel process. Chinese Physics Letters, 2007, Vol. 24, No. 7, Article 049, p. 1964–1966.
17. DUYAR, Ö., PLACIDO, F., ZAFER Durusoy, H. Optimization of TiO₂ films prepared by reactive electron beam evaporation of Ti₃O₅. Journal of Physics, D, 2008, Vol. 41, No. 9, Article ID 095307.
18. COJOCARU, B., NEATU, Ş., Neaţu, SACALIUC-PARVULESCU, E., LEVY, F., PARVULESCU, V.I., GARCIA, H. Influence of gold particle size on the photocatalytic activity for acetone oxidation of Au/TiO₂ catalysts prepared by dc-magnetron sputtering. Applied Catalysis B, 2011, Vol. 107, p. 140–149.



19. D.Y. Chen, C.C. Tsao, and C.Y. Hsu, “Photocatalytic TiO₂ thin films deposited on flexible substrates by radio frequency (RF) reactive magnetron sputtering. *Current Applied Physics*, 2012, Vol. 12, p. 179–183.
20. FARBOD, M., KHADEMALRASOOL, M. Synthesis of TiO₂ nanoparticles by a combined sol-gel ball milling method and investigation of nanoparticles size effect on their photocatalytic activities. *Power Technology*, 2011, Vol. 214, p. 344–348.
21. YU, J.C., HO, W., YU, J., HARK, S.K., IU, K. Effects of trifluoroacetic acid modifications on the surface microstructures and photocatalytic activity of mesoporous TiO₂ thin films. *Langmuir*, 2003, Vol. 19, No. 9, p. 3889–3896.
22. ZHAN, S., CHEN, D., JIAO, X., TAO, C. Long TiO₂ hollow fibers with mesoporous walls: sol-gel combined electrospun fabrication and photocatalytic properties. *Journal of Physical Chemistry B*, 2006, Vol. 110, No. 23, p. 11199–11204.
23. ZHU, J., CHEN, F., ZHANG, J., CHEN, H., ANPO, M. Fe³⁺-TiO₂ photocatalysts prepared by combining sol-gel method with hydrothermal treatment and their characterization. *Journal of Photochemistry and Photobiology A*, 2006, Vol. 180, No. 1–2, p. 196–204.
24. ARCONADA, N.; DURAN, A.; SUAREZ et al. Synthesis and photocatalytic properties of dense and porous TiO₂-anatase thin films prepared by sol-gel. *Applied Catalysis*, 2009, Vol. 86, No. 1–2, p. 1–7.
25. LUO, Z., CAI, H., REN, X.; LIU, J.; HONG, W.; ZHANG, P. Hydrophilicity of titanium oxide coatings with the addition of silica. *Materials Science and Engineering B*, 2007, Vol. 2, No. 138, p. 151–156.
26. FALCONER, J.L. Falconer and K.A. Magrini-Bair, “Photocatalytic and thermal catalytic oxidation of Acetaldehyde on Pt/TiO₂. *Journal of Catalysis*, 1998, Vol. 179, No. 1, p. 171–178.
27. ZHANG, J., PAN, C., FANG, P., WEI, J., XIONG, R. Mo + C codoped TiO₂ using thermal oxidation for enhancing photocatalytic activity. *ACS Applied Materials and Interfaces*, 2010, Vol. 2, No. 4, p. 1173–1176.
28. KUMAR, M.; KUMAR, M.; KUMAR, D. The deposition of nanocrystalline TiO₂ thin film on silicon using sol gel technique and its characterization,” *Microelectronics Engineering*, March 2010, Vol. 87, p. 447–450, Elsevier Publications.
29. <http://www.aerogel.org/?p=992>. Date viewed:23/02/2013.
30. BRINKER, M.; HARRINGTON, S. *Solid Energy Mater. S*, 1981, p 159.
31. PATIL, P.S.; *Mater. Chem. Phys.* 59 (1999) 185-198.
32. MOONEY, J.B.; RADDING, S.B.; *Annu. Rev. Mater. Sci*, 1982, Vol. 12, p. 81–101.
33. KIJATKINA, O. Deposition of Copper Indium Disulphide Films by Chemical Spray Pyrolysis. 2004.
34. PATIL, G.E.; KAJALE, D.D.; CHAVAN, D.N. Synthesis, characterization and gas sensing performance of SnO₂ thin films prepared by spray pyrolysis, *Bulletin of Materials Science*, 2011, Vol. 34, No. 1, p. 1–9.
35. DESHMUKH, H.P.; SHINDE, P.S.; PATIL, P.S. *Mater. Sci. Eng. B*, 2006, 130, p. 220-227.
36. CASTANEDA, L.; ALONSO, J.C.; ORTIZ, A.; ANDRADE, E., SANIGER, J.M.; BANUELOS, J.G. *Mater. Chem. Phys.* 2002, Vol. 77, p. 38–944.
37. CONDE-GALLARDO, A.; GUERRERO, M.; CASTILLO, N., SOTO, A.B.; FRAGOSO, R.; CABANAS-SOLID Moreno J.G. *Thin Films*, 2005, Vol. 473, p. 68–73.
38. ABOU-HELAL, M.O.; SEEBER, W.T. *Appl. Surf. Sci.*, 2002, Vol. 195, p. 53–62.
39. MARTINEZ, A.I.; ACOSTA, D.R.; LOPEZ, A. A. *J. phys. Condens. Matter*, 2004, Vol. 16, p. S2335–S2334.
40. C.H. Chen, E.M. Kelder, J. Schoonman, *thin Solid Films*, 1999, Vol. 342 (1999), p. 35–41.



41. OKUYA, M.; SHIOZAKI, K.; HORIKAWA, N.; KOSUGI, T.; ASOKA KUMURA, G.R.; MADARASZ, J.; KANEKO, S.; POKOL, S. *Solid State Ionics*, 2004, Vol. 172, p. 572–531.
42. MORE, A.M.; GUNJKAR, J.L.; LOKHANDE, C.D.; MANE, R.S.; HAN, S-H. *Micron* 2007.
43. OKUYA, M.; PROKUDINA, N.A.; MUSHIKA, K.; KANEKO, S. *J. Eur. Ceram. Soc.*, 1999, Vol. 19, p. 903–906.
44. KAVAN, L.; GRATZEL, M. *Electrochim. Acta*, 1995, Vol. 40, p. 643–652.
45. GOLEGO, N.; STUDENIKIN, S.A.; COCIVERA.M. *J. Mater. Res*, 1999, Vol. 14, p. 698–707.
46. ROGERS, K.D; LANE, D.W.; PAINTER, J.D.; CAHPMAN, A. *Thin Solid Films*, 2004, Vol. 466, p. 97–102.
47. NATARAJAN, C., FUKUNAGA, N., NOGAMI, G. *Thin Solid Films*, 1998, 322, p. 6–8.
48. ACIK, Oja I., KIISK, V., KRUNKS, M., SILDOS, I., JUNOLAINEN, A., DANILSON, M., MERE, A., MIKLI, V. *Applied Surface Science*, 2012, Vol. 261, p. 732–741.
49. BURGOS, M., LANGLET, M. *Thin Solid Films*, 1999, Vol. 349, p. 19.
50. HARIZANOV, O., HARIZANOVA, A. *Sol. Energy Mat. And Solar Cells*, 2000, Vol. 63, p. 185.
51. DJAOUED, Y., TAJ, R., BRUNING, R., BADILESCU, S., ASHRIT, P.V., BADER, G., VO-VAN, T.J. *Non- Cryst. Solids*, 2002, Vol. 297 (2002), p. 55.
52. RAUTA, N.C., TOM MATTEWS, A., CHANDRAMOHANB, P., SRINIVASANB, M.P.B, DASHA, S., TYANGI, A.K. Effect of temperature on the growth of TiO₂ thin films synthesized by spray pyrolysis. *Materials Research Bulletin*, 2011, Vol. 46, p. 2057–2063.
53. Oja, I., MERE, A., KRUNKS, M., SOLTERBECK, C-H., C-H., SOUNI, Es. M. Properties of TiO₂ films prepared by the spray pyrolysis method, *Solid State Phenom*, 2004, Vol. 99–100, p. 259–262.
54. LU TAIJING, TOMOYA OGAWA, KOICHI TOYODA and ZHENGUO WANG. Effect of surface structures upon ultrathin film interference fringes. *Journal of Materials Research*. *Journal of Materials Research Volume 8, Issue 09, 1993, p. 2315–2318.*



ELECTROPHYSICAL PROPERTIES OF THE ZnTe/CdTe THIN FILM HETEROSTRUCTURES

D. Scortescu, A. Mirzac, N. Spalatu and T. Potlog
Moldova State University
A. Mateevici str. 60, MD 2009 Chisinau – Moldova

V. Mikli
Tallinn University of Technology
Ehitajate tee 5, 19086 Tallinn – Estonia

ABSTRACT

Current–voltage characteristics at different temperatures and capacity-voltage characteristics of ZnTe/CdTe thin film heterostructures have been investigated. ZnTe/CdTe thin film heterostructures were obtained by close space sublimation method. The current-voltage and capacity-voltage analysis indicates to existence of a high resistive layer at the interface of ZnTe/CdTe. It has revealed that direct current–voltage characteristics of such structures are described by exponential dependence at small voltage (to 0.4 V) and then, at greater voltage (to 0.8 V) they have sublinear behaviour. From the capacity-voltage analysis, width of the layer has been estimated. These experimental results have been explained on the basis of the theory of injection depletion. The dependence, probably, is related to the injection-depletion effect taking place when diffusion current of the injected carriers is directed contrary to the drift current. Such a result has been obtained in wide range of temperature and it is the evidence of drift-diffusion model of the current transport.

Keywords: ZnTe/CdTe thin film heterostructures; Depletion layer, Drift-diffusion transport model

1. INTRODUCTION

As CdTe has a near optimal band gap (1.45 eV) for solar absorption, may be doped *n*- or *p*-type and has high (direct) optical absorption above the band gap ($\sim 10^4 \text{ cm}^{-1}$), it was recognized early on as a good solar cell absorber layer [1]. Recently, one of the most perspective heterojunction used for photovoltaic solar energy conversion is CdS/CdTe. The maximum experimental efficiency for CdS/CdTe-based solar cells is 16.5% [2]. Another material of $A_{II}B_{VI}$ compounds which can be used as a substrate for the growth of CdTe is ZnTe. Zinc telluride has a direct bandgap of 2.26 eV at room temperature and can be used for the fabrication of the heterostructures ZnTe/CdTe [3]. The theoretical limit for the solar energy conversion efficiency is relatively high – it exceeds 20%. Because of these reasons the *p*-ZnTe/*n*-CdTe heterojunctions (HJ) are interesting candidates for solar applications [4]. The current–voltage measurements permit to study the transport mechanism in the heterostructure, the basic physical parameters and junction features. The gained information is essential for understanding the photovoltaic loss mechanism, thus to improve the PV-device performance to get higher efficiencies.

1. EXPERIMENTAL DETAILS

The close spaced sublimation (CSS) method is considered one of the most promising techniques for A_2B_6 thin film deposition. We prepared two sets of glass/SnO₂/ZnTe/CdTe and glass/SnO₂/ZnTe(ZnCl₂ activated)/CdTe samples by the CSS technique. In our previous work [5], the optimal growth conditions for CdTe for high-performance CdS/CdTe solar cells were $T_s = 340 \text{ }^\circ\text{C}$ substrate temperature and $T_{ev} = 590 \text{ }^\circ\text{C}$ evaporator temperature. This technological regime was also used for the preparation of both type of ZnTe/CdTe heterosystems. The ZnTe layers were deposited at $T_s = 450 \text{ }^\circ\text{C}$ and $T_{ev} = 760 \text{ }^\circ\text{C}$. Also, the cleaned glass slides (for XRD study)

were used as substrates for the deposition of ZnTe films in order to adjust optimal condition for ZnCl₂ activation and thickness for obtaining solar cells with higher performance. The ZnCl₂ was applied to the surface of the ZnTe/SnO₂/glass structures by dipping in a water/ZnCl₂ solution. The sheet resistance of as-grown ZnTe thin films is higher than 10⁹ Ω. The investigation of the sheet resistance with ZnCl₂ concentration showed that resistance of ZnTe decreases till ~10⁶ Ω at 35 Wt % ZnCl₂ concentrations. The upper CdTe thin films were deposited directly on polycrystalline sublayers of glass/SnO₂/ZnTe substrates and then a thin layer of indium was deposited by thermal evaporation and treated in vacuum for 40 min at 300 °C. SnO₂ served as ohmic contact for ZnTe. An In contact was obtained by thermal evaporation on the CdTe.

The morphology of the surface and cross section were studied using a scanning electron microscope. The optical transmission spectra were recorded using a JASCO V-670 spectrophotometer. The study of the current – voltage characteristics of solar cells was carried out according to standard methods.

2. ZnTe THIN FILMS

It is known [6–7], that the charge-transport mechanism through HJ is determined by the interface quality of semiconductor materials. With increase of the quantity of surface defects on the interface the change of a charge-transport mechanism through HJ occurs. Therefore we present the morphology of ZnTe thin films from the viewpoint that in manufacturing of the ZnTe/CdTe heterojunctions ZnTe high quality with large grains was used. Fig. 1 (a) and (b) compare the morphology of ZnTe films deposited on glass and SnO₂/glass substrates. One can see that all the ZnTe films consist of crystallites with different sizes. The SEM micrograph shows the surface without any pinholes when are deposited on SnO₂/glass substrate.

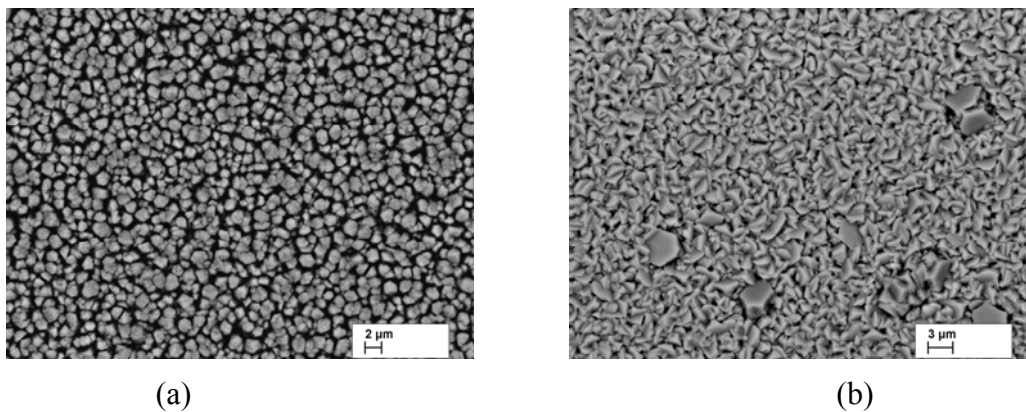


Fig. 1 SEM image of ZnTe thin films deposited on glass (a) and SnO₂/glass (b) substrates

The EDS analysis shows that both, those as-deposited ZnTe thin films and those chlorides activated are Zn-deficient. The chemical composition analysis shown in Fig. 2 revealed the presence of only Zn and Te elements in ZnTe films before ZnCl₂ activation. After ZnCl₂ activation ZnTe films contains Cl impurity at the sensitivity level of the EDS system and have more homogeneous grain structure and larger grains. But an average grain size for them is less than for CdTe films.

The optical transmission spectra of as-grown at 450 °C substrate temperature and ZnCl₂ activated ZnTe thin films were measured in the range of 400–1000 nm and shown in Fig. 3. The transmittance of the layers varies between 60%–70%, maximum of 70% being reached for non activated ZnTe layer. The transmission slightly decreases for the activated ZnTe film. One obvious result from the $(\alpha hv)^2 = f(hv)$ dependence (Fig. 4) for ZnCl₂ activated ZnTe films is that the energy gap decreases from 2.248 eV to 2.224 eV.

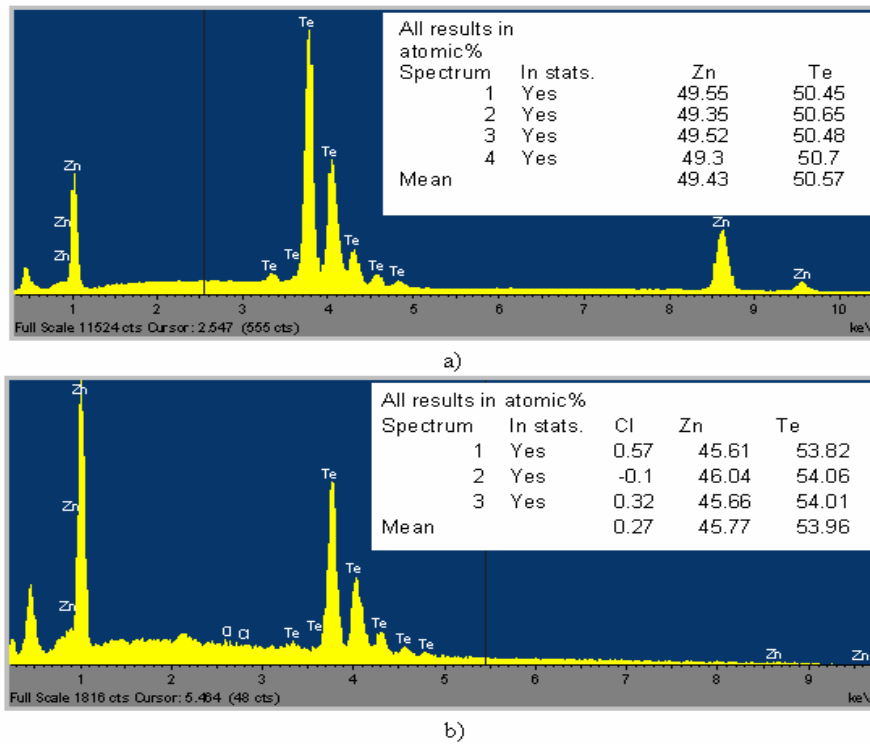


Fig. 2. Chemical composition of the as-grown (a) and ZnCl₂ activated ZnTe thin films (b)

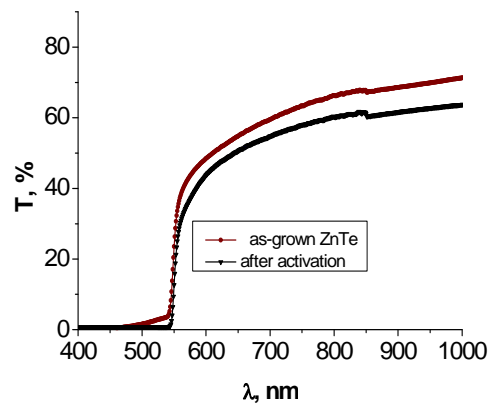


Fig. 3. The transmission spectra of as-grown and ZnCl₂ activated ZnTe thin films

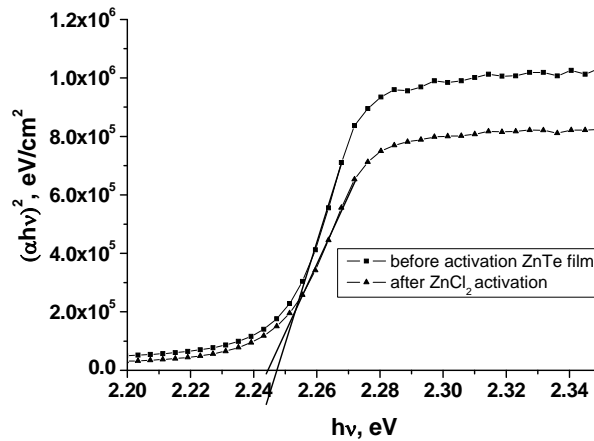


Fig. 4. The α^2 vs. photon energy ($h\nu$) spectra of as-grown and ZnCl_2 activated ZnTe thin film

3. PHOTOVOLTAIC CHARACTERISTICS AND PARAMETERS OF ZnTe/CdTe THIN FILMS HJs

The photovoltaic characteristics of ZnTe/CdTe thin film HJs were investigated through the wide band gap components at the room temperature (300 K) and 100 mW/cm^2 illumination.

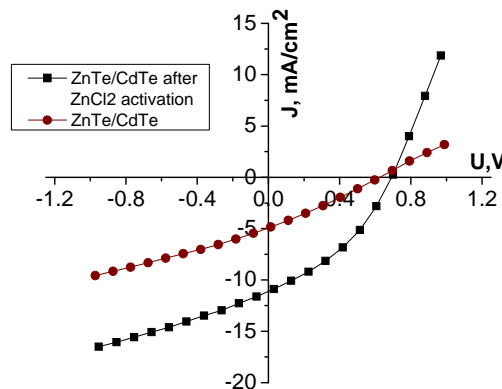


Fig. 5. Current-voltage characteristics of the ZnTe/CdTe thin film HJs under AM1.5 condition

Table 1. Photovoltaic parameters of ZnTe/CdTe solar cells

ZnTe/CdTe	J_{sc} , mA/cm^2	U_{oc} , V	FF	η , %	R_{sh} , $\Omega \cdot \text{cm}^2$	R_s , $\Omega \cdot \text{cm}^2$
Before ZnTe activation	7.8	0.61	0.18	0.86	172	98
After ZnCl_2 activation	12.03	0.64	0.36	2.81	91	20

The best photovoltaic parameters for ZnTe/CdTe solar cells were achieved for with ZnTe chlorine activated. As one can see from Table 1 the value of the open circuit voltage (U_{oc}) and the current density (J_{sc}) achieve 0.64 V and 12.03 mA/cm^2 , respectively. The ZnTe/CdTe solar cells

with efficiency (η) of $\sim 3\%$ were obtained. The fill factor (FF) is low in general. As one can see from the table, the low value of FF is mainly determined by the high value of the series resistance which is due to the high resistivity of components. The achievement of high efficiency solar cells requires the understanding of the junction current mechanism transport. Since the investigated thin film heterostructures are intended to work as solar cells, the temperature dependence of the current-voltage and the capacitance-voltage characteristic measurements were carried out.

4. TRANSPORT MECHANISMS IN THE ZnTe/CdTe THIN FILMS HJs

The I-U-T measurements were performed in dark in (100–300) K interval. Fig. 6 shows the current-voltage ($I = f(U)$) characteristics of the ZnTe/CdTe thin films HJs with ZnSe chloride activated. It can be seen that in forward direction current increases exponentially with the bias voltage. In the temperature range studied, two different slopes at low and high bias can be observed. I-U characteristics of a p-n junction at low bias can be described by the expression [8]

$$I = I_s \left(\exp \frac{eU}{nkT} - 1 \right), \quad (1)$$

where I_s is the device saturation current, n the ideality factor, k the Boltzmann constant and T the temperature. In order to extract the diode parameters we have plotted a semi-logarithmic I-U plot (Fig. 7). The ideality factor is determined by the dominant current transport mechanism. The ideality factor n equals 2 when generation and recombination of electron-hole pairs in the junction depletion region dominates and n equals 1 when the diffusion current dominates [8].

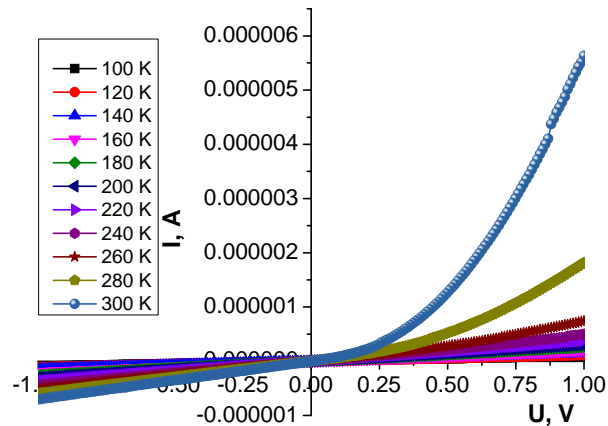


Fig. 6. Current-voltage characteristics of the ZnTe/CdTe thin film HJs with ZnSe chloride activated at different measurement temperatures

The values of n and I_s are evaluated from I-U plots by fitting the data to Eq. (1). In order to identify the dominant dark current transport mechanism, the I-U characteristics were examined using various conduction models. The values of ideality factor lie between 1.1 at 300 K and 2.9 at 100 K. The values of n lying between 1 and 2 suggest that the current is due to recombination within the depletion region [8].

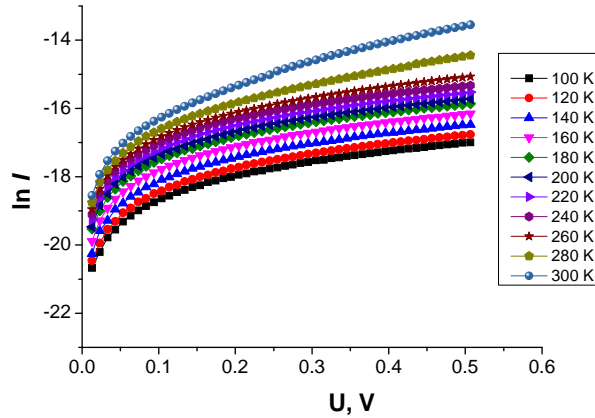


Fig. 7. Dependence $\ln I_d = f(U_d)$ at different temperatures of the ZnTe/CdTe thin films HJs

A plot of $\ln(I_s)$ versus $1/T$ is shown in Fig. 8. The activation energy determined from such a plot should be equal to approximately half the band gap if the current is controlled by the generation-recombination in the depletion region and it should be close to the band gap if the current is controlled by diffusion. The saturation current I_s , obtained by extrapolating the forward current curves $\ln I = f(U)$ to zero voltage is found to vary exponentially with $\frac{1}{T}$ in (100–300) K temperature interval according to the relation [9]:

$$I_s(T) \approx I_{oo} \exp\left(-\frac{\Delta E_A}{kT}\right), \quad (2)$$

where ΔE_A is the activation energy of the charge carriers in the forward bias. The activation energy calculated from the slope of the $\ln I_s$ versus $1/T$ plot is found to be 0.638 meV close to half the band gap of CdTe. This suggests that the generation-recombination of carriers in the depletion region determines the dark current. From the Fig. 7 it can be seen that at higher voltages (> 0.25 V) the sublinear portions appear after the usual exponential dependence in all I-U characteristics irrespective of temperature. These portions of I-U characteristics can be well described within the context of the theory of injection depletion for the first time predicted theoretically by A.Yu. Leiderman for the *p-i-n* structures [10], later observed in the structures based on silicon doped with Zn [11] and *n*-CdS/*p*-CdTe HJ [12]. In the case of this effect the I-U characteristics have a very specific shape and is described by the equation

$$V \approx V_0 \exp(JaW), \quad (3)$$

where the thickness of the *i* layer:

$$a = \frac{1}{2qD_p N_t} \quad (4)$$

is the parameter dependent only of the diffusivity of the minority carriers ($D_p = \left(\frac{kT}{q}\right)\mu_p$) and the deep impurity concentration N_t , J is the current density. One of the major conditions for observations of the sublinear portion in I-U characteristics is the requirement

$$JaW > 2,$$

which is fulfilled at all temperatures. As follows from the theory, the appearance of such I-U characteristics is possible only in the case of the opposite directions of ambipolar diffusion of nonequilibrium carriers and their ambipolar drift, which is determined by the injection modulation of the deep-impurity charge. Using equation (3) is possible to estimate the parameter a from the I-U characteristics

$$a = \frac{\ln\left(\frac{U_2}{U_1}\right) \cdot S}{(I_2 - I_1) \cdot W}. \quad (5)$$

The values of the parameter a in function of the temperature is presented in Table 2.

Table 2. Values of the parameter a depending of the temperature

T, K	300	280	260	240	220	200	180	160	140
a	$5.7 \cdot 10^4$	$11.6 \cdot 10^4$	$62.8 \cdot 10^4$	$10 \cdot 10^5$	$60 \cdot 10^5$	$10.6 \cdot 10^6$	$16.6 \cdot 10^6$	$20 \cdot 10^6$	$23.5 \cdot 10^6$
N_i, cm^{-3}	$3.4 \cdot 10^{15}$	$1.6 \cdot 10^{15}$	$3.1 \cdot 10^{14}$	$9.7 \cdot 10^{13}$	$3.2 \cdot 10^{13}$	$1.8 \cdot 10^{13}$	$1.2 \cdot 10^{13}$	$9.7 \cdot 10^{12}$	$8.2 \cdot 10^{12}$

It's seen a strong dependence of the parameter a on the temperature variations. Knowing the value of the parameter a we estimated the deep impurity concentration N_i (See Table 2). The appearance of the sublinear portion in I-U characteristics clearly indicates the presence of i -layer at the interface of the ZnTe/CdTe junction, which is very sensitive on the temperature.

The depletion layer capacitance of a junction at a voltage U is given by [13]:

$$C_j(U) = A \left[\frac{q \varepsilon_0 \varepsilon_r N_D}{2(U_{bi} + U)} \right]^{\frac{1}{2}}, \quad (6)$$

where A is the effective diode area, N_D the carrier concentration, ε_r the dielectric constant of CdTe, ε_0 the vacuum permittivity and V_{bi} the built-in potential. Fig. 9 shows the dependence of $1/C^2$ on voltage at various frequencies. $1/C^2 = f(U)$ plots are linear for the samples in the measured frequencies range. It can be seen that at 10 kHz there is a slight deviation from linearity. It is possible to use the data of Fig. 9 to get an estimate of how the doping density varies within the depletion layer. This is done by calculating $N_D(W)$ from [14–15]:

$$N_D(W) = \frac{2}{q \varepsilon_0 \varepsilon \left(\frac{dC^{-2}}{dU} \right) A^2} \quad (7)$$

and

$$W = \frac{\varepsilon_0 \varepsilon}{C(U)}, \quad (8)$$

where $N_D(W)$ is the ionized-charge concentration at position W in the depletion layer measured from the interface; q is the electron charge, ε is the semiconductor permittivity; A is the junction area;

$\frac{dC^{-2}}{dU}$ is computed at each voltage at which W is computed.

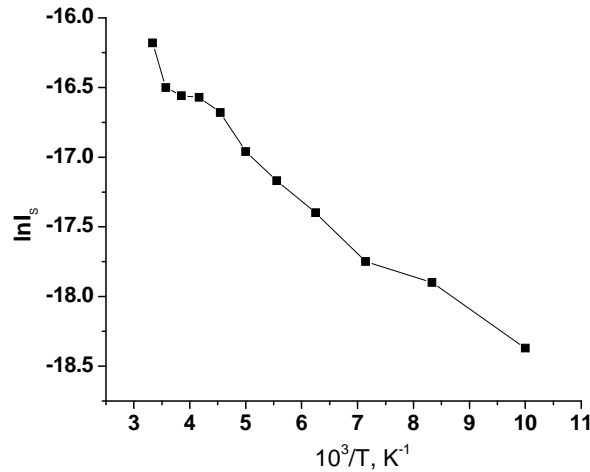


Fig. 8. Dependence $\ln I_s = f(10^3/T)$ in the range of (0.01–0.25) V of the ZnTe/CdTe thin film HJs

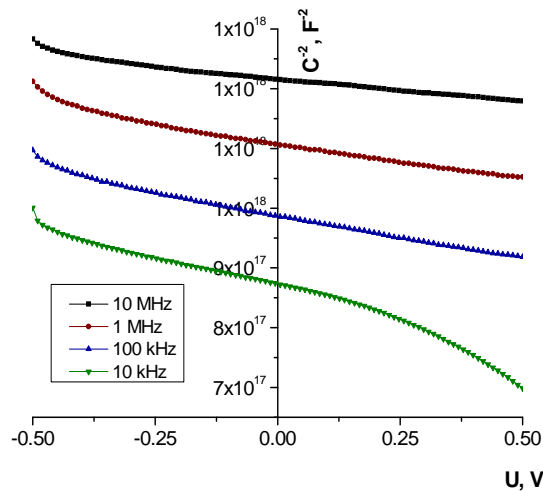


Fig. 9. Dependence of $\frac{1}{C^2} = f(U)$ of the ZnTe/CdTe thin film HJs at different frequencies

The estimation of the ionized-charge concentration (N_D) allowed the plotting of the dependence (N_D) versus depth of the junction. Note that the equations given assume a one-sided junction approximation. We can notice that the ionized-charge concentration profile (N_D) is not constant, but it is increasing together with the enlarging of the depth of heterojunction. The decreasing of the ionized-charge concentration suggests to a high density of the states that result at the junction interface of ZnTe/CdTe. Such behavior of the capacity in correspondence with the measure voltage is explained by the variation of the concentration of deep recombination centers that are present in the space region, which is situated in CdTe.

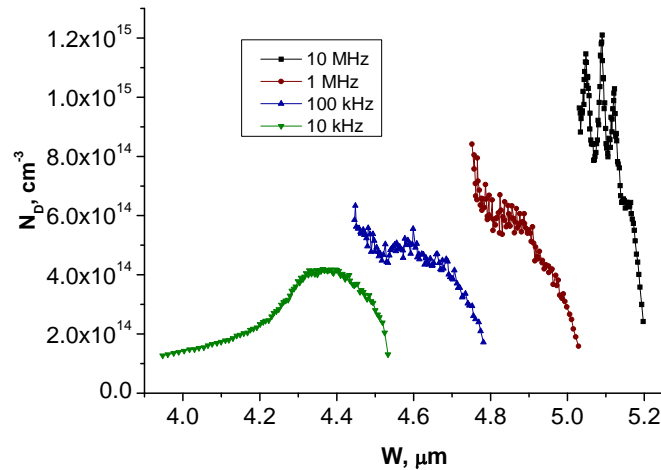


Fig. 10. Dependence of ionized charge concentration for ZnTe/CdTe sample derived from data of Fig. 9

Capacitance-voltage characteristics indicate as current-voltage characteristics the considerable numbers of deep recombination centers in the depletion region of the ZnTe/CdTe HJs.

CONCLUSIONS

From the analysis of I-U and C-U characteristics the current transport mechanism and the deep impurity concentration N_i were determined. The concentration of defects at the p -ZnTe/ n -CdTe interface is as high as $3 \cdot 10^{13} \text{ cm}^{-3}$. The investigation of the I-U characteristics shows that the ideality parameter n of ZnTe/CdTe HJ varies in the range 1–2 at the voltages $< 0.25 \text{ V}$ and suggests that the generation-recombination of carriers in the depletion region occurs. At higher voltages ($> 0.25 \text{ V}$) the characteristics have a sublinear behavior and indicate the strong carrier accumulation in the high resistive region of ZnTe/CdTe HJ which give rise to field-opposed diffusion of free carriers. Also, the frequency-dependence of the junction capacitances of the ZnTe/CdTe HJ shows that the effect of traps is present. The ionized-charge concentration profile (N_D) determined from C-U measurement is not constant, but it is increasing together with the enlarging of the depth of heterojunction and suggests to a high density of the states at the junction interface of ZnTe/CdTe HJ. The high defect density together with the high series resistance of the ZnTe/CdTe HJ limit the solar conversion efficiency to 3–4%. It is possible to achieve the further quality improvement of the material interface and, correspondingly, the device effectiveness based on ZnTe/CdTe system by the creation of new solid solutions on the interface.

ACKNOWLEDGEMENT

This research was supported by the EU 7th Framework Program PEOPLE International Research Staff Exchange Scheme project GA-2008, No. 230861.

REFERENCES

1. U. JAHN, T. OKAMOTO, A. YAMADA, et al., J. Appl. Phys. 90 (2001), 2553.
2. X. WU, J.C. KEANE, R.G. DHERE, et al., 17th European Photovoltaic Solar Energy Conference, Munich, Germany, 22–26 October, Proceedings, 2001, p. 995.
3. T.A. GESSERT, S. ASHER, S. JOHNSTON, M. YOUNG, P. DIPPO, C. CORWINE, Thin Solid Films 515 (2007) 6103.



4. B. SPATH, J. FRITSCHE, F. SAUBERLICH, A. KLEIN, W. JAEGERMANN. *Thin Solid Films* 480–481 (2005) 204.
5. T. POTLOG¹, N. SPALATU¹, N. MATICIUC¹, J. HIIE², A. MERE², V. VALDNA², V. MIKLI² *Physica Status Solidi (a)*, V. 209, Iss. 2, p. 272–276, 2012.
6. FAHRENBRUCH A. L. and BUBE R.H., *Fundamentals of Solar Cells* (Academic Press, New York, (1983).
7. SIMASHKEVICH A.V. *Geteroperehody na osnove poluprovodnikovyh soedinenii A₂B₆ Shtiintsa*, Kishinev, (1980).
8. R.H. MILES, G.Y. WU, M.B. JOHNSON, T.C. MCGILL, J.P. FAURIE et al. *Appl. Phys. Lett.* 48, 1383 (1986), p. 1383–1385;
9. T. SCHWARZ, E. KAUFMANN, G. SPRINGHOLZ, K. KOIKE, T. HOTEL, M. YANO AND W. HEISS, *Phys. Rev. B* 78, 165320, (2008).
10. A. YU. LEIDERMAN, P.M. KARAGEORGY-ALKALAEV. *Sol. St. Commun.*, 27, 339 (1976).
11. P.M. KARAGEORGY-ALKALAEV, I.Z. KARIMOVA, P.I. KNIGIN, A.YU. LEIDERMAN. *Phys. Status Solidi A* 36, 391 (1976).
12. SH. A. MIRSAGATOV, A. YU. LEĪDERMAN, B.U. AĪTBAEV, M.A. MAKHMUDOV. *Physics of the Solid State Vol. 51*, Iss. 10, (2009), p. 2032–2039.
13. S. M. SZE, "Physics of Semiconductor Devices", Publ. John Wiley & Sons Inc. (1981).
14. F. ZENIA, C. LEVY-CLEMENT, R. TRIBOULET, R. KONENKAMP, *ELECTROCHEM. Solid-State Lett.* 3 (2000), 73.
15. MILNES A.G. AND FEUCHT D.L. *Heterojunctions and Meral Semiconductor Jijnctions* (New York Academic) (1972).



OPTICAL PROPERTIES OF SPRAYED ZNO THIN FILMS

T. Unt, M. Kriisa, A. Mere, M. Krunka

*Tallinn University of Technology
Ehitajate tee 5, 19086 Tallinn – Estonia*

ABSTRACT

ZnO semiconductor material is inexpensive and abundant material that is being widely studied as a candidate to replace indium tin oxide (ITO) or tin oxide as a transparent conductive oxide (TCO) layer in thin film solar cells. In TCO layer it is important to achieve high electrical conductivity and optical transparency. Along with transparency it is required to have good light scattering ability to make light path longer and light absorption in solar cell more efficient. Current study focuses on the optical properties of chemically sprayed ZnO films. ZnO can be easily deposited at moderate growth temperatures (~400 °C) by inexpensive chemical spray pyrolysis method on glass or polymeric substrates. Indium doped ZnO films (ZnO:In) on glass substrates with thickness ca 1 micron show electrical resistivity in the order 10^{-3} Ωcm and transmittance of ca. 85% in visible spectral region. It appears that the concentration of carriers in ZnO:In films, at constant dopant amount in precursor solution, is controlled by the solution spray rate. The band gap of ZnO:In films increases from 3.28 eV to 3.36 eV and carrier concentration increases from $1 \cdot 10^{19}$ to $1 \cdot 10^{20}$ cm⁻³ as the solution spray rate changes from 0.5 ml/min to 4.7 ml/min. The decrease of optical transmittance in the near infrared spectral region (NIR) corresponds to the increase in concentration of free carriers. ZnO:In films on polyimide (PI) substrate can be grown onto ZnO buffer layer to form ZnO/ZnO:In bilayer. Depending on the buffer layer morphology ZnO/ZnO:In bilayer has mixed surface texture from smooth to scrolled belt-like grains with size up to 2–3 microns. The bilayers deposited on PI show high light scattering ability with haze factor of 85–95% in the spectral region of 350–1500 nm.

Keywords: ZnO, thin films, optical properties, chemical spray pyrolysis, spraying rate, ZnO:In

1. INTRODUCTION

Zinc oxide (ZnO) is widely used semiconductor material for different optoelectronic devices, such as transparent conductive oxide (TCO) layers as window layers in photovoltaic devices. Various methods like atomic layer deposition [1], pulsed laser deposition (PLD) [2], chemical bath deposition [3], radio frequency magnetron sputtering [4], spray pyrolysis [5] have been used for deposition of ZnO thin films. Chemical spray pyrolysis (CSP), used in this study, is fast and inexpensive method to obtain electrically conductive and highly transparent ZnO thin films.

ZnO thin films can be obtained electrically conductive by doping with suitable elements (e.g. Al, Ga, In) Regardless of dopant, it is reported that 3 at.% of dopant in spray solution is optimal to grow electrically conductive ZnO thin films. Optimal growth temperature for different set-ups varies between 350 and 500 °C. However, the effect of solution spray rate on the optical properties of ZnO thin films has been less studied. It is found that it affects the film surface morphology.

First aim was to understand the spray rate effect to optical properties of single layer ZnO thin film.

Currently polymers are substituting glass in the deposition of TCO-s due to its low weight, mechanical toughness and ductility. Different deposition methods mentioned above are being used to grow different TCO-s on polyimide substrates.

Second aim of the paper was to study the growth of ZnO and ZnO:In film on flexible polyimide substrates and it's optical properties at certain technological parameters.

2. METHODOLOGY

The CSP set-up used in this study is described elsewhere [6] and the deposition conditions were selected based on our previous studies on growth of ZnO:In films on glass substrate [7]. ZnO:In layers were deposited on soda-lime glass (SLG) substrates that were placed on melted tin bath at 400 °C. The SLG substrate thickness was 1 mm. The corresponding film growth temperature was ca. 20 °C lower due to cooling by air (flow rate of 8 l/min) used as a carrier gas; hence the film growth temperature (T_{Sn}) was kept at ca. 380 °C. ZnO:In film was deposited from 100 ml of solution. The spray rate was varied from 0.5 to 6.7 ml/min. ZnO layers and ZnO/ZnO:In bilayers were deposited onto polyimide (PI) substrates that were placed on melted tin bath at 400 °C. For reference, the ZnO, ZnO:In films and ZnO/ZnO:In bilayers were grown on (SLG) from 50 ml and 50+50 ml of solution respectively. ZnO buffer layers were grown from 50 ml (marked as buffer layer type A) and 30 ml (marked as buffer layer type B) of spray solution for PI substrates. We verified that the solution spray rate did not affect the film growth temperature. Since the spray deposition requires substrate temperatures of 300–450 °C, the polyimide film (Kapton® with a thickness of 150 µm supplied by Katco Ltd) was selected as polymer substrate due to its stability up to 400 °C. For the deposition of ZnO and ZnO:In layers, zinc acetate was dissolved in a mixture of deionized water and 2-propanol (volume ratio 2/3). The zinc acetate concentration was 0.2 mol/l. A few drops of acetic acid was added to the spray solution to prevent the precipitation of Zn(OH)₂. As a dopant source, InCl₃ was introduced into the spray solution with the atomic ratio of indium to zinc, $[In^{3+}]/[Zn^{2+}] = 3$ at. %.

X-ray diffraction (XRD) patterns of sprayed ZnO thin films and bilayers (ZnO/ZnO:In) on PI and glass substrates were recorded using a Rigaku Ultima IV diffractometer with monochromatic Cu K α radiation ($\lambda = 1.5406$ Å, 40 kV at 40 mA). Data were gathered in the 2θ range of 30°–70° with scan speed 4°/min and scan step 0.01° using the silicon strip detector D/teX Ultra. The X-ray diffractograms were analyzed using the software on the Rigaku system (PDXL 1.4.0.3). The morphology was characterized and the thickness of the layers was determined with scanning electron microscopy (SEM) using EVO MA 15 Zeiss apparatus at operating voltage of 7 kV. The optical specular reflectance, diffuse and total reflectance spectra were recorded in the wavelength range of 250–2500 nm on Jasco V-670 spectrophotometer using an integrating sphere. Electrical resistivity, charge carrier mobility and charge carrier concentration were measured using standard 4-probe method at room temperature using Hall, van der Pauw Controller H-50 from MMR. The contacts for van der Pauw and Hall measurements were made from graphite.

3. RESULTS AND DISCUSSION

3.1. Optical properties of ZnO:In on glass substrate

The XRD pattern of ZnO:In thin film deposited at 0.5 ml/min at 400 °C is presented in Fig. 1c. According to Fig. 1, ZnO:In film is preferably orientated in the (101) plane parallel to the substrate irrespective of the solution spray rate. Solution spray rates below 3 ml/min, lead to smaller crystallites with an average size of 20 nm while the use of solution spray rates above 3 ml/min result in the crystallite sizes of ca. 35 nm (Table 1).

Optical transmittance spectra of the ZnO:In films are presented in Fig. 2. Different solution spray rates were used and shown in this graph. Specular transmittance is above 75% in visible light region for ZnO:In films irrespective of the solution spray rate. Interference fringes number indicate that films grown at solution spray rates above 3 ml/min are thicker compared to those obtained at lower spray rates (see Table 1).

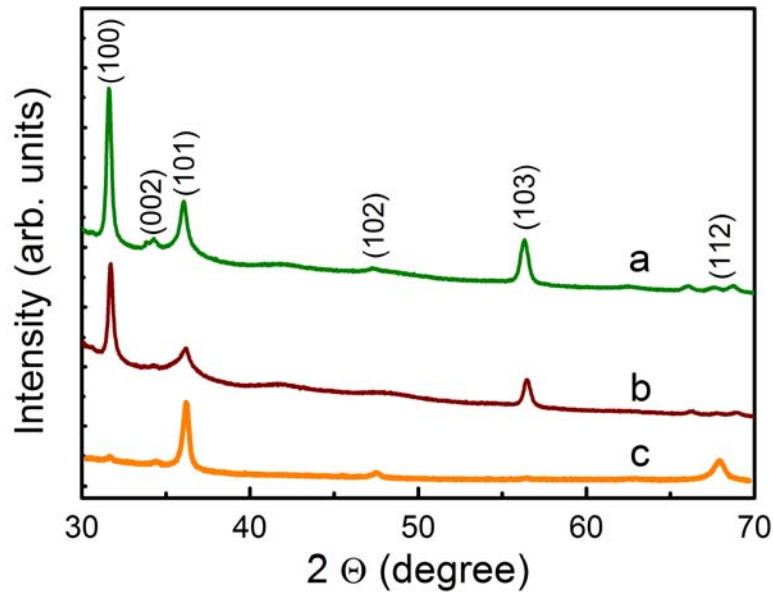


Fig. 1. XRD patterns of the ZnO/ZnO:In bilayer and its buffer layer type B on the PI substrate, a and b accordingly. ZnO:In single layer on glass substrate, pattern c

Table 1. The effect of the solution spray rate on the sprayed single layer ZnO:In film on glass substrate thickness, crystallite size (according to XRD), grain size (according to SEM), main carrier concentration (n) and mobility (μ), and optical band gap (E_g)

Solution spray rate (ml/min)	Film thickness (nm)	Crystallite size (nm)	Grain size (nm)	n (cm^{-3})	μ ($\text{cm}^2\text{V}^{-1}\text{s}^{-1}$)	E_g (eV)
0.5	700	22	115	$2.3 \cdot 10^{19}$	4.4	3.28
1.5	940	21	120	$6.9 \cdot 10^{19}$	7.7	3.31
3.3	1360	34	250	$1.1 \cdot 10^{20}$	16	3.34
4.7	1440	35	250	$1.4 \cdot 10^{20}$	15	3.36
6.7	1480	36	250	$1.2 \cdot 10^{20}$	12	3.32

The film grown at spray rate 0.5 ml/min shows comparable transmittance both in near infrared and UV-VIS region at 85%. Increasing the solution spray rate results in decrease of film transmittance in NIR region. Film deposited with spray rate 3.3 ml/min shows the biggest decrease from 80% in UV-VIS region down to 15% at 2500 nm. Optical transmittance decrease in the NIR spectral region is in correlation with the increased concentration of carriers in the films sprayed at higher solution spray rates (Table 1). The decrease of transmittance is due to increase of free carrier absorption [8].

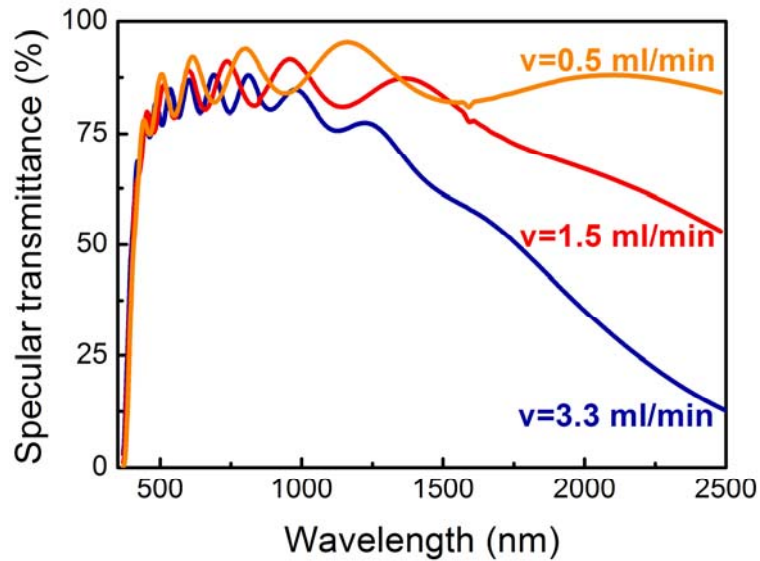


Fig. 2. Specular transmittance of ZnO:In thin films deposited at solution spray rates of 0.5 ml/min, 1.5 ml/min and 3.3 ml/min

The optical band gap of the films is determined from transmittance spectra. The optical band gap values were determined from commonly used equation $\alpha hv = A \cdot (hv - E_g)^{1/n}$, where A is the constant related to the effective mass of charge carrier, h is Planck constant, E_g is the band gap energy, hv is the incident photon energy and $1/n$ is the exponent that depends on the nature of the optical transition ($n = 0.5$ for direct transition). Fig. 3 shows the determination of the E_g from $(\alpha hv)^2$ vs. hv plot. The E_g values of ZnO:In films depending on the solution spray rate are given in Table 1. Solution spray rate increase from 0.5 ml/min up to 4.7 ml/min results in ZnO:In films band gap increase from 3.28 eV up to 3.36 eV. The band gap increase is in accordance with the increase of carrier concentration, Table 1, which can be explained by the Burstein-Moss effect. This result is in good agreement with the results of previous study where the increase in E_g is reported to be in correlation with the concentration of carriers controlled by doping level [8].

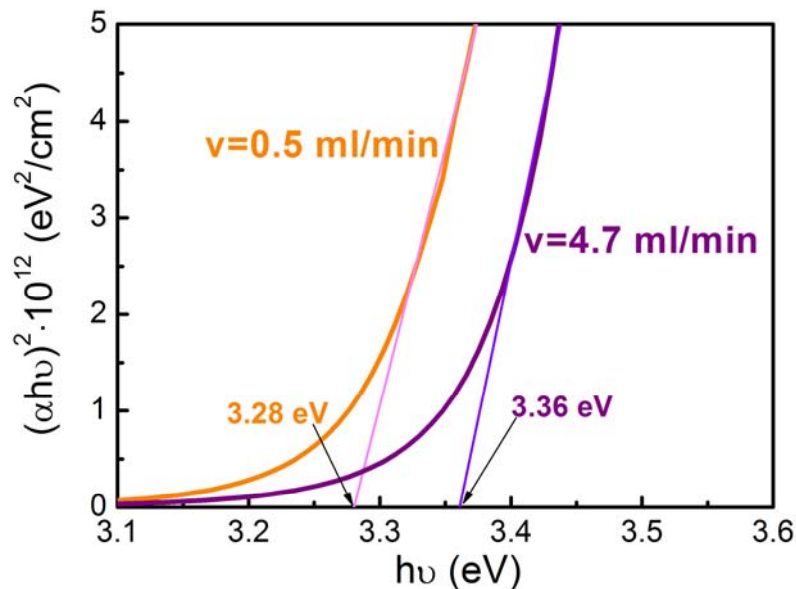


Fig. 3. Graphical determination of direct optical band gap of ZnO:In thin films deposited with solution spray rates of 0.5 ml/min and 4.7 ml/min

3.2. Optical properties of ZnO/ZnO:In on polyimide substrate

Zinc oxide thin films grown on PI at 380 °C were visually smooth, crack-free and showed good adhesion independent of solution volume sprayed and spray rate. However, ZnO:In thin films cracked and peeled off from the PI within a few minutes after deposition independent of the deposition conditions. To be able to grow adhesive ZnO:In film by spray on PI, an undoped ZnO film showing good adherence to PI was sprayed and used as a buffer layer. XRD patterns of the sprayed crack-free ZnO/ZnO:In bilayer and its buffer layer type B on the PI substrate are presented in Fig. 1 (a and b accordingly). Both films are preferably orientated in the (100) plane parallel.

Fig. 4 compares the total reflectance spectra of ZnO/ZnO:In bilayers grown onto PI from buffer layer type A and type B (spectra a and b, respectively) and glass from buffer layer type A (spectrum c), and a ZnO:In single layer on glass (spectrum d). The total reflectance spectra of bilayers on PI (a and b) are similar and show reflectance of 10–17% in the spectral region of 400–1500 nm. At the same time, the average total reflectance of both, the bilayer and the ZnO:In single layer on glass (spectra c and d, respectively) slightly decreases, from ca. 15% at 400 nm to ca. 10% at 1500 nm. The interference is less pronounced in the spectrum of the bilayer (spectrum c) compared to a single ZnO:In layer on glass (spectrum d), and could be explained by more granular structure of the bilayer (see SEM image of bilayer in Fig. 7d and SEM image of ZnO:In in [9]).

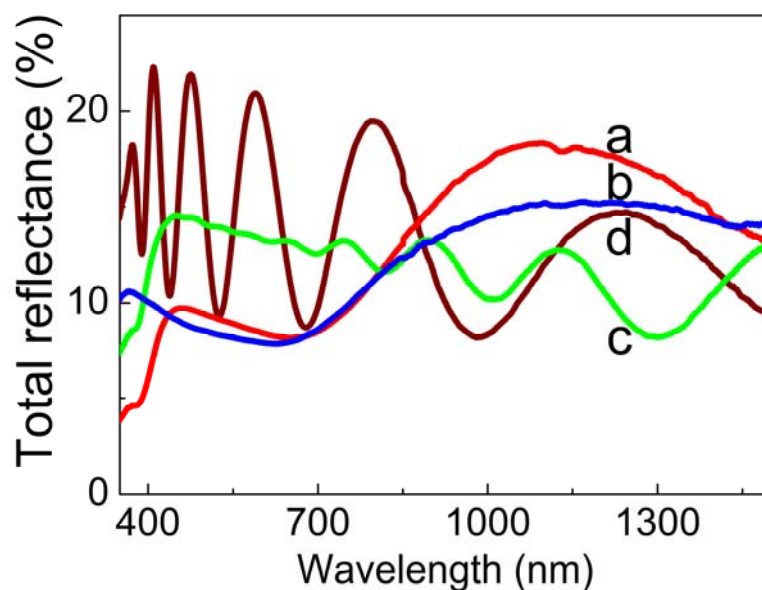


Fig. 4. Total reflectance spectra of ZnO/ZnO:In bilayer on PI using buffer layer of type A (line a), bilayer on PI using buffer layer of type B (line b), bilayer on glass substrate using buffer layer of type A (line c) and ZnO:In film on glass substrate (line d). All the layers were grown at 380 °C, ZnO:In layer from 50 ml of spray solution

Fig. 5 shows wavelength-dependent Haze factor spectra for same thin films in the same order as in total reflectance spectra. Haze factor is defined as the ratio of diffused reflectance with respect to total reflectance ($H = R_{diff}/R_{total}$). The Haze factor expresses the ZnO films capability to scatter light.

The presence of interference in the haze spectra of layers grown on glass (see Fig. 5 c and 5 d) originates from the specular component of the total reflectance (see Fig. 4 c and 4 d) and indicates that the layers are relatively smooth and uniform in thickness, compared to bilayers grown on PI (see Fig. 5 a and 5 b). The lack of any interference in the haze spectra of the bilayers grown

on PI refer to high surface roughness. This observation is in accordance with the SEM when comparing Fig. 6 d with Fig. 7 d that correspond to bilayers grown on PI and glass, respectively.

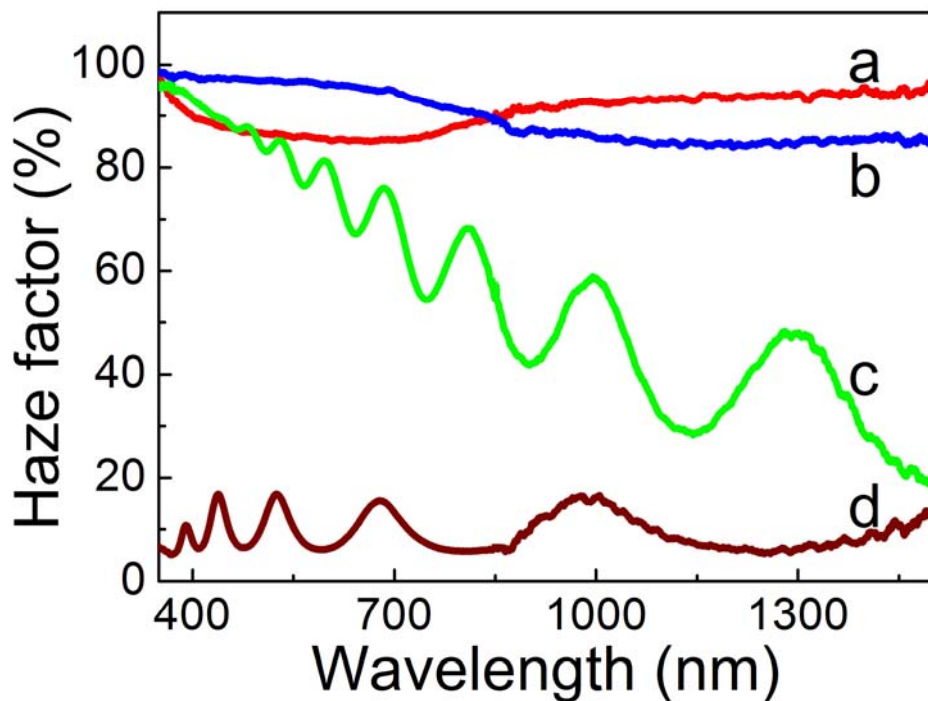


Fig. 5. Haze factor spectra of ZnO/ZnO:In bilayer on PI using buffer layer of type A (line a), bilayer on PI using buffer layer of type B (line b), bilayer on glass substrate using buffer layer of type A (line c) and ZnO:In on glass substrate (line d). All the layers were grown at 380 °C, ZnO:In layer from 50 ml of spray solution

Haze factor of the bilayer on PI (see corresponding SEM image in Fig. 6 d) is about 85% and 95% in the visible part of the spectrum and in the wavelength region of 800–1500 nm, respectively (see Fig. 5 a). The light scattering is highest when the incident light wavelength is similar to the feature dimension where the light is reflected [10]. Thus, it could be proposed that higher haze factor in the spectral region of 800–1500 nm is due to the higher share of features with sizes of 800–1500 nm. In contrary, the bilayer on PI with characteristic SEM image shown in Fig. 7 b demonstrates haze factor of ca. 95% in the visible part of the spectrum (Fig. 5 b) while the haze factor is ca. 85% at wavelengths between 900 nm and 1500 nm. In this case, the light scattering is slightly higher from features with the size of 350–700 nm.

For bilayer on glass (see SEM image on Fig. 7 d) the haze factor decreases rapidly from 95% down to 20% at wavelengths 350 nm up to 1500 nm, respectively, indicating the increased light scattering from the fine-scale features. The single ZnO:In layer on glass shows relatively low haze factor of ca. 10% over the spectral region 350–1500 nm.

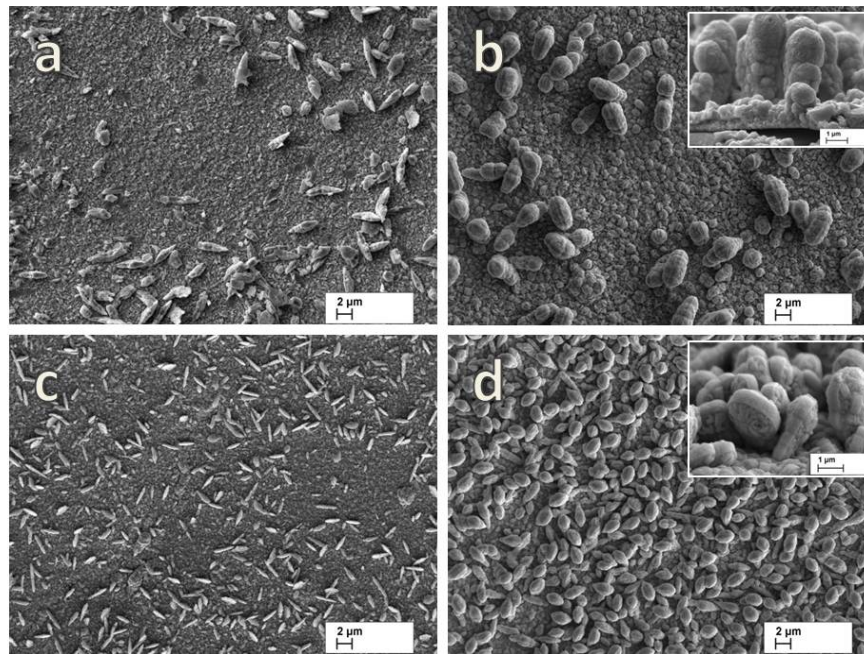


Fig. 6. SEM images of ZnO buffer layers of type A (a, c) and the corresponding ZnO/ZnO:In bilayers (b, d) grown at TS = 380 °C on PI substrate. Solution spray rate(s) of 2 ml/min (a, b) and 3 ml/min (c, d) were used, respectively. The SEM cross-sectional images of bilayers are presented as insets

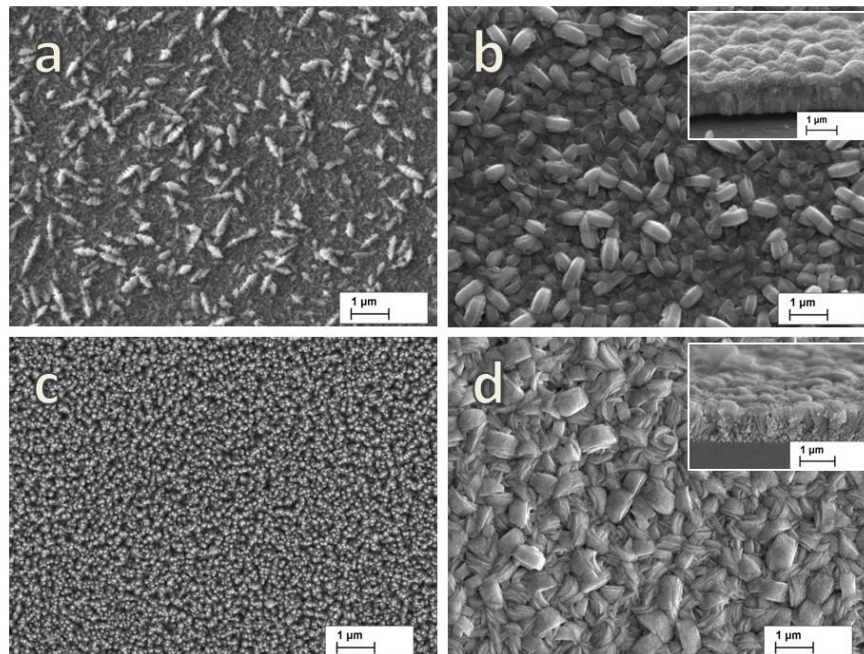


Fig. 7. SEM images of ZnO buffer layer of type B (a) and ZnO/ZnO:In bilayer (b) grown on PI substrate; and of ZnO buffer layer type B (c) and ZnO/ZnO:In bilayer (d) grown on glass. The films were grown at TS = 380 °C. The SEM cross-sectional images of bilayers are presented as insets

4. CONCLUSIONS

Optically transparent and electrically conductive indium doped ZnO thin films were grown on glass substrate by chemical spray pyrolysis. We showed that solution spray rate is a technological parameter that has an effect on the properties of ZnO:In thin films. An increase in solution spray rate from 0.5 ml/min up to 3.3 ml/min led to decreased transmittance in NIR region that was in accordance with the carrier concentration (increased from $2.3 \cdot 10^{19} \text{ cm}^{-3}$ to $1.1 \cdot 10^{20} \text{ cm}^{-3}$). The band gap of ZnO:In thin film increases from 3.28 eV up to 3.36 eV for ZnO:In films with solution spray rates of 0.5 ml/min and 4.7 ml/min, respectively.

Current work showed that ZnO films can be grown by CSP method on polyimide substrate at 380 °C. It appears that ZnO:In films cracked and peeled off when deposited directly onto polyimide. The ZnO:In films were grown onto an undoped ZnO layer acting as a buffer layer on top of polyimide. The ZnO:In layer shows mixed morphology from smooth canvas-like surface to large grains. According to SEM, the large grains with diameters from 1 μm up to 6 μm are bundles of scrolled belts. When grown on the polyimide substrate, the bilayers exhibit haze factor of 85–95% in the spectral region of 350–1500 nm indicating high light scattering capability.

REFERENCES

1. NIINISTÖ, L., NIEMINEN, M., PÄIVÄSAARI, J., NIINISTÖ, J., PUTKONEN, M. Advanced electronic and optoelectronic materials by Atomic Layer Deposition: An overview with special emphasis on recent progress in processing of high-k dielectrics and other oxide materials. *Physica Status Solidi (a)*, 2004, Vol. 201, No. 7, p. 1443–1452.
2. ZHAO, J.-L., LI, X.-M., BIAN, J.-M., YU, W.-D., ZHANG, C.-Y. Comparison of structural and photoluminescence properties of ZnO thin films grown by pulsed laser deposition and ultrasonic spray pyrolysis. *Thin Solid Films*, 2006, Vol. 515, No. 4, p. 1763–1766.
3. DRICI, A., DJETELI, G., TCHANGBEDJI, G., DEROUICHE, H., JONDO, K., NAPO, K., BERNÉDE, J. C., OURO-DJOBO, S., GBAGBA, M. Structured ZnO thin films grown by chemical bath deposition for photovoltaic applications. *Physica Status Solidi (a)*, 2004, Vol. 201, No. 7, p. 1528–1536.
4. JAYARAJ, M. K., ANTONY, A., RAMACHANDRAN, M. Transparent conducting zinc oxide thin film prepared by off-axis rf magnetron sputtering. *Bulletin of Materials Science*, 2002, Vol. 25, No. 3, p. 227–230.
5. HAFDALLAH, A., YANINEB, F., AIDA, M.S., ATTAFF, N. In doped ZnO thin films. *Journal of Alloys and Compounds*, 2011, Vol. 509, No. 26, p. 7267–7270.
6. OTTO, K., KATERSKI, A., MERE, A., VOLOBUJEVA, O., KRUNKS, M. Spray pyrolysis deposition of indium sulphide thin films. *Thin Solid Films*, 2011, Vol. 519, No. 10, p. 3055–3060.
7. VENT, M., KÄRBER, E., UNT, T., MERE, A., KRUNKS, M. The effect of growth temperature and spraying rate on the properties of ZnO:In films. *Physica Status Solidi (c)*, 2012, Vol. 9, No. 7, p. 1604–1606.
8. MINAMI, T. Transparent conducting oxide semiconductors for transparent electrodes. *Semiconductor Science and Technology*, 2005, Vol. 20, No. 4, p. S35–S44.
9. DEDOVA, T., KLAUSON, J., BADRE, C., PAUPOURTE, T., NISUMAA, R., MERE, A., VOLOBUJEVA, O., KRUNKS, M. Chemical spray deposition of zinc oxide nanostructured layers from zinc acetate solutions. *Physica Status Solidi (a)*, 2008, Vol. 205, No. 10, p. 2355–2359.
10. SODERSTROM, T., HAUG, F.-J., NIQUILLE, X., TERRAZZONI, V., BALLIF, C. Asymmetric intermediate reflector for tandem micromorph thin film silicon solar cells. *Applied Physics Letters*, 2009, Vol. 94, No. 6, p. 063501.



EXPERIMENTAL RESULTS AND MATHEMATICAL MODEL FOR THE PROCESS OF CARBON BLACK PRODUCTION IN HIGH TEMPERATURE FLOW REACTOR

S.I. Dmitriyev, P.S. Grinchuk, N.V. Pavljukevich
A.V. Luikov Heat & Mass Transfer Institute of NAS of Belarus
Brovki str. 15, Minsk 220072 – Belarus

ABSTRACT

Carbon black is one of the main components for productions of tires, rubbers and plastics. Properties of the final manufacturing product depend on the physicochemical properties of carbon black. That is why it is important to investigate and to modernize regimes of carbon black production. The most common way of producing is the growth of carbon black particles in high temperature flow reactor after evaporation of liquid hydrocarbonic raw material.

For an investigation of carbon black producing regimes two installations with productivity up to 10 kg/h were designed and operated. Their construction allows spraying a liquid hydrocarbonic raw material into high temperature gas flow having the temperature of 1300–1500 °C. Droplets of this raw material are evaporated and dissolved due to pyrolysis reaction. Obtained gas mixture is saturated with carbon. Then the growth of finely-divided carbon black takes place in the terms of a carbon nucleation from gas phase. Finally this mixture is cooled by spraying water into it and formed carbon black particles are caught by bag filter.

A number of experiments of carbon black production were carried out. Some physicochemical values of this process such as temperature, pressure, composition of gas mixture (H_2 , CO , CO_2 , CH_4 concentrations) were registered.

A mathematical model of hydrocarbonic droplets evaporation was formulated. The calculation revealed a fact, that these droplets are evaporated rapidly and this evaporation does not limit the technological process of carbon black producing in the flow reactor.

Keywords: carbon black, furnace black, pyrolysis reaction, flow reactor

1. INTRODUCTION

Carbon black (furnace black, further CB) is fine-grained carbonic material. It is widely used in industry as reinforcing filler in rubber products and tires as well as a black pigment for paints and toners. Physicochemical characteristics of CB have an influence on quality and properties of final good, for instance tensile strength and elasticity of rubbers, resistance to abrasion of tire tread electroconductivity, etc. Major CB characteristics are the average particle diameter and the surface-area-to-volume ratio. These values define criteria of sorting carbon black materials by different standardized types. For example, a popular standard ASTM D1765-03 classifies CB depending on the surface-area-to-volume ratio. There is also a classification in terms of physicochemical factors and the degree of reinforcing effect for rubbers [1].

A basic method of CB production is furnace method. This method is used for CB manufacture of about 96% of total volume [1]. The principle of this method is following. At one side of reactor a gas or a liquid fuel are burnt out with condition of slight excess of air. In the other zone of reactor that contains combustion products some portion of liquid hydrocarbonic (further HC) fuel are injected. HC fuel droplets are evaporated and decomposed by means of thermal-oxidative pyrolysis and number of chemical reactions. This results in a formation of solid fine-dispersed carbon material and assist gases.

The furnace method is widely used due to whole set of advantages in comparison with others methods of CB manufacturing: high productivity as result of backup fuel for reactor heating usage

as well as recuperative heating of supplied air, gas and fuel; reduction of harmful emissions into the atmosphere. Such a method allows producing CB with surface-area-to-volume ratio in the range from 12 to 500 m²/g [1]. A possibility of setting in wide range flows of coming to the reactor fuel, gas, air, cooling water, temperatures in the injection fuel reactor zone (from 1400 to 1750 °C) and cooling reactor zone plays an important role in managing of properties of obtained CB.

Scores of described in literature installations for CB manufacturing are designed with old-fashioned elements and mechanisms and they are totally aimed for producing CB in short range of standardized types. Moreover adjusting of technologies for producing CB with narrowly defined characteristics as rule is realized by empirical identification. This problem can be alleviated by using of state-of-the-art materials and control facilities with proven physicochemical explanation. And resulting conception is expected to provide with a well minded technology of CB producing when one can effectively obtain required characteristics of CB by means of managing of initial parameters.

The objective of the work is investigation of processes and regimes that correspond of CB production. Working installation design involves modern technologies as described further and this aspect gives novelty for experiments carried out. Another purpose is an investigation of obtained CB species for a final determination of applied manufacturing technologies. For precise understanding of physicochemical processes that occur during formation of CB particles a physico-mathematical model is formulated and presented in this paper. The model comprises complex of hydrodynamic and mass transfer equations and allows estimating a contribution of some key factors (e.g. the rate of HC droplet evaporation) that are notable for CB producing technology by furnace method.

2. EXPERIMENTS ON CB PRODUCTION

2.1. Installation for CB production

During last three years at the A.V. Luikov Heat and Mass Transfer Institute of NAS of Belarus two experimental installations for investigation of regimes of CB producing by furnace method were developed. Created experimental installations work on basis of known technological method – high-temperature non-oxidation pyrolysis of HC fuel. Moreover, modern technologies (automatic control system, fibrous insulation materials, lightweight refractory concretes, etc.) were used. The first installation (inst. #1) has productivity 1.9 kg of CB per hour, the second one (inst. #2) – up to 10 kg/h.

The principle of CB producing is the same for both of them. An explanation of their highlights is given further on the example of inst. #2. Channel reactor has a cylindrical geometry and is made of lightweight refractory concrete. The concrete is insulated outside by insulating fiber materials. Natural gas and air with controlled flow rates are supplied at the gas burner (2 in Fig. 1) established at the beginning of the reactor. A burning of natural gas / air mixture results in creation of high-temperature smoke fumes containing a certain amount of uncombined oxygen. Obtained gas mixture flows in the reactor channel due to running of exhaust fans (8, 9 in Fig. 1). In the reaction zone (3 in Fig. 1) a HC fuel is scattered from water-cooled centrifugal nozzles. After injection of fine-dispersed droplets of HC fuel into gas flow that has temperature of about 1500 °C they evaporate and decompose under pyrolysis conditions forming a gas mixture oversaturated with uncombined carbon. Then the growth of finely-divided CB takes place in the terms of a carbon nucleation from gas phase [2]. After passing of reactor channel the CB / smoke fumes mixture comes to the scrubber (4 in Fig. 1) where it is cooled down to the temperature of 250 °C by means of water spraying directly into the gas flow. Then formed carbon black particles are caught by sleeve filter (5 in Fig. 1). Smoke fumes are catalytically afterburned and released into the atmosphere.

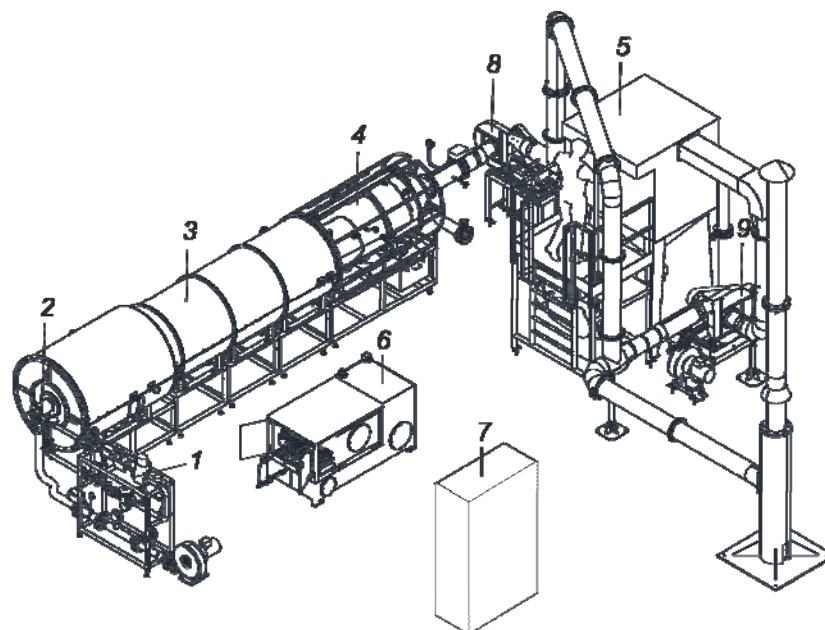


Fig. 1. Layout of inst. #2: 1 – gas-distributing system, 2 – gas burner, 3 – reactor, 4 – scrubber, 5 – bag filter for CB catching, 6 – HC fuel and cooling water supply system, 7 – automatic control system, 8 – high-temperature exhaust fan, 9 – fan after filter

Table shows comparative data for inst. #1 and #2. The second installation has a high level of automation and allows one to register up to 10 parameters (temperatures, pressures, flow rates of operating environments) and the control is realized by 15 actuators (butterfly valves, solenoid valves, gas and hydraulic systems, exhaust fans, pneumatic regeneration of sleeve filter, etc.).

Comparative data of technological parameters of inst. #1 and #2

	Inst. #1	Inst. #2
Diameter of reactor channel, mm	80	200
Length of reactor channel, m	3.4	4.2
Natural gas at burner inlet flow rate, nm ³ /h	up to 8	up to 25
Air flow rate, nm ³ /h	up to 90	up to 290
Liquid HC fuel flow rate, kg/h	5	25
Temperature at the reaction zone, °C	~1450	~1500
Productivity of CB, kg/h	1.9	10

2.2. Experimental data

A number of experiments of carbon black production were carried out. Some physicochemical values of this process such as temperature, pressure, composition of gas mixture (H₂, CO, CO₂, CH₄ concentrations) were registered. For example, Fig. 2 refers to temperatures (according to thermocouples ##1–3, sequentially set in the channel of reactor at the distance from its beginning 0.87 m, 1.425 m and 4.0 m respectively) in the regime of warming-up and with HC fuel spraying for one of the experiments on inst. #2. A measurement of H₂, CO₂ and CO gases concentration was also made by a portable gas analyzer. The accuracy of concentration measurements was ±1% for H₂ and ±2% for CO₂ and CO.

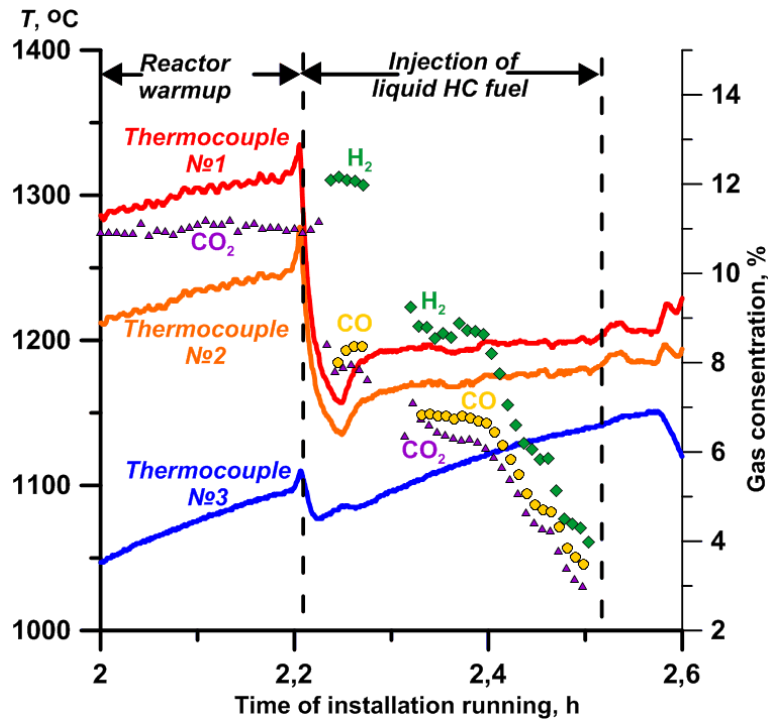


Fig. 2. Temperatures and gas concentrations for inst. #2 for regimes of warming-up and liquid HC fuel spraying. Natural gas flow rate – $14.5 \text{ nm}^3/\text{h}$, air flow rate $160 \text{ nm}^3/\text{h}$, excess-air factor – 1.2, HC fuel flow rate – 25 kg/h

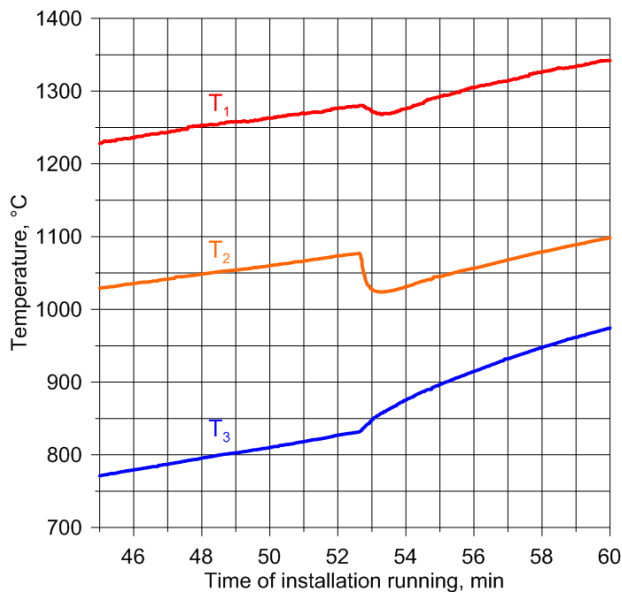


Fig. 3. Temperatures vs. time of inst. #1 running. $T_1 - T_3$ correspond to thermocouples ##1–3 respectively. Beginning of HC fuel spraying – 52nd min (gas flow rate $4 \text{ nm}^3/\text{h}$, air flow rate – $61 \text{ nm}^3/\text{h}$, excess-air factor – 1.38, HC fuel flow rate – 4.8 kg/h)

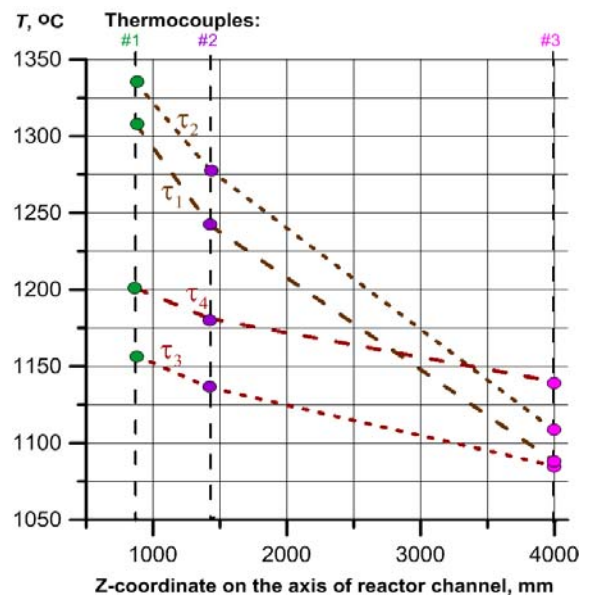


Fig. 4. Temperature profile on the channel length for inst. #2 at different moments of time (grouped with corresponding dashed line): τ_1 (130 min from start) – reactor warming-up, τ_2 (132 min), τ_3 (135 min), τ_4 (150 min) – HC fuel injection

Temperatures in the reactor channel of inst. #1 (Fig. 3) were registered by control system. Thermocouples ##1–3 are sequentially set in the channel of reactor at the distance from the beginning of reactor channel: thermocouple #1 – 0.92 m, #2 – 2.76 m, #3 – 3.4 m. It is important to note that when HC fuel began spraying there was a dip of temperature curves of about 30–50 °C (thermocouples #1 and #2) at the beginning and middle of channel. Meanwhile at the end of channel a temperature increase took place (thermocouple #3).

Temperature profiles along the channel length of the reactor for experiment mentioned in Fig. 2 are shown in Fig. 4. These temperatures are measured at different times during operation of inst. #2 for three points (thermocouples ##1–3). In the regime of reactor warming-up there is a harsh decline of temperatures on the length (about 200 °C or 70 °C/m). Profiles at the moments τ_3 and τ_4 are registered in the mode of HC fuel injection with the mass flow rate comparable to the mass flow rate of initial gas mixture. The temperature profile along the channel length is more uniform for these moments (differential decreases to 100 °C or about 35 °C/m). Temperature gradient on reactor channel is important for CB production. For period τ_1 its value was 89 °C/m, τ_2 – 84 °C/m, τ_3 – 29 °C/m and τ_4 – 26 °C/m.

3. RESULTS AND DISCUSSION

3.1. Experimental results

Shown concentrations in Fig. 2 characterize the intensity of the pyrolysis of raw materials and the process of CB formation. The higher degree of HC fuel decomposition corresponds to the higher level of hydrogen concentration.

The dip of temperature curves in Fig. 3 for beginning of the reactor is considered to be connected with liquid HC fuel evaporation while the temperature growth at the reactor end (thermocouple #3) can be caused by a partial combustion (oxidation) of the products of fuel decomposition. Another reason for the increase in temperature at the reactor end is an evolution of heat due to carbon vapour condensation into CB particles. By the way the reasons of such a temperature distribution during the regime of HC fuel spraying needs to be investigated thoroughly in the near future.

Since the thermal inertia of the reactor is high enough, even after several hours of work, it does not go out on a stationary temperature profile along the length of the channel – a gradual warming continues (Fig. 4). The period of time for steady state reaching is important information for stable technology of CB producing as a manufacturing of certain standardized CB type requires stable technological conditions (temperature gradients in the reactor channel, flow rates of working agents, etc.).

3.2. Characteristics of obtained CB

The resulting samples of CB were studied by scanning electron microscopy (SEM) and analysis of surface area. In Fig. 5 (*a, b*) are SEM images of CB obtained in the inst. #2.

It is revealed that obtained by this technology CB has globe structure with typical diameter 120–300 nm. It correlates to existing model of CB particle declaring that these particles have globe structure [3].

The surface-area-to-volume ratios are following: 40–120 m²/g (inst. #1) and 25–80 m²/g (inst. #2). These figures fall in the range of those that correspond to existing standardized types of CB.

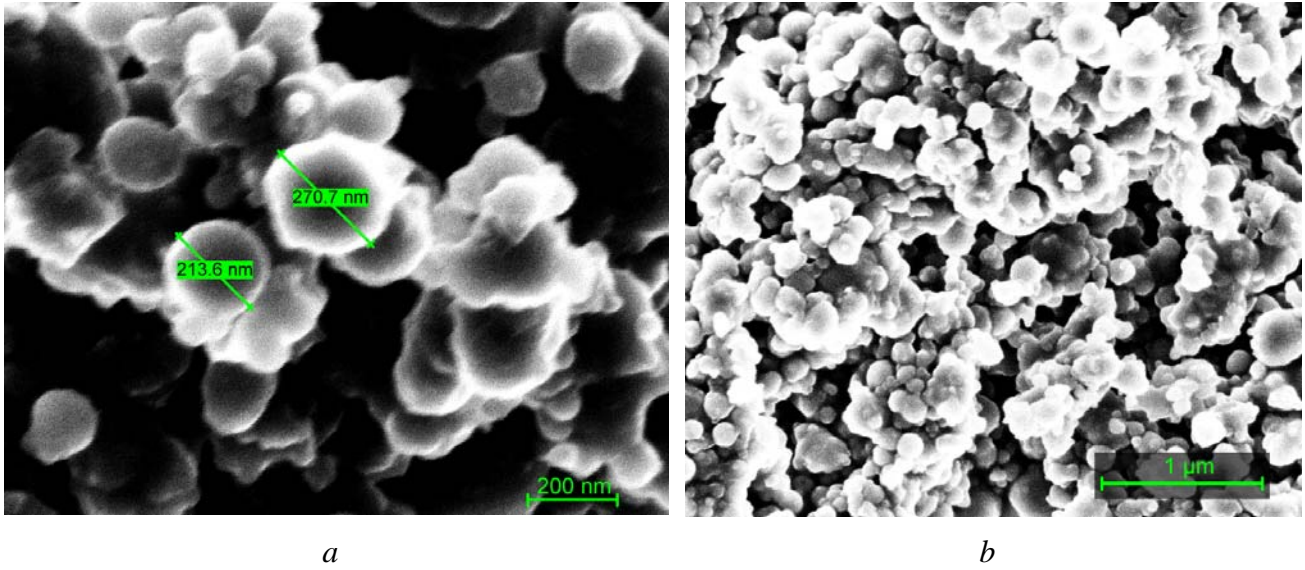


Fig. 5. SEM images of CB obtained in the inst. #2: *a* – nanoscale CB globes, *b* – CB conglomerates

3.3. Mathematical model of HC droplets evaporation in flow reactor

Another aspect of the problem of CB obtaining is the right choice of design parameters for the reactor. The main question is also determining the stage that is limitative for the entire process of CB production. The idea is to consider the evaporation of the HC droplets, as some researchers believe that it is the limitative stage of such a process [4]. In accordance with the geometry and the design of inst. #2 a mathematical model of HC droplet evaporation in a high-temperature gas flow was formulated:

$$\frac{1}{2} \rho_f v_{fz} \frac{dd_f}{dZ} = -\frac{ShD}{d_f} (\rho_{ev} - \rho_v), \quad d_f|_{Z=0} = d_{f0}; \quad (1)$$

$$v \frac{d\rho_v}{dZ} = \pi d_f n_f ShD (\rho_{ev} - \rho_v), \quad \rho_v|_{Z=0} = \rho_v|_{300K}; \quad (2)$$

$$\frac{dv_{fz}}{dZ} = -\frac{3}{4} C(Re_f) \frac{\rho_g (v_{fz} - u)^2}{\rho_f d_f v_{fz}}, \quad v_{fz}|_{Z=0} = 0.1 \text{ m/s}; \quad (3)$$

$$c_{pf} \rho_f v_{fz} \frac{dT_f}{dZ} = \frac{6}{d_f} \left[\alpha(T - T_f) - (Q_v + Q_l) \frac{ShD}{d_f} (\rho_{ev} - \rho_v) \right], \quad T_f|_{Z=0} = 300 \text{ K}; \quad (4)$$

$$T = 1500 - 20Z. \quad (5)$$

Equation (1) describes changing of droplet diameter d_f , (2) – a change in the density ρ_v of HC fuel vapour in the channel during the evaporation of cloud of droplets ($n_f = 10^{10} \text{ 1/m}^3$) and (3) – change of velocity v_{fz} of the particle moving along the channel, the drag coefficient here is

$C(\text{Re}) = \frac{24}{\text{Re}_f} \left(1 + \frac{1}{6} \text{Re}_f^{\frac{2}{3}} \right)$. In the balance equation (4) for the temperature droplet T_f the first term

on the right describes the convective heat transfer, and the second – the cooling of droplet due to both the phase transition and the heat of HC molecules bond breaking [5]. Even though the breaking of molecules of HC droplet vapour into individual atoms of H_2 and C occurs in the flow of gas mixture, this loss of heat is included in the equation for T_f because the heat transition in gas flow is not considered in this model (the distribution of the gas mixture (5) is taken from the experiments).

In the equations (1)–(4) $\rho_g = \rho_B + \rho_v$, $\text{Sh} = 2 + 0,6\text{Re}_f^{\frac{1}{2}}\text{Sc}^{\frac{1}{3}}$, $\text{Sc} = \frac{\nu}{D}$, $\text{Re}_f = \frac{d_f \sqrt{(v_{fz} - v)^2}}{\nu_g}$,

$\alpha = \frac{\lambda}{d_f} \text{Nu}$, $\text{Nu} = \frac{\ln(1 + B_T)}{B_f} \left(2 + 0,6\text{Re}_f^{\frac{1}{2}}\text{Pr}^{\frac{1}{3}} \right)$ and $B_T = \frac{c_{pv}(T - T_f)}{Q_v}$ – Spalding number for heat

transfer which takes into account the influence of blowing more cold vapour (with $B_T > 1$ number Nu decreases). The pressure of saturated vapour of HC fuel P_{ev} is calculated from the known empirical formulas [6].

In the equations (1), (2), (4) for concerned hydrodynamic conditions ($p \sim 1$ atm), the expression for the coefficient of mass transfer $\alpha_m = \frac{\text{Sh}D}{d_f}$ is used. A similar formula for α_m and the equation (1) are used in [7] for calculation of the evaporative cooling of water droplets in a cooling tower.

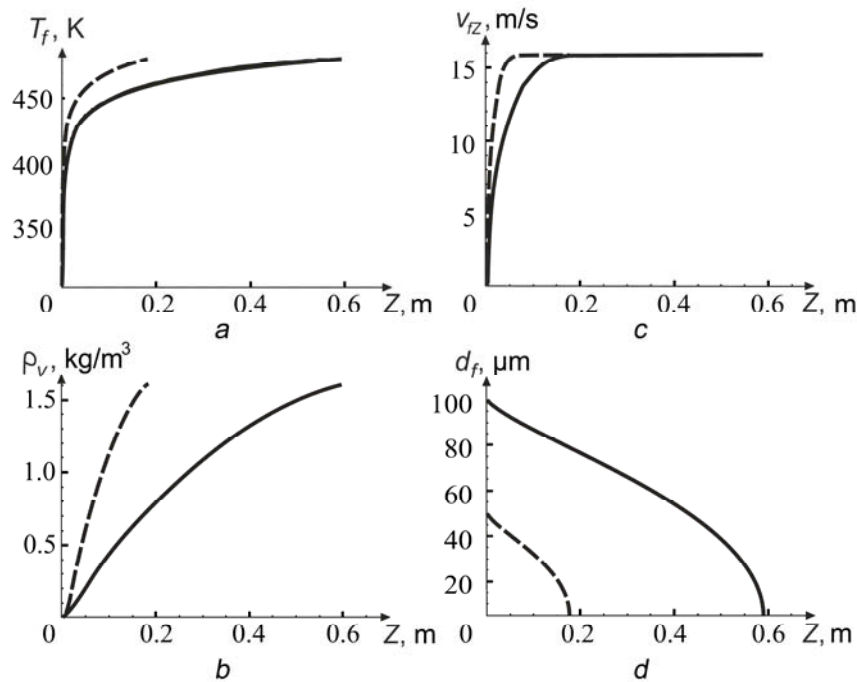


Fig. 6. Results of calculations on formulated model: *a* – temperature of HC droplet T_f , *b* – density of vapour ρ_v , *c* – velocity v_{fz} , *d* – droplet diameter d_f . Dashed line – result for diameter $d_{f0} = 50 \mu\text{m}$, solid line – $d_{f0} = 100 \mu\text{m}$.

There is an analysis of results of the application (instead of α_m) the expressions for the flow of steam on the basis of the molecular-kinetic theory in [8]. It is noted that the kinetic effect on

diesel fuel droplet evaporation are always noticeable despite the fact that evaporation takes place at high pressures. Kinetic models predict a longer evaporation time and higher temperature drop compared to a hydrodynamic model for tiny droplet sizes (about 5 microns). However, this applies to the case of single drop, a constant vapour density in the environment and the lack of gas flow.

Calculated results according to this model for dependence of d_f , ρ_v , v_{fz} and T_f on the channel length (its maximum value is $L = 3$ m) with $d_{f0} = 50$ and $100 \mu\text{m}$ ($n_f = 3 \cdot 10^{10}$ and $0,4 \cdot 10^{10} \text{ 1/m}^3$ respectively), velocity of flow $v = 16$ m/s are shown in Fig. 6. It is obvious that HC droplets evaporate too quickly and do not limit the entire process.

4. CONCLUSIONS

The possibilities of controlling a set of technological parameters (temperature gradient in the reactor channel, flow rates of operating agents, gas concentration) that are available on described installations are important for adjusting technologies for CB producing by furnace method. The obtained species were recognized as CB material and further research will be intended to producing specified CB material.

The results of experimental research will be used for the verification of mathematical models describing the complex physical and chemical processes occurring in the reactor channel while producing CB. Estimation based on given model proves that HC droplets evaporate too quickly and do not limit the entire process. The formulated model can be expanded for obtaining more rigorous view of involved processes. The goal of such research is intimate understanding of the processes taking place in the synthesis of nanoparticles of CB and look for opportunities to control the properties of the resulting product.

Competition between manufacturers of CB as well as of any other raw materials on the world market requires continuous improvement of production technology, aimed not only at the output with improved performance, but also to reducing of the production cost. And applied by us technologies and the approach are an apparent leap toward modern science development and viable manufacturing.

DESIGNATIONS

Z – coordinate on the axis of reactor channel in longitudinal direction with the beginning in the point of HC fuel injection; d_{f0} – initial diameter of HC droplet; d_f – diameter of HC droplet; n_f – concentration of HC droplets; T – temperature of the smoke fumes in the reactor channel, K; ν – gas mixture viscosity; v_{fz} – velocity of moving HC droplets in towards Z-axis; T_f – temperature of HC droplet, K; ρ_{ev} – density of saturated vapour of HC fuel; ρ_v – density of mixture of smoke fumes and HC fuel vapour; ρ_f – density of liquid HC fuel; ν – kinematic viscosity coefficient of the gas mixture; Sh – Sherwood number; ρ_B – density of smoke fumes without HC fuel vapour; Re – Reynolds number; Sc – Schmidt number; Nu – Nusselt number; Pr – Prandtl number; B_T – dimensionless criteria; D – diffusion coefficient; Q_1 – specific bond energy of HC fuel molecule, $842 \cdot 10^3$ J/kg; Q_v – heat of vaporization of HC fuel, $254 \cdot 10^3$ J/kg; α – heat-transfer coefficient for HC fuel; c_{pv} – heat capacity of HC vapour; c_{pf} – heat capacity of liquid HC fuel; λ – molecular heat conductivity of smoke fumes.



REFERENCES

1. IVANOVSKIJ V. I. *Tehnicheskii uglerod. Processy i apparty: Uchebnoe posobie. (Carbon black. Processes and devices: tutorial)*. Omsk: JSC “Tehuglerod”, 2004. 228 p.
2. TESNER P. A. *Obrazovanie ugleroda iz uglevodorodov gazovoi fazy. (Carbon formation from hydrocarbonic gas phase)*. Moscow, “Khimiya”, 1972. 136 p.
3. DONNET J. B. Do we need more research in the carbon black field? *Carbon black world*, 2002.
4. BASS YU. P., GILYAZETDINOV L. P. K raschetu dliny reaktora dlya proizvodstva saji. (For calculation of reactor length for carbon black production). *Journal of Engineering Physics and Thermophysics*, 1964. V. 7, No. 8, p. 114–120.
5. KEL'CEV V.V., TESNER P.A. *Saja: svoistva, proizvodstvo i primeneniye. (Carbon black: properties, manufacture and appliance)* M.-L.: Gostoptehizdat, 1952.
6. SAZHIN S. S. Advanced models of fuel droplet heating and evaporation. *Progress in energy and combustion science*, 2006. Vol. 32, p. 162–214.
7. FISENKO S.P., BRIN A.A., PETRUCHIK A.I. Evaporative cooling of water in a mechanical draft cooling tower. *Int. Journal of Heat and Mass transfer*. 2004. V. 47, p. 165–177.
8. KRYKOV A.P., LEVASHOV V.YU., SAZHIN S.S. Evaporation of diesel fuel droplets: kinetics versus hydrodynamic models. *Int. Journal of Heat and Mass transfer*. 2004. V. 47, p. 2541–2549.



CARBON NANOTUBES AND NANOFIBERS SYNTHESIS BY CHEMICAL VAPOR DEPOSITION IN REACTOR WITH CLOSE GAP BETWEEN CATALYTIC WALLS

P.S. Grinchuk, M.V. Kiyashko

*A.V. Luikov Institute of Heat and Mass Transfer of the NAS of Belarus
P. Brovki street, 220072 – Belarus*

ABSTRACT

Carbon nanotubes and nanofibers have been grown by thermal CVD inside slit-like space between Ni-coated copper walls of a plane flowing reactor under atmospheric pressure at 710 °C. No additional plasma excitation and no other catalyst were used. For comparison, carbon nanomaterials were obtained in a traditional tubular reactor under the same conditions. It is shown greater efficiency of CVD-process in the plane reactor as compared with the tubular one. High hydrocarbon feedstock conversion (70 at.%) and yield of nanostructured carbon (6.9 g/(m²·min)) is achieved in case of the plane reactor, that is by 22–23% more than in the tubular reactor. Carbon materials grown in both reactors have similar microstructures and contain nanofibers and nanotubes of diameter 20–400 nm. Theoretical estimation of gas dynamics and diffusion flow is implemented for tubular and plane configurations of CVD-reactor. Approximate relationship is found between reactor dimensions and physical parameters such as temperature, pressure, flow rate, chemical composition and properties of working gas mixture. It allows to define a simple criterion when the plane geometry of CVD-reactor is more effective than the tubular one under the same conditions. Theoretical analysis reveals that slit-like reactor configuration is more suitable for large-scale carbon nanotubes production as compared with the tubular reactor.

Keywords: thermal CVD, carbon nanotubes, tubular furnace, plane reactor, diffusion

1. INTRODUCTION

Production, examination and application of carbon nanomaterials are perspective and intensively developing directions. Carbon nanotubes (CNT) and nanofibers (CNF) can effectively be used in manufacturing of flat panel displays [1, 2], X-ray sources [3], gas-discharge tubes [4], electrodes for Li-ion batteries [5], etc., and as modifying admixtures upon manufacturing of polymeric materials, varnishes, dyes, resins [6]. Furthermore, for some purposes it is desirable to obtain a CNT/CNF layer on a flat substrate [7, 8]. One of the most widespread methods of producing carbon nanomaterials is a chemical vapour deposition (CVD) in the presence of a catalytic agent (Ni, Fe, Co and compounds thereof). This process can be stimulated by plasma (Plasma Enhanced CVD) [9] or other means [10]. However, to decrease the cost of a gained material, it is better and simpler to synthesize carbon nanostructures by means of a thermoresistive heating of the reactor (thermal CVD). Thermal CVD involves fewer controlling parameters than PECVD, though in general a large number of characteristics have an influence on carbon nanomaterials synthesis, such as temperature, pressure, feedstock composition, carrier gas type, catalyst, support, surface morphology.

Temperature plays a key role in thermal CVD. Depending on other parameters, there is an optimal temperature for high yield and quality of CNTs [11, 12]. In [11] CNTs were grown from ethanol on Fe-coated Si/Al₂O₃ support under the pressure 10 mm Hg at the temperatures between 580 and 805 °C, the temperature 655 °C being the optimal one. At the lower temperature, the catalyst nanoparticles size was bigger and their density was lower. So grown CNTs were short and sparse. Elevating the temperature above 655 °C also resulted in shorter and more sparse CNTs and an increased formation of amorphous carbon. In another work

[12], where Fe-Mo-MgO powder catalyst was used to grow CNTs from ethanol under atmospheric pressure, the yield of carbon permanently increased with the temperature raising from 750 to 950 °C. But the optimal temperature was 900 °C because of the significant formation of amorphous carbon at higher temperature. As a rule, multi-walled CNTs (MWCNTs) and CNFs with the diameter of few tens nm grow at lower temperatures, while at higher temperatures single-walled CNTs (SWCNTs) of 5–10 nm in diameter are formed [13].

The structure and yield of CNTs are strongly affected by the gas pressure. At low pressure the CNTs have completely hollow cores, whereas at high one the CNTs have a bamboo structure [14]. The density of the compartments in the bamboo-structured CNTs increases with the increase of the gas pressure.

Gaseous hydrocarbons are often used as a feedstock. The optimum experimental conditions vary for different gas precursors because of difference in mechanisms and kinetics of hydrocarbon pyrolysis. Methane molecule is very stable, so high temperature (> 900 °C) is required to decompose it on a catalyst, whereas ethanol starts self-decomposing at temperatures near 800 °C [15]. Linear hydrocarbons such as methane, ethylene, acetylene thermally decompose into atomic carbons or linear dimers/trimers of carbon, and generally produce straight hollow CNTs. Cyclic hydrocarbons such as benzene, xylene, cyclohexane produce relatively curved CNTs with the tube walls often bridged inside [16].

The main objective of the present research is to find out a role of the reactor geomtric influence on CVD efficiency and to improve carbon nanomaterials production on a flat catalytic surface. The classical reactor for thermal CVD represents a heated quartz tube through which a mixture of hydrocarbonic and inertial gases flow. CNT and CNF are formed on a catalyst placed within a tube. Wide application of reactors with circular cross-section is caused by the historical reasons (tubular reactors are used for a long time in different fields of researches and manufactures), simplicity of thermal and gas-dynamic modelling and calculations, easiness of manufacturing [17]. However, the cylindrical reactor has some deficiencies, especially manifested in the case when carbon nanomaterials are required on a flat substrate [17, 18]. It is related to the small ratio of a deposition surface area (S) and a reactionary volume (V). Because of this, only a small part of reactor volume is effectively used. As a result, longer periods of time for reactor filling and purging as well as greater flow rates are required. Only a small part of the hydrocarbonic gas participates in carbon deposition on the surface. It can result not only in inefficient use of raw materials, but also in formation of undesirable byproducts in reactor volume, including amorphous carbon polluting grown nanomaterials. Improving relationship (S/V) and, hence, efficiency of CVD-process is possible by replacement of the circular cross-section shape of the reactor with the rectangular cross-section [17, 19]. Hydrocarbon molecules transportation to a catalytic surface is more effective in the flat reactor with a close gap between its walls. Surface reactions should be more intensive than in the tubular reactor, and volumetric reactions should be suppressed.

2. EXPERIMENTAL

An experimental installation with a slit-like construction (Fig. 1) has been made to investigate characteristics of carbon growth in the reactor with the rectangular cross-section. Two identical copper plates (1) with dimensions 8×78×504 mm are nicked galvanically. The average thickness of the Ni-coating (2) is about 5 μm. Plates are fixed plane-parallel at the distance of 6 mm by means of a copper spacer (3) along the plates perimeter. Gas injection tube (4) and exhaust tube (5) pass through the spacer. High-temperature gaskets are arranged between the spacer and each of the plates to prevent inleakage of environmental air. Gas mixture is fed into the gap between the plates through triangular channel to uniformly distribute gas flow inside the reactor. Heating is carried out by electroresistance heaters (6).

All this construction is encapsulated into heat-insulating shell (7) and then into a case (8) to which each plate is attached with screws (9). At the inlet and the outlet of the reactor, thermocouples (10) are installed to measure the plate temperature. The differential pressure unit (11) measures a pressure drop between the inlet and the outlet of the reactor. The gas analyser (12) continuously detects hydrogen concentration at the outlet. The computerised control system supports temperature regime and flow rates, and records measured parameters.

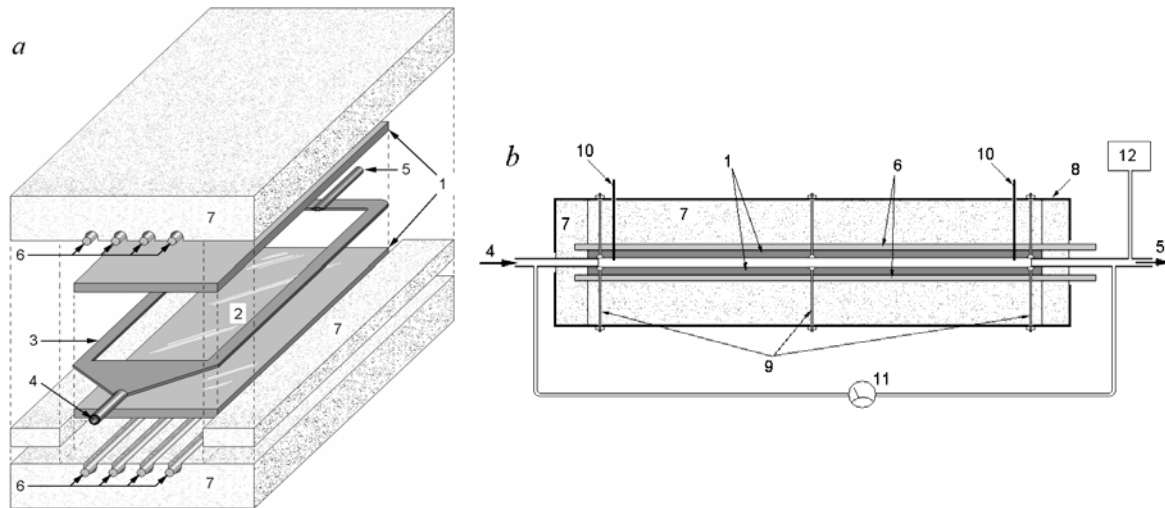


Fig. 1. The schematic drawing of the slit-like CVD-reactor: *a* – the three-dimensional outline; *b* – the longitudinal section. 1 – copper plates; 2 – nickel coat; 3 – spacer; 4 – gas inlet; 5 – exhaust; 6 – heaters; 7 – heat insulation; 8 – case; 9 – screws; 10 – thermocouples; 11 – differential pressure unit; 12 – gas analyser

Another investigations were conducted with the tubular reactor (Fig. 2) to compare CVD effects inside the reactors with rectangular and circular cross-sections. The reactor is a quartz tube of 0.8 m lengthwise and 0.112 m I. D. For more uniform heating, the tube is entirely disposed inside the furnace, and its ends are closed by the removable heat-insulated covers equipped with gas fittings. For an adequate comparison of carbon nanomaterials formation in reactors of different geometry, one of the same plates used in the slit-like reactor was placed inside the quartz tube. The plate was installed in a horizontal plane at the centre of the tube with a nickel coat upwards by means of the attached legs. In the same manner as in the previous case, the pressure drop between the inlet and the outlet of the reactor and the hydrogen concentration in an exhaust gas mixture were measured. Plate temperature near the reactor inlet was controlled by the same automatic system used for the slit-like reactor.

In both cases CVD-process was carried out at the atmospheric pressure. The temperature of a plate was maintained at 710 °C. Standard K-type thermocouples were mounted inside blind holes in the plates to control the temperature. The reactor was heated under N₂ flowing. O₂ concentration measured by gas analyzer Testo-350XL before raw material feeding did not exceed 0.1 vol.%. Gaseous hydrocarbon mixture (household fuel gas) diluted with nitrogen was used as the feedstock. As the thermal self-decomposing of used hydrocarbon mixture is accompanied by precipitation of polycyclic hydrocarbons at temperatures > 720 °C [18] and as the intensity of CVD increases with the temperature raising, we chose temperature 710 °C for the experiments. The flow rates of N₂ and hydrocarbon mixture were maintained at the fixed values of 1.5 slm and 0.5 slm respectively by means of massflowcontrollers Omega FMA-5400. During the experiments, gas samples from the inlet and the outlet of the reactor were taken and analyzed using gas chromatograph Agilent GC-7890A. H₂ concentration in exhaust gases was continuously measured using gas analyzer Hitech Instruments K1550.

Hydrocarbon feeding duration was 42 min in the experiment with the slit-like reactor and 55 min in the experiment with the tubular one. Carbon material was weighed and analyzed using scanning electron microscope (SEM) Carl Zeiss Supra-55.

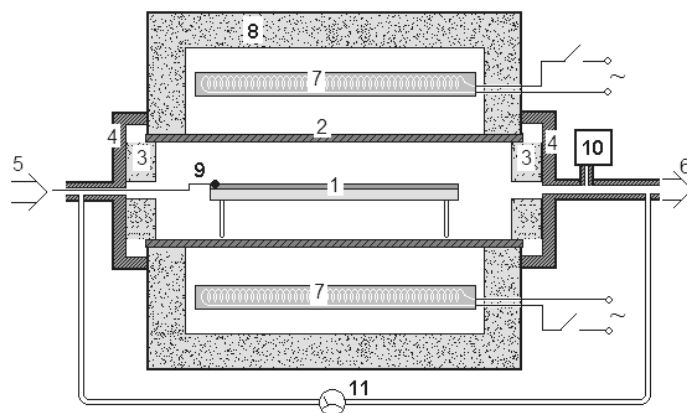


Fig. 2. The schematic drawing of the tubular reactor. 1 – Ni-coated plate; 2 – quartz tube; 3 – heat-insulating insertions; 4 – covers; 5 – gas inlet; 6 – exhaust; 7 – calefactores; 8 – furnace lining; 9 – thermocouple; 10 – gas analyser; 11 – differential pressure unit

Growth of temperatures, pressure drop and H_2 concentration during hydrocarbon feeding are shown in Fig. 3 for experiments with both slit-like (*a*) and tubular (*b*) reactors. H_2 concentration dips are caused by sampling of gas for chromatographic analysis. Periodical temperature oscillations are caused by turning the heaters on and off to maintain the given regime. In the slit-like reactor the temperature at the outlet was controlled, while the temperature at the inlet was measured to determine nonisothermality along the plates. For the cylindrical reactor, we have earlier found [18] that the difference between plate temperature at the outlet and at the inlet do not exceed $10\text{ }^\circ\text{C}$. The main difference between the experiments carried out in the slit-like and in the tubular reactors is a rapid pressure growth in the slit-like reactor after a certain period. It is caused by filling up the space between plates with carbon and decreasing of the reactor flow area. In the cylindrical reactor the change in flow area is negligible, so no rapid pressure growth is observed.

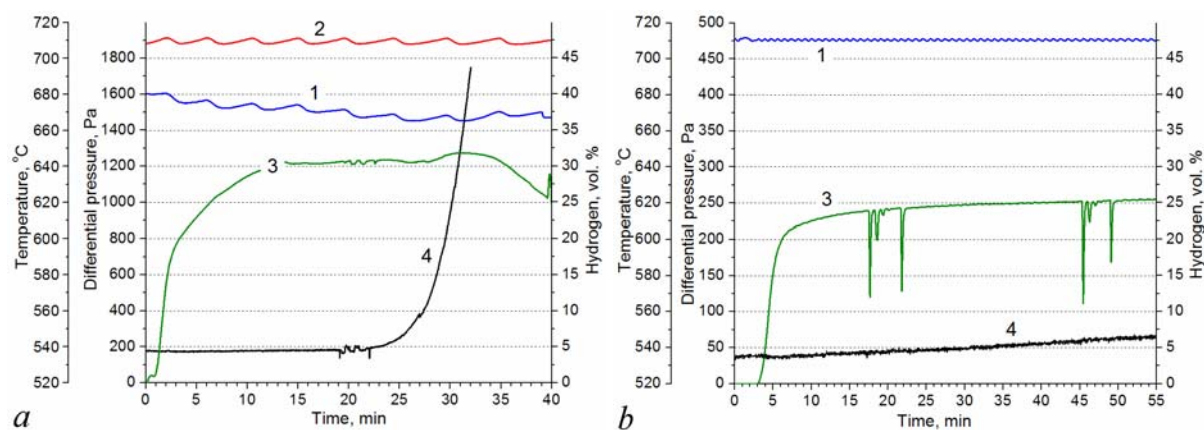


Fig. 3. Temperature of a plate nearby the reactor inlet (1) and the outlet (2), hydrogen concentration (3) and pressure drop (4): *a* – in the slit-like reactor; *b* – in the tubular reactor

3. RESULTS AND DISCUSSION

3.1. Experimental results

A friable carbon layer was formed upon nickel surfaces in either of the experiments. In a case with the slit-like reactor carbon material completely filled the space between plates from the inlet to approximately the middle of the plates. Towards the outlet, carbon layer became thinner on both plates. However, it remained uniform in a direction across the plates. At the outlet the layer almost disappeared. Such surface distribution of carbon indicates that the feedstock was intensively consumed while flowing through the reactor, and the gas mixture was carbon depleted at the outlet. The zinc-coated heads of all screws were pure that means no formation of carbon particles in the reactor volume. In a case with the tubular reactor, carbon was distributed non-uniformly on the substrate as lengthways so across, but no tendency was observed. Authors of [20] found out clear tendency in distribution of CNTs on support in the radial direction of cylindrical reactor. CNTs count was maximum in the center and decreased towards the reactor walls. This distribution strongly correlated with the gas velocities profile. Probably, we do not see such a tendency because of very low gas velocity in our reactor (~ 0.01 m/s that is by two orders less than gas velocity in [20]).

It was not revealed any basic difference in a microstructure of the carbon material grown in the slit-like reactor and in the tubular one. Fig. 4 shows SEM images of carbon structures, all of them being typical both for the slit-like and for the tubular reactor. Carbon material contained two general fractions. The first fraction consisted mainly of fibers of 100–400 nm in diameter with a rough outer surface (Fig. 4 *a–c*). Some of these fibers had junctions (Fig. 4 *c*). Similar junction-like structures were described in [21], where their formation was caused by simultaneous carbon growth upon different crystallographic planes of Ni-Cu alloy particles. Since we used Ni-coated copper plates, Ni-Cu particles may be a probable reason of formation of such joined carbon fibers. The second observed fraction was CNTs and CNFs of 20–100 nm in diameter (Fig. 4 *d, e*).

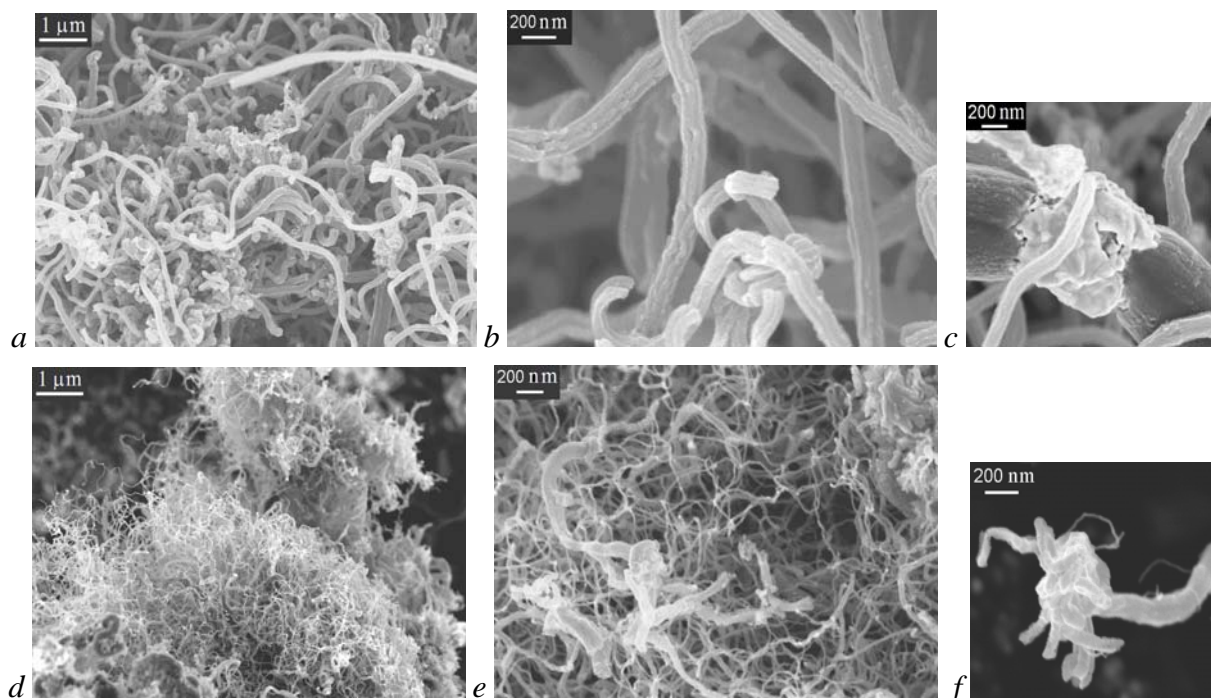


Fig. 4. SEM images of grown carbon materials

A lot of fibers of different diameters had branched tips (Fig. 4 f). Most probably, it is because of the presence of catalytic particles at the fibers tips that initiated secondary growth of thinner carbon fibers. Very similar branched CNFs were grown in [22] from acetylene on Ni-coated silicon substrates at 650 °C. The controlled growth of branched CNFs via PECVD involved four stages, including the initial growth of CNFs, coating CNFs with TiO₂, hydrogen plasma etching, and finally subsequent growth of CNFs.

The main quantitative experimental results are presented in Fig. 5 and in Table 1. The chromatographic analysis shows more hydrogen and less methane and ethane in gas flowing out of the slit-like reactor than in gas flowing out of the tubular one. In addition, ethylene is detected in the exhaust gas mixture out of the cylindrical reactor and is absent in a case of the slit-like reactor. All these findings indicate higher feedstock conversion into solid carbon in the slit-like reactor in comparison with the tubular one. Atomic percent of carbon yield is calculated on the basis of chromatographic analysis data. In case of the slit-like reactor the yield is 70 at.%, and for the tubular reactor it is 56 at.%. These absolute values differ by 23%. The same difference (22% of value) is observed in the specific productivity i.e. mass of the formed carbon nanomaterials per unit time upon unit area of a catalytic surface. For comparison, specific productivity of 4.8 g/(m²·min) was reported in [23] for CNTs grown on mechanically treated nickel via thermal CVD from polyethylene at 800 °C. Maximum specific productivity of experimental setup in [24] for synthesis of CNTs on stainless steel via low-temperature PECVD was 5.5 g/(m²·min).

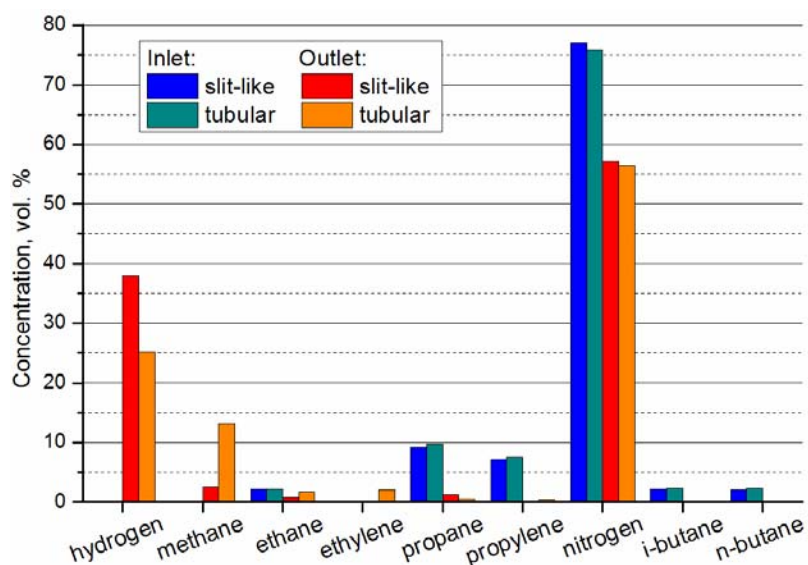


Fig. 5. Composition of input and exhaust gas mixture in both experiments

Table 1. Geometrics and experimental results for both reactors

	Slit-like	Tubular
Reactor cross-sectional area, cm ²	4.2	98.5
Reactor volume, l	0.2	7.0
The relation of a catalytic area to a total reactor volume S/V, m ⁻¹	336	6
Carbon yield, at. %	70	56
Specific productivity, g/(m ² ·min)	6.9	5.4

3.2. Theoretical estimation and analysis

The efficiency of solid carbon formation on a catalytic substrate depends on the transport of raw materials molecules towards the catalyst. In the laminar conditions, it is determined by a diffusion flow of these molecules towards the substrate. A theoretical estimate can be implemented for the slit-like reactor with the channel having a length L , a width B and an altitude H , the surface of two wide walls being coated by a catalyst and two other narrow walls being free from the catalyst (Fig. 6 a). In this estimation, we will consider only diffusion isothermal transport, and will not take into account the influence of chemical reactions on physical parameters. The characteristic residence time of a gaseous mixture in the reactor is

$$t_g = \frac{L}{U}, \quad (1)$$

where U (m/s) is the average gas stream velocity. Subject to the Clapeyron equation, it is equal to

$$U = \frac{GRT}{pM_{mix} S_{cross}} \frac{1}{S_{cross}}, \quad (2)$$

where G (kg/s) is a mass flow rate of gas mixture, M_{mix} (kg/mol) is an average molar mass of mixture, p (Pa) is a pressure, T (K) is a temperature, R (J/(mol·K)) is the universal gas constant, S_{cross} (m²) is the cross-sectional area of the reactor channel.

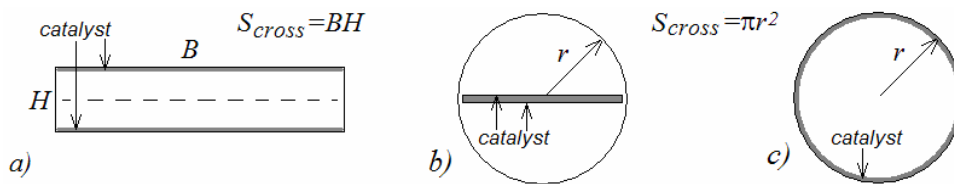


Fig. 6. Cross-sections of reactors and variants of catalyst disposition

The characteristic time of carbonaceous molecules diffusion [25] from the central plane of the channel towards the catalytic walls of the reactor is

$$t_d = \frac{(H/2)^2}{D_c}, \quad (3)$$

where D_c (m²/s) is the diffusion constant in the gas mixture. The necessary requirement that carbonaceous molecules had enough time to attain the substrate while gas flowing along the full length of the reactor is $t_d \ll t_r$, or

$$\frac{1}{4} \frac{H}{LB} \ll \frac{pM_{mix} D_c}{GRT}. \quad (4)$$

At the conditions of experiment in the slit-like reactor the inequality (4) is equivalent to the criterion $H \ll 0.1$ m, the specified value being determined within the accuracy of an order. Since the actual clearance between plates is on some orders less than this value, the basic part of raw materials is consumed much earlier than the gas mixture reaches the outlet of the reactor. In other words, the clearance can be increased several times without significant losses of efficiency of feedstock use. Moreover, the reactor productivity can be increased just against the probability of longer carbon deposition until complete filling the inner reactor space with carbon nanomaterials.

Transport of hydrocarbons towards the flat substrate in the tubular reactor can be analysed similarly. Optimum alternative for carbon deposition corresponds to the arrangement of the substrate at the centre of the tube, the substrate width being equal to the double radius r of the tube and the catalytic coating being present on both surfaces of the substrate (Fig. 6 *b*). As the mean-square distance between the substrate and the tube wall along the substrate normal is equal to $2/3r^2$, expressions (3) and (4) will be substituted accordingly for

$$t_d = \frac{2}{3} \frac{r^2}{D_c}, \quad (5)$$

$$\frac{2}{3\pi L} \ll \frac{pM_{mix}D_c}{GRT}. \quad (6)$$

Comparisons (4) and (6) allow to conclude that, under equal conditions of deposition (equal values in the right sides of inequalities) and equal length of the reactor, the slit-like geometry is more effective from the point of view of raw materials transport to the catalyst than the cylindrical one if the following condition is satisfied

$$\frac{B}{H} > \frac{3\pi}{8} \approx 1. \quad (7)$$

The slit-like geometry is less effective when the inverse inequality is carried out. It can be seen that the condition (7) is true whenever the channel altitude (H) is less than its width (B).

For this case, the criterion (7) seems trivial, however it is necessary to note that its aspect depends not only on reactor geometry, but also on the disposition of a catalyst within it. As an example, we will compare the discussed above slit-like reactor and the cylindrical reactor with the catalyst deposited uniformly on its inner wall (Fig. 6 *c*). The diffusion time in such reactor is

$$t_d = \frac{r^2}{\pi^2 D_c} \quad (8)$$

and then the expression (7) is written as

$$\frac{B}{H} > \frac{\pi^3}{4} \approx 8. \quad (9)$$

In other words, the transport of gaseous raw materials towards the catalyst in the cylindrical reactor with a catalytic inner wall is more effective than one in the cylindrical reactor with a flat catalytic substrate. Similar comparative criteria can be analogously created for other reactors and substrate configurations.

However, the examined conditions for a good transport of carbonaceous molecules towards a catalyst are not the only requirements for an effective carbon deposition and nanomaterials growth. Besides a catalytic hydrocarbon pyrolysis on a surface, there are undesirable pyrolysis reactions in the reactor volume. The contribution of the surface reactions to the total process of pyrolysis is estimated by the ratio (S/V) of the catalytic area to the reactionary volume. For the slit-like reactor, per a unit of its length

$$\frac{S}{V} = \frac{2B}{BH} = \frac{2}{H}. \quad (10)$$

In the above case of a flat substrate in the tubular reactor



$$\frac{S}{V} = \frac{4r}{\pi r^2} = \frac{4}{\pi r} \quad (11)$$

i.e. this ratio is inversely proportional to the radius of the reactor tube. Upon increasing the reactor radius with the same parameters of deposition, transit and diffusion times increase simultaneously. The transport of raw materials towards the catalyst is retarded, and the velocity of the gas stream in the reactor decreases also, therefore the requirement (6) is carried out in the same degree, as for the reactor with a small radius. But the retarding of the diffusion flow upon increasing the reactor radius raises the probability of the fact that hydrocarbon molecules react before they will attain the catalyst. Thus, besides the fulfilment of the conditions (4), (6) it is necessary to provide an enough great value (S/V) for the effective conversion of raw materials into the solid carbon on the catalyst.

The productivity improvement of the installation is related, first of all, to extending of the catalytic surface. When carbon nanomaterials are required on a flat substrate, the catalytic surface can be expanded by increasing the length (L) of the catalytic plate and by increasing its width (B). The first way becomes complicated by feedstock consuming upon its transport along the reactor. This requires distributed along the reactor supplying of raw materials and enlarges the linear gabarits of the installation. The increase of the catalytic plates width is less inconvenient, but for the tubular reactor it means increase of its radius, and consequently, decrease of the ratio (S/V). For the slit-like reactor, according to (10), this ratio does not depend on the choice of the length and width of plates and this provides the possibility to create package and effective units.

4. CONCLUSIONS

Experiments for producing carbon nanostructures via thermal CVD in a slit-like reactor and in a tubular one were carried out. The carbon yield in the slit-like reactor was 70 at.%, and the productivity was 6.9 g/(m²·min) that is by 22–23% more than in the tubular reactor under the same conditions. In the slit-like reactor the hydrocarbon raw materials are consumed before the gas mixture reaches the end of the reactor, and the space between catalytic surfaces is filled with carbon material. The approximate estimation has shown that with the given physical properties, the distance between catalytic surfaces can be increased several times, that should raise efficiency of CVD-process in the slit-like reactor. It is shown that the slit-like reactor is more suitable for large-scale production of carbon nanomaterials than the classical tubular one is.

ACKNOWLEDGMENTS

Authors express thanks to S.I. Shabunya and V.I. Kalinin, Members of the A.V. Luikov Institute of Heat and Mass Transfer of the NAS of Belarus, for valuable ideas and suggestions used in this research.

REFERENCES

1. McCARTHY, M.A.; LIU, B.; DONOGHUE, E.P.; KRAVCHENKO, I.; KIM, D.Y.; SO, F.; RINZLER, A.G. Low-voltage, low-power, organic light-emitting transistors for active matrix displays. *Science*, 2011, Vol. 332, No. 6029, p. 570–573.
2. ZHANG, Yu; DENG, S. Z.; XU, N. S.; CHEN, Jun. Fully sealed carbon nanotube flat-panel light source and its application as thin film transistor–liquid-crystal display



- backlight. *Journal of Vacuum Science & Technology B*, 2008, Vol. 26, Iss. 3, p. 1033–1037.
3. HYUN JIN KIM; JUN MOK HA; SUNG HWAN HEO; SUNG OH CHO. Small-sized flat-tip CNT emitters for miniaturized X-ray tubes. *Journal of Nanomaterials*, 2012, Vol. 2012, Article ID 854602.
 4. ROSEN, R.; SIMENDINGER, W.; DEBBAULT, C.; SHIMODA, H.; FLEMING, L.; STONER, B.; ZHOU, O. Application of carbon nanotubes as electrodes in gas discharge tubes. *Applied Physics Letters*, 2000, No. 76, p. 1668.
 5. EVANOFF, K.; BENSON, J.; SCHAUER, M.; KOVALENKO, I.; LASHMORE, D.; JUD READY, W.; YUSHIN, G. Ultra strong silicon-coated carbon nanotube nonwoven fabric as a multifunctional lithium-ion battery anode. *ACS Nano*, 2012, Vol. 6, Iss. 11, p. 9837–9845.
 6. SABU, Thomas; RANIMOL, Stephen; editors. *Rubber nanocomposites: preparation, properties, and applications*. Singapore: John Wiley & Sons (Asia). 2010. 705 p. ISBN 978-0-470-82345-3.
 7. SANGWAN, V. K.; BALLAROTTO, V. W.; HINES, D. R.; FUHRER, M. S.; WILLIAMS, E. D. Controlled growth, patterning and placement of carbon nanotube thin films. *Solid-State Electronics*, 2010, Vol. 54, Iss. 10, p. 1204–1210.
 8. XUE, Wei; CUI, Tianhong. Thin-film transistors with controllable mobilities based on layer-by-layer self-assembled carbon nanotube composites. *Solid-State Electronics*, 2009, Vol. 53, Iss. 9, p. 1050–1055.
 9. SAN HUA LIM; ZHIQIANG LUO; ZE XIANG SHEN; JIANYI LIN. Plasma-assisted synthesis of carbon nanotubes. *Nanoscale Research Letters*, 2010, Vol. 5, p. 1377–1386.
 10. LIN, Chao Hsun; CHANG, Hui Lin; HSU, Chih Ming; LO, An Ya; KUO, CHENG Tzu. The role of nitrogen in carbon nanotube formation. *Diamond Related Materials*, 2003, Vol. 12, p. 1851–1857.
 11. GOLABADI, M.; AJEIAN, R.; NAKHAIEBADRABADI, M. Study of Temperature effect on Synthesis of Carbon Nanotubes by Iron Catalyst and Ethanol vapor by Chemical Vapor Deposition (CVD). ICNS4 2012. Proceedings of the 4th International Conference on Nanostructures. Iran, Kish Island: Sharif Institute of Technology. 2012 March 12–14.
 12. SETAREH MONSHI TOUSSI; A. FAKHRU’L-RAZI; A. LUQMAN CHUAH; A.R. SURAYA. Effect of synthesis condition on the growth of SWCNTs via catalytic chemical vapour deposition. *Sains Malaysiana*, 2011, Vol. 40 (3), p. 197–201.
 13. HARRIS, Peter J.F. *Carbon nanotube science. Synthesis, properties and applications*. Cambridge: Cambridge University Press. 2009. 301 p. ISBN-13 978-0-511-51691-7.
 14. LI, W. Z.; WEN, J. G.; TU, Y.; REN, Z. F. Effect of gas pressure on the growth and structure of carbon nanotubes by chemical vapor deposition. *Applied Physics A*, 2001, Vol. 73, p. 259–264.
 15. KUMAR, M.; ANDO Y. Chemical vapor deposition of carbon nanotubes: a review on growth mechanism and mass production. *Journal of Nanoscience and Nanotechnology*, 2010, Vol. 10, p. 3739–3758.
 16. CHANDRA, B. *Synthesis and electronic transport in known chirality single wall carbon nanotubes*. Proquest, Umi Dissertation Publishing. 2009. 154 p. ISBN-13 9781244081291.
 17. SHAH, T.K.; GARDNER, S.H.; ALBERDING, M.R.; MALECKY, H.C. CNT-infused carbon fiber materials and process therefor. Patent US 20110168089A1. Assignee Lockheed Martin Corporation, Bethesda, MD. Patent Application Publication. 2011. 11 p. Int. Cl. B05C 13/02, B82Y 30/00, U.S. Cl. 118/620, 118/500, 977/843.



18. KIYASHKO, M.V.; GRINCHUK, P.S. Obtaining of nanostructured carbon materials on catalytic surfaces by CVD. Experimental results for the reactor of cylindrical geometry. Preprint No. 3. Minsk: A. V. Luikov Institute of Heat and Mass Transfer of the NAS of Belarus, 2012. 53 p.
19. ZHDANOK, S.A.; BUYAKOV, I.F.; KRAUKLIS, A.V.; LAKTYUSHIN, A.N.; BORISEVICH, K. O.; KIYASHKO M. V. Obtaining carbon nanomaterials in a plant with a plasma generator and a working zone of rectangular cross section. *Journal of Engineering Physics and Thermophysics*, 2010, Vol. 83, Iss. 1, p. 6–9.
20. ILLAYATHAMBI KUNADIAN, RODNEY ANDREWS, DALI QIAN, M. PINAR MENGUC. Growth kinetics of MWCNTs synthesized by a continuous-feed CVD method. *Carbon*, 2009, Vol. 47, p. 384–395.
21. CHESNOKOV, V. V.; BUYANOV, R. A. Characteristics of formation of carbon nanofilaments with different crystallographic structure from hydrocarbons on catalysts containing metals of Fe group. *Critical technologies. Membranes (Russian Academy of Sciences)*, 2005, Vol. 4 (28), p. 75–79.
22. ABDI, Y.; MOHAJERZADEH, S.; KOOHSHORKHI, J.; ROBERTSON, M. D.; ANDREI C. M. A plasma enhanced chemical vapor deposition process to achieve branched carbon nanotubes. *Carbon*, 2008, Vol. 46, p. 1611–1625.
23. KUKOVITSKY, E.F.; L'VOV, S.G.; SAINOV, N.A.; SHUSTOV, V.A. CVD growth of carbon nanotube films on nickel substrates. *Applied Surface Science*, 2003, Vol. 215, p. 201–208.
24. ZHDANOK, S.A.; BUYAKOV, I.F.; KRAUKLIS, A.V.; BORISEVICH, K.O. Transfer processes in low-temperature plasma on the formation of carbon nanostructures on the steel surface of a reactor as a result of the decomposition of hydrocarbons in the low-temperature plasma. 2. Modernization of the experimental setup, search for optimum operating conditions, determination of additional controlling factors of the process. *Journal of Engineering Physics and Thermophysics*, 2009, Vol. 82, Iss. 3, p. 414–418.
25. KRAINOV, V.P. *Qualitative Methods in Physical Kinetics and Hydrodynamics*. New York: American Institute of Physics. 1992. 224 p. ISBN-10 0-88318-953-4.



PROPERTIES OF NiO THIN FILMS PREPARED BY CHEMICAL SPRAY PYROLYSIS

J. Soon, M. Krunkas, V. Mikli
Tallinn University of Technology
Department of Materials Science
Ehitajate tee 5, 19086 – Estonia

ABSTRACT

A simple and inexpensive spray pyrolysis technique was used to deposit NiO thin films from $\text{NiCl}_2 \cdot 6\text{H}_2\text{O}$ or $\text{Ni}(\text{CH}_3\text{COO})_2 \cdot 4\text{H}_2\text{O}$ solutions on preheated glass substrates placed onto soldered tin bath at temperatures of 400–550 °C. NiO thin films synthesized by spray pyrolysis could be used as stable photocathode material for dye-sensitized photoelectrochemical cells. The precursor salt was dissolved in deionized water or in mixture of alcohol (ethanol or isopropanol) and deionized water. All films were deposited using precursor concentration of 0.05 M and spraying rate of ~1 ml/min. The effect of the precursor solution and growth temperature on the NiO thin film structural, morphological and optical properties was studied using X-ray diffraction (XRD), scanning electron microscopy (SEM), energy dispersive X-ray spectroscopy (EDX) and optical spectroscopy (UV-VIS) techniques. According to XRD, NiO films possess the cubic bunsenite crystal structure, crystallites show preferential orientation along (111) plane parallel to the substrate independent of the growth temperature and precursor. The increase of the bath temperature from 450 °C to 550 °C decreases the film thickness from 1.1 to 0.05 μm , and increases crystallite size from 4 to 25 nm. According to SEM, NiO films from nickel acetate solution have significantly smoother surface than films prepared from nickel chloride solutions. NiO films grown at 400 °C from nickel chloride solution contain 3 at.% of chlorine, at bath temperature of 550 °C chlorine concentration in the film is below 1 at.%. Optical transparency of NiO films is 70% in visible spectral region for the films obtained at tin bath temperature around 500 °C. The optical band gap of the NiO films sprayed from nickel acetate solution changes from 3.41 to 4.14 eV increasing the deposition temperature from 400 to 550 °C.

Keywords: Nickel oxide, spray pyrolysis, Thin films, XRD, SEM, UV-VIS

1. INTRODUCTION

Nickel oxide is p-type semiconductor having wide band gap from 3.5 to 4.0 eV [1]. It crystallizes in a rocksalt structure and has excellent durability and electrochemical stability [2]. Nickel oxide thin films are very useful for many applications such as active material in gas sensors, anode in oxygen fuel cells, buffer layer in organic solar cells, electrochromic material for smart windows and cathode for dye-sensitized photoelectrochemical cells [2–3]. In present work, the NiO films were synthesized by chemical spray pyrolysis. This method has found to be an efficient and cost effective to produce large area thin films [1–2]. Studies have reported that spray parameters like substrate temperature, precursor type, concentration of precursor and solution flow rate have strong influence on deposited NiO film morphological, structural and optical properties [1–11]. In present study, we report results on formation of compact and transparent NiO thin films by chemical spray pyrolysis.

NiO thin films have been sprayed onto glass substrates using nickel chloride and nickel acetate as starting chemicals. Influence of the type of precursor and deposition temperature on the structural, optical and morphological properties of sprayed NiO film has been investigated and discussed.

2. METHODOLOGY

Nickel acetate tetrahydrate [$\text{Ni}(\text{CH}_3\text{COO})_2 \cdot 4\text{H}_2\text{O}$, Merck, 98%] and nickel chloride hexahydrate [$\text{NiCl}_2 \cdot 6\text{H}_2\text{O}$, Merck, 99.9%] were used as precursor to deposit NiO films. The concentration of

nickel salt in the spraying solution was kept constantly 0.05 mol/L. The volume of the solution for each deposition was 50 ml and the rate of spray was ~1ml/min. The prepared solution was sprayed onto cleaned pre-heated glass substrates with the size of 20×15×1 mm using compressed air as carrier gas. Glass substrates were placed onto molten tin bath, the bath temperature was varied from 400 to 550 °C with step of 50 °C. The growth temperature of NiO film was about 100 °C lower than tin bath temperature.

The sprayed films were characterized by using Rigaku Ultima IV diffractometer (XRD) with monochromatic Cu K α radiation ($\lambda = 0.1540$ nm). Total optical transmission of the prepared NiO films were recorded over the wavelength range from 200 to 800 nm using the Jasco V-670 UV-VIS-NIR spectrophotometer equipped with an integrating sphere. Scanning electron microscope (Zeiss HR FESEM Ultra 55) was used to analyze the surface morphology and the thickness of the sprayed NiO films.

3. RESULTS AND DISCUSSIONS

3.1. The properties of NiO thin films deposited from NiCl₂·6H₂O aqueous solution

Fig. 1 presents the photo of NiO films deposited from nickel chloride solution at different temperatures and it can be seen that films sprayed at 400 °C and 450 °C tin bath temperature are black-brown in colour. It has been found in earlier studies that NiO has not the expected translucent colour due to the formation of the Ni³⁺ ions in the film [4, 5].

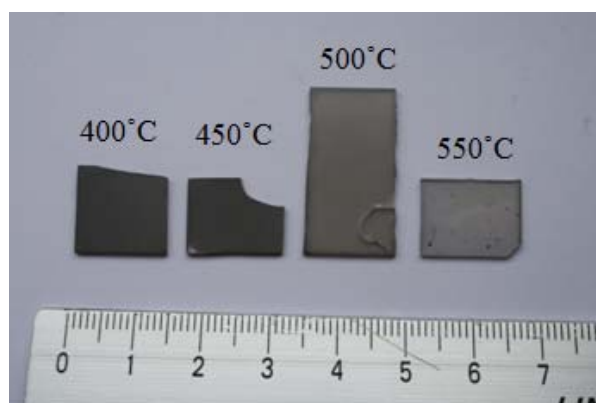


Fig. 1. Photo of NiO films deposited from NiCl₂·6H₂O aqueous solution at different tin bath temperatures $T_{Sn} = 400\text{--}550$ °C

According to XRD analysis results in Fig. 2 all the diffraction peaks belong to the bunsenite with cubic crystal structure of NiO (JCPDS 00-047-1049). No other crystalline phases were detected. The ratio of the intensities of the (111) and (200) diffraction peaks ($I_{(111)}/I_{(200)}$) varies from 16 to 2 for the films deposited at temperatures 400 to 550 °C. For the powder reference, the $I_{(111)}/I_{(200)} = 0.6$. These results show that all NiO films deposited from NiCl₂ solution show the preferential orientation of the crystallites along the (111) plane parallel to the substrate. The decrease of the intensity of diffraction peaks at higher growth temperatures indicates the decrease in the film thickness as also confirmed by the SEM analysis (Table 1).

Table 1. NiO thin film optical and crystal properties depending on tin bath temperature. (Crystallite size D , preferred orientation of NiO crystallites, film thickness d , total optical transmittance TT at $\lambda = 500$ nm and optical band-gap E_g). The films were deposited using two precursors: $\text{NiCl}_2 \cdot 6\text{H}_2\text{O}$ and $\text{Ni}(\text{CH}_3\text{COO})_2 \cdot 4\text{H}_2\text{O}$. The $[\text{Ni}]^{2+}$ concentration in the solution was 0.05 mol/l

Precursor salt	Object name	T_{Sn} , °C	D , nm	Orientation	t , nm	TT , %	E_g , eV
NiCl_2	JP-5-2	400	16	(111)	610	20	3.43
	JP-5-3	450	16	(111)	600	20	3.45
	JP-5-4	500	20	(111)	Not measured	50	3.59
	JP-5-5	550	26	(111)	50	60	3.66
$\text{Ni}(\text{CH}_3\text{COO})_2$	JP-4-2	400	4	Not orientated	Not measured	20	3.38
	JP-4-3	450	10	(200)	1000	20	3.51
	JP-4-4	500	16	Not orientated	Not measured	50	3.74
	JP-4-5	550	10	Weak (111)	75	60	4.14

The mean crystallite size was calculated from the full- width at half- maximum (FWHM) of the (111) diffraction peak using the Scherrer formula. The crystallite sizes were found to vary between 16 and 26 nm as the film growth temperature changed from 400 to 550 °C. The values are given in Table 1.

Total optical transmittance spectra of the NiO films deposited at different tin bath temperature are shown in Fig. 3. The total optical transmittance of the NiO films increases from 20 to 60% (at $\lambda = 500$ nm) with increasing the deposition temperature from 400 to 550 °C. The general increase in the transmittance could be caused by decrease of the film thickness (Table 1).

The formula below was used to determine the α value for E_g calculation [2]:

$$T = \exp(-\alpha \cdot d),$$

where T is the value of total transmittance, α is the absorption coefficient calculated from the optical spectra and d is NiO film thickness. The optical bandgap (E_g) values of NiO films were calculated from the recorded optical data using classical equation for the direct transitions:

$$\alpha \cdot hv = A(hv - E_g)^{1/2},$$

where A is a constant, h is the Planck constant, hv is the direct photon energy and $1/2$ is the exponent what corresponds to the direct transition for the NiO film. The value of optical bandgap energy (E_g) changes from 3.43 to 3.66 eV with increase of NiO film growth temperature from 400 to 550 °C. The graphical determination of NiO film E_g value for direct transitions is presented in Fig. 4.

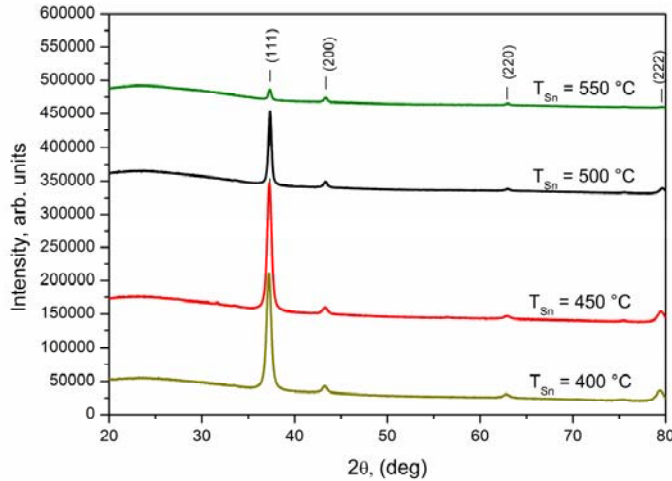


Fig. 2. XRD patterns of NiO films deposited from $\text{NiCl}_2 \cdot 6\text{H}_2\text{O}$ aqueous solution at different tin bath temperatures $T_{\text{Sn}} = 400\text{--}550$ °C

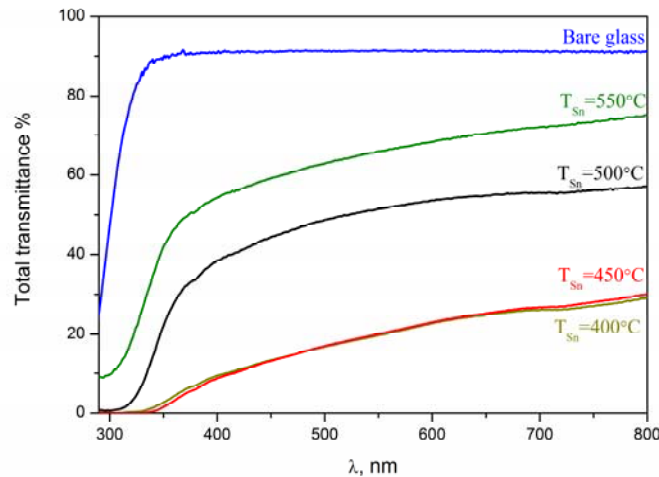


Fig. 3. Total optical transmittance spectra of the NiO films deposited from $\text{NiCl}_2 \cdot 6\text{H}_2\text{O}$ aqueous solution at different tin bath temperatures $T_{\text{Sn}} = 400\text{--}550$ °C

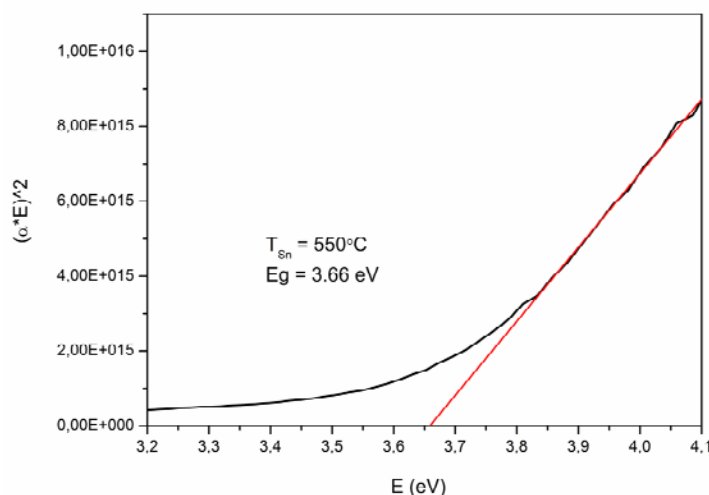


Fig. 4. Graphical determination of direct optical bandgap of NiO film deposited from $\text{NiCl}_2 \cdot 6\text{H}_2\text{O}$ aqueous solution at tin bath temperature 550°C

3.2. The properties of NiO thin films deposited from $\text{Ni}(\text{CH}_3\text{COO})_2 \cdot 4\text{H}_2\text{O}$ aqueous solution

Fig. 5 presents the photo of NiO films deposited from $\text{Ni}(\text{CH}_3\text{COO})_2$ at different deposition temperatures and as can be seen the clear and transparent NiO films were obtained at temperatures 500°C and 550°C . Visually the films in Fig. 5 are very similar to the films deposited using NiCl_2 precursor.

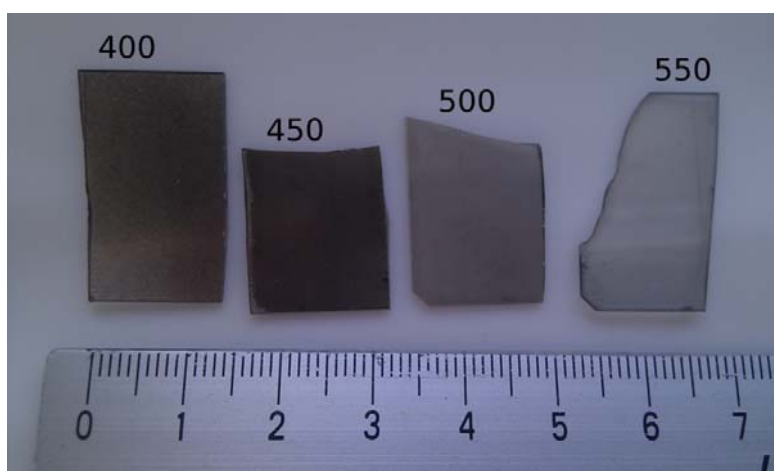


Fig. 5. Photo of NiO films deposited from $\text{Ni}(\text{CH}_3\text{COO})_2 \cdot 4\text{H}_2\text{O}$ aqueous solution at different tin bath temperatures $T_{\text{Sn}} = 400\text{--}550^\circ\text{C}$

X-ray diffraction profiles of NiO thin films grown at different temperatures are presented in Fig. 6. According to the XRD patterns all the diffraction peaks belong to the bunsenite with cubic crystal structure of NiO phase (JCPDS 00-047-1049). No other crystalline phases were detected. It can be seen in Fig. 6 that the diffraction peaks are very broad with low intensity at heater temperature of 400°C . This indicates low crystallinity in the films with average crystallite size 4 nm (Table 1). The XRD patterns show that the diffraction peaks of nickel oxide film become sharper with increasing deposition temperature. The average crystallite size was found to increase from 4 to 16 nm with increasing the tin bath temperature from 400°C to 500°C . The ratio of the intensities of the (111) and (200) diffraction peaks ($I_{(111)}/I_{(200)}$) varies from 0.5 to 0.9 for the films deposited at temperatures 400 to 550°C . For the powder reference, the $I_{(111)}/I_{(200)} = 0.6$. These

results indicate that deposited NiO films sprayed using nickel acetate show that practically the crystallites in the film do not have preferred orientation or it is very weak (Table 1).

Fig. 7 presents the optical transmission spectra of the sprayed NiO films grown at different tin bath temperature using $\text{Ni}(\text{CH}_3\text{COO})_2$ as nickel source. Spray-deposited NiO films optical transparency increased slightly with increasing deposition temperature (Fig. 7). The increase of tin bath temperature from 400 to 550 °C leads to an increase in optical transparency from 20 to 60% (at $\lambda = 500$ nm). The value of optical bandgap energy changes from 3.38 to 4.14 eV with increase of the NiO film growth temperature from 400 to 550 °C.

It has been found that film deposition temperature has great influence on growing film thickness, crystallite size, preferential orientation of the crystallites and optical properties of NiO thin films.

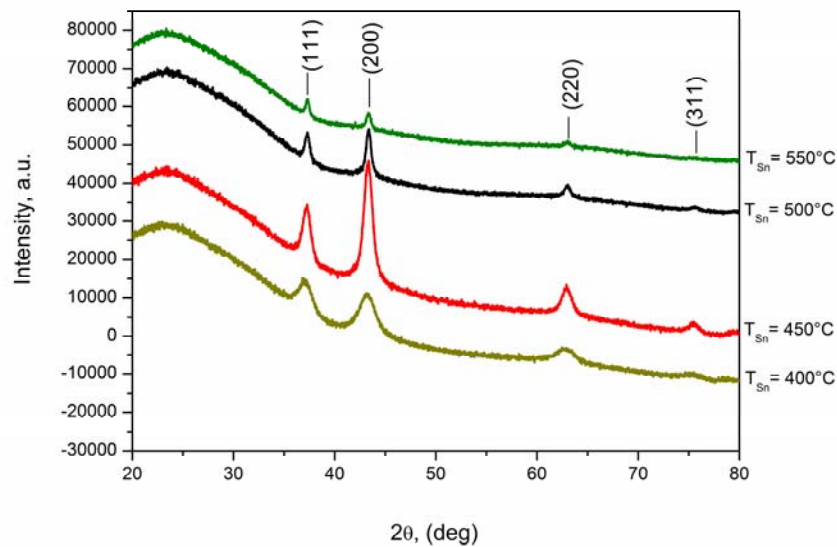


Fig. 6. XRD patterns of NiO films deposited from $\text{Ni}(\text{CH}_3\text{COO})_2 \cdot 4\text{H}_2\text{O}$ aqueous solution at different tin bath temperatures $T_{\text{Sn}} = 400\text{--}550$ °C

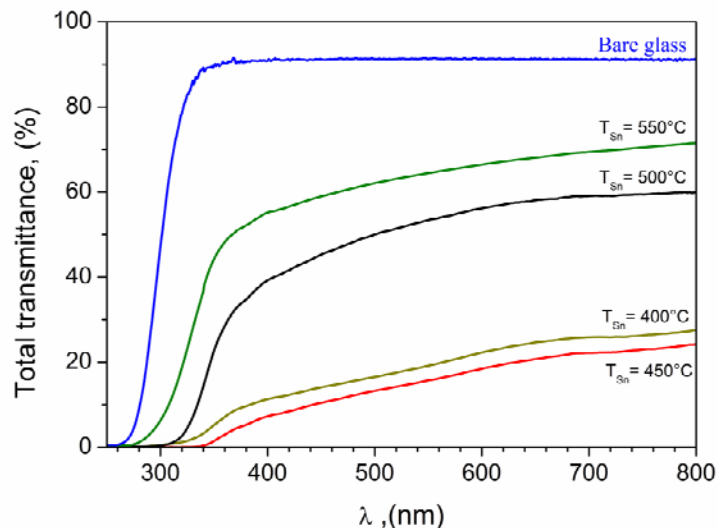


Fig. 7. Total optical transmittance spectra of the NiO films deposited from $\text{Ni}(\text{CH}_3\text{COO})_2$ salt aqueous solution at different tin bath temperatures $T_{\text{Sn}} = 400\text{--}550$ °C

3.3. Comparison of properties of NiO films deposited using different nickel source

To study the influence of the type of nickel salt on the properties of nickel oxide films, precursor containing different nickel salts $\text{Ni}(\text{CH}_3\text{COO})_2$ and NiCl_2 were deposited under the similar spray conditions. In all cases deposition parameters like concentration of nickel in precursor (0.05 mol/l), solution spraying rate (~ 1 ml/min) and volume of spraying solution (50 ml) were kept constant. The effect of precursor salt on the structural, optical and morphological properties of NiO thin films was studied.

According to XRD pattern in Fig. 2 and Fig. 6 the orientation of the crystallites in the NiO films was affected by the type of precursor and also by the deposition temperature.

All NiO films deposited from NiCl_2 show preferential growth along (111) plane. Films deposited from $\text{Ni}(\text{CH}_3\text{COO})_2$ solution show that practically the crystallites in the film do not have preferred orientation or it is very weak, depending on the tin bath temperature. Similar orientation of NiO film crystallites has been obtained in earlier studies [3–6]. It can be seen from Table 1 that the NiO films prepared from NiCl_2 precursor at the same temperature exhibit greater crystallite size than films issued from $\text{Ni}(\text{CH}_3\text{COO})_2$.

In both cases the clear and transparent NiO films were achieved at temperatures higher than 450°C . The optical transparency of NiO thin films deposited from different precursors at the same temperature is similar. The total optical transmittance of the NiO films deposited from both precursor solution increases from 20 to 60% (at $\lambda = 500$ nm) with increasing the bath temperature from 400 to 550°C . It was found from SEM analysis that increase of transparency is caused by decrease of the film thickness. Independent of the precursor the calculated optical bandgap of sprayed NiO films increases with deposition temperature (Table 1). The change of NiO film optical energy gap from about 3.5 to 4.3 eV depending on the deposition temperature is also reported by studies [2, 5, 6]. The results of the present study are in correlation with results obtained by other research groups.

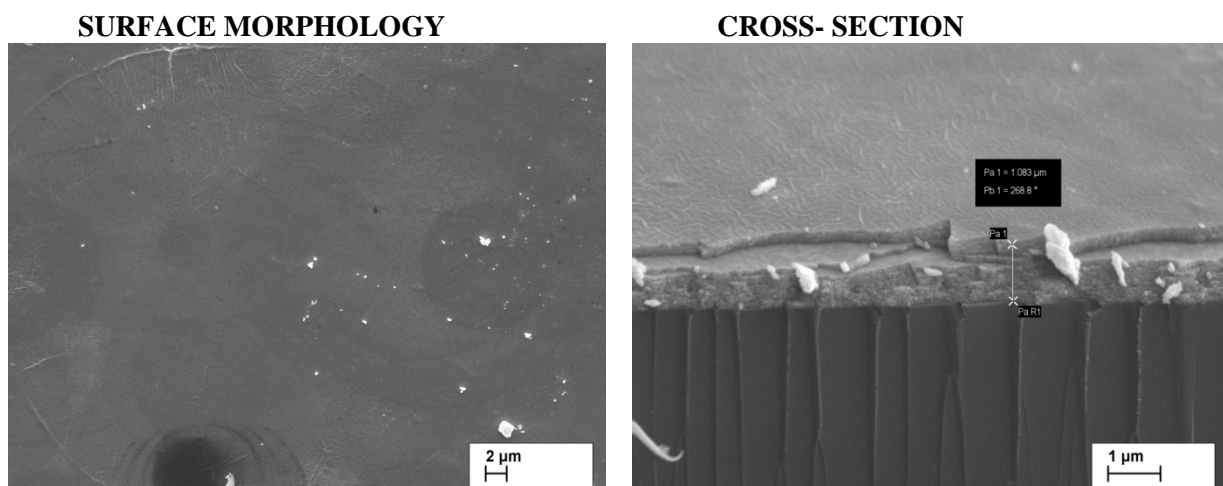


Fig. 8. SEM images of NiO films sprayed from nickel acetate [$\text{Ni}(\text{CH}_3\text{COO})_2$] aqueous solution at $T_{\text{Sn}} = 450^\circ\text{C}$ with nickel concentration of 0.05 mol/l and spraying speed ~ 1 ml/min

It can be clearly seen in Fig. 8 and Fig. 9 that the average thickness of the NiO film sprayed from NiCl_2 at 450°C is about 400 nm thinner than film deposited at same tin bath temperature using $\text{Ni}(\text{CH}_3\text{COO})_2$ solution. As can be seen, two different types of surface morphology have been obtained depending on the nickel source in the starting solution. Compared with films prepared from nickel acetate the surface morphology of the NiO films deposited from NiCl_2 is highly porous with a very rough surface and inhomogeneous film thicknesses. Improvement in film homogeneity

can be achieved when $\text{Ni}(\text{CH}_3\text{COO})_2$ is used as precursor. NiO films achieved from $\text{Ni}(\text{CH}_3\text{COO})_2$ are more compact and less porous than films issued from NiCl_2 . According to literature the similar morphological results obtained for NiO thin films [1, 3, 4].

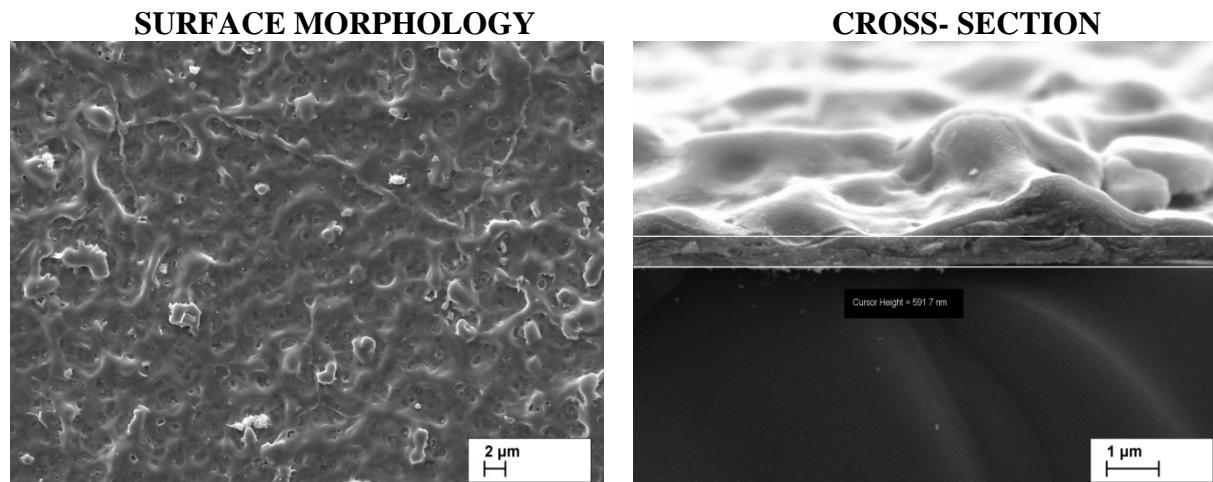


Fig. 9. SEM images of NiO films sprayed from nickel chloride (NiCl_2) aqueous solution at $T_{\text{Sn}} = 450^\circ\text{C}$ with nickel concentration of 0.05 mol/l and spraying speed ~ 1 ml/min

4. CONCLUSIONS

In this study the NiO thin films were deposited by chemical spray pyrolysis at different tin bath temperatures using aqueous solutions of nickel acetate and nickel chloride. According to the XRD patterns all the diffraction peaks belong to the bunsenite with cubic crystal structure of NiO (JCPDS 00-047-1049) and no other crystalline phases were detected. XRD analysis shows that precursor salt character affects the crystallites orientation and size in the film. All NiO films sprayed from NiCl_2 solution show preferential orientation of the crystallites along the (111) plane, independent on the deposition temperature. The crystallite size, depending on the tin bath temperature, was varied from 3.43 to 3.66 when temperature changed from 400 to 550 $^\circ\text{C}$. When $\text{Ni}(\text{CH}_3\text{COO})_2$ was used as precursor, the crystallites in the film do not have preferred orientation or it is very weak, depending on the tin bath temperature. The crystallite size also was depending on the tin bath temperature and was changed from 3.38 to 4.14 when temperature increased from 400 to 550 $^\circ\text{C}$.

The optical measurements indicate that NiO films, deposited from both precursor solution, show increase of optical transmittance from 20 to 60% when film deposition temperature increases from 400 $^\circ\text{C}$ to 550 $^\circ\text{C}$. As same time film thickness decreases drastically with increasing deposition temperature up to 550 $^\circ\text{C}$ (Table 1).

SEM analysis results indicates that the films deposited using nickel acetate are more homogeneous and compact with a smoother surface than films sprayed from nickel chloride solution.

5. REFERENCES

1. J. MATHIYAN, D. SIVALINGAM, J. B. GOPALAKRISHNAN, J. B. B. RAYAPPAN. Spray Coated Nanostructured Nickel Oxide Thin Films for Ethanol Sensing. *Journal of Applied Sciences*, 2012, Vol. 12, p. 1686–1690.



2. R. ROMERO, F. MARTIN, J.R. RAMOS-BARRADO, D. LEINEN. Synthesis and characterization of nanostructured nickel oxide thin films prepared with chemical spray pyrolysis. *Thin Solid Films*, 2010, Vol. 518, p. 4499–4502.
3. L. CATTIN, B.A. REGUIG, A. KHELIL, M. MORSLI, K. BENCHOUK, J.C. BERNE`DE. Properties of NiO thin films deposited by chemical spray pyrolysis using different precursor solutions. *Applied Surface Science*, 2008, Vol. 254, p. 5814–5821.
4. B.A. REGUIG, M. REGRAGUI M. MORSLI, A. KHELIL, M. ADDOU, J.C. BERNE`DE. Effect of the precursor solution concentration on the NiO thin film properties deposited by spray pyrolysis. *Solar Energy Materials & Solar Cells*, 2006, Vol. 90, p. 1381–1392.
5. P.S. PATIL, L.D. KADAM. Preparation and characterization of spray pyrolyzed nickel oxide (NiO) thin films. *Applied Surface Science*, 2002, Vol. 199, p. 211– 221.
6. SAFWAT A MAHMOUD, SHEREENALSHOMER, MOU`AD A. TARAWNH. Structural and Optical Dispersion Characterization of Sprayed Nickel Oxide thin films. *Journal of Modern Physics*, 2011, Vol. 2, p. 118–1186.
7. YI-MU LEE, CHENG-HSING HSU, HUNG-WEI CHEN. Structural, optical, and electrical properties of p-type NiO films and composite TiO₂/NiO electrodes for solid-state dye-sensitized solar cells. *Applied Surface Science*, 2009, Vol. 255, p. 4658–4663.
8. WON-SUB YOON, KYUNG-WAN NAM, JAMES MCBREEN, JONATHAN HANSON, AND XIAO-QING YANG. Investigation of the Thermal Decomposition of Nickel- Based Layered Cathode Materials by Time Resolved XRD. *The Electrochemical Society*, Brookhaven National Laboratory, Upton, New York 11973.
9. DAINIUS PEREDNIS, Thin Film Deposition by Spray Pyrolysis and the Application in Solid Oxide Fuel Cells. *DISS. ETH* No. 15190.
10. G.A.M. HUSSEIN, A.K.H. NOHMAN AND K.M.A. ATTYIA. Characterization of the Decomposition course of nickel acetate tetrahydrate in air. *Journal of Thermal Analysis*, 1994, Vol. 42, p. 1155–1165.
11. XUAN- HAO CHAN, J.R.JENNINGS, MD. ANOWER HOSSAIN, K.K. ZHEN YU, QINGWANG. Characteristics of p-NiO Thin Films Prepared by Spray Pyrolysis and Their Application in CdS-sensitized Photocathodes. *Journal of The Electrochemical Society*, 2011, Vol. 158, p. 733–740.

INFLUENCE OF THE PRECIPITATION CONDITIONS ON THE MORPHOLOGY, PHASE PURITY AND PHYSICAL PROPERTIES OF MAGNETITE NANOMATERIALS

S. Lagzdina, A. Sutka, G. Mezinskis

*Riga Technical University
Azenes 14/24, LV-1048 – Latvia*

J. Kleperis

*University of Latvia
Kengaraga 8, LC-1063 – Latvia*

ABSTRACT

In the present investigation, influence of the synthesis conditions on the morphology, phase purity and physical properties of the magnetite (Fe_3O_4) nanosized particles obtained from only ferrous salt solutions were investigated. It was found, that particle size, its distribution and phase composition is strongly influenced by different reaction conditions such as cation salt/precipitation agent molar ratio and temperature. Obtained powder products were characterized by X-ray diffraction (XRD) and scanning electron microscopy (SEM) analysis. By regulating synthesis conditions it is possible to obtain monophasic magnetite nanoparticles with spinel type structure and size < 30 nm, as well as admixture containing different crystal phases such as maghemite ($\gamma\text{-Fe}_2\text{O}_3$), hematite ($\alpha\text{-Fe}_2\text{O}_3$) or goethite (FeOOH). For synthesized compounds different physical characteristics such as magnetic, optical and photocatalytic properties were studied. Saturation magnetization of magnetite nanopowders was close to that of bulk value, thus showing that synthesized Fe_3O_4 is close to its stoichiometric composition. Also, obtained magnetite nanosized particles show some photocatalytic activity for water splitting under visible light for hydrogen production.

Keywords: Magnetite, nanoparticles, precipitation, photoelectrochemical properties, photocatalytic activity

INTRODUCTION

Iron oxides, such as magnetite (Fe_3O_4), hematite ($\alpha\text{-Fe}_2\text{O}_3$), maghemite ($\gamma\text{-Fe}_2\text{O}_3$), goethite (FeOOH), have been widely studied [1]. Iron oxides, especially nanoparticles, have been used in many technological and scientific fields [2]: in high-density magnetic recording materials [3], ferrofluids, magnetic refrigeration, magnetic resonance imaging, cancer therapy and catalysis [4, 5], photocatalytic water splitting [6], biomedicine as a magnetic drug delivery system [7], electrochemical displays, wave absorption, and electromagnetic shielding [8].

Magnetite form of these oxides is one of the most important magnetic materials. The compound has exhibited unique electric and magnetic properties. Its nanoparticles widely used for medical and non-medical applications. The main medical application is as a magnetic contrast agent in diagnosis, in therapy of hyperthermia, delivery and carrier of drug [9].

Controlling the morphology of material nanocrystallites is an important problem of modern material research. An optical, electronic, magnetic and catalytic property, which peculiar to iron oxides, depends critically not only on particle size but also on particle shape and phase purity [10]. All these properties can be controlled with choosing synthesis or changing its conditions.

Various methods have been reported for the synthesis of Fe_3O_4 nanoparticles, such as sol-gel, reduction of hematite by CO/CO_2 or H_2 [4], hydrothermal technique and the thermal decomposition [3]. Many of these methods need special equipment, expensive supplies or complicated processes, which is difficult to control. One of the most popular is co-precipitation method due to its ease, large volume capability and economy [5]. Using co-precipitation method it's easy to control phase composition, the size and shape of particle in the room temperature.

Usually Fe_3O_4 can obtain with co-precipitation method using a solution of ferrous/ferric mixed salt with the $\text{Fe}^{2+}/\text{Fe}^{3+}$ ratio 1:2. Reaction occurs in alkaline solution, as base using NaOH or NH_4OH [11]. There is two types co-precipitation technique: normal co-precipitation and reverse coprecipitation. In the first case, the pH value gradually increases, because an alkali solution is dropped into the mixed metal solution. In the second case, the mixed metal solution is directly dropped into an alkaline solution [12].

There are some problems in this case of method. It's difficult to obtain pure phase magnetite, using mixed ferrous/ferric salt because the initial ratio of Fe^{2+} and Fe^{3+} ions need to be 0.5. If the initial ratio of Fe^{2+} and Fe^{3+} ions not accurate, there can be formed other phases such as maghemite, goethite, hematite or the mixture of these phases with iron oxides because of Fe^{2+} oxidation. The ultimate aim is to obtain the pure phase magnetite. Some of the articles maintain that the reaction occurs in the air atmosphere but the obtained precipitates need to dry under the inert atmosphere or vacuum [2, 13].

Lately, some of scientists detected that is possible to obtain pure phase of magnetite using only ferrous salt and synthesis occurs in the room temperature and air atmosphere [14, 15]. From this reason the aim of the present work is to obtain monophasic magnetite, find out how ambient conditions affect to particle shape and size synthesized by using only ferrous salt aqueous solutions and in the air atmosphere. Structural, microstructural and physical properties will be determined during research. Practical use of the obtained magnetite nanopowders as photocatalysts was studied as well.

EXPERIMENTAL

In the present work co-precipitation method was used to obtain magnetite particles. In the synthesis $\text{FeCl}_2 \cdot 4\text{H}_2\text{O}$ dissolved in the distilled water obtaining 0.1 and 0.5 molar ratio, magnetically stirred 10 minutes. NaOH was dissolved into another distilled water to prepare the alkali solution with the mass ratio of $m(\text{NaOH})/m(\text{FeCl}_2)$ equal to 3.5. Then the alkali solution was poured into FeCl_2 solution. Mixture was stirred in the magnetic blender at room temperature and $60\text{ }^\circ\text{C}$ in the air atmosphere 5 and 24 h.

The product was filtered and washed with distilled water several times till precipitates are pH neutral. Then precipitates were dried 24 h in air at $60\text{ }^\circ\text{C}$.

Investigations of microstructural features of the synthesized powders were carried out by using Scanning Electron Microscope (SEM). In these experiments a field emission gun SEM (Tescan Mira/Lmu, Czech Republic) was used. SEM measurements were carried out by using electronbeam energy respective to 15 kV high voltages in case of all samples.

Phase compositions of the samples were characterized by using X-Ray powder Diffraction (XRD) recorded at 2θ from 10° to 60° at scanning rate of 1° min^{-1} by using an Ultima+ X-ray diffractometer (Rigaku, Japan) with $\text{Cu K}\alpha$ radiation.

The magnetic properties of the powders were defined by employing the vibration sample magnetometer (Lake Shore Cryotronic Co., Model 7404 VSM, USA) at room temperature in magnetic field varying from -10 to $+10$ kOe.

To measure light absorbance of samples, the instrument UV-VIS Spectrophotometer SPECORD® 210 (Analytik Jena) with integrating sphere coated with polytetrafluoroethylene (PTFE) was used. Measurements were performed for wavelengths varying from 350 up to 1100 nm. Spectralon© was used as white reference. In diffuse reflectance spectroscopy the measured intensity depends on both scattering and absorption processes being difficult to analyse separately for pressed samples, thus parameter called absorbance A_s , was introduced:

$$A_s = \log\left(\frac{I_s}{I}\right),$$

where I_s – incident light radiation (intensity measured from reference sample Spectralon®), I – light radiation reflected from sample. A_s is parameter without dimensions (a.u. or arbitrary units is used to describe the scale division).

The photo activity was performed in a double walled and small-sized reactor (Fig. 1). The water solution containing sacrificial donor ethanol (0.5 M) and photocatalyst (0.5 g/l) was deoxygenated in advance by argon bubbling for 30 min.

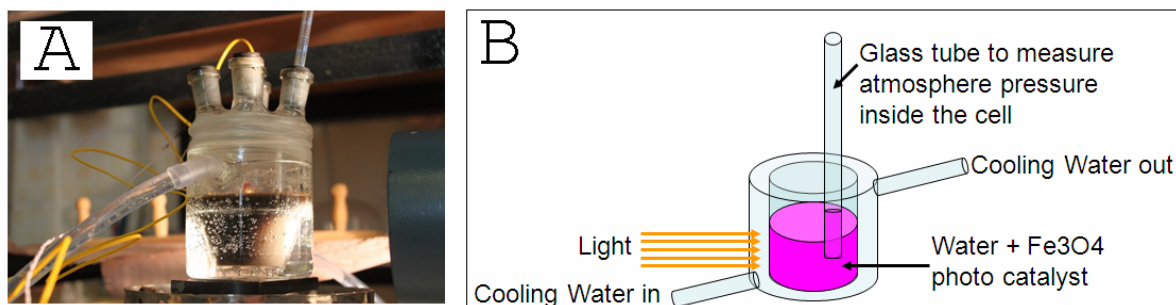
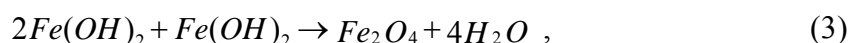


Fig. 1. Water photo-electrolysis cell for water splitting experiments

RESULTS AND DISCUSSIONS

First the stirring time influence on the phase purity and particle size was investigated. In this case the magnetite powders were synthesized from 0.1 M $\text{FeCl}_2 \cdot 4\text{H}_2\text{O}$ and NaOH solutions. Different stirring times 5 h and 24 h were chosen. XRD patterns of these samples indicate that stirring 5 h there is only magnetite phase, but stirring 24 h there is additional impurity peaks from goethite phase (Fig. 2 (a)).

Magnetite from ferrous salts can be synthesized according to following reactions (1), (2) and (3).



As synthesis process is performed in the air atmosphere, it is also possible to obtain goethite by reaction (4). By increasing stirring time there can be higher possibility for oxidation and formation of the goethite [5].



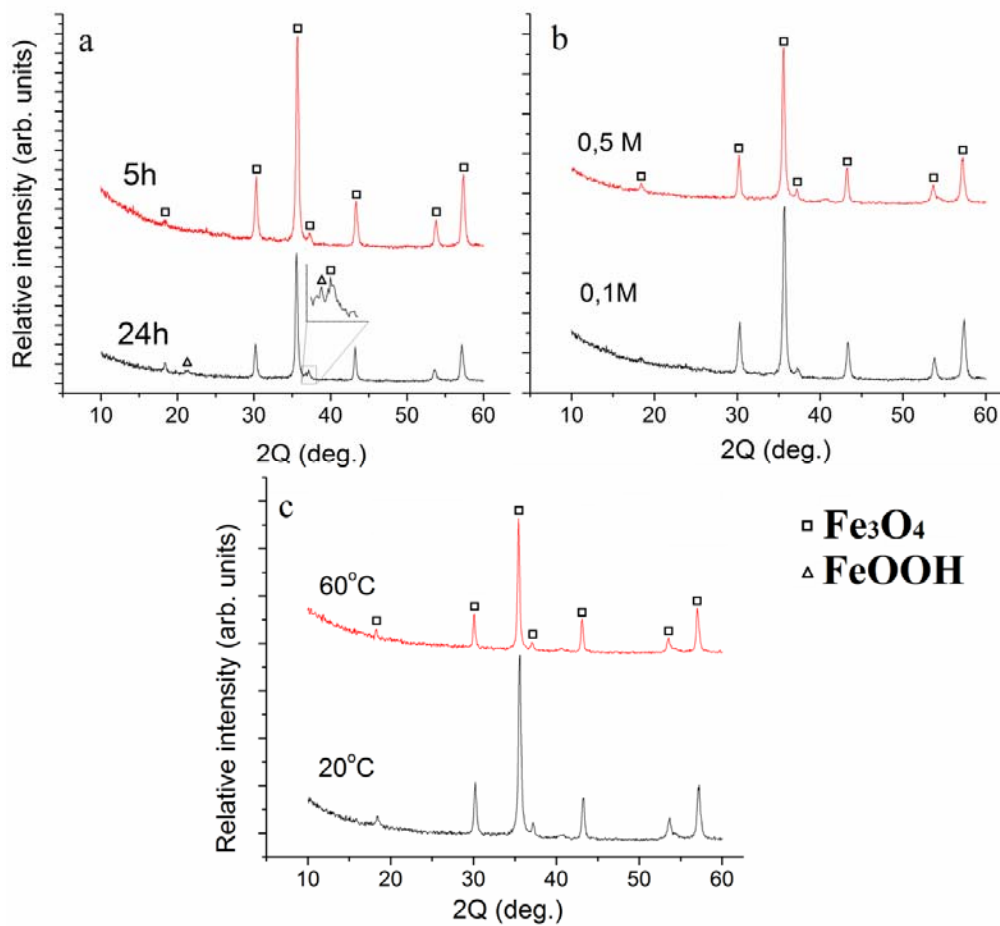


Fig. 2. XRD patterns of 24 h and 5 h magnetic stirred 0.1 M samples (a), 0.1 M and 0.5 M samples magnetic stirred 5 h (b) and 0.5 M at 60 °C and 20 °C 5 h stirred samples (c)

As we can see in SEM micrograph shown in the Fig. 3 (a), stirring for 5 h leads to the formation of the nanosized and monodisperse particles. For longer stirring times size of the particles, as well as polydispersity and shape anisotropy increases (Fig. 3 (c)). Stirring 24 h increases particle size.

Further we investigated influence of the molarity of the iron salts which was set on 0.1 and 0.5 M, respectively. Due to previous results for these experiments we chose stirring time 5 h. As we can see in Fig. 2 (b) for both molarities pure Fe_3O_4 phase was formed. Also, particle size, polydispersity and shape anisotropy was not influenced when molarity 0.5 of the solutions was chosen (Fig. 3 (b)).

One more parameter which can influence phase purity, particle size and shape is temperature. In synthesis at room temperature obtained pure magnetite phase with monodisperse, nanosized particles. When temperature was increased phase anisotropy of the particles was influenced. As we can see in Figure 3 (d) there is presence of needle shaped particles into the final product. The XRD pattern of sample which was stirred at 60 °C also exhibited only peaks corresponding to magnetite phase (Fig. 2 (c)).

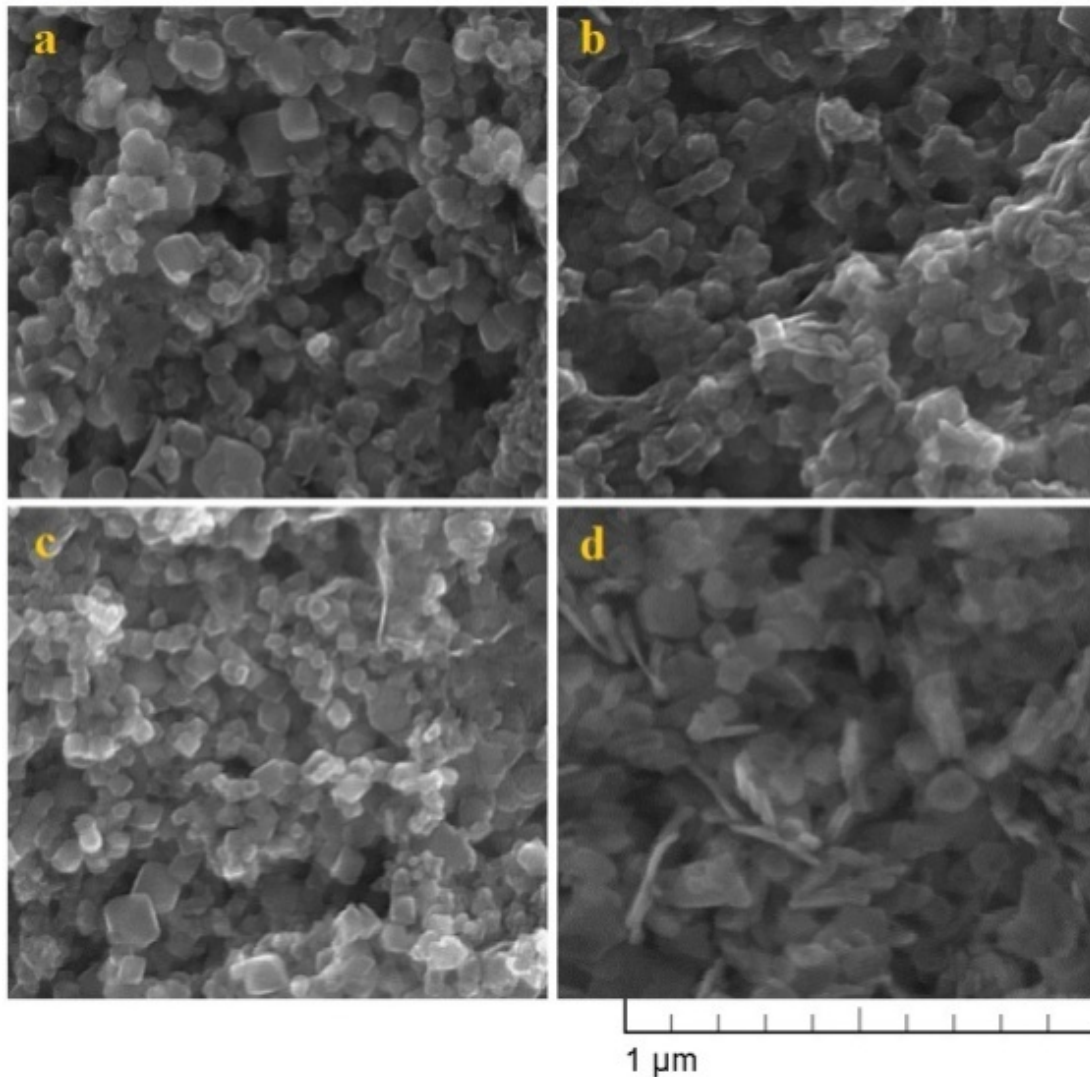


Fig. 3. SEM image of 0,1 M 24 h (a) and 5 h (c) stirred samples in room temperature. 0.5 M in room temperature (b) and in 60 °C (d) stirred samples

From the XRD patterns crystalline sizes and lattice parameters were calculated (Table 1). The crystallite sizes were determined by using Debye–Scherrer equation (2).

$$D = \frac{\lambda}{B \cos \theta}, \quad (2)$$

where λ is the wavelength of $\text{CuK}\alpha$, B is the diffraction peak width at half height on it and θ is the diffraction angle of a corresponding (hkl) plane.

The lattice constant a for all compositions was calculated from diffraction planes by using formula: $\alpha = d\sqrt{h^2 + k^2 + l^2}$ (3), where d is the interplane spacing; h , k , and l are the Miller indices of the crystal planes. Lattice constants were plotted against Nelson–Riley function:

$$F(\theta) = \frac{1}{2 \left(\frac{\cos^2 \theta}{\sin \theta} + \frac{\cos^2 \theta}{\theta} \right)}. \quad (4)$$

To obtain the exact values of the lattice constant, the plot of a lattice constant versus $F(\theta)$ is extrapolated to $F(\theta) = 0$ [16].

Table 1. Crystalline size and lattice parameter of the samples

Parameters	Crystalline size D, nm	Lattice parameter a, Å
0.1 M, 24 h	22.75	8.37
0.1 M, 5 h	18.84	8.34
0.5 M, 5 h, 20 °C	19.22	8.38
0.5 M, 5 h, 60 °C	24.90	8.37

It can be observed that lattice parameter for the all samples vary within the error borders, but the stirring time and the temperature are the parameters which changes crystalline sizes. With increasing stirring time and temperature crystallite size increased.

For further investigations we chosen sample 0.1 M 5 h stirred in room temperature, because of phase purity, monodispersity and nano-dimensionality of the particles.

Fig. 4 shows the magnetization, M (emu/g), as a function of the applied magnetic field H (Oe). The coercivity (H_c), the remanent magnetization (M_r) and magnetization saturation (M_s) of the present sample is determined from Fig. 4 and their values are 150 Oe, 20 emu/g and 87 emu/g, respectively. Obtained saturation magnetization is little bit lower than that of the bulk (93 emu/g) [16]. Smaller saturation magnetization could be due to small particle sizes of the magnetite or cation vacancies [5, 17].

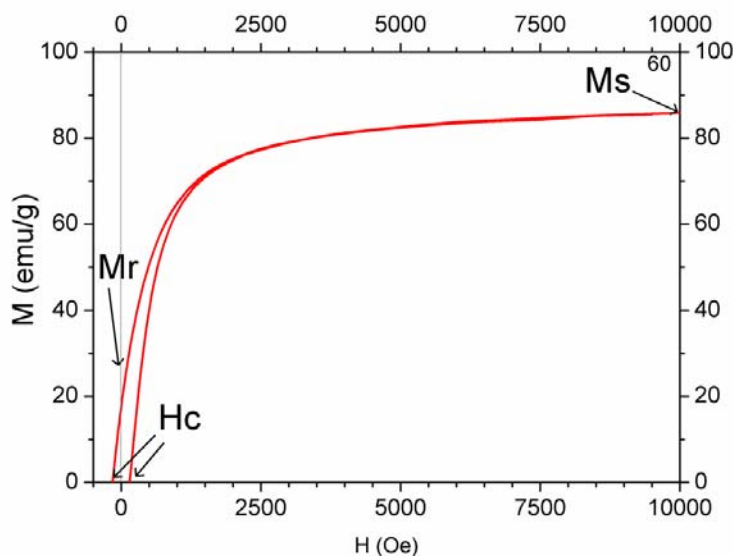


Fig. 4. Magnetization of the magnetite nanoparticles

Water splitting using metal semiconductors photocatalysts occurs in accordance with following reactions [18]:



To provide these reactions in sunlight, material should absorb visible light. Most popular photocatalysts as TiO_2 or ZnO absorb light only in the UV region. They can absorb only about 5% of sunlight, which greatly limits its practical applications. By now the main task in the science is to develop photocatalysts with enhanced visible light activity. From this point of view iron oxides stand out as promising materials for water splitting [6].

Fig. 5 shows the absorption spectra for the synthesized Fe_3O_4 nanoparticles. As we can see sample shows absorption in the visible region, thus water oxidation under sunlight could be expected.

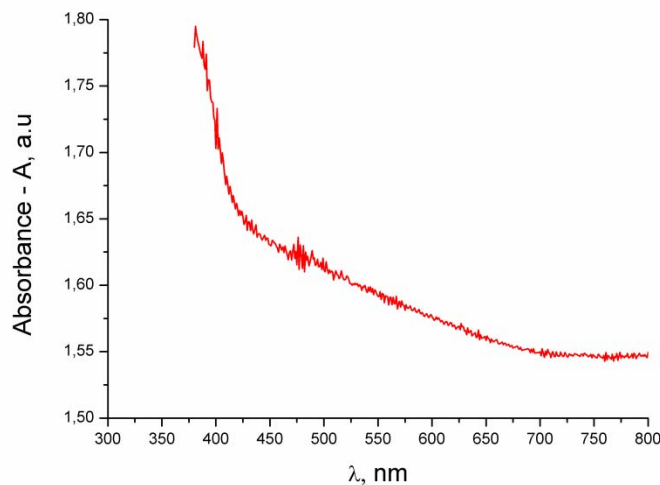


Fig. 5. Absorption spectrum of Fe_3O_4 nanoparticles

The UV-VIS absorbance spectrum was used to obtain band gap energy (E_g) of the magnetite nanoparticles. The crystalline material zone theory, where the forbidden gap is defined, only relatively is applicable to amorphous (nanocrystalline) materials. Small grains and large grain surfaces result in formation of defect levels in gap and additional light absorption below the edge (430–600 nm), however, most of the light is absorbed at energy, which is equal to the width of forbidden gap. In case of direct transitions the determination of the direct band gap for magnetite sample is shown in Fig. 6. Accordingly to Tauc [19] the direct band gap energies can be obtained from the dependencies $(\alpha h\nu)^2$ on $h\nu$, where α is absorption coefficient, but $h\nu$ is photon energy in eV. The energy gap from this relation was estimated by plotting $(\alpha h\nu)^{1/m}$ vs $h\nu$ and extrapolating to a straight line for $m = \frac{1}{2}$ (Fig. 6). The value of direct band gap is 2.74 eV. Calculated value is comparable with the results obtained by other authors for magnetite nanoparticles [20].

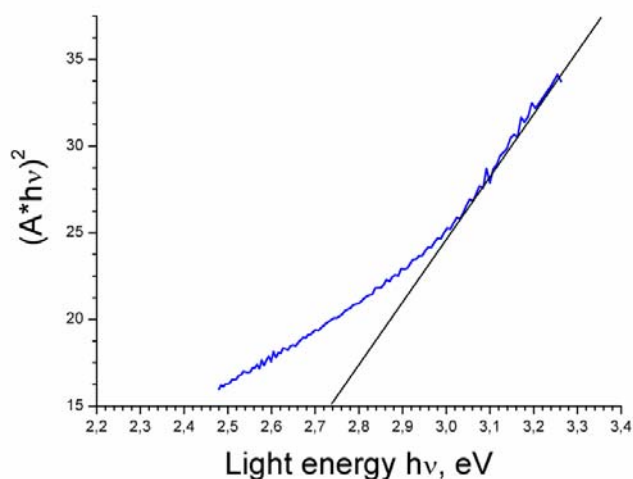


Fig. 6. Determination of the direct band gap for magnetite nanoparticles

Obtained magnetite nanosized particles show some photocatalytic activity for water splitting under visible light for hydrogen production. However, for precise hydrogen yield values the experiment conditions should be optimized and thus future work is necessary.

CONCLUSIONS

Pure and monodisperse nanosized magnetite was precipitate from only ferrous salt by co-precipitation method. Synthesis was performed in the room temperature and in the air atmosphere. Increasing molarity of the ferrous salt, as well as stirring time, increases particle size and forms impurity phases. These parameters also affect crystalline size. Temperature influenced the shape anisotropy of the particles. Besides spherical particles also needle shaped particles were formed. All parameters, stirring time, molarity and temperature influence the morphological and structural properties of the product.

Best results were achieved when stirring was performed in the room temperature for 5 h and molarity 0.5 M was chosen. This sample characterizes with high saturation magnetization, light absorption in the visible region and some photocatalytic activity for water splitting. It can be concluded that in the future Fe_3O_4 nanoparticles could be useful to split the water.

ACKNOWLEDGEMENT

Authors acknowledge National Research Program in material sciences IMIS for financial support of scientific experiments and ERDF project Nr. 2010/0204/2DP/2.1.1.2.0/10/APIA/VIAA/010 for financial support of travel expenses.

REFERENCES

1. M. CHANG, N.F. HSU, C.C. CHUNG, J.R. DEKA, Rapid growth of Fe_2O_3 nanowires with oxide assisted vapour-solid process. *Materials Letters*, 2010, 64, p. 1077–1080.
2. A.BEE, R.MASSART, S.NEVEN, Synthesis of very fine maghemite particles. *Journal of Magnetism and Magnetic Materials*, 1995, 149, p. 6–9.
3. K. PETCHAROEN, A. SIRIVAT, Synthesis and characterization of magnetite nanoparticles via the chemical co-precipitation method. *Materials Science and Engineering*, 2012, B 177, p. 421–427.
4. X. CHEN, Z. ZANG, X. LI, C. SHI, Hollow magnetite spheres: synthesis, characterization and magnetic properties. *Chemical Physics Letters*, 2006, 422, p. 294–298.
5. S. ALIBEIGI, M.R. VAEZI, Phase transformation of iron oxide nanoparticles by varying the molar ratio of $\text{Fe}^{2+}:\text{Fe}^{3+}$. *Chem.Eng.Technol.*, 2008, No. 11, p. 1591–1596.
6. P.A. MANGRULKAR, V.POLSHETTIWAR, N.K. LABHSETWAR, S. RAJENDER, V.SADHANA S. RAYALU, Nano-ferrites for water splitting: unprecedented high photocatalytic hydrogen production under visible light. *Nanoscale*, 2012, 4, p. 5202.
7. R. VALENZUELA, M.C. FUENTES, C. PARRA, J. BAEZA, N. DURAN, S.K. SHARMA, M. KNOBEL, J. FREER, Influence of stirring velocity on the synthesis of magnetite nanoparticles (Fe_3O_4) by the co-precipitation method. *Journal of Alloys and Compounds*, 2009, 488, p. 227–231.
8. W. SHEN, M. SHI, M. WANG, H. CHEN, A simple synthesis of Fe_3O_4 nanoclusters and their electromagnetic nanocomposites with polyaniline. *Materials Chemistry and Physics*, 2010, 122, p. 588–594.
9. D. FICAI, A. FICAI, B.S. VASILE, M. FICAI, O. OPREA, C. GURAN, E. ANDRONESCU. Synthesis of rod-like magnetite by using low magnetic field. *Digest Journal of nanomaterials and biostructures*, 2011, Vol. 6, p. 943–951.
10. J.FENG, X.GUO, J.HONG, W.DING, One-step wet chemistry for preparation of magnetite nanorods. *Materials Letters*, 2005, 59, p. 985–988.
11. I. NEDKOV, T. MERODIISKA, L. SLAVOV, R.E. VANDERBERGE, Y. KUSANO, J. TAKADA, Surface oxidation, size and shape of nano-sized magnetite obtained by co-precipitation. *J.Magn.Magn.Mater.*, 2006, 300, p. 358–367.

12. H. AONO, H. HIRAZAWA, T. NAOHAVA, T. MAEHAVA, H. KIKKAWA, Y. WATANABE, Synthesis of fine magnetite powder using reverse co-precipitation method and its heating properties by applying AC magnetic field. *Materials Research Bulletin*, 2005, 40, p. 1126–1135.
13. D. MAITY, D.C. AGRAWAL, Synthesis of iron oxide nanoparticles under oxidizing environment and their stabilization in aqueous and non-aqueous media. *Journal of Magnetism and Magnetic Materials*, 2007, 308, p. 46–55.
14. Q. LI, W. WANG, W. YONGFEI, Fabrication and characterization of $\text{Ni}_{0.5}\text{Zn}_{0.5}\text{Fe}_2\text{O}_4$ nanofibers. *Journal of Alloys and Compounds*, 2010, 494, p. 315–318.
15. U. SCHWETMAN; R.M. CORNELL. *Iron Oxides in the Laboratory*. Great Britain: Wiley-VCH, 2000. 188 p. ISBN 978-527-29669-9.
16. A. ŠUTKA, G. MEŽINSKIS, A. LŪSIS, M. STINGACIU, Gas sensing properties of Zn-Doped p-type nickel ferrite. *Sensors and Actuators*, 2012, p. 1–7.
17. H. IIDA, K. TAKAYANAGI, T. NAKANISHI, T. OSAKA, Synthesis of Fe_3O_4 nanoparticles with various sizes and magnetic properties by controlled hydrolysis, *J. Colloid Interf. Sci.*, 2007, 314, p. 274–280.
18. K. MAEDA, Photocatalytic water splitting using semiconductor particles: History and recent developments. *Journal of Photochemistry and Photobiology*, 2011, 12, p. 237–268.
19. J. TAUC, Optical properties and electronic structure of amorphous Ge and Si". *Materials Research Bulletin*, 1968, 3, p. 37–46.
20. H.E. GHANDOOR, H. M. ZIDAN, M.M.H. KHALILAND, M.I.M. ISMAIL, Synthesis and some physical properties of magnetite (Fe_3O_4) nanoparticles. *Int. J. Electrochem. Sci.*, 2012, 7, p. 5734–5745.



DEVELOPMENT OF ALGORITHMS FOR SIMULATION OF IRON ROD COMBUSTION IN OXYGEN WITH THE DETACHMENT OF THE DROP

V.I. Ignatenko, S.I. Shabunja, V.V. Martynenko

A.V. Luikov Heat and Mass Transfer Institute

P. Brovka str. 15, 2000072 Minsk – Belarus

ABSTRACT

The present work is a part of a research program to study the combustion of steel in oxygen at high pressure. A fundamental understanding of iron and steel combustion in oxygen is important to the safe selection and specification of these materials for oxygen service. The problem is studied for a long time, but the actual working models for the simulation of the combustion process a little.

In the paper standard upward-burning ignition tests were considered on cylindrical iron rods in oxygen with non-flowing test conditions. There were presented combustion model with the separation drops to investigate influence of different burning factors on the combustion process. The model results were compared with the NASA experiments to clarify the values that were introduced parametrically. The present model allow us to calculate and visualize the combustion parameters such as the velocity of the reaction front (front of burning) along the rod, the rate of the mass increasing of the drop and drop detachment, heat distribution along the rod, etc. For simulation there were used The Wolfram Mathematica 9.0 program.

Keywords: iron, metal combustion, heat conduction, burn criteria, flammability, melting drop formation

1. INTRODUCTION

Present paper is part of a research program designed to study safety of industrial production and transport of oxygen. Metal components (steel, aluminium, bronze, etc) in the oxygen-rich environment at high pressure are also at high temperatures. Under certain conditions there are processes of combustion or fast ignition that can more or less seriously damaged or completely destroyed the component in question. This finding is critical in terms of serviceability, if this component plays an important role in the mechanical behaviour of a given structure, such as for example a pipeline at high pressure where the gas flows at high velocity, oxygen production or distribution plants.

Despite the fact that the problems of ignition and combustion of solid metals are engaged more than half a century, most of the research was to carry out standard tests aimed to determine whether the combustion process to occur under certain conditions and finding burn criteria [1–2]. A lot of experiments were also devoted to the regression rate of the melting interface (RRMI) definition and finding the limiting mechanisms in a particular configuration of a metal rod and the environment conditions [3–8]. But it is more interesting to understand the mechanism of combustion, answer questions exactly how it proceeds and what the parameters affecting it. Unfortunately articles on this subject are not so much.

This paper presents an approach to the problem, as well as modelling of the combustion process, which allows us to understand and determine the conditions for the combustion propagation of the metal in oxygen under high pressure.

2. THEORETICAL PRINCIPLES AND MATHEMATICAL MODELLING

2.1. The model of combustion. Basic concepts

Typical rod combustion experiments are mainly carried out in a vertical position with non-flowing test conditions [2–8]. They deal with the upwards combustion, that is, the lower surface of the sample was ignited. This configuration is justified if the purpose is to create conditions for sustainable long-term process of combustion. The drop is formed at the lower end of the rod, and it separated from the sample under the influence of gravity, providing a better supply of oxygen to the interface reaction (Fig. 1). Just after the greater part of the molten mass drops, the remaining molten mass starts to increase again. This behaviour is repeated at regular intervals [3].

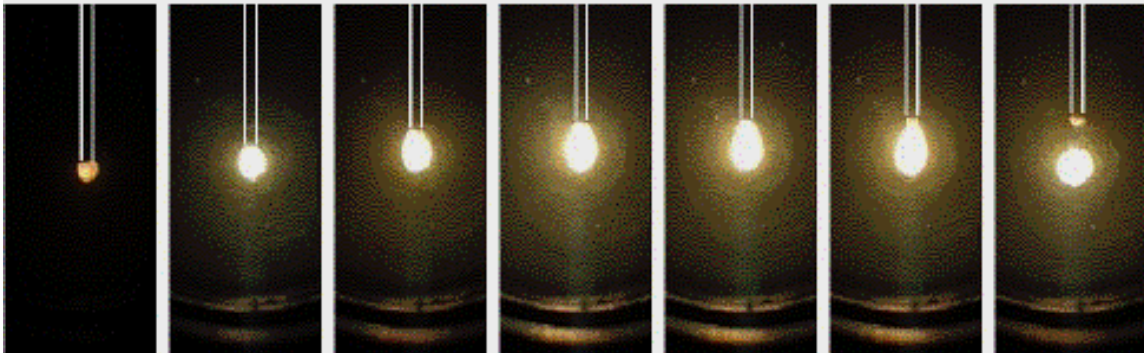


Fig. 1. Typical aspects of fire spread along iron rods

As shown by numerous experiments [9–14], the rods of different materials can be characterized by certain threshold pressure (TP) of oxygen at which steady burning of rod begins to exist.

NASA conducted experiments with the same configuration of the rod, which is further blown by the flow of oxygen down along the rod [15–16]. These experiments showed that the rate of gas flow affects the TP of oxygen (minimum); in addition there is a second limit – the maximum pressure at which the flame disappeared.

If there is a self-sustaining combustion process, two continuous mass flows come into the drop: $\dot{m}_{Fe}(t)$ – iron flow from the rod and $\dot{m}_{O_2}(t)$ – oxygen flow from the surrounding rod environment.

Component structure of the test rods affects their ability to burn for several reasons:

- a) the oxidation of different metals released different amounts of energy, which affects the energy balance in the combustion region;
- b) different metals may require different amounts of oxygen for the oxidation;
- c) forming oxides of different metals have different melting and boiling points, and this can affect the properties of the melt: diffusion, viscosity, evaporation, etc.;
- d) the course of the different metals oxidation due to the different requirements of the kinetic (different activation energies), i.e. require different temperatures.

The model can be brought closer to reality by taking into account geometric factors and the specific removal of the melt. The presence of the drop, in which through one surface (contact with the rod) comes molten iron or steel, and through another (contact with the gaseous medium) comes oxygen, makes it unlikely assumption of stoichiometry products. In this case, removed products contain some unoxidized alloy components; if they are oxidized later, energy from this reaction will not be transferred to the combustion region. As the drops can continue to burn in flight and on the bottom of the experimental setup, then the analysis of solidified oxides after the experiment will provide incorrect information about the composition of the drops. If it is assumed that the melt intensively mixed, it is likely the chemical balance in the drop.

As a result, we formulate the following model:

- ✓ Quasi-stationary combustion of the rod;
- ✓ The energy balance is written to the field of combustion, which is called "the melting drop";
- ✓ The melting drop absorbs material of the rod and oxygen from the environment, and the melt removed from it depends on the total mass of droplet;
- ✓ All the droplet characteristics depend only on time, i.e. averaged over the volume of the drop;
- ✓ Chemical composition (oxygen distribution between the metal melt) is calculated by thermodynamic equilibrium model at the average drop temperature.

2.2. Experiments

To refine the model parameters were used NASA movie and test reports [15–16], as well as data obtained by T. Suvorovs [17–18].

NASA reports describe the methodology and experimental setups to study the combustion of metal samples in oxygen. The experiments were conducted both in flowing and non-flowing oxygen atmosphere. There were fixed such parameters as operating pressure of oxygen in the chamber, oxygen flow rate, sample material, its geometry. Combustion process was recorded using high-speed video.

The Suvorovs thesis presents the results of experiments on cylindrical rod combustion of various diameters from 2 mm to 7 mm. There are data on the burning rate and the intensities of the separation of drops.

There were analyzed test reports, the experimental data and video in order to identify the basic physical processes to create a model that can describe the evolution of the test rod burning in oxygen.

2.3. Modelling of the combustion process

It's considered the physical and chemical processes that accompany the burning of cylindrical iron rods in an oxygen atmosphere at the pressure. These processes include the heating and melting of iron, oxygen diffusion into molten iron, oxide formation, the radiation in the environment. Correct account of all these processes is very complicated for mathematical modelling. Therefore, it is necessary to make some simplifications. In formulated model, the initial process of heating the metal and the initiation of combustion is not considered. Also it's believed that the energy released by the combustion of the metal enough to compensate for energy losses due to radiation into the environment as well as conductive and convective heat transfer. Actually the iron combustion process is in the form of drop formation of the oxidation products FeO . This product has a certain characteristic temperature T_{drop} , which is above the iron melting point T_{melt} .

The amount of iron consumed in the process of drop formation is controlled by the velocity of melting front V_{melt} and is proportional to the cross-sectional area of the rod S_{rod} . Evolution of the iron mass in a drop:

$$\frac{dm_{Fe}}{dt} = V_{melt} \rho_{Fe} S_{rod}, \quad (1)$$

were $S_{rod} = \frac{\pi d_{rod}^2}{4}$, ρ_{Fe} is the density of iron.

The amount of oxygen consumed for the formation of the melting drop is controlled such processes as the characteristics of oxygen atmosphere around the rod, surface area of the drop,

transport of oxygen into the drop. There is optimal form of the differential equation that models the evolution of the oxygen mass consumed for the formation of the drop:

$$\frac{dm_O}{dt} = \gamma_{stoh} (m_{Fe}, m_O) C_{ac} \rho_{O_2}^{amb} S_{drop} (m_{drop}), \quad (2)$$

where $S_{drop} = \beta_{shape} \left(\frac{m_{drop}}{\rho_{FeO}} \right)^{2/3}$, $\rho_{O_2}^{amb}$ is the oxygen density at the ambient temperature and γ_{stoh} is the stoichiometric factor that introduced to control the oxygen supplied to the droplet. It takes the value 0 when the ratio of oxygen and iron molecules equal 1 or more and takes the value 1 otherwise.

In this way the value m_O will be controlled by geometrical characteristics (reaction surface area), reactant stoichiometry and density of the oxygen atmosphere.

The evolution of the drop enthalpy over time due to the next factors: the iron and oxygen flows, radiation heat that is lost to the environment (T_0) and convective heat transfer from a drop (T_{drop}) in rod across the melt boundary (T_{melt}):

$$\frac{dH_{drop}}{dt} = h_{Fe}(T_{melt}) \frac{dm_{Fe}}{dt} + h_O(T_{melt}) \frac{dm_O}{dt} - S_{drop} \sigma_{Boltzman} \varepsilon (T_{drop}^4 - T_0^4) - S_{rod} a_{ht} (T_{drop} - T_{melt}). \quad (3)$$

Rewrite (3) using (1) and (2) as:

$$\begin{aligned} \frac{dH_{drop}}{dt} = & h_{Fe}(T_{melt}) V_{melt} \rho_{Fe} S_{rod} + h_{O_2}(T_0) \gamma_{stoh} (m_{Fe}, m_{O_2}) \langle C_{ac} \rangle \rho_{O_2}^{amb} S_{drop} (m_{drop}) - \\ & - S_{drop} \sigma \varepsilon (T_{drop}^4 - T_0^4) - S_{rod} \langle a_{ht} \rangle (T_{drop} - T_{melt}) \end{aligned} \quad (4)$$

Note that the model range 2 parameters: the accommodation coefficient C_{ac} and the coefficient a_{ht} that responsible for the heat transfer to the rod. Accommodation coefficient is responsible for carrying oxygen to the surface reaction.

Heat flow in the rod can be described as dimensional quasi-stationary solution for the melting of the rod with the front velocity V_{melt} :

$$J_{therm_cond} = \lambda \frac{dT}{dx} = \rho_{Fe} V_{melt} (h_{Fe}(T_{melt}) + h_{Fe}^{melting} - h_{Fe}(T_0)), \quad (5)$$

which takes into account hitting and the phase transition.

On the other hand heat flow is proportional to the difference between the drop and the molten iron temperatures:

$$J_{ht} = a_{ht} (T_{drop} - T_{melt}). \quad (6)$$

The factor a_{ht} includes all the mechanisms of convective-conductive heat transfer between the molten drop and rod.

The flows are equal $J_{therm_cond} = J_{ht}$, it gives the value of burning velocity (the velocity of the melting front):

$$V_{melt} = \frac{a_{ht} (T_{drop} - T_{melt})}{\rho_{Fe} (h_{Fe}(T_{melt}) + h_{Fe}^{melting} - h_{Fe}(T_0))}. \quad (7)$$

The drop temperature can be found from the transcendental equation:

$$T_{drop} = f(H_{drop}, m_{Fe}, m_O). \quad (8)$$

During the combustion gravity affects the drop $F_{gravity} = m_{drop}g$ and tends to deform the shape of the interface between the liquid and the surrounding oxygen atmosphere. Gravity counteracts the surface tension

$$F_{SurfTens} = \frac{2\sigma_{drop}(R_{rod} + R_{drop})}{R_{rod}R_{drop}}S_{rod}, \quad (9)$$

which prevents detachment of the drop from the rod. With the growth of the drop mass its size increases, and the surface tension decreases. In the non-flowing test conditions detachment of the drop occurs when the gravity $F_{gravity}$ and surface tension $F_{SurfTens}$ become equal. The condition of drop detachment:

$$\frac{2\sigma_{drop}(R_{rod} + R_{drop})}{R_{rod}R_{drop}}S_{rod} = m_{drop}g. \quad (10)$$

As noted above, the process of combustion initiation of the rod is not considered in this model. It is assumed that the rod is burning already. Moreover it is simulated steady periodic behavior, that is, it's covered the period between two successive drop detachments. As the characteristics of the melt after the sdetachment are not known, it is performed iteration specification of initial conditions. The first calculation is performed with starting initial conditions:

$$m_{Fe}|_{t=0} = m_{Fe}^0, \quad m_O|_{t=0} = m_O^0, \quad T_{drop}|_{t=0} = T_{drop}^0 \Rightarrow H_{drop} = H(T_{drop}, m_{Fe}, m_O). \quad (11)$$

The calculation is performed until the drop detachment $t = \tau$, which correspond to the detachment parameters m_{Fe}^τ , m_O^τ , T_{drop}^τ .

2.4. Results and discussion

Modelling was carried out in Wolfram Mathematica 9.0. Simulation of rod combustion and formation of drop is reduced to the numerical integration of differential equations (1), (2), (4) with initial conditions (11). During the integration the program calculates the drop mass and its enthalpy. The temperature of the drop can be determined from the enthalpies. The integration is terminated at a time when the relation (9) occurs.

During the simulation, there were calculated next fields (a/n experimental data were taken into account):

$$V_{melt}^{numeric} = f(C_{ac}, a_{ht}) - \text{the velocities field and}$$

$$\tau_{detachment}^{numeric} = f(C_{ac}, a_{ht}) - \text{the field of drop detachment times.}$$

For a rod diameter of 3.2 mm, these values are 12.2 mm/s and 0.2 s respectively.

The calculated values of the time of drop detachment, drop temperature at the beginning and at the end of the prop formation cycle, average velocity of burning, and also the values of accommodation and heat transfer coefficients are shown on the Table 1.

Table 1. The values of the combustion parameters obtained in the mathematical modelling for the rod diameter 3.2 mm

$t_{droplet}$, s	T_{start} , K	T_{end} , K	V, mm/s	C_{Ac}	a_{ht}
0.211664	3129.28	3129.60	12.1481	0.2536623	1.15×10^5

The examples of the calculated results of the different combustion parameters are presented on the Fig. 2–Fig. 5. Two main forces affecting the moment drop: the surface tension (red line) and the gravity (green) are shown on the Fig. 2. Droplet detachment occurs at the time when these forces are equal. The velocity of oxygen flow downward the rod will be taken into account with further improvement of the model. Thereby a third force that is directed downwards will appear and it will reduce the time of drop detachment.

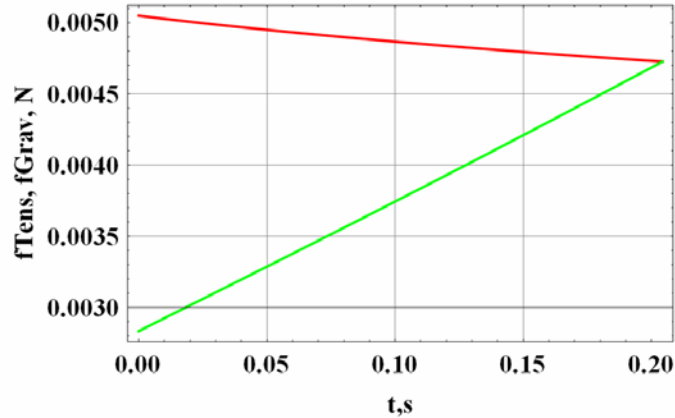


Fig. 2. The surface tension (red line) and the gravity (green line) during the drop formation cycle

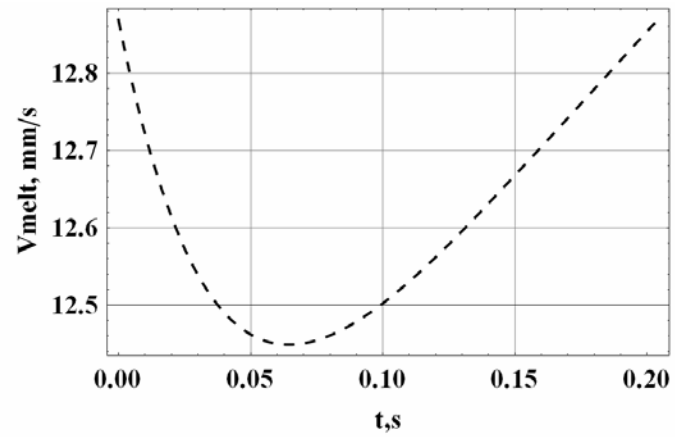


Fig. 3. Velocity of the melting front during the drop formation cycle

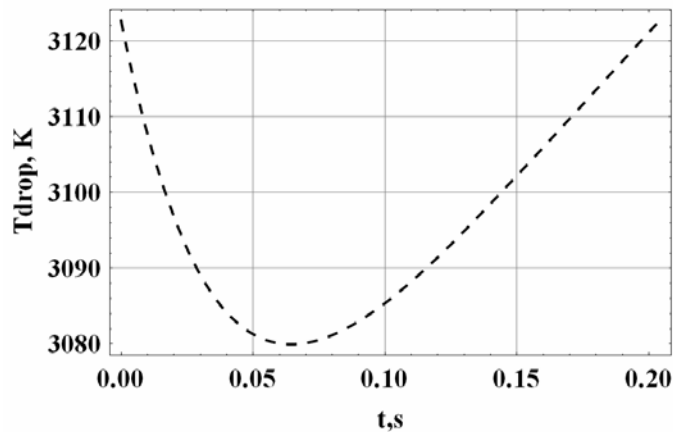


Fig. 4. Temperature of the drop during the drop formation cycle

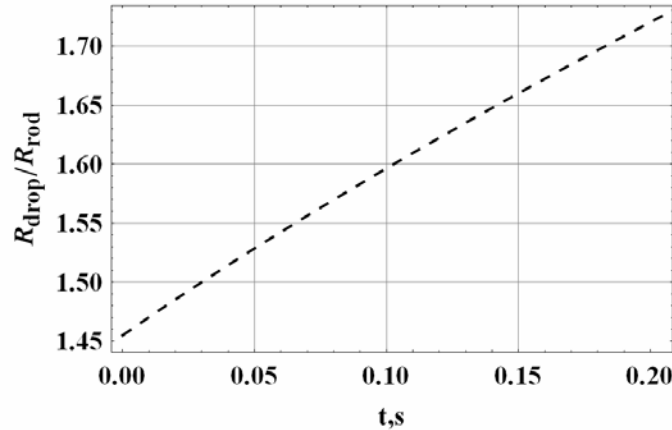


Fig. 5. Reduced value of the drop radius

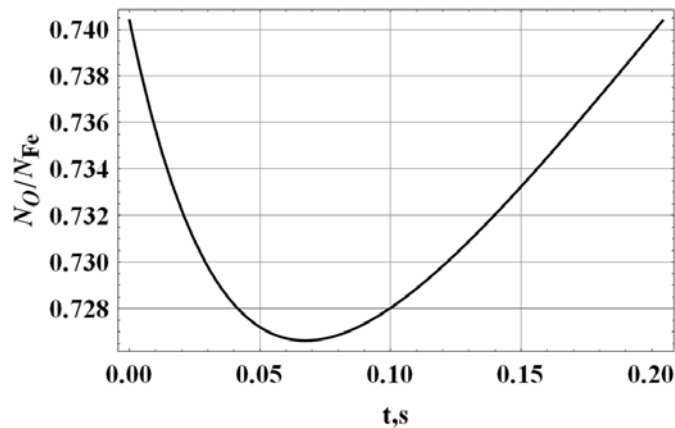


Fig. 6. The ratio of oxygen and iron in the drop

Thus, during the simulation, it can be obtained almost all the rod combustion parameters, determine the trend of the droplet formation and its time of separation. The program at the moment is not displaying graphics of heat distribution in the rod, but this parameter is present in the model and it can be visualized, as well as values of the droplet mass and some other parameters.

2.5. CONCLUSIONS

This paper presents a model of iron rod combustion with non-flowing test conditions. It contains the basic concepts and findings. Simulation was carried out in Wolfram Mathematica 9.0.

Modelling allows to take into account the configuration of the rod, oxygen pressure, ambient temperature, the rod alloy. The program facilitates to determine the burning rate, time of drop separation, the component structure of drop, its temperature, radius, mass over the cycle of drop formation and some other.

With further improvement of the model, the velocity of oxygen flow downward the rod will be taken into account, the model will be refined based on the improved mechanism of the oxygen transport to the surface of the reaction and generally amendments will be made on a larger number of experimental data.



REFERENCES

1. DEANN, L.E. and THOMPSON, W. R. Ignition Characteristics of Metals and Alloys. *ARS Journal*, July 1961, Vol. 31, No. 7, p. 917–923.
2. SLOCKERS, M. J., and ROBLES-CULBRETH, R. Ignition of Metals at High-Temperatures in Oxygen, *Flammability and Sensitivity of Materials in Oxygen-Enriched Atmospheres*, 2006, Vol. 11, p. 62–79.
3. SATO, J. and HIRANO, T. Fire Spread Mechanisms Along Steel Cylinders in High Pressure Oxygen, *Combustion and Flame*, 1989, p. 279–287.
4. STEINBERG, T. A. [et al.] Multiphase Oxidation of Metals, *Metallurgical and Materials Transactions*, 1997, Vol. 28, p. 1–6.
5. STEINBERG, T.A. [et al.] The combustion of iron in high-pressure oxygen. *Combustion and Flame*, 1992, Vol. 89, p. 221–228.
6. WILSON, D.B., STEINBERG, T.A. Thermodynamics and Kinetics of Burning Iron, *Flammability and Sensitivity of Materials in Oxygen-Enriched Atmospheres*, 1997, Vol. 8, p. 240–257.
7. SATO, J., SATO, K., HIRANO, T. Fire Spread Mechanisms Along Steel Cylinders in High Pressure Oxygen. *Combustion and Flame*, 1983, Vol. 51, p. 279–287.
8. WARD, N.R. and STEINBERG, T.A. The Rate-Limiting mechanisms for the Heterogeneous Burning of Cylindrical Iron Rods, *Journal of ASTM International*, 2009, Vol. 6.
9. SIRCAR, S., STOLTZFUS, J., BRYAN, C., KAZAROFF, J. Promoted Combustion of Pure Metals in Oxygen-Enriched Atmospheres, *Flammability and Sensitivity of Materials in Oxygen-Enriched Atmospheres*, 1995, Vol. 7, p. 100–106.
10. WERLEY, B.L., HANSEL, J.G. Flammability limits of Stainless Steel Alloys 304, 308 and 316, *Flammability and Sensitivity of Materials in Oxygen-Enriched Atmospheres*, 1997, Vol. 8, p. 203–224.
11. STEINBERG, T.A., RUCKER, M.A., and BEESON, H.D. Promoted Combustion of Nine Structural Metals in High Pressure Gaseous Oxygen, *Flammability and Sensitivity of Materials in Oxygen-Enriched Atmospheres*, 1989, Vol. 4, p. 54–75.
12. MC ILROY, K., RUCKER and ZAWIERUCHA, R. The Effects of Testing Methodology on the Promoted Ignition-Combustion Behavior of Carbon Steel and 316L Stainless Steel in Oxygen Gas Mixtures. *Flammability and Sensitivity of Materials in Oxygen-Enriched Atmospheres*, 1989, Vol. 4, p. 38–53.
13. DE WIT, J.R., STEINBERG, T.A., and HAAS, J.P. ASTM G-124 Test Data For Selected Al-Si Alloys, Al-Composites, Binary Alloys and Stainless Steels. *Flammability and Sensitivity of Materials in Oxygen-Enriched Atmospheres*, 2000, Vol. 9, p. 179–189.
14. SAMANT, A.V., ZAWIERUCHA, R. and MILLION, J.F. Thickness Effects on the Promoted Ignition-Combustion Behavior of Engineering Alloys. *Flammability and Sensitivity of Materials in Oxygen-Enriched Atmospheres*, 2003, Vol. 10, p. 177–191.
15. NASA White Sands Test Facility. Promoted Ignition in Flowing Oxygen Special Tests Data Report, *WHA Test Reports*, December 2, 2004.
16. Industry-Sponsored Metals Test Program 05-1. Promoted Combustion of Metals in Flowing and Nonflowing Oxygen Environments. *WHA Test Reports*, April 13, 2007.
17. SUVOROV, T., [et al.] Effects of Sample Geometry on Regression Rate of the Melting Interface for Carbon Steel Burned in Oxygen. *Journal of ASTM International*, Vol. 3(4), April 2006.
18. SUVOROV, T. Promoted Ignition Testing: An Investigation of Sample Geometry and Data Analysis Techniques. A Thesis Submitted for the Degree of Doctor of Philosophy, Queensland University of Technology, 2007.



RAPID COMPRESSION MACHINE STUDY OF AUTO-IGNITION AND COMBUSTION OF LIQUID FUELS WITH ULTRADISPERSE ADDITIVES

V.V. Leschevich, O.G. Penayzkov, S.V. Shushkov

*Heat and Mass Transfer Institute
15 P. Brovki, 220072, Minsk, Belarus
Phone +375172841520
E-mail: V.Leschevich@dnf.itmo.by*

ABSTRACT

The influence of nanosized carbon additives, obtained by different methods, on the ignition and combustion properties of ethanol was investigated. An analysis of fuel suspensions has been performed by a transmission and scanning electron microscopes before studying of their combustion behaviour in rapid compression machine. Experiments were carried out for stoichiometric fuel/air compositions at compression ratio 27:1. A specimen of liquid fuel was placed in a cup put into the combustion chamber before compression event. It was found that the rate of fuel combustion after electrical discharge treatment could be increased (about 10%). Any significant changes in ignition delay time were not observed at these experimental conditions.

Keywords: combustion, auto-ignition, ethanol, carbon nanoparticles

1. INTRODUCTION

In order to improve the commercial properties of fuels, they are often supplemented with additives in the form of particles of ultra disperse materials. For example, additions of a nanodisperse aluminium powder make it possible to obtain a prospective solid rocket fuel, since with these additives the rate of combustion increases by an order of magnitude (as compared with compositions involving aluminium particles of micron size) [1]. Dispersion of aluminium in a liquid fuel decreases the ignition delay by 30%, with the heat transfer through particles and additional energy release during their combustion being considered as the main mechanisms of efficient combustion [2]. Nanoparticles of other metals too are used as combustion catalysts [3]. A fuel is also admixed with nanosized carbon additives, for example, fullerenes C60 and C70, which have already become marketable. Additions of carbon nanotubes also increase the efficiency of combustion [4]. Graphene particles of size 200–500 nm increase the rate of combustion, which is attributable to the high thermal conductivity and emissivity of graphene, as well as to the absence of a solid phase in the combustion products [5]. In this study nanosized carbon additives were synthesized by different methods in ethanol which was selected as a model fuel, because it is widely used as a biofuel.

2. EXPERIMENTAL SETUP AND MATERIALS

2.1 Fuel. Nanosized Solid Additives

Several techniques were used to synthesize nanosized carbon additives in a fuel. The obtainable fuel suspensions were studied by a JEM100CX transmission electron microscope (TEM) and a LEO1455VP scanning electron microscope (SEM).

2.1.1. Technique A

Fuel A was produced by depositing graphitized films from a CH₄/He mixture onto a nickel surface in a gas discharge [6]. Thereafter, the films were separated from the substrate by etching in hydrochloric acid (HCl), washed with distilled water, dried, and dispersed in ethanol by treating in an ultrasonic bath for 1 h. As is seen from Fig. 1, the particles have different shapes and a marked spread in the size, hence the fuel was additionally cleaned of the largest particles by passing it through a filter paper.

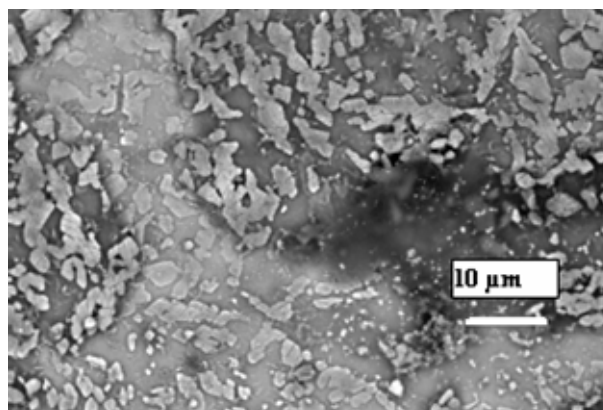


Fig. 1. Ultradispersed particles of fuel suspension A (SEM image)

2.1.2. Technique B and D

Nanosized particles were synthesized during the exposure of ethanol to an electric d.c. discharge. The cathode electrode made from the stainless steel was mounted at a distance of several millimeters above the ethanol surface, whereas the anode was put deeper into the ethanol. The gas volume of the reactor was filled with argon. On supply of voltage of 1000 V to the electrodes, a gas discharge was developed between the cathode and the liquid phase surface and, depending on the intensity of current, plasma synthesis of various particles occurred. A typical time of treating 10-ml specimens was approximately 1 h.

It is seen that in fuel B produced after treating ethanol with a current of 1–2 mA, different-structure clusters of size of up to 1 μm were synthesized (Fig. 2). Planar structures appear in fuel D when ethanol is treated by a high current of approximately 10 mA (Fig. 3).

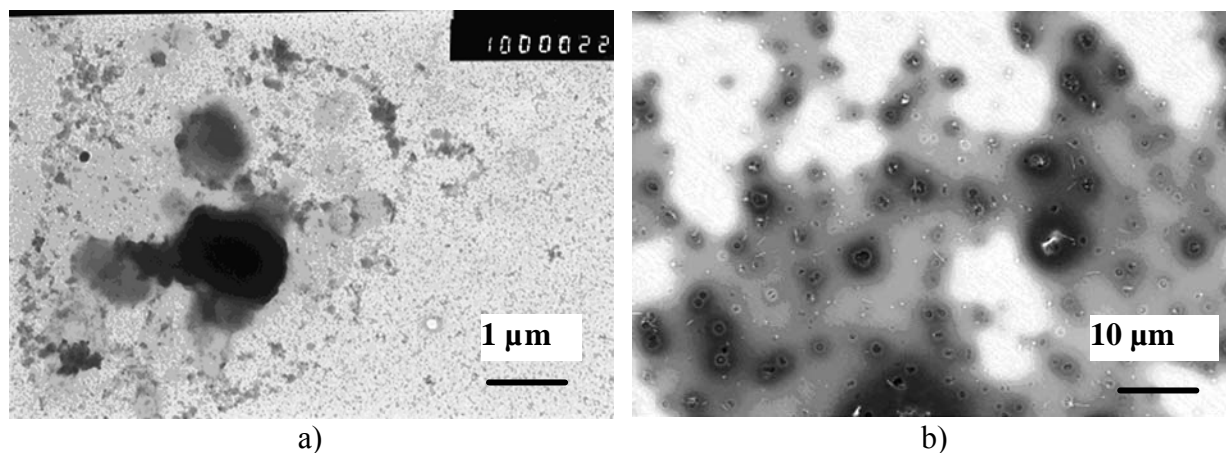


Fig. 2. Solid-phase carbon structures formed on electric-charge treatment of ethanol in fuel B obtained with the aid of TEM (a) and SEM (b)

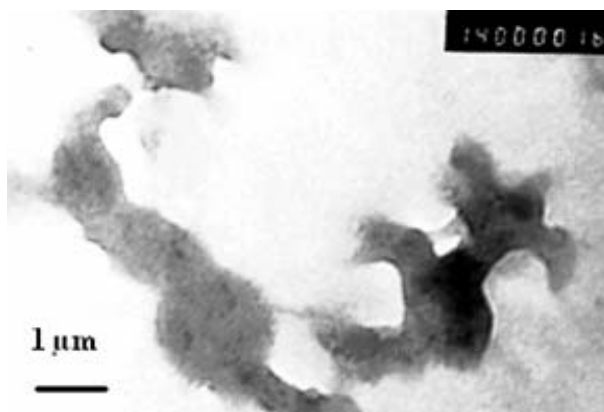


Fig. 3. Solid phase in fuel D (TEM image)

2.1.3. Technique C

A pair of stainless steel electrodes with an interelectrode gap of 1–10 mm was immersed into ethanol at a depth of 1 cm, and a d.c. voltage of 1000 V was applied to them. In the zone between the electrodes, the supply of a high-voltage initiating pulse caused the formation of gas bubbles which consisted of ethanol vapour and the products of its decomposition through which a quasi-stationary discharge was initiated. Under these conditions, the discharge current varied within 20–50 mA. In this high-current regime, the formation of a certain amount of soot-like particles was observed; they were removed by filtering as in the case of fuel A. After the electric discharge treatment, clusters of predominantly spherical shape and submicron size were detected in fuel C (Fig. 4).

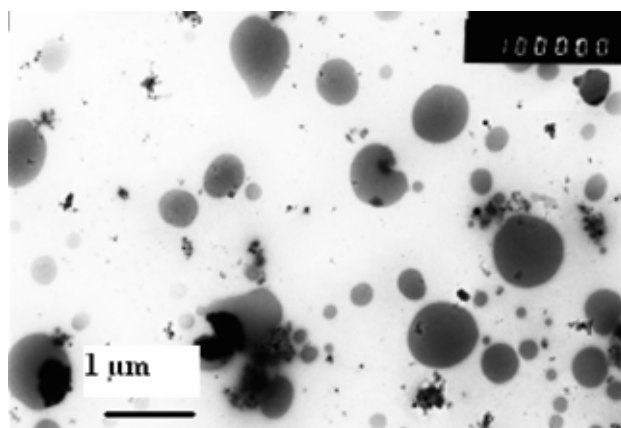


Fig. 4. Solid phase in fuel C (SEM image)

In our case, the recovery of solid particles occurs due to a relatively high specific power density of about 10 W/cm^3 of the discharge in ethanol vapours. Here, a chain mechanism of formation of radicals that leads to the formation of linear macromolecules and solid phase nuclei can take place [7]. Particles can also be formed via nucleation and polymerization by way of successive addition of acetylene (C_2H_2) fragments [8], which is usually the case where there is an excess of hydrogen and which is confirmed by the presence of C_2 dimer lines in the spectrum of a similar weak current hydrocarbon plasma [9].

The obtained specimens of fuel were transparent yellowish suspensions, which being illuminated by a laser beam, displayed the Tyndall effect, that is, the side visibility of the beam because of light scattering on the nanoparticles. Since in the course of time, the colloid solution develops aggregation, which leads to an increase in the size of particle agglomerates and their

sedimentation, experiments in rapid compression machine were conducted not later than several days after the suspension was obtained.

In the case of electric discharge treatment, the fuel, apart from solid particles, contains liquid synthesized compositions, which are detected by the chromatography and mass spectrometry methods. Stream chromatography by a "Crystal-2000M" for all types of fuel revealed the presence of a certain amount of higher components after electric discharge treatment. It was established that the treatment of the ethyl alcohol by technique B results in the formation of glycols, a complex acid, and an aldehyde. Compounds of glycol series were also detected in the specimen obtained by technique D. Tetradecanol $\text{CH}_3\text{-(CH}_2\text{)}_{12}\text{-CH}_2\text{-OH}$ was detected, in particular, in specimen C. Thus, in our case, the electric-discharge synthesis of intermediate ethanol compounds proceeds with the formation of molecules predominantly in the form of linear chains of carbon atoms.

2.2 Rapid compression machine facility

The combustion properties of synthesized fuels were investigated by rapid compression machine. The schematic diagram of its compression cylinder is presented in Fig. 5. The combustion chamber (1) was equipped with: a valve for evacuation and inflow of gas mixture (2), a Kistler 6031U18 high-temperature piezoelectric pressure sensor (3), and a quartz window (6) that provides access for optical measurements. A bifurcated fiber cable (8) was used to transfer light radiation from the interior of the chamber to photometric devices (9). All signals were recorded by a multichannel storage oscilloscope (10). In the experiments, the compression cylinder was filled with air up to atmospheric pressure, and a specimen of liquid fuel was placed in a metal cup (5) put into the combustion chamber. The quantity of fuel was calculated based on the stoichiometric ethanol/air relationship at the given atmospheric pressure, temperature, and humidity.

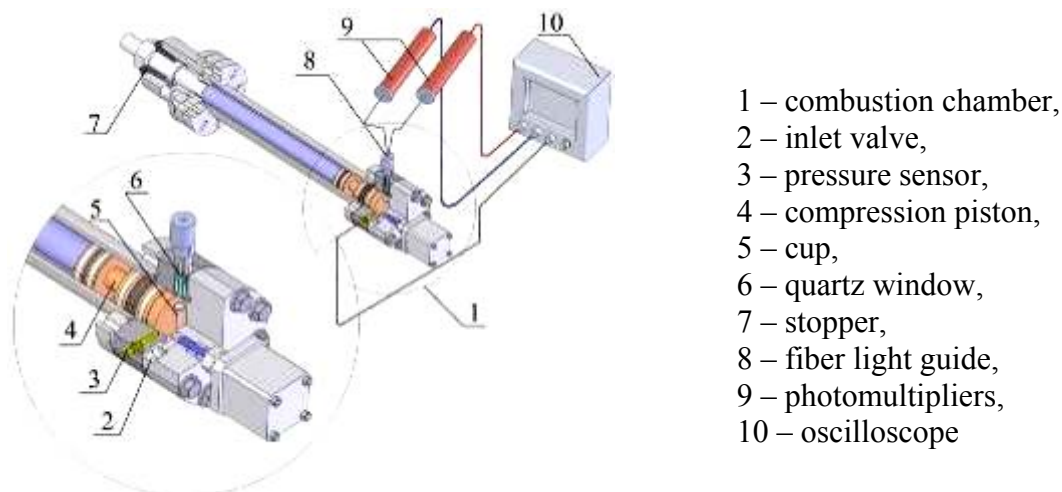


Fig. 5. Compression cylinder of a rapid compression machine and measuring equipment

In the each experiment, the change in the pressure in the combustion chamber caused by compression and ignition of fuel, as well as the glow within the chamber, was recorded. As photometric devices, two photomultipliers were used, before whose photocathodes narrow-band interferential filters transmitting radiation with wavelengths $\lambda = 308.9 \text{ nm}$ and $\lambda = 431.5 \text{ nm}$ were placed. These wavelengths correspond to transitions between the energy levels of excited OH ($A^2\Sigma - X^2\Pi$) and CH ($2\Delta - 2\Pi$) molecules, with the former being the basic intermediate radicals in the chemical reactions during the self-ignition of mixture and the latter being the intermediate radicals in the reactions of the formation of combustion products. Three criteria were used to measure the time of mixture induction: the pressure increase in the chamber due to the mixture ignition and the appearance of light emission within the chamber at two wavelengths.

During the preparatory tests, the parameters at which the self-ignition of an initial fuel (ethanol) occurs, as well as the repeatability of experimental results were determined. It was found that the original fuel ignites spontaneously at degrees of air compression above 27:1. In this case, at the end of the compression stroke, the pressure in the chamber attains 8.5 MPa and the temperature amounts to 980 K (estimates based on the adiabaticity of the compression process). The signals from the pressure sensor and photomultiplier with 308.9 nm filter recorded during four experiments are depicted in Fig. 6 where the dashed lines correspond to the signals in the experiment without a fuel. It was established that the maximal pressure in the chamber because of fuel compression is reproduced with an accuracy of 3.5% and the ignition delay, with an accuracy of about 5%. Thus, we may state that the given procedure will make it possible to carry out a comparative analysis of the combustion properties of different specimens if the resulting effect exceeds the 5% level.

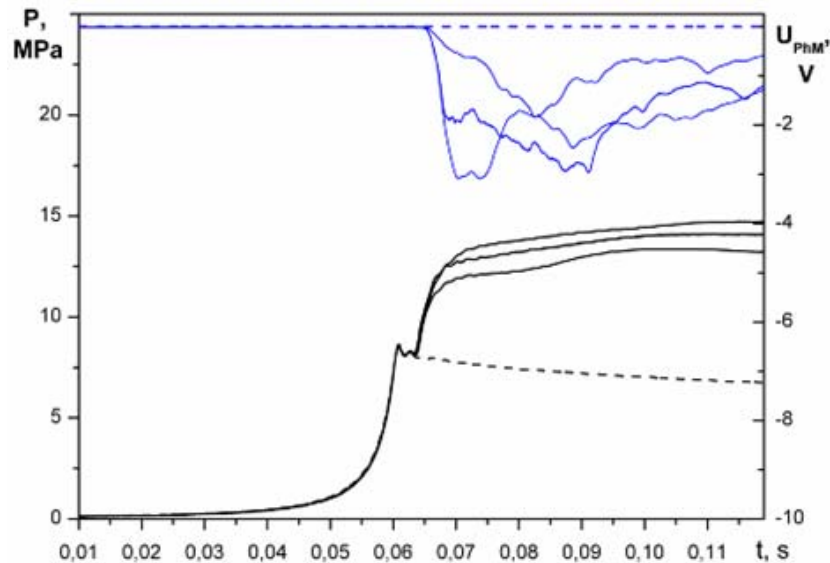


Fig. 6. Pressure (black lines) and photomultiplier (blue lines) signal registered during experiments with pure ethanol

3. RESULTS AND DISCUSSION

The experiments with the specimens of modified fuels were carried out at the same conditions as experiments with ethanol. Moreover, each series was run during one day and always started from ethanol. Fig. 7 a presents the results of a comparative analysis of self-ignition and combustion of specimens A (blue dashed line) and B (red dashed line) relative to the original specimen 0 (black solid line). The auto-ignition delay time and the maximum level of pressure in the chamber are identical within the procedure error for all specimens. However, in the case of combustion of specimen B, the rate of pressure rise in the chamber is much higher as compared with the original fuel 0 and sample A. This can be associated with the more intense evaporation of sample B. The results of measurements for specimens C and D are presented in Fig. 7 b. As with the previous specimens, the auto-ignition delay time lies within the limits of the error of the method, which points to the fact that it depends on the ethanol evaporation rate. However, during the subsequent combustion of samples C and D, the pressure in the chamber increases more rapidly as compared to the original fuel. As is seen, the level of specimen C is approximately 10% higher than that of specimen 0. As is seen from the experimental data, the rate of fuel combustion after electrical discharge treatment can increase substantially. There are several explanations for the effect observed. The dynamics of combustion experiences the effect from both liquid synthesized substances and solid nanoparticles. Liquid light fractions can accelerate the evaporation of fuel during its combustion in a bowl. Some components synthesized by an electric discharge, e.g.,

tetradecanol, have a higher enthalpy in comparison with the original ethanol, and during combustion they produce a higher thermal effect. Various mechanisms of combustion acceleration for solid particles can be considered. In our experiments, synthesized particles are predominantly represented by porous clusters composed of chain structures. Their influence on the fuel combustion rate can manifest itself as acceleration of heterogeneous reactions on the developed solid surface of nanoparticles as compared to purely gas-phase combustion. However, since the material of the particles can contain uncontrolled impurities, for example, of metals sputtered by the electrodes, the catalytic mechanism of the accelerated combustion must also be taken into account.

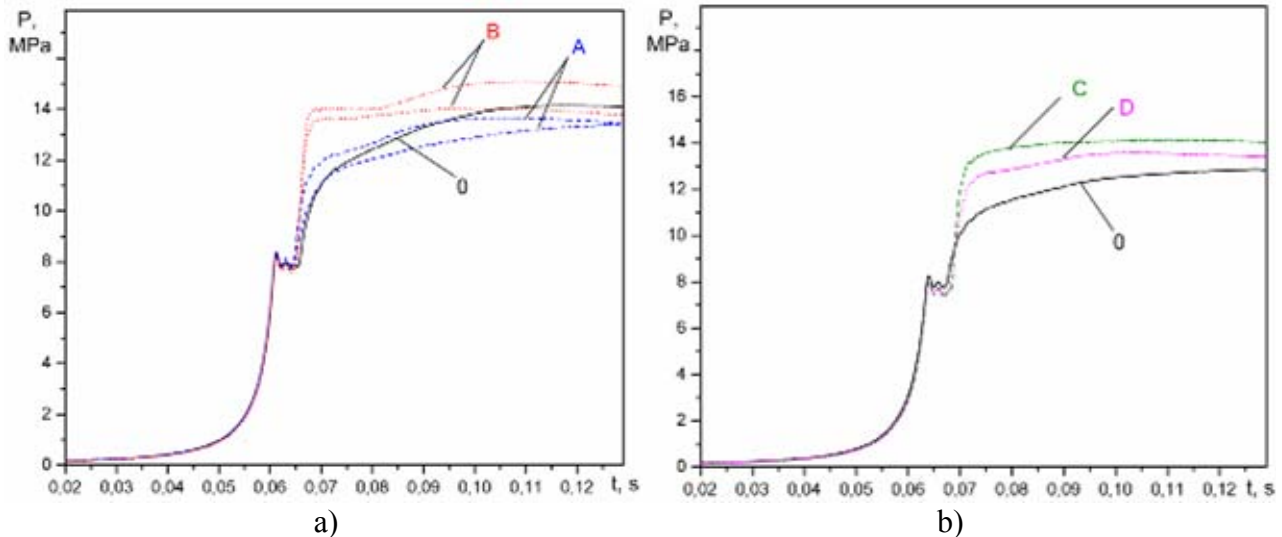


Fig. 7. Pressure signals registered during rapid compression machine experiments with ethanol (0) and modified fuels (A, B, C and D)

In order to make a more distinct separation of the above-mentioned factors, it is necessary to carry out experiments on combustion of a fuel under conditions of diffuse fuel injection into combustion chamber of rapid compression machine. It is also necessary to investigate specimens of fuels after their long storage in order to determine the factor of sedimentation of solid particles. It should be noted that in future modification of bioethanol seems to be imperative, because its production in a pure state is nonprofitable; therefore, only ethanol with improved characteristics will turn out to be competitive as an additive to a traditional fuel. It is of interest to estimate the magnitude of additional energy expenditures on electric discharge treatment of a fuel as compared to the own calorific value of the latter. For example, for technique C of obtaining a fuel at an electric discharge power of about 1–10 W, with the heat of combustion of ethyl alcohol assumed to be equal to 27.2 MJ/kg (without expenditures on evaporation of inherent water), the fraction of the additional energy input equals several percent.

4. CONCLUSION

The dynamics of pressure increase on combustion of ethanol preliminarily treated by electric discharge can be improved by the formation of both nanosized carbon solid particles and liquid synthesized substances. Catalytic heterogeneous reactions on the surface of solid nanoparticles can be an important mechanism underlying the improvement of the rate of combustion. Liquid volatile fractions can ensure accelerated evaporation of a fuel.



REFERENCES

1. FROLOV, YU.V., PIVKINA, A.N., IVANOV, D.A., et al. Structure of particles and combustion parameters of nanoaluminum. *Russian Journal of Physical Chemistry B*, 2008, Vol. 2, No. 3, p. 463–469.
2. ALLEN, C., MITTAL, G., SUNG, C. J., TOULSON, E., LEE, T. An aerosol rapid compression machine for studying energetic-nanoparticle-enhanced combustion of liquid fuels. *International Journal of Chemical Kinetics*, 2011, Vol. 33, p. 3367–3374.
3. REN, YONG-QIANG, HUANG, ZHI-NING, FU, YAN. Evaluation on combustion properties of nanoparticle as fuel additive. *Advanced Materials Research*, 2011, Vols. 335–336, p. 1516–1519.
4. MOY, D., NIU, CH., TENNENT, H., HOCH, R. Carbon Nanotubes in Fuels. *Patent 6419717 US*, 2002.
5. SABOURIN, J.L., DABBS, D.M., YETTER, R.A., DRYER, F.L., AKSAY, I.A. Functionalized graphene sheet colloids for enhanced fuel/propellant combustion. *ACS Nano*, 2009, Vol. 3, No. 12, p. 3945–3954.
6. ZHDANOK S.A., KRYLOV I.S., SILENKOV M.A., FILATOV S.A., SHUSHKOV S.V. Deposition of cathode carbon films in the plasma of a low-current gas discharge at atmospheric pressure. *Journal of Engineering Physics and Thermophysics*, 2011, Vol. 84, No. 3, p. 540–545.
7. TESNER P.A. *Formation of Carbon from Gas-Phase Hydrocarbons* [in Russian], Moscow: Khimiya, 1972, 136 p.
8. KRESTININ A.V. Formation of soot particles as a process involving chemical condensation of polylines. *Chemical Physics Reports*, 1998, Vol. 17, No. 8, p. 1441–1461.
9. ZOLOTUKHIN, A.A., OBRAZTSOV, A.N., VOLKOV, A.P., USTINOV, A.O. Formation of nanocarbon film materials in a gas-discharge plasma. *Journal of Experimental and Theoretical Physics*, 2003, Vol. 124, No. 6, p. 1291–1297.



NUMERICAL MODELS OF WOOD PELLET SHRINKING ON PYROLYSIS

R. Paulauskas, A. Džiugys, N. Striūgas

Lithuanian Energy Institute

Breslaujos str. 3, LT-44403 Kaunas – Lithuania

ABSTRACT

The shrinkage of the wood pellet impacts the pyrolysis in several ways. The properties as porosity, permeability, density, mass diffusivity, specific heat capacity, thermal conductivity, the total volume of the particle changes continuously. The density of the char increases during pyrolysis due to the chemical restructuring process. The temperature profile of the particle changes too. Therefore, an explicit understanding of the transport mechanisms and chemical processes of impact in wood pellet shrinking is needed. Researchers analyze the wood pellets shrinking on pyrolysis using a kinetic model coupled with heat transfer model. The numerical models are used to study the impact of shrinkage on particle size, volume, pyrolysis time, product yields and specific heat capacity. These numerical models are validated with experimental results later.

The shrinkage models of wood pellet are discussed in this paper. The simplest model is one-dimensional (1D) using constant properties and considering bare minimum processes. The shape of wood pellet is mostly chosen in spherical for 1D model. Three models are formulated for dry wood pellets. Other models for wet pellets are presented too. More complex model is two-dimensional formulated in cylindrical coordinates and used to predict the progress of conversion in a cylindrical wood particle undergoing pyrolysis. Some models are used for single wood particle reactor with low heating-rate. Several researchers suggested model for pyrolysis in packed bed, others formulated for pyrolysis in a fluidized bed. Shrinking effect is included in these models.

All mentioned models shows the influence of anisotropy on the product yield and conversion time. One-dimensional and two-dimensional models are presented in this work in order to identify suitable model for numerical simulations of particles dynamics and conversion. The differences between these models are presented too.

Keywords: shrinkage, wood pellet, pyrolysis, numerical model

1. INTRODUCTION

Products of biomass pyrolysis are used for energy recovery, power generation and etc. Also pyrolysis takes first place in combustion and gasification. During pyrolysis wood pellets are decomposed into mixture of volatile species (gases and tar) and a solid carbonaceous residual (char). It is important to point out that the wood pellet decomposition depends on three main parameters (the heating rate of the pellets; the residence time of the pellets and of the pyrolysis products in the reactor; the temperature of the reactor). Among these, the heating rate is surely the most difficult to control since it depends on many variables including the thermochemical properties of the solid, the content in humidity, the particle size, the kind of reactor [1].

The decomposed products cause shrinking, which involves such parameters as porosity, permeability, density, mass diffusivity, the volume occupied by the volatiles and solid, in wood pellet. Also particles size as well particles shrinking has important influence on particles dynamics, residence time, mixing, segregation [2]. The numerical models are used to study the impact of shrinkage on these parameters and investigate how it effects pyrolysis process. The most usable models of particle conversion are one-dimensional or two dimensional models. Also there are three-dimensional models, but it requires too much computing resources for numerical simulation dynamics and conversion of big number particles by Discrete Elements Method (DEM). The purpose of this work is to investigate shrinking models for the wood pellet and compare them in order to identify suitable model for numerical simulations of particles dynamics and conversion.

2. NUMERICAL MODELS

2.1. One-dimensional models

Shrinking of wood pellet is simulated by one-dimensional model in two ways: using modified heat transfer model or modified thermal decomposition model by chemical reaction kinetics. Wood pellet maintains the shape of a sphere in both models. Boundary conditions as surface temperature, surface pressure are the same in both models and their values are equal to measured temperature and atmospheric pressure.

Modified model of heat transfer is used to simulate pyrolysis and the influence from structural changes of dry wood pellet. This model consists equation of energy conservation and expressions for solid phase and species concentration in the gas phase. Formulation of temperature T from energy equation is showed below[3]:

$$\frac{\partial T}{\partial t} \cdot (c_{ps}\rho_s + c_{pg}\epsilon_g\rho_g) + \frac{\partial T}{\partial r} \cdot (c_{pg}u\rho_g) = \frac{1}{r} \cdot \frac{\partial}{\partial r} \left(rk_{eff} \frac{\partial T}{\partial r} \right) - \omega_p \Delta h_p, \quad (1)$$

where ρ_s is the sum of wood density ρ_w and charcoal density ρ_c , ϵ_g – porosity, u – gas velocity in the radial direction of the pellet, which are calculated from Darcy's law, c_{ps} – specific heat of solid, c_{pg} – specific heat of gas, k_{eff} – effective heat conductivity and h_p – heat of pyrolysis. The expression of solid phase is written:

$$\frac{\partial \rho_s}{\partial t} = \omega_p - \frac{\rho_s}{V} \cdot \frac{\partial V}{\partial t}, \quad (2)$$

where ω_p – decomposition of solid phase during pyrolysis and V – pellet volume, which is included to account for shrinking. The concentration of species j is calculated below:

$$\frac{\partial \epsilon_g \rho_j}{\partial t} + \frac{1}{r} \cdot \frac{\partial ur \rho_j}{\partial r} = \frac{1}{r} \cdot \frac{\partial}{\partial r} \left(r D_{eff} \rho_g \cdot \frac{\partial \rho_j / \rho_g}{\partial r} \right) + \omega_j - \frac{\epsilon_g \rho_j}{V} \cdot \frac{\partial V}{\partial t}, \quad (3)$$

where D_{eff} – binary diffusivity of species j in the gas phase, ω_j – the production of species j . The last term on equation accounts for the shrinking. Model of shrinking is developed on three empirical shrinking parameters: α , β , γ . These parameters are used to describe volume changes included in Eqs. (1) and (2). The equation of solid volume is written [3]:

$$V_s = V_s^i \cdot \frac{V(\rho_w + \alpha \rho_c)}{\rho_s^i V^i}. \quad (4)$$

The second model is used to describe wood thermal degradation to gas, tar and char by primary reactions and tar changes to gas or to char by second reactions in fluidized bed reactor. This model consists kinetic equations with mass transfer phenomenon. The mass is expressed to pellet volume and density. The equation is written as [4]:

$$\frac{\partial(\rho_w V)}{\partial t} = -(k_1 + k_2 + k_3) \rho_w V, \quad (5)$$

$$\frac{\partial(\rho_c V)}{\partial t} = -k_1 \rho_w V + k_5 \epsilon \rho_0 V. \quad (6)$$

The solid particle undergoes shrinkage with devolatilization, which influences enthalpy balance. Also endothermic and exothermic reactions take place in wood pellet pyrolysis process. All these are described as [4]:

$$\frac{DH}{Dt} = \text{div}(\lambda \text{grad } T) + \sum_{i=1,5} Q_i - \frac{H}{V} \cdot \frac{\partial V}{\partial t}, \quad (7)$$

where DH/Dt represents enthalpy change rate and enthalpy flow, $\text{div}(\lambda \text{grad } T)$ represents thermal conduction flux, the sum of Q_i – heat effect during particle thermal-degradation, and the last one

describes the effect of shrinkage. Then particle shrinkage is assumed with the densities of char and wood and pellet volume is calculated below:

$$V = V_0 + \frac{m_s - m_{w0}}{m_{cs} - m_{w0}} \cdot (V_s - V_0). \quad (8)$$

2.2. Two-dimensional models

Two-dimensional model has the same initial conditions, solid definition and kinetic expressions as 1D model, but boundary conditions and equations for energy and mass are modified. These modifications are performed for the shape of cylindrical wood pellet, which is discretised by hollow cylinders. The volume of pellet is defined as [5]:

$$V = 2\pi r \Delta z \Delta r, \quad (9)$$

where r – inner radius, $r + \Delta r$ – outer radius Δz – height of hollow cylinder. At the pellet surface boundary conditions is written:

$$-h_t(T - T_{ext}) - \omega\sigma(T^4 - T_{ext}^4) = -[\lambda_{eff} \cdot \nabla T] \cdot \mathbf{n}, \quad (10)$$

where ω is the emissivity, σ – the Stefan–Boltzmann constant, h_t – the heat transfer coefficient and \mathbf{n} – the unitary vector orthogonal to the surface. In the middle of the pellet boundary conditions are used:

$$\mathbf{n} \cdot \nabla T = 0, \quad (11)$$

$$\mathbf{n} \cdot \nabla m_i = 0. \quad (12)$$

The temperature, wood and char densities are constant in the control cylinders. The heat flow is calculated at the centre and the surfaces of the cylinders using central differences. The divergence of the flow is approximated at the centre of the cylinders by central differences. Boundary conditions are included in the discretised equations and solved by implicit method [5]. The energy conservation in a control volume is used:

$$\frac{\partial T}{\partial t} = \frac{-V \nabla \cdot Q - \sum_{i=1}^3 w_i \Delta H_i}{m_w c_{pw} + m_c c_{pc}}, \quad (13)$$

where T is the temperature, V – the volume of the pellet, ΔH_i – the reaction heat and Q – the heat flow.

Three different models are used for shrinking simulations. All these models calculate shrinkage coefficients for changes of volume. The simplest one is uniform shrinkage model, where the conversion is averaged over the whole particle and ratio of control and total volume is constant [5].

$$\frac{V}{V_{tot}} = \frac{V}{\sum V} = \frac{s_r^2 s_z V_0}{\sum s_r^2 s_z V_0} = \frac{V_0}{V_{tot,0}} = const, \quad (14)$$

where s_z is longitudinal and s_r radial shrinkage coefficients, V_{tot} – total volume which is calculated by:

$$V_{tot} = s_r^2 s_z \pi r_0^2 l_0. \quad (15)$$

The shrinkage coefficients are carried out at each time step. The order differential equation system is implicitly solved at each time step and the shrinkage is calculated explicitly. The same radial and longitudinal shrinking coefficients are used for all volumes.

The shrinking shell model calculates the radial shrinkage coefficient at radius r by averaging the conversion over a hollow cylinder with an inner radius $r - \Delta r/2$ and an outer radius $r + \Delta r/2$ and with a length l_0 . The longitudinal coefficient at length z is calculated on a flat cylinder of upper

surface $z + \Delta z/2$ and lower surface $z - \Delta z/2$ with radius r_0 . In this model the coefficient is S_r and S_z can be different for each node while the global cylindrical shape of the particle still remains [5].

The shrinking cylinders model calculates radial and longitudinal shrinkage coefficients at radius r and height z with a conversion averaged over a hollow cylinder with an inner radius $r - \Delta r/2$ and with an outer radius $r + \Delta r/2$ and with a length l_0 . In this model, the particle is seen as a series of hollow cylinders, which linearly shrink with conversion. It physically means that shrinkage occurs along the fibres and that they shrink independently from each other [5].

3. DISCUSSIONS

The wood pellets use the shape of sphere in discussed one-dimensional models. The shrinking are described by mass and density changes, which shows reduction in volume of wood pellet by 52–77%. The model for dry pellets is simpler to use than the model for fluidized reactor. The convective terms are discretised by first order upwinding but diffusive terms by central differentiation. Equations are calculated by implicit method.

Three models of shrinkage for 2D models are presented too. The uniform shrinkage model is simple to implement comparing to other 2D models. Also the ratio of control and total volume is constant over the whole pyrolysis, what gives the same shrinking effect in all hollow cylinders and changes during time step as it shown in Fig. 1.

The shrinking shell model is more realistic than uniform shrinkage since shrinkage is likely to follow the pyrolysis wave and to occur as a shrinking shell. This model is more difficult to implement and needs more time for calculations since each control volume has to be evaluated and the central difference approximation for unequal space step requires more calculations and is less accurate.

The shrinking cylinders model is the most complicated to implement since the grid is neither orthogonal nor evenly spaced making gradient and divergence calculations much more difficult. The particle is also no longer cylindrical except at the beginning and the end of pyrolysis.

Differences of these three 2D models are shown in scheme (Fig. 1) below:

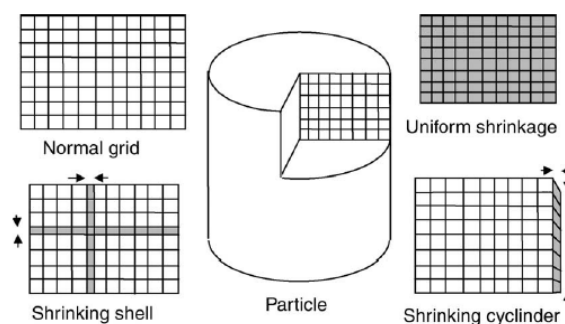


Fig. 1. Different schemes for calculating shrinkage coefficients. Grey zones represent the part of the grid used for averaging the conversion [5]

The shrinkage has an opposite influence on pyrolysis whether it is uniformly or locally modelled. Using uniform shrinkage model the rate of pyrolysis decreases but it increases for shrinking shell and cylinders models. The outer part of the wood pellet shrinks using models of shrinking shell and cylinders during pyrolysis. This happens due to the greater temperature gradient in the outer part of pellet.

4. CONCLUSIONS

One-dimensional models are simpler to use for shrinking comparing with two-dimensional models for the shape of sphere. Also shrinking of wood pellet volume is calculated by mass and



density changes. Furthermore two-dimensional models involve radial and longitudinal shrinkage coefficients what effect in more time of calculations. Besides it requires more computing resources for numerical simulation dynamics and conversion of big number particles by DEM.

REFERENCES

1. SREEKANTH, M.; KOLAR, Ajit Kumar. *Progress off conversion in a shrinking wet cylindrical wood particle pyrolyzing in a hot fluidized bed*. Journal of Analytical and Applied Pyrolysis 84, 2009, p. 53–67.
2. PETERS, B.; DŽIUGYS, A.; HUNSINGER, H.; KREBS, L. *An Approach to Qualify the Intensity of Mixing on a Forward Acting Grate*. Chemical Engineering Science 60, 2005, p. 1649–1659.
3. LARFELDT, J.; LECKNER, B.; MEAAEN, M.C. *Modelling and measurements of the pyrolysis of large wood particles*. Fuel 79, 2000, p. 1637–1643.
4. LUO, Zhongyang; WANG, Shurong; CEN, Kefa. *A model of wood flash pyrolysis in fluidized bed reactor*. Renewable Energy 30, 2005, p. 377–392.
5. BELLAIS, Micheal; DAVIDSSON, K.O.; LILIEDAHL, T.; PETERSON, J.B.C. *Pyrolysis of large wood particles: a study of shrinkage importance in simulations*. Fuel 82, 2003, p. 1541–1548.
6. PETERS, B.; DŽIUGYS, A.; NAVAKAS, R. *A shrinking model for combustion/gasification of char based on transport and reaction time scales*. Mechanika 18, 2012, p. 177–185.
7. BABU, B.V.; CHAURASIA, A.S. *Heat transfer and kinetics in the pyrolysis of shrinking biomass particle*. Chemical Engineering Science 59, 2004, p. 1999–2012.
8. PETERS, B.; DŽIUGYS, A.; HUNSINGER, H.; KREBS, L. *Evaluation of the Residence Time of a Moving Fuel Bed on a Forward Acting Grate*. Granular Material 8, 2006, p. 125–135.



OPTIMIZATION OF COMBUSTION PROCESS BY CHARACTERIZATION OF THE FLAME PARAMETERS USING CHEMILUMINESCENCE PHENOMENON

A. Saliamonas, N. Striūgas, R. Navakas

*Lithuanian Energy Institute,
Laboratory of Combustion Processes
Breslaujos str. 3, LT-44403 Kaunas – Lithuania*

ABSTRACT

Combustion is one of the most important energy and industrial processes. Currently all combustion devices must fit main requirements: they must be cost-effective and environmentally friendly. In process of improving the construction of combustion facilities, it is imperative that they operate environmentally, economically and reliably under different modes of operation and use of fuels with different chemical composition and physical properties. Most suitable for achieving these goals are combustion devices that can automatically adapt to the operating mode. Such devices have an integrated active control system, consisting of flame diagnostic equipment, signal processing, parameter selection and management system, which, according to measured parameters of the combustion process sets the operation mode for a burner.

Most of the currently used burners have a diagnostic combustion system which uses flue gas composition analysis. In this manner, the data does not adequately describe the ongoing process. A more accurate way is to directly measure the flame parameters using chemiluminescence phenomenon.

This article presents the recent achievements in the field of chemiluminescence and the preliminary results obtained in the investigation of flame radicals chemiluminescent radiation patterns, depending on the combustion conditions, and how it can be used to measure the emission intensity levels of excited radicals, assessing the potential combustion process control limits.

Keywords: Chemiluminescence, combustion process, flame monitoring, combustion management, spectroscopy

1. INTRODUCTION

Chemiluminescence is widely used in a variety of combustion applications. It naturally occur in the flame (there is no need for external illumination) and it is easy to exploit in the harsh environments, because it is an non-intrusive optical diagnostic method. It has been used for identification of the reaction zone, to compute Rayleigh index maps, as a marker of heat release rate, and to measure flame equivalence ratios. By use of a Cassegrain optics-based Chemiluminescence Sensor (CS), Orain demonstrated in their chemiluminescence study that the intensity ratio of the two excited radicals OH^* and CH^* is independent of strain rate in premixed counterflow flames at atmospheric pressure, in contrast to that of OH^* and C_2^* , which is a function of strain rate [1]. Alessandro Schönborn et al visualised autoignition of propane in air was in a turbulent flow reactor using natural OH^* -chemiluminescence imaging. The spatial and temporal development of autoignition kernels was studied in an optically accessible tubular section of the reactor [2]. Real time measurement of local fuel–air equivalence ratios are helpful in prevention of damages to combustors, monitoring pollutant formation in premixed combustors, and in the development of advanced combustion strategies, amongst other applications. Markandey M. Tripathi et al. [3] investigated a new partial least square regression (PLS-R) based multivariate sensing methodology and compared it with an OH/CH^* intensity ratio-based calibration model for sensing equivalence ratio in atmospheric methane–air premixed flames, ranging from fuel-lean to fuel-rich conditions. It was found that the equivalence ratios predicted with the PLS-R based multivariate calibration model matched the experimentally measured equivalence ratios within 7%; whereas, the OH/CH^* intensity ratio calibration grossly underpredictes equivalence ratios in comparison to measured

equivalence ratios, especially under rich conditions. Ji Zhang et al [4] studied on spray combustion of ultra low sulphur diesel (ULSD) fuel under low oxygen conditions with low temperature combustion (LTC) mode in an optically accessible constant volume combustion chamber. The ambient oxygen concentration was configured as 10% and 15% to achieve low flame temperature. The ambient gas temperature varied from 800 K to 1200 K. High speed imaging of OH* chemiluminescence and natural luminosity (NL) was used to visualize the instantaneous spray combustion process. The heat release rate was analyzed using the transient combustion pressure and the flame structure was studied based on the combustion images. Results show that a higher oxygen concentration case features a shorter ignition delay and higher heat release rate. The LTC mode can be realized by decreasing the oxygen concentration and ambient temperature simultaneously and it features a longer ignition delay, a slower reaction rate, and apparently lower soot radiation heat loss. The visualization results of NL and OH* show that the high temperature reaction occurs mainly in the mid-stream and downstream of the spray combustion, but not in the region very close to the chamber wall. This study validated the LTC process by showing very weak OH* chemiluminescence signal. The results also indicate that in order to realize LTC mode, it is important to control the ambient oxygen and ambient temperature at the same time. By only reducing the ambient oxygen concentration it may not be effective to suppress soot generation.

Henriques et al. [5] presented an accurate model for correlation between chemiluminescence intensity of OH* and CH*, mass flow and excess ratio (ER) of the premixed swirlstabilized flame. They gathered all available knowledge and measuring techniques, including studies on the CO₂* broadband emission, to obtain the best correlation. Despite all this work, chemiluminescence is still not clearly understood. While working on his accurate model, Guyot uncovered an important limitation: each correlation is restricted to each combustor and flame configuration. Understanding these problems is essential since all major work is done over laminar flames but the final target are high turbulent flame environments.

This paper shows results of primary chemiluminescence measurements of Bunsen burner methane/air flame and a comparison between measured results and CFD model by using Ansys Fluent partially premixed combustion model.

2. METHODOLOGY

Flame chemiluminescence was researched by burning natural gas with different air/fuel ratios and measuring the chemiluminescence spectra of OH⁻ in experimental stand and by modelling the same experiment with CFD software. The results both from modelling and experiment were compared.

2.1 Experimental setup

The experimental set-up consists of three main parts: spectrograph and ICCD camera system (Fig. 1 elements 1–4) natural gas combustion chamber (Fig 1 elements 5–10), and a flue gas analyzer (Fig. 1 elements 11–13). Flame chemiluminescence monitoring experiments are carried out in the following way:

Natural gas is supplied to Bunsen burner (7) by the flow of 2.8 l/min. Air is supplied from ambience through the adjustable size Bunsen burner holes and also through the gap between hole in the combustion chamber stand (6) and Bunsen burner head (Fig. 2, Fig. 3).

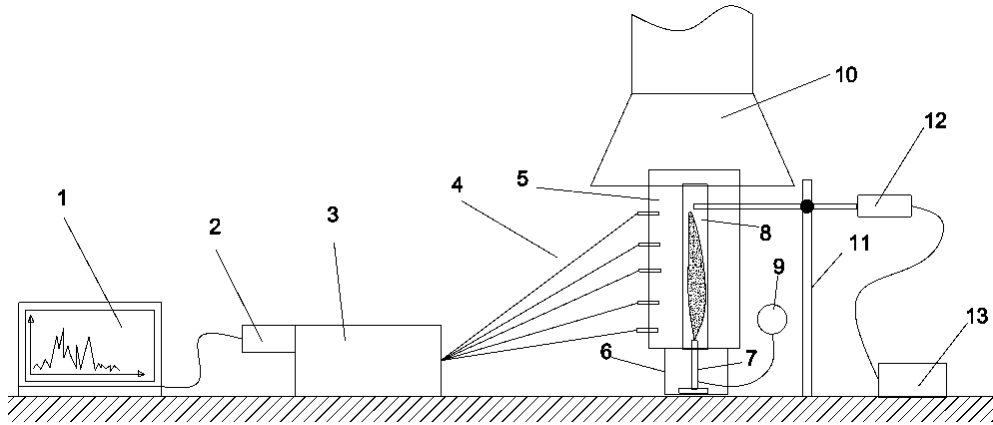


Fig. 1. Experimental setup: 1 – computer; 2 – ICCD camera; 3 – spectrograph; 4 – Optic fibers; 5 – protective screen; 6 – combustion chamber stand; 7 – Bunsen burner; 8 – quartz glass pipe; 9 – natural gas source; 10 – ventilation; 11 – gas analyzer stand; 12 – gas analyzer probe; 13 – flue gas analyzer

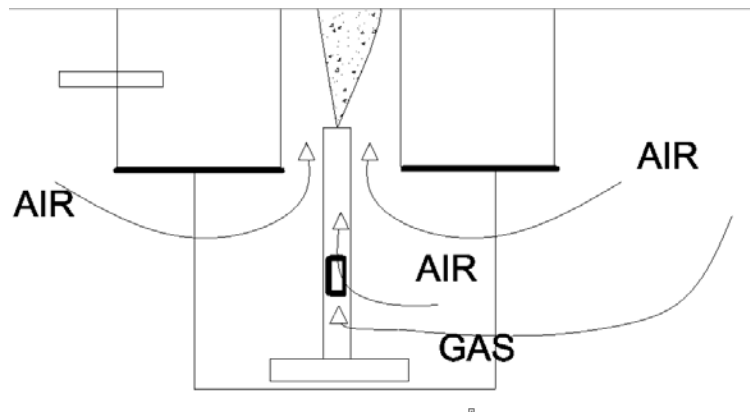


Fig. 2. Fuel and air entrance points scheme

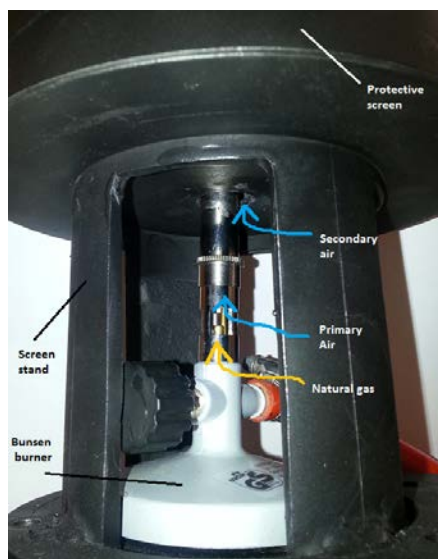


Fig. 3. Laboratory stand fuel and air entrance points

After ignition the flame is monitored with five optic fibers (4) mounted into dark screen (5) to prevent measurements from ambient light pollution. The light from flame travels through optic fibers to “Andor Shamrock 303” spectrograph (3). The spectrograph disperses light from flame into spectral lines and then the signal through mirror system is transferred to “Andor iStar ICCD” camera’s (2) sensor (Fig. 1). Finally the digitalized signal from camera is transferred to PC (1) and analyzed with “Solis” spectroscopy software.

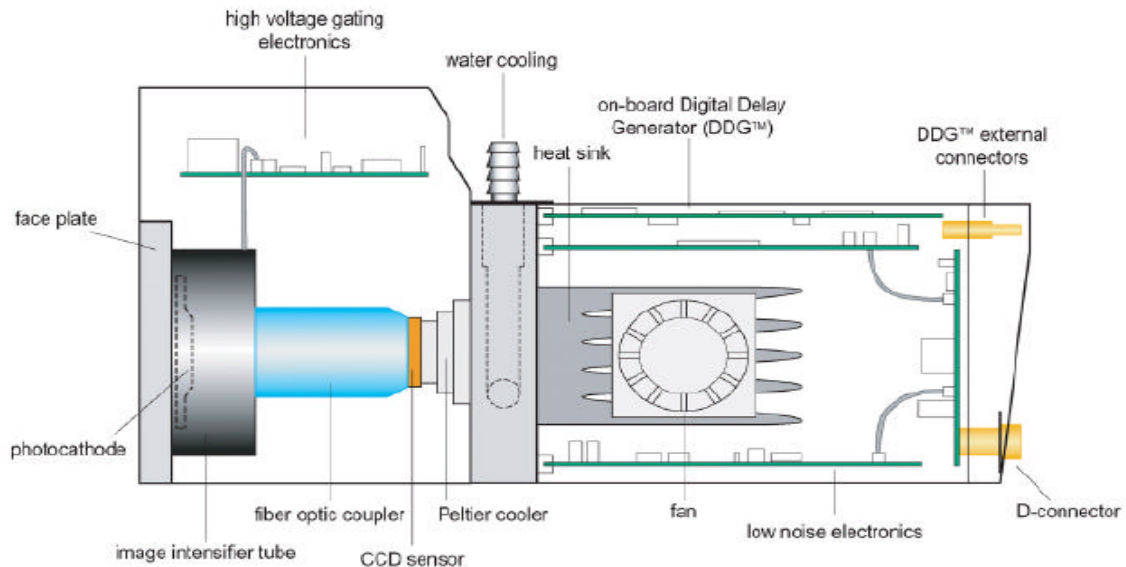


Fig. 4. ICCD camera's main parts [7]

The flue gas parameters (composition, temperature) are measured at the top of the quartz pipe with gas analyzer TESTO 350-XL (12, 13).

The measurements were taken at different air /fuel ratio. The air flow was controlled by closing the air inflow hole in the Bunsen burner. Parameters were measured at fully open, 80% open, 50% open, 10% open and closed air flow hole. When Bunsen burner's air hole was closed, only the secondary air flow was flowing through the gap between screen stand and burner's head.

2.2 Modelling setup

Experimental setup is modelled with CFD software “FLUENT”. Partially premixed combustion model was used for modelling the case the physical model considered here is represented in (Fig. 5). The cylindrical combustion chamber has two inflow planes and one outflow plane. It is assumed, that center plane represents the Bunsen burner top part, where premixed air and CH_4 mixture flows in 4.333 m/s speed. The outer plane represents the gap between Bunsen burner and hole in combustion chamber stand trough which secondary air naturally flows in at constant rate into the combustion chamber.

To simplify the CFD analysis the following hypothesis and assumptions are used:

Since modelled geometry is symmetrical in 2 planes, the modelling takes only a quarter of volume. That makes calculation 4 times faster.

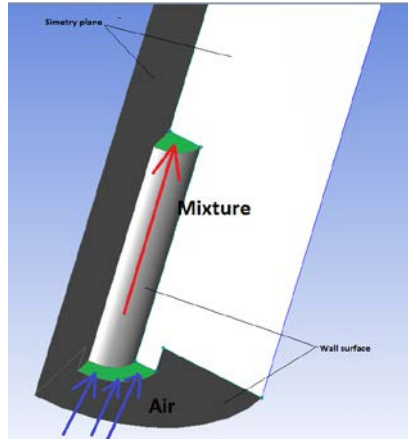


Fig. 5. Physical model of combustion chamber

Species fractions, temperature and other density weighted mean scalars are calculated from the probability density function (PDF) of mass f and mean progress variable c

$$\bar{\phi} = \int_0^1 \int_0^1 \phi(f, c) p(f, c) df dc. \quad (1)$$

Under the assumption that only unburnt reactants and burnt products exist, the $\bar{\phi}$ are determined from

$$\bar{\phi} = \bar{c} \int_0^1 \phi_b(f) p(f) df + (1 - \bar{c}) \int_0^1 \phi_u(f) p(f) df. \quad (2)$$

In this equation subscript u denotes unburnt and b denote burnt.

The burnt scalars, ϕ_b , are functions of the mixture fraction and are calculated by mixing a mass f of fuel with a mass $(1-f)$ of oxidizer and allowing the mixture to equilibrate. When non-adiabatic mixtures and/or laminar flamelets are considered, ϕ_b is also a function of enthalpy and/or strain, but this does not alter the basic formulation. The unburnt scalars, ϕ_u , are calculated similarly by mixing a mass f of fuel with a mass $(1-f)$ of oxidizer, but the mixture is not reacted.

The mean unburnt scalars, ϕ_u , are functions of \bar{f} only. Because turbulent fluctuations are neglected for the unburnt mixture. It means that the unburnt density, temperature, specific heat, and thermal diffusivity are fitted in ANSYS FLUENT to third-order polynomials of \bar{f} using linear least squares:

$$\bar{\phi}_u = \sum_{n=0}^3 c_n \bar{f}^n. \quad (3)$$

Since the unburnt scalars are smooth and slowly-varying functions of \bar{f} , these polynomial fits are considered to be generally accurate [7].

3. RESULTS AND DISCUSSION

First measurement was taken when Bunsen burner's air inflow holes were fully open. The flame was short, blue. Maximum OH emission was registered at the bottom part of the flame, near the burner. The light blue line represents signal from lowest optic fiber (Fig. 6).

Table 1. Results of Gas analyzer measurements with various amounts of air

Air flow through Bunsen's burner hole, %	O ₂ , %	CO, ppm	NO _x , ppm	SO ₂ , ppm	T, °C
100	14.54	6	30	1	412.2
80	14.27	6	33	2	418.9
50	13.54	13	31	1	474.4
10	11,36	4	44	2	467.3
0	9.94	420	36	5	404.3

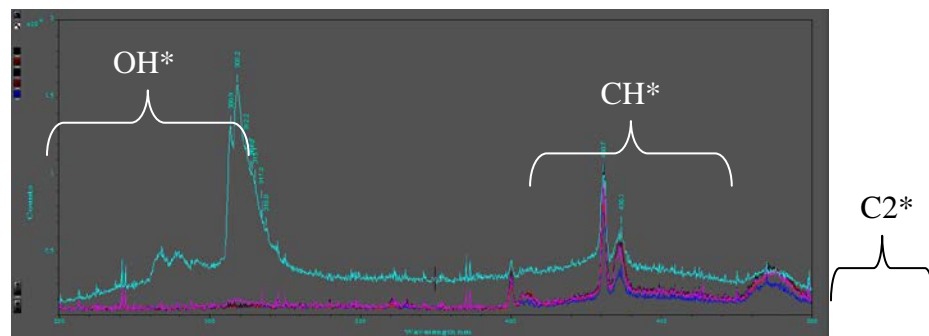


Fig. 6. Chemiluminescent spectra captured on first measurement in 250–500 nm wavelength range

The CFD simulation shows highest OH concentration in the middle and at the secondary air inflow (Fig. 6).

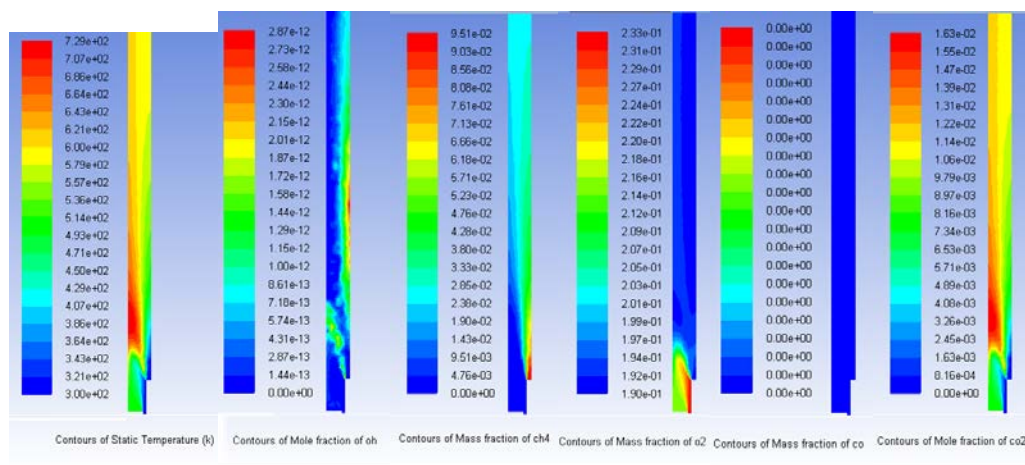


Fig. 7. CFD modeling results of temperature field and spatial distribution of fuel, oxidizer and OH, CO, CO₂ species in measurement case 1

After first measurement, the Bunsen burner's air inflow hole was slightly closed, the inflow air was reduced by 20%. The unchanged CH and C₂ and significant decrease of the OH spectral intensity was registered by spectroscopic system (Fig. 8). The CFD model also shows significantly increased OH and CO generation (Fig. 9). The control measurement of flue gas shows unchanged generation of CO (Table 1). It seems that model at such conditions works incorrectly.

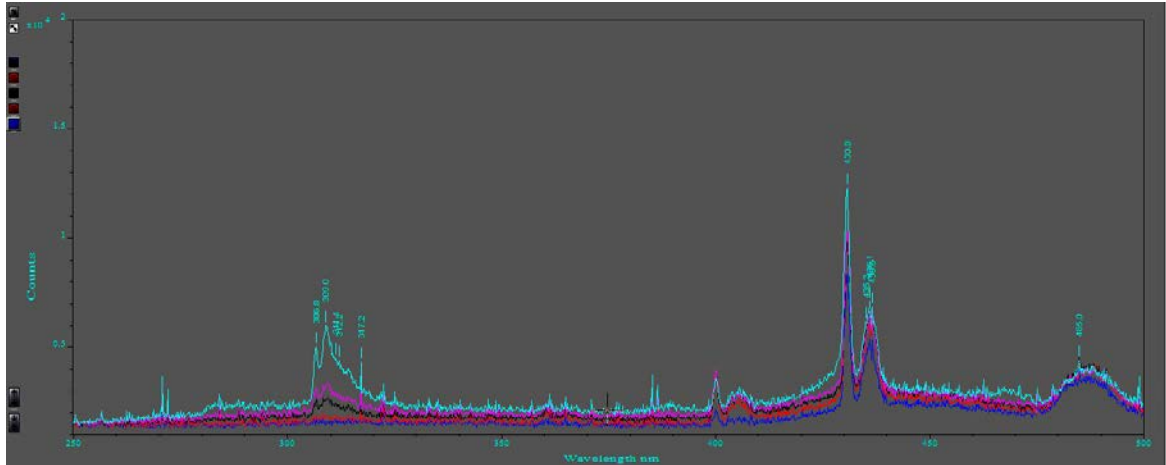


Fig. 8. Chemiluminescent spectra captured on second measurement in 250–500 nm wavelength range

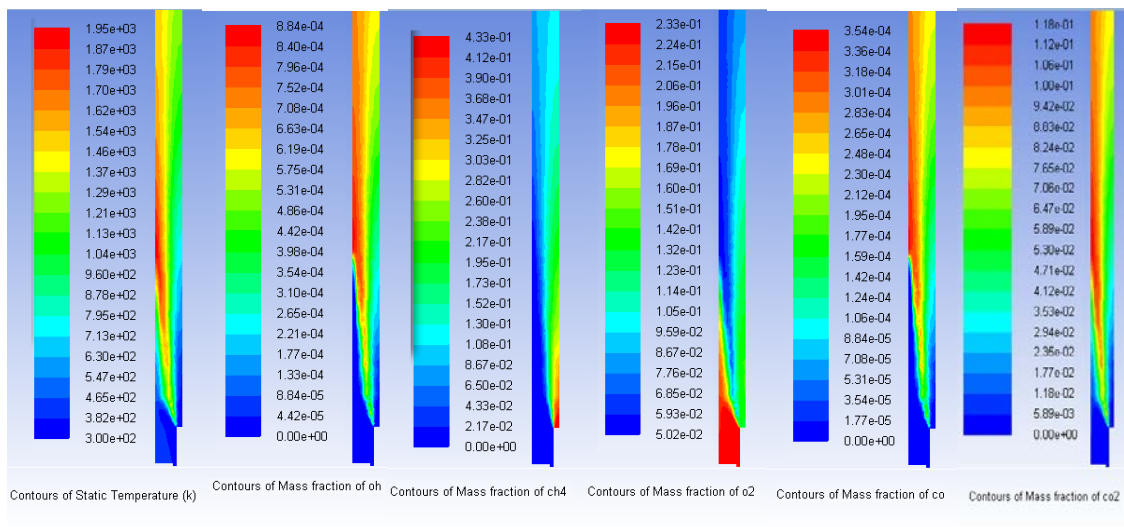


Fig. 9. CFD modelling results of temperature field and spatial distribution of fuel, oxidizer and OH, CO, CO₂ species in measurement case 2

When air flow was decreased 50% at Bunsen burner air inlet, the chemiluminescent information was almost same as in case with 80% (Fig. 10). Although the CFD model and gas analyzer registered temperature increase. (Table 1, Fig. 11). CFD analysis also shows significant OH concentration decrease.

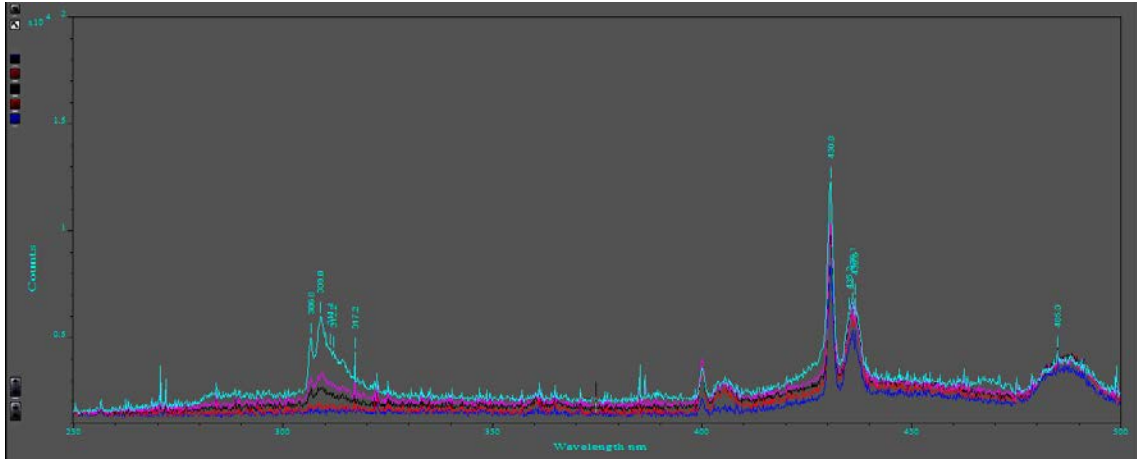


Fig. 10. Chemiluminescent spectra captured on third measurement in 250–500 nm wavelength range

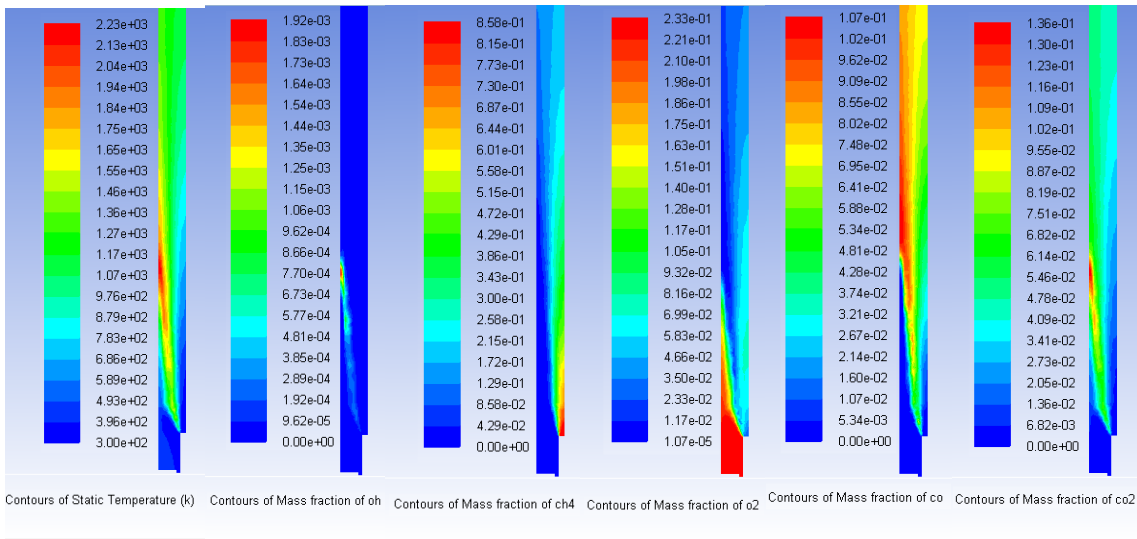


Fig. 11. CFD modeling results of temperature field and spatial distribution of fuel, oxidizer and OH, CO, CO₂ species in measurement case 3

When air flow is reduced to 10%, spectroscopic equipment, gas analyzer and CFD model shows similar results like measurement case 3. From chemiluminescence data it can be seen that CH and C₂ spectra is getting more intense along the flame. It can be seen in Fig. 2 – the lines representing different zones of flame start to separate, showing that C₂ generation is most intensive at the middle part of flame. This also can be seen in CFD model results.

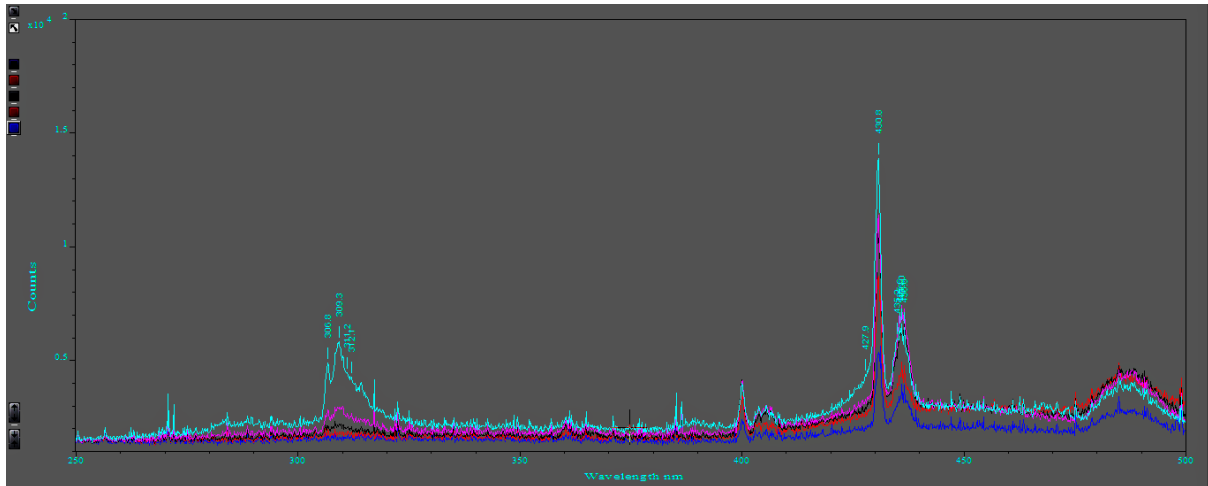


Fig. 12. Chemiluminescent spectra captured on fourth measurement in 250–500 nm wavelength range

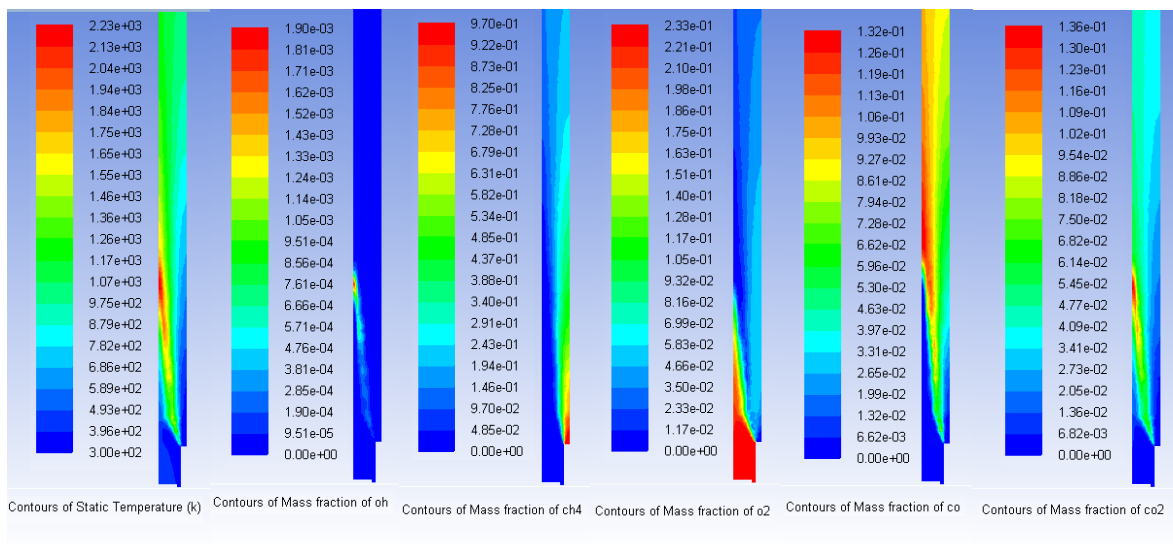


Fig. 13. CFD modeling results of temperature field and spatial distribution of fuel, oxidizer and OH, CO, CO₂ species in measurement case 4

Finally when Bunsen burner's air inflow holes are completely closed, the flame in chamber is bright orange colour. The chemiluminescence data shows intense generation of C₂ and CH, and the OH intensity is slightly decreased (Fig. 14). The CFD model shows only slight increase of CO. The gas analyzer measurements show large increase of CO generation.

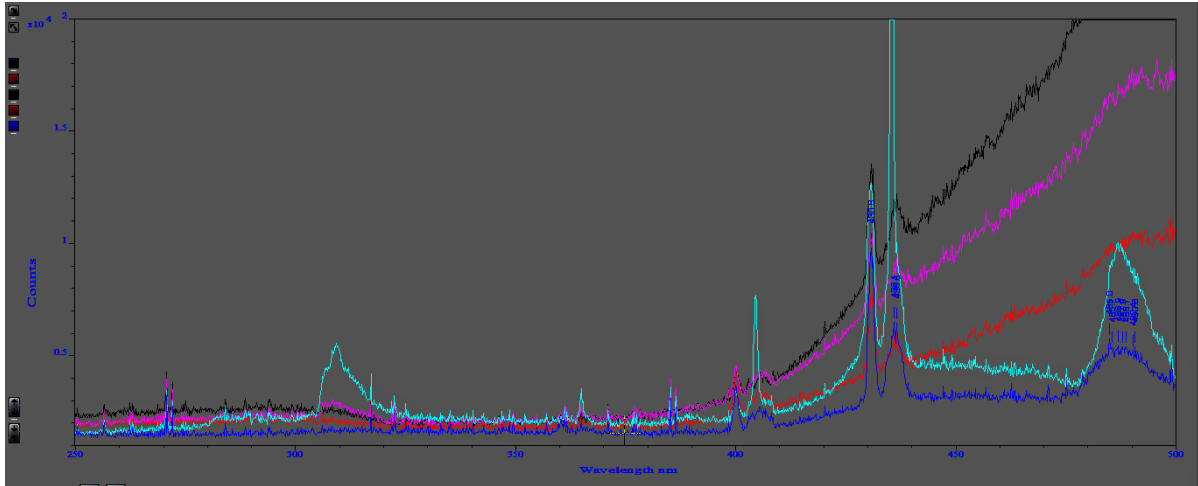


Fig. 14. Chemiluminescent spectra captured on last measurement in 250–500 nm. wavelength range

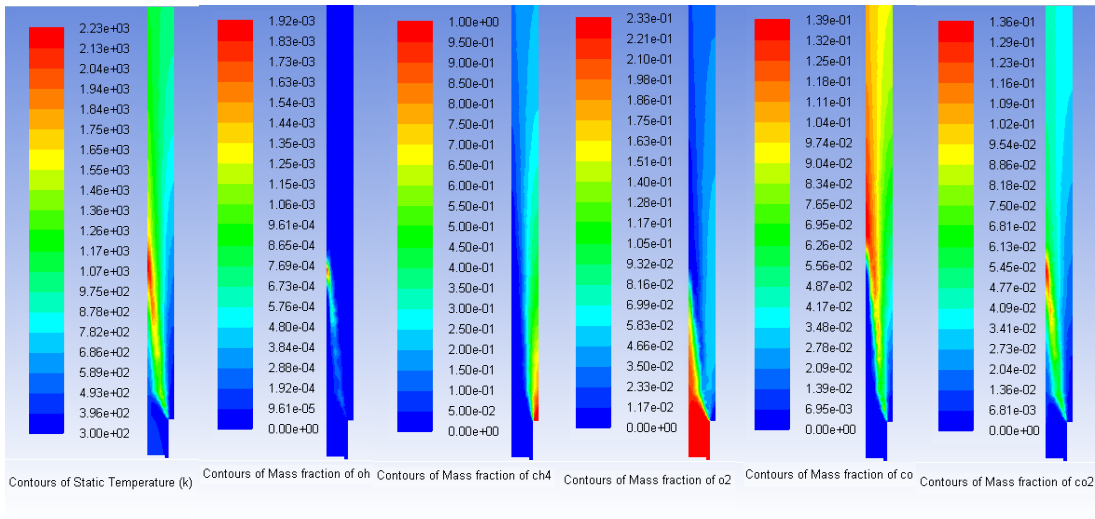


Fig. 15. CFD modelling results of temperature field and spatial distribution of fuel, oxidizer and OH, CO, CO₂ species in measurement case 5

4. CONCLUSIONS

- Experiment showed that there is a correlation between emission intensity levels of excited OH, CH, C₂ radicals and fuel/air ratio.
- Measuring of combustion product composition with flue gas analyzer is slower than doing same thing with ICCD camera. It means that combustion process monitoring and control can be faster when using chemiluminescence based sensors instead of traditional flue gas analyzers.
- The CFD model can show the tendency of species generation and temperature fields in combustion chamber but it needs improvements for more accurate results. Main problem is that model reacts too slowly and to get same results as in experiment it needs to have lower excess ratio than in reality.
- The OH spectrum is most intense when there is enough air for stoichiometric combustion.
- The CH and C₂ spectra intensity increases with excess ratio decrease.
- Highest OH spectral intensity is measured at flame beginning.
- To have more accurate predictions it is necessary to improve the CFD model.
- For more accurate calculations the experimental stand must be upgraded with more accurate air and gas flow measurement and control equipment.



5. REFERENCE

1. PANOUTSOS, C.S., HARDALUPAS Y. Numerical evaluation of equivalence ratio measurement using OH* and CH*chemiluminescence in premixed and non-premixed methane–air flames. *Combustion and Flame*, 2009, Vol. 156, p. 273–291.
2. ALESSANDRO SCHÖNBORN, PARISA SAYAD Visualization of propane autoignition in a turbulent flow reactor using OH* chemiluminescence imaging. *Combustion and Flame* xxx (2013) xxx–xxx
3. MARKANDEY M. TRIPATHI, SUNDAR R. KRISHNAN Chemiluminescence-based multivariate sensing of local equivalence ratios in premixed atmospheric methane–air flames. *Fuel* 2012, Vol. 93, p. 684–691.
4. JI ZHANG, WEI JING, High speed imaging of OH chemiluminescence and natural luminosity of low temperature diesel spray combustion. *Fuel* 2012, Vol. 99, p. 226–234.
5. ANTÓNIO MIGUEL HENRIQUES Chemiluminescence for flame control. Thesis, Instituto superior tecnico, Universidade tecnica de Lisboa.
6. Ansys FLUENT theory guide <https://www.sharenet.ca/Software/Fluent12/html/th/node1.htm>
7. COLIN DUNCAN Physical sciences imaging and high energy detection. Andor academy training material, Belfast, February 2013.



THE APPLICATION OF THE TALBOT-IMAGES METHOD TO THE METHANE-AIR FLAME DIAGNOSTIC

I.N. Shatan

*A.V.Luikov Heat and Mass Transfer Institute of National Academy of Sciences of Belarus
P. Brouki str. 15, BY-220072 Minsk – Belarus*

ABSTRACT

The article describes the experimental system based on the Talbot effect which is used to measure the temperature distribution in premixed methane-air flame. In the paper the principles of the Talbot effect-based technique for analysis of optical inhomogeneity are discussed and the optical scheme for the technique is represented. The results of nonintrusive measurements for axisymmetric reacting methane-air jet issuing from the nozzle with a critical cross-section diameter 4 mm are reported. The equivalence ratio of the investigated mixture was $\phi = 2.2$. The flow velocity at the nozzle exit was approximately 10 m/s. Experimentally measured distribution of deflection angles of probe radiation was used to determine refractive index field in the flame. Temperature calculation is based on the assumption that refractive index in the flame slightly differs from the refractive index of air at the same local temperature. The applicability of such approach is discussed. The paper illustrates the application of Talbot effect-based method for experimental diagnostic of reacting gas flows.

Keywords: Talbot-images, flame temperature, premixed methane-air flame, combustion diagnostic

1. INTRODUCTION

The temperature spatial distribution is an important characteristic of combustion processes. There are a lot of non disturbing methods for temperature diagnostic with high spatial and temporal resolution. Among them are: schlieren methods [1–4], methods based on Rayleigh light scattering [5, 6], CARS methods [7, 8], moiré methods [9–11], interferometric methods [12–15], speckle methods [16, 17], methods of Talbot and Lau interferometry [18–21] and etc.

Some established methods, like methods based on Rayleigh and Raman scattering, laser induced fluorescence, or CARS methods, require complex optical systems and provide point-by-point but not spatial measurements. Because of inability of simultaneous measurements in entire region, scanning of area of interest is necessary for local characteristics field measurements.

There are also methods based on the simultaneous measurement of entire area, which provide accurate measurements of temperature distribution in a flame. Schlieren and interferometric methods, moiré methods, speckle methods and other allow to reconstruct spatial distribution of refractive index, which can be used to calculate temperature field.

For example, in the work [13] the method of laser holographic interferometry is used to measure refractive index distribution in planar two-dimensional methane-air flame and to obtain temperature field. In the [14] the measurements of temperature distribution in diffusive flame of methane issued from small metallic capillary are performed by laser holographic interferometer. In the [9] the moiré deflectometry method is described and the temperature distribution is retrieve for premixed methane-air flame. In the [10] the method of moiré deflectometry is used for diagnostic of a premixed hydrogen-oxygen axially symmetric flame. In the paper [18] the temperature distribution of an axially symmetric Bunsen burner flame of liquefied petroleum gas is derived by means of Lau interferometer. The paper [16] uses the method of speckle-photography for determining refractive index and temperature in cylindrical flame of propane.

Existing methods based on a wave front comparison, including interferometric methods, provide simultaneous measurements for entire test area but very sensitive to vibrations and require high mechanical stability. This requirement limits possible application of the methods for flame

diagnostic. Methods based on moiré effect, methods of Talbot and Lau-interferometry don't have such severe requirements on mechanical stability of optical components but are confined of one predetermined direction in which measurements of refractive index gradient can be performed. Sensitivity and direction, in which the deflection of light will be measured, should be determined before the experiment and correspond to the task.

Talbot-images method [22, 23] also can be used for accurate measurements of refractive index distribution and subsequent calculating of temperature field in reacting gas flows. This method provides ability of simultaneous measurements for entire field of view, does not require high mechanical stability of optical components and does not require prior selection of the direction in which deflection of probe radiation will be registered.

The Talbot effect is well known in the coherent optics and is used in the various applications [24]. Methods based on the analysis of Talbot image behind a single grating, were used to determine the angles of deflection of the laser light transmitted through the lens [25], for the recovery of the wavefront of the laser radiation at a microscope slide [26], to measure the distribution of concentrations of the components in the binary gas flows [22, 23], to determine the mean-square fluctuations in the concentrations of the components of turbulent jet [22, 27].

In this work the results of using method of Talbot-images for temperature field measurement in premixed methane-air flame are presented. Though this method is applicable for a wide range of diagnostic problems, the aim of this work was to demonstrate the possibility of quantitative measurements in flames.

2. THEORY

The main information measured by the method of Talbot-images is distribution of deflection angles of coherent probe radiation that passes through an investigated object. Detection of wave front distortion is based on the self-reproduction effect of intensity distribution of coherent radiation behind two-dimensional periodic object (Talbot effect [28]). The experimental setup consists of a wide aperture laser beam and a two-dimensional periodic object – Talbot grating. The periodic structure of the Talbot grating is reproduced in an interference pattern on a light sensitive matrix of a digital camera. A phase object is placed before the grating in the range of the laser beam. The position of the camera is adjusted in such a way to correspond to a self-imaging plane of the Talbot-grating.

A probe radiation is registered in a reference Talbot-image and in a Talbot-image which is distorted due to an object under the test. If there is no object, the radiation intensity in the self-imaging plane forms regular structure of bright spots, which corresponds to the structure of openings in the Talbot-grating. A refractive index inhomogeneity in a flame produces wave front distortion that results in displacements of bright spots on the Talbot-image. Determination of radiation deflection is based on the measurements of bright spots shift.

Though registered angles of light deflection correspond to the wave front distortion integrated over the optical path of probe radiation, local characteristics of the investigated object can be retrieved by the means of tomographic reconstruction. For planar and axially symmetric objects the relation between angles of deflection and gradients of refractive index has the simplest form. In the case of axially symmetry with the axis perpendicular to the optical axis of the setup z and directed straight up along the coordinate y , the relation between refractive index $n(r)$ and deflection angles ε_x can be expressed by the solution of Abel integral equation for radial component [29]:

$$n(r) - n_0 = -\frac{n_0}{\pi} \int_r^R \frac{\varepsilon_x dx}{\sqrt{x^2 - r^2}}, \quad (1)$$

where ε_x is projection of light deflection angle on coordinates x , n_0 – refractive index for non disturbed area, $R = R(y)$ – radial distance in which gradient of refractive index is equal to zero. Numerical solution of (1) is performed using interpolating of ε_x by cubic spline and following analytical integration of constructed polynomials on corresponded regions [23].

Taking into account that refractive index n of gases is close to unity, the equation of Lorentz-Lorentz [29] for mixture can be written as:

$$(n - 1) = 2\pi \sum N_i a_i, \quad (2)$$

where N_i – number of molecules of component i in volume unit, a_i – molecular polarizability. By using the state equation for ideal gas, the relation between refractive index, temperature and gas mixture composition can be expressed in the following equation:

$$(n - 1) = \frac{T_0}{T} \frac{p}{p_0} \sum X_i (n_{0i} - 1), \quad (3)$$

where T – gas mixture temperature, n_{0i} – index of refraction of component i which corresponds to temperature T_0 and pressure p_0 , X_i – mole fraction of component i . For flames at atmospheric pressure with moderate gas flow rate refractive index $n(x, y, z)$ can be written in the form:

$$(n - 1) = \frac{T_0}{T} \sum X_i (n_{0i} - 1) = \frac{T_0}{T} (n_{mix} - 1), \quad (4)$$

where $n_{mix} \equiv n_{mix}(x, y, z)$ is refractive index of gas mixture at temperature T_0 and pressure p_0 .

This equation demonstrates that index of refraction in flames has non uniform distribution which depends on temperature and composition of gas mixture. As spatial distribution of components in flames is usually unknown, direct use of equation (4) for temperature measurements is not possible.

If the refractive index of major components differs slightly or there is one dominant component, which makes the main contribution to the refractive index value, the value of $n_{mix}(x, y, z)$ can be substituted by space independent value n_{av} . In this case the temperature T will be in inverse proportion to the refractive index of the flame:

$$T = T_0 \frac{(n_{av} - 1)}{(n - 1)}. \quad (5)$$

The approach based on neglecting of mixture composition variation and its impact on the measured temperature is used in many works [2, 4, 9-11, 13, 14, 16-20]. The widely used assumption for the methane-air flame diagnostic is using refractive index of air at temperature T_0 as value n_{av} [4, 13]. This corresponds to the assumption that local value of refractive index in the flame is equal to the refractive index of air at the same temperature.

The assumption of the constant value of n_{mix} causes small errors for premixed methane-air flames and can lead to large discrepancies in the case of diffusive flames. In the [13, 30] are shown that though the discrepancies can reach high values for diffusion flames diagnostic, the accurate measurements of temperature are feasible for partially premixed flames. The estimation of inaccuracy of temperature determination for axially symmetric methane-air flame is presented in the [13]. The maximum values are 6.3% in the case of $\phi = 1.5$ and 8.0% for $\phi = 2.0$. Temperature data obtained from refractive index is less than temperature determined by numerical simulation of the flame [30, 13]. For rich premixed and diffusive flames the error can reach large values. In the [13]

is shown that temperature measurements by using equation (5) for diffusive methane-air flames leads to maximum error 34%.

In addition the [30] demonstrates that the error in temperature determination decreases from the some lengthwise distance. In this region the intermediate and final products predominate and the refractive index of this composition has approximately the same value as air at the same temperature. It indicates that composition impact on temperature field reconstruction is significant only in the initial part where methane is a dominant component.

The equation (5) is applicable for diagnostic of a wide range of air premixed flames since significant impact on refractive index in entire area is produced by molecules of nitrogen N_2 . It leads to $n_{mix}(x, y, z) \approx n_{air}$. In this work the temperature determination is based on equation (5) and the value of refractive index of air as n_{av} .

3. EXPERIMENTAL SETUP

The experimental setup consists of the optical system and the burner. The optical scheme of experimental setup for flame diagnostic is shown in the figure 1.

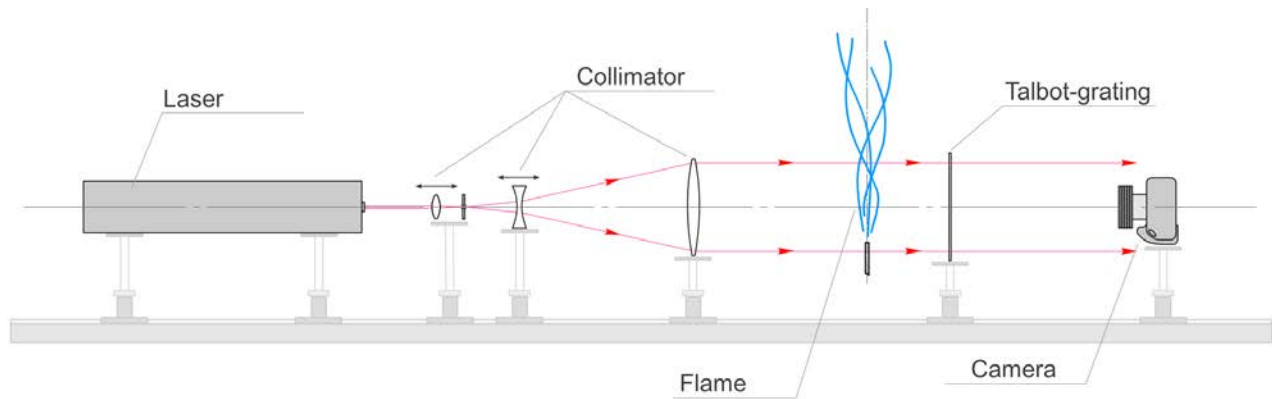


Fig. 1. Optical scheme of the experimental setup

The gas discharge laser with a wavelength $\lambda = 632.8$ nm is used to generate the probe radiation. The laser radiation is transformed into a wide aperture beam with approximately plane wave front by a collimator. The diameter of the probe radiation beam is about 200 mm. The Talbot-grating is placed perpendicularly to the direction of the probe radiation. The optical grade glass plate with reflecting layer ($D = 4$) is used as a Talbot-grating. The reflecting layer consists of a periodically spaced equal round holes system. The schematic representation of Talbot-grating is shown on Fig. 2. The period of holes is $p = 250$ μm and their diameter is $d = 50$ μm . The indicated parameters correspond to the period of self-imaging $L_T = p^2 \lambda^{-1} = 0.099\text{m}$.

The probe radiation intensity distribution is registered by the light sensitive matrix of digital camera "Nikon-D700" with dimensions of 24×36 mm and a number of active pixels are 12.1 Mpx. The position of camera corresponds to the plane of self-imaging and is adjusted according to the desired sensitivity.

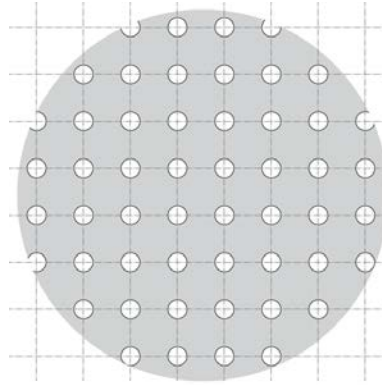


Fig. 2. Two-dimensional periodic structure of the Talbot-grating

At some distance from the collimator the burner is placed. Methane-air gas mixture with equivalence ratio $\phi = 2.2$ issues from a cylindrical tube with inner diameter $D = 4$ mm and length 400 mm. Visually stable non flickering flame is established by controlling the flow velocities and the equivalence ratio of the mixture. The flow rate of the mixture at the exit of the nozzle is approximately $u = 10$ m/s for reported experiments. The combustion took place in the atmosphere, and the flame is laminar. The picture of the flame is shown in the Fig. 3.



Fig. 3. The picture of illumination of the investigated rich premixed methane-air flame

4. RESULTS

In the Figs. 4 and 5 distribution of deflection angles of light ε_x and ε_y for premixed methane-air flame are presented. The angles are determined based on the experimental Talbot-images. The data are shown by the three-dimensional surface corresponded to the entire field of view and by the cross-sections $y = 1D$; $5D$.

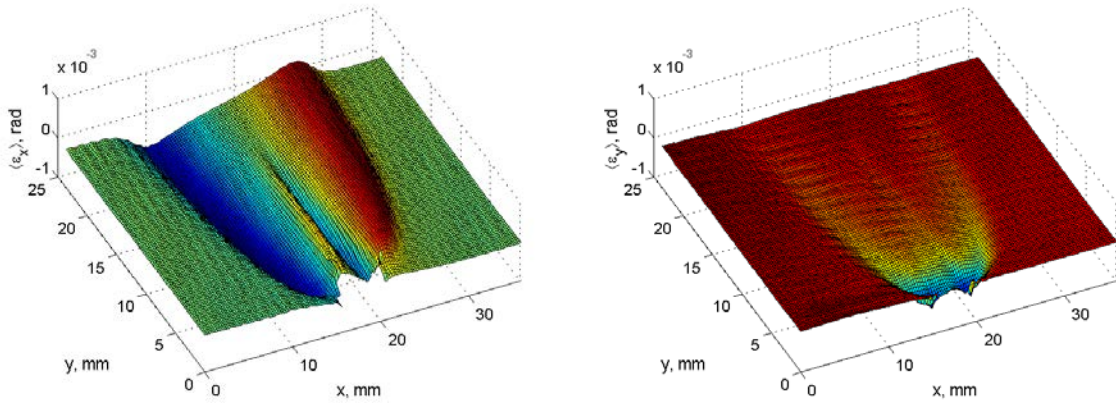


Fig. 4. Distribution of light deflection angles ε_x (left) and ε_y (right) for entire field of view

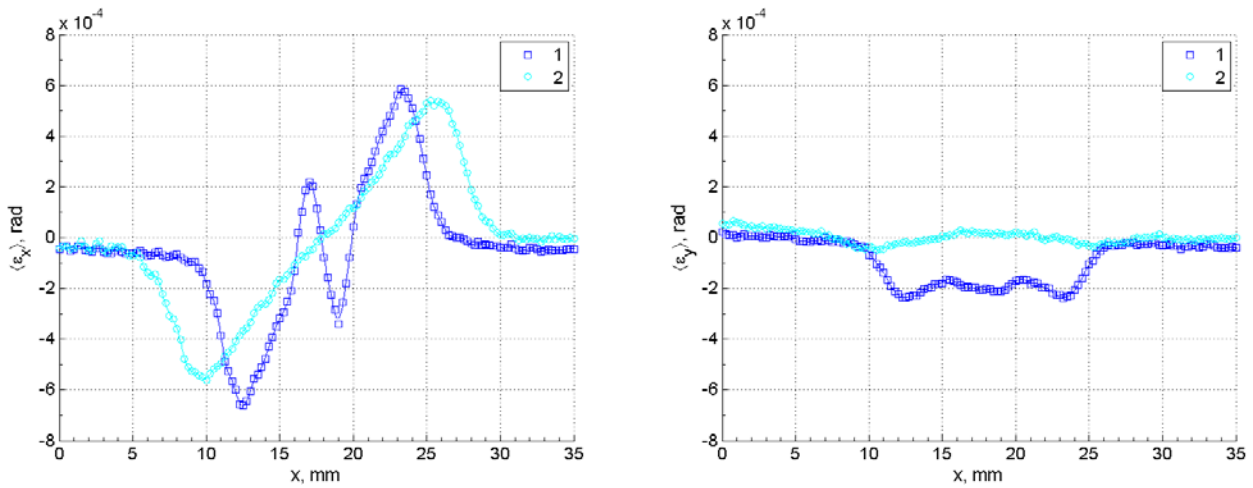


Fig. 5. Distribution of deflection angles ε_x (left) and ε_y (right) for cross-sections $y = 1D$ (1) and $y = 5D$ (2)

Maximum values of deflection angles along x axis does not exceed $8 \cdot 10^{-4}$ rad ($170''$), and along y axis – $3 \cdot 10^{-4}$ rad ($60''$). There is an axis of symmetry on which ε_x values are equal to zero. In the Fig. 6 the refractive index distribution corresponding to investigated axially symmetric flame is presented.

The temperature in the flame is calculated by the equation (5). The results for the premixed methane-air flame are presented in the Fig. 7. The left part demonstrates temperature distribution for the entire field of view. In the right part temperature vs. radius is shown for the flame cross-sections $y = 5$ mm; 10 mm; 20 mm.

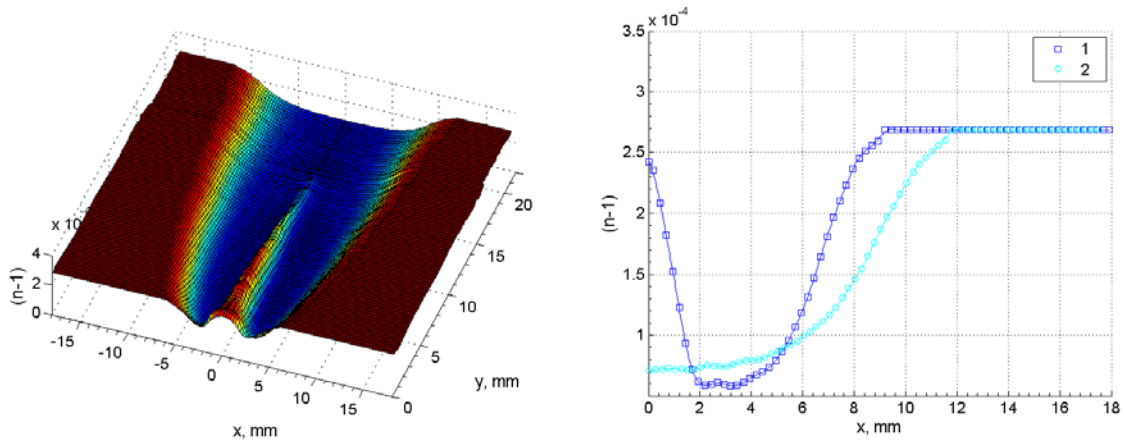


Fig. 6. Distribution of refractive index in axially symmetric flame for the entire field of view (left) and for cross- sections: 1 – $y = 1D$ and 2 – $y = 5D$ (right)

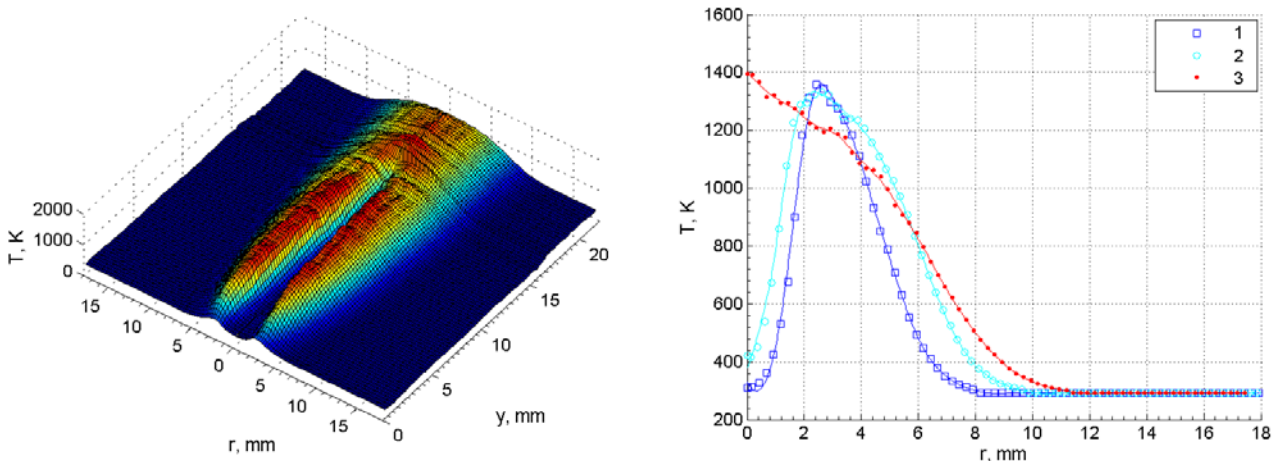


Fig. 7. Temperature distribution in the flame for the entire field of view (left) and for cross-sections: 1 – $y = 5$ mm; 2 – 10 mm; 3 – 20 mm (right)

Fig. 7 shows that the gas flow with temperature T_0 is presented near the nozzle exit. The temperature in this region reaches maximum values outside the axis of symmetry. For lengthwise distance $y \geq 18$ mm from the nozzle exit the temperature maximum in cross-sections moves to the axis of symmetry. The centreline temperature for $y = 18$ mm is 1540 K and it is maximum temperature measured in the flame. The presented data contains an error caused by the influence of components variations on the flame temperature. The maximum relative error can be assumed by substituting n_{av} on refractive index that maximally differs from reference refractive index n_{air} . This evaluation leads to the maximum value of relative error less than 9.4%. The data presented here should be different in the lower side of the actual temperature.

5. CONCLUSIONS

The results of using the Talbot-images method for combustion diagnostic are presented in the work. The experimental study was carried out for the rich premixed methane-air flame ($\phi = 2.2$) issuing from the axially symmetric nozzle. The distribution of the refractive index in the flame was retrieved from the distribution of deflection angles of probe radiation by using solution of integral



Abel equation. To calculate the temperature field the approach was chosen in which the refractive index of the flame is assumed to be equal to the refractive index of air at the same local temperature. Estimation of error caused by this approach gives the maximum value $< 10\%$. The results show the possibility of using the method of Talbot-images for non disturbing temperature field measurement in reacting gas flows with sufficient accuracy and high spatial resolution.

The presented method is simple to implement and easy. Due to a small number of optical components the method is resistant to external perturbations, and therefore can be used for industrial applications. The technique can also be applied for measurements of phase objects that arise in the study of heat transfer and gas dynamics.

REFERENCES

1. GIGLIO, M., MUSAZZI, S., PERINI, U. A white light speckle Schlieren technique. *Opt. Commun.*, 1981, Vol. 36, No. 2, p. 117–120.
2. IBARRETA, A.F., SUNG, C.J. Flame temperature and location measurements of sooting premixed Bunsen flames by rainbow schlieren deflectometry. *Applied Optics*, 2005, Vol. 44, No. 17, p. 3565–3575.
3. WONG, T., AGRAWAL, A.K. Quantitative measurements in an unsteady flame using high-speed rainbow schlieren deflectometry. *Meas. Sci. Technol.* 2006. Vol. 17, p. 1503–1510.
4. XIAO, X., PURI, I.K., AGRAWAL, A.K. Temperature Measurements in Steady Axisymmetric Partially Premixed Flames by Use of Rainbow Schlieren Deflectometry. *Applied Optics*. 2002. Vol. 41, No. 10, p. 1922–1928.
5. KAMPMANN, S., LEIPERTZ, A., DOBBLING, K., HANUMANN, J., SATTELMAYER, T. Two-dimensional temperature measurements in a technical combustor with laser Rayleigh scattering. *Appl. Opt.* 1993. Vol. 32, No. 30, p. 6167–6172.
6. DIBBLE, R.W., HOLLENBACH, R.E. Laser Rayleigh thermometry in turbulent flames *Symposium (International) on Combustion*. 1981. Vol. 18, No. 1, p. 1489–1499.
7. SEEGER, T., JONUSCHEIT, J., SCHENK, M., LEIPERTZ, A. Simultaneous temperature and relative oxygen and methane concentration measurements in a partially premixed sooting flame using a novel CARS-technique. *Journal of Molecular Structure*. 2003. Vol. 661–662, p. 515–524.
8. ECKBRETH, A. C., HALL, R. J. CARS Thermometry in a Sooting Flame. *Combustion and Flame*. 1979. Vol. 36, p. 87–98.
9. BAR-ZIV, E., SGULIM, S., KAFRI, O., KEREN, E. Temperature mapping in flames by moire deflectometry. *Applied Optics*. 1983. Vol. 22, No. 5, p. 698–705.
10. KEREN, E., BAR-ZIV, E., GLATT, I., KAFRI, O. Measurements of temperature distribution of flames by moire deflectometry. *Applied Optics*. 1981. Vol. 20, No. 24, p. 4263–4266.
11. SHARMA, D.K., STEPHEN, S., NATARAJAN, R. Structure of Burning n-hexane Droplet by Moire Deflectometry. *Combustion Science and Technology*. 1998. Vol. 131, No. 1–6, p. 305–321.
12. FARRELL P. V., SPRINGER G.S., VEST, C.M. Heterodyne holographic interferometry: concentration and temperature measurements in gas mixtures. *Applied Optics*. 1982. Vol. 21, No. 9, p. 1624–1627.
13. XIAO, X., CHOI, C.W., PURI, I.K. Temperature measurements in steady two-dimensional partially premixed flames using laser interferometric holography. *Combustion and Flame*. 2000. Vol. 120, No. 3, p. 318–332.
14. POSNER, J.D., DUNN-RANKIN, D. Temperature Field Measurements of Small, Nonpremixed Flames with use of an Abel Inversion of Holographic Interferograms. *Applied Optics*. 2003. Vol. 42, No. 6, p. 952–959.



15. XIAO, X., PURI, I.K. Systematic Approach Based on Holographic Interferometry Measurements to Characterize the Flame Structure of Partially Premixed Flames. *Applied Optics*. 2001. Vol. 40, No. 6, p. 731–740.
16. FARRELL, P.V., HOFELDT, D.L. Temperature measurement in gases using speckle photography. *Applied Optics*. 1984. Vol. 23, No. 7, p. 1055–1059.
17. SHAKHER, C., NIRALA, A.K., PRAMILA, J., VERMA, S. K. Use of speckle technique for temperature measurement in gaseous flame. *J. Optics (Paris)*. 1992. Vol. 23 No. 2, p. 35–39.
18. THAKUR, M., VYAS, A.L., SHAKHER, C. Measurement of Temperature Profile of a Gaseous Flame with a Lau Phase Interferometer that has Circular Gratings. *Applied Optics*. 2002. Vol. 41, No. 4, p. 654–657.
19. SHAKHER, C., DANIEL, A.J. Talbot interferometer with circular gratings for the measurement of temperature in axisymmetric gaseous flames. *Applied Optics*. 1994. Vol. 33, No 25, p. 6068–6072.
20. SHAKHER, C., DANIEL, A.J., ANGRA, S.K. Measurement of the temperature profile of an atomic absorption spectrophotometer burner using a Talbot interferometer with circular gratings. *Optical Engineering*. 1994. Vol. 33 No. 8, p. 2663–2669.
21. SILVA, D.E. Talbot Interferometer for Radial and Lateral Derivatives. *Applied Optics*. 1972. Vol. 11, No 11, p. 2613–2624.
22. DOROSHO M.V., KHRAMTSOV P.P., PENYAZKOV O.G., SHIKH I.A., Measurements of admixture concentration fluctuations in a turbulent shear flow using an averaged Talbot image. *Experiments in Fluids*. 2008. Vol. 44, p. 461–468.
23. ХРАМЦОВ, П.П., ПЕНЯЗЬКОВ, О.Г., ШАТАН, И.Н., ШИХ, И.А. Тальбот-метод исследования распределения концентрации метана в турбулентной осесимметричной струе. *ИФЖ*. 2013. Vol. 86, No. 2, p. 247–255.
24. PATORSKI, K. The self-imaging phenomenon and its applications. *Progress in Optics XXVII*. Amsterdam: Elsevier, 1989. p. 2–108.
25. SALAMA N.H., PATRIGNANI D., De PASQUALE L., SICRE E.E., Wavefront sensor using the Talbot effect. *Optics & Laser Technology*. 1999. Vol. 31, No. 4, p. 269–272.
26. SIEGEL Ch., LOEWENTHAL F., BALMER J.E. A wavefront sensor based on the fractional Talbot effect. *Optics Communications*. 2001. Vol. 194, No. 4–6, p. 265–275.
27. ДОРОШКО М.В., ПЕНЯЗЬКОВ О.Г., ХРАМЦОВ П.П., ШИХ И.А. Измерение пульсаций концентрации в сдвиговом турбулентном потоке методом осредненных тальбот-изображений. *ИФЖ*. 2008. Vol. 81, No. 1, p. 49–54.
28. TALBOT, H.F. Facts relating to Optical Science No. IV. *Philos. Mag.* 1836. Vol. 9, No. 56, p. 401–407.
29. ВАСИЛЬЕВ, Л.А., *Теневые методы*. М.: Наука, 1968. 400 p.
30. QIN, X., XIAO, X., PURI, I.K., AGGARWAL, S.K. Effect of varying composition on temperature reconstructions obtained from refractive index measurements in flames. *Combustion and Flame*, 2002. Vol. 128, No. 1, p. 121–132.



ELECTRICAL AND THERMAL CHARACTERISTICS OF WATER VAPOR PLASMA TORCH USED FOR THERMAL PLASMA REFORMING

A. Tamošiūnas, P. Valatkevičius, V. Grigaitienė, V. Valinčius

*Lithuanian Energy Institute
Breslaujos str. 3, LT-44403 Kaunas – Lithuania*

ABSTRACT

The electrical and thermal characteristics of the atmospheric pressure plasma torch with a direct current arc discharge stabilized by water vapour vortex are experimentally investigated. Water vapour overheated up to 450 K was used as plasma forming gas. Plasma torch design is one of the most important factors leading to a stable operation of the device. The electrical and thermal characteristics of the plasma torch have been determined during the experimental investigations. The design and the basic characteristics of the water vapour plasma torch are presented in the paper. Plasma torches including the electric arc stabilized by water vapour vortex provide special performance characteristics for some plasma processing applications such as thermal plasma neutralization and destruction of organic wastes enabling to extract high caloric value synthesis gas as by-product of the process. Syngas may be used as a surrogate fuel partly replacing the dependence on the fossil fuels or used as a feedstock for hydrogen, methanol production etc.

Keywords: atmospheric pressure thermal plasma, arc discharge, water vapour, plasma torch

1. INTRODUCTION

Constantly increasing use of fossil fuels becomes an issue. Therefore, it is necessary to develop new technologies for clean energy production in regard to Sustainable Development and EU regulations of environmental pollution. Hydrogen energy is considered to be a next-generation fuel, partly reducing the dependence on the crude oil [1].

In a number of existing conventional fuel-reforming technologies, such as partial oxidation [2], steam reforming [3], autothermal reforming [4], dry reforming [5] etc. there are some economical and technical limitations, including requirement of external high-heat source inducing thermal absorption reaction, catalyst sensitivity to contaminants, and large size of equipment as well as high investment and exploitation costs.

As alternative atmospheric pressure thermal plasmas have attracted the attention as an important tool overcoming such limitations typical to conventional means. Thermal plasma, with such unique properties as the high energy density, high enthalpy and high chemical reactions rates initiates processes generating radicals and reactive species which can accelerate chemical reactions with low energy costs. Despite the mentioned advantages, thermal plasmas face some disadvantages regarding the use of expensive electricity and reduced life-time of the electrodes asserted by the arc erosion [6].

During the development of the thermal plasma reforming technology it is important to determine the parametric characteristics of the plasma torch enabling a stable operation within the reforming process. So, the goal of this experimental research is determine the electrical and thermal characteristics of the atmospheric pressure direct current water vapour plasma torch used for thermal plasma reforming of propane.

2. EXPERIMENTAL SETUP AND METHODOLOGY

The experimental setup used in the research is shown in Fig. 1. A non-transferred direct current thermal arc plasma torch of a linear design operates at atmospheric pressure. The torch consists of the following major parts: a cylindrically shaped copper cathode with inserted 2.5 mm in

diameter tungsten rod, which emits electrons initiating gas ionization; a cylindrical stair-shaped anode used to fix the mean arc length; and neutral section with insulating rings used for the arc stabilization in the discharge chamber by tangentially supplying plasma forming gas. Sudden expansion of the anode channel helps to minimize a large-scale shunting of the arc [7].

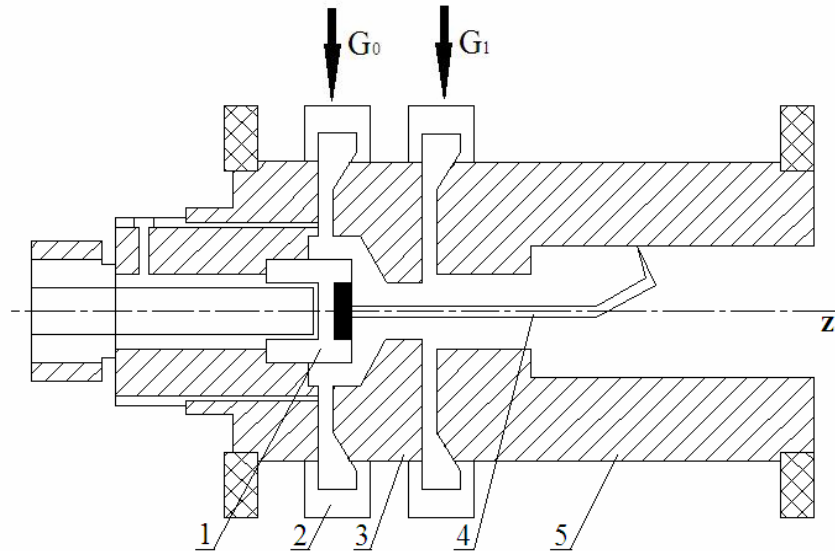


Fig. 1. Scheme of the water vapour plasma torch: 1 – cathode, 2 – insulating rings, 3 – neutral section, 4 – electric arc, 5 – anode. G_0 , G_1 – gas supply

Noble gas argon, with flow rate of $0.52 \cdot 10^{-3} \text{ kg} \cdot \text{s}^{-1}$, was used to protect the tungsten cathode from erosion, whereas water vapour as main plasma forming gas with flow rates in range of 2.63 to $4.48 \cdot 10^{-3} \text{ kg} \cdot \text{s}^{-1}$. Dry saturated water vapour was produced by 5-bar pressure steam generator GAK-50. It was overheated to 450 K by a superheater in order to prevent the condensation on the walls of the discharge chamber of the torch. Condensation determines the shorter life-time of the copper anode and initiates the pulsations of the plasma flow asserted by the shunting of the arc.

During the experiments, arc current and voltage were measured using a remote control block with voltmeter and ammeter inside connected to the electrical power source (VTPE 400-750). Thermal and electrical characteristics of the water vapour plasma torch were generalized using a theory of similarity.

3. RESULTS AND DISCUSSION

The operating parameters of the atmospheric pressure DC water vapor plasma torch during the experiments were maintained as follows: electric arc current intensity varied from 120 to 200 A, voltage range 220–400 V, power available for plasma torch 38–63 kW, and thermal efficiency 0.76. The generated plasma flow mean temperature and mean velocity at the exhaust nozzle of the torch varied from 2400 K and $200 \text{ m} \cdot \text{s}^{-1}$ to 3000 K and $400 \text{ m} \cdot \text{s}^{-1}$, respectively.

3.1. Electrical characteristics of the water vapour plasma torch

The most important electrical characteristic of the plasma torch is the volt-ampere characteristic (VAC). The form of this characteristic determines the selection of the parameters of the power source and the electrical efficiency of the torch.

Since the existing analytical methods are not capable to describe the processes occurring in the electric arc plasma torches, we can refer to the theory of similarity to generalize the volt-ampere

characteristics of the arc (Fig. 2) and deduce these experimental results in the criterial form expressed by the following relation:

$$\frac{Ud}{I} = 34 \left(\frac{I^2}{Gd} \right)^{-0.7} \left(\frac{G}{d} \right)^{0.23} (pd)^{0.48}, \quad (1)$$

where U is the voltage, d – the diameter, I – the current intensity, G – the gas flow rate, p – the pressure.

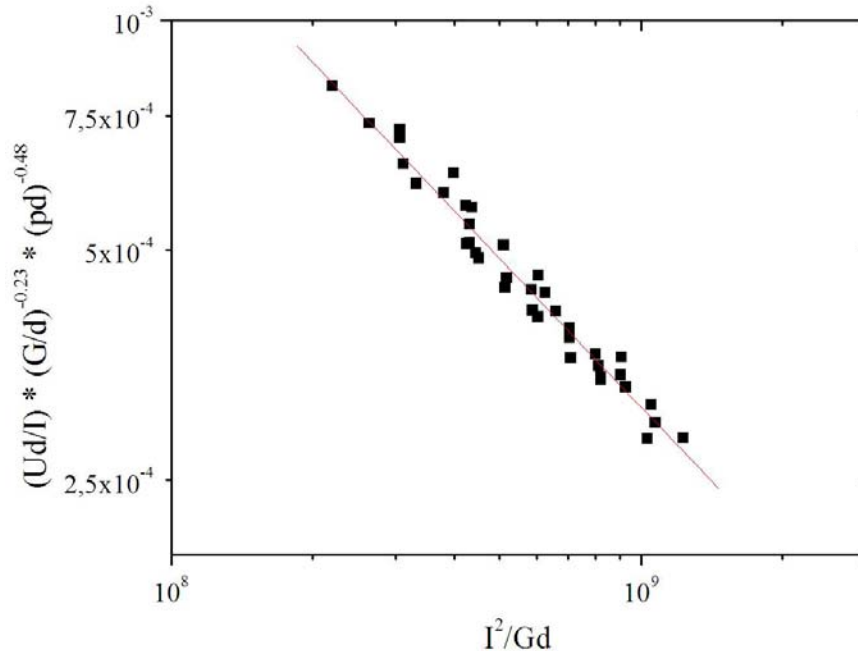


Fig. 2. The generalized VAC characteristics of the water vapour plasma torch

The obtained experimental voltage-current characteristic Eq. (1) was modified to Eq. (2) in order to compare to the generalized VAC commonly used for the steam plasma generators Eq. (3) [7].

$$U = 34 \left(\frac{I^2}{Gd} \right)^{-0.2} \left(\frac{G}{d} \right)^{0.73} (pd)^{0.48}, \quad (2)$$

$$U = 70 + 26.4 \left(\frac{I^2}{Gd} \right)^{-0.13} \left(\frac{G}{d} \right)^{0.2} (pd)^{0.48}. \quad (3)$$

The range of variation of the complexes in the equations proposed is as follows:

$$\begin{aligned} I^2 / Gd &= (3.0 \div 367) \cdot 10^8 \text{ A}^2 \text{ s} / (\text{kg} \cdot \text{m}); \\ G / d &= (0.017 \div 0.22) \text{ kg} / (\text{m} \cdot \text{s}); \\ pd &= (1.7 \div 4.9) \cdot 10^3 \text{ N} / \text{m}. \end{aligned} \quad (4)$$

Comparison of the equations (2) and (3) shows that the substantial difference in exponents at (G/d) , representing the Re_d number, is observed. It could reflect the stronger effect of large-scale shunting (arc to wall) of the arc in the output anode electrode. Therefore, the pulsations of the arc voltage were observed during the experiments. The other complexes remained are quite in a good agreement with the Eq. (3).

3.2. Thermal characteristics of the water vapour plasma torch

Electrical characteristics of the plasma torch were studied simultaneously with thermal characteristics. Thermal coefficient of the efficiency of plasma torch was determined by processes taking place in the column of the electric arc taking into account the heat exchange between the arc, the gas and the walls of the discharge chamber. Therefore, the integral coefficient of heat transfer of the atmospheric pressure DC water vapour plasma torch presented in Fig. 3 was expressed in a general form as the function of the main criteria complexes:

$$\frac{(1-\eta)}{\eta} = 2,22 \cdot 10^{-2} \left(\frac{I^2}{Gd} \right)^{0,22} \left(\frac{G}{d} \right)^{-0,38} \left(\frac{l}{d} \right)^{-0,8}, \quad (5)$$

where η is the thermal efficiency of the plasma torch, I – the current intensity, G – the gas flow rate, d – the diameter, l – the electric arc length.

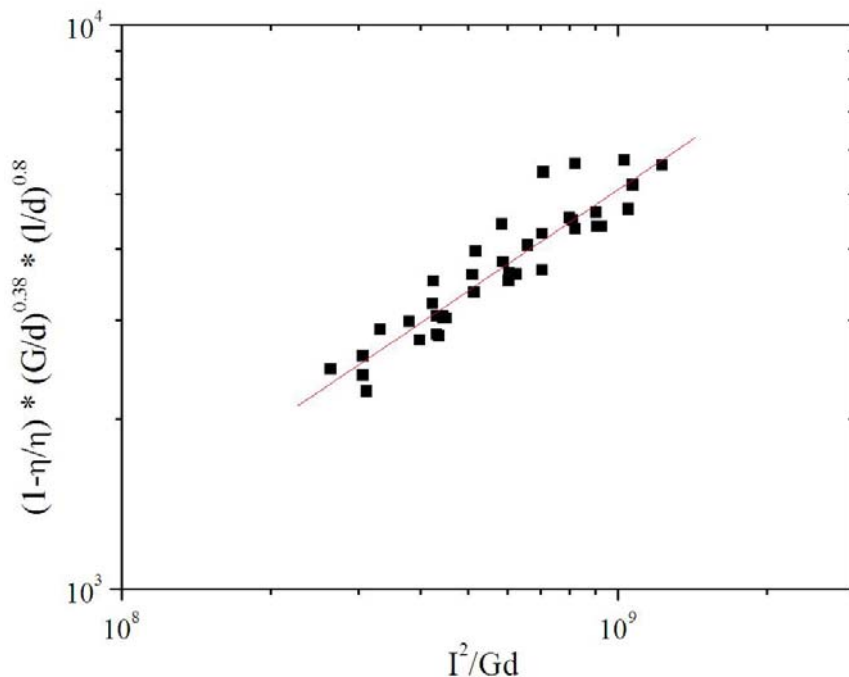


Fig. 3. The generalized thermal characteristics of the water vapour plasma torch

Thermal characteristic of the water vapour plasma torch obtained experimentally was compared to the method used for VAC calculations which is expressed in the form of the dependence of the relative heat losses on the main criteria complexes Eq. [6]. The range of variation of the parameters is the same for VAC used.

$$\frac{1-\eta}{\eta} = 3.02 \cdot 10^{-6} \left(\frac{I^2}{Gd} \right)^{0,32} \left(\frac{G}{d} \right)^{-0,57} (pd)^{0,4}. \quad (6)$$



One can see that, the exponents at complexes (I^2/Gd) and (G/d) are different from those presented in Eq. 6. It could be explained by the poor heat transfer mechanism between the arc and the walls of the discharge chamber which is a reason for initiating the negative shunting effect.

The presence of the generalized thermal characteristics for the water vapor plasma torch helped to optimize the energy losses of any plasma process giving attention not only to the total losses of energy determined by the VAC of the plasma torch.

4. CONCLUSIONS

The electrical and thermal characteristics of the DC linear arc plasma torch with water vapour vortex stabilization operating at atmospheric pressure were investigated. The obtained experimental results, which were compared to the results generally describing the electrical and thermal processes in the steam plasma generators, will help to improve the design of the thermal plasma reforming system by increasing the heat exchange between the arc and the walls of the discharge chamber. Consequently, the shunting of the arc will be suppressed.

ACKNOWLEDGEMENTS

This research was funded by the grant (No. ATE-10/2012) from the Research Council of Lithuania.

REFERENCES

1. MIDILLI, A., DINCER, I. Key strategies of hydrogen energy for sustainability. *International Journal of Hydrogen Energy*, 2007, Vol. 32, p. 511–524.
2. SHIRAGA, M., LI, D., SHISHIKO, T., OUMI, Y., SANO, T., TAKEHIRA, K. Partial oxidation of propane to synthesis gas over noble metals-promoted Ni/Mg(Al)O catalysts – High activity of Ru-Ni/Mg(Al)O catalyst. *Applied Catalysis A: General*, 2007, Vol. 318, p. 143–154.
3. RABIK, M.A., GRACE, J.R., LIM, C.J., ELNASHAIE, S.S.E.H., GAIASI, B. Steam reforming of propane in a fluidized bed membrane reactor for hydrogen production. *International Journal of Hydrogen Energy*, 2010, Vol. 35, p. 6276–6290.
4. LIM, S.S., LEE, H.J., MOON, D.J., KIM, J.H., PARK, N.C., SHIN, J.S., KIM, Y.C.H. Autothermal reforming of propane over Ce modified Ni/LaAlO₃ perovskite-type catalysts. *Chemical Engineering Journal*, 2009, Vol. 152, p. 120–126.
5. RABERG, L.B., JENSEN, M.B., OLSBYE, U., DANIEL, C., HAAG, S., MIRODATOS, C., OLAFSEN SJASTAD, A. Propane dry reforming to synthesis gas over Ni-based catalysis: Influence of support and operating parameters on catalyst activity and stability. *Journal of Catalysis*, 2007, Vol. 249, p. 250–260.
6. SHUTSE, A., JEONG, J.Y., BABAYAN, S.E., PARK, J., SELWYN, G.S., HICKS, R.F. The atmospheric-pressure plasma jet: A review and comparison to other plasma sources. *IEEE Transactions on Plasma Science*, 1998, Vol. 26, No. 6, p. 1685–1694.
7. ZHUKOV, M.F., ZASYPKIN, I.M. *Thermal Plasma Torches: Design, Characteristics, Applications*. Cambridge International Science Publishing Ltd, 2007. 600 p. ISBN-13: 978-1-904602-02-6.



NUMERICAL AND EXPERIMENTAL STUDIES OF BIOMASS PYROLYSIS

U.M. Bahach, S.V. Vasilevich, M.V. Malko

*Institute of Power Engineering, NAS of Belarus
Akademicheskaya str. 15/2, 220072, Minsk – Belarus*

ABSTRACT

Pyrolysis is one of the most efficient thermochemical processes of organic compounds conversion, which occurs at high temperatures without oxygen.

The results of a comprehensive study of the biomass pyrolysis to produce high yield of liquid fuels are presented in the article. A mathematical model was developed that adequately describes the process of biomass pyrolysis. Experimental studies of biomass pyrolysis were carried out.

The optimal biomass particle size for high liquid products yield was defined as 1–3 mm. The effect of biomass moisture was studied.

Found that in order to maximize the yield of liquid pyrolysis products of good quality biomass, process temperature should not exceed 600 °C.

Chromatographic studies conducted tests of liquid pyrolysis products, which showed that the composition of the products greatly depends on the humidity of raw materials. With rapid heating and temperatures of about 500 °C (the technology of fast pyrolysis), the dominant product is a liquid with a high calorific value, consisting of complex organic compounds and water. In this case, gas-vapour mixture of products should quickly (within seconds) to cool.

Keywords: biomass, pyrolysis, mathematical model, liquid products

INTRODUCTION

Pyrolysis is one of the most efficient thermochemical processes of organic compounds conversion, which occurs at high temperatures in inert environment. Burning gases and high calorific value liquids as well as coke are formed during this process. Yields of different products of pyrolysis as well as their energy and chemical properties depend on temperature of process, rate of heating as well as from properties of medium that is used for creating of fluidized bed.

Liquid products having high combustion heat are dominating products of pyrolysis at high rate of heating, moderate temperature in the vapour phase (around 500 °C), small time of residence in reaction zone (approximately 1 seconds) and rapid quenching of reaction products [1]. These products consist of complex organic compounds and water. At higher temperatures and longer residence liquid organic products of pyrolysis undergo a number of chemical reactions transforming them into gaseous products such as carbon oxide, carbon dioxide, hydrogen and light hydrocarbons. Slow and super slow pyrolysis (carbonization) performed at low temperature (approximately 300 °C and lower) resulted in formation the highest amount of solid product (coke) [2].

At present main efforts in research of biomass pyrolysis are devoted to development of effective technologies for fuel production for different kind of engines and as inhibitors of fuel [1]. However pyrolysis of biomass allows to produce a number of chemical compounds that can be used in medicine, in food processing industry, in paint industry, in plastics industry etc. For example such phenolic organic compounds formed in the biomass pyrolysis process as tyrosol, butylated hydroxytoluene, thiolane etc are antioxidants that used in medicine for treatment of different diseases [3, 4].

Using of bioantioxydants generated in process of biomass pyrolysis can be very important for Belarus that develops its own medical production. Compounds having antioxidant properties are also important for other sectors of economy of Belarus.



Computer simulation and experimental study of optimal producing such and other compounds by using the technology of fast pyrolysis of biomass was the main goal of the present investigation. For this purpose a mathematical model has been developed. This model describes the pyrolysis conditions in the fluidized bed of the laboratory facility which was constructed at the Institute of Power Engineering of the National Academy of Belarus. Experimental studies of the pyrolysis were conducted with the aim to determine the effect of the process conditions on the composition of the liquid products.

1. COMPUTER SIMULATION OF BIOMASS FAST PYROLYSIS

At present a number of models of biomass pyrolysis have been developed which describe adequately results of experimental studies [5]. Two main problems are considered by elaboration of such models: kinetic scheme of biomass thermo chemical destruction and process of pyrolysed particles heating. Analysis demonstrates that results of numerical simulations performed by using such models agree quite well. Using of them is determined mostly by necessity to reach the wished accuracy of modelling.

The model used in the present research is based on the Miller-Bellan kinetic scheme of biomass pyrolysis [6]. This kinetic scheme gives good results in case of pyrolysis of small particles (spheres with radius up to 3 millimetres). Pyrolysis of such particles is limited by chemical reaction and allows producing a maximal yield of liquid products.

We have developed a simplified model of particle heating and gases transport inside the constructed reactor. Products of burning of gaseous products of pyrolysis and gaseous products of pyrolysis were considered as the gaseous agent for creation of fluidized bed. Together with the Miller-Bellan kinetic scheme these models allowed to conduct a computer simulation of the pyrolysis process.

1.1. Kinetic scheme of biomass pyrolysis

Cellulose, hemicelluloses and lignin are the main components of organic material of wood. As can be seen from Table 1 fractions of these components vary slightly in different kinds of wood that are common for Belarus [7].

Table 1. Composition of wood kinds

Kinds of wood	Cellulose, %	Hemicelluloses, %	Lignin, %
pine	51.4	24.4	26.9
birch	45.8	26.0	21.2
fir	52.4	23.5	28.1
alder	43.6	19.6	24.6
oak	37.1	28.8	22.5
asp	47.2	22.8	21.3
maple	41.5	33.3	23.1

In accordance with accepted kinetic scheme at elevated temperature components of biomass transform themselves into activated state and then undergo conversion into liquid products, coke and non condensable gaseous products. When liquid products of pyrolysis remain at high temperatures for a long time, they undergo a further transformation into non-condensable gases and coal. Therefore, a rapid cooling of products of pyrolysis is necessary in order to receive significant amount of liquid products. Fig. 1 shows a simplified kinetic scheme of biomass pyrolysis that was used in the present research.

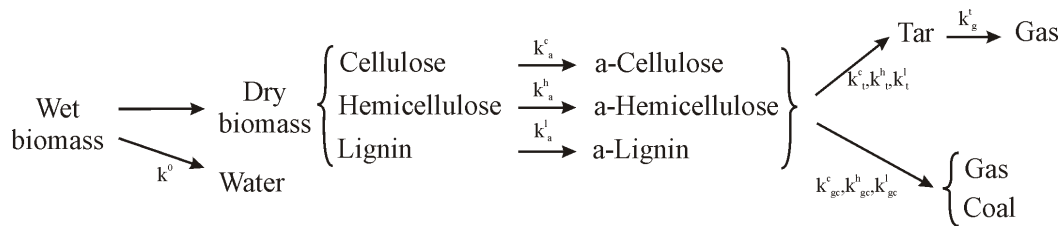


Fig. 1. Kinetic scheme of biomass pyrolysis

One needs to notice here that the word tar shown in the kinetic scheme means all liquid products of pyrolysis including water. The word water shown in the kinetic scheme means water which was received during biomass drying.

Rates of chemical and phase transformation shown in Fig.1 are described on the basis of the Arrhenius equation:

$$k = A \cdot \exp\left(-\frac{E_a}{RT}\right) \quad (1)$$

Activation energies (E_a) and pre-exponential factors (A) of the equation (1) for evaluation of constant rates of chemical processes were taken from the paper [6]. Vaporization rate was calculated by using data given in the paper [8]. Gaseous agent composition at different temperatures of process was taken from the paper [9].

In accordance of the kinetic scheme of Miller-Bellan coke and gaseous products are generated simultaneously. It is also believed that each component of wood gives different mass fraction of coke: $X^c = 0.35(\text{cellulose})$; $X^h = 0.60(\text{hemicelluloses})$; $X^l = 0.75(\text{lignin})$ [6].

In case of small size of particles (up to 3 mm) and moderate temperatures (up to 600–700 °C) diffusion rate of gaseous compounds is higher than rates of chemical transformation. This means that pyrolysis of small biomass particles is limited by chemical reactions. Therefore one does not need to assess chemical reactions of liquid products and coke inside of particles. Such reactions occur mostly only in vapour phase of reaction zone. Rapid cooling of pyrolysis products freezes chemical reactions between products of pyrolysis and increases yield of liquid products.

The kinetic scheme adopted in the present research allows to estimate mass fractions of coke (X_{coal}), liquid products (X_{tar}), non condensable gases (X_{gas}) and water vapour (X_{vapor}) as a result of pyrolysis of a single particle.

1.2. Model of particle heating

Using in case of fast pyrolysis of small particle causes high rate of their heating that is higher than the rate of their chemical destruction. This allows assuming that temperature distribution inside of particles is uniform.

Last assumption allows assessing the thermal energy delivered per unit time to heated particle by fluidized bed on the basis of equation:

$$\frac{dQ}{dt} = \alpha \cdot S \cdot (T_0 - T_p), \quad (2)$$

where α – coefficient of heat exchange of particle with the fluidized bed that considers efficiency of heat exchange from fluidized bed to the particle surface as well as efficiency of transfer of heat from the surface of particle by means of thermal conductivity;

T_0 – temperature of fluidized bed;

T_p – temperature of particle;

S – surface area of particle.



Thermal energy delivered to particle is used for increase of its temperature and vaporization. The balance equation describing these processes has the following form:

$$\frac{dQ}{dt} = C_{eff} \cdot V \cdot \frac{dT_p}{dt} + LV \cdot \frac{d\rho_w}{dt}, \quad (3)$$

where V – volume of particle;

L – specific heat of vaporization;

C_{eff} – specific isochoric heat capacity of particle.

The value of C_{eff} is estimated on the basis of current phase concentrations and their specific volumetric heats by using the equation:

$$C_{eff} = (\rho_c + \rho_h + \rho_l + \rho_{*c} + \rho_{*h} + \rho_{*l}) \cdot c_{wood} + \rho_{coal} \cdot c_{coal} + \rho_{water} \cdot c_{water}, \quad (4)$$

where ρ_c, ρ_h, ρ_l – are mass concentrations of cellulose, hemicelluloses and lignin;

$\rho_{*c}, \rho_{*h}, \rho_{*l}$ – are mass concentrations of activated cellulose, hemicelluloses and lignin;

$\rho_{coal}, \rho_{water}$ – are mass concentration of coal and water;

$c_{wood}, c_{coal}, c_{water}$ – are specific heat capacities of wood, coal and water.

For estimation of the coefficient of heat exchange α the method analogous to the method for describing of external heat exchange of spherical body. In accordance with [10], the effective coefficient of heat exchange of spherical particle can be assess on the basis of formula:

$$\alpha = \frac{\alpha_{int} \cdot \alpha_{ext}}{\alpha_{int} + \alpha_{ext}}, \quad (5)$$

where α_{int} и α_{ext} – are coefficients of external and internal heat exchange respectively.

Assessment of the internal coefficient of heat exchange α_{int} is given by expression:

$$\alpha_{int} = \frac{\pi^2 \cdot \lambda_{eff}}{3r_p}. \quad (6)$$

The external coefficient of heat exchange α_{ext} can be evaluated by using Nusselt criterion:

$$\alpha_{ext} = \frac{\lambda_0}{2r_p} \cdot Nu, \quad (7)$$

where λ_0 – is coefficient of thermal conductivity of gaseous compounds,

It is necessary to consider in case of fluidized layer consisting of small particles heat exchange from the gaseous medium to particles as well as heat exchange between particles by their collision. The role of heat transfer by radiation at temperatures around 500 °C is quite small and therefore it was not considered in the present investigation. For an estimation of the Nusselt criteria at such conditions one can use the formula [11]:

$$Nu = 0,016 \cdot (Re/\varepsilon)^{1,3} \cdot Pr^{1/3}, \quad (8)$$

where ε – is the porosity of fluidized layer, Re is a Reynolds number and Pr is the Prandtl number.

The following expression can be used for evaluation of the Reynolds number:

$$Re = \frac{Ar \cdot \varepsilon^{4,75}}{18 + 0,61\sqrt{Ar \cdot \varepsilon^{4,75}}}. \quad (9)$$

Here Ar is the Archimedes number. If the density of gaseous medium is much lower than the density of particles and particles are ball-shaped the Archimedes number is determined by expression:



$$Ar = \frac{8gr_p^3}{\mu_0^2} \cdot \rho_p \rho_0, \quad (10)$$

where μ_0 – is dynamic viscosity of gaseous medium,
 ρ_0 – is density of gaseous medium,
 ρ_p – is density of biomass particles.

The Prandtl number is determined by expression:

$$Pr = \frac{c_0 \cdot \mu_0}{\lambda_0}, \quad (11)$$

where c_0 – is specific isobaric heat of gaseous medium.

1.3. Transport model of gases

It was mentioned previously that rapid cooling of pyrolysis products prevents their destruction into non condensable gases. This operation is performed usually with help of some cyclones that can cool products of pyrolysis very quickly. This means that products pyrolysis remain at high temperatures only some short time. In case of fast pyrolysis this time is approximately 1–2 seconds.

Time that is needed for products of pyrolysis to leave pyrolytic reactor can be assessed by using the expression:

$$\tau = \frac{H - h}{v_0}, \quad (12)$$

where H – is the height of reactor,
 h – is the height of fluidized layer.

This expression is based on the assumption that flow of gaseous medium outside of fluidized layer as well as close to outlet from the reactor is laminar. In case of big velocities of gaseous medium and low diameter of transitional socket between reactor and cyclone it is necessary to take into account the effect of turbulence at the outlet of reactor.

For assessment of destruction grade of tar (liquid product) during the time τ it is necessary to use the value $Y(t)$, that is the fraction of non destructed tar at the time t . For estimation of this value it is necessary to solve the following differential equation:

$$\frac{dY}{dt} = -Y(t) \cdot A_{tg} \cdot \exp\left(-\frac{E_{tg}}{RT}\right), \quad (13)$$

where A_{tg} и E_{tg} – are Arrhenius parameters of thermochemical transformation of tar into non condensable gases and T is the temperature of vapour phase in reactor.

The initial condition for solving of equation (13) is:

$$Y(0) = 1. \quad (14)$$

Solving of the equation (13) at this initial condition gives:

$$Y(\tau) = \exp\left[-\tau \cdot A_{tg} \cdot \exp\left(-\frac{E_{tg}}{RT}\right)\right]. \quad (15)$$

The amount of tar or mixture of liquid products and water at the outlet of reactor can be evaluated using the formula:

$$m_{tar} = m_{biomass} \cdot X_{tar} \cdot Y(\tau), \quad (16)$$

where m_{tar} – mass of tar,

$m_{biomass}$ – initial mass of particle.

Amount of non condensable gases at the outlet of reactor is then determined by expression:

$$m_{tar} = m_{biomass} \cdot [X_{gas} + X_{tar} \cdot (1 - Y(\tau))]. \quad (17)$$

1.4. Computer simulation of biomass fast pyrolysis

A computer program was written on the base of described mathematical models using the Delphi programming language. This program was used for computer simulation of fast pyrolysis of wooden particles. In course of this study influence of such parameters on yield of liquid products such as process temperature, velocity of gaseous medium flow, size of biomass and kind of pyrolysed wood have been studied.

The Fig. 2 shows dependence of mass yield of condensable products of pyrolysis (organic substances and water) on temperature of process. The left panel of this figure gives evaluated data for different kinds of wood. One can see that pyrolysis of conifer give higher yield of liquid products than pyrolysis of broad-leaved trees. It is also to notice that this effect does not depend on temperature.

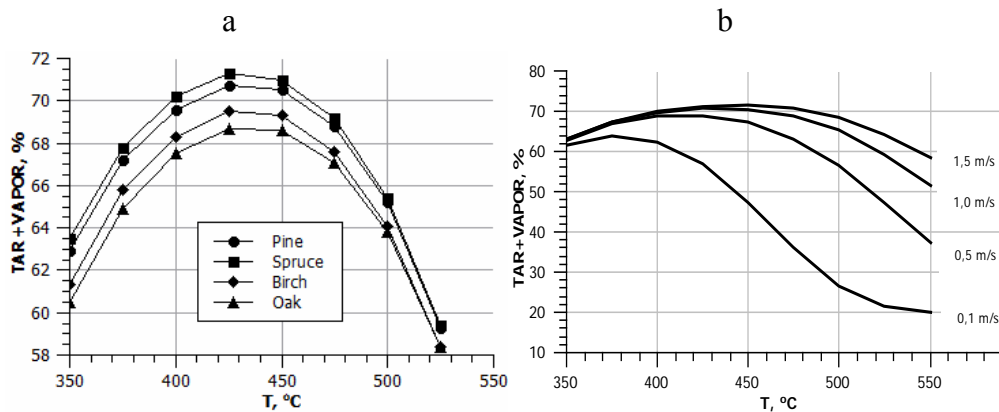


Fig. 2. Dependence of the mass yield of condensable products of biomass pyrolysis from the process temperature: a) for different kinds of wood, $r_p = 0.5$ mm, $V = 1$ m/s, $\phi = 20\%$; b) for different velocities of gaseous medium, Pine, $r_p = 0.5$ mm, $\phi = 20\%$

The right panel of Fig. 2 demonstrates the yield of liquid products (tar and water vapor) from the velocity of gaseous agent used for creation of fluidized bed. One can see that decreasing of the velocity of gaseous agent decreases significantly the yield of liquid products. This effect simply reflects occurring of thermochemical destruction of liquid products of pyrolysis. Results presented in the right panel of Fig. 2 were evaluated for distance 1 meter that had to move gaseous medium inside of reactor zone. This data indicates that in case of pyrolysis performed at temperature 550 °C, velocity of gaseous medium must be more than 0.5 m/s, thus vaporized liquid products must leave reactor zone during 2 seconds.

Fig. 3 presents data on mass yield of condensable products of pyrolysis (tar and water) assessed for particles of different sizes. Established data demonstrate that maximal yield of liquid products required pyrolysis of particles having size of 1–3 mm.

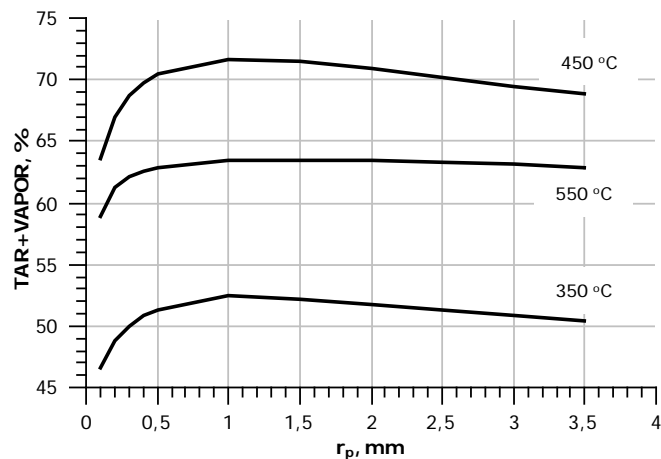


Fig. 3. Dependence of the mass yield of condensable products of biomass pyrolysis from the size of particles: Pine, $V = 1$ m/s, $\varphi = 20\%$

2. EXPERIMENTAL STUDIES OF BIOMASS PYROLYSIS

Preliminary experimental studies of biomass pyrolysis were performed by using an experimental laboratory facility developed at the Institute of Power Engineering of the National Academy of Sciences of Belarus. The facility has reactor with fluidized bed and allows to pyrolyse 1 kilogram of biomass per hour. As gaseous agent for creation of fluidized bed it uses products of pyrolytic gases burning. At the initial stage of pyrolysis the air played the role of gaseous medium for creation of fluidized bed. The simplified scheme of the facility is shown on Fig. 4.

The described facility was used for experimental study of fast pyrolysis of biomass in the temperature range from 350 to 600 °C and humidity of biomass in the range from 10 to 25%. Pine sawdust with size 0.5–3 mm was taken as raw material by performing this study.

Liquid products of biomass pyrolysis after sedimentation during some time at room temperature divide in two layers with different density and colour. The upper layer looks like some aqueous semitransparent liquid of buff or red colour. This liquid consists of low fraction of organic compounds (10–15 mass%) and high water fraction (85–90 mass%). The lower layer looks like some dense resinous liquid of dark blue colour. It consists of big fraction of organic compounds (85–90 mass%) and low fraction of water (10–15 mass%).

Fig. 5 demonstrates photos of experimental samples of such layers after sedimentation of liquids products of pyrolysis performed at temperatures 350 °C and 400 °C.

It was found that the process of sedimentation does not change the composition of mixture of liquid products of pyrolysis. However it changes absolute amounts of these compounds as well as relation in mass percent of them. The last effect indicates occurring of some separation of liquid products of pyrolysis between layers having different concentrations of water. Table 2 demonstrates existence of such separation in case of phenolic organic compounds.

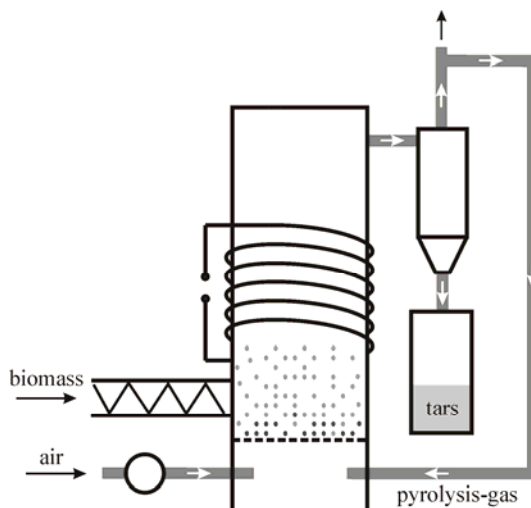


Fig. 4. The scheme of facility

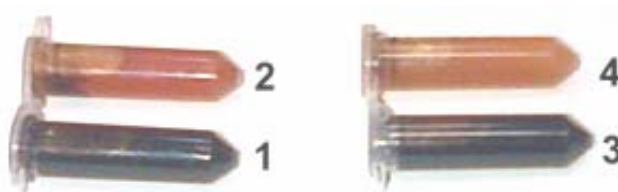


Fig. 5. Photos of experimental samples of liquid products of wooden sawdust pyrolysis:
 1 – 350 °C, lower layer; 2 – 350 °C, upper layer;
 3 – 400 °C, lower layer; 4 – 400 °C, upper layer

Table 2. Concentrations of phenolic organic compounds in samples of liquid products of sawdust pyrolysis

Sample	1	2	3	4
Temperature of process	350 °C		400 °C	
Fraction (layer)	Lower	Upper	Lower	Upper
Compounds	Concentration, mg/ml			
1. Tyrosol	26.25	3.14	28.65	1.34
2. (2,6-di-tert-butylphenyl)propane	1.67	1.33	0.75	1.06
3. Butylated hydroxytoluene	2.07	0.19	1.00	0.02
4. Fenozan 28	0.80	0.19	0.60	0.02
5. Cyclohexanone + Fenozan 30	0.36	0.19	0.58	0.01
6. Fenozan 43	0.72	0.20	0.86	0.02
7. Thiolane	0.96	0.58	0.10	0.04
8. Tetramethylene disulfide	4.79	0.69	3.35	0.01
9. Fenozan 23	1.12	0.08	1.27	0.01

Analysis of liquid products of pyrolysis was performed by using of reversed phase liquid chromatography (chromatograph LC-20A, Shimadzu Corporation, Japan). Separation of phenols

was performed on a column Nusleodur 100–5 C₁₈ ec, 250×5.0 mm at 25 °C. A linear gradient of mobile phase was used for this purpose. Process time was 25 minutes with the rate of mobile phase of 0.5 ml/min. The mobile phase consisted of 100–0% A solution (distilled water + 0.09% trifluoroacetic acid), and 0–100% B solution (acetonitrile ≥ 99.9% + 0.09% trifluoroacetic acid). Quantity of phenols was determined from the chromatogram using standard gallic acid. Samples of established chromatograms are shown in Fig. 6.

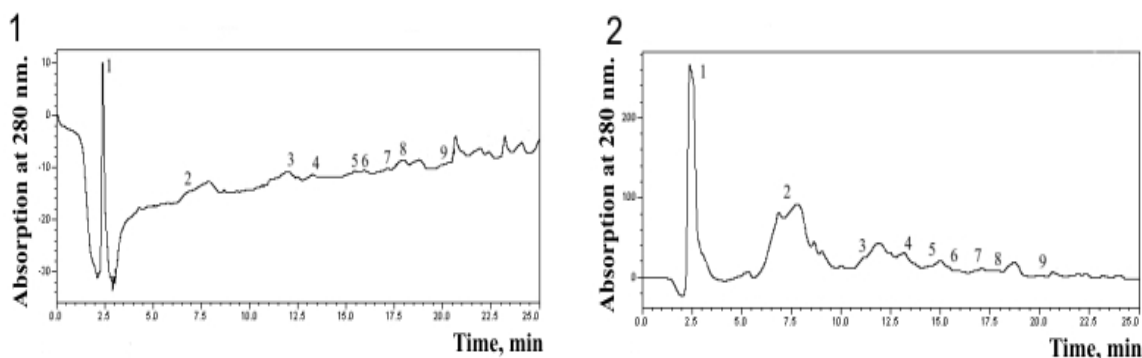


Fig. 6. Chromatograms of experimental samples of liquid products of pyrolysis performed at temperature 350 °C: 1 – lower layer; 2 – upper layer

Experimental results established in the described study show that increasing of the process temperature from 350 °C to 400 °C decreases amount of phenolic compounds in liquid products of pyrolysis. For example, amount of phenolic organic compounds in the lower fraction (lower layer) was at the pyrolysis temperature 400 °C by 17.3% lower than by temperature 350 °C. However, the relative fraction of them in the tar generated at temperature 400 °C was by 16.1% higher than in case of pyrolysis conducted at temperature 350 °C. Similar change was to see also in case of liquid products that collect in the upper layer. Total amount of phenolic organic compounds in the upper fraction in case of pyrolysis temperature equal to 400 °C is by 4.8% less than in case of pyrolysis process performed at temperature 350 °C. The fraction of phenolic organic compounds in the tar in the upper fraction increases by increase of pyrolysis temperature from 350 °C to 400 °C.

Significant influence on the amount of phenolic compounds makes also humidity of pyrolysed biomass. It was found in the experimental study that an increase of humidity of sawdust from 10 to 25% percent decreases concentration of phenolic component in liquid mixture of pyrolysis from 4.5 to 0.4 mg/ml.

Similar influence of temperature and humidity was also established for such important products of pyrolysis as toluene, benzene, alkene and alkadien. This allows to produce necessary liquid products by choosing pyrolysis temperature and humidity of pyrolysed material.

CONCLUSION

The optimal conditions of the pyrolysis with maximized yield of liquid products were defined during the computer simulation and experimental research.

Modelling of the pyrolysis process of different wood species showed that under the same conditions, the total yield of liquid products is practically unchanged. The defined optimum biomass particle size to obtain high yield of liquid products is 1–3 mm. Moreover, it is established that in order to maximize the yield of liquid products of biomass pyrolysis, process temperature should not exceed 600 °C. To prevent secondary decomposition of tars at such temperatures, vaporized liquid products must leave reactor zone during 2 seconds.

Conducted chromatographic studies of pyrolysis liquid samples show that the yield of important phenolic compounds depends greatly on temperature in reaction zone, on velocity of gaseous medium used for creation of fluidized bed and humidity of pyrolysed biomass. Increasing



of the process temperature from 350 °C to 400 °C decreases amount of phenolic compounds in liquid products of pyrolysis. An increase of humidity of sawdust from 10 to 25% percent decreases concentration of phenolic component in liquid mixture of pyrolysis from 4.5 to 0.4 mg/ml.

REFERENCES

1. BRIDGWATER, A.V. Biomass fast pyrolysis. *Thermal Science*, Vol. 8, No. 2, 2004, p. 21–49.
2. MOHAN, Dinesh; PITTMAN, Charles U.; STEELE, Philip H. Pyrolysis of wood/biomass for bio-oil: A critical review. *Energy and Fuels*, Vol. 20, No. 3, 2006, p. 848–889.
3. ЗЕНКОВ, Н.К.; КАНДАЛИНЦЕВА, Н.В.; ЛАНКИН, В.З.; МЕНЬЩИКОВ, Е.Б.; ПРОСЕНКО, А.Е. Фенольные биоантиоксиданты. Новосибирск: СО РАМН, 2003. 328 с.
4. ОРЛОВА, Т.Н.; ТОЛСТИКОВА, Т.Г.; СОРОКИНА, И.В. и др. Фармакинетика нового фенольного антиоксиданта СО-3. *Химико-фармацевтический журнал*, Том 34, № 9, 2000, с. 9–11.
5. BABU, B.V.; CHAURASIA, A.S. Heat transfer and kinetics in the pyrolysis of shrinking biomass particle. *Chemical Engineering Science*, Vol. 59, 2004, p. 1999–2012.
6. MILLER, R. S.; BELLAN, J. A generalized biomass pyrolysis model based on superimposed cellulose, hemicellulose and lignin kinetics. *Combustion Science and Technology*, 1997, Vol. 126, 1997, p. 97–137.
7. НИКИТИН, В.М.; ОБОЛЕНСКАЯ, А.В.; ЩЕГОЛЕВ, В.П. Химия древесины и целлюлозы. Москва: Лесная промышленность, 1978. 366 с.
8. CHAN, Wai-Chun R.; KELBON, Marcia; KRIEGER, Barbara B. Modelling and experimental verification of physical and chemical processes during pyrolysis of a large biomass particle. *Fuels*, Vol. 64, No. 11, 1985, p. 1505–1513.
9. LEWIS, F. Michael; ABLOW, Clarence M. Pyrogas from biomass. A conference on capturing the sun through bioconversion. Washington, D.C. 1976 March 10–12.
10. ЛЫКОВ, А.В. Теория теплопроводности. Москва: Высшая школа, 1967. 600 с.
11. МУХЛЕНОВ, Б.С.; САЖИН, Б.С.; ФРОЛОВ, В.Ф. Расчеты аппаратов кипящего слоя: Справочник. Ленинград: Химия, 1986. 352 с.



OPTIMIZATION OF THERMAL DECOMPOSITION PROCESS OF BIOMASS PYROLYSIS TARS FOR THE PRODUCTION OF HIGH CALORIFIC GASES

K. Zakarauskas, N. Striūgas, G. Stravinskas
Lithuanian Energy Institute
Laboratory of Combustion Processes
Breslaujos str. 3, LT-44403 Kaunas – Lithuania

ABSTRACT

Biomass and bio-waste gasification is one of alternatives in heat and electricity generation, by developing local renewable energy sources. This technology has not been worked out fully, therefore, a lot of problems are faced that prevent from mass spread of gasification technologies in industry. One of aforementioned problems is the presence of tar in gasification gas. The permissible tar concentration in gasification gas is from 0 to 500 mg/m³, depending on where it is intended to use the obtained gas (e.g., in case of gas turbines, it is allowed only up to 5 mg/m³). Seeking to optimize the gasification processes, new methods for tar removal from gas are looked for. One of them is catalytic reforming, when hydrocarbons, comprising the tar, are additionally gasified till end products of reaction.

The article presents the results of research on catalytic reforming of thermal decomposition of tar, obtained during biomass gasification and present in the composition of gas. For research the catalyst of activated char of tires was used at two thermochemical processes: partial oxidation and steam reforming. What is more, the change of composition of gas-tar mix during tar decomposition was assessed, their mass balance before and after thermal decomposition was formed. The analysis of obtained results was also carried out the generalization of which enables to define the optimal parameters at which the cleaning of gasification gas from tar is the most effective and the gas output is the best.

Keywords: Biomass gasification, tars, steam reforming, partial oxidation, char

1. INTRODUCTION

Biomass gasification is one of alternatives, seeking to develop its usage possibilities. Gasification is a complex thermo-chemical process, when biomass is converted to the following main components: CO, H₂, CO₂, CH₄, N₂, and tar. In order to use the obtained gas in internal combustion engines, gas turbines, in production of synthetic diesel, chemical materials, it must be cleaned from tar [1, 2].

Tar is defined as generic term, including all organic compounds, present in gasification gas, except gaseous hydrocarbons [3]. Tar removal or conversion is one of the greatest technical obstacles for successful development of gasification. As tar gets on technological equipment, it condenses, burns, thus, shortening the life time of the equipment.

One of the methods of tar removal is its condensation in scrubbers. This is quite effective, but uneconomical cleaning method, since a part of calorific substances is got out. Especially, when the end usage of gas requires that the gas would remain of high temperature. In this case, the most optimum way is to use the catalytic thermal decomposition of tar by decomposing it up to gaseous hydrocarbons. One more advantage of this process is adjustment of gas composition, which influences not only tar, but also gas conversion.

The aim of this article is to assess the change in composition of gas-tar mixture, which takes place during catalytic tar decomposition, by using the catalyst of activated tyre carbon and by making gas mass balances, as well as to determine the influence of these processes on gross calorific value of gas at three different temperatures and two thermochemical processes, i.e., partial oxidation and steam reforming.

2. METHODOLOGY

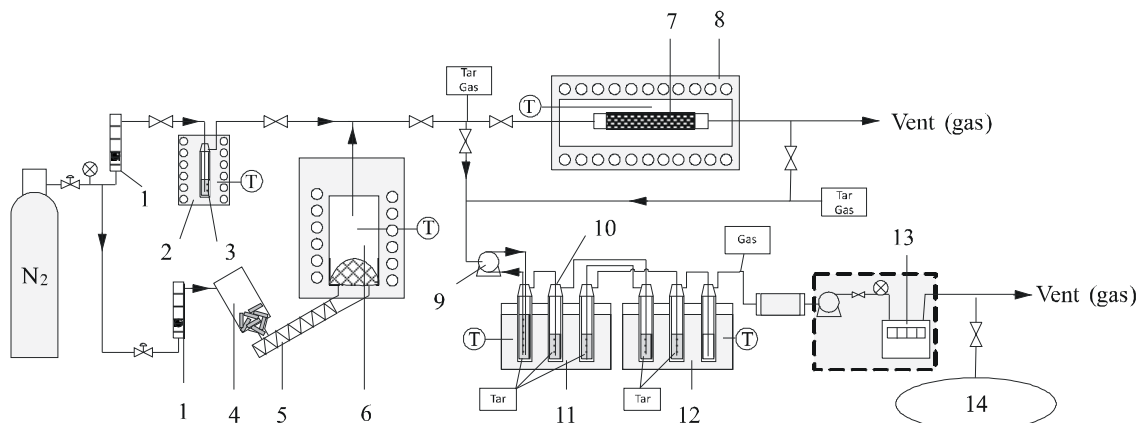


Fig. 1. Scheme of the experimental rig

1 – rotameter; 2 – heater; 3 – water evaporator; 4 – biomass pellet container; 5 – screw conveyor; 6 – pyrolysis reactor; 7 – catalytic bed; 8 – catalytic reactor; 9 – peristaltic pump; 10 – gas washing bottles; 11 – heated bath (+30 °C); 12 – cooled bath (-20 °C); 13 – gas flowmeter; 14 – gas bag

The experimental stand consists of four main parts: biomass pyrolysis reactor, catalytic reactor and tar condensers. Biomass tar decomposition experiments are carried out in the following way: nitrogen is supplied to evaporator 3 by the flow of 0.9 l/min. Water is evaporated at constant temperature in evaporator. Nitrogen flow, flowing through evaporator, saturates with certain water quantity. Other measured nitrogen flow (1.8 l/min) for pyrolysis gas transportation is supplied to container 4 with fuel pellets. As the experiments of partial oxidation are carried out, air is supplied instead of water vapour.

Coniferous wood pellets are used in experimental studies. Screw conveyor 5 supplies a constant quantity of fuel pellets, i.e., 5 g/min, to pyrolysis reactor 6. Constant temperature of 850 °C is maintained in pyrolysis reactor. The obtained pyrolysis gas with tar is mixed with nitrogen – water vapour or air before going to catalytic reactor. The obtained gas mixture goes to tar catalytic reactor. Catalyst layer [5] of activated tyre carbon is mounted inside the reactor, where the constant required temperature (700–900 °C) is maintained. Tar and gas concentrations are determined before and after catalytic reactor [5].

The analysis of gaseous samples was performed using Agilent 7890A gas chromatograph with dual channel thermoconductivity detectors (TCD) and valve system: front channel is used for separating of O₂, N₂, CO₂, CH₄, CO and light hydrocarbons, while back channel – for hydrogen separation.

3. RESULTS AND DISCUSSION

While analyzing the catalytic-thermal decomposition of tar, experimental studies were carried out by using the catalyst of activated tyre carbon and two thermochemical processes: partial oxidation and steam reforming at different temperatures (700, 800 and 900 °C). The experiments of partial oxidation were carried out at a constant excess air ratio ER = 0.067 [6], while the ones of steam reforming – at the amount of steam H₂O/C = 0.5 [5].

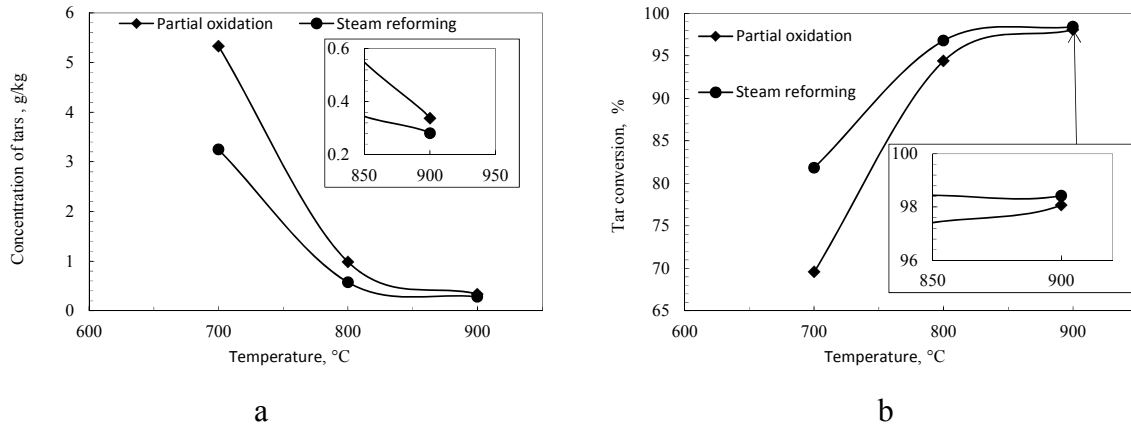


Fig. 2. Impact of temperature on tar destruction: gas concentrations (a); effectiveness of tar conversion (b)

Seeking to assess the effectiveness of catalysts, tar concentrations were converted to the percentage value of decomposition effectiveness:

$$X(\%) = \frac{(C_{in} - C_{out})}{C_{in}} \cdot 100\%, \quad (1)$$

where C_{in} – inlet concentrations of total tars (g/m^3) and C_{out} – outlet concentrations of total tars (g/m^3).

The obtained results of calculations are presented in Fig. 2. As it may be seen from the Figure, tar decomposition is more effective, when using the steam reforming at the temperature of 700–800 °C, comparing with partial oxidation. The effectiveness of tar decomposition at the temperature of 900 °C is similar in case of both thermochemical processes: steam reforming 98.4% and partial oxidation 98.0%, respectively. The influence of temperature is obvious in both cases. Further, the main attention in this article is paid on analyzing the influence of gas decomposition processes on the change in gas composition.

3.1. Partial oxidation

The results of mass balance after reactor are presented in Fig. 3. The gas composition was maintained constant before reactor, i.e.: H_2 – 1.5%, CO – 18.8%, CH_4 – 4.8%, CO_2 – 16.7%, N_2 – 51.9% and O_2 – 2.5% (mass).

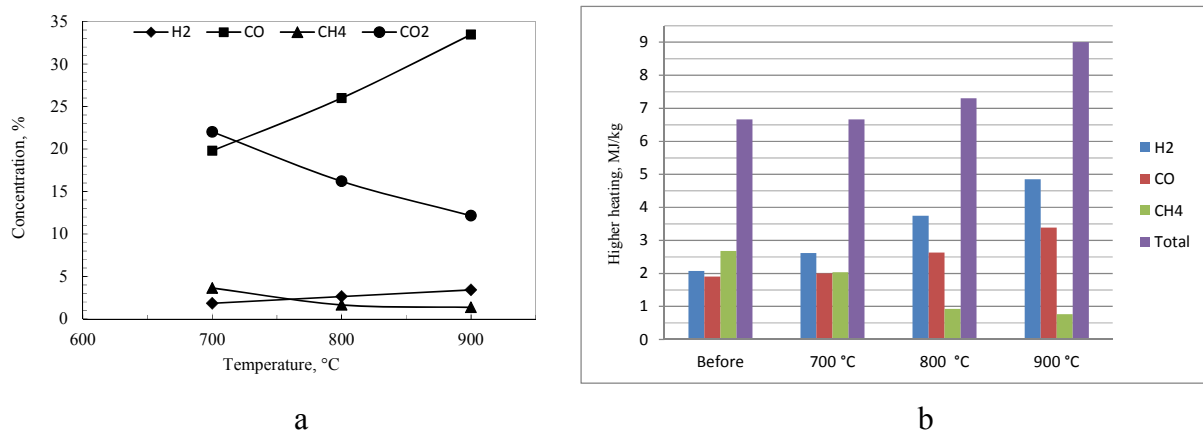


Fig. 3. Gas composition in percentage values (a) and higher calorific value (b) obtained at different process temperatures, when air excess ratio is $\text{ER} = 0.0667$

The concentrations of CO and H₂ slightly increase in gas at the temperature of 700 °C, while the calorific value of gas remains the same due to decrease of CH₄. The increase of CO₂ shows that a part of oxygen, supplied with air, took part in complete combustion. The opposite processes take place at higher temperatures: the concentration of CO₂ decreases from initial value of 16.7% to 15.3% at the temperature of 800 °C and to 12.2% at the temperature of 900 °C, respectively. Therefore, it might be stated that not only a partial oxidation, but also a reaction of dry reforming (2) takes place, during which CO₂ reacts with hydrocarbons, therefore the concentrations of H₂ or CO especially increase at the temperature of 900 °C, thus, increasing the calorific value to 9 MJ/kg.



As gas composition changed due to additional air and thermochemical process, its density also changed. While calculating the mass balances and the calorific value of kilogram of gas, the calorific value of gas from pyrolysis reactor and the calorific value of air mixture were assessed. Seeking to assess the influence of aforementioned process, the term of gas output was introduced, which defines how much gas is obtained from one cubic meter of gasification gas (V_b) after catalytic cleaning (V_a). At the same time, the higher volumetric calorific value was calculated.

$$\beta = \frac{V_a}{V_b}; \quad (3)$$

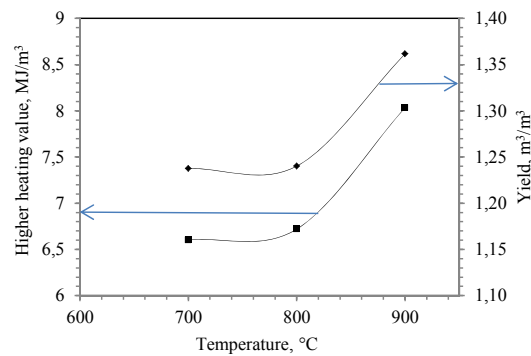


Fig. 4. Gas output and higher volumetric calorific value at different temperatures, when air excess ratio is ER = 0.0667

The results in Fig. 4 show that under normal conditions at the temperature of 700–800 °C the calorific value of gas is about 7.0 MJ/m³, while the one of gasification gas is equal to 8.0 MJ/m³. At first glance, it seems that the calorific value of gas decreases after catalytic cleaning, however, due to increase of gas output the gross energy value remained the same at 700 °C and even increased at the temperature of 800 °C. At the temperature of 900 °C, the calorific value of gas was 8.0 MJ/m³, similar to the one of gasification gas. However, the gas output is 1.36, thus, the gross energy value increases to 10.89 MJ.

Teo-Young [6] performed similar research on tar decomposition by using partial oxidation and activated wood carbon, only at air excess ratio of ER = 0.17 and other interval of temperatures (643–793 °C). When comparing the results, the temperatures, which are the closest to our experiments, were selected, i.e., 698 °C and 793 °C. In both cases, the decrease of hydrocarbons, increase of hydrogen concentration and decrease of higher calorific value of gas (MJ/m³) is observed.

3.2. Steam reforming

The results of mass balance after reactor are presented in Figure 5. The gas composition was maintained constant before reactor, i.e.: H₂ – 1.5%, CO – 19.2%, CH₄ – 4.9%, CO₂ – 17.1%, N₂ – 46.2% (mass).

In case of steam reforming, the changes of gas at the temperature of 700–800 °C were similar. In both cases, the gas reforming reaction took place, according to equation 4. Therefore, the concentration of methane CH₄ respectively decreased in gas. The increase of hydrogen was determined not only by aforementioned reaction, but also by interaction of CO and water vapour, according to equation 5 [7], during which CO₂ and H₂ hydrogen were formed. As the mass balance confirms, CO decreases, while CO₂ increases. This observations suggest that the amount of water vapour was too high at these temperature, it is sought that only steam reforming would take place. The calorific value of gas slightly increased in both cases, 6.91 and 6.98 MJ/kg, respectively, when it was 6.83 MJ/kg before. As in case of partial oxidation, the decrease of methane and CO was compensated by almost twice increase of hydrogen.

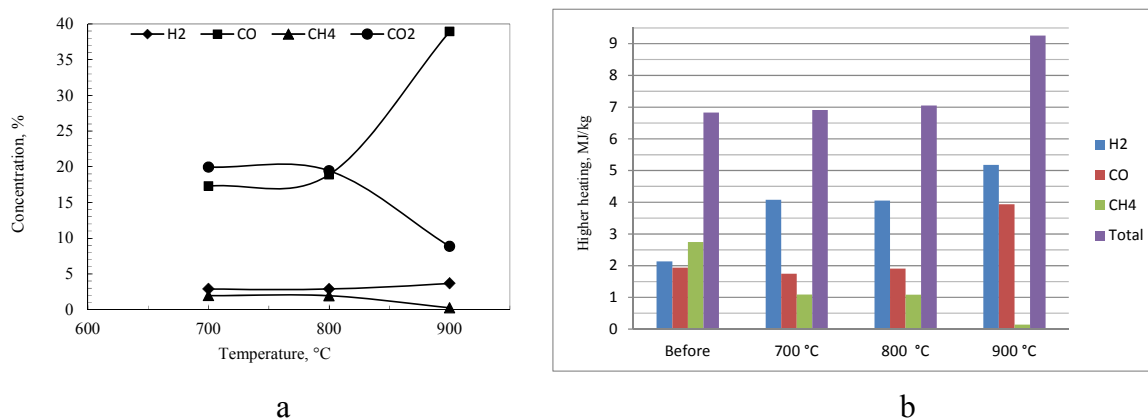
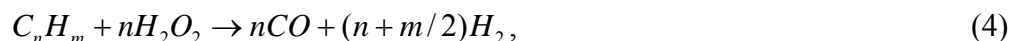
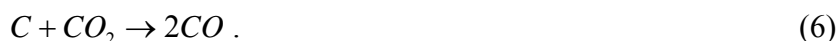


Fig. 5. Gas composition in percentage values (a) and higher calorific value (b) at different temperatures, when H₂O/C = 0.5

CO concentration increases twice at the temperature of 900 °C, i.e., from 19.2% to 38.9%, unlike at lower temperatures. The concentration of hydrogen increases from 1.5% to 3.7% at the same time. However, it cannot be stated that only a reaction of steam reaction took place, since dry reforming also took place due to decrease of CO₂ concentration from 17.1% to 8.8%. Despite the fact, in order to confirm this consumption more detailed research is required, since it is possible that CO₂ reacted with carbon of catalyst and, thus, the so-called Boudouard reaction took place 6.



As in case of partial oxidation, here the gas output and higher volumetric calorific value of gas under normal conditions was assessed. The results in Figure 6 show that under normal conditions at the temperature of 700–800 °C the calorific value of gas is about 6.6 and 6.7 MJ/m³, respectively, while the one of gasification gas is equal to 8.07 MJ/m³. At first glance, it seems that the calorific value of gas decreases after catalytic cleaning, however, due to increase of gas output the gross energy value slightly increased at 700–800 °C, 8.17 and 8.33 MJ/m³, respectively. At the

temperature of 900 °C, the calorific value of gas was 8.03 MJ/m³, similar to the one of gasification gas. However, the gas output is 1.36, thus, the gross energy value is 10.94 MJ.

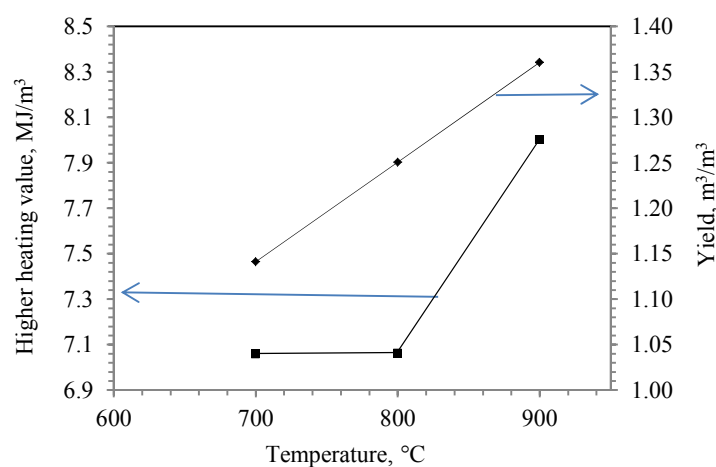


Fig. 6. Gas output and higher volumetric calorific value at different temperatures, when H₂O/C = 0.5

4. CONCLUSIONS

After carrying out experimental studies and balance calculations, it was determined:

- In case of partial oxidation the volumetric calorific value of gas decreased after catalytic cleaning at the temperature of 700–800 °C, however, due to increase of gas output the gross energy value remained the same at 700 °C and even increased at the temperature of 800 °C. At the temperature of 900 °C, the calorific value of gas was 8.0 MJ/m³, but due to increase of output, the gross energy value increases to 10.89 MJ.
- In case of steam reforming the calorific value of gas is about 6.6 and 6.7 MJ/m³, respectively, at the temperature of 700–800 °C, while the one of gasification gas is equal to 8.07 MJ/m³. However, due to increase of gas output the gross energy value slightly increased at 700–800 °C, 8.17 and 8.33 MJ/m³, respectively. At the temperature of 900 °C, the calorific value of gas was 8.03 MJ/m³, similar to the one of gasification gas. However, due to increase of output, the gross energy value increases to 10.94 MJ.
- The performed analysis shows that the effectiveness and calorific value of gas is similar in case of both thermochemical processes (partial oxidation and steam reforming), at the temperature of 900 °C. At lower temperatures, a partial oxidation is characterized by lower effectiveness in respect of tar decomposition. Taking into account the aforementioned results, it might be stated that tar decomposition does not reduce the gross energy value of gas and even increases it at higher temperatures.

REFERENCES

1. LIM M.T., ZAINAL Z.A., Bubbling fluidized bed biomass gasification-performance, process findings and energy analysis, *Renewable Energy*. 2008 Vol. 33, October 2008, p. 2339–2343.
2. GIL J., CORELLA J., AZNARA M.P., CABALLEROA M.A. Caballero Biomass gasification in atmospheric and bubbling fluidized bed: effect of the type of gasifying agent on the product distribution. *Biomass and Bioenergy*. 1999 Vol. 17, p. 389–403.



3. RABOU, L.P.L.M., ZWART, R.W.R., VREUGDENHIL, B.J., BOS, L., 2009. Tar in biomass producer gas, the Energy research centre of the Netherlands (ECN) experience: an enduring challenge, *Energy Fuels*, 2009 Vol. 23, p. 6189–6198.
4. DEVI L., J.K. PTASINSKI, JANSSEN J.J.G.F., A Review of the Primary Measures for Tar Elimination in Biomass Gasification Processes. *Biomass and Bioenergy*, 2003 Vol. 24, p. 125–140.
5. ZAKARAUSKAS K., STRIŪGAS N., STRAVINSKAS G. CYSENI 2012. Investigation of thermal cracking of syngas tar from biomass gasification by catalytic steam reforming Proceedings of annual conference of young scientists on energy issues. [CD]. Kaunas: Lithuanian Energy Institute. 2012 May 24–25.
6. MUN T., KANGB.S, KIM J.K., Production of a producer gas with high heating values and Less tar from dried sewage sludge through air gasification using a two-stage gasifier and activated carbon. *Energy & Fuels*. 2009, Vol. 23, p. 3268–3276.
7. DAYTON D. A review of the literature on catalytic biomass tar destruction. Milestone completion report. Milestone Completion Review (2002), NREL/TP-510-32815.



FEATURES OF MAXIMUM DISCHARGES CHANGE OF MOUNTAIN RIVERS IN THE CARPATHIAN REGION: A CASE STUDY OF THE WATER COURSES IN THE UPPER PART OF THE RIKA RIVER BASIN

T. Bauzha, L. Gorbachova
*Ukrainian Hydrometeorological Institute
Nauki Prospect 37, 03028 Kyiv – Ukraine*

ABSTRACT

The research of the flood discharges is one of the important problems in hydrology, because it gives an idea of the general characteristics of the runoff regime of a region, especially mountainous. The floods are a threat for human life and national economy. Therefore, the analysis of tendencies of the flood discharges in present conditions has important scientific and practical importance. In this paper the estimation of the results of the long-term observations of the maximum discharges of mountain rivers in the Carpathian region (by the example of the watercourses in the upper part of the Rika River Basin, which is the right tributary of the Tysa River) is presented. For the rivers of the Tysa River Basin the spring flood is not typical, because of the frequent winter thaw accompanied by the liquid precipitation, which constitute 50–60% of the mixed flood runoff. Therefore, within this region for the warm (rain floods) and cold (rain and snowmelt floods) periods the maximum discharges were calculated. The estimation of the homogeneity and stationarity of the observations data of the flood discharges by the hydrological genetic (the general integral curves, the difference integral curves, the combined chronological graphs) and statistical methods (the statistical criteria by the Fisher's and Student's, the statistical significance of linear trends) was carried out. For the first time this complex application of these methods for the comparative analysis is carried out. For all gauging stations the statistical parameters were calculated and analyzed. The phases of cyclical fluctuations of the maximum discharges of the rivers and streams were defined.

Keywords: maximum discharges; climate change; small mountain catchments; stationarity.

1. INTRODUCTION

The Ukrainian Carpathians belong to the flood danger regions of Europe. The flash floods on the Carpathian Rivers are the largest in the height and intensity in Ukraine. It is observing several times a year. Their frequency is subject to certain regularities that are associated with the periodic change of periods of increase and decrease of the phases of the cyclical fluctuations of the maximum discharges. In cold and warm season due to intense rains the floods are dangerous. Sometimes the floods even are the disasters. It is causing the considerable damage for agriculture (flooded lands, granaries, warehouses of mineral fertilizers) and also is by threat for human life. In this period the situation is complicated by the emergence of landslides and powerful mudflow that is destroys buildings, roads, railways, high voltage line and other engineering communications. Not only on the large and the medium rivers, but also on the small mountain watercourses sometimes can be observed the stormy rain floods. The values of the maximum discharges these floods are very often exceeding floods of snowmelt water because the water yield during the rainstorms is much more intense than during snowmelt.

The present researches of the maximum discharges on the rivers of Ukrainian Carpathian is carried out by numerous authors, for example, the analysis of the flood discharges on the Tysa River Basin is in the papers Gopchenko, Grebin, Susidko at al. [1–5]. However, for small rivers of the research of the maximum discharges did not carry out. The goal of this paper is the analyses the flood discharges of warm and cold periods on the small and medium rivers of the upper part of the Rika River Basin and the calculation of their statistical characteristics (average discharge,

coefficient of variation, coefficient of asymmetry, etc.). It will allow to define the possible changes of the maximum discharges and is analyzing the reasons for such changes.

The main tasks of the research:

- the estimate of the homogeneity of the observations data by the general integral curve and by the statistical criteria the Fisher and the Stjudent;
- the estimation of the stationarity of the long-term fluctuations of the maximum discharges of the rain floods and rain and snowmelt floods by an assessment of the statistical significance of the linear trends;
- the analysis of the difference integral curves of the observations series to reveal the regularity of the cyclical fluctuations of the maximum discharges;
- the statistical hydrologic characteristics of the maximum discharges of the rivers and streams are determining;
- the phases of cyclical fluctuations of the maximum discharges of flood of the water objects are analyzing.

2. STUDY AREA AND DATA

For the statistical analysis of the maximum discharges of warm (the positive of air temperature and the liquid precipitation) and cold (the negative of air temperature and the liquid and snow precipitation or only snow precipitation) periods the data of 16 gauges located on the mountain watercourses were used (Fig. 1): 4 small ($F_{basin} = 10\text{--}100 \text{ km}^2$) and 2 medium ($F_{basin} = 100\text{--}1000 \text{ km}^2$) rivers (according to classification of the EU Water Framework Directive 2000/60/EC) [6] and 5 streams within Zakarpatska water-balance station (ZWBS). The period of observation on these water bodies is from 47 to 50 years. The station is located in the upper part of the Rika River with the closing gauge in the village Mizhgirya ($F_{basin} = 550 \text{ km}^2$). It covers the main part of the Mizhgirya region of the Zakarpattya area (the western part of Ukraine) and occupies the south-west slopes of the East Carpathians within heights from 434 to 1598.9 m above sea level which are the chain of the mountains with the steep slopes that cuted the valleys of the rivers and streams. The river network is presented by the ten rivers (Rika, Rypynka, Lopushna, Golyatynka, Studenny, Pylypets, etc.) with the lengths from 7.1 to 31.3 km and the more 500 of the streams by length from 2 to 3 km. The total length of the river network exceeds 300 km. The density of the river network varies from 0.2 to 2.7 km/km². The catchment areas are changing in the greater limits – from 10–15 to 550 km² [7]. The detailed description of the characteristics of the study area are presented in the paper [8].

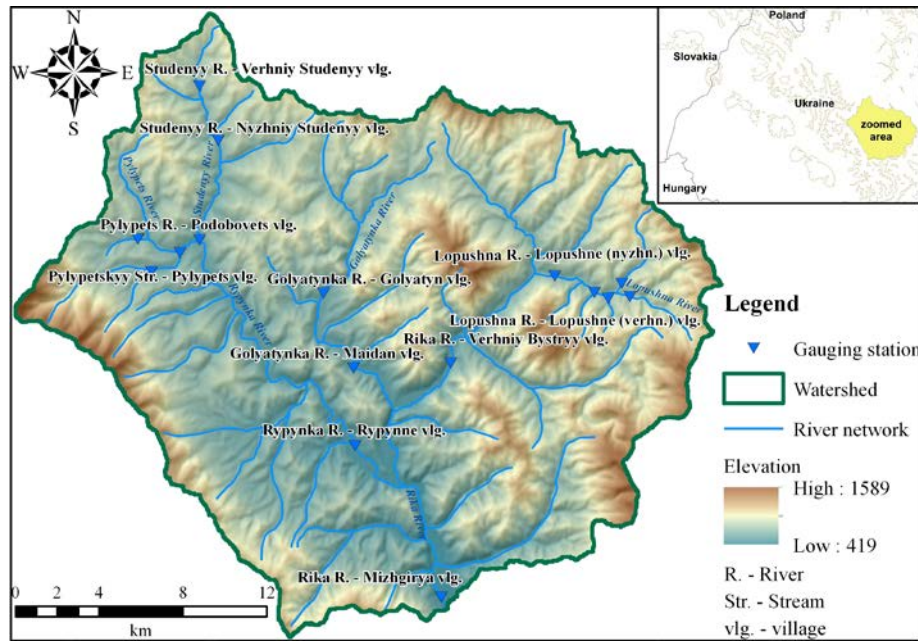


Fig. 1. The gauging stations in the upper part of the Rika River Basin

3. METHODOLOGY

The observations data were formed on the basis of complex graphs (discharge, air temperature, precipitation) for calendar period of year. In some years for several rivers and streams the observations were not carried out. Thus, the omissions in the observations data were restored by method of the regression on the variable on the base of the data of the streams and analogues rivers according to [9] and using of the program HydroStatCalc (developer is the State Hydrological Institute, Russia). This method consists in the calculating the regression equation by using the data of the analogues rivers. The restore of the data is carrying out provided that

$$R \geq 0.7, n \geq 10, k/\sigma_k \geq 2, \quad (1)$$

were R is the correlation factor between the values of the discharges in the brought gauge and analogue gauge; n is the number of the joint years of the observations in the brought gauge and analogue gauge; k is the regression coefficient; σ_k is the standard deviation of the regression coefficient.

The estimation of the statistical hydrologic characteristics are carried out by the homogeneous data to receive accurate and reliable results [10]. The estimation of the homogeneity and stationarity of the observations series of the flood discharges was carried out by the hydrological genetic and statistical methods.

Hydrological genetic methods include:

- 1) the general integral curves. Their review (presence or absence of any points of the fracture in the directions) allows to find out the influence the anthropogenic factors and the manifestations of the global climate change on the formation of the river runoff;
- 2) the difference integral curves which allows to reveal the regularity in the cyclical fluctuations of the runoff on the catchment;
- 3) the combined chronological graphs.

Statistical methods include the statistical significance of linear trends and the statistical criteria by the Fisher's (for dispersions) and Student's (for averages) with provision the autocorrelation coefficient $r(1)$:

$$r(1) = \left[\sum_{i=1}^{n-1} (Q_i - \bar{Q}_1)(Q_{i+1} - \bar{Q}_2) \right] / \sqrt{\sum_{i=1}^{n-1} (Q_i - \bar{Q}_1)^2 \sum_{i=2}^n (Q_i - \bar{Q}_2)^2}, \quad (2)$$

where $\bar{Q}_1 = \left(\sum_{i=1}^{n-1} Q_i \right) / (n-1)$; $\bar{Q}_2 = \left(\sum_{i=2}^n Q_i \right) / (n-1)$.

According to the criteria of the time series is divided into two equal parts. For each part of series are calculated averages (\bar{x} and \bar{y}) and dispersions (σ_x^2 and σ_y^2). It is later used to calculated values of the Student statistics (t) and the Fisher statistics (F). In general form they are as follows:

- the criterion of homogeneity of dispersions:

$$F = \frac{\sigma_x^2}{\sigma_y^2} \quad (3)$$

- the criterion of homogeneity of averages:

$$t = \frac{|\bar{y} - \bar{x}|}{\sqrt{n_1 \sigma_x^2 + n_2 \sigma_y^2}} \sqrt{\frac{n_1 \cdot n_2 (n_1 + n_2 - 2)}{n_1 + n_2}}, \quad (4)$$

where σ_x^2 and σ_y^2 are the dispersions of the time series of the maximum discharges; n_x and n_y are the volume of the first and second half of the series; \bar{x} and \bar{y} are the averages of the first and second parts of the series.

The calculated values of these criteria are compared with the critical values for 5 % of the significance level. If empirical values (t_{emp} and F_{emp}) exceed the critical values (t_{cr} and F_{cr}), it is considered as the disturbance of the stationarity in these observations series. The critical value of the Student criterion and the Fisher criterion should be determined by the special tables, taking into account the significance level α .

The estimation of the stationary of the long-term fluctuations of the maximum discharges is carried out by the assessment of the statistical significance of the linear trends [10]. In turn, the statistical significance of the trends is defined by the statistical significance of the correlation factor (R). The correlation factor of this dependence is estimating on the relation to the standard deviation (σ_R):

$$R / \sigma_R \geq \beta. \quad (5)$$

For 5 % of the significance level or for the 95 % confidential limit $\beta = 2$. If as a result of the calculations it will appear that $2\sigma_R < R$, it indicates no stationarity of the long-term fluctuations of the runoff, and on the contrary, if $2\sigma_R > R$ is the homogeneity of the runoff in the time. The standard deviation of the correlation factor for $n > 25$ is defining by the formula:

$$\sigma_R = (1 - R^2) / \sqrt{n - 1}, \quad (6)$$

where n is the total number of the members of the row.

For comparison of the results the graphs of the long-term dynamics and of the difference integral curves were created in the modulus coefficients (K_A) according to:

$$K_A = A_i / \bar{A}, \quad (7)$$

where A_i is the value i -element of the series; \bar{A} is the average of the series.

4. RESULTS AND DISCUSSION

The comparative analysis of the largest to research period the maximum discharges of warm and cold periods on the existing gauges was carried out. It is showed that the maximum discharges of warm period on average 1.6 times higher than the maximum discharges of cold period. However, in three points of observations are located on the medium rivers the largest statistical maximum of the rain and snowmelt floods exceeds the largest statistical maximum of the rain floods (Table 1).

Table 1. The largest statistical maximum discharges of warm and cold periods of the rivers and streams of the upper part in the Rika River Basin

The name of gauge	The largest $Q_{max. \text{ warm. period, m}^3/\text{s}}$	The largest $Q_{max. \text{ cold. period, m}^3/\text{s}}$	$\frac{Q_{max. \text{ warm. period}}}{Q_{max. \text{ cold. period}}}$
Rika River – Mizhgirya village	555	735	0.76
Rypynka River – Rypynne village	248	253	0.98
Golyatynka River – Golyatyn village	160	64.9	2.47
Rika River – Verhniy Bystryy village	131	142	0.92
Golyatynka River – Maidan village	130	127	1.02
Pylypets River – Pylypets village	88	60.8	1.45
Studenyy River – N. Studenyy village	62.7	26.9	2.33
Pylypets River – Podobovets village	41.5	22.0	1.89
Ploshanka Stream – Pylypets (nyzhn.) village	37.5	30.3	1.24
Studenyy River – Verhniy Studenyy village	34.2	12.3	2.78
Lopushna River – Lopushne (nyzhn.) village	27.5	26.5	1.04
Lopushna River – Lopushne (verhn.) village	20.9	13.4	1.56
Branysche Stream – Lopushne village	16.5	11.3	1.46
Pylypetsky Stream – Pylypets village	13.7	8.12	1.69
Zyubrovets Stream – Lopushne village	7.50	3.42	2.19
Seredniy Zvir Stream – Lopushne village	3.73	2.26	1.65

The graphs of the general integral curves of the maximum discharges of cold and warm periods for all rivers and streams in the Rika River Basin were created. It don't have any significant

points of the fracture of the directions of the curves, i.e. the observations series are the homogeneous. Examples of such curves are shown in Fig. 2 for some rivers and streams of the Zakarpatska water-balance station.

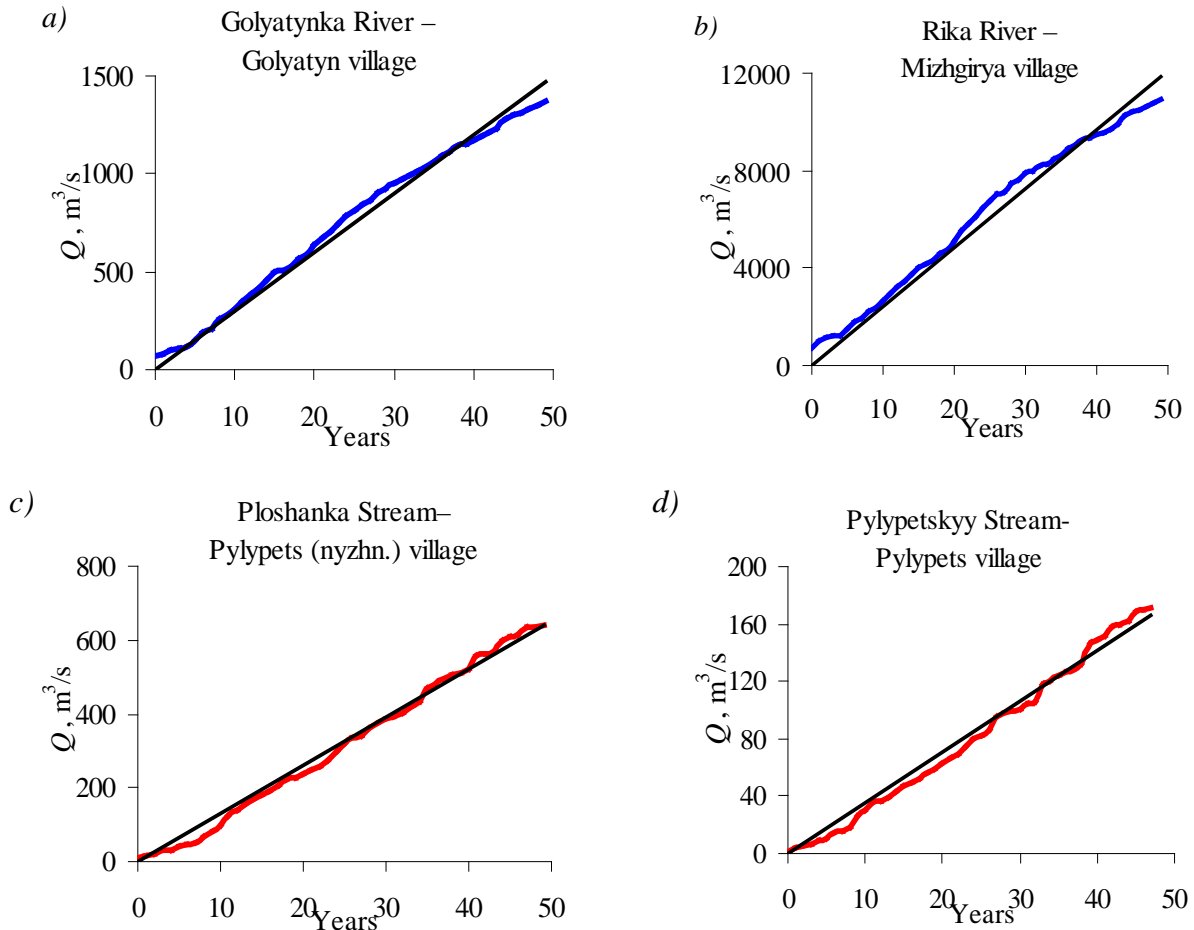


Fig. 2. The general integral curves of the flood discharges of cold (*a, b*) and warm (*c, d*) periods on the rivers and streams of the ZWBS

The estimation of the homogeneity of the observations series of the maximum discharges were carried out by parametric statistical generalized criteria by the Fisher's and Student's with provision the in-row correlation (Table 2). As a result the inhomogeneous observations data were found (Table 3), namely the series the maximum discharges for warm period – in four of the gauges (Ploshanka Stream – Pylypets (nyzhn.) village, Pylypetsky Stream – Pylypets village, Golyatynka River – Golyatyn village and Zyubrovets Stream – Lopushne village) by the Fisher criterion; and the series of maximum discharges for cold period – in six of the gauges (Rika River – Mizhgirya village, Rika River – Verhniy Bystryy village, Rypynka River – Rypynne village, Studenyy River – Nyzhniy Studenyy village, Golyatynka River – Golyatyn village, Golyatynka River – Maidan village) by the criteria the Fisher's and Student's and – the gauges Pylypets River – Pylypets village by the Student criterion.

Table 2. The in-row correlation of the observation data of the maximum discharges of warm and cold periods of the rivers and streams of the Zakarpatska water-balance station

№	The name of the gauge	Period	
		cold	warm
		$r(I)$	
1	Pylypets River – Pylypets village	0.2	0.1
2	Golyatynka River – Golyatyn village	0.2	0.0
3	Golyatynka River – Maidan village	0.2	0.0
4	Rika River – Mizhgirya village	0.2	0.0
5	Rypynka River – Rypynne village	0.2	0.0
6	Rika River – Verhniy Bystryy village	0.2	0.0
7	Studenyy River – Nyzhniy Studenyy village	0.2	0.0
8	Lopushna River – Lopushne (verhn.) village	0.1	0.0
9	Zyubrovets Stream – Lopushne village	0.1	0.0
10	Seredniy Zvir Stream – Lopushne village	0.1	0.0
11	Pylypets River – Podobovets village	0.0	0.2
12	Ploshanka Stream – Pylypets (nyzhn.) village	0.0	0.1
13	Branysche Stream – Lopushne village	0.0	0.1
14	Studenyy River – Verhniy Studenyy village	0.0	0.0
15	Pylypetsky Stream – Pylypets village	0.0	0.0
16	Lopushna River – Lopushne (nyzhn.) village	0.0	0.0

 Table 3. The inhomogeneous data of the maximum discharges of warm and cold periods in the Rika River Basin by the statistical criteria the Fisher (F) and the Student (t)

The name of the gauge	t_{emp}	t_{cr}	F_{emp}	F_{cr}	The results of the check	
					the Student's	the Fisher's
Warm period						
Golyatynka River – Golyatyn village	0.59	2.01	4.24	2.27	+	–
Zyubrovets Stream – Lopushne village	1.12	2.02	6.05	2.39	+	–
Ploshanka Stream – Pylypets (nyzhn.) village	0.77	2.20	2.33	2.29	+	–
Pylypetsky Stream – Pylypets village	1.18	2.02	4.05	2.39	+	–
Cold period						
Rika River – Mizhgirya village	2.54	2.42	2.58	2.34	–	–
Rika River – Verhniy Bystryy village	2.72	2.42	2.54	2.34	–	–
Rypynka River – Rypynne village	2.79	2.42	2.51	2.34	–	–
Golyatynka River – Golyatyn village	2.54	2.42	2.58	2.34	–	–
Studenyy River – N. Studenyy village	3.27	2.42	2.44	2.34	–	–
Golyatynka River – Maidan village	3.33	2.42	2.44	2.34	–	–
Pylypets River – Pylypets village	2.87	2.42	1.39	2.34	–	+

+ – the homogeneous series of observations; – – the inhomogeneous series of observations.

At the same time, the estimation of the stationary of the long-term fluctuations of the maximum discharges were carried out by the assessment of the statistical significance of the linear trends (at 5 % of the significance level). In the course of research of the maximum discharges of

warm period no statistically significant trends were found. It indicates the homogeneity of the series of observations in time, i.e. their stationarity. In the observations series of the maximum discharges of cold period the statistically significant trends were observed in eight of the gauges (Golyatynka River – Maidan village, Golyatynka River – Golyatyn village, Rika River – Mizhgirya village, Pylypets River – Pylypets village, Studenyy River – Nyzhniy Studenyy village, Rika River – Verhniy Bystryy village, Ploshanka Stream – Pylypets (nyzhn.) village, Rypynka River – Rypynne village) (Table 3). However, the view of the general curves for these gauges (Fig. 2) and also synchronous fluctuations of the maximum discharges (Fig. 3) at all observation points indicates the homogeneity of the conditions of their formation, i.e. in accord with the hydrological genetic methods the series of observations are homogeneous. Examples of such fluctuations are shown in Fig. 3 for some rivers and streams of the ZWBS. The statistical inhomogeneity of the series (Table 4), which were found in some observation points, occurs due to the comparison of the increasing and decreasing of phases of cyclical fluctuations of the maximum discharges (Fig. 4). The same results are received in the papers [4, 8, 11].

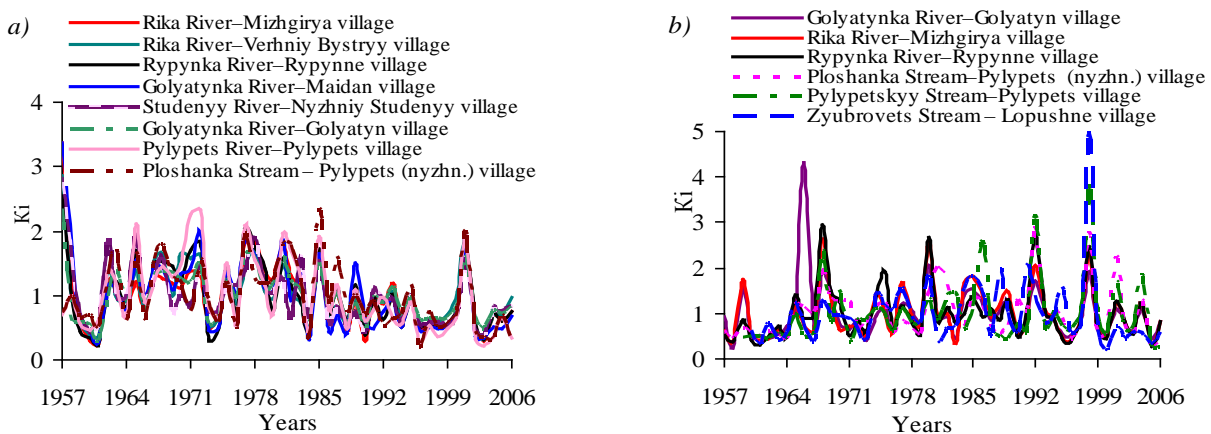


Fig. 3. The long-term dynamics of the flood discharges of the rivers and streams in the Rika River Basin of cold (a) and warm (b) periods

Table 4. The statistically significant linear trends of the maximum discharges of cold period of the rivers and streams in the Rika River Basin, 1957–2006

The name of the gauge	The equation of the trend	R ²	R	σ _R	2σ _R	3σ _R
Golyatynka River – Maidan village	Y=-0.017x+35.5	0.18	0.42	0.12	0.24	0.35
Golyatynka River – Golyatyn village	Y=-0.008x+17.3	0.09	0.29	0.13	0.26	0.39
Rika River – Mizhgirya village	Y=-0.012x+25.1	0.11	0.32	0.13	0.26	0.38
Pylypets River – Pylypets village	Y=-0.014x+28,4	0.12	0.35	0.13	0.25	0.38
Studenyy River – N. Studenyy village	Y=-0.015x+30.1	0.20	0.44	0.12	0.23	0.35
Rika River – Verhniy Bystryy village	Y=-0.011x+22.3	0.10	0.32	0.13	0.26	0.38
Ploshanka Stream – Pylypets (nyzhn.) village	Y=-0.010x+20.9	0.08	0.28	0.13	0.26	0.40
Rypynka River – Rypynne village	Y=-0.012x+24.8	0.11	0.33	0.13	0.26	0.38

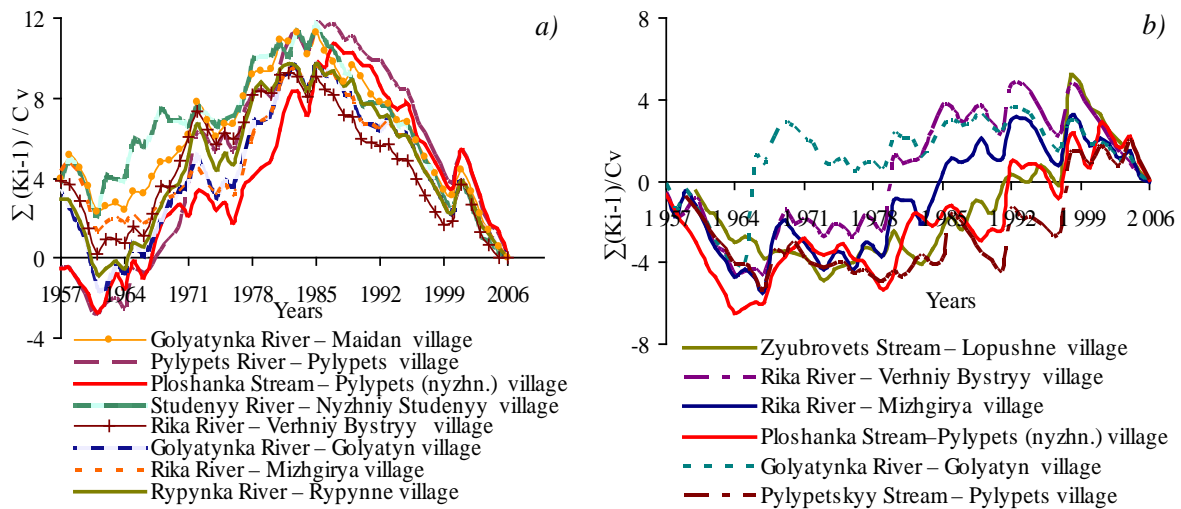


Fig. 4. The difference integral curves of the maximum discharges of the rivers and streams in the Rika River Basin of cold (a) and warm (b) periods

So, as a result all of the above-indicated, the series of observations of the maximum discharges of the rain floods and of the rain and snowmelt floods of the rivers and streams in the Rika River Basin are in general homogeneous and stationary. The same results are received in the paper [12], but the analysis of the trends has been done by using one statistical method (non-parametric Mann-Kendall test). So, it allows to use the apparatus of mathematical statistics for further calculations. The definition of the statistical parameters of the maximum discharges was carried out by the three-parameter gamma distribution and binomial distribution with using the methods of the maximal probability or method of moments by the HydroStatCalc [13].

The statistical parameters of the rivers and streams in the Rika River Basin is changing in the range: a) warm period the coefficients of variation (C_v) are changes from 0.44 (Lopushna River – Lopushne (nyzhn.) village) to 1.01 (Studenyy River–Verhniy Studenyy village) and the coefficients of asymmetry (C_s) – from 0.99 (Lopushna River – Lopushne (nyzhn.) village) to 5.06 (Zyubrovets Stream – Lopushne village); b) cold period: C_v – from 0.41 (Golyatynka River – Golyatyn village) to 0.62 (Studenyy River – Verhniy Studenyy village) and C_s – from 0.97 (Rypynka River – Rypynne village) to 2.63 (Studenyy River – Verhniy Studenyy village) (Table 5). The calculated probability characteristics of the maximum discharges will be corrected with lengthening of the series of observations because the researched data are not representative (absence full cycle fluctuations) to definition the average value.

The flood discharges of warm period of the rivers and streams of the studied region is characterized by three periods: 1) from the start of observations till 1967 was the phase decrease of cyclical fluctuations of the maximum discharges; 2) from 1967 till 1998 and from 1967 till 1998 was the phases increase of cyclical fluctuations; 3) from 1998 to present time is observing the phase decrease of cyclical fluctuations. The flood discharges of the warm period has two phase of cyclical fluctuations: the phase increase is observing from early 60's to mid-80's of the 20th century, with a few notable decrease in 1974–1977, and the phase decrease – since the mid 80's to present time (Fig. 4.).

Table 5. The statistical parameters of the maximum discharges of the rivers and streams in the Rika River Basin of warm and cold periods, 1957–2006

The name of gauge	Q_{average}		C_v		C_v/C_v		$P, 1\%$	
	Flood period							
	cold	warm	cold	warm	cold	warm	cold	warm
Golyatynka River– Golyatyn village	27.5	37.2	0.41	0.68	2.36	6.52	61.5	150
Golyatynka River – Maidan village	37.8	43.7	0.61	0.70	2.81	4.56	117	158
Studenny River – N. Studenny village	9.56	14.9	0.49	0.86	3.69	4.60	25.7	70.5
Rypynka River – Rypynne village	99	84.5	0.54	0.62	2.21	3.17	269	274
Rika River – Mizhgirya village	218	210	0.54	0.59	2.62	3.35	610	644
Rika River – Verhniy Bystryy village	49.6	47.2	0.49	0.49	2.96	4.58	129	128
Pylypets River – Pylypets village	26.1	30.0	0.59	0.69	2.35	3.94	77.0	106
Studenny River – V. Studenny village	3.86	6.61	0.62	1.01	4.27	4.25	12.5	36.1
Ploshanka Stream – Pylypets (nyzhn.) village	12.9	12.8	0.53	0.59	2.10	3.88	34.3	40.3
Pylypetsky Stream – Pylypets village	3.42	3.56	0.54	0.74	2.27	3.91	9.32	13.5
Pylypets River – Podobovets village	7.91	10.3	0.59	0.78	1.94	3.03	22.5	39.8
Branysche Stream – Lopushne village	4.09	5.09	0.51	0.60	2.92	2.34	11.1	15.2
Seredniy Zvir Stream – Lopushne village	0.83	0.73	0.54	0.95	2.35	2.71	2.25	2.83
Lopushna River – Lopushne (verhn.) village	4.64	6.00	0.60	0.60	2.89	2.96	14.1	18.7
Zyubrovets Stream – Lopushne village	1.24	1.50	0.58	0.83	2.69	6.09	3.67	7.18
Lopushna River – Lopushne (nyzhn.) village	11.5	12.9	0.47	0.44	2.49	2.25	28.2	30.0

CONCLUSIONS

1. The statistically significant trends which were found in some of the observations series have the periodic natures, which depend not only on duration of the observations, but also on the length of the separate full hydrological cycles and of their phases.
2. On the watercourses of the upper part of the Rika River Basin in cold (mid 80's of the 20th century) and warm (from 1998) periods are observing the phases decrease of cyclical fluctuations of the maximum discharges.
3. According to observations of the gauges the floods of warm period are on the average 1.6 times higher (for the maximum discharges) than the floods of cold period.
4. The view of all the general curves without any significant points of the fracture of the directions and synchronicity of the chronological charts and the difference integral curves of series of the maximum discharges of the rivers and streams of the Zakarpatska water-balance station indicates on the homogeneity of data.



5. During estimation of the homogeneity and stationarity of runoff the preference should be given to the hydrological and genetic methods, because such methods allow, unlike the statistical methods, to consider conditions of the hydrological characteristics formation of the runoff.
6. The calculated statistical parameters of time series of the flood discharges will become more reliable in the presence of the full hydrological cycles in consequence of lengthening the series of observations.

REFERENCES

1. GOPCHENKO, E.D., ROMANCHUK, M.E., KHARITONOVA, A.S. The calculation of maximal runoff of rain flood of Zaccarpathia rivers. *Proceeding of VOSEU*, 2010, Vol. 10, p. 181–186 (in Russian).
2. GREBIN, V.V. The present of the change of the separate characteristics of the rain floods on the rivers of Ukraine. *Hydrology, hydrochemistry, hydroecology*, 2010, Vol. 2 (19), p. 74–85 (in Ukrainian).
3. SUSIDKO, M.M., POLYAKOVA, S.O., SCHERBAK, A.V. The catalogue of the characteristics of the rain and snow-rain floods on the rivers of Carpathian Region for 1989–2002 years. *Proceeding of UHMI*, 2006, Vol. 255, p. 298–309 (in Ukrainian).
4. BAUZHA, T.O. Flood flow the cold period in the Rika River Basin and its calculated characteristics. *Hydrology, hydrochemistry, hydroecology*, 2012, Vol. 2 (27), p. 73–80 (in Ukrainian).
5. MELNYK, T.P. The general analysis, the ways and manners of the decision of the problems of the snow-rain floods of the territory in the Tysa River Basin. *Hydraulics and engineering hydrology*, 2009, Vol. 63, p. 1–10 (in Ukrainian).
6. EU Water Framework Directive 2000/60/EC. Definitions of Main Terms, 2006, Kyiv, 240 p.
7. Materials of observations of the Zakarpatska water-balance station. Kyiv. 1964. Vol. 2, 1960. p. 6 (in Russian).
8. BAUZHA, T., GORBACHOVA, L. Estimation of the homogeneity of the average annual runoff of the rivers and streams of the Zaccarpatska station. BALWOIS 2012, Proceedings of International Conference on water, climate and environment. Ohrid, Republic of Macedonia. 2012 28 May – 2 June, edited by M. Morell, ISBN 978-608-4510-10-9, <http://www.balwois.com/2012>
9. BNR (The building norm and rules 2.01.14-83) The determination of the calculation hydrologic characteristics. State committee USSR on the construction, 1983. p. 97 (in Russian).
10. The methodological recommendations for assessment the homogeneity of the hydrological characteristics and definition of their calculation values for the non-homogeneous data, State Hydrological Institute, Saint Petersburg, 2010. p. 39–40 (in Russian).
11. GORBACHOVA, L., KOLIANCHUK, O. Long-term dynamics of the main hydrometeorological characteristics of spring flood in the Desna River's Basin. Proceedings of International Conference "Water resources and wetlands". Tulcea, Romania. 2012, 14–16 September.
12. ZABALETA, A. Regional hydrological signs for climate change (Basque Country). BALWOIS 2012, Proceedings of International Conference on water, climate and environment. Ohrid, Republic of Macedonia. 2012 28 May – 2 June, edited by M. Morell, ISBN 978-608-4510-10-9, <http://www.balwois.com/2012>.
13. User's Guide. Software for automation of engineering hydrological calculations HydroStatCalc. State Hydrological Institute, Saint Petersburg, 2010. Link to the internet <http://www.hydrology.ru/metodic/manual_2010.pdf> (in Russian).



ABATEMENT COST ANALYSIS FOR GREENHOUSE GAS EMISSION REDUCTIONS IN UKRAINE

A.V. Epik

*Institute of Engineering Thermophysics of
National Academy of Sciences of Ukraine
Kyiv-67, 03067, P.O. box 66, Ukraine*

ABSTRACT

Cost analysis approach is the common instrument used in project planning and technological selection process. The standard approach for doing this on the project pre-implementation phase is development of classical feasibility study which provides typical benchmarks, such as IRR, NPV, simple and discounted payback periods, etc. However pre-feasibility study usually does not include the emission reduction trading component. In some cases this component could have a significant impact on resulting financial indicators of planned project and could even lead to suspension of implementation of planned technology due to large variety of options with different carbon emission reduction potentials and costs of emission reductions per output product. Abatement cost analysis may demonstrate not only the potential of emission reductions for each specified technology but also to show the expenditures (in \$ USD/tCO₂) for such emission reductions. These figures could be used then by installation operators to assess whether their technology provides optimal emission reductions from the financial point of view. In other words, is 1 t CO₂ reduced by certain technology the cheapest among other options with the same output or not? Current work proposes quantitative analysis of emission reduction potential and emission reduction cost with respect to selected roster of available and some perspective (demonstrating-level) technologies for primary energy generation in Ukrainian conditions. Obtained results could be helpful for scientists, governmental bodies, investors and operators of installations to assess the place of definite technology among other options with respect to carbon emission reductions and expenditures for achieving of these reductions.

Keywords: greenhouse gases, emission reductions potential, cost of emission reductions, abatement cost

1. INTRODUCTION

Climate change mitigation as well as the 20-20-20 goals of the EU-27 established in the EU Directive 2009/28/EC of the European Parliament and the Council [1] set up the task to find the optimal way to achieve targets by most cost-effective and energy efficient way. Under this task the choice of the cheapest type of technology with satisfactory parameters and minimal payback period is usually understood while the collateral effect on climate change mitigation by the chosen technology type, especially greenhouse gas (GHG) emission reductions is ignored or not properly managed. A good effort to increase the impact of last issue is the EU Emission Trading Scheme (EU ETS) already entered into Phase 3. The quantitative GHG emission obligations under EU ETS could serve as an incentive for operators that are willing to reduce GHG emissions at their production site providing additional value for the output product of operator's installation. Those who does not comply with the individual emission obligations or does not want to comply has an option to buy deficient amount of emission units (EU Emission Allowances – EUA, 1 EUA is equivalent of 1 metric ton of CO₂) from another operator/installation with the GHG emissions below obligatory limits or in other words surplus of GHG allocations. EU ETS approach is good because it provides annually fixed and strictly defined figures of CO₂ emission limits for each operator/installation however it does not show the cost of GHG emissions reduction (so-called “abatement costs”). From the other hand the cost of emissions reduction (usually measured in \$ USD/tCO₂) is highly dependent on technology applied in some limited area (it is obvious that the cost of the same technology is different for Russia and Germany). And, in its turn, each type of technology in limited area generates different volumes of emission reductions. So we are coming to



the classic optimization problem, where cost of emission reduction is dependent from the generated volumes of emission reductions and vice versa.

Cost analysis is useful and widespread instrument to make such optimization demonstrating not only the potential of emission reductions for each specified technology but also to show the expenditures (in \$ USD/tCO₂) for achieving of such emission reductions. These figures could be used then by installation operators to assess whether their concrete technology provides most cost-efficient emission reductions or not. In other words, is 1 t CO₂ reduced by certain technology the cheapest among other options? In current work we made an effort to answer on such frequently asked question of project owners and operators: where is my technology among the group of technologies with the same output product? Does it provide the cheapest 1 t CO₂ reduction, or the most expensive one? The explicit answer on this question could not be given due to influence of infinite factors depending on final value of emission reductions cost. However making some assumptions and strictly disseminating them on the chosen sector we could at some level of approximation obtain mentioned Figures.

2. ASSUMPTIONS AND METHODOLOGY

As it was stated earlier the problem of emission reduction cost analysis is complex and requires introducing of some assumptions to obtain steady solving. The influence of number of external factors on the final figures, such as specific considered territory (country), adopted policies, tariffs, level of technologies development and commercialization in considered sector, general financial situation, etc. is significant and in some cases may cause contradictory results. As the problem is multiparametric at first it is necessary to set up some assumptions to simplify solving process. The principal assumptions are the following:

- Only power (electricity) generation sector is considered;
- Country chosen is Ukraine; (calculation is doing as per tier 2 – on national level);
- The solving is performed for present time (for end of 2012);
- Currency of calculation is \$ USD, rate of inflation is not taking into account;
- Construction time for all considered power generation technologies is assumed to be equal and thus is not taking into account;
- Power generation efficiency and capacity factor are dependent only from technology type;
- The capacity factor is defined as 1 (100 %) for 8 000 hours of operation per year.

The first assumption is obvious – in any case all sectors could be included but power generation activity is chosen as most energy intensive sector which provide major portion of emissions in the total GHG balance. The choice of Ukraine is done because in the nearest future the internal emission trading scheme is to be introduced here (the appropriate Law of Ukraine “On Regulation of Energy Efficiency” # 7231 is already adopted in the first reading by Ukrainian Parliament). It should be emphasized that at the first stage of such internal emission trading system formation in Ukraine the monitoring and reporting processes are to be conducted for all sectors of economical activity. It will require subsequent and comprehensive knowledge of potential of GHG emission reductions for each technology or group of technologies and, which is more important, the cost of GHG emission reductions for each technology to make a decision where is so-called “painful points” of each sector: what technologies should be prioritized for implementation and what technologies should “wait” due to high GHG emission reductions cost or low GHG emission reduction potential. The availability of some kind of spreadsheet of GHG emissions potential-cost could be very useful at this stage. Later on, Ukrainian emission trading scheme (UETS) is going to be linked with EU ETS therefore the technologies implemented in Ukraine should be also linked with EU technologies and this connection could be easily traversed on the basis of specific indicators such as cost of emission reductions and potential for each technology type. Such data is



now absent in available sources. That's why in current conditions the calculation for Ukrainian emission cost-potential for 2012 is extremely needed.

Other assumptions are in some meaning the consequence of the let's conditionally call it "stationary" calculation for present time (2012). Concerning the choice of efficiency for roster of technologies it should be mentioned that generally speaking efficiency could be dependent also on various factors, such as regimes of equipment operation, quality of manufacture, mounting and maintenance, local fuel quality, etc. But in current work we are focused not on the technological cycle analysis but on the calculation of specific emission indicators so efficiency is taken as constant value for each technology type. The capacity factor is taken as 100 % for 8000 hours/year due to practical reasons.

Since the considered sector and assumptions are stated let's form the roster of power generation technologies:

- 1) Supercritical pulverized coal combustion (hereinafter SC PCC);
- 2) Ultrasupercritical pulverized coal combustion (hereinafter USC PCC);
- 3) Integrated gasification combined cycle (hereinafter IGCC);
- 4) Natural gas combined cycle – combined cycle with gas turbine (hereinafter NGCC (CCGT));
- 5) Gas turbine;
- 6) USC PCC with post-combustion carbon capture and storage (hereinafter USC PCC+ post comb CCS);
- 7) IGCC with pre-combustion CCS (hereinafter IGCC+ pre comb CCS);
- 8) NGCC with post-combustion CCS (hereinafter NGCC+ post comb CCS);
- 9) Renewable generation technology group:
 - Solid biomass thermal power plant (hereinafter TPP);
 - Solid biomass co-firing;
 - Solid biomass combined heat and power plant of medium scale (CHP medium);
 - Solar PV large scale;
 - Solar PV buildings;
 - Hydro large scale;
 - Hydro small scale;
 - Wind onshore;
 - Wind offshore.
- 10) Nuclear power generation.

The roster of technologies is formed on the basis of the International Energy Agency (IEA) classification as close as possible. Later we will also come back to the IEA simplified cost analysis approach that will be used in calculation. Some technologies are removed from consideration due to unprofitableness (for example, biogas for power, small biomass CHP) [2] or absence of enough generation potential (geothermal power generation) in current Ukrainian conditions. At the same time medium biomass CHP are already implemented in Ukraine as working projects: due to "green" tariff availability this technology is becoming very attractive for investments [3]. Nuclear power generation despite it's exclusion from emission reduction roster of technologies according to international emission trading rules is presented here for informational and comparative purposes. Although some activity in Ukraine is observed in this direction but due to complex of reasons currently nuclear power development is frozen for unknown term.

Below in Table 1 the technical data on the chosen technologies is presented. The capital costs of technologies and net efficiencies are taken from [4]. Annual working hours are taken where possible from the field investigations (hydro large and small scale, nuclear, medium biomass CHP) and where not possible recalculated by capacity factor taken from [4] bearing in mind the assumption of 100 % capacity correspondence to 8000 hours/year of installation operation.

Table 1. Technical input data for chosen technological types in power generation sector

Type of technology (installation)	Specific investments, \$ USD/kW _{el}	Net Efficiency, %	Annual operation hours	Capacity factor
SC PCC	2070	42%	8000	100%
USC PCC	2266	45%	8000	100%
IGCC	2588	45%	8000	100%
NGCC (CCGT)	828	57%	8000	100%
Gas Turbine	473	36%	8000	100%
USC PCC+post comb CCS	3726	33%	8000	100%
IGCC+pre comb CCS	3757	37%	8000	100%
NGCC+post comb CCS	1490	49%	8000	100%
Biomass TPP	2308	35%	5600	70%
Biomass co-firing	581	37%	5600	70%
Biomass CHP medium	3031	70%	5200	65%
Solar PV Large scale	3329	100%	960	12%
Solar PV buildings	4161	100%	720	9%
Hydro Large scale	2081	100%	3440	43%
Hydro Small scale	3305	100%	3200	40%
Wind onshore	1563	100%	2000	25%
Wind offshore	3080	100%	3040	38%
Nuclear	3623	33%	6800	85%

According to [5] and [6] absolute emissions for i type of technological unit and k type of fuel used by technology to produce electricity (tCO₂/year) are defined as:

$$E_{i,y} = \frac{0,036 \cdot N_i \cdot EF_{k,y} \cdot OA_{i,y}}{\eta_{i,y}}, \quad (1)$$

where:

$E_{i,y}$ – emissions of i technology in y year, tCO₂/year;

N_i – capacity of i considered technological unit, kW_{el}; in case of specific emissions determination always equals to 1 kW_{el};

EF_k – emission factor of k type of fuel used for power generation, tCO₂/GJ [6];

$OA_{i,y}$ – average annual operational hours of i technological unit in y year, h/year;

$\eta_{i,y}$ – net efficiency of power generation of i technological unit in year y , %.

Obviously specific emissions $SE_{i,y}$ (tCO₂/kW_{el}/year) equal absolute emissions $E_{i,y}$ in one case, when $N_i=1$ kW_{el}. The calculation is done for 1 year so hereinafter we will skip “year” from the dimension units of specific emissions and for definition of $SE_{i,y}$ will use tCO₂/kW_{el}. Strictly speaking for cases where calculation is done for 2 and more years it is necessary to replicate the calculation according to equation (1) as it contains variables depending on year for which calculation is done.

Simple cost of emissions $SC_{i,y}$ in \$ USD/tCO₂ for i technology in year y is defined as:

$$SC_{i,y} = \frac{SI_{i,y}}{SE_{i,y}}, \quad (2)$$

where $SI_{i,y}$ is specific investments per unit of installed capacity for i technology in year y , \$ USD/kW_{el}. The values of $SI_{i,y}$ are available in Table 1.

Generally speaking $SC_{i,y}$ could oneself be a parameter for comparison analysis of different technologies concerning cost of emission generation by each technology. However, this parameter does not provide information on the emission **reductions** for certain technology in comparison with some “base” technology for sector, so-called “base case”, which could serve as the reference point or benchmark. This approach is close to the baseline and project line setting used in emission reduction projects under Kyoto Protocol and EU ETS. The inconvenience of mentioned value usage also lies in the fact that in some cases resulting value from equation (1) become zero or nearly zero. Such situation occurs, for example when emission factor of fuel EF_k equals zero (for electricity generation without any fuel utilization) or comprises very low value. In current analysis we are dealing with both cases – first case is observed when we consider solar, wind and hydro renewable power generation activities, which do not require any fuel for electricity production process; the second one – for biomass generation activities bearing in mind standard assumption on biomass nearly-zero CO₂ emissions [7]. This make the value $SC_{i,y}$ not applicable as it turns into infinity when specific CO₂ emissions equals zero. At the same time for fossil fuel power generation the value of emissions obtained according to equation (1) is defined strictly. How to compare such technologies? Such inconsistency could be avoided if the value in denominator of equation (2) will be replaced by difference between current value of specific emissions for each technology $SE_{i,y}$ and some base fixed parameter, let’s name it “average emission factor by sector”. Such approach is very flexible and could be disseminated on any random sector in any country, but is especially comfortable with respect to power generation sector analysis. A lot of countries have already calculated this value which is commonly called “grid emission factor”. Hereinafter we will use this term marking it as GEF_y , tCO₂/kWh_{el}, where y – is appropriate year of calculation. Application of grid emission factor also account the national peculiarities of sector and thus make the cost of GHGs emission reduction more close to reality for chosen territorial area. Grid emission factor is available for Ukraine on the national level and for 2012 equals 1.063 tCO₂/kWh_{el} [8]. This value is easily transferred to $GEF_{i,y}$ tCO₂/kWh_{el} (bearing in mind average operational hours for each technology) as follows:

$$GEF_{i,y} = GEF_y \cdot OA_{i,y}. \quad (3)$$

The value $GEF_{i,y}$ is dependent not only on the year of calculation but also on the type of technology applied due to inclusion in calculation operational hours per annum for each technology. $GEF_{i,y} = GEF_y$ when $OA_{i,y} = 8000$ h/year.

The final equation for GHG emission reduction costs determination will be the following:

$$SC_{i,y} = \frac{SI_{i,y}}{SE_{i,y} - GEF_{i,y}}. \quad (4)$$

According to equation (3) it should be noted that the minus sign of $SC_{i,y}$ means that applied type of technology result in emission reductions in comparison with average grid-connected power generation technologies in country for year y and plus sign means that technology applied result in additional emission generation in comparison with average technology used in sector.

3. RESULTS AND DISCUSSION

Once all boundary conditions and assumptions have been set, the calculation of GHG emission reduction potential and cost is up to elementary algebraic operations. Table 2 contains the results of such calculations. It could be seen, that for Ukraine all selected technologies provide emission reductions as all values of emission reduction potential are negative. It is obvious, that if reference country changes, for example to one with large renewable share, then some technologies (primary coal-based) will result in additional emission generation in comparison with “average base case”. This is a little disadvantage of applied method as it provides results only for specific territory and average sectoral base case.

Now let’s do some analysis of obtained results. The lowest GHG emission reduction potential is for solar technologies due to very low capacity factor (9 %) and as a consequence very low amount of grid power generation per year (here it is important to stipulate that if the calculation will be done, let’s say for 30 years (project lifetime), reduction potential in specific values will not significantly increase because together with solar technologies efficiency increasing, the efficiency of “base case” technologies represented here by $GEF_{i,y}$ will also simultaneously increase; this statement could be applied for any time frame, i.e. for month, day, hour, we will obtain almost the same resulting values accurate within finite approximation defined by the efficiency increasing ratio between current technology and “base case technology”); to obtain steady solving it is necessary just to select uniform time interval and make it constant throughout all calculation; this is obvious advantage of solving in current specific representation which is dependent only on technology type and independent from time interval).

Table 2. Resulting GHG emission reduction potential and cost for the roster of technologies in Ukrainian conditions

Type of technology (installation)	$GEF_{i,y}$, tCO ₂ /kW _{el}	Emission reduction potential $SE_{i,y} - GEF_{i,y}$, tCO ₂ /kW _{el}	GHG emission reduction cost $SC_{i,y}$, \$ USD/tCO ₂
SC PCC	8.5040	-1.763	-1173.8
USC PCC	8.5040	-2.213	-1024.0
IGCC	8.5040	-2.348	-1102.3
NGCC (CCGT)	8.5040	-5.669	-146.0
Gas Turbine	8.5040	-4.016	-117.8
USC PCC+post comb CCS	8.5040	-6.216	-599.4
IGCC+pre comb CCS	8.5040	-7.009	-536.0
NGCC+post comb CCS	8.5040	-8.041	-185.3
Biomass TPP	5.9528	-5.903	-391.0
Biomass co-firing	5.9528	-5.906	-98.4
Biomass CHP medium	5.5276	-5.505	-550.6
Solar PV Large scale	1.0205	-1.020	-3262.2
Solar PV buildings	0.7654	-0.765	-5436.7
Hydro Large scale	3.6567	-3.657	-569.1
Hydro Small scale	3.4016	-3.402	-971.6
Wind onshore	2.1260	-2.126	-735.2
Wind offshore	3.2315	-3.232	-953.1
Nuclear	7.2284	-7.228	-501.2

There is a group of technologies with high emission reduction cost and low emission reduction potential. This group is coal-based power generation. Such result is logical and could be explained as follows: coal-based power generation is already in place in Ukraine and is nearly “technological saturation” so the cost of every additional capacity with higher efficiency than existing one is connected with higher and higher (like snow ball) cost per 1 kW_{el}.

The second conditional group includes technologies with low carbon emission reduction cost and high potential. The lowest GHG emission reduction cost and the best ratio $\frac{SC_{i,y}}{SE_{i,y} - GEF_{i,y}}$

(which is only indicative value without any sense) has biomass co-firing with fossil fuels. However in current Ukrainian conditions implementation of biomass co-firing is almost impossible due to complex of reasons (cheap fossil fuel, absence of mature biomass market, absence of “green tariff” provision for co-combustion, etc.). Pretty unexpected result is presence in low carbon abatement cost group natural gas-based generation, notably standard gas turbine technology, NGCC and, which is very strange, NGCC with CCS which has the highest GHG emission reduction potential from all selected technologies. This could be explained by nearly-zero current share of natural gas utilization in Ukraine in power generation sector and very high share of coal utilization in total fuel balance (it could be also seen from the value of average grid emission factor which is very close to pure coal power generation emission factor). Thus gas utilization as a primary resource for power production with almost two times lower emission factor (56,1 for gas against 98,3 tCO₂/TJ for coal) and higher efficiency of gas power generation technologies in comparison with coal generation results in large GHG emission reduction potential and as a consequence in very cheap GHG emission reduction cost. At first glance carbon capture and storage technologies are attractive for implementation with respect to low cost of emission reductions achieving. But due to current status of international emission trading market which in some cases may be a single source of payback for such project do not compensate significant initial investments for such technology. With decreasing of initial investments and introduction of emission trading scheme with high cost of 1 t CO₂ it is expected that CCS will become primary source of emission reduction on the way on low carbon economy.

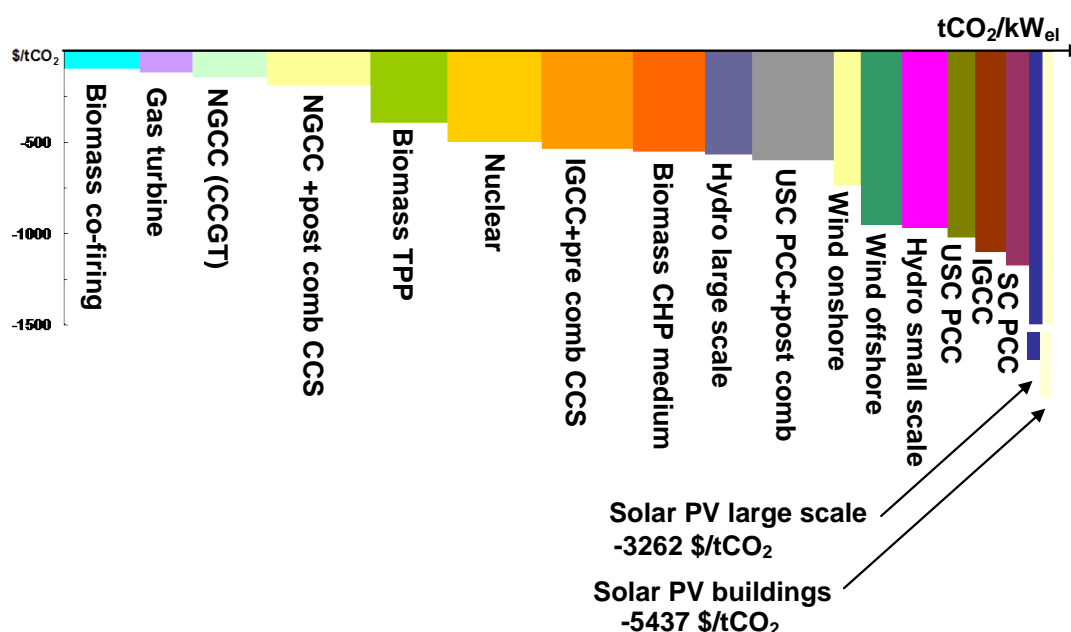


Fig. 1. Abatement curve for the roster of technologies in Ukrainian conditions

Other technologies occupy in-between position with the range of carbon reduction cost 400–1000 \$ USD/tCO₂ and relatively high carbon emission reduction potential. To make the perception and further analysis easier let's draw up the commonly used in cost analysis abatement curve (Fig. 1). Vertical axis represents the cost of reduction, and horizontal axis – the potential of GHG emission reductions. Then let's put all considered technologies at the diagram. The wider is the column the higher will be emission reduction potential, the lower is the column the cheaper will be cost of emission reduction by current technology.

During analyzing of abatement curve for the roster of selected technologies the conclusions of optimal options are visually obvious. Depending on established goal, for example maximization of emission reductions, minimization of emission abatement cost or both one can choose the appropriate technology for each case. Additionally such graphical representation could be useful for projects on the pre-implementation or pre-investment stage to assess where the place of applied technology is in the variety of technologies with the same output product regarding GHG emission reductions. This quick check of different options can be included in pre-feasibility study and somehow change financial indicators of planned project for some technologies (of course with the condition of carbon market existence and adequate emission reduction price). This may cause additional financial attractiveness of not early considered options or in some cases even change of technology for planned project on more energy efficient one.

4. CONCLUSIONS

As the result of performed analysis the following outcomes could be formulated:

- Power generation sector of Ukraine has a huge potential for almost all greenfield power generation technologies (with range of 1-8 tCO₂/kW_{el} and average value of 4.8 tCO₂/kW_{el}) and relatively cheap indicators of achieving of emission reductions (with range 100-1100 \$ USD/tCO₂ without solar and nuclear generation);
- Applying of new coal-based generation technologies without CCS for emission reduction in power generation sector has limited potential (in average 2 tCO₂/kW_{el}) and high abatement cost (in average 1100 \$ USD/tCO₂);
- According to current conditions for 2012 the lowest GHG emission reduction cost (98 \$ USD/tCO₂) has biomass co-firing with fossil fuels at TPPs with the appropriate annual emission reduction potential 5.9 tCO₂/kW_{el}; the highest abatement cost has solar PV technology for buildings (5436 \$ USD/tCO₂) with the potential of emission reduction 0.765 tCO₂/kW_{el};
- Carbon capture and storage technology is attractive for coal and gas based generation with respect to cheap abatement cost and high potential of reductions however still the emission trading market conditions are not enough to compensate large initial investments for implementation of this expensive technology.

REFERENCES

1. *Directive 2009/28/EC* of the European Parliament of the Council of 23 April 2009 on the promotion of the use of energy from renewable sources and amending and subsequently repealing Directives 2001/77/EC and 2003/30/EC. Link to the internet: http://ec.europa.eu/energy/renewables/background_documents_en.htm
2. KUTSIY D.V., MATVEEV YU.B., PUKHNYUK O.YU. Tendencies of Technologies Development for Municipal Solid Waste Biogas Energy Utilization for Power Production. *Industrial Heat Engineering*, 2011, Vol. 33, No. 6, p. 64–72.
3. A.V. EPIK, S.M. CHAPLYGIN, E.N. OLEJNIK. Technical and Economical Assessment of Biomass Projects Implementation in Ukraine // Proceedings of XIX International Conference



- “Innovation ways of actual ecology, energy saving and resources saving problems solving”, 6–10 of June 2011, Crimea, Ukraine (in three Volumes). Vol. 1, p. 147–154.
4. *Energy technology perspectives 2012. Pathways to a clean energy system*. International Energy Agency, 2012. ISBN 978-92-64-17488-7, 690 p.
 5. A. EPIK. Greenhouse Gas Emission Potential for the Energy Generation Activities // Proceedings of the International Conference of Bucharest Polytechnical Institute “First International Conference of Thermal Equipment, Renewable Energy and Rural Development”, 5–7 of July 2012, Bucharest city, Romania.
 6. *Guidelines for National Greenhouse Gas Inventories*. Volume 2. Energy. Chapter 2. Stationary Combustion. Intergovernmental Panel on Climate Change, 2006, 47 p. Link to the internet: www.ipcc-nggip.iges.or.jp/public/2006gl/pdf/2_Volume2/V2_2_Ch2_Stationary_Combustion.pdf
 7. *International project of European Commission Directorate-General XII Science, Research and Development “ExternE. Externalities of Energy”*. Vol. XX: National Implementation, prepared by CIEMAT, ES, 1999, p. 184, 507.
 8. *Order of National Environmental Investment Agency of Ukraine # 75 from 2011/05/12 “On approval of specific grid carbon emission factors”*.



LONG-TERM VARIATIONS OF THE HEAT RUNOFF TRANSFERRED BY THE RIVERS NEMUNAS AND MERKYS

A.J. Jurgelėnaitė

Lithuanian Energy Institute

Breslaujos str. 3, LT-44403 Kaunas – Lithuania

ABSTRACT

The heat runoff is a process of heat transfer in the river water. Heat runoff, as a synthetic measure of discharge and water temperature, is useful to define the characteristics of a watershed's in response to climate change. It varies depending on the season and the river hydrological regime. Heat runoff of the river has a particularly strong influence on the formation of the ice-thermal regime in the lower reaches of rivers below the dams. The aim of this work is to assess the heat runoff and the character of its temporal variation in the rivers Nemunas and Merkys. In this paper, based on the average monthly and warm season (May–October) water discharge and water temperature data for the period of 1945–2011, the heat runoff regime was defined and its changes were quantified. Relations between heat runoff and water temperature and water discharge values were analyzed as well as reliable correlations of these parameters were obtained. Temporal changes of heat runoff of the rivers Nemunas and Merkys were studied, and the factors influencing the heat runoff were revealed.

Keywords: heat runoff, river, warm season, water temperature, discharge

1. INTRODUCTION

Rivers are now considered to be among the most sensitive of all ecosystems to the effects of climate change [1]. Scientists estimate that the global average surface temperature has increased over the 20th century by about 0.6°C [2]. Projected global average surface warming at the end of the 21st century according different scenarios can increase from 1.8°C to 4°C [3]. River water temperatures follow air temperature. Rising water temperatures affect aquatic life, because every aquatic organism has preferred water temperature range in which it can survive. The most aquatic organisms are ectotherms, so they may be especially affected by climatic-driven temperature increases, as ambient temperature directly controls body temperature of these organisms [4]. Metabolic activity, spawning, growth rate, production, migration, composition of aquatic organisms are temperature dependent.

Rivers are also linked inextricably to climate effects on flow pattern and all related processes: discharge variations, flood and drought effects, hydraulics, flow-mediated connectivity, and fluxes of solutes and energy between land and water [1]. Hydraulic conditions and water temperature is two major physical factors that regulate the life cycles of lotic biota [5]

Heat runoff, as a synthetic measure of discharge and water temperature, is useful to define the characteristics of a watershed's in response to climate change [6]. Rivers carry a large amount of heat with water, that can be used for various applications (as a heat source for power plants, source of energy which can be used for heat pumps et al).

Heat runoff depends on the water abundance and the water temperature of the river and varies depending on the season and the river hydrological regime. The flow direction and the hydrographic network structure determine the changes of heat runoff along the river. Rivers flowing from the south to the north carry of a large amount of heat, helping to mitigate the ice conditions at the mouth and exerting some influence on the climatic conditions of the river valleys [7]. Significant changes in heat flow can be at the confluence of tributaries [8].

In recent decades, human activities have a significant impact on the hydrothermal regime. Regulation of the river flow and construction of the water reservoirs have played a significant role in the change of natural conditions of aquatic life: reduced rivers water runoff, decreased summer heat flow, decreased water temperature [9].

Heat runoff of the rivers is one of the components of heat balance of the lakes and reservoirs [10]. Heat balance of the lake is evaluated/calculated when the lake is used as a cooling pond for the nuclear power plant (NPP) to assess the impact of NPP on the hydrothermal regime of the lake [11]. River heat runoff is used for the calculation of evaporation from the lake water surface [12].

Heat runoff as hydrothermal characteristic of the river water may be useful in assessing the impact of power plants on water regime. The nominal 1,000 MWe nuclear generating station must discharge nearly 2,000 MW the environment as waste heat. There is a need to evaluate environmental impact of cooling water in terms of thermal, chemical and radionuclide pollution, and impact on biota [13].

Many studies are done for evaluation of heat runoff of Russian rivers. The long-term variations of heat runoff of warm season (June-September) transferred by the Lena River are presented in [14]. In June the heat runoff of the Lena River increased during the period of 1950-1992 in all water gauging stations except the station which is influenced by reservoir regulation. The influence of regulation of the Volga River runoff on the thermal regime and heat runoff was evaluated in [15]. Average heat runoff of the River Volga decreased 16 % after the regulation of the river, whereas the maximum heat runoff increased by 30 %. Relations between heat runoff of North European and Siberian rivers and their discharge values and water temperature were studied and reliable correlation of these parameters were obtained in [16].

The heat runoff of Lithuanian rivers has not been investigated at all. River water runoff was researched quite well, but the water thermal regime of Lithuanian rivers has not been sufficiently analyzed. Only in recent years the thermal regime of Lithuanian rivers was studied [17, 18, 19, 20].

The aim of this work is to evaluate the long-term variation of heat runoff transferred by the main and largest Lithuanian river Nemunas which basin covers approximately 71.6% of the Lithuanian territory and to assess the impact of Kaunas hydropower plant (HPP) on the heat runoff of this river. According to [18] this river depends to the warm water river group. There are plans to use the water of the River Nemunas for cooling purposes of new Baltic nuclear power plant (NPP), which is under construction in Kaliningrad district (Russia), 11 km from Lithuanian border. Smalininkai WGS heat runoff data will be useful as background reading for assessing of the warming effect of NPP on the hydrothermal regime of the River Nemunas as the receiving water body for cooling waters of NPP. The River Merkys was chosen (it depends to the cold water river group) to comparison of the variation of warm and cold water rivers heat runoff. The total annual value of the heat runoff is defined for the warm season of the year (May – October) as during this period the most intensive hydrological and biological processes occur in the water bodies. In the river hydrological regime this period is the maximum heat transfer period.

DATA AND METHODS

Two rivers of different size were selected for the study of heat runoff during warm season (May-October) period. The River Nemunas is warm water river (average water temperature of warm season – 16.0°C) and the River Merkys - cold water river (13.6°C) [18]. In [18] the classification of Lithuanian rivers was performed according warm season (May-October) water temperature data in the standard normal period (1961-1990). Rivers were divided into three groups: the warm water ($t \geq 14.9^\circ\text{C}$), cool water ($13.4^\circ\text{C} < t < 14.9^\circ\text{C}$) and cold water ($t \leq 13.4^\circ\text{C}$) rivers.

The Smalininkai water gauging station (WGS) and Kaunas WGS on the River Nemunas and Puvočiai WGS on the River Merkys were selected to evaluate the impact of climate change and anthropogenic activity on heat runoff of rivers. The Smalininkai WGS (the river basin area of 81130 km²) is located 111.0 km from the mouth and Kaunas WGS (the river basin area of 46328 km²) is located 208.6 km from the mouth of the River Nemunas. Puvočiai WGS on the River Merkys (basin area 4297 km²) is located 13.6 km from the mouth of the river. The Kaunas WGS was chosen for

the evaluation of impact of Kaunas Hydropower Plant (HPP) on the heat runoff of the River Nemunas.

The data series of average monthly water discharge and water temperature of the River Nemunas at Smalininkai WGS (1946–2011), at Kaunas WGS (1945–2010) and of the River Merkys at Puvočiai WGS (1945–2011) derived from the Hydrological yearbooks of Lithuanian Hydrometeorological Service (LHMS) were used for the calculation of the heat runoff.

Basing on the long-term and reliable monthly average discharge and stream temperature data, long-term mean heat runoff and inter-annual variation (C_v) is calculated for the gauging stations of the River Nemunas and the River Merkys.

For the rivers, where the distribution of water temperature in the watercourse practically homogeneous, the heat runoff is calculated as

$$\theta = c \cdot \rho \cdot Q \cdot t \cdot T \quad , \quad (1)$$

where t – the average water temperature of cross-section ($^{\circ}\text{C}$); Q – water discharge (m^3/s), T – time interval (s), c – heat capacity of water (cal), ρ – water density (kg/m^3) [7]. Heat capacity and density of water are taken as constant values ($\rho = 1$, $c = 1000000$ cal) for calculation of heat runoff [8].

According to average monthly water discharge and water temperature data, the average monthly heat runoff for warm season (May–October) was calculated, evaluating that month duration in seconds is different. The heat runoff for individual years was calculated as the mean of average monthly values during warm season (May–October).

An average annual mean of heat runoff was established for the warm (May–October) season because at that time the most intensive vital activities take place in the water bodies.

2. RESULTS

The temporal analysis of long-term data series of heat runoff was applied to the warm River Nemunas (Smalininkai WGS) and the cool River Merkys (Puvočiai WGS). The chronological variations of warm season (May–October) heat runoff of these rivers are presented in the Fig. 1. This figure shows that there are similar tendencies of synchronic variation of heat runoff in the River Nemunas at Smalininkai WGS and the River Merkys at Puvočiai WGS. Heat runoff slightly increases during the investigated period in both rivers (Fig. 1).

The simplest method of analysis is the comparison of the norms, calculated for different periods. The heat runoff depends on the water discharge and water temperature therefore the averages of these parameters for different periods were presented in the Table 1. The parameters were calculated for different periods: entire period of observations; the 30 year (1961–1990) period, which is considered a standard normal period; 1945–1979 and 1980–2011 periods. [21] maintains that more intensive warming has occurred in Lithuania from 1980 s.

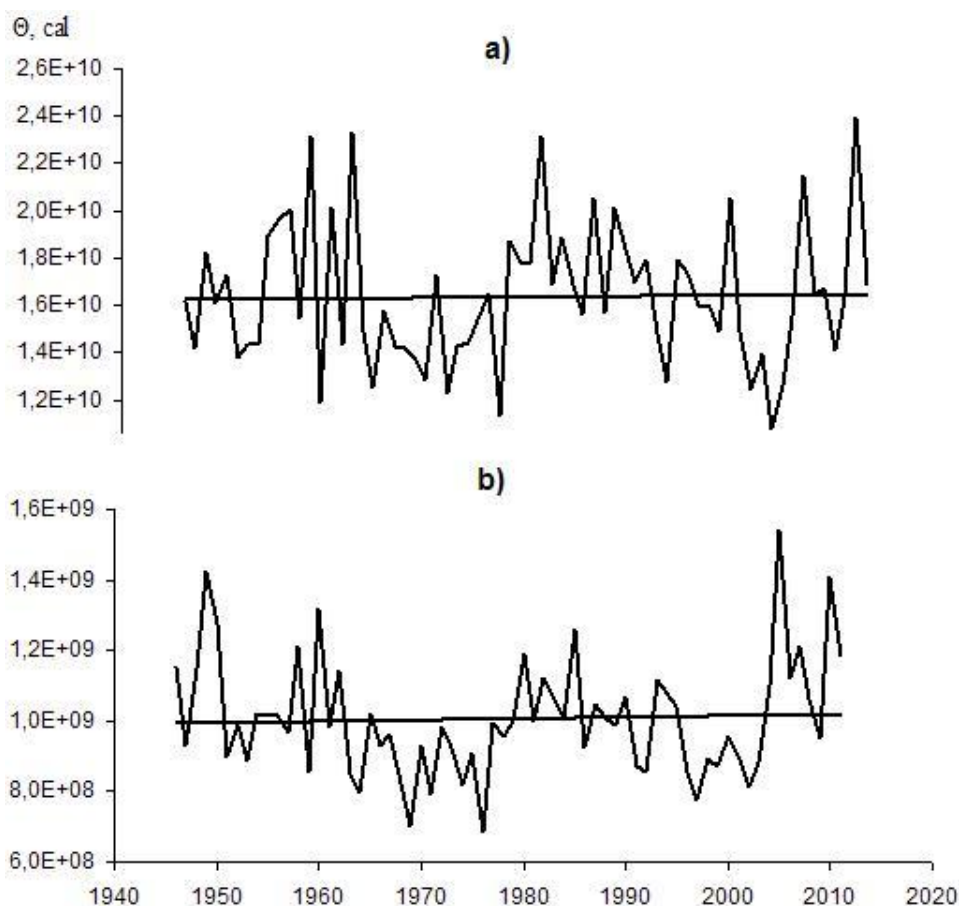


Fig. 1. Variations and trends of average heat runoff of the River Nemunas (Smalininkai WGS) and the River Merkys (Puvočiai WGS) during warm season (May–October)

Table 1. Long-term average heat runoff (cal), water discharge (m^3/s) and temperature ($^{\circ}\text{C}$) during warm season (May–October) for different periods

River – WGS	Parameter	Periods			
		Entire period	1961–1990	1945–1979	1980–2011
Nemunas at Smalininkai WGS	Heat runoff	1.64E+10	1.64E+10	1.60E+10	1.68E+10
	Discharge	395	401	390	399
	Water temperature	16.0	15.9	16.0	16.1
Merkys at Puvočiai WGS	Heat runoff	1.01E+09	0.96E+09	0.99E+09	1.04E+09
	Discharge	28.4	27.6	27.6	29.3
	Water temperature	13.6	13.3	13.6	13.5

The results of analysis show that long-term average mean of heat runoff of warm season in the River Nemunas at Smalininkai WGS and the River Merkys at Puvočiai WGS is 5% higher comparing to the periods of 1945–1979 and 1980–2011. Meanwhile, the long-term average water discharge in the River Nemunas is 2% and in the River Merkys 6% higher for the same periods. Whereas the long-term average water temperature in the River Nemunas is only 1% higher and in the River Merkys 1% lower for the same periods.

The average and extreme values of heat runoff, water discharge and temperature are presented in the Table 2.

Table 2. Average heat runoff of the warm season (May–October) of the River Nemunas and the River Merkys (1945–2011)

River - WGS	Parameter	Average	max	Year	min	Year	Ratio (max/min.)
Nemunas at Smalininkai WGS	Heat runoff	1.64E+10	2.39E+10	2010	1.08E+10	2002	2.2
	Water discharge	395	623	1962	249	2002	2.5
	Water temperature	16.0	17.4	1999	14.5	1962	1.2
Merkys at Puvočiai WGS	Heat runoff	1.01E+09	1.54E+09	2005	0.68E+09	1976	2.2
	Water discharge	28.4	42.9	2005	20.0	1969	2.1
	Water temperature	13.6	14.9	1948	12.0	1974	1.2

The long-term average mean of heat runoff of warm season in the River Nemunas at Smalininkai WGS for the 1946–2011 was 1.64E+10 cal. The maximal annual mean was in 2010 and it was 46% higher than average mean while the minimum heat runoff was derived in 2002 and it was 34% lower than average value. The water discharge was minimal in this year as well. The year of 1962 was particular – the highest water discharge and the lowest water temperature were during 67 year period. The heat runoff of this year was the second highest. It can be concluded that the heat runoff depends more on discharge than on the water temperature. This is confirmed by data in the 2002 than minimal heat runoff and water discharge were determined.

In the period of 1945–2011 the average mean of heat runoff of warm season in the River Merkys at Puvočiai WGS was 1.01E+09 cal and it was 16 times lower than one of the River Nemunas (Smalininkai WGS). The maximal heat runoff of the River Merkys at Puvočiai WGS was in 2005 and it was 53% higher than average mean while the minimum heat runoff was derived in 1976 and it was 32% lower than average value. The water discharge was maximal in 2005 as well.

Correlation coefficients between the heat runoff and water discharge as well as heat runoff and water temperature were calculated on purpose to determine most significant parameter affected the heat runoff (Table 3).

Table 3 Coefficients of correlation between different parameters (1945–2011)

River - WGS	Heat runoff – water discharge		Heat runoff – water temperature	
	R	Regression relationship	R	Regression relationship
Nemunas at Smalininkai WGS	0.95	$y=3E-08x-22.72$	0.11	$y=-3E-11x+16.475$
Merkys at Puvočiai WGS	0.95	$y=3E-08x-2.45$	0.23	$y=8E-10x-12.747$
Nemunas at Kaunas WGS	0.95	$y=4E-07x+1E+09$	0.19	$y=-9E-11x+17.033$

The conclusion could be done that heat runoff depends more on the water discharge than on the water temperature regardless of the size of the river and its thermal regime.

River heat runoff changes may be caused by the water discharge and temperature changes which occur due to the variation of meteorological conditions and anthropogenic activity (HPP construction on the river, thermal pollution and etc.) [8]. For the analysis of influence of Kaunas Hydroelectric Power Plant (constructed in 1959) on the heat runoff of the River Nemunas at Kaunas WGS the multi-annual averages of heat runoff and other parameters were calculated for the different periods: entire, standard normal, natural water regime (1945 to 1959) and the period after HPP construction (1960–2010). The results are presented in the Table 4 and Fig. 2.

Table 4. Average heat runoff of warm season (May-October) of the River Nemunas at Kaunas WGS

Parameter	Period			
	Entire period	1961–1990	1945–1959	1960–2010
Heat runoff	8.82E+09	8.67E+09	9.59E+09	8.59E+09
Water discharge	210	210	229	204
Water temperature	16.3	16.0	16.3	16.2

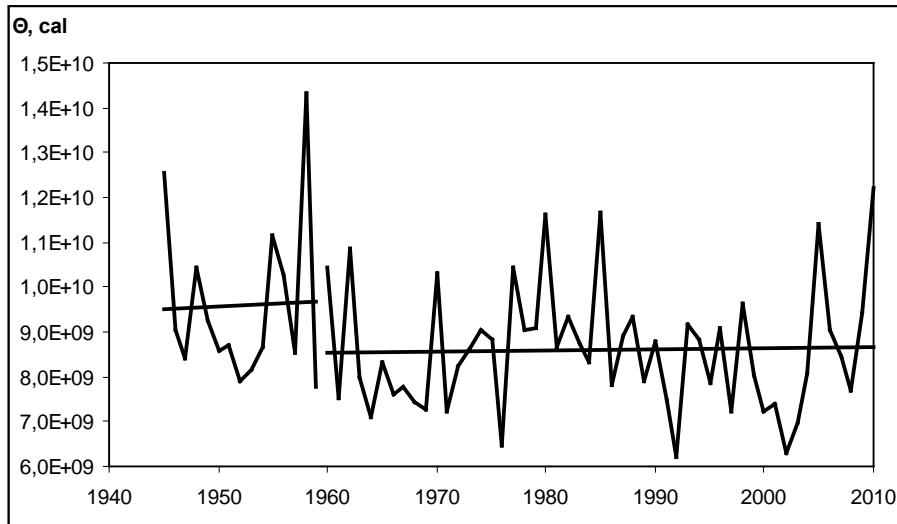


Fig. 2. Heat runoff (cal) of the River Nemunas at Kaunas WGS before and after construction of Kaunas HPP

The comparison of averages of heat runoff (Fig. 2) and other parameters of two periods revealed, that average values of all parameters decreased after construction of Kaunas HPP: heat runoff decreased to 10%, discharge -11% and temperature -1%.

The influence of HPP on the heat runoff are well apparent through comparing the heat runoff values of the individual years with equal water runoff (modulus coefficient) during the period of natural hydrological regime (before the plant start-up) and the period of influence of anthropogenic activity (after HPP start) (Table 5).

Table 5. Heat runoff of the River Nemunas at Kaunas WGS before and after construction (1959) of the Kaunas Hydroelectric Power Plant in the year with same stream flow (modulus coefficient)

Parameter	Before construction of HPP					After construction of HPP				
	1948	1953	1954	1955	1959	1964	1973	1990	1992	2003
Modulus coefficient	1.00	0.80	0.85	1.10	0.76	0.85	0.99	1.10	0.75	0.79
Heat runoff	10.4E+09	8.2E+09	8.7E+09	11.1E+09	7.8E+09	7.1E+09	8.6E+09	8.8E+09	6.2E+09	7.0E+09



Heat runoff of the River Nemunas at Kaunas WGS after Kaunas HPP construction was lower in all investigated individual years with the same water flow (modulus coefficient). For example, the heat runoff of 1990 was 21% lower than one of 1955.

CONCLUSIONS

1. Warm season (May-October) heat runoff variations among the River Nemunas at Smalininkai WGS and the River Merkys at Puvočiai WGS were highly synchronous and it slightly increases during the investigated period in both rivers. In the period of 1945–2011 the average mean of heat runoff of warm season in the River Nemunas at Smalininkai WGS was $1.64E+10$ cal and it was 16 times higher than one of the river Merkys at Puvočiai ($1.01E+09$ cal).
2. Heat runoff of warm season has been getting warmer more intensive over the last 30 years in both rivers, regardless to which the temperature group it belongs. The results of analysis show that long-term average mean of heat runoff of warm season in the River Nemunas at Smalininkai WGS for the period of 1980–2011 is 5% higher comparing to the periods of 1945-1979, indicating climate warming.
3. Rivers heat runoff depends more on the water discharge (both rivers $R=0.95$) than on the water temperature (Nemunas at Smalininkai – $R=0.11$ Merkys at Puvočiai – $R=0.23$).
4. Heat runoff of warm season of the River Nemunas at Kaunas WGS decreased to 10% after the construction of Kaunas HPP.

REFERENCES

1. ORMEROD, S.J.; DURANCE, I. Understanding and Managing Climate Change Effects on River Ecosystem. *River Conservation and Management*. 2012, p. 107–119.
2. IPCC Third Assessment Report. [*Climate Change 2001: Working group 1: The Scientific Basis*](#). 2001.
3. IPCC, 2007: Summary for Policymakers. In: *Climate Change 2007: The Physical Science Basis. Contribution of Working Group I to the Fourth Assessment Report of the Intergovernmental Panel on Climate Change* [Solomon, S., D. Qin, M. Manning, Z. Chen, M. Marquis, K.B. Averyt, M. Tignor and H.L. Miller (eds.)]. Cambridge University Press, Cambridge, United Kingdom and New York, NY, USA. 18 p.
4. REISER, S.; TEMMING, A.; ECKHARDT, A.; HERMANN, J.-P. Automation and critical evaluation of an annual chamber for aquatic ectotherm temperature preference experiments. *Methods in Ecology and Evolution*. 2013. 11 p.
5. GORE, J.A.; MEAD, J.; PENCZAK, T.; HIGLER, L.; KEMP, J. Processes Influencing Aquatic Fauna. *Ecohydrology: Processes, Models and Case Studies*. 2008. 391 p.
6. LIU, B.; YANG, D. Siberian Lena River heat flow regime and change. *Cold Region Hydrology in a changing Climate Symposium in Melbourne, Australia*. 2011, p. 71–76.
7. ODROVA, Tatjana V. Гидрофизика водоемов суши, 1979, 312 p.
8. ODROVA, Tatjana V. Условия формирования теплого стока рек Сибири, 1984, p. 239–246.
9. VYŠĚGORODCEV, A. A. Рыбы Енисея. 2000, 188 p.
10. DVINSKICH, S.A.; NOSKOV, V.M. Структура водохранилища и ее роль в формировании температурного режима. 2008, 12 p.
http://www.geovestnik.psu.ru/files/vest/115_struktura_vodohranilisa_i_ee_rolb_v_formirovanii_temperaturnogo_rezima.pdf
11. Базовое гидрофизическое состояние озера Друکشяй. 1989б 188 p.
12. FINCH, J.; CALVER A. Methods for the quantification of evaporation from lakes. 2008. 41 p.



13. TURNPENNY, A.W.H.; COUGHLAN, J.N.B.; CREWS, P.; BAMBER, R.N.; ROWLES, P. Cooling Water Options or the New Generation of Nuclear Power Stations in the UK. Environment Agency. 2010, 214 p.
14. LIU, B.; YANG, D.; YE, B.; BEREZOVSKEYA, S. Long-term open-water season stream temperature variations and changes over Lena River Basin in Siberia. *Global and Planetary Change*. Vol. 48, Iss. 1–3 September, 2005, p. 96–111.
15. ČERNOVA, J.V.; JOLIN M.M. Влияние зарегулирования стока Волги на термический режим дельтовых водотоков. *Современное состояние и стратегии сохранения природных ресурсов и антропогенных экосистем : материалы всероссийской научно-практической конференции*. 2010, p. 90–94.
16. MAGRICKII, D.V. Тепловой сток рек в моря российской Арктики и его изменения. *Вестник Московского университета*. 2009. Ser. 5. География, p. 69–77.
17. MEILUTYTĖ-BARAUSKIENĖ, D.; KOVALENKOVIENĖ, M.; ŠARAUSKIENĖ, D. The impact of runoff regulation on the thermal regime of the Nemunas. *Environmental research, engineering and management*. 2005. No 4 (34)p. 43–50.
18. JABLONSKIS, J.; JURGELĖNAITĖ, A. Water Temperature Peculiarities of Lithuanian Rivers. *Energetika*. 2010. 56 (2). p. 163–171.
19. VANAGAITĖ, J.; VALIUŠKEVIČIUS, G. Assessment of river water temperature compliance with ecological requirements in Lithuania. *Geografija*. 2011 47 (2), p. 62–70.
20. JURGELĖNAITĖ, A.; KRIAUCIŪNIENĖ, J.; ŠARAUSKIENĖ, D. Spatial and temporal variation in the water temperature of Lithuanian rivers. *BALTICA*. 2012. Vol. 25, Nr. 1. p. 65–76.
21. GALVONAITĖ, A.; MISIŪNIENĖ, M.; VALIUKAS, D.; BUITKUVIENĖ, M.S. Lietuvos klimatas: monografija, 2007. 180 p.



HYDRO-GENETIC RESEARCH METHODS OF THE MAIN FACTORS OF THE SPRING FLOOD IN THE DESNA RIVER BASIN

O. Koshkina, L. Gorbachova

*Ukrainian Hydrometeorological Institute
37, Nauki Prospect, Kyiv-28, 03028, Ukraine
Phone +380445258670*

Email: olga.koshkina@ukr.net, lyudgor@list.ru

ABSTRACT

The results of the complex analysis of the spring flood trends of the main factors in the Desna river basin are present in this paper. Assessment of homogeneity and stationarity of the spring flood main factors was made using the hydro-genetic methods. The stationarity of the hydrometeorological characteristics was researched on the base of the estimation of the linear trends significance at the 5% significance level. Phases of cyclical fluctuations of hydrometeorological characteristics based on the difference-integral curves were analyzed. In all gauges and stations synchronous fluctuations of the spring flood formation factors are observed. It indicates that the conditions of their formation are homogeneous. Trend analysis showed that such parameters as the maximum water discharges and the sum of negative air temperatures in winter have statistically significant trends for all the stations. However, analysis of the total integral curves showed that all observation series are homogeneous because of any significant inflection lines curves were found. However, analysis of the total integral curves showed that all the observation series are homogeneous, so as they don't have any points of the fracture in the directions.

Keywords: stationarity, homogeneity, spring flood, Desna River, discharge trends

1. INTRODUCTION

The Desna River is the longest and the second largest basin of the left bank tributary of the Dnieper River. Length of the river is 1130 km, basin area – 88.900 km², the fall of water surface – 146 m [1]. The river flows into the Dnieper River in 920 km from the estuary, in 10 miles above the city of Kiev (Fig. 1). It is especially important to have knowledge about changes in the maximum river runoff, because high floods lead to negative consequences such as flooding of settlements, destruction of hydraulic structures, bridges, etc., which causes considerable material damages for the states and public. Therefore, analysis of trends of the spring flood main factors in the basin of the Desna River has important scientific and practical value. The characteristics of the research area were described in details in the work [2].

The formation conditions as well as analysis of long-term fluctuations of the spring flood characteristics of the river Desna were explored in such publications [3–9]. One of the first information about the spring flood in the Desna river basin was presented in the paper G.I. Schvetz's paper [10]. This paper presents the maximum water levels in Chernihiv. In the paper of Fomenko [5] the formation features of the prominent flood in 1970 in the basin of the Desna river were analyzed. It was also considered the work of S.S. Kutoviy [11], which analyzed the impact assessment of the economic activities on an annual and seasonal runoff of the Desna river. The results showed that the potential anthropogenic changes, including spring runoff, are within the accuracy of hydrological calculations, so they can not be taken into calculation. Series of papers of Chornomorets are devoted to Desna River Basin [3, 6, 7, 12, 13]. One of these papers is devoted to the long-term dynamic of alimentation regime of the Desna river [7]. The author of this work concluded that the value of total underground alimentation of the river increased by 10% by reducing the value of snow alimentation in the last 20 years. In recent years, the study of the terms of passing of spring floods in the basin of the Desna River researched by Shakirzanova J.R. and

Chornomorets Yu.O. [3, 9]. However, the work [9] is generalized to the whole territory of Ukraine and in [3] the analysis of long-term dynamics of the terms of passing of floods was performed in two periods. While, the analysis of homogeneity of observations series was not performed. It is clear that last approach does not allow to obtain reliable results. In previous studies only the Desna River basin on Ukrainian territory was used. In this paper the analysis is carried out throughout Desna River Basin.

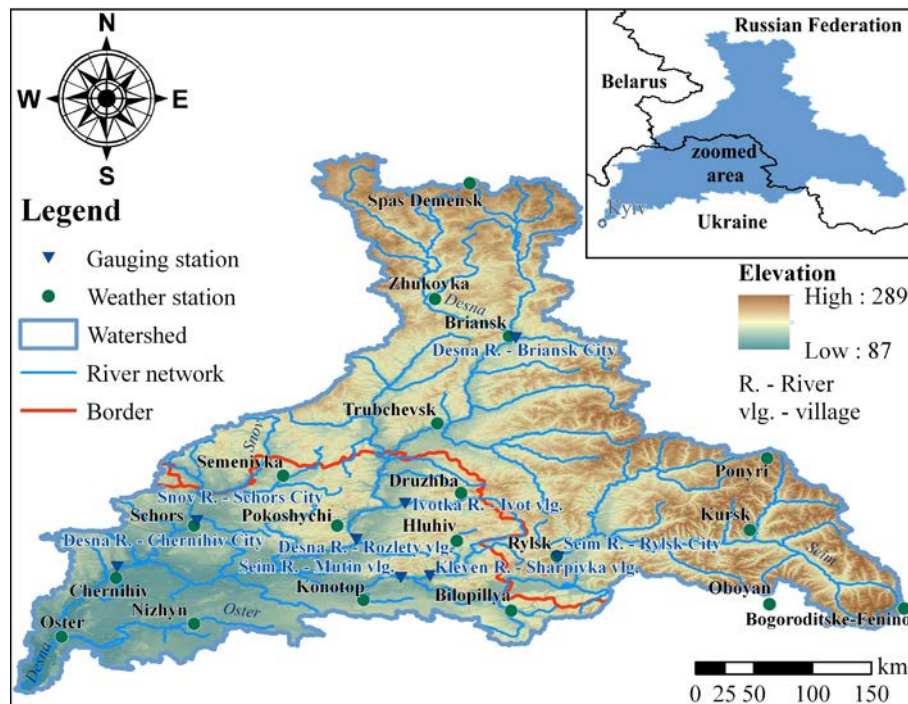


Fig. 1. The gauging and weather stations in the Desna River Basin

It is clear that to determine any parameters condition required for statistical analysis in any field must be met. It is the condition of homogeneity of members of a statistical series [14]. In these studies were used mainly only statistical methods, but for better results you need to use hydro-genetic methods too. That is why a complex analysis of trends of the spring flood hydrometeorological parameters in the Desna river basin based on the assessment of stationarity, homogeneity and cyclical fluctuations of observations data was made.

The same results by using complex analysis for the other water objects were obtained in such works [15–17].

The main goal of this research was to assess stationarity of the main factors of the spring flood. And also research the time variation of their values in the Desna River basin. It will allow to identify any changes in their distribution and to analyze the reasons of such changes.

The following tasks were solved: the homogeneity of the observations data by the total integral curve was estimated; the difference integral curves of the main factors of the spring flood to identify patterns of their fluctuations were analyzed; estimation of stationarity of long-term fluctuations of the main factors of spring flood based on assessment of statistical significance of linear trends was carried out; the gauge-analogue was chosen for the restoration of observational data on the basis of paired regression method for separate years; average date of the maximum water equivalent of snow cover occurrence, date of the maximum spring flood water discharges occurrence, dates of the beginning and the end of the flood were calculated.

The materials of stationary hydrological observations of 6 gauges (Desna river – Chernihiv city, Desna river – Rozlety village, Ivotka river – Ivot village, Snov river – Schors city, Seim river –

Mutin village, Kleven river - Sharpivka village) and 10 meteorological stations (Bilopillya, Hluhiv, Druzhba, Konotop, Nizhyn, Oster, Pokoshychi, Semenivka, Chernihiv, Schors) on the territory of Ukraine and 2 gauges (Desna river – Briansk city, Seim river – Rylsk city) and 8 meteorological stations (Briansk, Zhukovka, Kursk, Oboyan, Ponyri, Rylsk, Spas Demensk, Trubchevsk) on the territory of the Russian Federation were used with the period of observations from 50 to 125 years (Table 1).

Table 1. Information about stations

Gauge, Meteorological Station	WMO index	Years
Desna river - Chernihiv city	80131	1884–2009
Desna river – Rozlety village	80123	1954–2009
Ivotka river - Ivot village	80179	1959–2009
Snov river - Schors city	80259	1956–2009
Seim river - Mutin village	80209	1927–2009
Kleven river - Sharpivka village	80255	1956–2009
Desna river – Briansk city	80118	1895–2009
Seim river – Rylsk city	80204	1935–2009
Bilopillya	33271	1947–1989
Hluhiv	33156	1947–2009
Druzhba	33058	1947–2009
Konotop	33261	1947–2009
Nizhyn	33246	1947–2009
Oster	33236	1947–2009
Pokoshychi	33146	1925–2009
Semenivka	37708	1956–2009
Chernihiv	33135	1947–2009
Schors	33136	1947–2009
Briansk	26898	1937–2009
Zhukovka	26894	1966–2009
Kursk	34009	1892–2009
Oboyan	34109	1966–2009
Ponyri	34003	1966–2009
Rylsk	33166	1960–2009
Spas Demensk	26795	1966–2009
Trubchevsk	26997	1966–2009

2. METHODOLOGY

Because of the lack of observational data in some years in the territory of Russian Federation after the collapse of the Soviet Union the restoration of series of the maximum water discharge through the application of paired regression method according to the rivers analogs was carried out according to [18] (Table 2).

Table 2. Information about the restore of the observations data on the gauges in the basin of the Desna River

№	The name of the gauge	The name of the gauge-analogue	Conditions			The years for which data were restored
			$n \geq 10$	$R \geq 0.7$	$k/\delta_k \geq 2$	
1.	Desna river – Briansk city	Seim river – Mutin village	32	0.76	162.8	1981–2009
2.	Seim river – Rylsk city	Seim river – Mutin village	32	0.72	151.2	1981–2009



This method consists in the calculating the regression equation by using the data of the analogues rivers. The quantitative characteristics of the runoff were restored, on condition according to current building norm and rules 2.01.14-83 [18, 19]:

$$R \geq 0.7, n \geq 10, k/\sigma_k \geq 2, \quad (1)$$

where R is the correlation coefficient between the values of the discharges in the brought gauge and analogue gauge; n is the number of the joint years of the observations in the brought gauge and analogue gauge; k is the regression coefficient; σ_k is the standard deviation of the regression coefficient.

The correlation coefficient was calculated by the formula:

$$R = \frac{\sum (q_i - \bar{q})(q_{ia} - \bar{q}_a)}{\sqrt{\sum (q_i - \bar{q})^2 \sum (q_{ia} - \bar{q}_a)^2}}, \quad (2)$$

where q_i and q_{ia} are the corresponding values of annual runoff modules of the main river and of the river-analogue; \bar{q} and \bar{q}_a are the average values of annual runoff of each series for the period of simultaneous observations.

Regression coefficient was calculated by the formula:

$$k = \frac{R \cdot \sigma}{\sigma_a}, \quad (3)$$

where σ and σ_a are standard deviation of annual runoff values of the main river and river-analogue for the period of simultaneous observations.

The estimation of the statistical hydrologic characteristics were carry out by the homogeneous data to receive accurate and reliable results [18]. The estimation of the homogeneity and stationarity of the observations series of the main factors of the flood was carried out with the using of the hydro-genetic methods.

The hydrological genetic methods consist of the total integral curves, their view (presence or absence of the any points of the fracture in the directions) allows to find out the influence of the anthropogenic factors and the manifestations of the global climate change on the river runoff formation; the difference integral curves that allows to reveal the regularity in the cyclical fluctuations of the runoff on the catchment; the combined chronological graphs.

The concept of cyclical fluctuations without the effect of the displacement between phases of the cycles of high and low duration enables the use of difference integral curves, or the total curves of deviations from the center. The method of the difference integral curve to estimate the cyclical fluctuations of many nature phenomena for the first time was proposed by V.G. Glushkov. V.G. Andreianov first started to make a comparative analysis of heterogeneous material based on the valuation of difference integral curves of the modular coefficient [14].

Method of calculating of the difference integral curve is that the first of all for current series of observations carried out the calculation of the modular coefficients:

$$K = \frac{M_i}{\bar{M}}, \quad (4)$$

where M_i is the value of the series, \bar{M} is the average value of the series.

Then determine their deviations from the middle $K - 1$. After builds the integral curve by successive summation of these deviations by the formula:

$$\sum_1^i (K - 1) = f(i) \quad (5)$$

In addition, to exclude the effect of different variability, the integral curves, when they are compared to each other, should be given in the normalized deviations (ie lead to $C_v = 1$). Thus, the expression for the normalized difference integral curves in modular coefficients assumes the following form:

$$\frac{\sum_1^n (K-1)}{C_v} = f(i) \quad (6)$$

Therefore, the difference integral curve represents the cumulative sum of the modular coefficients deviations from the mean annual values of the series for each Mi years.

The estimation of the stationarity of the long-term fluctuations of the hydrometeorological characteristics in the basin of the Desna River was carried out by an assessment of the statistical significance of the linear trends [19]. The statistical significance of the trends was defined by the statistical significance of the correlation coefficient (R). The correlation coefficient of this dependence was estimated on the relation to the standard deviation (σ_R):

$$R / \sigma_R \geq \beta \quad (7)$$

If as a result of the above-stated calculations it will appear that the trend significantly (at the given significance level) differs from zero, i.e. the double of standard deviation of the correlation coefficient is much less than the correlation coefficient, it indicates no stationarity of the long-term fluctuations of the main factors of the flood, i.e. the inhomogeneity its at time, and on the contrary, if $2\sigma_R > R$ is the homogeneity of the main factors of the flood at time.

For 5 % of the significance level or for the 95 % confidential limit $\beta = 2$ [19].

The standard deviation of the correlation coefficient for $n > 25$ was defined by the equation:

$$\sigma_R = (1 - R^2) / \sqrt{n - 1}, \quad (8)$$

where n is the total number of the members of the row.

2. RESULTS

In all meteorological stations synchronous fluctuations of the main factors of spring flood were observed in spite of fact that they all are located in different parts of researched area. It indicates that conditions of their formation are homogeneous. Long-term dynamics of maximum spring flood water discharges, depth of soil freezing at the beginning of flood, maximum water equivalent of snow cover, sums of precipitation for the spring floods period, sums of negative and positive air temperatures in winter, dates of the beginning and the end of the flood at all observation stations in the basin of the Desna River have statistically significant trends. It indicates a violation of the stationarity of the spring flood formation (Fig. 2).

However, trend analysis (Table 3) showed that statistically significant trends in all stations have such factors as the sum of negative air temperatures for the winter period and maximum water discharges. The depth of soil freezing only at two stations (Hluhiv, Konotop) has a statistically significant trends. The sum of positive air temperatures for the winter period has a statistically significant trend at 6 meteorological stations from 11. Only long-term dynamics of the dates of the maximum spring flood water discharges occurrence and maximum water equivalent of snow cover for all hydrological stations characterized by the absence of statistically significant trends in the 5 % significance level for all gauging and meteorological stations. So ranks are homogeneous.

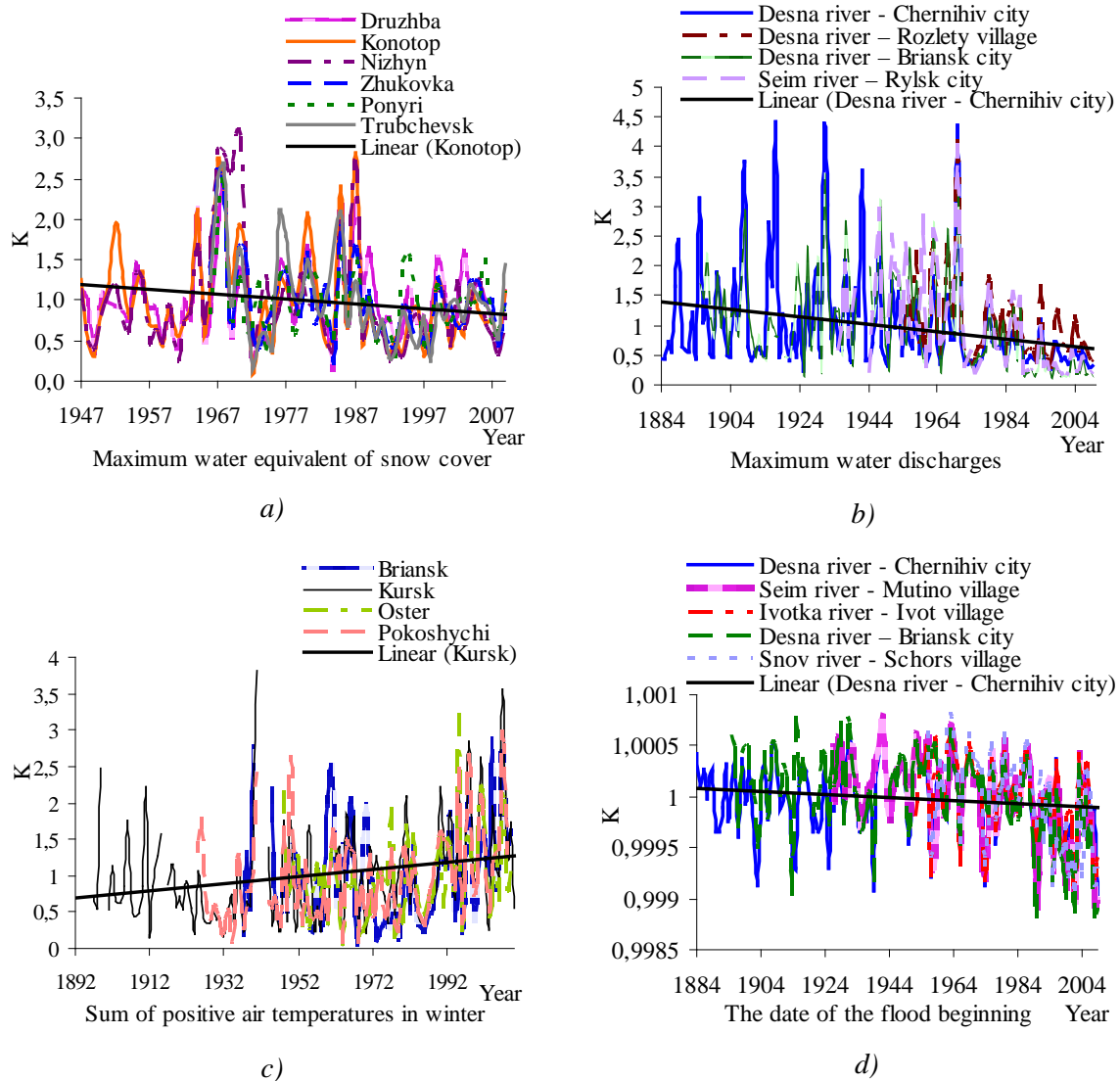


Fig. 2. Long-term dynamics and linear trends of the factors of the spring flood formation in the basin of the Desna River

Table 3. The estimation of the significance linear trends of the spring flood hydrometeorological characteristics in the basin of the Desna river

The name of gauge and station	The equation of the trend	R	σ_R	$2\sigma_R$	The result
Maximum water discharges					
Desna river - Chernihiv city	$y = -0.0064x + 1.4092$	0.271	0.08	0.165	“A”
Seim river - Mutin village	$y = -0.0196x + 1.8235$	0.519	0.08	0.60	“A”
Kleven river - Sharpivka village	$y = -0.0246x + 1.6766$	0.460	0.11	0.215	“A”
Snov river - Schors city	$y = -0.0306x + 1.8418$	0.574	0.09	0.182	“A”
Ivotka river - Ivot village	$y = -0.0187x + 1.486$	0.447	0.11	0.224	“A”
Desna river – Rozlety village	$y = -0.0147x + 1.4199$	0.359	0.12	0.233	“A”
Desna river – Briansk city	$y = -0.0091x + 1.5326$	0.392	0.08	0.158	“A”
Seim river – Rylsk city	$y = -0.021x + 1.8153$	0.509	0.09	0.171	“A”



Sum of negative air temperatures in winter					
Chernihiv	$y = -0.0067x + 14.281$	0.298	0.12	0.231	“A”
Briansk	$y = -0.0067x + 14.283$	0.400	0.10	0.197	“A”
Rylsk	$y = -0.0089x + 18.672$	0.346	0.12	0.249	“A”
Kursk	$y = -0.0025x + 5.821$	0.271	0.08	0.170	“A”
Oster	$y = -0.0067x + 14.352$	0.273	0.12	0.235	“A”
Pokoshychi	$y = -0.0049x + 10.564$	0.316	0.10	0.196	“A”
Konotop	$y = -0.008x + 16.837$	0.362	0.11	0.221	“A”
Druzhba	$y = -0.0068x + 14.541$	0.346	0.11	0.224	“A”
Nizhyn	$y = -0.0076x + 16.065$	0.326	0.11	0.227	“A”
Hluhiv	$y = -0.0073x + 15.414$	0.342	0.11	0.224	“A”
Depth of soil freezing at the beginning of flood					
Hluhiv	$y = -0.009x + 18.849$	0.335	0.11	0.224	“A”
Druzhba	$y = -0.0058x + 12.552$	0.162	0.13	0.260	“0”
Konotop	$y = -0.0084x + 17.577$	0.350	0.11	0.225	“A”
Schors	$y = -0.0023x + 5.6086$	0.062	0.14	0.271	“0”
Oster	$y = -0.0074x + 15.581$	0.213	0.12	0.241	“0”
Semenivka	$y = -0.007x + 14.838$	0.195	0.13	0.262	“0”
Pokoshychi	$y = -0.0052x + 11.208$	0.160	0.12	0.247	“0”
Sum of positive air temperatures in winter					
Chernihiv	$y = 0.0068x - 12.449$	0.200	0.12	0.244	“0”
Pokoshychi	$y = 0.0079x - 14.509$	0.300	0.10	0.199	“0”
Briansk	$y = 0.0044x - 7.7479$	0.128	0.12	0.230	“0”
Rylsk	$y = 0.0054x - 9.7033$	0.150	0.14	0.276	“0”
Kursk	$y = 0.005x - 8.7006$	0.234	0.09	0.173	“A”
Oster	$y = 0.0083x - 15.391$	0.248	0.12	0.238	“A”
Konotop	$y = 0.0103x - 19.451$	0.275	0.12	0.235	“A”
Druzhba	$y = 0.0102x - 19.244$	0.281	0.12	0.234	“A”
Nizhyn	$y = 0.0093x - 17.447$	0.273	0.12	0.235	“A”
Hluhiv	$y = 0.0103x - 19.29$	0.270	0.12	0.235	“A”
Bilopillya	$y = -0.0032x + 7.2925$	0.059	0.15	0.308	“0”
Maximum water equivalent of snow cover					
Hluhiv	$y = -0.0059x + 12.654$	0.179	0.12	0.244	“0”
Druzhba	$y = 0.0005x + 0.0038$	0.017	0.13	0.252	“0”
Briansk	$y = -0.0072x + 15.269$	0.211	0.14	0.288	“0”
Ponyri	$y = -0.0076x + 16.037$	0.222	0.14	0.287	“0”
Konotop	$y = -0.006x + 12.784$	0.179	0.12	0.244	“0”
Schors	$y = -0.0017x + 4.4064$	0.048	0.13	0.251	“0”
Nizhyn	$y = -0.0053x + 11.447$	0.146	0.12	0.249	“0”



Oboyan	$y = -0.0068x + 14.518$	0.155	0.15	0.294	“0”
Spas Demensk	$y = -0.0019x + 4.8021$	0.053	0.15	0.301	“0”
Sum of precipitation during the spring flood					
Chernihiv	$y = 0.0106x + 0.6601$	0.451	0.10	0.201	“A”
Semenivka	$y = 0.0198x + 0.4554$	0.514	0.10	0.200	“A”
Oster	$y = 0.0111x + 0.6444$	0.433	0.10	0.205	“A”
Briansk	$y = 0.0066x + 0.9016$	0.104	0.18	0.367	“0”
Nizhyn	$y = 0.0116x + 0.6284$	0.459	0.10	0.199	“A”
Pokoshychi	$y = 0.0055x + 0.8492$	0.240	0.13	0.257	“0”
Schors	$y = 0.0202x + 0.4436$	0.521	0.10	0.198	“A”
Hluhiv	$y = -0.0082x + 0.2622$	0.271	0.12	0.234	“A”
Rylsk	$y = 0.015x + 0.6178$	0.456	0.11	0.224	“A”
Date of maximum water equivalent of snow cover occurrence					
Hluhiv	$y = -4E - 06x + 1.0076$	0.087	0.126	0.252	“0”
Konotop	$y = -7E - 06x + 1.0135$	0.158	0.124	0.248	“0”
Druzhba	$y = -8E - 07x + 1.00116$	0.022	0.127	0.254	“0”
Nizhyn	$y = -8E - 06x + 1.0163$	0.182	0.123	0.246	“0”
Oster	$y = -1E - 06x + 0.9978$	0.022	0.127	0.254	“0”
Schors	$y = -1E - 05x + 1.0255$	0.281	0.117	0.234	“A”
Semenivka	$y = -3E - 05x + 1.0518$	0.418	0.119	0.238	“A”
Pokoshychi	$y = -2E - 05x + 1.0448$	0.370	0.125	0.249	“A”
Briansk	$y = -1E - 05x + 1.0294$	0.373	0.131	0.263	“A”
Zhukovka	$y = -9E - 06x + 1.0179$	0.216	0.145	0.291	“0”
Oboyan	$y = -1E - 05x + 1.0242$	0.303	0.138	0.277	“A”
Ponyri	$y = -7E - 06x + 1.0148$	0.191	0.147	0.294	“0”
Trubchevsk	$y = -1E - 05x + 1.0218$	0.218	0.145	0.291	“0”
Spas Demensk	$y = -1E - 05x + 1.0237$	0.277	0.141	0.282	“0”
Date of the flood beginning					
Desna river – Chernihiv city	$y = -1E - 06x + 1.0028$	0.146	0.088	0.175	“0”
Desna river – Rozlety village	$y = -1E - 05x + 1.0229$	0.493	0.102	0.204	“A”
Ivotka river – Ivot village	$y = -9E - 06x + 1.0174$	0.372	0.114	0.228	“A”
Kleven river – Sharpivka village	$y = -8E - 06x + 1.0154$	0.312	0.124	0.248	“A”
Seim river – Mutin village	$y = -9E - 06x + 1.0169$	0.480	0.084	0.169	“A”
Snov river – Schors city	$y = -1E - 05x + 1.0297$	0.504	0.102	0.205	“A”
Desna river – Briansk city	$y = -5E - 06x + 1.0106$	0.423	0.077	0.154	“A”
Seim river – Rylsk city	$y = -9E - 06x + 1.0184$	0.465	0.091	0.182	“A”
Date of the flood ending					
Desna river – Chernihiv city	$y = -3E - 06x + 1.0059$	0.252	0.090	0.179	“A”



Desna river – Rozlety village	$y = 5E-06x + 0.9903$	0.203	0.129	0.259	“0”
Ivotka river – Ivot village	$y = -1E-05x + 1.0251$	0.567	0.090	0.180	“A”
Kleven river – Sharpivka village	$y = -1E-05x + 1.0189$	0.314	0.124	0.248	“A”
Seim river – Mutin village	$y = -4E-06x + 1.0087$	0.311	0.099	0.198	“A”
Snov river – Schors city	$y = 1E-05x + 0.9786$	0.341	0.121	0.243	“A”
Desna river – Briansk city	$y = 1E-06x + 0.9976$	0.117	0.094	0.189	“0”
Seim river – Rylsk city	$y = 2E-06x + 0.9961$	0.117	0.115	0.229	“0”
Date of the maximum water discharges occurrence					
Desna river – Chernihiv city	$y = -4E-07x + 1.0007$	0.041	0.089	0.179	“0”
Desna river – Rozlety village	$y = -2E-06x + 1.0047$	0.137	0.132	0.265	“0”
Ivotka river – Ivot village	$y = -4E-06x + 1.0083$	0.184	0.128	0.256	“0”
Kleven river – Sharpivka village	$y = -5E-06x + 1.0108$	0.217	0.131	0.262	“0”
Seim river – Mutin village	$y = -2E-06x + 1.0047$	0.201	0.106	0.212	“0”
Snov river – Schors city	$y = -2E-07x + 1.0004$	0.009	0.137	0.275	“0”
Desna river – Briansk city	$y = -5E-07x + 1.001$	0.065	0.095	0.191	“0”
Seim river – Rylsk city	$y = 1E-06x + 0.998$	0.081	0.115	0.231	“0”
Flood duration					
Desna river – Chernihiv city	$y = -0.0005x + 1.0295$	0.11	0.09	0.177	“0”
Desna river – Rozlety village	$y = 0.0076x + 0.7844$	0.54	0.08	0.155	“A”
Ivotka river – Ivot village	$y = -0.0037x + 1.1079$	0.171	0.13	0.257	“0”
Kleven river – Sharpivka village	$y = -0.0015x + 1.041$	0.076	0.14	0.273	“0”
Seim river – Mutin village	$y = 0.002x + 0.9161$	0.248	0.10	0.205	“A”
Snov river – Schors city	$y = 0.0156x + 0.572$	0.587	0.09	0.180	“A”
Desna river – Briansk city	$y = -0.0008x + 1.0312$	0.085	0.11	0.221	“0”
Seim river – Rylsk city	$y = -0.002x + 1.0433$	0.107	0.15	0.309	“0”

«A» – the statistically significant trend, i.e. inhomogeneous; «0» – the statistically insignificant trend, i.e. homogeneous

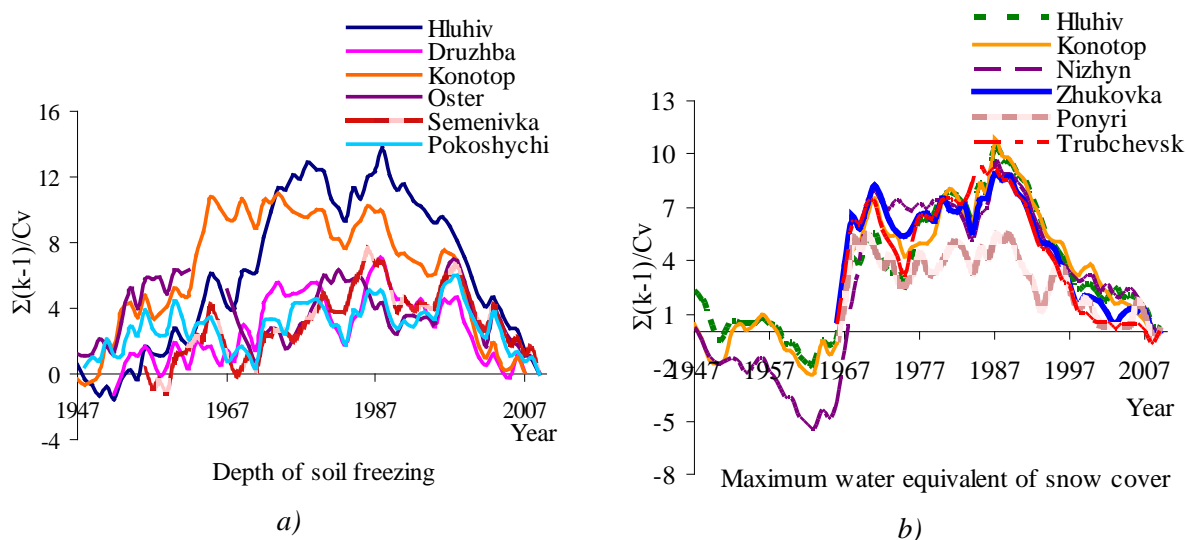
Analyzing the linear trends we can see that the depth of soil freezing, the maximum water equivalent of snow cover, sums of negative and positive air temperatures in winter and maximum water discharges are characterized by the decreasing trends. In other words due to increase of air temperature in winter, decrease of the depth of soil freezing and the maximum water equivalent of snow cover are observed, which reduces the maximum water discharge during the period of spring flood. Decrease of the maximum water equivalent of snow cover is the main reason for the reduction of the spring flood.

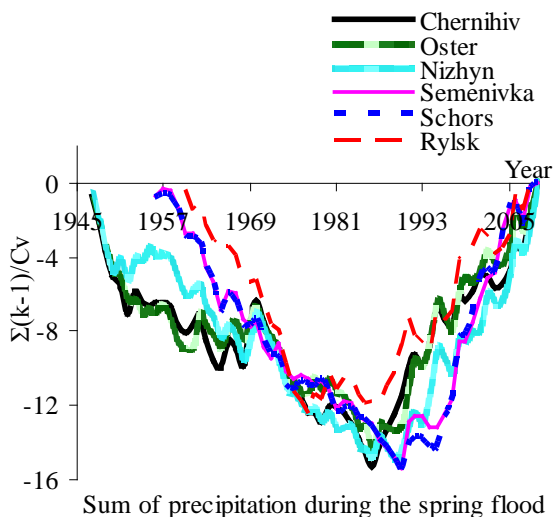
Analysis of the difference integral curves showed that the depth of soil freezing at the beginning of flood, maximum water equivalent of snow cover and sums of negative air temperatures in winter have a decreasing phase of the cyclical fluctuations. Analysis of the difference integral curves of the maximum spring flood water discharges showed that for all rivers in 1970 a transition from high to low water phases of the hydrological cycle was found. (Fig. 3f). Starting from 70 years of the last century for such indicators as maximum water equivalent of snow cover and the sums of negative air temperatures in winter a decreasing phase of the cyclical fluctuations was observed, (Fig. 3b, d). That is, decreases of the sums of negative air temperatures leads to the decrease of solid precipitation, and as a result to the decrease of the maximum water

equivalent of snow cover. All this causes the reduction of the maximum water discharges in the basin of the Desna River since 1970. At the same time the sum of precipitation for the period of spring flood and the sum of positive air temperatures in winter have the increasing phases of cyclical fluctuations from 1986-1988 (Fig. 3 *c, e*). However, the growth of these parameters does not have a significant impact on the spring flood formation, for example, the proportion of rainfall during the spring flood in the general flood runoff is only a 12–20%.

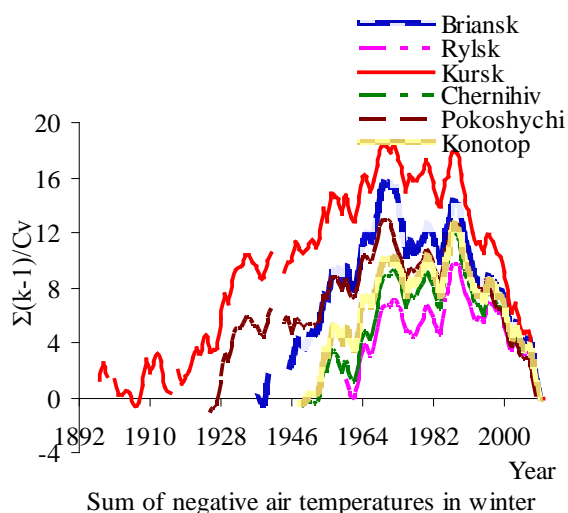
Observational data of the maximum runoff does not have a full closed cycle. Hydrological gauges Desna River – Chernihiv city and Desna river – Briansk city also does not have a full hydrological cycle, although have an observational data from 1884 and 1895 duration 128 and 115 years respectively (Fig. 3 *f*).

The difference integral curves of the dates of the beginning and the end of the flood (Fig. 3 *i, j*) shows that they have synchronous fluctuations. In the period from 1884 to 1944 the date of the beginning of the flood in the hydrological gauge Desna River – Chernihiv city has stable character. At the same time, the end date of the flood have increasing phase of the fluctuations, so it is moving to a later date (June–July). It leads to an increase in the duration of flood. Since 1945, there is a shift of the dates of the flood beginning to a later dates. So, there was a increasing phase, which lasted until 1988. At the same time, the end dates of the flood have decreasing phase. It indicates about the earlier dates of the flood ending, thereby reducing the duration of the flood. Since 1988, the date of the flood beginning has shifted to an earlier date (February–March). The end of the flood in the same period has a stable fluctuations which leads to an increase in the flood duration.

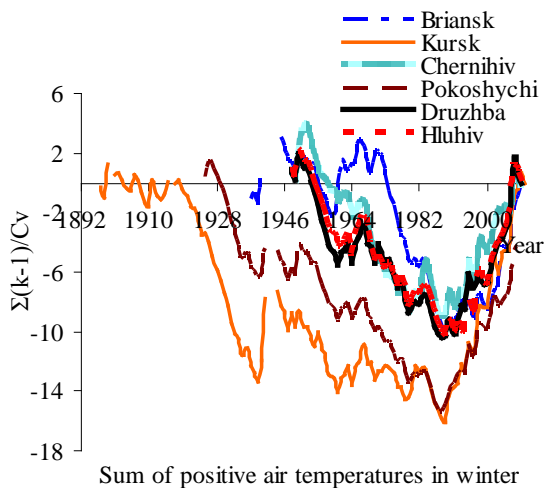




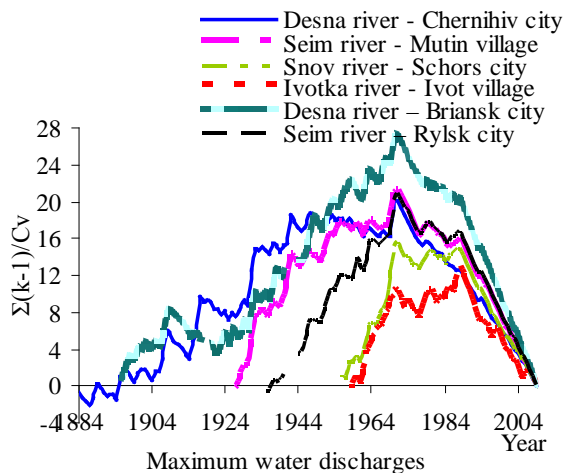
c)



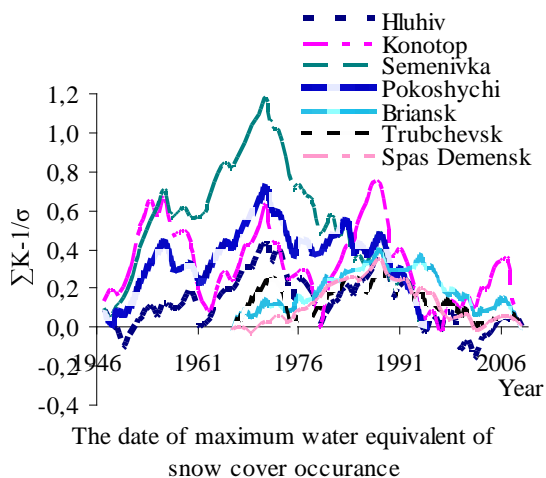
d)



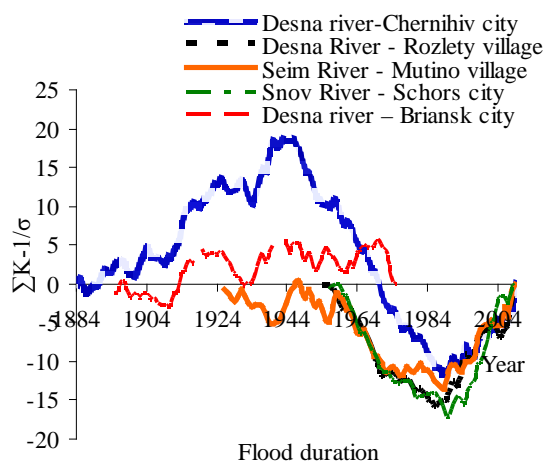
e)



f)



g)



h)

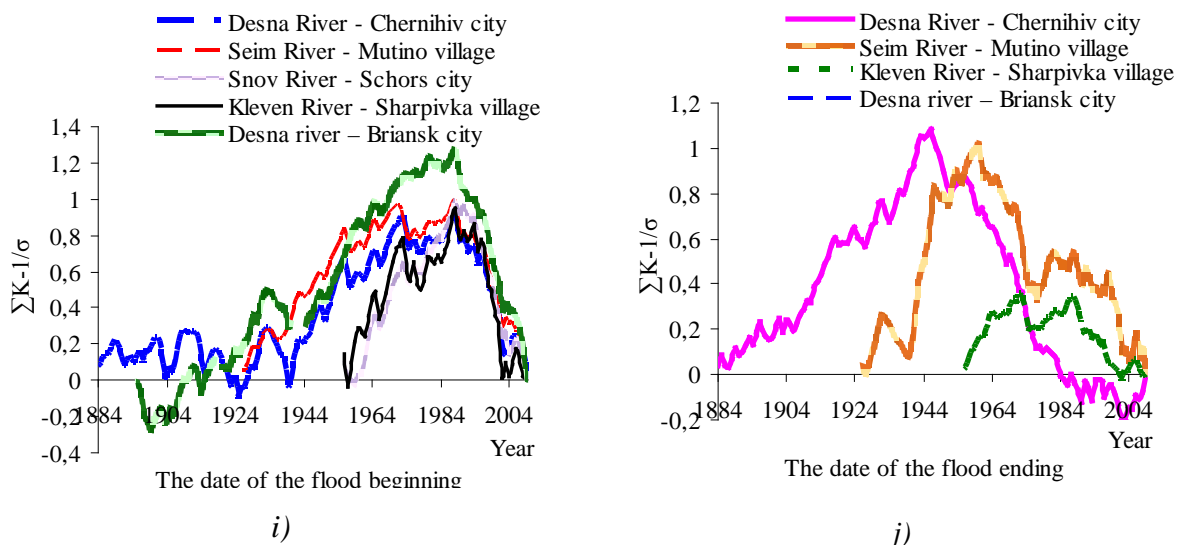
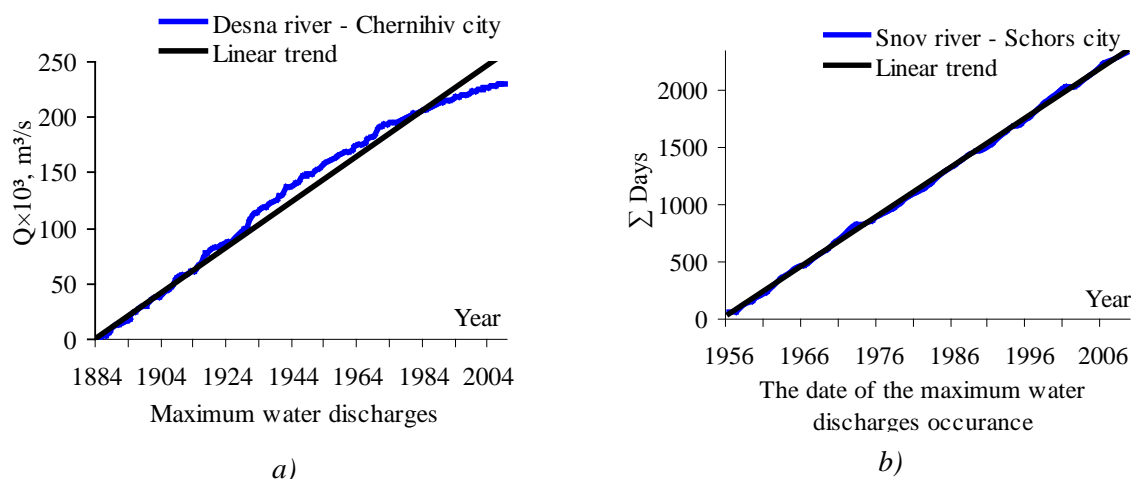


Fig. 3. Difference-integral curves of the factors of the spring flood formation in the basin of the Desna River

The presence of statistically significant trends indicates the inhomogeneity of the observations data. The analysis of the homogeneity of the main factors was carried using total integral curves. It is showed that all observational data are homogeneous, because of any significant points of curves trends fractures are not detected. Some examples of such curves are presented at the Fig. 4. Some doubt causing the form of total curves of maximum water discharge of the spring flood. However, all the main factors of flood formation have homogeneous series of observations, that is, the reasons which could cause inhomogeneity ranks are missing. So, this type of total curves can be explained only by the fact that the maximum water discharge in comparison, for example, with the average annual discharges have higher values, variability and incomplete cycle of fluctuations. Consequently, the total value of maximum water discharge on the curves are more deviated from the straight line. With the extension of observational data total values will have cyclical form, which will synchronously coincide with fluctuations on the integral curves. We can assume that the statistical significance of trends are determined by comparing of the high-water and low-water phases of cyclical fluctuations, that is temporary in nature (Fig. 3).





6. CHORNOMORETS Yu.O., LUK'YANETS O.I. Estimation of spring discharge distribution timing for Desna river. *Hydrology, hydrochemistry, hydroecology*, 2010. Vol. 4(21), p. 56–67 (in Ukrainian).
7. CHORNOMORETS Yu.O., GREBIN' V. V. Long-term dynamic of alimentation regime of Desna river. *Hydrology, hydrochemistry, hydroecology*, 2010. Vol. 3(20), p. 59–67 (in Ukrainian).
8. VISHNEVSKIY V.I. Climate and river runoff changes on the territory of Ukraine and Belarus. *Proceeding of UHMI*, 2001. Vol. 249, p. 89–105 (in Ukrainian).
9. SHAKIRZANOVA J.R. Analysis and spatial generalization of dates of passing of the spring floods on the flat rivers of Ukraine. *Bulletin of the OSEU*, 2008. Vol. 6, p. 157–164 (in Ukrainian).
10. SCHVETZ G.I. Characteristics of water content of the rivers of Ukraine. Kyiv. 1964, p. 192 (in Russian).
11. KUTOVIY S.S. An estimation of the influence of agricultural, industrial and other activities on the yearly and Seasonal drainage of the Desna River. *Hydrology, hydrochemistry, hydroecology*, 2002. Vol. 4, p. 101–102 (in Ukrainian).
12. CHORNOMORETS Yu. The characteristic of basic elements of a water regime time dynamics of the river Desna. *Hydrology, hydrochemistry, hydroecology*, 2009, Vol. 17, p. 80–93 (in Ukrainian).
13. CHORNOMORETS Yu.O. GREBIN' V. V. Elements of water river balance annual distribution of Desna Basin and their annual fluctuations. *Hydrology, hydrochemistry, hydroecology*, 2010. Vol. 1(18), p. 98–107 (in Ukrainian).
14. ANDREIANOV V.G. Cyclical fluctuations of annual runoff and their consideration in the hydrological calculation. *Proceedings of State Hydrological Institute*, 1959, Vol. 68, p. 3–49 (in Russian).
15. BAUZHA T., GORBACHOVA L. Estimation of the homogeneity of the average annual runoff of the rivers and streams of the Zaccarpatska station. BALWOIS 2012, Proceedings of International Conference on water, climate and environment. Ohrid, Republic of Macedonia. 2012 28 May–2 June, edited by M. Morell, ISBN 978-608-4510-10-9, <http://www.balwois.com/2012>.
16. GORBACHOVA L., BIBIK V. Temporary homogeneity of the characteristics of the water flow in the Borzhava river basin. *Proceeding of UHMI*, Vol. 262 (in Ukrainian).
17. GORBACHOVA L., BAUZHA T. The reasons of the instationarity of the seasonal runoff of rivers and streams in the Rika River Basin. Proceedings of International Conference “Water resources and wetlands”. Tulcea, Romania. 2012, 14–16 September.
18. BNR (The building norm and rules 2.01.14-83) The determination of the calculation hydrologic characteristics. State committee USSR on the construction, 1983, p. 97 (in Russian).
19. The methodological recommendations for assessment the homogeneity of the hydrological characteristics and definition of their calculation values for the non-homogeneous data, State Hydrological Institute, Saint Petersburg, 2010, p. 39–40 (in Russian).



ANALYSIS OF THERMAL HYDRAULIC PROCESSES DURING DIFFERENT OPERATION MODES OF WENDELSTEIN 7-X EXPERIMENTAL FUSION REACTOR

T. Kaliatka

Lithuanian Energy Institute

Laboratory of Nuclear Installation Safety

Breslaujos str. 3, LT-44403 Kaunas – Lithuania

ABSTRACT

Fusion is the energy production technology, which could potentially solve problems with growing energy demand of population in the future. Wendelstein 7-X (W7-X) is an experimental stellarator type nuclear fusion facility currently being built in Greifswald, Germany, which is supposed to demonstrate that in the future energy could be produced in such type of fusion reactors. This article presents the model of W7-X target modules cooling system and plasma vessel, developed with RELAP5 code. The analysis of loss-of-coolant accident (rupture of the 40 mm target cooling pipe) during “baking” (no-plasma operation), “normal” and “hot linear” operation mode were performed. During “baking” operation mode the in-vessel components are heated up to 160 °C in order to clean the surface of in-vessel components. During “normal” and “hot linear” operation modes (plasma initiated in plasma vessel) the in-vessel components are cooling down. During “hot linear” operation mode the one of in-vessel components (wall panels) could reach 150 °C temperature, this is main difference from “normal” operation mode. The performed analysis allows to investigate the processes in cooling system and to evaluate the increase of pressure in plasma vessel during loss-of-coolant accident in different operation modes of W7-X experimental fusion reactor. The calculations results showed that in W7-X experimental fusion reactor designed safety measures are sufficient to maintain the plasma vessel integrity during loss-of-coolant accident in all three operation modes. The biggest discharged of hot water through the break is calculated during the “hot liner” operation mode. In this article presented models could be used for further analyses of other accidents of W7-X fusion facility.

Keywords: Wendelstein 7-X, cooling system, plasma vessel, RELAP5

1. INTRODUCTION

Fusion power is the power generated by nuclear fusion reactions, i.e. two light atomic nuclei fuse together to form a heavier, more stable nucleus releasing the binding energy [1]. At present, several experimental fusion reactors are under construction, among them ITER, which is built in France, KSTAR in South Korea, Wendelstein 7-X (W7-X) in Germany. There are two main types of devices initiating fusion in the plasma confined by magnetic field – tokamaks and stellarators. Both types of magnetic confinement fusion devices have toroidal geometry. However, while the cross-section of the tokamak device stays constant along the circumference of the torus, devices of the stellarator type have varying cross-sections. Wendelstein 7-X (which is currently being developed and built by IPP in Greifswald [2]) is stellarator type experimental nuclear fusion device (see Fig. 1). The purpose of the development of the W7-X device is to demonstrate the feasibility of the stellarator devices for the creation of stable plasma conditions for as long as half an hour.

One of the organizations performing research and development of the nuclear fusion technologies in Europe is European Fusion Development Agreement (EFDA). Starting 2007, Lithuanian energy institute (LEI) is a member of this organization. LEI is cooperating with Max Planck plasma physics institute (IPP, Germany) in the frame of EFDA project by performing safety analysis of fusion device WENDELSTEIN 7-X (W7-X),

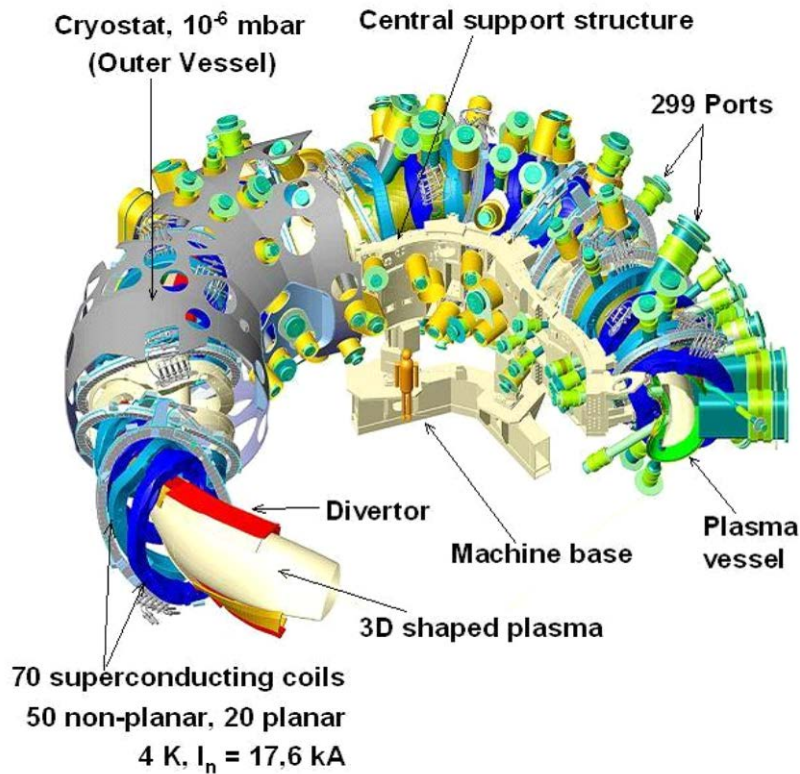


Fig. 1. Fragment of the 3D schematic view of the W7-X device [3]

Prior to the commissioning of the facility its safe operation has to be proved by dedicated safety analysis. The ingress of water into the plasma vessel represents one of the critical failure events, since primary and secondary steam production leads to a rapid increase of the inner pressure in the plasma (vacuum) vessel. A rupture of the 40 mm target module cooling pipe (pipe with largest diameter) could lead to the loss of vacuum condition up to an overpressure in the plasma vessel, damage of in-vessel components and diagnostics devices [4, 5]. When plasma is initiated in plasma vessel, cooling system is working in “normal” or “hot liner” operation modes. The aim of this work is to investigate the processes in W7-X experimental fusion reactor target cooling system and to evaluate the increase of pressure in plasma vessel during the rupture of the 40 mm target module cooling pipe in three (“baking”, “normal”, “hot liner”) cooling system operation modes. It was performed by employing the computer models, based on thermal hydraulic system code RELAP5. The processes in cooling system and plasma vessel during the rupture of the 40 mm target cooling pipe in “baking” operation mode were analyzed in the previously works and presented in papers [6 - 9]. This paper is focused on the investigation of processes in cooling system and plasma vessel during the same pipe rupture, but then cooling system working in “normal” and “hot liner” operation modes. The results of the presented study may be used to evaluate the capacity of designed protection measures and instructions in order to ensure safe operation.

2. MODELLING OF W7-X TARGET MODULES COOLING SYSTEM

The main parameters of W7-X are: average major radius 5.5 m, average plasma radius 0.53 m, total weight 725 t (see Fig. 1). Wendelstein7-X facility is composed of 2×5 so-called divertor units located in the plasma vessel with the bean-shaped cross section. The maximal height of the torus is 7 m (the highest point of pipes to the upper ports of the outer vessel is at elevation about +3.5 m, while the connections to the lower ports are at -3.5 m). Each divertor unit is assembled from 12 separate horizontal and vertical target modules (see Fig. 2) capable to remove maximum 10 MW/m² convective stationary power load [4].

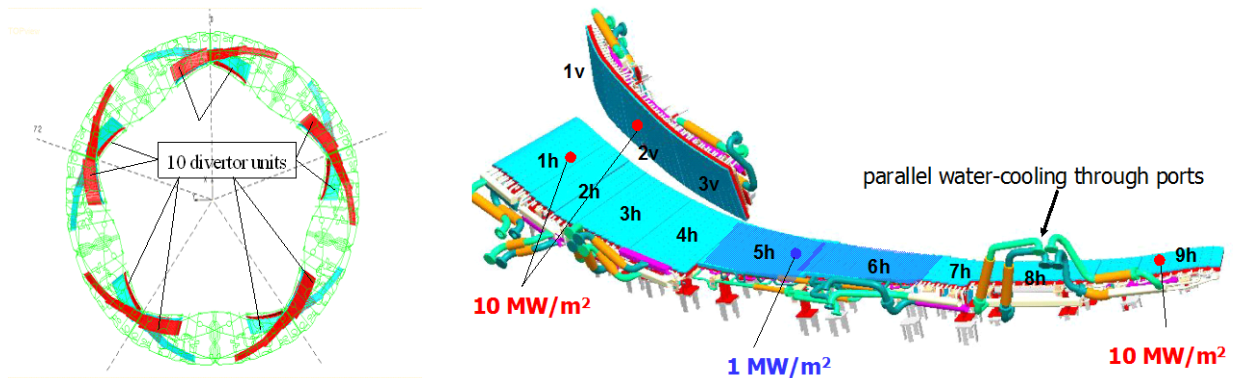


Fig. 2. W7-X top view and scheme of single divertor unit with horizontal (1h-9h) and vertical (1v-3v) target modules [3]

The W7-X facility target modules cooling system consists of two coolant circuits: The Main Cooling Circuit (MCC) and the so-called “baking” circuit. The MCC is used for cooling of the target modules when the W7-X facility under normal operation. Before plasma operation, the target modules and other in-vessel components must be heated up in order to ‘clean’ the surfaces by thermal desorption and the subsequent pumping out of the released volatile molecules. The “baking” circuit is mainly used for this purpose. Both MCC and “baking” circuits are connected together and supply water to the same target modules. During operation of W7-X in the “baking” mode (no-plasma in plasma vessel), the heat, necessary for target modules heating is generated in electrical heater. There is only one pump for all target modules loops in the “baking” operation mode. To maintain constant pressure in cooling system, the pressurizer is used. The height of the pressurizer is 2.85 m, the diameter is 1.25 m and the total volume – 2.5 m³ [5]. According the drawings presented by facility developers, the volume of water in two divertor units with 12 target modules each is approximately 0.457 m³, thus, the total volume of water in all 2×5 divertor modules is 0.457 * 5 = 2.28 m³. The water is provided to the upper and lower target modules in each divertor unit through lower and upper ports. A simplified scheme of the circuits is shown in Fig. 3.

The amount of water in the all pipelines, connecting the target modules with the both MCC and the “baking” circuits is 1.66 m³. The largest amount of water is used in the MCC – 63.1 m³, while the amount of water in “baking” circuit is very small – 1.06 m³.

Before plasma initiation the cooling system is working in “baking” operation mode. During this mode only “baking” circuit is used and only one pump for water circulation in “baking” circuit. The maximum water temperature is 160°C (water is heated in electrical heaters), the water pressure is about 1.0 MPa. The corresponding mass flow of water in the “baking” circuit is 177 m³/h (44.6 kg/s) [5].

Then plasma in plasma vessel is initiated the MCC circuit is used for the cooling of in-vessel components. In-vessel components are heated by the plasma. During the cooling of in-vessel components there are two possible operation modes: 1) “normal” and 2) “hot liner”. During “normal” operation mode the maximum water temperature is about 35°C, the water pressure is about 1.0 MPa. The corresponding mass flow of water in the MCC circuit is 1382 m³/h (348 kg/s), when 3 circulation pumps in MCC circuit are working. The “hot liner” operation mode is an additional situation where some of the in-vessel components (wall panels) are heated with water up to 150 °C and this provides a thermal radiation load to other in-vessel components. Other water parameters are the same as in “normal” operation mode. This case of operation will be used for more than 10% of all plasma experiments. This operation mode is performed for more rapid achievement of equilibrium of adsorbed and desorbed wall particles.

The designed working pressure in the plasma vessel is about 10⁻² Pa (deep vacuum) and pressure increase can lead to the break of plasma vessel and damage of in-vessel components and diagnostics

devices as well as bellows of the ports. A rupture of the 40 mm diameter target module pipe near the port flange of the outer vessel, right at a place at the inner surface of the target module, during plasma vessel “baking” operation mode was selected for the analysis. The response of “baking” circuit and the evaluation of the amount of discharged water in the plasma vessel are presented in the following sections.

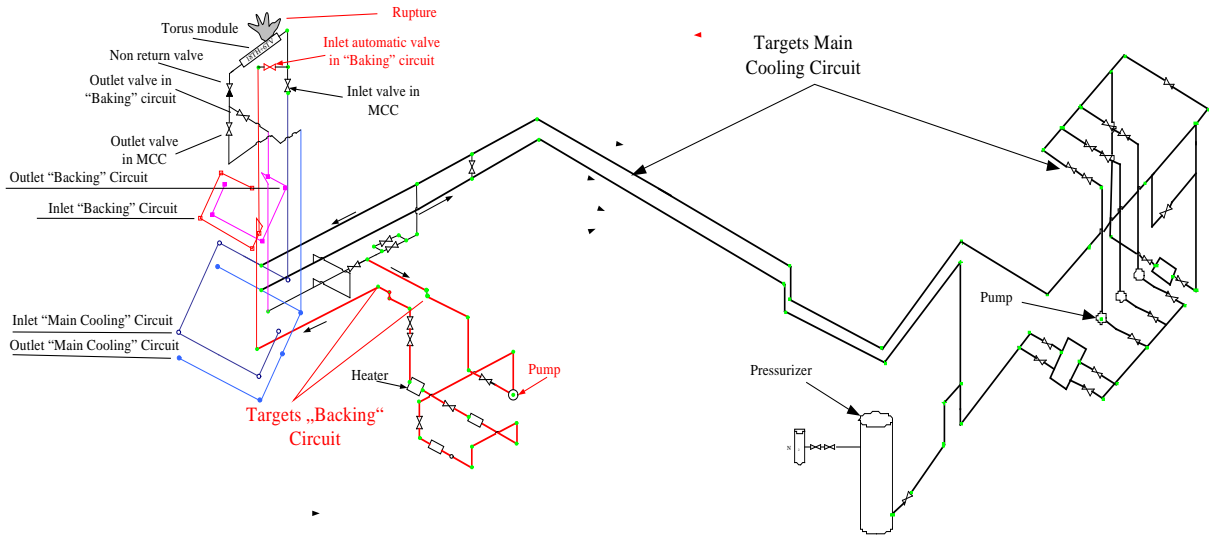


Fig. 3. Simplified scheme of main cooling and “baking” circuits

The analysis of accident with water ingress to the plasma vessel was performed using thermal-hydraulic state-of-the-art RELAP5 Mod3.3 code. RELAP5 [10] is a “best estimate” system code for the analysis of all transients and postulated accidents in light water reactor systems, including both large and small-break loss-of-coolant accidents as well as the full range of operational transients. Because the W7-X facility divertor cooling system is filled by water (coolant accepted in RELAP5 code) and can be described by above mentioned RELAP5 components (pumps, valves, pipes, heat structures, etc.), it was decided to develop the model of main cooling and “baking” circuits for RELAP5 code.

For the modelling of the selected accident (40 mm target module pipe rupture) in “baking” operation mode it is sufficient to develop a detailed model of the “baking” circuit. However both MCC and “baking” circuit are connected together (see Fig. 3). Thus, it was decided to develop a detailed model of both connected circuits. The measurements (pipe lengths, elevations, pump parameters, heater power and valves parameters) and the configuration of pipes (necessary for evaluation of form loss coefficients) were taken from the drawings provided by the W7-X design office [11].

The W7-X cooling system supplies 10 divertor units. The divertors can be grouped into two groups – upper and lower divertor units. One single upper divertor unit, connected with lower divertor unit creates one torus segment. Thus, each torus segment is composing of 18 horizontal (9 upper and 9 lower) target modules and 2x3 vertical target modules. In the developed RELAP5 nodalisation, four torus segments are modelled as equivalents (with the corresponding water volume and hydraulic resistance). One single torus segment is modelled in more extended format. In this torus segment, the upper and lower, horizontal and vertical target modules were modelled separately. From horizontal target modules two single target modules were selected: one in upper and one in lower position. These elements of single target modules allow to model rupture of single target module. In the Fig. 3 only one torus segment is shown. The each torus segment is connected to the MCC and “baking” circuit using valves, which are at the segment inlet and outlet. The valves

at the inlet to torus segment are automatic. In the case of pressure increase in the plasma vessel (it indicates the injection of water into vessel through rupture in cooling circuit) the automatic valves are closing, reducing the discharge of water. The description of the model of MCC and “baking” circuit, developed using RELAP5 code, in more details is presented in [6, 7]. During “baking” operation mode the valves from “baking” circuit on the inlet and outlet of torus are opened, the inlet valves from the MCC circuit is closed, outlet valves are opened. During “normal” and “hot liner” operation modes the valves from “baking” circuit on inlet and outlet are closed.

The complicated three-dimensional geometry of the plasma vessel volume in the stellarator (see Fig. 1 and 2) in the developed model is simplified to the geometry of horizontal cylinder. Ends of the cylinder are open and joined together, simulating closed circle of torus geometry (see Fig. 4). Whole volume (108 m^3) of the plasma vessel was modelled using one element “pipe 199”. The inner surface area (215.3 m^2) and wall thickness (0.019 m) of vessels structures in the model correspond to the available design data [5, 11]. One additional small volume (0.026 m^3) – element “196” models the volume into which the water release from the ruptured pipe. It is defined for the aims of simulation – it helps to more realistically model the steam – water mixture flowing from the ruptured pipe into the volume on back side of divertor. The plasma vessel is connected to the plasma vessel venting system. This system consists of pipelines with the drainage outlet, chimney and two burst disks. These burst disks, are installed to protect the plasma vessel from overpressure. The opening pressure of first burst disk is 110 kPa, while the opening pressure of second burst disk is 120 kPa (absolute pressure). Diameter of both burst disks is 250 mm. In case of a loss of coolant accident and the water ingress in the plasma vessel the opening pressure of the burst disk would be reached and after disk opening steam would enter piping of the venting system and would be directed outside the building. The steam would be condensing on the colder surfaces of the piping, therefore the piping are designed with inclination, which ensures that water flows to the drainage outlet (see Fig. 4).

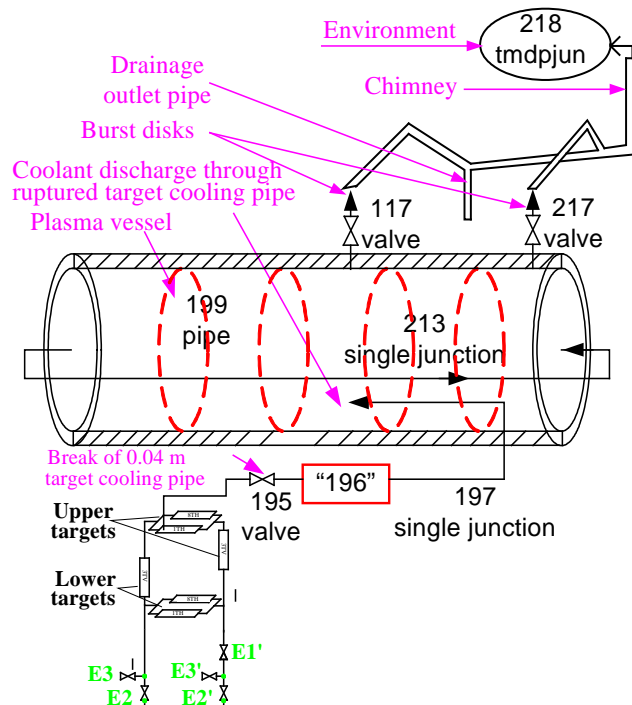


Fig. 4. Nodalization scheme of stellarator with rupture in 40 mm diameter feeder pipe

The burst disks are simulated using valves “117” and “217”, which are closed at the beginning and opens if pressure difference in plasma vessel and plasma vessel venting system exceeds 10 kPa

(for “117”) and 20 kPa (for “217”). Flow area of these valves is equal to the area of the burst disks. The environment is simulated in RELAP5 model using time dependent volume “218” with atmospheric pressure. Due to limitation of RELAP5 code it was assumed that the pressure in plasma vessel is equal to 1000 Pa – lowest possible pressure used in RELAP5 computer code. In Fig. 4 the main cooling circuit inlet valve is marked as E2, the outlet valve – E2’, the “baking” circuit inlet automatic valve – E3, outlet valve at the “baking” circuit – E3’. The check valve at the outlet from torus segment targets is marked as E1’. The identical valves are installed in the each torus segments. At “baking” operation mode the MCC inlet valves are closed and “baking” circuit inlet automatic valves – opened.

3. MODEL ASSUMPTIONS

Information regarding measurements of plasma vessel used for analysis of consequences of the W7-X in-vessel 40 mm coolant pipe break was taken from reports [11, 12] and from correspondence between D. Naujoks, J. Boscary and L. Topilski:

- Plasma vessel volume 108.375 m³;
- Plasma vessel inner surface area 708.1 m²;
- Plasma vessel perimeter 34 m;
- Plasma vessel weight 32600 kg;
- Plasma vessel average wall thickness 0.0174 m;

For the calculation of different operation modes different water parameters and different valve positions in cooling system were used, for example: during “baking” operation mode – “baking” circuit is working (Table 1.).

Table 1. Initial parameters for calculation of different operation modes

Parameter	“Baking” operation	“Normal” operation	“Hot liner” operation
Temperature, °C	160	35	150
Density, kg/m ³	907	994	917
Pressure, MPa	1	1	1
Position of valves	Baking circuit: Inlet – open Outlet – open MCC circuit: Inlet – close Outlet – open	Baking circuit: Inlet – close Outlet – close MCC circuit: Inlet – open Outlet – open	Baking circuit: Inlet – close Outlet – close MCC circuit: Inlet – open Outlet – open

4. CALCULATION RESULTS

As it was already mentioned the processes in cooling system and plasma vessel during the rupture of the 40 mm target cooling pipe in “baking” operation mode were analyzed in the previously works [6 - 9]. The comparison of calculation results computed using RELAP5 and ASTEC codes was presented in the article [9]. It was stated that comparison of calculation results received using RELAP5 and ASTEC codes, demonstrated the reasonable agreement (see Fig. 5). Some calculation divergences can be caused by different models of plasma vessel, and differences between RELAP5 and ASTEC program codes (in RELAP5 code non-homogeneous and non-equilibrium models are used for the two-phase system, while in the ASTEC code homogeneous approach is used).

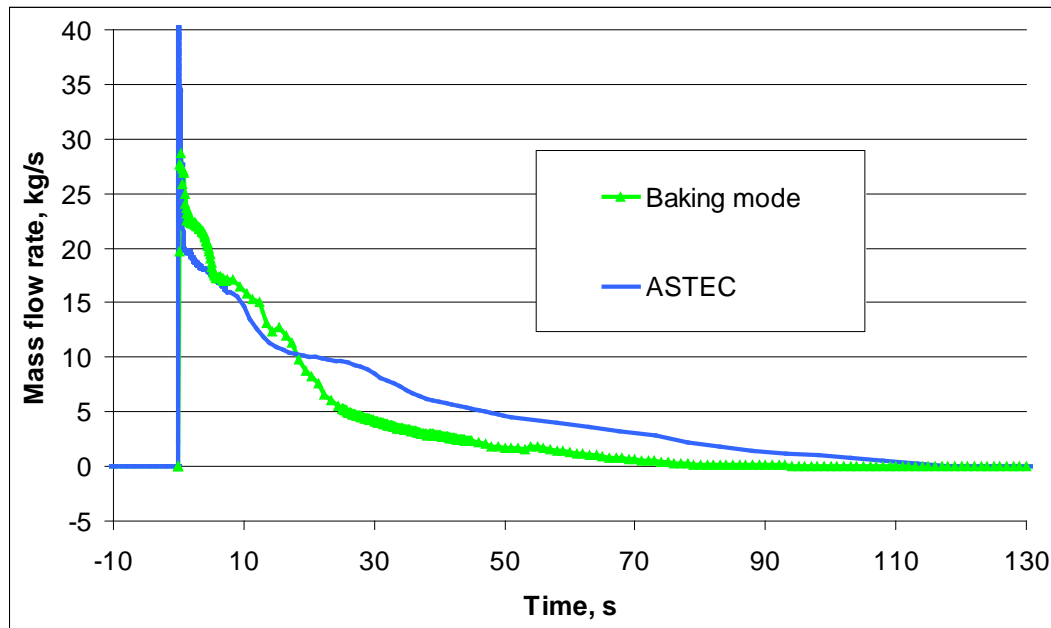


Fig. 5. Water mass flow rate through the break to the plasma vessel

In this article using RELAP5 code the processes in cooling system and plasma vessel during the rupture of the 40 mm target cooling pipe was modelled then cooling system working in “normal” and “hot liner” operation modes. Calculations of three different (“baking”, “normal” and “hot liner”) operational modes are presented in Figs. 5–7.

Water mass flow rate through the break to the plasma vessel is presented in Fig. 6. As it is shown in the figure mass flow rate during the first 20 s after the break is larger in the “normal” or “hot liner” operation modes comparing to the mass flow rate calculated during “baking” operation mode. After 20 s the mass flow rate in all operation modes is the same. Water injection in plasma vessel from the brake terminates ~90 s after the break.

In Fig. 7 the pressure in the affected target during different operation modes are presented. During “normal” and “hot liner” operation modes the pressure in the affected target before the break are bigger comparing to pressure during “baking” operation mode. However after the break pressure decreases and the pressure values in all operation modes are very similar till 80 s after the break. At this moment the pressure in affected target reaches atmospheric pressure and does not fall down. In normal operation mode, 80 s after the break, the pressure continuously decreases. This is related to the pressure in the plasma vessel (Fig. 8). As it is shown in Fig. 8 the pressure in the plasma vessel at “normal” operation mode reaches only ~8 kPa. At this pressure water saturation temperature is ~ 35 °C, so water is not evaporating and pressure is not rising also there is big margin before burst disc activation. The biggest pressure increase rate is observed in the “hot liner” operation mode (Fig. 8), the burst disc is activated 5 s earlier then in the “baking” mode operation. This is due to the bigger discharge through the break into plasma vessel in “hot liner” operation mode (Fig. 6). However calculation showed that during “hot liner” and “baking” operation modes the selected area of burst disks and proposed plasma vessel venting system are sufficient to prevent pressure inside the plasma vessel of simulated 40 mm target cooling pipe rupture.

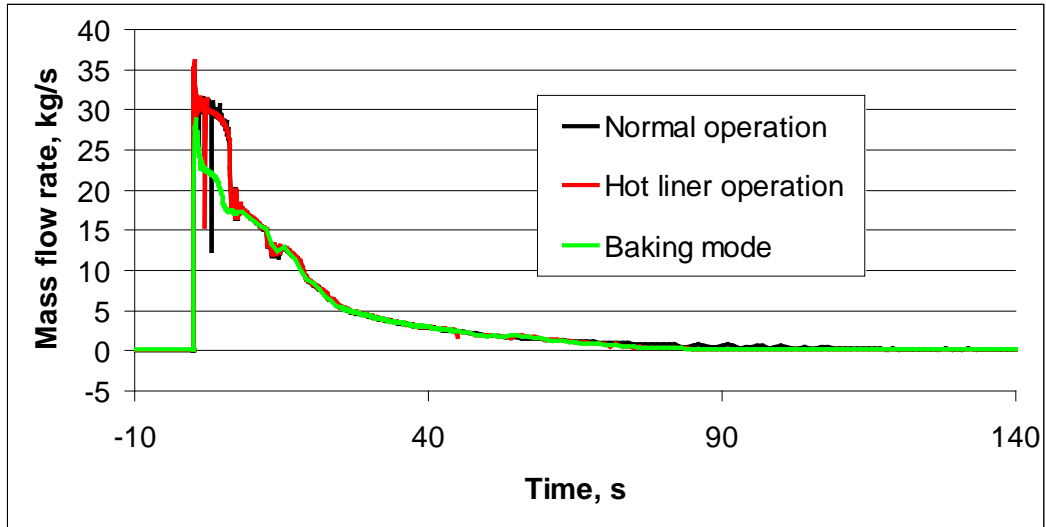


Fig. 6. Water mass flow rate through the break to the plasma vessel during different (“normal”, “hot liner” and “baking”) operation modes

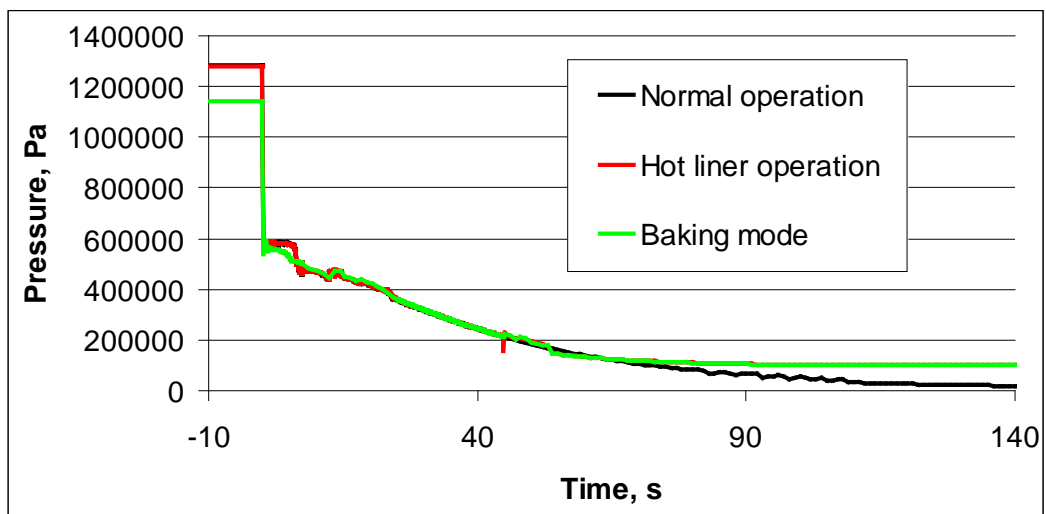


Fig. 7. Pressure in affected target during different (“normal”, “hot liner” and “baking”) operation modes

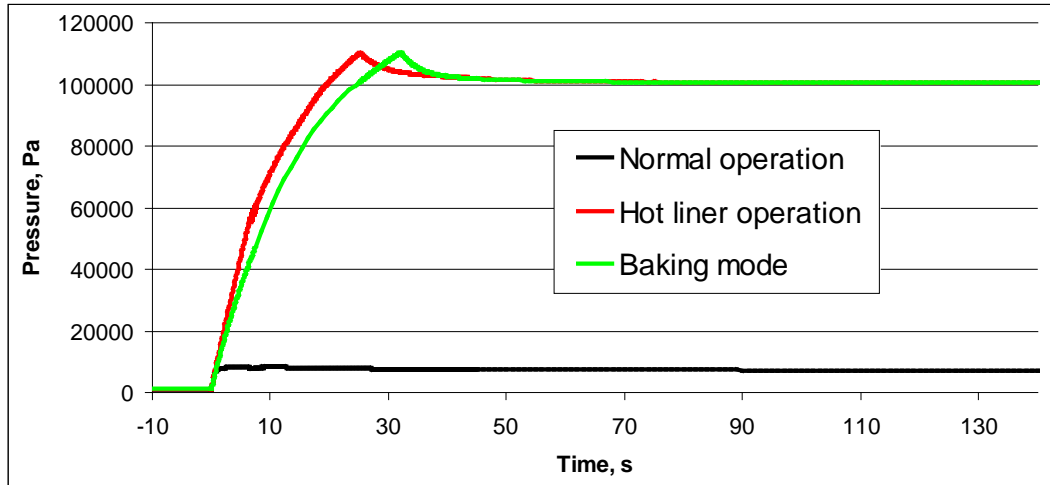


Fig. 8. Pressure in plasma vessel during different (“normal”, “hot liner” and “baking”) operation modes

5. CONCLUSIONS AND SUMMARY

The analysis of accident with water ingress into the plasma vessel in Wendelstein nuclear fusion device W7-X was performed. The rupture of the 40 mm target module cooling pipe (pipe with largest diameter) was selected as one of the critical failure events with loss of coolant, since primary and secondary steam production leads to a rapid increase of the inner pressure in the plasma vessel. To reach this goal the model of W7-X divertors, MCC and “baking” circuits, the plasma vessel and venting system were developed using thermal-hydraulic state-of-the-art RELAP5 Mod3.3 code. The performed analysis of rupture of 40 mm diameter pipe in the single upper horizontal target module during different („baking“, „hot liner“ and „normal“) operation modes demonstrates that the selected area of burst disks and proposed plasma vessel venting system are sufficient to prevent pressure inside the plasma vessel exceeding 110 kPa in the case of simulated accident. The calculation showed that the rupture of the 40 mm target module during „hot liner“ operation mode distinguishes by the biggest amount of discharged hot water through the break to the plasma vessel that leads to the highest pressure increase rate in plasma vessel. The burst disk is opened 26 s after the accident.

The prepared models will be used for further analyses of other accidents to prove the safety of W7-X fusion facility.

REFERENCES

1. BOSCH, H.-S., DINKLAGE, A., KLINGER, T., WOLF, R. and the W7-X Team, *Contributions to Plasma Physics*, 2010.
2. ERCKMANN, V., et al., The W7-X Project: Scientific Basis and Technical Realization, *Proceedings of 17th IEEE/NPSS Symposium on Fusion Engineering*, San Diego, CA, October 6–10, 1997.
3. The WENDELSTEIN 7-X Project: <http://www.ipp.mpg.de/ippcms/eng/for/projekte/w7x/> last checked 2013.
4. STREIBL, B., et al., Manufacturing of the W7-X divertor and wall protection, *Proceedings of 23rd Symposium of Fusion Technology*, Venice, Italy, 2004.
5. TOPILSKI, L., Consequences of the W7X in-vessel coolant pipe break at baking conditions, *Report I-NBF-T0015*, Max-Planck-Institut für Plasma Physik, 2006.



6. KALIATKA, T., KALIATKA, A., KAČEGAVIČIUS, T., NAUJOKS, D., Analysis of the processes in the target cooling system of the W7-X fusion experiment, *Kerntechnik*. ISSN 0932-3902, Vol. 75, Iss. 5, p. 255–263, 2010.
7. KALIATKA, A., USPURAS, E., KALIATKA, T., Pressure surge in Wendelstein 7-X experimental stellarator facility, *Kerntechnik*. ISSN 0932-3902. Vol. 77, No. 2, p. 134–140, 2012.
8. KALIATKA, T., POVILAITIS, M., KALIATKA, A., URBONAVIČIUS, E., Simulation of targets feeding pipe rupture in Wendelstein 7-X facility using RELAP5 and COCOSYS codes, *Journal of Fusion Energy*, ISSN 0164-0313, Vol. 31, No. 5, p. 506–517, 2012.
9. KAČEGAVIČIUS, T., KALIATKA, T., Integral analysis of the W7-X fusion experiment with ASTEC and RELAP5 codes, *8th international conference of young scientists on energy issues (CYSENI 2011)*, LEI, Kaunas, ISSN 1822-7554, p. 449–457, 2011.
10. FLETCHER, C.D., et. al., RELAP5/MOD3 code manual user's guidelines, *Report NUREG/CR-5535*, Idaho National Engineering Lab, 1992.
11. NAUJOKS, D., Initial and Boundary Conditions, *Report 1-NBF-T0008.0*, Max-Planck-Institut für Plasma Physik, 2006.
12. KALIATKA, A., KALIATKA, T., OGNERUBOV, V., KAČEGAVIČIUS, T., Accident analysis and evaluation of consequences for W7-X, Development of model for thermo-hydraulic analysis of processes in W7-X target cooling circuits in “baking” mode, *Report No. S/17-887.7.8-01-V:01*, LEI, Kaunas, 17 July, 2009.



PREPARATION OF EFFECTIVE CROSS-SECTION LIBRARIES FOR CALCULATION OF SPENT NUCLEAR FUEL INVENTORY OF RBMK TYPE REACTORS

V. Barkauskas, A. Plukis

*Center for Physical Sciences and Technology
Savanorių ave. 231, LT-02300 Vilnius – Lithuania*

ABSTRACT

Depletion of RBMK-1500 spent nuclear fuel (SNF) with and without erbium burnable absorber was modelled and one group burnup dependent cross-section libraries for Origen-ARP were created. Calculations were performed using SCALE 6.1 code package. Depletion calculations for generation of cross-section libraries were performed using TRITON control module, which employs NEWT deterministic 2D transport code with 238-group energy library based on ENDF-B VII library and ORIGEN-S nuclide composition calculation code. Fuel irradiation conditions were simulated using 4x4 channels RBMK-1500 reactor lattice with 14 fuel channels and 2 special purpose channels. Cross-section libraries were prepared depleting one fuel bundle while keeping constant average RBMK-1500 reactor fuel burnup in surrounding fuel channels and using different coolant densities. Generated ARP (Automatic Rapid Processing) cross-section libraries may be used for fast burnup inventory modelling used in source term, criticality safety and other calculations. Concentrations of most important isotopes for criticality safety were calculated using these libraries and were compared with the ones of non-erbium fuel values obtained from pre-generated and experimentally validated libraries for RBMK-1000 type reactor available within SCALE 6.1 code package. Initial fuel enrichment was different: 2.4–2.8% of ^{235}U for erbium fuel libraries and 1.8–2.2% of ^{235}U for non-erbium fuel libraries. Composition differences were evaluated for different fuel enrichments and water densities. Evolution differences of most important actinides for both types of libraries were identified.

Keywords: RBMK-1500, nuclear fuel, depletion modelling, burnup credit

1. INTRODUCTION

As both RBMK-1500 reactors of Ignalina nuclear power plant (NPP) are permanently shutdown, one of the most important issues regarding nuclear safety is spent nuclear fuel (SNF) storage. There are about 22000 assemblies of SNF which have to be safely stored until final decision regarding SNF management (reprocessing, disposal, etc.) is made. At present most of the SNF assemblies are stored in SNF pools inside the units, and part of SNF assemblies is stored at existing interim dry type SNF storage facility. This facility contains only 2% ^{235}U initial enrichment uranium assemblies, stored in CASTOR[®]RBMK-1500 and CONSTOR[®]RBMK-1500 type SNF storage casks.

Issues of nuclear safety of SNF storage facilities are ones of the most challenging for Ignalina NPP in decommissioning stage. One of the key elements of safety analysis of these facilities is SNF characterization regarding composition and related activity and neutron emission. These characteristics are needed for solving different problems in the field of nuclear safety analysis. For example in criticality analysis of SNF storage cask taking into account burnup credit, in source term analysis of accidents related with SNF, etc. SNF composition determination using direct or indirect experimental techniques is rather expensive and complicated. Therefore computer simulations are often used to obtain information needed. Results of these calculations have to be validated, i.e. results of calculations of varying complexity should correspond with available experimental knowledge [1].

Only limited experimental data is available for RBMK type reactor fuel [2, 3], especially regarding fuel with erbium burnable absorber, used in Ignalina NPP RBMK-1500 type reactors. Some modelling was recently performed in this area: MCNP and ORIGEN codes were used for



depletion calculations for RBMK-1000 fuel and comparison with experimental data was performed by A. Plukis et al. [4]. RBMK-1500 type reactor SNF depletion calculations and SNF storage cask criticality calculations were performed by A. Šmaižys et al. [5, 6]. Also there were some studies related with Ignalina NPP decommissioning projects [7].

Performing analysis of operational conditions for new SNF storage facility for RBMK-1500 SNF, fresh fuel assumption was used, that is very conservative approach. Tendency of using burnup credit is observable worldwide [1, 8]. Burnup credit application is related with positive economical effect without compromising nuclear safety. Availability of accurate and validated calculation results is essential for possible use of burnup credit in SNF storage facilities analysis. One of the possible ways of taking burnup credit into account is the use of “actinide-only” burnup credit. This approach is less conservative than fresh fuel assumption but more conservative compared to burnup credit calculations taking into account fission products. “Actinide-only” approach reduces unnecessary conservatism and also gives acceptable safety margin in criticality calculations. Actinides used for “actinide-only” calculations may be different in different countries, but most of them are the same [9].

New computational codes, improved computational speed and improved capabilities (e.g. 3D modelling geometry) for burnup analysis allows to evaluate fuel depletion more precisely and to extend the understanding of fuel burnup in the reactor.

In this paper calculations of fuel depletion in RBMK-1500 type reactor were performed and one group cross-section libraries were created for SNF composition calculations. Concentrations of actinides important to burnup credit were calculated for RBMK-1500 erbium fuel and for non-erbium fuel. Different fuel composition comparison was made, taking into account results obtained using experimentally validated RBMK-1000 SNF libraries [10].

2. MODELLING TOOLS AND PROCEDURE

2.1. Calculations codes

SCALE 6.1 code package which is widely used for criticality and burnup calculations to justify safety of various activities in nuclear field was used for calculations. TRITON control module employing NEWT (2D geometry and deterministic calculation method to solve neutron transport equations and calculate neutron flux) and ORIGEN-S (depletion calculations) codes was used to generate cross-section libraries [11]. ENDF/B-VII 238 energy group data library was used for calculations.

ORIGEN-ARP was used to perform point-depletion calculations with the ORIGEN-S code using problem-dependent cross-section libraries which were generated using the ARP (Automatic Rapid Processing) module. ARP utilises an interpolation algorithm that operates on prepared libraries created during aforementioned depletion calculations [12].

ARP reads the prepared libraries and interpolates a problem-dependent library for ORIGEN-S using defined parameters. This procedure simplifies and accelerates calculations. There are number of prepared cross-section libraries available within SCALE for different reactors and fuels. Library for RBMK-1000 fuel depletion modelling is also available, however there are no libraries for erbium fuel used in RBMK-1500 type reactors. Results (concentration and absorption fractions) for library analysis were obtained using ORIGEN-ARP module.

2.2. Model

Geometrical model of RBMK-1500 reactor core was created assuming several simplifications in order to achieve acceptable calculation time. 2D model (see section of the model in Fig. 1) of the RBMK-1500 reactor core fragment consists of 14 fuel channels with fuel assemblies and 2 CPS (Control and protection system) channels with control rods, distributed in accordance to the real

distribution of fuel and CPS channels in the RBMK-1500 reactor core. RBMK-1500 fuel assembly consists of 2 fuel bundles each of them has 18 fuel rods arranged in two concentric rings with central carrier rod at the centre. Fuel rod was treated as zirconium alloy tube homogeneously filled with uranium dioxide with or without burnable erbium absorber. Pellet density was reduced to ensure that amount of fuel material inside the tube corresponds to real conditions. Central carrier rod was defined as hollow tube made from zirconium alloy. Triangular pitch with half-pitch $h = 0.802$ cm was chosen for lattice cell parameters to assist self-shielding calculations [13]. For self-shielding calculations water as a moderator was selected. Periodical boundary conditions were applied for reactor segment walls, which corresponds to an infinite lattice comprised of such segments and is suitable for modelling of neutron fluxes in the RBMK-1500 reactor core. Inserted CPS rod with neutron absorber B_4C was used. This assumption was made for both CPS channels, B_4C was chosen as absorber used in original design of RBMK.

The power of the fuel assembly was chosen to be constant. The graphite and cooling water temperatures were kept equal to 873 K and 567 K, respectively, which correspond to the real operating conditions of the RBMK-1500 reactor [14]. The density of the cooling water in the model was changed from 0.2 g/cm^3 to 0.8 g/cm^3 and density of graphite was 1.675 g/cm^3 .

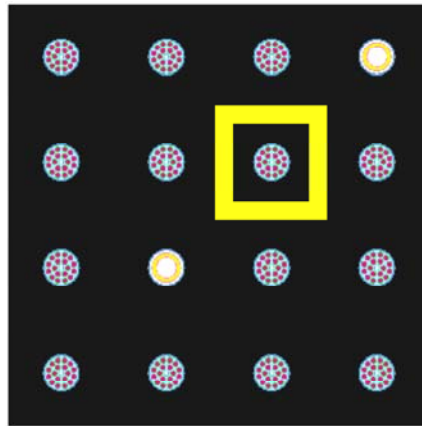


Fig. 1. RBMK-1500 reactor lattice with fuel (14) and CPS (2) channels. Fuel assembly in marked channel was used for depletion calculations to obtain cross-section libraries

2.3. Preparation of cross-section libraries

Depletion calculations for cross-section libraries preparation consisted of two steps. First step was depletion of fresh fuel in all fuel channels to average burnup (12 GWd/tU). Second step was depletion of fuel in one fuel channel (marked channel in Fig. 1) while constant composition (set of 100 nuclides consisting of initial fuel material, activation and fission products) taken from first step calculations and corresponding to average fuel burnup was kept in remaining fuel channels. The neutron fluxes were calculated by NEWT module using three 160 day time steps (power was kept constant: 25 MW/tU) for first step calculations. Second step calculations were performed using 100 day time step (except for first step, as for preparation of cross-section libraries for ORIGEN-ARP 10^{-15} day first time step is recommended by SCALE developers), keeping constant 25 MW/tU power up to 30 GWd/tU burnup. The same procedure was applied for non-erbium fuel with 2% enrichment and 2.4% (with 0.41% mass of Er_2O_3 burnable absorber), 2.6% (0.5% Er_2O_3) and 2.8% (0.6% Er_2O_3) enrichment fuel with erbium burnable absorber. Uranium isotopic composition was chosen with constant ^{234}U content (0.005%), ^{238}U content was determined by ^{235}U enrichment which was specified before (2.0%, 2.4%, 2.6%, 2.8%). Natural erbium isotopic composition was used for calculations (1.7% ^{164}Er , 33.4% ^{166}Er , 22.9% ^{167}Er , 26.9% ^{168}Er , 15.1% ^{170}Er).

Table 1. Irradiation and composition data for Sample 20 and Sample 26 [10]

	Sample 20	Sample 26
Coolant density	0.45	0.76
Burn (days)	278	1281
Power (MW/t)	20.91	16.69
Burnup (GWd/t)	5.81	21.38
^{234}U (g/g ^{238}U)	$1.506 \cdot 10^{-4}$	$1.117 \cdot 10^{-4}$
^{235}U (g/g ^{238}U)	$1.410 \cdot 10^{-2}$	$3.527 \cdot 10^{-3}$
^{236}U (g/g ^{238}U)	$1.213 \cdot 10^{-3}$	$2.792 \cdot 10^{-3}$
^{237}Np (g/g ^{238}U)	$2.970 \cdot 10^{-5}$	$1.913 \cdot 10^{-4}$
^{238}Pu (g/g ^{238}U)	$1.465 \cdot 10^{-6}$	$4.611 \cdot 10^{-5}$
^{239}Pu (g/g ^{238}U)	$1.615 \cdot 10^{-3}$	$2.429 \cdot 10^{-3}$
^{240}Pu (g/g ^{238}U)	$3.441 \cdot 10^{-4}$	$1.982 \cdot 10^{-3}$
^{241}Pu (g/g ^{238}U)	$7.681 \cdot 10^{-5}$	$5.976 \cdot 10^{-4}$
^{242}Pu (g/g ^{238}U)	$7.067 \cdot 10^{-6}$	$3.815 \cdot 10^{-4}$
^{243}Am (g/g ^{238}U)	$5.121 \cdot 10^{-7}$	$3.763 \cdot 10^{-5}$

3. RESULTS AND DISCUSSION

Depletion of RBMK-1500 non-erbium nuclear fuel with 2% ^{235}U enrichment and with 2.4%, 2.6% and 2.8% enrichment fuel with erbium burnable absorber was modelled and one group burnup and water density dependent cross-section libraries for Origen-ARP were created using procedure described above.

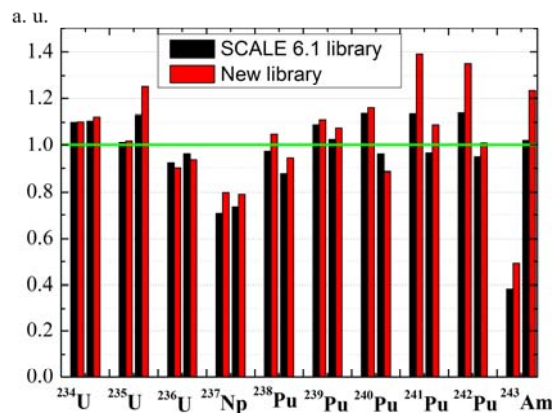


Fig. 2. New library and SCALE library comparison with experimental data for 2% enrichment RBMK fuel: calculated and experimental concentrations ratio of actinides important for burnup credit. Left pair of columns represents Sample 20 and right pair of columns represents Sample 26

In order to ensure, that calculation results with created model are acceptable and created libraries correspond to libraries available with SCALE and with experimental data, comparison with two cases was performed. These two cases represent two sets of experimental data of two samples destructive analysis – Sample 20 and Sample 26. Data of these samples (see Table 1) was taken from [10].

Sample 20 provides data for relatively low burnup (5.81 GWd/t) SNF, while Sample 26 for relatively high burnup (21.38 GWd/t) RBMK-1000 fuel. ORIGEN-ARP calculations were performed using irradiation conditions given for Sample 20 and Sample 26. RBMK-1000 and RBMK-1500 reactor and fuel assembly designs are in principle the same therefore we assume, that depletion results should be similar, for the same type of fuel and irradiation conditions.

Comparison was performed between calculated and experimentally measured concentrations expressed as grams of certain isotope per gram of ^{238}U . Ratios of calculated concentrations using different libraries and experimental results are given in Fig. 2.

Left pair of columns represents Sample 20 irradiation conditions and right pair of columns represents Sample 26 irradiation conditions. Differences between two libraries are not significant, highest differences are observable for plutonium isotopes at low burnup. Newly created library gives overestimated concentration for ^{235}U at high burnup. Results of comparison show that predicted concentrations of fissile isotopes are higher than measured, i.e. created model gives conservative results. It is possible to claim, that this model is valid, and modelling results are acceptably accurate compared to the experimental data.

Next step was comparison of concentrations of important for burnup credit actinides for different fuel types (see Fig. 3).

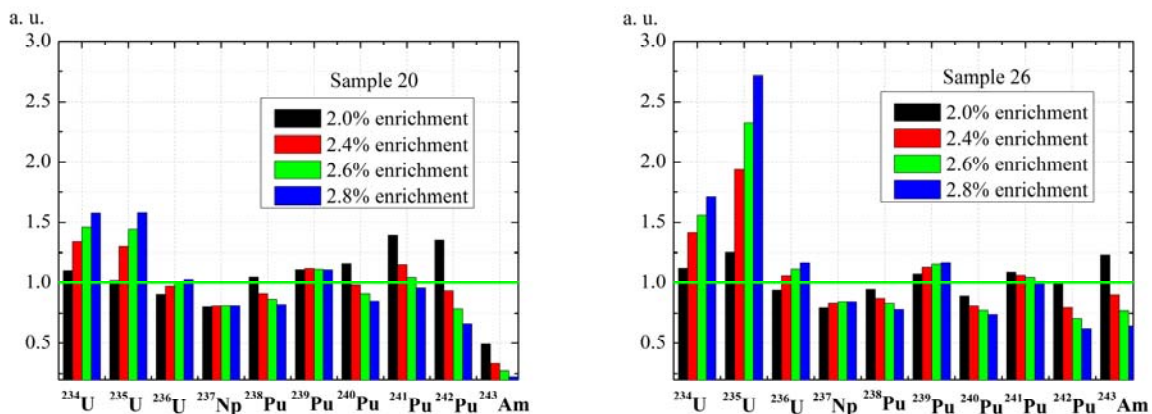


Fig. 3. Comparison of actinides important for burnup credit concentrations for different enrichment RBMK fuel: calculated and experimental (for 2% enrichment fuel only) concentrations ratios for Sample 20 and Sample 26 irradiation conditions

The comparison was performed in previously described manner, plotting ratios of modelled and experimental concentrations for Sample 20 and Sample 26. This is the convenient way to perform comparison between different isotopes concentrations which may differ by several orders of magnitude. Largest differences for different fuel types are observable for ^{235}U isotope. Difference is proportional to different initial enrichment, so this is due to the fact that while calculating concentrations ratio 2.4–2.8% enriched fuel data was used in numerator and 2% enriched fuel data – in denominator. Also it may be seen, that buildup of plutonium isotopes other than ^{239}Pu decreases with increasing erbium content in the fuel. Calculations show that buildup of ^{239}Pu and ^{237}Np is almost independent from fuel type.

In order to identify which elements are the most important for burnup credit application, neutron absorption fractions were calculated for Sample 20 and Sample 26 irradiation conditions (see Fig. 4).

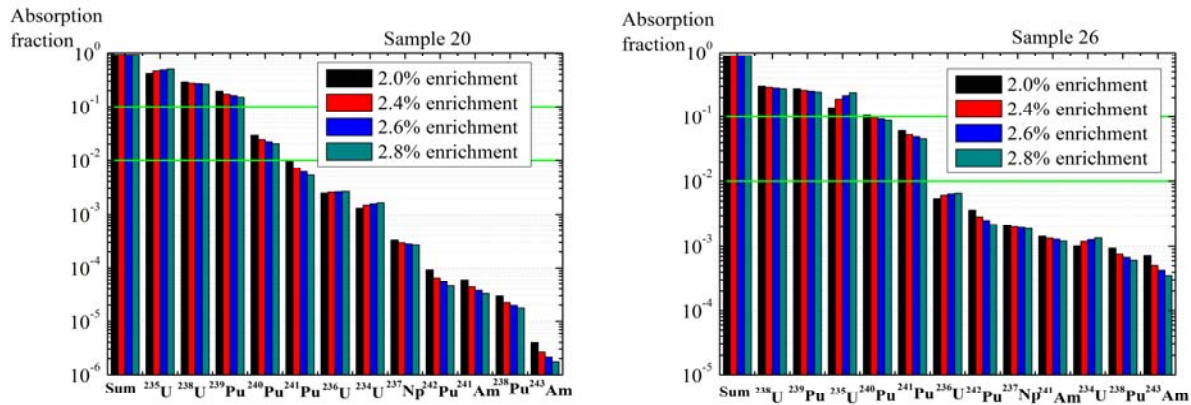


Fig. 4. Calculated neutron absorption fraction of different actinides important for burnup credit for different enrichment RBMK SNF for Sample 20 and Sample 26 irradiation conditions. Green lines represent values 0.1 and 0.01

It may be seen that importance of isotopes is different depending on burnup. For lower burnup SNF (Sample 20) most absorbing isotope is ^{235}U , and for higher burnup – ^{238}U and ^{239}Pu . Initial enrichment also plays role in this case – higher initial enrichment increases absorption of ^{235}U . Also for higher burnup fuel, importance of other actinides increases by several orders of magnitude, but most of these actinides are responsible for less than 1% of absorptions.

Further the evolution of absorption was evaluated for 2% and 2.8% (limiting cases) enrichment fuel and for different irradiation conditions (Fig. 5 and 6). This data is useful evaluating SNF characteristics for repositories, because significant changes in concentrations of actinides important for burnup credit calculations are observable only in scale of hundred years.

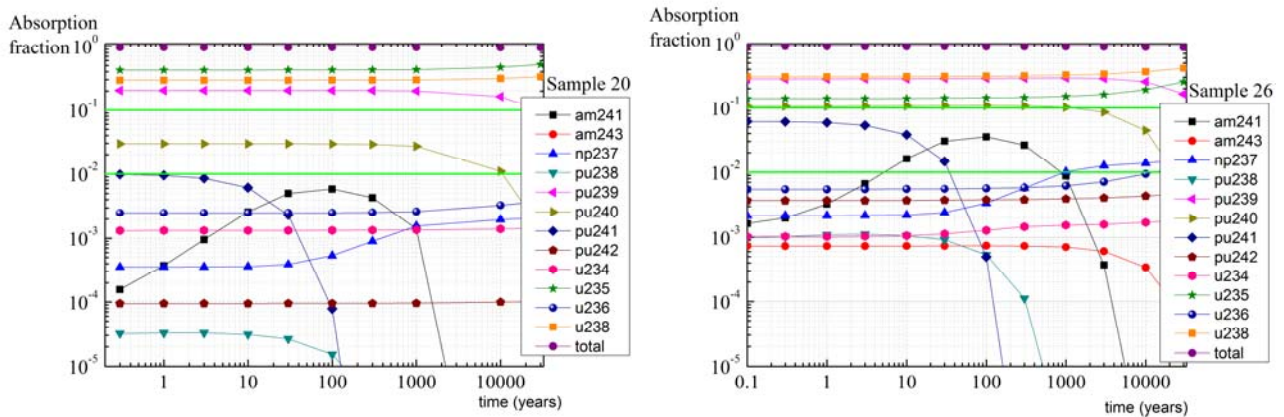


Fig. 5. Neutron absorption fraction of different actinides important for burnup credit for 2% enrichment RBMK non-erbium fuel for Sample 20 and Sample 26 irradiation conditions. Green lines represent values of 0.1 and 0.01

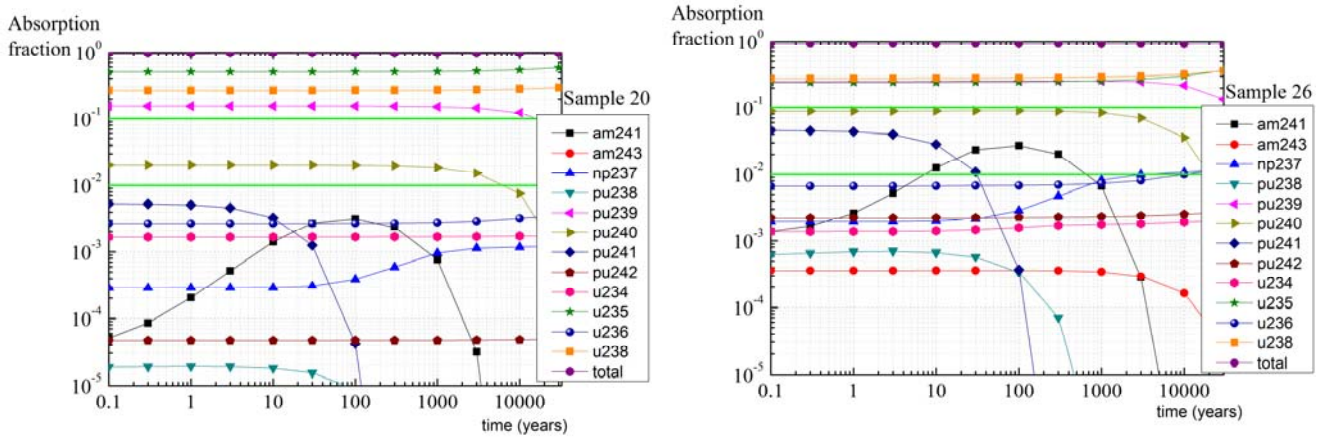


Fig. 6. Neutron absorption fraction of different actinides important for burnup credit for 2.8% enrichment RBMK erbium fuel for Sample 20 and Sample 26 irradiation conditions. Green lines represent values of 0.1 and 0.01

Additionally, cross-section libraries were created using different water densities in the channel to take into account possible real coolant densities in the reactor. Comparison of concentrations calculated for different water densities was performed in order to evaluate the influence of coolant density on SNF composition. Results are given in Fig. 7 (for 2% enrichment fuel) and Fig. 8 (for 2.8% enrichment fuel). Results show that higher water density during operation and higher erbium burnable absorber content reduce buildup of plutonium isotopes, except ^{239}Pu which is almost not affected by water density. This seems to be due to increased absorption of thermal neutrons, but to confirm this more detailed spectral analysis is needed. Generally water density plays an important role on actinide build up. Also burnup of ^{235}U isotope for 2.8% enrichment fuel is lower for fuel with higher burnup.

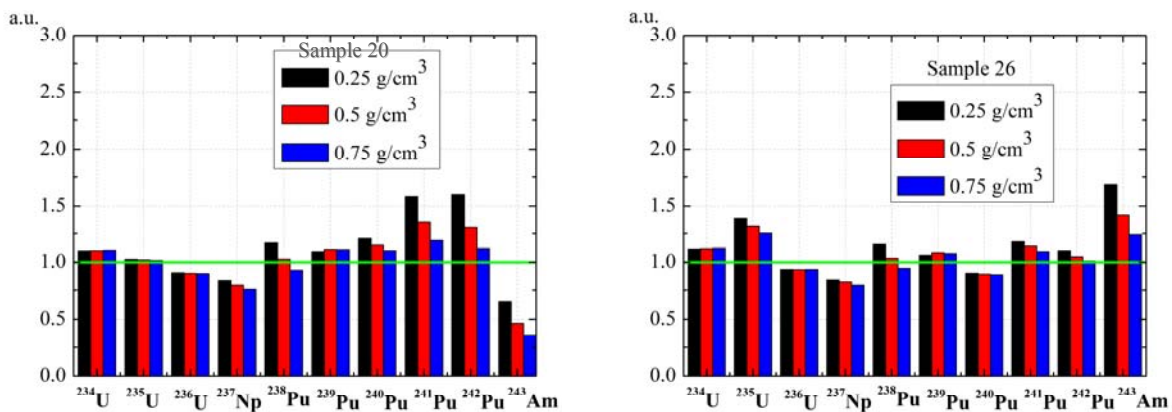


Fig. 7. Comparison of actinides concentrations of irradiated RBMK 2% enrichment non-erbium fuel for different water densities during operation in the reactor: calculated and experimental concentrations ratio for Sample 20 and Sample 26 irradiation conditions

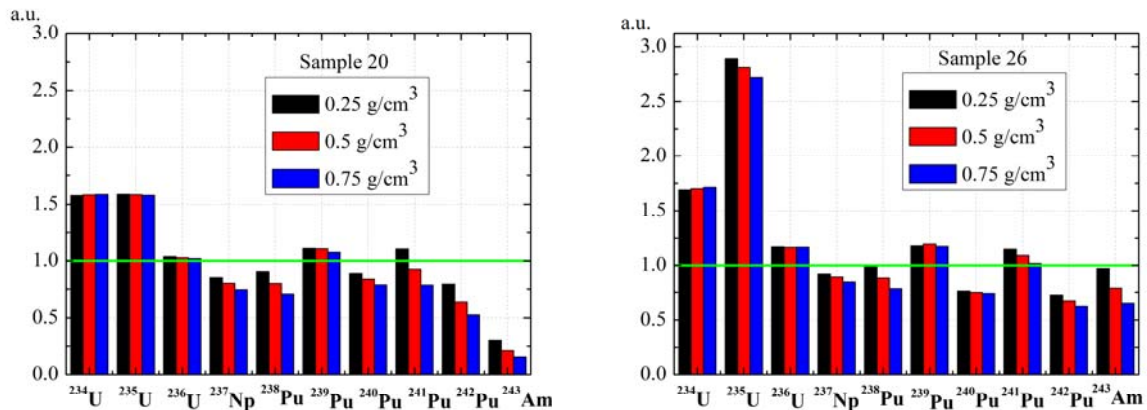


Fig. 8. Comparison of actinides concentrations of irradiated RBMK 2.8% enrichment erbium fuel for different water densities during operation in the reactor: calculated and experimental (for 2% enrichment fuel only) concentrations ratio for Sample 20 and Sample 26 irradiation conditions

4. CONCLUSIONS

Depletion of RBMK-1500 nuclear fuel was modelled and one group burnup dependent cross-section libraries for Origen-ARP were created.

Concentrations of actinides important for burnup credit analysis were calculated using these libraries and were compared with values obtained from experimentally validated libraries for RBMK-1000 type reactor available within SCALE 6.1 code package. Comparison show acceptable agreement between values obtained from libraries available with SCALE and prepared libraries for 2% enrichment fuel without erbium. Most important isotopes for RBMK-1500 „actinide-only“ burnup credit analysis were identified evaluating neutron absorption in the SNF, quantitative values of the isotopes importance changes with fuel burnup. Change of water density in the fuel channel during operation plays an important role on actinide buildup. Due to the lack of experimental information of SNF with erbium burnable absorber, cross-section libraries still needs further validation.

REFERENCES

1. *Spent Nuclear Fuel Assay Data for Isotopic Validation*, NEA State of the art Report, OECD (2011).
2. MAKAROVA, T.P., BIBICHEV, B.A., DOMKIN, V.D. Destructive Analysis of the Nuclide Composition of Spent Fuel of WWER-440, WWER-1000, and RBMK-1000 Reactors, *Radiochemistry*, 2008, Vol. 50, No. 4, p. 414–426.
3. KORENKOV, A.G., MAKAROVA, T.P., STEPANOV, A.V., PEVTSOVA, E.V., BELYAEV, B.N., VORONKOV, A.A. Destructive Analysis Determination of Neutron Emission from Spent RBMK Fuel, *Atomic Energy*, 2002, Vol. 93, No. 4, p. 815–822.
4. PLUKIS, A., PLUKIENĖ, R., REMEIKIS, V., RIDIKAS, D. MCNP and ORIGEN codes validation by calculating RBMK spent nuclear fuel isotopic composition, *Lithuanian Journal of Physics*, 2005, Vol. 45, No. 4, p. 281–287.
5. ŠMAIŽYS, A., POŠKAS, P. Possibility for BUC implementation in RBMK-1500 fuel dual purpose storage casks, *Practices and developments in spent fuel burnup credit applications: Proceedings of a Technical Committee meeting held in Madrid, 22–26 April 2002*, IAEA Tecdoc-1378.



6. ŠMAIŽYS, A. Analysis of nuclear and radiation characteristics of RBMK-1500 spent nuclear fuel casks and storage facilities, *PhD thesis*, 2004, Kaunas.
7. *Interim Storage of RBMK Spent Nuclear Fuel from Ignalina NPP Units 1 and 2*, Environmental Impact Assessment Report, Consortium GNS – NUKEM, Lithuanian Energy Institute, 2007.
8. *Advances in Applications of Burnup Credit to Enhance Spent Fuel Transportation, Storage, Reprocessing and Disposition*: Proceedings of a Technical Meeting held in London, 29 August – 2 September 2005, IAEA Tecdoc-1547.
9. *Topical Report on Actinide-Only Burnup Credit for PWR Spent Nuclear Fuel, Rev. 2*, 1998, DOE Office of Civilian Radioactive Waste Management.
10. MURPHY, B. D. *ORIGEN-ARP Cross-Section Libraries for the RBMK-1000 System*, 2006, Prepared by Oak Ridge National Laboratory.
11. DEHART, M., D. *Triton: a two-dimensional transport and depletion module for characterization of spent nuclear fuel*, 2009, Prepared by the Oak Ridge National Laboratory.
12. BOWMAN, S. M., GAULD, I. C. *OrigenArp Primer: How to Perform Isotopic Depletion and Decay Calculations with SCALE/ORIGEN*, 2010, Prepared by the Oak Ridge National Laboratory.
13. PLUKIENĖ, R., PLUKIS, A., GERMANAS, D., REMEIKIS, V. Numerical sensitivity study of irradiated nuclear fuel evolution in the RBMK reactor, *Lithuanian Journal of Physics*, 2009, Vol. 49, No. 4, p. 461–469.
14. ALMENAS, K., KALIATKA, A., UŠPURAS, E. *Ignalina RBMK-1500. A source book*, 1998, Lithuanian Energy Institute.



INFLUENCE OF POROUS MEDIUM PERMEABILITY ON GAS MIGRATION IN THE DISPOSAL TUNNEL OF CONCEPTUAL GEOLOGICAL REPOSITORY

D. Justinavičius

*Laboratory of Nuclear Engineering
Lithuanian Energy Institute
Breslaujos str. 3, LT-44403 Kaunas – Lithuania*

ABSTRACT

The long-term safety of the disposal of nuclear waste is a crucial issue for most of countries worldwide. Repositories for the disposal of high-level and long-lived radioactive waste generally rely on a multi-barrier system projected for the waste isolation from the biosphere. The multi-barrier system comprises the natural geological barrier provided by the repository host rock and an engineered barrier system, i.e. engineered materials placed within a repository, including the waste form, waste canisters, backfill and seals. Most recent studies have revealed that in such conditions significant amounts of gas are expected to be produced due to the corrosion of metallic components (e.g. steel linings, waste containers) used during the implementation of the repository. Gas generation will continue for a long period after the repository closure. The accumulation of the gas may lead to a significant desaturation and unacceptable build-up of gas pressure in the disposal tunnels if the gas cannot escape through the low-permeability host rock.

While modelling the complex behaviour of geological disposal system some uncertainties related to physical parameters could arise. In order to optimise the further research the sensitivity analysis is performed usually. The objective of sensitivity analysis is to rank the input parameters with respect to their importance to the gas transfer and how they affect the output indicators. In this paper the influence of intrinsic permeability coefficient in geological repository materials on peak pressure and gaseous/dissolved hydrogen flux out of disposal system was investigated. Numerical modelling of gas migration in single disposal tunnel of repository situated in the clay rock was performed by computer code PETRASIM (USA).

Keywords: Gas migration modelling, geological repository, intrinsic permeability, sensitivity analysis

1. INTRODUCTION

Gas influence on the long-term safety of geological repositories has been investigated for almost fifteen years. EVAGAS [1], MEGAS [2], PEGASUS [3], GASNET [4], PAMINA [5] and FORGE [6] are the international projects which were held to investigate gas problem in the perspective of geological repository safety. During these investigations it was established that radioactive waste and their disposal packages (steel canisters), as well as reinforcement steel used in the construction of the repository, are the principal sources of gas generation. Among four possible ways of gas generation (corrosion of metal components, microbial degradation, radiolysis and radioactive decay), anaerobic corrosion of the steel components in the engineered barrier system (EBS) is a dominant source of hydrogen gas. The impact on the geological repository long-term safety could be grouped into categories according to the type of effect caused by the generation of gas: (a) the mechanical effects on repository and rock structures caused by the pressure build-up that may follow if gas cannot escape through the low-permeability host rock in dissolved state (disruption of the EBS, fracturing of the host rock), (b) the direct effect of gas on groundwater flow around the repository (induced groundwater flow, forcing of contaminated water from the repository or canisters, transport associated with bubbles), (c) the release of volatile radionuclides and toxic gas up to the biosphere.

Lithuanian energy institute (LEI) participated in numerical modelling section of recent EU-FP7 project FORGE. Investigations carried out within this project were concentrated on the analysis

of generated gas behaviour in the geological repository. Two benchmark exercises – at cell scale (single disposal tunnel) and at module scale (50 inter-connected disposal tunnels) – were analyzed. LEI results of the first exercise (reference case¹ and some sensitivity cases) are already presented in [8, 9 and 10]. In this paper additional sensitivity analyses – influence of intrinsic permeability coefficient in geological repository materials on peak pressure and gaseous/dissolved hydrogen flux out of disposal tunnel is investigated.

2. TASK DEFINITION

To be able to understand water and gas flow at the repository scale it is necessary to understand water and gas flow at cell scale (e.g. on the scale of a tunnel). The type of cell considered [7] is a generic high-level waste (HLW) cell in a clay host rock (Fig. 1). According to this concept, HLW canisters 2 are transported by shafts down to the main tunnel at 500 m depth below ground level, from which they are transported by access drifts 7 to the disposal cell situated in the clay rock 1. The HLW canisters are placed in these cells one after another and finally they are sealed with bentonite plug 5. As the diameter of disposal cell is slightly more than diameter of HLW canisters, there are thin engineered gaps 3, 4 between the HLW and engineered disturbed zone (EDZ) 6 and between the bentonite plug and EDZ after the placement of the canisters. During the operational phase of the repository, shafts, main tunnel and drifts are ventilated. The undisturbed clay and the EDZ are depressurized and desaturated. After the emplacement of the HLW canisters, the access drift, main tunnel and shafts are backfilled with the mixture of crushed rock and compacted bentonite. Then resaturation of the clay rock and backfill materials starts. At the same time the corrosion of steel canisters causes hydrogen to be generated in the repository.

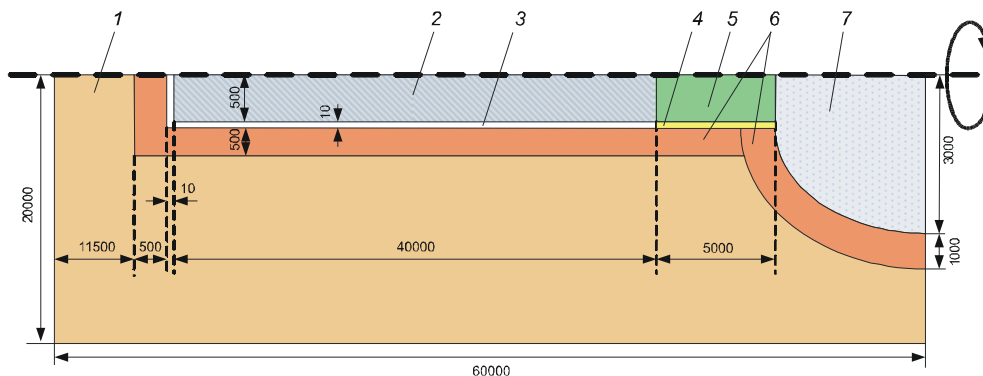


Fig. 1. Conceptual model of disposal tunnel: 1 – clay rock; 2 – HLW canisters; 3 – interface between HLW canisters and EDZ; 4 – interface between bentonite plug and EDZ; 5 – bentonite plug; 6 – EDZ; 7 – access drift

The objective of this exercise is to model gas migration in single disposal tunnel. The following questions concerning long term behaviour of the system should be answered: (a) what is the peak pressure expected in disposal cell during the gas generation phase and could this pressure affect the mechanical stability of the repository, (b) what are the main migration pathways for gaseous/dissolved hydrogen.

3. METHODOLOGY

3.1. Modelling tool

Gas transport modelling was performed with original version of TOUGH2 [11] code using PETRASIM [12] as the graphical interface. The TOUGH2 is a numerical simulator for

¹ Case with base values of parameters (proposed in FORGE benchmark specification [7])

nonisothermal flows of multicomponent, multiphase fluids in one, two and three-dimensional porous and fractured media. The EOS5 fluid property module was selected for the description of the thermodynamics of hydrogen gas.

Fluid flow in the repository involves multiphase transient flow processes. For gas flow, a mixture of gases is evolved from corrosion, with hydrogen being the main constituent. In this study all the gases are treated as hydrogen. Hydrogen dissolution in the pore-water follows Henry's law. Gas and water flow are governed by a multiphase extension of Darcy's law:

$$V_{\beta} = -\frac{kk_r^{\beta}(S_{\beta})}{\mu_{\beta}}(\nabla P_{\beta} + \rho_{\beta}g\nabla z), \quad (1)$$

where β denotes the phase of the fluid (aqueous or gaseous), k is the intrinsic permeability [m^2], k_r^{β} is relative permeability for phase β , S_{β} is saturation level for phase β , μ_{β} is dynamic viscosity of the fluid [$\text{kg}\cdot\text{m}^{-1}\cdot\text{s}^{-1}$], P_{β} is the phase pressure [Pa], ρ_{β} is the fluid density [$\text{kg}\cdot\text{m}^{-3}$], g is acceleration of gravity [$\text{m}\cdot\text{s}^{-2}$], z is the altitude [m], and V_{β} is Darcy's velocity for phase β [$\text{m}\cdot\text{s}^{-1}$].

Diffusion processes in the gas and water phases are described by Fick's Law. The diffusive flux for the binary mixture of hydrogen and water vapour f^g [$\text{kg}\cdot\text{m}^{-2}\cdot\text{s}^{-1}$] can be written as:

$$f^g = \rho_g D_{H_2}^g \nabla X_{H_2}^g, \quad (2)$$

where g represents the gas phase, $D_{H_2}^g$ is the diffusion coefficient of hydrogen in the water vapour [$\text{m}^2\cdot\text{s}^{-1}$], and $\nabla X_{H_2}^g$ is the gradient of mass fraction of hydrogen gas [m^{-1}].

The diffusive flux for the dissolved hydrogen f^w [$\text{kg}\cdot\text{m}^{-2}\cdot\text{s}^{-1}$] is written as:

$$f^w = \rho_w D_{H_2}^w \nabla X_{H_2}^w, \quad (3)$$

where w represents the liquid phase, $D_{H_2}^w$ is the diffusion coefficient of hydrogen in the water [$\text{m}^2\cdot\text{s}^{-1}$], and $\nabla X_{H_2}^w$ is the gradient of mass fraction of dissolved hydrogen [m^{-1}].

The TOUGH2 solves mass-balance equations by the integrated finite difference method. The equations are set up by combining mass balance, advection flux and diffusion flux, and solved by supplementing with a number of constitutive equations.

3.2. Numerical model

The numerical model representing the system being analyzed was developed according to the given technical specification [7], that defines model geometry, description of physical processes and their mathematical expression, characteristic of materials and the initial and boundary conditions.

As most of the materials in this exercise are of very low permeability, the capillary process will be dominant over the gravity. Therefore two-dimensional symmetric disposal cell model in cylindrical r-z system was analyzed. As the scale is quite small (few tens of meters) it is possible to represent fine geometric features and especially the interfaces. Both interfaces considered as centimetre-thick regions and are represented with one layer of grid elements. The modelling domain was meshed with 4.836 rectangular grid elements and is refined in engineered materials due to higher gradients of the physical variables and a finer result resolution required.

The radioactive waste canisters are constituted of a material impermeable to both liquid and gas flow and are not explicitly represented in the model. Gas transport analysis is considered to be isothermal with a constant temperature of 20 °C, i.e. residual heat removal from canisters is neglected. The gas source term (100 mol/year/disposal cell) is represented by a simple step function

covering 10.000 years. In the numerical model it is assumed that hydrogen gas is injected directly into interface between the canisters and EDZ. The outer radial boundary condition (constant water pressure) and the condition on the boundary of the access drift (time varying gas pressure and gas saturation) are implemented precisely as they are described in specification. All other boundary conditions are designated as no-flow (Fig. 2).

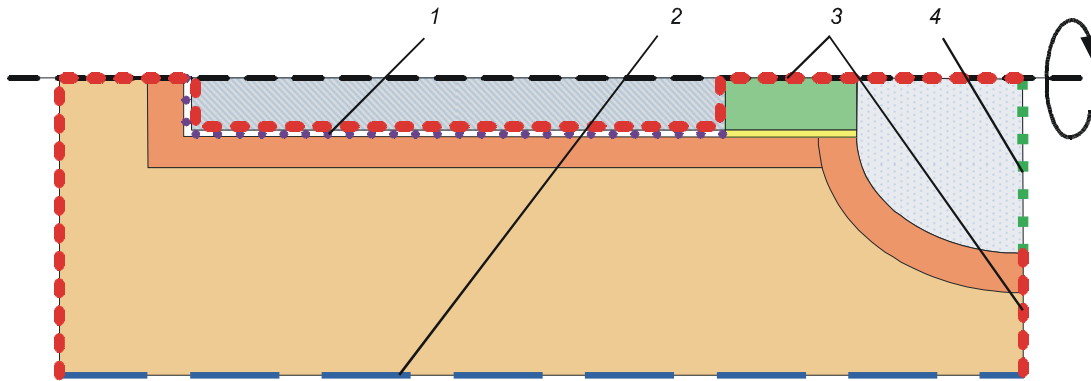


Fig. 2. Schematic representation of boundary conditions: 1 – hydrogen gas injection area; 2 – constant water pressure; 3 – no flow boundary conditions; 4 – time varying boundary conditions

It is assumed that initially gas saturation is 30% in the bentonite plug and the access drift and 95% in both interfaces. The remaining part of modelling domain is fully water saturated. Initial groundwater pressure is set to be 5 MPa in all fully water saturated parts of the model (according to a continuous formulation, the gas and water pressures are the same if there only dissolved gas appears). In parts of the model that initially is not fully water saturated, gas pressure is set to be 0.1 MPa. In this case water pressure is in capillary equilibrium with the gas pressure and is deduced from the gas pressure and the saturation by applying van Genuchten model associated with each material.

3.3. Input data for sensitivity analysis

In this paper the influence of intrinsic permeability coefficient k in geological repository materials on peak pressure and gaseous/dissolved hydrogen flux out of disposal system is investigated. Coefficient k selected because it is one of the most uncertain parameter in analyzed system according to the experimental data. Uncertainties of intrinsic permeability coefficient in four different materials (disturbed and undisturbed host rock and both interfaces) are analyzed. Table 1 provides the nominal, maximal and minimal values of intrinsic permeability coefficient for selected materials used in sensitivity analysis. Nominal (reference) values are defined in benchmark specification. Maximal and minimal values are settled from [13]:

Table 1. Values of intrinsic permeability coefficient for sensitivity analysis

Parameter	Material	Intrinsic permeability coefficient k (m^2)		
		Nominal value	Maximal value	Minimal value
k_{rock}	Undisturbed clay rock	$1 \cdot 10^{-20}$	$1 \cdot 10^{-19}$ (S1)	$1 \cdot 10^{-21}$ (S2)
k_{EDZ}	Disturbed clay rock (EDZ)	$1 \cdot 10^{-17}$	$1 \cdot 10^{-16}$ (S3)	$1 \cdot 10^{-18}$ (S4)

Parameter	Material	Intrinsic permeability coefficient k (m^2)		
k_{int1}	Interface between HLW canisters and EDZ	$1 \cdot 10^{-15}$	$1 \cdot 10^{-13}$ (S5)	$1 \cdot 10^{-17}$ (S6)
k_{int2}	Interface between bentonite plug and EDZ	$1 \cdot 10^{-17}$	$1 \cdot 10^{-16}$ (S7)	$1 \cdot 10^{-18}$ (S8)

As solution of the exercise requires long computation time, local (deterministic) sensitivity analysis was performed. It means that only one parameter is varying simultaneously. Due to this eight cases (S1–S8) were analysed additionally to the reference case (using nominal k values in all materials).

4. RESULTS AND DISCUSSIONS

The simulation time was limited up to 100.000 years after repository closure. The results obtained using nominal values of intrinsic permeability coefficient were summarized as: (1) observed peak pressure was 5.71 MPa within modelled domain; (2) significant levels of gas saturation were reached in the interfaces, minor amount of free gas concentrates in access drift and some parts of the EDZ, and very small amount of free gas was detected in undisturbed clay rock; (3) a big amount of generated hydrogen (1.694 kg out of 2.000 kg) was flowing toward the access drift (through surface S_{cell}) and major part of this hydrogen (1.617 kg) was flowing over very thick interface (surface S_{int1}). As hydrogen arrived to the plug interface, which permeability is much lower (equal to permeability of the EDZ), part of this hydrogen (990 kg) was flowing through plug interface (surface S_{int2}). Remaining part (472 kg out of 1.462 kg) of hydrogen was flowing toward the drift over the EDZ. Overall, 73% of generated hydrogen was transported from disposal cell toward the access drift in gaseous form while remaining part dissolved in pore-water and transported out of the system over radial boundary (surface S_{out}) (Fig. 3).

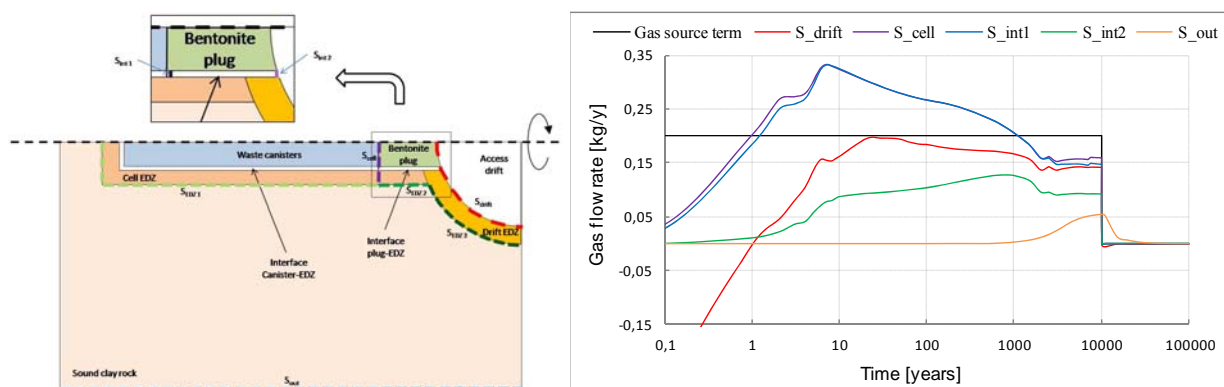


Fig. 3. Comparison of gas flow rate through different surfaces

Observed peak pressure over all analyzed cases was compared using tornado chart, which shows relative importance of variable on the evaluation results. It could be seen (Fig. 4) that pressure increases by 0.52–1.55 MPa from initial groundwater pressure (5 MPa). In most of cases, the peak pressure was achieved in waste interface by the end of gas generation (after 10.000 years). In all cases peak pressure does not exceed allowed (lithostatic) pressure which is ~10 MPa in this repository concept. Thus mechanical effects on repository and rock structures caused by the pressure build-up that may follow from gas generation are not presumable.

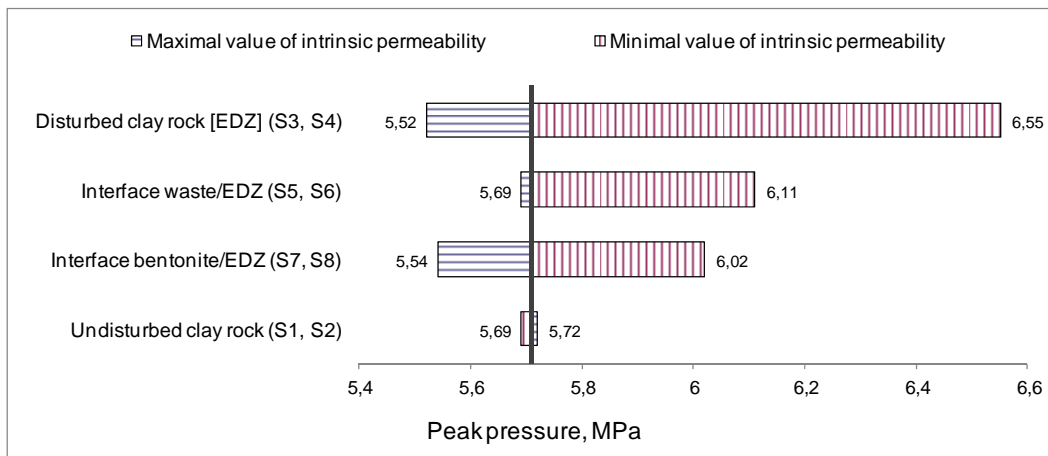


Fig. 4. Comparison of peak pressure in the system for all analysed cases

The highest peak pressure (6.55 MPa) was determined in the case of less permeable EDZ (*S4*). Also higher peak pressure in comparison to reference case was achieved using minimal value of intrinsic permeability coefficient k in both interfaces (*S6*, *S8*). In cases of maximal value of k in interfaces and EDZ (*S3*, *S5*, *S7*), lower peak pressure were determined in comparison with reference case. It is important to notice that changes of permeability coefficient in undisturbed clay rock (*S1*, *S2*) have minor impact on peak pressure. Obtained results confirm the fact, that interfaces and EDZ are primary pathways for gas migration in analyzed system. Increased permeability in this media accelerates gas transport and determines pressure reduction while lower permeability decelerates gas transport and determines build-up of gas and higher pressure as well.

Concerning gaseous hydrogen flux toward the drift (Fig. 5), the highest amount of total transported mass was observed in case of less permeable EDZ (*S4*).

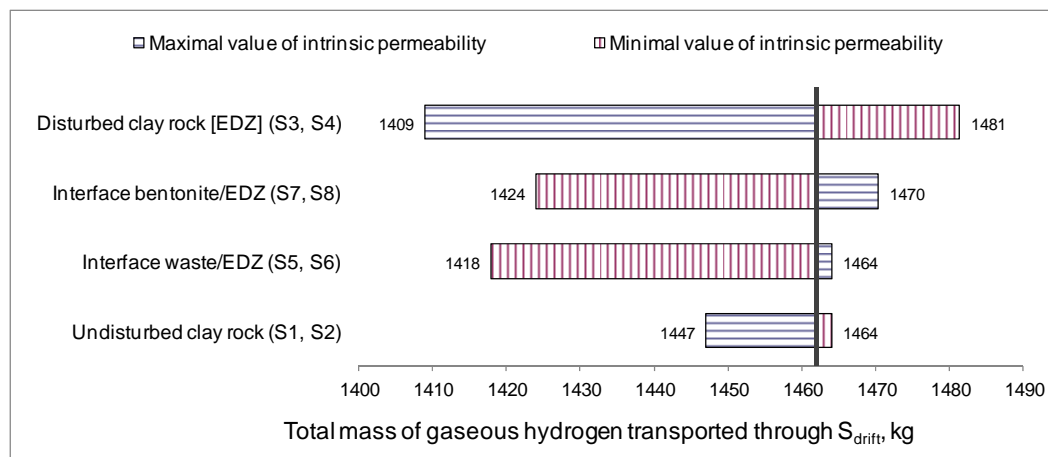


Fig. 5. Comparison of gaseous H_2 flux through S_{drift} for all analysed cases

The importance of second transport pathway over EDZ was reduced in case *S4*, but the primary transport pathway through interfaces was more dominant and higher flux toward the drift was determined. Reduced permeability of undisturbed clay rock (*S2*) blocks gas flow outside the EDZ thus slightly higher amount of gas was transported toward the drift in comparison with reference case. Increased permeability of disturbed and undisturbed clay rock (*S1*, *S3*) reduce gaseous hydrogen transport toward the drift in comparison with reference case. Concerning permeability variations in both interfaces situation was opposite. Increased permeability (*S5*, *S7*) impacts on slightly higher fluxes toward the drift while reduced permeability (*S6*, *S8*) influence on much lower fluxes in comparison with reference case. The reason for this is that interfaces are most

permeable component in the system and preferential pathway for gaseous hydrogen as well. Increased permeability does not change these facts significantly while decreased permeability does. However, intrinsic permeability coefficient in the EDZ has highest impact on total gaseous hydrogen transport among all analyzed materials.

Fig. 6 shows impact of intrinsic permeability coefficient on dissolved hydrogen flux through outer boundary (surface S_{out}).

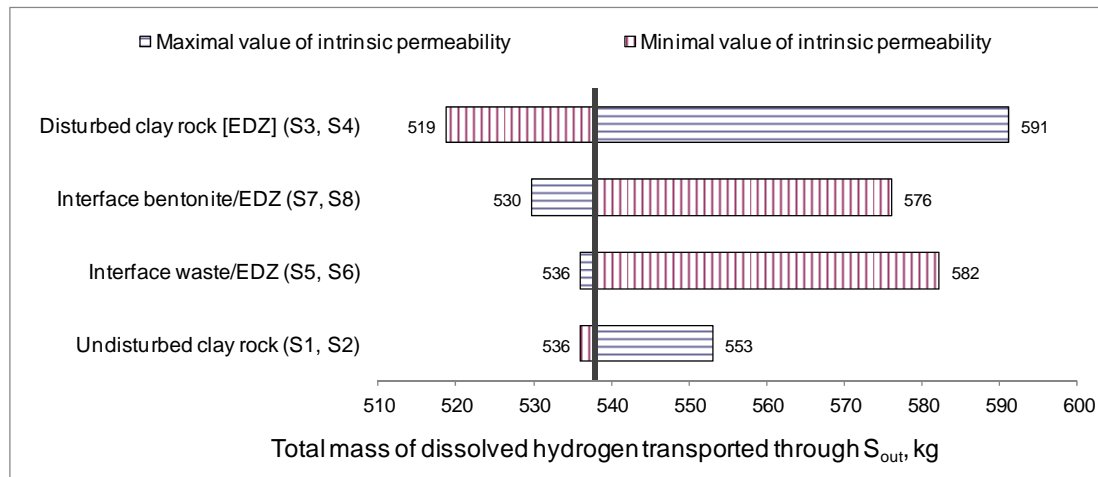


Fig. 6. Comparison of dissolved H_2 flux through S_{out} for all analysed cases

These results are strongly related to gaseous hydrogen fluxes toward the drift. Reduced fluxes of gaseous hydrogen toward the drift ($S1, S3, S6, S8$) impact on increased fluxes of gaseous/dissolved hydrogen outside the EDZ and out of radial boundary as well. Increased fluxes of gaseous hydrogen toward the drift ($S2, S4, S5, S7$) were related to decreased fluxes of hydrogen out of radial boundary. It is important to notice that due to very low permeability of undisturbed clay rock hydrogen migrates only by diffusive flow in dissolved form toward the outer boundary.

5. SUMMARY AND CONCLUSIONS

The assessment of the influence of porous medium permeability on gas migration in the disposal cell of conceptual geological repository for radioactive waste has shown that:

- 1) Peak pressure was 5.71 MPa within modelled domain using nominal values of intrinsic permeability coefficient while the highest peak pressure (6.55 MPa) was observed in case of less permeable interface. This pressure has no mechanical impact on repository and rock structures;
- 2) Using nominal values of intrinsic permeability coefficient, most of generated gas (~73%) was transported in gaseous phase toward the drift while the rest of the gas dissolved and was transported by diffusion into the host rock. The primary transport pathway of gaseous H_2 was over the interface (~50% of total generated gas transported) while the secondary transport pathway was over EDZ (~24% of total generated gas transported);
- 3) Intrinsic permeability coefficient in disturbed clay rock (EDZ) has strongest impact on gaseous/dissolved hydrogen transport out of the system while permeability changes in undisturbed clay rock have lowest impact among all analyzed materials.

REFERENCES

1. MANAI, T. EVEGAS – European Validation Exercise of GAS Migration Model through Geological Media. Final Report. Luxembourg: European Commission, 1997. 49 p.



2. ORTIZ, L., VOLCKAERT, G. et al. MEGAS: Modelling and Experiments on GAS Migration in Repository Host Rocks. Final Report. Luxembourg: European Commission, 1997. 445 p.
3. HAJTINK, B., RODWELL, W. Project on the Effects of GAS in Underground Storage Facilities for Radioactive Waste (Pegasus Project). Final Report. Luxembourg: European Commission, 1998. 247 p.
4. RODWELL, W., NORRIS, S. et al. A Thematic Network on Gas Issues in Safety Assessment of Deep Repositories for Radioactive Waste (GASNET). Final Report. Luxembourg: European Commission, 2003. 49 p.
5. DYMITROVSKA, M., GENTY, A., LUKIN, D., NAVARO, M., WEETJENS, E. PA Approach to Gas Migration. PAMINA (Performance Assessment Methodologies in Application to Guide the Development of the Safety Case) Deliverable Report D3.2.1. Luxembourg: European Commission, 2009. 74 p.
6. LEMY, F. et al. Summary of gas generation and migration. Current state-of-the-art. FORGE (Fate Of repository Gases) milestone M15. Luxembourg: European Commission, 2010. 183 p.
7. WENDING, J. Draft report on definition of benchmark studies on repository-scale numerical simulations of gas. FORGE deliverable report D1.1. Luxembourg: European Commission, 2009. 19 p.
8. JUSTINAVIČIUS, D. Modelling of two-phase flow of hydrogen gas in the disposal cell of repository for high level radioactive waste. CYSENI 2012. Proceedings of annual conference of young scientists on energy issues. [CD]. Kaunas: Lithuanian Energy Institute. 2012 May 24–25. p. 658–667.
9. JUSTINAVIČIUS, D., POŠKAS, P. Gas migration modelling in the disposal cell of conceptual geological repository for high-level radioactive waste. *Energetika*, 2012, Vol. 58, No. 2, p. 97–107 (in Lithuanian).
10. JUSTINAVIČIUS, D., NARKŪNIENĖ, A., POŠKAS, P. Impact of different factors on gas migration in the disposal cell of conceptual geological repository for high level radioactive waste. *Mechanika*, 2012, Vol. 18, No. 6, p. 650–656.
11. PRUESS, K., OLDENBURG, C., MORIDIS, G. TOUGH2 Users's guide, Version 2.0. Berkeley, California: Lawrence Berkeley National Laboratory, 1999. 198 p.
12. Thunderhead engineering. PETRASIM user manual. Version 5.0, 2010. 112 p.
13. TREILLE, E., WENDLING, J., TRENTY, L., et al. Probabilistic analysis based on simulations of the long-term gas migration at repository-scale in a geological repository for high and intermediate level radioactive waste disposal in a deep clay formation. Tough Symposium 2012, September 17–19, 2012, Lawrence Berkeley National Laboratory, Berkeley, USA, 2012, p. 416–424.



MODELLING OF HEAT TRANSFER PROCESSES IN THE DRY STORAGE SPENT NUCLEAR FUEL CONTAINERS USING RELAP5 CODE

A. Šutas

*Lithuanian Energy Institute
Breslaujos str. 3, LT-44403 Kaunas, Lithuania*

ABSTRACT

Ignalina nuclear power plant uses CASTOR RBMK-1500 and CONSTOR RBMK-1500 containers for spent nuclear fuel interim storage. The container thermal evaluation may be carried out using a variety of numerical simulation codes (such as ALGOR, ANSYS, NEPTUNE). This paper presents the attempt to perform thermal analysis of CASTOR RBMK-1500 and CONSTOR RBMK-1500 containers using thermal hydraulic safety analysis code RELAP5. The RELAP5 code package is designed for the thermal hydraulic analysis of the processes in nuclear reactor cooling circuit. Some difficulties arise when using model where heat removal from spent nuclear fuel storage cask by air is modelled.

The purpose of this paper is to determine whether RELAP5 code package is suitable for simulating heat transfer processes in CASTOR RBMK-1500 and CONSTOR RBMK-1500 containers. For a description of a heat exchange inside a container and heat transfer to the environment, special RELAP5 model simulating the container and surrounding environment was developed. Calculations were performed for different parameters of the model and also changing the model itself. The results of calculations were compared with the calculations results of other author, presented in open literature. It was also attempted to find out the influence of various model parameters to the final simulation results.

Final results showed that due to RELAP5 specifics this code package is not particularly handy with this type of analysis. Finally, RELAP5 code package limitations are discussed and recommendations for development of a numerical simulation using RELAP5 code for the heat transfer processes in CASTOR RBMK-1500 and CONSTOR RBMK-1500 containers are provided.

Keywords: container, storage, spent nuclear fuel, numerical simulation, RELAP5 code package

1. INTRODUCTION

Ignalina nuclear power plant uses CASTOR RBMK-1500 and CONSTOR RBMK-1500 containers for spent nuclear fuel interim storage. CASTOR container is made of cast iron and CONSTOR container consists of an outer and an inner shell made of steel with reinforced concrete filling inside. Thermal evaluation of these containers is carried out using RELAP5 code [1].

The RELAP5 code package is designed for the thermal hydraulic analysis of the processes in nuclear reactor cooling circuit, where coolant is water. In particular case with CASTOR and CONSTOR containers cooling of spent nuclear fuel is carried out by air and it is important to assess whether RELAP5 code is appropriate for such a type thermal analysis.

2. METHODOLOGY

2.1. Containers design

The containers design is presented on Fig. 1 according to [2]. Container CONSTOR is slightly higher than CASTOR container, but the inner volume of both containers is the same.

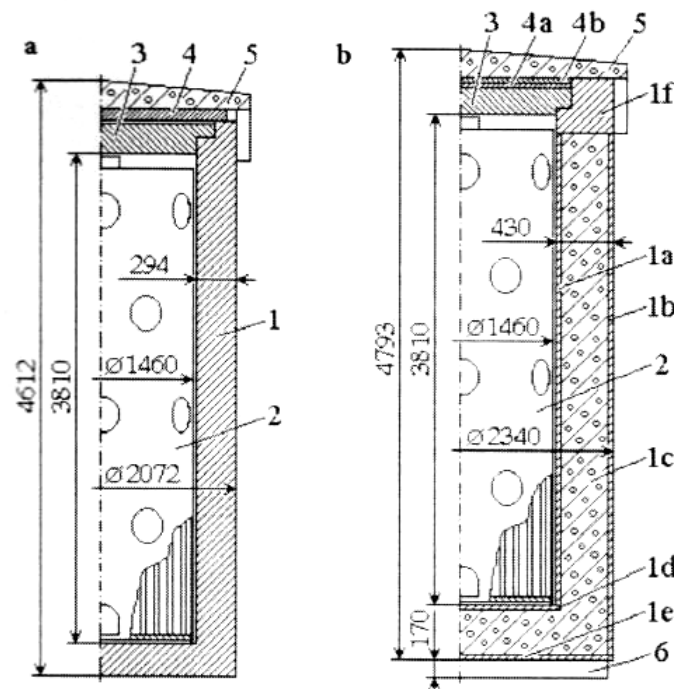


Fig. 1. Principal schemes of CASTOR RBMK-1500 (a) and CONSTOR RBMK-1500 (b) containers: 1 – container wall (1a, 1b – inner and outer surfaces; 1c – heavy concrete; 1d, 1e – bottom plates; 1f – forged ring); 2 – basket; 3 – lid; 4 (4a, 4b) – primary and secondary plates; 5 – protective cover; 6 – steel plate

The body of a CASTOR container (Fig. 1, a) is made from malleable cast iron *1*, which height is greater than 4 meters, diameter about 2 meters and wall thickness is 0.3 m. The wall of CONSTOR container (Fig. 1, b) is comprised of inner *1a* and outer *1b* surfaces with heavy concrete filling inside, and wall thickness is 0.43 m. A bottom wall of CONSTOR container has analogous construction as a side wall. The containers are designed to keep spent nuclear fuel bundles in a fixed basket *2* made of stainless steel. This basket contains 102 fuel bundles (51 halved fuel assemblies). After filling, container is tightly closed with a lid *3* and covered with a protective plate *4*. Further water is sucked out of container, and then traces of water are dried out. Finally, container is fully evacuated of air and filled with helium. Then filled container is transported to the interim storage site, where it is placed and covered with a reinforced concrete protective cover *5*. The weight of loaded CASTOR container is about 75 tons, while CONSTOR container weighs about 88 tons. It is assumed that total residual heat of spent fuel bundles (after 5 years storage in cooling pool) in a container is equal to 7.14 kW, the ambient temperature is conservatively chosen equal to 27 °C and heat from a heat source is transferred to environment by convection.

According to Regulations for the safe transport of radioactive material [3], the maximum fuel rod temperature must not exceed 300 °C and the maximum temperature of outer surface of the container must be lower than 85 °C.

2.2. Modelling methodology

Simulation is performed using RELAP5 code package. Numerical model of the CASTOR container (Fig. 2) is composed of mutually interconnected hydrodynamic component and two heat structures (no. 12221 and no. 12032).

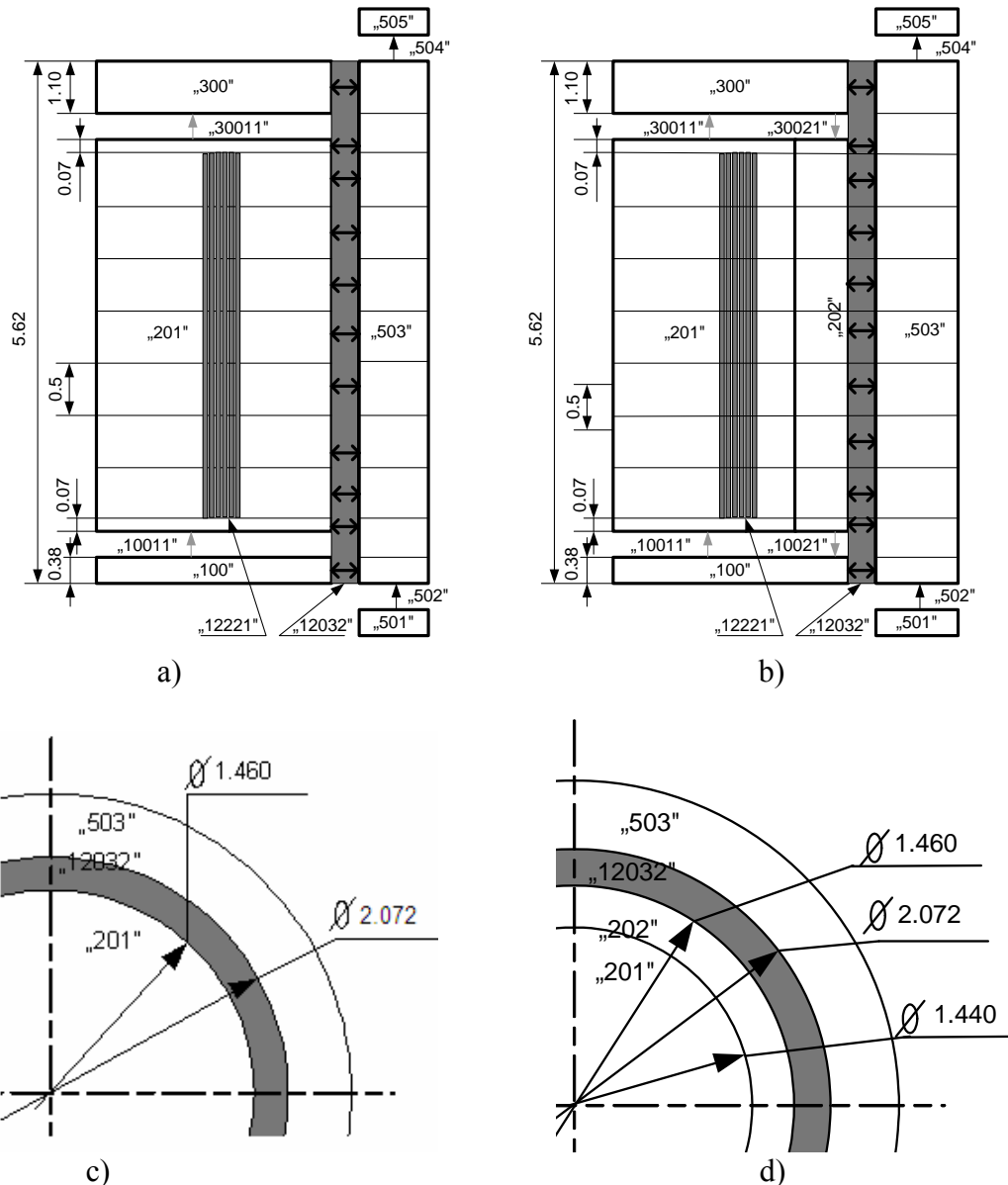


Fig. 2. Models of a CASTOR container for use in RELAP5: view from the side (a) and from above (c) of one camera model; view from the side (b) and from above (d) of a model with an internal heat circulation inside the container

Parts (a) and (c) of Fig. 2 presents one camera model, parts (b) and (d) are representing model with an internal heat circulation inside the container. Thermal structure no. 12221 simulates nuclear fuel bundles in a container, which is represented by a hydrodynamic component no. 201. It is assumed that volume of all 1836 heat structures (fuel rods) occupies about 6.7% of the container inner volume. RELAP5 code does not take into account the order of heat structures layout. Heat structures heat the container gaseous environment. Hot gas is concentrated in the upper part of the container, which is simulated by the hydrodynamic component no. 300. Heat structure no. 12032 simulates wall of the container. Gap between basket with fuel bundles and wall of the container is a place where hot gas cools and descends to the bottom of the container, which is modelled by hydrodynamic component no. 100. Cool gas in a component no. 100 slowly warm up and then begin to rise again as described repeating cycle of internal circulation. Hydrodynamic component no. 503 simulates ambient atmosphere of a container. Components no. 501 and no. 505 are characterized by different pressures and so atmosphere air ascends along the outer surface of a container. Components nos. 10011, 30011, 502 and 504 correspond to junctions between

hydrodynamic components. Height of the container is increased compared to real case due to need of correct assessment of horizontal heat transfer (it is assumed that heat is transferred only in horizontal direction).

The RELAP5 code package is designed for the thermal hydraulic analysis of the processes in nuclear reactor cooling circuit, so in an attempt to simulate similar processes in a container, which is stored in an open court, some difficulties arise when the heat removal from the spent fuel storage container by air is modelled. As already mentioned, CASTOR and CONSTOR containers are filled with helium while environment around the containers is atmospheric air. However, difficulties in calculations revealed, that RELAP5 code package is not applied for calculations where heat transfer process involves several different types of gas. Two cases have been simulated in order to evaluate the influence of the gas to modelling results: atmospheric air is selected in a 1st case and a mixture of 60% helium and 40% nitrogen gas is used in the 2nd case. These cases were modelled for CASTOR container. Modelling of the CONSTOR container was performed with 3 different values of container wall thickness: 0.2 m, 0.3 m and 0.4 m.

3. MODELLING RESULTS AND DISCUSSION

Modelling results are summarized in Table 1, Fig. 3, and Table 2. Both tables present maximum temperatures of fuel cladding surface and containers inner and outer surfaces.

Modelling of CONSTOR container results presented in Table 1 indicates that maximum fuel cladding temperature and minimum container outer surface temperature is observed when container wall thickness is 0.4 m. This case presents minimum thermal conductivity of the CONSTOR container. By reducing the thickness of the heavy concrete wall of the CONSTOR container fuel cladding temperature and temperature of inner surface of the container decreases while temperature of outer surface of the container wall increases.

Table 1. Maximum temperatures at different points of the containers

Point in a container	Parameter	a)	b)	c)	d)
Fuel cladding	T_1 (°C)	324	338	351	280
Container inner surface	T_2 (°C)	156	171	184	107
Container outer surface	T_3 (°C)	98	92	87	98

Comments to Table 1:

- CONSTOR container heavy concrete wall thickness is 0.2 m;
- CONSTOR container heavy concrete wall thickness is 0.3 m;
- CONSTOR container heavy concrete wall thickness is 0.4 m;
- CASTOR container cast iron wall thickness is 0.3 m.

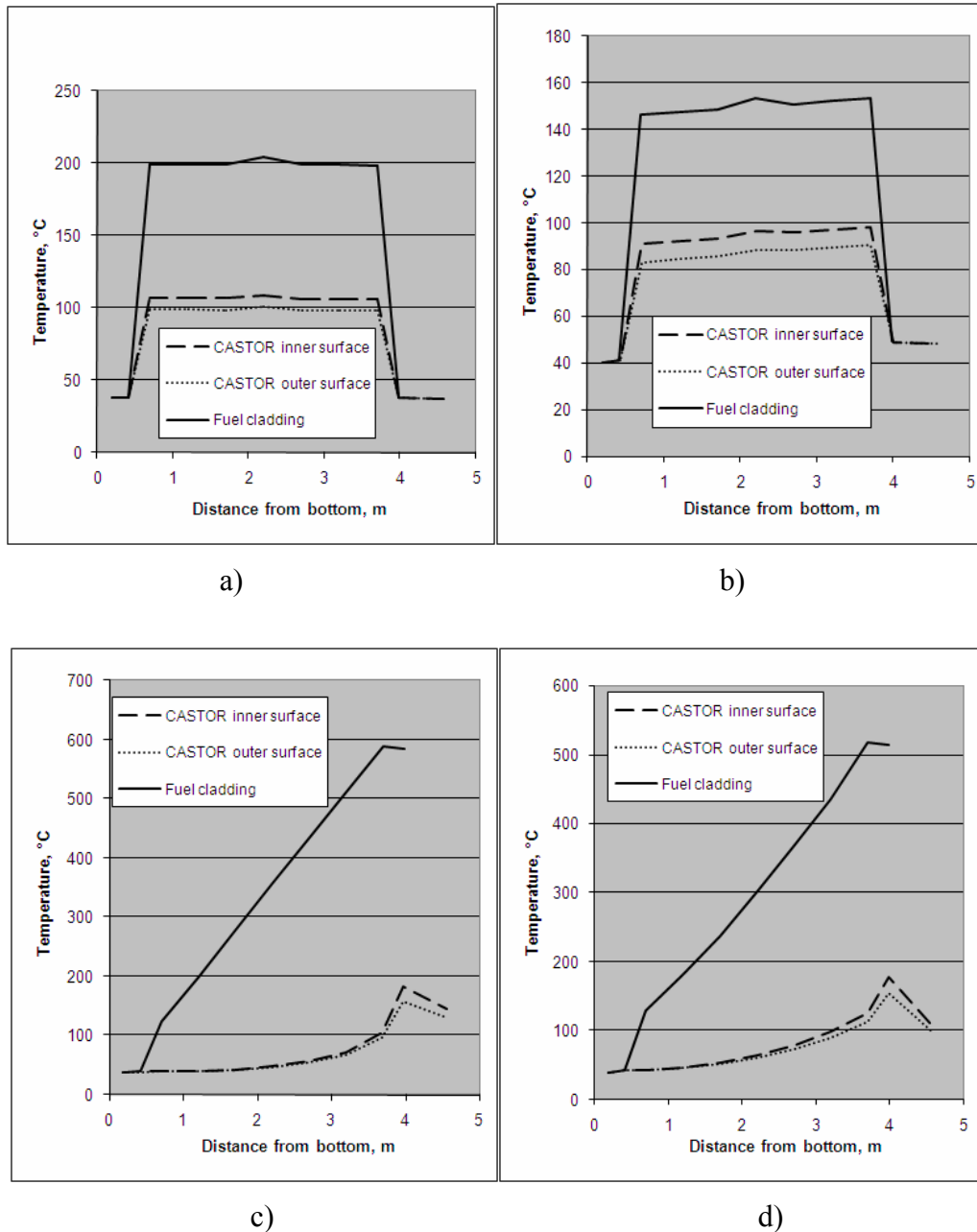


Fig. 3. CASTOR container temperatures at different points: one camera model with air (a) and mixture of 60% helium and 40% nitrogen gas (b); model with an internal heat circulation inside the container using mixture of 60% helium and 40% nitrogen gas without (c) and with (d) cross flow inside a container

In comparison with the simulation results presented by other author calculations, Table 2 was made where maximum temperatures (T_1 ; T_2 ; T_3) of fuel cladding, container inner and outer surfaces in CASTOR container are calculated. In addition Table 2 presents heat transfer coefficients from fuel cladding to container inner surface (α_1), from container inner surface to outer surface (α_2) and from container outer surface to atmosphere (α_3). Heat transfer coefficients present the middle point of container (according to the height of container).

Table 2. Maximum temperatures and heat transfer coefficients at different points of the CASTOR container

Point in a container	Parameter	a)	b)	c)	d)	e)
Fuel cladding	T_1 (°C)	204	153	589	518	231.5
	α_1 (W/(m ² K))	2.5	4.8	6.9	6.0	
Container inner surface	T_2 (°C)	109	98	182	178	
	α_2 (W/(m ² K))	5.4	8.9	28.7	30.5	
Container outer surface	T_3 (°C)	101	90	158	155	80.7
	α_3 (W/(m ² K))	5.1	6.9	3.7	5.6	

Comments to Table 2:

- a) One camera model with air;
- b) One camera model with a mixture of 60% helium and 40% nitrogen gas;
- c) Model with an internal heat circulation inside the container using mixture of 60% helium and 40% nitrogen gas without cross flow inside a container;
- d) Model with an internal heat circulation inside the container using mixture of 60% helium and 40% nitrogen gas with cross flow inside a container;
- e) CASTOR container simulation results of the other authors presented in scientific paper [2].

Comparing the container temperatures from a model with internal heat circulation with other author results it is obvious that for both air and helium – nitrogen models maximum temperatures are inadequately high. Maximum temperature is observed at the top of container what shows that the process of internal heat circulation inside a container is not modelled accurately. When heat transfer is modelled using an internal heat circulation inside a container model without (Table 2, c) and with (Table 2, d) cross flow inside container, maximum temperatures are lower than in a previous case. However, such an approach for heat transfer from container to environment modelling is not satisfactory too.

Results with one camera model demonstrates better correspondance with other author results. When modelling a mixture of 60% helium and 40% nitrogen gas it is important to take into account that in a reality container is surrounded by air which heat transfer coefficient is lower than helium, so, in order to minimize heat transfer from outer surface of a container, velocity of ascending gas flow along container outer surface must be low.

4. CONCLUSIONS AND RECOMMENDATIONS

1. RELAP5 code package is not designed for the calculations where heat exchange process involves gas of different composition.
2. In order to model heat transfer in CASTOR RBMK-1500 and CONSTOR RBMK-1500 containers more accurately, it is recommended to use one camera container model.

REFERENCES

1. FLETCHER C. D. et al., *RELAP5/MOD3 Code Manual User's Guidelines*, NUREG/CR-5535, Idaho National Engineering Lab., 1992.
2. POŠKAS, P., ŠIMONIS, V., MAKAREVIČIUS, R. Panaudoto branduolinio kuro saugojimo konteinerių šiluminis įvertinimas. *Energetika*. 1999. Nr. 4, p. 20–25.
3. TS-R-1, 2009. Regulations for the safe transport of radioactive material. *In: Safety Requirements, 2009 Edition, IAEA Safety Standards Series*. International Atomic Energy Agency, Vienna.